

ASPECTS OF THE STUDY OF SURFACES

ADVANCES IN CHEMICAL PHYSICS

VOLUME XXVII

EDITORIAL BOARD

THOR A. BAK, H. C. Oersted Institute, Copenhagen, Denmark

J. DUCHESNE, University of Liège, Liège, Belgium

H. C. LONGUET-HIGGINS, Department of Machine Intelligence, University of Edinburgh, Edinburgh, Scotland

M. MANDEL, University of Leiden, Leiden, Holland

V. MATHOT, Université Libre de Bruxelles, Brussels, Belgium

P. MAZUR, Institut Lorentz, Leiden, Holland

A. MÜNSTER, Institut für theoretische physikalische Chemie, Frankfurt-am-Main, Germany

S. ONO, Institute of Physics, College of General Education, Tokyo, Japan

B. PULLMAN, Institute de Biologie Physico-Chimique, Université de Paris, Paris, France

J. W. STOUT, The James Franck Institute, University of Chicago, Chicago, Illinois, U.S.A.

G. SZASZ, General Electrical Company, Zurich, Switzerland

M. V. VOLKENSTEIN, Institute of Macromolecular Chemistry, Leningrad, U.S.S.R.

B. H. ZIMM, School of Science and Engineering, University of California at San Diego, La Jolla, California, U.S.A.

ASPECTS OF THE STUDY OF SURFACES

EDITED BY

I. PRIGOGINE

University of Brussels,
Brussels, Belgium

AND

STUART A. RICE

Department of Chemistry
and
The James Franck Institute
The University of Chicago
Chicago, Illinois

VOLUME XXVII

AN INTERSCIENCE® PUBLICATION

JOHN WILEY AND SONS

NEW YORK · LONDON · SYDNEY · TORONTO

An Interscience* Publication
Copyright © 1974, by John Wiley & Sons, Inc.

All rights reserved. Published simultaneously in Canada.

No part of this book may be reproduced by any means, nor transmitted, nor translated into a machine language without the written permission of the publisher.

Library of Congress Cataloging in Publication Data:

Main entry under title:

Aspects of the study of surfaces.

(Advances in chemical physics, v. 27)

"An Interscience publication."

Includes bibliographical references.

I. Surface chemistry—Addresses, essays, lectures.

I. Prigogine, Ilya, ed. II. Rice, Stuart Alan,
1932— ed. III. Series.

QD453.A27 vol. 27 [QD508] 541'.08s [541'.3453]

ISBN 0-471-69932-2

74-5292

Printed in the United States of America

10 9 8 7 6 5 4 3 2 1

PREFACE

From time to time fields of investigation that have long lain fallow are reactivated. This may be kindled by a theoretical advance, a technical innovation, or both. Whatever the source of the inspiration, reports of the new results are often spread so widely in the scientific literature that it is difficult to follow all of the developments. Recent research on the properties of surfaces is a case in point.

Although a volume in the *Advances in Chemical Physics* usually contains contributions on many subjects, occasionally it may be appropriate to concentrate attention on one subject of immediate importance. Accordingly, this volume is devoted to recent findings relevant to the properties of surfaces. Only a small portion of the new information is surveyed, but it should serve as an introduction to the recent findings, enabling the reader to delve further into the literature to pursue individual interests. The contributors to this volume were urged to express points of view and to speculate, where appropriate. The book thus should serve, at least partially, the three purposes of surveying and interrelating new results, suggesting fruitful lines of new inquiry, and being useful as a textbook at the advanced level.

STUART A. RICE

Chicago, Illinois
October 1974

CONTRIBUTORS TO VOLUME XXVII

AARON N. BLOCH, Department of Chemistry, Johns Hopkins University, Baltimore, Maryland

C. B. DUKE, Xerox Research Laboratories, Xerox Square, Rochester, New York

E. N. ECONOMOU, Department of Physics, University of Virginia, Charlottesville, Virginia

R. FUCHS, Department of Physics, Iowa State University, Ames, Iowa

R. GOMER, Department of Chemistry, The James Franck Institute, The University of Chicago, Chicago, Illinois

DANIEL GUIDOTTI, The James Franck Institute, The University of Chicago, Chicago, Illinois

K. L. KLIEWER, Department of Physics, Iowa State University, Ames, Iowa

HOWARD L. LEMBERG, The James Franck Institute, The University of Chicago, Chicago, Illinois

WILLIAM C. MURPHY, Department of Chemistry, Johns Hopkins University, Baltimore, Maryland

K. L. NGAI, Naval Research Laboratory, Washington, D.C.

STUART A. RICE, Department of Chemistry and The James Franck Institute, The University of Chicago, Chicago, Illinois

CONTENTS

DETERMINATION OF THE STRUCTURE AND PROPERTIES OF SOLID SURFACES BY ELECTRON DIFFRACTION AND EMISSION <i>By C. B. Duke</i>	1
ELECTRON SPECTROSCOPY OF CHEMISORPTION ON METALS <i>By R. Gomer</i>	211
SURFACE PLASMA OSCILLATIONS AND RELATED SURFACE EFFECTS IN SOLIDS <i>By E. N. Economou and K. L. Ngai</i>	265
THEORY OF DYNAMICAL PROPERTIES OF DIELECTRIC SURFACES <i>By K. L. Kliewer and R. Fuchs</i>	355
SOME COMMENTS ON THE ELECTRONIC PROPERTIES OF LIQUID METAL SURFACES <i>By Stuart A. Rice, Daniel Guidotti, Howard L. Lemberg, William C. Murphy, and Aaron N. Bloch</i>	543
AUTHOR INDEX	635
SUBJECT INDEX	649

ASPECTS OF THE STUDY OF SURFACES

ADVANCES IN CHEMICAL PHYSICS

VOLUME XXVII

DETERMINATION OF THE STRUCTURE AND PROPERTIES OF SOLID SURFACES BY ELECTRON DIFFRACTION AND EMISSION

C. B. DUKE

Xerox Research Laboratories, Webster, New York

CONTENTS

I.	Introduction	2
II.	The Characterization of Solid Surfaces: Survey of Techniques	8
	A. Preliminaries and Assumptions	8
	B. Particle-Solid Interactions.	12
	1. Scope and Organization	12
	2. Electrons	13
	3. Photons	20
	4. Atoms, Molecules, and Ions	22
	C. Surface Atomic Composition.	25
	D. Surface Geometry	28
	E. Surface Atomic Motion	30
	F. Surface Electronic Structure	32
	G. The Multiple-Technique Strategy	33
III.	Low-Energy Electron Diffraction: Concepts and Definitions	35
	A. Intensity Analysis	35
	1. Data Displays	35
	2. Definition of the Analysis Problem	39
	B. Models of Electron-Solid Interactions.	42
	C. Elastic Diffraction from a Rigid Lattice: Born Approximation	47
	D. Correspondence between Calculated and Measured Intensities: Instrumental Effects	52
	E. Inelastic Electron-Solid Collisions	54
	F. Quasielastic Diffraction from a Vibrating Lattice: Born Approximation	58
IV.	Dynamical Theory of Elastic Electron-Solid Scattering at Planar Surfaces	73
	A. Motivation	73
	B. Distorted-Wave Multiple-Scattering Analysis	77
	C. Wave-Function-Matching Analyses	81
	D. Laminar Multiple-Scattering Analyses	83
V.	Model Elastic Low-Energy Electron Diffraction Calculations: Inputs, Outputs, and Critique	86

A.	Construction of the Electron-Ion-Core Potential	86
B.	Empirical Models of the Optical Potential	89
C.	Sensitivity Analyses	91
1.	Boundary Conditions	91
2.	Number of Phase Shifts: Rigid Lattice	98
3.	Lattice Vibrations	101
4.	Number of Phase Shifts: Vibrating Lattice	103
5.	Bulk Electron-Ion-Core Potentials	106
6.	Specifically Surface Phenomena: Clean Surfaces	110
7.	Adsorbed Overlayer Potentials	112
D.	Critique	118
VI.	Model Inelastic Low-Energy Electron Diffraction Calculations	124
A.	Two-Step Inelastic Diffraction	124
B.	Dynamical Inelastic Diffraction.	136
C.	Consequences of Line-Broadening Mechanisms	139
VII.	Surface Crystallography via Elastic Low-Energy Electron Diffraction	141
A.	Scope and Organization	141
B.	The Atomic Geometry and Symmetry of Ideal Surfaces	142
C.	The Atomic Geometry of Nonideal Surfaces	142
1.	Classification of Imperfections	142
2.	Single-Step Imperfections	145
3.	Multistep Topographies	150
D.	Structure Determination for Uniform Surfaces Exhibiting Long-Range Order	151
1.	Relation between Intensity Pattern Symmetry and Atomic Geometry	151
2.	Analytical Approaches to Surface Crystallography	154
3.	Structure Determination via Dynamical Models of Elastic Low-Energy Electron Diffraction	159
4.	Structure Determination via Data Reduction and Kinematical Methods	173
E.	Structural Analysis for Disordered Surfaces.	181
F.	Synopsis.	183
VIII.	Dispersion Relations of Electronic Surface Excitations via Inelastic Low-Energy Electron Diffraction	185
A.	Determination of Surface Excitation Dispersion	185
1.	Nature of the Problem	185
2.	Selection of the Level of Analysis	189
3.	Analytical Procedure	190
B.	Surface Plasmon Dispersion: Al(111)	193
IX.	Epilogue: Patterns of the Future.	198
	References.	200

I. INTRODUCTION

This article deals with the determination of the structure and properties of solid surfaces by measuring and analyzing the scattering and emission of electrons from them. In order to render these processes sensitive to the surface rather than bulk properties of the sample, electrons in the energy range $10 \text{ eV} \lesssim E \lesssim 10^3 \text{ eV}$ usually are used in the measurements. The coherent scattering of such electrons from the surfaces of crystalline solids is referred to as "low-energy electron diffraction" or "LEED." The energy

of such electrons is indeed "low" from the perspective of nuclear and particle physics, although it is rather high relative to that of concern in electronic structure calculations characteristic of chemical and solid-state physics.

Before embarking on our main task of reviewing the theory and applications of LEED, it seems appropriate to recall the context in which current studies of this topic are carried out. The discipline of chemical physics traditionally has concerned itself with two subjects: structures and reactions. The introduction of a solid surface as an ingredient of a system under study often creates dramatic alterations in both. Reactive gases adsorbing on the surfaces of both metals and insulators form "surface complexes" of unique structure and properties. Moreover, metallic and oxide surfaces find common use as catalysts. Yet decades of traditional measurements of the thermodynamic and kinetic properties of surface reactions have led to little understanding of the reaction mechanisms in terms of the microscopic (e.g., electronic) properties of the reactants. It is not difficult to discern the origin of this unhappy situation. The properties of one of the reactants (i.e., the surface) are essentially unknown. Only in the past few years has the atomic composition of surfaces been determined even approximately. Their atomic geometry and the mobility of adsorbed reactants and reaction products are just beginning to be explored. Indeed, the poor characterization of surface composition and structure must be regarded as a major barrier to a predictive description of surface reactions.

Recognizing this barrier, it is of particular interest that within the past decade advances in ultrahigh vacuum technology have provided the setting for dramatic improvements in the techniques for characterizing *quantitatively* the nature and properties of both "clean" and adsorbate-covered surfaces.¹ The ability to produce ultrahigh vacuum ($p \sim 10^{-10}$ torr) on a routine basis permits even the smallest university or industrial laboratory to generate the stable environment necessary for the preparation and study of controlled surfaces. Moreover, electron-solid scattering has proved to be one of the most versatile and quantitative of the techniques for examining such surfaces. As such, it commands the interest and consideration of the host of workers interested in the quantitative description of the "surface" reactants, intermediates, or products in surface-mediated reactions.

In any examination of gas-surface reactions, however, we immediately encounter a formidable obstacle: the dynamic character of a solid-gas interface. During the course of a reaction the atomic composition and structure of the surface is changing continually as it reacts with the constituents of a contiguous gas phase. At the present time, electron scattering spectroscopies are incapable of monitoring this dynamic process *in situ* except in special simple cases (e.g., the determination of changes in

the atomic composition of a sample as it is eroded away by an ion beam). Thus some procedure must be introduced for stopping the reaction at appropriate stages to monitor the condition of the surface. Typically this "freezing" of the reaction process is accomplished by admitting small, controlled amounts of gas into an ultrahigh vacuum system for reaction with a previously prepared sample. Studies of the structure of the resulting gas-solid adsorption system may be related to surface reactions per se in that the initial, final, and possible intermediate states of a reaction process are appropriate candidates on which to carry out these studies.

Electron-solid scattering is only one of a variety of experimental techniques utilized to characterize adsorbed species on solid surfaces. A complete description of a surface involves answering the following questions:

1. What atomic species are present on the surface?
2. How are they arranged?
3. How are their valence electrons distributed?
4. What are their atomic motions?

Different experimental measurements are appropriate for responding to each of these questions.¹ Elastic low-energy electron diffraction (ELEED) provides the most satisfactory probe of the atomic geometry²⁻⁷ and surface vibrational properties⁸⁻¹⁰ of macroscopic crystalline samples. Inelastic low-energy electron diffraction (ILEED) is currently the only high-precision, surface-sensitive technique for measuring the energy-momentum relation of surface branches of the electronic excitation spectra of solids.^{7,11-13} Core-level excitation and emission spectroscopies are appropriate for identifying the atomic species present on a surface.^{1,5,14,15} The results obtained by using all of the various techniques in concert must be fitted together in a consistent fashion in order to characterize adequately a solid-gas adsorption system.

The nature of electron diffraction from crystals can be understood most simply by regarding a crystal as comprised of geometrically equivalent layers of atoms parallel to a given surface. An incident electron of wave vector \mathbf{k} (i.e., momentum $\mathbf{p} = \hbar\mathbf{k}$) is diffracted from the array of these two-dimensional gratings stacked together to form the crystal.¹⁶ The periodic translational symmetry of these diffraction gratings is manifested in the electron-solid scattering cross-sections by virtue of the reflected electrons emerging from the solid in a series of diffracted beams as indicated in Fig. 1. Low-energy electron diffraction (LEED) is the study of the electrons coherently scattered from the solid into these beams. The configuration of the diffracted beams relative to the beam of incident electrons may be predicted from the translational symmetry of the system

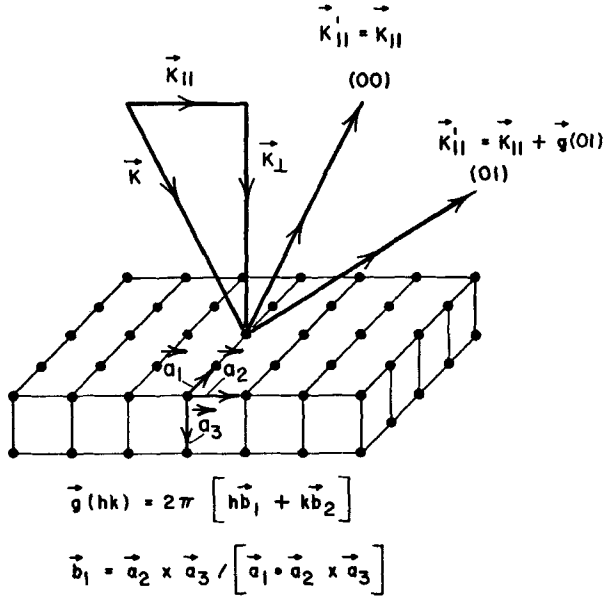
KINEMATICS OF ELASTIC LOW-ENERGY
ELECTRON DIFFRACTION

Fig. 1. Schematic illustration of an incident electron beam of wave-vector $\mathbf{k} = \mathbf{k}_\perp + \mathbf{k}_\parallel$, scattered elastically from a single crystal into a state characterized by the wave-vector $\mathbf{k}' = \mathbf{k}'_\parallel + \mathbf{k}'_\perp$. The construction of the reciprocal lattice associated with the single-crystal surface also is shown. The vectors $\mathbf{g}(hk)$ designate the reciprocal lattice vectors associated with the lowest-symmetry bravais net parallel to the surface.

which leads to the momentum conservation law

$$\mathbf{k}'_\parallel = \mathbf{k}_\parallel + \mathbf{g} \quad (1a)$$

$$k_\parallel = \left(\frac{2mE}{\hbar^2} \right)^{1/2} \sin \theta \quad (1b)$$

for electrons of energy E incident on a planar surface at an angle θ relative to its exterior normal. The vectors \mathbf{g} are the reciprocal lattice vectors of the two-dimensional atomic diffraction gratings as indicated in Fig. 1. We return to a more careful examination of the diffraction process in Part III. For our present purposes only one point is of importance: the distinction between the structural information contained in the configuration of the diffracted beams and that which can be extracted only by an analysis of their intensities.

Examination of (1) and Fig. 1 reveals that the only information conveyed by the configuration of the diffracted beams is the translational symmetry parallel to the surface of the two-dimensional atomic diffraction gratings that comprise the solid. Determination of the unit-cell structure within each of these gratings and of the packing sequence of the gratings relative to each other requires analysis of the diffracted intensities. The deduction of possible translational symmetries of adsorbate-solid systems from measurements of the configuration of the diffracted electron beams has been a standard surface characterization experiment since Davisson and Germer's initiation of the field of LEED in 1927.¹⁶ Only in the past few years, however, has the theory of the electron-solid diffraction process been developed to the point that an analysis of the *intensities* of the diffracted beams is feasible. It is the description of this theory and its application to extract surface structural parameters from measured intensities which is the primary topic of this review.

For years experimental workers have deplored the complexity of theoretical models of LEED.^{4,5} Unfortunately, most of the complexity is an inevitable concomitant of the surface sensitivity of the technique. In particular, the use of the first Born approximation for the electron-solid scattering cross-section is widely regarded as a suitably "simple" theory of low-energy electron diffraction.⁴ Often called the "kinematical" model, the use of this (single scattering) approximation implies that the electron-solid interaction is weak. Spectroscopies based on the applications of the first Born approximation, however, measure the bulk, not surface, properties of solids. For example, the interaction between X-rays and matter is weak, so that X-ray diffraction is a suitable technique for determining the crystallographic structure of bulk solids rather than the positions of atoms in their uppermost few layers.

Both X-ray and electron diffraction spectroscopy are examples of the characterization of solids by scattering experiments. For scattering experiments to probe the surface rather than the bulk regions of a solid, the interaction of its constituents with the incident and/or exit particles must be strong. "Low-energy," $10 \text{ eV} \lesssim E \lesssim 10^3 \text{ eV}$, electrons exhibit suitably strong electron-solid interactions. Both their elastic¹⁷ and inelastic^{17,18} atomic scattering cross-sections are comparable to the geometrical size of the atom. The same is true for condensed atoms, for example, solids, although the nature of the inelastic scattering processes is altered.¹⁹ Therefore, in the case of elastic low-energy electron-solid scattering (e.g., ELEED), the scattered electrons must have emanated from the surface region of the solid. If not, they would have suffered an inelastic collision. Consequently, the large inelastic electron-solid cross-sections are the fundamental cause of the surface sensitivity both of LEED and also of

other electron scattering and emission spectroscopies (e.g., X-ray or Auger spectroscopy^{1,14,15}) in which a clear distinction between the "elastic" and "inelastic" outgoing electrons can be made.

We now can understand the correlation between the complexity of the theory of LEED and the surface sensitivity of the technique itself. Surface sensitivity is a consequence of large inelastic electron-solid cross-sections. These in turn are caused by the strong interactions between the incident electron and the electrons in the solid. Such interactions also result, however, in large elastic electron scattering cross-sections from the ion-cores in the solid. Because of these large elastic cross-sections, even a distorted-wave version of the Born approximation does not describe adequately ELEED from crystalline solids. Consequently, any accurate theoretical model calculation of ELEED intensities must be intrinsically more complicated than the corresponding evaluation of X-ray diffraction intensities. As we shall see, however, such "dynamical" ELEED intensity calculations exist, and their use to determine simple surface structures is becoming routine.

From the discussion above we infer that three ingredients are required in order to utilize LEED as a quantitative probe for the characterization of crystalline solid surfaces. First, the intensities of electrons diffracted from a controlled sample surface must be measured in a suitable ultrahigh vacuum instrument. Second, a rather complete theory must be constructed to relate these intensities to the microscopic parameters (e.g., atomic positions, vibrations, and elastic scattering factors) characterizing the surface of the sample. Finally, appropriately simplified versions of the theory must be reduced to computational algorithms suitable for the routine analysis of measured intensities. The potential of the LEED technique can be realized only when all three steps have been completed and the LEED measurements themselves supplemented with independent techniques for the determination of the atomic composition and ground-state electronic structure of the sample.

A complete description of these three ingredients of surface structure spectroscopy via electron scattering and emission would require a treatise devoted to the topic. Our aim is more modest: to provide an annotated survey of the literature for those who wish to inspect the scope and consequences of LEED theory and its applications without working through all of the concomitant details. The experimental aspects of ELEED have been reviewed by Somorjai and Farrell⁴ in this series and, more recently, by Sickafus and Bonzel.⁵ Moreover, a detailed review of the theoretical literature on both ELEED^{6,8} and ILEED¹¹ has been given elsewhere. The major new aspect of LEED since these reviews is its increasing use in concert with other techniques to derive a more complete

characterization of a surface and in concert with theoretical data analysis efforts to provide a quantitative characterization of various types of surface structure. Therefore, we focus our attention on these two trends toward completeness and quantitateness which seem to be the patterns of the future in surface studies.

We proceed in three steps. In Part II we survey the general problem of the characterization of solid surfaces and discuss the role of LEED as one of the more powerful techniques used to accomplish this objective for macroscopic crystalline surfaces. Second, in Parts III to VI we describe the theory of LEED and examine its ability to interpret experimentally measured intensities. Part III includes the introductory material usually found in review articles on LEED²⁻⁵ and hence can be read selectively by readers already acquainted with this topic. In Part IV, however, we get to the heart of our subject matter with a description of the dynamical theory of electron-solid scattering and a critical discussion of the current state of our knowledge of the electron-solid force law. Our treatment of the dynamical theory is continued in Parts V and VI which contain descriptions of the calculations of ELEED and ILEED intensities, respectively, performed using this theory. Finally, in Parts VII and VIII we survey the applications of ELEED and ILEED to determine surface geometries and surface branches of electronic elementary excitation spectra. The review concludes with a brief epilogue in which current research trends are summarized and used as the basis for conjectures concerning future developments in surface spectroscopy.

II. THE CHARACTERIZATION OF SOLID SURFACES: SURVEY OF TECHNIQUES

A. Preliminaries and Assumptions

In this section we examine three issues which must be introduced prior to our survey of surface characterization techniques. First, by examining distance scale lengths of various phenomena associated with interfaces we sharpen our definition of the "surface" properties of a solid. Then we comment on the nature of surfaces produced in different fashions. Finally, we consider several alternative sample geometries with the intent of reducing our survey of techniques to those appropriate for the characterization of large-area (e.g., 10 cm²) planar high-vacuum interfaces of crystalline solids.

Consider a hypothetical "atomically flat surface" of a single-crystal solid obtained by truncating that solid along a crystallographically allowed atomic plane. The atomic geometries of such surfaces can be specified easily,²⁰ and are often used as the basis for estimating the surface energies

of crystals.²¹ Suppose we wish to examine this surface by scattering or emission experiments. Electromagnetic radiation in and above the range of visible frequencies penetrates a solid for distances $\lambda_{\text{em}} \sim 10^4 \text{ \AA}$.^{22,23} Static electric fields penetrate metals for $\lambda_m \sim 1$ to 10 \AA ²⁴ and semiconductors and insulators by $\lambda_{\text{sc}} \sim 10^3$ to 10^6 \AA .²⁵ Low-energy ($10 \text{ eV} \lesssim E \lesssim 10^3 \text{ eV}$) electrons exhibit inelastic collision mean free paths $\lambda_{ee} \sim 2$ to 10 \AA .¹⁹ Low-energy ($E \lesssim 10 \text{ eV}$) atoms²⁶ (obtained, e.g., from atomic beams) and kiloelectron-volt ions²⁷ do not penetrate the surface although mega-electron-volt ions can if the incident beam is aligned along a crystallographic axis of high symmetry.²⁸ Thus we immediately see that scattering experiments using the various probes will measure properties of the solid characteristic of different depths below its surface. In an operational sense "surface" properties exist only to the extent that they can be measured by our hypothetical experiments. Consequently, the concept of "surface" properties of even an atomically flat solid is defined only relative to the probe being used to examine it.

These considerations serve to emphasize one central theme: The depth resolution (i.e., "surface sensitivity") of any given experimental probe depends primarily on the nature of the interaction of the probe with the constituents of the solid rather than on externally controllable parameters characteristic of the experiment itself. For example, ELEED experiments with 50-eV electrons examine features of the upper 1 to 10 atomic layers of a solid independent of the intensity of the incident beam or the energy resolution of the source or detector. If a more precise depth scale is desired, some other technique must be used.

This theme has three important implications which we shall explore several times during the course of this review. First, by linking the spatial depth resolution of a scattering or emission experiment with the interaction with the solid of the incident and/or exit particles used in the measurement, attention is focused on the microscopic particle-solid force law. This force law is known rather poorly for both electrons^{29,30} and atoms.^{21,26} Consequently, a central issue in the evaluation of any surface-sensitive spectroscopy is the assessment of the magnitude of errors in the determination of the quantities of interest introduced by uncertainties in the relevant particle-solid force laws. Second, since the various techniques probe rather different aspects of a surface, a sensibly complete description of the surface can be achieved only by using multiple techniques in concert. In particular, surfaces that appear "flat" or "clean" using one technique may seem quite "rough" or "dirty" using another. Third and finally, since sensitivity to the properties of the surface atomic layers of a solid implies strong interactions of the probe particles with the constituents of these layers, as the number of atomic layers explored by a given technique

decreases, the probability of damage to these layers increases. Both photon-³¹ and electron-stimulated³² desorption are well-known phenomena, and secondary ion mass spectrometry³³ is based on the erosion of surfaces by incident ions. Thus the possibility and consequences of changes in a surface wrought by the technique used to examine it always must be considered when evaluating, designing, and interpreting experiments which measure surface properties. The first of these three issues is of central importance in any discussion of the theory of LEED and is developed in parts III and V. The latter two are relevant in the evaluation of LEED relative to other techniques for surface studies and, as such, are considered in the remainder of this part.

Turning to our second topic in this introductory section, that is, the distinction between different types of surfaces, we begin by recalling that studies of heterogeneous catalysis provide a major motivation for chemists' interest in solid surfaces. One of the unifying themes in such studies lies in the broad question of influence of the geometrical and electrical structure of a solid surface on catalytic action at that surface.³⁴ In this context, it is widely believed that the determination of the geometrical and electronic structure of chemisorbed intermediates and the systematic relating of this structure to catalytic activity comprise the main ingredient in establishing models of catalytic reactions with predictive capability. Conventional catalysts occur in the forms of gels, powders, and polycrystalline films. Their surfaces exhibit complicated geometries and compositions. Usually they are ill suited for systematic studies of the electronic and geometric factors in catalytic reactions *per se*. Consequently, scientific work has increasingly centered on simpler, better characterized systems, especially polycrystalline films and wires. Yet these samples also exhibit the severe limitation that they are both structurally and electronically heterogeneous. In fact, some recent work suggests that the surface properties of polycrystalline thin films and small particles of copper are essentially unlike those of the low-index single-crystal faces of which most studies presume them to consist.³⁵ Moreover, it has been speculated that high-index single-crystal faces are associated with essentially different types of adsorption behavior than low-index faces.³⁶ Thus we see that the fabrication method and morphology of a given sample may exert strong influences on the reactions of gases with its surfaces.

A similar situation exists in the examination of the surface properties of interest in semiconductor electronics. Here, it is customary to distinguish between "real" and "clean" surfaces.³⁷ Real surfaces are those produced by the mechanical polishing and chemical etching treatments characteristic of semiconductor device fabrication. They are usually polycrystalline and are covered with a thin layer of adsorbed gases. Clean surfaces are

generated under ultrahigh vacuum, usually on a single-crystal face, by cleavage, ion bombardment, chemical cleaning, and heating. The appellation "clean" often is used in reference to single-crystal faces of known chemical composition rather than to chemically pure faces of amorphous or polycrystalline samples.

Electron diffraction experiments are useful only for the examination of crystalline surfaces. Moreover, interpretations of LEED intensities usually invoke the implicit assumption of an atomically flat surface associated with a defect-free single-crystal sample. Indeed, almost all of the theoretical analyses described in this review are based on models embodying this assumption. Chemisorption systems are regarded as fixed coverages of adsorbate at an atomically flat surface of a single-crystal substrate. Obviously, these are not the "real" surfaces of interest in heterogeneous catalysis and semiconductor electronics. The examination of such highly idealized systems is motivated by the philosophy that "real" catalytic and semiconductor systems, while too complex to be described in detail, can be manipulated in a qualitatively predictive fashion on the basis of insight achieved from the quantitative description of the properties of well-characterized if simpler surfaces. Although the success of this philosophy is not assured, the history of the development of semiconductor electronics and high-temperature, high-strength materials indicates that it has proved fruitful in analogous situations.

As our final topic in this section we summarize the assumptions inherent in our treatment of surface characterization. We have limited our scope to the examination of ultrahigh vacuum ($p \sim 10^{-10}$ torr) surfaces. This restriction is caused by the constraint that gas adsorption not alter the state of the surface during the measurements ($t \sim 1$ hr) performed to characterize it. We implicitly assume that the measurements themselves do not alter the state of the surface being studied—an assumption that must be tested in each individual case. We presume that the sample is a single crystal, defect free unless otherwise specified. Finally, we consider only the characterization of macroscopic-area (1 to 100 cm²) atomically flat surfaces. This restriction eliminates the field emission³⁸ and field ionization^{38,39} experiments in which the sample is a small, more or less hemispherical tip of radius approximately 1000 Å. Such tips consist of many atomically flat planar regions containing up to 100 atoms. A great deal of valuable information can be learned from them, especially about lattice imperfections and surface diffusion.³⁹ Obviously, the "tip" geometry is dictated by the requirements of strong electric fields and large magnification in the field emission and ionization experiments, and is inappropriate for the macroscopic samples whose characterization we are considering. We conclude by emphasizing, however, that the generation of a macroscopic

atomically flat surface is not simple, nor is the task of verifying the "flatness" of a given sample.⁴⁰

B. Particle-Solid Interactions

1. Scope and Organization

Large-area planar surfaces are characterized almost exclusively by scattering and particle-stimulated emission experiments. Three generic types of incident and/or emitted projectiles are employed for this purpose: electrons, photons (i.e., quanta of electromagnetic radiation), and chemical species (i.e., neutrons, atoms, molecules, and ions). Consequently, it is necessary to review briefly the nature of the interaction of these entities with condensed matter as a preliminary to our survey of techniques for the characterization of surfaces.

This section is devoted to such a review. It is organized by considering each type of particle in turn. Three types of information are important. First, since for large-area surfaces the geometrical structure of the surface is inferred statistically by diffraction experiments,^{1,40} we must examine the possibility of such experiments. The parameters needed for this examina-

TABLE I

Physical Parameters Describing the Energy-Momentum Relations of Particles of Energy E and Momentum $p = \hbar k = h/\lambda^a$

Particle	Dispersion relation	Typical wavelengths	Predominant particle-solid interaction
Electron	$E = \frac{h^2}{2m\lambda^2}$	$E = 1 \text{ meV}: \lambda = 387 \text{ \AA}$	Diffraction by ion-cores and energy loss to phonons
		$E = 1 \text{ eV}: \lambda = 12 \text{ \AA}$	Diffraction by ion-cores
		$E = 10 \text{ keV}: \lambda = 0.12 \text{ \AA}$	Energy loss to valence electrons
Photon	$E = \frac{hc}{\lambda}$	$E = 1 \text{ meV}: \lambda = 0.0124 \text{ cm}$	Free carrier and defect absorption
		$E = 1 \text{ eV}: \lambda = 1.24 \times 10^4 \text{ \AA}$	Absorption via interband transitions
		$E = 10 \text{ keV}: \lambda = 1.24 \text{ \AA}$	Diffraction by ion-cores
Chemical species	$E = \frac{h^2}{2MA\lambda^2}$	$E = 1 \text{ meV}: (A=2) \lambda = 6.4 \text{ \AA}$	Energy loss to phonons
		$E = 1 \text{ eV}: (A=2) \lambda = 0.2 \text{ \AA}$	Usually energy loss
		$E = 10 \text{ keV}: (A=2) \lambda = 2 \times 10^{-3} \text{ \AA}$	Scattering by ion-cores

^aThe qualitative nature of the particle-solid interaction also is noted. Cogent parameters are $h = 6.625 \times 10^{-27} \text{ erg-sec}$, $c = 3 \times 10^{10} \text{ cm/sec}$, $m = 9.11 \times 10^{-28} \text{ g}$, $M = 1.67 \times 10^{-24} \text{ g}$, and A is the atomic mass.

tion are summarized in Table I and discussed in each of the succeeding three subsections. Second, we must specify the features of a given measurement which render it surface sensitive. Third, we must consider the nature of the excitations of the solid created by the various incident projectiles in order to utilize these excitations as a characterization of the sample and to estimate the damage done by the particle. We now turn to a consideration of these three issues for each type of incident particle.

2. Electrons

In this subsection we review three features of electron interactions with solids. A synopsis of the major contributions to these interactions is presented in Fig. 2. We defer consideration of the electron-surface-charge interaction until Part III. Here, we begin by estimating the strength and consequences of elastic electron scattering from the ion-cores in the solid. Then we examine the energy-loss processes undergone by the incident electrons. We conclude by discussing the probability that some of the electrons emitted from the solid result from an Auger process associated with the filling of a hole in a low-energy orbital of one of the ion-cores.

Surprisingly few calculations have been performed of the elastic scattering cross-sections of "low-energy" ($10 \text{ eV} \lesssim E \lesssim 10^3 \text{ eV}$) electrons from either free atoms or the ion-cores in a solid. Most of the latter calculations^{41,42} have been performed using one-electron potentials appropriate for the description of the energy band structure near the Fermi energy of

THE ELECTRON-SOLID FORCE LAW

1. LONG-RANGE PART:
ELECTRON - SURFACE - CHARGE INTERACTION
2. SHORT-RANGE PART:
ELECTRON - ION - CORE INTERACTIONS
3. DISSIPATIVE PART:
ELECTRON - ELECTRON
INTERACTIONS
(INELASTIC COLLISIONS)

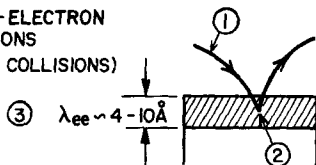


Fig. 2. Schematic indication of the three parts of the electron-solid force law for electrons in the energy range, $10 \text{ eV} < E < 10^3 \text{ eV}$, of interest in low-energy-electron diffraction (LEED). The symbol λ_{ee} designates one half of the mean free path of the incident electron before it undergoes an inelastic collision with one in the solid.

the solid. A few⁴³⁻⁴⁵ are based on more sophisticated model potentials. Although the various potentials can lead to rather different energy band structures, we shall see that for clean metals all reasonable models lead to almost indistinguishable LEED intensities.^{46,47} Finally, a few calculations of the elastic electron scattering cross-sections have been performed for free atoms.^{17,48,49} Although the differential cross-sections vary widely as functions of energy, model potential and atomic number, all of the calculations predict total cross-sections which lie in the range $10^{-15} \text{ cm}^2 \lesssim \sigma_e \lesssim 10^{-17} \text{ cm}^2$ and decrease slowly with increasing energy for fixed atomic number.

From the discussion above and Table I we see that low-energy electrons, $10 \text{ eV} \lesssim E \lesssim 10^3 \text{ eV}$, should diffract elastically from an atomic crystalline lattice with high intensity. They do so, of course, as noted in the discussion of Fig. 1. Models embodying only elastic diffraction were employed almost exclusively in the literature from the early works of Bethe⁵⁰ and Morse⁵¹ to the modern sophisticated calculations of Pendry⁵² and of Hoffstein and Boudreaux.⁵³ Summaries of the extensive literature on these models have been given by Duke,⁶ Estrup and McRae,³ and Laramore.⁷ Unfortunately, in such models the ion-cores in the lattice scatter the incident electrons too efficiently, leading to the prediction of excessive structure in the LEED cross-sections and of scattered intensities several orders of magnitude larger than those observed. The elimination of these discrepancies between the model predictions and the experimental data awaited the recognition by Duke and Tucker^{19,54} that the inelastic rather than elastic electron-solid scattering dominated the motion of a "low-energy" electron near a solid surface. Why this advance in the conceptual basis of the theory did not occur until 41 years after Davisson and Germer's original work¹⁶ is difficult to understand. Indeed, a phenomenological (optical model) framework for the description of the consequences of inelastic processes was proposed by Slater⁵⁵ in 1937. Workers in the field certainly were aware of the possibility of inelastic processes^{56,57} but evidently failed to regard them as of sufficient importance to estimate their magnitude in the energy range of interest in LEED.

An outstanding attribute of the scattering of low-energy electrons by matter is the preference of these electrons to excite electronic excitations of energy $\Delta E \sim 5$ to 10 eV in the target. This preference can be expressed quantitatively by examining, as an example, the electron impact ionization of atoms. As described in a recent review by Rudge,¹⁸ a fairly satisfactory description of the total ionization cross-section for an ionization threshold energy E_i is given by

$$\sigma_i(E) = \frac{\xi a}{E_i \cdot E} \ln \left(\frac{E}{E_i} \right), \quad E > E_i \quad (2)$$

in which a is a constant and ξ is a parameter tabulated by Lötž.⁵⁸ Both Lötž⁵⁸ and Rudge¹⁸ discuss numerous refinements of this formula, but it suffices for our purpose of showing that σ_i decreases as E_i increases so that valence-electron ionization processes lead to much larger cross-sections than core-electron ionizations. Moreover, (2) exhibits a maximum at $E_m \approx 4E_i$ such that for a shell of ξ equivalent electrons,

$$\sigma_i(E_m) \approx \left(\frac{-13.6 \text{ eV}}{E_i} \right)^2 \xi \pi a_0^2 \quad (3)$$

in which $a_0 = \hbar^2 / me^2 = 5.29 \times 10^{-9} \text{ cm}$ is the Bohr radius. Therefore we see that the total electron impact ionization cross-sections for valence-electron ionization ($E_i \lesssim 10 \text{ eV}$) are comparable to or larger than the elastic scattering cross-sections at the same energy.

When atoms condense to form a liquid or solid, the nature of the valence-electron excitations changes but the large cross-sections for these excitations remain a characteristic feature of electron-solid interactions. Although the details vary from one material to another,⁵⁹ most of the inelastic electron scattering occurs via the excitation of collective oscillations, called plasmons, of the valence-electron fluid in the solid. The total cross-section for creating a bulk plasmon excitation of energy ΔE is given by

$$\sigma_{\text{pl}}(E) = \frac{2\pi e^4}{\Delta E \cdot E} \ln \left(\frac{k_c}{k} \cdot \frac{2E}{\Delta E} \right) \quad (4a)$$

$$k \equiv \left(\frac{2mE}{\hbar^2} \right)^{1/2} \quad (4b)$$

in which e is the charge of an electron and $k_c \sim 10^8 \text{ cm}^{-1}$ is a cutoff wave vector.⁶⁰ The similarity of (4a) and (3) is evident. The plasmon energy ΔE in (4a) is the analogue of the ionization threshold E_i in (3). In simple materials, ΔE is related to the electron density n by

$$(\Delta E)^2 = \frac{4\pi n e^2 \hbar^2}{m} \quad (5)$$

Thus in typical solids,⁵⁹ $5 \text{ eV} \lesssim \Delta E \lesssim 15 \text{ eV}$. From (4) we see that plasmon creation total cross-sections occur in the range $\sigma_{\text{pl}} \sim 10^{-16} \text{ cm}^2$ for low-energy electrons.

Recalling the results of our discussion to this point, we see that both the elastic and valence-electron excitation total cross-sections for a low-energy incident electron are $\sigma \sim 10^{-16} \text{ cm}^2$. Since atomic densities are $\rho \sim 10^{22}$ to

10^{23} atoms/cm³, we expect the elastic and inelastic mean free paths, λ_e and λ_{ee} respectively, to satisfy

$$\lambda = (\rho\sigma)^{-1} \sim 10 \text{ \AA} \quad (6)$$

Thus an incident electron will undergo both elastic and inelastic collisions in the uppermost one to five layers of the solid. On the other hand, its cross-section for exciting a core electron ($100 \text{ eV} \lesssim E_i \lesssim 10^4 \text{ eV}$) is $\sigma_e \sim 10^{-17}$ to 10^{-18} cm^2 . Consequently, we anticipate that these processes will be considerably weaker than valence-electron excitation.

Equations (2) to (6) and our estimates of the elastic electron-ion-core cross-sections permit us to address another issue—the relation between the criterion of surface sensitivity and that of the applicability of the Born approximation for the elastic electron-solid cross-sections. Surface sensitivity requires that either the elastic or the inelastic collision mean free path, (λ_e and λ_{ee} , respectively) satisfies

$$\lambda\rho^{1/3} \lesssim 10 \quad (7)$$

The applicability of the Born approximation for elastic scattering requires

$$\rho^{2/3}\sigma_e \ll 1 \quad (8a)$$

or, from (6),

$$\lambda_e\rho^{1/3} \gg 1 \quad (8b)$$

Equations (7) and (8) are compatible if $\sigma_e \ll \sigma_i \sim 10^{-16} \text{ cm}^2$, in which case we have weak elastic but strong inelastic scattering. In this situation the distorted-wave Born approximation would provide an adequate description of the cross-sections. A related situation in which a given electron polarizes both the valence-electron fluid and the lattice “prior” to undergoing isolated single elastic scattering events is thought to prevail in the scattering of valence electrons in a solid from a low concentration of defects. In the case of LEED, however, we have seen that $\lambda_e\rho^{1/3} \sim 1$, so (8) are not satisfied. Thus, not even a distorted-wave version of the Born approximation suffices to describe the elastic scattering cross-sections.

We can also apply our estimates to interpret the secondary emission (or loss) spectrum of a solid. A schematic diagram of a display-type LEED instrument being used to measure this spectrum is shown in Fig. 3. If a total current I at voltage V (electron energy $E \sim 100 \text{ eV}$) is incident on the target, about 99% of the current passes through the target and 1% is reflected for collection by the hemispherical screen behind the target; that is, $I_r \cong (0.01)I_i$. The reason for this, of course, is that most of the electrons lose their incident energy by a cascade of electronic energy losses, $\Delta E \sim 10$

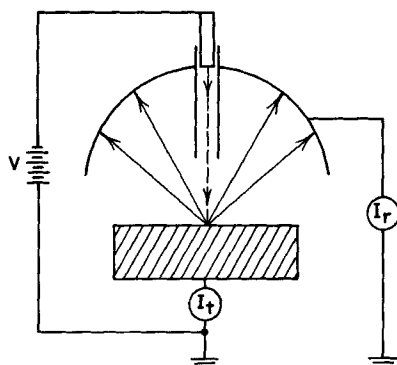
SCHEMATIC DIAGRAM OF AN ELECTRON
DIFFRACTION APPARATUS

Fig. 3. Schematic diagram of a low-energy electron diffraction apparatus illustrating that most of the current drawn from the gun, $I = I_t + I_r$, passes through the target to ground (I_t) rather than being reflected back from the target (I_r).

eV. They thereby become “trapped” at energies near and below the work function of the material and must exit the target via the back electrode (at least for metal targets: insulators have an unhappy tendency to become charged). An energy scan of the total reflected current is called the secondary emission or “loss” spectrum $N(E)$, that is,

$$I_r(V) = \int_0^{eV} N(E') dE' \quad (9)$$

Examples of such a secondary emission spectrum and its derivative are shown in Fig. 4. They indicate clearly the consequences of our previous estimates. Pronounced elastic and plasmon excitation peaks occur because of electron backscattering from the upper one to five layers of the solid. These processes are comparable in intensity, their relative magnitudes depending on the energy of the incident beam and its angle relative to the surface normal. The fine structure in dN/dE corresponds to transitions associated with the filling of empty core-electron states generated by the impact ionization of these states by the incident beam. Finally, the “true secondary” peak results from the cascade loss processes of the incident electron which create a large population of low-energy “secondary” electrons, most of which exit the sample as contributors to I_r , but some of which, in particular those evident in Fig. 4, contribute to I_t . Thus the

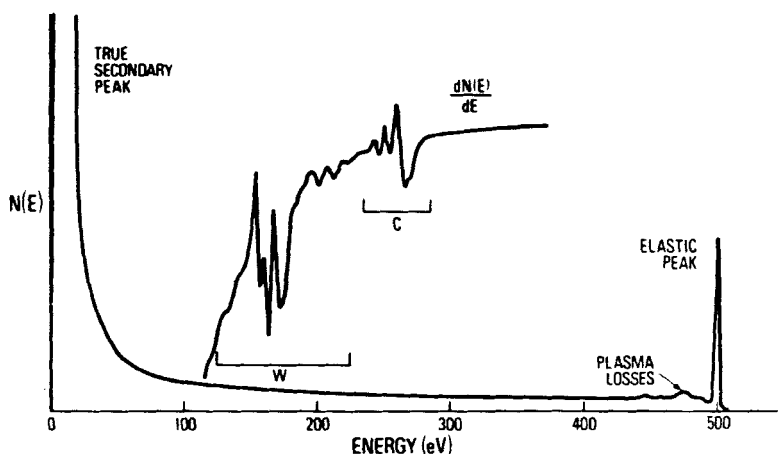


Fig. 4. Secondary electron or "loss" spectrum of a tungsten surface bombarded with 500 eV electrons. Most of the secondaries are contained in the low-energy or "true" secondary peak. The energy derivative of the spectrum exhibits distinct structure corresponding to the characteristic Auger energies of tungsten and a carbon contaminant. (These plots were obtained by R. L. Gerlach, Sandia Laboratories.) (After Duke and Park¹.)

features of this secondary electron spectrum reflect, quite directly, the order of magnitudes of the various elastic and inelastic cross-sections. At sufficiently high incident beam energies, however, more secondaries are emitted than there are incident electrons since each incident electron can create approximately $E/\Delta E$ secondaries. In this case, the sign of I_i is reversed relative to the convention indicated in Fig. 3.

We now turn to our final topic in this subsection, the filling of an empty core state (called a core "hole") by Auger processes.⁶¹ The possibilities for the creation and subsequent filling of such a core hole are indicated schematically in Fig. 5. We are concerned here with the mechanisms for filling an initially empty core hole (i.e., diagrams *c* and *d* of Fig. 5).

The two possible mechanisms for this process are radiative recombination (X-ray fluorescence, Fig. 5*c*) and Auger recombination (Fig. 5*d*). For a given core hole, in general many initial states are available to fill it, leading to a considerable array of possible recombination lines of both the X-ray and Auger type. Two issues usually are examined in the literature: the energies and intensities of the various recombination processes.

Since these topics have been reviewed quite extensively,^{62,63} and are of peripheral interest to LEED per se, it seems inappropriate to examine them in detail. The most important result for our purposes is that for core holes

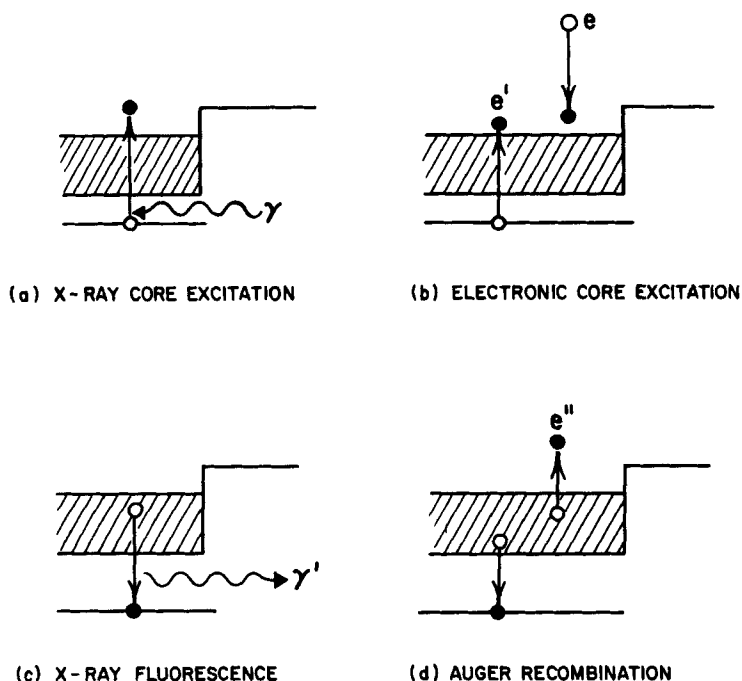


Fig. 5. Schematic diagram of core-level excitation (a & b) and recombination (c & d) processes in a metal. The core holes also can be excited by heavy particle (e.g., proton) bombardment. The recombination processes shown involve valence electrons. For heavier elements these processes also can involve core electrons from higher-energy core states. Atomic species can be identified from the energies of the ejected core electrons or from the characteristic X-rays or Auger electrons resulting from recombination of the core hole. Only X-ray recombination following X-ray excitation is insensitive to the surface region.

with binding energies $E_h \lesssim 1500$ eV, over 90% of the recombination processes are of the Auger type.^{62,63} Therefore the intensities of the associated electron emission lines (i.e., the electron designated by e'' in Fig. 5) are a direct measure of the impact ionization cross-sections [given in the case of electron impact ionization by (2) or a more refined version thereof^{64,65}]. Quantitative interpretations of the individual energies and intensities of the various possible Auger lines associated with a given core hole are rare and often inconclusive.⁶⁶⁻⁷⁰ Qualitative identification of the major features of the observed emission spectra with the atomic number of the excited ion-core is fairly simple,⁷¹ however, and recently has become almost routine.^{5,15,72-74} Thus in Fig. 4, it is easy to distinguish Auger emission contributions to the loss spectra associated with tungsten from those associated with a carbon contaminant on the tungsten substrate. A de-

tailed interpretation of the observed dN/dE structure in terms of the electronic structure of the carbon-contaminated tungsten surface is beyond the capability of existing models.

Like the LEED intensities, the Auger emission contributions to the loss spectrum are characteristic of surface species. From (2) and (6) we see that the mean free path for core-level excitation by an incident electron is $\lambda_c \gtrsim 100$ to 1000 \AA . Therefore unless a glancing incidence electron beam is used, core holes are produced for hundreds of atomic layers within the surface. The emitted Auger electrons associated with only the surface atoms contribute to the structure in dN/dE shown in Fig. 4, however, because once such an electron undergoes loss processes of any kind (e.g., plasmon excitation) it usually is lost into the background secondary electron distribution. Consequently, it is the low-energy-loss processes undergone by the emitted electron more than the magnitude of the electron impact ionization cross-sections associated with the incident electron which are instrumental in rendering electron-stimulated Auger spectroscopy a surface-sensitive analytical technique.

In summary, both LEED and electron-stimulated Auger spectroscopy are surface-sensitive techniques probing the uppermost 1 to 10 atomic layers of a solid. In addition, LEED provides a suitable diffraction spectroscopy of atomic positions at crystalline surfaces provided one analyzes the diffracted intensities using a multiple-scattering model.

3. Photons

Electromagnetic radiation in the visible ($\lambda \sim 6000 \text{ \AA}$, $h\nu \sim 2 \text{ eV}$) spectrum interacts with condensed matter by exciting electronic transitions between occupied and unoccupied low-energy eigenstates of the valence electrons.^{22,23} As the frequency of the radiation increases, the excited electrons can escape from the sample giving rise to the photoelectric effect. As this frequency is increased further (i.e., $h\nu \gtrsim 100 \text{ eV}$) into the soft X-ray region its absorption occurs predominately by the excitation of the core-level electrons in the target.⁷⁵ Therefore Auger electrons as well as photoelectrons are contained in the photostimulated secondary electron emission spectrum.^{14,66-68,76} Increasing the energy of the quanta of radiation, that is, photons, still further to $E = h\nu \sim 10^4 \text{ eV}$ in the X-ray region leads to decreasing cross-sections for absorption of the radiation and the predominance of its (elastic) diffraction by crystalline solids. As this energy approaches the "hard" X-ray region, $h\nu \gtrsim 10^5 \text{ eV}$, however, Compton scattering and, eventually, electron-positron pair production emerge as the predominant mechanisms for the interaction between radiation and matter. Our interest centers around the X-ray region $10^3 \text{ eV} \lesssim h\nu \lesssim 25 \times 10^3$

eV. From Table I we see that photons of this energy exhibit the correct wavelengths to diffract coherently from a crystalline solid.

Just as in the case of electrons, in order to assess the surface sensitivity of photon-solid scattering, we must estimate the elastic scattering and absorption cross-sections. To estimate the elastic scattering cross-sections we use the Raman-Compton classical model⁷⁷ of X-ray scattering from atoms:

$$\sigma_{pe}(\mathbf{q}) = \sigma_0 [Z^2 |f(\mathbf{q})|^2 + Z(1 - |f(\mathbf{q})|^2)] \quad (10a)$$

$$\sigma_0 = \frac{2}{3} \left(\frac{e^2}{mc^2} \right)^2 = 5.30 \times 10^{-26} \text{ cm}^2 \quad (10b)$$

$$f(\mathbf{q}) = \int e^{i\mathbf{q}\cdot\mathbf{r}} p(r) d^3r \quad (10c)$$

in which Z is the atomic number of the atom, $p(r)$ is the normalized radial probability of finding an electron a distance r from the nucleus, and \mathbf{q} is the momentum transfer

$$q = \frac{4\pi}{\lambda} \sin \frac{\theta}{2} \quad (10d)$$

for scattering through an angle θ . Considering the limit of point atoms, that is, $q \ll \langle r \rangle^{-1}$, we obtain the desired estimate

$$\sigma_{pe} \approx Z^2 (6.65 \times 10^{-25} \text{ cm}^2) \quad (11)$$

For light elements ($Z \lesssim 10$) the X-ray absorption cross-section may be estimated by considering the photoionization cross-section for a K -shell orbital. We find the differential cross-section⁷⁸

$$\sigma_{pi}(q) = \frac{64}{3} \alpha k \left(\frac{E}{h\nu} \right) \left(\frac{Z}{a_0} \right)^5 \left[\frac{Z^2}{a_0^2} + q^2 \right]^{-4} \quad (12a)$$

$$\alpha = \frac{e^2}{\hbar c} = \frac{1}{137} \quad (12b)$$

Or, for $h\nu > E_i(Z)$,

$$\sigma_{pi} = \frac{64\pi}{9} \alpha \left[\frac{h\nu - E_i(Z)}{h\nu} \right] \cdot \frac{a_0}{Zk} \quad (12c)$$

in which $E = \hbar^2 k^2 / 2m = [h\nu - E_i(Z)]$ is the energy of the photoemitted

electron, $E_i(Z)$ is the ionization energy of the orbital,⁷⁶ and $h\nu$ is the energy of the incident photon. More sophisticated formulas are readily available⁷⁹⁻⁸¹ for heavier elements (i.e., $Z \gtrsim 10$). They all lead to $\sigma_{pi} \sim 10^{-18}$ to 10^{-20} cm² in the X-ray energy range (i.e., 10^3 eV $\lesssim E \lesssim 25 \times 10^3$ eV).

Using these estimates in (6) for the mean free path gives

$$\lambda_e \sim \frac{100}{Z^2} \text{ cm} \quad (13a)$$

$$\lambda_a \sim 10^{-3} \text{ cm} \quad (13b)$$

Thus we can have the situation alluded to in the previous subsection in which $\lambda_e \gg \lambda_a$. The surface-sensitivity criterion for photons, analogous to (7) for electrons, is

$$\lambda_a \rho^{1/3} \lesssim 10 \quad (14)$$

which, since $\rho \sim 10^{22}$ atoms/cm³, is clearly not satisfied. The criterion for the validity of the Born approximation, (8b), is satisfied by both λ_e and λ_a , however, so both elastic X-ray diffraction and X-ray absorption cross-sections may be calculated using the Born approximation, a well-known and extensively used result.⁷⁷

Summarizing, we find that for electromagnetic radiation in the far ultraviolet to the hard X-ray region ($50 \text{ eV} \lesssim h\nu \lesssim 5 \times 10^4 \text{ eV}$) the predominant absorption mechanism in solids is photoelectric emission of atomic core electrons. The photostimulated secondary emission spectrum consists of both these photoelectrons and Auger electrons generated by the filling of the resulting core holes. In the X-ray region, $h\nu \sim 10^4 \text{ eV}$, the wavelengths of the radiation are appropriate for observing its diffraction from crystalline solids. This diffraction occurs, associated with an atomic elastic scattering cross-section roughly proportional to Z^2 . Both diffraction and absorption are characteristic of the bulk solid because the associated mean free paths lie in the range $10^{-4} \text{ cm} \lesssim \lambda \lesssim 1 \text{ cm}$ for almost all solids. Sharp features in the secondary electron emission spectrum, however, tend to be characteristic of the surface layers of the solid because of the short inelastic collision mean free path, $\lambda_{ee} \sim 10 \text{ \AA}$, of the secondary electrons themselves.

4. Atoms, Molecules, and Ions

The use of massive particles as a probe of the elementary excitation spectra of solids is well known within the context of neutron diffraction measurements of lattice-vibration and spin-wave spectra.^{82,83} Neutrons interact too weakly with matter to be broadly useful in surface studies, but

the reflection of atoms, molecules, and ions from condensed matter is primarily a surface phenomenon. Interest in atom- and molecule-solid collisions centers around studies of energy transfer²⁶ and chemical reactions, including adsorption, at surfaces.⁸⁴ Ions are most widely used for cleaning a surface by eroding its upper atomic layers and for mass analysis by examination of either the chemical species generated thereby³³ or the energy distribution of the backscattered ions.^{85,86}

Three energy ranges for these projectiles are commonly used in surface studies. Most atomic and molecular beam scattering experiments utilize thermal beams of energies, $0.025 \text{ eV} \lesssim E \lesssim 1 \text{ eV}$, although "hyperthermal" energies up to about 20 eV are possible.⁸⁷ "Low-energy" ion-solid scattering studies are carried out with ions of energy $E \sim 10^3 \text{ eV}$, although neutral beams of this energy can be produced by successive ionization, acceleration, and neutralization.⁸⁸ Ion energies in the range $E \sim 10^6 \text{ eV}$ are also used in backscattering studies.^{28,86} This is the upper currently useful range of energies, however, because of the onset of nuclear reactions at energies $E \sim 10^6$ to 10^8 eV .

Inspection of Table I reveals that at thermal energies, $1 \text{ meV} \lesssim E \lesssim 1 \text{ eV}$, light species, especially H, He, H_2 , and D_2 , are expected to diffract from crystalline surfaces. Following the initial observations of the diffraction of He and H_2 from LiF by Estermann and Stern⁸⁹ in 1929, numerous workers attempted to observe this phenomenon on other materials, with rather limited success.^{26,90-92} Elastic atomic scattering cross-sections in this energy range are large,⁹³ $\sigma_e \gtrsim 10^{-16} \text{ cm}^2$, rendering the associated atom-solid scattering highly surface sensitive. The detailed behavior of the atom-solid force law is essentially unknown, however, except for its dependence on z^{-4} for large perpendicular distances z from the surface,⁹⁴ and its repulsive nature within a few angstroms of the surface.⁹³ Most model calculations utilize either superpositions of static two-body forces between the incident atom and those in the solid^{95,96} or even simpler schematic interactions.⁹⁵ These models attribute the commonly observed absence of elastic atom-solid diffraction phenomena to the predominance of inelastic scattering events in which lattice vibrations are excited by the collision. All existing data, while fragmentary, are consistent with this hypothesis⁹¹ although other alternatives have been suggested.^{21,90}

The interaction of slow ($E \lesssim 10^3 \text{ eV}$) ions with surfaces is dominated by the large cross-sections⁹³ ($\sigma_n \sim 10^{-15} \text{ cm}^2$) for neutralization by electrons emanating from the solid.^{85,97,98} Thus the net yield of scattered ions results from a competition between the elastic and ion neutralization cross-sections. Lowering the ion energy increases the elastic scattering cross-section but increases the neutralization probability still faster. Smith⁸⁵ uses

the "binary collision" model formulas

$$\sigma_i(E) = P_n(E) \sigma_e(E) \quad (15a)$$

$$P_n(E) = \exp \left[\frac{-v_0}{(2ME)^{1/2}} \right] \quad (15b)$$

to analyze his ion yields as a function of the energy E of the incident ions. The quantity $P_n(E)$ is the neutralization probability and v_0 is an empirical parameter, $v_0 \sim 10^7$ cm/sec. According to this model the maximum value of $\sigma_i(E)$ occurs for energies in the range $500 \text{ eV} \lesssim E \lesssim 2000 \text{ eV}$ for noble gas ions incident on most materials. The details of the ion-solid interaction are unknown, however, because when the ion is close to the solid, the valence electrons in the solid screen the ionic charge in a complicated fashion, depending on the energy and incidence angle of the ion, and the nature of the solid. This fact plus uncertainties associated with the neutralization of the incident ions have rendered impossible quantitative calculations of ion-solid backscattering intensities.

Turning to our discussion of ion-induced excitations, we note that incident ions have been used also to create optical fluorescence^{88,99} and Auger electrons.¹⁰⁰ The former is thought to be caused by the decay of excited neutral species sputtered from the surface.⁹⁹ The cross-section for the excitation of core holes (and hence Auger electrons) by charged ions is given by a formula like (2). At high energies, however, ions of equal charge and equal velocity give equal impact ionization cross-sections.¹⁸ Thus heavier ions exhibit much larger cross-sections at a given energy, as may be described by requiring the constant a in (2) to be proportional to the mass of the incident ion times the logarithm of its reciprocal. We expect, therefore, that a charged ion creates considerably more core holes and Auger electrons than an electron of the same energy. Of course, this does not imply that Auger yields from ion beams are higher than those from electrons beams of the same energy because many ions become neutralized when in close proximity to the target. Indeed, any calculation of ion beam Auger yields must include a consideration of this neutralization of the incident ions as described, for example, in (15b). These neutralization processes are sufficiently complicated^{97,98} that their importance has proved a substantial barrier to quantitative analysis of any type of ion-solid collision cross-sections.

Summarizing, light chemical species of thermal energies can diffract from crystalline solid surfaces. The diffraction is obscured, however, by the tendency of incident atoms and molecules to scatter inelastically from a surface, creating lattice vibrations or internal excitations. Higher energy

atomic and molecular beams are difficult to generate and hence are rarely used in surface studies. Ions of energy below about 100 to 300 eV are neutralized close to surfaces and hence are rarely used in ion scattering surface studies per se (although the electrons they create are often examined^{101, 102}). Ion-solid scattering in the energy range $500 \text{ eV} \lesssim E \lesssim 10^7 \text{ eV}$, however is utilized for examining surfaces for examining surfaces with the high-energy limit being dictated by the onset of nuclear reactions.

C. Surface Atomic Composition

Elements are characterized by the mass and charge of their nuclei. The latter may be determined either from the energy required to create a hole in a "deep" or core electronic state of the element in question^{76, 103, 104} or from the energies of the electronic transitions involved in the recombination of the hole with a valence or higher energy core electron.^{14, 15, 66-74} The mass is ascertained either from the recoil momentum given an incident ion^{28, 85, 86} or by bodily removing surface atoms for analysis by a mass spectrometer.^{33, 39, 105} In this section we briefly survey the techniques utilized to determine the atomic composition of the upper 1 to 10 layers of a planar solid surface.

In principle the simplest means of determining the charge of surface atoms (except H and He) is the measurement of the inelastic impact ionization cross-section of an incident particle exciting core levels of the atom in question (see, e.g., Fig. 5*b*). Since we found in the preceding section that X-ray absorption is not surface sensitive and a low-energy final-state ion would be neutralized before leaving the surface, electrons are the natural candidates for such a measurement. Indeed, the electron impact ionization of surface atoms has been observed.^{65, 103, 106-110} The inelastic electron scattering cross-sections associated with these processes are characterized by two important features. First, the loss energy at threshold is independent of the primary beam energy: A fact that can be exploited for either the detection^{103, 107} or elimination^{72, 107} of such loss processes. Second, both the incident and core electrons must have empty final states into which to be scattered. Therefore the observed line shapes will be influenced by the availability of these states, and hence by the electronic as well as chemical structure of the target. No quantitative line shape analyses and only the most rudimentary comparisons with other core-level spectroscopies^{107, 109} have been carried out to date.

The measurement of the inelastic cross-sections and their use to characterize impurity species on surfaces has been called ionization spectroscopy^{103, 107, 109} and also has been included in the more generic area of characteristic loss spectroscopy.^{106, 110} The resulting structures in the secondary emission ("loss") spectrum are small, however, relative to the

prominent Auger features shown in Fig. 4. Currently, this analytical method is used almost exclusively in conjunction with Auger spectroscopy to clarify the interpretation of complicated, overlapping Auger line shapes. It is neither theoretically nor experimentally a well-developed tool for surface analysis at the present time.

Once a core hole is excited, it can decay by either X-ray fluorescence (Fig. 5c) or Auger electron emission (Fig. 5d). Appearance potential spectroscopy¹¹¹⁻¹¹⁶ is a surface analytical technique based on the former mechanism, whereas Auger spectroscopy^{15,71} is based on the latter. Of the two, Auger spectroscopy is by far the most widely used.^{5,14,15,72,73} Its comparison with other surface analytical techniques is the topic of a review by Kane and Larrabee.¹¹⁷

In the previous section we noted that the core hole filled by the Auger process could be created by electrons, photons, or massive particles, and we estimated the impact ionization cross-sections for all three. Only one preliminary report of ion-stimulated Auger spectra has been given,¹⁰⁰ although several authors^{14,118-121} have compared electron- and X-ray-induced spectra. Two criteria are most relevant for this comparison: absolute intensity of the Auger lines and the ratio of this intensity to the background. Typical X-ray core ionization cross-sections are $\sigma_{pi} \sim 10^{-18}$ to 10^{-20} cm², whereas electron impact ionization cross-sections for electrons of comparable energies ($E \sim 10^4$ eV) are $\sigma_{ei} \sim 10^{-20}$ to 10^{-22} cm². The ion-induced ionization cross-sections probably lie between these two. X-ray-tube line spectra give maximum photon fluxes at the sample of $\dot{N}_{ph} \sim 10^6$ photons/sec.¹²² A microampere current of incident electrons corresponds to an electron flux of about 6×10^{12} electrons/sec. Therefore although the photoionization cross-sections can be as much as 10^4 larger than the impact ionization cross-sections, this advantage is offset by the fact that photon sources are, at best, 10^6 to 10^7 counts/sec weaker than electron sources. In addition, the incident X-ray beam usually is spread over larger areas of the sample. Consequently, electrons give the largest absolute Auger signal using convenient electron and X-ray sources. Unfortunately, they also give the largest background,^{14,118,119} so that X-ray-stimulated Auger spectra often exhibit larger ratios of signal to background. Moreover, we found in (2) and (4) that electrons of a given energy exhibit much larger cross-sections ($\sigma \sim 10^{-16}$ cm²) for low-energy valence-electron excitation than for core-electron impact ionization. This is not true of X-ray photons which exhibit rather small cross-sections ($\sigma \lesssim 10^{-20}$ cm²) for valence-electron excitation.⁸¹ Consequently, electrons are considerably more damaging to a surface than photons for two reasons: An increased incident flux is required to achieve the same signal (a factor of 10^2 to 10^4) and the probability per incident particle of a valence-electron

excitation is enhanced (a factor of 10^3 to 10^5). We see, therefore, that the selection of the means to use in exciting Auger spectra depends on the requirements of sensitivity, signal-to-background ratio, and nondestructiveness imposed on the experiment under consideration.

Quantitative interpretation of Auger electron spectra involving only core electrons is hampered by several complicating features: the excitation of core holes by secondary electrons ("backscattering corrections")^{123,124}; the possibility that discrete loss processes¹²⁵⁻¹²⁷ or multiple-ionization events^{68,127} cause low-energy side bands associated with the prominent Auger lines; the absence of an adequate description of the multiplet fine structure of both the initial core hole and final pair of core holes^{66,67,69}; the occurrence of Coster-Kronig transitions that modify the initial distribution of core holes prior to the Auger event^{62,63}; and the angular dependence of the cross-sections involved in the excitation and emission processes.¹²⁸⁻¹³⁰ If valence electrons are involved in the Auger transition, one encounters the added difficulty that their wave functions are poorly known, especially in the case of adsorbed impurities. In spite of these complications, however, the qualitative identification of trace impurities using prominent features of observed Auger spectra is both straightforward and routine.^{15,72,73} The determination of their positions and concentrations, however, is a considerably less reliable undertaking, requiring thorough calibration even in the simplest of cases.^{124,131-133} Studies of the influence of the chemical state of an element on its Auger spectrum, although widely undertaken,^{126,134-147} have yet to prove a fruitful source of any but the most qualitative information about this state.

In appearance potential spectroscopy the total X-ray fluorescence yield from a sample is measured as a function of the energy of a beam of incident electrons (or ions). When the energy of these particles increases through an ionization threshold, the X-ray yield abruptly becomes larger. Therefore the derivative of this yield with respect to the incident beam energy (i.e., target potential) can produce sharp structure at an ionization threshold, thereby permitting the deduction of the energy of that threshold.

This technique has been applied to examine impurities on the surface of the third-period transition elements.^{113,114,116} In addition, a qualitative line-shape analysis has been provided for the case of clean surfaces.¹¹⁵ A central feature predicted by this analysis is the dependence of the threshold yield on the self-convolution of the density of unoccupied states at the Fermi energy: that is, at threshold both the incident and core electrons must find an empty final state into which they can be scattered. This fact makes the technique most sensitive for materials with large densities of unoccupied states at or near the Fermi level. The transition metals exhibit precisely this property. For such systems, appearance poten-

tial spectroscopy and Auger spectroscopy have been shown to be mutually complementary techniques for the detection of impurities.¹⁴⁸ The utility of appearance potential spectroscopy for materials other than the 3-*d* transition metals, however, remains to be demonstrated.

Since appearance potential spectroscopy is based on electron-stimulated photons, it would seem natural to reverse the roles of these probes and examine the electrons emitted by X-ray photons (i.e., X-ray photoemission). Such measurements have been made for about a decade by Siegbahn and his group, and interpreted in terms of the bulk properties of the target material.⁷⁶ The short inelastic collision mean free path of the photoelectrons, however, renders X-ray photoemission as well as Auger spectroscopy sensitive to the surface rather than bulk properties of the sample. Recognition of this fact by the X-ray photoelectron spectroscopists is beginning to appear in the literature.¹⁴⁹⁻¹⁵³

Finally, we recall that whereas core-level spectroscopies can determine the charge of surface species, in the case of planar targets ion scattering experiments are used to measure their mass. In ion scattering spectrometry,^{85, 86, 117, 154} the elastic scattering from surface species of ions in the energy range $10^3 \text{ eV} \lesssim E \lesssim 10^6 \text{ eV}$ is measured. The recoil energy given the incident ion is a direct measure of the mass of the particle with which it collided.^{27, 28} In secondary ion mass spectrometry^{33, 117} (or "ion probe microanalysis"), the species sputtered from a surface by an incident ion beam are mass analyzed directly. Both techniques are surface sensitive, damaging to the surface, and in need of further calibration for quantitative analysis. It is evident, however, that a combination of core-level and ion scattering techniques can provide a fairly reliable measure of the charges and masses of species in the upper few layers of a solid surface with accuracies in the parts-per-thousand range. If the surface is eroded by an ion beam, they can also provide depth profiles of comparable accuracy and a spatial resolution of $\Delta d \gtrsim 10 \text{ \AA}$ normal to the surface with beam diameters of about 10^{-3} to 10^{-4} cm .

D. Surface Geometry

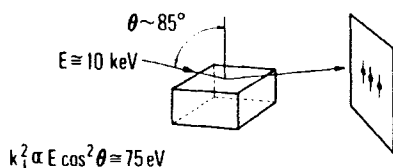
Electron diffraction is the most widely used technique for determining the geometry of large-area, planar surfaces.¹⁻⁶ Since diffraction methods provide statistical rather than imaging characterizations of a structure, they are more sensitive to the existence of regions of order than to the occurrence of defects. In this sense, electron diffraction is complementary to field ion microscopy, the only other popular technique for the characterization of the atomic structure of a surface.³⁹ In field ion microscopy, the atomic structure associated with a tip of radius $r \sim 1000 \text{ \AA}$ is imaged

directly on a fluorescent screen. Thus it provides an elegant technique for examining defect structures (including adsorbed species) on this tip. Since, as discussed in Section II.A, we are focusing our attention on large-area surfaces, however, it seems most appropriate to terminate our consideration of field ion microscopy by referring to Müller and Tsong's review treatise on the subject.³⁹

In our discussion of particle-solid interactions (Section II.B) we found that light chemical species (e.g., H, H₂, He) of thermal energies also could provide a surface-sensitive diffraction spectroscopy. Such experiments have not yet proved useful for determining surface structures because of the widespread failure to observe diffraction of atomic beams from metal surfaces.^{26,90-92} Several reasons can be advanced for this,⁹¹ including experimental ones like the failure to prepare and maintain clean surfaces and the lack of sufficient energy resolution to permit the distinction between elastic and phonon-assisted scattering. At the present time, however, the application of atom-solid scattering experiments to characterize surface geometry remains an interesting possibility rather than an accomplished fact.

In order for electron diffraction to be sensitive to the properties of the upper few atomic layers of a solid, the energy of the electron associated with the component of its motion normal to the surface must lie in the energy range¹⁹ $25 \text{ eV} \lesssim E_{\perp} \lesssim 500 \text{ eV}$. The two experimental arrangements that have been used to achieve this goal are indicated schematically in Fig. 6. The more common of the two, referred to as "low-energy electron diffraction" (LEED), consists of using electrons in the desired energy range incident nearly normal to the target. The theory underlying the use of this technique for surface structure determination is the main topic of subsequent sections in this chapter. Less commonly used is "reflection high-energy electron diffraction" (RHEED). In this case kilovolt electrons incident on the surface near grazing angles are diffracted from the surface.¹⁵⁵ Rather few studies have been carried out using this experimental arrangement,¹⁵⁵⁻¹⁶¹ probably because of its extreme sensitivity to the morphology (e.g., "flatness") of the surface. The LEED arrangement does not exhibit similar sensitivity to the surface morphology.^{156,157,159} This fact suggests that in cases where this information is important, the use of LEED should be supplemented with that of another technique, either RHEED or possibly a direct imaging method based on either RHEED or field emission.⁴⁰ We return to a detailed examination of the applications of LEED in surface crystallography in Part VII, following our discussions of the theory of electron-solid scattering in which we separate the consequences of uncertainties in the electron-solid force law from those of unknown surface geometry.

1. Reflection High-Energy Electron Diffraction
(RHEED)



2. Elastic Low-Energy Electron Diffraction
(ELEED)

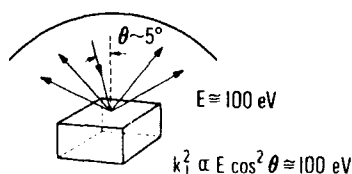


Fig. 6. Schematic indication of the two electron-diffraction techniques used to determine the geometry of single-crystal surfaces: reflection high-energy-electron diffraction (RHEED) and elastic low-energy-electron diffraction (ELEED). The diffraction patterns in both cases usually are imaged on a fluorescent screen. In the case of ELEED, this imaging requires retarding energy analysis (to eliminate inelastically scattered electrons) followed by reacceleration.

E. Surface Atomic Motion

Since scattering experiments provide a statistical rather than imaging characterization of surfaces, they are used to examine average atomistic properties (e.g., the vibrational amplitudes of atoms in the surface layer) rather than the behavior of individual atoms on the surface (as, e.g., in field ion microscope studies of surface diffusion³⁹). Particle-solid scattering experiments are influenced by the thermal motion of the ion-cores in two ways.⁸ First, their elastic particle-ion-core scattering amplitudes are reduced by the Debye-Waller factor, $\exp[-\langle(\mathbf{q} \cdot \mathbf{u})^2\rangle_T]$ in which \mathbf{q} is the momentum transfer in the scattering event, \mathbf{u} is the vibrational amplitude of the ion-core under consideration, and $\langle \rangle_T$ designates an average over the equilibrium lattice motions of the solid. Second, the scattering can be "assisted" by one or more phonons, that is, quanta of lattice vibrational energy. In this case an inelastic scattering event occurs which must be discussed using the appropriate energy and momentum conservation laws. We proceed by indicating the extent to which these two types of process can be distinguished in common scattering experiments and surveying the use of these experiments to determine the values of $\langle u^2 \rangle_T$ associated with surface species. The experimental determination of these surface values of

$\langle u^2 \rangle_T$ is interesting because they are expected to be several times the corresponding values for bulk ion-cores.²¹

Since atoms and molecules interact strongly with surface species on a solid and phonon-assisted processes usually dominate the associated cross-sections, atom-solid scattering experiments might seem the most natural technique for examining surface vibrational motion.¹⁶² The use of energy or velocity discrimination among the scattered particles, however, is rare in such measurements.²⁶ Only a few determinations of the velocity distribution of atoms scattered in different directions from single-crystal surfaces have been reported.¹⁶³⁻¹⁶⁵ The available velocity resolution seems adequate to detect surface-induced modifications of the phonon spectrum of a crystal, although model analyses appropriate for the extraction of such information from observed velocity distributions have yet to be undertaken. Indeed, the only reported observation of surface phonons by atom-solid scattering is based on the measurement of energy-integrated cross-sections.¹⁶⁶ Thus the analysis of atom-solid scattering experiments to extract from them a characterization of the surface vibrational motion seems to lie beyond current practice. The only detailed analysis attempted thus far is one of the total, energy-integrated, differential cross-sections of He scattered from the (111) face of Ag.^{167,168} This analysis is consistent with values of surface $\langle u^2 \rangle_T$ of approximately twice the corresponding bulk values. Moreover, the predicted values of $\langle u^2 \rangle_T$ are in agreement with LEED measurements of this quantity.^{169,170} Thus we find that atom-solid scattering is indeed a possible, although rather undeveloped, technique for determining the vibrational properties of surface atoms.

The most widely used technique for exploring surface vibrational properties is low-energy electron diffraction. The energy resolution of typical display-type LEED instruments is $\Delta E \sim 0.5$ eV. Therefore in these instruments phonon-assisted inelastic scattering processes cannot be distinguished from the elastic events. The use of cylindrical monochromators and analyzers leads to improved resolution of $\Delta E \sim 10$ meV so that inelastic electron scattering by local modes of adsorbed species^{171,172} and optical surface phonons in semiconductors¹⁷²⁻¹⁷⁴ can be observed directly. The great majority of LEED studies of surface atomic vibrations,^{169,170,175-196} however, are carried out by observing the temperature dependence of the "quasielastic" differential cross-sections defined by^{8,9}

$$\left(\frac{d\sigma}{d\Omega} \right)_{qe} = \int_{-\Delta E/2}^{\Delta E/2} dw \left(\frac{d^2\sigma}{d\Omega dw} \right)$$

in which $d^2\sigma/(d\Omega dw)$ is the differential inelastic scattering cross-section associated with an energy loss of $w = E - E'$. Almost all of these mea-

measurements are analyzed in terms of Born approximation (single scattering) models. Although it is well known^{8-10,197,198} that multiple-scattering phenomena influence the values of $\langle u^2 \rangle_T$ extracted from the data using this model, an extensive error analysis⁸ vindicates the accuracy of the resulting interpretation that in the surface layer $\langle u^2 \rangle_T \cong 2\langle u_{\text{bulk}}^2 \rangle_T$ and the values of $\langle u^2 \rangle_T$ monotonically decrease to $\langle u_{\text{bulk}}^2 \rangle$ within increasing distance from the surface. A more detailed specification of the $\langle u^2 \rangle_T$ is impossible at the present time because of uncertainties in the other ingredients of the electron-solid force law.^{8,47,197,199}

F. Surface Electronic Structure

The electronic structure of the surface region of condensed matter can be examined by two distinctly different types of scattering experiment. In the first, one measures the cross-section associated with processes in which the incident or exit particle interacts directly with the valence electrons in the target. Examples of this kind of experiment are elastic and inelastic low-energy electron diffraction, the photomission of valence band electrons,²⁰⁰⁻²⁰⁴ and Auger processes involving two valence electrons.^{101,102,205-211} In the second, one examines valence-electron-induced changes in the lineshapes of electronic transitions between core levels or of the initial excitation of a core electron. The classic example of this kind of measurement is the observation of "chemical shifts" of core-level electrons emitted in X-ray photoemission.^{76,151,152} Such core-level transitions involve electrons localized around a given ion-core. Therefore they tend to measure local properties of the valence-electron fluid. On the other hand, techniques involving the direct excitation of valence electrons usually examine nonlocal properties of the electronic structure. The participation of two valence electrons in an Auger transition to a core hole inside the sample (i.e., not on an external ion as in ion neutralization spectroscopy^{101,102}) is intermediary between these two limits. Thus we arrive at our central observation about the juxtaposition of the terms "surface" and "electronic structure" in the heading of this section: The nature of the physical interactions in a given experiment determines the region of space sampled by that experiment (e.g., its surface sensitivity). Since the detailed nature of many of these interactions is obscure, the determination of the size of this region for techniques involving direct excitation of the valence-electron fluid can become complicated indeed.

It seems premature to attempt to systematic survey of techniques used to measure surface electronic structure because the surface sensitivity of most of the possible measurements is poorly known. For example, we have noted in Sections II.B.2 and II.D that, although elastic low-energy electron

diffraction measures the properties of the outer 1 to 10 atomic layers of a solid, it seems remarkably insensitive to the changes in the electronic structure of the ion-cores in these layers relative to bulk ion-cores or free atoms of the same element.⁴⁷ Indeed, this result is essential for the technique to be useful for surface crystallography. The requirement that a detailed description of the electronic structure of surface atoms is a necessary prerequisite for determining the geometrical structure of the surface has a bulk analogue: that the energy band structure of a solid be established before its crystal structure can be determined. Were this the case, we would be fortunate to know the crystal structure of Al, Si, Ge, and possibly GaAs and Cu. The determination of the structure of more complicated materials would be almost hopeless. The implications of the corresponding requirement for surface structures are obvious. That no such requirement exists is fortunate for surface crystallography, but is indicative of the difficulties inherent in assessing the surface sensitivity of techniques designed to measure electronic structure.

The most extensive attempt to characterize quantitatively a surface feature of the electronic structure of solids has been the application of inelastic low-energy electron diffraction to determine the relationship between energy and momentum (i.e., dispersion relation) of a surface plasmon.^{12,13} The important feature of this study is the demonstration that by using an appropriate mathematical model this dispersion relation may be extracted from the intensity data rather than the interpretation being terminated with a qualitative indication of the physical origin of a given peak in the loss (or Auger or photoemission) spectrum. Quantitative data analyses also have been carried out for ultraviolet photoemission energy distributions from "clean" metals under the assumption, however, that surface phenomena were irrelevant for the interpretation.^{213,214} Despite numerous observations of adsorbate-induced changes in Auger emission,^{126,136-147} appearance potential,^{113,114,116} photoemission,^{200,215-223} ion neutralization,^{101,102} and loss^{126,224-230} spectra only one²³¹ quantitative interpretation of any of these observations has been attempted thus far. The unified, semiquantitative interpretation of combinations of these measurements using a single theoretical model would seem to be the next logical step in the development of the various spectroscopies of electronic surface structure.

G. The Multiple-Technique Strategy

If there is any single pervasive theme in modern high-vacuum surface science it is that "one technique alone is never enough." The trend is toward combining as many as four or five measurements in the same vacuum chamber at the same time in order to be able to characterize more

completely the sample surface being examined. As we have seen, low-energy electron diffraction (LEED), the main topic of this review, is only one of the possible techniques for surface analysis. It seems appropriate, therefore, to conclude our survey of these techniques with a brief indication of the role of LEED in fulfilling the requirements that dictate the design of surface analytical instruments.

A list of these requirements in their broadest sense might read:

1. Surface sensitivity
2. completeness (or uniqueness)
3. quantitateness
4. convenience
5. nondestructiveness.

Our survey has been concerned, thus far, primarily with the first two. We examined the surface sensitivity of each technique, in turn, and organized the survey to display the nature of the surface characterization information generated by the various types of measurement. Evidently, completeness requires that we include in our hypothetical instrument at least one experiment to determine the chemical, geometrical, vibrational, and electronic structure, respectively, of a sample. The role of LEED was particularly evident in our considerations of surface geometry because of its suitability and almost universal acceptance for this purpose in studies of crystalline samples. The temperature dependence of LEED intensities provides, moreover, the major source of information about surface atomic vibrations. Thus, on the basis of the surface sensitivity and completeness criteria alone, LEED is an essential ingredient of any instrument designed to study large-area single-crystal surfaces.

In addition, LEED is currently the most quantitative of the surface analysis methods. Error analyses have been given for its applications to surface crystallography,⁶ the spectroscopy of surface atomic vibrations,⁸ and the spectroscopy of surface plasmon dispersion and damping.^{12,13} Analyses of observed elastic and inelastic LEED intensities have been carried out within a single theoretical framework (the inelastic collision model⁶⁻¹³) and utilized to determine the geometrical, electronic, and vibrational parameters characterizing single-crystal surfaces. This analysis for the low-index faces of clean aluminum is essentially complete at this writing.^{6-8,12,13,47,199} Similar analyses probably will be provided for several simple chemisorption systems within the next few years. The only remaining major (but straightforward) task on the theoretical front is the construction of a description of the emission spectroscopies (e.g., photoemission and Auger emission) based on the existing LEED theory. When this is accomplished, the parameters obtained from emission and scattering ex-

periments can be combined into a single unified mathematical model. It is difficult to believe that this task will long remain undone.

Finally, LEED is convenient but tends to be destructive to fragile adsorption and organic systems. It is readily compatible with Auger spectroscopy (for the determination of the surface atomic composition) and photoemission or ion neutralization spectroscopy (for the measurement of the electronic ground-state parameters to supplement the surface excitation spectra obtained via inelastic LEED). As discussed in Sections II.B.2 and II.C, however, all electron spectroscopies tend to be more destructive than photon spectroscopies because of the large electron cross-sections for valence-electron excitation. In this context we ultimately encounter the fundamental incompatibility between the criterion of surface sensitivity and that of nondestructiveness (Section II.B). Strong particle-solid interactions are required for the first, but weak interactions are the guarantee of the second. Doubtless this difficulty, when it arises, will be circumvented by using probes whose particular strong interaction with the solid is minimally destructive to the sample being examined.

In summary, there is no doubt that LEED is a necessary but not sufficient ingredient in any ultrahigh vacuum instrument designed to examine crystalline surfaces. We have argued, moreover, that the examination of such surfaces is a major part of any systematic study of the electronic and geometrical factors in catalysis. We have seen already that an experimenter must measure the intensities as well as spot pattern of the diffracted LEED beams in order to determine the geometrical and vibrational structure of the surface. The remainder of this article is devoted to the task of indicating what one must do to analyze them, once they have been measured.

III. LOW-ENERGY ELECTRON DIFFRACTION: CONCEPTS AND DEFINITIONS

A. Intensity Analysis

1. Data Displays

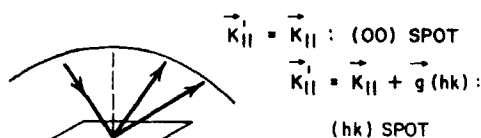
We have seen in previous sections that an analysis of observed low-energy electron diffraction (LEED) intensities is both necessary and sufficient to determine many features of the geometrical, vibrational, and electronic structure of a presumably planar surface of a single-crystal solid. In this subsection we describe the parameters on which the intensities depend and the common methods of displaying these intensities in forms suitable for analysis. The following subsection is devoted to a synopsis of the analytical procedure per se.

Schematic diagrams of the LEED experiment have been given in Figs. 3 and 6. Descriptions of the instruments used for this purpose may be found in earlier reviews.^{4,5} It is conventional to distinguish between "intensity patterns" (or "spot patterns") and "intensity profiles" as indicated in Fig. 7. We recall from (1) in Part I that the intensity pattern determines only the translational symmetry parallel to the surface. Analysis of the magnitudes of the scattered intensities themselves is required to determine the geometry of surface atoms. We return to a more extensive discussion of the interpretation of intensity patterns in Part VII. Here, we concentrate on a description of the electrons scattered in the vicinity of the (00) (i.e., "specular," $\mathbf{k}'_{\parallel} = \mathbf{k}_{\parallel}$) beam.

The parameters describing the incident (unprimed variables) and exit (primed variables) beams are indicated in Fig. 8. The energy, polar angle,

EXPERIMENTALLY MEASURED QUANTITIES IN ELASTIC LOW-ENERGY ELECTRON DIFFRACTION (ELEED)

1. INTENSITY PATTERN: FIXED INCIDENT BEAM ENERGY



2. INTENSITY PROFILE: ENERGY DEPENDENCE OF THE INTENSITY OF A GIVEN SPOT

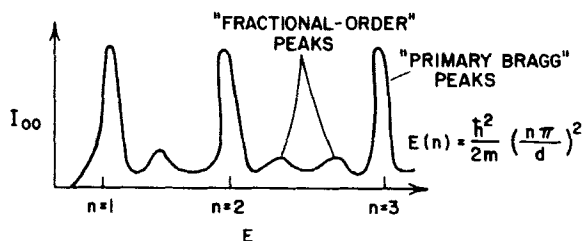


Fig. 7. Illustration of the distinction between an intensity pattern and an intensity profile. In both cases, the detector is biased relative to the gun in such a fashion that only the electrons in the quasi-elastic peaks, indicated in Figs. 4 and 9, are collected. The diffracted beams are labeled by the Miller indices of the reciprocal lattice vectors of the Bravais net for translational symmetry parallel to the surface as defined in Fig. 1 (see pg. 5.)

and azimuthal angle for the incident (exit) beam are designated by E , θ , and ψ (E' , θ' , and ψ'), respectively. For elastic low-energy electron diffraction (ELEED) we see that $E' = E$ by definition. Moreover, the exit angles θ' and ψ' are determined from the incident beam parameters by conservation of momentum parallel to the surface, that is,

$$\mathbf{k}'_{\parallel} = \mathbf{k}_{\parallel} + \mathbf{g} \quad (16a)$$

$$k_{\parallel} = \left(\frac{2mE}{\hbar^2} \right)^{1/2} \sin \theta \quad (16b)$$

$$k'_{\parallel} = \left(\frac{2mE'}{\hbar^2} \right)^{1/2} \sin \theta' \quad (16c)$$

in which \mathbf{g} is a reciprocal lattice vector of the Bravais net describing the translational symmetry parallel to the surface (see, e.g., Fig. 1). Therefore the diffracted intensities are functions of only three independent variables: E , θ , and ψ . In the case of inelastic low-energy electron diffraction (ILEED), however, the scattered intensities depend on all six of the independently variable beam parameters defined in Fig. 8.

LEED: BEAM PARAMETERS AND SPECULAR BEAM GEOMETRY

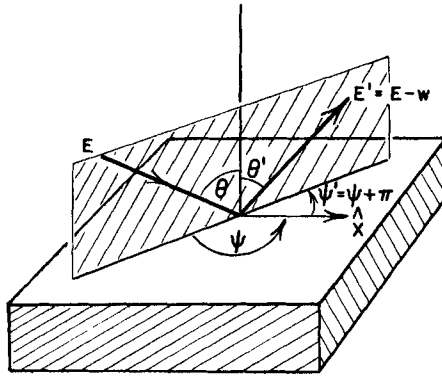


Fig. 8. Schematic diagram of the geometry of the specular beam for both elastic low-energy electron diffraction (ELEED: $w \equiv 0$) and inelastic low-energy electron diffraction (ILEED: $w \neq 0$). The energy E ($E' \equiv E - w$), polar angle θ (θ'), and azimuthal angle ψ (ψ') of the incident (exit) beam are indicated.

The ELEED intensities are customarily displayed as plots of the intensity of a given diffracted beam as a function of one of the three independent incident beam variables with the other two held fixed. Varying the incident beam energy for fixed θ , ψ leads to the intensity profiles (or “IV curves” or “pseudorocking curves”). “Rocking curves” are generated by varying θ for fixed values of E and ψ . Finally, plots of a beam’s intensity versus azimuthal angle (ψ) for prescribed E, θ are referred to as “rotation diagrams.” Historically, intensity profiles have been the predominant form of data display used in the literature.

The most remarkable feature of ILEED is its existence: Inelastically as well as elastically scattered electrons emerge from the solid in a series of well-defined beams. Larger values of the energy loss, $w = E - E'$, usually are associated with broader beams, of course, because of multiple-loss processes. The existence of such beams is well documented, however, for values of w up to 25 to 50 eV.^{16,232–238}

We have seen that the diffracted intensity in the ILEED beams is a function of six independent variables: E , $w \equiv E - E'$, θ , θ' , ψ , and ψ' . The results of both experiments and calculations are presented for a fixed direction of the incident beam (θ , ψ fixed) and scattering in a plane ($\psi' = \psi + \pi$). This procedure reduces to three (E , w , and θ') the number of independent variables specifying the inelastically diffracted intensities. By holding two of these variables fixed while sweeping the third, we generate “energy (intensity) profiles,” “loss profiles,” and “angular profiles,” respectively, as indicated in Fig. 9. In detail, these three modes of presenting the data are defined as follows: (a) In the case of an *energy profile* the direction (θ, ψ) of the incident beam, the direction of the scattered beam (θ', ψ'), and the loss energy w are held fixed. The scattered intensity is presented as a function of incident beam energy E . (b) In the case of a *loss profile* the direction (θ, ψ) and the energy E of the incident beam and the direction (θ', ψ') of the scattered beam are held constant. Then the scattered intensity is plotted as a function of the loss energy w . (c) In the case of an *angular profile*, the direction (θ, ψ) and energy E of the incident beam as well as the loss energy w are taken to be constant. The scattered intensity is given in this case as a function of the final angle θ' (with $\psi' = \psi + \pi$). Although these forms of data display are not the only ones possible, they are those commonly used in the literature. The secondary electron (or “loss”) spectra, $N(E' \equiv E - w)$, like that shown in Fig. 4, are obtained by summing over the angular integrals of the loss profiles of all of the various ILEED beams as indicated in Fig. 3, that is,

$$N(E - w) = \sum_{(hk)} \int d\Omega' I_{hk}^{E, \theta'}(w) \quad (17)$$

EXPERIMENTALLY MEASURED QUANTITIES IN INELASTIC
LOW-ENERGY ELECTRON DIFFRACTION (ILEED)

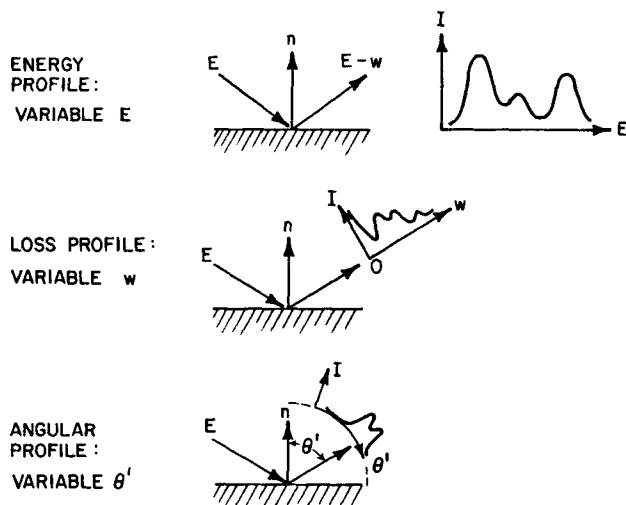


Fig. 9. Schematic diagram of the three types of display of ILEED intensity data. The "loss profile" display is called the secondary electron (or "loss") spectrum if all final angles (θ', ψ) are integrated over. Obviously, the measurement of the three types of ILEED profile indicated in this figure requires the use of a movable small-area detector rather than the hemispherical screen shown in Fig. 3.

in which $I_{hk}^{E, \theta'}(w)$ is the loss profile of the beam labeled by the (hk) miller indices (see, e.g., Fig. 1). We use in (17) a notation for the various profiles in which subscripts designate the beam indices, superscripts indicate the variables held constant by definition, and the quantity in parentheses is the running variable for the profile in question. Finally, we see that the elastic "intensity profile" (see Fig. 7) is the inelastic "energy profile" for $w \equiv 0$.

2. Definition of the Analysis Problem

Having described the modes of displaying the intensity data, we now can examine the issues involved in their interpretation. We proceed in three stages. First, we expose the analysis problem in its complete generality. Then we explore two pervasive themes about its solution which characterize the current literature. Finally, we establish the focus of our emphasis in this review, and outline the approach which we follow.

Broadly stated, the objective of LEED intensity analysis is the formulation of a mathematical model of LEED and the determination of the

values of the parameters in that model that are associated with a given set of observations. Five types of parameters occur in such a model. We already have defined the *beam parameters* (E , E' , θ , θ' , ψ , ψ') in the preceding subsection. Moreover, the surface itself is characterized by *thermodynamic parameters* like the temperature T , the sample area A , and the various state functions (e.g., entropy) associated with the surface properties of the target. On the "atomic" scale, there are *structural parameters* describing the chemical identity, geometrical positions, and lattice vibrations of the ion-cores at the sample surface. Given the atomic structure, it is *electronic parameters* which describe the interaction of the incident electron with the constituents of the target. Finally, *instrumental parameters* (e.g., energy and angular resolution) determine the relationship between elemental (e.g., calculated) cross-sections and the diffracted intensities observed in a given apparatus. The sophistication with which these different types of parameters are incorporated into a given model calculation depends on the purpose which that calculation is designed to serve.

Surveys²⁻⁸ of the literature on LEED reveal two persistent, yet distinctly different, themes concerning the purposes of model analyses. Experimental workers tend to view them as vehicles for determining the structural parameters from experimental data (under the implicit although seldom stated assumption that the other four types of parameters are known a priori). Theoretical workers, on the other hand, usually regard them as exercises in the technology of mathematical solid-state physics: testing grounds for theoretical formalisms and possibly vehicles for determining the electronic structure of solids. Given this situation, it is not difficult to see, either logically or from a perusal of the literature, that the advocates of one theme do not always value highly studies undertaken in the context of the other.

Although the tension between these two themes is historical in origin,⁶ its resolution rests exclusively in the nature of electron-solid interactions. With suitable care the beam, thermodynamic and instrumental parameters can be obtained to arbitrary accuracy. The structural and electronic parameters, however, can be determined only within the context of the analysis of the measurements themselves because of the surface sensitivity of the LEED technique and the dependence of these parameters on the state of the surface.^{21,29} Therefore the crucial issue for practical data analysis is the relative sensitivity of predicted LEED intensities to the structural versus electronic parameters in the model. For example, surface crystallography via LEED is feasible if and only if these intensities are substantially more sensitive to changes in the lattice parameters, $\Delta d \sim 0.1 \text{ \AA}$, than to plausible alterations in the electron scattering cross-sections

of surface species (associated with uncertainties in the exact nature of their chemical bonding to those in the substrate).

In spite of considerable discussion and vacillation in the literature, the enhanced sensitivity of predicted ELEED intensities to the structural relative to the electronic parameters has been documented thoroughly for clean Al,⁴⁷ Cu,²³⁹ Ag,²⁴⁰ and Ni²⁴¹ as well as chemisorbed layers of Na, O, and S on Ni(100) and Al(100).²⁴² Models of electron-ion-core potentials based on simple overlapping atomic charge densities predict ELEED intensities quite comparable to those obtained using more sophisticated potentials. Moreover, the changes in potential associated with differing and bulk atomic coordination cause negligible alterations in the predicted intensities. The physical origin of these results resides in the short inelastic collision mean free path, $\lambda_{ee} \sim 2$ to 10 \AA , discussed in Section II.B.2 (6). Their main consequence is that surface crystallography via ELEED differs from bulk crystallography via X-ray diffraction only in the technical complexity of the analytical procedure. The essential input ingredients in both analyses are identical: a simple model of the electronic charge density around the atoms (obtained from standard references like the book by Herman and Skillman²⁴³) and a set of computer programs that convert these charge densities plus a hypothetical structure into model intensities for comparison with experimental data. As indicated in the Introduction and described later, because of the large electron-ion-core elastic scattering cross-sections the computer programs for surface crystallography are considerably more complicated than those for a comparable bulk crystallographic analysis. Nevertheless, they exist and their use is quite elementary, subject only to the availability of large-scale electronic computers using the "FORTRAN" compiler.

Our considerations concerning the nature and importance of model parameters suggest that we adopt a four-step approach to the analysis of LEED intensity data.

1. The nature of electron-solid interactions is examined in order to construct a suitable model on which to base a calculation of the intensities.

2. Given the model Hamiltonian, an accurate evaluation of these intensities is performed via the solution of the resulting (nonrelativistic) Schrödinger equation.

3. The sensitivity of the predicted intensities to the values of the model parameters is investigated in order to determine the consequences of anticipated uncertainties in the precise description of the electron-solid interactions.

4. For each proposed data analysis (e.g., to extract surface geometries, atomic thermal displacements, or surface plasmon dispersion from mea-

sured intensities) an analytical procedure is constructed together with a corresponding error analysis.

During the remainder of this part we describe the performance of the first two steps in the simplest and broadest of terms. Then in Part IV we examine step 1 in more detail. A thorough discussion of steps 2 and 3 for ELEED and ILEED is given in Part V and VI, respectively. Finally, the analytical procedures for use in surface crystallography and in the determination of surface plasmon dispersion are developed in Parts VII and VIII.

B. Models of Electron-Solid Interactions

In this section, we first discuss the main physical features of the electron-solid interaction. Then we describe how these features are incorporated into model Hamiltonians describing electron diffraction. Finally, we indicate the uncertainties in our present knowledge of the details of the electron-solid force law and their consequences for the applications of low-energy electron diffraction to determine the geometry of surface atoms and the dispersion relation of surface plasmons.

The three important parts of the electron-solid interaction for electrons in the energy range of interest in LEED, that is, $10 \text{ eV} \lesssim E \lesssim 10^3 \text{ eV}$, have been indicated already in Fig. 2 (see page 13). The long-range contributions due to the interaction of the incident electron with the charge it induces on the surface cause the image force (even for a fast electron) if it is far from the surface outside of the solid.³⁰ However, as an electron approaches within a few angstroms of the surface, the emission of surface plasmons becomes likely, leading to the description of elastic electron-solid scattering in terms of a complex, highly nonlocal, effective one-electron "optical" potential.³⁰ Such inelastic excitation of plasmons occurs because of the interaction of the incident electron with the valence electrons in the solid. Thus it is the electron-electron interactions that give rise to the major dissipative contributions to the electron-solid force law by virtue of an incident electron's energy loss to bulk as well as surface plasmons, and to other types of excitation of the valence-electron fluid, e.g., interband transitions.²⁴⁴

The electron-electron interactions produce predominately small momentum transfer (i.e., forward scattering) events. Therefore in a large-scattering-angle reflection spectroscopy like LEED another mechanism must exist to "turn the electron around." The backscattering of the electron from the ion-cores in the solid performs this function. Indeed, the simplest type of model for electron-solid scattering is obtained by considering the atoms in the solid to be rigid, static potentials situated on a periodic lattice. Such a model is referred to as a *static potential model*. It constitutes the basis for band structure calculations for a bulk solid as well

as for electron-solid scattering. The Hamiltonian which defines this model is

$$H_0 = H_{00} + V \quad (18a)$$

$$H_{00} = \frac{-\hbar^2 \Delta}{2m} \quad (18b)$$

$$V = V(\mathbf{r}) = \sum_n v_n(\mathbf{r} - \mathbf{R}_n) \quad (18c)$$

in which H_0 is the kinetic energy of the incident electron and $v_n(\mathbf{r} - \mathbf{R}_n)$ is the static potential of an atom whose nucleus is at the position \mathbf{R}_n . In (18) magnetic interactions (e.g., due to the spin-orbit coupling of the incident electron with the "atomic" potential) are neglected. An equivalent form of the potential, (18c), for a periodic lattice is

$$V(\mathbf{r}) = \sum_{\mathbf{G}} V_{\mathbf{G}} e^{-i\mathbf{G} \cdot \mathbf{r}} \quad (19)$$

in which \mathbf{G} is a reciprocal lattice vector of the bulk (i.e., three-dimensional) lattice. This is the form of the potential used in "multiple-beam" analyses of LEED intensities which have been reviewed recently by Stern, Perry, and Boudreaux.²⁴⁵ The Fourier expansion given by (19) applies only if the potential is perfectly periodic, that is, the surface ion-core potentials are identical to those in the bulk. We found in Part II that such is not the case. The surface scatterers can be chemically different from those in the bulk (e.g., in the presence of adsorbed overlayers) and they are always vibrationally and electronically inequivalent because of their reduced coordination. Since the electron-electron-interaction-induced inelastic collisions render LEED a measure of the properties of the upper 1 to 10 atomic layers of a solid, we see that (19) is not a suitable expansion for use in a complete theory of low-energy electron reflection from solids.

The static potential model can be extended to describe the influence of lattice vibrations by writing the nuclear coordinates in "second-quantized" notation.²⁴⁶ In the case of a monatomic lattice we find

$$\mathbf{R}_n(t) = \mathbf{R}_n^{(0)} + \mathbf{u}_n(t) \quad (20)$$

$$\mathbf{u}_n(t) = \sum_{\mathbf{p}, \lambda} \epsilon_{\mathbf{p}\lambda} \left(\frac{\hbar}{2MN\omega_{\lambda}(\mathbf{p})} \right)^{1/2} [b_{\mathbf{p}\lambda}^+ e^{-i\mathbf{p} \cdot \mathbf{R}_n^{(0)}} + b_{\mathbf{p}\lambda} e^{i\mathbf{p} \cdot \mathbf{R}_n^{(0)}}] \quad (21a)$$

$$H_L = \sum_{\mathbf{p}\lambda} \hbar\omega_{\lambda}(\mathbf{p}) [b_{\mathbf{p}\lambda}^+ b_{\mathbf{p}\lambda} + \frac{1}{2}] \quad (21b)$$

The $b_{\mathbf{p}\lambda}$ are the annihilation operators of phonons of quasiwave vector \mathbf{p} , polarization index λ , and energy $\hbar\omega_\lambda(\mathbf{p})$. They satisfy the commutation relations

$$[b_{\mathbf{p}\lambda}, b_{\mathbf{p}'\lambda'}] = [b_{\mathbf{p}\lambda}^+, b_{\mathbf{p}'\lambda'}^+] = 0 \quad (22a)$$

$$[b_{\mathbf{p}\lambda}, b_{\mathbf{p}'\lambda'}^+] = \delta_{\lambda\lambda'} \delta_{\mathbf{p}, \mathbf{p}'} \quad (22b)$$

For convenience, we usually suppress the polarization index λ . The electronic Hamiltonian specified by (18) can also be written in this notation as

$$H_0 = H_{00} + V \quad (23a)$$

$$H_{00} = \sum_{\mathbf{k}} \epsilon(\mathbf{k}) c_{\mathbf{k}}^+ c_{\mathbf{k}} \quad (23b)$$

$$\epsilon(\mathbf{k}) = \frac{\hbar^2 k^2}{2m} \quad (23c)$$

$$V = \sum_{\mathbf{q}, \mathbf{k}} \langle \mathbf{k} + \mathbf{q} | V | \mathbf{k} \rangle c_{\mathbf{k} + \mathbf{q}}^+ c_{\mathbf{k}} = \sum_{\mathbf{q}, \mathbf{k}, n} v_{\mathbf{q}} e^{-i\mathbf{q} \cdot \mathbf{R}_n} \quad (23d)$$

$$v(\mathbf{r}) \equiv \sum_{\mathbf{q}} v_{\mathbf{q}} e^{i\mathbf{q} \cdot \mathbf{r}} \quad (24)$$

$$[c_{\mathbf{k}}, c_{\mathbf{k}'}]_+ = [c_{\mathbf{k}}^+, c_{\mathbf{k}'}^+]_+ = 0 \quad (25a)$$

$$[c_{\mathbf{k}}, c_{\mathbf{k}'}^+]_+ = \delta_{\mathbf{k}, \mathbf{k}'} \quad (25b)$$

Thus the Hamiltonian including electron-phonon interactions may be written as

$$H_1 = H_0 + H_L = H_{00} + H_L + V \quad (26)$$

with H_0 given by (23) and H_L given by (21). Equation (26) is referred to as the rigid-ion approximation because the potential $v(\mathbf{r} - \mathbf{R}_n(t))$, associated with a given ion position $\mathbf{R}_n(t)$, rigidly moves as the ion vibrates. This model is inadequate for some purposes (e.g., the description of superconductivity) but its refinements require consideration of electron-electron interactions.

The inclusion of electron-electron interactions in the model Hamiltonian is rather complicated because careful distinctions must be drawn between the consequences of real and induced charge densities.³⁰ Therefore this aspect of analysis is treated phenomenologically in existing models of low-energy electron diffraction.⁶ The consequences of electron-electron

interactions on elastic electron-solid scattering are simulated by use of empirical optical potentials⁵⁵ or an equivalent propagator-renormalization procedure.^{19,247,248} In the former case the one-electron Hamiltonian H_{00} given by (18b) is supplemented by a complex, energy-dependent ("optical") potential usually taken to be constant inside the solid (i.e., for $z > 0$). A common form taken for this Hamiltonian is^{6,19,248}

$$H_{00} = \frac{-\hbar^2 \Delta}{2m} + \Sigma(E)\theta(z) \quad (27)$$

$$\Sigma(E) = -V_0 - \frac{i\hbar}{m\lambda_{ee}} [2m(E + V_0)]^{1/2} \quad (28)$$

The real part of the optical potential, $-V_0$, is caused primarily by the exchange interaction of the incident electron with the valence electrons in the solid. As such, it provides the major contribution to the cohesive energy of simple metals.²⁴ The imaginary part of the optical potential describes the removal of electrons from the elastic beam by inelastic electron-electron collisions. It is expressed in terms of the inelastic collision damping length λ_{ee} in (28). (The inelastic collision mean free path is half the inelastic collision damping length because the former describes the modulus square of the wave function of the incident electron.²⁴⁸ The symbol λ_{ee} is used in the literature to designate the damping length, not the mean free path. We did not introduce this distinction in Part II because it is irrelevant for the order-of-magnitude estimates presented there.) Typically both V_0 and λ_{ee} (or equivalent parameters) must be taken to be adjustable parameters to achieve a good description of experimental ELEED intensities.^{42,47,249-251}

In the case of inelastic electron-solid scattering, the incident electrons' coupling to the loss modes of the solid is incorporated explicitly into the Hamiltonian by means of an interaction term

$$U_{el} = \sum_{\mathbf{q}, \mathbf{k}, n} c_{\mathbf{k}+\mathbf{q}}^+ c_{\mathbf{k}} T(n; \mathbf{k} + \mathbf{q}, \mathbf{k}) \quad (29a)$$

$$T(n; \mathbf{k} + \mathbf{q}, \mathbf{k}) = \exp[-i\mathbf{q} \cdot \mathbf{R}_n] h(n) \quad (29b)$$

$$h(n) = \sum_{\mathbf{p}} \exp[-i\mathbf{p} \cdot \mathbf{R}_n] t(\mathbf{p}) [b_{\mathbf{p}}^+ + b_{-\mathbf{p}}] \quad (29c)$$

in which the $b_{\mathbf{p}}$ are the annihilation operators of the *electronic* excitations of the valence-electron fluid (e.g., bulk and surface plasmons). The Hamiltonian of these loss modes themselves is, in principle, of the form given in (21b). In practice, however, a more refined spectral density quantum field theory formalism is used^{11,30,247,252} in which the interactions of these loss mode excitations result in their damping.

The inclusion of the electron-electron interactions into the model Hamiltonian yields the formally complete Hamiltonian

$$H = H_{00} + H_L + V + U_{el} + V_{el-el} \quad (30)$$

in which we use V_{el-el} to designate those terms in the electron-electron interaction not included in U_{el} . An important aspect of the development of LEED theory is that the approximations which work well to describe the ground and low-lying excited states in a bulk solid *do not suffice* to provide even a qualitative theory of LEED. The big difference between the analysis of LEED and that of the low-temperature transport or optical properties of solids is that the excitation of collective and single-particle excitations of the valence-electron-ion-core plasma causes strong "inelastic collision" damping of the incident elastic wave field for electrons in the energy range of interest in LEED. This damping must be incorporated into the theory *ab initio* in order to achieve even a qualitative description of experimental results. As noted in previous sections, it results in the important property of LEED experiments that they are sensitive to the surface, not bulk, properties of the solid.

Surveying the numerous parameters in (18) to (30), it seems appropriate to conclude our discussion with an indication of the areas of greatest uncertainty. We emphasized in Section III.A.2 that relatively simple models of the electron-ion-core potential suffice to describe the line shapes of observed ELEED intensity profiles. In fact, this potential probably is the best established feature of the electron-solid interaction. The surface ion-core lattice displacements are not known in any detail beyond the fact that $\langle u_{\text{surface}}^2 \rangle_T \cong 2\langle u_{\text{bulk}}^2 \rangle_T$. Fortunately, by taking ELEED intensity data at low temperatures (e.g., $T \lesssim 100^\circ\text{K}$), the uncertainties in the thermal lattice displacements can be reduced to the point that their influence on the line shapes of the intensity profiles is negligible.^{47,242} Thus we are left with the electron-electron interactions as the major potential source of error in models of the electron-solid interaction.³⁰ In the case of ELEED, the electron-electron-interaction-induced optical potential is currently the weak link in the microscopic description of the diffracted intensities because "first principles" evaluations of this potential do not yield uniformly satisfactory descriptions of existing ELEED intensity data.^{30,42,47,250,251} The order of magnitudes $V_0 \sim 10$ eV and $\lambda_{ee} \sim 2$ to 10 Å are well documented, but variations seem to occur in V_0 and λ_{ee} with incident electron energy and in V_0 with angle of incidence and crystal face. These phenomena have not been interpreted in detail. Evidently, such uncertainties in V_0 create corresponding ones in the surface lattice parameters, especially in the case of adsorbed overlayers. In practice, V_0 and λ_{ee} are fixed empirically by analyzing ELEED intensities from the

“clean” substrate before the adsorbed layer is created—a workable although not entirely satisfying procedure. Finally, both the dispersion relations $\hbar\omega(\mathbf{p})$ and the electron vertex functions $t(\mathbf{p})$ of the surface excitations of the valence-electron fluid are almost “unknown.” In the case of aluminum, however, simple semiclassical models of $t(\mathbf{p})$ seem to suffice to extract sensible surface plasmon dispersion relations from experimental ILEED intensities.^{11–13,212} Thus it appears remarkable but true that for both ELEED and ILEED, the data analyses are sufficiently insensitive to the electron-ion-core and electron-excitation vertex functions, respectively, that sensible atomic geometries and surface plasmon dispersion relations can be extracted from measured intensities in spite of the host of uncertainties in the model electron-solid force law.

C. Elastic Diffraction from a Rigid Lattice: Born Approximation

Having constructed a model of electron-solid interactions in the preceding section, we now derive the consequences of these interactions in the simplest possible case: the Born approximation calculation of elastic low-energy electron diffraction (ELEED) intensities. In this approximation, sometimes referred to as the “kinematical model,” the incident electron is presumed to scatter once and only once from each ion-core in the target. We proceed in three steps. First we derive expressions for the Born approximation to the elastic electron-solid cross-sections. Then we evaluate the cross-sections for the scattering of an incident electron from a static two-dimensional planar array of ion-cores parallel to a hypothetical surface of a monatomic solid. Finally, the solid is “built up” by stacking these two-dimensional atomic diffraction gratings on top of each other. The electron diffraction cross-sections from this array of diffraction gratings are calculated and interpreted in terms of ELEED intensities from atomically flat surfaces of single-crystal solids.

The Schrödinger equation associated with the static potential model (18) is given by²⁵³

$$\psi_{\mathbf{k}}(\mathbf{r}) = \varphi_{\mathbf{k}}(\mathbf{r}) + \int d^3r' G_0(\mathbf{r}, \mathbf{r}', E) V(\mathbf{r}') \psi_{\mathbf{k}}(\mathbf{r}') \quad (31a)$$

$$V(\mathbf{r}) = \sum_{n, \mathbf{q}} v_n(\mathbf{q}) e^{i\mathbf{q} \cdot (\mathbf{r} - \mathbf{R}_n)} \quad (31b)$$

$$\begin{aligned} G_0(\mathbf{r}, \mathbf{r}', E) &= \lim_{\delta \rightarrow 0^+} \frac{1}{(2\pi^3)} \int d^3k \frac{e^{i\mathbf{k} \cdot (\mathbf{r} - \mathbf{r}')}}{E - \hbar^2 k^2 / 2m + i\delta} \\ &= \frac{-m}{2\pi\hbar^2} \frac{e^{ik(E)|\mathbf{r} - \mathbf{r}'|}}{|\mathbf{r} - \mathbf{r}'|} \end{aligned} \quad (32a)$$

$$k(E) \equiv \left(\frac{2mE}{\hbar^2} \right)^{1/2} \quad (32b)$$

The $v_n(\mathbf{q})$ are the Fourier transforms of the ion-core potentials at the sites $\{\mathbf{R}_n\}$. If we use scattering theory boundary conditions, $|\mathbf{r}| \gg |\mathbf{r}'|$, so that

$$G_0(\mathbf{r}, \mathbf{r}', E) \xrightarrow{|\mathbf{r}| \gg |\mathbf{r}'|} \frac{-m}{2\pi\hbar^2} \frac{e^{ik(E)r}}{r} e^{ik(E)\hat{\mathbf{r}} \cdot \mathbf{r}'} \quad (33)$$

where $\hat{\mathbf{r}}$ is a unit vector directed along \mathbf{r} . The scattered wave emerges along $\hat{\mathbf{r}}$ so that we define the final wave vector by

$$\mathbf{k}' \equiv k(E)\hat{\mathbf{r}} \quad (34)$$

Therefore in the asymptotic limit that $|\mathbf{r}| \gg |\mathbf{r}'|$ Eqs. (31) give

$$\psi_{\mathbf{k}}(\mathbf{r}) = \varphi_{\mathbf{k}}(\mathbf{r}) + f(\mathbf{k}', \mathbf{k}) \frac{e^{ik(E)r}}{r} \quad (35)$$

In the Born approximation we replace the exact wave function $\psi_{\mathbf{k}}(\mathbf{r}')$ by that of the incident electron $\phi_{\mathbf{k}}(\mathbf{r}')$ under the integral in (31a). In this case the scattering amplitude $f(\mathbf{k}', \mathbf{k})$ becomes

$$\begin{aligned} f(\mathbf{k}', \mathbf{k}) &= \frac{-m}{2\pi\hbar^2} \int d^3r' e^{-i\mathbf{k}' \cdot \mathbf{r}'} V(\mathbf{r}') e^{i\mathbf{k} \cdot \mathbf{r}'} \\ &= \frac{-m}{2\pi\hbar^2} \sum_n v_n(\mathbf{k}' - \mathbf{k}) e^{-i(\mathbf{k}' - \mathbf{k}) \cdot \mathbf{R}_n} \end{aligned} \quad (36)$$

In the limit that all of the scattering potentials are identical [i.e., $v_n(\mathbf{q}) = v(\mathbf{q})$ as in a monatomic crystal] the elastic scattering cross-section is given by

$$\frac{d\sigma}{d\Omega} = |f(\mathbf{k}', \mathbf{k})|^2 = \left| \frac{-m}{2\pi\hbar^2} \sum_n v(\mathbf{k}' - \mathbf{k}) e^{-i(\mathbf{k}' - \mathbf{k}) \cdot \mathbf{R}_n} \right|^2 \quad (37)$$

which is the usual expression for scattering from a periodic potential.⁸³ One often defines an interference function (sometimes called a structure factor in the solid-state literature²⁵⁴) $S(\mathbf{q})$ via

$$S(\mathbf{q}) = \frac{1}{N} \sum_n e^{-i\mathbf{q} \cdot \mathbf{R}_n} \quad (38)$$

Writing $\mathbf{k}' = \mathbf{k} + \mathbf{q}$ in (36) we obtain

$$\frac{d\sigma}{d\Omega} = \left(\frac{mN}{2\pi\hbar^2} \right)^2 |v(\mathbf{q})|^2 |S(\mathbf{q})|^2 \quad (39)$$

in which N denotes the number of atoms in the monatomic lattice. Thus the scattering amplitude factors into the interference function $S(\mathbf{q})$, which depends only on the lattice geometry, and a form factor $v(\mathbf{q})$, which depends only on the dynamics of the electron-ion-core interaction.

Following Davisson and Germer,¹⁶ we consider a monatomic solid to consist of a stacked array of two-dimensional atomic diffraction gratings. The top layer of atoms is associated with an interference function $S(\mathbf{q})$, given by

$$S(\mathbf{q}) = \frac{1}{N_{\parallel}} \sum_n e^{-i\mathbf{q} \cdot (\mathbf{R}_n)_{\parallel}} = \delta_{\mathbf{g}, \mathbf{q}} \quad (40)$$

We have defined the parallel and perpendicular components \mathbf{k} via

$$\mathbf{k}_{\parallel} \cdot \mathbf{R}_{\perp} = 0 \quad (41a)$$

$$\mathbf{k}_{\perp} \cdot \mathbf{R}_{\parallel} = 0 \quad (41b)$$

where the magnitude of \mathbf{k}_{\parallel} is specified by boundary conditions (Fig. 1) and that of \mathbf{k}_{\perp} is determined by energy conservation which, for free electrons, gives

$$k_{\perp}^2(\mathbf{g}, E) \equiv \frac{2mE}{\hbar^2} - (\mathbf{k}_{\parallel} + \mathbf{g})^2 \quad (42)$$

As anticipated, the scattered electrons emerge from the crystal in a series of beams each associated with a given value of \mathbf{g} . The intensities of these beams are determined by

$$|v(\mathbf{q})|^2 \rightarrow |v[\mathbf{q}_{\parallel} = \mathbf{g}, q_{\perp} = k_{\perp}(0, E) + k_{\perp}(\mathbf{g}, E)]|^2 \quad (43)$$

which is a slowly decreasing function of energy for a given beam index $\mathbf{g} = 2\pi(\hbar\mathbf{b}_1 + k\mathbf{b}_2)$. Thus we see that for a two-dimensional diffraction grating, the kinematical approximation predicts an intensity profile for each beam which is a monotonically decreasing function of the primary beam energy. This prediction is in strong disagreement with measured profiles such as the one indicated schematically in Fig. 7. Equations (39), (40), and (43) also reveal the major "physical" features of the Born approximation analysis of this model. The translational symmetry of the

scattering potential determines the intensity pattern, whereas the details of the electron-solid interaction determine the intensities of the various scattered beams as a function of the incident beam parameters and the beam index.

Having noted that in the Born approximation electron diffraction from a single atomic layer leads to monotonically decreasing intensity profiles, it is natural to inquire whether in this approximation multilayer scattering can improve the description of experimental data. In order to examine this question, we observe that (27) and (28) imply that the occurrence of inelastic collisions by the incident electron gives $k_{\perp}(\mathbf{g}, E)$, a small imaginary component. That is, if we focus our attention solely on the elastic scattering of an electron by the solid, inelastic collisions have the effect of "absorbing" particles from the incident beam. Therefore the electron's momentum normal to the surface is determined from energy conservation to be given by

$$[k_{\perp 1}(\mathbf{g}, E) + ik_{\perp 2}(\mathbf{g}, E)]^2 = \frac{2m}{\hbar^2} [E - \Sigma(E)] - (\mathbf{k}_{\parallel} + \mathbf{g})^2 \quad (44)$$

in which $\Sigma(E)$ is the complex potential describing the effects of both elastic and inelastic electron-electron collisions of the incident electron with the valence electrons of the solid [see (28)]. Because of these interactions, (44) replaces (42) for electronic motion "inside" the solid. Using (41) and noting that \mathbf{k}'_{\perp} has the opposite direction to \mathbf{k}_{\perp} for an electron reflected from a solid, we obtain for the interference function [(38)]

$$S(\mathbf{k}' - \mathbf{k}) = \delta_{\mathbf{k}_{\parallel}, \mathbf{k}_{\parallel} + \mathbf{g}} \sum_{\nu=0}^{\infty} \exp - i\mathbf{g} \cdot \mathbf{d}_{\nu} \exp \{ i[k_{\perp}(0, E) + k_{\perp}(\mathbf{g}, E)]d_{\nu\perp} \} \quad (45)$$

in which \mathbf{d}_{ν} is the radius vector from the origin of the central cell on the top atomic layer ($\nu=0$) to that on the ν th layer. For example, in the case of a (110) face of an fcc lattice, if a is the lattice spacing of the simple cubic basis, the primitive Bravais net of the surface layer is specified by

$$\mathbf{a}_1 = a \left(\frac{1}{\sqrt{2}}, 0 \right) \quad (46a)$$

$$\mathbf{a}_2 = a(0, 1) \quad (46b)$$

The layer spacing vector is

$$\mathbf{d}_{\nu} = \nu a \left(\frac{1}{2\sqrt{2}}, \frac{1}{2}, \frac{1}{2\sqrt{2}} \right) \equiv \nu \mathbf{d}_0 \quad (47)$$

That is, the origin of the central cell is shifted by $[(\mathbf{a}_1 + \mathbf{a}_2)/2]$ from layer to layer, and the layer spacing is $d = a/2\sqrt{2}$. Because the inelastic collision damping leads to complex $\mathbf{k}_\perp(\mathbf{q}, E)$, the series in (45) is a simple geometrical one with the sum

$$S(\mathbf{k}' - \mathbf{k}) = \delta_{\mathbf{k}'_\parallel, \mathbf{k}_\parallel + \mathbf{g}} [1 - R(0, \mathbf{g}, E)]^{-1} \quad (48)$$

$$\begin{aligned} R(\mathbf{g}, \mathbf{g}', E) = & \exp \{ i [k_{\perp 1}(\mathbf{g}, E) + k_{\perp 1}(\mathbf{g}', E)] d \} \\ & \times \exp \{ - [k_{\perp 2}(\mathbf{g}, E) + k_{\perp 2}(\mathbf{g}', E)] d \} \\ & \times \exp \{ - i(\mathbf{g} + \mathbf{g}') \cdot \mathbf{d}_0 \} \end{aligned} \quad (49)$$

Equation (48) predicts an interference function which exhibits maxima near energies which satisfy

$$\text{Re} \{ [k_{\perp}(0, E) + k_{\perp}(\mathbf{g}, E)] d \} - \mathbf{g} \cdot \mathbf{d}_0 = 2\pi n \quad (50)$$

which are the n th-order "primary" Bragg peaks indicated schematically in Fig. 7. In geometrical terms, this is the condition that

$$\mathbf{k} - \mathbf{k}' = \mathbf{G} \quad (51)$$

where \mathbf{G} is a reciprocal lattice vector of the full three-dimensional lattice.

Summarizing, from (39), (43), and (48) we obtain the expression for the Born approximation to the elastic differential electron-solid cross-section:

$$\frac{d\sigma}{d\Omega} = \left| \frac{m}{2\pi\hbar^2} v[\mathbf{g}, k_{\perp}^+(0, \mathbf{g})] \right|^2 [N \delta_{\mathbf{k}'_\parallel - \mathbf{k}_\parallel, \mathbf{g}}]^2 \frac{1}{|1 - R(0, \mathbf{g}, E)|^2} \quad (52a)$$

$$v(\mathbf{g}, k_{\perp}) = \int d^3r e^{-i\mathbf{g} \cdot \mathbf{r}} e^{-ik_{\perp} z} v(\mathbf{r}, z) \quad (52b)$$

$$k_{\perp}^+(\mathbf{g}, \mathbf{g}') \equiv k_{\perp}(\mathbf{g}, E) + k_{\perp}(\mathbf{g}', E) \quad (52c)$$

in which $R(\mathbf{g}, \mathbf{g}', E)$ is given by (49). Two main features are evident from (52). The existence of discrete final beams at fixed values of \mathbf{k}'_\parallel is the cause of the discrete spot pattern illustrated in Figs. 1 and 7. The occurrence of the $|1 - R|^{-2}$ factor in (52a) is the origin of the primary Bragg peaks noted in the intensity profile shown in Fig. 7. The widths of these peaks are determined in the Born approximation solely by the imaginary part of the $k_{\perp}(\mathbf{g}, E)$. A proper multiple-scattering analysis predicts considerably larger widths because broad maxima which "appear" to be primary Bragg peaks are comprised of several overlapping multiple-scattering maxima.^{6,255}

D. Correspondence between Calculated and Measured Intensities: Instrumental Effects

In principle, the coefficient of the square of the parallel momentum Kroneker delta in (52a) is a direct measure of the intensity of a diffracted beam [labeled by the Miller indices (hk) defined in Fig. 1] as a function of the incident beam parameters (E, θ, ϕ). In practice, a host of considerations associated with the design of the experimental apparatus intervenes. In this section we enumerate the most important of these and indicate their order of magnitude. Their detailed consequences can be evaluated only in the case of a specific instrument.

The electron gun which constitutes the source of incident electrons is characterized by two parameters. The energies of the electrons that it produces are contained within a range of width ΔE . For most electron guns this range is determined by the thermal spread of electrons emitted by the gun: that is, $\Delta E \sim 3\kappa T/2 \sim 0.1$ to 0.5 eV. Moreover, the source of electrons is of finite size, subtending an angle β at the target as illustrated in Fig. 10. For typical instruments $\beta \sim 0.001$ to 0.01 radians (i.e., sources of diameter $d \sim 0.5$ to 1 mm at distances $R \sim 10$ to 50 cm from the target).

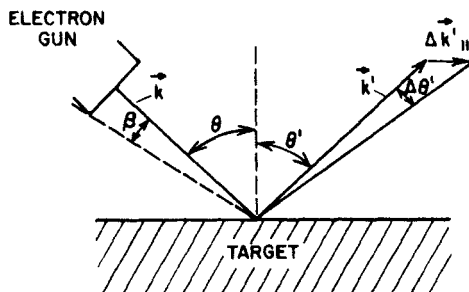


Fig. 10. Schematic indication of the angle β subtended by the source at the target and of the conversion from uncertainties Δk in momenta to uncertainties $\Delta \theta'$ in exit angle.

Because of the limited temporal coherence of the source (described by ΔE) and the incoherence of electrons emitted from different spatial points on it, the area of the target over which an incident electron wave is coherent, called the *coherence zone*, is finite.^{256,257} The uncertainty in k_{\parallel} caused by the spread in energy of the incident electrons is

$$\Delta k_{\parallel} = \left(\frac{m \Delta E}{\hbar^2 k} \right) \sin \theta = 2\pi \left[\frac{E(\text{eV})}{150} \right]^{1/2} \frac{\Delta E \sin \theta}{2E} \quad (53a)$$

The corresponding uncertainty associated with the extended source is

$$\Delta k_{\parallel} = k\beta \cos \theta = 2\pi \left[\frac{E \text{ (eV)}}{150} \right]^{1/2} \beta \cos \theta \quad (53b)$$

If both sources of uncertainty in \mathbf{k}_{\parallel} can be described by Gaussian momentum distributions, then the total uncertainty from the two is given by

$$\Delta k_{\parallel} = \left[\frac{k^2}{4} \left(\frac{\Delta E}{E} \right)^2 \sin^2 \theta + k^2 \beta^2 \cos^2 \theta \right]^{1/2} \quad (54)$$

The diameter Δx of the coherence zone is estimated from the uncertainty principle to be

$$\Delta x = \frac{2\pi}{\Delta k_{\parallel}} = \lambda \left[\left(\frac{\Delta E}{2E} \right)^2 \sin^2 \theta + \beta^2 \cos^2 \theta \right]^{-1/2} \quad (55)$$

in which $\lambda = 2\pi/k$ is the wavelength of the incident electron ($\lambda = 1 \text{ \AA}$ at $E = 150 \text{ eV}$). At modest energies ($E \geq 50 \text{ eV}$) near normal incidence we can neglect the temporal coherence term to estimate $\Delta x \sim \lambda/\beta \sim 50$ to 500 \AA . Therefore we find that low-energy electron diffraction is sensitive to the state of order over very small areas of the sample (containing, e.g., as few as 1000 atoms). This fact is sometimes expressed in the literature by remarks to the effect that LEED "enhances" the apparent perfection of a surface: that is, if any small flat crystalline areas do exist on a given sample, a diffraction pattern will be created by these areas and only by them. Consequently, LEED is a technique for measuring the atomic structure, not the topography, of a surface.

Two additional instrumental effects need to be considered in the interpretation of measured LEED intensities. The finite diameter of the detector causes the detector to subtend an angle β' at the surface (analogous to β for the electron gun illustrated in Fig. 10). This effect causes an uncertainty in \mathbf{k}_{\parallel}' given by

$$\Delta k_{\parallel}' = 2\pi \left[\frac{\Delta E \text{ (eV)}}{150} \right]^{1/2} \frac{\Delta E \sin \theta'}{2E} \quad (56)$$

In addition, however, the finite diameter of the incident beam as it

impinges on the surface gives rise to an uncertainty in k'_{\parallel} as well as k_{\parallel} . If this beam diameter is taken to be the projection of the source on the sample, we obtain

$$\Delta k'_{\parallel} = \left(\frac{kd}{R'} \right) \left(\frac{\cos \theta'}{\cos \theta} \right) = 2\pi \left[\frac{E \text{ (eV)}}{150} \right]^{1/2} \beta \left(\frac{R}{R'} \right) \frac{\cos \theta'}{\cos \theta} \quad (57)$$

in which d is the source diameter and R (R') is the distance of the source (detector) from the point of impact of the beam on the surface of the sample.

Equations (53), (56), and (57) express instrumental uncertainties in the initial and final momenta parallel to the surface. In an actual instrument, these fluctuations "smear out" the parallel momentum delta function derived in (40). Consequently, the measured intensities do not correspond directly to those obtained from a model calculation like (52). Typically the instrument discards some of the predicted intensity by virtue of the collector being too small to observe all of the scattered intensity associated with a given beam. Moreover, it is evident from (53), (56), and (57) that the magnitude of the resulting discrepancy can depend sensitively on the incident and exit beam parameters—a result that always should be considered when evaluating comparisons between measured and calculated intensities in which these instrumental effects have not been removed from the raw intensity data.

E. Inelastic Electron-Solid Collisions

An incident electron in the energy range of interest in low-energy electron diffraction, $10 \text{ eV} \leq E \leq 10^3 \text{ eV}$, creates both electronic ($\hbar\omega_{\text{el}} \sim 10 \text{ eV}$) and atomic ($\hbar\omega_{\text{ph}} \sim 0.01 \text{ eV}$) excitations of the target.²¹ In addition, the energy uncertainty of the incident beam, $\Delta E \sim 0.5 \text{ eV}$, in a typical low-energy electron diffraction instrument satisfies the inequality

$$\hbar\omega_{\text{el}} \gg \Delta E \gg \hbar\omega_{\text{ph}} \quad (58)$$

Therefore in most instruments electronic excitations of the solid are associated with clearly resolved inelastic scattering cross-sections, whereas atomic excitations lead to inelastic electron scattering events that cannot be distinguished from elastic processes. The resulting asymmetry in the view of these two kinds of excitations afforded by LEED has already been indicated in Sections II.E and II.F. This section is devoted to a description of the manifestations of these excitations in inelastic low-energy electron diffraction intensities and the conservation laws which govern them. Section III.A.1 contains the necessary definitions of the

variables and geometries used in this description.

A schematic diagram of an ILEED experiment is shown in Fig. 11. For a given position of the gun generating incident electrons of fixed (and controllable) energy, the scattered electrons are detected by a movable collector which contains a retarding grid, phase-sensitive-detection apparatus. The measured quantity is the intensity $I_{hk}^{E,\theta'}$ ($w \equiv E - E'$) scattered into a particular final angle. A typical $I_{hk}^{E,\theta'}(w)$ curve (i.e., loss profile) for scattering angles near the elastic diffraction condition is indicated in Fig. 11. Its similarities to the angular integrated loss spectrum shown in Fig. 4 are evident. Since typical experimental resolutions are

$$\Delta E \sim 0.5 \text{ eV} \quad (59a)$$

it is not possible to resolve elastic scattering from the inelastic scattering "assisted" by quanta of lattice vibrational energy (i.e., phonons). The

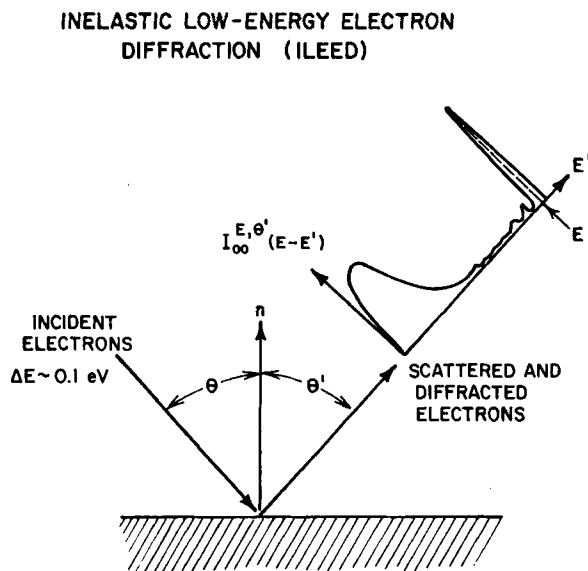


Fig. 11. Schematic diagram of the experimental arrangement for an ILEED measurement. The energies E of the incident electrons lie in the range $10 \text{ eV} < E < 10^3 \text{ eV}$. The scattering cross-sections are determined by the number of electrons with energy $E' < E$, that is, $I_{hk}^{E,\theta'}(E-E')$, scattered into a given solid angle $d\Omega'$ at the final-state polar (θ') and azimuthal (ψ') angles. A schematic curve for $I_{00}^{E,\theta'}(E-E')$ when $\theta' \approx \theta$ is shown in the figure. This curve is characteristic of inelastic diffraction which occurs when $\mathbf{k}_{\parallel}' \approx \mathbf{k}_{\parallel} + \mathbf{g}(hk)$. For a general direction (θ', ψ') only the low-energy "true secondary" peak described in Fig. 4 occurs for scattering from a single-crystal surface.

instrument measures the quasielastic scattering cross-sections

$$\left(\frac{d\sigma}{d\Omega} \right)_{qe} = \int_{\Delta E/2}^{\Delta E/2} dw \left(\frac{d^2\sigma}{d\Omega dw} \right) \quad (59b)$$

Consequently, the large “quasielastic” peak in the measured intensity for $E' \cong E$ ($E - E' \equiv w \sim 0$) contains electrons arising from both elastic and phonon-assisted scattering events. The fine structure indicated just below the quasielastic peak, that is at $w \sim 10$ to 20 eV, is called the discrete—or “characteristic”—loss region of the loss profile. It consists of electrons that have scattered inelastically by creating a small number (usually one) of electronic excitations of the solid. The large low-energy maximum is referred to as the true secondary region of the profile consisting of “secondary” electrons emitted from the solid following their excitation by the incident electron. The Auger electron fine structure (see, e.g., Fig. 4) is not shown in Fig. 11.

Turning to our discussion of the consequences of the appropriate conservation laws, we see in Fig. 12 a schematic diagram of an inelastic electron reflection process. An incident electron of energy E and component of momentum parallel to the surface, \mathbf{k}_{\parallel} , is reflected back from the surface with energy

$$E' = E - w \quad (60a)$$

and momentum parallel to the surface

$$\mathbf{k}'_{\parallel} = \mathbf{k}_{\parallel} - \mathbf{p}_{\parallel} + \mathbf{g} \quad (60b)$$

In (60) \mathbf{p}_{\parallel} is the momentum parallel to the surface of the excitation(s) of the solid responsible for the electron's energy loss w , and \mathbf{g} is a reciprocal lattice vector associated with the translational symmetry of the planes of ion-cores in the target solid parallel to its surface.

If we assume that both w and $\mathbf{k}'_{\parallel} - \mathbf{k}_{\parallel}$ are known precisely and that only a single excitation of the solid is created by the incident electron, then we can draw some general conclusions from the conservation laws independent of the detailed dynamics of the electron-solid interaction. Consider first the case of a bulk excitation of the solid characterized by the dispersion relation

$$w = \hbar\omega_b(\mathbf{p}_{\parallel}, p_{\perp}) \quad (61)$$

The excitation's momentum parallel to the surface, \mathbf{p}_{\parallel} , is determined from momentum conservation. Thus, in general, if $w > \hbar\omega_b(0)$, there exists an

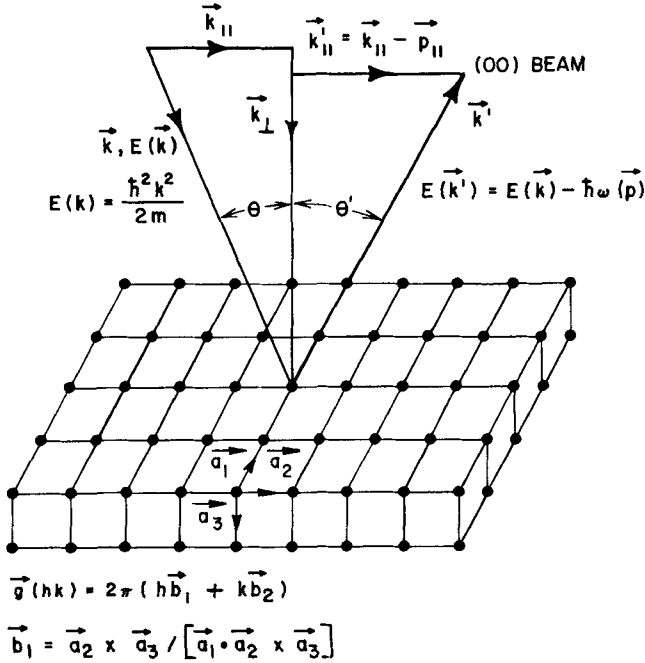
KINEMATICS OF INELASTIC LOW-ENERGY
ELECTRON DIFFRACTION

Fig. 12. Schematic diagram of the kinematics for an electron loss process in which an excitation of parallel momentum $\vec{p}_{||}$ and energy $\hbar\omega(\vec{p})$ is excited.

excitation of energy w whose momentum normal to the surface, p_{\perp} , is specified by (61). The conservation of momentum normal to the surface plays no obvious role in this process because the symmetry of the solid in this direction is broken by the surface. This fact suggests that the excitation of bulk loss processes (e.g., in the quasielastic or characteristic loss regions of the energy-loss profile shown in Fig. 11) merely broadens the angular width of scattered beam relative to that width which is characteristic of elastically scattered electrons.

In the case of surface excitations, the loss mode dispersion relation is of the form

$$w = \hbar\omega_s(\vec{p}_{||}) \quad (62)$$

The quantity $\vec{p}_{||}$ is determined by momentum conservation. If w is fixed and the detector angle is varied, a surface loss will be observed only at

those angles for which (60b) and (62) are satisfied simultaneously. Therefore the excitation of surface modes causes a conelike distribution of inelastically scattered electrons such that the axis of the cone is the "inelastic specular" direction defined by

$$\mathbf{k}'_{\parallel} = \mathbf{k}_{\parallel} + \mathbf{g} \quad (63a)$$

$$E' = E - \hbar\omega_s(0) \quad (63b)$$

The considerations given above presume a measuring instrument which exhibits infinitely good angular and energy resolution. In practice, the angular resolution ($\Delta\theta \sim 1^\circ$) of existing spectrometers is consistent with this presumption. For phonon excitations, however, $w \cong \hbar\omega_{\text{ph}} \sim 10$ meV, whereas in most cases the energy resolution of slow-electron spectrometers is $\Delta E \sim 500$ meV $\gg \hbar\omega_{\text{ph}}$. Therefore phonon-assisted diffraction appears as part of the quasielastic peak and is significant in determining the angular profile of electrons in this peak. Phonon-assisted processes also lead to the introduction of a temperature dependence of the "elastically" scattered intensities. The physical origin of this temperature dependence is the phonon-assisted scattering of the incident electrons outside the angular aperture of the detector. If both the angular aperture and energy resolution are of such magnitudes that phonon-assisted scattering from wide regions of the Brillouin zone are observed as "elastic" events, then the measured intensity profiles become almost independent of temperature and the angular dependence of the beam intensity is no longer a meaningful observation.²⁵⁸

In summary, existing LEED spectrometers exhibit enough angular resolution to examine the consequences of parallel momentum conservation in all cases of inelastic diffraction. Moreover, their energy resolution suffices to determine those of energy conservation for electronic excitations. In analyzing LEED from a vibrating lattice, however we must incorporate in the theory an explicit consideration of the fact that $\Delta E \gg \hbar\omega_{\text{ph}}$. We discuss this topic in the following section, deferring until Part VI our examination of ILEED via the creation of large-energy ($w \sim 10$ eV) electronic excitations in the target.

F. Quasielastic Diffraction from a Vibrating Lattice: Born Approximation

This section is devoted to an outline of the calculation of the quasielastic scattering cross-section of low-energy electrons from a vibrating lattice of

ion-cores. The model Hamiltonian describing this system is given by (20) to (26). The calculation is performed using the Born approximation for the scattering of the incident electron from each ion-core. Within this approximation, however, closed-form expressions are obtained for both the inelastic and quasielastic scattering cross-sections describing the emission and adsorption of an arbitrary number of phonons (i.e., energy quanta associated with the normal modes of the lattice) by an incident electron. Our analysis is a special case of a computational technique known as linear response theory.²⁵⁹ It provides the analogue for a vibrating lattice of the rigid-lattice Born approximation calculation presented in Section III.C: the simplest possible example of the evaluation of low-energy electron diffraction intensities. We proceed by first deriving suitable expressions for the inelastic differential scattering cross-sections, then reducing these formulas to the corresponding ones for the quasielastic cross-sections [(59)], and finally discussing applications of the results to the analysis of beam widths and to the extraction of values of $\langle u^2 \rangle_T$ for surface scatterers from observed LEED intensities.

In terms of the Hamiltonian specified by (20) to (26), the Born approximation to the differential inelastic scattering cross-section for scattering by an angle (θ, φ) with energy loss w is given by⁸³

$$\left(\frac{d^2\sigma}{d\Omega dw} \right)_{fi} = \left(\frac{E-w}{E} \right)^{1/2} \left(\frac{m}{2\pi\hbar^2} \right)^2 |\langle \mathbf{k} + \mathbf{q}, f | V | \mathbf{k}, i \rangle|^2 \delta(w - E_i + E_f) \quad (64)$$

The electron makes a transition from a state (\mathbf{k}, E) to the state $(\mathbf{k} + \mathbf{q}, E - w)$, while the lattice makes a transition from the state $|i\rangle$ to the state $|f\rangle$. Thus the initial and final wave functions are

$$\psi_i = \exp(i\mathbf{k} \cdot \mathbf{r}) \varphi_i \{ \mathbf{R} \} \quad (65a)$$

$$\psi_f = \exp[i(\mathbf{k} + \mathbf{q}) \cdot \mathbf{r}] \varphi_f \{ \mathbf{R} \} \quad (65b)$$

The $\{ \mathbf{R} \}$ denote a complete set of variables describing the crystal. In the present case, they consist of a set of equilibrium positions for the ion-cores, $\{ \mathbf{R}_n^{(0)} \}$, and occupation numbers of the phonons associated with the lattice displacements, \mathbf{u}_n , as defined by (20) and (21).

In terms of the electron-lattice interaction, (18c) and (23), and the lattice

displacement operators, (21), we obtain the expression for the matrix elements of V in a plane-wave basis:

$$\begin{aligned}\langle \mathbf{k} + \mathbf{q}, f | V | \mathbf{k}, i \rangle &= \int d\{\mathbf{R}\} \int d\mathbf{r} e^{-i(\mathbf{k} + \mathbf{q}) \cdot \mathbf{r}} \bar{\varphi}_f\{\mathbf{R}\} \sum_n v(\mathbf{r} - \mathbf{R}_n) e^{i\mathbf{k} \cdot \mathbf{r}} \varphi_i\{\mathbf{R}\} \\ &= v(\mathbf{q}) \int d\{\mathbf{R}\} \bar{\varphi}_f\{\mathbf{R}\} \sum_n e^{-i\mathbf{q} \cdot \mathbf{R}_n} \varphi_i\{\mathbf{R}\} \\ &\equiv v(\mathbf{q}) \langle f | \sum_n e^{-i\mathbf{q} \cdot \mathbf{R}_n} | i \rangle\end{aligned}\quad (66)$$

In deriving the final form of (66) we assumed that all of the ion-cores have the same potential form factor $v(\mathbf{q})$. More generally we must use form factors which depend on the site index:

$$\langle \mathbf{k} + \mathbf{q}, f | V | \mathbf{k}, i \rangle = \sum_n v_n(\mathbf{q}) \langle f | e^{-i\mathbf{q} \cdot \mathbf{R}_n} | i \rangle \quad (67)$$

Equation (66) does not specify the experimentally measured differential inelastic electron scattering cross-section for two reasons. First, the final state only of the electron is observed in the experiment. Therefore the lattice may be in any final state consistent with a momentum-energy transfer of (\mathbf{q}, w) to the electron. Consequently, we must sum (64) over the final state "f" indices of the lattice. Second, the lattice was not in a given state prior to the scattering event but was in an incoherent superposition of such states characteristic of its temperature T . Thus in (64) we must average over the initial-state indices, in accordance with

$$\langle M \rangle_T \equiv \sum_i \langle i | M | i \rangle \frac{e^{-E_i/\kappa T}}{Z} \quad (68a)$$

$$Z = \sum_i e^{-E_i/\kappa T} \quad (68b)$$

Performing these two operations leads to the final expression for the observed differential inelastic electron scattering cross-section:

$$\begin{aligned}\frac{d^2\sigma}{d\Omega d\omega} &= \left[\frac{E - w}{E} \right]^{1/2} \left[\frac{m}{2\pi\hbar^2} \right]^2 \sum_{fi} e^{-E_i/\kappa T} \delta(w - E_i + E_f) \\ &\times |\langle f | \sum_n v_n(\mathbf{q}) e^{-i\mathbf{q} \cdot \mathbf{R}_n} | i \rangle|^2 Z^{-1}\end{aligned}\quad (69)$$

If we could remove the delta function in energy, we could use the final-state completeness relation to remove the sum over “ f ” in (69). This objective may be achieved by using the integral representation for the delta function:

$$\delta(E) = \frac{1}{2\pi\hbar} \int_{-\infty}^{\infty} e^{-iEt/\hbar} dt \quad (70)$$

and noting that the E_i and E_f are eigenvalues of the lattice Hamiltonian, (21b), that is,

$$H_L \Phi_\alpha \{\mathbf{R}\} = E_\alpha \Phi \{\mathbf{R}\} \quad (71)$$

Consequently, we may write (69) as

$$\begin{aligned} \frac{d^2\sigma}{d\Omega dw} &= \left[\frac{E-w}{E} \right]^{1/2} \left[\frac{m}{2\pi\hbar^2} \right]^2 \frac{1}{2\pi\hbar} \int_{-\infty}^{\infty} dt e^{-iwt/\hbar} \\ &\times \sum_{fi} \langle i | e^{iE_i t/\hbar} \sum_m \bar{v}_m(\mathbf{q}) e^{i\mathbf{q}\cdot\mathbf{R}_m} e^{-iE_f t/\hbar} | f \rangle \langle f | \sum_n v_n(\mathbf{q}) e^{-i\mathbf{q}\cdot\mathbf{R}_n} | i \rangle \frac{e^{-E_i/\kappa T}}{Z} \\ &= \left[\frac{E-w}{E} \right]^{1/2} \left[\frac{m}{2\pi\hbar^2} \right]^2 \frac{1}{2\pi\hbar} \int_{-\infty}^{\infty} dt e^{-iwt/\hbar} \sum_{m,n} \bar{v}_m(\mathbf{q}) v_n(\mathbf{q}) \\ &\times \langle e^{i\mathbf{q}\cdot\mathbf{R}_m(t)} e^{-i\mathbf{q}\cdot\mathbf{R}_n(0)} \rangle_T \end{aligned} \quad (72)$$

The second line of (72) is obtained from the first line by using

$$\begin{aligned} \langle i | e^{iE_i t/\hbar} e^{i\mathbf{q}\cdot\mathbf{R}_m} e^{-iE_f t/\hbar} | f \rangle &= \langle i | e^{iH_L t/\hbar} e^{i\mathbf{q}\cdot\mathbf{R}_m} e^{-H_L t/\hbar} | f \rangle \\ &\equiv \langle i | e^{-i\mathbf{q}\cdot\mathbf{R}_m(t)} | f \rangle \end{aligned}$$

in which $\mathbf{R}_m(t)$ is given by (20) and (21). Stated in words, the final form of (72) is constructed by introducing the Heisenberg representation for the lattice position operators:

$$A(t) \equiv e^{iH_L t/\hbar} A e^{-iH_L t/\hbar} \quad (73)$$

From now on we suppress the superscript (0) on the equilibrium positions of the ion-cores.

The reason that it is convenient to write the cross-section in the form of (72) is that for harmonic oscillator systems the thermal average can be evaluated in closed form. In the case of a monatomic lattice the final result is given by⁸³

$$\frac{d^2\sigma}{d\Omega dw} = \left(\frac{E-w}{E} \right)^{1/2} \left(\frac{m}{2\pi\hbar^2} \right)^2 \left(\frac{1}{2\pi\hbar} \right) \times \sum_{m,n} \bar{v}_m(\mathbf{q}) v_n(\mathbf{q}) e^{i\mathbf{q}\cdot(\mathbf{R}_m - \mathbf{R}_n)} \int dt e^{-i\omega t/\hbar} e^{-Q_{mn}(t)} \quad (74a)$$

$$Q_{mn}(t) = \frac{\hbar^2 q^2}{2MN} \sum_{\mathbf{p}, \lambda} [\hbar\omega_\lambda(\mathbf{p})]^{-1} [-i \sin[\theta_{mn}(t)]] + \{1 - \cos[\theta_{mn}(t)]\} \{2N[\omega_\lambda(\mathbf{p})] + 1\} \quad (74b)$$

$$\theta_{mn}(\mathbf{p}, t) = \omega_\lambda(\mathbf{p})t + \mathbf{p} \cdot (\mathbf{R}_m - \mathbf{R}_n) \quad (74c)$$

$$N(\omega) = [\exp(\hbar\omega/\kappa T) - 1]^{-1} \quad (74d)$$

This expression gives the inelastic electron scattering cross-section accurate to second order in the $v(\mathbf{q})$ but to all orders in the electron-phonon interaction as described by the rigid-ion model. Strictly speaking, (74) are valid only for bulk phonons. The extension to include surface vibrations, however, is tedious but routine^{212,260,261} and need not concern us here.

It is appropriate to note at this point that if the potential form factors $v_m(\mathbf{q})$ are independent of the atomic position index, the electron scattering properties factor out of the expression for the cross-section, giving

$$\frac{d^2\sigma}{d\Omega dw} = \left(\frac{E-w}{E} \right)^{1/2} \left(\frac{m}{2\pi\hbar^2} \right)^2 \frac{1}{\hbar} |v(\mathbf{q})|^2 S(\mathbf{q}, w) \quad (75a)$$

$$S(\mathbf{q}, w) \equiv \frac{1}{2\pi} \int_{-\infty}^{\infty} dt e^{-i\omega t/\hbar} \sum_{n,m} \langle e^{i\mathbf{q}\cdot\mathbf{R}_m(t)} e^{-i\mathbf{q}\cdot\mathbf{R}_n(0)} \rangle_T \\ = \sum_{n,m} e^{i\mathbf{q}\cdot(\mathbf{R}_m - \mathbf{R}_n)} \int_{-\infty}^{\infty} \frac{dt}{2\pi} e^{-i\omega t/\hbar} e^{-Q_{mn}(t)} \quad (75b)$$

The quantity $S(\mathbf{q}, w)$ is the well-known pair correlation function.⁸³ It

describes the linear response of the atomic lattice to a time-dependent potential of wave vector \mathbf{q} and frequency $\omega = w/\hbar$.

In order to extract from (75) the expression for the elastic scattering cross-section, we decompose $Q_{mn}(t)$ into its time-independent and time-dependent terms:

$$Q_{mn}(t) = 2W(\mathbf{q}) - F_{mn}(t) \quad (76a)$$

$$W(\mathbf{q}) = \left(\frac{\hbar^2 q^2}{4M} \right) \frac{1}{N} \sum_{\mathbf{p}, \lambda} \frac{2N [\omega_\lambda(\mathbf{p})] + 1}{\hbar \omega_\lambda(\mathbf{p})} \quad (76b)$$

$$F_{mn}(t) = \left(\frac{\hbar^2 q^2}{2M} \right) \frac{1}{N} \sum_{\mathbf{p}, \lambda} [\hbar \omega_\lambda(\mathbf{p})]^{-1} \{ (1 + N[\hbar \omega_\lambda(\mathbf{p})]) \\ \times \exp[i\theta_{mn}(t)] + N[\hbar \omega_\lambda(\mathbf{p})] \exp[-i\theta_{mn}(t)] \} \quad (76c)$$

The classification of contributions to the cross-section as “s”-phonon terms arises from expanding

$$\exp[-Q_{mn}(t)] = \exp[-2W(\mathbf{q})] \sum_{s=0}^{\infty} \frac{1}{s!} [F_{mn}(\mathbf{q}, t)]^s \quad (77)$$

and identifying the s th-order term with processes associated with s -phonons. For example, the elastic scattering cross-section arises from the $s=0$ term in (77):

$$\left(\frac{d^2 \sigma}{d\Omega d\omega} \right)_{\text{elastic}} = \left(\frac{mN}{2\pi \hbar^2} \right)^2 |v(\mathbf{q}) e^{-W(\mathbf{q})}|^2 |S(\mathbf{q})|^2 \delta(w) \quad (78a)$$

$$S(\mathbf{q}) = \frac{1}{N} \sum_n e^{-i\mathbf{q} \cdot \mathbf{R}_n} \quad (78b)$$

which is identical to the result that would be derived for a rigid lattice, except for the vertex renormalization factor, $\exp[-W(\mathbf{q})]$, that measures the reduction in the total intensity of the elastic scattering due to the occurrence of inelastic scattering. The expression $\exp[-2W(\mathbf{q})]$ is called the Debye-Waller factor.

The single-phonon emission and absorption processes result from the $s=1$ term in (77). The t integral gives energy conservation and the n, m

sums give momentum conservation. We obtain

$$\begin{aligned} \left(\frac{d^2\sigma}{d\Omega dw} \right)_{\text{phonon}} &= \left[\frac{E-w}{E} \right]^{1/2} \left[\frac{mN}{2\pi\hbar^2} \right]^2 |v(\mathbf{q})e^{-w(\mathbf{q})}|^2 \frac{\hbar^2 q^2}{2M} \\ &\times \frac{1}{N} \sum_{\mathbf{p}, \lambda} \frac{1}{\hbar\omega_\lambda(\mathbf{p})} \{ (1 + N[\omega_\lambda(\mathbf{p})]) \delta[w - \hbar\omega_\lambda(\mathbf{p})] |S(\mathbf{p} + \mathbf{q})|^2 \\ &+ |S(-\mathbf{p} + \mathbf{q})|^2 N[\omega_\lambda(\mathbf{p})] \delta[w + \hbar\omega_\lambda(\mathbf{p})] \} \end{aligned} \quad (79)$$

The m, n sums are absorbed in the "phonon-assisted" interference functions

$$S(\pm \mathbf{p} + \mathbf{q}) = \frac{1}{N} \sum_n \exp[-i(\mathbf{q} \pm \mathbf{p}) \cdot \mathbf{R}_n] \quad (80)$$

The first term in (79) describes phonon emission by the electron and the second term describes phonon absorption. The evaluation of both terms has been described in detail by Duke.⁸ Hence, it is not repeated here.

Our next task is the combination of (59), (74), and (76) to construct an expression for the quasielastic scattering cross-section. Recalling from inequality (58) that $\Delta E \gg \hbar\omega_{\text{ph}}$, we can replace the limits in (59b) by infinity and use (74) and (76) for $(d^2\sigma/d\Omega dw)$ to obtain

$$\left(\frac{d\sigma}{d\Omega} \right)_{\text{qe}} = \left(\frac{m}{2\pi\hbar^2} \right)^2 \sum_{m, n} e^{i\mathbf{q} \cdot (\mathbf{R}_m - \mathbf{R}_n)} \bar{v}_m(\mathbf{q}) v_n(\mathbf{q}) e^{-2W(\mathbf{q})} \exp[F_{mn}(t=0)] \quad (81a)$$

$$\begin{aligned} F_{mn}(0) &= \frac{\hbar^2 q^2}{2M} \frac{1}{N} \sum_{\mathbf{p}, \lambda} [\hbar\omega_\lambda(\mathbf{p})]^{-1} \{ (1 + N[\omega_\lambda(\mathbf{p})]) e^{i\mathbf{p} \cdot (\mathbf{R}_m - \mathbf{R}_n)} \\ &+ N[\omega_\lambda(\mathbf{p})] e^{-i\mathbf{p} \cdot (\mathbf{R}_m - \mathbf{R}_n)} \} \end{aligned} \quad (81b)$$

By expanding $\exp[F_{mn}(0)]$ we recover the usually quoted^{258, 260} expressions for the multiphonon scattering of low-energy electrons. The conventional procedure^{258, 260} is to expand $\exp[F_{mn}(t=0)]$ and perform the multiple integrals over (\mathbf{p}, λ) and (m, n) term by term. The contribution to the quasielastic scattering cross-section of the term linear in $F_{mn}(0)$ is called the *thermal diffuse* scattering cross-section. A more complete discussion of sum rules and comparisons with experiment can be found in the literature.⁸

Although (81) provide a useful version of the desired expression for the quasielastic differential cross-section, it is also convenient to rewrite them in a form in which the dependence of the cross-section on the atomic displacements, $\mathbf{u}_n(t)$, is displayed explicitly. To accomplish this objective, we reexamine (72) written in the form

$$\begin{aligned} \frac{d^2\sigma}{d\Omega dw} = & \left(\frac{E-w}{E} \right)^{1/2} \left(\frac{m}{2\pi\hbar^2} \right)^2 \frac{1}{2\pi\hbar} \sum_{m,n} e^{i\mathbf{q}\cdot(\mathbf{R}_m-\mathbf{R}_n)} \bar{v}_m(\mathbf{q}) v_n(\mathbf{q}) \\ & \times \int_{-\infty}^{\infty} dt e^{iwt/\hbar} \langle e^{i\mathbf{q}\cdot\mathbf{u}_m(t)} e^{-i\mathbf{q}\cdot\mathbf{u}_n(0)} \rangle_T \end{aligned} \quad (82)$$

Using standard combinatorial techniques,⁹ the thermal average in (82) can be reduced to a form equivalent to (74):

$$\langle e^{i\mathbf{q}\cdot\mathbf{u}_m(t)} e^{-i\mathbf{q}\cdot\mathbf{u}_n(0)} \rangle_T = e^{-W_m(\mathbf{q},t)} e^{-W_n(\mathbf{q},0)} \exp[i\mathbf{q}\cdot\mathbf{D}(m,n,t)\cdot\mathbf{q}] \quad (83a)$$

$$W_m(\mathbf{q},t) = \frac{1}{2} \langle [\mathbf{q}\cdot\mathbf{u}_m(t)]^2 \rangle_T \quad (83b)$$

$$\mathbf{D}(m,n,t) = -i \langle \mathbf{u}_m(t) \mathbf{u}_n(0) \rangle_T \quad (83c)$$

Equation (83b) for $W_m(\mathbf{q})$ is independent of m for bulk phonons, thereby reducing to the factor given by (76b). In the harmonic approximation [i.e., H_L is given by (21b) or its generalization to include surface modes] $W_m(\mathbf{q},t)$ is independent of t , so we shall suppress the time variable by setting $W_m(\mathbf{q},t) \rightarrow W_m(\mathbf{q})$. The quasielastic scattering cross-section is found from (81) to (83) to be given by

$$\begin{aligned} \left(\frac{d\sigma}{d\Omega} \right)_{\text{qe}} = & \left(\frac{m}{2\pi\hbar^2} \right)^2 \sum_{m,n} e^{i\mathbf{q}\cdot(\mathbf{R}_m-\mathbf{R}_n)} \bar{v}_m(\mathbf{q}) e^{-\bar{W}_m(\mathbf{q},0)} v_n(\mathbf{q}) \\ & \times e^{-W_n(\mathbf{q},0)} \exp[i\mathbf{q}\cdot\mathbf{D}(m,n,0)\cdot\mathbf{q}] \end{aligned} \quad (84)$$

In the case that only bulk phonons are included in the lattice vibration Hamiltonian H_L and all of the $v_m(\mathbf{q})$ are taken to be the same, (84) is identical with (81) provided we select

$$D_{\alpha\beta}(m,n,0) = \left(\frac{-i\hbar}{2MN} \right) \delta_{\alpha\beta} \sum_{\mathbf{p}} \frac{1}{\omega(\mathbf{p})} \coth \left[\frac{\hbar\omega(\mathbf{p})}{2\kappa T} \right] \exp[i\mathbf{p}\cdot(\mathbf{R}_m-\mathbf{R}_n)] \quad (85)$$

for the matrix elements of the \mathbf{D} matrix. Since the $W_m(\mathbf{q})$ factors are specified by

$$2W_m(\mathbf{q}) = iq^\alpha D_{\alpha\beta}(m, m, 0)q^\beta \quad (86)$$

it is evident that in the diagonal term in the sum over m and n in (84) the $\exp[iq^\alpha D_{\alpha\beta}(m, m, 0)q^\beta]$ factor precisely cancels the $\exp[-2W_m(\mathbf{q})]$ term in the prefactor.

Equations (81) and (84) are the expressions for the quasielastic scattering cross-section which we sought. Having derived these formulas, we conclude our discussion in this section by applying them to examine the phonon-induced beam width and the temperature dependence of the resulting cross-sections. In particular, we consider the intensities predicted by two quite different models of the lattice vibration spectra. The dispersion relation describing an Einstein phonon spectrum is

$$\omega(\mathbf{p}) = \omega_0, \quad p \leq p_m = (6\pi^2 n)^{1/3} \quad (87)$$

in which n is the atomic density of the model lattice. This model describes optical phonons in solids with more than one atom per unit cell. The dispersion relation describing a Debye phonon spectrum is

$$\omega_\lambda(\mathbf{p}) = v_\lambda p; \quad p \leq p_m \quad (88)$$

for one longitudinal ($\lambda=1$) and two transverse ($\lambda=2,3$) branches. The associated average speed of sound v_s is defined by

$$v_s^{-2} = \frac{1}{3} \sum_{\lambda=1}^3 v_\lambda^{-2} \quad (89)$$

The Debye model describes acoustical phonons. Both the Einstein and Debye models are appropriate only for bulk lattice vibration spectra. They will prove adequate, however, for our purpose of illustrating the qualitative features of phonon-assisted quasielastic diffraction.

Perhaps the most important feature of phonon-assisted quasielastic LEED is its determination of the angular width of the individual scattered beams in the absence of surface disorder. The quasielastic scattering cross-sections associated with Einstein phonons can be evaluated by inspection of (81). Since $\omega(\mathbf{p}) = \omega_0$ is independent of \mathbf{p} , $F_{mn}(0)$ is diagonal in

the m and n indices. Consequently, for a lattice of identical scatterers we obtain

$$\left(\frac{d\sigma}{d\Omega}\right)_{qe} = \left| \frac{mv(\mathbf{q}) \exp[-W(\mathbf{q})]}{2\pi\hbar^2} \right|^2 \left\{ N[\exp[2W(\mathbf{q})] - 1] + \sum_{m,n} \exp[i\mathbf{q} \cdot (\mathbf{R}_m - \mathbf{R}_n)] \right\} \quad (90)$$

The second term in (90) describes the coherent diffraction of the electron from the lattice. It is unaffected by the phonon-assisted scattering events which serve only to cause the incoherent background scattering from the total lattice of N ion cores described by the first term in (90). Thus Einstein phonons extract spectral density from the coherent elastic intensity and place it in a completely incoherent background.

Turning to a consideration of Debye acoustical phonons it is convenient, but not necessary, to work in the high-temperature limit

$$N(\omega) \cong \frac{\kappa T}{\hbar\omega} \quad (91)$$

Direct evaluation of the sum over \mathbf{p} in (81b) gives, for identical scatterers,

$$\left(\frac{d\sigma}{d\Omega}\right)_{qe} = \left| \frac{mv(\mathbf{q}) \exp[-W(\mathbf{q})]}{2\pi\hbar^2} \right|^2 \times \left\{ N \exp[2W(\mathbf{q})] + \sum_{m \neq n} \exp[i\mathbf{q} \cdot (\mathbf{R}_m - \mathbf{R}_n)] \exp\left[\frac{\alpha(\mathbf{q})}{|\mathbf{R}_m - \mathbf{R}_n|}\right] \right\} \quad (92a)$$

$$\alpha(\mathbf{q}) = \frac{\pi W(\mathbf{q})}{2p_m} \quad (92b)$$

Therefore in marked contrast to the case of optical phonons, the emission of multiple low-energy acoustical phonons causes an R^{-1} long-range correlation between ion-cores separated by a distance R . This long-range correlation in the coordinate representation leads to short-range correlations in the momentum representation—that is, to beam broadening.

Unfortunately, the R^{-1} term in the exponent in (92a) has the consequence that the sums over m and n thus far have eluded closed-form

evaluation. The presense of acoustical phonon-induced beam broadening can be demonstrated, however, by formal power series expansion of the exponential in (92a). Using the identity

$$\frac{1}{|\mathbf{R}_m - \mathbf{R}_n|} = 4\pi \int \frac{d^3p}{(2\pi)^3} \frac{\exp[i\mathbf{p} \cdot (\mathbf{R}_m - \mathbf{R}_n)]}{p^2}$$

we can write

$$\begin{aligned} S(\mathbf{q}) &= \sum_{m,n} \exp[i\mathbf{q} \cdot (\mathbf{R}_m - \mathbf{R}_n)] \\ &\times \exp \left\{ 4\pi\alpha(\mathbf{q}) \int \frac{d^3p}{(2\pi)^3} \frac{\exp[i\mathbf{p} \cdot (\mathbf{R}_m - \mathbf{R}_n)]}{p^2} \right\} \\ &= \sum_t S_t(\mathbf{q}) \end{aligned} \quad (93)$$

The sum over t designates terms in the power series expansion of the latter exponent in (92a). For a single layer of N_{\parallel} scatterers we obtain

$$S_0(\mathbf{q}) = N_{\parallel} (2\pi)^2 A^{-1} \delta(\mathbf{q}_{\parallel} - \mathbf{g}) \quad (94a)$$

$$S_1(\mathbf{q}) = \frac{4N_{\parallel}\alpha(\mathbf{q})}{A} \sum_{\mathbf{g}} \frac{1}{|\mathbf{q}_{\parallel} - \mathbf{g}|} \tan^{-1} \left[\frac{p_m}{|\mathbf{q}_{\parallel} - \mathbf{g}|} \right] \quad (94b)$$

$$S_2(\mathbf{q}) \cong \frac{2\pi N_{\parallel}\alpha^2(\mathbf{q})}{A} \sum_{\mathbf{g}} \ln \left[\frac{p_m}{|\mathbf{q}_{\parallel} - \mathbf{g}|} \right] \quad (94c)$$

in which

$$\mathbf{q}_{\parallel} \equiv \mathbf{k}'_{\parallel} - \mathbf{k}_{\parallel} \quad (95)$$

is the momentum transfer parallel to the planar solid surface. The S_2 term is calculated presuming $|\mathbf{q}_{\parallel} - \mathbf{g}|$ to be small in order to isolate the divergence as $|\mathbf{q}_{\parallel} - \mathbf{g}| \rightarrow 0$. The higher order S_t are convergent functions (i.e., $u^{n-2} \ln u$) of $|\mathbf{q}_{\parallel} - \mathbf{g}|$ when $\mathbf{q}_{\parallel} \rightarrow \mathbf{g}$. It is evident from (94), however, that both the one- and two-phonon contributions to $S(\mathbf{q})$ diverge as $\mathbf{q}_{\parallel} \rightarrow \mathbf{g}$, that is, as a reciprocal lattice rod is approached by varying the external beam parameters. Because they result from an infrared catastrophe, these phonon-assisted diffraction divergences are more severe for $\kappa T > \hbar v_s p_m$ than for $\kappa T \lesssim \hbar v_s p_m$. In the low-temperature limit ($\kappa T \ll \hbar v_s p_m$) they are reduced by one order, that is, $S_1(\mathbf{q})$ is proportional to $\ln[p_m/|\mathbf{q}_{\parallel} - \mathbf{g}|]$, whereas $S_2(\mathbf{q})$, being proportional to $|\mathbf{q}_{\parallel} - \mathbf{g}| \ln |\mathbf{q}_{\parallel} - \mathbf{g}|$, converges as $\mathbf{q}_{\parallel} \rightarrow \mathbf{g}$.

These divergences do not disappear when multilayer diffraction is considered. In the case of the single-phonon term (i.e., thermal diffuse scatter-

ing), we obtain for $q_{\parallel} \ll p_m, \kappa T \lesssim \hbar v_s p_m$, the result

$$\left(\frac{d\sigma}{d\Omega} \right)_{\text{qe}}^{\text{tds}} = N_{\parallel} \left[\frac{mv(\mathbf{q}) \exp[-W(\mathbf{q})]}{2\pi\hbar^2} \right]^2 \times \left(\frac{2\pi\alpha(\mathbf{q})}{Aq_{\parallel}} \right) \cdot |1 - \exp[(2ik_{\perp}(0, E) - q_{\parallel})d]|^{-2} \quad (96)$$

for the specular beam (i.e., $\mathbf{q}_{\parallel} = \mathbf{k}'_{\parallel} - \mathbf{k}_{\parallel}$) cross-section predicted by our simple model. The expected [see (76b), (92b), and (94)] and observed²⁶² linear dependence on q^2 , T , and q_{\parallel}^{-1} are all present. A more sophisticated model of the lattice dynamics would change only the numerical constants.²⁶⁰ Note that departures from the specular direction (i.e., $\mathbf{q}_{\parallel} \neq 0$) act to further damp out, not tune, the Bragg resonance associated with coherent multilayer scattering.

From (90), (92), and (96) we discern two types of phenomena associated with phonon-assisted quasielastic diffraction. The flat, higher frequency phonon modes give rise to short-range correlations between atomic scatterers. These correlations extract intensity from the coherent scattering and place it in an incoherent background. The low-frequency (long-wavelength) acoustical modes introduce long-range atomic correlations which emanate from an infrared catastrophe associated with the copious emission of low-energy phonons. Such correlations lead to the broadening of the coherently diffracted electron beams, rather than the enhancement of the incoherent background intensity. Often, however, the instrumental angular resolution $\Delta\theta$ is wider than the phonon-induced beam broadening.¹⁶⁹ In this case the properties of the measuring instrument rather than the physical state of the surface determine the width of the observed angular profile.

A subsidiary consequence of the occurrence phonon-assisted diffraction processes is the removal from the elastic ("zero phonon") scattering cross-section of the intensity associated with the phonon-assisted events. This phenomenon is described by the Debye-Waller factors, $\exp[-2W_m(\mathbf{q})]$. Consequently, the values of $\langle u_m^2 \rangle_T$ associated with surface scatterers can be estimated from the observed temperature dependence of elastic low-energy electron diffraction intensities. For example, in the case of the (00) beam \mathbf{q} is normal to the surface so that

$$W_m(\mathbf{q}) \rightarrow 2|k_{\perp}(0, E)|^2 \langle u_{m\perp}^2 \rangle_T \quad (97)$$

where we used the fact in the presence of inelastic collision damping

$$W_m(\mathbf{q}) = \frac{1}{2} \mathbf{q} \cdot \langle \mathbf{u}_m(0) \mathbf{u}_m(0) \rangle_T \cdot \bar{\mathbf{q}} \quad (98a)$$

$$F_{mn}(t) = -i \mathbf{q} \cdot \mathbf{D}(m, n, t) \cdot \bar{\mathbf{q}} \quad (98b)$$

From (84) we see that if we pick a simple form for $\langle u_{m\perp}^2 \rangle$, for example,

$$\langle u_{m\perp}^2 \rangle_T = \langle u^2 \rangle_T [1 + AF_m] \quad (99)$$

the sums over m and n can be performed numerically provided we neglect thermal diffuse and multiphonon contributions to the quasielastic cross-section. The resulting expression is just the differential elastic scattering cross-section

$$\left(\frac{d\sigma}{d\Omega} \right)_{qe}^{(0)} = \left(\frac{m}{2\pi\hbar^2} \right)^2 \left| \sum_{m=0}^N e^{-i\mathbf{q} \cdot \mathbf{R}_m} v_m(\mathbf{q}) e^{-W_m(\mathbf{q})} \right|^2 \quad (100)$$

Jones et al.¹⁶⁹ performed this calculation for various values of F_n using a form for $k_{\perp 2}(0, E)$ in which $k_{\perp 2}$ linearly decreased with increasing energy E of the incident electrons. The comparison of these calculations with some of their experimental data is shown in Fig. 13. In this figure, the effective value of $\langle u_{m\perp}^2 \rangle$ has been converted into an effective value of the Debye Θ parameter via the use of the Debye spectrum in the high-temperature limit to set [see, e.g., (76b) and (88)]

$$\langle u_{\perp \infty}^2 \rangle = \frac{\hbar^2 T}{M \kappa \Theta_{\infty}^2} \quad (101a)$$

$$\Theta_{\infty} = \frac{\hbar v_s p_m}{\kappa} \quad (101b)$$

in which v_s denotes the average speed of sound defined by (89). All of the atomic scatterers in each layer parallel to the surface [of clean Ag(111) in this case] are taken to exhibit identical vibrational and electronic properties. The various layers are labeled by the index ν which may be regarded as the component normal to the surface of the atomic index m in (100). Inserting (99) into (101) gives

$$\frac{1}{\Theta_{\nu}^2} = \frac{1}{\Theta_{\infty}^2} [1 + AF_{\nu}] \quad (102)$$

which is used to calculate the curves shown in Fig. 13.

The analysis leading to these graphs consists of five steps. First, the intensity profiles associated with one or more beams are measured at several different temperatures. Second, the prominent maxima in these profiles are identified at energies $\{E_p\}$. The intensities of these peaks, that is, $I_{hk}(E_p)$, are plotted on semilog paper as a function of temperature. At sufficiently high temperatures a straight line results. Third, the slopes of these lines [one line for each set of values (h, k, E_p)] are determined. (Figure 13 illustrates data only for $h = k = 0$.) Fourth, from (98), (100), and (101) these slopes, that is, $d[\ln I(E_p)]/dT$, are converted into values of $\langle u_{\text{eff}}^2 \rangle_T$ or Θ_{eff} for each peak individually. The resulting values of Θ_{eff} are the experimental points shown in Fig. 13. Fifth and finally, using a construction like (99) in (98) and (100), kinematical intensity profiles are calculated. The temperature dependence of the peaks in the resulting model intensities for various values of A and functional forms of F_m leads to the solid lines in Fig. 13. These lines are drawn through points obtained from $d[\ln I]/dT$ for the Bragg maxima predicted by (100).

The interpretation of plots like that shown in Fig. 13 of the values of either $\langle u_{\perp}^2 \rangle_{\text{eff}}$ or Θ as a function of the energy of their associated peak in the elastic intensity profile usually involves the three concepts indicated in Fig. 14. First, each point on the plot is obtained by examining the

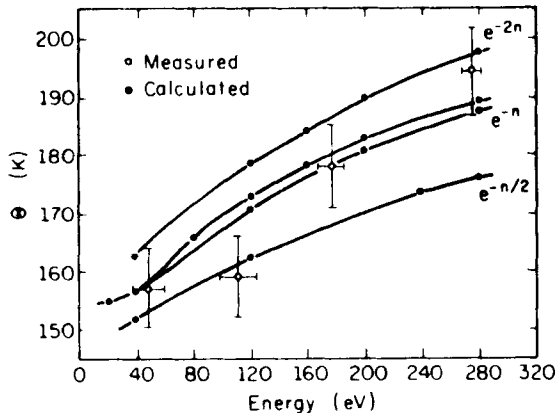


Fig. 13. Comparison of effective Debye temperatures calculated from (100) and (102) in the text with the experimental values (denoted by open circles with error bars) extracted from data by using a model in which all atomic form factors are identical, all atoms have the same $\langle u_{\perp}^2 \rangle_T = \hbar^2 T / M \kappa \Theta^2$, and $k_{\perp 2}(0, E)$ decreases linearly with increasing electron energy. The selection of the F_n and evaluation of $k_{\perp}(0, E)$ are described in detail in Ref. 169. (After Jones et al.¹⁶⁹)

Vibronic Properties of Surface Atoms via ELEED Temperature Dependence

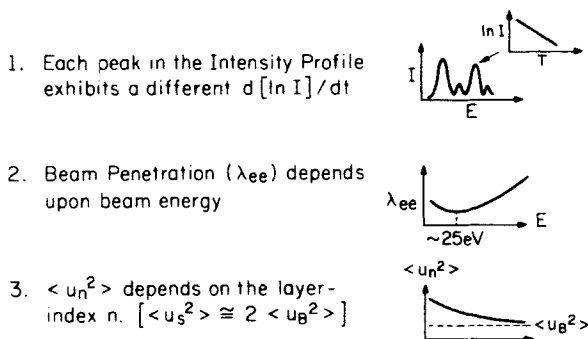


Fig. 14. Schematic indication of the three central concepts used in interpreting plots of the exponential temperature dependence of maxima in ELEED intensity profiles as a function of the energy of the peak.

temperature dependence of a particular peak in the intensity profile as indicated by item 1 in Fig. 14. It is found universally that the higher energy peaks tend to yield smaller values of $\langle u^2 \rangle_{\text{eff}}$ (larger values of Θ). Figure 13 provides an example of this result. The conventional rationalization of these observations is that since with increasing energy the elastic beam of electrons penetrates further into the lattice (item 2, Fig. 14), they are scattered increasingly by bulk rather than surface ion-cores. Hence, the decrease in $\langle u_{\text{eff}}^2 \rangle_T$ with increasing beam energy reflects a decrease in $\langle u_\nu^2 \rangle_T$ with increasing ν (i.e., distance from the surface). This conclusion is indicated by item 3 of Fig. 14. Thus if one knows λ_{ee} and the form factors $v_n(\mathbf{q})$ as a function of energy, then by using the appropriate complex optical potential in (44), for example (28), one can extract the $\langle u_\nu^2 \rangle_T$ from the data by using (100). The solid curves in Fig. 13 are generated in a similar fashion by taking $\lambda_{ee}(E)$ from empirical considerations and the $\langle u_\nu^2 \rangle_T$ from model calculations. The fact that this type of analysis is qualitatively but not quantitatively correct is evident from Fig. 13. Such a conclusion has also been reached by numerous other workers.^{170, 175-194} In particular, the analysis suffers from the fatal flaw that multiple-scattering effects, ignored in linear response calculations, usually are of critical importance in achieving a quantitative description of ELEED intensities.^{6, 8} An example of the consequences of multiple scattering is the fact that an increase in the surface $\langle u_0^2 \rangle_T$ relative to bulk $\langle u^2 \rangle_T$ leads to reduced scattering by the surface atoms and hence increased penetration of the elastic beam inside the solid. In a multiple-scattering analysis, this effect alone provides a decrease in $\langle u_{\text{eff}}^2 \rangle_T$ for peaks in the ELEED intensities at

increasingly larger energy.^{10,199} Therefore the energy dependence of λ_{ee} serves only to complicate, not to cause, the observed trend for the observed $\langle u_{\text{eff}}^2 \rangle_T$ to decrease with increasing peak energy. A critique of the determination of $\langle u_v^2 \rangle_T$ via Born approximation analyses of the temperature dependence of ELEED intensities has been given by Duke.⁸ He finds that from such analyses one can conclude reliably that $\langle u_0^2 \rangle_T \cong 2\langle u_{\text{bulk}}^2 \rangle_T$ but that the extraction of specific values of $\langle u_v^2 \rangle_T$ from those of $\langle u_{\text{eff}}^2 \rangle_T$ can be performed only to within an accuracy of about 25%. The fundamental origin of the large uncertainties in the values of $\langle u_v^2 \rangle_T$ obtained from observed ELEED intensities is the occurrence of multiple elastic scattering phenomena associated with the large electron-ion-core cross-sections (see, e.g., Section II.B.2). Indeed, the complicating effects of multiple scattering are evident in many features of LEED intensities. Therefore we turn to a discussion of them in the next section.

IV. DYNAMICAL THEORY OF ELASTIC ELECTRON-SOLID SCATTERING AT PLANAR SURFACES

A. Motivation

The criterion that a scattering spectroscopy be surface sensitive is mutually exclusive with the requirement that the Born approximation provide an adequate interpretation of the associated cross-sections. As noted in Parts I and II, surface sensitivity and strong particle-solid interactions are inseparable companions. Since strong interactions imply multiple collisions, a dynamical (i.e., multiple-scattering) theory inevitably is needed for the determination of surface structure via scattering and emission spectroscopies.

We demonstrated in Part II that the reflection and emission of "low-energy," $10 \text{ eV} \lesssim E \lesssim 10^3 \text{ eV}$, electrons from surfaces provide a surface-sensitive spectroscopy for the determination of the chemical, geometrical, vibrational, and electronic structure of the outermost 1 to 10 layers of crystalline solids. From Section II.B.2 we recall, however, that although the large ($\sigma \sim 10^{-16} \text{ cm}^2$) inelastic electron-electron cross-sections render these experiments surface sensitive, the correspondingly large ($\sigma \sim 10^{-17} \text{ cm}^2$) elastic electron-ion-core cross-sections require the use of a multiple elastic scattering analysis to evaluate the scattered intensities. Since an analysis of the measured intensities is a necessary prerequisite for the determination of the positions of surface scatterers, surface crystallography constitutes an example of a surface structure spectroscopy that requires an adequate dynamical theory of electron-solid scattering for its successful realization.

Inspection of observed elastic low-energy electron diffraction (ELEED)

intensities often indicates explicitly the necessity of a dynamical theory for their interpretation. An appropriate example is shown in Fig. 15. Experimental elastic intensity profiles²⁶³ for the (00) (i.e., specular) beam of electrons diffracted from the (001) face of LiF are displayed in Fig. 15a. The occurrence of complicated structure in these profiles, not obviously related to the kinematical Bragg peaks considered in Section III.C, is evident from the figure. Such Bragg peaks are evident, however, in the results of the model calculations²⁶⁴ shown in Fig. 15c. The intensity profiles shown in Fig. 15c were calculated using a model in which multiple elastic scattering *within* planar layers of ion-cores was accounted for, but an electron was presumed to scatter once and only once from each layer. Evidently, the calculated profiles shown in Fig. 15c bear little resemblance to the observed ones displayed in Fig. 15a. The dramatic consequences of including in the model multiple scattering between layers are revealed by comparing Fig. 15b with 15c. The complete calculations shown in Fig. 15b, obtained using the isotropic scatterer inelastic collision model,¹⁹ exhibit a much improved correspondence with the measurements. Never-

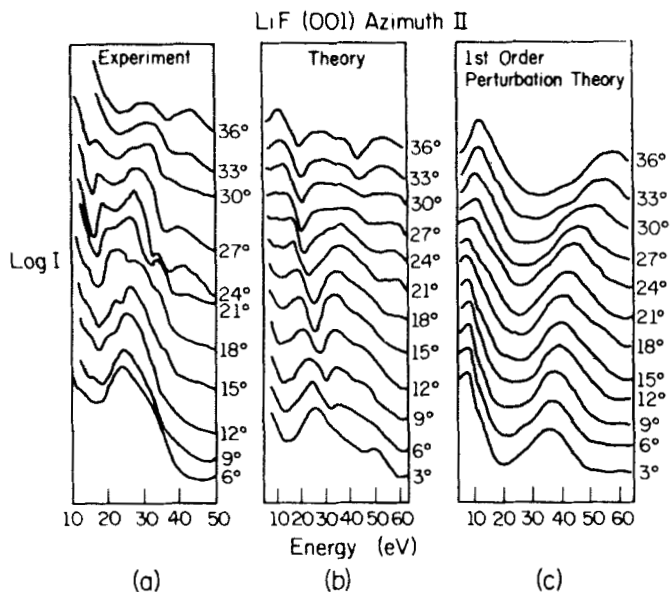


Fig. 15. Analysis of experimental²⁶³ LEED intensities from LiF (a), using a complete multiple-scattering theory (b), and the Born approximation (c). All panels show the logarithm of the specularly reflected intensity as a function of the incident electron's energy. The polar angles of incidence are indicated in the figure. The azimuthal angles are specified in Ref. 263. (After Holland et al.²⁶⁴)

theless, quantitative descriptions of the data require a still more accurate description of the electron-solid force law.²⁶⁵

In addition to the general lack of resemblance between observed intensity profiles and those predicted by the Born approximation, the measured intensities often exhibit fine structure which changes markedly with small variations in the angle or energy of the incident beam. Such an effect for the specular beam of electrons reflected from Cu(100) is illustrated by the doublet shown in Fig. 16. That such structures are associated with coherent

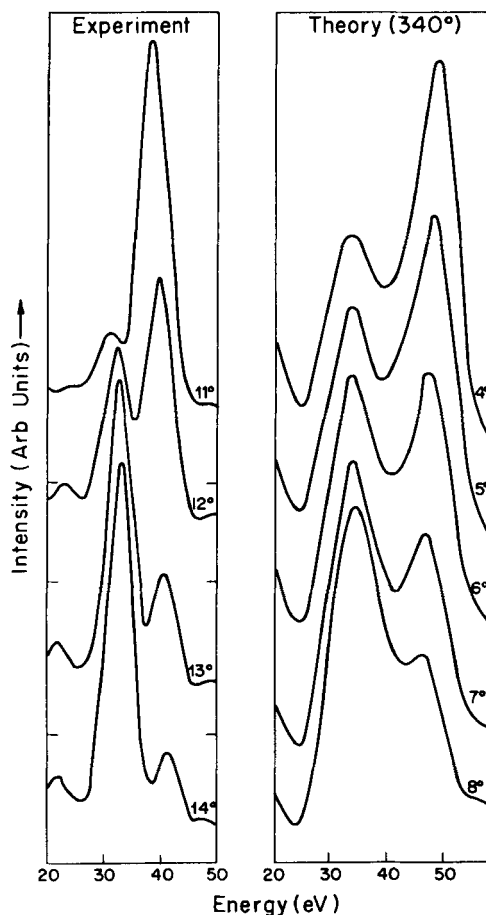


Fig. 16. The intensity-voltage profiles for the (00) beam from Cu(100) for a series of angles of incidence. The zeros for different curves are displaced arbitrarily. The experimental results were taken at room temperature. (After Holland.¹⁹⁸)

multiple-scattering elastic diffraction may be demonstrated either by theoretical arguments^{6,255} or by observing the highly nonkinematical temperature dependence of this doublet^{196,198} as shown in Fig. 17. The results of the model calculations displayed in the right-hand panels of Figs. 16 and 17 reveal that a theory which incorporates the consequences both of inelastic collisions and of multiple elastic scattering phenomena indeed can describe the qualitative features of such observations. Their quantitative description, however, requires a more refined characterization of the electron-solid force law. Nevertheless, Figs. 15 to 17 suffice to illustrate the necessity of incorporating a description of multiple elastic scattering phenomena in any theory of either isothermal ELED intensities or their temperature dependence.

Having convinced ourselves that a consideration of multiple-scattering effects is essential to any microscopic theory of LEED, we next must ask

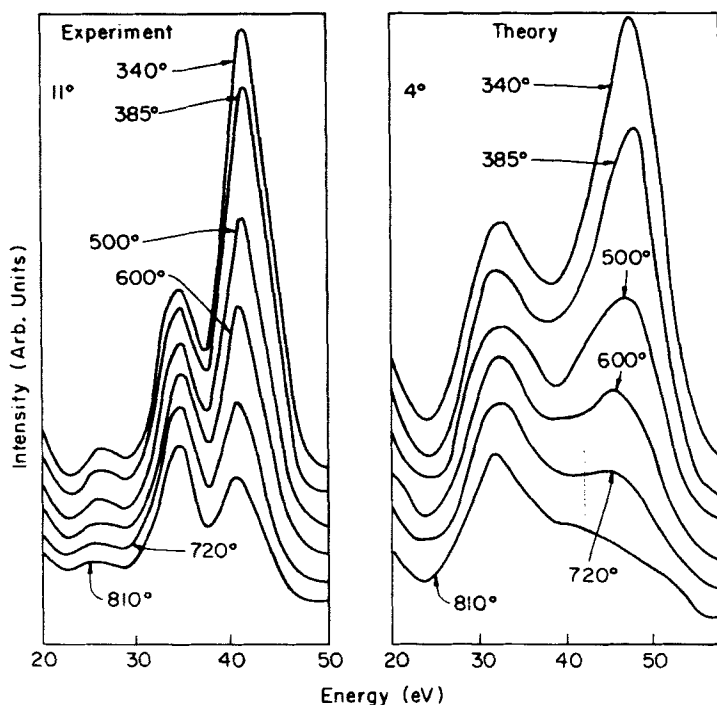


Fig. 17. The effect of temperature changes on an intensity-voltage profile for the (00) beam from Cu(100). Corresponding experimental and theoretical curves refer to the same temperature and have the same base line, but curves for different temperatures have slightly different base lines. (After Holland.¹⁹⁸)

another, in many respects more important, question if we propose to develop LEED as a technique for surface crystallography. "Given the significance of multiple-scattering phenomena in the LEED process, do we know the electronic parameters characterizing the electron-solid interactions with sufficient accuracy to extract structural parameters from an analysis of observed ELEED intensities?" (See also Section III.A.2.) The response to this query depends on two factors: the extent to which the surface is characterized by the other techniques described in Part II and the intrinsic sensitivity of the predicted ELEED intensities to the electronic parameters in the model Hamiltonian. The first factor can be discussed only within the context of analyzing individual experimental measurements. The second is examined in Section V.C which deals with sensitivity analyses. We see, however, that the availability of an adequate dynamical theory of ELEED from planar single-crystal surfaces is a necessary, but not necessarily sufficient, condition for the determination of surface structures. Nevertheless, we shall find in Part VII that after a 40-year delay following Davisson and Germer's vision of LEED as a technique for surface crystallography,¹⁶ within the past two years the theoretical models described in this chapter have been applied successfully for the determination of several structures.

B. Distorted-Wave Multiple-Scattering Analysis

This section is devoted to a brief outline of the nature of the mathematical formalism used in three-dimensional multiple-scattering analyses of elastic low-energy electron diffraction. The details of this formalism need not concern us directly because their specification is not required for the comprehension of either the physical interpretation or the conceptual content of its predictions, and because they are displayed explicitly in a series of papers by Duke and co-workers.^{6, 8—12, 19, 30, 247, 248, 252, 255, 266} It is useful, however, to develop some appreciation of the structure of the theory, of the approximations that must be made in order to reduce the complete formalism to useful computational algorithms for calculating ELEED intensities, and of the complexity of the resulting computer programs used in structure analyses. In this section we explore only the first of these three topics, deferring our consideration of the latter two until Part V in which we discuss specific model calculations.

Let us begin by examining the description of electron-electron interactions by the multiple-scattering formalism. We recall from Section II.B.2 that an incident electron is rather likely to undergo inelastic collisions with the valence electrons in the target. Indeed, an appreciable probability of the excitation of surface plasma oscillations can exist even when the electron is well outside the sample. These features of the electron-solid

force law are included in the cross-section calculation by considering the wave function of the incident electron to be "distorted" by the electron-electron interactions before, in between, and after its multiple elastic scattering by the ion-cores in the solid. This effect is incorporated into the mathematical formalism by considering the motion of an electron of energy E from position \mathbf{r}' to position \mathbf{r} to be described by the distorted-wave propagator, $G_0(\mathbf{r}, \mathbf{r}', E)$, defined by

$$G_0(\mathbf{r}, \mathbf{r}', E) = G_{00}(\mathbf{r}, \mathbf{r}', E) + \int d^3r_1 d^3r_2 G_{00}(\mathbf{r}, \mathbf{r}_1, E) \Sigma(\mathbf{r}_1, \mathbf{r}_2, E) G_0(\mathbf{r}_2, \mathbf{r}', E) \quad (103)$$

$$\left(E - \frac{\hbar^2 \Delta}{2m} \right) G_{00}(\mathbf{r}, \mathbf{r}', E) - \int d^3r_1 V_0(\mathbf{r}, \mathbf{r}_1) G_{00}(\mathbf{r}_1, \mathbf{r}', E) = \delta(\mathbf{r} - \mathbf{r}') \quad (104)$$

in which $\Sigma(\mathbf{r}', \mathbf{r}, E)$ is the retarded proper self-energy or "optical potential" due to electron-electron interactions and $V_0(\mathbf{r}, \mathbf{r}')$ is any prescribed static potential. A rather complete description of the evaluation of $\Sigma(\mathbf{r}', \mathbf{r}, E)$ and $V_0(\mathbf{r}, \mathbf{r}')$ is given by Feibelman et al.³⁰ Roughly speaking $G_{00}(\mathbf{r}, \mathbf{r}', E)$ describes the propagation of an electron in the "best" static one-electron potential in between the ion-cores and $G_0(\mathbf{r}, \mathbf{r}', E)$ includes the additional consequences of inelastic collisions in these regions of the target. The elastic scattering of an electron by the ion-core potentials as well as the electron-electron interactions is described by the complete propagator of the system, $G(\mathbf{r}, \mathbf{r}', E)$, which satisfies the integral equation

$$G(\mathbf{r}, \mathbf{r}', E) = G_0(\mathbf{r}, \mathbf{r}', E) + \int d^3r_1 d^3r_2 G_0(\mathbf{r}, \mathbf{r}_1, E) V_L(\mathbf{r}_1, \mathbf{r}_2) G(\mathbf{r}_2, \mathbf{r}', E) \quad (105)$$

In (105) $V_L(\mathbf{r}, \mathbf{r}')$ is the change in potential caused by decomposing a uniform positive "jellium" background into positive ions of the appropriate charge and position. A multiple-scattering analysis of (105) can be performed if $V_L(\mathbf{r}, \mathbf{r}')$ is of the form

$$V_L(\mathbf{r}, \mathbf{r}') = \delta(\mathbf{r} - \mathbf{r}') \sum_{\mathbf{R}} V_{\mathbf{R}}(\mathbf{r} - \mathbf{R}) \quad (106)$$

The elastic electron-solid cross-section is obtained by examining the asymptotic form of

$$\psi_{\text{scatt}}(\mathbf{r}, E) - \varphi_{\mathbf{k}}(\mathbf{r}) = \int d^3r_1 d^3r_2 G(\mathbf{r}, \mathbf{r}_1, E) V_L(\mathbf{r}_1, \mathbf{r}_2) \varphi_{\mathbf{k}}(\mathbf{r}_2) \quad (107a)$$

$$\varphi_{\mathbf{k}}(\mathbf{r}) = e^{i\mathbf{k} \cdot \mathbf{r}} + \int d^3r_1 d^3r_2 G_{00}(\mathbf{r}, \mathbf{r}_1, E) \Sigma(\mathbf{r}_1, \mathbf{r}_2, E) \varphi_{\mathbf{k}}(\mathbf{r}_2) \quad (107b)$$

in which \mathbf{k} is the wave vector of the incident electron. Therefore in this formulation of the calculation of the elastic electron-solid cross-section, all effects of both the induced charge on the solid's surface and the inelastic loss processes are described by the coordinate representation of the electronic proper self-energy, $\Sigma(\mathbf{r}, \mathbf{r}', E)$, for semi-infinite jellium.

From (103) to (107) we see that the fundamental "inputs" to this formalism are the functions $V_{\mathbf{R}}(\mathbf{r}-\mathbf{R})$, $V_0(\mathbf{r}, \mathbf{r}')$, and $\Sigma(\mathbf{r}, \mathbf{r}', E)$. The evaluation of the former has been discussed most extensively by Duke et al.^{29,47} and Pendry.⁴⁵ The last two functions are treated as adjustable functions by most workers⁶ although Feibelman et al.³⁰ have provided a formally complete theory for their evaluation in terms of the microscopic parameters characterizing the target. Different workers select different forms for these functions so that considerable discussion of these choices exists in the literature.^{6,29,30,44-47} Moreover, the arbitrariness associated with such choices constitutes a far more serious source of error in modern calculations of ELEED intensities than the technical approximations made in evaluating $\psi_{\text{scatt}}(\mathbf{r}, E)$ from (107a).

Although complicated in detail,^{9,10,250,266,267} the solution to (107) by the multiple-scattering method is conceptually simple. It proceeds in five steps. First, (107a) is expanded as a perturbation series with summations over scattering sites indicated explicitly. In practice, this step is accomplished by writing (107a) in terms of a "T" matrix, $T(\mathbf{r}, \mathbf{r}')$, via

$$\psi_{\mathbf{k}}(\mathbf{r}) = \varphi_{\mathbf{k}}(\mathbf{r}) + \int d^3r' d^3r'' G_0(\mathbf{r}, \mathbf{r}', E) T(\mathbf{r}', \mathbf{r}'') \varphi_{\mathbf{k}}(\mathbf{r}'') \quad (108)$$

and subsequently expanding the equation for T which is analogous to (105), that is,

$$\begin{aligned} T(\mathbf{r}, \mathbf{r}') &= \delta(\mathbf{r}-\mathbf{r}') \sum_{\mathbf{R}} v_{\mathbf{R}}(\mathbf{r}-\mathbf{R}) + \int d^3r'' \sum_{\mathbf{R}} v_{\mathbf{R}}(\mathbf{r}-\mathbf{R}) G_0(\mathbf{r}, \mathbf{r}'', E) T(\mathbf{r}'', \mathbf{r}') \\ &= \delta(\mathbf{r}-\mathbf{r}') \sum_{\mathbf{R}} v_{\mathbf{R}}(\mathbf{r}-\mathbf{R}) + \sum_{\mathbf{R}, \mathbf{R}'} v_{\mathbf{R}'}(\mathbf{r}-\mathbf{R}') G_0(\mathbf{r}, \mathbf{r}', E) v_{\mathbf{R}}(\mathbf{r}'-\mathbf{R}) + \dots \end{aligned} \quad (109)$$

The second step consists of defining a "single-site" t matrix which accounts for all of the diagonal terms in (109). It satisfies

$$\begin{aligned} \langle \mathbf{k}' | t_{\mathbf{R}}(E) | \mathbf{k} \rangle &= \int d^3r' d^3r e^{-i\mathbf{k}' \cdot \mathbf{r}'} t_{\mathbf{R}}(\mathbf{r}'-\mathbf{R}, \mathbf{r}-\mathbf{R}) e^{i\mathbf{k} \cdot \mathbf{r}} \\ &\equiv e^{-i(\mathbf{k}'-\mathbf{k}) \cdot \mathbf{R}} t_{\mathbf{R}}(\mathbf{k}', \mathbf{k}; E) \end{aligned} \quad (110a)$$

$$t_{\mathbf{R}}(\mathbf{k}', \mathbf{k}; E) = v_{\mathbf{R}}(\mathbf{k}' - \mathbf{k}) + \int \frac{d^3 k''}{(2\pi)^3} v_{\mathbf{R}}(\mathbf{k}' - \mathbf{k}'') G_0(\mathbf{k}'', E) t_{\mathbf{R}}(\mathbf{k}'', \mathbf{k}; E) \quad (110b)$$

$$v_{\mathbf{R}}(\mathbf{q}) = \int d^3 r v_{\mathbf{R}}(\mathbf{r}) e^{-i\mathbf{q}\cdot\mathbf{r}} \quad (110c)$$

The third step consists of inserting these expressions for the single-site t matrix back into the integral equation (109) for T and converting that integral equation into an algebraic equation by use of partial-wave expansion techniques. It is worth noting that the *major* effects of the lattice vibrations for *low-energy* ($E \lesssim 100$ eV) electrons are inserted into the theory⁹ by replacing the t matrix in (110b) by

$$t_{\mathbf{R}}(\mathbf{k}', \mathbf{k}; E) \rightarrow t_{\mathbf{R}}(\mathbf{k}', \mathbf{k}; E) \exp[-W_{\mathbf{R}}(\mathbf{k}' - \mathbf{k})] \quad (111a)$$

$$W_{\mathbf{R}}(\mathbf{q}) = \frac{1}{2} \mathbf{q} \cdot \langle \mathbf{u}_{\mathbf{R}}(0) \mathbf{u}_{\mathbf{R}}(0) \rangle_T \cdot \bar{\mathbf{q}} \quad (111b)$$

in which $W_{\mathbf{R}}(\mathbf{q})$ is a factor associated with the root-mean-square (rms) lattice displacements $\mathbf{u}_{\mathbf{R}}(t)$ at the site \mathbf{R} . Therefore the temperature effects are put into the theory prior to the execution of the third step in the cross-section calculation. Their presence merely changes some of the details of the partial-wave expansions performed during this step.

The fourth step in the solution to (107a) is the partial performance of the sums that appear in the algebraic equations at the completion of the third step. In particular, the lattice is divided into repeating layers of geometrically identical "subplanes" of scattering centers. All of the multiple scattering in each subplane is summed analytically with the result that the atomic scattering matrices $t_{\mathbf{R}}$ are replaced by subplane scattering matrices τ_{ν} of the generic form

$$\tau_{\nu} = t_{\mathbf{R}=(\mathbf{P}, \nu)} [1 - G^{\text{sp}} t_{\mathbf{R}=(\mathbf{P}, \nu)}]^{-1} \quad (112)$$

in which \mathbf{P} labels the sites of the scatterers in a given subplane, ν labels the subplanes, and G^{sp} is an appropriate propagator defined in terms of $G_0(\mathbf{k}, E)$.^{6,9,248,266} This step in the three-dimensional multiple-scattering analysis renders it equivalent to the laminar analyses discussed in Section IV.D for those model potentials which currently are commonly used in the calculation of ELED intensities.

The complete layer scattering amplitudes T_{ν} are obtained by summation of the remaining terms in the perturbation expansion (109) for $T(\mathbf{r}, \mathbf{r}')$.

Moreover, the T_ν themselves are matrices labeled by the $L \equiv (l, m)$ components of the spherical harmonics used in the angular momentum expansion in step 3. This summation can be cast into the form of a set of coupled linear matrix equations. The final step in the calculation is the solution of these equations and the insertion of their solutions back into (108) for the wave function. The Fourier transform of $T(\mathbf{r}, \mathbf{r}')$ is simply related²⁵⁰ to the electron-ion-core scattering contribution to the electron-solid reflection coefficient. The bulk of the time consumed in any computer calculation of ELEED intensities is used for the evaluation of the layer scattering amplitude matrices T_ν via the construction and solution of the set of coupled, linear algebraic equations that they satisfy. The scattering amplitude $T(\mathbf{r}, \mathbf{r}')$ is obtained as a sum over both the layer indices ν and the angular momentum indices L .

A complete account of the derivation of the equations for $T(\mathbf{r}, \mathbf{r}')$ and T_ν is given by Duke and Tucker¹⁹ for a rigid lattice of isotropic ion-core scatterers and is extended to the general case by Laramore and Duke¹⁰ and by Duke et al.²⁶⁶ Their numerical solution is described by Laramore and Duke.²⁵⁰ The outline just given provides an indication of the relationship between the structure of these equations and the nature of the electron-electron and electron-ion-core interactions that govern the scattering of low-energy electrons from solids. The approximations needed to reduce their formal structure into satisfactory computational algorithms for ELEED intensities are discussed in Part V. First, however, we examine in the next two sections alternatives to the multiple-scattering method of calculating ELEED intensities.

C. Wave-Function-Matching Analyses

The multiple-scattering method described in the previous section is by no means the only mathematical formalism which is commonly used for calculating elastic low-energy electron diffraction (ELEED) intensities. We discussed the multiple-scattering method first because it constitutes the only theory of ELEED in which microscopic descriptions of electron-electron interactions have been introduced in a systematic rather than empirical fashion.^{19,30,44,247} Historically, the importance of these interactions for the evaluation of ELEED intensities was recognized only very recently.^{19,54,268} The original analyses of ELEED by Bethe,⁵⁰ Morse,⁵¹ and Kronig and Penny,²⁶⁹ performed in the early years of quantum mechanics (1928 to 1930), were based on the rigid-lattice, static potential model specified by (18) and (19). They used a technique to solve the Schrödinger equation for the electron which is usually referred to as the "wave-function-matching" method. In this section we indicate the nature of this technique and provide a brief historical account of its development in more recent years.

The model Schrödinger equation solved by this method is given by

$$\left\{ -\frac{\hbar^2 \Delta}{2m} + \theta(z) [V + V_p(\mathbf{r})] - E \right\} \psi_E(\mathbf{r}) = 0 \quad (113)$$

in which $V_p(\mathbf{r})$ is a periodic potential existing only in the half-space $z > 0$. The quantity V designates a constant, although not necessarily real, optical or "inner" potential. Both the early^{50, 51, 269} and many recent^{52, 53, 270-274} authors consider V to be real, however, so initially we shall also.

The reflection coefficients, $R_g(E)$, associated with the diffracted beams labeled by the planar reciprocal lattice vectors $\mathbf{g}(hk)$ defined in Fig. 1 are obtained by matching the external wave function

$$\psi_E(\mathbf{r}) = e^{i\mathbf{k} \cdot \mathbf{r}} + \sum_{\mathbf{g}} R_g(E) e^{-i\mathbf{k}_{\perp}(\mathbf{g}, E)z} e^{i(\mathbf{k}_{\parallel} + \mathbf{g}) \cdot \mathbf{r}}; \quad z < 0 \quad (114)$$

to that inside the crystal along the planar surface at $z=0$. The wave functions inside the crystal are written as linear combinations of Bloch waves,²⁷⁵ $\psi_{n\mathbf{k}}(\mathbf{r})$, that is,

$$\psi_E(\mathbf{r}) = \sum_{n, \mathbf{k}} [F_{n\mathbf{k}}^+ \psi_{n\mathbf{k}}^+(\mathbf{r}) + F_{n\mathbf{k}}^- \psi_{n\mathbf{k}}^-(\mathbf{r})]; \quad d > z > 0 \quad (115)$$

in which n is the band index and \mathbf{k}^+ (\mathbf{k}^-) indicates waves moving to the right (left). Only outgoing waves are presumed to occur at the rear of the target of thickness d :

$$\psi_E(\mathbf{r}) = \sum_{\mathbf{g}} T_g(E) e^{i\mathbf{k}_{\perp}(\mathbf{g}, E)z} e^{i(\mathbf{k}_{\parallel} + \mathbf{g}) \cdot \mathbf{r}}; \quad z > d \quad (116)$$

If the $\psi_{n\mathbf{k}}(\mathbf{r})$ are known from energy band theory,²⁷⁵ then the continuity of ψ_E and ψ'_E at the two surfaces determines $R_g(E)$, $T_g(E)$, and the $F_{n\mathbf{k}}^{\pm}$. The bulk of actual calculations is devoted to evaluating the Bloch functions and these coefficients.

In 1930, by using an approximate version of this method, Morse⁵¹ constructed a qualitative interpretation of multiple-scattering effects evident in Davisson and Germer's original data.¹⁶ The more modern calculations^{52, 53, 270-274, 276-279} based on the static potential model for real values of V have been carried out with the objective of determining the consequences of improved models of $V_p(\mathbf{r})$. Unfortunately, they have added little to the insight obtained by Morse because their neglect of inelastic collision damping¹⁹ renders the correspondence of their predictions with observed ELEED intensities tenuous at best for incident electron energies $E \gtrsim 10$ eV.

As indicated in Section III.B, the consequences of inelastic collision

damping may be introduced into the static potential model [e.g., (113)] by the simple device of taking V to have a negative-definite imaginary part. This fact was recognized in the 1930s by Slater⁵⁵ and Moliere²⁸⁰ whose papers were undeservedly neglected by subsequent workers. While providing no microscopic model of the cause of the damping or estimates of its magnitude, both they and Hirabayashi²⁸¹ found that imaginary potentials of the order of a few electron volts would reduce the heights of peaks in ELEED intensity profiles and broaden these peaks considerably. Indeed, in 1967 Hirabayashi used this device to achieve a quite good description of ELEED intensity data on graphite taken by Lander and Morrison.²⁸² Several years later this procedure also became popular in the West, leading to a variety of wave-function-matching calculations,^{43,45,249,283-287} some of which we reconsider in Part V.

It seems appropriate to note in closing that the main applications of the static potential model have occurred in the realm of high-energy (i.e., $E \sim 10\text{keV}$) electronic-solid scattering. In this energy regime the inelastic collision damping lengths are much larger, $\lambda_{ee} \gtrsim 100 \text{ \AA}$, so that the scattering is characteristic of the bulk rather than surface of the sample. The truncated periodic potential model provides a much closer approximation to the experimental situation in this case, and Bethe-type multiple internal beam analyses have been performed extensively within the context of electron microscopy.^{288,289} The extension of these analyses into the energy range of ELEED has been carried out by Stern and his colleagues,²⁴⁵ but little direct contact with experimental data has been achieved.

D. Laminar Multiple-Scattering Analyses

Within a year of Morse's wave-function-matching analysis⁵¹ of Davisson and Germer's elastic low-energy electron diffraction (ELEED) data,¹⁶ a critique of his model calculation was advanced²⁹⁰ asserting that it described the bulk properties of the sample, whereas some features of the data were determined by surface properties. In this paper²⁹⁰ von Laue constructed a laminar model of ELEED from a single planar array of atomic scatterers, which is indeed the forerunner of modern multiple-scattering theories used in the analysis of surface structures. In this section, we indicate the mathematical structure of the laminar multiple-scattering method and trace the history of its subsequent development and ultimate blending into a momentum space representation of the formalism described in Section IV.B.

The fundamental ingredient of the laminar formalism is the incorporation of the two-dimensional space group symmetry of the crystal into the construction of the Schrödinger equation describing the motion of the incident electron. Therefore if $\{\mathbf{g}\}$ designates the set of reciprocal lattice

vectors associated with this symmetry (see, e.g., Fig. 1 or Wood^{291,292}), then the scattering potential admits the expansion

$$V(\mathbf{r}) = \sum_{\mathbf{g}} V_{\mathbf{g}}(z) e^{i\mathbf{g}\cdot\boldsymbol{\rho}} \quad (117)$$

in which z is the distance normal to the surface and $\boldsymbol{\rho}$ is a position vector lying in the surface, that is, $\mathbf{r} = \boldsymbol{\rho} + z\hat{\mathbf{n}}$. Using this expansion plus the ansatz

$$\psi_E(\mathbf{r}) = \sum_{\mathbf{g}} \psi_{E,\mathbf{g}}(z) e^{i(\mathbf{k}_{\parallel} + \mathbf{g})\cdot\boldsymbol{\rho}} \quad (118)$$

in the static potential model Schrödinger equation

$$\left(\frac{-\hbar^2 \Delta}{2m} + v(\mathbf{r}) - E \right) \psi_E(\mathbf{r}) = 0 \quad (119)$$

yields a set of coupled differential equations for the $\psi_{E,\mathbf{g}}(z)$:

$$\left[\frac{d^2}{dz^2} + k^2 - (\mathbf{k}_{\parallel} + \mathbf{g})^2 \right] \psi_{E,\mathbf{g}}(z) = \sum_{\mathbf{g}'} \left[\frac{2m}{\hbar^2} V_{\mathbf{g}-\mathbf{g}'}(z) \right] \psi_{E,\mathbf{g}'}(z) \quad (120)$$

The solution of these equations (or an equivalent integral form thereof) by iteration is the content of laminar multiple-scattering analyses. Our use of the plural "analyses" indicates that a variety of mathematical methods have been employed for this purpose. Similarly, different authors construct different models of the potential $V_{\mathbf{g}}(z)$.

Von Laue treated (120) by use of the method of successive approximations, arriving at a result equivalent to our Born approximation analyses presented in Section III.C. The next step in the development of the analysis for purely real potentials $V_{\mathbf{g}}(z)$ was made 35 years later by Kambe^{293,294} who reformulated the problem of multiple scattering within the atomic laminae in terms of a KKR (Korringa,²⁹⁵ Kohn and Rostoker²⁹⁶) Green's function method. He demonstrated that for isotropic scatterers (in the absence of inelastic collision damping) the resulting laminar KKR method is identical to the multiple-scattering analysis described in Section IV.B. McRae extended the theory to describe scattering from multiple atomic layers²⁹⁷ and developed a systematic momentum representation multiple-scattering perturbation analysis to discuss the interlayer scattering events.²⁹⁸ Numerical calculations (based on models in which inelastic collision damping is neglected) have been carried out by Kambe⁴⁸ and by McRae and his colleagues.^{277,279}

As in the case of the wave-function-matching formalism, the consequences of inelastic collision damping can be incorporated into the

laminar scattering method by introducing a negative-definite imaginary component of $V_{\mathbf{g}=0}(z)$ in (120). This was first done by Hirabayashi and Takeishi²⁹⁹ during the course of an analysis of Lander and Morrison's ELEED intensity data for graphite.²⁸² They achieved a qualitative description of both the shape and magnitude of the observed intensities in what proved to be the first reasonably successful dynamical description of experimental ELEED intensities. A more systematic development of the multiple-scattering analysis and its consequences was constructed by Ohtsuki³⁰⁰ who, however, did not pursue the calculation beyond the identification of its simpler general consequences. Hirabayashi subsequently performed isotropic scatterer calculations of ELEED intensities from a variety of materials.^{301,302} These analyses are equivalent to and appeared about the same time as the early isotropic scatterer calculations based on the multiple-scattering theory developed in Section IV.B.^{19,29,54,197,248,255,264,303} Small numerical differences between the predictions of the two methods, enhanced with decreasing electron energy,³⁰³ are caused by the use of different boundary conditions to relate the intensity of the external beams to that of the internal beams at the surface of the sample.

One of the most interesting features of the development of the three types of "dynamical" theories of ELEED discussed in this section is their increasing similarity to each other. A good example of this trend is the layer KKR method developed by Marcus and Jepsen.^{42,304-306} Written in the formalism of von Laue's laminar model, much of the actual analytical detail is taken from the work of Kambe^{293,294} for scattering within a plane of atoms parallel to the surface, and from that of McRae²⁹⁷ for a description of the multiple scattering between these layers. Yet the joining conditions used at the solid-vacuum surface are those of the wave-function-matching method, thereby rendering the "layer KKR" analysis essentially identical to the most recent wave-function-matching calculations of Pendry.^{45,249} Yet in his latest work,³⁰⁷⁻³⁰⁹ on which structure analyses have been based,^{240,310} Pendry also has adopted a momentum representation multiple-scattering technique completely equivalent to a particular approximate solution to the multiple-scattering series, (109), developed in Section IV.B. Current operative structural analysis computer programs are based on the formalisms of Duke and co-workers,^{9,10,19,250} Marcus and Jepsen,^{42,304-306} and Pendry.^{45,307-309} Regardless of their historical origin, therefore, all presently used "dynamical" theories of ELEED intensities are based on multiple-scattering analyses of electron scattering from planes of ion-cores. In terms of mathematical techniques these theories differ only in that the wave-function-matching condition is employed by the layer KKR method but not by the other two, and different calculations embody different technical approximations as de-

scribed in the following part. In practice, moreover, the different model electron-solid interactions used in the various calculations usually cause discrepancies between their predictions which are large relative to discrepancies associated with their use of different mathematical formalisms.^{47,242}

The most significant technical distinction between the various methods is, from a practical point of view, the amount of computer time and memory required to operate the program used to generate the ELEED intensities. In this regard, the programs of Jepsen, Marcus, and Jona^{42,306} are inaccessible to the average laboratory because of their large memory requirements and length of operation. The "exact" calculations of Duke and co-workers^{241,242,250} and Pendry²⁴⁹ are based on programs which may be used by most laboratories with modern electronic computers (e.g., the Xerox Sigma-7 series, the IBM 360-70 series, the Digital Equipment PDP-10 series, or larger computers like the Control Data CDC-6600 series). Perturbation treatments based on either the laminar^{307,308} or the three-dimensional^{284,285,311} multiple-scattering methods promise still further increases in speed of computation once their regions of convergence have been documented for a variety of incident beam parameters and model potentials. Consequently, the formalisms described in this part of the review are practically useful as well as mathematically accurate in their present form. Moreover, further improvements doubtless will be forthcoming.

V. MODEL ELASTIC LOW-ENERGY ELECTRON DIFFRACTION CALCULATIONS: INPUTS, OUTPUTS, AND CRITIQUE

A. Construction of the Electron-Ion-Core Potential

The construction of a suitable short-range electron-ion-core potential has attracted substantial attention in the theoretical literature on elastic low-energy electron diffraction (ELEED). The central issue is whether or not the large energies, $E \sim 100$ eV, of the incident electrons render inadequate models of this potential appropriate for the description of the optical and transport properties of the solid (i.e., for the description of electronic motion at energies within 5 to 10 eV of the Fermi energy). Two features of this question are noteworthy. First, its resolution may depend on the particular system being examined. Second, whether or not a given potential is regarded as "adequate" is essentially a subjective matter. It depends on the intended use of the calculated ELEED intensities, the alternatives that are available, and the judgment of individual workers. One person's "excellent agreement between predicted and observed in-

tensities" may be another's disaster. These features of the issue complicate both the use of the literature and its review. In this section we adopt the conventions that the intended use of calculated ELEED intensities is structure analysis and that two potentials are regarded as "indistinguishable" if they lead to predicted intensities which lie within the experimental uncertainties associated with reproducing a given measurement at two different laboratories. These uncertainties currently are roughly $\pm 50\%$ in peak heights and ± 2 to 3 eV in the energies of maxima in ELEED intensity profiles.⁶

Given these two conventions, there is no firm evidence in the literature that conventional energy band structure potentials are inadequate for the calculation of ELEED intensities. Two claims to the contrary have been advanced. The first, for the system Ag(111), is simply a passing remark in a paper on the structure analysis of a $(\sqrt{3} \times \sqrt{3})$ 30° iodine overlayer.²⁴⁰ The second is a comparison of Slater and Hartree-Fock exchange potentials for Cu(100) reported by Pendry.²⁴⁹ Other workers have failed to be able to reproduce Pendry's Hartree potential,^{239,241} however, and explicit checks of this point for Al(100),⁴⁶ Al(111),⁴⁷ and Ni(100)^{241,312} led to the conclusion that, if anything, the Slater exchange potential provides a better description of the existing data in all three cases. Moreover, Capart finds only small differences between the two models for Cu(100) itself.⁴³ Therefore we regard the claims that special potentials are necessary for ELEED intensity calculations in Ag(111) and Cu(100) as unproven at the present time and, in any case, not generalizable to all systems.

The electron-ion-core potential is inserted into an ELEED intensity analysis in one of two ways. In wave-function-matching pseudopotential calculations the V_G coefficients in (19) are evaluated. This approach has been taken by Pendry,^{52,287,313} Strozier and Jones,²⁸⁴⁻²⁸⁶ and Hoffstein and Boudreaux.^{53,274} In multiple-scattering calculations, the electron-ion-core potential is reduced to a spherical form. Electron scattering from these spherical potentials is described by the scattering amplitude²⁵³:

$$f(\mathbf{k}', \mathbf{k}) = \frac{-2\pi i}{k} \sum_{l,m} [\exp[2i\delta_l(E)] - 1] Y_{lm}^*(\hat{k}') Y_{lm}(\hat{k}) \quad (121)$$

in which the $\delta_l(E)$ are the energy-dependent phase shifts associated with spherical potential and the $Y_{lm}(\hat{k})$ are the spherical harmonics. Most workers use this formula to convert their model electron-ion-core potential into sets of phase shifts, $\{\delta_l(E)\}$, for each scatterer. Since the scattering

amplitude $f(\mathbf{k}', \mathbf{k})$ given by (121) is related to the renormalized ion-core t matrices [(111a)] via

$$t_{\mathbf{R}}(\mathbf{k}', \mathbf{k}; E) = \frac{-2\pi\hbar^2 f_{\mathbf{R}}(\mathbf{k}', \mathbf{k})}{m} \quad (122)$$

we see that the phase shifts $\{\delta\}$ are the direct inputs to a multiple-scattering computer program.

Although band structure potentials provide satisfactory descriptions of ELEED from the low-index faces of clean metals, in order to perform structure analyses of adsorbed overlayers we must devise a still simpler model of the potential because it seems unlikely that an accurate self-consistent calculation of the electron-ion-core potentials can be performed without an a priori knowledge of the atomic geometry of these systems. For this purpose, Duke and co-workers^{47,242} have proposed the use of an overlapping atomic charge density model. First, the crystal potential $V_c(r)$ is calculated, and then it is reduced to the muffin-tin form for evaluation of the phase shifts. The crystal potential is calculated using the expression²⁴³

$$V_c(r) = -\frac{Ze^2}{r} + \frac{e^2}{r} \int_0^r \sigma(t) dt - e^2 \int_r^\infty \frac{\sigma(t)}{t} dt - 3e^2 \left[\frac{3\sigma(r)}{32\pi^2 r^2} \right]^{1/3} \quad (123)$$

in which $\sigma(r)$ is the electronic radial number density at a distance r from an ion-core at $r=0$. The last term in (123) is the Slater approximation³¹⁴ to the exchange energy. The symbol Ze designates the nuclear charge and e is the elemental electronic charge. The overlapping atomic charge density model is defined by the use of a crystal charge density $\sigma(\mathbf{r})$ at a given point \mathbf{r} which is the superposition of atomic charge densities of the constituents of the crystal, that is,

$$\sigma(\mathbf{r}) = \sum_n \sigma_{\text{atomic}}(\mathbf{r} - \mathbf{R}_n) \quad (124)$$

The atomic charge densities $\sigma_{\text{atomic}}(r)$ are calculated using a computer program essentially identical to that of Herman and Skillman.²⁴³ Only the spherically symmetric component of the crystal charge density at a given site is used in (124) and this component is evaluated using Löwdin's alpha-function expansion³¹⁵ as described by Mattheiss.³¹⁶ The expansion over lattice sites in (124) is carried out over the three nearest shells of neighbors of a given ion-core.

Once the crystal potential in a given Wigner-Seitz cell has been obtained, however, it still must be reduced to muffin-tin form in order to

achieve the spherical symmetry required for the calculation of the electron scattering phase shifts. This reduction requires that a muffin-tin radius and the constant potential between the spheres be chosen. Duke et al.^{47,242} describe several possible choices of these parameters and demonstrate that provided the charge on the ion-cores is held fixed, the procedure used to select them exerts negligible influence on the predicted ELEED intensities. Moreover, for the low-index clean surfaces of aluminum, the overlapping atomic charge density model reproduces almost exactly the ELEED intensities predicted by Snow's self-consistent band structure potential.⁴⁷

Summarizing, the surface structure computer programs described in the previous sections use as input data sets of spherical wave phase shifts obtained from models of the electron-ion-core potentials. This fact already implies assumptions about the solution to the single-site t -matrix equation [i.e., (110b)] which are not correct in a dissipative medium or near a surface. Therefore all models of the electronic scattering factors of surface ion-cores are unmistakably if subtly empirical in character. Moreover, no definitive studies have yet been advanced to support the occasional claim that potentials more sophisticated than those obtained from overlapping atomic charge densities need to be used for the calculation of ELEED intensities. Consequently, the facilities not only to operate the multiple-scattering programs but also to construct simple, but adequate, model potentials for surface crystallography exist in any laboratory equipped with modern electron computers within the (Sigma-7)-(IBM-360-70)-(PDP-10)-(CDC-6600) range of capabilities.

B. Empirical Models of the Optical Potential

The electron-electron interaction-induced optical potential, $\Sigma(\mathbf{r}, \mathbf{r}', E)$ in (103) and (107b) is the least well-understood ingredient of the electron-solid force law. In spite of extensive theoretical attempts to evaluate this quantity from microscopic models³⁰ only four of its features are known with certainty: (1) It is nonlocal; (2) far outside the solid electronic motion in the nonlocal optical potential is identical to that in a local image potential, $V(z) = -e^2/4z$; (3) its real part is determined predominately by the bulk exchange-correlation energy of the valence electrons in the solid; and (4) its imaginary part is determined primarily by the excitation of both bulk and surface plasma oscillations in the valence-electron fluid. Because of the large uncertainties in its precise form, it is incorporated into models of elastic low-energy electron diffraction (ELEED) exclusively by the use of empirical formulas. Sometimes these formulas have a microscopic basis^{19,44,248} but usually they are phenomenological in character, containing at least two parameters [analogous to V_0 and λ_{ee} in (28)] which are chosen by comparison of the model predictions with observed ELEED intensities.

The *local complex potential model* is defined by specifying, a priori, that the retarded proper self-energy $\Sigma(\mathbf{r}, \mathbf{r}', E)$ be of the form

$$\Sigma(\mathbf{r}, \mathbf{r}', E) \equiv \delta(\mathbf{r} - \mathbf{r}') \Sigma(\mathbf{r}, E) \quad (125)$$

In practice, the further assumption is made that if the target extends over the half-space $z > 0$, then

$$\Sigma(\mathbf{r}, E) = V(E) \theta(z) \quad (126)$$

in which $V(E)$ either is chosen completely empirically,^{42, 43, 240-242, 249, 251, 264, 265, 281, 283-287, 299, 301-303, 310} or else is related to the bulk self-energy of the valence-electron fluid.^{19, 44, 46, 197, 248, 250} The energy dependence of the real part of $V(E)$ reflects that of the exchange-correlation energy of a valence electron.³¹⁸ Its imaginary part is obtained primarily from the probability of plasmon emission.^{19, 30} It is a simple, and often surprisingly adequate, approximation to take $V(E)$ as a constant,^{42, 43, 46, 250, 251} that is,

$$V(E) = V_1 - iV_2 \quad (127)$$

in which $V_1 \sim 10$ to 20 eV and $V_2 \sim 3$ to 5 eV.

Another common model described in the literature is the *inelastic collision model* proposed heuristically by Duke and Tucker¹⁹ and derived microscopically from a quantum field theory by Duke and Laramore.²⁴⁷ It consists of avoiding the solution of (103) and (104) by use of the ansatz

$$G_0(\mathbf{r}, \mathbf{r}', E) = \int \frac{d^3k}{(2\pi)^3} G_0(\mathbf{k}, E) e^{i\mathbf{k} \cdot (\mathbf{r} - \mathbf{r}')} \quad (128a)$$

$$G_0^{-1}(\mathbf{k}, E) = E - \frac{\hbar^2 k^2}{2m} - \Sigma(\mathbf{k}, E) \quad (128b)$$

in which $\Sigma(\mathbf{k}, E)$ is the proper self-energy of the incident electron in bulk jellium.^{19, 318} Equation (128a) exhibits the important analytical feature that $G_0(\mathbf{r}, \mathbf{r}', E)$ depends only on $\mathbf{R} = \mathbf{r} - \mathbf{r}'$. Therefore (105) for the full electron-solid Green's function can be solved by standard multiple-scattering methods in either the configuration²⁶⁷ or momentum^{6, 10, 266} representations. Use of the momentum representation exhibits the important advantage that the consequences of the thermal vibrations of the short-range ion-core potentials can be incorporated into the analysis. The nonlocality of the bulk self-energy,

$$\Sigma(\mathbf{r}, \mathbf{r}', E) \equiv \int \frac{d^3k}{(2\pi)^3} e^{i\mathbf{k} \cdot (\mathbf{r} - \mathbf{r}')} \Sigma(\mathbf{k}, E) \quad (129)$$

is neglected in all but one⁴⁴ of the numerical applications of (128) because the energy shell self-energy, $\Sigma(E) \equiv \Sigma(k(E), E)$, is used in (128b) where $k(E)$ is the value of k for which $G^{-1}[k(E), E] = 0$ [see, e.g., (28)].

It seems appropriate to conclude this section by noting a few features of both the inelastic collision and local complex potential models as they are analyzed in the literature. The only difference between the models lies in their expressions for G_0 and $\varphi_{\mathbf{k}}(\mathbf{r})$ given by (103) and (107b), respectively (Section IV.B). This difference enters the final expressions for the cross-sections in three places: formulas (110) for the site scattering amplitudes, expressions for the propagators like G^{sp} in the final algebraic equations for the T_{ν} , and in the boundary conditions implicit in (107a). All existing microscopic model calculations use free electron propagators in (110b) for the site scattering amplitudes. To this extent they are all empirical and perhaps inadequate²⁹ models of the electron-solid scattering process. The local complex potential model calculations are performed using the distorted-wave propagators (103) rather than the plane-wave (inelastic collision model) propagators (128) in solving the algebraic equations for the layer scattering amplitudes T . Nevertheless, most users of the local complex potential models^{42, 249, 251, 284-286} ultimately revert back to the boundary conditions of the inelastic collision model in order to avoid (unwanted) fine structure in their predicted intensity profiles caused by quantum interference effects associated with the sharp change in the optical potential, (126), at $z = 0$. This strictly empirical change in boundary conditions is accomplished by various ad hoc prescriptions in all of the most recent major calculations.^{42, 249, 251, 284-286, 310} Earlier calculations are reviewed by Estrup and McRae.³ Thus, none of the existing ELEED calculations are actually microscopic in character. They all involve semiempirical treatments of the short-range electron-ion-core interactions, of both the spatial and energy dependence of the inelastic collision optical potential, and of the boundary conditions. None of these calculations actually displays the consequences of the models of which they nominally are supposed to be an analysis, and none of the existing models embodies an adequate electron-electron-induced optical potential. Therefore it remains for us to demonstrate in the followig section that their deficiencies reduce only slightly the utility of these models for surface crystallography.

C. Sensitivity Analyses

1. Boundary Conditions

We recall from Part IV that the multiple-scattering and wave-function-matching methods employ different boundary conditions at the solid-vacuum interface. Moreover, the boundary conditions used in the inelastic

collision model (see Section V.B) are to a certain degree arbitrary because the electrons are always regarded as moving in a dissipative medium surrounding the ion-cores rather than being permitted to escape into the vacuum. Consequently, it seems appropriate to initiate our sensitivity analyses by examining the extent to which any discrepancies in the elastic low-energy electron diffraction (ELEED) intensities predicted by various models can be attributed to the different boundary conditions used in these models rather than to uncertainties in the electron-solid interactions.

Turning to an examination of the consequences of the wave-function-matching conditions at the solid-vacuum interface, we illustrate in Fig. 18 intensity profiles evaluated using three different but roughly equivalent matching procedures in the layer KKR method.⁴² The curves labeled *a* are those obtained using the local complex potential model defined by (126) and (127). Those labeled *c* were evaluated by setting $V_1=0$ in (127), but shifting the energy scale after the completion of the calculation by

$$\Delta \equiv \frac{V_1}{\cos^2 \theta} \quad (130)$$

corresponding to the value of V_1 used in curves *a*. Finally, the “no-reflection” curves labeled *b* were calculated by using the inelastic collision model boundary condition

$$k^2(E) \equiv \frac{2m[E + \Sigma(E)]}{\hbar^2} \quad (131)$$

to define the propagation wave number inside the crystal associated with $\Sigma(E) \equiv V(E) = V_1 - iV_2$. In the layer KKR method, however, a convention must be adopted to deal with the matching conditions at the vacuum interface for those beams with $E_\perp < V_1$ (i.e., beams which cannot escape the solid). Jepsen et al.⁴² select the convention that the components of the wave function associated with these beams join on to evanescent waves in the vacuum. This boundary condition distinguishes the layer KKR “no-reflection” model from the inelastic collision model (see also Section V.B). Inspection of Fig. 18 reveals shifts in peak position by several electron volts and alterations in intensity by as much as 50% at energies $E \lesssim 80$ eV for the specular [i.e., (00)] beam. At higher energies for the (00) beam and at almost all energies for the nonspecular beams, however, the consequences of these three different boundary conditions appear to be negligible for electron beams incident normal to the surface.

It is also instructive to scrutinize more closely the common procedure^{42, 249, 284–286} of calculating the intensity profiles for $V_1=0$ [(127)] and subsequently shifting the energy scale in compensation. Using the inelastic

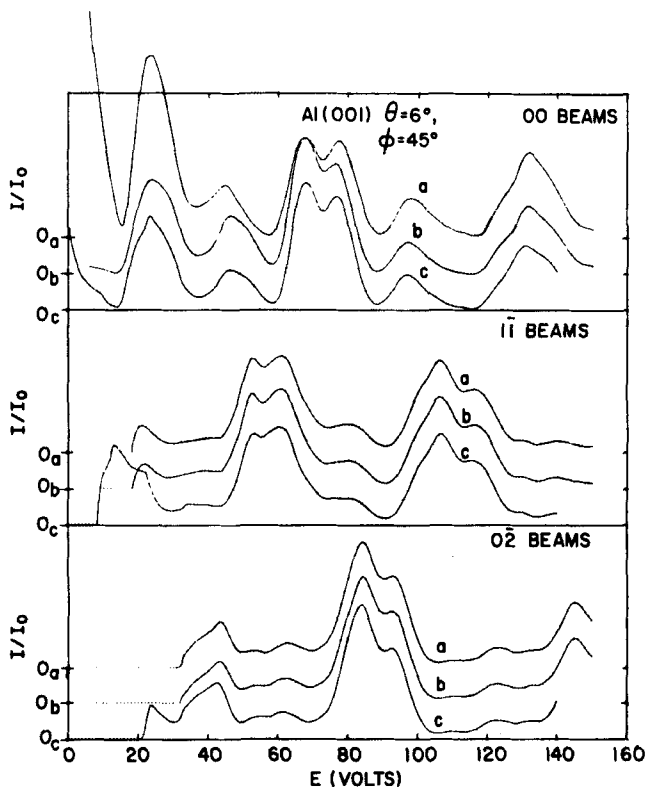


Fig. 18. Effects of different matching procedures on calculated Al(100) intensity profiles at $\theta = 6^\circ$, $\varphi = 45^\circ$, $\text{Im}[V(E)] = 4.1$ eV for the (00), ($\bar{1}\bar{1}$), and ($0\bar{2}$) beams. Plots *a*: abrupt step at surface in the real and imaginary part of the potential of magnitude $[-7.5 - 4.1i]$ eV. Plots *b*: “no-reflection” matching. The intensity profiles are calculated with $V_1 = V_2 = 0$ in (126) and (127) but using a complex $k_\perp(\mathbf{g}, E)$ equivalent to taking $V_2 = 4.1$ eV to calculate the transfer matrix for electron motion inside the crystal. After the completion of the calculation the intensity profiles are shifted by $\Delta = -7.5$ eV corresponding to the value of V_1 used in curves *a*. Plots *c*: $\text{Im}[V(E)]$ reflection matching. The intensity profiles are calculated using $V_1 \equiv 0$ and then shifted by $\Delta = -7.5$ eV. (After Jepsen et al.⁴²)

collision model we relate the total inner potential V_0 [(28)] to the propagator renormalization value V_1 and the shift of the energy scale Δ for the (00) beam via

$$V_1 + \frac{\Delta}{\cos^2 \theta} = V_0 \quad (132)$$

In Fig. 19 we illustrate the consequences of selecting three pairs of (V_1, Δ) values associated with a V_0 of 16.7 eV for Al(100). Comparison of the

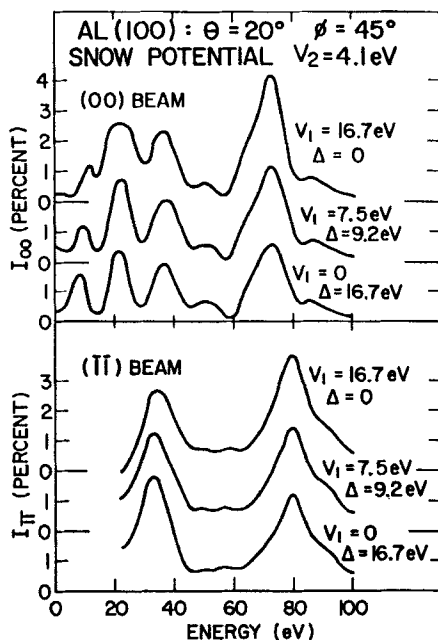


Fig. 19. Intensity profiles for electrons incident on Al(100) at an angle of incidence of 20° along a $\langle 010 \rangle$ azimuth. The three profiles for each of the (00) and $\bar{1}\bar{1}$ beams illustrate the consequences of using various combinations of real self-energies and shifts in the energy scale as discussed in association with (132) in the text. The electron-ion-core potential used in the calculations is that of Snow³¹⁷ as applied by Jepsen et al.⁴² The thermal motions of the ion-cores were neglected in these computations. (After Duke et al.⁴⁷)

($V_1 = 7.5$ eV, $\Delta = 9.2$ eV) results with those obtained for ($V_1 = 0$, $\Delta = 16.7$ eV) provides a direct comparison of the spectra calculated using the boundary conditions of Laramore and Duke²⁵⁰ ($V_1 = 7.5$ eV) and those of Jepsen et al.⁴² ($V_1 = 0$) for the value of the inner potential shift used by the latter. The observed differences in the two sets of spectra, while leaving the qualitative appearance of the intensity profiles unaltered, prove to be much larger than those between the spectra predicted by different plausible models of the electron-ion-core potential.⁴⁷ Moreover, it is significant that these differences persist to quite large energies (because of the influence of the value of V_1 on that of $\text{Im}[k(E)]$). For example, the intensity of the (00) beam at $E = 73$ eV is reduced by 50% when V_1 is taken to be zero and Δ to be 16.7 eV rather than conversely. Therefore we find that seemingly innocent changes in the treatment of the real part of the inner potential can induce quite noticeable alterations in the shape of the resulting intensity profiles.

Although we thus far have focused our attention on boundary condition ambiguities associated with the wave-function-matching method, the inelastic collision model also contains certain somewhat arbitrary conventions. They stem from the fact that if (128) are used to define $G_0(\mathbf{r}, \mathbf{r}', E)$, then it is not possible to evaluate the scattered intensities outside the electron-electron-interaction-induced dissipative optical potential by taking the large- r limit in (107) (Section IV.B). The expression used for these intensities is²⁵⁰

$$I(\mathbf{g}) = \frac{J_{\text{out}}}{J_{\text{in}}} = \frac{k_{\perp}^{\text{ext}}(\mathbf{g}, E)}{k_{\perp}^{\text{ext}}(0, E)} |R(\mathbf{g}, E)|^2 \quad (133)$$

where J_{in} and J_{out} are, respectively, the incident current per unit area and the reflected current per unit area of the \mathbf{g} th beam. In (133) the k_{\perp}^{ext} are determined external to the crystal:

$$k_{\perp}^{\text{ext}}(\mathbf{g}, E) \equiv \left[\frac{2mE}{\hbar^2} - (\mathbf{k}_{\parallel} + \mathbf{g})^2 \right]^{1/2} \quad (134)$$

The reflection amplitude $R(\mathbf{g}, E)$ is given by

$$R(\mathbf{g}, E) = \frac{-miR_{\mathbf{g}}(\mathbf{k}_{\parallel} + \mathbf{g} + k_{\perp}(\mathbf{g}, E)\hat{\mathbf{z}}, \mathbf{k})}{\hbar^2 A k_{\perp}(\mathbf{g}, E)} \quad (135a)$$

$$R_{\mathbf{g}}(\mathbf{k}', \mathbf{k}) = \sum_{\nu} \exp[-i(k'_{\perp} - k_{\perp})d_{\nu} - i\mathbf{g} \cdot \mathbf{a}_{\nu}] T_{\nu}(\mathbf{k}', \mathbf{k}) \quad (135b)$$

$$T_{\nu}(\mathbf{k}', \mathbf{k}) = \sum_{L, L'} T_{\nu}^{L'L} [k(E)] Y_L(\hat{\mathbf{k}}') Y_L(\hat{\mathbf{k}}) \quad (135c)$$

in terms of the matrix elements in the spherical wave representation (i.e., $L = l, m$) of the T matrices obtained from the solution of (109). Inside the solid the wave vectors are obtained from the condition that $G_0^{-1}(\mathbf{k}, E) = 0$ in (128b) as discussed in Section III.C, that is,

$$k_{\perp}^2(\mathbf{g}, E) = k^2(E) - (\mathbf{k}_{\parallel} + \mathbf{g})^2 \quad (136a)$$

$$k^2(E) = \frac{2m}{\hbar^2} \{ E - \Sigma[k(E), E] \} \quad (136b)$$

rather than from (134). The quantities \mathbf{a}_ν designate the shifts in the origin of the layer labeled by ν relative to the top layer [see, e.g., (47)]. Equations (133) to (136) illustrate the issue at hand: Since $k_\perp(\mathbf{g}, E)$ is complex inside the solid, how do we define the $Y_L(\hat{k})$ so that they correspond to the observed beam directions outside the solid?

Although several alternatives have been suggested,^{47,250,319} the most appropriate of them seems to be the use of those complex arguments in the $Y_L(\hat{k})$ associated with outgoing spherical and planar scattered waves.²⁵⁰ Thus if the $Y_L(\hat{k})$ are written as polynomials in $k(E)$, $k_\perp(E)$, and k_\parallel , we select $\text{Im}[k(E)] > 0$ and $\text{sgn}\{\text{Im}[k_\perp(E)]\} = \text{sgn}\{\text{Re}[k_\perp(E)]\}$ so that both spherical waves and those scattered in the $\pm z$ direction always decay as they propagate away from the scatterer. The consequences of this and the alternative conventions for the $Y_L(\hat{k})$ are indicated in Fig. 20 where they are labeled by "Snow-1" to "Snow-4." As in the cases illustrated by Figs. 18 and 19, we find that the details of the low-energy ($E \lesssim 50$ eV) intensity profiles are influenced substantially by the choice of boundary conditions.

Given the results documented above, we might wonder how well the results of different groups' analyses compare with each other relative to their description of observed ELEED intensities. Using the beam indexing shown in Fig. 21, a comparison for Al(111) of the layer KKR analysis of Jepsen et al.²⁵¹ with the inelastic collision model analysis of Duke et al.⁴⁷ and the data of Jona³²⁰ is shown in Fig. 22. As we shall see in Section V.C.2, the most significant difference between the two calculations is their use of different numbers of partial waves.⁴⁷ (Duke et al.⁴⁷ employed only three whereas Jepsen et al.²⁵¹ utilized eight.) Considering the uncertainties induced by boundary conditions and slightly different computational details, the agreement between the two model predictions and the quality of their description of the observed intensities are indeed a tribute to the adequacy of modern mathematical models of ELEED from clean metals. When the numerical accuracy of the individual calculations is good (i.e., to within a few percent for a fixed optical potential and set of ion-core phase shifts) and the model force laws are comparable, the analyses of different groups agree quite well.

Summarizing, the use of different boundary conditions in various groups' ELEED analyses causes quantitative but not qualitative alterations in the predicted intensity profiles. These effects are largest for the specular beam at low incident electron energies, $E \lesssim 50$ eV. Since other uncertainties, (e.g., surface electronic effects⁴⁷ and the onset of new inelastic loss channels⁶) are also large in this energy region, surface crystallography via ELEED is perhaps best carried out by analyzing the nonspecular beams over wide ranges of electron energies $E \gtrsim 50$ eV. In this range of parameters only uncertainties in the electron-solid force law, that is, not those

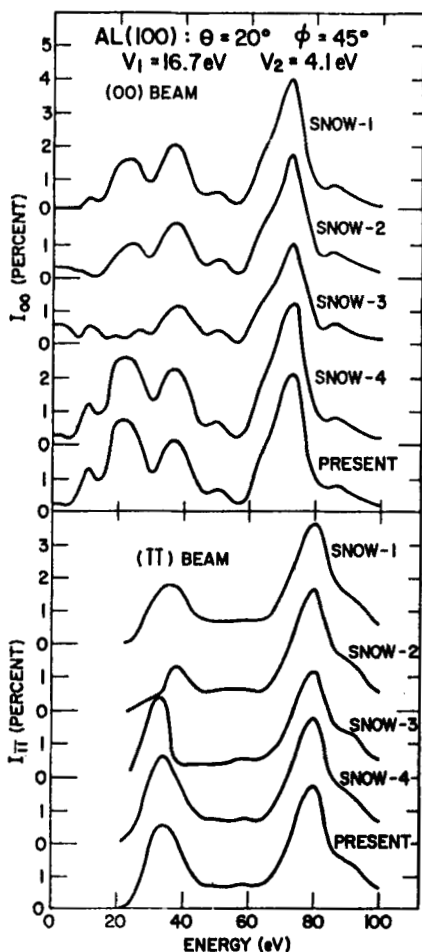


Fig. 20. Intensity profiles for the (00) and (11) beams associated with electrons incident on Al(100) at an angle of incidence of 20° along a $\langle 010 \rangle$ azimuth. The curves labeled SNOW-1 are calculations of these intensities based on Snow's potential³¹⁷ as used by Jepsen et al.⁴² performed using the computer program written by Laramore and Duke.²⁵⁰ Those labeled SNOW-2 are based on the same potential but performed using a version of the Laramore-Duke program in which complex values of k and k_\perp in the upper half-complex k plane are used consistently to calculate both $Y_{lm}(\hat{k})$ and $Y_{lm}^*(\hat{k})$. Laramore and Duke used $-k_\perp'/k$ in calculating $Y_{lm}^*(\hat{k})$, thereby rendering $-k_\perp'$ a number in the lower half-complex k plane. The profiles labeled SNOW-3 were calculated using the real asymptotic values of k outside the solid in evaluating the $Y_{lm}(\hat{k})$. Those designated as SNOW-4 were obtained using the same $Y_{lm}(\hat{k})$ as in the SNOW-2, but defining $Y_{lm}^*(\hat{k}) \equiv \bar{Y}_{lm}(\hat{k})$ for complex values of k . The set of curves labeled PRESENT were evaluated using the latter boundary conditions but with the electron-ion-core phase shifts for bulk aluminum predicted by an overlapping atomic charge density model. All calculations were performed neglecting the thermal motions of the ion-cores. (After Duke et al.⁴⁷)

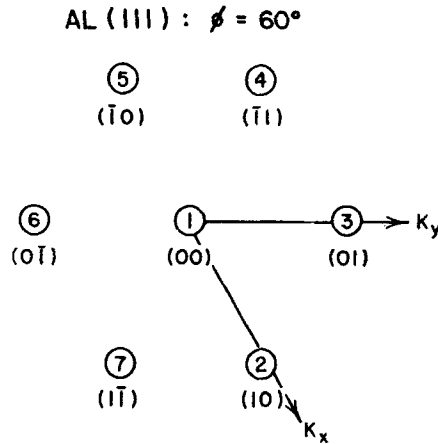


Fig. 21. Schematic diagram of the indexing of the nonspecular beams for an incident beam azimuth of $\phi = 60^\circ$ on Al(111). The numbering of the beams is that of Jepsen et al.,²⁵¹ whereas the indexing is due to Jona.³²⁰ (After Duke et al.⁴⁷)

associated with the scattering theory per se, can cause ELEED to become an inadequate technique for surface crystallography.

2. Number of Phase Shifts: Rigid Lattice

We recall from (121) (Section V.A) that after a model electron-ion-core potential has been constructed, it is approximated by a spherical potential and the resulting electron scattering phase shifts $\{\delta_l(E)\}$ are used as inputs to calculations of the elastic low-energy electron diffraction intensities. The selection of the number of phase shifts to be used in a given calculation is an important technical question both for the minimization of computer operating time and for the informed comparison of ELEED intensity calculations using different mathematical techniques or different model potentials.^{47,321,322} Therefore in this section we indicate the major issues involved in performing this selection.

The dimensionality of the individual sublattice $\tau_p^{L'L}$ matrices [(112) in Section IV.B] is given by

$$D_\tau = \left[\sum_l (2l+1) \right] \times \left[\sum_l (2l+1) \right] \quad (137a)$$

In “exact” multiple-scattering calculations^{47,250} of ELEED intensities from

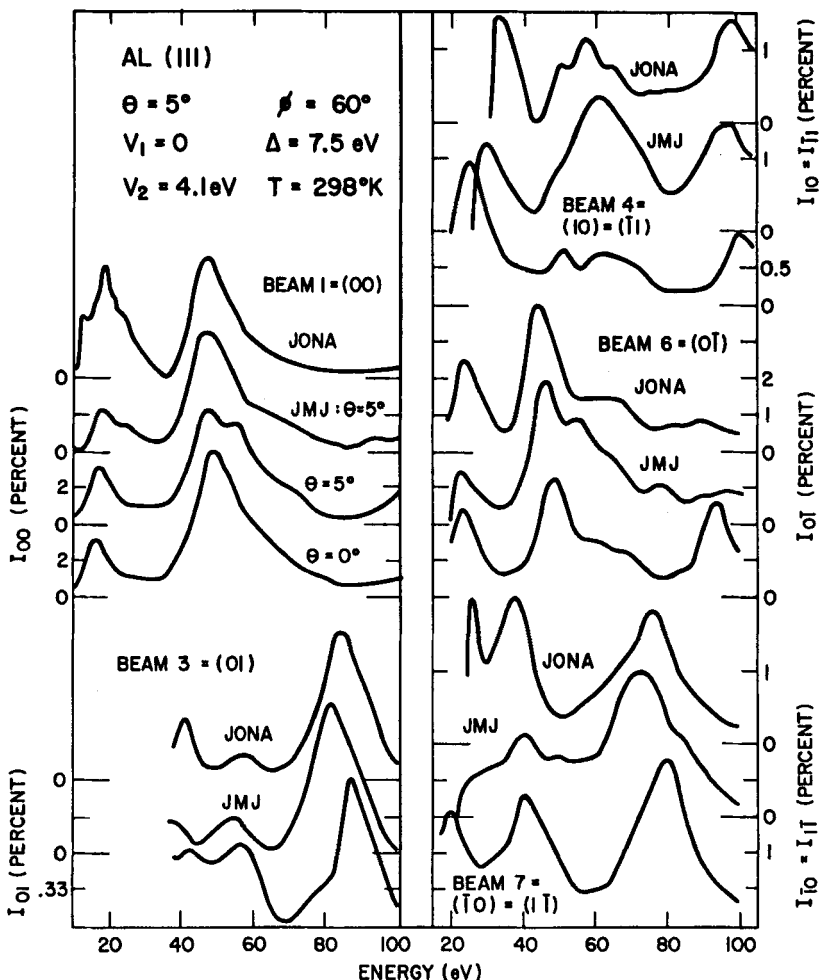


Fig. 22. Intensity profiles for electrons incident on Al(111) at an angle of incidence $\theta = 5^\circ$ along a $\langle 11\bar{2} \rangle$ azimuth. The curves labeled JONA are the experimental data of Jona³²⁰ whereas those labeled JMJ are the calculations of Jepsen et al.²⁵¹ The unlabeled curves are calculations performed using the potential predicted by an overlapping atomic charge density model using the local average potential to define the constant potential in a muffin-tin model of the electron-ion-core interaction. The models of the inner potential and thermal vibrations were chosen to correspond directly with those used by Jepsen et al., that is, $V_1 = 0$, $V_2 = 4.1$ eV, $\Delta = 7.5$ eV, and $\Theta_D' = 418^\circ$ for all layers. The intensity scales for the unlabeled calculations are in percent, whereas those for Jona's data and Jepsen et al.'s calculations are arbitrary. (After Duke et al.⁴⁷)

n equivalent planar sublattices the dimensionality of the complete scattering matrices $T_v^{LL'}$ is

$$D_T = \left[n \sum_l (2l+1) \right] \times \left[n \sum_l (2l+1) \right] \quad (137b)$$

Since the time used by the multiple-scattering computer program²⁵⁰ to evaluate the ELEED intensities scales as D_T , it is economical to employ as few partial waves as possible in the calculations. Moreover, a similar although less restrictive consideration applies to some of the perturbation expansions.^{307,308} Therefore the central criterion for the selection of the number of partial waves to include in a structure analysis is the use of only as many as is necessary to achieve a tolerable description of the electron-ion-core scattering amplitudes [(121)].

It is evident that even for a fixed electron-ion-core potential, the results of a multiple-scattering calculation of ELEED intensities depend on the number of phase shifts included in the analysis. A specific illustration of this fact for Al(100) is shown in Fig. 23. The alterations in the intensity profile incurred by changing from one to three partial waves suggest that it is not very useful to compare the results of different mathematical methods unless equivalent electron-ion-core potentials and an adequate number of partial waves are incorporated in all of the calculations. Although this conclusion may seem trivial, it is not always recognized in the literature.^{321,322}

There is no general prescription for deciding a priori how many partial waves should be included in a calculation of ELEED intensities intended for use in an atomic structure analysis. In aluminum, three seem to suffice for $E \lesssim 100$ eV because of the large d -wave phase shifts. For Ni and Cu, however, at least four phase shifts must be included in a structure analysis^{241,242} and five seem adequate to provide an excellent description of the observed line shapes of the intensity profiles³¹² for $E \lesssim 200$ eV. Obviously at higher energies more phase shifts are required to describe the increased forward scattering cross-sections from the ion-core.¹⁷ Nevertheless, the routine use of four or five phase shifts obtained from overlapping atomic charge density models of the potential^{47,312} describes quite adequately observed room-temperature ELEED intensities from clean metals. We expect, therefore, that this level of description also will suffice to perform structure analyses of low-temperature ($T \lesssim 100^\circ\text{K}$) ELEED intensity data from adsorbed overlayers.

In practice, the decision of how many phase shifts to use for a given rigid lattice of ion-core scatterers usually can be made by calculating and

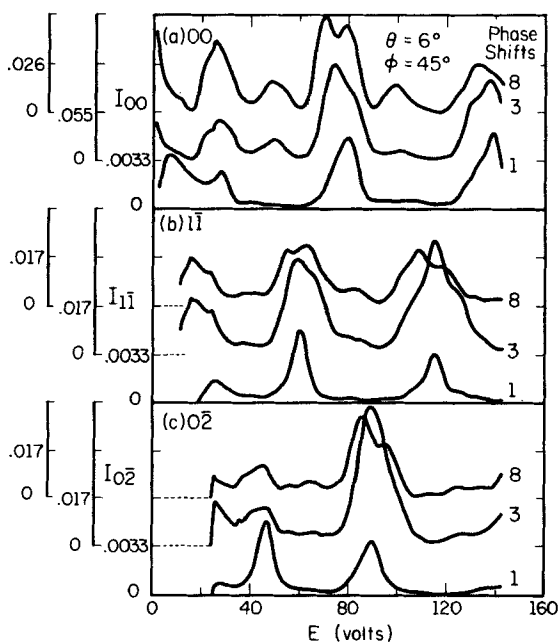


Fig. 23. Effect on the intensity profiles from Al(100) of using different numbers of phase shifts from the Marcus-Jepsen-Snow potential for Al in the theoretical calculation. The three curves in each panel were calculated with one, three, and eight phase shifts as indicated beside the individual intensity profiles. The various panels correspond to (a) 00 beam, (b) $1\bar{1}$ beam, and (c) $0\bar{2}$ beam. For all profiles $\theta = 6^\circ$, $\phi = 45^\circ$ (see Ref. 320). Note that the three zeros on the left refer to the origins of the scales of intensities for the three curves in each box. The profiles are calculated using $V_1 = 0$ between the atomic scatterers but a constant imaginary potential of $V_2 = 4.1$ eV. They are shifted by -7.5 eV to align the peaks with those in Jona's data.³²⁰ (After Jepsen et al.³⁰⁶)

inspecting the phase shifts for $l \lesssim 8$, retaining only those that are substantially larger (e.g., by factors of 3 or 4 at least) than the others. The occurrence of lattice vibrations complicates this issue, however, so we next must turn to an examination of their insertion into the model calculation.

3. Lattice Vibrations

The major effect of lattice vibrations on elastic low-energy electron diffraction at modest energies ($E \lesssim 100$ eV) is the renormalization of the electron-ion-core t matrices.⁹ This renormalization was discussed in Section IV.B and specified by (111). In our present notation the renormalized t matrices are given by

$$t_{\mathbf{R}}(\mathbf{k}', \mathbf{k}; E) = -\frac{2\pi\hbar^2}{m} f_{\mathbf{R}}(\mathbf{k}', \mathbf{k}) \exp[-W_{\mathbf{R}}(\mathbf{k}' - \mathbf{k})] \quad (138a)$$

$$W_{\mathbf{R}}(\mathbf{k}' - \mathbf{k}) = \frac{1}{2} \left\{ [k'_{\perp}(\mathbf{g}', E) - k_{\perp}(\mathbf{g}, E)]^2 \langle u_{\perp \mathbf{R}}^2 \rangle_T + \langle [(\mathbf{g}' - \mathbf{g}) \cdot \mathbf{u}_{\mathbf{R}}]^2 \rangle_T \right\} \quad (138b)$$

in which $f_{\mathbf{R}}(\mathbf{k}', \mathbf{k})$ is given by (121), $k_{\perp}(\mathbf{g}, E)$ by (136), and the beam reciprocal lattice vector \mathbf{g} by Fig. 1. The \mathbf{u} are the thermal lattice displacements defined by (20) and (21) in Section III.B. The most important result illustrated by (138) is the reduction of the backward scattering of the electron [e.g., $k'_{\perp}(0, E) = -k_{\perp}(0, E)$; $\mathbf{g}' = \mathbf{g} = 0$] relative to its forward scattering ($\mathbf{k}' = \mathbf{k}$). This phenomenon further enhances the maxima at small momentum transfer in the effective ion-core t matrices. Moreover, these maxima become more pronounced with increasing energy of the incident electron. Especially at higher temperatures, they can require the inclusion of additional partial waves in ELED intensity calculations.

We recall from Section III.F that the values of $\langle u_{\nu}^2 \rangle_T$ for surface scatters ($\nu=0$) typically are twice those associated with bulk scatterers. Stated in terms of the normal mode (i.e., phonon) spectrum of the lattice vibrations, this fact is a manifestation of the occurrence of surface phonon branches of this spectrum. In a complete theory, these surface phonon modes would be incorporated into the lattice vibration Hamiltonian, (21) in Section III.B, which in turn would be used to evaluate the $\langle u_i^2 \rangle_T$ in (138b). In practice, however, it has been customary to adopt an empirical approach in which an effective Debye temperature is assigned to each separate planar sublattice of equivalent ion-cores.^{8,10,47} Thus we write

$$W_{\nu}(\mathbf{k}' - \mathbf{k}) \equiv (\mathbf{k} - \mathbf{k}')^2 W_{\nu}(T) \quad (139a)$$

$$W_{\nu}(T) = \frac{3\hbar^2}{2M_{\nu}\kappa\Theta_{\mathbf{D}\nu}} \left[\frac{1}{4} + \left(\frac{T}{\Theta_{\mathbf{D}\nu}} \right)^2 \int_0^{(\Theta_{\mathbf{D}\nu}/T)} \frac{x dx}{e^x - 1} \right] \quad (139b)$$

in which M_{ν} is the mass of the atoms in the sublattice labeled by ν , $\Theta_{\mathbf{D}\nu}$ is the Debye temperature describing the motion of the atoms in this layer, T

is the temperature, and κ is Boltzmann's constant. The enhanced lattice vibration amplitudes of surface ion-cores are described in this model by letting $\Theta_D^{r=0} < \Theta_D^{r=1}$ as discussed in association with (101) and (102) in Section III.F.

The lattice vibrations exert two different types of influence on the calculated ELEED intensities. Obviously they cause these intensities to depend on the temperature and on the phonon spectrum of the sample (see Section III.F). They also can effect pronounced changes in the appearance of the intensity profiles as illustrated in Fig. 17. The detailed nature of both effects depends, however, on the optical potential and on the rigid-lattice electron-ion-core scattering phase shifts as well as on the lattice vibrational spectrum of the solid.^{10,11,197} The only important general result to emerge thus far from studies of these phenomena^{10,47,197-199,242} is that for $E \lesssim 100$ eV the intensity profiles predicted for a rigid lattice deviate from those predicted for a vibrating lattice primarily by an overall scale factor of the order of $\frac{1}{2}$ at temperatures much less than any of the Θ_D^r used in the vibrating lattice calculation. This conclusion has the important consequence that ELEED intensity data measured at low temperatures [e.g., 4.2°K (liquid He) or perhaps 77°K (liquid N₂)] can be used in atomic structure analyses even though the vibrational amplitudes of the surface scatterers are not known in detail. For clean metals this situation can persist up to room temperature (see, e.g., Fig. 22). In most cases, however, significant changes in the line shapes as well as in the absolute magnitudes of the intensity profiles occur for temperatures near and above the effective Debye temperature $\Theta_D^{r=0}$, associated with the surface ion-cores. Because of their dependence on so many of the model parameters, the high-temperature intensity profiles must be examined individually in each separate case. Their only universal feature is the disappearance of both intralayer and interlayer interference maxima with increasing electron energy because of the factors of $(k'_\perp - k_\perp)^2$ and $(\mathbf{g}' - \mathbf{g})^2$ in (138b).

4. Number of Phase Shifts: Vibrating Lattice

We found in Section V.C.3 that the thermal vibrations of the ion-cores in the sample cause the renormalization of the electron-ion-core t matrices. This renormalization is described by (138) and (139). Its primary effect is the enhancement of the maxima in the t matrices at small scattering angles. Since the description of these maxima is the predominant cause of the need to use many phase shifts in the partial-wave representation of the t matrix (see Section V.C.2), we must examine the influence of the t matrix renormalization procedure on the determination of the number of partial waves required in a multiple-scattering calculation of elastic low-energy electron diffraction (ELEED) intensities.

For temperatures large relative to Θ_D^ν the expression for $W_\nu(T)$ given by (139b) becomes

$$W_\nu(T) = \frac{3\hbar^2}{2M_\nu\kappa\Theta_D^\nu} \left[\frac{1}{4} + \frac{T}{\Theta_D^\nu} \right]; \quad T \geq \Theta_D^\nu$$

$$= \frac{10^{-17}}{A_\nu} \left(\frac{723}{\Theta_D^\nu} \right) \left[\frac{1}{4} + \frac{T}{\Theta_D^\nu} \right] \quad (139c)$$

in which A_ν is the atomic number of the ion-cores on the sublattice labeled by ν . For typical materials the magnitude of the prefactor of the square brackets in (139c) is about 10^{-18} cm^2 . Therefore the t matrix renormalization becomes appreciable for momentum transfers $q \sim 10 \text{ \AA}^{-1}$ at zero temperature but for $q \sim 1 \text{ \AA}^{-1}$ at $T = 2\Theta_D^\nu$. Values of $q \sim 10 \text{ \AA}^{-1}$ correspond to an incident electron energy of $E \sim 100 \text{ eV}$, whereas $q \sim 1$ corresponds to $E \sim 1 \text{ eV}$. Therefore we see quite explicitly that temperatures $T \gtrsim \Theta_D^{\nu=0}$ will exert an appreciable influence on the renormalized ion-core t matrices and hence on the multiple-scattering analyses. At these temperatures three to nine partial waves are required in the expansion of the $\exp[-W_R(\mathbf{k}' - \mathbf{k})]$ factor in (138a).^{10,199}

The final quantities which enter the multiple-scattering calculations of ELEED intensities are the partial-wave expansion coefficients of the renormalized ion-core t matrices given by (138a). Therefore the number of partial waves required for $T \gtrsim \Theta_D^{\nu=0}$ is approximately the number required for a rigid lattice plus two (or more, depending on the value of T). In the case of aluminum, we have argued that three partial waves are adequate for the description of ELEED from a rigid lattice. Therefore five is the minimal number for the analysis of ELEED from a vibrating lattice at $T \gtrsim \Theta_D^{\nu=0}$. The intensity profiles predicted for Al(100) by two such model calculations are compared with measured intensities in Fig. 24. The importance of the extra two partial waves in describing the calculated line shapes for $T > \Theta_D^{\nu=0} \equiv \Theta_S$ is evident from a comparison of the three- and five-phase-shift calculations using $\Theta_D^{\nu=0} = 180^\circ$ and $\Theta_D^{\nu>0} = 380^\circ$.

Summarizing, the description of ELEED from a vibrating lattice at temperatures comparable to and above the Debye temperature associated with the *surface* ion-cores requires the use of at least two additional partial waves relative to the corresponding description of ELEED from a rigid lattice (Section V.C.2). This fact as well as uncertainties in the description

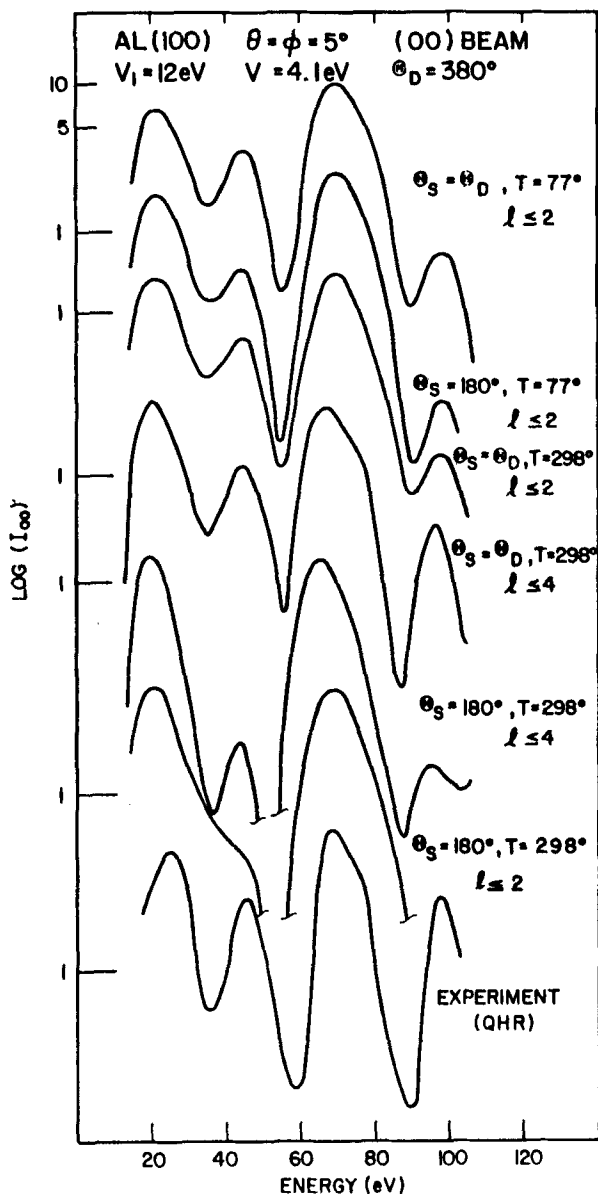


Fig. 24. Intensity profiles for the (00) beam of electrons incident on Al(100) at an angle of incidence of 5° along an azimuth which is 5° off a $\langle 010 \rangle$ direction. The upper six profiles are calculated using the potential predicted by an overlapping atomic charge density model.⁴⁷ The lowest panel illustrates intensities measured at 298°K by Quinto et al.¹⁹⁴ The optical potential parameters, effective Debye temperatures, and number of phase shifts (i.e., three for $l < 2$ or five for $l < 4$) are indicated in the figure. The value of $\theta_s = 180^\circ = \theta_D^{z=0}$ is obtained from an analysis of the temperature dependence of the larger peaks in the intensity profile.¹⁹⁹ (After Duke et al.⁴⁷)

of the vibrations of surface scatterers indicates that studies of surface crystallography should be carried out at low temperatures ($T \lesssim 100^\circ$) for most materials.

5. Bulk Electron-Ion-Core Potentials

The construction of the electron-ion-core potential was described in Section V.A. In this section we examine the dependence of predicted elastic low-energy electron diffraction intensities on the model potential used in the calculation.

Three distinct levels of approximation are commonly used in the construction of model electron-ion-core potentials.

1. A simple overlapping atomic charge density model, such as that described in Section V.A, is used directly to construct a muffin-tin potential with spherical ion-cores.^{47,242,265,312} The phase shifts resulting from this model are obtained by integration of the Schrödinger equations for the individual (i.e., isolated) ion-core potentials.

2. A self-consistent "band structure" potential is constructed by iterative calculations of the ground-state energy and charge distribution.^{42,43,46,250,251} The associated phase shifts are evaluated as for potentials in class 1.

3. Special "high-energy" potentials involving various modified treatments of electron-electron exchange interactions are constructed using atomic charge densities but analyzing electron scattering from these by using the Hartree-Fock approximation or a simplification thereof.^{43-45,52} Other models including pseudopotentials^{53,274,284-286} and strictly empirical atomic scattering factors (like the isotropic scatterer model^{197,248,255}) also have been discussed in the literature. The pseudopotential models have not yet achieved extensive application, however, and the empirical scattering factors have been used primarily to examine general features of the predicted intensities rather than to provide detailed descriptions of specific ELEED intensity data.

As indicated in Section V.A, it appears that the use of either an overlapping atomic charge density or a pseudopotential model (or empirical version thereof) is both necessary and sufficient for the description of ELEED intensities with enough accuracy to be adequate for applications in surface crystallography. Specifically, neither the complete self-consistency of a band structure potential nor a special accounting for the high energy of the incident electrons seems to be required for these applications. In the case of metals, this result for Al(111) is illustrated by Fig. 22 (see Section V. C.1) in which the theoretical curves labeled JMJ are obtained using a band structure potential²⁵¹ and the unlabeled curves are obtained from an overlapping atomic charge density model.⁴⁷ The same

conclusion also has been documented for the low-index face of transition metals as indicated in Figs. 25 and 26 for Ni(100). Figure 25 illustrates the comparison of intensity profiles calculated using two independently constructed overlapping atomic charge density potentials (labeled LARAMORE and DLLT in the figure) and those evaluated using Pendry's Hartree-Fock phase shifts.^{45,310} The intensities resulting from the "high-energy" Hartree-Fock potential are clearly distinguishable from those obtained using the overlapping atomic charge density model. Comparison of these latter calculated intensities with the data of Demuth et al.³²³ and of Andersson and Kasemo³²⁴ is given in Fig. 26 for the (00) diffracted beam. The correspondence with Andersson and Kasemo's data on the nonspecular beams is comparable to that shown in Fig. 26.³¹² Figures 22 and 26 reveal clearly the extent of the description of experimental ELEED intensities by simple "atomic" local potentials provided the two constants associated with the optical potential [e.g., V_0 and λ_{ee} in (28) or V_1 and V_2 in (127)] are treated as adjustable parameters.

The situation for insulators is less clear than that for metals primarily because no adequate body of ELEED intensity data exists on which to base a definitive analysis for any insulator or semiconductor. In this case,

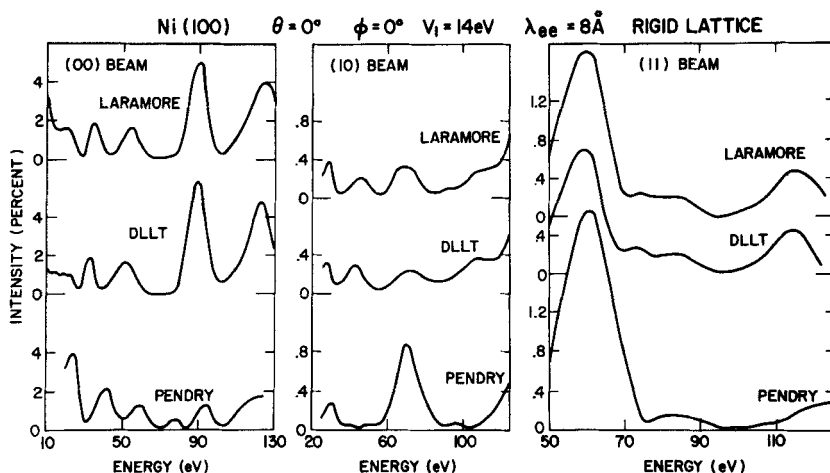


Fig. 25. Calculated intensity profiles for the elastic diffraction of normally incident electrons from the (100) face of atomically flat Ni. The profiles labeled LARAMORE were obtained using the model potential described in Ref. 312; those labeled DLLT were evaluated using the potential discussed in Ref. 242; and those labeled PENDRY were obtained using the phase shifts associated with the calculations reported in Ref. 310 as communicated by Dr. S. Y. Tong. All calculations were performed using the multiple-scattering computer programs of Duke et al.²⁴²

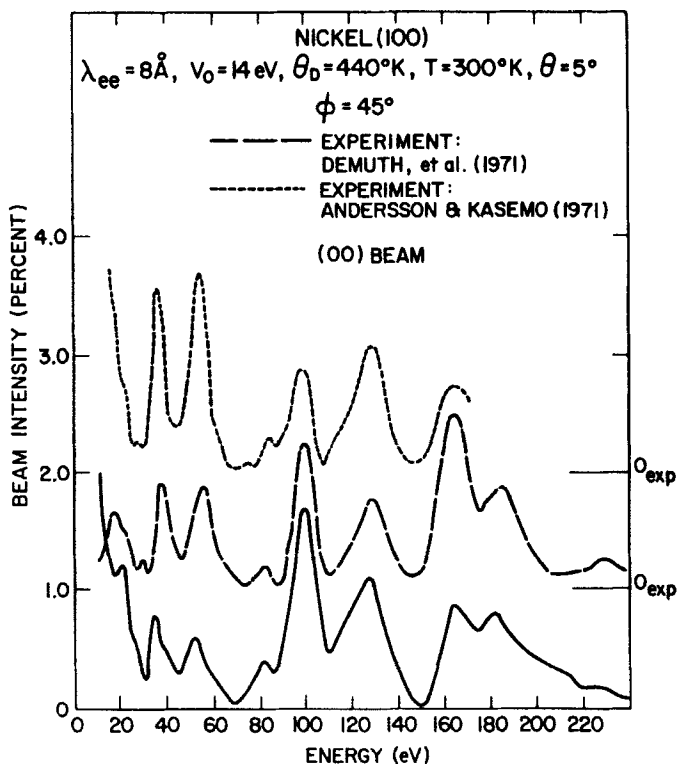


Fig. 26. Comparison of calculated (solid line) and observed (dashed lines) intensity profiles for the (00) beam of electrons diffracted from Ni(100). The experimental intensities were reported by Demuth et al.³²³ and by Andersson and Kasemo,³²⁴ respectively, as indicated in the figure. The calculations were performed by Laramore³¹² using a relativistic overlapping atomic charge density model potential and a five-phase-shift, five-layer multiple-scattering computer program. (After Laramore.³¹²)

however, the opportunity exists for large changes in the potential due to the transfer of charge from one ion-core to another in ionic solids. An analysis (based on the use of local atomic potentials) of a few data for LiF reported by McRae and Caldwell³²⁵ has been given by Laramore and Switendick.²⁶⁵ A comparison with these data of the intensity profiles for the (00) beam calculated using both neutral atom " Li^+F^- " and ionic scatterer " Li^+F^- " potentials is shown in Fig. 27. The most obvious and important feature of the intensity profiles predicted by these two potentials is their similarity. Essentially the only difference between them is a rigid shift of the energy scales associated with their differing values of the real part of the optical potential. Thus we reach the important conclusion that

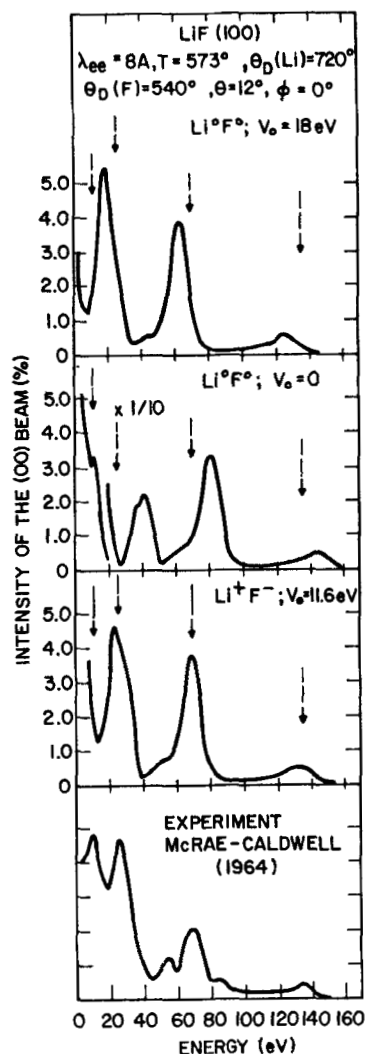


Fig. 27. Comparison with experimental intensities of calculated intensity profiles for the (00) beam of electrons diffracted from LiF(100). Those profiles predicted by neutral atom potentials are designated by $\text{Li}^\circ\text{F}^\circ$ whereas those associated with an ionic potential are indicated by Li^+F^- . The azimuthal angle φ is measured relative to an axis of the primitive square lattice of the surface Bravais net. The dashed arrows indicate the energies of prominent experimental maxima. All calculations were performed using overlapping atomic (ionic) charge density model potentials reduced to muffin-tin form. The resulting phase shifts were inserted into a two-sublattice, three-phase-shift, five-layer version of a multiple-scattering computer program.³²⁶ (After Laramore and Switendick.²⁶⁵)

if the parameters of the optical potential are adjusted to describe the most prominent peaks in the experimental intensity profiles, then even large changes in the potential like those induced by altering the charge states of the scatterers introduce relatively minor alterations in the predicted intensities.

In summary, we find that the use of simple overlapping atomic charge density models of the electron-ion-core potentials and the direct evaluation of electron scattering phase shifts for the resulting local spherical potentials provide a quite adequate description of experimental ELEED intensities from nominally clean, atomically flat solid surfaces. For both metals and insulators modest changes in these potentials act primarily to shift the energy scales of the intensity profiles. Consequently, such changes can be absorbed by selecting a different (constant) value for the real part of the optical potential. Since the optical potential cannot be calculated accurately from microscopic models (see Section V.B), however, most models of the electron-ion-core potential are equivalent from the perspective of using them together with an empirical optical potential in an atomic structure analysis.

6. Specifically Surface Phenomena: Clean Surfaces

We anticipate that the major application of analyses of elastic low-energy electron diffraction (ELEED) intensities will be for the purpose of determining the atomic structure of surfaces. In such a case, all of the parameters characterizing the electron-ion-core potential and the optical potential are regarded as fixed a priori, whereas those describing the positions of the ion-cores are considered unknowns to be determined from the observed intensities. The surface scatterers differ from those in the bulk, however, in their electronic and vibrational properties as well as in their positions. In this section we indicate the extent to which uncertainties in the electronic and vibrational properties of these surface ion cores influence an analysis of ELEED intensities whose purpose is the determination of their geometrical structure.

Even for a clean, atomically flat surface the electron-ion-core potentials of surface atoms differ from those in the bulk because of the reduced atomic coordination near the surface. The influence of this effect on the ELEED intensities from the low-index faces of aluminum has been studied by Duke et al.⁴⁷ Examples of their results for two models of the bulk and surface potentials are shown in Fig. 28. It is evident from the figure that within the context of the overlapping atomic charge density model the reduced atomic coordination at the surface exerts negligible influence on the calculated intensity profiles. This result remains valid even at low incident electron energies $E \lesssim 50$ eV for which the discrepancies between

the phase shifts of the surface and bulk scatterers are largest.⁴⁷ Indeed, Fig. 28 constitutes a graphic illustration of why models of ELEED from clean metals embodying bulk electron-ion-core potentials provide a satisfactory description of observed low-temperature, low-energy ($E \lesssim 100$ eV) intensities from these materials.

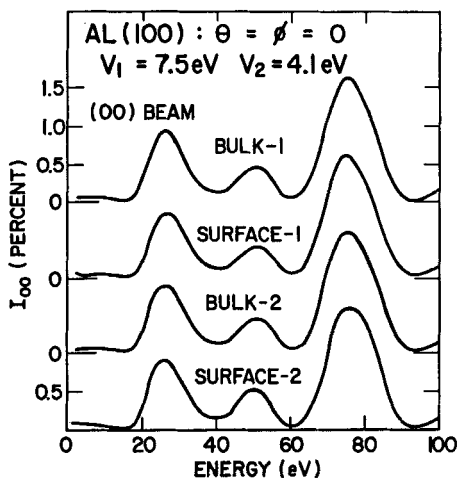


Fig. 28. Intensity profiles for the (00) beam of normally incident electrons elastically diffracted from Al(100). The profiles labeled BULK-1 and BULK-2 were evaluated using bulk phase shifts obtained from the overlapping atomic charge density model using methods "1" and "2", respectively, described in Ref. 47. Those labeled SURFACE-1 and SURFACE-2 were calculated using phase shifts obtained from this model by following these same methods. The parameters describing the optical potential are noted in the figure. All calculations were performed for a rigid lattice using a multiple-scattering computer program. (After Duke et al.⁴⁷)

We already have introduced the topic of the enhanced vibrational amplitudes of surface ion-cores in Sections III.F, V.C.3, and V.C.4. In particular, we recall from the discussion of Fig. 24 in Section V.C.4 that for temperatures high relative to the effective Debye temperature of the surface scatterers the large lattice vibrations of these atoms can introduce substantial modifications of the intensity profiles. This fact is readily verified by comparing the $T=298^\circ$ profiles shown in Fig. 24 for the two cases $\Theta_s \equiv \Theta_D^{r=0} = \Theta_D^{r>0} \equiv \Theta_D = 380^\circ$ and $\Theta_s = 180^\circ$, $\Theta_D = 380^\circ$, respectively. The value $\Theta_s = 180^\circ$ was selected¹⁹⁹ to describe the temperature dependence of the experimental intensities measured by Quinto et al.¹⁹⁴ Consequently, the lower three curves in Fig. 24 indicate a potentially serious

and as yet unresolved problem in the theoretical analyses of high-temperature ELED intensities from Al(100): The parameters Θ_D' that describe the temperature dependence of the prominent peaks in the intensity profile for the (00) beam fail to describe its changing line shape with increasing temperature. Therefore we obtain another argument for performing structure analyses on low-temperature ($T \leq \Theta_D'^{=0}$) ELED intensity data. Only in this case do the enhanced vibrations of the surface ion-cores fail to distort the low-energy ($E \lesssim 100$ eV) line shapes of the intensity profiles from those obtained for a rigid lattice.

In conclusion, Figs. 24 and 28 reveal that, provided a structure analysis for the low-index faces of aluminum is confined to observed ELED intensities for $E \lesssim 100$ eV taken at nitrogen temperatures ($T = 77^\circ\text{K}$) or below, uncertainties in the electronic and vibrational properties of surface atoms exert negligible influence on the analysis. Although one example hardly suffices to prove a theorem, the relatively low atomic number and Debye temperature of aluminum suggest that this conclusion is valid far more generally.

7. Adsorbed Overlayer Potentials

In constructing the electron-ion-core potentials associated with adsorbed species on crystalline surfaces, two considerations are of paramount importance. First, what is the appropriate level of sophistication to be incorporated into models of these potentials? Second, to what extent does the local coordination of the adsorbate influence the associated electron-ion-core phase shifts to be used in a multiple-scattering analysis of its geometrical structure? We proceed in this section by examining each of these issues in turn.

A thorough discussion of these questions thus far has been given in only one case: $c(2 \times 2)$ adsorbed monolayers of Na, S, and O on Ni(100).²⁴² The space group symmetry of such $c(2 \times 2)$ overlayers and the symmetry of the associated reciprocal lattice are indicated in Fig. 29. We recall from the Introduction, however, that the space group-symmetry does not suffice to determine the positions of the adsorbed species. The three most probable adsorption sites are specified and labeled in Fig. 30. Moreover, for each of these sites the question arises as to whether or not the surface is "reconstructed." That is, Ni atoms from the substrate can occupy the "empty" sites in the top layer which are not filled by the (half-monolayer coverage of) adsorbed species. One of our central tasks in this section is the illustration that changes in the geometrical positions of the adsorbates create sufficiently minor changes in the electron-ion-core phase shifts that the consequences of the electronic and geometrical structure of

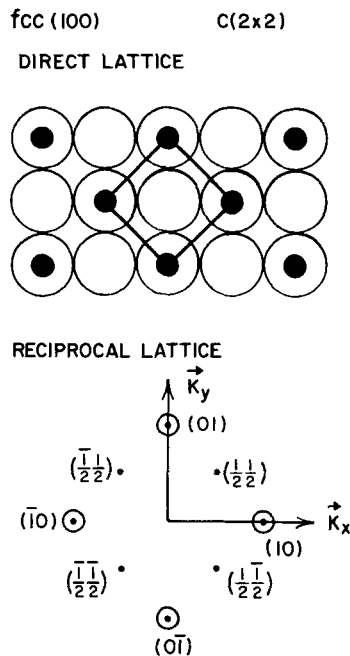


Fig. 29. Schematic indication of the space group symmetry (top panel) and its associated ELEED intensity pattern (lower panel) for a $c(2 \times 2)$ adsorbate structure on the (100) face of an fcc crystal. These structures typically appear at half-monolayer coverage when, as indicated in the figure, one adsorbate species (small heavy circles) is associated with two atoms (large open circles) in the substrate.

SITES OF HIGH COORDINATION

fcc (100) : $C(2 \times 2)$

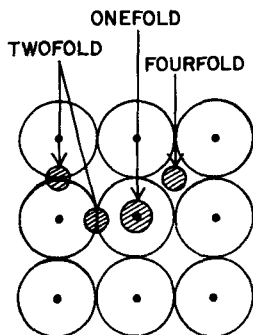


Fig. 30. Schematic indication and labeling of the sites of high coordination for adsorbates on the (100) face of an fcc crystal.

these overlayers can be distinguished with enough accuracy to perform a determination of their atomic geometry using observed elastic low-energy electron diffraction (ELED) intensities.

We recall from Section V.C.5 that three levels of approximation characterize commonly used models of the electron-ion-core potentials. In overlapping atomic charge density or pseudopotential models the potentials and their associated phase shifts are constructed by fiat and then used in the ELED calculations. The next more complicated models are those in which self-consistency criteria are imposed on the charge densities used to obtain the potentials. The final class of models consists of those constructed by eliminating the self-consistency requirements but utilizing a Hartree-Fock analysis of electron scattering from the individual ion-core potentials in order to treat more correctly the alterations in the electron-electron exchange forces associated with the high energies of electrons in the $10\text{ eV} \lesssim E \lesssim 10^3\text{ eV}$ range of interest in ELED.

Self-consistent model potentials have not yet been used in the analysis of ELED intensities from adsorbed overlayers. Moreover, our considerations of self-consistency and surface phenomena in Sections V.C.5 and V.C.6, respectively, do not suggest an overwhelming need for such potentials in surface structure analyses via ELED. A comparison of local potential and Hartree-Fock analyses of ELED from an overlapping atomic charge density model of a $c(2 \times 2)$ Na structure on Ni(100) is presented in Fig. 31. We again find, as in the case of clean Ni(100) (Section V.C.5), that the two calculations yield intensity profiles that are of comparable utility in surface structure analysis. The interpretation of the profiles shown in Fig. 31 is complicated by the use of perturbation theory for $E > 15\text{ eV}$ in the calculations labeled PENDRY.³¹⁰ Nevertheless, the great similarity of the predictions of the local and nonlocal (i.e., Hartree-Fock) analyses is evident in all three diffracted beams. They are "identical" for the purpose of structure determination provided the parameters of the optical potential are determined empirically.

Finally, let us turn to an examination of the relationship between surface structure and the nature of the electron-ion-core potentials. Since the local coordination and bonding of an adsorbate species depend on its geometrical structure, it is entirely possible that the electronic and geometrical structures of adsorbed overlayers are inextricably intertwined. Fortunately, in the four cases subjected to extensive sensitivity analysis,^{241,242} that is, $c(2 \times 2)$ layers of Na on Ni(100) and Al(100) and of S and O on Ni(100), the intensity profiles have been shown to be influenced far more substantially by plausible alterations in the geometrical parameters than by those in the electronic parameters.

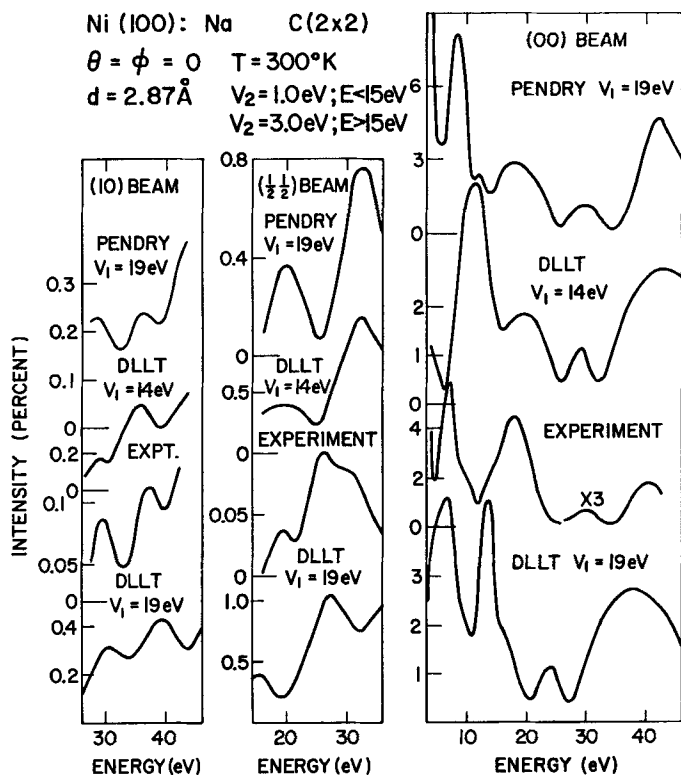


Fig. 31. Comparison of experimental and calculated intensity profiles for electrons normally incident on a $c(2 \times 2)$ overlayer of Na on Ni(100). Both the measured intensities and the calculated ones labeled PENDRY were reported in Ref. 310. These calculations were performed using a perturbation theory multiple-scattering analysis^{307,308} of a Hartree-Fock electron-ion-core potential.⁴⁵ The intensity profiles labeled DLLT were evaluated using a five-phase-shift, five-layer multiple-scattering analysis³²⁶ based on an overlapping atomic charge density potential.²⁴² The consequences of lattice vibrations are included in these latter calculations using $\Theta_D^{T=0} = 300^\circ\text{K}$ and $\Theta_D^{T=0} = 440^\circ\text{K}$. The parameters used in the empirical optical potential are indicated in the figure. The Na overlayer was taken to be situated in the fourfold coordination sites at a distance $d = 2.87 \text{ \AA}$ above the surface.

The key ingredient in our discussion of coupled electronic and geometrical effects on ELEED intensities is the word "plausible." The presence of adsorbates characterized by potentials dramatically different from those associated with the substrate atoms can create quite substantial changes in the intensity profiles. This fact is illustrated vividly in Fig. 32 in which

predicted ELED intensities from a simple cubic lattice of isotropic scatterers are displayed as functionals of the s -wave phase shifts characterizing the surface (δ_s) and substrate (δ_B) scatterers. The electronic structure of both the adsorbate and substrate atoms obviously exerts marked influence on the predicted intensity profiles.

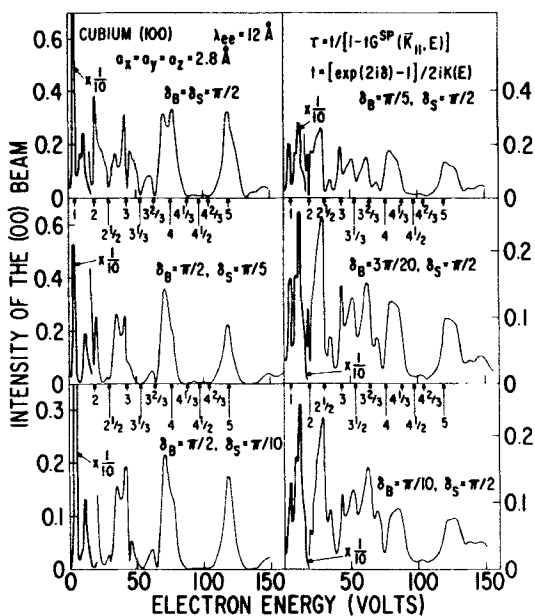


Fig. 32. Intensities of the (00) beam normally incident on the (100) face of a simple cubic lattice. Scattering from the top layer of ion-cores is described by the phase shift δ_s and that from the "bulk" ion-cores by δ_B . The intensities are calculated using (15), (30), (44), and (45) given by Duke, Anderson, and Tucker²⁴⁸ using the parameters shown in the figure. (After Duke and Tucker.⁵⁴)

Our interest lies not in the large modifications of electronic structure wrought by alterations in the atomic number of scatterers, however, but rather in the changes of this structure induced by differences in coordination and, by implication, in the character of the adsorbate-substrate bond. In Fig. 33 we illustrate the relative significance for typical intensity profiles of changing the electronic potential alone (upper two profiles) or the geometrical structure alone (lower two profiles) of a $c(2 \times 2)$ monolayer of

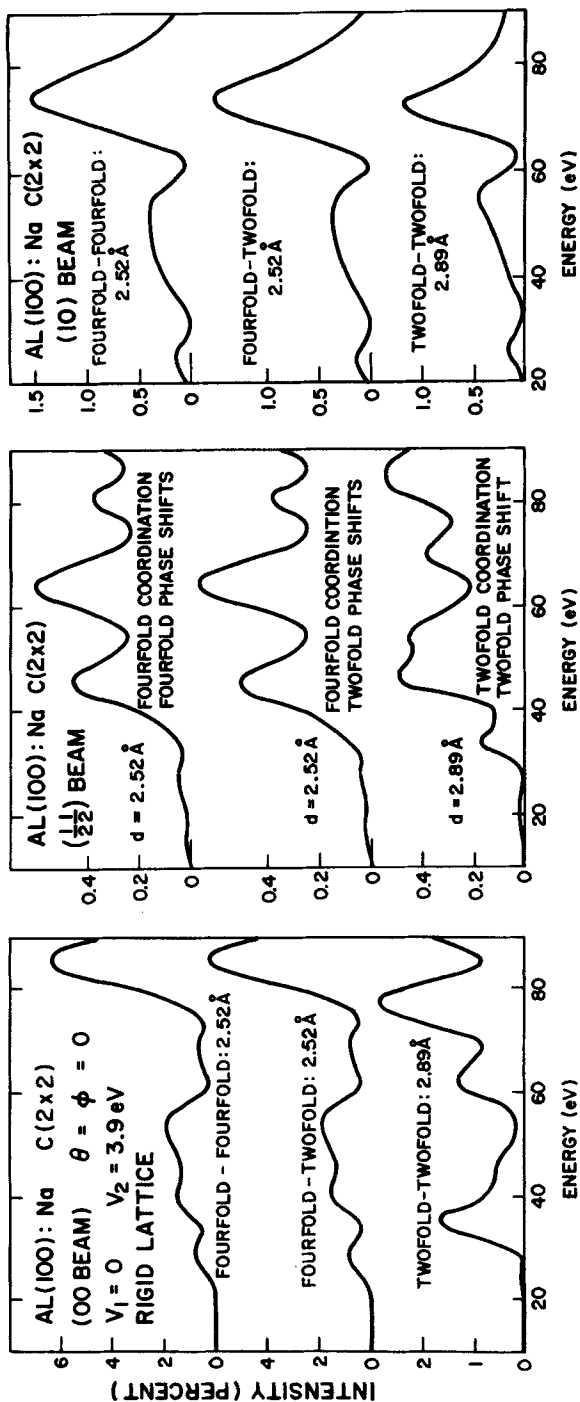


Fig. 33. Comparison of calculated intensity profiles for electrons normally incident on a $c(2 \times 2)$ overlayer of Na on Al(100). All calculations were performed for a rigid lattice of scatterers described by overlapping atomic charge density electron-ion-core potentials. A three-phase-shift, five-layer multiple-scattering program was used to perform the calculations. The electron-ion-core potentials (i.e., phase shifts) and the site symmetry of the Na atoms are indicated in the center panel and abbreviated in the others. The optical potential parameters are indicated in the figure. The quantity d given in the figure specifies the height of the Na overlayer above the Al(100) substrate.

Na on Al(100). Evidently the use of the twofold coordination potential for Na atoms at the fourfold sites (see Fig. 30) creates negligible modifications of the predicted intensities. Subsequent transfer of the Na atoms from the fourfold to the twofold sites, however, generates quite substantial changes in these profiles. Since the potentials used to construct Fig. 33 were obtained using an overlapping atomic charge density model, the resulting variation in the intensity profiles with different coordination does not simulate alterations in the chemical bonding. A study of ionic as opposed to covalent bonding for Ni(100)-c(2×2)-O reveals, however, that provided $50 \text{ eV} \lesssim E$ even this modification of the adsorbate potential does not materially influence the predicted ELEED intensities.^{241,242}

Summarizing, although the electronic structure of surface species can exert a marked influence on ELEED intensities, within the context of the (spherical scatterer) overlapping atomic charge density model changes in this structure induced by altered surface atomic coordination create barely discernible modifications of these intensities. On the other hand, changes in the geometrical positions of the surface scatterers produce marked alterations in the predicted intensities. It would be tempting to argue from these results that the alterations in adsorbate electronic structure with varying atomic coordination can be neglected in surface structure analysis via ELEED. We should recognize, however, that the approximation of the actual (anisotropic) surface electronic charge density with an array of spherical ion-cores in a muffin-tin potential eliminates by construction some of the distinction between the potentials obtained for varying coordination. This reduced sensitivity of the model ELEED intensities to the electronic structure of surface species is exacerbated by the use of empirical optical potentials (Section V.B). Thus at the present time it remains to be demonstrated that the insensitivity of the ELEED intensities to coordination-induced changes in the electron-ion-core potentials is not a peculiar, if attractive, feature of the overlapping atomic (ionic) charge density model.

D. Critique

Since this part of the review has been devoted to describing the construction and applications of model calculations of elastic low-energy electron diffraction (ELEED) intensities, it seems appropriate to conclude it with a brief assessment of their extent and utility. We first consider possible criteria on which to base such a critique, and then indicate the degree of their satisfaction in those cases which have been examined most extensively in the literature.

It is useful to isolate three separate standards for the assessment of model ELEED intensity calculations: (1) Do they describe the qualitative

features (e.g., trends, order of magnitude, variation with incident electron energy and target material) of observed intensities? (2) To what degree do they reproduce the quantitative details (e.g., absolute intensities, peak energies, and line shapes) of a given set of measured intensity data? (3) Is the extent of the data and the quantitateness of its description by the calculation adequate for the intended use of the analysis?

It is now well established that almost any model of ELEED incorporating strong inelastic collision damping, modest electron-ion-core scattering, and the correct geometry of the lattice produces a qualitative description of intensity profiles from clean, atomically flat single-crystal surfaces. Since the documentation of this result constitutes a major theme of a recent review,⁶ we do not pursue the topic further. The central issue in most current ELEED studies is the quantitative rather than qualitative aspects of the description of observed intensities by model calculations.

With the exceptions of a single paper²⁵⁰ and review⁶ in which different data and analyses are compared statistically, assessments of the quantitative description of a particular set of data by a given calculation have been based solely on the subjective judgments of individual authors. In comparing these assessments the response to several questions may prove helpful: (1) What is the extent of the (isothermal) intensity data used in a given analysis? In particular, are rotation diagrams as well as intensity profiles examined (Section III.A.1)? If only intensity profiles are utilized, several incident polar ($\theta \lesssim 25^\circ$) and azimuthal angles should be considered. An example of a fairly complete analysis of this type for the specular beam of electrons diffracted from Al(100) is shown in Fig. 34. Consideration of a wide selection of data is usually advisable in view of the empirical nature of models of the optical potential (Section V.B). Choices of the parameters in these models that provide a satisfactory description of one beam, crystal face, or set of data may prove less adequate in analyses of others. (2) Do the calculations reproduce the absolute magnitudes as well as the line shapes of the various displays of the measured isothermal intensities (Section III.A.1)? (3) How many adjustable parameters are included in the model potential and how are these determined? This issue is particularly important if only a small amount of data is analyzed. For example, often only one or two beams are examined over a small range of incident energies ($\Delta E \lesssim 50$ eV) and of angles of incidence ($\Delta\theta \lesssim 10^\circ$) for a given azimuth on a single-crystal face at only one temperature. Adjustments in the parameters of the optical potential, the vibrational amplitudes of surface scatterers, and the boundary conditions can create remarkable alterations in the comparison of model calculations with such a limited data base. (4) What are the ranges of temperature considered? If data taken at room temperature and above are examined, we found in Sections

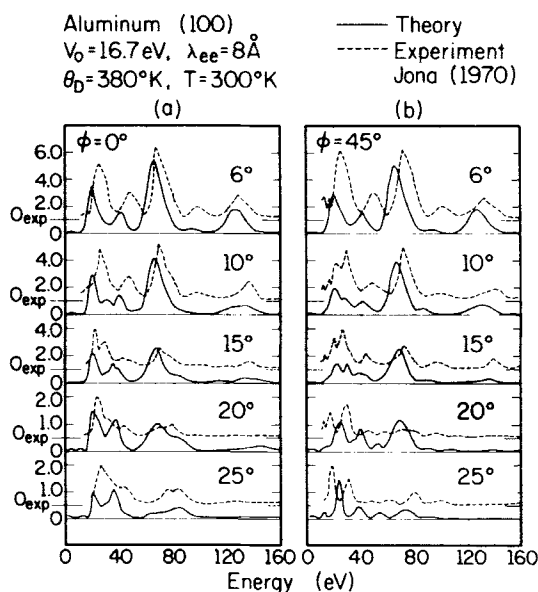


Fig. 34. Comparison between the predictions of the Laramore-Duke-Snow model²⁵⁰ and Jona's data³²⁰ for the specular beam of electrons diffracted from Al(100). The model parameters are indicated in the figure and the method of calculation in Ref. 250. The two panels show the diffracted intensities as a percentage of that for an incident beam along a diagonal ($\phi = 0^\circ$) and side ($\phi = 45^\circ$) of a primitive unit surface cell. The real inner potential, V_0 in (28) in the text, was taken to equal the Fermi energy plus the work function of Al(100). An empirical value of $V_0 \approx 12 \text{ eV}$ would produce alignment of all major theoretical and experimental maxima to within the intrinsic accuracy of the data ($\Delta E = \pm 2 \text{ eV}$).

V.C.3 and V.C.6 that the analysis should incorporate a description of the enhanced vibrations of surface ion-cores. Moreover, in this case the internal consistency of the predicted isothermal intensity profiles and the temperature dependence of major peaks in these profiles are a possible source of concern. In short, the model electron-solid interactions contain enough uncertainties and adjustable constants that quantitative conclusions about these interactions should be drawn from an examination of a sizable data base of absolute intensity measurements. In particular, these data should encompass modest ranges of incident electron energy ($\Delta E \gtrsim 100 \text{ eV}$) and polar angle ($\Delta\theta \gtrsim 20^\circ$), at least two or three azimuths, and (unless the measurements are taken at low temperatures, $T \lesssim 100^\circ \text{K}$), a span of temperatures corresponding to orders-of-magnitude changes in prominent peaks in the intensity profiles.

Fortunately, for many purposes the accumulation of such a massive array of data may prove unnecessary. Once the influence on calculated ELEED intensities of the basic ingredients of the model force law has been established, those aspects of the model which are unimportant for a given application may be treated with less concern. This hypothesis motivated the sensitivity analyses presented in Section V.C. in which we found that for applications to the surface crystallography of adsorbed overlayers, the combination of a simple overlapping atomic charge density evaluation of the electron-ion-core potential and an empirical optical potential obtained from an analysis of ELEED from the clean substrate provides a necessary and generally sufficient description of the electronic parameters of the model. Moreover, the use of low-temperature ($T \lesssim 100^\circ\text{K}$) intensity data renders the vibrational parameters relatively unimportant. Consequently, the intent to use the calculations for surface structure determination permits a significant relaxation of the requirement that they provide a quantitative description of all aspects of the measured intensities.

TABLE II
Tabulation of Dynamical Calculations of Isothermal ELEED
Intensity Profiles from Clean Single-Crystal Surfaces

Material	References
Ag(100)	42, 301
Ag(111)	255
Al(100)	29, 42, 46, 47, 54, 197, 199, 248, 250, 255 274, 278, 283, 301, 302, 306, 311, 322
Al(110)	53, 54, 197, 248, 250, 251, 255, 311
Al(111)	47, 53, 54, 248, 250, 251, 255
Au(100)	301
Be(0001)	29, 284, 285, 286
Cu(100)	42, 43, 46, 198, 249, 301
Ni(100)	51, 301, 311, 312, 323
Ni(110)	303, 311
Ni(111)	52, 287, 303, 312
Pd(100)	301
Rh(210)	255
W(100)	54, 248, 279
LiF(100)	264, 265, 301
NaF(100)	301
PbSe(100)	301
Graphite(0001)	281, 299, 301

Although calculations of ELEED intensities have been performed for low-index faces of several metals and insulators, at the present time only the analyses of ELEED from the low-index faces of aluminum are sufficiently comprehensive to permit definitive assessment of their quantitative description of experimental measurements. A tabulation of the existing dynamical model calculations of intensity profiles from atomically flat, clean surfaces is presented in Table II for convenient reference. The preponderance of analyses for Al(100) is evident. Moreover, for Al(100) the rotation diagrams also have been observed^{321,322,327} and calculated.^{322,328} It is evident from Figs. 22, 24, and 34 that if the constants in the optical potentials specified by either (28) or (127) are treated as adjustable parameters, a quite precise description of the shape of the room-temperature intensity profiles can be achieved for Al(100) and Al(111). A similar conclusion has been reached from a study³²⁸ of the room-temperature rotation diagrams for Al(100) taken at an angle of incidence of $\theta = 32^\circ$. For larger angles of incidence, the correspondence between the measured and calculated intensities tends to diminish.^{250,328}

Unfortunately, the application of the same model which successfully describes the close-packed faces Al(100) and Al(111) to analyze intensity profiles associated with the more open face Al(110) has proved disappointing.^{197,250,251} Even the qualitative features of the observed³²⁰ intensity profiles are described poorly: A result that can be attributed to either incomplete characterization of the experimental surface,^{197,250} contraction of the uppermost layer spacing,^{197,250,251} or the presence of steps on the surface.³²⁹ Therefore on the basis of isothermal line-shape considerations alone, the models described in Sections V.A. and V.B. describe "quantitatively" the measured intensities from Al(100) and Al(111) but a reconstructed surface geometry must be hypothesized in order to achieve a quantitative description of those from Al(110).

The absolute magnitudes of the diffracted intensities have been measured for both Al(100)³³⁰ and Al(111).³³¹ In both cases the measured maximum intensities are about 0.5 to 0.05% of that of the incident beam, that is, an order of magnitude smaller than the calculated ones shown in Figs. 22, 24, and 34. A resolution of this discrepancy has been suggested by Duke et al.⁴⁷ based on the microscopic theory of the optical potential.³⁰ The excitation of surface plasmons causes the adsorptive part of the optical potential to extend into the vacuum beyond the geometrical boundary of the solid. Figure 35 illustrates the consequences of such extensions as well as those of the enhanced vibrational amplitudes of surface scatterers. Simulating surface plasmon creation by the incident electron via initiating the adsorptive optical potential about one lattice spacing in front of the geometrical surface of the crystal brings into

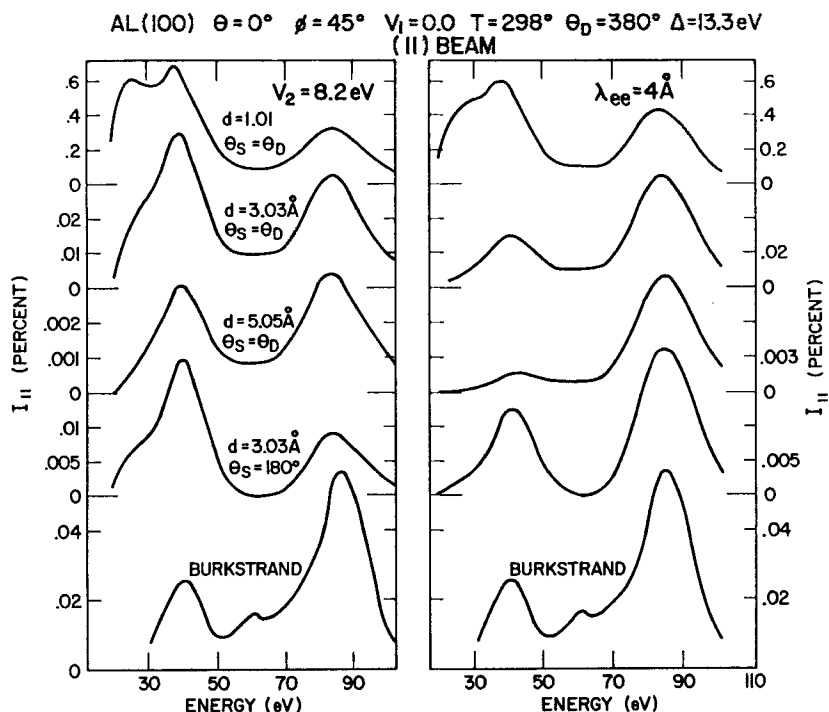


Fig. 35. Intensity profiles for the (11) beam of electrons normally incident on Al(100). The left-hand panel contains profiles evaluated using (127) for the optical potential, whereas the right-hand panel contains those calculated from (28). The parameters used in these optical potentials as well as the vibration parameters $\theta_S = \theta_D^{-1}$, $\theta_D = \theta_D^{*2}$ are indicated in the figure. The lower intensity profiles labeled BURKSTRAND are those measured by Burkstrand.³³⁰ The notation d designates the depth of the upper layer of ion-cores below the position of the onset of the inelastic collision damping. (After Duke et al.⁴⁷)

satisfactory correspondence the calculated and observed absolute intensities from both Al(100) and Al(111).⁴⁷

Only one examination of the temperature dependence of ELEED from aluminum has been reported: that of Al(100) by Quinto et al.¹⁹⁴ These data have been analyzed by Laramore¹⁹⁹ and by Duke et al.⁴⁷ Sample results for the intensity profiles are shown in Fig. 24. Both analyses lead to the conclusion that the selection of the parameters θ_D (Section V.C.3) which describes the temperature dependence of the prominent peaks in the intensity profiles fails to describe temperature-induced changes in the line shapes of these profiles. The most probable causes of this unhappy result are the breakdown of the theory leading to (138) or the occurrence of

increased thermal diffuse scattering at high temperatures, rendering inadequate the calculation of the elastic rather than the quasielastic scattering cross-sections (Section III.F). The compatibility of the analyses of the isothermal line shapes of observed intensities with those of their temperature dependence has not yet been established either for aluminum or for any other target material.

In summary, we find that the qualitative description of observed ELEED intensities by the models described in this part of the review is thoroughly documented. Moreover, these models often provide a quantitative description of the shapes and magnitudes of measured intensity profiles from both clean surfaces (Table II) and adsorbed overlayers.^{240-242,310} Such aspects of the data certainly seem to be reproduced with sufficient accuracy for ELEED to be a useful technique for the surface crystallography of clean and adsorbate-covered metals. Nevertheless, we must recognize that quantitative tests of the models are rare; their applicability to high-temperature ($T \gg \Theta_D$) data is not yet established; and they occasionally experience unexpected failures [e.g., in the description of the intensity profiles from Al(110) and of the temperature dependence of those on Al(100)]. On balance it seems fair to conclude, however, that the basic outline of both the multiple-scattering formalism described in Part IV and the electron-ion-core and optical potential models considered in this part are firmly established at the present time. Refinements of both undoubtedly will be forthcoming as a wider range of their applications is undertaken. We return to a discussion of such applications in Part VII, following our introduction to the theory of inelastic low-energy electron diffraction in Part VI.

VI. MODEL INELASTIC LOW-ENERGY ELECTRON DIFFRACTION CALCULATIONS

A. Two-Step Inelastic Diffraction

Perhaps the most surprising aspect of inelastic low-energy electron diffraction (ILEED) is that it occurs at all. The fact that electrons which have experienced an energy loss continue to diffract from the crystal lattice implies that the energy-loss process preserves the phase coherence of the incident beam. Yet we recall from Figs. 9, 11, and 12 (Sections III.A.1 and III.E) that, indeed, for energy losses $w = (E - E') \sim 25$ to 50 eV those electrons which have been scattered inelastically as well as elastically by a single-crystal solid emerge from it in a series of well-defined beams. The relevant conservation laws which describe such diffraction processes have been discussed in Section III.E [see, e.g., (60) to (63)]. The convenient

methods of displaying the inelastic diffraction intensity data were indicated in Section III.A.1. In this part we consider the mechanisms and general features of inelastic diffraction processes (Section VI.A), dynamical calculations of ILEED intensities (Section VI.B), and the consequences of various instrumental and intrinsic line-broadening mechanisms which must be considered in order to relate the calculated intensities to those observed using an ILEED spectrometer (Section VI.C). Our discussion of the important application of ILEED for surface characterization, that is, the determination of the dispersion relation of electronic surface excitations, is deferred until Part VIII.

The simplest mechanism for inelastic diffraction is that it occur via two sequential steps of energy loss and elastic diffraction.^{16,232} The physical nature of such a "two-step" mechanism is indicated schematically on the left-hand side of Fig. 36. Thus the scattering amplitude describing inelastic diffraction is the sum of those for the diffraction-before-loss (DL) processes and the loss-before-diffraction (LD) processes. In terms of the Hamiltonian defined by (23) to (30) in Section III.B it is most convenient to describe the calculation of these scattering amplitudes in the nomenclature of diagrammatic perturbation theory.^{247,252,332} In this notation open circles containing crosses delineate elastic scattering vertices [(23d)], solid lines designate electron propagators [(128)], wavy lines indicate loss mode

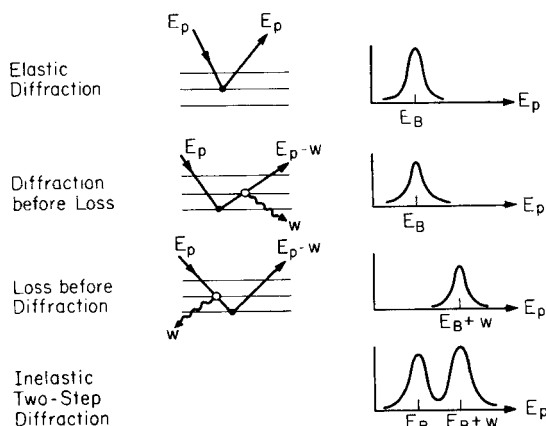


Fig. 36. Schematic indication of the relationship between a diffraction resonance in the elastic energy ("intensity") profile (top panel), the diffraction before loss (DL) energy profile (second panel), the loss before diffraction (LD) profile (third panel), and total inelastic energy profile (bottom panel) predicted by a two-step-diffraction model. The profiles are illustrated for a bulk plasmon emission process in the direction of the specular beam ($\mathbf{k}'_{||} = \mathbf{k}_{||}$).

propagators,²⁴⁷ and the intersections of wavy and solid lines are associated with loss mode vertices^{212,247} [(29)]. Panels (a) and (b) in Fig. 37 illustrate the perturbation theory symbolism for the diffraction before loss and loss before diffraction contributions, respectively, to the scattering amplitude. The expressions for the cross-sections associated with these diagrams are given by (16) to (20) in a paper by Bagchi and Duke.²¹²

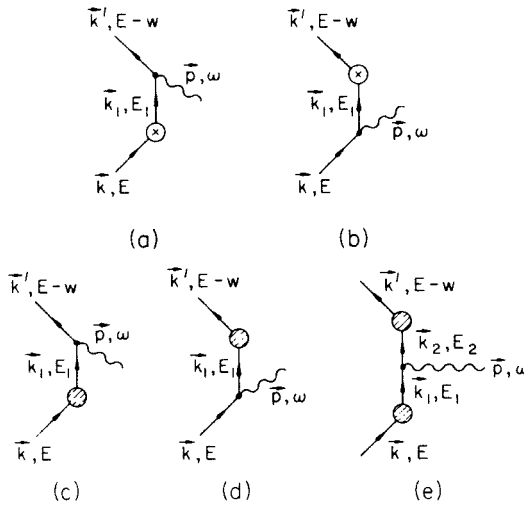


Fig. 37. Diagrams contributing to the scattering amplitudes of ILEED: (a) two-step, diffraction before loss; (b) two-step, loss followed by diffraction; (c) multiple elastic diffraction before loss; (d) loss followed by multiple elastic diffraction; (e) multiple elastic diffraction both before and after loss. The perturbation theory definition of the expressions for the cross-sections associated with these diagrams is given by Duke and Laramore.²⁴⁷ The shaded circle indicates the summation of an arbitrary number of individual elastic scattering events (designated by the circled cross in Figs. 37a and 37b). (After Duke and Landman.²⁵²)

Electronic-excitation-assisted diffraction differs from lattice-vibration-(phonon)-assisted diffraction in two important ways. First, whereas the probability of a phonon-assisted scattering event increases with increasing momentum transfer [(96) in Section III.F], the vertex functions for electronic excitations [$\iota(\mathbf{p})$ in (29c) in Section III.B] exhibit sharp maxima for forward scattering, that is, $\mathbf{p} \rightarrow 0$.^{212,247} Therefore the elastic scattering event in the two-step mechanism is necessary in order to “turn the electron around” so it can be reflected from the target. Second, the energies $\hbar\omega_{el}$ of the electronic excitations are large relative to the energy resolution of

conventional spectrometers [(58) in Section III.E]. This has the consequences that not only can the inelastic cross-sections be resolved from the elastic ones, but also ELEED resonant intensity maxima which are functions of the incident beam parameters (E, θ, ψ) lead to companion resonances in the ILEED intensities.^{12, 212, 252, 332–337} Since these coupled ELEED-ILEED resonances play a central role in the determination of excitation dispersion relations from observed ILEED intensities, we examine them more closely.

In the two-step model of inelastic diffraction, two separate types of resonance occur. The mechanism for the first kind, which we refer to as “*energy-tuned*” resonances, is illustrated in Fig. 36. In the inelastic energy profile, $I_{hk}^{w, \theta'}(E)$, the loss energy w and exit polar angle θ' are held fixed while the energy of the incident beam is varied. If a maximum in the elastic intensity profile exists at energy E_B , similar ones will occur in the inelastic energy profile at the energies E_B (diffraction before loss) and $E_B + w$ (loss before diffraction) as indicated in Fig. 36. Thus a single peak in the intensity profile causes a double peak in the inelastic energy profile. This behavior is illustrated in Fig. 38 for various values of w associated with calculated ILEED intensities for bulk plasmon emission by electrons incident on Al(100). The second type of resonance is associated with momentum conservation normal to the surface in the case that a bulk electronic excitation is created by the incident electron. These *momentum-tuned resonances* occur when

$$\text{Re} [k_{\perp}(0, E_{\pm}) + k'_{\perp}(\mathbf{g}, E_{\pm} - w)] \pm p_{\perp} = \frac{2\pi n}{d_{\perp}} \quad (140)$$

in which p_{\perp} is determined from energy and momentum conservation via (60) and (61), that is

$$\mathbf{p}_{\parallel} = \mathbf{k}_{\parallel} + \mathbf{g} - \mathbf{k}'_{\parallel} \quad (60b)$$

$$w = \hbar\omega_b(\mathbf{p}_{\parallel}, p_{\perp}) \quad (61)$$

The quantity d_{\perp} is the lattice spacing normal to the surface and \mathbf{g} is the planar reciprocal lattice vector associated with the diffracted beam (see, e.g., Fig. 1). If w is large enough and the bulk excitations are weakly damped, the momentum-tuned resonances are predicted to be distinguishable from the energy-tuned ones as illustrated in Fig. 39: a phenomenon called side-band diffraction in analogy to the occurrence of side bands on optical absorption lines in solids.^{332, 333} In practice, however, the occurrence of side-band diffraction resonances in inelastic energy profiles seems unlikely because of the large damping of bulk electronic excitations²¹² and

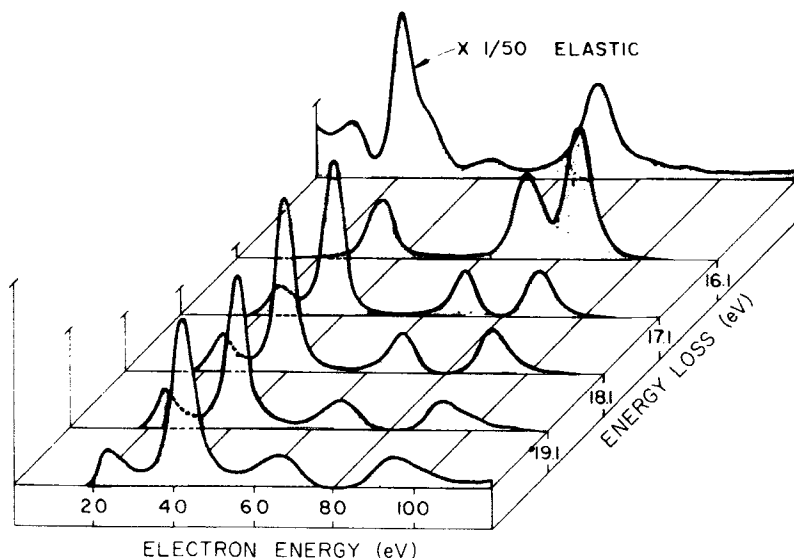


Fig. 38. Calculated elastic and inelastic energy profiles for the (00) beam of electrons diffracted from Al(100) accompanied by bulk plasmon emission. Subplane elastic scattering amplitudes (τ) have been employed to describe the elastic vertex. The profiles are evaluated for $\theta = \theta' = 15^\circ$, $\psi = 45^\circ$. The scaling of the profiles is indicated by the bars on the left-hand side of the panel. (After Laramore and Duke.³³³)

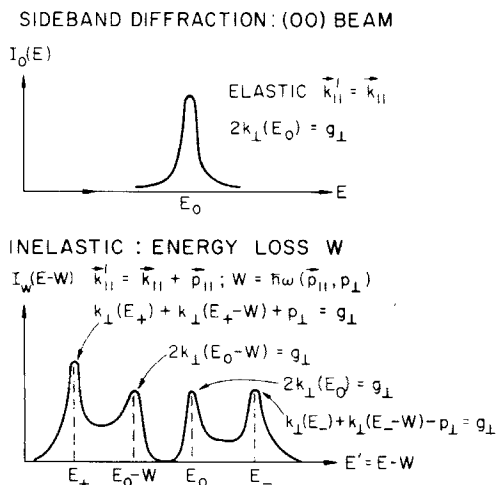


Fig. 39. Schematic illustration of the side-band diffraction splitting of the doublet structure in the inelastic energy profile. This splitting occurs only for bulk plasmons, and even then only if $\omega \gg \hbar\omega_b$ ($\mathbf{p} = 0$) so that the resonance conditions in the figure hold for modest values of p_{\perp} . The quantity g_{\perp} is $2\pi m/d_{\perp}$ where d_{\perp} is the layer spacing normal to the surface and m is an integer.

the complicating effects of multiple elastic scattering.^{252,336} They are not visible in Fig. 38, for example.

The modulation of ILEED intensities by resonant structure characteristic of ELEED renders the simple conservation law arguments advanced in Section III.E seriously inadequate for the detailed interpretation of ILEED intensities. This fact is illustrated in Fig. 40 for the surface-plasmon-assisted diffraction from Al(100). The elastic scattering modulates quite unequally the two components of the doublet predicted by (60) and (62). Moreover, when instrumental, plasmon damping, and lattice vibration broadening are inserted into the analysis, only the very large low-angle peaks survive above the background,³³⁷ a result quite consistent with observed ILEED intensities.^{234,236—238} Angular profiles for a larger loss energy associated with bulk plasmon emission are shown in Fig. 41. Comparison with Fig. 40 reveals that as suggested in Section III.E, the

ANGULAR PROFILES—SURFACE PLASMONS

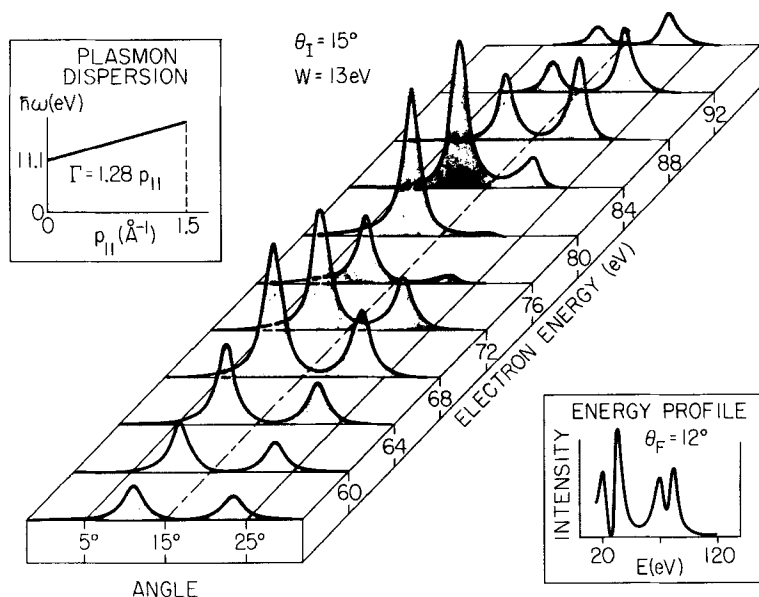


Fig. 40. Calculated inelastic angular profiles for the (00) beam of electrons diffracted from Al(100) accompanied by surface plasmon emission. Layer elastic scattering amplitudes (τ) have been used to describe the elastic vertex. The profiles are calculated for $\theta = 15^\circ$, $\psi = 45^\circ$. The insert on the lower right shows an inelastic energy profile taken at $\theta' = 12^\circ$. The insert on the upper left illustrates the plasmon dispersion curve and the plasmon damping parameter used in the calculation. (After Laramore and Duke.³³³)

ANGULAR PROFILES-BULK PLASMONS

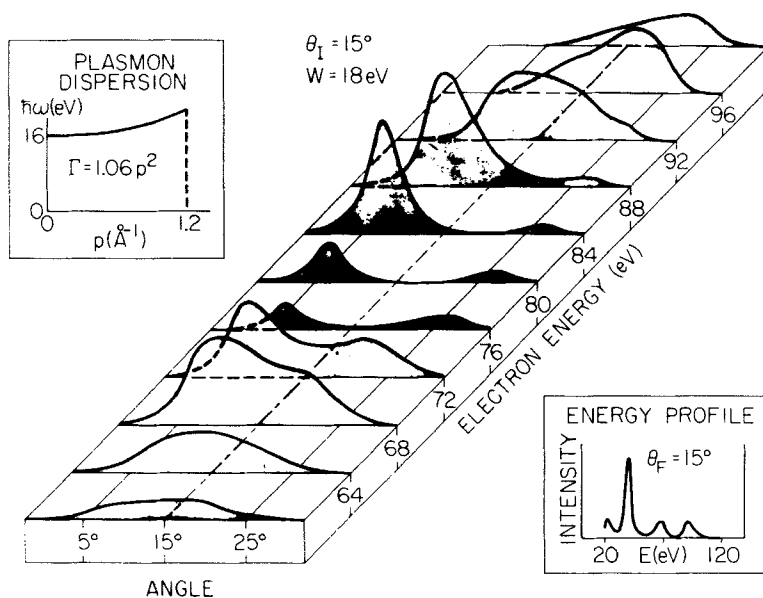


Fig. 41. Calculated inelastic angular profiles for the (00) beam of electrons diffracted from Al(100) accompanied by bulk plasmon emission. The parameters used in the calculation are indicated in the caption of Fig. 38. The insert on the lower right shows an inelastic energy profile and the insert on the upper left illustrates the plasmon dispersion curve and the plasmon damping parameter. (After Laramore and Duke.³³³)

bulk-plasmon-assisted diffraction tends to broaden the emerging beams without introducing excessive structure in their angular profiles. Nevertheless, prominent low-angle maxima occur near $E = 70$ and 86 eV. These are associated with momentum-tuned side-band-diffraction resonances³³³ and should be observable in measured ILEED intensities.

Having noted the major consequences of the two-step model, it is appropriate to inquire into the extent to which they are realized in experimental data. In this context, it is significant that the model calculations shown in Fig. 38, 40, and 41 were reported³³⁴ over a year prior to the subsequent confirmation of all of their main predictions by three separate experimental groups.²³⁶⁻²³⁸ The procedure used to select experimental data to analyze is simple. Initially, elastic intensity profiles for one or more diffracted beams associated with several incident beam directions are measured. Next, from these data one chooses a few prominent peaks at

energies $\{E_i\}$ and examines the corresponding loss profiles for various initial beam energies $(E_i - 20 \text{ eV}) \leq E \leq (E_i + 20 \text{ eV})$ and several final angles θ' in the angular range $(\theta - 10^\circ) \lesssim \theta' \lesssim (\theta + 10^\circ)$. For aluminum one discovers a prominent surface plasmon peak at $w \approx 11 \text{ eV}$ and bulk plasmon peak at $w \approx 15 \text{ eV}$. The accumulation of the data is completed by measuring angular profiles for incident beam energies in the same energy range $(E_i - 20 \text{ eV}) \leq E \leq (E_i + 20 \text{ eV})$ for various values of w near those of the prominent loss peaks: for example $8 \text{ eV} \leq w \leq 18 \text{ eV}$ in the case of aluminum.

The analysis of such a set of data proceeds in three steps. First, using a reasonable electron-ion-core potential (Section V.A) the theoretical elastic intensity profiles corresponding to the selected peaks in the experimental data are evaluated using the Born approximation (Section III.C). Second, the values of V_0 and λ_{ee} in (28) [or V_1 and V_2 in (127)] are chosen so that the Born approximation intensities "fit" the observed elastic intensity profile in the vicinity of one of those maxima for which the associated ILEED intensities were measured. Third, having parametrized the ELED data in this fashion, the cross-section formulas of Bagchi, Duke, and Landman^{12,212} permit the calculation of the ILEED intensities associated with bulk- and surface-plasmon-assisted diffraction as functionals of the plasmon dispersion and damping:

$$\hbar\omega_b(p) = \hbar\omega_b + A_1 p^2 + A_2 p^4 \quad (141a)$$

$$\Gamma_b(p) = \Gamma_b + B_1 p^2 + B_2 p^4 \quad (141b)$$

$$\hbar\omega_s(p_{\parallel}) = \hbar\omega_s + C_1 p_{\parallel} + C_2 p_{\parallel}^2 \quad (142a)$$

$$\Gamma_s(p_{\parallel}) = \Gamma_s + D_1 p_{\parallel} + D_2 p_{\parallel}^2 \quad (142b)$$

In typical analyses of ILEED from Al³³²⁻³³⁷ the bulk plasmon parameters are taken insofar as possible from kiloelectron-volt electron transmission data to be given by²¹² $\hbar\omega_b = 14.2 \text{ eV}$, $A_1 = 3.048 \text{ eV}\text{\AA}^2$, $A_2 = 0$, $\Gamma_b = 0.53 \text{ eV}$, $B_1 = 0.103 \text{ eV}\text{\AA}^2$, and $B_2 = 1.052 \text{ eV}\text{\AA}^4$. The surface plasmon parameters are regarded as unknowns to be extracted from the data analysis as described in Part VIII. Thus we have constructed a simple prescription for converting a hypothetical surface plasmon dispersion relation, (142), into calculated ILEED intensities for comparison with experimental ILEED data.

The burning issue, of course, is how well this prescription describes measured ILEED intensities. A global response to this question is provided in Figs. 42 and 43 for the loss and angular profiles, respectively, associated

with the (11) beam of electrons inelastically diffracted from Al(100).^{212,236} From Fig. 42 we see that both the intensities and energies of the maxima in the loss profile depend on the incident beam parameters (E, θ). Moreover, the qualitative features of the measured loss profiles are reproduced faithfully by the two-step model calculations. This fact is significant because all of the parameters used in these calculations were obtained

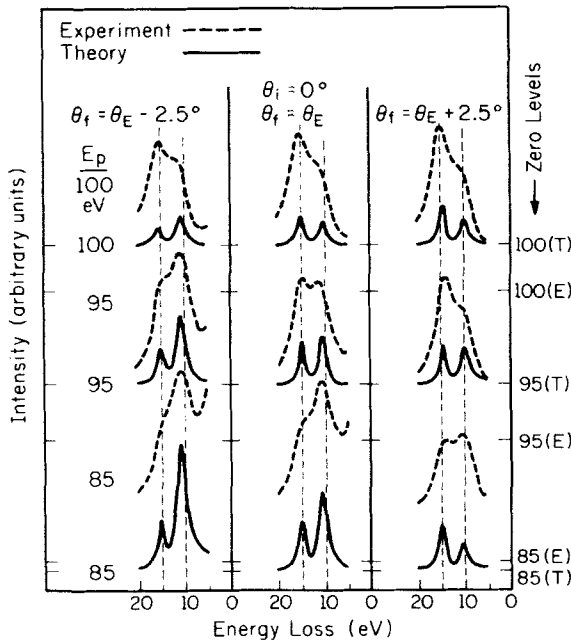


Fig. 42. A comparison of theoretical (solid lines) and experimental (dashed lines) loss profiles of electrons incident normally on Al(100) and scattered inelastically in the (11) beam. The primary beam energy is denoted by E_p which also labels the zero levels on the right-hand side of the graph. The notation $T(E)$ designates the theoretical (experimental) curve. The exit angles in the experiment are denoted by θ_i while θ_E defines the direction of the elastically diffracted beam. The theoretical curves in each vertical panel are computed for an emergence angle 1° above the measured exit angle. (See Ref. 212. The absolute value of this angle may be in error by as much as $\pm 4^\circ$.) The parameters characterizing the surface plasmon dispersion and damping used in the theory are given by $\hbar\omega_s = 10.1 - 0.7p_{\parallel} + 10p_{\parallel}^2$ and $\Gamma_s = 1.6 + 0.94p_{\parallel}$. Those characterizing the bulk plasmon are taken from kiloelectron-volt electron transmission measurements. Elastic electron-ion-core scattering is described by the s -wave inelastic collision model with $\lambda_{ee} = 8 \text{ \AA}$, $V_0 = 16.7 \text{ eV}$ and $\delta = \pi/4$. For these parameters a Bragg peak exists at $E_B = 86 \text{ eV}$. A large peak occurs in the experimental (11) intensity profile at this energy. (After Bagchi and Duke.²¹²)

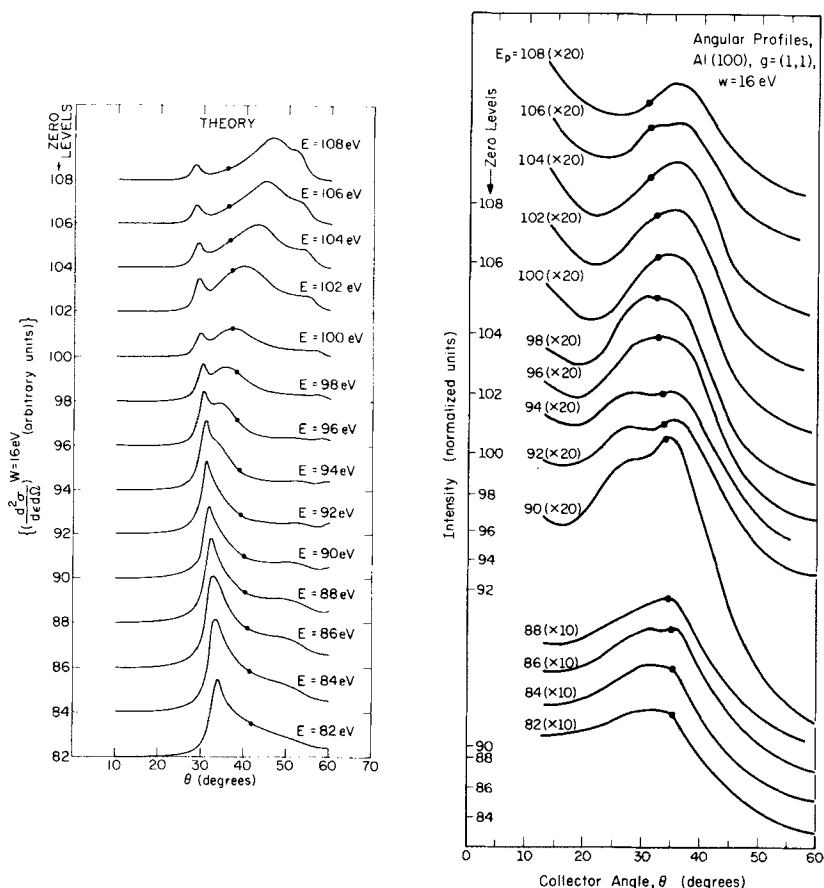


Fig. 43. Theoretical and experimental curves for the angular profiles of electrons incident normally on Al(100) and scattered inelastically in the (11) beam. The loss energy is fixed at 16 eV and the primary beam energy E is varied. Dots indicate the direction of emergence of the elastically scattered (11) beam. All parameters that are used in the model calculations are indicated in the caption of Fig. 42. The experimental collector angle is uncertain to within $\pm 4^\circ$ because of uncertainties in target and beam alignment and the angular spread of the incident beam. (After Bagchi and Duke.²¹²)

independently of the experimental data shown in the figure. Similar conclusions about the angular profiles may be drawn from Fig. 43. In particular, the movement of the observed maxima to higher angles with increasing incident beam energy is described by the model calculation and is a direct manifestation of the side-band diffraction phenomenon. The narrow peak near $\theta' = 30^\circ$ in the theoretical profiles is caused by surface-

plasmon-assisted diffraction. The broad structure arising for $\theta' < \theta_E$ at $E = 94$ eV and subsequently moving to $\theta' > \theta_E$ at $E = 102$ eV is a side band diffraction resonance analogous to that evident in Fig. 41 between 84 and 96 eV.

Although a qualitative description of the data by the model is evident from Figs. 42 and 43, the calculations must be refined further to achieve a quantitative one. The most sophisticated two-step model analysis of experimental measurements to date is that of ILEED data for Al(111) films given by Duke et al.^{13,337} Typical loss and angular profiles evaluated during the course of this study are shown in Figs. 44 and 45, respectively.

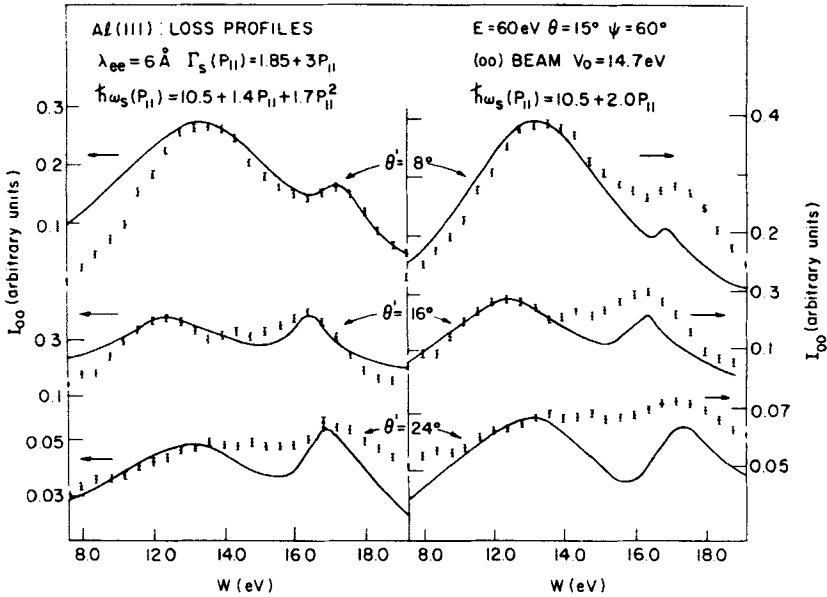


Fig. 44. Experimental (points) and theoretical (solid lines) loss profiles for the (00) beam of electrons scattered from Al(111) for three values of the exit angle ($\theta' = 8^\circ, 16^\circ, 24^\circ$). The incident beam parameters are primary energy $E = 60$ eV, polar angle $\theta = 15^\circ$, and azimuthal angle $\psi = 60^\circ$. A four-phase-shift (Snow's APW potential³¹⁷) two-step model was used in the calculations. The values of the other parameters used in the analysis are indicated in the figure. Results are shown for two surface plasmon dispersion relations, $\hbar\omega_s(p_{||}) = 10.5 + 1.4p_{||} + 1.7p_{||}^2$ (left-hand panel) and $\hbar\omega_s(p_{||}) = 10.5 + 2.0p_{||}$ (right-hand panel). Both dispersion relations are consistent with the regions of ambiguity described by Duke et al.¹³ and with the damping $\Gamma_s(p_{||}) = 1.85 + 3p_{||}$. The experimental surface-to-bulk peak height ratios and trends as a function of exit angle are predicted by both dispersions. The sensitivity of the quantitative line shapes to the dispersion relation used in the calculation, however, is evident from the figure. (After Duke and Landman.³³⁷)

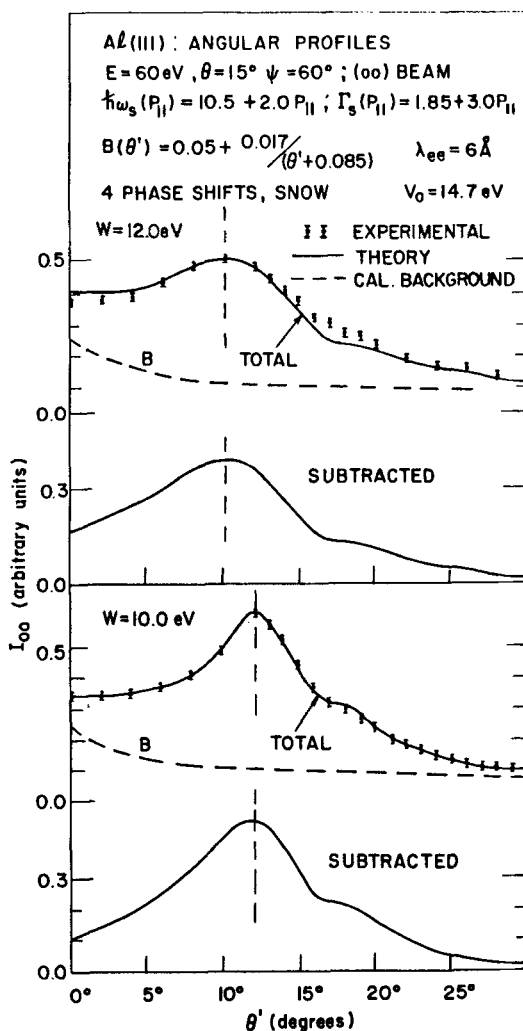


Fig. 45. Angular profiles of the (00) beam of electrons scattered from Al(111) for two values of loss energy ($w=10, 12 \text{ eV}$). The primary beam parameters are $E=60 \text{ eV}$, $\theta=15^\circ$ and $\psi=60^\circ$. The calculations were performed using the two-step model with four phase shifts derived from Snow's APW potential. The parameters used to describe the plasmon dispersion and elastic electron-ion-core scattering are indicated at the top of the figure. For each value of the loss energy, experimental and theoretical results were compared. The dashed theoretical curves illustrate the background subtraction procedure associated with eliminating incoherent scattering from the target. Vertical dashed curves are drawn for ease in locating the positions of the peaks. (After Duke and Landman.³³⁷)

The use of an accurate surface plasmon dispersion relation [(142)] can render the two-step model's description of ILEED intensities quite comparable to that of ELEED intensities by the dynamical multiple-scattering model discussed in the previous part. An important ingredient of the analytical procedure, however, is the focusing of attention on individual resonances in the ELEED intensity profile which can be described empirically by a kinematical (i.e., Born approximation) calculation of the elastic scattering amplitude. This prescription permits the accurate description of the ILEED intensities associated with a given ELEED resonance even in the absence of a detailed multiple-scattering description of the resonance itself.

In summary, the theory of ILEED is relatively young and immature relative to that of ELEED. Nevertheless, the two-step model has been refined to the point that it provides quantitative descriptions of the line shapes of the loss and angular profiles associated with ILEED from Al(111) films. Whether similar accuracy can be achieved in other systems remains to be seen. Indeed, at first sight this degree of accuracy might seem rather surprising considering the well-documented inadequacy of single-scattering (Born approximation) models of ELEED. Thus, we turn in the next section to a consideration of the dynamical theory of ILEED and a demonstration that the accuracy of the two-step model is not accidental, provided loss profiles are used as the basic experimental data in an analysis.

B. Dynamical Inelastic Diffraction

In the preceding section we found that a two-step model of inelastic diffraction describes experimental inelastic low-energy electron diffraction (ILEED) intensities with unanticipated accuracy. Since the two-step model of ILEED corresponds to a single-step (Born approximation) analysis of elastic low-energy electron diffraction, however, the considerations presented in Section IV.A lead us to expect that an adequate treatment of multiple elastic scattering events would be as necessary in models of ILEED as in those of ELEED. Consequently, in this section we review the results obtained from such a treatment in order to delineate the limitations of the two-step model.

A dynamical theory of ILEED and illustrative numerical applications thereof have been constructed by Duke and Landman.^{252,336} They evaluated the scattering cross-sections of electrons that are inelastically reflected from a single-crystal solid surface after having excited a bulk or surface plasmon. In particular, they summed all perturbation theory contributions to these cross-sections in which the incident electron scatters elastically from the ion-cores in the solid an arbitrary number of times but

creates only one plasmon. This analysis revealed that the consideration of multiple elastic scattering processes led to two main consequences relative to the two-step model of inelastic diffraction. First, for those classes of perturbation theory diagrams in which all of the multiple elastic scattering events occur before (after) the loss, the summation over these events leads simply to the renormalization of the elastic electron-ion-core scattering vertices. This result is indicated by panels (c) and (d) of Fig. 37 in which the shaded circles designate the sum over an arbitrary number of individual elastic scattering events [which, in turn, are denoted by open circles containing crosses in panels (a) and (b) of Fig. 37]. In these cases our interpretation of inelastic diffraction in terms of two-step diffraction-before-loss (loss-before-diffraction) processes remains intact.

A second consequence of multiple elastic scattering, however, is the occurrence of diagrams describing elastic events both before and after the loss. When summed, these diagrams lead to the "three-step" processes indicated in panel (e) of Fig. 37. In these processes a renormalized elastic scattering vertex occurs both before and after the loss vertex. An important conclusion reached by Duke and Landman³³⁶ is that these three-step events lead to contributions to the inelastic scattering amplitudes which usually are small relative to those associated with the (renormalized) two-step processes. This result indicates that the concept of "two-step" inelastic diffraction emerges naturally from the complete multiple-scattering analysis.

We now can understand why the two-step model described in Section VI.A provides an adequate description of the qualitative features of observed ILEED intensities. By virtue of "fitting" a single-step ELEED resonance to an observed maximum in the intensity profile we empirically constructed the renormalized electron-ion-core vertices noted in panels (c) and (d) of Fig. 37. Therefore if we confine our attention to ILEED intensities dominated by a particular ELEED resonance, we are utilizing an (imprecisely specified) approximation to these diagrams in our evaluation of the inelastic diffraction cross-sections. Since, moreover, the contributions to the cross-section of the two-step diagrams in panels (c) and (d) generally exceed those of the three-step diagram in panel (e), by following such a procedure we can achieve a tolerable description of observed ILEED intensities.

While this rationale for the two-step model provides a satisfying interpretation of its qualitative success, inspection of Figs. 15 to 17 (Section IV.A) should raise considerable misgivings concerning its quantitative validity. The central issue bearing on the quantitative accuracy of an empirical two-step model is that of determining the range of parameters over which the single-step (i.e., kinematical) elastic diffraction resonance

simulates the behavior of an observed (dynamical) resonance. A detailed examination of this point has been given by Duke and Landman,^{12,336} typical results of which are shown in Fig. 46. The lower panel illustrates the correspondence between calculated kinematical and dynamical intensity profiles. Such results are typical of the correspondence between the kinematical model intensity profiles and experimental ELEED data.³³⁷ In spite of the rather qualitative description of the ELEED intensity profiles

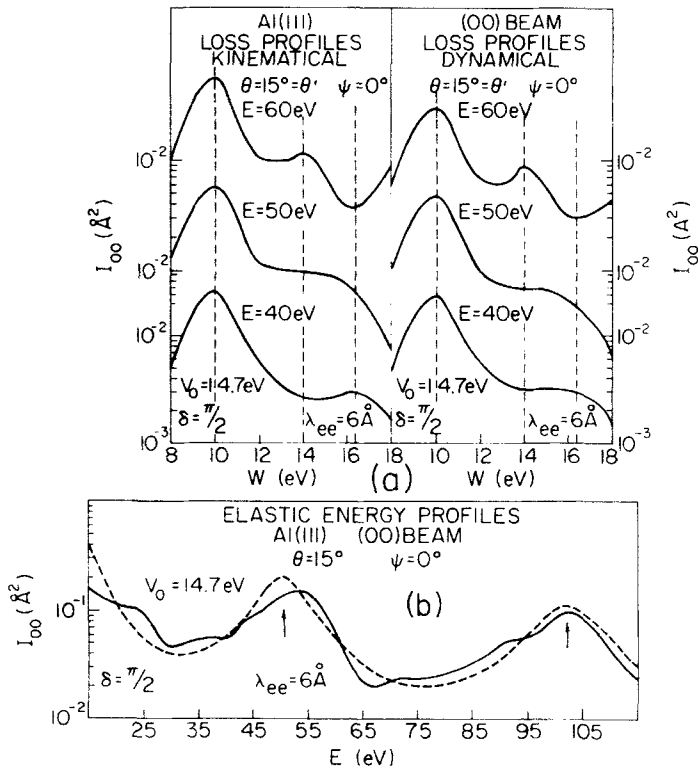


Fig. 46. Panel (a) displays the kinematical and dynamical loss profiles for electrons diffracted in the (00) beam from Al(111). The profiles are shown for various energies above and below the kinematical Bragg energy ($E_B = 50 \text{ eV}$) in the elastic energy profile of the (00) beam. The plasmon dispersion relations used in constructing the figure are $\hbar\omega_s(p_{\parallel}) = 10.1 - 0.7p_{\parallel} + 10p_{\parallel}^2$; $\Gamma_s(p_{\parallel}) = 1.6 + 0.74p_{\parallel}$; $\hbar\omega_b(p) = 14.2 + 3.048p^2$; and $\Gamma_b(p) = 0.53 + 0.103p^2 + 1.052p^4$. The parameters used in describing the elastic electron-solid scattering are indicated in the figure. Vertical dashed lines are included for convenience in visualization. Panel (b) contains a plot of the kinematical (dashed line) and dynamical (solid line) elastic intensity profiles obtained using these parameters. Arrows indicate the kinematical primary Bragg energies. All beam parameters are noted in the figure. (After Duke and Landman,³³⁶)

by the kinematical model, the upper panel of Fig. 46 reveals a quantitative description of the surface plasmon peak in the dynamical loss profiles by the two-step model. Moreover, this result remains valid on an energy-loss grid of $\Delta w = 50$ meV.¹² Correspondence between the two-step and dynamical inelastic energy profiles is comparable to that shown in the lower panel of Fig. 46 for the elastic intensity profiles. Similar but smaller discrepancies occur between the dynamical and two-step angular profiles. Thus the bulk plasmon ILEED intensities are reproduced at best qualitatively by the two-step model which, however, can describe the energies of surface plasmon maxima in the loss profiles quantitatively to within approximately ± 50 meV.

The mathematical basis of the quantitative validity of the semiempirical two-step model only for surface excitation loss profiles is easy to understand.³³⁶ The elastic scattering contribution to the diffraction-before-loss scattering amplitude is independent of w if all other beam parameters are held fixed. Moreover, for surface excitations (but not bulk excitations) the elastic scattering contribution to the loss-before-diffraction amplitude varies only as $E - w$. Since the variation in w over the surface plasmon peak in the loss profile is small [i.e., $\Delta w / (E - w) \ll 1$], the elastic vertex functions influence the loss profiles near the surface plasmon maximum only as an overall scale factor. The energy and shape of the maximum are almost unaffected by the choice of these functions provided they exhibit maxima for the correct incident beam energies and angles.

Summarizing, the construction and examination of a multiple-scattering theory of ILEED lead naturally to the predominance of two-step diffraction processes in which the elastic diffraction vertex is renormalized to describe multiple elastic scattering events. A two-step model based on a single-scattering elastic vertex yields qualitative reproductions of the main features of ILEED data provided the parameters describing the elastic vertex are chosen empirically to simulate observed multiple-scattering ELEED resonances. This model can provide quantitative descriptions of the energies of surface excitation maxima in the loss profiles, however, because of their insensitivity to the precise form of the elastic scattering vertices.

C. Consequences of Line-Broadening Mechanisms

The calculations described in the preceding two sections do not correspond directly to measured inelastic low-energy electron diffraction (ILEED) intensities because the characteristics of the experimental apparatus have not yet been incorporated into the analysis. Similarly, deviations of the geometry of any given sample from a rigid, defect-free single crystal influence the observed intensities. Since applications of ILEED to

measure surface excitation dispersion and damping require precise determinations of the energies of peaks in the loss profiles (i.e., to within $\delta w \sim 50$ to 100 meV as discussed in Part VIII), the determination of the influence of the various line-broadening mechanisms on these profiles constitutes the central ingredient in the establishment of ILEED as a quantitative technique for surface characterization. In this section we survey the results of such determinations.

Perhaps the most evident causes of the broadening of experimental ILEED profiles are the finite angular extent of the electron gun and detector, and the thermal spread of incident electron energies. These phenomena cause broadening of the angular profiles as discussed in Section III.D. Their influence on the loss profiles has been examined by Duke and Landman¹² who find that on a loss energy scale of $\delta w = 50$ meV they broaden but do not shift surface plasmon maxima in these profiles.

Another important instrumental parameter is the loss energy resolution Δw of the detector. The fact that $\Delta w \sim 1$ eV is large relative to typical phonon energies, $\hbar\omega_{\text{ph}} \sim 0.01$ eV, has the consequence that phonon-assisted diffraction as well as the scattering of the incident electron by lattice defects provide sources of both beam broadening and incoherent background. The phonon-assisted contributions to the quasielastic scattering cross-sections have been described via (90) to (96) in Section III.F. We recall that the excitation by the incident electron of optical phonons or multiple acoustical phonons leads to an incoherent background of scattered electrons. This contribution to the observed ILEED intensities is subtracted out of the raw data by use of the formula

$$\left(\frac{d\sigma}{d\Omega} \right)_{\text{incoh}} = A_0(E, \theta) + \frac{A_1(E, \theta)}{\theta' + \theta_0(E, \theta)} \quad (143)$$

in which the parameters A_0 , A_1 , and θ_0 are taken to be independent of the loss energy w . An application of the background subtraction procedure is illustrated in Fig. 45. The incoherent scattering described by (143) is caused by surface defects as well as by phonons. Only examinations of its temperature dependence can distinguish between the various sources of background, and such studies have not yet been attempted except for the quasielastic cross-sections^{258, 338} (i.e., $w = 0$).

The emission of one or possibly two acoustical phonons can be regarded as contributing to the angular width of the diffracted beam rather than to the incoherent scattering of the incident electrons. A Born approximation analysis of this effect is given by (92) to (96) in Section III.F. Its consequences on the ILEED profiles were examined by Duke and Landman¹² and found to be equivalent to those of the instrumental broadening

mechanisms described earlier in this section.

Typical experimental values of $\Delta\omega \sim 1$ eV are large relative to the desired resolution of the loss profile analysis, $\delta\omega \sim 0.05$ eV, as well as to the phonon energies. Nevertheless, Duke and Landman¹² were able to establish that for instrumental resolution $\Delta\omega \lesssim 2$ eV the surface plasmon maxima in the loss profiles could be located to an accuracy of $\delta\omega = 0.05$ eV, provided the electronics were sufficiently stable to obtain good statistical accuracy of the loss profiles. Such accuracy has been realized in the ILEED spectrometer built by J. O. Porteus for which the resolution is $\Delta\omega \cong 1$ eV.^{13,339}

In conclusion, we see that neither multiple elastic scattering phenomena nor the effects of various broadening mechanisms prohibit the two-step model from providing a quantitative description of surface excitation contributions to the ILEED loss profiles. The energies of surface-excitation-induced maxima in these profiles can be established to a precision of $\delta\omega \cong 0.1$ eV in spite of an instrument loss energy resolution of $\Delta\omega \cong 1$ eV, uncertainties in the elastic electron-solid force law, and a host of instrumental and intrinsic sources of both beam broadening and incoherent background. The derivation of this result, which is essential to the applications of ILEED for surface characterization (Part VIII), provides an illuminating example of the role of microscopic electron-solid scattering theory in the development of quantitative surface-sensitive spectroscopies.

VII. SURFACE CRYSTALLOGRAPHY VIA ELASTIC LOW-ENERGY ELECTRON DIFFRACTION

A. Scope and Organization

Inspection of almost any review of the literature on low-energy electron diffraction (LEED) from solid surfaces reveals a pervasive emphasis on its applications for the determination of the atomic geometry of solid surfaces.^{1-6,340-344} Yet we found in Parts I, III, IV, and V that definitive structure determinations require analyses of the diffracted intensities—analyses which have become possible only in the past few years. Consequently, the focus of our attention in this section is the use of intensity calculations to ascertain the atomic geometry of clean and adsorbate-covered single-crystal surfaces.

Having decided on this central theme, we proceed by first reviewing the specification of the atomic positions at single-crystal surfaces and subsequently examining the manifestations of the atomic geometry on observed elastic low-energy electron diffraction (ELED) intensities. Since it is convenient to consider defect-free (“ideal”) and imperfect surface structures separately, we examine each in turn. Moreover, we attempt to catalog

systematically the literature on ELEED from imperfect surfaces by introducing a classification scheme for defect structures based both on surface topography and on the consideration of whether or not a particular structure exhibits long-range (i.e., crystalline) order parallel to the surface. We make no effort to organize and reference the enormous experimental literature on (presumably) observed surface structures because extensive catalogs of such studies may be found in earlier reviews^{2,4,341,344}. Similarly, we do not reproduce the substantial body of reference material on atomic geometry^{2,20,340,341} and on spot-pattern interpretation^{2,4,5,340,341,344} which has been reviewed and tabulated by others.

B. The Atomic Geometry and Symmetry of Ideal Surfaces

An *ideal* surface is defined to be that obtained by cutting a perfect, rigid single crystal by a plane and subsequently removing all atoms whose centers lie on one side of this plane. This prescription defines an *atomically flat* surface even if the initial crystal contains defects or the atoms comprising the crystal are permitted to vibrate. Ideal surfaces are designated by the chemical symbol of the material and the Miller indices (*hkl*) of the dividing plane, for example, Al(100). A detailed discussion of the mathematical specification of such surfaces has been given by Nicholas.²⁰ We use his conventions and notations throughout this review. A thorough tabulation of the atomic geometry of the low-index surfaces of monatomic and diatomic solids crystallizing in the fcc, bcc, hcp, NaCl, and diamond (zinc blende) lattices is given in Nicholas's book.²⁰

All ideal surfaces are characterized by both translational and point group symmetry in the plane of the surface.^{291,292} The combined (space group) symmetry operations restrict the possible surface geometries to five two-dimensional (Bravais) *nets* of points. The association with each point in this net of a *basis* of atoms defines the actual crystal surface. These bases extend throughout the crystal in the direction normal to the chosen surface. The unit areas in the five Bravais nets are called *unit meshes*. A tabulation of the five possible meshes is given by Wood^{291,292} and quoted in nearly every subsequent review. The specification of both the unit mesh and the elements of the space group results in a unique characterization of the symmetry of an ideal surface. In order to describe its atomic geometry, however, the basis also must be prescribed.

C. The Atomic Geometry of Nonideal Surfaces

1. Classification of Imperfections

The ideal surfaces described in the preceding section are obtained in practice rarely, if at all.^{1,40} Nevertheless, almost all calculations of elastic

low-energy electron diffraction (ELED) intensities from clean surfaces have been based on models embodying atomically flat surfaces. We found in Part V, moreover, that these calculations described quite adequately observed ELED intensities from clean metals. The origin of this pleasant surprise lies in the small coherence zone, $(\Delta x)^2 \sim 10^4 \text{ \AA}^2$, of the incident electron beam and the poor angular resolution of most ELED spectrometers (Section III.D). Generally speaking, ELED is rather insensitive to the presence of many types of surface imperfections.^{1,40} Conversely, in a study of surface crystallography it is important to determine the conditions which must be satisfied in order to render a prescribed level of structural detail observable by the ELED technique.

In classifying defect structures, it is convenient to visualize a surface as comprised of close-packed two-dimensional atomic diffraction gratings stacked on top of each other. Therefore these two-dimensional layers constitute the building blocks of a surface just as the atomic scatterers are the units out of which the layers themselves are constructed. An example of this concept is shown in Fig. 47 which illustrates the construction of the (755) face of a monatomic fcc solid out of close-packed (111) layers of atomic scatterers. This view of surfaces being composed of arrays of close-packed atomic planes is often referred to as the terrace-ledge-kink (TLK) model.³⁴⁵ The flat expanses of the close-packed planes are the "terraces"; the abrupt atomic steps from one terrace to another are the "ledges" (often referred to as "steps"); and both intersections of two ledges and atomic vacancies in the individual ledges form the "kinks." The close-packed faces [e.g., (111) and (110) in fcc and bcc structures, respectively] exhibit a preferred status in this model because all other atomically flat faces are considered to be constructed from individual close-packed atomic layers. The model is most useful for the description of high-index faces [i.e., those inclined at a small angle relative to the (100), (110), and (111) faces] and surface defects. Low-index faces are more easily described by considering them to be composed of two-dimensional atomic layers parallel to the surface.

The TLK model permits us to classify surface structures according to the number and spatial extent of their low-index terraces. Surfaces that consist of such terraces whose spatial extent is large relative to the coherence zone [$(\Delta x)^2 \sim 10^4 \text{ \AA}^2$] are considered to exhibit *single-step topography*. Those for which the areas of the terraces are small relative to the coherence zone are said to exemplify *multistep topography*. By basing this definition on the area of the coherence zone, we have recognized explicitly the instrumental restrictions on LEED as a technique for surface defect crystallography. Although optical and electron microscope techniques are capable of detecting considerably larger terraces, their resolution

THE TERRACE-LEDGE-KINK MODEL OF A
HIGH-INDEX [I.E., (755)] FACE OF AN
FCC CRYSTAL

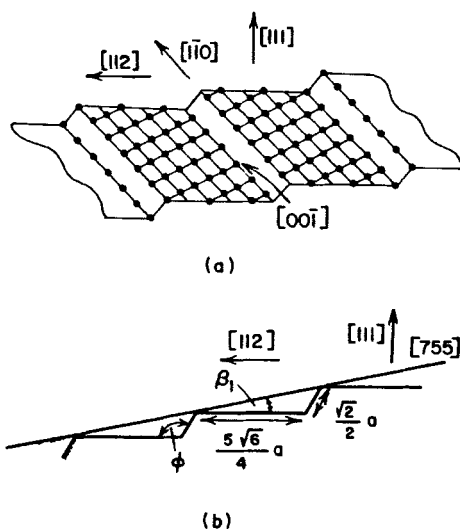


Fig. 47. Schematic diagrams of the construction of the (755) surface of a monatomic fcc solid in terms of layers of close-packed (111) planes. Various crystallographic directions are indicated in the figure. The quantity a designates the simple cubic lattice distance of the fcc crystal. Panel (a) indicates the atomic structure of the (755) face, whereas in panel (b) the relevant structural parameters are indicated on a cross-sectional view of this face. (After Duke and Landman.³⁵⁷).

horizontal to the surface is greater than or comparable to the size of the LEED coherence zone.⁴⁰ Therefore a surface that appears “flat” to them can exhibit multistep topography from the perspective of LEED, and conversely.

All calculations of ELED intensities except one³²⁹ have been based on models of the surface geometry which assume a priori the existence of single-step topography. Even within this class of models, however, several different types of surface imperfections (i.e., deviations from the ideal surface geometry) can occur. Two of these exist even for atomically flat, chemically clean surfaces: imperfections caused by a nonuniform spacing of the upper few atomic layers parallel to the surface and by a nonuniform stacking sequence of these layers. Both of these types of defect structure manifest themselves as alterations in the atomic basis associated with the surface Bravais net. Therefore both are discernible only via an analysis of LEED intensities since neither modifies the spot patterns. Imperfections caused by alterations in the structure of the surface atomic layers them-

selves may, however, change the spot patterns. Such defects can be classified in one of two ways. *Uniform overlayer structures* preserve the periodic long-range order parallel to the surface of an atomically flat single crystal, although they may reduce the space group symmetry of this surface (i.e., increase the size of the unit mesh and possibly alter its shape). Such structures can occur via the adsorption of new surface species, the spontaneous rearrangement of surface atoms, or the diffusion of impurities to the surface. *Nonuniform overlayer structures* arise via the same physical mechanisms, but fail to preserve long-range order parallel to the surface. They can be characterized by the degree of order in the overlayer structure itself. We examine this topic in the following section and indicate in Section VII.D.1 the influence of the atomic structure on the intensity patterns.

2. Single-Step Imperfections

As noted in the preceding section, in the case of planar, "single-step" surface topography, it is convenient to distinguish between uniform ordered surface structures, which exhibit long-range periodic order parallel to the plane of the surface, and nonuniform structures, which do not. We restrict our considerations of nonuniform structures to those described by lattice gas models of the positions of atoms in an overlayer on an otherwise ideal crystal face.³⁴⁶ Models in which the atoms in an overlayer exhibit only short-range order analogous to that in liquids or gasses can, of course, be constructed.³⁴⁷ They have not yet been used to analyze elastic low-energy electron diffraction (ELEED) intensities, however, so there is little reason to examine them here. Given this restriction, we proceed by stating our assumptions and then examining the uniform and nonuniform structures in turn.

Since our discussion is based on certain hypotheses about the surface atomic geometry, it seems appropriate to begin by enumerating them. The model which provides the foundation for our visualization of single-step surface structures consists of an atomically flat, low-index face of a crystal on which a fraction of a monolayer coverage of atomic or molecular adsorbates has been deposited to form an "overlayer." Typically, the underlying atomically flat crystal is referred to as the *substrate* and the overlayer is called the *selvedge*.²⁹¹ Considerably more general models of planar surfaces have been proposed in the literature.²⁹¹ Indeed, few if any of our considerations will depend on either the chemical nature of the overlayer or its thickness. Therefore our discussion describes equally well rearranged low-index surfaces of clean solids, simple monatomic overlayers on such surfaces, and reconstruction of the underlying substrate by the adsorbate. It does not describe, however, clean or adsorbate-covered

high-index crystal faces or surfaces whose topography is nonplanar on a distance scale $\Delta x \sim 100 \text{ \AA}$ comparable to the diameter of the coherence zone (Section III.D). These are considered in Section VII.C.3.

The most general description of the periodic space group symmetry of a uniform (ordered) overlayer-substrate system is given in terms of a matrix notation.³⁴⁸ Consider a substrate whose primitive (i.e., smallest possible) unit mesh is described by the translation vectors **a** and **b**. On this substrate there is an overlayer associated with the unit mesh vectors **a_s** and **b_s**. (We follow the notation developed by Wood.²⁹¹) If we fix a set of Cartesian unit vectors \hat{x} and \hat{y} , then the unit meshes of the substrate and the overlayer may be described by matrices **A** and **B**, respectively, whose matrix elements are determined by

$$\mathbf{a} = A_{11}\hat{x} + A_{12}\hat{y} \quad (144a)$$

$$\mathbf{b} = A_{21}\hat{x} + A_{22}\hat{y} \quad (144b)$$

and similarly for **B**. The relationship between the unit meshes of the overlayer and substrate may be expressed in terms of the matrix transformation **G** between them, that is

$$\mathbf{G} = \mathbf{B}\mathbf{A}^{-1} \quad (145)$$

The determinants of these matrices are designated according to $G \equiv \det |\mathbf{G}|$.

The matrix **G** permits us to classify the different possible types of relationships between the substrate and overlayer Bravais nets. If G is an integer, the nets are said to be *simply related* and the combined structure is referred to as *simple*. If G is a rational number, the nets are *rationally related* and the composite is called a *coincidence-site structure*.³⁴⁹ Finally, if G is an irrational number, the nets are *irrationally related* and the structure is designated as *incoherent*.³⁵⁰ In the first two of these three cases the combined system is itself characterized by a Bravais net and the overlayer structure is said to be *in register* with that of the substrate. In all three cases, however, the composite system can be described by a symbol of the form $M(hkl) - (\mathbf{G}) - S(\gamma)$ in which $M(hkl)$ designates the (hkl) face of a substrate of substance M ; **G** is defined by (144) and (145); and S is the chemical symbol of the overlayer whose atomic coverage is γ (in units of a monolayer).

Wood²⁹¹ uses a more common although less general notation which we designate as the *net quotient* overlayer labeling procedure. In the case that the unit mesh vectors of the overlayer can be expressed as rational linear combinations of those of the substrate, we can identify the combined

substrate-overlayer system by the symbol

$$M(hkl)-\overset{p}{c}\left(\frac{a_s}{a}\times\frac{b_s}{b}\right)\zeta-S(\gamma) \quad (146)$$

In this notation $M(hkl)$ and $S(\gamma)$ are defined as in the preceding paragraph, p , (c) designate primitive (p) and centered (c) unit meshes of the composite system, $((a_s/a)\times(b_s/b))$ denotes the ratios of the sides of the unit surface mesh vectors to those of the substrate mesh, and ζ is the angle between the overlayer and substrate unit vectors \mathbf{a}_s and \mathbf{a} , respectively (which is omitted if it is zero).

Figure 29 provides an illustration of the use of both notations. If a Na overlayer is deposited on a Ni(100) substrate, then the structure shown in the top panel of this figure is designated as

$$\text{Ni}(100)-\begin{pmatrix} 1 & 1 \\ -1 & 1 \end{pmatrix}-\text{Na}(\frac{1}{2}) \quad (147a)$$

$$\text{Ni}(100)-p(\sqrt{2}\times\sqrt{2})45^\circ-\text{Na}(\frac{1}{2}) \quad (147b)$$

$$\text{Ni}(100)-c(2\times 2)-\text{Na}(\frac{1}{2}) \quad (147c)$$

Equations (147b) and (147c) reveal that the overlayer structure shown in Fig. 29 can be regarded as either a primitive or centered unit mesh. A more extensive discussion of the applications of the matrix and net quotient nomenclatures has been given by Estrup and McRae.³

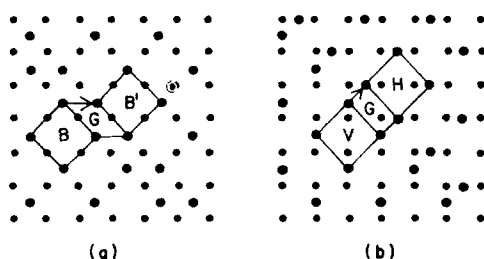
Turning to our discussion of nonuniform single-step imperfections, we identify the major cause of such structures as the occurrence of disorder in the overlayer atomic positions for an arbitrary temperature and coverage. Only at low temperatures and for coverages which are rational fractions of a monolayer are uniform overlayer structures to be expected. Different mathematical descriptions of such disorder have been proposed, the most common of which are the lattice gas model^{256,346,348,351-355} and the domain model.^{256,356} Rather than explore the consequences of the various versions of these models, however, we proceed by giving examples of the common types of nonuniform single-step structures.

The overlayer and substrate structures are said to be in *translational register* when the Bravais net of the composite system is invariant under translations by prescribed multiples of the unit mesh vectors of both the overlayer and the substrate. Often, however, the species in the overlayer may coalesce into islands or *domains*, each of which is in register with the

substrate, but which are not separated from each other by the translation vectors of the overlayer unit mesh. In this case, examples of which are illustrated in Fig. 48, we refer to them as *out-of-phase domains*. Evidently the vector connecting the domains B and B' as well as that linking V and H do not belong to the overlayer translational symmetry group. Park and Houston²⁵⁶ have formalized the description of such domains by introducing the concept of equivalence. Two domains are said to be related by *equivalent* transformations if the atomic positions in one can be mapped into those in the other by an element of the overlayer symmetry group. All other transformations relating two domains are called *inequivalent*. The *registry degeneracy* of a given overlayer structure is defined to be the minimal number of nonequivalent transformations required to relate all possible domains consisting of this structure on a perfect substrate. Thus the registry degeneracy is a measure of the number of different composite overlayer-substrate structures that can be constructed from a given overlayer structure, substrate structure, and set of symmetry equivalent positions of the overlayer species in the substrate unit cell.

In addition to translational registry degeneracy, similar degeneracies

OUT - OF - PHASE DOMAINS



$$B = B' = \begin{pmatrix} 1 & 1 \\ -1 & 1 \end{pmatrix} \quad G = \begin{pmatrix} 1 & 1 \\ 0 & 1 \end{pmatrix} \quad V = H = \begin{pmatrix} 1 & 1 \\ -1 & 1 \end{pmatrix} \quad G = \frac{1}{2} \begin{pmatrix} 22 \\ -11 \end{pmatrix}$$

Fig. 48. Illustration of out-of-phase $c(2 \times 2)$ domains on the (100) face of an fcc or bcc crystal. The direct nets for the $c(2 \times 2)$ structure are indicated. Small and large dots represent substrate and overlayer sites, respectively. In panel (a) the overlayer atoms are located in positions of maximum fourfold coordination. Unit meshes B and B' , representative of two overlayer domains, are connected by the unit mesh G . In panel (b) the overlayer atoms are located in nearest-neighbor twofold bridged positions: vertical bridged positions (V) and horizontal ones (H). The two overlayer domains are connected by a unit mesh G . The representation matrices of the unit meshes with respect to the substrate mesh are included for reference. (After Duke and Landman.³⁵⁷)

occur because domains occur which are not related to each other by the elements of the point group of the overlayer. Figures 49 and 50 illustrate *rotational registry degeneracy* and *reflection registry degeneracy*, respectively, arising from this cause. A complete discussion of the analysis of both translational and point group domain equivalence has been given by Duke and Landman,³⁵⁷ on whose work our considerations are based. Figures 48 to 50 illustrate adequately, however, the nature of the various types of disorder which can occur because of defects in the packing of overlayer domains on periodic substrates.

ROTATIONAL REGISTRY DEGENERACY

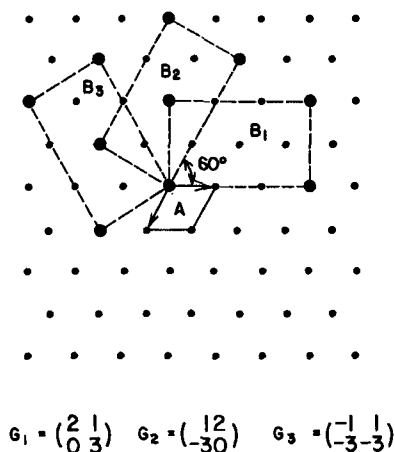


Fig. 49. Schematic model of a structure exhibiting rotational registry degeneracy. Dots represent the (111) face of an fcc crystal with unit mesh A (solid lines). The rectangular unit meshes (dashed lines) designated by B_i ($i=1,2,3$) are representative of domains related to each other by anticlockwise rotations of 60° . The matrices relating B_i ($i=1,2,3$) to the substrate net (A), are given by G_i ($i=1,2,3$). The superposition of diffraction patterns from these three rotationally degenerate domains results in a hexagonal pattern. (After Duke and Landman.³⁵⁷)

Summarizing, in this section we have cataloged common types of overlayer structures on periodic substrates characteristic of single-step topography. The various notations and terminologies commonly used in the literature were introduced, and their application illustrated. Our main interest, of course, is the influence of these structures on ELEED intensities. We examine this topic in Section VII.D following a brief consideration of the specification of multilayer topographies.

REFLECTION REGISTRY DEGENERACY

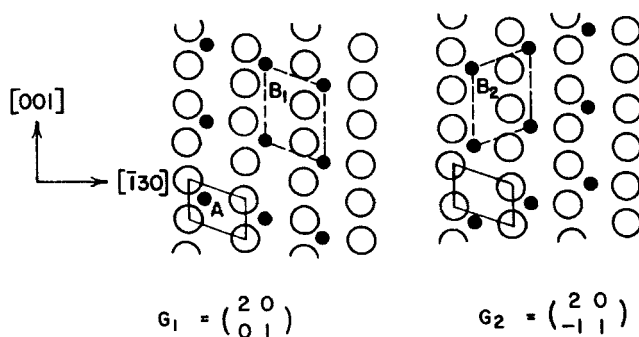


Fig. 50. An example of a surface structure exhibiting reflection registry degeneracy. The arrangement of the substrate sites, represented by solid circles, is that of the (310) face of a bcc crystal. The unit mesh of the substrate is denoted by *A*. Open circles denote overlayer sites. Two domain orientations with unit meshes *B*₁ and *B*₂ are shown. The matrices relating *B*₁ and *B*₂ to the substrate net are given by *G*₁ and *G*₂, respectively. (After Duke and Landman.³⁵⁷)

3. Multistep Topographies

Interest in multistep topographies has been stimulated recently by a series of studies of elastic low-energy electron diffraction spot patterns from high-index crystal faces.^{36, 358–361} If these crystal faces are atomically flat, then they can be regarded as comprised of a regular sequence of terraces of close-packed planes as described in Section VII.C.1. The mathematical description of such surfaces has been developed by Nicholas.²⁰ They are uniquely and completely described by the Miller indices (*hkl*) of the surface plane. An example of this description is illustrated in Fig. 47. Lang et al.³⁶ introduced a rather combersome notation for high-index surfaces based on (*h*₁*k*₁*l*₁) terraces in which they are designated by *M*(*S*)-[*m*(*h*₁*k*₁*l*₁) × *n*(*h*₂*k*₂*l*₂)] for a crystal designated by the chemical symbol *M*. The index *m* is the number of atomic rows in the (*h*₁*k*₁*l*₁) terraces and *n* is the number of atomic layers in the (*h*₂*k*₂*l*₂) ledges. Thus a (755) surface of Ni such as that shown in panel (a) of Fig. 47 is designated by Ni(*S*)-[6(111) × (100)] in the notation of Lang et al.³⁶ The adsorption of foreign species on high-index faces is a complicated topic.^{36, 360} If the area of the low-index terraces is large and the unit mesh of the overlayer is small, then the overlayer structures may be those characteristic of the low-index terraces. If, in addition, out-of-phase domains are common, the notation of Lang et al.³⁶ may prove appropriate. In the case that size of the overlayer mesh is comparable to or larger than that of the terraces,

however, we recover the situation described in the preceding section, that is, the structure of the overlayer is described best in terms of atomic planes parallel to the substrate surface. No extensions of the conventional notations developed in Sections VII.B and VII.C.2 are required for the specification of the atomic geometry of either these latter structures or of clean high-index crystal faces.

Since high-index surfaces are energetically unstable,³⁴⁵ they are likely to be imperfect, in which case it is necessary to specify statistically the parameters describing the terraces and the ledges. Such a description also is required for disordered low-index crystal faces. In these cases the surface topography is prescribed by the Miller indices of the close-packed terrace faces and the combined distribution of terrace widths, lengths, and orientations and of ledge heights. Several simplified models in which the terraces are taken to exhibit a random distribution of sizes and orientations,³⁶¹ or, more generally, this distribution is taken to be separable from that of their heights,³⁶² have been considered in the literature. Determinations of average step heights and widths have been based on kinematical analyses of elastic low-energy electron diffraction intensities from high-index surfaces.^{36, 358-360} No serious attempt has yet been made, however, to utilize ELEED as a technique for the quantitative determination of statistical multistep surface topographies.

D. Structure Determination for Uniform Surfaces Exhibiting Long-Range Order

1. Relation between Intensity Pattern Symmetry and Atomic Geometry

In this and the following three subsections we examine the determination of the atomic geometry of the surfaces of crystalline solids via analysis of elastic low-energy electron diffraction (ELEED) intensities from these surfaces. In particular, we consider the surface to exhibit an atomically flat single-step topography (see Section VII.C.1), consisting of a uniform surface structure. Therefore we do not examine the consequences of steps (see, e.g., Fig. 47) or of domain degeneracies (see, e.g., Figs. 48 to 50). Treatments of the former can be found in the original literature,^{36, 329, 356-363} whereas adequate reviews of the latter are available elsewhere.^{2,3}

We discovered in our Born approximation analysis of ELEED from a rigid lattice (Section III.C) that the diffracted beams emanating from the solid provide a direct measure of the translational symmetry of the solid parallel to the surface. In detail, the angle these beams make with the surface is determined from the momentum conservation law

$$\mathbf{k}'_{\parallel} = \mathbf{k}_{\parallel} + \mathbf{g} \quad (1a)$$

$$k_{\parallel} = \left(\frac{2mE}{\hbar^2} \right)^{1/2} \sin \theta \quad (1b)$$

as described in Part I. The \mathbf{g} are vectors in the reciprocal lattice of one of the five possible two-dimensional Bravais nets discussed in Section VII.B. The unit meshes associated with these nets are illustrated in Fig. 51. Each unit mesh is associated with a reciprocal lattice which may be constructed using the matrix notation introduced in Section VII.C.2.³⁴⁸ If we use (144) to define the matrix \mathbf{A} which describes a given surface unit mesh, then the associated reciprocal lattice is comprised of translations by multiples of the vectors

$$\mathbf{a}^* = A_{11}^* \hat{x} + A_{12}^* \hat{y} \quad (148a)$$

$$\mathbf{b}^* = A_{21}^* \hat{x} + A_{22}^* \hat{y} \quad (148b)$$

The matrix \mathbf{A}^* is defined by

$$\mathbf{A}(\mathbf{A}^*)_t = \mathbf{I} \quad (149)$$

in which a subscript t indicates the transpose. The vectors \mathbf{g} in the

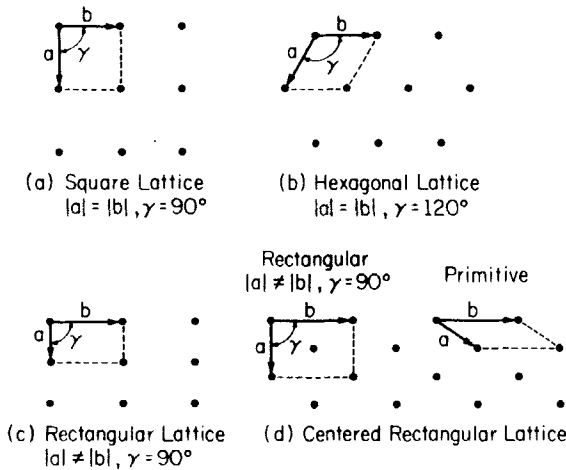


Fig. 51. The five two-dimensional Bravais nets. Note the convention for the axes.

reciprocal lattice are specified by

$$\mathbf{g}_{hk} \equiv 2\pi(h\mathbf{a}^* + k\mathbf{b}^*) \quad (150)$$

Using this notation, the construction of the reciprocal lattice associated with a given Bravais net is elementary. If we take \hat{y} to be horizontal and \hat{x} to be vertical (pointing downward), then the net vectors shown in Fig. 51 can be written as

$$\mathbf{a} = a_0(s\hat{x} - t\hat{y}) \quad (151a)$$

$$\mathbf{b} = a_0r\hat{y} \quad (151b)$$

in which a_0 is a unit of length. We find from (148), (149), and (151) that

$$\mathbf{A} = a_0 \begin{pmatrix} s & -t \\ 0 & r \end{pmatrix} \quad (152a)$$

$$\mathbf{A}^* = (rsa_0)^{-1} \begin{pmatrix} r & 0 \\ t & s \end{pmatrix} \quad (152b)$$

leading to the direct and reciprocal nets shown in Fig. 52 for the square rectangular and hexagonal unit meshes.

For normally incident electrons, the symmetry of the intensity pattern (Fig. 7) is identical to that of the reciprocal lattice of a uniform substrate-overlayer target system. Moreover, since in this case the sine of the exit polar angle is given by

$$\sin \theta'_g = \frac{|\mathbf{g}|}{(2mE/\hbar^2)^{1/2}} \quad (153)$$

the slopes of plots of $\sin^{-2} \theta'_g$ versus energy yield a direct determination of the lengths of \mathbf{a} and \mathbf{b} via (151) and (152). Therefore for all surface structures exhibiting long-range order parallel to the surface the unit mesh vectors in principle can be constructed by inspection from the intensity pattern provided domain degeneracies can be neglected. The practice of this art is described in several recent reviews. Unfortunately, in the absence of an analysis of the magnitudes of the scattered intensities we can say no more. In general many atomic geometries are consistent with a given Bravais net. Indeed, the literature contains numerous examples of attempts to remove the ambiguity by the use of physical argu-

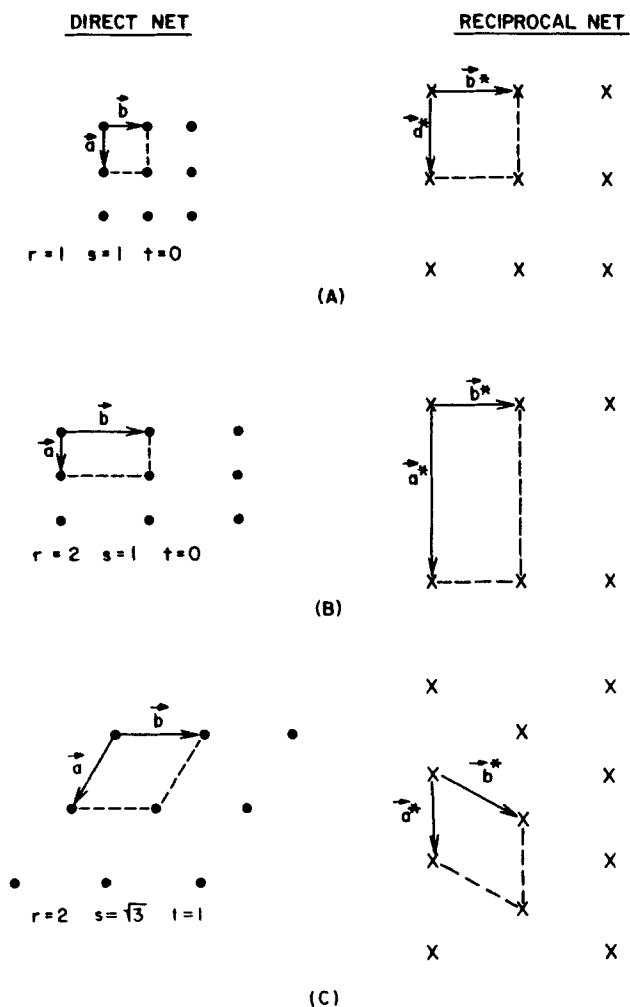


Fig. 52. Schematic indication of the direct lattice (left-hand panels) and reciprocal lattice (right-hand panels) unit meshes for three two-dimensional Bravais nets. The construction of the reciprocal net from the direct one is indicated by (148) to (152) in the text. (After Duke and Landman.³⁵⁷)

ments.^{2-5, 340-342} We next turn to our discussion of intensity analysis as an appropriate quantitative technique for the determination of surface atomic geometry.

2. Analytical Approaches to Surface Crystallography

As in the case of X-ray crystallography of bulk solids,^{364, 365} it is convenient to decompose the determination of surface structures into two

parts: that of the space group symmetry (i.e., Bravais space lattice) and that of the structure of the unit cells that occupy the individual points on the Bravais lattice. For uniform surface structures the space group symmetry is that characteristic of the (two-dimensional) periodicity parallel to the surface. In the cases of incoherent uniform structures (Section VII.C.2) or of nonuniform structures (e.g., domains), however, this symmetry does not exist. We limit our considerations to the two-dimensional periodic structures for which the space group symmetry exists and is determined from the intensity pattern as indicated in Section VII.D.1.

Formally, the unit cells which occupy the sites on the resulting two-dimensional Bravais net extend throughout the sample normal to the surface. In practice this point of view is never adopted. Rather, as indicated in Section VII.C.2, the surface is regarded as a selvedge of specified symmetry on an otherwise ideal single-crystal substrate.²⁹¹ We refer to such a visualization of the surface structure as the *uniform overlayer model*. In this model the determination of the contents of the unit cells is reduced to that of the structure of the selvedge layer and the registry of this layer relative to the substrate. Moreover, we regard the selvedge itself as comprised of individual monatomic planes of identical symmetry parallel to the surface. The unit-cell structure of the selvedge, therefore, is expressed by using multiple "subplanes" of identical scatterers, displaced relative to each other but all exhibiting the space group symmetry of the selvedge as a whole.²⁶⁷

Given the problem of determining the structure and registry of the selvedge in the context of the uniform overlayer model, two rather different approaches have been proposed for its solution. We refer to these as microscopic model and data reduction methods of surface crystallography, respectively. Within the framework of each method, various specific techniques for structure determination have been utilized. In the remainder of this subsection we catalog these techniques according to the extent of input information about the electron-solid interaction which they require. Further distinction between them, based on technical details like the nature and extent of ELED intensity data used in the analysis, is deferred until the following two subsections.

The objective of the microscopic model approach is the development of a model of electron-solid scattering which describes, in detail, measured ELED intensities from solid surfaces. This approach, which was described in Parts IV and V, evidently utilizes a complete specification of the electron-solid interaction subject to the relaxations of this requirement permitted by the sensitivity analysis described in Section V.C. Because of the large quantity of input information which they embody, applications of the microscopic model techniques to surface crystallography encounter two obstacles. First, they require a precise characterization of the experi-

mental surface and a detailed knowledge of the electron-solid force law, neither of which is currently available except for simple systems like the close-packed faces of elemental metals. Second, from the point of view of crystallography, they are excessively ambitious in that they characterize the electronic and vibrational structure of the surface as well as its geometrical structure. Since a wealth of dynamical information about the force law is required by (or, in principle, extracted from) a model calculation, certain ambiguities concerning the geometrical structure per se can arise in actual data analyses. On the one hand, if one examines a small quantity of measured ELEED intensities, ambiguities usually occur between the values of dynamical parameters (e.g., values of the inner potential between muffin-tin ion-core scatterers) and geometrical parameters (like the spacing of the upper two layers of the solid). On the other hand, as the analysis is extended to more data, it inevitably works more adequately for some parts of the data than for others. Thus the major conceptual difficulties encountered with the microscopic model approach to surface crystallography are those of the uniqueness and intrinsic accuracy of the values of the geometrical parameters extracted from data analyses. Technical difficulties (e.g., the requirement of extensive computer computations) also occur, but can be overcome just as similar ones in X-ray crystallography have been. We described in Sections V.A to V.C the construction of techniques embodying this approach. We discuss their applications in Section VII.D.3.

Data reduction approaches to surface crystallography are based on exploitations of the fact that despite the occurrence of strong dynamical phenomena, both model calculations^{6, 29, 54, 197, 248, 250, 255, 326, 366-369} and ELEED intensity data^{368, 370-376} exhibit unmistakable and universal residual manifestations of the purely geometrical conditions for intensity maxima which characterize the Born approximation ("kinematical") analyses. By manipulating observed ELEED intensities to enhance these geometrical effects while smoothing or ignoring the dynamical ones, analytical procedures based on kinematical concepts can be used for structure determination. Two types of analysis have been examined in the literature. In the first, either raw^{368, 370, 371} or averaged^{366-369, 372-376} ELEED intensities are compared directly with the predictions of a kinematical (Born approximation) calculation. The model intensities are given by

$$I_{hk}^{\text{kin}}(E) = |F_{hk}(E)|^2 \quad (154a)$$

$$F_{hk}(E) = \sum_{\alpha} f_{\alpha}(E, \theta_{hk}) \exp [2\pi i(hx_{\alpha} + ky_{\alpha})] \\ \times \exp \{i[k_{\perp}(0, E) + k_{\perp}(\mathbf{g}_{hk}, E)]z_{\alpha}\} \quad (154b)$$

In (154) the quantity $f_\alpha(E, \theta)$ is the atomic scattering amplitude as a function of energy and scattering angle for the ion-core scatterer labeled by α [see, e.g., (121)]; h and k are the Miller indices corresponding to the reciprocal lattice vector \mathbf{g} which designates the scattered electron beam [(150)]; and x_α, y_α , and z_α are the fractional coordinates of the atoms in the unit cells which extend an arbitrary depth below the surface. The quantity $k_\perp(\mathbf{g}, E)$ is the component of momentum normal to the surface for electrons of energy E in the beam labeled by \mathbf{g} , as given by (44), that is,

$$k_\perp^2(\mathbf{g}, E) = \frac{2m[E - \Sigma(E)]}{\hbar^2} - (\mathbf{k}_\parallel + \mathbf{g})^2 \quad (44)$$

In (44) $\Sigma(E)$ is the one-electron optical potential as given by (28) or (127). For example, in the case of (28) we have

$$\Sigma(E) = -V_0 - \frac{i\hbar^2}{m\lambda_{ee}} \left[\frac{2m(E + V_0)}{\hbar^2} \right]^{1/2} \quad (28)$$

From (28), (44), (121), and (154) we see that the inputs of a kinematical analysis are models for the optical potential and ion-core scattering factors, whereas the outputs are the atomic positions $\{x_\alpha, y_\alpha, z_\alpha\}$ which are selected to "fit" the ELEED data in a prescribed fashion.³⁶⁸ In the second kind of analysis, the Patterson or Fourier transform methods,³⁷⁷⁻³⁷⁹ the use of a model for the atomic scattering factors is avoided by using the Fourier-Laplace transform of the measured intensities $I_{hk}(E)$, or averages thereof, that is,

$$P(x, y, z) = \sum_{h,k} \int_0^\infty \frac{Z(E) dE}{k_\perp(\mathbf{g}_{hk}, E)} I_{hk}(E) \exp \{ -i[2\pi hx + 2\pi ky] \} \\ \times \exp \{ -i[\bar{k}_\perp(0, E) + \bar{k}_\perp(\mathbf{g}_{hk}, E)] z \} \quad (155a)$$

$$Z(E) = \frac{m}{\pi\hbar^2} \left[1 - \frac{\partial \Sigma(E)}{\partial E} \right]^{-1} \quad (155b)$$

Because of the combined effect of inelastic collision damping and the half-space nature of the electron diffraction problem, the conventional X-ray Patterson sum³⁸⁰ in the direction normal to the surface becomes a Laplace inversion. Moreover, the use of an energy-dependent optical potential leads to the occurrence of the density of states renormalization factor $Z(E)$ in the quasiparticle approximation.¹⁹ The complex nature of

k_{\perp} and the definition of the integral transformation render the Patterson function $P(x,y,z)$ defined by (155) a complex quantity. Clarke et al.^{378,379} arbitrarily take the real part of $P(x,y,z)$, neglect the density-of-states factor, and truncate the integral over E according to the extent of their data. The validity of such procedures is not obvious, especially since the range and extent of the observed intensity data are well known to influence the validity of "kinematical" analyses thereof,^{255,368} and other real quantities can be constructed from the complex function $P(x,y,z)$.

The major advantages of the data reduction techniques are simplicity and suitability for automatic digital processing. Indeed, Patterson function methods are ideally suited for completely automated structural analysis which, moreover, can be performed quite economically by use of fast Fourier transform methods if the inelastic collision damping is described via a layer-by-layer reduction in the atomic scattering factors in (155). An attractive feature of both data reduction techniques is their analogy to the X-ray structure literature. Because of this, well-tested methodologies are available for the assessment of the adequacy of proposed structures and for structure refinement.^{326,368}

The major disadvantage of data reduction techniques is their implicit assumption that all variations in the intensity profiles are geometrical in origin. In cases for which the atomic structure is known a priori the validity of this assumption, and of data averaging procedures necessary to enforce it, can be checked. Only as a body of successful experience with both experimental data and dynamical calculations is acquired for the various structure determination algorithms, however, can confidence in them be established in the general case of adsorbed overlayers. The Patterson function methodology is particularly subject to the confusion of dynamical and geometrical phenomena unless the data sampling techniques needed to evaluate (155) (or a variant thereof) are subjected to explicit tests to ensure suitable "kinematical" character of the raw or averaged intensity profiles. Moreover, on the basis of X-ray experience³⁸⁰ we would expect that the chemical identity of the species in the unit cell and plausible models for their atomic scattering factors must be inserted into the analysis in order to determine any but the simplest, nonreconstructed overlayer structures.

In short, each of the various microscopic model and data reduction approaches to surface crystallography exhibits its own unique assets and liabilities. None of them has been applied to examine a wide range of model systems. Nevertheless, in the following two subsections we discuss the available literature on their applications, recognizing that the large amount of current activity in this area probably will bring about additional developments in the near future.

3. *Structure Determination via Dynamical Models of Elastic Low-Energy Electron Diffraction*

The major application envisaged for elastic low-energy electron diffraction (ELEED) is the determination of the structure of adsorbed overlayers. Nevertheless, many useful studies of clean surfaces can be undertaken, such as the search for expanded or contracted upper layer spacings,^{29, 197, 250, 251, 265, 381, 382} or the examination of the validity of data reduction techniques.^{326, 366-369} Therefore we proceed by discussing structure determination calculations for clean surfaces and adsorbed overlayers in turn.

Interest in the structure of clean surfaces recently has been stimulated by a host of model calculations of layer spacings near these surfaces²¹ and by the recognition that unlike the situation for Al(100) and Al(111), observed ELEED intensities for Al(110) cannot be described adequately by use of a model in which the surface is regarded as a truncated but otherwise ideal bulk solid.^{197, 250} Three hypotheses have been advanced to interpret these data. First, the surfaces involved are not adequately characterized^{197, 250} (i.e., free of contaminants). Second, the upper layer spacing on Al(110) is contracted by approximately 10%.^{197, 250, 251} Third, deviations of the surface topography from that of a plane (in particular, the occurrence of steps) cause the discrepancy between model calculations for planar surfaces and experimental data for real (i.e., "stepped") surfaces.^{329, 363} Subsequent studies^{145, 383} of aluminum surfaces with Auger spectroscopy have rendered the first hypothesis rather unlikely. Although both of the latter two interpretations remain viable possibilities, neither produces a description of the observed intensities comparable to those shown in Fig. 22 [Al(111)], Figs. 24 and 34 [Al(100)], and Fig. 26 [Ni(100)] for the unreconstructed close-packed faces of clean metals. Therefore no compelling indication has yet been given of either expansions or contractions by greater than 5% (the intrinsic accuracy of the analysis) of the surface layer spacings of clean single-crystal solids. The intensity patterns alone, however, indicate that the surfaces of covalent semiconductors and possibly the (100) faces of Au, Ir, and Pt are reconstructed relative to their bulk counterparts.²¹

The situation is more promising in the case of adsorbed overlayers because the geometrical effects are intrinsically greater. In general, the adsorbates are expected to occupy sites of high symmetry (see, e.g., Fig. 30) which differ from each other by distances of the order of 0.2 to 2.0 Å. Since these are larger than the anticipated resolution of the analysis ($\Delta a \sim 0.1$ Å), we expect intensity analyses in their present state of development to permit a distinction between the various possible types of structures. Therefore the question of interest to us in the remainder of this

section is "given the occurrence of a reduced symmetry ordered adsorbate structure as revealed by the spot pattern, can the positions of the adsorbate and substrate species be determined by analysis of the intensities of the diffracted beams?"

During the past two years substantial advances have occurred in the art of surface structure determination via ELEED intensity analysis. At the present time the structure of small (low-coverage) overlayer structures [like, e.g., $c(2 \times 2)$, $p(2 \times 2)$, $(\sqrt{3} \times \sqrt{3})$] can be inferred from dynamical, multiple-scattering analyses of the intensities of the diffracted beams.^{240-242,310,382} Moreover, the structure of the more complex (high-coverage) coincidence lattice structures can be determined by suitable data averaging procedures.^{326,366-368} Indeed, the first example of the determination of the atomic geometry of an adsorbed overlayer was an analysis of such a coincidence lattice: Rh(100)- $c(2 \times 8)$ -0.³⁶⁸ Consequently, by a judicious choice of analytical techniques it currently is possible to attempt an analysis of even fairly complex overlayer structures.

The selection of the method to be used in a particular structure determination is based on both technical and physical considerations. At the present time, computational limitations restrict microscopic model structure analyses to cases characterized by small selvedge unit cells in each layer parallel to the surface, (i.e., those containing four atoms or less). The use of data reduction methods, however, is limited by physical constraints. Whereas these methods are quite applicable in the high-energy region ($150 \text{ eV} \lesssim E$), the surface sensitivity of ELEED diminishes in this region due to increases in the inelastic collision damping length (λ_{ee}) and decreases in the atomic elastic scattering cross-sections caused by thermal vibrations of the ion-cores. Consequently, the desire that the kinematical model be applicable for the analysis of measured ELEED intensities tends to be mutually exclusive with the requirement that the ELEED technique be surface sensitive. This observation is evidently more restrictive for adsorbed overlayers than for undistorted clean surfaces. Therefore an assessment of the prospects for microscopic model calculations is of substantial importance for the development of a crystallography of adsorbate-covered surfaces.

The most popular microscopic model technique^{240,310,382} pertains to the case in which a simple adsorbed overlayer is considered to lie "on top" of an underlying substrate. The unit-cell contents of the overlayer are regarded as known a priori, so that it is necessary to determine only its vertical and horizontal registry with respect to the substrate. Its vertical position is determined by comparison of the calculated and measured (00) beam intensities for a specified horizontal position (usually chosen to be that of maximum coordination). The final selection of the site symmetry of the atoms in the overlayer is performed by comparing calculations for the

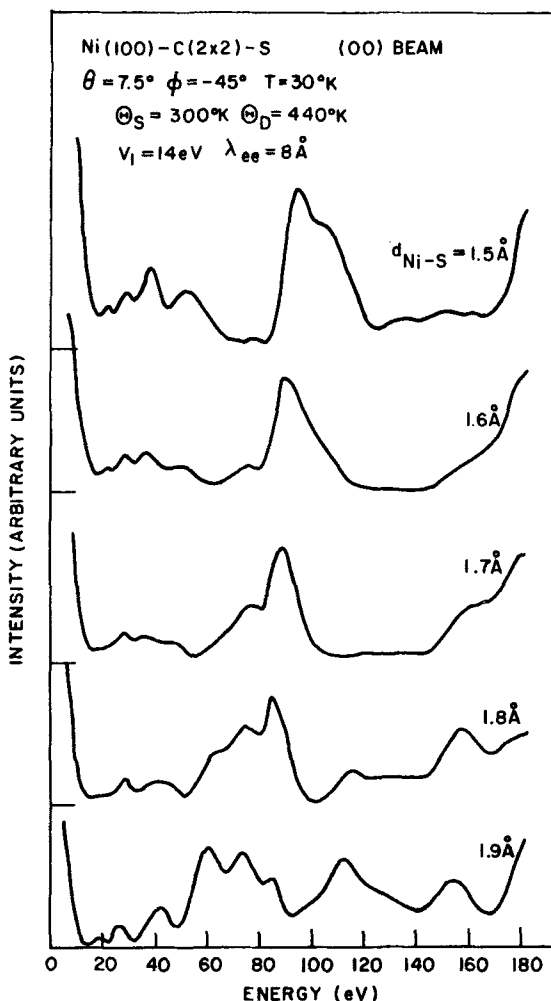


Fig. 53. Calculated intensities of the (00) beam of electrons diffracted from Ni(100)-c(2×2)-S. The azimuthal angle, $\phi = -45^\circ$, is measured with respect to the side of a c(2×2) square surface unit mesh. The phase shifts used in the calculations were obtained from an overlapping atomic potential. The intensities were evaluated using a four-phase-shift, six-layer multiple-scattering computer program. The vibrational and optical model parameters, the temperature, and the beam parameters are indicated in the figure. The sulfur-nickel distance for the unreconstructed c(2×2) overlayer of sulfur at the fourfold coordinated sites is indicated beside the individual intensity profiles. The layer spacing of the Ni substrate is taken to be $d_{\text{Ni-Ni}} = 1.76 \text{ \AA}$, leading to Bragg envelope maxima at about 35 and 95 eV. (After Duke et al.²⁴¹)

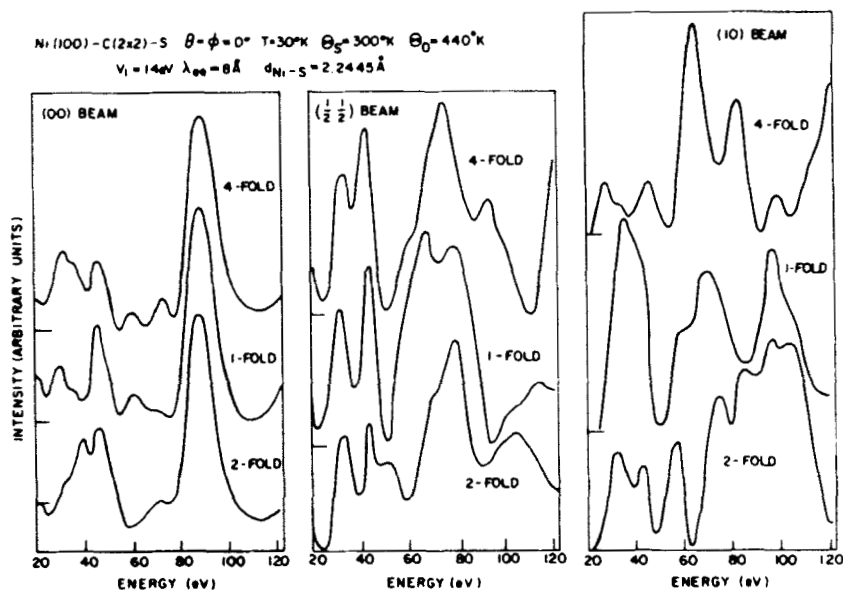


Fig. 54. Calculated intensities of the (00), $(\frac{1}{2} \frac{1}{2})$, and (10) beams of electrons diffracted from Ni(100)-c(2 \times 2)-S. The azimuthal angle, $\phi = 0$, is measured with respect to the side of a c(2 \times 2) square surface unit mesh. The phase shifts used in the calculations were obtained from an overlapping atomic potential. The intensities were evaluated using a four-phase-shift, six-layer multiple-scattering computer program. The vibrational and optical model parameters, the temperature, and the beam parameters are indicated in the figure. The sulfur-nickel distance for the unreconstructed c(2 \times 2) overlayer of sulfur is $d_{\text{S-Ni}} = 2.2445 \text{ \AA}$. The site symmetry of the S atoms in the overlayer is indicated beside the individual intensity profiles. The layer spacing of the Ni substrate is taken to be $d_{\text{Ni-Ni}} = 1.76 \text{ \AA}$, leading to Bragg envelope maxima in the specular beam at about 35 and 95 eV. (After Duke et al.²⁴¹)

various symmetries (usually at the height fixed in the preceding step) with the observed intensities.

The initial application of this method, that is, to Ni(100)-c(2 \times 2)-Na,³¹⁰ led to the results discussed in Section V.C.7. The space group and site symmetries of c(2 \times 2) overlayers on the (100) face of fcc crystals are shown in Figs. 29 and 30, respectively. An indication of the accuracy of the procedure of determining the spacing and coordination of the overlayer is given in Figs. 53–55 for Ni(100)-c(2 \times 2)-S. It is evident from Fig. 53 that the major consequences of altering the height of the overlayer by $\pm 0.1 \text{ \AA}$ are changes in the shapes of prominent peaks in the (00) beam rather than shifts in their energies. Moreover, these changes are similar to those obtained from variations in the boundary conditions from one model to another and from the use of atomic as opposed to ionic ion-core potentials. The alterations in the intensity profiles associated with different site

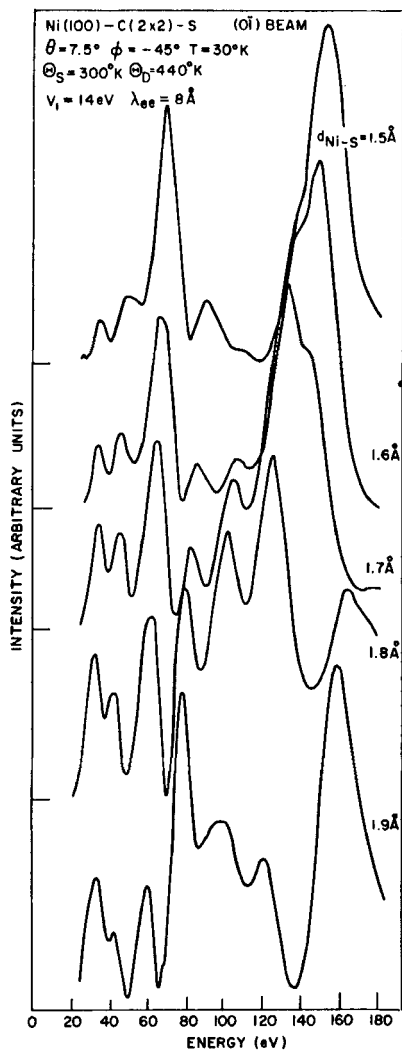


Fig. 55. Calculated intensities of the $(0\bar{1})$ beam of electrons diffracted from Ni(100)- $c(2 \times 2)$ -S. The azimuthal angle, $\phi = -45^\circ$, is measured with respect to the side of a $c(2 \times 2)$ square surface unit mesh. The phase shifts used in the calculations were obtained from an overlapping atomic potential. The intensities were evaluated using a four-phase-shift, six-layer multiple-scattering computer program. The vibrational and optical model parameters, the temperature, and the beam parameters are indicated in the figure. The sulfur-nickel distance for the unreconstructed $c(2 \times 2)$ overlayer of sulfur at the fourfold coordinated sites is indicated by the individual intensity profiles. The layer spacing of the Ni substrate is taken to be $d_{\text{Ni-Ni}} = 1.76 \text{ \AA}$, leading to Bragg envelope maxima at about 70 and 150 eV. (After Duke et al.²⁴¹)

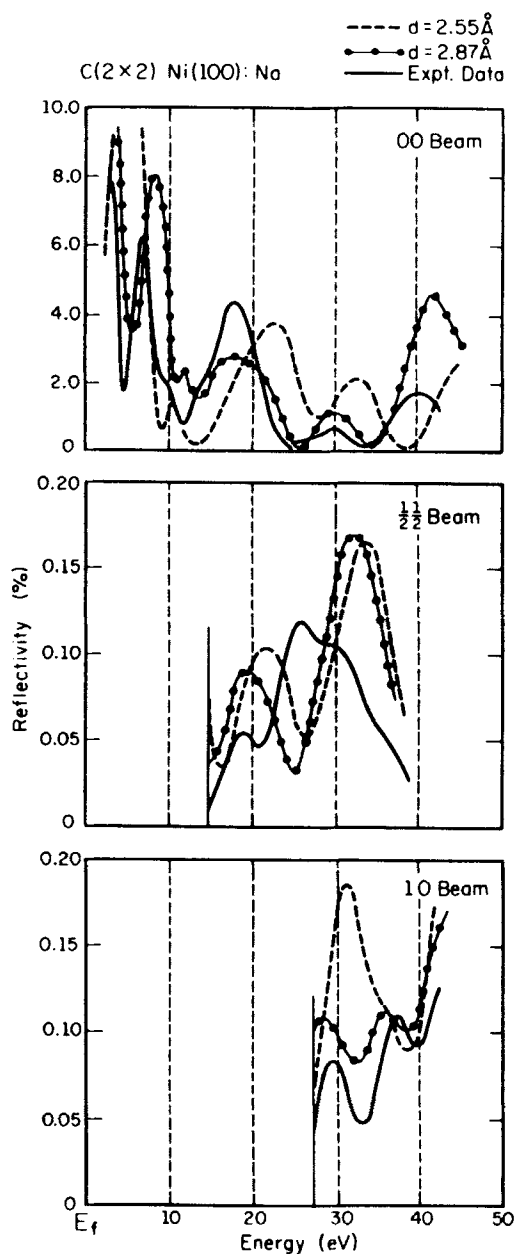


Fig. 56. LEED spectra calculated and observed for normal-incidence electrons diffracted from a $c(2 \times 2)$ sodium structure on a nickel (100) surface: — experiment; --- theory, $d = 2.55 \text{ \AA}$; - · - · theory, $d = 2.87 \text{ \AA}$. Experimental (00) beam $\times 3$ above 25 eV; theoretical ($\frac{1}{2} \frac{1}{2}$) beam $\times 4$; theoretical (10) beam $\times 2$. The theory curves were obtained from the electron-solid potential described in Ref. 310. (After Andersson and Pendry.³¹⁰)

symmetries for a vertical height equal to the covalent radius close-packed spacing (i.e., $d = r_S + r_{Ni}$; $r_S = 1.0$ Å and $r_{Ni} = 1.245$ Å) at the onefold site are shown in Figs. 54, 55, which reveals that given the uncertainties in the potential and boundary conditions described in Section V.C. variations among the sites of high symmetry coordination are unambiguously discernible in the calculations. We see from Fig. 53, however, that effects in the (00) beam caused by changes in vertical spacing of $\Delta a = 0.1$ Å are difficult to distinguish from those associated with different potentials for $E \lesssim 100$ eV. Fortunately, Fig. 55 demonstrates that such differences in spacings generate clearly identifiable effects in the nonspecular (0 $\bar{1}$) beam. Therefore the multiple-scattering-analysis methodology is feasible, although perhaps less emphasis should be placed on descriptions of the (00) beam for incident beam energies below about 50 to 100 eV.

The calculations of Andersson and Pendry^{310,382} led them to conclude that for Ni(100)-c(2×2)-Na the Na atoms occupy fourfold sites a distance $d = 2.87$ Å above the center of the plane of substrate Ni atoms. Their "best fit" structures are shown in Fig. 56. Forstman et al.²⁴⁰ applied the same technique to examine Ag(111)-($\sqrt{3} \times \sqrt{3}$)30°-I structures. The relevant site symmetries are indicated in Fig. 57. Forstman et al. concluded that the

$$fcc(111) : (\sqrt{3} \times \sqrt{3}) 30^\circ$$

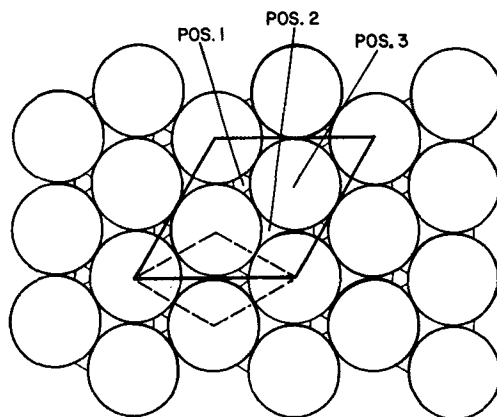


Fig. 57. The local high-coordination site symmetries of ($\sqrt{3} \times \sqrt{3}$)30° structures on atomically flat (111) faces of fcc crystals. These structures correspond to third-monolayer coverage of adsorbates in a simple overlayer. Position 2 exhibits maximum coordination from both the top layer and the one below it. (After Forstmann et al.²⁴⁰)

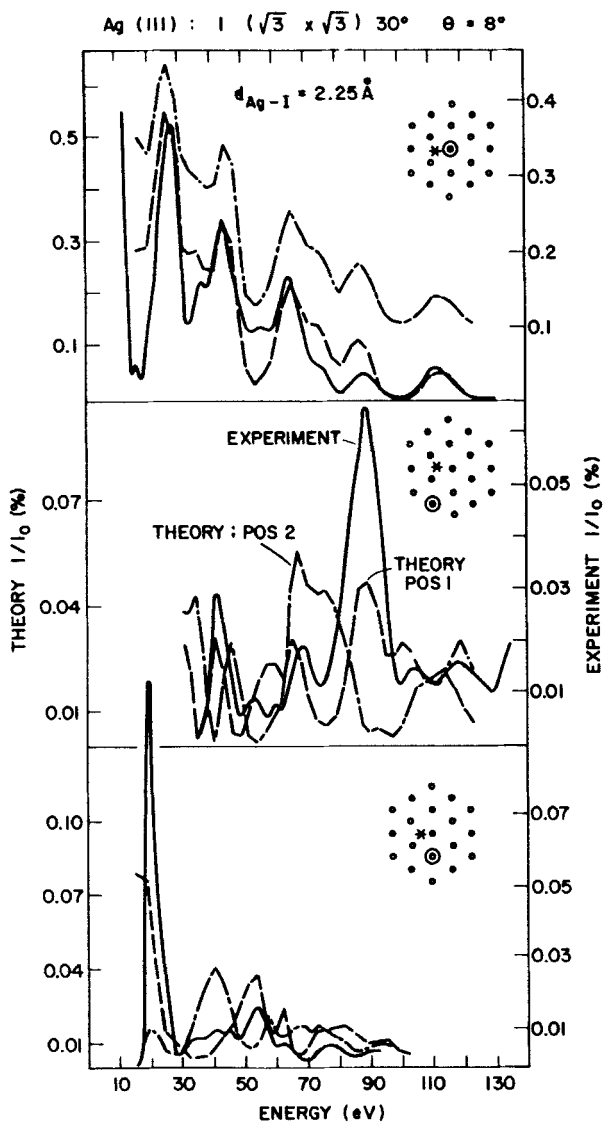


Fig. 58. Intensity profiles from a $(\sqrt{3} \times \sqrt{3})30^\circ$ iodine structure on a silver (111) surface at an incidence angle of 8° from normal. The corresponding diffraction spot is encircled in the pattern. The asterisk indicates the electron gun position. Solid line, experiment; dashed line, theory for iodine atoms in position 1; dot-dashed line, theory for iodine atoms in position 2. The ratio between theoretical and experimental scales is 1.45. (After Forstmann et al.²⁴⁰)

iodine atoms occupy site 1 at a distance of 2.25 Å from the center of the underlying Ag layer. Their best-fit structures are displayed in Fig. 58. The fact that an extended range of data is considered (14 clearly discernible "peaks") provides added confidence in the results of their analysis. Of these peaks, the preferred model structure predicts only eight (i.e., 57%) to within 3 to 4 eV because its description of the specular beam is, by construction, considerably better than that of the other two beams. Considering the visual impact of the model description of the observed ELEED intensities, however, we conclude that a dynamical model description of 50 to 60% of the observed intensity maxima probably establishes a plausible structure.

In the technique used to obtain Figs. 56 and 58 it is assumed that the structure of the overlayer is known a priori. Although such an assumption is sensible for metallic and inert adsorbates at low coverages, these species at higher coverages and reactive adsorbates at all coverages create structures associated with overlayer unit cells of uncertain contents and positions. Since currently it is technically feasible to examine only small structures using a microscopic model methodology, we next extend the technique described above to the consideration of the possibility of reconstructed surface structures for Ni(100)-c(2×2)-S.^{241,242}

We hypothesize that the S atoms form an adsorbed overlayer on an otherwise ideal Ni(100) surface. In the case of reactive gases like S, the unit-cell contents within the overlayer are uncertain even if the coverage is known. Hagstrum and Becker³⁸⁴ regard c(2×2)S layers on Ni(100) as comprised of a single S atom for every two substrate Ni ion cores. Perdereau and Oudar,³⁸⁵ on the other hand, consider such overlayers to be "reconstructed" one-dimensional NiS structures comprised of planar arrays of interpenetrating square lattices of Ni and S, respectively. The objective of a complete structure analysis is the determination of the structure of this hypothetical overlayer, and its registry (vertical and horizontal) relative to the Ni(100) substrate.

Duke et al.^{241,242} analyzed this structure by proceeding in three steps. First, various models of the overlayer constitution and registry were used to evaluate LEED intensities for comparison with the (01) and ($\frac{1}{2}$ $\frac{1}{2}$) beams measured for normally incident electrons. These models included both simple and planar reconstructed overlayers at the fourfold, twofold (two sites), and onefold coordinated sites. For each site the vertical spacing of the overlayer was adjusted in 0.1 Å steps to achieve the best "fit" to the observed intensities. Then the S atoms in the planar reconstructed overlayers were moved vertically and the S atoms in both model overlayers adjusted horizontally to examine the possibility of improving the descrip-

tion of the data. Second, the LEED intensities at incident angles $\theta = 7.5^\circ$ and 12.5° were evaluated for the strongest "candidate" structures and a separate suboptimization carried out for $\theta = 7.5^\circ$. Third, for the resulting "best" S-Ni structure (fourfold coordinated, unreconstructed, $d_{\text{Ni-S}} = 1.7 \text{ \AA}$) the spacing of the uppermost two Ni layers was allowed to expand or contract in order to improve the description of the data. In all, over 50 model structures were examined and over 500 calculated intensity profiles were compared with the experimental data.

An indication of the accuracy of this procedure is provided by Figs. 53 to 55 and by Table III in which we note experimental and predicted peak energies in the $(\frac{1}{2} \frac{1}{2})$ and (10) diffracted beams associated with normally incident electrons. The four model structures used to obtain the results indicated in this table were chosen to illustrate the nature of changes in peak energies caused by vertical translation and by reconstruction, respectively, of the atoms in the overlayer. Similar results are obtained for other beams and angles of incidence. Agreement between the observed and predicted peak energies to within 2 to 4 eV is regarded as the intrinsic resolution of the method which is limited by uncertainties in data reproducibility and in the construction of the model electron-solid potential. As evident from the table, this precision corresponds to an uncertainty of approximately $\Delta a = 0.1 \text{ \AA}$ in the atomic position coordinates.

Table III indicates that given Theeten's experimental intensity data as the basis for a structure analysis, the survey of structures leads to a clear choice of $d_s = 1.70 \pm 0.1 \text{ \AA}$ for the overlayer-substrate spacing. The determination of the structure of the overlayer, however, is more difficult. A typical comparison between calculated and measured intensities is shown in Fig. 59 for the "optimum" unreconstructed and reconstructed structures obtained neglecting the possibility of adsorbate-induced relaxations of the underlying Ni(100) crystal. A representative survey of calculated and observed intensity profiles for likely structures of Ni(100)-c(2×2)-S is presented in Figs. 60 and 61. In the unreconstructed structures the S atoms occupy a c(2×2) array of fourfold sites at a distance d_s above a plane passing through the center of the underlying Ni(100) layer. The structure labeled "reconstructed" has Ni atoms also at the other c(2×2) array of fourfold sites but at a bulk layer spacing $d = 1.76 \text{ \AA}$ above the plane below it. The expanded substrate structure consists of an unreconstructed c(2×2) layer of S in the fourfold sites over a Ni(100) substrate whose upper layer spacing is $d_{\text{Ni-Ni}} = 1.90 \text{ \AA}$ rather than $d = 1.76 \text{ \AA}$.

From a survey of results like those given in Figs. 33, 53 to 55, and 59 to 61 and in Table III, Duke et al.²⁴² concluded that on the basis of an analysis of Theeten's data the sulfur atoms would seem to occupy a c(2×2) array of fourfold sites at a distance $d_{\text{Ni-S}} = 1.70 \pm 0.1 \text{ \AA}$ above the Ni(100)

TABLE III

Peak Energies (in eV) for Experimental and Model ELEED Intensities for Normally Incident Electrons Diffracted from Ni(100)-c(2×2)-S^a

Experiment $T = 30^\circ\text{K}$	Unreconstructed, fourfold site			Reconstructed fourfold sites $d_{\text{Ni-S}} = 1.70 \text{ \AA}$, $d_{\text{Ni-Ni}} = 1.76 \text{ \AA}$
	$d_s = 1.60 \text{ \AA}$	$d_s = 1.70 \text{ \AA}$	$d_s = 1.80 \text{ \AA}$	
$(\frac{1}{2}\frac{1}{2})$ beam				
20	22	20	20	—
30	(35)	(32)	—	30
41	42	41	35	(37)
54	58	54	49	(60)
70	78	74	72	72
94-(110)	122	118	114	(99)-112
139-150-(160)	157	152-(160)	145	150-162
(10) beam				
44	44	44	42	42
57	62	59	57	61
74-79	82	78	74	80
96	98	97	94	99
124-131-(152)	142	118-137	(114)-130	134-142

^aThe table includes the two "optimal" structures (unreconstructed, $d = 1.70 \text{ \AA}$; reconstructed, $d_{\text{Ni-S}} = 1.70 \text{ \AA}$, $d_{\text{Ni-Ni}} = 1.76 \text{ \AA}$) obtained in Ref. 242 by neglecting adsorbate-induced alterations of the substrate. Smaller structure is designated in parentheses and split peaks by hyphens. (After Duke et al. 242)

layer beneath. Further assertions are less certain. For a data base containing 64 prominent maxima using the unreconstructed structure the model predicts 83% of these peaks, the reconstructed structure 56%, and the expanded-substrate structure 68% of them. A typical nonoptimized structure describes about 30% of these maxima. Thus all three structures provide descriptions of the ELEED intensities comparable to or better than the optimal one illustrated in Fig. 58 for Ag(111)- $(\sqrt{3} \times \sqrt{3})30^\circ\text{-I}$. Only further experience will permit a definitive assessment of the adequacy of the data base of the significance of these three optimal structures for Ni(100)-c(2×2)-S, although it would seem that a reconstructed overlayer can be ruled out in spite of its quite acceptable description of many of the ELEED intensity profiles.

The three studies just described, plus two^{242,386,387} on Ni(100)-c(2×2)-O, constitute the portfolio of microscopic model analyses of overlayer structures reported to date. (i.e., June 1973). The oxygen structures on Ni

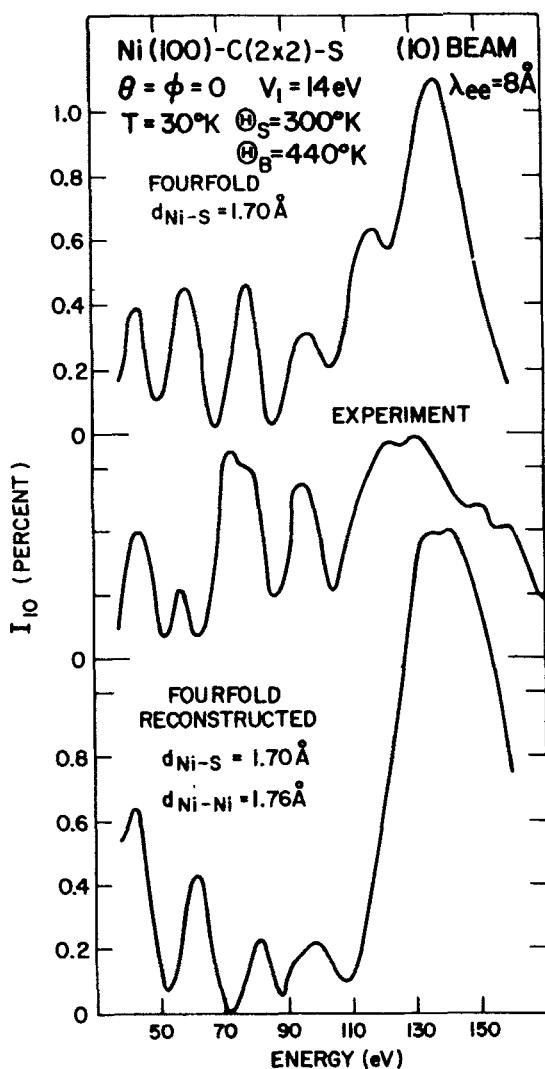


Fig. 59. Comparison of the observed and calculated intensity profiles of normally incident electrons scattered into the (10) substrate beam associated with a Ni(100)-c(2x2)-S structure. The dynamical and geometrical parameters used in the model calculations are indicated in the figure. The multiple-scattering computer program used in the analysis incorporates four phase shifts and six layers of scatterers. The electron-ion-core potential was obtained using an overlapping atomic charge density model. The designation "fourfold" indicates that the adsorbate c(2x2) lattices consist of atoms in the geometrical "holes" above the uppermost layer of Ni atoms in the substrate as shown in Fig. 30. (After Duke et al.²⁴²)

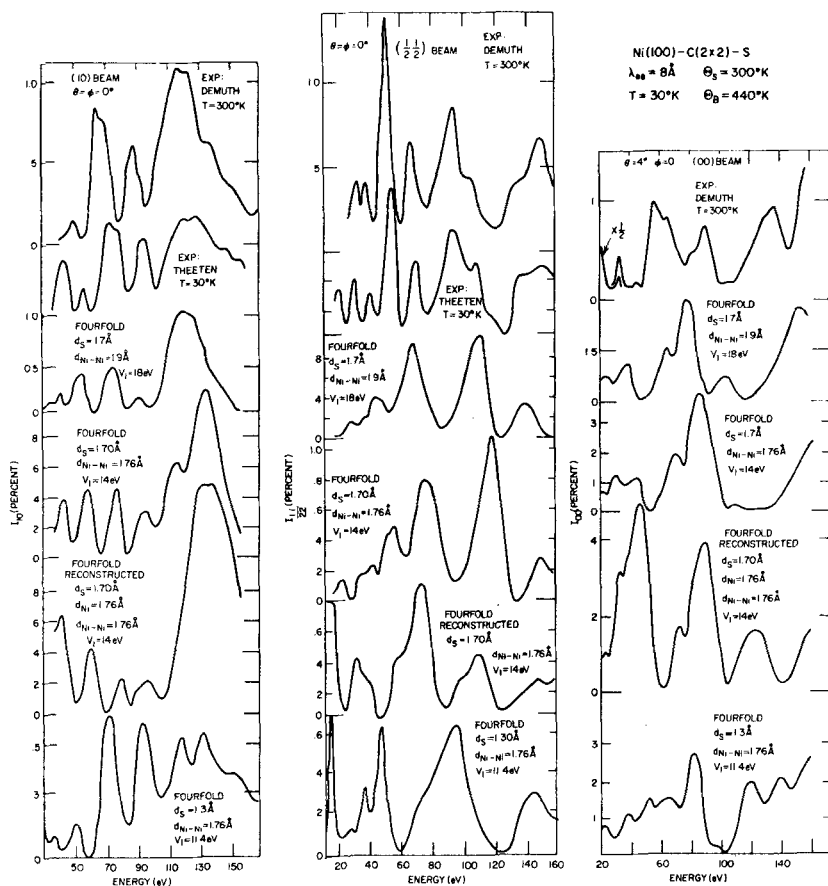


Fig. 60. Comparison with observed ELED intensity profiles for Ni(100)-c(2x2)-S of those calculated using the optimum structures without (lower three curves) and with (fourth curves from the bottom) relaxation of the upper layer spacing of the Ni(100) substrate. In all cases but that shown in the lower panel, the sulfur occupies the four-fold coordinated sites at a height $d_s = 1.70\text{\AA}$ above a plane passing through the center of the underlying layer of Ni atoms. For the lower panel $d_s = 1.3\text{\AA}$. All potentials were obtained from an overlapping atomic charge density model. The calculations were performed using a four-phase-shift, six-layer multiple-scattering computer program. The real part of the optical potential, V_1 , was allowed to increase to 18eV in order to align maxima in the $\theta = 7.5^\circ$, $\phi = -45^\circ$ specular beam intensity profile when the upper Ni layer spacing was taken to be expanded. The beam parameters, overlayer structures, and temperatures are indicated in the figure. The experimental data are labeled by the names of the workers who obtained them, and are reproduced here with the kind permission of Drs. Theeten and Demuth. (After Duke et al.²⁴²)

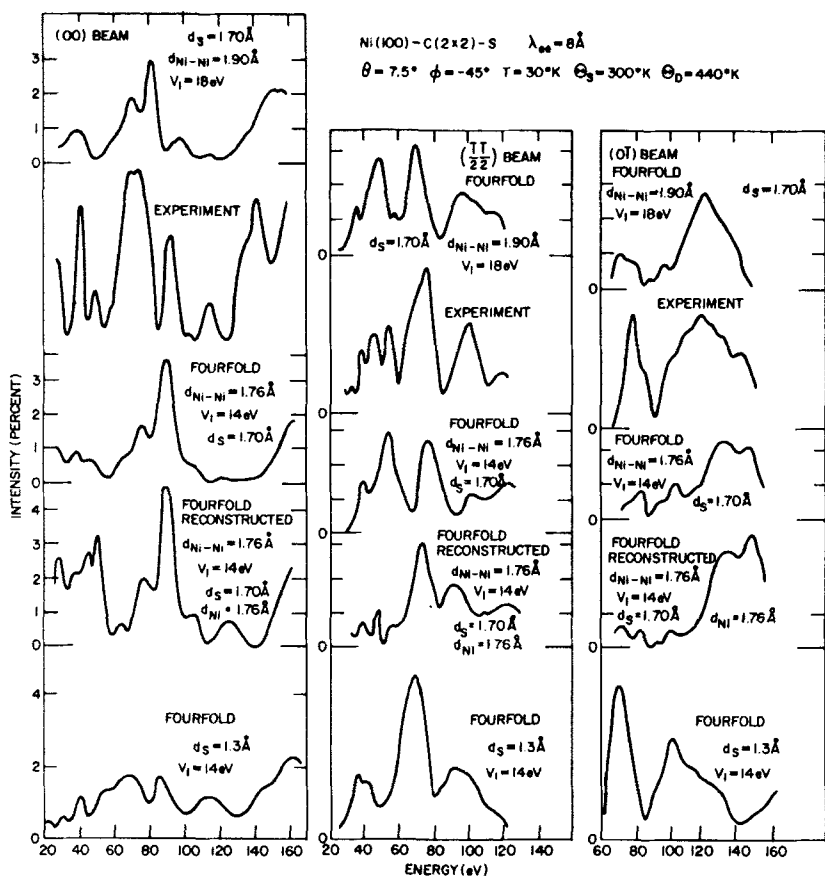


Fig. 61. Comparison with observed ELED intensity profiles at $\theta = 7.5^\circ$ for Ni(100)-c(2 \times 2)-S of those calculated using the optimum structures without (lower three curves) and with (upper curves) relaxation of the upper layer spacing of the Ni(100) substrate. In all cases but that shown in the lower panel, the sulfur occupies the four-fold coordinated sites at a height $d_s = 1.70 \text{ \AA}$ above a plane passing through the center of the underlying layer of Ni atoms. All potentials were obtained from an overlapping atomic charge density model. The calculations were performed using a four-phase-shift, six-layer multiple-scattering computer program. The real part of the optical potential, V_1 , was allowed to increase to 18 eV in order to align maxima in the specular beam intensity profile in the case that the upper Ni layer spacing was taken to be expanded. The beam parameters, overlayer structures, and temperature are indicated in the figure. (After Duke et al.²⁴²)

appear intrinsically more complicated than those discussed above because the ELEED data suggest that more than one unit-cell structure corresponds to an observed $c(2 \times 2)$ intensity pattern. These examples reveal that structure determinations by comparison of dynamical model calculations of ELEED intensities with measurements thereof clearly are feasible. Moreover, such procedures seem capable of generating a small group of plausible structures for any given data base. The distinction between structures which predict to within a few electron volts over 60% of 50 or more observed maxima in the ELEED intensities is less certain, although for a given experimental data base these structures generally differ from each other by geometrical changes $\Delta a \sim 0.1$ to 0.2 Å which are comparable to the stated uncertainty in the methodology. The major limitations on the application of this analytical technique are the adequacy of the experimental intensities and the present restriction of the computations to overlayer structures containing four or less atoms per unit cell in a given plane of the seldge. To examine larger structures data reduction methods currently are required, so we turn next to a discussion of the present state of development of these techniques.

4. Structure Determination via Data Reduction and Kinematical Methods

In spite of the considerable discussion in the literature about structure analyses based on kinematical (i.e., Born approximation, Section III.C) models^{2-5, 340-342} few applications of these methods to examine either clean or adsorbate-covered surfaces have been performed. The origin of this situation seems to reside in the substantial body of elastic low-energy electron diffraction (ELEED) intensity data required for a definitive analysis of this type³⁶⁶⁻³⁷⁶ and the difficulty of obtaining such data without automated equipment³⁴³ and low-temperature crystal manipulators (see Sections V.C.4 and V.C.6). Consequently, the use of these techniques remains thus far an attractive idea whose time is yet to come. We proceed in this subsection by indicating the nature and extent of the existing applications of such methods for clean surfaces and adsorbed overlayers, respectively.

It is convenient to decompose the problem of determining the atomic geometry of defect-free planar single-crystal surfaces into three steps. First, the Bravais net of the two-dimensional atomic planes parallel to the surface is constructed from the intensity pattern (Section VII.D.1). The solid is visualized as being composed by stacking these planes on top of each other. Second, the chemical identities, electron-ion-core scattering factors, and positions of the atomic species in each layer must be evaluated. Finally, the registry (i.e., packing sequence and spacing) of the various layers must be determined. For simplicity, we discuss each of these

steps in the limiting case of a monatomic metal.

In the case of an unreconstructed clean metal surface, the chemical identities and positions of the atomic scatterers within an individual two-dimensional layer are regarded as "known" a priori (once, of course, the cleanliness of the surface has been established by, e.g., Auger spectroscopy). Moreover, the observed intensity profiles usually exhibit such clearly discernible kinematical features that the layers' registry can be ascertained by kinematical indexing of prominent maxima in the non-specular beams. Specific examples have been discussed by Farrell and Somorjai,³⁸⁸ and by Tucker and Duke.^{255,366-368} Thus the kinematical aspects of the intensity profiles observed from many clean metals are both apparent and pervasive, and their existence is crucial to the success of the data reduction methodologies described in Section VII.D.2. Consequently, Duke and co-workers^{197,248,250,255,326,366-369} performed a variety of schematic model calculations in order to examine the generality of observations of kinematical behavior and their compatibility with dynamical models of ELEED. They concluded that the dynamical intensity profiles consist of numerous "interlayer multiple-scattering peaks" (ILMSP) whose dynamical origin is the multiple scattering of the incident electron between atomic layers parallel to the crystal surface. The detailed shapes of these peaks depend on all of the dynamical parameters in the models and hence are not simply related to the atomic geometry. Nevertheless, these peaks often are most intense for energies close to those predicted by the kinematical Born approximation analysis. Tucker and Duke abstracted this general feature of the model calculations under the shorthand notation "Bragg envelope concept."²⁵⁵ that is, the dynamical intensities behave as if the "kinematical" scattering cross-section predicted by the first Born approximation modulates an array of closely spaced multiple-scattering peaks which otherwise would exhibit fairly uniform intensities. Indeed, the registry of the upper layers of the surfaces of clean materials has, thus far, been determined either by direct analysis of kinematical features in the intensity profiles^{255,368,370-374,388-390} or by their implicit utilization in a Patterson function analysis.^{378,379}

Like all generalizations, the Bragg envelope concept has its limitations. Thus its application to surface structure determination is facilitated by distinguishing between characteristic features of the intensity profiles in three separate ranges of energy of the incident electrons. The low-energy region, $0 \lesssim E \lesssim 25$ eV, is characterized by long electron inelastic collision mean free paths, for example, $\lambda_{ee} \sim 200$ Å, as $E \rightarrow 0$, and the occurrence of inelastic threshold phenomena. Therefore the dynamic effects associated with the electronic structure of the constituents of the solid and the discrete electronic inelastic loss processes dominate the behavior of the intensity profiles. Consequently, we do not expect this region to be broadly

useful for the study of surface crystallography.

The intermediate-energy region, $25 \text{ eV} \lesssim E \lesssim 100$ to 300 eV , is characterized by strong inelastic collision damping ($\lambda_{ee} \sim 2$ to 8 \AA), and strong elastic electron-ion-core scattering. It is in this energy region that ELEED is most surface sensitive. However, in this region the intensity profiles generally appear highly "dynamical" in character as described in Section IV.A. (That is, the fine structure in between the clusters of peaks near the kinematical Bragg energies is comparable in intensity to these "kinematical" clusters.) Also, as initially noted by Farnsworth,³⁹¹ the intensity profiles from geometrically similar but electronically distinct materials can differ substantially. The key to utilizing this region of the intensity profiles to determine surface crystallography lies in the application of data averaging^{366-369,372-376} to eliminate the unwanted dynamical fine structure while preserving maxima at the energies of the Bragg envelope clusters.

A number of simplifications in the intensity profiles occur in the high-energy region $E \gtrsim 100$ to 500 eV . The precise definition of this region varies from one crystal face and material to the next, occurring for energies above about 100 eV in carbon but not until about 450 eV for W(100). In this region the inelastic collision mean free path is increasing so that ELEED is becoming less sensitive to the surface properties of the solid. This effect is enhanced by the large vibrational amplitudes of surface scatterers which reduce the scattering from the surface atoms relative to that from bulk atoms. Thus, the elastic as well as inelastic scattering of the electron is diminishing in this energy region, leading to intensity profiles which "appear" kinematical. This observation renders the high-energy region of the intensity profiles directly useful for surface crystallography without the need for data averaging.^{255,368} The disadvantage of using this energy region for surface crystallography, however, is the concomitant loss of sensitivity to surface effects (because of the increasing values of λ_{ee} and the enhanced lattice vibrations of surface scatterers).

The Bragg envelope concept and that of three energy ranges constitute the foundation for assessing the suitability of data reduction techniques in specific cases. Evidently, if the bulk of the intensity data to be examined is obtained at high energies and/or predominately for nonspecular beams, either a direct kinematical analysis or its indirect application via a Patterson inversion may be appropriate without further inquiry. If, however, considerations of surface sensitivity or convenience lead to an emphasis on the intermediate-energy region, the raw intensity data should be smoothed by an appropriate averaging procedure prior to performing either a kinematical or Patterson analysis. One class of these procedures has been applied exclusively to the analysis of ELEED from clean metals. Therefore we consider them next.

A *constant-momentum-transfer averaging method* has been proposed by Lagally et al.³⁷²⁻³⁷⁴ who applied it to analyze data on Ag(111) and Ni(111). The fact that averaging the intensity profiles of the specular beam over the azimuthal angle ψ smooths out fine structure in the observed intensity is illustrated by Fig. 62. The manifestations of the Bragg envelope concept are evident in the original intensity profiles (Fig. 62a) as well as in the azimuthal average (Fig. 62b).

An additional average over pairs of (E, θ) values can be performed by recalling that the kinematical intensities of the (hk) beam depend only on the momentum transfer:

$$\mathbf{S} = \mathbf{g}_{hk} + [k_{\perp}(0, E) + k_{\perp}(\mathbf{g}_{hk}, E)]\mathbf{n} \quad (156)$$

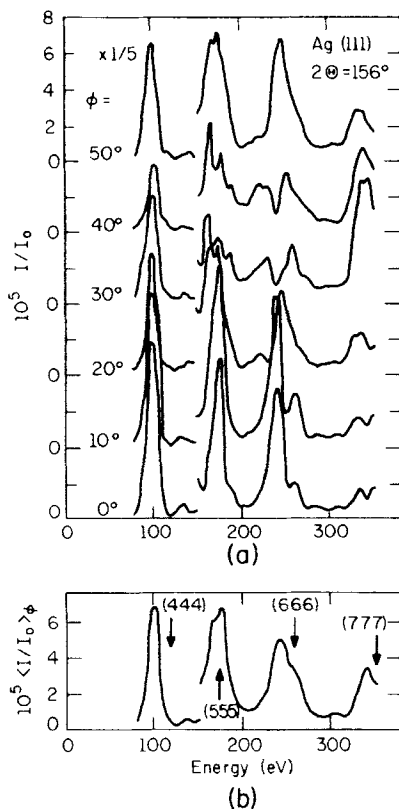


Fig. 62. Intensity profiles for electrons scattered from Ag(111) at incident and exit angles of $\theta = 12^\circ$. The azimuthal angles, ψ , are indicated in the figure. The original raw data are shown in (a). In (b) is illustrated the angular average over azimuthal angles, ψ , of the data shown in (a). (After Lagally et al.³⁷²)

in which \mathbf{n} is the exterior surface normal and the $k_{\perp}(\mathbf{g}, E)$ are given by (44). The momentum transfer \mathbf{S} often is measured in units of

$$S_0 = \frac{2\pi}{d} \quad (157a)$$

in which d designates the spacing between two equivalent layers parallel to the surface. Thus, for an ideal clean crystal surface, the kinematical Bragg

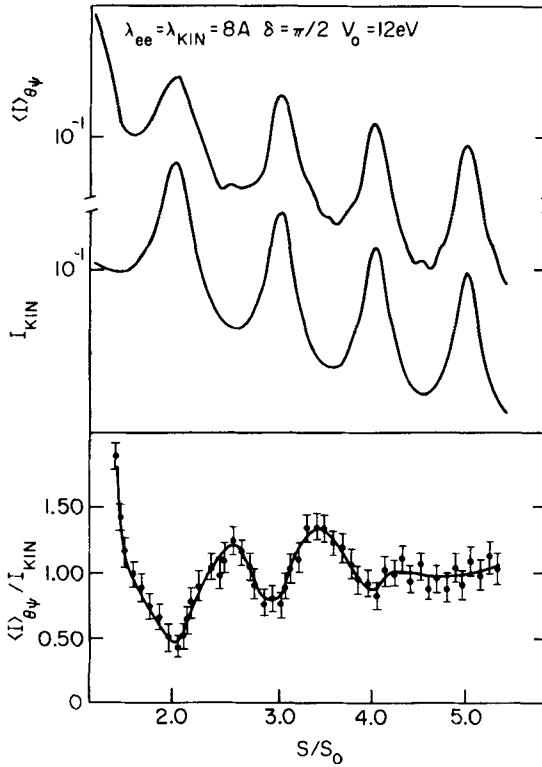


Fig. 63. Comparison of the grand averaged intensity of the (00) beam with the kinematic intensity (upper panel) and the ratio of the grand averaged intensity to the kinematic intensity (lower panel). The six values of $\psi = 0, 10^\circ, 20^\circ, 30^\circ, 40^\circ$, and 50° were used in constructing the azimuthal averages. Then six azimuthal averages for angles of incidence $\theta = 12^\circ, 14^\circ, 16^\circ, 18^\circ, 20^\circ$, and 22° were in turn averaged by selecting energies and incidence angles corresponding to fixed momentum transfer. Intensities are plotted as a function of a normalized momentum transfer S/S_0 chosen so that the Bragg peaks occur at integral values of S/S_0 . Error bars in the ratio indicate the estimated uncertainty in performing the average from the given set of 36 intensity profiles. Values of the dynamical parameters are indicated in the figure. (After Duke and Smith.³⁶⁹)

peaks occur at

$$\frac{S}{S_0} = m \quad (157b)$$

in the specular ($\mathbf{g} \equiv 0$) beam if m is an integer. The important feature of (157) for our present purposes is that S is not only independent of ψ for $\mathbf{g} = 0$, but in general is constant along certain trajectories in the E - θ plane. Therefore the most complete average possible is a combined "grand" average over both ψ and some appropriate measure of arc length along these trajectories.

Lagally et al.³⁷²⁻³⁷⁴ demonstrated that an additional "constant S " E - θ average does indeed smooth further observed ELEED intensity data. Moreover, Duke and Smith³⁶⁹ examined the quantitative comparison between the corresponding averaged dynamical calculated intensities and those predicted by the kinematical model. Typical results of the latter analysis are shown in Fig. 63 which indicates that although the averaging does smooth the intensities, it does not reduce them to precisely the kinematical form. As anticipated from Tucker and Duke's formulation of the Bragg envelope concept,²⁵⁵ the multiple elastic scattering processes usually spread the intensity in a "Bragg" maximum over a wider range of energies than predicted by the kinematical model—an effect that becomes more pronounced with decreasing values of the inelastic collision damping length λ_{ee} . This phenomenon is responsible for the minima in the ratio $\langle I \rangle_{\theta\psi} / I_{\text{kin}}$ near integral values of S/S_0 evident in Fig. 63. Nevertheless, Duke and Smith concluded that for physically reasonable ranges of the parameters used in the dynamical model calculation, a suitably complete "grand" averaging procedure could reproduce the predictions of the kinematical analysis to within about 25 to 50%. As indicated in Fig. 64, this accuracy is quite sufficient to detect changes in the upper layer spacing at the surface of an unreconstructed clean metal crystal by 5 to 10%. Nevertheless, neither of the clean surfaces studied thus far by the averaging method [Ag(111) and Ni(111)] have been found to exhibit upper layer spacings or registries detectably different from those characteristic of the bulk metal.³⁷²⁻³⁷⁴

In summary, to within an accuracy of about 5% both the layer spacing and registry of the uppermost layers of unreconstructed close-packed surfaces of clean metals can be determined directly from kinematical features evident in observed ELEED intensities. This result can be interpreted in terms of dynamical model calculations by application of the Bragg envelope and three energy range concepts. It also would emerge from more elaborate data reduction procedures such as constant-

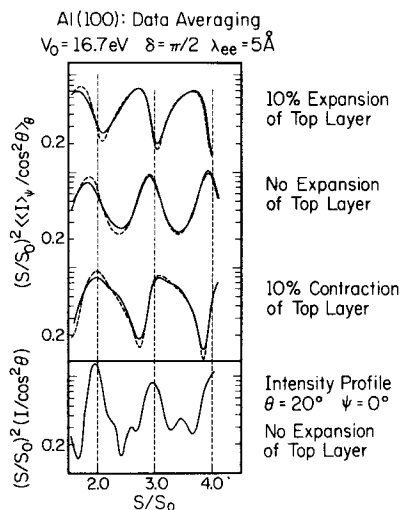


Fig. 64. Averaged dynamical intensities (solid lines) and their kinematical analogues (dashed lines) for electrons reflected in the (00) beam from Al(100). Both the averaged dynamical intensities and the kinematical averages have been multiplied by $(S/S_0)^2$ in order to obtain a function analogous to the kinematical interference function. The lower panel shows an intensity profile for a particular set of values of θ and ψ in order to illustrate how extensively the averages shown in the upper three panels smooth out the individual intensity profiles. The top panel shows the dynamical and kinematical averages for a crystal in which the upper layer spacing is expanded 10% relative to the bulk. The second panel shows the averages for a truncated bulk solid. The third panel shows the averages for the case in which the upper layer spacing is contracted 10% relative to the bulk value. The dynamical averages were evaluated using the azimuthal (ψ) grid $0(9^\circ)45^\circ$ and the polar grid for $\cos\theta = 0.6(0.025)1.0$. The kinematical averages were performed using the $\cos\theta$ grid $0.6(0.01)1.0$. A check on the mesh size indicated an accuracy of a few percent relative to the use of smaller grid meshes. The dynamical parameters are indicated in the figure. The peaks in $\langle I \rangle_\psi / \cos^2 \theta$ for the truncated bulk lattice do not fall at integral values of S/S_0 because of the range of values for $\cos\theta$ used in the polar angle average. (After Duke and Smith.³⁶⁹)

momentum-transfer averaging or Patterson function analysis, and has done so in all cases examined thus far.

Turning to our discussion of uniform overlayer structures for which the combined overlayer-substrate system is periodic parallel to the surface, we recall that the Bravais net of the composite system is determined from the intensity pattern as described in Section VII.D.1. In contrast to the case for most clean surfaces, however, the atomic geometry of the overlayer itself often is unknown. This situation appears most often at high coverages at which coincidence structures occur, but also is common at low coverages of reactive adsorbates which can cause surface reconstruction. (See, e.g., Sections VII.D.1 and VII.D.3) In these cases the geometry of the

overlayer per se can be examined by using the *energy averaging method* introduced by Tucker and Duke³⁶⁶⁻³⁶⁸ or a variant thereof (e.g., a Patterson function analysis employing a data smoothing or sampling procedure³⁷⁸). The registry between the overlayer and the substrate always must be determined either by a dynamical model calculation or a version of the kinematical analyses described earlier in this section.³⁶⁸

The fundamental idea underlying the energy averaging method is the observation that in the limit of strong inelastic collision damping multiple scattering between the overlayer and the underlying substrate layers primarily redistributes the "kinematic" intensity as a function of incident beam energy within a given scattered beam rather than redistribute appreciable intensity from one beam to another. Consequently, Tucker and Duke proposed that by averaging out this fine structure in the dynamical intensities, $I_{hk}(E)$, over a range of energies $(E_0 + \Delta/2) \geq E \geq (E_0 - \Delta/2)$ ($\Delta \sim 80\text{eV}$) they could construct a set of quantities

$$M_{hk} = \int_{E_0 - \Delta/2}^{E_0 + \Delta/2} I_{hk}(E) dE \quad (158)$$

directly proportional to the average kinematical intensities

$$\bar{I}_{hk}^{\text{kin}} = \int_{E_0 - \Delta/2}^{E_0 + \Delta/2} I_{hk}^{\text{kin}}(E) dE \quad (159)$$

in which the kinematical intensities themselves are obtained from (154). If such a proportionality occurs, then the atomic structure of the overlayer itself can be extracted from a kinematical analysis of the M_{hk} .

Studies by Tucker and Duke³⁶⁶⁻³⁶⁸ and by Duke and Laramore³²⁶ have established two important characteristics of the method as applied to uniform overlayers on otherwise ideal single-crystal substrates. First, for an overlayer of lower symmetry than the substrate, the averaged intensities of the additional overlayer beams are essentially independent of either the geometry or the composition of the substrate. Second, if $\lambda_{ee} \lesssim 8 \text{ \AA}$, the M_{hk} are indeed proportional to the $\bar{I}_{hk}^{\text{kin}}$ to within about 10 to 25% for a wide variety of ion-core scattering factors. This accuracy is quite sufficient to define a four or five-level gray scale for the diffracted beams. Such a scale, in turn, can provide structure determinations to within $\Delta a \sim 0.1 \text{ \AA}$.³⁶⁸

A final aspect of the energy averaging method of interest to us is its application to analyze experimental ELEED data. Because of a lack of suitable data, only one system has been analyzed thus far—an oxygen $c(2 \times 8)$ structure on Rh(100). The results of Tucker and Duke's analysis³⁶⁸ of this case are summarized in Fig. 65. The value of 0.28 for the reliability index was obtained by optimizing the vertical position of the oxygen atom

COMPARISON OF OBSERVED AND CALCULATED STRUCTURE FACTORS
FOR C(2×8) OXYGEN STRUCTURE ON THE RHODIUM (100) SURFACE

OXYGENS AT (0,0), (1/7,0), (2/7,0) AND (3/7,0)												
OXYGEN AT (3/7,0) RAISED 0.35 Å												
(hk)	(00)	(20)	(40)	(60)	(80)	(11)	(31)	(51)	(71)	(02)	(22)	(42)
F _{OBS}	50	15	0	13	39	23	0	8	44	49	9	0
F _{CALC}	44	17	6	24	24	24	6	17	44	44	17	6

$$R = \frac{\sum |F_{OBS} - F_{CALC}|}{\sum F_{OBS}} = 0.28$$

Fig. 65. Comparison of observed and calculated structure factors for a c(2×8) oxygen structure on Rh(100) consisting of surface oxygens at (0,0), (1/7,0), (2/7,0), and (3/7,0) with the oxygen at (3/7,0) raised 0.35 Å. The experimental intensities are taken from photographic plates. (After Tucker and Duke.³⁶⁸)

at ($\frac{3}{7}$, 0). Since a value of $R \leq 0.5$ indicates a structure which is basically correct but needs refinement, it is clear that the energy averaging method constitutes a *practical* method of determining the unit-cell structure of the top layer of a solid. Obviously, a refined structure could be obtained in this particular case if a more accurate form factor for electron scattering from adsorbed oxygen and more extensive data were available. In addition, we still must rely on either a microscopic model calculation or a constant-momentum-transfer data averaging analysis in order to determine definitively the registry of this overlayer with the underlying Rh(100) substrate. Nevertheless Tucker and Duke's study of Rh(100)-c(2×8)-O constitutes the first example of the determination of the atomic geometry of an adsorbed overlayer from an analysis of observed ELEED intensities. As such, it illustrates both the practical consequences of the recent advances in the theory of ELEED (Parts IV and V) and the type of insight and results that can be extracted from measured intensities by using suitably refined data-reduction and kinematical concepts.

E. Structural Analysis for Disordered Surfaces

We recall from Sections VII.C.2 and VII.C.3 that structural disorder is common in both single-step and multistep surface topographies. So little work has been done for multistep topographies, however, that we do not pursue their discussion beyond that given in Section VII.C.3. Consequently, in this section we examine the literature on elastic low-energy

electron diffraction (ELEED) from either isolated disordered overlayers or from such overlayers situated on otherwise ideal periodic substrates (the *nonuniform overlayer model*, Section VII.C.1).

The predominant experimental evidence for disordered overlayer structures arises from studies of ELEED from adsorbate-covered surfaces as a function of the adsorbate coverage γ and/or the temperature T . In the first case, with increasing adsorbate coverage (at fixed temperature) the overlayer beams are observed to sharpen,^{340,352} elongate ("streak"),^{340,392-394} split,^{352,392,393} and/or broaden.³⁹⁵ In the second case, as the temperature increases (for fixed coverage) the overlayer beams may disappear entirely^{179,195,340,394} (order-disorder transitions) or may be transformed into those characteristic of another structure^{340,396} (order-order transitions). A complete dynamical theory of ELEED must describe the dependence of the diffracted intensities on the thermodynamic variables γ and T as well as on the beam and electronic parameters discussed in preceding sections.

With a single exception,³⁹⁷ all analyses of ELEED from disordered overlayers have been based on kinematical (i.e., Born approximation) analyses of the diffracted intensities.^{256,340,351-356,398} Even within this context two quite different types of description of the structure of disordered overlayers have been used. In a *statistical model*, the occupation probabilities of the various sites are specified a priori by means of empirical statistical distributions (e.g., of domain lengths^{256,356,398}). In a *statistical mechanical model*,^{354,355} a force law between the adsorbates is prescribed, and the site occupation probabilities are evaluated from equilibrium statistical mechanics. The relationship between these two types of models as used in the literature is by no means clear at the present time. In particular, the domain distributions postulated by Park and Houston^{256,356} are not consequences of simple statistical mechanical models embodying finite-range interactions between adsorbed species.^{354,355,397,398}

The problem of evaluating ELEED intensities from disordered overlayers closely resembles that of describing X-ray diffraction from solid-state alloys. Indeed, kinematical analyses of ELEED associated with order-disorder transitions in adsorbed overlayers^{179,351-356,398} are essentially identical to those of X-ray diffraction from disordered solids.³⁹⁹ An important qualitative result which emerges from these analyses is a classification scheme for models of lattice disorder. In the Born approximation description of electron diffraction from an isolated overlayer the ELEED intensities depend on only two statistical quantities which characterize the structure of the overlayer³⁵⁶: the average site occupancy function (i.e., the coverage)

$$f_0(\mathbf{R}, T) \equiv \langle e_{\mathbf{R}} \rangle_T \equiv \gamma \quad (160a)$$

and the average two-site autocorrelation function

$$f_1(\mathbf{R}, \mathbf{R}', T) \equiv \langle e_{\mathbf{R}} e_{\mathbf{R}+\mathbf{R}'} \rangle_T \quad (160b)$$

The position of a scatterer in the overlayer is designated by the vector \mathbf{R} , and e is an index which is unity if a site is occupied, and is zero otherwise.³⁹⁷ *Disorder of the first kind* is characterized by a two-site autocorrelation function that can be specified in terms of deviations from a periodic "average lattice." These deviations can be either *displacements* (as in lattice-vibration-induced disorder) or *substitutions* (as in homogeneous solid binary alloys). *Disorder of the second kind* is characterized by a two-site autocorrelation function that becomes constant as the distance between the two sites increases. Liquids, gases, and sputter-damaged surface layers⁴⁰⁰ are examples of this type of disorder. Houston and Park's concept³⁵⁶ of *disorder of the third kind*, characteristic of lattice gas domain models of adsorbed overlayers, is a special case of substitutional disorder of the first kind as defined in the literature on X-ray crystallography. These two types of disorder lead to rather different consequences in the calculated intensities as described by Guinier³⁹⁹ and Houston and Park.³⁵⁶

The only existing dynamical model of ELEED from disordered overlayers³⁹⁷ (on otherwise ideal single-crystal substrates) is based on an approximation method that renders the dynamical intensities dependent on the structure of the overlayer solely via the geometry of the substrate and the statistical functions specified in (160). It utilizes a lattice gas model formulation of the multiple-scattering analysis and, consequently, is suitable for the description of disorder of the first but not the second kind.

Thus far, no quantitative structure analyses have been constructed from model calculations embodying a disordered overlayer. Except for the work of Ertl and Küppers³⁵⁴ all of the theoretical analyses have been based on one-dimensional models of the adsorbed overlayer. They reveal that the qualitative features of the phenomena of beam splitting, beam broadening, beam streaking, and order-disorder transformations can be interpreted in terms of Born approximation calculations which incorporate statistical descriptions of surface disorder. Nevertheless, many puzzles remain,^{179,398} the resolutions of which await the description of more complete sets of intensity data by multiple-scattering theories.³⁹⁷

F. Synopsis

We have seen that the principal application envisaged for elastic low-energy electron diffraction (ELEED) is the determination of the atomic geometry of the uppermost few layers of a single-crystal solid. This anticipation is based on measurements of marked changes in the intensity

pattern upon the adsorption of foreign species. Such observations date from the work of Davisson and Germer¹⁶ in 1927, and have proliferated during the past two decades.^{2-5, 340-344} From measurements of the intensity patterns alone, however, one can infer only the space group symmetry for translations along a planar surface. Determinations of the actual positions of the atomic species in either the adsorbed layers or the substrate have been delayed over four decades by the absence of a reliable theory of ELEED intensities and a suitable standard of experimental surface characterization.

Modern theoretical work on ELEED has eliminated uncertainties in the theory per se as a major source of delay in the applications of ELEED to surface crystallography. Moreover, we found in Section VII.D.3 that microscopic model calculations currently can be utilized to determine to within $\Delta a \sim 0.1$ Å the atomic geometry of well-characterized clean surfaces and overlayer structures which contain four or less atoms per unit cell in each layer of the selvage. From Section VII.D.4 we see that a variety of data reduction methods have been proposed to examine larger structures or to provide a simpler, more rapid analysis of the smaller ones. Such techniques directly or indirectly rely on the hypothesis that either the observed ELEED intensities or suitable averages thereof can be described by the Born approximation. Physical restrictions which render this assumption incompatible with the requirement of surface sensitivity may, however, limit the applicability of these methods in practice.

Perhaps the most serious deficiencies of structure determinations based on the analysis of ELEED intensities stem from an ignorance of surface topography. Existing model calculations usually assume the surface to be planar and free of defects. The occurrence of steps on clean surfaces can invalidate this hypothesis, and the presence of domains in adsorbed overlayers is a well-known phenomenon. A proper treatment of the consequences of such defects requires both refinement of the existing dynamical models and improvement in the current experimental techniques for surface characterization.

The overriding limitation on the use of both the microscopic model and data reduction methods, however, has been a lack of ELEED intensity data suitable for structure analysis. An assessment of the severity of the problems associated with both surface defects and fundamental uncertainties in the electron-solid force law awaits the accumulation of experience on model systems. Given the current widespread availability of computer programs for intensity calculations and the apparent adequacy of simple model force laws for such calculations, workers in almost any laboratory with a modern electronic computer can attempt their own structure determinations. Consequently, it seems reasonable to anticipate that in the

near future suitable intensity data will be obtained for various clean surface and overlayer systems. From the results of the analyses of such data there will emerge both surface structures and refinements to the methodologies for the determination of these structures.

VIII. DISPERSION RELATIONS OF ELECTRONIC SURFACE EXCITATIONS VIA INELASTIC LOW-ENERGY ELECTRON DIFFRACTION

A. Determination of Surface Excitation Dispersion

1. Nature of the Problem

We found in Section II.F that a variety of experimental techniques are useful for the characterization of the electronic structure of solid surfaces. Of these, however, inelastic low-energy electron diffraction (ILEED) currently permits the most quantitative analysis of observed spectra by virtue of the theory described in Sections VI.A to VI.C. Consequently, in this part of the review we indicate the nature and results of applications of this theory to extract the dispersion and damping of surface branches of the collective excitation spectra of crystalline solids from measured ILEED intensities.

Two major difficulties are encountered in any attempt to extract excitation dispersion relations [see, e.g., (142)] from measured ILEED intensities: those of uniqueness and internal consistency. The former arises because many dispersion relations may describe a small data base of ILEED intensities such as those associated with one of the elastic scattering resonances shown in Fig. 46. The latter occurs because the dispersion relations extracted from one of these sets of ILEED data may not agree with those obtained from a comparable set associated with another elastic low-energy electron diffraction (ELEED) resonance. Therefore any procedure designed to determine excitation dispersion relations must be constructed in such a fashion to display explicitly both the uncertainties in and the internal consistency of an analysis of a particular block of ILEED intensity data.

For any given values of the incident beam variables (E, θ, ψ) (see, e.g., Section III.A) the dispersion relations of the collective excitations stimulated by the inelastic scattering of the incident electrons in principle can be obtained by analysis of the differential inelastic scattering cross-sections as functions of the exit beam variables ($w = E - E', \theta', \psi' \equiv \psi + \pi$). We found in Section VI.B, however, that any such analysis embodying the two-step model should be based on a consideration only of the observed loss profiles (variable w , fixed θ', ψ'). Therefore we examine the loss profiles for each set of incident beam parameters (E, θ, ψ) individually and expect each

such examination to lead to a family of dispersion relations specified by the values of the parameters A_i , B_i , C_i , and D_i in (141) and (142) (see Section VI.A).

For the purpose of determining the dispersion relation describing a particular class of surface excitations, we must adopt a priori a model of the dispersion and damping of any other excitations whose maxima in the loss profiles overlap substantially those under consideration. Thus, it is evident from Figs. 42, 44, and 46 that in the case of aluminum a description of bulk plasmon dispersion and damping is implicitly required as an input to an analysis of surface plasmons. Consequently, the values of the A_i and B_i in (141) are obtained from fast (i.e., kiloelectron volt) electron transmission experiments on thin films as indicated below (142) and described by Bagchi and Duke.²¹²

Having eliminated all of the other unknowns in the model (i.e., the A_i and B_i in the Al example), we next must discuss the presentation of the range of surface plasmon dispersion relations (i.e., values of C_i and D_i) consistent with the ILEED data associated with a prescribed set of incident beam variables (E, θ, ψ). Data analyses are often insensitive to the value of D_2 in (142b), so Duke et al.¹³ arbitrarily set $D_2 \equiv 0$ and regarded the surface plasmon dispersion relation as a function of the five parameters ω_s , C_1 , C_2 , Γ_s , and D_1 . These quantities are determined by comparing calculated and observed values of the loss energy, w , at which peaks occur in the loss profile.

Given a grid of loss energies, $w_{l+1} = w_l + \delta w$, and the associated statistical errors $\Delta I(w_l)$ in the ILEED intensities $I(w_l)$, the peak of the loss profile is located by passing a smooth curve $I(w)$ through the data points. The surface excitation maxima in the loss profiles are regarded as lying within the loss energy interval $(w_p - w_e, w_p + w_e)$ where w_p is the loss energy at which the smooth curve exhibits its peak and w_e is defined by $I(w_p \pm w_e) = I(w_p) - \Delta I(w_p)$. Stated in words, $2w_e$ is the range of loss energies over which deviations in the loss profile from its maximum value are less than the statistical uncertainty of the data point nearest the maximum value itself. Typically, $w_e \lesssim 2\delta w$.^{12, 13, 337}

The definition of w_e permits us to define precisely the circumstances in which two surface excitation dispersion relations provide equivalent descriptions of a set of loss profile data. A given dispersion relation is said to describe the loss profiles associated with prescribed incident beam parameters (E, θ, ψ) if and only if the experimental (w_p) and theoretical (w_p') energies of the peaks in the loss profiles satisfy

$$|w_p(\theta') - w_p'(\theta'; \omega_s, C_1, C_2, \Gamma_s, D_1)| \leq w_e \quad (161)$$

for all values of θ' for which these peaks are clearly defined. Therefore all descriptions of the loss profiles for prescribed (E, θ, ψ) values lie in a volume, called the *region of ambiguity*, of a five-dimensional parameter space spanned by the variables ω_s , C_1 , C_2 , Γ_s , and D_1 .

In order to construct a practical data display, Duke et al.¹³ reduced the number of independent parameters from five to two. The value of $\hbar\omega_s$ usually is defined to within ± 0.2 eV by an analysis of the loss profiles for which $\theta' \cong \theta$. Moreover, the values of C_1 and C_2 are relatively insensitive to those of Γ_s and D_1 provided D_1 (measured in units of eVÅ) is less than Γ_s . Therefore calculations of the regions of ambiguity are presented as two-dimension projections in the C_1 - C_2 plane for fixed values of $\hbar\omega_s$, Γ_s , and D_1 . An example of such a projection is shown in Fig. 66 for $(E=60$ eV, $\theta=15^\circ$, $\psi=60^\circ)$ on Al(111).¹² The construction of this projection is based on analyses of loss profiles like those illustrated in Fig. 67. Typical angular profiles predicted by the same analysis used to construct Fig. 67 are presented in Fig. 68 in order to indicate the extent of compatibility between these two types of data display.

Summarizing, Figs. 67 and 68 reveal clearly that a variety of quite different surface excitation dispersion relations can provide comparable descriptions of observed ILEED intensities for fixed incident beam parameters (E, θ, ψ) . In order to characterize this result quantitatively,

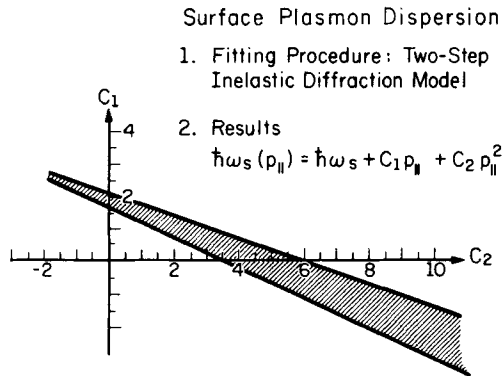


Fig. 66. Region of ambiguity in the surface plasmon dispersion relation of Al(111). Any dispersion relation whose coefficients lie in the shaded region yields a good fit between the theoretical and observed loss and angular profiles as described in association with inequality (161) in the text. The calculations were performed using the two-step model with four phase shifts derived from the Laramore-Duke-Snow APW potential, for the (00) beam of electrons with an inner potential $V_0 = 14.7$ eV, mean free path $\lambda_{ee} = 6$ Å, and damping $\Gamma_s = 1.4 + 0.74p_{\parallel}$. The theoretical loss and angular profiles were fitted to experimental ones for incident energy $E = 60$ eV with $\theta = 15^\circ$ and $\psi = 60^\circ$. (After Duke and Landman.¹²)

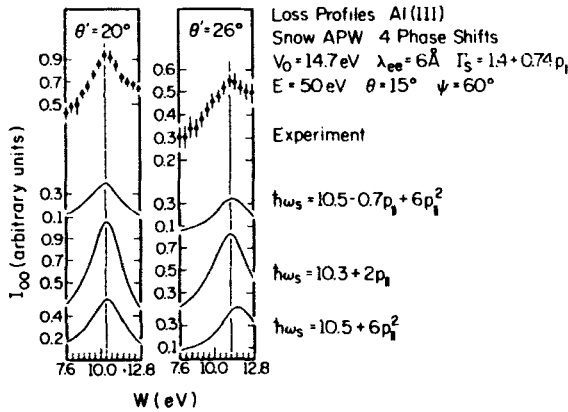


Fig. 67. Comparison with Porteus's data on Al(111) of supersonic loss profiles associated with three surface plasmon dispersion relations all of which are compatible with the data. The beam parameters and dynamical parameters used in the (two-step) model calculations are indicated in the figure. The loss energy grid is $d\bar{w} = 400 \text{ meV}$. (After Duke and Landman.¹²)

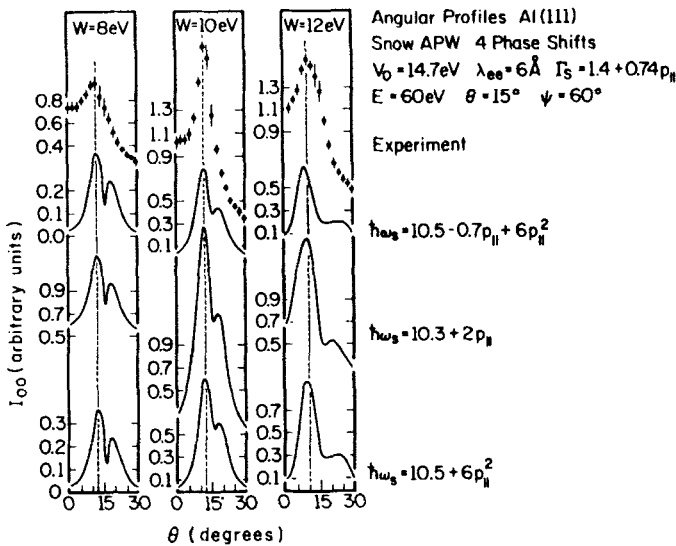


Fig. 68. Comparison with Porteus's data on Al(111) of angular profiles associated with three surface plasmon dispersion relations all of which are compatible with the data. The parameters used in the model calculations are noted in the figure. The two-step model provided the basis for these calculations. The angular profile grid is $d\theta = 2^\circ$. The incident beam parameters are given in the figure. (After Duke and Landman.¹²)

Duke et al.^{12,13} introduced the concept of a region of ambiguity which is that volume of the parameter space associated with the excitation dispersion relations in which the observed and calculated maxima in the loss profiles correspond as indicated by the inequality (161). For practical purposes, one can show at best two-dimensional projections of this region. The most useful such projection seems to be the one in the C_1 - C_2 plane [see (142)] like that shown in Fig. 66.

2. Selection of the Level of Analysis

Once we recognize that within the context of a given theoretical model many excitation dispersion relations are consistent with a given body of measured ILEED intensities, we must inquire into the nature of the model used to predict the "theoretical" intensities. In particular, how detailed must this model be? Three proposals have appeared in the literature: (1) the conservation laws alone are enough^{235,238,401} (the conservation law model), (2) the process must be described by a model in which it is considered to occur in the two steps of kinematical elastic diffraction either before (DL) or after (LD) the loss process (the two-step model),^{12,13,212,233,332-337} and (3) a description must be given of the multiple elastic scattering which occurs both before and after loss^{12,252,336} (the "dynamical" model). The greater the accuracy which we require in the determination of $\hbar\omega_s(\mathbf{p}_{\parallel})$, the more refined the models which we must use in the analysis.

In order to determine the C_i in (142a) to an accuracy of 25% or better, it is necessary to analyze the ILEED intensities using an energy-loss scale of $50 \text{ meV} \leq \delta w \leq 100 \text{ meV}$ and an exit angle scale of $\delta\theta' \sim 1^\circ$.¹² The conservation law model is inadequate to analyze data with this precision because variations in the elastic scattering cross-sections cause motion of the ILEED resonance peaks on a scale of $\Delta w \sim 100$ to 200 meV , $\Delta\theta' \sim 1$ to 2° for typical surface excitation dispersion relations.¹² Consequently, the use of the microscopic two-step model is *necessary* in order to achieve the level of precision implied by a $\delta w \sim 50 \text{ meV}$, $\delta\theta' \sim 1^\circ$ grid of distinguishable intensity data points.

Its use also appears to be *sufficient* to attain this precision. Comparisons^{12,336} of the predictions of the dynamical model with those of the two-step model (in the case of isotropic electron-ion-core scattering) reveal that the values of w at which surface excitation peaks occur in the ILEED intensities (all other parameters, E , θ , θ' , ψ , ψ' , remaining fixed) are identical to within $\Delta w = 50 \text{ meV}$. This close correspondence between the two-step and dynamical predictions of surface excitation ILEED intensities occurs, however, only for the loss profile mode of data presentation. Therefore the use of the two-step model is sufficient to achieve a precision

of $\delta w \sim 50$ meV, $\delta\theta' \sim 1^\circ$ only if the analysis is confined to locating the peak positions in the loss profiles. Moreover, it does not appear sensible to improve the precision further. Uncertainties in the elastic (Part V) and inelastic^{30,212} electron-solid interactions, and instrumental limitations (e.g., the absolute accuracy of θ' and the stability of the power supply) create an intrinsic imprecision of this order of magnitude in the measurements and their analysis by any model.

In summary, several levels of model description of ILEED intensities have been proposed for the determination of surface excitation dispersion. For a "first-try" preliminary analysis, direct use of the conservation laws [(60)] suffices to describe the energies of maxima in the loss profiles. This procedure, however, introduces spurious uncertainties into the resulting dispersion relation because of the dependence on the elastic diffraction conditions of maxima in the loss profiles. A more accurate analysis of surface excitation dispersion as well as an evaluation of the damping of such excitations is provided by the two-step model. Refinement of the analysis beyond the two-step model seems unrewarding because of both instrumental and physical uncertainties.

3. Analytical Procedure

Having established the two-step model as a suitable basis for a determination of surface excitation dispersion, we conclude our discussion of this topic by reviewing the data analysis procedure developed by Duke and co-workers.^{12,13,212,337} They decompose the analysis into five steps. First, the data to be analyzed are selected. Second, given these data the incoherent inelastic background scattering is subtracted from the measured intensities to obtain the diffracted intensities. Third, a preliminary estimate of the surface plasmon damping is performed. Fourth, using this estimate the range of surface plasmon dispersion consistent with the data is determined. Fifth and finally, the third and fourth steps are iterated in order to ensure that the damping and dispersion are internally consistent.

Turning to the first topic, we must decide what measurements are to be taken and analyzed. This is an important task because the inelastic differential electron-solid cross-sections are functions of six variables ($E, \theta, \psi, E' = E - w, \theta', \psi'$). Our problem is to decide what values of $E, \theta, \psi = \psi' - \pi, w$, and θ' to use in the analysis.

The values of the incident beam parameters (E, θ, ψ) for which we wish to analyze ILEED data are selected by examining the elastic low-energy electron diffraction intensities. If the incident angles are held fixed and the energy is varied, prominent peaks appear in the resulting "intensity profiles" or IV curves. Such maxima are caused by elastic scattering from the substrate (Parts III and V). As described in Section VI.A, this scattering

also generates related maxima in the ILEED intensities because of the "two-step" nature of the inelastic diffraction process. Duke et al.'s analysis of surface excitation dispersion is based on a consideration of the ILEED intensities in the vicinity of these resonant maxima. Therefore they select the values of the incident beam parameters (i.e., E, θ, ψ) by requiring that these parameters be associated with a prominent peak in the ELEED intensity profile. The analysis proceeds by first selecting values of the real inner potential V_0 and inelastic collision damping length λ_{ee} in order to describe the elastic intensities in the vicinity of a prominent resonant maximum. The phase shifts describing the elastic electron-ion-core scattering are taken from a plausible ion-core potential. In Duke and Landman's analysis of Al(111) they used the potential that was constructed by Snow.³¹⁷ The resulting parametrization of the ELEED data of Porteus and Faith is shown in Fig. 69.

Given the choice of incident beam parameters, we next must select the range of exit beam parameters to be studied. Duke et al. utilized both angular and loss profiles for incident beam parameters (E_B, θ, ψ) and $(E_B \pm 10, \theta, \psi)$ where the symbol (E_B, θ, ψ) designates the incident beam energies and angles which characterize a prominent resonance in the (elastic) intensity profile. (See, e.g., Fig. 69.) The angular profiles are used to determine the incoherent "background" inelastic scattering intensities to be subtracted from the coherent inelastic diffraction intensities. This background is due to the deviations of the surface geometry from that of an ideal single-crystal plane. Its subtraction is described by (143) in Section VI.C and is illustrated in Fig. 45. Since the background is taken to be independent of w , it evidently exerts no influence on the values of w at which peaks occur in the loss profiles. Only loss profile data are used subsequently in the analysis for the reasons discussed in the preceding subsection.

The third step in the analysis consists of estimating the plasmon damping prior to the precision determination of its dispersion. The dispersion relation is parametrized by the form (Section VI.A)

$$\hbar\omega_s(p_{\parallel}) = \hbar\omega_s + C_1 p_{\parallel} + C_2 p_{\parallel}^2 \quad (142a)$$

$$\Gamma_s(p_{\parallel}) = \Gamma_s + D_1 p_{\parallel} \quad (142b)$$

Energies are measured in electron volts and momenta in reciprocal angstroms. The parameter Γ_s is obtained by analyzing the loss profile line shapes for values of θ' such that $p_{\parallel} \cong 0$. The quantity D_1 is determined by examining the dependence on θ' of the width of the excitations' maxima in the loss profile. An example of the evaluation of Γ_s and D_1 is indicated in Fig. 44. In it we see the loss profiles near $p_{\parallel} = 0$ (i.e., $\theta' = 16^\circ$) and at

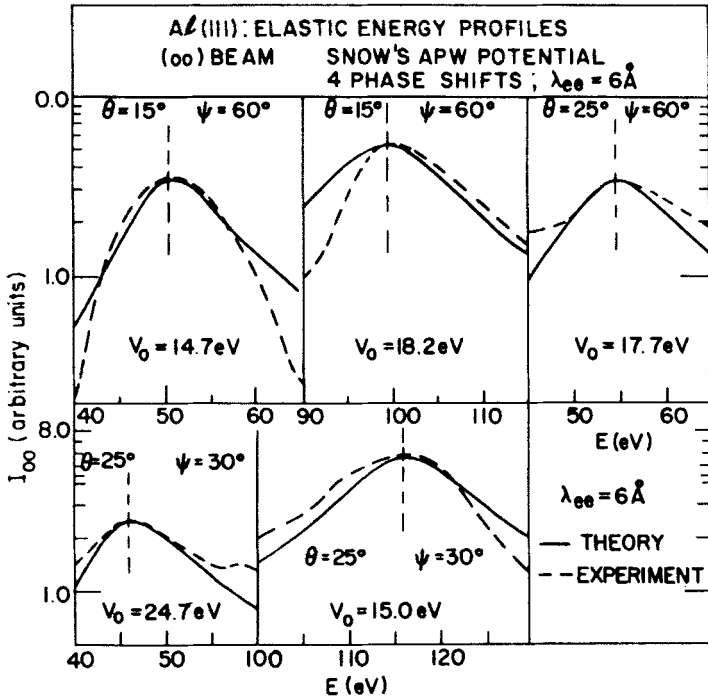


Fig. 69. Elastic intensity profiles for the (00) beam of electrons scattered from an Al(111) surface. Experimental (dashed) and theoretical (solid) kinematical curves for three sets of (θ, ψ) angles are shown. The calculations were performed using four phase shifts, $l < 3$, derived from Snow's APW potential and the beam parameters indicated in the figure. The values of the inner potential (V_0) leading to alignment of experimental and kinematical peaks' positions also are indicated in the figure. Vertical dashed lines were drawn to guide the eye in locating the positions of the maxima. A complete description of the theoretical model and its associated parameters may be found in Ref. 337. The value $\psi = 60^\circ$ corresponds to a $\langle 11\bar{2} \rangle$ azimuth and that of $\psi = 30^\circ$ to a $\langle 11\bar{0} \rangle$ azimuth. (After Duke and Landman.³³⁷)

extremal values of θ' (i.e., 8° and 24°) for which good data occur. Two important results are illustrated by this figure. First, the surface plasmon damping $\Gamma_s = 1.85$ eV and $D_1 = 3$ eVÅ is consistent with the observed loss profiles for two forms of the real part of the plasmon energy, $\hbar\omega_s(p_{\parallel})$, which are representative of the range of possibilities resulting from the complete data analysis.¹³ Second, we find that the detailed loss profile line shape depends on $\hbar\omega_s(p_{\parallel})$ as well as on $\Gamma_s(p_{\parallel})$. Therefore the two cannot be determined independently and hence the necessity for the fifth step (i.e., the self-consistency loop) in the analytical procedure. It is the failure of a given plasmon damping to be completely consistent with a range of

plasmon dispersions which is the determining factor in estimates of the uncertainties in Γ_s and D_1 .

The fourth step in the analysis consists of the evaluation of the remaining three parameters in the dispersion relation [ω_s , C_1 , and C_2 in (142a)] given initial estimates of Γ_s and D_1 . This evaluation proceeds in two stages. First, for each of the values of (E_B, θ, ψ) and $(E_B \pm 10 \text{ eV}, \theta, \psi)$, the loss profiles are analyzed to determine the individual C_1 - C_2 plane projections of the region of ambiguity. This study is carried out in accordance with the inequality (161) as discussed in Section VIII.A.1. At its completion, one obtains a plot like that shown in Fig. 66 for each set of (E, θ, ψ) values. Second, these plots are tested for internal consistency. They are internally consistent if and only if there exists a "region of overlap" in the C_1 - C_2 plane in which all the data are consistent with the same surface plasmon dispersion relation. Precisely speaking, this region is the union of all of the individual regions of ambiguity for the various values of (E, θ, ψ) .

The fifth and final step in the analytical procedure is the repetition of the fourth step for various values of the surface excitation damping. Thus, in principle, a complete map of the region of ambiguity for each value of (E, θ, ψ) may be obtained. From such maps, we could visualize constructing the union of these regions of ambiguity for the various values of (E, θ, ψ) utilized in the analysis. In practice^{13,337} a simpler procedure is employed in which loss profiles associated with one or two values of (E, θ, ψ) are evaluated using various values of Γ_s and D_1 and a compromise choice of these parameters is selected for use in the study of the loss profiles for other values of (E, θ, ψ) . Then at the conclusion of the calculation, the line shapes as well as peak energies of the loss profiles are examined to ensure that the "compromise" values of Γ_s and D_1 are, in fact, consistent with the observed ILEED intensities for values of C_1 , C_2 , and $\hbar\omega_s$ in the final composite region of ambiguity. The application of this procedure in an individual case is described in the following section.

B. Surface Plasmon Dispersion: Al(111)

Thus far the only detailed application of the analytical procedure proposed in the preceding section has been an analysis by Duke and Landman^{13,337} of inelastic low-energy electron diffraction (ILEED) intensity data for Al(111) taken by Porteus.^{13,339} Indeed, although it had been proposed prior to this application,¹² the procedure was refined during the course of the Al(111) analysis and doubtless will be improved still further as additional applications are attempted.

Following the logic outlined in Section VIII.A.3, Duke and Landman selected for analysis the eight independent sets of loss profile data (for various values of θ') indicated in Table IV. The regions of ambiguity

TABLE IV

Incident Beam Parameters (E, θ, ψ) and Loss Energy Grid Size (δw) Characteristic of the Eight Sets of Loss Profiles as Functionals of θ' Which Were Used in Duke and Landman's Analysis of the ILEED Data on Al(111) taken by Porteus and Faith³³⁹ (After Duke and Landman³³⁷)

E (eV)	θ (deg.)	ψ (deg.)	δw (eV)
50	15	60	0.4
60	15	60	0.4
60	15	60	0.05
110	15	60	0.4
55	25	60	0.4
56	25	30	0.4
56 ^a	25	30	0.05
115	25	30	0.4

^aThe statistical scatter in these data precluded their providing additional accuracy over corresponding analyses of the $\delta w = 0.4$ eV data taken using the same incident beam parameters, except that $C_1 < 0$ is clearly incompatible with these fine-grid data.

obtained from their analysis of each of these sets of data individually are shown in Figs. 70 to 73. The only region of the C_1 - C_2 plane in which the regions of ambiguity associated with all of these analyses overlap is that near $C_1 \sim 2$ to 3 eV and $C_2 \sim 0$. There is no area of complete overlap because the (55 eV, 25°, 60°) region is mutually exclusive with that associated with (56 eV, 25°, 30°). A closer examination of the data, however, revealed several difficulties with those associated with the (55 eV, 25°, 60°) incident beam parameters.^{337, 387} Thus Duke and Landman argued that the results shown in Fig. 72 could be disregarded in the final determination of the surface plasmon dispersion relation.

The final results given by Duke and Landman for the surface plasmon dispersion and damping on Al(111) films are

$$\hbar\omega_s(p_{\parallel}) = 10.5(\pm 0.1) + 2(\pm 1)p_{\parallel} + 0(+2)p_{\parallel}^2 \quad (162a)$$

$$\Gamma_s(p_{\parallel}) = 1.85(\pm 0.5) + 3(\pm 2)p_{\parallel} \quad (162b)$$

in which energies are measured in electron volts and momenta in reciprocal angstroms.

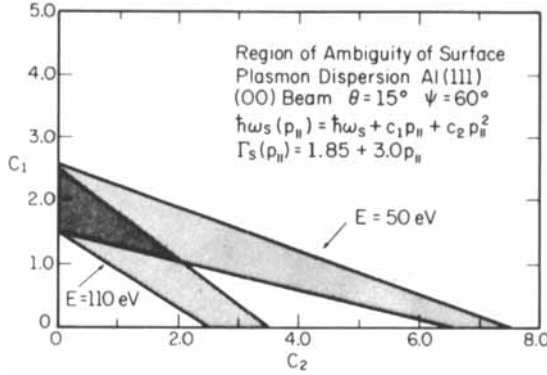


Fig. 70. Regions of ambiguity in the surface plasmon dispersion relation of Al(111) associated with two distinct resonances in the ELEED intensities. Any dispersion relation whose coefficients lie in the shaded regions yields a good theoretical description of the observed loss profiles as defined by inequality (161) in the text. The calculations were performed using the two-step model with four phase shifts derived from Snow's APW potential for the (00) beam of electrons with inner potentials $V_0 = 14.7$ eV for the $E = 50$ eV analysis and $V_0 = 18.2$ eV for the $E = 110$ eV analysis, mean free path $\lambda_{ee} = 6$ Å, and damping $\Gamma_s = 1.85 + 3.0p_{||}$. The loss profiles examined in the analysis were obtained for incident energies $E = 50$ and 110 eV with $\theta = 15^\circ$ and $\psi = 60^\circ$. The grid sizes in the loss profiles used to construct the regions of ambiguity shown in this figure are $\delta\omega = 400$ meV and $\delta\theta' = 2^\circ$. The dark shaded zone resulting from the intersection of the two regions of ambiguity defines a region in which both analyses yield internally consistent results. Each of the two individual regions of ambiguity extends to negative values of $C_1 \approx -1$, although these extensions are not shown in the figure. (After Duke and Landman.³³⁷)

The surface plasmon damping, (162b), is subject to large errors for two reasons. Fluctuations in the loss profiles when $|\theta' - \theta| \gtrsim 6^\circ$ for the various values of (E, θ, ψ) are the primary source of the uncertainties in the term linear in $p_{||}$. The erratic behavior exhibited by these profiles for θ' greater than 6 to 7° away from the specular direction precludes an accurate determination of D_1 in (142b). The origin of the uncertainty in the value of Γ_s is illustrated by Fig. 44: The shape of the maxima in the loss profile is influenced substantially by the dispersion as well as damping of the surface plasmons. Consequently, uncertainties in C_1 and C_2 are inevitably associated with similar ones in Γ_s and D_1 .

The uncertainties in the surface plasmon dispersion, (162a), are obtained directly from Figs. 70 to 73 as described by Duke and Landman.³³⁷ The values quoted in (162a) are upper limits on the errors actually expected because they are based on treating the uncertainties in C_1 and C_2 as statistically independent (when, in fact, they are strongly correlated²¹²). Nevertheless, Figs. 70 to 73 and (162) illustrate quite adequately the

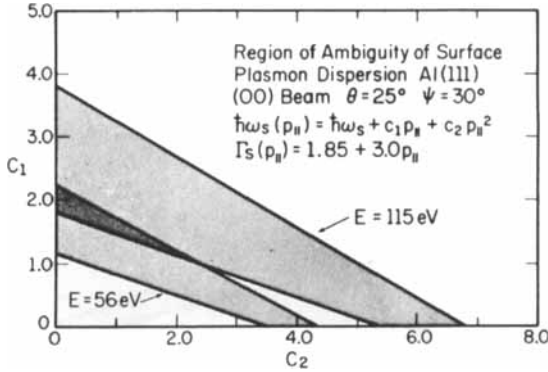


Fig. 71. Regions of ambiguity in the surface plasmon dispersion relation of Al(111) associated with two distinct resonances in the ELED intensities. The model parameters are those described in the caption to Fig. 70, but using $V_0 = 24.7$ eV for the $E = 56$ eV analysis and $V_0 = 15.0$ eV for the $E = 115$ eV analysis. The loss profiles of the (00) beam for incident electron energies of $E = 56$ and 115 eV with $\theta = 25^\circ$ and $\psi = 30^\circ$ were examined in the analysis. (After Duke and Landman.³³⁷)

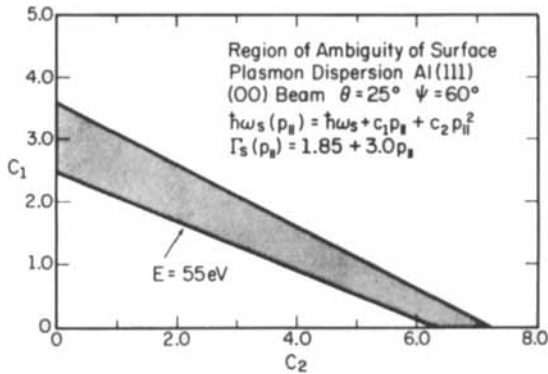


Fig. 72. Regions of ambiguity in the surface plasmon dispersion relation of Al(111). The model parameters are those described in the caption to Fig. 70 but using $V_0 = 17.7$ eV. The loss profiles of the (00) beam for incident electron energies of $E = 55$ eV with $\theta = 25^\circ$ and $\psi = 60^\circ$ were examined in the analysis. (After Duke and Landman.³³⁷)

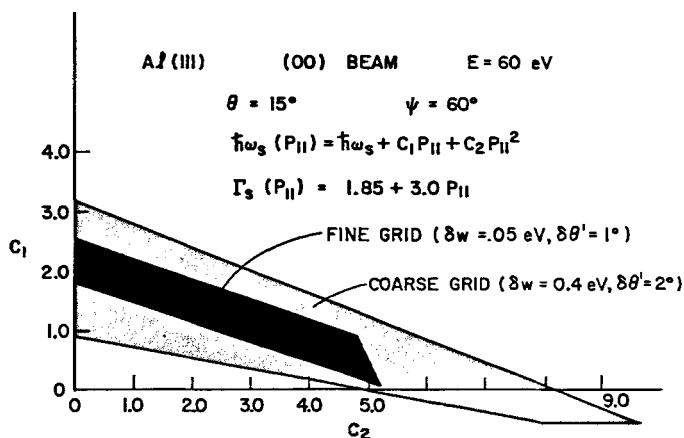


Fig. 73. Regions of ambiguity in the surface plasmon dispersion for the (00) beam of electrons scattered from Al(111). The two regions of ambiguity were determined by analyzing the coarse ($\delta w = 400$ meV, $\delta\theta' = 2^\circ$) and fine ($\delta w = 50$ meV, $\delta\theta' = 1^\circ$) grid presentations of the ILEED loss profiles associated with the ELEED resonances at $E_B = 50.5$ eV, $\theta = 15^\circ$, $\psi = 60^\circ$. The calculations were performed using the two-step model with four phase shifts. The model parameters are those given in the caption to Fig. 70 except that $V_0 = 14.7$ eV is used for the inner potential. The loss profiles examined in the analysis were obtained for an incident energy $E = 60$ eV with $\theta = 15^\circ$ and $\psi = 60^\circ$. A considerable reduction in the uncertainties in the surface plasmon dispersion relation is achieved by superimposing the results of the coarse and fine-grid analysis resulting in the inner dark shaded region shown in the figure. (After Duke and Landman.³³⁷)

precision and accuracy which can be expected for surface excitation dispersion relations extracted from modern high-precision ILEED intensity data. Moreover, from Figs. 70 to 73 we see graphically the immense importance of basing any such extraction on the self-consistent description of a large data base.

Finally, an interesting feature of the resulting surface plasmon dispersion relation is the occurrence of substantial damping ($\Gamma_s \sim 1$ to 2 eV). Such rapid damping can be caused either by surface plasmon decay into interband particle-hole excitations,⁴⁰² by surface diffuseness on an atomic scale,⁴⁰³ or by both. Since the damping and dispersion of the surface plasmons are strongly correlated, the results given by (162) reveal immediately that simple specular reflection free electron models of surface plasmons^{30,402,403} are quite inadequate. In particular, the distance along the surface moved by a surface plasmon in its lifetime is approximately $d = C_1/\Gamma_s \sim 1$ Å. Thus we are led to the rather surprising concept that the

motion of surface plasmons parallel to the surface is more highly localized than the extent of these plasmons perpendicular to it. Indeed, if we take the range of 1 Å at face value we are forced to conclude that the range of these excitations is an atomic dimension. This result has immediate and important consequences like the limitation of the range of the nonlocality of the imaginary part of the electron-solid optical potential to atomic dimensions and the elimination of virtual surface plasmon creation as an important source of retarded long-range interactions between adsorbed species.

IX. EPILOGUE: PATTERNS OF THE FUTURE

This review constitutes an attempt to provide a broad perspective on the characterization of "planar" solid surfaces by scattering experiments. Because of the surface sensitivity, convenience, and generally nondestructive nature of electron scattering measurements, we have focused our attention on their analyses for the purpose of quantitative surface structure determination. Indeed, our major theme has been the apparent adequacy of modern mathematical models of electron-solid scattering for this purpose—an encouraging and important result which has been realized only in the past few years.

An equally significant recent occurrence is the development of a wide variety of surface-sensitive spectroscopic techniques and their combination within the same ultrahigh vacuum system. The combination of this trend toward a more comprehensive characterization of surfaces and the increasing skill in the preparation of well-characterized surfaces is introducing a new era in surface science analogous to that opened in solid-state physics by the purification of silicon and germanium in the late 1940s.⁴⁰⁴ Thus, for the first time, it has become possible to measure "simultaneously" and reproducibly enough different types of particle-solid cross-sections to determine the chemical, electronic, geometrical, and vibrational structure of carefully prepared surfaces of inorganic crystalline solids. This accomplishment in turn permits acquisition of the reproducible and interpretable data required to examine reaction processes under controlled conditions at these surfaces.

It is evident from the body of this review that systematic applications of modern theoretical analyses to interpret suitable comprehensive data are in their infancy. Nevertheless, such applications are no longer "just around the corner": They are upon us. Any group with access to modest electronic computing equipment can, using packaged programs, perform electronic

and geometrical structure analyses. Moreover, rather complete surface analytical instruments embodying electron, photon, and ion scattering facilities together with versatile low-temperature sample holders can be designed and purchased commercially for about \$100,000. A logical next step in the design of such instrumentation is the automation of the acquisition of the data and their processing in "real time" as the measurements are underway. With such facilities it might well become feasible to trace the individual steps in some of the simpler catalytic reactions. Even with existing instrumentation, however, the static aspects of these reactions can be studied by utilizing preprogrammed sequential doses of reactants incident on single-crystal surfaces.

As more laboratories become equipped to perform sophisticated, comprehensive surface characterizations, it seems reasonable to anticipate further advances in technique. Two trends which we have emphasized are the use of more measurements in the same vacuum chamber and the development of less destructive experimental methods for the study of fragile molecular and organic solids. Specifically, the increased use of photoemission measurements and of lower beam currents (and/or higher incident energies) in electron scattering experiments seems likely, as does considerably more extensive examination of the surfaces of both organic and inorganic insulators. The use of electron diffraction and core-level spectroscopic measurements to monitor, *in situ*, the fabrication of thin film structures is already a reality, and probably will become increasingly pervasive.

Finally, the theory of particle-solid scattering and emission, while understood in broad outline, is far from complete. Models of photoemission and Auger emission intensities have yet to reach the maturity of those of electron diffraction. Moreover, the construction of dynamical models of electron scattering from disordered overlayers has just begun. The development of these models requires not only further attention to the mathematical representation of the structure of such an overlayer but also a considerably more complete specification of the limitations on the analysis imposed by the characteristics of the measuring instrument. Both of these aspects of the developing theory are becoming increasingly significant as attention is turned from the nearly "ideal" low-index faces of solids to their high-index faces which contain "defects" in the form of ledges and kinks. These defects are widely suspected to be necessary participants in both surface-mediated catalysis and in the preparation or operation of "useful" insulator surfaces (e.g., in semiconductor passivation, epitaxial growth of heterojunctions, and xerographic charging). Therefore it is the further development and application of surface-sensitive

spectroscopies for the examination of such defects and their consequences which appears to be one of the most probable patterns of the future in high-vacuum surface science.

Acknowledgments

The author is greatly indebted to Ms. P. VanDeusen for splendid typing and to the Xerox art and photo services groups for preparation of the figures, both tasks being performed under severe time constraints. I also am indebted to G. E. Laramore and N. O. Lipari for permission to use their figures prior to publication. I would like to thank Drs. R. L. Park, D. L. Adams, and P. Nielson for educating me on many of the details of surface characterization instrumentation, Dr. Brian Theeten for providing the data on Ni(100)-c(2×2)-S discussed in Parts V and VII, and Dr. J. O. Porteus for his continuing collaboration in ILEED studies such as those discussed in Parts VI and VIII. Finally, many figures in this chapter are taken from the works of numerous friends and colleagues. The sources of these figures are acknowledged in their captions, and I am indebted to the authors and their publishers for the use thereof.

References

1. C. B. Duke and R. L. Park, *Phys. Today*, **25**, 23 (August 1972).
2. J. W. May, *Adv. Catal.*, **21**, 151 (1970).
3. P. J. Estrup and E. G. McRae, *Surf. Sci.*, **25**, 1 (1971).
4. G. A. Somorjai and H. H. Farrell, *Adv. Chem. Phys.*, **20**, 215 (1971).
5. E. N. Sickafus and H. P. Bonzel, *Prog. Surf. Membrane Sci.*, **4**, 115 (1971).
6. C. B. Duke, in *LEED: Surface Structures of Solids*, Vol. 2, M. Laznicka, Ed., Union of Czechoslovak Mathematicians and Physicists, Prague, 1972, pp. 125–291, 361–387.
7. G. E. Laramore, *J. Vac. Sci. Technol.*, **9**, 625 (1972).
8. C. B. Duke, in *LEED: Surface Structures of Solids*, Vol. 2, M. Laznicka, Ed., Union of Czechoslovak Mathematicians and Physicists, Prague, 1972, pp. 1–72.
9. C. B. Duke and G. E. Laramore, *Phys. Rev.*, **B2**, 4765 (1970).
10. G. E. Laramore and C. B. Duke, *Phys. Rev.*, **B2**, 4783 (1970).
11. C. B. Duke, in *LEED: Surface Structures of Solids*, Vol. 2, M. Laznicka, Ed., Union of Czechoslovak Mathematicians and Physicists, Prague, 1972, pp. 73–124.
12. C. B. Duke and U. Landman, *Phys. Rev.*, **B7**, 1368 (1973).
13. C. B. Duke, U. Landman, and J. O. Porteus, *J. Vac. Sci. Technol.*, **10**, 183 (1973).
14. M. Pessa, *J. Appl. Phys.*, **42**, 5831 (1971).
15. P. W. Palmberg, in *Electron Spectroscopy*, D. A. Shirley, Ed., North Holland, Amsterdam, 1972, pp. 835–859.
16. C. J. Davisson and L. H. Germer, *Phys. Rev.*, **30**, 705 (1927).
17. N. F. Mott and H. S. W. Massey, *The Theory of Atomic Collisions*, Clarendon Press, Oxford, 1965, Chapters 16–18.
18. M. R. H. Rudge, *Rev. Mod. Phys.*, **40**, 564 (1968).
19. C. B. Duke and C. W. Tucker, Jr., *Surf. Sci.*, **15**, 231 (1969).
20. J. F. Nicholas, *An Atlas of Models of Crystal Surfaces*, Gordon and Breach, New York, 1965.
21. C. B. Duke, *Ann. Rev. Mater. Sci.*, **1**, 165 (1971).
22. J. I. Pankove, *Optical Processes in Semiconductors*, Prentice-Hall, Englewood Cliffs, New Jersey, 1971, Chapter 3.
23. F. Wooten, *Optical Properties of Solids*, Academic Press, New York, 1972, Chapters 3 and 5.
24. C. B. Duke, *J. Vac. Sci. Technol.*, **6**, 152 (1969).

25. A. Many, Y. Goldstein, and N. B. Grover, *Semiconductor Surfaces*, North Holland, Amsterdam, 1965, Chapter 4.
26. J. N. Smith, Jr., and H. Saltsburg, in *Fundamentals of Gas Surface Interactions*, H. Saltsburg, J. N. Smith, Jr., and M. Rogers, Eds., Academic Press, New York, 1967, pp. 370-391.
27. G. Carter, *J. Vac. Sci. Technol.*, **7**, 31 (1970).
28. J. A. Davies, *J. Vac. Sci. Technol.*, **8**, 487 (1971).
29. C. B. Duke and C. W. Tucker, Jr., *Phys. Rev.*, **B3**, 3561 (1971).
30. P. J. Feibelman, C. B. Duke, and A. Bagchi, *Phys. Rev.*, **B5**, 2436 (1972).
31. F. S. Stone, *Adv. Catal.*, **13**, 40 (1962).
32. T. E. Madey and J. T. Yates, Jr., *J. Vac. Sci. Technol.*, **8**, 525 (1971).
33. R. Castaing and J. H. Hennequin, *Adv. Mass Spectry.*, **5**, 419 (1971).
34. G. C. Bond, *Catalysis by Metals*, Academic Press, New York, 1962, Chapters 1-3 and 21.
35. J. Pritchard, *J. Vac. Sci. Technol.*, **9**, 895 (1972).
36. B. Lang, R. W. Joyner, and G. A. Somorjai, *Surf. Sci.*, **30**, 454 (1972).
37. A. Many, Y. Goldstein, and N. B. Grover, *Semiconductor Surfaces*, North Holland, Amsterdam, 1965, Chapter 3.
38. R. Gomer, *Field Emission and Field Ionization*, Harvard University Press, Cambridge, 1961.
39. E. W. Müller and T. T. Tsong, *Field Ion Microscopy*, American Elsevier, New York, 1969.
40. R. D. Young, *Phys. Today*, **24**, 42 (November 1971).
41. E. Bauer, *J. Vac. Sci. Technol.*, **7**, 3 (1970).
42. D. W. Jepsen, P. M. Marcus, and F. Jona, *Phys. Rev.*, **B5**, 3933 (1972).
43. G. Capart, *Surf. Sci.*, **26**, 429 (1971).
44. S. Y. Tong and T. N. Rhodin, *Phys. Rev. Lett.*, **26**, 711 (1971).
45. J. B. Pendry, *J. Phys. C*, **4**, 2501 (1971).
46. G. E. Laramore, C. B. Duke, A. Bagchi, and A. B. Kunz, *Phys. Rev.*, **B4**, 2085 (1971).
47. C. B. Duke, N. O. Lipari, and U. Landman, *Phys. Rev.* **B8**, 2454 (1973).
48. K. Kambe, *Surf. Sci.*, **20**, 213 (1970).
49. M. Fink, M. R. Martin, and G. A. Somorjai, *Surf. Sci.*, **29**, 303 (1972).
50. H. Bethe, *Ann. Phys.*, **87**, 55 (1928).
51. P. M. Morse, *Phys. Rev.*, **35**, 1310 (1930).
52. J. B. Pendry, *J. Phys. C*, **2**, 2273 (1969).
53. V. Hoffstein and D. S. Boudreaux, *Phys. Rev.*, **B3**, 2447 (1971).
54. C. B. Duke and C. W. Tucker, Jr., *Phys. Rev. Lett.*, **23**, 1163 (1969).
55. J. C. Slater, *Phys. Rev.*, **51**, 840 (1937).
56. H. Yoshioka, *J. Phys. Soc. Japan*, **12**, 618 (1957).
57. J. Lander and J. Morrison, *J. Appl. Phys.*, **34**, 925 (1963).
58. W. Löt, *Astrophys. J. Suppl.*, **14**, 207 (1967).
59. H. Raether, *Springer Tracts in Modern Physics*, **38**, 84 (1965).
60. R. A. Ferrell, *Phys. Rev.*, **107**, 450 (1957).
61. E. H. S. Burhop, *The Auger Effect and Other Radiationless Transitions*, University Press, Cambridge, 1952.
62. R. W. Fink, R. C. Jopson, H. Mark, and C. D. Swift, *Rev. Mod. Phys.*, **38**, 513 (1966).
63. W. Bambynek, B. Craesmann, R. W. Fink, H. U. Freund, H. Mark, C. D. Swift, R. E. Price, and P. V. Rao, *Rev. Mod. Phys.*, **44**, 716 (1972).
64. W. Löt, *Z. Phys.*, **232**, 101 (1970).
65. R. L. Gerlach and A. R. Ducharme, *Phys. Rev. Lett.*, **27**, 290 (1971).
66. O. Hörnfeldt, A. Fahlman, and C. Nordling, *Ark. Fys.*, **23**, 155 (1962).

67. A. Fahlman, R. Nordberg, C. Nordling, and K. Siegbahn, *Z. Phys.*, **192**, 476 (1966).
68. A. Fahlman, K. Hamrin, G. Axelsson, C. Nordling, and K. Siegbahn, *Z. Phys.*, **192**, 484 (1966).
69. C. J. Powell and A. Mandl, *Phys. Rev. Lett.*, **29**, 1153 (1972).
70. C. J. Powell, *Appl. Phys. Lett.*, **20**, 335 (1972).
71. L. A. Harris, *J. Appl. Phys.*, **39**, 1419 (1968).
72. C. C. Chang, *Surf. Sci.*, **25**, 53 (1971).
73. T. E. Gallon and J. A. D. Matthew, *Rev. Phys. Technol.*, **3**, 31 (1972).
74. P. W. Palmberg, G. E. Riach, R. E. Weber, and N. C. Mac Donald, *Handbook of Auger Electron Spectroscopy*, Physical Electronic Industries, Edna, 1972.
75. U. Fano and J. W. Cooper, *Rev. Mod. Phys.*, **40**, 441 (1968).
76. K. Siegbahn, C. Nordling, A. Fahlman, R. Nordberg, K. Hamrin, J. Hedman, G. Johansson, T. Bergmark, S. E. Karlsson, I. Lindgren, and B. Lindberg, *ESCA, Atomic, Molecular, and Solid State Structure Studied by Means of Electron Spectroscopy*, Almqvist and Wiksells, Upsalla, 1967.
77. H. Curien, in *International Tables for X-Ray Crystallography*, K. Lonsdale, C. H. Macgillivray, and G. D. Rieck, Eds., Kynock Press, Birmingham, 1962, pp. 247–253.
78. E. Merzbacher, *Quantum Mechanics*, Wiley, New York, 1970, pp. 470–472.
79. R. D. Schmickley and R. H. Pratt, *Phys. Rev.*, **164**, 104 (1967).
80. M. Ya. Amus'ya, N. A. Cherepkov, and L. V. Chernysheva, *Zh. Eksp. Teor. Fiz.*, **60**, 160 (1971) [*Sov. Phys. JETP*, **33**, 90 (1971)].
81. D. J. Kennedy and S. T. Manson, *Phys. Rev.*, **A5**, 227 (1972).
82. C. G. Schull and E. O. Wollan, *Solid-State Phys.*, **2**, 137 (1956).
83. C. Kittel, *Quantum Theory of Solids*, Wiley, New York, 1963, Chapter 19.
84. H. Wise and B. J. Wood, *Adv. At. Mol. Phys.*, **3**, 291 (1967).
85. D. P. Smith, *Surf. Sci.*, **25**, 171 (1971).
86. M. A. Nicolet, J. W. Mayer, and I. V. Mitchell, *Science*, **177**, 841 (1972).
87. W. L. Hays, W. E. Rodgers, and E. L. Knuth, *J. Chem. Phys.*, **56**, 1652 (1972).
88. C. W. White, D. L. Simms, and N. H. Tolk, *Science*, **177**, 481 (1972).
89. I. Estermann and O. Stern, *Z. Phys.*, **61**, 95 (1930).
90. R. L. Palmer, D. R. O'Keefe, H. Saltsburg, and J. N. Smith, Jr., *J. Vac. Sci. Technol.*, **7**, 91 (1970).
91. W. H. Weinberg and R. P. Merrill, *J. Chem. Phys.*, **56**, 2893 (1972).
92. D. V. Tendulkar and R. E. Stickney, *Surf. Sci.*, **27**, 516 (1971).
93. N. F. Mott and H. S. W. Massey, *The Theory of Atomic Collisions*, Clarendon Press, Oxford, 1965, Chapter 19.
94. D. Raskin and P. Kusch, *Phys. Rev.*, **179**, 712 (1969).
95. F. O. Goodman, *Surf. Sci.*, **26**, 327 (1971).
96. F. O. Goodman, W. S. Liu, and N. Cabrera, *J. Chem. Phys.*, **57**, 2698 (1972).
97. H. D. Hagstrum, *Phys. Rev.*, **96**, 336 (1954).
98. H. D. Hagstrum, *Phys. Rev.*, **123**, 758 (1961).
99. C. W. White and N. H. Tolk, *Phys. Rev. Lett.*, **26**, 486 (1971).
100. R. G. Musket and W. Bauer, *Appl. Phys. Lett.*, **20**, 455 (1972).
101. H. D. Hagstrum, *J. Res. Natl. Bur. Stand.*, **74A**, 433 (1970).
102. H. D. Hagstrum, *Science*, **178**, 275 (1972).
103. R. L. Gerlach, *J. Vac. Sci. Technol.*, **8**, 599 (1971).
104. R. L. Park and J. E. Houston, *Adv. X-Ray Anal.*, **15**, 462 (1972).
105. E. W. Müller, J. A. Panitz, and S. B. McLane, *Rev. Sci. Instrum.*, **39**, 83 (1968).
106. H. E. Bishop and J. C. Riviere, *Appl. Phys. Lett.*, **16**, 21 (1970).
107. R. L. Gerlach, J. E. Houston, and R. L. Park, *Appl. Phys. Lett.*, **16**, 179 (1970).
108. W. P. Ellis and B. D. Campbell, *J. Appl. Phys.*, **41**, 1858 (1970).

109. R. L. Gerlach, in *Electron Spectroscopy*, D. A. Shirley, Ed., North Holland, Amsterdam, 1972, pp. 885-894.
110. J. P. Coad and J. C. Riviere, *Phys. Status Solidi (a)*, **7**, 571 (1971).
111. R. L. Park, J. E. Houston, and D. G. Schreiner, *Rev. Sci. Instrum.*, **41**, 1840 (1970).
112. R. L. Park and J. E. Houston, *Surf. Sci.*, **26**, 664 (1971).
113. J. E. Houston and R. L. Park, *J. Chem. Phys.*, **55**, 4601 (1971).
114. J. E. Houston and R. L. Park, *J. Vac. Sci. Technol.*, **9**, 579 (1972).
115. R. L. Park and J. E. Houston, *Phys. Rev.*, **B6**, 1073 (1972).
116. J. E. Houston and R. L. Park, in *Electron Spectroscopy*, D. A. Shirley, Ed., North Holland, Amsterdam, 1972, pp. 895-901.
117. P. F. Kane and G. B. Larrabee, *Ann. Rev. Mater. Sci.*, **2**, 33 (1972).
118. N. G. Nakhodkin and P. V. Mel'nik, *Fiz. Tverd. Tela*, **5**, 2441 (1963) [*Sov. Phys. Solid State*, **5**, 1779 (1964)].
119. N. G. Nakhodkin and P. V. Mel'nik, *Fiz. Tverd. Tela*, **10**, 1859 (1967) [*Sov. Phys. Solid State*, **10**, 1462 (1968)].
120. C. R. Brundle, *Surf. Sci.*, **27**, 681 (1971).
121. T. E. Gallon and J. A. D. Matthew, *J. Phys. D*, **5**, L69 (1972).
122. L. G. Parratt, *Rev. Sci. Instrum.*, **30**, 297 (1959).
123. T. E. Gallon, *J. Phys. D*, **5**, 822 (1972).
124. F. Meyer and J. J. Vrakking, *Surf. Sci.*, **33**, 271 (1972).
125. W. M. Mularie and W. T. Peria, *Surf. Sci.*, **26**, 125 (1971).
126. M. Suleman and E. B. Pattinson, *J. Phys. F*, **1**, L24 (1971).
127. L. H. Jenkins and M. F. Chung, *Surf. Sci.*, **33**, 159 (1972).
128. L. A. Harris, *Surf. Sci.*, **15**, 77 (1969).
129. H. E. Bishop and J. C. Riviere, *Surf. Sci.*, **17**, 446 (1969).
130. L. A. Harris, *Surf. Sci.*, **17**, 448 (1969).
131. R. E. Weber and W. T. Peria, *J. Appl. Phys.*, **38**, 4355 (1967).
132. R. E. Weber and A. L. Johnson, *J. Appl. Phys.*, **40**, 314 (1969).
133. M. Perdereau, *Surf. Sci.*, **24**, 239 (1971).
134. A. Fahlman, K. Hamrin, R. Nordberg, C. Nordling, and K. Siegbahn, *Phys. Lett.*, **20**, 159 (1966).
135. R. G. Albridge, K. Hamrin, G. Johansson, and A. Fahlman, *Z. Phys.*, **209**, 419 (1968).
136. T. W. Haas and J. T. Grant, *Appl. Phys. Lett.*, **16**, 172 (1970).
137. J. T. Grant and T. W. Haas, *Surf. Sci.*, **24**, 332 (1971).
138. J. P. Coad and J. C. Riviere, *Surf. Sci.*, **25**, 609 (1971).
139. R. J. Fortner and R. G. Musket, *Surf. Sci.*, **28**, 339 (1971).
140. T. W. Haas, J. T. Grant, and G. J. Dooley in *Adsorption-Desorption Phenomena*, F. Ricca, Ed., Academic Press, New York, 1972, pp. 359-368.
141. T. W. Haas, J. T. Grant, and G. J. Dooley, III, *J. Appl. Phys.*, **43**, 1853 (1972).
142. H. E. Bishop, J. C. Riviere, and J. P. Coad, *Surf. Sci.*, **24**, 1 (1971).
143. J. T. Grant and T. W. Haas, *Surf. Sci.*, **23**, 347 (1970).
144. B. A. Joyce and J. H. Neave, *Surf. Sci.*, **27**, 499 (1971).
145. D. T. Quinto and W. D. Robertson, *Surf. Sci.*, **27**, 645 (1971).
146. M. A. B. Whitaker, *J. Phys. C*, **5**, L102 (1972).
147. J. M. Baker and J. L. McNatt, *J. Vac. Sci. Technol.*, **9**, 972 (1972).
148. R. G. Musket, *J. Vac. Sci. Technol.*, **9**, 603 (1972).
149. R. G. Steinhardt, J. Hudis, and M. L. Perlman, in *Electron Spectroscopy*, D. A. Shirley, Ed., North Holland, Amsterdam, 1972, pp. 557-567.
150. Y. Baer, P. F. Heden, J. Hedman, M. Klasson, and C. Nordling, *Solid-State Commun.*, **8**, 1479 (1970).
151. T. A. Carlson, in *Electron Spectroscopy*, D. A. Shirley, Ed., North Holland, Amsterdam, 1972, pp. 53-77.

152. K. Siegbahn, D. Hammon, H. Fellner-Feldegg, and E. F. Barnett, *Science*, **176**, 245 (1972).
153. T. Robert, M. Bartel, and G. Offergeld, *Surf. Sci.*, **33**, 123 (1972).
154. D. J. Ball, T. M. Buck, D. MacNair, and G. H. Wheatly, *Surf. Sci.*, **30**, 69 (1972).
155. T. B. Sewell and M. Cohen, *Appl. Phys. Lett.*, **7**, 32 (1965).
156. D. F. Mitchell, G. W. Simmons, and K. R. Lawless, *Appl. Phys. Lett.*, **7**, 173 (1965).
157. G. W. Simmons, D. F. Mitchell, and K. R. Lawless, *Surf. Sci.*, **8**, 130 (1967).
158. P. B. Sewell and M. Cohen, *Appl. Phys. Lett.*, **11**, 298 (1967).
159. G. E. Hill, I. Marklund, J. Martinson, and B. J. Hopkins, *Surf. Sci.*, **24**, 435 (1971).
160. J. F. Menadue, *Acta Crystallogr. A*, **28**, 1 (1972).
161. A. E. Lee, *Phil. Mag.*, **25**, 291 (1972).
162. N. Cabrera, V. Celli, and R. Manson, *Phys. Rev. Lett.*, **22**, 346 (1969).
163. S. S. Fischer and J. R. Bledsoe, *J. Vac. Sci. Technol.*, **9**, 814 (1972).
164. R. B. Subbarao and D. R. Miller, *J. Vac. Sci. Technol.*, **9**, 808 (1972).
165. R. B. Subbarao and D. R. Miller, *J. Chem. Phys.*, **51**, 4679 (1969).
166. B. R. Williams, *J. Chem. Phys.*, **55**, 3220 (1971).
167. F. O. Goodman, *J. Vac. Sci. Technol.*, **9**, 812 (1972).
168. F. O. Goodman, *Surf. Sci.*, **30**, 1 (1972).
169. E. R. Jones, J. T. McKinney, and M. B. Webb, *Phys. Rev.*, **151**, 476 (1966).
170. R. M. Goodman, H. H. Farrell, and G. A. Somorjai, *J. Chem. Phys.*, **48**, 1046 (1968).
171. F. M. Propst and T. C. Piper, *J. Vac. Sci. Technol.*, **4**, 53 (1967).
172. H. Ibach, *J. Vac. Sci. Technol.*, **9**, 713 (1972).
173. H. Ibach, *Phys. Rev. Lett.*, **24**, 1416 (1970).
174. H. Ibach, *Phys. Rev. Lett.*, **27**, 253 (1971).
175. A. U. MacRae and L. H. Germer, *Phys. Rev. Lett.*, **8**, 489 (1962).
176. A. U. MacRae, *Surf. Sci.*, **2**, 522 (1964).
177. H. B. Lyon and G. A. Somorjai, *J. Chem. Phys.*, **44**, 3707 (1966).
178. J. M. Morabito, Jr., R. F. Steiger, and G. A. Somorjai, *Phys. Rev.*, **179**, 638 (1969).
179. P. J. Estrup, in *The Structure and Chemistry of Solid Surfaces*, G. A. Somorjai, Ed., Wiley, New York, 1969, Chapter 19.
180. D. P. Woodruff and M. P. Seah, *Phys. Lett.*, **30A**, 263 (1969).
181. D. P. Woodruff and M. P. Seah, *Phys. Status Solidi (a)*, **1**, 429 (1970).
182. S. Andersson and B. Kasemo, *Solid-State Commun.*, **8**, 1885 (1970).
183. R. J. Reid, *Phys. Status Solidi (a)*, **2**, K109 (1970).
184. R. J. Reid, *Phys. Status Solidi (a)*, **4**, K211 (1971).
185. D. Tabor and J. M. Wilson, *Surf. Sci.*, **20**, 203 (1970).
185. D. Tabor and J. M. Wilson, *Surf. Sci.*, **20**, 203 (1970).
186. J. M. Wilson and D. Tabor, *Surf. Sci.*, **26**, 461 (1971).
187. D. Tabor, J. M. Wilson, and T. J. Bastow, *Surf. Sci.*, **26**, 471 (1971).
188. D. Tabor and J. M. Wilson, *J. Vac. Sci. Technol.*, **9**, 695 (1972).
189. J. B. Theeten, J. L. Domange, and J. Bonnerot, *Solid-State Commun.*, **8**, 643 (1970).
190. R. Baudouin, C. Corotte, and A. Mascall, *Colloq. J. Phys.*, **31**, C1-21 (1970).
191. J. B. Theeten, J. Bonnerot, J. L. Domange, and J. B. Hurault, *Solid-State Commun.*, **9**, 1121 (1971).
192. R. Kaplan and G. A. Somorjai, *Solid-State Commun.*, **9**, 505 (1971).
193. A. Ignatjevs, T. M. Rhodin, S. Y. Tong, B. I. Lundquist, and J. B. Pendry, *Solid-State Commun.*, **9**, 1851 (1971).
194. D. T. Quinto, B. W. Holland, and W. D. Robertson, *Surf. Sci.*, **32**, 139 (1972).
195. J. Henrion and G. A. Rhead, *Surf. Sci.*, **29**, 20 (1972).
196. R. J. Reid, *Surf. Sci.*, **29**, 623 (1972).

197. C. B. Duke, G. E. Laramore, B. W. Holland, and A. M. Gibbons, *Surf. Sci.*, **27**, 523 (1971).
198. B. W. Holland, *Surf. Sci.*, **28**, 258 (1971).
199. G. E. Laramore, *Phys. Rev.*, **B6**, 1097 (1972).
200. W. E. Spicer, *J. Res. Natl. Bur. Stand.*, **74A**, 397 (1970).
201. D. E. Eastman, in *Electron Spectroscopy*, D. A. Shirley, Ed., North Holland, Amsterdam, 1972, pp. 487-514.
202. S. B. M. Hagström, in *Electron Spectroscopy*, D. A. Shirley, Ed., North Holland, Amsterdam, 1972, pp. 515-534.
203. J. Hedman, M. Klasson, R. Nilsson, C. Nordling, M. F. Sorokina, O. I. Kijushnikov, S. A. Nemnov, V. A. Trapezikov, and V. G. Zyryanov, *Phys. Scr.*, **4**, 195 (1971).
204. G. K. Wertheim and S. Hüfner, *Phys. Rev. Lett.*, **28**, 1028 (1972).
205. J. J. Lander, *Phys. Rev.*, **91**, 1382 (1953).
206. R. G. Albridge, K. Hamrin, G. Johansson, and A. Fahlman, *Z. Phys.*, **209**, 419 (1968).
207. G. F. Amelio and E. J. Scheibner, *Surf. Sci.*, **11**, 242 (1968).
208. R. G. Musket and R. J. Fortner, *Phys. Rev. Lett.*, **26**, 80 (1970).
209. G. F. Amelio, *Surf. Sci.*, **22**, 301 (1970).
210. H. G. Maguire and P. D. Augustus, *J. Phys. C*, **4**, L174 (1971).
211. E. J. LeJeune and R. D. Dixon, *J. Appl. Phys.*, **43**, 1998 (1972).
212. A. Bagchi and C. B. Duke, *Phys. Rev.*, **B5**, 2784 (1972).
213. N. V. Smith and W. E. Spicer, *Opt. Commun.*, **1**, 157 (1969).
214. A. R. Williams, J. F. Janak, and V. L. Moruzzi, *Phys. Rev. Lett.*, **28**, 671 (1972).
215. T. A. Callcott and A. U. MacRae, *Phys. Rev.*, **178**, 966 (1969).
216. D. E. Eastman and J. K. Cashion, *Phys. Rev. Lett.*, **27**, 1520 (1971).
217. D. E. Eastman, J. K. Cashion, and A. C. Switendick, *Phys. Rev. Lett.*, **27**, 35 (1971).
218. D. E. Eastman, *Solid-State Commun.*, **10**, 933 (1972).
219. C. R. Helms and W. E. Spicer, *Phys. Rev. Lett.*, **28**, 565 (1972).
220. J. M. Baker and D. E. Eastman, *J. Vac. Sci. Technol.*, **10**, 223 (1973).
221. D. E. Eastman and W. D. Grobman, *Phys. Rev. Lett.*, **28**, 1378 (1972).
222. B. J. Wacławski and E. W. Plummer, *Phys. Rev. Lett.*, **29**, 783 (1972).
223. B. Feuerbacher and B. Fitton, *Phys. Rev. Lett.*, **29**, 786 (1972).
224. L. N. Tharp and E. J. Scheibner, *J. Appl. Phys.*, **38**, 3320 (1967).
225. E. J. Scheibner and L. N. Tharp, *Surf. Sci.*, **8**, 247 (1967).
226. J. J. Lander and J. Morrison, *Surf. Sci.*, **14**, 465 (1969).
227. A. U. MacRae, K. Müller, J. J. Lander, J. Morrison, and J. C. Phillips, *Phys. Rev. Lett.*, **22**, 1048 (1969).
228. P. S. P. Wei, *Surf. Sci.*, **20**, 157 (1970).
229. F. Steinrissler and E. N. Sickafus, *Phys. Rev. Lett.*, **27**, 992 (1971).
230. E. N. Sickafus and F. Steinrissler, *Phys. Rev.*, **B6**, 3714 (1972).
231. K. L. Ngai, E. N. Economou, and M. H. Cohen, *Phys. Rev. Lett.*, **24**, 61 (1970).
232. J. C. Turnbull and H. E. Farnsworth, *Phys. Rev.*, **54**, 509 (1938).
233. W. H. Weber and M. B. Webb, *Phys. Rev.*, **177**, 1103 (1969).
234. M. P. Seah, *Surf. Sci.*, **17**, 161 (1969).
235. J. O. Porteus, in *The Structure and Chemistry of Solid Surfaces*, G. A. Somorjai, Ed., Wiley, New York, 1969, Chapter 12.
236. J. M. Burkstrand and F. M. Propst, *J. Vac. Sci. Technol.*, **9**, 731 (1972).
237. R. J. Stein and R. M. Stern, *J. Vac. Sci. Technol.*, **9**, 743 (1972).
238. J. O. Porteus and W. N. Faith, *J. Vac. Sci. Technol.*, **9**, 1062 (1972).
239. P. M. Marcus, D. W. Jepsen, and F. Jona, unpublished.
240. F. Forstmann, W. Berndt, and P. Büttner, *Phys. Rev. Lett.*, **30**, 17 (1973).

241. C. B. Duke, G. E. Laramore, and N. O. Lipari, *J. Vac. Sci. Technol.*, **11**, 180 (1974); *Phys. Rev.* (submitted).
242. C. B. Duke, N. O. Lipari, G. E. Laramore, and J. B. Theeten, in *Abstracts of the Thirty-Third Annual Conference on Physical Electronics Berkeley, 1973*, p. 46; *Solid-State Commun.*, **13**, 579 (1973); *Phys. Rev.* (submitted).
243. F. Herman and S. Skillman, *Atomic Structure Calculations*, Prentice-Hall, Englewood Cliffs, New Jersey, 1963.
244. E. Bauer, *Z. Phys.*, **244**, 19 (1969).
245. R. M. Stern, J. J. Perry, and D. S. Boudreaux, *Rev. Mod. Phys.*, **41**, 275 (1969).
246. C. Kittel, *Quantum Theory of Solids*, Wiley, New York, 1963, Chapters 2 and 5.
247. C. B. Duke and G. E. Laramore, *Phys. Rev.*, **B3**, 3183 (1971).
248. C. B. Duke, J. R. Anderson, and C. W. Tucker, Jr., *Surf. Sci.*, **19**, 117 (1970).
249. J. B. Pendry, *J. Phys. C*, **4**, 2514 (1971).
250. G. E. Laramore and C. B. Duke, *Phys. Rev.*, **B5**, 267 (1972).
251. D. W. Jepsen, P. M. Marcus, and F. Jona, *Phys. Rev.*, **B6**, 3684 (1972).
252. C. B. Duke and U. Landman, *Phys. Rev.*, **B6**, 2956 (1972).
253. L. I. Schiff, *Quantum Mechanics*, McGraw-Hill, New York, 1955, pp. 161-168.
254. W. A. Harrison, *Pseudopotentials in the Theory of Metals*, Benjamin, New York, 1963.
255. C. W. Tucker, Jr., and C. B. Duke, *Surf. Sci.*, **24**, 31 (1971).
256. R. L. Park and J. E. Houston, *Surf. Sci.*, **18**, 213 (1969).
257. A. Delong, in *LEED: Surface Structures of Solids*, Vol. I, M. Laznicka, Union of Czechoslovak Mathematicians and Scientists, Prague, 1972, pp. 128-165.
258. R. F. Barnes, M. G. Lagally, and M. B. Webb, *Phys. Rev.*, **171**, 627 (1968).
259. C. B. Duke, *Tunneling in Solids*, Academic Press, New York, 1969, Chapter 19.
260. D. L. Huber, *Phys. Rev.*, **153**, 772 (1967).
261. V. Roundy and D. L. Mills, *J. Vac. Sci. Technol.*, **9**, 699 (1972).
262. J. T. McKinney, E. R. Jones, and M. B. Webb, *Phys. Rev.*, **160**, 523 (1967).
263. E. G. McRae and C. W. Caldwell, Jr., *Surf. Sci.*, **7**, 41 (1967).
264. B. W. Holland, R. W. Hannum, and A. M. Gibbons, *Surf. Sci.*, **25**, 561 (1971).
265. G. E. Laramore and A. C. Switendick, *Phys. Rev.*, **B7**, 3615 (1973).
266. C. B. Duke, D. L. Smith, and B. W. Holland, *Phys. Rev.*, **B5**, 3358 (1972).
267. J. L. Beeby, *J. Phys. C*, **1**, 82 (1968).
268. R. O. Jones and J. A. Strozier, Jr., *Phys. Rev. Lett.*, **22**, 1186 (1971).
269. R. de L. Kronig and W. G. Penny, *Proc. Roy. Soc.*, **130**, 499 (1931).
270. D. S. Boudreaux and V. Heine, *Surf. Sci.*, **8**, 426 (1967).
271. G. Capart, *Surf. Sci.*, **13**, 361 (1969).
272. K. S. Pogorel'skii, V. F. Dvoryankin, and A. Yu. Mityagin, *Fiz. Tverd. Tela*, **11**, 3225 (1969) [*Sov. Phys. Solid State*, **11**, 2614 (1970)].
273. A. Yu. Mityagin and K. S. Pogorel'skii, *Fiz. Tverd. Tela*, **13**, 1532 (1970) [*Sov. Phys. Solid State*, **13**, 1284 (1971)].
274. V. Hoffstein and D. S. Boudreaux, *Phys. Rev. Lett.*, **25**, 512 (1970).
275. C. Kittel, *Quantum Theory of Solids*, Wiley, New York, 1963, Chapters 9, 10, 13, and 14.
276. E. G. McRae, *J. Chem. Phys.*, **45**, 3258 (1966).
277. E. G. McRae and D. E. Winkel, *Surf. Sci.*, **14**, 407 (1969).
278. P. M. Marcus, D. W. Jepsen, and F. Jona, *Surf. Sci.*, **17**, 442 (1969).
279. P. J. Jennings and E. G. McRae, *Surf. Sci.*, **23**, 363 (1970).
280. K. Moliere, *Ann. Phys.*, **34**, 461 (1939).
281. K. Hirabayashi, *J. Phys. Soc. Japan*, **24**, 846 (1968).
282. J. J. Lander and J. Morrison, *J. Appl. Phys.*, **35**, 3593 (1964).
283. F. Hoffman and H. P. Smith, Jr., *Phys. Rev.*, **B1**, 2811 (1970).
284. J. A. Strozier, Jr., and R. O. Jones, *Phys. Rev. Lett.*, **25**, 516 (1970).
285. J. A. Strozier, Jr., and R. O. Jones, *Phys. Rev.*, **B3**, 3228 (1971).

286. F. Jona, J. A. Strozier, Jr., J. Kumar, and R. O. Jones, *Phys. Rev.*, **B6**, 407 (1972).
287. J. B. Pendry, *J. Phys. C*, **2**, 2283 (1969).
288. Z. G. Pinsker, *Electron Diffraction*, Butterworths, London, 1953, Chapter 8.
289. P. H. Dederichs, *Solid-State Phys.*, **27**, 135 (1972).
290. M. von Laue, *Phys. Rev.*, **37**, 53 (1931).
291. E. A. Wood, *J. Appl. Phys.*, **35**, 1306 (1964).
292. E. A. Wood, *Bell Syst. Tech. J.*, **43**, 541 (1964).
293. K. Kambe, *Z. Naturforsch.*, **22a**, 422 (1967).
294. K. Kambe, *Z. Naturforsch.*, **22a**, 322 (1967).
295. J. Korrinda, *Physica*, **8**, 392 (1947).
296. W. Kohn and N. Rostoker, *Phys. Rev.*, **94**, 1111 (1954).
297. E. G. McRae, *Surf. Sci.*, **11**, 479 (1968).
298. E. G. McRae, *Surf. Sci.*, **11**, 492 (1968).
299. K. Hirabayashi and Y. Takeishi, *Surf. Sci.*, **4**, 150 (1966).
300. Y. H. Ohtsuki, *J. Phys. Soc. Japan*, **24**, 1116 (1968).
301. K. Hirabayashi, *J. Phys. Soc. Japan*, **30**, 211 (1971).
302. K. Hirabayashi, *Surf. Sci.*, **28**, 621 (1971).
303. B. W. Holland, R. W. Hannum, A. M. Gibbons, and D. P. Woodruff, *Surf. Sci.*, **25**, 576 (1971).
304. P. M. Marcus and D. W. Jepsen, *Phys. Rev. Lett.*, **20**, 925 (1968).
305. D. W. Jepsen and P. M. Marcus, in *Computational Methods in Band Theory*, P. M. Marcus, J. F. Janak, and A. R. Williams, Eds., Plenum Press, New York, 1971, pp. 416-443.
306. D. W. Jepsen, P. M. Marcus, and F. Jona, *Phys. Rev. Lett.*, **26**, 1365 (1971).
307. J. B. Pendry, *Phys. Rev. Lett.*, **27**, 856 (1971).
308. J. B. Pendry, *J. Phys. C*, **4**, 3095 (1971).
309. J. B. Pendry in *LEED: Surface Structures of Solids*, Vol. 2, M. Laznicka, Ed., Union of Czechoslovak Mathematicians and Physicists, Prague, 1972, pp. 305-346.
310. S. Andersson and J. B. Pendry, *J. Phys. C*, **5**, L41 (1972).
311. R. H. Tait, S. Y. Tong, and T. N. Rhodin, *Phys. Rev. Lett.*, **28**, 553 (1972).
312. G. E. Laramore, *Phys. Rev.*, **B8**, 515 (1973).
313. J. B. Pendry, *J. Phys. C*, **2**, 1215 (1969).
314. J. C. Slater, *Phys. Rev.*, **81**, 385 (1951).
315. P. O. Löwdin, *Adv. Phys.*, **5**, 1 (1956).
316. L. F. Mattheiss, *Phys. Rev.*, **133**, A1399 (1964).
317. E. C. Snow, *Phys. Rev.*, **158**, 683 (1967).
318. L. Hedin and S. Lundquist, *Solid-State Phys.*, **23**, 2 (1969).
319. S. Y. Tong and T. N. Rhodin, *Phys. Rev.*, **B8**, 421 (1973).
320. F. Jona, *IBM J. Res. Dev.*, **14**, 444 (1970).
321. R. Baudouin, L. de Bersuder, G. Gaubert, V. Hoffstein, J. Lauzier, and H. Taub, *J. Vac. Sci. Technol.*, **9**, 634 (1972).
322. Group d'Etude des Surfaces, *Surf. Sci.*, **32**, 297 (1972).
323. J. E. Demuth, S. Y. Tong, and T. N. Rhodin, *J. Vac. Sci. Technol.*, **9**, 639 (1972).
324. S. Andersson and B. Kasemo, *Surf. Sci.*, **25**, 273 (1971).
325. E. G. McRae and C. W. Caldwell, Jr., *Surf. Sci.*, **2**, 509 (1964).
326. C. B. Duke and G. E. Laramore, *Surf. Sci.*, **30**, 659 (1972).
327. L. de Bersuder, V. Hoffstein, and J. Lauzier, *Surf. Sci.*, **27**, 338 (1971).
328. G. E. Laramore, *Phys. Rev.*, **B6**, 2950 (1972).
329. G. E. Laramore, J. E. Houston, and R. L. Park, *J. Vac. Sci. Technol.*, **10**, 196 (1973).
330. J. M. Burkstrand, Ph.D. Thesis, University of Illinois, Urbana, 1972; Ph.D. Thesis, *Phys. Rev.*, **B7**, 3443 (1973).

331. J. O. Porteus, unpublished.
332. C. B. Duke, G. E. Laramore, and V. Metze, *Solid-State Commun.*, **8**, 1189 (1970).
333. G. E. Laramore and C. B. Duke, *Phys. Rev.*, **B3**, 3198 (1972).
334. C. B. Duke, A. J. Howsmon, and G. E. Laramore, *J. Vac. Sci. Technol.*, **8**, 10 (1971).
335. C. B. Duke and A. Bagchi, *J. Vac. Sci. Technol.*, **9**, 738 (1972).
336. C. B. Duke and U. Landman, *Phys. Rev.*, **B6**, 2968 (1972).
337. C. B. Duke and U. Landman, *Phys. Rev.*, **B8**, 505 (1973).
338. R. L. Dennis and M. B. Webb, *J. Vac. Sci. Technol.*, **10**, 192 (1973).
339. J. O. Porteus and W. N. Faith, *Phys. Rev.*, **B8**, 491 (1973).
340. J. J. Lander, in *Progress in Solid State Chemistry*, Vol. II Pergamon Press, New York, 1965, pp. 26–118.
341. V. F. Dvoryankin and A. Yu Mityagin, *Kristallografiya*, **12**, 1112 (1967) [*Sov. Phys. Crystallogr.*, **12**, 982 (1968)].
342. E. Bauer, in *Techniques in Metals Research*, Vol. II, Part 2, Wiley-Interscience, New York, 1969, pp. 559–639.
343. W. D. Robertson, *J. Vac. Sci. Technol.*, **8**, 403 (1971).
344. M. Prutton, *Met. Rev.*, **152**, 57 (1971).
345. W. J. Dunning, in *The Solid-Gas Interface*, Vol. I, E. A. Flood, Ed., Marcel Dekker, New York, 1967, pp. 271–306.
346. J. M. Honig, in *The Solid-Gas Interface*, Vol. I, E. A. Flood, Ed., Marcel Dekker, New York, 1967, pp. 371–412.
347. L. Schwartz and H. Ehrenreich, *Ann. Phys. (N. Y.)*, **64**, 100 (1971).
348. R. L. Park and H. H. Madden, Jr., *Surf. Sci.*, **11**, 188 (1968).
349. C. W. Tucker, Jr., *J. Appl. Phys.*, **35**, 1897 (1964).
350. E. Bauer, in *Adsorption et Croissance Crystalline*, Centre de la Recherche Scientifique, Paris, 1965, p. 1.
351. P. J. Estrup and J. Anderson, *Surf. Sci.*, **8**, 101 (1967).
352. P. J. Estrup and J. Anderson, *J. Chem. Phys.*, **45**, 2254 (1966).
353. P. J. Estrup, J. Anderson, and W. E. Danforth, *Surf. Sci.*, **4**, 286 (1966).
354. G. Ertl and J. Küppers, *Surf. Sci.*, **21**, 61 (1970).
355. C. E. Carroll, *Surf. Sci.*, **32**, 119 (1972).
356. J. E. Houston and R. L. Park, *Surf. Sci.*, **21**, 209 (1970).
357. C. B. Duke and U. Landman, (unpublished).
358. W. P. Ellis and R. L. Schwoebel, *Surf. Sci.*, **11**, 82 (1968).
359. M. Henzler, *Surf. Sci.*, **19**, 159 (1970).
360. J. Perdereau and G. A. Rhead, *Surf. Sci.*, **24**, 555 (1971).
361. M. Henzler, *Surf. Sci.*, **22**, 12 (1970).
362. J. E. Houston and R. L. Park, *Surf. Sci.*, **26**, 269 (1971).
363. J. E. Houston, G. E. Laramore, and R. L. Park, *Surf. Sci.*, **34**, 481 (1973).
364. M. J. Buerger, *Crystal Structure Analysis*, Wiley, New York, 1960.
365. M. J. Buerger, *Contemporary Crystallography*, McGraw-Hill, New York, 1970.
366. C. W. Tucker, Jr., and C. B. Duke, *Surf. Sci.*, **23**, 411 (1970).
367. C. B. Duke and C. W. Tucker, Jr., *J. Vac. Sci. Technol.*, **8**, 5 (1971).
368. C. W. Tucker, Jr., and C. B. Duke, *Surf. Sci.*, **29**, 237 (1972).
369. C. B. Duke and D. L. Smith, *Phys. Rev.*, **B5**, 4730 (1972).
370. L. H. Germer, S. Goldstaub, J. Escard, G. David, and J. P. DeVille, *Compte Rendus*, **262**, 1059 (1966).
371. R. M. Goodman, H. H. Farrell, and G. A. Somorjai, *J. Chem. Phys.*, **49**, 692 (1968).
372. M. G. Lagally, T. C. Ngoc, and M. B. Webb, *Phys. Rev. Lett.*, **26**, 1557 (1971).
373. M. G. Lagally, T. C. Ngoc, and M. B. Webb, *J. Vac. Sci. Technol.*, **9**, 645 (1972).
374. T. C. Ngoc, M. G. Lagally, and M. B. Webb, *Surf. Sci.*, **35**, 117 (1973).

- 375. D. T. Quinto and W. D. Robertson, *Surf. Sci.*, **34**, 501 (1973).
- 376. D. Aberdam and R. Baudoing, *Solid-State Commun.*, **10**, 1199 (1972).
- 377. C. W. Tucker, Jr., *J. Appl. Phys.*, **37**, 3013 (1966).
- 378. T. A. Clarke, R. Mason, and M. Tescari, *Surf. Sci.*, **30**, 553 (1972).
- 379. T. A. Clarke, R. Mason, and M. Tescari, *Proc. Roy. Soc. (London)*, **A331**, 321 (1972).
- 380. H. Lipson and W. Cochran, *The Determination of Crystal Structures*, G. Bell and Sons, London, 1966, Chapters 7, 8, and 10.
- 381. P. M. Marcus, D. W. Jepsen, and F. Jona, *Surf. Sci.*, **31**, 180 (1972).
- 382. S. Andersson and J. B. Pendry, *J. Phys. C*, **6**, 601 (1973).
- 383. F. Jona, J. A. Strozier, Jr., and C. Wong, *Surf. Sci.*, **30**, 225 (1972).
- 384. H. D. Hagstrum and G. E. Becker, *J. Chem. Phys.*, **54**, 1015 (1971).
- 385. M. Perdereau and J. Oudar, *Surf. Sci.*, **20**, 80 (1970).
- 386. J. B. Pendry, S. Andersson, B. Kasemo, and M. W. Van Hove, in *Abstracts of the Thirty-Third Annual Conference on Physical Electronics*, p. 47, *Phys. Rev. Lett.*, **31**, 595 (1973).
- 387. C. B. Duke, in *Proceedings of the International School of Physics Enrico Fermi*, Course LVIII, Academic Press, New York, 1974.
- 388. H. H. Farrel and G. A. Somorjai, *Phys. Rev.*, **182**, 751 (1969).
- 389. R. M. Stern and S. Sinharoy, *Surf. Sci.*, **33**, 131 (1972).
- 390. S. Andersson and B. Kasemo, *Surf. Sci.*, **25**, 237 (1971).
- 391. H. E. Farnsworth, *Phys. Rev.*, **43**, 900 (1933).
- 392. L. H. Germer, J. W. May, and R. J. Szostak, *Surf. Sci.*, **8**, 430 (1967).
- 393. J. C. Tracy and J. M. Blakely, in *The Structure and Chemistry of Solid Surfaces*, G. A. Somorjai, Ed., Wiley, New York, 1969, Chapter 65.
- 394. D. E. Andersson and S. Andersson, *Surf. Sci.*, **23**, 311 (1970).
- 395. R. L. Park, in *The Structure and Chemistry of Solid Surfaces*, G. A. Somorjai, Ed., Wiley, New York, 1969, Chapter 28.
- 396. J. V. Florio and W. D. Robertson, *Surf. Sci.*, **22**, 459 (1970).
- 397. C. B. Duke and A. Liebsch, *Bull. Am. Phys. Soc.*, **18**, 364 (1973); *Phys. Rev.* **B9**, 1126 (1974); *Phys. Rev.* **B9**, 1150 (1974).
- 398. R. Heckingbottom, *Surf. Sci.*, **27**, 370 (1971).
- 399. A. Guinier, *X-Ray Diffraction*, W. H. Freeman, San Francisco, 1963, Chapters 6, 8, and 9.
- 400. R. L. Park, *J. Appl. Phys.*, **37**, 295 (1966).
- 401. J. O. Porteus and W. N. Faith, *Phys. Rev.*, **B2**, 1532 (1970).
- 402. J. M. Elson and R. H. Ritchie, *Surf. Sci.*, **30**, 178 (1972).
- 403. J. Heinrichs, *Solid-State Commun.*, **12**, 167 (1973).
- 404. C. B. Duke, *CRC Crit. Rev. Solid State Sci.*, **4**, June (1974).

ELECTRON SPECTROSCOPY OF CHEMISORPTION ON METALS

R. GOMER

*The James Franck Institute and The Department of Chemistry
 The University of Chicago, Chicago, Illinois*

CONTENTS

I.	Introduction	211
II.	Theory of Chemisorption	212
	A. Newns-Anderson Model	214
	B. Valence-Bond (Schrieffer-Paulson-Gomer) Approach	224
	C. Linear Response (Kohn-Smith-Ying) Method	225
III.	Theory of Energy Distributions in Field Emission	225
	A. Field Emission	226
	B. Total Energy Distribution	227
	C. Transfer Hamiltonian	231
	D. Energy Distribution in the Presence of Adsorbates	233
IV.	Experimental Considerations	237
	A. Field Emission Microscope	237
	B. Energy Analyzers	239
V.	Photoemission	244
	A. Experimental Aspects of Photoemission	245
VI.	Field and Photoemission Distributions from Selected Systems	246
	A. Ba on W	246
	B. H ₂ on W	248
	C. Carbon Monoxide on Tungsten	250
	D. Other Systems	261
VII.	Conclusion	262
	References	262

I. INTRODUCTION

The study of chemisorption on clean, single-crystal surfaces of metals has progressed to the point where it becomes meaningful to inquire into the electronic structure of the adsorption complex. Such knowledge serves not only as an aid in identifying different adsorption states but is fundamental to any real understanding of chemical bonding on surfaces. This article discusses two of the three principal methods now available, namely energy distributions in field emission from adsorbate-covered surfaces, and

in less detail, photoemission spectroscopy. The third, ion neutralization spectroscopy¹ developed by H. Hagstrum, is not discussed here. In order to give a feeling for the kinds of questions that a knowledge of local density of states at the adsorbate can help to answer we start by sketching the present status of the theory of chemisorption on metals.

II. THEORY OF CHEMISORPTION

Chemisorption is defined, somewhat loosely, as the adsorption of atoms or molecules on surfaces with a binding energy in excess of 1 eV. In many cases energies as high as 3 or 4 eV are observed, so that the process clearly corresponds to electron sharing, that is, chemical bonding. The difference between bonding on a surface and "ordinary" chemical bonding is that, in principle at least, about 10^{23} electrons can participate in one ad-bond. Nevertheless the usual concepts of chemical bonding can be generalized to include chemisorption. A qualitative picture is given in Fig. 1. If an adsorbate atom A approaches a metal surface its sharp level at ϵ_a broadens by interaction with the metal. Very crudely the half-width Δ of the broadened level is related to the tunneling time τ of an electron on A into the metal, or vice versa, by

$$\Delta \cong \frac{\hbar}{\tau} \quad (1)$$

In addition to being broadened, the original adsorbate level will also be shifted for three reasons, which, in a one-electron approach at least, are more or less separable. First, there is a downward shift because of interaction with the metal, related in an essential way to the bonding;

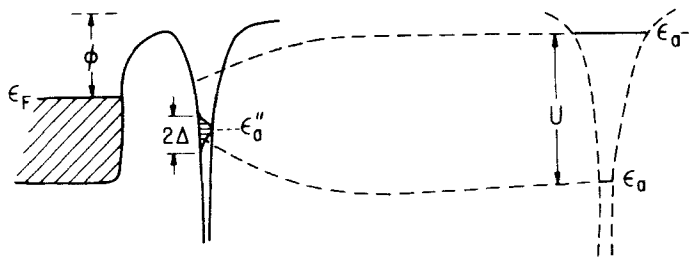


Fig. 1. Schematic potential energy diagram of chemisorption on a metal. ϵ_a and ϵ_{a^-} are energies of highest filled levels of neutral adsorbate A and ion A^- , respectively, separated by the intra-atomic Coulomb repulsion U . ϵ_F is the Fermi energy ϕ is the work function of metal. ϵ_a'' is the adsorbate level, shifted by interaction with the metal and by Coulomb repulsion; its broadening is represented by 2Δ .

second the fact that two electrons can be on the adsorbate simultaneously leads to an intra-atomic Coulomb repulsion U which shifts the level upward. Finally, the fact that ionization of A leads to an attractive image interaction with the surface reduces the effective ionization potential, that is, shifts ϵ_a upward by an amount $V_{im} = e^2/4x$. If $\pi\Delta > U$, that is, if the average time spent by an electron on the adsorbate is sufficiently short, it turns out that the chemisorption problem can be treated by a generalization of the LCAO-MO scheme in Hartree-Fock approximation. If only for this reason, a knowledge of the shape and position of the adsorbate "resonance" is clearly of greatest importance. If, on the other hand, the inequality is reversed, electron correlation on the adsorbate becomes very important and we must resort to better approximations than Hartree-Fock.

Before going into further details it is necessary to define the term broadened adsorbate level, or resonance, more quantitatively. This is most conveniently done in terms of a local density of states, at the adsorbate, ρ_a which is defined as the modulus squared of the projection of the wave function at the adsorbate φ_a on a system state φ_m at energy ϵ , multiplied by the density of states at ϵ :

$$\rho_a(\epsilon) = \sum_m |\langle a|m \rangle|^2 \delta(\epsilon - \epsilon_m) \quad (2)$$

ρ_a can be expressed very conveniently in terms of the Green's function of the metal-adsorbate system. For our purposes the one-electron approximation suffices so that the Green's operator is defined by

$$G(E - H - i\alpha) = 1 \quad (3)$$

where H is the Hamiltonian of the metal-adsorbate system and α is a small quantity which will be allowed to approach 0 at the appropriate point. Thus

$$G = \frac{1}{\epsilon - H - i\alpha} \quad (4)$$

and

$$G_{mm} = \frac{1}{\epsilon - \epsilon_m - i\alpha} \quad (5)$$

if $|m\rangle$ is an eigenvector of H . Multiplying numerator and denominator of G_{mm} by $\epsilon - \epsilon_m + i\alpha$ yields for the imaginary part of G_{mm} , $\text{Im } G_{mm}$,

$$\text{Im } G_{mm} = \frac{i\alpha}{(\epsilon - \epsilon_m)^2 + \alpha^2} \quad (6)$$

so that

$$\frac{1}{\pi} \text{Im } G_{mm} = \delta(\epsilon - \epsilon_m) \quad (7)$$

as can be verified by integrating (6) and then letting $\alpha \rightarrow 0$. Consequently, we can write for ρ_a , (2)

$$\begin{aligned}\rho_a &= \frac{1}{\pi} \text{Im} \sum_m \langle a|m \rangle \langle m|G|m \rangle \langle m|a \rangle \\ &= \frac{1}{\pi} \text{Im} G_{aa}\end{aligned}\quad (8)$$

This is a central result, since the experimental information obtainable from field emission and photoemission will be shown to yield $\text{Im} G_{aa}$ rather directly.

A. Newns-Anderson Model

It should be noted that we have not been very specific in defining our basis set. In the simplest model this is chosen as a single free adsorbate wave function φ_a plus the Bloch states of the metal $|k\rangle$, and a system state $|m\rangle$ is written as

$$|m\rangle = b_m|a\rangle + \sum_k c_m|k\rangle \quad (9)$$

An immediate difficulty is that this basis is overcomplete and (equivalently) that $\langle k|a\rangle \neq 0$. If this difficulty is neglected for the moment, the problem becomes tractable in the self-consistent field Hartree-Fock approximation. The problem is physically and formally quite similar to that of an impurity in the metal, which has been considered by a number of authors, particularly Friedel² and Anderson.³ The adaptation of Anderson's formalism to the chemisorption problem is due to Newns,⁴ whose approach we follow here. It should be added that the chemisorption problem, neglecting Coulomb interaction of electrons, has been treated along more orthodox chemical lines by a number of authors, for instance Grimley.⁵

Following Anderson and Newns, we neglect all but intra-atomic Coulomb repulsions of up-spin with down-spin electrons, and write a Hamiltonian for up-spin (\uparrow) electrons (with an analogous expression for H^\downarrow)

$$H^\uparrow = H_{(m)} + V + \langle n_\downarrow \rangle U \quad (10)$$

where $H_{(m)}$ is the metal Hamiltonian and V can be regarded as the difference between the metal and the adsorbate potential; $\langle n_\downarrow \rangle$ is the average population of down-spin electrons on A. If we neglect all off-diagonal matrix elements of H except those coupling $|k\rangle$ to $|a\rangle$, $H_{ak} = V_{ak}$, and write $H_{kk'} = \epsilon_k \delta_{kk'}$, $H_{aa}^\uparrow = \epsilon_a^\uparrow + \langle n_\downarrow \rangle U \equiv \epsilon_a^\uparrow$, we can obtain G_{aa}

straightforwardly, for instance by taking appropriate matrix elements of both sides of (3). The result is

$$G_{aa}^{\uparrow} = \left(\epsilon - \epsilon_a^{\uparrow} - \sum_k \frac{|V_{ak}|^2}{\epsilon - \epsilon_k - i\alpha} \right)^{-1} \quad (11)$$

with an analogous expression for G_{aa}^{\downarrow} . Multiplying numerator and denominator in the sum over k in (11) by $\epsilon - \epsilon_k + i\alpha$ leads to

$$G_{aa}^{\uparrow} = \frac{1}{\epsilon - \epsilon_a^{\uparrow} - \Lambda - i\Delta} \quad (12)$$

where

$$\Delta(\epsilon) = \pi \sum_k |V_{ak}|^2 \delta(\epsilon - \epsilon_k) \approx \pi \overline{|V_{ak}|^2} \rho_k(\epsilon) \quad (13)$$

and

$$\Lambda(\epsilon) = P \sum_k \frac{|V_{ak}|^2}{\epsilon - \epsilon_k} = \frac{P}{\pi} \int_{-\infty}^{\infty} \frac{\Delta(\epsilon') d\epsilon'}{\epsilon - \epsilon'} \quad (14)$$

Here P stands for the Cauchy principal value, for example,

$$\lim_{\alpha \rightarrow 0} \sum_k \frac{|V_{ak}|^2 (\epsilon - \epsilon_k)}{(\epsilon - \epsilon_k)^2 + \alpha^2}$$

and so on. As the last equality in (14) indicates $\Lambda(\epsilon)$ is the Hilbert transform of $\Delta(\epsilon)$. Equation (12) enables us to find ρ_a^{\uparrow} as

$$\rho_a^{\uparrow} = \frac{\text{Im}}{\pi} G_{aa}^{\uparrow} = \frac{\Delta/\pi}{(\epsilon - \epsilon_a^{\uparrow})^2 + \Delta^2} \quad (15)$$

where $\epsilon_a^{\uparrow} \equiv \epsilon_a + \langle n_{\downarrow} \rangle U + \Lambda(\epsilon)$. If the energy dependence of $\Lambda(\epsilon)$ and $\Delta(\epsilon)$ could be neglected, ρ_a^{\uparrow} would have a simple Lorentzian line shape centered on ϵ_a^{\uparrow} , the shifted adsorbate level, with a half-width at half-maximum of Δ , which would be related to the average, that is, energy-independent, tunneling time by the "golden rule" expression

$$\frac{1}{\tau} = \frac{2\pi}{\hbar} \rho_k \overline{|V_{ak}|^2} \quad (16)$$

as indicated in (1).

In general the energy dependence of Δ and Λ cannot be neglected and ρ_a will be more complicated, even in the simple model depicted here. This fact is responsible for the variety of behavior which may occur. Equations

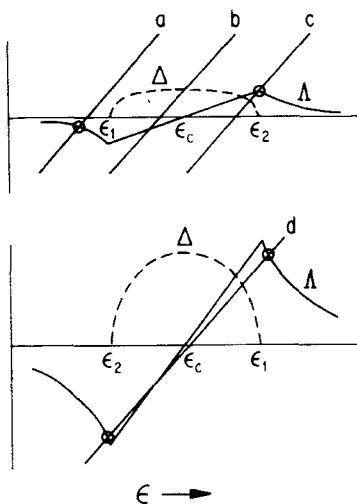


Fig. 2a. Relations between Δ and Λ for small and large Δ . ϵ_1 and ϵ_2 are the upper and lower limits of the relevant band, ϵ_c is the energy of the band center. Four possible intersections of $\epsilon - \epsilon_a$ with Λ are shown: (a) a single localized state below the band; (b) no localized states; (c) a localized state above the band; (d) localized states above and below the band.

(5) and (8) show that the energy eigenvalues ϵ_m correspond to poles of G_{aa} . These can occur not only in the band but also outside it where $\Delta=0$ if, from (12),

$$\epsilon - \epsilon_a^{\uparrow} - \Lambda(\epsilon) = 0 \quad (17)$$

has real roots. This situation corresponds to the intersection of the line $\epsilon - \epsilon_a^{\uparrow}$ versus ϵ with $\Lambda(\epsilon)$. Possible situations are shown in Fig. 2. It is seen that one, two, or zero states may detach themselves from the band. It is not

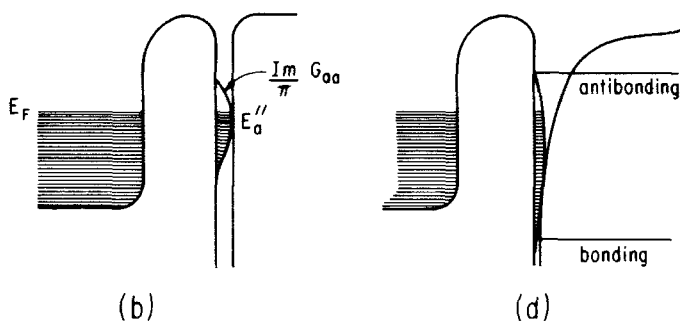


Fig. 2b. Schematic potential diagrams indicating local densities of state for two of the situations depicted in Fig. 2a. The labeling is identical.

difficult to show that only one state below the band generally corresponds to very weak interaction while a state below (filled) and above the band (empty) corresponds to very strong chemisorption, that is, the formation of a surface molecule between the adsorbate and its neighboring substrate atoms.

It is worthwhile to show this more explicitly. If the localized states are far above and below the band, we may approximate $\Lambda(\epsilon)$ in their vicinity by

$$\Lambda(\epsilon) \cong (\epsilon - \epsilon_c)^{-1} \pi^{-1} \int \Delta(\epsilon') d\epsilon' \quad (18)$$

where ϵ_c is the energy of the band center (in the case of a half-filled band ϵ_F) and the integral runs only over the band. Then we have from (17)

$$\epsilon - \epsilon'_a - (\epsilon - \epsilon_c)^{-1} \pi^{-1} \int \Delta(\epsilon') d\epsilon' = 0 \quad (19)$$

or, from the definition of Δ , (13),

$$(\epsilon - \epsilon'_a)(\epsilon - \epsilon_c) = \sum_k |V_{ak}|^2 \quad (20)$$

We next represent the states $|k\rangle$ in terms of a set formed by taking the most relevant atomic orbitals, say $5d$ orbitals in the case of tungsten, from each substrate atom in the metal. We shall pretend that these form a complete orthonormal set, which is of course only an approximation. It is possible to construct orthonormal sets along such lines, for instance Wannier orbitals (which are not localized enough for our purposes), but we shall ignore such refinements. With this approximation we have

$$V_{ak} \cong \sum_j \beta'_j \langle j|k \rangle \quad (21)$$

where

$$\beta'_j = V_{aj} \quad (22)$$

Then (20) becomes, since the $|k\rangle$ form a complete set,

$$(\epsilon - \epsilon'_a)(\epsilon - \epsilon_c) = \sum_j |\beta'_j|^2 \quad (23)$$

or

$$\epsilon_i = \frac{1}{2} \left\{ \epsilon_c + \epsilon'_a \pm \left[(\epsilon'_a - \epsilon_c)^2 + 4 \sum_j |\beta'_j|^2 \right]^{1/2} \right\} \quad (24)$$

These are just the bonding and antibonding levels of a surface molecule formed between the adsorbate and those substrate atoms for which $\beta'_j \neq 0$. This is a very important result since it brings out the localized nature of the interaction between adsorbate and substrate in the case of strong bonding.

It provides the mathematical underpinning for the fact that different adsorption states can exist not only on different crystal planes but on one and the same plane. These correspond to different geometric arrangements in which both the magnitudes and number of the β 's vary, depending on the configuration.

Finally we must consider in slightly more detail the location of ϵ_a . At large adsorbate-surface separations x , $\epsilon_a^\uparrow = \epsilon_a + U\langle n\downarrow \rangle$ with $\langle n\downarrow \rangle = 0$ (neutral A) or 1 (negative ion, A^-). Considering the neutral case for the moment, as A approaches the surface, ϵ_a' is pushed up in energy by the image potential, $V_{im} = e^2/4x$, as already noted. Similarly, the affinity level, that is, the ionization level of A^- , is pulled down, since the affinity increases by V_{im} . As x approaches the equilibrium adsorbate-surface separation, the classical image potential undoubtedly breaks down but can be replaced by an effective interaction, V'_{im} . Thus we find that

$$\epsilon_a^\uparrow = \epsilon_a + V'_{im} + (U - 2V'_{im})\langle n\downarrow \rangle \quad (25)$$

since the effective U is the separation of the ionization and affinity levels. In particular if $\langle n\uparrow \rangle = \langle n\downarrow \rangle = \frac{1}{2}$ we find the interesting result that

$$\epsilon_a^\uparrow = \epsilon_a^\downarrow = \epsilon_a + \frac{1}{2}U \quad (26)$$

If ϵ_a lies near ϵ_F , that is, if $I - \phi$ is small, I being the ionization potential of A and ϕ the work function of the metal, an upward shift of ϵ_a as A approaches the surface may result in an appreciable fraction of ρ_a lying above ϵ_F . This situation, which is encountered with alkali adsorption on transition metals for instance, corresponds to highly polar electropositive adsorption. Analogously, an empty affinity level of A lying not too far above ϵ_F can be pulled down enough to be partially filled, corresponding to strongly electronegative adsorption. In the case of electropositive adsorption Λ tends to pull ϵ_a'' down while V_{im} pushes it up. In the second case both Λ and V_{im} pull the affinity level down. It should be apparent that this description is simply another way of looking at U ; we are not justified in thinking of electrons on A in the same orbitals as nonequivalent. This statement does not mean, however, that multiple bonds cannot be formed by an atom, by utilizing different atomic orbitals.

In principle the procedure for evaluating the binding energy is also straightforward. We first note that

$$\langle n\uparrow \rangle = \int^{\epsilon_F} \rho_a^\uparrow d\epsilon \quad (27)$$

with a similar expression for $\langle n\downarrow \rangle$. Since $\epsilon_a^\uparrow = \epsilon_a + \langle n\downarrow \rangle U$, $\langle n\uparrow \rangle$ and $\langle n\downarrow \rangle$ are related and must be solved for self-consistently. There will always be a root of the resultant equations which is nonmagnetic, that is, for which $\langle n\uparrow \rangle = \langle n\downarrow \rangle$. It may also happen that there are two symmetric

magnetic roots for which this is not the case. It can be formally shown that the magnetic roots have the lower energy. This is obvious from simple physical considerations: The extreme limit of the magnetic case corresponds to occupation of the adsorbate atom by only one electron at a time, spin-up or spin-down, and thus avoids most intra-atomic repulsion. The less extreme case still manages to reduce the intra-atomic repulsion. Unfortunately it can be shown⁶ that the magnetic limit in Hartree-Fock approximation (unrestricted Hartree-Fock) is not likely to be valid. This is best seen by starting at the nonmagnetic limit, which can be shown⁶ to be valid when $\pi\Delta > U$, as already mentioned. Physically this situation corresponds to the fact that electrons hop on and off the adsorbate sufficiently rapidly to correlate their motion adequately in Hartree-Fock approximation (for given U). When this condition is not met, correlation becomes so important that Hartree-Fock breaks down. But the reversal of the inequality is just the condition under which Hartree-Fock would try to "go magnetic."

In principle an experimental check of sorts on $\sum \langle n \rangle$ exists, since the integral in (27) summed over both spin states gives the total electronic charge at the adsorbate. If the adsorbate-surface distance and the screening length of the surface were known, the dipole moment per ad-particle could be calculated and compared with the experimental value which can be found from the work function increment and the number density of adsorbed particles:

$$\Delta\phi = 4\pi NP \quad (28)$$

where N is the number of adsorbate particles per square centimeter and P is the dipole moment per ad-particle.

Once $\langle n \rangle$ and hence ϵ'_a are found the adsorption energy ΔE can be evaluated as the difference between the system energy when the adsorbate is not interacting and with interaction turned on:

$$\Delta E = 2 \sum_m \epsilon_m - U \langle m \downarrow \rangle \langle n \uparrow \rangle - 2 \sum_k \epsilon_k - V_{im} - \epsilon_a \quad (29)$$

The U term appears with a negative sign since it is counted twice in the sum over system states, m . The factors of 2 arise because m and k do not include spin. The salient quantity in (29) is the difference between the sums over m and k , which we can call $\Delta E'$:

$$\Delta E' = \sum_m \epsilon_m - \sum_k \epsilon_k \quad (30)$$

$\Delta E'$ can be obtained from G_{aa} by making use of a theorem of contour integration,⁴ which goes as follows: If $f(z)$ is an analytic function of z with a contour C and if $\varphi(z)$ is analytic in C , except for a finite number of

poles, then

$$\frac{1}{2\pi i} \int_c f(z) \frac{\varphi'(z)}{\varphi(z)} dz = \sum_j r_j f(a_j) - \sum_j s_j f(b_j) \quad (31)$$

where a_j corresponds to the j th zero and b_j to the j th pole of φ in C and r_j and s_j are the respective multiplicities. The zeros of G_{aa}^{-1} correspond to the ϵ_m as already noted, while its poles obviously correspond to the ϵ_k . Thus

$$\Delta E' = \frac{1}{2\pi i} \int_c \epsilon \frac{d}{d\epsilon} \ln G_{aa}^{-1} d\epsilon \quad (32)$$

if the contour encloses all the occupied eigenvalues. It can be shown⁴ that the contour integral then reduces to

$$\Delta E' = \frac{1}{\pi} \int_{\epsilon_1}^{\epsilon_f} \tan^{-1} \left[\frac{\Delta(\epsilon)}{\epsilon - \epsilon'_a - \Lambda(\epsilon)} \right] d\epsilon + \epsilon_l \quad (33)$$

where ϵ_1 corresponds to the bottom of the band and ϵ_l to localized states, if any, below it.

The foregoing should suffice to show the importance of G_{aa} , both as a quantity to be calculated and one to be measured. We have ignored so far the problem of overcompleteness or nonorthogonality, which will not shock many chemists. Since the "hopping integrals" β'_{aj} are difficult to calculate in any case and would be treated as parameters, the general structure of a calculation and any numerical (i.e., parametrized) estimates are probably not very seriously affected. It turns out, however, that a calculation of energy distributions in field or photoemission is much more sensitive to this neglect, and that in fact spurious terms enter if it is neglected. For this reason we complete our discussion of the Hartree-Fock approximation by taking nonorthogonality into account.

As we have seen the problem arises from the fact that $|a\rangle$ is not orthogonal to the set $|k\rangle$. Since the latter is complete we can always expand H and G in it even if the resultant matrices are not diagonal. The density of states for instance would still be given by $\text{tr } G$ since the trace is invariant. The problem then is to bring $|a\rangle$ into the picture somehow. There are various methods of doing so, which turn out to be, if not equivalent, at least closely related. Perhaps the simplest to understand, if not to justify, is an approximation due to Penn⁷: If V is defined as before by

$$V^\dagger \equiv H - H_{(m)} + U \langle n \downarrow \rangle \quad (34)$$

the approximation consists of assuming that

$$V_{kk'} \approx \frac{V_{ka} V_{ak'}}{V_{aa}} \quad (35)$$

A rough justification for (35) can be given somewhat as follows: Assume that $V_{kk'}$ is expanded in some complete set, say the eigenstates $|b\rangle$ of the free adsorbate A of which $|a\rangle$ is the most relevant member,

$$V_{kk'} = \sum_b \langle k|b\rangle \langle b|V|k'\rangle \approx \langle k|a\rangle \langle a|V|k'\rangle \quad (36)$$

Inserting the unit operator $\sum_b |b\rangle \langle b|$ between k and V in $\langle k|V|a\rangle$ gives

$$V_{ka} = \sum_b \langle k|b\rangle \langle b|V|a\rangle \approx V_{aa} \langle k|a\rangle \quad (37)$$

so that the right-hand side of (35) becomes approximately $\langle k|a\rangle V_{ak'}$, establishing the approximate equality. The validity of this approximation seems to hinge on the neglect of all terms in the expansion over $|b\rangle$ except that involving $|a\rangle$. It turns out that this is not as stringent a restriction as might appear, since the same final result can also be obtained by a number of other approaches.⁸ Insertion of (35) for $V_{kk''}$ in the equation of motion of the Green's function

$$\sum_{k''} (\epsilon - H_{(m)} - V)_{kk''} G_{k''k'} = \delta_{kk'} \quad (38)$$

[which is obtained from (3) by insertion of $\sum_{k''} |k''\rangle \langle k''|$ between $(\epsilon - H)$ and G] then leads, after some algebra⁷ to an expression for $G_{kk'}$:

$$G_{kk'}^\dagger = g_k \delta_{kk'} + \frac{g_k V_{ka} V_{ak'} g_{k'}}{\epsilon - \epsilon_a^\dagger - \sum_k g_k |V'_{ak}|^2} \quad (39)$$

Here

$$g = (\epsilon - H_{(m)} - i\alpha)^{-1} \quad (40)$$

and

$$g_k \equiv \langle k|g|k\rangle = (\epsilon - \epsilon_k - i\alpha)^{-1} \quad (41)$$

while

$$V'_{ak} \equiv (H - \epsilon)_{ak} = V_{ak} + (\epsilon_k - \epsilon) \langle a|k\rangle \quad (42)$$

We can easily obtain G_{aa} by multiplying both sides of (39) by $\langle a|k\rangle \langle k'|a\rangle$ and summing over k and k' :

$$G_{aa}^\dagger = \sum_{k,k'} \langle a|k\rangle \langle k|G|k'\rangle \langle k'|a\rangle = g_{aa}^\dagger + \frac{[(gV)_{aa}]^2}{\epsilon - \epsilon_a^\dagger - \sum_k g_k |V'_{ak}|^2} \quad (43)$$

Equations (39) and (43) are equivalent⁷ to those obtainable from a paper by Anderson and McMillan⁹ if $H_{ak} \sim V_{ak}$ and $H_{kk} \sim \epsilon_k \delta_{kk'}$ and can be shown to go over into the Kanamori equations¹⁰ with certain other approximations.⁷

It is worthwhile to examine the structure of G_{aa} . The first term g_{aa} can be written

$$g_{aa} = \sum_k |\langle k|a\rangle|^2 g_k \quad (44)$$

and amounts to a projection of the substrate density of states on $|a\rangle$. The main term has a denominator which is only a slight modification of (11). In particular, the self-energy term, $\sum_k |V'_{ak}|^2 g_k$, has real and imaginary parts Λ' and Δ' very similar in structure to Λ and Δ given by (13) and (14). If we ignore the imaginary part of g in the numerator of (43), it can be expressed as $|\langle a|a'\rangle|^2 = 1$ where

$$|a'\rangle \equiv gV|a\rangle \quad (45)$$

Thus the G_{aa} of (43) is very similar to the simple form (11) obtained previously. It must be emphasized that our formal development has not in any way fixed $|a\rangle$ except through the identification of H_{aa} with ϵ'_a . This is evidently reasonable when ϵ_a is the relevant free adsorbate level. Further this identification also allows us to replace V'_{ak} by V_{ak} when (a) $\langle a|k\rangle$ is small or (b) $\epsilon_k \sim \epsilon$. Near resonance the important $|k\rangle$ states will be those for which condition (a) fails, but condition (b) holds.

We are not limited to this approximation. If the set $|k\rangle$ is taken to be complete, the term $\sum_k g_k |V'_{ak}|^2$ in the denominator of G_{aa} can be expanded, yielding after some trivial algebra

$$G_{aa} = g_{aa} + \frac{\langle a|a'\rangle^2}{V_{aa} - \sum_k g_k |V_{ak}|^2} \quad (46)$$

where V_{ak} without the prime is just the hopping integral. The term $\epsilon - \epsilon'_a$ has vanished entirely! Nevertheless, the possibility of a resonance in the band or of bound states outside remains, corresponding to the intersection of the horizontal line V_{aa} with Λ . Outside the band where $\Delta=0$ this is obvious. In the band the nature of the resonance can be seen by expanding $(V_{aa} - \Lambda)^2$ about the energy of intersection, ϵ_a'' . Then near ϵ_a'' $\text{Im } G_{aa}$ looks like

$$\frac{\text{Im}}{\pi} G_{aa} = \frac{\Delta/\pi}{(\epsilon - \epsilon_a'')^2 (\partial \Lambda / \partial \epsilon)_{\epsilon_a''}^2 + \Delta^2} \quad (47)$$

which is Lorentzian.

We can now see that the modified denominator $\epsilon - \epsilon'_a - \sum_k |V'_{ak}|^2 g_k$ plays the same role in determining chemisorption energies and all other relevant quantities as the simple G_{aa}^{-1} of (11) since its zeros and poles correspond to the ϵ_m and ϵ_k . The only slight modification occurs in the calculation of $\langle n \rangle$ where the numerator of (43) must be used. Despite this great similarity we will see that taking overcompleteness into account is worthwhile when it comes to calculating energy distributions in field and photoemission, where its neglect leads to difficulties.

Finally the explicit recognition of nonorthogonality removes a logical difficulty, namely the fact that chemical intuition tells us that bonding depends on overlap, and that matrix elements like V_{ak} can be approximated by $\langle V \rangle \langle a|k \rangle$.

At this point it is useful to summarize very briefly the physical content of the Hartree-Fock theory we have formulated. In essence we have considered bonding to involve hopping of electrons to and from the adsorbate and we have allowed two electrons (spin-up and spin-down) to occupy an adsorbate orbital simultaneously, so that an intra-adsorbate Coulomb repulsion U enters importantly into the resultant shift of the adsorbate level. By taking for U the experimental difference between ionization and affinity level the intra-atomic correlation is in fact taken into account perfectly, since we have allowed nature rather than a model to do the correlation for us. Nevertheless this may still be inadequate even if metal electron-adsorbate electron repulsion could be ignored. As already mentioned the condition of validity of our approach so far is that $\pi\Delta \geq U$. (For the case that localized states split off above and below the substrate band the separation between these takes the place of Δ in this inequality.) In the case of H adsorbed on transition metals U would seem to be $13.6 - 0.5 = 13.1$ eV, so that a $\Delta \geq 4$ eV would be required to make Hartree-Fock theory valid. In fact the effective U will be somewhat less because of the image interaction already discussed. In electron volt-angstrom units this reduces U by about $7.2/x$ eV. The true reduction will be less, not only because the classical image potential breaks down at small distances from the surface, but also because it is static. When electrons hop on and off the adsorbate rapidly the metal electrons may not adjust sufficiently fast to turn on the full static screening, so that the effective reduction in U will be less than our estimate. An exact calculation, however, would be very difficult and has not been attempted to my knowledge.

A final comment on LCAO-MO theories seems in order. For obvious reasons we wish to retain the concept of one-electron energy levels, that is, molecular orbitals, if at all possible, because of the ease of visualizing and dealing with them. In particular our discussion of field and photoemission would be very difficult to couch in other terms. We shall encounter

situations in which a simpleminded adherence to integrals over ρ_a would indicate many more electrons on the adsorbate than can in fact be reconciled with reasonable adsorbate charges. The difficulty once again is the correct definition of $|a\rangle$. Simple LCAO-MO models for small molecules suffer from the same difficulty: We know that bonding electrons spend much of their time between rather than on atoms, but cannot easily take account of this with a very restricted basis set. Thus integrals like $(\text{Im}/\pi)G_{aa}(\epsilon)$ give the correct number of electrons in $|a\rangle$ but it would be naive to equate this with the number *on* the adsorbate A.

B. Valence-Bond (Schrieffer-Paulson-Gomer) Approach^{11,12}

We have seen from the foregoing that the validity of the LCAO-MO approach in Hartree-Fock approximation is limited to broad resonances, small U , or localized states straddling the substrate band. The basic problem is to take proper account of the kind of correlation which results from electrons hopping off the adsorbate into the metal. In principle this can be handled in LCAO-MO by including configuration interaction or by more sophisticated definitions of $|a\rangle$. A different approach is to exaggerate correlation from the beginning by setting up the analogue of a valence-bond (VB) wave function. It is well known that the LCAO-MO method exaggerates ionic contributions, while the Heitler-London function omits ionic terms altogether. Thus the latter approach has (excessive) correlation built into it. In the valence-bond approximation it is customary to consider only electron pair bonds, the spin singlet leading to bonding because of the symmetric space part of the wave function. This is not an ironclad rule but arises in most cases from quantitative considerations, that is, the actual magnitudes of the Coulomb and exchange integrals. While HeH is not stable, either in the MO or valence-bond schemes, He_2^+ is bonding in both. If the requirement for the electron pair bond is waived, the VB approximation becomes largely equivalent to the LCAO-MO scheme with postulated infinite U , which can be treated more or less along the lines outlined in the preceding section. If we insist, however, on the importance of spin pairing, the substrate metal as it stands is not a suitable partner since, at ordinary temperatures, there are effectively no unpaired spins available. Consequently, it is necessary to create electron-hole pairs by promoting electrons above the Fermi energy in order to create free spins which can then pair with the adsorbate spin to form a valence bond. One may think of the adsorbate spin as inducing spin in the substrate. This process would cost energy, of course, were it not that the attendant bond formation leads to a net lowering.

A quantitative formulation of this theory¹² is a rather difficult many-body problem, and considerably beyond the scope of this review. Since the

basic approach abandons the concept of one-electron energy levels, the theory is also difficult to couch in the language of local densities of state. Very qualitatively, a level spectroscopy should indicate some disturbance in the substrate densities near ϵ_F and should show an electron on the adsorbate near ϵ_a . In the tight-binding case, where the VB method also predicts a local state below the band, this quasi-one-electron level could be shifted below ϵ_a of the free atoms.

C. Linear Response (Kohn-Smith-Ying) Method

An entirely different approach to chemisorption applied to date only to hydrogen has been taken by Kohn and his co-workers.¹³ In this method a bare proton is allowed to embed itself in the electron gas at a metal surface in such a way as to minimize the total energy. The resultant charge density is automatically self-consistent. In essence the method is an elaboration of linear response, and thus of the Fermi-Thomas approach and takes correlation into account somewhat empirically. Although the calculated binding energy (relative to H^+ and M^-) is not very good, the method deals rather effectively with the charge density at and near the adsorbate and thus explains observed dipole moments rather well. In principle, the self-consistent potential which results can be used to calculate quasi-one-electron energy levels, and thus a local density of states could be extracted (for energies near ϵ_F —the quasiparticle lifetimes are too short for meaningful results far from ϵ_F), although this has not yet been done. In principle the method is extendible to other cases, although actual calculations will undoubtedly be very difficult.

III. THEORY OF ENERGY DISTRIBUTIONS IN FIELD EMISSION

In this section we show how field emission measurements can provide information on the electronic structure of adsorption complexes. The notion that resonance tunneling through adsorbates should yield information of this kind was first proposed by Duke and Alferieff¹⁴ in 1968. More recently Duke and Fauchier¹⁵ have elaborated this by considering the substrate in Kronig-Penney approximation, with the adsorbate represented by a potential of different strength. Tunneling through a barrier containing impurities has also been considered by Hurault¹⁶ and Modinos.¹⁷ An attempt to consider the chemisorption case explicitly was made by Gadzuk¹⁸ in 1970, but suffered from the defect that the coupling of the adsorbate to the substrate was treated as if coming exclusively from the applied field used in field emission. A more quantitative calculation which ignored the problem of overcompleteness was made by Penn, Gomer, and Cohen.¹⁹ This calculation had the advantage of being applicable to a more general

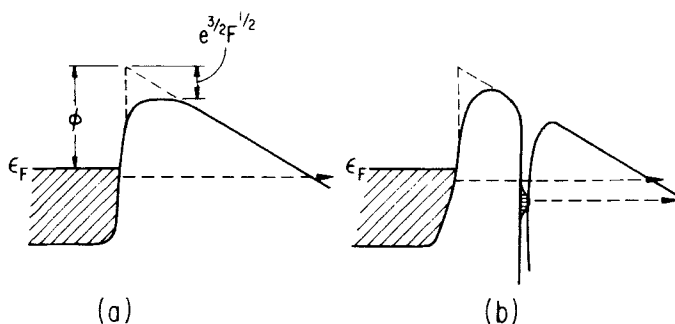


Fig. 3. Schematic potential diagrams illustrating field emissions (a) in the absence and (b) in the presence of an adsorbate. Diagram (a) indicates the reduction in barrier height arising from the image potential.

case than Hartree-Fock, but the neglect of overcompleteness led to difficulties in the energy dependence of the wave function component representing an electron on A. This dependence had to be adjusted arbitrarily. Recently Penn²⁰ has overcome this difficulty by a formalism very similar to that which is presented here. The present treatment is largely based on that of Penn, but while less rigorous has the advantage of great simplicity. The field emission problem has also been treated by Caroli et al.²¹

A. Field Emission

We review here briefly the fundamentals of field emission from a metal.^{22,23} In the presence of an applied field electrons in the metal see a potential barrier of finite width as well as height and consequently can tunnel (Fig. 3a). The probability of tunneling is given in WKB approximation by

$$D(\epsilon_x) \cong \exp\left(-2 \int k'_x dx\right) \quad (48)$$

where

$$k'_x = \left(\frac{2m_e}{\hbar^2}\right)^{1/2} [V(x) - \epsilon_x]^{1/2} \quad (49)$$

in the classically forbidden region and the integral extends over the classical turning points as shown in Fig. 3. For a triangular barrier D becomes

$$D \cong \exp\left[\frac{-(4/3)(2m_e/\hbar^2)^{1/2}(-\omega_x)^{3/2}}{Fe}\right] = \exp\left[\frac{-6.8 \times 10^7(-\omega_x)^{3/2}}{F}\right] \quad (50)$$

where ω_x is the energy in the tunneling direction, measured from the vacuum level, and F is the applied field. For $-\omega$ in electron volts and F in electron volts per centimeter the coefficients have the value shown. The total emitted current density for a "free electron" metal can be found very simply by multiplying the penetration coefficient D by a supply function, expressed in terms of the forward energy ϵ_x , and integrating over the conduction band. Since we are not particularly interested in the forward energy distributions we state only the result (for low temperatures), which is the familiar Fowler-Nordheim equation:

$$i = 6.2 \times 10^6 \left(\frac{\epsilon_F}{\phi} \right)^{1/2} (\epsilon_F + \phi)^{-1} F^2 \exp \left[\frac{-6.8 \times 10^7 \phi^{3/2}}{F} \right] \quad (51)$$

As expected the barrier height seen by electrons with $\epsilon_x = \epsilon_F$ dominates, so that the emitted current depends on the work function ϕ . Largely for this reason the Fowler-Nordheim equation gives reasonably good values of ϕ even in cases where the energy distribution differs appreciably from the simple free electron model we have discussed so far. It should also be pointed out that the equation, although strictly valid only for 0°K, is a good approximation to room temperature and above since the number of electrons with energies greater than ϵ_F is then still quite small.

Since the potential at a metal surface does not rise abruptly, but can be represented to a reasonable approximation by a classical image potential, the actual barrier shape is rounded and decreased (Fig. 3a). The resultant image correction can be taken into account by multiplying the exponent in (50) by a term $v(y)$ which is a slowly varying function²² of the quantity $y = (e^3 F)^{1/2} / |\omega| = 3.8 \times 10^{-4} F^{1/2} / |\omega|$ for F in volts per centimeter and ω in electron volts. A reasonable correction to the Fowler-Nordheim equation can then be obtained by multiplying the exponent in (49) by $v(y_0)$ where $y_0 = 3.8 \times 10^{-4} F^{1/2} / \phi$. $v(y)$ is almost a linear function of F :

$$v(y) = s(y) - c(y)F \quad (52)$$

where $c(y)$ and $s(y)$ are very slowly varying functions of y . Thus the $1/F$ term of the Fowler-Nordheim exponent is multiplied by $s(y_0)$ rather than by $v(y_0)$. Values of $v(y)$ and $s(y)$ are shown in Table I.

B. Total Energy Distribution

Although we subsequently derive the energy distribution equations in a more general way, the a priori use of the WKB barrier penetration coefficient leads to a very simple explicit result of considerable usefulness, and we start with this approach. The derivation given here is that of Stratton.²⁴

TABLE I
Values of the Functions $v(y)$, $s(y)$, $t(y)$

y	$v(y)$	$t(y)$	$s(y)$
0	1.0000	1.0000	1.0000
0.1	0.9817	1.0036	0.9981
0.2	0.9370	1.0111	0.9926
0.3	0.8718	1.0207	0.9835
0.4	0.7888	1.0319	0.9711
0.5	0.6900	1.0439	0.9554
0.6	0.5768	1.0565	0.9366
0.7	0.4504	1.0697	0.9149
0.8	0.3117	1.0832	0.8903
0.9	0.1613	1.0969	0.8630
1.0	0	1.1107	0.8330

The velocity in the tunneling direction, v_x , of an electron with total energy ϵ , measured from the bottom of the band, is

$$v_x = \frac{\partial \epsilon}{\partial p_x} \quad (53)$$

where $p_x = m_e v_x$ so that the total energy distribution is

$$j_0(\epsilon) d\epsilon = f(\epsilon) \int_{\epsilon}^{\epsilon + \epsilon_m} \frac{2}{h^3} D(\epsilon_x) \frac{\partial \epsilon}{\partial p_x} dp_x dp_y dp_z$$

$$= \frac{2}{h^3} f(\epsilon) D(\epsilon_x) d\epsilon dp_y dp_z \quad (54)$$

where $f(\epsilon)$ is the Fermi-Dirac function $[1 + e^{(\epsilon - \epsilon_F)/kT}]^{-1}$. Transforming to polar coordinates φ and p_{yz} in the p_y, p_z plane yields, after letting $p_{yz}^2/2m \equiv \epsilon_t$,

$$j_0(\epsilon) = \frac{4\pi m}{h^3} f(\epsilon) \frac{1}{2\pi} \int_0^{2\pi} d\varphi \int_0^{\epsilon_m(\epsilon, \varphi)} D(\epsilon - \epsilon_t) d\epsilon_t \quad (55)$$

where $\epsilon_x = \epsilon - \epsilon_t$ and ϵ_m is the maximum transverse kinetic energy for a given polar angle. For spherical constant energy surfaces ϵ_m would be independent of angle and given by ϵ . By writing the integral over ϵ_t in two parts, the first running from 0 to ϵ and the second, subtracted from the first, from ϵ_m to ϵ and changing the variable of integration from ϵ_t to ϵ_x ,

one obtains

$$j_0(\epsilon) = \frac{4\pi m_e}{h^3} \left[\int_0^\epsilon D(\epsilon_x) d\epsilon_x - \frac{1}{2\pi} \int_0^{2\pi} d\varphi \int_0^{\epsilon - \epsilon_m} D(\epsilon_x) d\epsilon_x \right] \quad (56)$$

Unless the energy surfaces have extremely peculiar shapes ϵ_m will not differ very much from ϵ and consequently the second term in (56) will be negligible because D decreases so rapidly with decreasing ϵ_x . Thus we are left with a very straightforward expression, first derived by R. Young²⁵ on the basis of a free electron gas.

The integral over ϵ_x can be carried out by a Taylor's expansion to first order of $v(y)|\omega_x|^{3/2}$ about the total energy $|\omega|$. Writing $v(\omega)$ for $v(y(\omega))$ and $v(\omega_x)$ for $v(y(\omega_x))$

$$\begin{aligned} v(y)|\omega_x|^{3/2} &\cong v(\omega)|\omega|^{3/2} + (|\omega_x| - |\omega|) \left[\frac{\partial(v(\omega)|\omega|^{3/2})}{\partial\omega} \right]_{|\omega|} \\ &= v(\omega)|\omega|^{3/2} + \left(\frac{3}{2}\right)|\omega|^{1/2}t(\omega)(|\omega_x| - |\omega|) \end{aligned} \quad (57)$$

where $t(y(\omega))$ is defined as $t(y) = v(y) - (\frac{2}{3})y(dv/dy)$; $t(y)$ is a slowly varying function of y whose value is close to unity²² (Table I). Thus the first integral in (54) becomes trivial and, neglecting the second integral,

$$j_0(\epsilon) \cong \frac{8\pi m}{3b|\omega|^{1/2}h^3} e^{-b|\omega|^{3/2}v(\omega)} \quad (58)$$

where $b = 6.8 \times 10^7 / F$. If ω lies near $\omega_F = -\phi$, we can further expand about ϕ and obtain

$$j_0(\epsilon) = \frac{8\pi m e^{-b\phi^{3/2}v(y_0)} f(\epsilon)}{3b\phi^{1/2}h^3} e^{\epsilon'/d} \quad (59)$$

where $\epsilon' \leq 0$ is the energy measured from the Fermi level, and

$$\frac{1}{d} = \frac{3}{2} b \phi^{1/2} t(y_0) \quad (60)$$

With this version, the distribution can be normalized in terms of the total current since

$$i = \int_{-\infty}^0 j_0(\epsilon') d\epsilon' \quad (61)$$

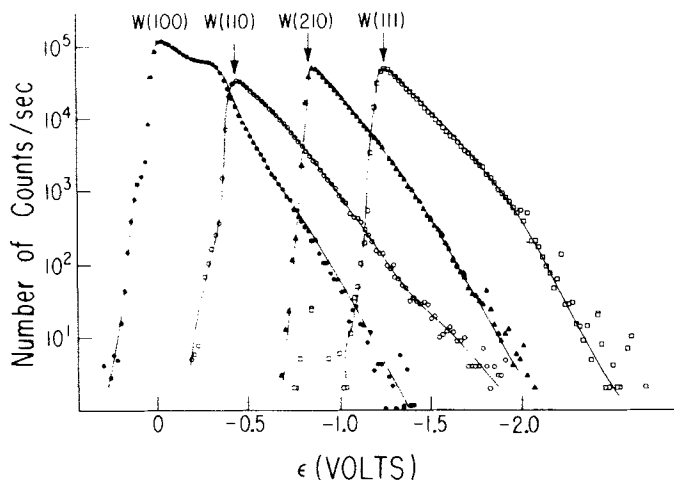


Fig. 4. Total energy distributions in field emission from several planes of clean tungsten.⁵⁵

Thus we finally arrive at

$$j_0(\epsilon') = \frac{i}{d} f(\epsilon) e^{\epsilon'/d} \quad (62)$$

which is the form of Young's original derivation.²⁵

It will be noted that this expression does not contain the density of metal states at all. In the approximation we have used this comes about because we have multiplied a velocity by a density of states to obtain a flux arriving at the surface. Since the velocity is proportional to $\text{grad}_p E$ while the density of states is proportional to $1/\text{grad}_p E$ the density of states does not appear in the final result. Experimental energy distributions from clean metal surfaces do show some structure, however (Fig. 4), and Penn²⁶ has recently shown how this can be explained by a more exact calculation.

It was pointed out by Young²⁷ that energy distributions obeying (59) can be used to determine work functions of single-crystal planes without explicit knowledge of the field-voltage proportionality factor, which will vary slightly from plane to plane on a real field emitter, because of its geometry. Since the slope S_{FN} of a $\ln i/V^2$ versus $1/V$ plot is, from (49),

$$S_{FN} = \frac{6.8 \times 10^7 \phi^{3/2} s(y)}{k} \quad (63)$$

where $k = F/V$ and since the slope of a plot of $\ln(\epsilon')$ versus ϵ' , obeying

(59), yields $1/d$ in the form

$$d = \frac{\frac{2}{3} (6.8 \times 10^7)^{-1} kV}{\phi^{1/2} t(y)} \quad (64)$$

we see that

$$S_{\text{FN}} \cdot d = \frac{2}{3} V \frac{s(y)}{t(y)} \phi \approx \frac{2}{3} V \phi \quad (65)$$

ignoring image terms so that ϕ can be obtained. Plummer²⁸ has recently shown that it is possible to obtain work functions by a generalization of this procedure, despite the structure in the energy distributions.

C. Transfer Hamiltonian

In order to proceed we now formulate the tunneling probability by what is essentially a perturbation treatment, in terms of the transfer Hamiltonian. While the result looks exactly like the "golden rule" formula, the method avoids the logical difficulty inherent in perturbation theory for energy-conserving transitions to a continuum: The initial and final state functions extend, in the presence of the applied field, over all space and thus cannot be normalized, except by fiat, that is, by confining the initial function to the metal and the final state function to the region outside of it. The transfer Hamiltonian method legalizes this by defining a Hamiltonian for the left-hand system (namely the metal) $H_L = T + V_{(m)}$ and a Hamiltonian for the right-hand system $H_R = T - F_{\text{ex}}$ where T is the kinetic energy, $V_{(m)}$ is the metal potential, and F is the applied field. Both Hamiltonians extend over all space. At $t \leq 0$ an electron in the metal is in an eigenfunction of H_L , φ_L . When the field is turned on at $t = 0$ transitions occur to a state closely describable as an eigenstate of H_R , so that we may write, for $t \geq 0$,

$$\varphi = a(t) \varphi_L e^{-i\epsilon_L t/\hbar} + b(t) \varphi_R e^{-i\epsilon_R t/\hbar} \quad (66)$$

with $a(0) = 1, b(0) = 0$. A development entirely analogous to that of standard time-dependent perturbation theory then shows that the probability per unit time of making transitions from left to right, P_{LR} , is given by

$$P_{LR} = \sum_{\epsilon_R} \frac{2\pi}{\hbar} |\langle \varphi_R | H - \epsilon_L | \varphi_L \rangle|^2 \delta(\epsilon_L - \epsilon_R) \quad (67)$$

Since $H_L \varphi_L = E_L \varphi_L$ we may replace $H - \epsilon_L$ by $H - H_L$ in the matrix

element of (67). But

$$H - H_L = -Fex\theta(x) \equiv \tau \quad (68)$$

where

$$\theta(x) = \begin{cases} 1 & x > 0 \\ 0 & x \leq 0 \end{cases} \quad (69)$$

if H is the total Hamiltonian of the metal in the presence of an external applied field. Consequently

$$P_{LR} = \sum_R \frac{2\pi}{\hbar} |\langle \varphi_R | \tau | \varphi_L \rangle|^2 \delta(\epsilon_L - \epsilon_R) \quad (70)$$

The density in energy of the emitted current, $j_0(\epsilon)$, is obtained by summing over initial metal states k at energy ϵ , and multiplying by the Fermi function $f(\epsilon)$ to ensure that only filled states contribute. Then

$$j_0(\epsilon) = \frac{2\pi}{\hbar} f(\epsilon) \sum_k \sum_R |\langle \varphi_k | \tau | \varphi_R \rangle|^2 \delta(\epsilon - \epsilon_R) \delta(\epsilon - \epsilon_k) \quad (71)$$

a result we could have written down immediately, if less justifiedly, from Fermi's "golden rule."

In order to evaluate expression (71) Airy functions must be used for $\varphi_R(x)$. If plane-wave functions are used for the components of φ_L and φ_R parallel to the surface, the conservation of parallel momentum occurs automatically through factors of the form $e^{i(k_{\parallel L} - k_{\parallel R})\rho}$ (where $\rho^2 = y^2 + z^2$) so that total energy conservation also requires conservation of energy in the tunneling direction.* The final result turn out to be²⁶

$$j_0(\epsilon) = \frac{2\hbar}{m_e} f(\epsilon) \sum_k D(\epsilon_x) N^2(\epsilon_k) \delta(\epsilon - \epsilon_k) \quad (72)$$

where $D(\epsilon_x)$ is the WKB barrier penetration coefficient, (55), and N a normalization constant for the metal wave functions. If WKB wave func-

* In this connection the following point must be noted. It has been stated by Gadzuk²⁹ that tunneling will not occur from metal states describable by p or d orbitals so oriented relative to the surface as to expose lobes of opposite sign parallel to the surface since the matrix element in (68) would vanish because of symmetry. It is perfectly true that metal states of this kind will not couple to plane-wave final states of $k_{\parallel} = 0$ since this would violate angular momentum conservation about the x direction. (The metal states of such symmetry amount to states with $m \neq 0$.) However, the final state functions can always be expanded in $m \neq 0$ states, and coupling to final state functions conserving angular momentum will occur. However, the fact that $k_{\parallel} \neq 0$ reduces ϵ_x for given total ϵ , and hence decreases the tunneling probability.

tions are used, $N^2 \propto \epsilon_x^{1/2}$. Writing $\delta(\epsilon - \epsilon_k)$ as $\delta(\epsilon - \epsilon_x - \epsilon_{\parallel})$ and summing over $k_x = (2m\epsilon_x/\hbar)^{1/2}$ leaves a sum over k but multiplies the result by a one-dimensional density of states which is proportional to $\epsilon_x^{-1/2}$. The result is that $j_0(\epsilon)$ reduces to the previous result, (59), which does not contain the density of metal states

$$j_0(\epsilon) = \frac{2}{\hbar} \sum_{k_{\parallel}} D \left(\frac{\epsilon - \hbar^2 k_{\parallel}^2}{2m_e} \right) \quad (73)$$

In general the potential near the classical turning point on the metal side of the barrier changes quite rapidly and the WKB approximation may be inadequate in the metal. It can then be shown²⁶ that (70) becomes

$$j_0(\epsilon) = \sum_k D(\epsilon_x) |\varphi_k(x_0)|^2 \delta(\epsilon - \epsilon_k) \quad (74)$$

Since the steep dependence of D on ϵ_x selects out states with k_{\parallel} very close to zero, $j_0(\epsilon)$ thus measures to a reasonable approximation the one-dimensional density of states at the turning point. As pointed out by Penn and Plummer,²⁶ this can account for most of the structure observed in energy distributions from clean surfaces.

D. Energy Distribution in the Presence of Adsorbates

Our main interest in energy distributions comes from the fact that they can reveal information on the local density of states in adsorption. Qualitatively this becomes obvious from Fig. 3b. Electrons with appreciable amplitude at the adsorbate see a smaller tunneling barrier than electrons confined to the metal, and thus we would expect the energy distribution to mirror the local density of states at the adsorbate. It is not difficult to put the matter more quantitatively. We start by writing the density in energy in terms of true eigenvectors $|m\rangle$ of the metal adsorbate system, by adapting (71):

$$j(\epsilon) = \frac{2\pi}{\hbar} f(\epsilon) \sum_{m,f} |\langle m|\tau|f\rangle|^2 \delta(\epsilon - \epsilon_m) \delta(\epsilon - \epsilon_f) \quad (75)$$

where we have written $|f\rangle$ for final (free) states. Since $\delta(\epsilon - \epsilon_m) = \frac{\text{Im}}{\pi} G_{mm}$, we have

$$\begin{aligned} j(\epsilon) &= \text{Im} \left\{ \frac{2}{\hbar} f(\epsilon) \sum_{m,f} \langle f|\tau|m\rangle \langle m|G|m\rangle \langle m|\tau|f\rangle \delta(\epsilon - \epsilon_f) \right\} \\ &= \text{Im} \left\{ \left(\frac{2}{\hbar} \right) f(\epsilon) \sum_f \langle f|\tau G \tau|f\rangle \delta(\epsilon - \epsilon_f) \right\} \end{aligned} \quad (76)$$

We now insert the complete sets of metal states $|k\rangle$ and $|k'\rangle$ on both sides of G and obtain

$$j(\epsilon) = \text{Im} \left\{ \frac{2}{\hbar} f(\epsilon) \sum_{k,k'} \langle f|\tau|k\rangle G_{k,k'} \langle k'|\tau|f\rangle \delta(\epsilon - \epsilon_f) \right\} \quad (77)$$

We now insert for $G_{kk'}$ expression (39) and obtain after extracting $|k\rangle$, $|k'\rangle$

$$j(\epsilon) \cong \text{Im} \left\{ \frac{2}{\hbar} f(\epsilon) \sum_{k,f} \left[g_k |\langle f|\tau|k\rangle|^2 + \frac{|\langle f|\tau|a'\rangle|^2}{\epsilon - \epsilon'_a - \sum_k g_k |V'_{ak}|^2} \right] \delta(\epsilon - \epsilon_f) \right\} \quad (78)$$

The first term in the brackets is just $j_0(\epsilon)$. The second term represents tunneling from a fictitious state $|a'\rangle$, weighted by the factor

$$\text{Im} \left(\epsilon - \epsilon'_a - \sum_k g_k |V'_{ak}|^2 \right)^{-1} = \frac{\Delta'}{(\epsilon - \epsilon'_a - \Lambda')^2 + \Delta'^2} \quad (79)$$

where Λ' and Δ' have the significance already discussed. Thus

$$\frac{j-j_0}{j_0} \cong \frac{\Delta j}{j_0} = \left(\frac{1}{j_0} \right) \left(\frac{2}{\hbar} \right) f(\epsilon) \sum_f |\langle f|\tau|a'\rangle|^2 \delta(\epsilon - \epsilon_f) \frac{\Delta'^2}{(\epsilon - \epsilon'_a)^2 + \Delta'^2} \quad (80)$$

The state $|a'\rangle = gV|a\rangle$ looks somewhat like a Lippman-Schwinger function. Its significance is that it represents $|a\rangle$ with its asymptotic energy dependence fixed up to correspond to the particular ω for which $j(\omega)$ is being found, that is, $|a'\rangle \rightarrow \exp[-(2m_e/\hbar^2)^{1/2}(-\omega)^{1/2}r]$. This can be seen by transforming to a coordinate representation so that

$$\varphi_a(r) = \int d^3x' g_\omega(x, x') V(x') \varphi_a(x') \quad (81)$$

Since

$$g_\omega(x, x') \cong \frac{e^{-k'|\mathbf{x}-\mathbf{x}'|}}{|\mathbf{x}-\mathbf{x}'|} \quad (82)$$

with $k' = (2m|\omega|/\hbar^2)^{1/2}$ the asymptotic r dependence becomes plausible. A more detailed calculation³⁰ shows that this is in fact the case for various bounded potentials. The reason we emphasize this point can be seen from Fig. 3b. An electron with energy $-\omega$ must have a wave function whose asymptotic form is

$$\varphi_\omega(r) \rightarrow \exp - \left(\frac{2m}{\hbar^2} \right)^{1/2} (-\omega)^{1/2} r \quad (83)$$

On the other hand, the asymptotic form of $\varphi_a(r)$ is that of (83) with ω replaced by ω_a . If this were the correct form to use for tunneling, the enhancement would be incorrectly given, except in the immediate energy vicinity of ϵ_a . In the original work of Penn, Gomer, and Cohen,¹⁹ which neglected overcompleteness, the current energy dependence had to be inserted arbitrarily, whereas it comes out quite naturally in the present approach.

Up to this point we have replaced $\langle a|Vg$ by $\langle a'|$ which would be correct if g were real. In fact g has a small imaginary part, which can be neglected near resonance, since, at the adsorbate, $|m\rangle \approx |a\rangle$ so that

$$(\epsilon - H_{(m)} - V)|a\rangle \approx 0 \quad \text{for } x > 0 \quad (84)$$

or

$$|a\rangle \approx \frac{1}{\epsilon - H_{(m)}} V|a\rangle = gV|a\rangle \equiv |a'\rangle \quad (85)$$

Far from resonance, however, the imaginary part of g can introduce structure into the numerator of Δj , and contains the possibility of introducing negative terms, thus producing antiresonances. While the present method includes in principle the structure of Δj at and off resonance it is probably simpler to treat the problem far from resonance by a formally different approach, namely that of Duke and Alferieff.¹⁴ In this approach we consider an electron far from resonance to be just a metal electron which can tunnel through the potential provided (self-consistently) by the adsorbate and its population of electrons. This problem is tractable once an appropriate potential is known; in practice one proceeds the other way; that is, one tries to fit experimental distributions by strength parameters for the potential.

At the risk of belaboring this point, it should be reemphasized that the choice of $|a\rangle$ is quite arbitrary. In a recent paper Penn²⁰ has opted to let $|a\rangle$ be the eigenfunction of the total Hamiltonian at energy ϵ for $x > 0$, that is, to let $|a\rangle$ represent not a single state but a quasicontinuum. With this choice the proper energy dependence is assured automatically, but as previously noted, the term $\epsilon - \epsilon'_a$ in the denominator of G_{aa} vanishes, so that the poles of G_{aa} must now appear as zeros in the self-energy, $\Sigma_k g_k V'_{ak}$.² While Penn's definition of $|a\rangle$ makes this possible, the present treatment is considerably more transparent and directly applicable to chemisorption calculations.

The final step in evaluating $\Delta j/j_0$ consists of finding the matrix elements for tunneling from the adsorbate state $|a'\rangle$ which is approximated in first order by an s -like state, normalized over the region of the atom, with the

exponential r dependence already discussed. The result is $R(\epsilon) \equiv \Delta j/j_0$

$$R(\omega) = 4\pi^2 r_a^2 n_a W_m \frac{(5.12 \times 10^7 / F) |\omega|^{5/2} [1 + (5.12 \times 10^7 \pi |\omega|^{3/2} / F)^{1/2}]^2}{(|\omega| + W_m)^{1/2} [1 + (5.12 \times 10^7 |\omega|^{3/2} / \pi F)^{1/2}]} \\ \times \exp \left[2(2m/\hbar)^{1/2} |\omega|^{1/2} x_a - (4/3)(2m/\hbar)^{1/2} |\omega|^{3/2} (1 - v(\omega)) / F \right] \\ \times \text{Im}(G_{aa} - g_{aa}) \quad (86)$$

where n_a is the adsorbate density in particles/cm², r_a the adsorbate radius, W_m the metal band width, (in eV), F the applied field in volts/cm, and ω the energy measured from the vacuum level, (in eV). x_a is the metal-adsorbate distance $v(\omega)$ an image correction, $v = 3.8 \cdot 10^{-4} F^{1/2} / |\omega|$. The term $\exp[2(2m/\hbar)^{1/2} (-\omega)^{1/2} x_a]$ in (86) has a simple physical interpretation: It is the ratio of barrier penetration coefficients for an electron on the adsorbate and an electron of the same energy in the metal, assuming a triangular barrier. This can be seen qualitatively by comparing the exponents for the two cases: For the full barrier we have $\exp(-b|\omega|^{3/2})$ while for the barrier seen at the adsorbate we have $\exp[-b(|\omega| - x_a F)^{3/2}]$ where $b = (\frac{4}{3})(2m/\hbar^2)^{1/2} F$. Expansion of $(|\omega| - x_a F)^{3/2}$ then gives the desired ratio. The second exponential term can now be understood as well. Since the image correction is most important near the metal surface, it reduces the effective barrier for a metal electron more than for an electron at the adsorbate. A rough estimate is simply the ratio of image-uncorrected to image-corrected current density for the clean metal:

$$\sim \exp \left[\frac{-6.8 \times 10^7 |\omega|^{3/2}}{F} (1 - v(\omega)) \right]. \quad (87)$$

Plots of enhancement factors for $F = 0.3$ volt/Å and various values of x_a are shown in Fig. 5.

The final result of our considerations so far then is that $\Delta j/j_0$ is proportional to the local density of states at the adsorbate, although the energy-dependent factors in (86) may modulate and thus distort ρ_a to some extent.

A shift in the resonances, relative to the field-free case, is also produced by the fact that ϵ_a is shifted by the applied field. In first order this can be taken into account by including a term $-Fex_a$ in ϵ'_a . Unfortunately the exponential dependence of field-emitted current on $1/F$ makes it difficult

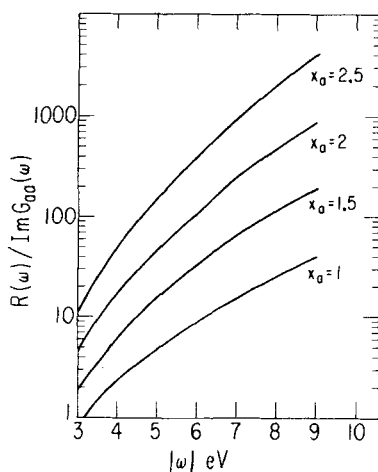


Fig. 5. Enhancement factors, based on Eq (86), for various values of x_a (in Angstrom) and for $F = 3 \times 10^7$ volts/cm, as function of energy ω .

to exploit this effect, since the experimentally accessible range of fields is quite small.

IV. EXPERIMENTAL CONSIDERATIONS

So far our discussion has been purely theoretical and it is time we turned to a discussion of the actual methods of obtaining energy distributions. We start with a very brief review of the field emission microscope, invented by E. W. Müller in 1937.^{22,23}

A. Field Emission Microscope

The dominant term in the Fowler-Nordheim equation, (49), governing field-emitted current, is $\exp(-6.8 \times 10^7 \phi^{3/2}/F)$ if ϕ is expressed in electron volts and F in electron volts per centimeter. Since $\phi = 4$ to 5 eV for most metals, it is easily seen that fields of the order of about 3×10^7 V/cm are needed for appreciable emission. A simple method obtaining fields of this magnitude (and greater) consists of etching a small wire to a sharp point. It is not difficult to obtain radii of curvature of the order of 10^{-5} cm or less; in the case of refractory metals cleaning by flashing to high temperatures is possible and leads, without excessive blunting, to hemispheroidal caps on conical or cylindrical shanks. The field at the apex of such structures is of the order²³ of

$$F \sim \frac{V}{5r_t} \quad (88)$$

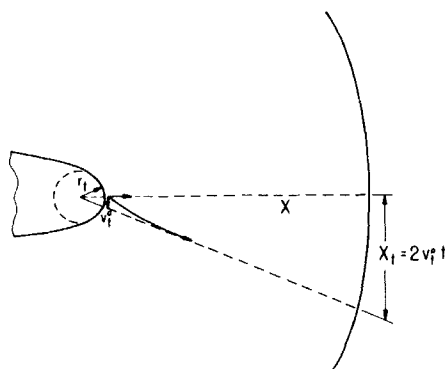


Fig. 6. Schematic diagram illustrating electron trajectories in the field emission microscope. r_t tip radius; x tip to screen distance; v_t transverse velocity at tip of emerging electron; x_t transverse displacement at screen resulting from v_t ; t time of flight. Magnification would be x/r_t if there were no compression of trajectories by the emitter shank.

where r_t is the tip radius, and thus very modest voltages suffice to produce the required fields. If a diode is constructed by surrounding the emitter by a hemispherical, conducting fluorescent screen, a field emission microscope results: Since electrons after tunneling have essentially no kinetic energy to start with, they follow, at least initially, the lines of force, which diverge from the emitter (Fig. 6). To a first approximation the magnification is thus given by the ratio l/r_t . The presence of the shank compresses the electron beam (without destroying axial symmetry) by a factor of $\beta \sim 1.5$, but this is not important. Thus one obtains a highly magnified emission map of the emitter cap where the field is sufficiently high for appreciable emission. For the usual emitter geometries this confines emission to a cone of half-angle of about 50° .

In general the emitter is etched from a polycrystalline wire. However, the tip is almost always much smaller than the grains composing the wire, so that it is part of a single crystal. The emitting region thus is hemispheroidal, exposing a few flat facets corresponding to the lowest energy planes, which blend smoothly into curved regions of varying orientation. Since different crystal planes have different work functions, the magnified pattern will show emission anisotropy which corresponds to the crystal symmetry. It is thus possible to index the emitter from the symmetry of the pattern.

Electrons arriving at the fluorescent screen have very short de Broglie wave lengths, and consequently diffraction plays little role in determining resolution, which depends primarily on the transverse velocity spread of emitted electrons. Since we are dealing with a Fermi gas, which can be

considered in first approximation to be at 0°K, the maximum allowed transverse energy for given ϵ_x is $\epsilon_F - \epsilon_x$. It turns out that the average transverse energy is $\frac{4}{9} (\epsilon_F - \epsilon_x)$ for given ϵ_x . Now the average forward energy $\langle \epsilon_x \rangle$ can be shown to decrease linearly with increasing field F , since a thinning of the barrier allows electrons of relatively lower ϵ_x to tunnel. Consequently, the average transverse momentum of escaping electrons increases as $F^{1/2}$. The time of flight t of electrons, on the other hand, is proportional to $V^{-1/2}$, V being the applied potential. Since $F = kV$ and since the lateral displacement of an electron on the screen turns out to be $2v_t t$ the resolution δ is independent of applied field. A more detailed calculation²³ shows that

$$\delta \cong 2.62 \times 10^{-4} \beta \left(\frac{r_t}{5\phi^{1/2}} \right)^{1/2} \text{ cm} \quad (89)$$

For emitter radii of 1000 Å δ is thus of the order of 30 Å.

A final point of considerable importance to us needs to be made. To a good approximation the emitter-anode configuration corresponds to a concentric spherical condenser, and thus the potential distribution to that of a central force law. Consequently, angular momentum about an origin at the center of the emitter is conserved. This means that the transverse velocity of an electron at a macroscopic distance r from the emitter is vanishingly small, being given by

$$v_t(r) = \frac{r_t}{r} v_t(r_t) \quad (90)$$

Thus the forces acting on an electron in flight rapidly throw it along a radius vector, and all its energy is converted, by the time it arrives at the screen or a collector, into forward energy. Thus for ordinary tip-collector geometries only the total, not the forward energy (referred to the emitter), can be measured. (Angular momentum conservation is also responsible for the fact that transverse displacement at the screen is $2v_t t$ rather than $v_t t$, as might at first be expected.²³)

B. Energy Analyzers

The high magnification of the field emission microscope and the fact that the emitter is a single crystal make it possible to analyze the emission from a small region of the emitter, corresponding to a portion of an individual crystal plane, by permitting a fraction of the beam to pass through a small hole in the first anode, that is, the screen, for further analysis. The first analyzers yielding reliable results were those of Müller

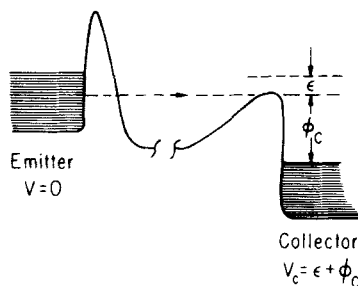


Fig. 7a. Schematic potential diagram illustrating the principle of a retardation analyzer for field emitted electrons. ϵ is the range of energy (relative to Fermi level) that is collected, ϕ_c is the collector work function and V_c is the collector bias.

and Young,³¹ and were of the retarding type. The principle of such an analyzer can be understood from Fig. 7. Electrons emitted from the tip are decelerated and allowed to impinge on a collector or equivalently to pass through a retarding mesh into a collector. The potential of the collector (or retarder) relative to the emitter determines the energy of electrons that can reach the collector and thus contribute to the collector current. At zero bias the Fermi levels of collector and emitter are equal. When the collector is made positive by an amount just equal to its own work function ϕ_c , electrons at or above the emitter Fermi level can just be collected. As the collector is made more positive electrons of lower energy will reach it. The fact that the collector rather than the emitter work function is relevant in a retardation experiment can be utilized to measure ϕ_c quite accurately.³² The first derivative of collector current with respect to bias voltage then yields the distribution. The differentiation can be carried out electronically

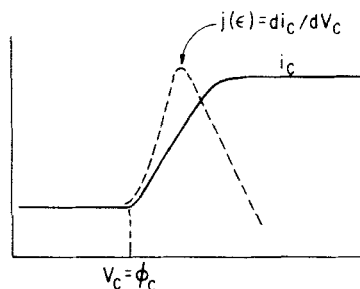


Fig. 7b. Collector current and its first derivative as functions of collector voltage V_c . Current will just be collected when $V_c = \phi_c$.

by modulating the collector bias with a small sinusoidal ac component of low frequency.

Ideally electron trajectories should be orthogonal to the retarder (or collector) surface since the resolution will be given by

$$\frac{\Delta E}{E} = \cos^2 \theta \quad (91)$$

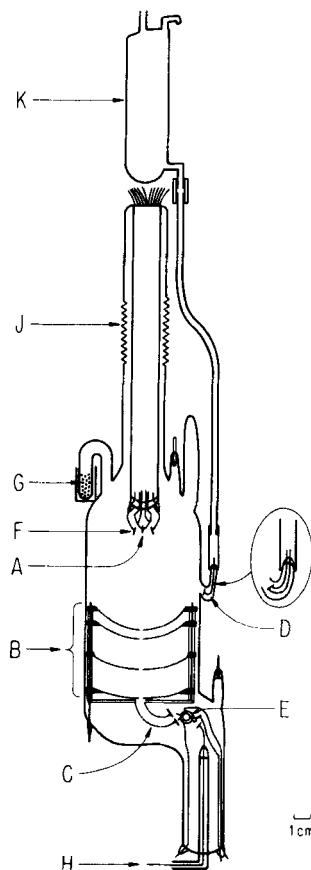


Fig. 8. Schematic diagram of differential field emission analyzer tube for use in a cryostat. *A* tip assembly; *B* concentric spherical shell electrodes; *C* 127° cylindrical electrostatic deflection velocity analyzer; *D* sublimation source; *E* channeltron electron multiplier; *F* steering electrodes (only one pair shown); *G* molecular sieve to getter H_2 released by channeltron or to facilitate source loading; *H* shielded current lead; *J* bellows for emitter positioning; *K* liquid H_2 reservoir for loading sublimation source.

θ being the angle of incidence. The trick then is to design lens systems which come close to fulfilling this requirement. A number of designs^{32,34,35} have proved quite successful, as attested by the fact that resolutions of 20 to 30 mV have been achieved for primary energies of 1 to 2 kV.

In recent designs^{33,35} conventional or channeltron electron multipliers are used for detection, and electrostatic steering of the beam is used. The former feature vastly increases the sensitivity and makes it possible to use much lower total currents, especially for probing low-emission planes. Electrostatic steering is achieved by two pairs of deflecting electrodes near the tip (Fig. 8): the potentials of a given pair are $V_{\text{anode}} \pm V_{\text{steering}}$. The steering voltages are appropriately adjusted to place a given portion of the emission pattern over the probe hole. To ensure paraxiality the entire tip assembly must be adjusted by means of a flexible bellows arrangement.

We have not gone into much detail here because retardation analyzers are of limited usefulness in field emission and have been superseded by differential types. The need for differential analyzers in field emission was first recognized by Plummer and Kuyatt³⁶ who also built the first differential type. Retardation analyzers are limited by the fact that $j(\epsilon')$ is such a steeply decreasing exponential function of ϵ' , that almost the entire current will have been collected by the time $\epsilon' = 0.5$ eV. Consequently shot noise makes it impossible to probe lower energies. This difficulty can be overcome up to a point by differential analyzers, which collect only electrons in a narrow energy range $d\epsilon'$ at ϵ' at any one setting. The limitation on the depth of the Fermi sea that can be probed now arises from the unavoidable presence of secondary or scattered electrons spuriously entering the collector. If 0.1% of electrons at $\epsilon' = 0$ (ϵ_F) wind up somehow at $\epsilon' = 2$ eV, they will swamp the true signal at this energy by a factor of about 10^2 . Consequently even differential analyzers are limited to probing five to six orders of magnitude in current. Depending on the work function of the region probed, this corresponds to an energy range of 2 to 4 eV below the Fermi level. Thus field emission is directly competitive with photons of about 8 eV energy. While this limited range is its chief drawback, the method remains highly attractive for a number of reasons: (1) It has very high resolution; (2) a number of different crystal planes can be examined under identical conditions without the need of preparing different specimens; (3) it is often much easier to obtain clean, nearly perfect surfaces on field emitters than on macroscopic substrates; and (4) the dependence of energy distributions from clean surfaces on bulk density of states, and other bulk properties of the substrate, is much less than in photoemission, and thus effects arising from adsorption show up more clearly.

The elements of a differential analyzer consist of emitter, screen, a lens system to retard and focus the beam onto the analyzer, the analyzer itself,

and a detector. In Plummer and Kuyatt's design³⁶ a cylindrical lens system was used to focus the electron beam onto an electrostatic velocity analyzer consisting of concentric spherical shells. Electrons of correct energy pass through the exit slit and are counted by a multiplier. A design employed in our laboratory (Fig. 8) uses a set of concentric spherical shells to retard the beam, which is focused by the last electrode onto a small 127° cylindrical electrostatic deflection analyzer. Electrons emerging from the exit slit are counted by a channeltron. The entire apparatus is mounted in a glass envelope small enough to fit into a 10-cm-diameter liquid H₂ cryostat, for reasons which are discussed shortly.

In order to maintain constant dispersion the potential difference between the analyzer plates is kept constant and the midpoint of this potential is varied relative to the emitter. By setting the analyzer to let about 0.2-eV electrons pass, the modest resolution of the analyzer itself (~10%) leads to an overall resolution of about 20 mV.

Both in Plummer's system and in that used in our laboratory data are acquired and stored electronically. We employ a Nova 1200 minicomputer to set analyzer voltage, store the counts received, proceed to the next analyzer setting, and so on. A preset energy range can be swept as often and as rapidly as desired, and the results can be disgorged on a storage oscilloscope, paper tape, or printed on an *x-y* recorder. Since a given distribution usually comprises 10⁴ datum points, this is a considerable convenience. Obviously further processing of the data is possible with the computer. For instance, background noise can be subtracted, the distribution can be integrated to obtain total current, and so on.

In any adsorption experiment it is necessary to clean the substrate and to maintain it free from contamination. Field emitters made from refractory metals can be cleaned by flashing to high temperature; contamination is prevented by ensuring adequate vacuum. This can be done by using conventional baked glass or metal ultrahigh vacuum systems. The latter have the advantage of greater flexibility, the former perhaps of simplicity. There is another route to ultrahigh vacuum,^{23,37} namely cooling to liquid H₂ temperature, where the vapor pressures of most gases are negligible. The real point of this procedure is that it makes measurements at controllable partial coverages relatively easy. In a typical experiment the apparatus is sealed off containing several torrs of the adsorbate gas. The latter is then condensed on a small heatable Pt platform (Fig. 8) by cooling the latter with liquid H₂ before the rest of the apparatus. When condensation is complete, the entire apparatus is cooled and ultrahigh vacuum established. It is now possible to heat the platform (sublimation source) electrically and to obtain very reproducible gas doses. Gas not striking the emitter on the first pass is condensed on the walls. By maintaining

effectively infinite pumping speed the relative coverage on the emitter surface can thus be controlled far more accurately than by conventional methods. A further advantage is the fact that for many adsorption systems binding modes are quite temperature sensitive so that cooling of the substrate to at least 77°K would be necessary in any case. Since thermal changes constitute an interesting aspect of chemisorption studies, provision must be made for controlling the emitter temperature. This can be accomplished by mounting it on a loop of its own material, equipped with potential leads. Resistive heating of the loop and temperature control can be achieved by a variety of servomechanisms.²³

V. PHOTOEMISSION

Although this article is primarily intended to present field emission spectroscopy, the theory of photoemission from adsorbate-covered surfaces is related to that of field emission and the two methods complement each other so much that a brief discussion of photoemission must be included. The method has long been and continues to be used for the study of the bulk density of states of solids³⁸; as higher energies become available through synchrotron radiation and discrete X-ray sources the probing is going deeper and deeper in energy. We confine ourselves here to a brief discussion only of the surface aspects, and more specifically of applications to adsorption. Much of the recent work in this area has been carried out by Eastman,³⁹ Plummer,⁴⁰ and Spicer.⁴¹ The principle of the method is quite straightforward. If monochromatic photons of energy $h\nu$ are absorbed by a solid, the photoelectron energy distribution mirrors the electron distribution in the states from which excitation occurred (Fig. 9). While photons penetrate fairly deeply into the bulk, the escape depth of electrons⁴² in the 20 to 40 eV energy range is 5 to 20 Å so that emission comes mostly from the surface and near-surface region. While transitions in the bulk must (probably!)⁴³ conserve crystal momentum, no such restrictions seem necessary for electrons that are excited directly into the vacuum. Moreover for such transitions the density of the final (free) states is the usual free electron one, so that emission from the surface should mirror the local density of the initial states, rather than a joint density of initial and final bulk states. For sufficiently high final-state energies ($\epsilon_F \geq \epsilon_F + 10$ eV) the final-state band structure seems to be sufficiently free-electron-like in most cases so that even for bulk emission the initial density of states seems to be mirrored, if $h\nu \geq 20$ eV.

By arguments entirely analogous to those used to arrive at the field emission distribution in the presence of adsorbates one obtains⁴⁴

$$j - j_0 = \frac{2}{\hbar} \sum_f \delta(\epsilon - \epsilon_f) |\langle f | \mathbf{A} \cdot \mathbf{p} | a' \rangle|^2 \left(\frac{\Delta'^2}{(\epsilon - \epsilon_a'')^2 + \Delta'^2} \right) \quad (92)$$

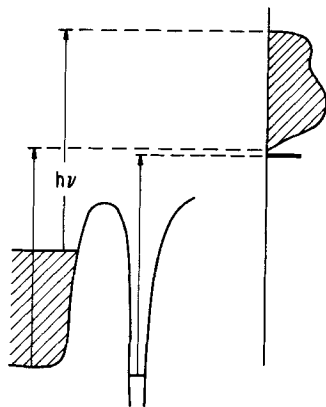


Fig. 9. Schematic diagram illustrating the principle of photoemission spectroscopy.

where A is the vector potential of the incident radiation.

The surface photoemission requires electrons to be accelerated normal to the surface,⁴⁵ so that the radiation must have a component of the electric field vector normal to the surface, that is, must *not* have normal incidence.

An extension of photoemission spectroscopy from the far ultraviolet to the X-ray range, commonly known as ESCA, is also capable in principle of giving information on the electronic structure of the bonding electrons. In practice, its generally lower resolution and high energy make it most suitable for probing the core states of adsorbates. Since these are subject to chemical shifts, which in turn are largely caused by electrostatic environment, that is, by the charge density at the adsorbate, ESCA can supply much useful information, if somewhat more indirectly. A discussion of the applications of ESCA to surface and adsorption problems is outside the scope of this article. The same applies to Auger spectroscopy and various inelastic electron loss techniques.

A. Experimental Aspects of Photoemission

The principal advantage of photo over field emission is the fact that it is possible to probe to lower energies. For surface work the He(I) resonance line at 21.2 eV is a convenient radiation source. Since the LiF cutoff lies at 11 eV, use of this line requires a windowless discharge tube.⁴⁶ In most arrangements a capillary discharge is separated from the substrate by differential pumping, the light path being provided by a number of aligned capillaries. In this way ultrahigh vacuum can be maintained in the sample chamber, even though the discharge tube pressure is 10 to 40 millitorrs. Energy analysis of the photoelectrons can proceed in a number of ways.

Since photoemission is not plagued by an exponential intensity drop with decreasing energy simple retardation analyzers⁴¹ can give very good results. Eastman³⁹ has used various differential analyzers, for instance double cylindrical mirrors. Plummer⁴⁰ has recently devised an ingenious arrangement, using a channel plate behind a spherical retardation analyzer to obtain the spatial as well as the energy distribution of photoelectrons.

Since surface photoemission seems to be mostly nondirect, there is not nearly as much need for varying photon energy as in the case of bulk studies. For fairly obvious reasons development has not been pushed very hard in the direction of continuously variable energy sources for surface work. Synchrotron radiation from electron accelerators coupled to vacuum monochromators provides one such source. The great technical difficulties of doing adsorption experiments in this way and the fact that only two such sources currently exist in the United States (the Stoughton storage ring in Wisconsin and SLAC at Stanford—until recently also the Cambridge Electron Accelerator) make these sources seem more useful for bulk work. In the relatively low energy region continuum discharges are also available. It is possible, however, to obtain some discrete energies in a discharge tube, either by changing the gas or the operating conditions. Thus the He(II) line at 40 eV can be obtained (with some difficulty) by lowering the gas pressure and increasing the discharge voltage, and 16.8-eV photons can be obtained by using Ne.

VI. FIELD AND PHOTOEMISSION DISTRIBUTIONS FROM SELECTED SYSTEMS

The thrust of this article is the study of chemisorption and we must omit discussion of a number of interesting observations and applications not directly connected to chemisorption. Some of these can be found in recent review articles by Gadzuk and Plummer³³ and Bell and Swanson.³² In the following we attempt to see what information has in fact been obtained for a number of adsorption systems.

A. Ba on W

The earliest study of adsorption was Plummer and Young's investigation of alkaline earth atoms on W and Mo substrates by means of a retardation analyzer.⁴⁷ Their results for Ba on the (111) and (103) planes of W are shown in Fig. 10 and seem to indicate a broad resonance and two small but sharp peaks slightly below ϵ_F . The positions of these narrow peaks correspond reasonably well to those of the free atom 3D and 1D states, respectively (corresponding to $5d^16s^2$ configurations), while the broad resonance can be associated with a broadened $6s$ level. Gadzuk and Plummer³³

speculate that the observed structure corresponds to promotion of a $6s$ electron to the $5d$ orbital. If one worries about self-consistency, this picture requires careful analysis. If the (broadened) $6s$ level, that is, the resonance arising from interaction of the Ba $6s$ level with the metal, lay wholly below ϵ_F , its average occupation would be 2 and the $5d$ level could not be seen by metal electrons because of the high U . In order for the $5d$ level to be available the average total occupation of Ba $6s$ must be at most one electron. This requires the $6s$ resonance to lie more than half-way above ϵ_F . This, however, is just what we would expect in the first place since all levels are pushed up by the image potential, as explained previously. It remains to ask why the $5d$ level, which is above $6s$ in the free atom, is not also pushed above the Fermi level by the image interaction. If the interpretation discussed here is correct, the implication is that the $5d$ level is pulled down by interaction with the metal, that is, $\Lambda' > V'_{im}$. Thus a consistent picture could be postulated in which a largely empty s resonance accounts for the net positive charge on adsorbed Ba, while most of the bonding comes from interaction of the d level with the metal. It should be emphasized that we are *not* speaking of configuration interaction, but are considering two sets of molecular orbitals, one with s character the other set having d character.

The issue is clouded somewhat by the fact that on Mo(110) the split between the small peaks is 0.1 eV rather than 0.3 eV as on W. It is possible that this corresponds to different shifting of the two D configurations, but this should also have been seen on different planes of W. In view of the

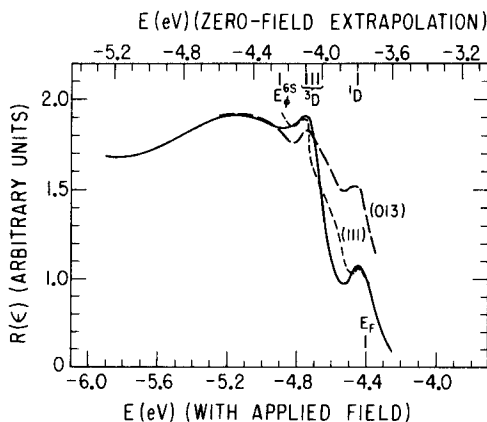


Fig. 10 Experimental enhancement factors $R(\epsilon)$ in field emission for Ba on two planes of tungsten, from Plummer and Young⁴⁷ (dashed curves), and a curve based on an interpretation by Gadzuk.³³

fact that the energy range probed was rather small, it is perhaps premature to speculate further until this system has been studied by a differential method.

However, this is as good a time as any to discuss some of the complications that may arise in field emission. An alternative explanation of the Plummer and Young Ba results is the following: Suppose that bonding involves in fact only the 6s level. When an electron tunnels out of this state the 5d "channel" opens momentarily and resonance tunneling through it can be observed. Note that this mechanism still requires the 5d level to be pulled below ϵ_F by interaction with the metal (unless it is postulated that the time between the tunneling of the first and second electron is less than that required to turn on the image interaction, which is unlikely). Yet another possibility is inelastic tunneling, as also pointed out by Gadzuk and Plummer.³³ This could consist of excitation of a Ba electron into a 5d level by an electron tunneling from the metal, followed by tunneling from the excited Ba. Since the primary event in these processes is proportional to emitted current, while the second step is also field dependent, the probability of these processes should be roughly proportional to i^2 . This dependence does not seem to have been investigated yet. Since 2-photon events at ordinary fluxes are negligible, the obvious way to distinguish between processes peculiar to field emission and those which truly reflect electron levels is to investigate the same system by photoemission spectroscopy. Unfortunately this has not yet been done for the alkaline earths on tungsten.

B. H₂ on W

Despite the possible complications of absorption rather than adsorption and of the possibility of molecular adsorption at high coverage, H atoms represent the simplest adsorbate, and the study of hydrogen adsorption is thus of considerable theoretical as well as practical interest. The adsorption of H on the (100) plane of W has been studied in field emission by Plummer and Bell⁴⁸ and photoemission by Plummer⁴⁰ and Eastman.³⁹ The salient findings are the following. Photoemission shows a peak centered 5.5 eV below ϵ_F , about 1.5 eV wide, which shifts upward by about 1 eV at high coverage.⁴⁰ The field emission results⁴⁸ indicate a peak about 1 eV wide at $\epsilon' = 1$ eV (Fig. 11). This peak builds in at a coverage of $\theta \sim 5 \times 10^{14}$ atoms/cm², weakens, and shifts upward toward the Fermi level with increasing θ and vanishes for $\theta > 10 \times 10^{14}$ atoms/cm². This peak has also been seen by Young and Gomer on the (102) plane. [There is also seen, in both field and photoemission, an effect which occurs on W(100) with all adsorbates, including inert gases,^{35,33} namely the quenching of the so called

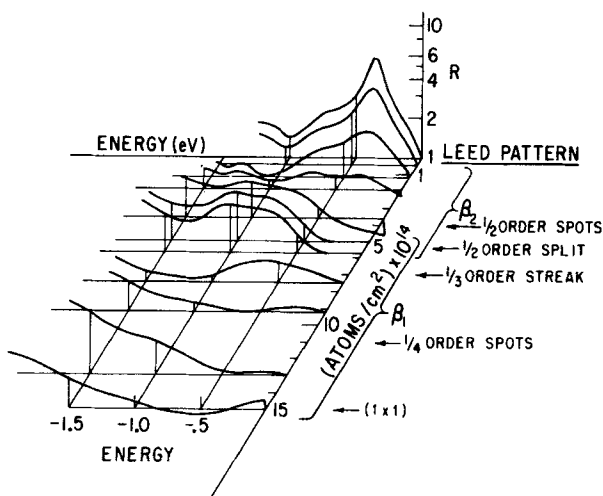


Fig. 11. Enhancement factors $R(\epsilon)$ for field emission from a hydrogen-covered (100) plane of tungsten. Hydrogen-atom densities and corresponding LEED patterns are shown on the right. From Plummer and Bell.⁴⁸

Swanson hump,³² a peak in the energy distribution at $\epsilon' = 0.35$ eV. This suggests that this peak is probably due to intrinsic surface states on (100).^{33,35]}

The absence of a broad resonance extending above ϵ_F and the peak at $\epsilon' = 5.5$ eV indicate that localized bonding occurs. At present it is impossible to determine whether this can be adequately described in the Hartree-Fock approximation. We now show that this certainly possible, and even not unreasonable. If the peak at $\epsilon' = 5.5$ eV corresponds to a state localized near the bottom of the d band, an empty, "antibonding" state must lie above it. In this situation the appropriate Δ' is the separation between bonding and antibonding levels, so that $\Delta' \geq 10$ eV. Thus $\pi\Delta$ would in fact exceed U which, as we have noted, is $13 - 2V'_{im}$ eV. On this basis the state at $\epsilon' = 5.5$ eV would correspond to ϵ_H'' . As we have seen for a neutral adsorbate in restricted Hartree-Fock approximation $\langle n\uparrow \rangle = \langle n\downarrow \rangle = 0.5$ and so $\epsilon_H' \cong \epsilon_H + U/2 \cong -13.5 + 7.5 = -6$ eV, relative to vacuum. Since $\epsilon_H'' = \epsilon_H' - \Delta'$ falls at -10.5 eV relative to vacuum [the work function of the (100) plane covered with H is ~ 5 eV] we conclude that $\Delta' \sim 4$ eV. An extremely rough estimate of the overlap integral β' can be made from the estimate of Δ' . It can be shown⁴ that

$$\int_{-\infty}^{\infty} \Delta'(\epsilon) d\epsilon = \pi n \beta'^2 \approx \Delta' \cdot l \quad (93)$$

where n is the number of substrate atoms directly bonding to one H atom and l the width of the d band. Taking $n=4$, $l=10$ eV, and $\Delta'=10$ eV we find $\beta'\sim 3$ eV. This is not an unreasonable value.

It is also possible of course that there is a single resonance at $\epsilon_F-5.5$ eV and no antibonding level (or resonance) above the d band. In that case the Hartree-Fock approximation would be inadequate, and a treatment like that of Schrieffer would become more appropriate. It is not clear, however, in the Schrieffer picture why a resonance should appear at ϵ_F-1 eV. If there were spin flipping excitations induced by the adsorbate, one would expect changes in the substrate density of states much closer to the Fermi level. The fact that this peak occurs on other planes as well indicates that it is not peculiar to the (100) face: it is probably a consequence of the shape of the $\Lambda(\epsilon)$ curve which leads to a resonance at this energy.

The shift in peak positions with coverage θ is also significant, since it probably corresponds to a change in the nature of binding with θ . While thermal desorption spectra,⁴⁹ LEED data,⁵⁰ and electron impact desorption⁵¹ show that different binding states exist for H on W(100), their nature has not been unequivocally established.

Plummer and Bell⁴⁸ have also attempted to investigate the vibrational spectra of adsorbed hydrogen and deuterium on tungsten by looking for inelastic tunneling, corresponding to vibrational losses. Since most tunneling comes from the vicinity of the Fermi level, and since it is reasonable to expect inelastic tunneling to involve most strongly the most energetic electrons, one might expect small bumps at $\epsilon_F-\nu$. It is known that a low-temperature high-coverage phase of hydrogen on the (111) plane of W is probably molecular.⁵² Plummer and Bell⁴⁸ were in fact able to see a loss peak at $\epsilon'=0.4$ eV for deuterium on (111) at 78°K and high θ , corresponding to the vibrational excitation of molecular D₂. On heating to 200°K this signal vanished, as expected. On (100) no molecular peaks were seen with D or H under any conditions, indicating the absence of molecular H₂ on that face. If correct, this is an interesting result, since a high-coverage phase of H on (100) desorbs with first-order kinetics⁴⁹; thus there is some possibility that it corresponds to H₂ adsorption.

C. Carbon Monoxide on Tungsten

This system is of great interest because it is one of the few known instances of nondissociative molecular adsorption. It has been investigated both by photo-emission and in field emission. The latter studies, despite their limited energy range, provide some interesting correlations with thermal and electron impact desorption studies. Baker and Eastman³⁹ have looked at the $\geq 300^\circ\text{K}$ phases on the (100) and (110) planes and

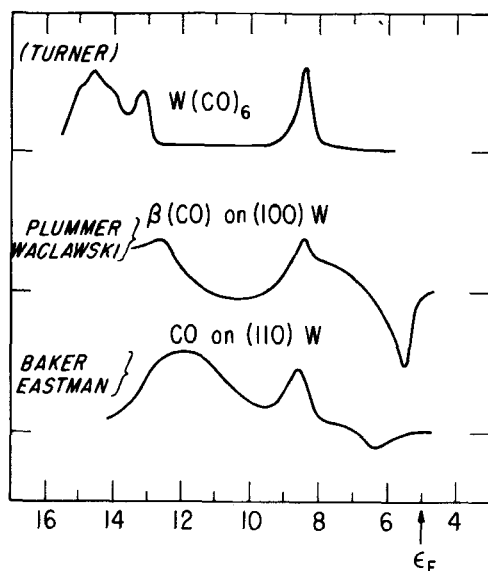


Fig. 12. Photoemission enhancements $j(\epsilon) - j_0(\epsilon)$ versus energy for gaseous $W(CO)_6$ (Turner⁵³), β -CO on (100) tungsten (Plummer and Waclawski⁴⁰), and CO on W (110) (at 300°K) (Baker and Eastman³⁹).

Plummer⁴⁰ has published data on the high-temperature phases on (100). In addition to possibly unresolved structures near ϵ_F and the customary suppression of the Swanson hump on (100) a peak at about -8.5 eV (below vacuum) is seen on both planes; in addition peaks at approximately -12 eV are also seen. Both these features bear striking resemblances to the main peaks seen in the gaseous tungsten hexacarbonyl electron emission spectrum⁵³ (Fig. 12).

While this is rather clear evidence of localized bonding, the similarity of the spectra on different planes and their similarity with the gas-phase carbonyl spectrum are in fact slightly disappointing. The reason is that $W(CO)_6$ is believed to bond mainly via a dative bond formed from the CO lone pair σ^2 orbital located on the C atom, with some π bonding involving the antibonding π^* -CO orbitals. While there is reason to believe that the low-temperature, "virgin" phase of CO on metallic W is bonded in this way, there is also evidence to show that the virgin phase transforms at temperatures ranging from 300 to 600°K (depending on the crystal plane) to other more tightly and complexly bound states. Some of these apparently involve bridge bonding via the C end or configurations in which both C and O bond; even dissociation has been postulated on (100).

Thus the photoemission results must be interpreted roughly as follows: The peak at -8.5 eV is probably largely due to an orbital involving mostly tungsten $5d-t_{2g}$ wave functions. The peak at -12 eV is probably due to bonding via $e_g 5d$ orbitals with either C or O; although this peak undergoes some changes with T , these are at present rather difficult to interpret. Plummer⁵⁴ has recently examined the photoemission spectra of C, O, and CO on (110) and (100). He concludes that on (100) the C and O spectra do add up to the CO spectrum, while on (110) they very nearly do. While this need not mean that β -CO is dissociated, it does indicate that both C and O bond to W simultaneously, that is, that CO is lying down, a conclusion reached previously from electron impact desorption and coverage data. It will be useful to obtain photoemission data on the low-temperature phases, both for comparison with the high-temperature data, and with the low T field emission results, which are described next. Young and Gomer⁵⁵ have examined in some detail the behavior of CO on the (110), (100), (111), and (102) planes of tungsten, using the apparatus and technique already referred to.

On the (110) plane a resonance peaking at $\epsilon' > 1$ (probably $\epsilon' \sim 2$ eV) was observed in the 20°K layer (Fig. 13). This showed little broadening with increasing coverage, but its intensity at first increased linearly to $\theta = 0.45$ and then dropped sharply, with the resonance gone entirely at $\theta = 0.7$ (Fig. 14). Heating a full low-temperature layer caused the resonance to reappear at 220°K. Further heating to 350°K caused its irreversible disappearance. Heating of a partial monolayer, $\theta = 0.4$, caused the resonance to disappear

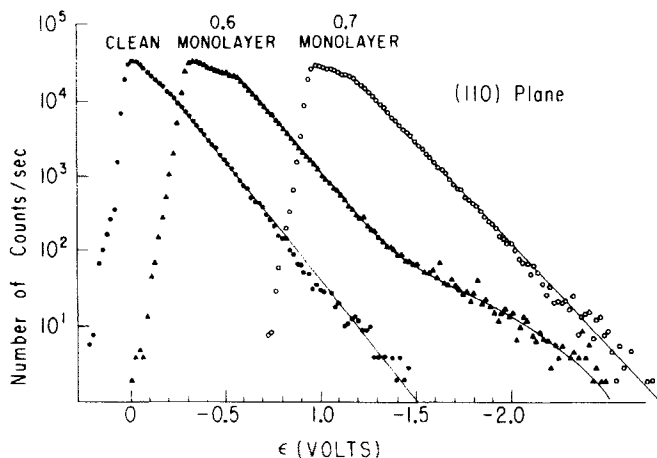


Fig. 13. Total energy distribution in field emission for virgin CO on (110) tungsten. Curves are displaced by arbitrary amounts; leading edges should coincide (Young and Gomer⁵⁵).

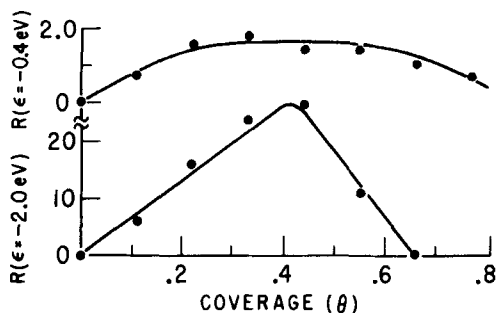


Fig. 14. Enhancements (at fixed energies) for the "shoulder" (upper curve) and main resonance (lower curve) in field emission from the (110) plane of tungsten as a function of virgin CO coverage, in arbitrary units relative to a monolayer (Young and Gomer⁵⁵). Absolute coverage at $\theta = 1$ is 1.56×10^{15} mol/cm², or CO/W = 1.1.⁵⁷

at 200°K. Redosing a layer heated to 400 to 600°K caused no particular changes; that is, no new resonance turned up.

In addition to this "main" resonance a shoulder in the distribution appeared at $\epsilon' = 0.2$ eV. Its width also varied with θ , but more or less symmetrically about $\theta = 0.5$ (Fig. 14). When a partial layer, $\theta = 0.3$, was heated to 100°K the resonance disappeared. At higher coverage, $\theta = 0.6$, the structure persisted to 350°K. Heating a full layer to 220°K brought the shoulder back, which then persisted to 350°K.

On the (120) plane a resonance centered at $\epsilon' = 2.7$ eV with a half-width at half-maximum of 0.47 eV occurred in the low-temperature layer (Fig. 15). Its intensity increased linearly with θ up to a monolayer. Heating caused its disappearance at 350°K. Redosing after heating a virgin layer to 350°K caused a strong resonance to reappear at $\epsilon' = 2.7$ eV. Similar behavior was found on the (123) plane.

On (111) a resonance centered at $\epsilon' = 2.5$ eV was found in the low-temperature layer (Fig. 16). Its intensity increased at first slowly, then more rapidly with coverage, then decreased and vanished at $\theta = 0.8$ (Fig. 17). Heating a full layer caused the resonance to reappear at 300°K and to persist to about 700°K (Fig. 18). Heating a partial layer, $\theta = 0.5$, caused irreversible disappearance of the resonance at 350°K. Redosing a virgin layer heated to 800°K again caused a resonance to appear at $\epsilon = 2.5$ eV (Fig. 16). The intensity of this peak was also coverage dependent (Fig. 17). Reheating a fully redosed, that is, alpha, layer caused the resonance to reappear at 100°K as shown in Fig. 18. It persisted to above 700°K.

On the (100) plane no resonance was observed in the low-temperature layer at any θ . As expected the Swanson hump disappeared for $\theta > 0.4$.

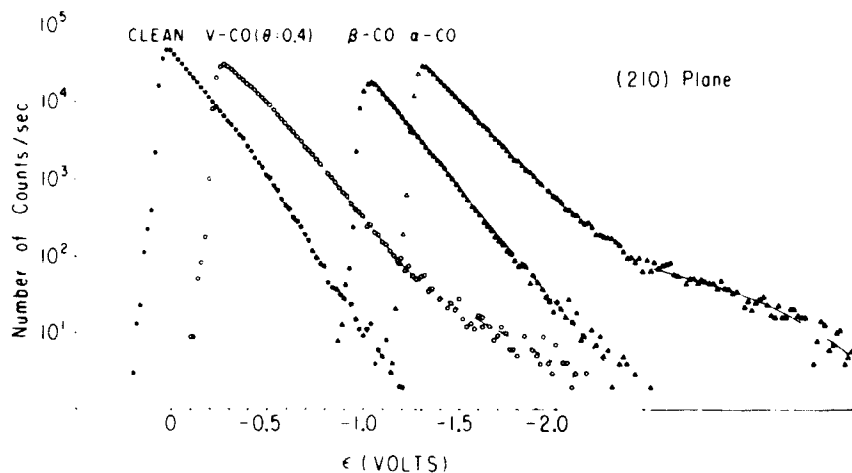


Fig. 15. Energy distributions in field emission from CO-covered W(210). Curves arbitrarily displaced; leading edges should coincide. β -CO: virgin layer heated to $T > 350^\circ\text{K}$; α -CO: β layer redosed at 20°K .

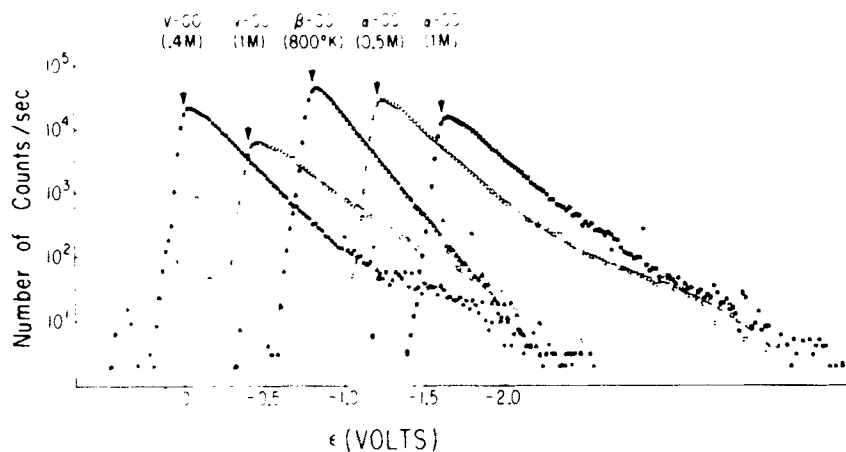


Fig. 16. Energy distributions in field emission from a tungsten (111) plane under various conditions of CO coverage and treatment. Coverages are indicated as fractional monolayers (M). Note the disappearance of the resonance in the virgin and α layers at (1M) (Young and Gomer⁵⁵).

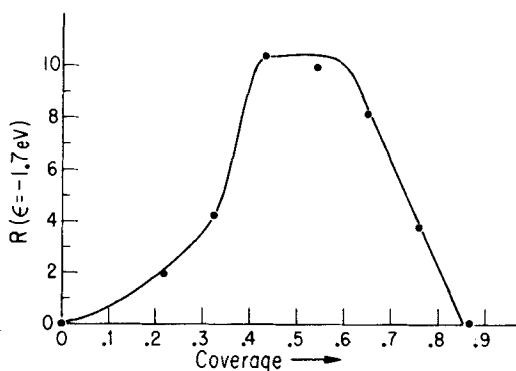


Fig. 17. Enhancement $R(\epsilon)$ for field emission (at fixed energy) on the (111) plane of tungsten as function of virgin CO coverage. Note the difference in shape from the analogous curve of Fig. 13 for (110) (Young and Gomer⁵⁵).

Heating a virgin layer produced a resonance at $\epsilon' = 2.0$ eV. This reached its maximum intensity after heating to 700°K (Fig. 19).

Before discussing the possible meaning of these results it is useful to summarize briefly the picture of CO adsorption which is emerging from thermal⁵⁵⁻⁵⁸ and electron impact desorption work.⁵⁹⁻⁶¹ While there seem to be quantitative differences from plane to plane many qualitative features seem to be preserved. Low-temperature adsorption leads to a rather weakly bound state ($H_a \sim 1$ eV) (virgin) for which the CO/W ratio, at least on

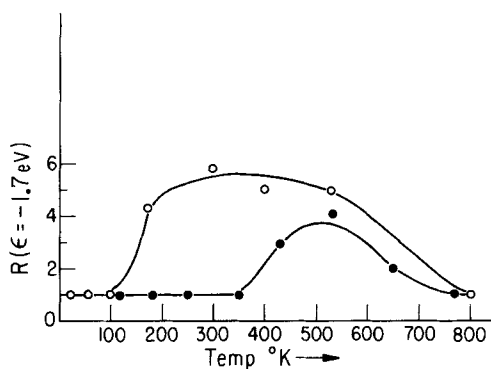


Fig. 18. Enhancement at fixed energy for CO on the (111) plane of tungsten as function of temperature for initially full monolayers. Open circles α -CO; full circles virgin layer (Young and Gomer⁵⁵).

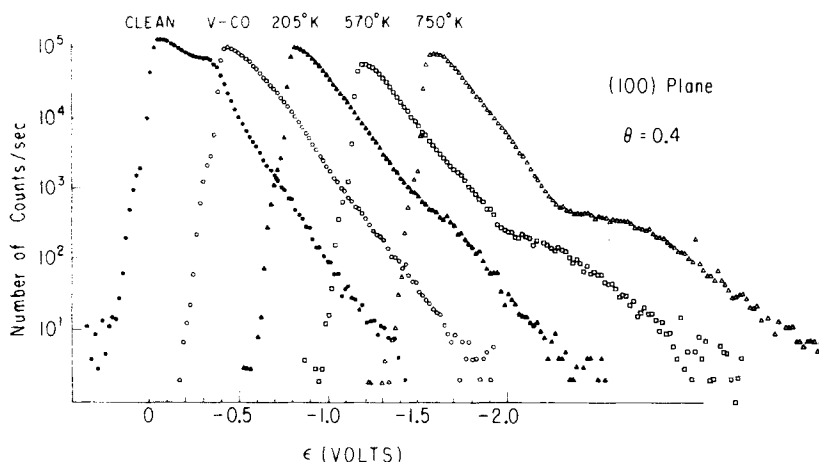


Fig. 19. Energy distributions in field emission from a CO-covered (100) plane, under various conditions of heating. Initial coverage of virgin layer $\theta = 0.4$. Curves arbitrarily displaced; leading edges should coincide (Young and Gomer⁵⁵).

(110), is about 1.1.⁵⁷ On heating to 400 to 600°K there is partial desorption and conversion of the remaining adsorbate to a more tightly bound state (beta, or beta precursor) for which $\text{CO}/\text{W} = 0.5$. Readsorption on a beta layer results in formation of a new state, alpha, such that $\alpha/\beta = 1$. The fact that a new state is created was first noticed from work function measurements.^{55,62} Virgin adsorption leads to an increase in ϕ , $\Delta\phi \sim 0.6$, 1 eV, depending on plane^{61,63}; in the beta layer $\Delta\phi$ is smaller, but still of the same sign. Alpha adsorption, on the other hand, leads to a decrease in ϕ relative to the beta layer, except on (110) where no change is observed.*⁶¹ Electron impact desorption data on (100) by Yates and King,⁵⁸ on polycrystalline W by Menzel,⁶⁰ and on (110) from our laboratory⁶¹ indicate that both virgin and alpha layers yield CO^+ as principal ionic desorption product. It is found, however, that the desorption cross-sections for α -CO differ from those of virgin CO on some planes.^{59,61} Heating a virgin layer

* Reference 63 reports work function measurements based on the Fowler-Nordheim equation. As was noted there the (110) plane acted anomalously. This behavior is now explained by the shoulder in the distribution. Consequently, the values for virgin and α -CO on (110) obtained in this way seem incorrect. The values reported here were obtained by a Kelvin vibrating condenser method⁶¹ and are therefore trustworthy. The measurements for other planes given in Ref. 63 have been confirmed⁵⁵ by use of (63). If the latter is applied to average slopes of energy distributions, it also gives results for (110) in agreement with the vibrating condenser measurements.

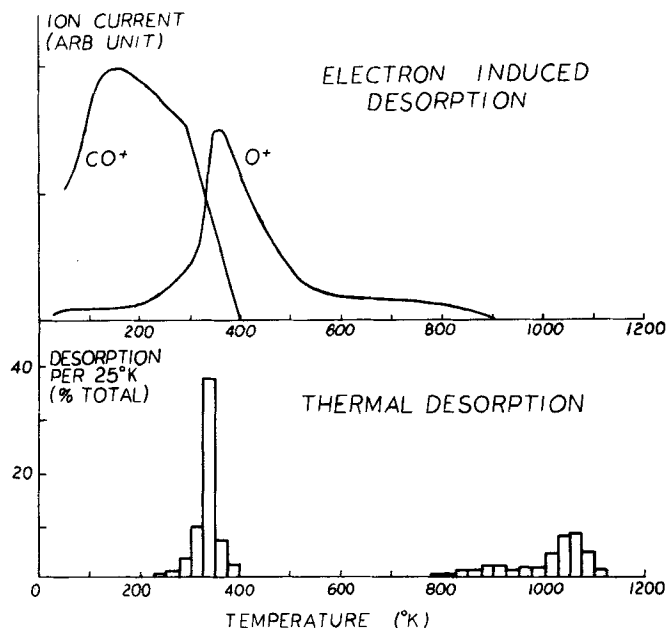


Fig. 20. Electron-induced and thermal step desorption spectra versus temperature for a full virgin CO layer on the (110) plane of tungsten.⁶¹

causes gradual disappearance of the CO^+ signal with a concomitant rise in O^+ (Fig. 20). The conversion from the CO^+ - to the O^+ -yielding species, on (110) for instance, is concomitant with virgin desorption (Fig. 20). Thus there is at least one precursor state to the high-temperature beta form; from the latter there is no appreciable electron impact desorption. The O^+ -yielding species in turn disappears on heating before thermal beta desorption sets in (Fig. 20).

While the details of this adsorption system are obviously very complex, it seems likely that virgin adsorption corresponds to bonding via the C end. Since CO^+ rather than O^+ is produced, since there is no activation energy of adsorption, and since the sticking coefficients are about 1, it seems likely that bonding to a single atom rather than bridge bonding is involved. Since the beta precursor state yielding O^+ still has almost the same dipole moment as the virgin state, we believe it to correspond to bridge bonding via carbon sp^2 orbitals to two W atoms, at least on (110). In this configuration, the surface coverage on (110) can still be $\text{CO}/\text{W}=1$. As desorption proceeds and space becomes available, this state converts to the beta

mode. The very small cross-sections for electron desorption from the beta state indicate that this probably corresponds to a lying down mode, in which two virgin sites are filled by one CO. Beta adsorption could also involve major surface reconstruction, or possibly even dissociation, as suggested for (100) by King and Yates.⁵⁸ The fact that first-order desorption kinetics seem to hold rigorously on (110)⁵⁷ makes it unlikely that dissociation occurs on this plane (however, see page 252). On the (100) plane the situation may be even more complex, with a number of intermediate states⁵⁸ occurring. Detailed results for the other planes are lacking at the moment.

In this picture alpha states correspond to adsorption in the interstices of the beta, or beta precursor, layer. Depending on the plane, this may or may not involve bonding to single W atoms. On (110), for instance, our picture would indicate bonding between two W atoms (Fig. 21).

Let us next attempt to describe the electronic structure of virgin CO, assuming that it corresponds in fact to adsorption on single W atoms. By analogy to schemes proposed for the molecular hexacarbonyls⁶⁴ we write a level diagram for W-CO (Fig. 22). We have simplified matters slightly by ignoring the tungsten *s* electrons. We assume that the situation on a surface can be related to the scheme shown in Fig. 22 by some shifting and some broadening of the levels shown. It now becomes possible to identify the peak seen in photoemission [and in $W(CO)_6$] at -8.5 eV with the W-CO orbital labeled π_2 . We postulate that this orbital has largely tungsten $5d\ t_{2g}$ character and is therefore seen not only in virgin but also in other configurations. It should be added that it has not been seen yet in virgin CO adsorption because photoemission experiments are lacking and

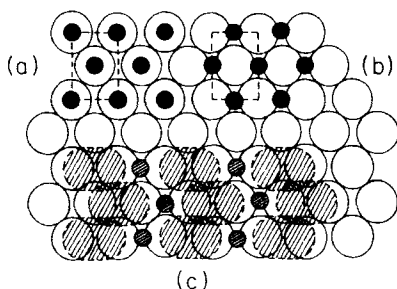


Fig. 21. Possible CO arrangements on the (110) plane of tungsten. (a) Adsorption upright on single W atoms; $CO/W=1$. (b) Bridge bonding between two W atoms; $CO/W=1$. (c) Large shaded objects represent van der Waals dimensions of CO "lying down," a probable configuration for β -CO; $CO/W=0.5$. Small circles represent additional sites on such a layer for upright adsorption, for example, α -CO, with $CO/W=0.5$. (From Kohrt and Gomer.⁵⁷)

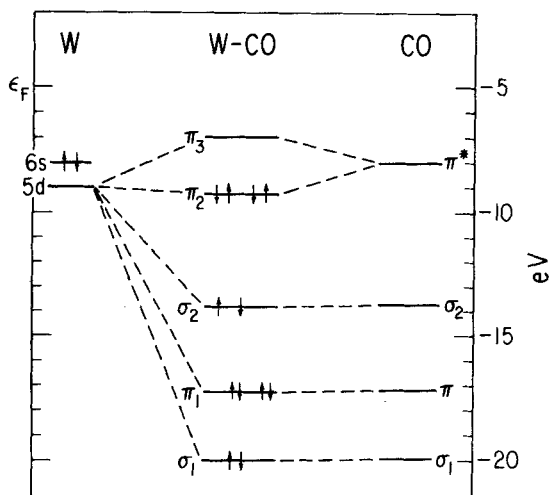


Fig. 22. Proposed energy level diagram for CO adsorbed on tungsten.

because the range of field emission distributions has not been pushed far enough below the Fermi level. It is hoped that both these situations will be remedied, however, and this writer at least is fairly confident that a level at -8.5 eV will be seen in virgin adsorption. The resonance at -7.9 to -7.5 eV, which is seen in field emission at $\epsilon' \sim 2$ to 2.5 eV, can now be explained if the orbital labeled π_3 in Fig. 22 is pulled below the Fermi level. This orbital would be expected to have largely CO- π^* character, and thus its presence or absence hinges sensitively on the CO configuration.

We are now able to interpret the main field emission results. First, the presence or absence of the resonance at $\epsilon' = 2.5$ eV has been postulated to correlate with (a) the existence of more or less unperturbed CO so that CO- π^* exists, and (b) the availability of suitable W t_{2g} orbitals for forming π_3 . We can thus conclude that the conversion of virgin to beta or beta precursor states involves sufficient rearrangement to kill this resonance, in agreement with the fact that its disappearance coincides with the disappearance of the CO $^+$ signal in electron impact desorption. Similarly, the reappearance of this resonance in alpha adsorption on some planes can be interpreted as single-site adsorption for α -CO on those planes. The structure of the (111) plane, for instance, makes it very plausible that this is the case there.

The absence of a resonance for virgin CO on (100) is most easily explained by assuming that adsorption occurs in the center of the unit mesh so that CO is recessed and partially shielded. The resonance at $\epsilon' \approx 2.0$ eV, seen on heating, seems similar to a peak produced also with

oxygen on heating, and may be due to surface reconstruction or to bonds having mainly tungsten character.

Perhaps the most interesting result of the field emission work is the coverage dependence of the resonances, which can be explained as follows. At high coverage, CO molecules come sufficiently near each other on some planes to cause spatial interference of the 3π orbitals either with each other or with π_2 orbitals (which are in effect π orbitals of CO). The resultant Pauli exclusion amounts to a strongly repulsive pseudopotential so that charge is squeezed out of the π_3 orbital. It is interesting to note that on the (110) plane, which is rather close packed, the peak intensity at first rises linearly to almost half-coverage. This indicates that incoming CO molecules, which can probably skitter over the surface for a small distance before becoming firmly adsorbed, are able to avoid each other. Above half-coverage each new addition makes contact with two already adsorbed molecules, thus accounting for the steep decrease in peak intensity. On the (102) plane, which consists of terraces of one unit cell of (110) and steps of one unit cell of (100), the (110)-like sites are sufficiently separated to prevent interference so that the intensity increases monotonically. On the (111) plane there are two types of adsorption sites (Fig. 23). If it is assumed that the recessed sites are filled first, and if it is further assumed, if only for geometric reasons, that the resonance intensity is less for recessed sites

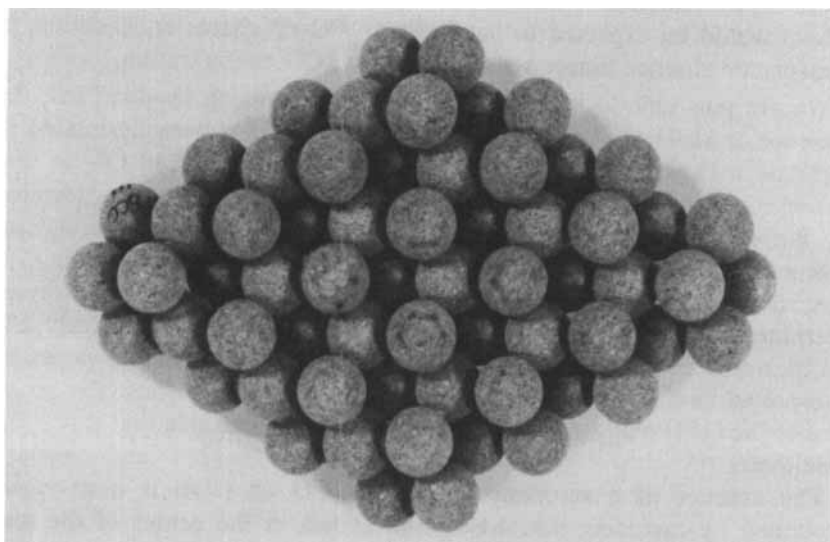


Fig. 23. Model of (111) plane of tungsten.

than for outermost ones in field emission, the shape of the intensity versus coverage curve on (111) is qualitatively explained. It should be noted that despite its open structure adsorption on (111) brings CO molecules into contact with at least three nearest CO neighbors at full coverage.

The reappearance of the resonances on heating full layers can be explained by the fact that some desorption from these will precede conversion to beta or beta precursor states; as θ is decreased, some remnant virgin CO molecules are freed from contact with other CO molecules (this could also occur by conversion to other states) and the resonance is restored. The fact that on partial layers resonances disappear at lower temperatures than on full layers is in agreement with thermal and electron impact desorption results which indicate that conversion to more tightly bound states occurs more easily and at lower temperature at partial coverage, where space for the conversion is more available.

Finally the shoulder observed near ϵ_F on the (110) plane deserves some discussion. The (110) plane is the most closely packed and highly symmetric one for a bcc lattice. It is therefore possible that a surface layer which destroys its symmetry could lead to an increase in the local density of tungsten states (of small $k_{||}$), for instance, by relaxing the requirement for admixing s and p to d orbitals in order to fulfill the symmetry requirements on clean (110), or a covered surface of identical symmetry. The behavior of the modulation with coverage and temperature points in this direction. At a low concentration of CO (low θ_{CO}) or of holes in the CO layer (high θ_{CO}) the intensity of the shoulder increases more or less linearly, while at intermediate coverages where a random CO layer would have little symmetry, the intensity is essentially independent of coverage. At sufficient temperature to cause rearrangement by surface diffusion the modulation vanishes, provided θ_{CO} is such that a more symmetric structure can be attained, but not otherwise. Thus it is likely that a change in ρ_k is involved here which is not directly related to chemisorption.

D. Other Systems

This article makes no pretense at discussing all the systems so far examined by field or photoemission. Nevertheless brief mention of some other studies must be made. As already mentioned Plummer⁵⁴ has compared the O, CO, and C photoemission spectra on W. Baker and Eastman³⁹ have examined photoemission from O, and NO on W, as well as H, CO, and N₂ on Ni. Their general conclusions are that most gases give very similar spectra on W while more striking differences show up on Ni. The explanation is very probably the following. It is known from a great deal of chemisorption work that much stronger chemisorption and more strongly differentiated binding states within a given system occur on bcc metals,

than on fcc metals. This is a consequence of the more open geometric structure of bcc surfaces. Thus the relatively high temperature states examined by Eastman correspond to very tightly bound, substrate-dominated configurations in which quantitative differences between different adsorbates are largely suppressed. For the weaker adsorption seen on fcc substrates the nature of the adsorbate probably plays a greater role in determining the observed densities of state.

Oxygen on tungsten has also been examined in field emission by Plummer.³³ Very complicated behavior occurs, indicating considerable changes in going from 78 to 300°K, and further changes at higher temperatures. The behavior varies from plane to plane, but has not yet been interpreted in detail.

VII. CONCLUSION

This article has attempted to convey some feeling for current thinking in chemisorption on metals and to describe two techniques of investigating the electronic structure of adsorption complexes. Very briefly, field emission has the advantage of high resolution and virtual freedom from bulk effects, so that adsorbate-caused effects stand out very clearly. Its chief disadvantage is the limited energy range, 2 to 4 eV below the Fermi energy, which can be probed. Photoemission has the advantage of effectively unlimited range, but as currently practiced has much lower, though still adequate resolution. Its chief drawback is that spectra from clean substrates have a great deal of structure so that the interpretation of the differences in spectra from clean and adsorbate-covered surfaces is more difficult. Despite their drawbacks both techniques and some other methods we have not had space to discuss are in the process of opening up an entirely new chapter in the understanding of chemisorption.

Acknowledgments

It is a pleasure to acknowledge many stimulating and valuable discussions with Drs. David Penn and Amitaba Bagchi. This work was supported by NSF Grant No. 32848.

References

1. H. D. Hagstrum, *Science*, **178**, 275 (1972).
2. A. Blandin and J. Friedel, *J. Phys. Radium*, **19**, 573 (1958), and previous papers.
3. P. W. Anderson, *Phys. Rev.* **124**, 41 (1961).
4. D. Newns, *Phys. Rev.* **178**, 1123 (1969).
5. T. B. Grimley, *Proc. Phys. Soc. (London)*, **90**, 751 (1967), and previous papers.
6. J. R. Schrieffer and D. C. Mattis, *Phys. Rev.*, **140**, 1412 (1965).
7. D. Penn, *Phys. Rev.* **B9**, 844 (1974).
8. A. Bagchi and M. H. Cohen, to be published.
9. P. W. Anderson and W. L. McMillan, *Scuola internazionale di fisica, Varenna, Italy*, W. Marshall, Ed., Academic Press, New York, 1967.

10. K. Terakura and J. Kanamori, *Prog. Theor. Phys.*, **46**, 1007 (1971), and previous papers.
11. J. R. Schrieffer and R. Gomer, *Surf. Sci.*, **25**, 315 (1971).
12. R. H. Paulson and J. R. Schrieffer, to be published.
13. J. R. Smith, S. C. Ying, and W. Kohn, *Phys. Rev. Lett.*, **30**, 610 (1973).
14. C. B. Duke and M. E. Alferieff, *J. Chem. Phys.*, **46**, 923 (1967).
15. C. B. Duke and J. Fauchier, *Surf. Sci.*, **32**, 175 (1972).
16. J. P. Hurault, *J. Phys.*, **32**, 421 (1971).
17. A. Modinos, *Surf. Sci.*, **22**, 473 (1970).
18. J. W. Gadzuk, *Phys. Rev.*, **B1**, 2110, (1970).
19. D. Penn, R. Gomer, and M. H. Cohen, *Phys. Rev.*, **B5**, 768 (1972).
20. D. Penn, *Phys. Rev.* **B9**, 839 (1974).
21. C. Caroli, D. Lederer, and D. St. James, *Surf. Sci.*, **33**, 228 (1972).
22. R. H. Good and E. W. Müller, *Handb. Phys.*, **21**, 176 (1956).
23. R. Gomer, *Field Emission and Field Ionization*, Harvard University, Press, Cambridge, 1961.
24. R. Stratton, *Phys. Rev.*, **135**, A794 (1964).
25. R. D. Young, *Phys. Rev.*, **113**, 110 (1959).
26. D. Penn and E. W. Plummer, *Phys. Rev.* **B9**, 1216 (1974).
27. R. D. Young and H. E. Clark, *Phys. Rev. Lett.*, **17**, 351 (1966).
28. E. W. Plummer, to be published.
29. J. W. Gadzuk, *Phys. Rev.*, **182**, 416 (1969).
30. A. Bagchi, D. Penn, and R. Gomer, *Surf. Sci.* **41**, 555 (1974).
31. R. D. Young and E. W. Müller, *Phys. Rev.*, **113**, 115 (1959).
32. L. W. Swanson and A. E. Bell, *Adv. Electron. Electron Phys.*, **32**, 193 (1973).
33. J. W. Gadzuk and E. W. Plummer, *Rev. Mod. Phys.*, **45**, 487 (1973).
34. A. van Oostrom, *Philips Res. Rep. Suppl.*, **11**, 102 (1966).
35. C. Lea and R. Gomer, *J. Chem. Phys.*, **54**, 3349 (1971).
36. C. E. Kuyatt and E. W. Plummer, *Rev. Sci. Instrum.*, **43**, 108 (1972).
37. R. Gomer, *Vacuum*, **22**, 521 (1972).
38. N. V. Smith, *CRC Crit. Rev. Solid-State Sci.*, **2**, 45 (1971).
39. J. M. Baker and D. E. Eastman, *J. Vac. Sci. Technol.*, **10**, 223 (1973), and to be published.
40. E. W. Plummer, AVS Symposium, Chicago, October 1972.
41. C. R. Helms and W. E. Spicer, *Appl. Phys. Lett.*, **21**, 327 (1972), and previous papers.
42. P. W. Palmberg, *Anal. Chem.*, **45** 549A (1973).
43. W. L. Schaich and N. W. Ashcroft, *Phys. Rev.*, **B3**, 2452 (1971).
44. D. Penn, *Phys. Rev. Lett.*, **28**, 1041 (1972).
45. I. Adawi, *Phys. Rev.*, **134**, A788 (1964).
46. J. A. R. Samson, *Techniques of Vacuum Ultraviolet Spectroscopy*, Wiley, New York, 1967.
47. E. W. Plummer and R. D. Young, *Phys. Rev.*, **B1**, 2088 (1970).
48. E. W. Plummer and A. E. Bell, *J. Vac. Sci. Technol.*, **9**, 583 (1972).
49. P. W. Tamm and L. D. Schmidt, *J. Chem. Phys.*, **51**, 5352 (1969); **52**, 1159 (1970).
50. P. J. Estrup and J. Anderson, *J. Chem. Phys.*, **45**, 2254 (1966).
51. W. Jelend and D. Menzel, *Surf. Sci.* **40**, 295 (1973).
52. T. E. Madey, *Surf. Sci.*, **29**, 571 (1972).
53. D. W. Turner, A. D. Baker, C. Baker, and C. P. Brundle, *Molecular Photoelectron Spectroscopy*, Wiley, New York, 1972, p. 372.
54. E. W. Plummer, 33rd Physical Electronics Conference, 1972, and private communication.
55. P. L. Young and R. Gomer, *Phys. Rev. Lett.*, **30**, 955 (1973), and *J. Chem. Phys.* In press.

56. A. E. Bell and R. Gomer, *J. Chem. Phys.*, **44**, 1065 (1966).
57. C. Kohrt and R. Gomer, *Surf. Sci.*, **24**, 77 (1971).
58. J. T. Yates and D. A. King, *Surf. Sci.*, **32**, 479 (1971).
59. D. Menzel and R. Gomer, *J. Chem. Phys.*, **41**, 3329 (1964).
60. D. Menzel, *Ber. Bunsenges. Phys. Chem.*, **72**, 591 (1968).
61. M. Vass, C. Leung, and R. Gomer, to be published.
62. L. W. Swanson and R. Gomer, *J. Chem. Phys.*, **39**, 2813 (1963).
63. T. Engel and R. Gomer, *J. Chem. Phys.*, **50**, 2428 (1969).
64. N. A. Beach and H. B. Gray, *J. Am. Chem. Soc.*, **90**, 5713 (1968).

SURFACE PLASMA OSCILLATIONS AND RELATED SURFACE EFFECTS IN SOLIDS*

E. N. ECONOMOU

*Department of Physics, University of Virginia, Charlottesville,
 Virginia and*

K. L. NGAI

Naval Research Laboratory Washington, D. C.

CONTENTS

I.	Introduction	266
A.	Solid-State Plasma: General Features	266
B.	Surfaces and Their Effects	268
C.	Purpose and Organization of This Review	269
II.	General Formulation of the Problem: Approximations	270
A.	The Hamiltonian; The Linear Response Approximations	270
B.	The Dielectric Function	273
C.	Boltzmann-Vlasov Equation Approach	276
D.	Summary	280
III.	Explicit Results for the Eigenmodes	282
A.	General Remarks	282
B.	Specific Cases	286
1.	Parallel Plane Surfaces	286
2.	Spherical Geometries	301
3.	Circular Cylinder.	305
IV.	Interactions of Plasma Oscillations with Charged Particles	308
A.	General Remarks	308
B.	Quantization of Surface Plasma Fields: Electron-Surface Plasmon Interaction Hamiltonian	312
C.	Transition Radiation	318
D.	High-Energy Electron Losses	320
E.	Surface Plasmon Interaction with Low-Energy Electrons	322
1.	Low-Energy Electron Diffraction (LEED)	322
2.	Electron Tunneling in Solids	324
3.	Photoemission.	326
4.	Field Ion Emission	326

*Work supported by the National Science Foundation: NSF-GH-34404.

V.	Interaction of Surface Plasmons with Photons and Electrons on Rough Surfaces	327
A.	Theory	327
B.	Optical Reflectance (Thick Film)	330
C.	Plasma Radiation Excited by Light (Thin Films) (PREL)	333
D.	Surface Plasma Radiation Excited by Electrons (SPREE)	334
E.	Optical Diffraction Grating and Wood's Anomalies	337
F.	Photoemission; Enhancement of Photoelectron Yield	338
G.	Rough Cylindrical Surfaces	339
VI.	Photon-Surface Plasmon Coupling; Attenuated Total Reflection (ATR)	339
VII.	Surface Excitations in Small Crystals	341
VIII.	Inelastic X-Ray Scattering by Surface Plasmons	342
IX.	Van der Waals Forces Between Surfaces: Surface Energy	343
X.	Quantum Effects	346
	References.	348

I. INTRODUCTION

A. Solid-State Plasma: General Features

Solids, which can be considered as made up from electrons and ions, form a plasma that is referred to as solid-state plasma (SSP). Metals, semimetals, and semiconductors are examples of SSP. There are several important differences between SSP and the gaseous plasma which is the subject matter of plasma physics. Platzman and Wolff¹ in their excellent monograph have pointed out that SSP, in contrast to gaseous plasma, is almost always near thermodynamic equilibrium and, as a result, the emphasis in research has been in near equilibrium phenomena mainly in the study of elementary excitations. Gaseous plasma can be easily driven out of equilibrium and, as a result, the emphasis there is on the study of instabilities.

The main physical characteristic of a plasma is the possibility of the existence of a nonzero local charge density which can create long-range Coulomb fields capable of organizing the system in a collective motion. The frequency ω_p of such a motion is given by $(k/m)^{1/2}$ where k is an effective "spring constant" and m is the mass of the electron. For the present case, where the restoring force is Coulombic in nature, $k \sim ne^2$ where n is the density of the electrons and e is the electronic charge. Thus $\omega_p \sim (ne^2/m)^{1/2}$; numerically $\hbar\omega_p \sim 10$ eV for a typical metal and 5 to 100 meV for doped semiconductors.

Another related effect is the existence of screening: If an external charge is brought within a plasma, induced charge is set up to screen the field of the external charge. This screening is practically complete within a distance λ_s from the external charge. The screening length λ_s depends on the conditions of the plasma. Numerically λ_s is of the order of 10^{-8} cm for a metal and of the order of 10^{-4} to 10^{-6} cm for a doped semiconductor.

The existence of screening has another important effect: Individual

particle excitations are strongly suppressed and, as a result, the system responds to an external perturbation like an idealized continuum distribution of mass and charge. Obviously this statement is correct only as long as the wavelength of the external perturbation is much larger than the screening length; when the wavelength of the external perturbation is comparable to or smaller than the screening length, screening becomes nonoperative and the discrete nature of the electronic charge is quite important. This discussion implies that there exists a characteristic wavelength of the order of the screening length λ_s (or a wave number of the order of $k_s \equiv 1/\lambda_s$) such that for excitations of $\lambda \gg \lambda_s$ (or $k \ll k_s$) the system is almost equivalent to an idealized continuum distribution of charge and matter. As λ becomes comparable to or less than λ_s (or k becomes comparable to or greater than k_s), the individual electron excitation becomes more and more important and the continuum approximation fails.

Another parameter characteristic of SSP is the collision time τ . It characterizes the scattering of the plasma particles (electrons) by imperfections, lattice vibrations (phonons), and so on, and represents a damping mechanism for the motion of each individual electron. For metals τ can be as high as 10^{-9} sec for low temperatures and pure samples. For semiconductors τ can seldom be made higher than 10^{-11} sec.

The presence of an external static magnetic field H_0 modifies the properties of the SSP. Another characteristic frequency is introduced, the cyclotron frequency $\omega_c = eH_0/mc$, and new modes of oscillation appear, the so-called helicon waves.

In setting up a theory for any plasma, it is useful to compare the kinetic energy K of the plasma with the Coulomb potential energy V . For the kinetic energy one can distinguish two regimes: the low-density high-temperature regime where $K/N \sim k_B T$ (nondegenerate classical plasma) and the high-density low-temperature regime where $K/N \sim E_F$ (degenerate plasma); N is the total number of particles, k_B is Boltzmann's constant, T is the temperature, and E_F is the Fermi level. For a metal we are always in the degenerate regime; for semiconductors at low doping we are in the nondegenerate regime, and eventually as the doping increases we may pass to the degenerate regime. The case $V/K \ll 1$ is the so-called weak coupling limit for which the system can be treated as a "gas" of weakly interacting particles; in the opposite case where $V/K \gg 1$ the kinetic energy can almost be omitted and the system forms a "crystalline solid"; the intermediate case where $V/K \sim 1$ is the most difficult one (Fermi liquid case). In practice the theories valid for $V/K \ll 1$ have some qualitative success even for values of $V/K \approx 5$ which is the upper limit for the ratio V/K in an SSP.

The points just given are discussed in a clear physical way in Ref. 1.

B. Surfaces and Their Effects

The existence of surfaces introduces two kinds of effects: (a) it modifies the bulk modes, that is the modes which exist even in the absence of surfaces; and (b) it creates new modes associated with the surfaces, called surface modes, which are absent in the bulk. For an SSP the (a)-type effect is rather small because usually the mean free path is much smaller than the geometrical dimensions of the sample. The surface modes,²⁻⁸ however, are easily observable in a number of different experiments; they can be used to obtain information about the nature of the surfaces. Certain physical properties of the materials can be found by using the concept of surface modes.

TABLE I

Summary of the Experimental Situations where Surface Effects (In Particular, Surface Plasmon Effects) Are Important



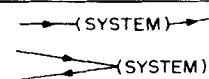




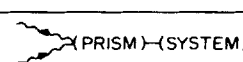

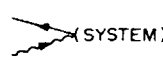

NAME	 electron  photon	MEASURED QUANTITIES E = energy \vec{p} = momentum
ELECTRON } HIGH ENERGY LOSS } LEED EXPS }		E of the incoming and outgoing electron \vec{p} of the incoming and outgoing electron
TUNNELING NORMAL SUPERCON- DUCTING		d^2I/dV^2 where I current and V applied voltage
TRANSITION RADIATION		\vec{p} of the incoming electron and \vec{p} of the outgoing photon.
REFLECTION, TRANSMISSION AND ABSORPTION		\vec{p} of the incident reflected and transmitted photon. No frequency shift. Snell's law obeyed.
PLASMA RADIATION EXCITED BY LIGHT		\vec{p} of the incident and emitted photon. No frequency shift. Snell's law not obeyed.
FRUSTRATED TOTAL REFLECTION		\vec{p} of the incident and reflected photon.
INELASTIC PHOTON (X-RAY) SCATTERING		\vec{p} of the ingoing and outgoing photon.
PHOTOEMISSION		\vec{p} of the incident photon; \vec{p} of the emitted electron
ATTRACTION OF SOLID SURFACES		Force of attraction or interaction energy.
SURFACE ENERGY OF SOLIDS		Energy of creating new surfaces

Table I summarizes the experiments where surface modes play an important role. The list of experiments in Table I constitutes essentially the subject matter of the present review. Since the interaction of a charged particle with our system takes place through the fields generated by the particle, we can conclude that the general problem under consideration is that of interaction of our material system with electromagnetic fields. For the plasma oscillations we consider here, the general problem can be attacked in two steps: First, one can find constitutive equations relating the currents and charges due to the particles of the systems in terms of the fields; second, one can solve Maxwell's equations using the constitutive equations obtained in the first step. We should point out that the first step is in general extremely difficult and one has to develop approximations of different degrees of sophistication in order to obtain the constitutive equations.

C. Purpose and Organization of This Review

As was explained above, Table I specifies the subject matter. The theoretical techniques used are Maxwell's equations and the special methods (such as hydrodynamic approximation, Boltzmann-Vlasov equation, quantum mechanical generalizations) required to obtain the constitutive equations. In this review we try to present the basic concepts employed for the study of surface plasma oscillations as they appear in the experiments summarized in Table I. Particular care is given in explaining the interrelation between different theoretical techniques in simple physical terms; we think that there is a need for putting in perspective the diverse theoretical methods and thereby define the conceptual framework on which our understanding is based. In other words, the theory is presented in a form appropriate for experimentalists or for theorists not specialized in the field. An effort is also made to collect the main results in the field in order to make this review useful as a reference. Since the two purposes stated above are somehow contradictory, a proper balance will be sought. Certain aspects are dealt with briefly because they are covered in detail in the existing review articles.²⁻⁸

The organization of this article is apparent from the Contents: The main properties of the physical systems under consideration are presented in the Introduction. The basic theoretical ideas together with the relevant approximations are presented in Section II. In Section III a systematic study of the properties of surface plasmons for different geometries is presented. Then the interaction of surface plasmons with incoming charged particles (usually electrons) is studied in Section IV. Surface roughness presents essentially a perturbation and as such a coupling mechanism between modes. This coupling leads to a host of interesting physical situations which are examined in Section V. In Section VI the simple

but ingenious idea of coupling photons with nonradiative surface modes through total reflection is presented; this subject is treated briefly since several detailed reviews are available. In Section VII a qualitative discussion is given on the effects occurring in small crystals. The problem of inelastic scattering of X-rays by surface plasmons is discussed briefly in Section VIII. The concept of surface plasmons has been employed recently to examine some problems which were traditionally considered in a different way. Some successes in this direction are presented in Section IX. Finally, in Section X we discuss qualitatively the regime in which examination of surface plasmons requires a full quantum mechanical many-body approach. This regime is important for some physical situations; the theoretical techniques employed, although very interesting, are sophisticated and lengthy and consequently are not presented in detail here.

II. GENERAL FORMULATION OF THE PROBLEM: APPROXIMATIONS

A. The Hamiltonian; The Linear Response Approximations

We consider here nonmagnetic materials where the magnetic susceptibility χ is¹ of the order of 10^{-6} ; the magnetic permeability $\mu = 1 + 4\pi\chi$ can be taken approximately equal to 1. This approximation means microscopically that we omit the orbital and spin angular momenta of the particles of the system.

We further assume that no external static field is applied. Note, however, that the application of a static magnetic field modifies the response function of the system drastically by introducing into the problem another characteristic frequency, the cyclotron frequency. New modes appear, the magnetoplasma modes, which have been studied extensively.¹ For an elementary discussion of the role of a static magnetic field in the electromagnetic properties of a system, see the book by Landau and Lifshitz.⁹ Most of the surface plasmon work, however, has been done with no external magnetic field applied; the reason is that the plasma frequency is much higher than the cyclotron frequency (except possibly in doped semiconductors), and consequently the effects of the static field are negligible at the frequency range of interest.

We consider first a material system consisting of ions and electrons. The ions occupy the sites of a lattice that may somehow be distorted near the surface. The electrons move under the influence of the fields of the ions and the other electrons. The Hamiltonian describing such an interacting system is¹⁰ for nonrelativistic particles,

$$H_{\text{tot}} = H_m + H_f + H_{m-f} \quad (2.1)$$

where

$$H_m = \sum_i \frac{\mathbf{p}_i^2}{2m_i} \quad (2.2)$$

$$H_f = \frac{1}{8\pi} \int d^3r \left[\frac{1}{c^2} \left(\frac{\partial \mathbf{A}}{\partial t} \right)^2 + (\nabla \times \mathbf{A})^2 \right] \quad (2.3)$$

$$H_{m-f} = \sum_i e_i \phi(\mathbf{r}_i, t) - \frac{1}{c} \sum_i \frac{e_i}{m_i} \mathbf{A}(\mathbf{r}_i, t) \cdot \mathbf{p}_i + \frac{1}{2c^2} \sum_i \frac{e_i^2}{m_i} \mathbf{A}^2(\mathbf{r}_i, t) \quad (2.4)$$

In the formulas above \mathbf{p}_i , m_i , e_i are the momentum, mass and charge of the i th particle (ion or electron) of the system; $\phi(\mathbf{r}, t)$, $\mathbf{A}(\mathbf{r}, t)$ are the scalar and vector potentials, respectively; the particular gauge $\nabla \cdot \mathbf{A} = 0$ has been chosen. In this gauge ϕ describes the so-called longitudinal fields and \mathbf{A} the so-called transverse fields. $\mathbf{H} = \nabla \times \mathbf{A}$ and $\mathbf{E} = \mathbf{E}_L + \mathbf{E}_T = -\nabla \cdot \phi - (1/c)(\partial \mathbf{A} / \partial t)$; note that $\nabla \cdot \mathbf{E}_T \equiv 0$ and $\nabla \times \mathbf{E}_L \equiv 0$.

From the Hamiltonian (2.1) to (2.4) one can derive the inhomogeneous Maxwell equations

$$\nabla^2 \phi(\mathbf{r}, t) = -4\pi \rho(\mathbf{r}, t) \quad (2.5)$$

$$\nabla^2 \mathbf{A}(\mathbf{r}, t) - \frac{1}{c^2} \frac{\partial^2}{\partial t^2} \mathbf{A}(\mathbf{r}, t) = -\frac{4\pi}{c} \mathbf{j}(\mathbf{r}, t) \quad (2.6)$$

where $\rho(\mathbf{r}, t)$ and $\mathbf{j}(\mathbf{r}, t)$ are the charge and current density associated with the particles of the system. A general problem of physical importance is to find the eigenmodes of the system described by the Hamiltonian (2.1). A second problem is to find the response of the system to some external probes. We consider first the problem of the eigenmodes. The eigenmodes can be classified in two groups: For eigenmodes of the first group any excess charge is screened within a microscopic length; as a result of this, the potential \mathbf{A} is practically zero¹¹ and the field $\phi(\mathbf{r}_i, t)$ is due essentially to the nearby charges only; that is, the Coulomb interaction can be replaced by an effective short-range interaction. In this case the material system decouples from the field and can be described by an effective Hamiltonian of the form

$$H = \sum_i \frac{\mathbf{p}_i^2}{2m_i} + \frac{1}{2} \sum_{ij} V_{ij} \quad (2.7)$$

where V_{ij} is an effective short-range potential. The eigenmodes of the

second group are associated with charges and currents extending over large (macroscopic) distances and, as a result, the system creates macroscopic fields in addition to the local microscopic fields. Examples of modes of this second group are the plasma oscillations (both bulk and surface), phonons in ionic crystals, magnetic excitations, and so on.¹² Among the different ways to study the modes belonging to this second group is to try to express the macroscopic current¹³ $\mathbf{j}(\mathbf{r}, t)$ in terms of the macroscopic fields ϕ and \mathbf{A} . This step is an extremely difficult one. Usually a linear *approximation*¹ is employed by writing

$$\mathbf{j}(\mathbf{r}, t) = \int_{-\infty}^t dt' d^3r' \boldsymbol{\sigma}(\mathbf{r}, \mathbf{r}', t - t') \cdot \mathbf{E}(\mathbf{r}', t') \quad (2.8)$$

or by Fourier transforming

$$\mathbf{j}(\mathbf{r}, \omega) = \int d^3r' \boldsymbol{\sigma}(\mathbf{r}, \mathbf{r}', \omega) \cdot \mathbf{E}(\mathbf{r}', \omega) \quad (2.8')$$

Even within the linear approximation (2.8) one has to determine the nonlocal conductivity tensor $\boldsymbol{\sigma}$ which can be decomposed into a longitudinal and a transverse part. For a translationally invariant system $\boldsymbol{\sigma}$ is a function of $\mathbf{r} - \mathbf{r}'$ only and, as a result, one can make a further Fourier transform and cast (2.8) into the form

$$\mathbf{j}(\mathbf{k}, \omega) = \boldsymbol{\sigma}(\mathbf{k}, \omega) \cdot \mathbf{E}(\mathbf{k}, \omega) \quad (2.8'')$$

For an isotropic system the tensor $\boldsymbol{\sigma}(\mathbf{k}, \omega)$ must have the form¹

$$\sigma_{ij}(\mathbf{k}, \omega) = \sigma^{(1)}(\mathbf{k}, \omega) \delta_{ij} + \frac{k_i k_j}{k^2} \sigma^{(2)}(\mathbf{k}, \omega) \quad (2.9)$$

where $\sigma^{(1)}(\mathbf{k}, \omega)$ and $\sigma^{(2)}(\mathbf{k}, \omega)$ are scalars. It follows from (2.9) that the combination $\sigma_L(\mathbf{k}, \omega) = \sigma^{(1)}(\mathbf{k}, \omega) + \sigma^{(2)}(\mathbf{k}, \omega)$ determines the response to longitudinal fields whereas $\sigma_T(\mathbf{k}, \omega) = \sigma^{(2)}(\mathbf{k}, \omega)$ gives the response to transverse ones. Thus even for a translationally invariant, isotropic system two scalar functions $\sigma_L(\mathbf{k}, \omega)$ and $\sigma_T(\mathbf{k}, \omega)$ are required to describe its linear response. The dielectric function tensor is generally defined as

$$\epsilon(\mathbf{r}, \mathbf{r}', \omega) = 1 + \frac{4\pi}{i\omega} \boldsymbol{\sigma}(\mathbf{r}, \mathbf{r}', \omega) \quad (2.10)$$

and the longitudinal and transverse dielectric scalars in the case of translationally invariant isotropic systems as

$$\epsilon_{L,T}(\mathbf{k}, \omega) = 1 + \frac{4\pi}{i\omega} \sigma_{L,T}(\mathbf{k}, \omega) \quad (2.11)$$

The definitions (2.10), (2.11) are equivalent to other definitions one can find in the literature.^{1,14} Having obtained an expression of $\mathbf{j}(\mathbf{r}, t)$ in terms of the fields, one can substitute back in (2.5), (2.6) and determine the fields.

Before we discuss in some detail the quantity σ or ϵ , it is worthwhile to consider briefly the validity of the linear approximation (2.8). For most of the cases (2.8) is adequate because the macroscopic fields are very weak. In particular the linear response approximation is completely satisfactory for the study of the eigenmodes of the system belonging to the second group, since for an eigenmode problem the strength of the associated field can be considered arbitrarily small. There are, however, phenomena of physical importance which cannot be considered at all within the linear response theory: Raman scattering, Compton scattering, and other *inelastic* light scattering are such examples. To study such effects one has to return to the general Hamiltonian (2.1).

For a somewhat different but illuminating discussion of the subjects of this section, the reader is referred to the papers by Bohm and Pines,¹⁵ Fano,¹⁶ and Ehrenreich and Cohen.¹⁷

B. The Dielectric Function

The determination of the tensor $\sigma(\mathbf{r}, \mathbf{r}', \omega)$ [or the tensor $\epsilon(\mathbf{r}, \mathbf{r}', \omega)$] is in general an extremely difficult problem. Both the electrons and the ions contribute to ϵ although the ionic contribution is usually negligible (one exception is the case of ionic crystals). We consider here the electronic contribution to ϵ . The determination of ϵ is extremely difficult because

1. each electron moves in a periodic pseudopotential due to the ions and the other electrons;
2. the electron-electron interactions make the motion of electrons correlated;
3. the presence of surfaces further complicates the problem;
4. lattice vibrations and impurities interact with the electrons.

If one omits the complications (1) to (4) above and considers an electronic gas without particle correlations embedded in an infinite uniform positive charge (ensuring overall electrical neutrality), then one can calculate the dielectric functions $\epsilon_L(\mathbf{k}, \omega)$, $\epsilon_T(\mathbf{k}, \omega)$. The resulting expressions are known as the random phase approximations (RPA) to ϵ_L and ϵ_T and are rather complicated.^{1,18} The main properties of the RPA for ϵ_L and ϵ_T are the following¹:

$$1. \quad \epsilon_L(0, \omega) = \epsilon_T(0, \omega) = 1 - \frac{\omega_p^2}{\omega^2} \quad (2.12)$$

where ω_p , the plasma frequency, is given by

$$\omega_p^2 = \frac{4\pi e^2 n}{m} \quad (2.13)$$

and n is the electronic density.

2. The expression for finite k depends on the plasma temperature. One can distinguish two limiting cases, the $T=0$ degenerate case applicable for metals, and the low-density, high-temperature nondegenerate case applicable for lightly doped semiconductors.

3. For $\omega/k \lesssim \omega_p/k_c$, where $1/k_c \sim \lambda_c$ is the screening length, the dielectric function acquires an appreciable imaginary part; this implies that the plasma oscillations have a rather short lifetime when $\omega/k \lesssim \omega_p/k_c$. This is to be expected on the basis of the discussion given previously. Plasma oscillations are associated with the generation of macroscopic fields. As the wavelength becomes smaller and smaller, the individual character of the electronic gas is more and more revealed and the collective plasma oscillations can decay by exciting individual electron eigenmodes. Strictly speaking, the plasma oscillation is an exact eigenmode only in the limit $k \rightarrow 0$. For finite k the plasma oscillation is only an approximate eigenmode. Finally, for $\omega/k \ll \omega_p/k_c$ the plasma oscillation lifetime is so short that we cannot even talk about an approximate eigenmode.

If one considers the electrons in our model as a continuous distribution of mass and charge,¹² then (2.12) would be valid for all k , and the lifetime would be infinite, in agreement with the reasoning above about the origin of the finite lifetime of plasma oscillations. The decay of plasma oscillations due to the excitations of individual particle modes is termed Landau damping¹ in the literature.

Let us briefly review the theoretical methods used to calculate $\epsilon(\mathbf{k}, \omega)$. For high-frequency $\omega/k \gg \omega_p/k_c$ we are always in the classical regime where quantum effects are negligible. Also for nondegenerate, low-density, high-temperature plasma one can always obtain an adequate description by classical mechanics. On the other hand, for $\omega/k \lesssim \omega_p/k_c$ and for degenerate plasma a quantum description is required. We discuss first the classical approach; the quantum approach is discussed in a separate section.

The most general and widely used classical approach to the problem of calculating the dielectric functions is the Boltzmann-Vlasov equation, which relates the particle distribution function in velocity and real space, $f(\mathbf{v}, \mathbf{r}, t)$, with the total field. From the distribution function f one can easily obtain the current \mathbf{j} ; thus a current-field relation results. For low k one can use a hydrodynamic approximation to the Boltzmann-Vlasov equation known as Bloch's equation.^{19,20} In the hydrodynamic approach one intro-

duces a function $\psi(\mathbf{r}, t)$ such that $\langle \mathbf{v} \rangle_{av} = -\nabla \cdot \psi$. Bloch's equation then connects ψ with the total field. The current density is given by $\mathbf{j} = -e\rho_0 \nabla \cdot \psi$. A further simplified approach adequate for $k \rightarrow 0$, is to consider the equation of motion of one electron under the influence of the total field. The velocity of the electron $\mathbf{v}(t)$ can be found trivially, and the current can be calculated by $\mathbf{j}(t) = e\rho_0 \mathbf{v}(t)$.

Before we present the Boltzmann-Vlasov equation approach in some detail, we discuss the effects of the complications 1 to 4 listed above. The existence of a periodic potential may or may not be important. Thus for materials like Al, Mg, Be, K, Na^{2,5} the band structure effects, as they are usually called, are negligible for frequencies around their plasma frequency. On the other hand, for Ag, Cu²¹ band structure contributions are quite important, modifying the real part of the dielectric function and increasing significantly the imaginary part of it. The theory of band-structure effects requires a quantum mechanical treatment, usually that of the RPA as in Ref. 21.

The effects of the electron-electron correlations require for their estimation extremely complicated many-body techniques going beyond the RPA.¹ It should be pointed out that in the weakly interacting case, $V/K \ll 1$, the RPA is quite adequate. It seems that the RPA gives reasonable results even for $V/K \sim 1$. Note also that the electron-electron correlations are always negligible for low k . Thus the only case where electron-electron correlations are important is for $V/K \gtrsim 1$ and for $k \sim k_c$.

The effect of lattice vibrations and impurity scattering is to provide a damping mechanism (collision damping) for the plasma oscillation.²² Usually this damping mechanism can be taken into account phenomenologically by introducing a collision time τ or a mean free path l where $l = v_c \tau$; v_c is equal to the Fermi velocity v_F for a degenerate plasma or to the thermal velocity $v_{th} = (2k_B T/m)^{1/2}$ for a low-density, high-temperature plasma. The collision time τ can be easily introduced in any formalism, be it the Boltzmann-Vlasov equation, the Bloch equation, or even the simple equation of motion. The Boltzmann-Vlasov formalism (as well as the quantum mechanical formalisms) permits a more sophisticated description of the role of the lattice vibrations or the impurities in terms of the scattering cross-section of an electron by a phonon or an impurity. Such a sophistication complicates the calculations considerably and it is not usually necessary. One exception to this rule occurs in doped semiconductors where a resonance scattering may take place if the plasma frequency matches some phonon frequency. In what follows we describe the role of lattice vibrations and impurities by using the collision time approximation.

Finally let us consider the role of surfaces in the determination of ϵ or σ . Generally speaking the existence of surfaces implies that σ is a function of

both \mathbf{r} and \mathbf{r}' in (2.8') and as a result, one cannot even define $\sigma(\mathbf{k}, \omega)$. In the quantum regime (short-wavelength excitations) there is no consistent way to overcome this difficulty; one has to solve the problem by taking into account explicitly at every step the existence of the surfaces. We present the relevant work in a later section.

In the classical regime the situation depends on the approximation: The simple equation of motion approach always gives a local conductivity [i.e., $\sigma(\mathbf{r}, \mathbf{r}', \omega) = \delta(\mathbf{r} - \mathbf{r}') \cdot \sigma(\omega)$ or $\sigma(\mathbf{k}, \omega) = \sigma(\omega)$] which is, of course, independent of the existence of surfaces.

On the other hand, for the Boltzmann-Vlasov equation approach (or for the hydrodynamic approximation of it) the existence of a surface modifies the current field relation giving a conductivity $\sigma(\mathbf{r}, \mathbf{r}', \omega)$ which is a function of both \mathbf{r} and \mathbf{r}' . In this general case one has to use the Boltzmann-Vlasov equation (or the hydrodynamic approximation of it) with the appropriate boundary conditions together with Maxwell's equations with the corresponding boundary conditions in order to study the properties of the plasma oscillations. Here we outline in some detail the most general case of the Boltzmann-Vlasov equation approach. The case of the hydrodynamic approximation is straightforward: one has to consider in addition to Maxwell's equation one more partial differential equation [the one connecting $\psi(\mathbf{r}, t)$ with the electric field $\mathbf{E}(\mathbf{r}, t)$] together with the known boundary conditions satisfied by the fields and the velocity potential $\psi(\mathbf{r})$.

C. Boltzmann-Vlasov Equation Approach

The Boltzmann-Vlasov equation relates the distribution function $f(\mathbf{r}, \mathbf{v}, t)$ with the total electric field as follows

$$\frac{\partial f}{\partial t} + \mathbf{v} \cdot \frac{\partial f}{\partial \mathbf{r}} + \frac{e}{m} \mathbf{E}(\mathbf{r}, t) \cdot \frac{\partial f}{\partial \mathbf{v}} = \left(\frac{\partial f}{\partial t} \right)_{\text{coll}} \quad (2.14)$$

where $(\partial f / \partial t)_{\text{coll}}$ is a complicated functional of f and the scattering amplitude. Usually a collision time approximation is employed for this term, that is,

$$\left(\frac{\partial f}{\partial t} \right)_{\text{coll}} \approx - \frac{f - f_0}{\tau} \quad (2.15)$$

where τ is the collision time and f_0 is the equilibrium distribution, $f_0(\mathbf{v}) = m^3 h^{-3} \{ \exp[\beta (\frac{1}{2} m v^2 - \mu)] + 1 \}^{-1}$. There are cases, however, where one has to go beyond the simple collision time approximation.²³

In the presence of surfaces one has to impose certain boundary conditions describing what happens to electrons colliding with the surface. One

assumes that a fraction p of the electrons arriving at the surface scatters specularly with reversal of the perpendicular velocity component while the rest are scattered diffusely with a complete loss of the drift velocity; for $p = 1$ we have the so-called specular reflection and for $p = 0$ the diffuse scattering.

Since we are interested in the linear response of the system to the total field, we write the solution of (2.14) in the form

$$f(\mathbf{r}, \mathbf{v}, t) = f_0(\mathbf{v}) + f_1(\mathbf{r}, \mathbf{v})e^{i\omega t} \quad (2.16)$$

where the term f_1 is assumed proportional to the electric field with higher terms in the field having been omitted. Substituting (2.16) into (2.14) and keeping only terms linear in the field, we obtain the linearized Boltzmann-Vlasov equation

$$i\omega f_1 + \mathbf{v} \cdot \frac{\partial f_1}{\partial \mathbf{r}} + \frac{e}{m} \mathbf{E} \frac{\partial f_0}{\partial \mathbf{v}} = \frac{-f_1}{\tau} \quad (2.17)$$

The current linear in the field is given by

$$j_a = 2e \int v_a f_1 d^3v \quad (2.18)$$

If f_1 varies slowly with \mathbf{r} , $\partial f_1 / \partial \mathbf{r}$ is small and can be neglected; in this case f_1 is given by

$$f_1 = \frac{-e\tau}{m(1+i\omega\tau)} \mathbf{E} \cdot \frac{\partial f_0}{\partial \mathbf{v}} \quad (2.19)$$

Substituting (2.19) into (2.18) and performing the integration we obtain

$$\mathbf{j}(\omega) = \frac{e^2 \tau n}{m(1+i\omega\tau)} \mathbf{E}(\omega) \quad (2.20)$$

Using (2.10) we obtain for $\epsilon(\omega)$

$$\epsilon(\omega) = 1 - \frac{\omega_p^2}{\omega^2} \frac{1}{1 - i/\omega\tau} \quad (2.21)$$

which is a local dielectric function identical with the one obtained through a simple equation of motion approach. The local approximation is justified whenever the term $\mathbf{v} \cdot (\partial f_1 / \partial \mathbf{r})$ is negligible compared to $(1/\tau)(1+i\omega\tau)f_1$. Now $\mathbf{v} \cdot (\partial f_1 / \partial \mathbf{r})$ is of the order of $(v/L)f_1$ where v is a typical velocity and

L is some characteristic length over which the function f_1 varies significantly. Thus the local approximation is valid when

$$L \gg \frac{v\tau}{|1+i\omega\tau|} \equiv \frac{l}{|1+i\omega\tau|} \quad (2.22)$$

The quantity $l/|1+i\omega\tau|$ is a dynamic mean free path over which an electron can move without suffering any collision. For $\omega\tau \ll 1$ this length is the ordinary mean free path $l = v\tau$; for high frequency it is v/ω , that is, the distance traveled by an electron in one period. The characteristic length L can be (a) the geometrical dimension of the sample d , (b) the wavelength of the plasma oscillation and (c) the classical penetration depth²⁴ $(\lambda_p/2\pi)(1+1/\omega^2\tau^2)^{1/4}$ where $\lambda_p \equiv 2\pi c/\omega_p$ is the plasma wavelength.²⁵ In order to have plasma oscillations at all, both the bulk scattering and the surface scattering should not overdamp the oscillation. This is achieved when

$$\omega\tau \gg \max\left(1, \frac{l}{d}\right) \quad (2.23)$$

Taking into account (2.23), the condition (2.22) for the validity of the local approximation becomes

$$\omega\tau \gg \max\left(\frac{l}{\lambda}, \frac{l}{\lambda_p}\right) \quad (2.24)$$

Thus when

$$\min(\lambda, \lambda_p) \gg \min(l, d) \quad (2.25)$$

all the plasma oscillations can be studied using the local approximation (2.21). On the other hand, when condition (2.25) is violated, there exist oscillations [i.e., (2.23) is satisfied] which do not satisfy (2.24) either because

$$\omega\tau \lesssim \frac{l}{\lambda} \quad (2.26)$$

or because

$$\omega\tau \lesssim \frac{l}{\lambda_p} \quad (2.27)$$

Equation (2.26) is equivalent to $\omega/k \lesssim v$; in this case, as was explained previously we are in the quantum regime, which is examined later. When (2.27) is satisfied, we are in the so-called anomalous skin effect regime which requires the complete solution of the Boltzmann-Vlasov equation without omitting the term $\mathbf{v} \cdot \partial f_1 / \partial \mathbf{r}$. The mathematical analysis is then considerably complicated.^{23,24,27,28} It should be noted that certain

geometries (e.g., the plane surface), in the case of specular surface reflection, allow the use of a technique which greatly facilitates the mathematical analysis. This technique is based on fictitiously extending the material beyond its boundary to infinity and then using symmetry considerations to find a field in the fictitious part of the material which will reproduce the same current in the real material as in the presence of the real boundaries. Since an equivalent infinite medium is introduced this way, one can use the current-field relation of the type (2.8'') as in the bulk and avoid completely the solving of the Boltzmann-Vlasov equation in the presence of the boundaries.^{23,29} The idea is similar to the introduction of image charges in electrostatics by which one avoids the complication arising from the presence of surfaces.

Up to now we have considered the contribution to the dielectric function arising from the electrons. The ions contribute also. For nonionic crystal the main contribution comes from the core polarization, the effect of which is to increase the dielectric function by a positive amount $\Delta\epsilon_c$ which, for the frequencies of interest, is small compared with unity and is frequency independent. For ionic crystals the main contribution to the dielectric function for low frequencies comes from the ions. The form of the dielectric function is quite different¹² since a new frequency is introduced in the problem, namely, that of the optical phonon oscillation. The oscillation in ionic crystals is an extensively studied problem. We do not present any details here; we simply point out that this problem can be treated within the framework of Maxwell's equations supplemented by a constitutive equation of the type (2.8).

The case of doped semiconductors deserves special mention. The contribution to $\epsilon(\mathbf{r}, \mathbf{r}', \omega)$ coming from the "impurity" electrons is of the form already examined. But in this case the impurity electrons of density n_i do not move in vacuum but in a background of bonding electrons that are highly polarizable. Thus in the simplest case, and for frequencies comparable to $\omega_{pi} = (4\pi e^2 n_i / m^*)^{1/2}$, the dielectric function, instead of the form (2.21), is

$$\epsilon(\omega) = \epsilon_0 \left[1 - \frac{\omega_{pi}^2}{\omega^2} \frac{1}{1 - i/\omega\tau} \right] \quad (2.28)$$

where ϵ_0 is the dielectric function of the undoped semiconductor which for $\omega \sim \omega_{pi}$ can be considered as frequency independent and usually considerably larger than unity. When $\hbar\omega \gg E_g$, where E_g is the energy gap, the contribution of "impurity" electrons is negligible; the bonding electrons can be considered as free and the dielectric function is of the form (2.21)

where the density n entering ω_p is now the density of bonding electrons.

Another special case worth mentioning is that of superconducting materials. For frequencies much higher than the gap Δ there is no essential difference from a normal metal. On the other hand, for $\hbar\omega < 2\Delta$ the situation is quite different. Economou²⁶ has shown, using the theory by Mattis and Bardeen,²⁹ that for $\hbar\omega < 2\Delta$

$$\epsilon_s(\omega) = 1 - \frac{\omega_{ps}^2}{\omega^2} \left(1 + i \frac{\sigma_1}{\sigma_2} \right) \quad (2.29)$$

where ω_{ps} is a temperature-dependent effective plasma frequency of the order of magnitude of $5 \times 10^{15} \text{ sec}^{-1}$ (i.e., comparable to that of a normal metal). The imaginary part σ_1/σ_2 is small in comparison with unity and can be omitted in a first approximation.

In many experiments, besides solid-state plasma materials, insulators (or dielectrics) are present. Those materials will be characterized by a real, frequency-independent, dielectric function which is larger than unity. This is a satisfactory assumption for various dielectric layers on metal surfaces.³⁰ Note, however, that, for frequencies exceeding the interband absorption frequency, the dielectric function becomes frequency dependent and acquires a significant imaginary part which may strongly attenuate the surface plasma oscillations.

D. Summary

Consider a coupled system consisting of a material body and the electromagnetic field. To study the eigenmodes of the system associated with macroscopic electromagnetic fields, one needs only to consider the set of Maxwell's equations

$$\nabla \cdot \mathbf{D} = 0 \quad (2.30a)$$

$$\nabla \cdot \mathbf{H} = 0 \quad (2.30b)$$

$$\nabla \times \mathbf{E} = - \frac{i\omega}{c} \mathbf{H} \quad (2.30c)$$

$$\nabla \times \mathbf{H} = \frac{i\omega}{c} \mathbf{D} \quad (2.30d)$$

supplemented by a constitutive equation relating \mathbf{D} with \mathbf{E}

$$\mathbf{D}(\mathbf{r}, \omega) = \int d^3r' \epsilon(\mathbf{r}, \mathbf{r}'; \omega) \cdot \mathbf{E}(\mathbf{r}', \omega) \quad (2.31)$$

where the magnetic permeability μ has been taken equal to unity in (2.30).

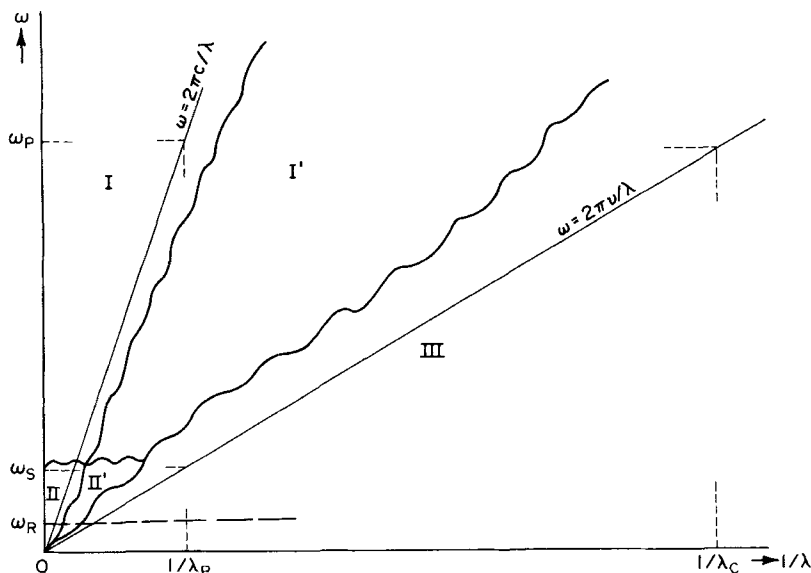


Fig. 1. Different regions in the $\omega\lambda$ plane, where ω is the frequency and λ is the wavelength of the oscillation. The region $\omega \lesssim \omega_R = (1/\tau) \max(1, l/d)$ is of no interest because the oscillations are strongly damped; τ is the collision time, $l = v\tau$ is the mean free path, v is the Fermi velocity (for a degenerate plasma) or the thermal velocity (for a classical Maxwellian plasma), and d is the geometric dimension of the system. In the regions I, I', II, II' ($\omega \gg 2\pi v/\lambda$) the particles of the system can be considered as obeying classical mechanics while in region III quantum effects are important. In regions I, I' the dielectric function is a local one given by (2.21). The regions II, II' are the anomalous skin effect regimes where the dielectric function is nonlocal. Finally, in regions I, II ($\omega \gtrsim 2\pi c/\lambda$) retardation effects are important while in regions I', II', III retardation effects can be omitted ($c \rightarrow \infty$).

For a solid-state plasma and in regions I and I' of Fig. 1 ($\omega \gg 2\pi v/\lambda$; $\omega \gg \omega_s = \omega_p v/c$) the dielectric tensor becomes a local scalar function

$$\epsilon(\mathbf{r}, \mathbf{r}'; \omega) = \delta(\mathbf{r} - \mathbf{r}') \epsilon(\omega) \quad (2.32)$$

In the free electron case $\epsilon(\omega)$ is given by (2.21), where $\omega_p^2 = 4\pi e^2 n/m$, n is the electronic density, m is the electronic mass, τ is the collision time, $l = v\tau$ is the near free path, and v is either the Fermi velocity (for a degenerate plasma) or the thermal velocity $(2k_B T/m)^{1/2}$ (for a classical high-temperature, low-density plasma). One does not need to consider frequencies below or comparable to $\omega_R = (1/\tau) \max(1, l/d)$, where d is the geometrical dimension of the material, because in this regime the damping is usually very strong. In the regions II, II' (anomalous skin effect regime) the dielectric function is a complicated nonlocal tensor which can be

calculated from the Boltzmann-Vlasov equation (or less satisfactorily by the hydrodynamic approximation). Note that whenever $\omega_R \gtrsim \omega_s$, as is usually the case, the anomalous skin effect regime does not appear at all. Finally in region III of Fig. 1 ($\omega \lesssim 2\pi v/\lambda$) the calculation of $\epsilon(\mathbf{r}, \mathbf{r}', \omega)$ requires a quantum mechanical treatment of the particles of the material body as well as a detailed microscopic description of the surface; this is the subject of a later section.

The electromagnetic fields \mathbf{E} and \mathbf{H} can be separated in two parts, the transverse part associated with the vector potential \mathbf{A} (in the gauge $\nabla \cdot \mathbf{A} = 0$) and the longitudinal part associated with the scalar potential ϕ . We have then $\mathbf{H} \equiv \mathbf{H}_T = \nabla \times \mathbf{A}$, $\mathbf{E} = \mathbf{E}_L + \mathbf{E}_T$, $\mathbf{E}_L = -\nabla\phi$, $\mathbf{E}_T = -(1/c)(\partial\mathbf{A}/\partial t)$. The transverse and the longitudinal parts are, in general, coupled.²⁶ In regions I', II', III of Fig. 1 ($\omega \ll 2\pi c/\lambda$) the transverse part is negligible (which is equivalent to setting $c = \infty$, i.e., no retardation effects) and only the longitudinal field survives, which means that we are in the electrostatic regime.

The separation of the $\omega\lambda$ plane into regions is very useful because in different experiments we are usually in only one regime and consequently one can make the corresponding approximations. Thus in optical experiments we are usually in region I or more rarely in region II and thus the particles of the system can be treated as classical objects, and the dielectric function is rather simple.

III. EXPLICIT RESULTS FOR THE EIGENMODES

A. General Remarks

In this section we examine the eigensolutions of the coupled system consisting of the electromagnetic field and material bodies which are completely characterized by a dielectric function. Unless explicitly stated otherwise, we assume for simplicity that the dielectric function is a function of the frequency only. When explicit results for the dispersion relation of the eigenmodes are given, it is assumed that $\epsilon(\omega) = 1 - \omega_p^2/\omega^2$. Surfaces bounding the different materials are present at which the dielectric function changes abruptly. At the surfaces the fields satisfy the well-known boundary conditions

$$H_{\perp} \text{ continuous} \quad (3.1)$$

$$D_{\perp} \text{ continuous} \quad (3.2)$$

$$E_{\parallel} \text{ continuous} \quad (3.3)$$

$$H_{\parallel} \text{ continuous} \quad (3.4)$$

$$\Delta E_{\perp} = 4\pi\rho_s \quad (3.5)$$

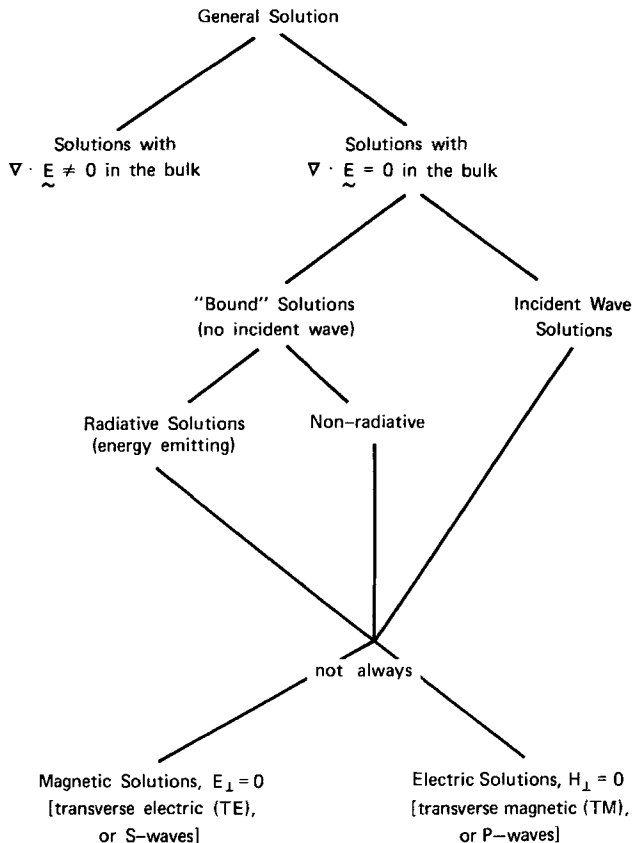
where ρ_s is the surface charge. From the five boundary conditions only two are independent; usually one considers (3.3) and either (3.2) or (3.4).

The eigensolutions of the problem stated above can be classified as in Table II.

The solutions with $\nabla \cdot \mathbf{E} \neq 0$ are the bulk plasma oscillations in the presence of surfaces. They are characterized by the following properties:

1. There is bulk and surface charge, $\rho \neq 0$, $\rho_s \neq 0$.
2. The field is purely longitudinal (electrostatics suffices), $\mathbf{E}_T = \mathbf{H} = 0$.

TABLE II
A Classification Scheme for the Solutions of the Coupled System
Consisting of EM Fields and Material Bodies Completely Described
by a Dielectric Function^a



^a Bulk plasma oscillations are of the type $\nabla \cdot \mathbf{E} \neq 0$ in the bulk. Surface plasma oscillations are "bound" nonmagnetic solutions of the type $\nabla \cdot \mathbf{E} = 0$ in the bulk.

3. Each plasma material sustains independent solutions of this type and the field is exclusively confined within the material; in other words, a surface charge is set up which completely screens the field outside.

4. The frequency of these oscillations is given by $\epsilon(\omega)=0$ as in the case of bulk plasma in a material of infinite extent.

The solutions with $\nabla \cdot \mathbf{E}=0$ in the bulk are not transverse solutions because the condition $\nabla \cdot \mathbf{E}=0$ is not satisfied in general at the boundaries which may sustain surface charges, thus making the solutions of this type a mixture of the transverse fields \mathbf{E}_T , \mathbf{H}_T and the longitudinal field \mathbf{E}_L . There are two different criteria to further classify the solutions with $\nabla \cdot \mathbf{E}=0$. One criterion is based on the existence or the nonexistence of an incident wave. In this case we may distinguish the incident wave solutions which have the general form

$$b_{\text{inc}} \mathbf{B}_{\text{inc}} + f b_{\text{inc}} \mathbf{B}_{\text{out}}$$

where b_{inc} is the strength of the incident wave \mathbf{B}_{inc} , \mathbf{B}_{out} is the outgoing wave which has a strength proportional to the incident wave strength, and f is the proportionality factor; f depends on the frequency, wavelength, geometry, and so on. We may also have solutions without an incident wave; we call them bound solutions in analogy with the classification of the solutions in ordinary quantum mechanics where bound solutions (no incident wave) and scattering solutions (incident wave present) exist. There is a basic distinction between bound and incident wave solutions. The bound eigenmodes are genuine surface modes which disappear when the surfaces disappear. On the other hand, the incident wave solutions are essentially bulk solutions modified because of the presence of surfaces. From the form of the incident wave solution given above, it is clear that the bound solutions correspond to the condition

$$f = \infty \tag{3.6}$$

since this is the only way to have a nonzero solution when $b_{\text{inc}}=0$. Thus bound solutions appear only for certain frequencies satisfying (3.6). This is again quite analogous to the quantum mechanical case: The bound solutions correspond to infinities of the scattering amplitude. Two remarks are in order here. As in the quantum mechanical case, the bound solutions can be found by means other than (3.6); however, if the incident wave solutions are already available, (3.6) provides a direct way of determining the eigenfrequencies of the bound solutions. The infinities of f may occur for complex values of the parameters on which f depends; for example, in quantum mechanics if f is expressed in terms of $k=(2mE/\hbar^2)^{1/2}$, then the

bound states correspond to complex k , which simply means negative energy values. We examine such examples later.

We pointed out that the bound solutions correspond to the infinities of f . In some cases f may exhibit sharp peaks (not real infinities) as a function of ω . These peaks correspond by definition to *virtual bound* solutions. These virtual bound solutions appear in quantum mechanics and in elementary particle physics and are called virtual levels or resonances. Note that in reality the distinction between real bound solutions and virtual solutions disappears. Whenever the dielectric function possesses a nonzero imaginary part, all the infinities of f are reduced to peaks and all bound eigenmodes become virtual. Another equivalent way of characterizing a virtual mode is to say that the infinities of f occur at a complex value of the frequency ω . The imaginary part of the complex eigenfrequency is the decay rate and is equal to the inverse of the lifetime of the considered eigenmode.

The bound solutions can be classified further as radiative or nonradiative, depending on whether or not energy is radiated in the form of electromagnetic waves.³¹ All the radiative solutions should be virtual solutions even in the limit $\text{Im}\epsilon \rightarrow 0$ as a result of the conservation of energy. Since the modes we consider here are solutions of Maxwell's equations, they satisfy the following relation

$$\frac{\partial}{\partial t} W_{\text{tot}}(t) = -P_{\text{coll}} - P_{\text{rad}}$$

where $W_{\text{tot}}(t)$ is the total field energy that can be expressed in terms of \mathbf{E} , \mathbf{H} , and \mathbf{D} , $P_{\text{coll}} \geq 0$ is the power lost to heat, and $P_{\text{rad}} \geq 0$ is the radiated power. If $\text{Im}\epsilon = 0$, $P_{\text{coll}} = 0$. A real mode as defined above exists only in the idealized situation where both $P_{\text{coll}} = 0$ ($\Leftrightarrow \text{Im}\epsilon = 0$) and $P_{\text{rad}} = 0$. Otherwise the mode is virtual. For a radiative mode the decay rate $\text{Im}\omega = \gamma_{\text{tot}}$ can be written as a sum of two parts; $\gamma_{\text{tot}} = \gamma_{\text{coll}} + \gamma_{\text{rad}}$, while for a nonradiative mode; $\gamma_{\text{tot}} = \gamma_{\text{coll}}$. As $\text{Im}\epsilon \rightarrow 0$, $\gamma_{\text{coll}} = 0$ and then the nonradiative modes become real while the radiative modes remain virtual even in this idealized case.

It should be emphasized here that the solutions of Maxwell's equations automatically give the total decay rate and that there is no need to use the energy conservation equation given above for calculating $\gamma_{\text{tot}} = \gamma_{\text{coll}} + \gamma_{\text{rad}}$. If, however, some approximation to Maxwell's equations was used such as the omission of retardation effects, a procedure should be found by which P_{rad} will be approximately calculated and then the energy conservation equation should be used for the determination of the radiative decay rate which the electrostatic approach completely omits.

Another way to classify the solutions with $\nabla \cdot \mathbf{E} = 0$ in the bulk is according to whether or not E_{\perp} , H_{\perp} are zero. E_{\perp} , H_{\perp} are the perpendicular components of the electric and magnetic field at the surfaces. We call magnetic waves [or transverse electric (TE)] those waves where $E_{\perp} = 0$ at every point of the separating surfaces. The magnetic waves are also called *S*-waves or *s*-polarization waves in optics. We call electric waves [or transverse magnetic (TM)] those with $H_{\perp} = 0$ at the surfaces. The electric waves are also called *P*-waves or *p*-polarization waves in optics. Note that for the general surface the solutions are a mixture of *S*- and *P*-waves. However, some simple surfaces as the plane (or a set of parallel planes) or the sphere (or a set of concentric spheres) allow pure magnetic and pure electric waves.³² The cylindrical geometry allows neither pure magnetic waves nor pure electric waves.³² The magnetic waves are transverse waves in the sense that $E_L \equiv 0$ (the electric charge is everywhere, both in the bulk and at the surfaces, equal to zero). On the other hand, the nonmagnetic solutions (or the electric waves if they exist) have both transverse and longitudinal components coupled together²⁶ (there is charge at the surface and there is a nonzero magnetic field).

The so-called surface plasma oscillations (SPO) are solutions with $\nabla \cdot \mathbf{E} = 0$ in the bulk, "bound," of nonmagnetic type (electric waves if the latter exist).

The SPO are characterized by the following properties, distinguishing them from the bulk plasma oscillations:

1. There is no bulk charge, $\rho = 0$, only surface charge, $\rho_s \neq 0$.
2. Both transverse and longitudinal fields are present and coupled together (the full set of Maxwell equations is required in general for their study) E_T , \mathbf{H} , $E_L \neq 0$.
3. The fields are not confined within the material but extend to both sides of the surface so that each surface (if more than one) cannot be considered independently.
4. The eigenfrequency of the SPO depends strongly on the geometry as well as on the form of the dielectric function.

Our main interest here is to study the SPO. Other solutions are examined to the extent that they are related with SPO.

B. Specific Cases

1. Parallel Plane Surfaces

We first examine very briefly the bulk plasma oscillations in these geometries. One set of solutions for an SSP film has an electric field inside the film of the form $\mathbf{E} = \mathbf{z}_0 E_0 e^{i(\omega t - k_z z)}$ where the *z*-axis is perpendicular to

the plane surfaces; the frequency is given as a solution of $\epsilon(\omega)=0$; the space charge inside the material is $\rho = -(ik_z/4\pi)E_0 e^{i(\omega t - k_z z)}$ and the surface charge at the two boundaries $z=a$, $z=a+d$ is $\rho_s = (E_0/4\pi)e^{i(\omega t - k_z a)}$ and $\rho_s = -(E_0/4\pi)e^{i(\omega t - k_z a - k_z d)}$, respectively. This surface charge completely screens the field so that $\mathbf{E}=0$ outside the film. Note that for $k_z=0$ the bulk charge is exactly equal to zero so that this particular bulk oscillation belongs also to the group of solutions with $\nabla \cdot \mathbf{E}=0$ in the bulk. We will see later that this is actually the case.

Let us now examine the solutions with $\nabla \cdot \mathbf{E}=0$ in the bulk. The plane geometry always allows the separation of the solution to *S*-waves and *P*-waves. Here we are interested in the *P*-waves. The solutions, due to the translational invariance in the direction parallel to the surfaces, contain a factor $e^{i(\omega t - \mathbf{k}_\parallel \cdot \mathbf{R})}$ where \mathbf{R} and \mathbf{k}_\parallel are two-dimensional vectors parallel to the plane surfaces. The position vector is given by $\mathbf{r} = \mathbf{R} + z_0 \mathbf{z}$. Within each material *i* one can use Maxwell's equations to express the component of the field in terms of

$$E_z = F(z) e^{i(\omega t - \mathbf{k}_\parallel \cdot \mathbf{R})} \quad (3.7)$$

Thus we have

$$\mathbf{E}_\parallel = -\frac{i\mathbf{k}_\parallel}{k_\parallel^2} \frac{dE_z}{dz} \quad (3.8)$$

$$\mathbf{H}_\parallel = \mathbf{z}_0 \times \mathbf{k}_\parallel \frac{\omega \epsilon_i}{ck_\parallel^2} E_z \quad (3.9)$$

with

$$\frac{d^2 F}{dz^2} - K_i^2 F = 0 \quad (3.10)$$

where

$$K_i = \left(k_\parallel^2 - \frac{\omega^2 \epsilon_i}{c^2} \right)^{1/2}; \quad \text{Re } K \geq 0 \quad (3.11)$$

The general solution of (3.10) is a linear combination of $e^{K_i z}$ and $e^{-K_i z}$. One can distinguish two cases:

$$(a) \quad k_\parallel^2 > \frac{\omega^2 \epsilon_i}{c^2} \quad (3.12)$$

$$(b) \quad k_\parallel^2 < \frac{\omega^2 \epsilon_i}{c^2} \quad (3.13)$$

A small imaginary part in ϵ_i is omitted for the sake of simplicity and clarity in the argument. For case (a) and $z \rightarrow +\infty$ or $z \rightarrow -\infty$ the solution is $e^{-K_i z}$ or $e^{+K_i z}$, respectively, that is it decays exponentially and therefore it is always a bound nonradiative solution. On the other hand, for case (b) the solution is of the form $Ae^{+iK_i|z} + Be^{-iK_i|z}$ and, for $z \rightarrow \pm\infty$, both terms may be present. Thus for case (b) we have always radiative solutions, either the incident wave solutions or, possibly, radiative bound solutions; the direction of propagation makes an angle θ with the z -axis which is given by

$$\sin \theta_i = \frac{k_{\parallel}}{(k_{\parallel}^2 + |K_i|^2)^{1/2}} = \frac{ck_{\parallel}}{\omega \sqrt{\epsilon_i}} \quad (3.14)$$

Note that case (a) corresponds to complex values of $\sin \theta_i$ which means that if one has already obtained the incident wave solutions [case (b), $\sin \theta_i$ real] and wants to use these solutions to obtain the bound nonradiative solutions [case (a)], it should allow $\sin \theta_i$ to become a complex number so as to describe a decaying solution. For the vacuum the condition (3.13) means that $\omega > ck_{\parallel}$ and for a plasma of dielectric function $\epsilon(\omega) = 1 - \omega_p^2/\omega^2$ it implies that $\omega^2 > \omega_p^2 + c^2 k_{\parallel}^2$. Since in all practical cases the system is surrounded by the vacuum, the condition for existence of radiative solutions is

$$\omega > ck_{\parallel}$$

In the following subsections we discuss briefly some specific cases.

a. Single Plasma-Vacuum Interface. For a single interface at $z=0$ and for bound solutions, $F(z)$ has the form

$$F(z) = \begin{cases} A_1 e^{K_p z}, & z < 0 \\ A_2 e^{-K_v z}, & z > 0 \end{cases} \quad (3.15)$$

where the plasma occupies the $z < 0$ half-space. The fields \mathbf{E}_{\parallel} and \mathbf{H}_{\parallel} can be calculated from (3.7) to (3.9); the continuity of \mathbf{E}_{\parallel} and \mathbf{H}_{\parallel} at $z=0$ gives two linear homogeneous equations for the constants A_1 and A_2 . In order to obtain a nonzero solution the determinant should be equal to zero which is equivalent to

$$R \equiv - \frac{(K/\epsilon)_{\text{plasma}}}{(K/\epsilon)_{\text{vacuum}}} = 1 \quad (3.16)$$

For $\epsilon(\omega) = 1 - \omega_p^2/\omega^2$, (3.16) is satisfied when

$$\omega = \omega_p \left[1 + \frac{2}{2q^2} + \left(1 + \frac{1}{4q^4} \right)^{1/2} \right]^{-1/2} \quad (3.17)$$

where $q = k_{\parallel}/k_p$ and $k_p = \omega_p/c$.

If electrostatic theory had been used, the condition (3.16) would become

$$\epsilon_{\text{plasma}} = -\epsilon_{\text{vacuum}} \quad (3.16')$$

since in the electrostatic case $K_i = k_{\parallel}$. The dispersion relation would be

$$\omega = \frac{\omega_p}{\sqrt{2}} \quad (3.17')$$

Note that the correct solution (3.17) approaches the approximate electrostatic solutions as ω/k_{\parallel} becomes much smaller than c , in agreement with the general remark made previously (see Fig. 2). Note also that all the bound solutions are not radiative. There are no virtual (radiative or not) modes for this geometry.

Ritchie³³ was the first to predict the SPO at $\omega_p/\sqrt{2}$. Stern and Ferrell³⁴ have discussed the mode in detail and Powell and Swan³⁵ have detected

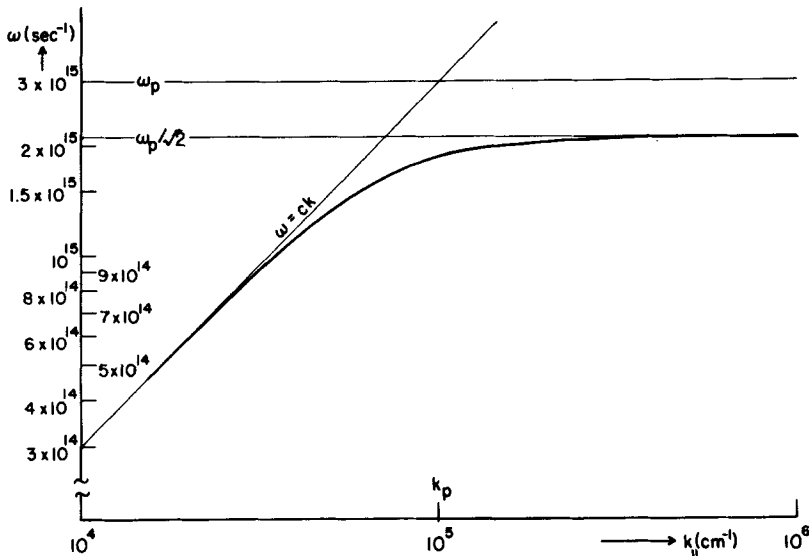


Fig. 2. ω versus k for the SP at the plane interface of a plasma [$\epsilon(\omega) = 1 - \omega_p^2/\omega^2$] and the vacuum; ω_p has been chosen to be $3 \times 10^{15} \text{ sec}^{-1}$.

the mode experimentally. For a discussion of the experimental situation, see the review articles listed in Refs. 2 to 7 as well as the papers by Raether³⁶ and Kunz.³⁷

The incident wave solutions (which are essentially modified bulk solutions) are of two types: The incident wave is coming from the vacuum or the incident wave is coming from the plasma. The incident wave in the first case is characterized by a 3-*d* vector $\mathbf{k} = \mathbf{k}_{\parallel} + \mathbf{z}_0 k_z$, a frequency $\omega = c|\mathbf{k}|$, and an amplitude b_{inc} . We can equivalently characterize the incident wave by the angle θ , which the vector k makes with the *z*-axis, the parallel component of \mathbf{k} , k_{\parallel} , its frequency, and its amplitude b_{inc} . The reflected and the refracted waves have directions which are determined by Snell's law (which is a consequence of the boundary conditions), and have the same frequency and amplitudes b_{refl} and b_{refr} which are proportional to b_{inc} , that is, $b_{\text{refl}} = f_{\text{refl}} b_{\text{inc}}$ and $b_{\text{refr}} = f_{\text{refr}} b_{\text{inc}}$; the reflectance is defined by

$$R = |f_{\text{refl}}|^2 \quad (3.18)$$

The result for R is given in all books on electrodynamics⁹

$$R = \left| \frac{\epsilon(\omega) \cos \theta - [\epsilon(\omega) - \sin^2 \theta]^{1/2}}{\epsilon(\omega) \cos \theta + [\epsilon(\omega) - \sin^2 \theta]^{1/2}} \right|^2 \quad (3.19)$$

According to the general discussion given in the previous subsection the bound solutions will appear as poles of R . We note that R does not blow up for real values of θ which means that there are no radiative bound solutions. R has poles, however, corresponding to imaginary values of θ . The poles are given by

$$\epsilon(\omega) \cos \theta + [\epsilon(\omega) - \sin^2 \theta]^{1/2} = 0 \quad (3.20)$$

which is identical to (3.16) if (3.14) is taken into account with $\epsilon_i = 1$.

Kliwer and Fuchs²³ have calculated the reflection coefficient in the anomalous skin effect regime by using a nonlocal dielectric function. They solve the problem both by the general approach based on the Boltzmann-Vlasov equation in the presence of the surface (specular reflection was assumed) and by a technique which allowed them to use the nonlocal bulk dielectric function. Their result for R is

$$R = \left| \frac{\cos \theta - z'_p}{\cos \theta + z'_p} \right| \quad (3.21)$$

where

$$z'_p = \frac{2i\Omega}{\pi} \int_0^\infty \frac{dQ_z}{Q} \left[\frac{Q_{\parallel}^2}{\Omega^2 \epsilon_L(\Omega, Q)} + \frac{Q_z^2}{\Omega^2 \epsilon_T(\Omega, Q) - Q^2} \right] \quad (3.22)$$

$\Omega = \omega/\omega_p$, $Q_z = k_z/k_p$, $Q = k_{\parallel}/k_p$, and ϵ_T, ϵ_L are the nonlocal transverse and longitudinal dielectric functions. If $\epsilon_L(\Omega, Q) = \epsilon_T(\Omega, Q) = \epsilon(\Omega)$, (3.21) reduces to (3.19). In the anomalous skin effect regime (3.21) shows a different behavior than the classical (3.19).

Melnyk and Harrison^{28,38} studied the reflection problem by using a nonlocal dielectric function tensor derived from the Boltzmann-Vlasov equation. They also eliminated the assumption of a surface capable of sustaining surface charge. As a result of this generalization, the solutions with $\nabla \cdot \mathbf{E} = 0$ and $\nabla \cdot \mathbf{E} \neq 0$ in the bulk are now coupled since the surface charge is spread over a finite volume.^{8,39} Mathematically, this is achieved through the boundary conditions which are now supplemented by E_{\perp} being continuous across a surface; this new boundary condition is satisfied only if both $\nabla \cdot \mathbf{E} = 0$ and $\nabla \cdot \mathbf{E} \neq 0$ solutions are present. The effects of this generalization are negligible for the case of a single interface.

The single-interface problem for the case of a high-temperature, low-density plasma has been studied by Guernsey⁴⁰ using the Boltzmann-Vlasov equation.

b. Thin Film in a Vacuum. Following a procedure similar to that of single interface, we find that, in order to have a bound solution (of P -type) in the case of a plasma slab characterized by $\epsilon(\omega)$, the following equation should be satisfied:

$$\frac{1-R}{1+R} = \pm e^{-K_p d} \quad (3.23)$$

where R is given by (3.16), $K_p = [k_{\parallel}^2 - \omega^2 \epsilon(\omega)/c^2]^{1/2}$, and d is the thickness of the film. The plus and minus signs correspond to a symmetric and antisymmetric solution, respectively.

The electrostatic limit can be obtained either from (3.23) by allowing $c \rightarrow \infty$ or independently from the boundary conditions of the electrostatic case. The result is

$$\frac{\epsilon_p(\omega) + 1}{\epsilon_p(\omega) - 1} = \pm e^{-k_{\parallel} d} \quad (3.24)$$

which can be solved explicitly to give the dispersion relation

$$\omega^{(\pm)}(k_{\parallel}) = \frac{\omega_p}{\sqrt{2}} [1 \mp e^{-k_{\parallel}d}]^{1/2} \quad (3.25)$$

Thus there are two branches, the symmetric (or tangential) branch, $\omega^{(+)}(k_{\parallel})$, corresponding to the upper sign, and the antisymmetric (or normal) branch, $\omega^{(-)}(k_{\parallel})$ corresponding to the lower sign in (3.24).

The modes resulting from (3.23) are considerably more complicated. They are plotted schematically in Fig. 3, together with the results of the electrostatic theory. The lower mode $\omega^{(+)}(k_{\parallel})$ is pushed down below the c line as a result of the retardation effects. The upper mode is modified in a more complicated way: It is pushed all the way to zero along the c line so that two submodes emerge; the one below the c line is a real nonradiative one; the other above the c line is a radiative virtual mode, as every bound solution above the c line should be. For this radiative mode $\omega^{(-)}(k_{\parallel})$ has

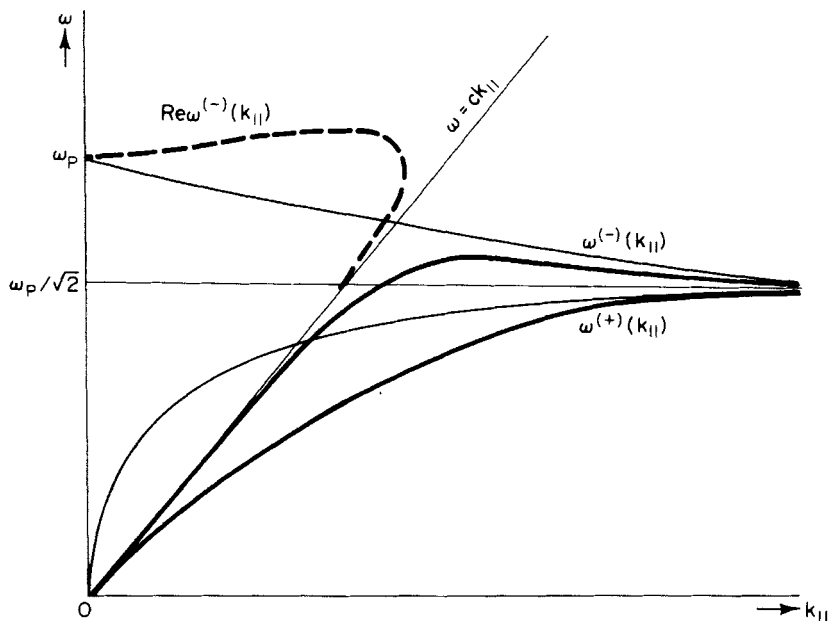


Fig. 3. Dispersion relations for SP of a plasma slab [$\epsilon_p(\omega) = 1 - \omega_p^2/\omega^2$] of thickness d (schematically). The light solid lines are the electrostatic results. The heavy lines are the full electromagnetic results; the heavy solid lines are nonradiative real eigenmodes; the dashed heavy line is a radiative virtual mode.

both a real and a small imaginary part. The dashed line in Fig. 3 is a plot of $\text{Re } \omega^{(-)}(k_{\parallel})$. The imaginary part of $\omega^{(-)}(k_{\parallel})$ is exactly zero at $k_{\parallel}=0$ and increases as we approach the c line until it becomes comparable to the real part, in which case we cannot talk about an eigenmode at all.

According to the general discussion given above, these modes would appear as peaks or infinities of the reflection coefficient for this geometry. In other words, if the reflection coefficient R is written as a function of k_{\parallel} [using (3.14) with $\epsilon_i = 1$], then R would blow up along the lines $\omega = \omega^{(\pm)}(k_{\parallel})$ of the ωk_{\parallel} plane, and it would exhibit a maximum along the line $\omega = \text{Re } \omega^{(-)}(k_{\parallel})$ of the ωk_{\parallel} plane. Note, however, that the infinities occur for nonreal values of $\sin \theta$ and as a result have no effect on the optical properties of the system. In contrast the virtual mode corresponds to real values of $\sin \theta$ and should influence the optical behavior of the system.

As the thickness of the film increases, $\omega^{(-)}(k_{\parallel})$ and $\omega^{(+)}(k_{\parallel})$ come closer together and in the limit $d \rightarrow \infty$ they become degenerate as they should since at $d \rightarrow \infty$ the charge oscillations of the two surfaces become decoupled. As d increases, the lifetime of the virtual mode decreases and, when d is such that $d\omega_p/c \gtrsim 1$, the lifetime is so short that the virtual mode disappears.

For thin foils and for $\theta < \pi/4$, the quantities $\text{Re } \omega^{(-)}$ and $\text{Im } \omega^{(-)}$ are given by⁴¹

$$\text{Re } \omega^{(-)} \approx \omega_p + \frac{1}{8} \omega_p \left(\frac{\omega_p d}{c} \right)^2 \tan^2 \theta \quad (3.26)$$

$$\text{Im } \omega^{(-)} \approx \omega_p \frac{\omega_p d}{4c} \sin \theta \tan \theta \quad (3.27)$$

where $\sin \theta = ck_{\parallel} / \text{Re } \omega^{(-)} \approx ck_{\parallel} / \omega_p$.

Analytical expressions for the $\omega^{(\pm)}$ modes just below the c line can be found in Ref. 26.

It should be noted that in addition to the modes illustrated in Fig. 3 a host of other virtual modes are predicted⁴¹ by (3.23). All these modes are lying well above ω_p (and above the c line of course); they have rather short lifetimes and are thickness dependent. The existence of these modes means physically that the reflection coefficient exhibits additional peaks for high frequencies. The short lifetime indicates that these peaks are rather broad and not so well defined. The physical origin of these virtual modes is a relative "confinement" of the electromagnetic field within the foil via a multiple reflection process. This physical interpretation is supported by the facts⁴¹ (a) that the modes depend strongly on the thickness of the film, and (b) that at the vicinity of Brewster's angle ($\tan \theta = \sqrt{\epsilon_p}$), where the slab

becomes more transparent and multiple reflection is weakened, the virtual modes are ill defined.

The thin film case and especially the virtual mode with $\text{Re } \omega^{(-)} \approx \omega_p$ have been discussed extensively starting with the classical paper by Ferrell.⁴² The reader is referred to the review papers^{5,8} and for more detailed information to Refs. 43 to 59. Note also that the bulk plasma oscillations have been observed for thin films.⁶⁰⁻⁶² The initial treatment by Ferrell⁴² was based on electrostatic theory. Some arguments were proposed that the upper mode is not affected by retardation effects, at least for small k_{\parallel} , and then the radiation was calculated from the vector potential $\mathbf{A} = (1/c) \int \mathbf{j} dV$. Having the radiation field one can easily obtain the radiative decay rate that agrees with (3.27).

The incident wave solutions can be obtained by the standard technique,⁹ already outlined. The results for the reflection and transmission coefficients R and T are summarized and discussed in Ref. 5. It is noted here that the vanishing of the denominator for the reflection coefficient is equivalent with (3.23), as is expected from the general discussion. For thin films the reflection coefficient has a sharp maximum at ω_p corresponding to the virtual mode. This maximum is equal to 1 if $\text{Im } \epsilon = 0$. The transmission coefficient shows a minimum at $\omega = \omega_p$ for the same reasons. The absorption $A \equiv 1 - R - T$, which is proportional to $\text{Im } \epsilon$, shows a peak at $\omega = \omega_p$. This resonance structure in the absorption coefficient appears in the experiments of photoemission since the latter is proportional to the strengths of the fields which exhibit a resonance structure at $\omega = \omega_p$. For a full discussion of this point, see the review paper by Steinmann⁵ and the references cited therein. This same structure in A has been used to explain the enhanced absorption of laser energy incident on solid targets.⁶³

More complicated expressions for R , T , and A have been obtained by Melnyk and Harrison^{28,38} in their generalized treatment previously outlined. In the case of a thin film, additional structure is predicted due to the coupling with the bulk plasmons. Before we proceed to other geometries, we consider certain questions that have been examined extensively in the literature.

The "coupling" of photons with SPO has been used to explain the peaks in the reflection coefficient. The word "coupling" may be misleading since both the photons and the SPO are eigenmodes of the same system, namely, the electromagnetic field in the presence of an inhomogeneous dielectric function $\epsilon(\omega)$. The use of Maxwell's equations suffices for the complete description of both eigenmodes. To demonstrate this point, we mention here that the peak in the reflection coefficient for P -waves can be "explained" without introducing the virtual mode concept at all. Thus one can easily see that the reflection coefficient for P -waves is exactly equal to

unity when $\epsilon(\omega)=0$ no matter what the thickness of the film. On the other hand, the penetration depth of the field inside the plasma is given by $|K_p^{-1}| \approx \lambda_p / \sin \theta$. When d is much smaller than $|K_p^{-1}|$, the field should easily penetrate the plasma and the reflection coefficient should be small. Therefore, for the case of thin films ($d|k_p| \ll 1$), we pass from a condition of total reflection to almost perfect penetration as ω changes from ω_p to lower or higher frequencies in agreement with the observation. The situation is, of course, different when the electrostatic equations (instead of Maxwell's equations) have been used for the description of the SPO. In this case, one should add by hand the coupling of the electrostatic field (longitudinal field) with the transverse part of the electromagnetic field to remedy the omission of this coupling at the very beginning. It should be pointed out that the use of Maxwell's equations is not considerably more complicated than the electrostatic approach; it is physically straightforward, it gives automatically the total radiation without calculating the fields, and can be used everywhere in contrast to the electrostatic approach which is valid only when the retardation effects (RE) are negligible or small.

As a matter of fact, it is not so trivial to recognize whether or not the RE are important when the geometry is complicated. In the case where the only length is the wavelength λ , as in an infinite system or in a single interface, the RE are unimportant when $\lambda \ll c/\omega$ and they become increasingly important as λ increases. We consider now the more complicated case where there may be different lengths λ_i characterizing the variation of the fields as well as a length d characterizing the geometrical dimension of the system. Whenever $\min(\lambda_i) \ll c/\omega$, then retardation effects are negligible. This is so because the field is appreciable only for distances comparable to or less than $\min(\lambda_i)$ from the surfaces and consequently this field is due to charges being no further away than $\min(\lambda_i)$. When $\min(\lambda_i) \gg c/\omega$ and $d \gtrsim c/\omega$, retardation effects are expected to be important since both characteristic lengths are longer than c/ω . The case $\min(\lambda_i) \gg c/\omega$ and $d \ll c/\omega$ is more subtle because the importance of RE depends on the nature of the mode as well. Consider, for example, the two modes $\omega^{(+)}$ and $\omega^{(-)}$ for a thin film geometry. For the $\omega^{(+)}$ mode the charges of the two surfaces are of the same sign and, as a result, the field inside the slab is due to contributions from charges at a distance comparable to the wavelength. Therefore, for the field inside the slab, as well as the distant field, the retardation effects are important. On the other hand, for the $\omega^{(-)}$ mode the field inside is due to contributions from charges at a distance d and, as a result, the field inside the slab is unaffected by RE. The distant field is affected by RE, but, for small k (large λ), the distant field as well as the modifications from RE are very small. This can be seen from the fact that for $k_{\parallel}=0$ and $\omega=\omega_p$ the eigenmode can be considered both as an SPO

(since there is no space charge) and as a bulk oscillation as well (since it occurs at $\omega = \omega_p$, the fields are confined exclusively within the slab, and are of purely longitudinal nature, i.e., no coupling with the transverse fields) and consequently, there are no retardation effects at $\omega = \omega_p$ and $k_{\parallel} = 0$. By continuity arguments we expect that the retardation effects are small for small $k_{\parallel}d$, as is actually the case. This discussion shows that the virtual mode becomes a real, nonradiative "bulk" mode at $k_{\parallel} = 0$. For this reason we simply call it a virtual mode without specifying it as surface or bulk mode.

From Fig. 3 we see that the most dramatic effects due to retardation appear when $\lambda \approx c/\omega$ independently of d . The physical explanation is as follows: When some dimension of the system is much larger than c/ω (in the present case the dimensions parallel to the plane surfaces) the field of a uniform charge or current distribution at large distances is attenuated because of destructive interference due to the finiteness of the velocity of light. As a result, the total radiation drops drastically and the field at large distances is negligible as in the electrostatic case. This is another way of explaining why retardation effects are negligible for the distant fields of the upper mode and for $k_{\parallel} \approx 0$. However, when the charge or current distribution exhibits a periodic variation itself, it may eliminate the destructive interference due to the finiteness of the velocity of light; this can only happen when $\lambda \approx c/\omega$. Thus when $\lambda \approx c/\omega$, strong radiation is expected and therefore a strong departure from the electrostatic behavior.

c. Tunneling Geometry. This geometry is shown in Fig. 4. Having in mind applications in semiconductor-metal tunneling,⁶⁴ the dielectric functions have been chosen as $\epsilon_M(\omega) = 1 - \omega_M^2/\omega^2(1 - i/\omega\tau_M)$, $\epsilon_S(\omega) = \epsilon_{\infty}[1 - \omega_S^2/\omega^2(1 - i/\omega\tau_S)]$, and $\epsilon_I = \epsilon_{\infty}$. The metal-vacuum-metal case can be easily obtained by putting $\epsilon_{\infty} = 1$. The dispersion relations are given⁶⁴ by the equation

$$R_S R_M - (R_M + R_S) \coth K_I d + 1 = 0 \quad (3.28)$$

where

$$R_S = \frac{-\epsilon_I K_S}{\epsilon_S K_I}, \quad R_M = \frac{-\epsilon_I K_M}{\epsilon_M K_I}$$

and

$$K_i = \left(k_{\parallel}^2 - \frac{\omega^2 \epsilon_i}{c^2} \right)^{1/2}, \quad i = I, S, M$$

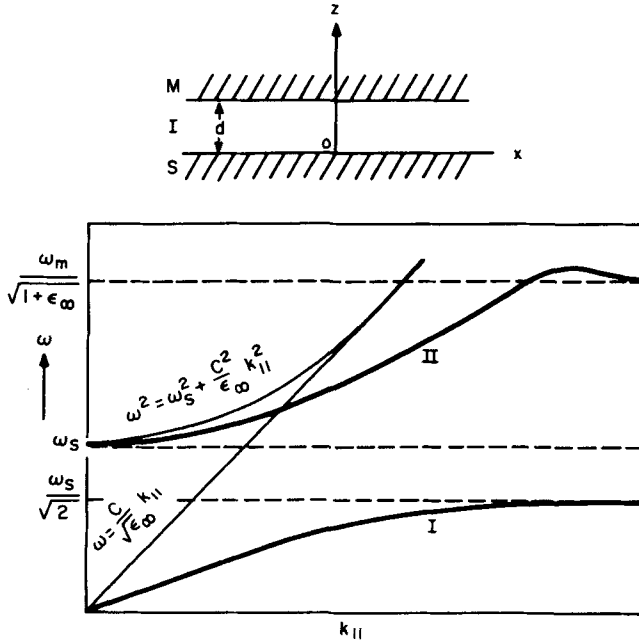


Fig. 4. Geometry and dispersion relations for SP of an idealized metal semiconductor junction. (After Ngai, Economou, and Cohen.⁶⁴)

The electrostatic result is

$$\frac{\epsilon_I^2}{\epsilon_S \epsilon_M} + \frac{\epsilon_I(\epsilon_S + \epsilon_M)}{\epsilon_S \epsilon_M} \coth k_{||} d + 1 = 0 \quad (3.29)$$

For the particular case $\epsilon_\infty = 1$, $\omega_S = \omega_M$, and $\tau_S = \tau_M = 0$, the solutions of (3.29) are

$$\omega = \frac{\omega_p}{\sqrt{2}} (1 \pm e^{-k_{||} d})^{1/2} \quad (3.30)$$

For the lower branch and for $\omega_S \ll \omega_M$ the solution of the electrostatic equation is

$$\frac{\omega}{\omega_S} = \frac{1}{\sqrt{2}} (1 - e^{-2k_{||} d})^{1/2} \quad (3.31)$$

The solutions of the full (3.28) are plotted schematically in Fig. 4. See also Ref. 26 for a plot and discussion of the modes in the case of a

metal-vacuum-metal junction; there are two modes, the lower of which is linear for small k_{\parallel} with a phase velocity given by

$$\bar{c} = c \left[\frac{d}{(d + \lambda_M + \lambda_S) \epsilon_{\infty}} \right]^{1/2} \quad (3.32)$$

where $\lambda_M = c/\omega_M$ and $\lambda_S = c/\omega_S$. This mode was first studied in connection with the I versus V characteristic of a Josephson tunnel junction⁶⁵⁻⁶⁷; it gives rise to the so-called Fiske steps. As is always the case for $\omega \ll ck_{\parallel}/\sqrt{\epsilon_{\infty}}$, RE are unimportant and the electrostatic equation (3.20) is adequate. In a later section we discuss the role of these eigenmodes in superconducting tunneling as well as metal-semiconductor tunneling. Here we note that the results predicted above seem to be valid even when the thickness of certain films becomes microscopic, in which case a full quantum mechanical treatment may be necessary.

d. Film on Substrate. This geometry is quite common. It simulates an oxidated film and it may even be considered as an approximation of the surface of certain materials. LEED studies⁶⁸⁻⁷⁰ on this geometry show a strong SPO influence. The geometry is shown in Fig. 5 where a metal film [$\epsilon_c(\omega) = 1 - \omega_c^2/\omega^2(1 - i/\omega\tau_c)$] is deposited on a metal substrate [$\epsilon_w(\omega) = 1 - \omega_w^2/\omega^2(1 - i/\omega\tau_w)$]. The dispersion relations are given⁶⁴ as solutions of

$$R_c R_w - (R_c + R_w) \coth K_c d + 1 = 0 \quad (3.33)$$

where

$$R_c = \frac{-\epsilon_c K_v}{K_c}, \quad R_w = \frac{-\epsilon_c K_w}{\epsilon_w K_c}$$

and $K_c = (k_{\parallel}^2 - \omega^2/c^2)^{1/2}$ and $K_i = (k_{\parallel}^2 - \omega^2\epsilon_i/c^2)^{1/2}$, $i = c, w$. The electrostatic result is

$$\frac{\epsilon_c^2}{\epsilon_w} + \frac{\epsilon_c \epsilon_w + \epsilon_c}{\epsilon_w} \coth k_{\parallel} d + 1 = 0 \quad (3.34)$$

In Fig. 5 we have plotted schematically the dispersion relations as resulting from (3.33) or its electrostatic limit (3.34). The region $\omega > ck_{\parallel}$ has not been investigated theoretically or experimentally for this geometry. It should be pointed out that the present "macroscopic" description seems to be valid even for thicknesses corresponding to a single monolayer. This assertion is supported by the calculations of Ngai et al.^{64,70} who have

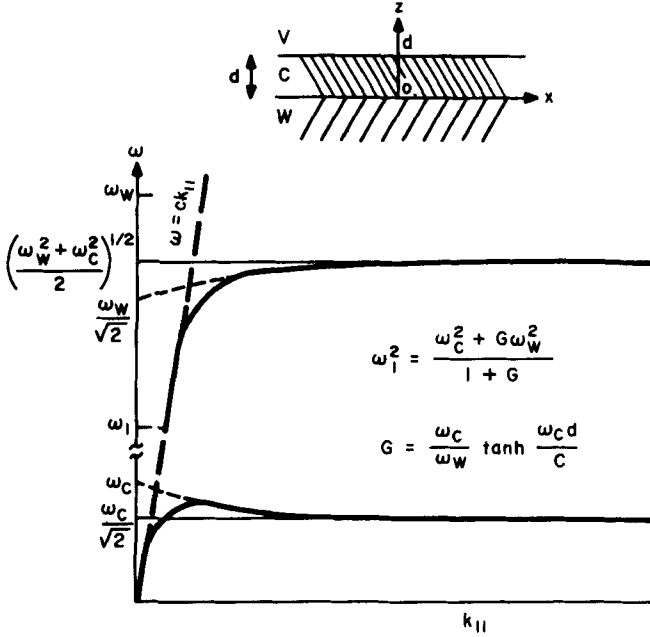


Fig. 5. Geometry and dispersion relation for SP at a deposited metal film on a metal substrate. (After Ngai and Economou.⁶⁴) Heavy solid lines are the full solutions including RE. Dashed lines are the electrostatic results.

shown that the present formulation reduces in the limit $d \rightarrow 0$ to a quantum mechanical treatment of a two-dimensional gas on the top of a metal surface. See in this connection the papers by Newns⁷¹ and Gadzuk.⁷²

e. Multiple Film Geometries. We present here results for a two-metal film geometry shown in Fig. 6. The dispersion relations are given implicitly by²⁶

$$\left(\frac{1-R}{1+R} \right)^4 - A_2 \left(\frac{1-R}{1+R} \right)^2 + \exp(-2K_p d_1 - 2K_p d_2) = 0 \quad (3.35)$$

where

$$A_2 = \exp(-2K_p d_1) + \exp(-2K_p d_2) \\ + \exp(-2K d_i) [1 - \exp(-2K_p d_1)] [1 - \exp(-2K_p d_2)]$$

and $K_p = [k_{||}^2 - \epsilon_p(\omega)\omega^2/c^2]^{1/2}$, $K = (k_{||}^2 - \omega^2/c^2)^{1/2}$, and $\epsilon_p(\omega)$ is the dielectric function of the metal. The resulting dispersion relations are shown

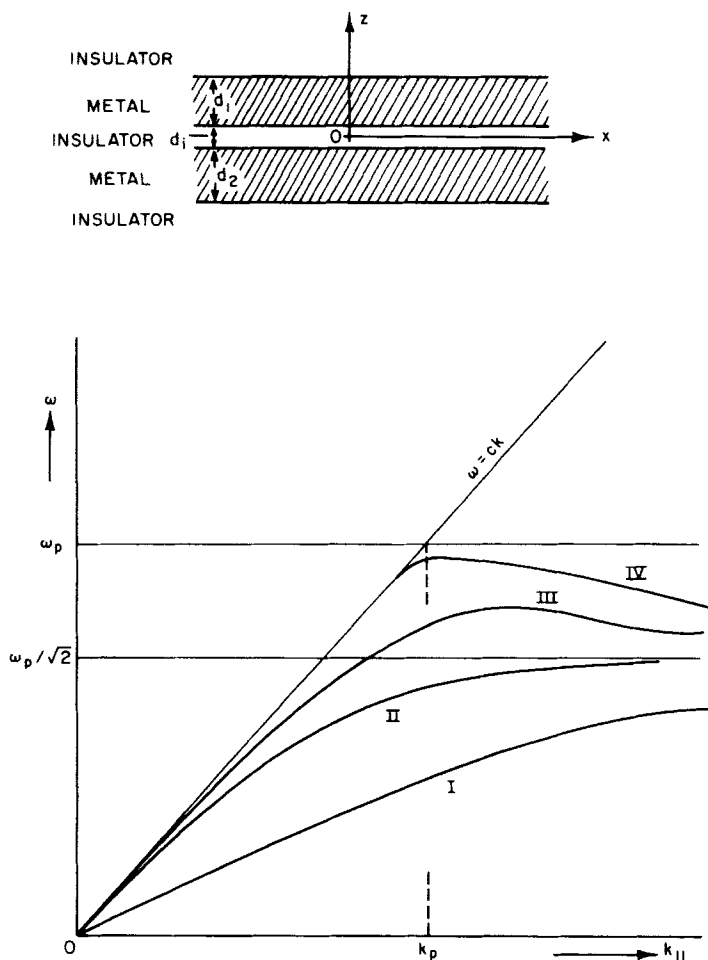


Fig. 6. Geometry and the dispersion relations for SP of two metal films separated by vacuum (schematically). The region $\omega \gtrsim ck$ has not been carefully investigated.

in Fig. 6. The region $\omega > ck_{||}$ has not been carefully investigated. However, one expects virtual radiative modes similar in nature with the ones in the single-film case, although more complicated due to the interference between the two films. The most interesting mode is the mode denoted by I in Fig. 6. For low $k_{||}$ it is linear with a phase velocity v_p given by

$$v_p = c \left[\frac{d_i}{d_i + \lambda_p (\coth k_p d_1 + \coth k_p d_2)} \right]^{1/2} \quad (3.36)$$

Note that in the electrostatic limit ($c \rightarrow \infty$)

$$v_p \xrightarrow{c \rightarrow \infty} \omega_p \left(\frac{d_1 d_2}{d_1 + d_2} \right)^{1/2} \quad (3.37)$$

This mode is important in connection with superconducting films. It influences the I versus V characteristic of Josephson junctions.⁶⁷ It may have observable effects in the thermodynamics of superconducting films because v_p may be as low as 10^8 cm/sec for extremely thin films; it may also influence the transition temperature of superimposed thin films since it provides an additional mechanism for electron attraction via exchange of surface plasmons. Finally, it should be mentioned that this mode is interesting from the theoretical point of view because it shows that in inhomogeneous systems the Coulomb force can create collective oscillations of linear dispersion relation $\omega \propto k_{\parallel}$, much like short-range interactions in homogeneous systems.²⁶

Other more complicated geometries of relevance to superimposed Josephson junctions have been studied in Ref. 26. It should be noted that the predictions in Ref. 26 for these more complicated geometries and for $\omega > ck_{\parallel}$ are incorrect.⁷³

2. Spherical Geometries

To study SPO in spherical geometries we have to write Maxwell's equations in spherical coordinates. It turns out³² that the spherical geometry allows the separation of the $\nabla \cdot \mathbf{E} = 0$ solutions into electric waves ($H_{\perp} \equiv H_r = 0$) and magnetic waves ($E_{\perp} \equiv E_r = 0$). As has been already discussed above, SPO are bound solutions with $\nabla \cdot \mathbf{E} = 0$ of the electric type. The fields of these solutions in spherical coordinates have³² the following general forms:

$$E_r^i = - \frac{l(l+1) Y_{ml}^i(\phi, \theta) b_l(\kappa_i r) e^{+i\omega t}}{\kappa_i r} \quad (3.38a)$$

$$E_{\theta}^i = - \left(\frac{\partial Y_{ml}^i}{\partial \theta} \right) \frac{e^{+i\omega t} [\kappa_i r b_l(\kappa_i r)]'}{\kappa_i r} \quad (3.38b)$$

$$E_{\phi}^i = - \sin^{-1} \theta \left(\frac{\partial Y_{ml}^i}{\partial \phi} \right) \frac{e^{+i\omega t} [\kappa_i r b_l(\kappa_i r)]'}{\kappa_i r} \quad (3.38c)$$

$$H_r^i = 0 \quad (3.38d)$$

$$H_{\theta}^i = \left(\frac{\kappa_i}{i\omega \sin \theta} \right) \left(\frac{\partial Y_{ml}^i}{\partial \phi} \right) b_l(\kappa_i r) e^{i\omega t} \quad (3.38e)$$

$$H_{\phi}^i = - \left(\frac{\kappa_i}{i\omega} \right) \left(\frac{\partial Y_{ml}^i}{\partial \theta} \right) b_l(\kappa_i r) e^{i\omega t} \quad (3.38f)$$

where

$$\kappa_i^2 = \frac{\omega^2 \epsilon_i(\omega)}{c^2}$$

$$Y_{ml}^i(\phi, \theta) = (A_{eml}^i \cos m\phi + A_{oml}^i \sin m\phi) P_l^m(\cos \theta)$$

$$b_l(x) = A_l j_l(x) + B_l h_l^{(2)}(x)$$

where l, m are nonnegative integers, $A_{eml}^i, A_{oml}^i, A_l^i, B_l^i$ are arbitrary constants, P_l^m is the Legendre polynomial, j_l and $h_l^{(2)}$ are the spherical Bessel and Hankel functions, and the prime denotes differentiation with respect to $\kappa_i r$. Note that

$$j_l(x) \xrightarrow{x \rightarrow 0} \frac{2^l l! x^l}{(2l+1)!} \quad (3.39a)$$

$$\xrightarrow{x \rightarrow \infty} \frac{1}{x} \cos \left(x - \frac{l+1}{2} \pi \right) \quad (3.39b)$$

and

$$h_l^{(2)}(x) \xrightarrow{x \rightarrow 0} \frac{-i(2l)!}{2^l l! x^{l+1}} \quad (3.40a)$$

$$\xrightarrow{x \rightarrow \infty} \frac{i^{l+1} e^{-ix}}{x} \quad (3.40b)$$

Because of (3.39) and (3.40), in regions including the origin $B_l^i = 0$ and in regions extending to infinity $A_l^i = 0$ (in order to have only an outgoing wave by definition of the "bound" solutions).

The continuity equations at the spherical surfaces separating different materials give us a system of linear homogeneous equations for the constants. In order to have a nonzero solution, the determinant of this system should be equal to zero. This is the condition that determines the eigenvalues of the SPO. Note that the eigenvalues do not depend on the number m . For a sphere of dielectric function $\epsilon_p(\omega)$ and radius R

surrounded by a material of dielectric function ϵ_0 , the procedure outlined above gives the eigenvalues implicitly as

$$\frac{[\kappa_p R j_l(\kappa_p R)]'}{\epsilon_p(\omega) j_l(\kappa_p R)} = \frac{[\kappa_0 R h_l^{(2)}(\kappa_0 R)]'}{\epsilon_0 h_l^{(2)}(\kappa_0 R)} \quad (3.41)$$

In the electrostatic limit ($c \rightarrow \infty$) with the help of (3.39) and (3.40), (3.41) reduces to

$$\epsilon_p(\omega) = -\frac{l+1}{l} \epsilon_0 \quad (3.42)$$

If $\epsilon_p(\omega) = 1 - \omega_p^2/\omega^2$ and ϵ_0 is constant, we obtain

$$\omega_l = \omega_p \left[\frac{l}{l + (l+1)\epsilon_0} \right]^{1/2} \quad (3.43)$$

which for $\epsilon_0 = 1$ and $l = 1$ (the lowest nonzero mode) becomes

$$\omega_1 = \frac{\omega_p}{\sqrt{3}} \quad (3.44)$$

The electrostatic solution is adequate when the RE are negligible. According to the general discussion given before, RE are negligible whenever the length over which the fields vary ($\pi R/l$ for the present case) is much smaller than ω/c . Thus the criterion for the omission of RE is

$$\frac{cR}{l\omega_p} \ll 1 \quad (3.45)$$

As can be seen from (3.38) and (3.40b), the SPO in a plasma sphere surrounded by a dielectric are always radiative. The radiative decay rate can be calculated directly from (3.41) as the imaginary part of the eigenvalue. The same quantity can be calculated approximately as follows: Use electrostatic theory to solve the problem; this is allowed only if (3.45) is satisfied. Then introduce the coupling of the electrostatic field with transverse fields from the equation $\mathbf{A} = (1/c) \int \mathbf{j} dv$, where \mathbf{j} is the current density in the sphere. From \mathbf{A} one can calculate the Poynting vector and the total radiation. Note that this procedure is necessary only because of the use of the electrostatic approximation. If Maxwell's equations are used, the radiative decay is given automatically and one should not talk about

coupling of photons with surface plasmons. In the case where (3.45) is satisfied, one solves (3.41) approximately by expanding the spherical Bessel functions in powers of the small quantities $\kappa_p R$ and $\kappa_0 R$. One then finds⁷⁴ that the correction to (3.43) has a real part which is of second order in cR/ω_p and an imaginary part which is of third order in cR/ω_p . This latter correction agrees with the result obtained by Crowell and Ritchie⁷⁵ using a variation of the electrostatic approach outlined above.

In addition to the bound solutions discussed above (which are always radiative and virtual), there are incident wave solutions. If the incident wave is a spherical wave, then the solutions will be of the type (3.38); but at infinity, the coefficient A_l^i in $b_l(x)$ will be equal to $2 \cdot A_{\text{inc}}$ where A_{inc} is the amplitude of the spherical incident wave. Then, from the continuity equations, all other constants will be expressed in terms of A_{inc} . In particular, the strength of the outgoing wave will be

$$B_l + A_{\text{inc}} = f_l A_{\text{inc}} \quad (3.46)$$

where f_l is the scattering coefficient. As was discussed above, whenever the frequency of the incident wave coincides with an eigenfrequency of the system corresponding to a bound solution, $f_l = \infty$. In the present case all the eigenfrequencies of bound solutions and consequently $f_l(\omega)$ will exhibit a peak whenever ω coincides with $\text{Re } \omega_l$. In practice, however, the incident wave is not a spherical wave but a plane wave. The solution then is obtained as follows: The plane incident wave is analyzed in spherical waves (partial-wave analysis); for each partial spherical wave the solution proceeds as outlined above and the total scattering wave is found by summing all the partial scattered waves. This procedure was followed by Mie,⁷⁶ who obtained the total scattering coefficient. The total scattering coefficient exhibits peaks whenever $\omega = \text{Re } \omega_l$, $l = 1, 2, \dots$.

When $\text{Im } \epsilon_p(\omega) \neq 0$, there would be absorption of electromagnetic energy in addition to scattering. The absorption can be easily calculated from the conservation of energy. If $\omega = \text{Re } \omega_l$, the absorption would have a maximum, since at $\omega = \text{Re } \omega_l$ the fields inside the sphere exhibit a maximum due to the resonance condition.

Natta⁷⁷ has examined the problem of SPO in spherical cavities. The dispersion relation for this geometry can be obtained from (3.41) or (3.42) by interchanging $\epsilon_p(\omega)$ and ϵ_0 . The result for the electrostatic regime studied by Natta is

$$\omega_l = \frac{\omega_p}{[1 + \epsilon_0 l / (l + 1)]^{1/2}} \quad (3.47)$$

For the case of a dielectric sphere surrounded by a spherical plasma shell Natta⁷⁷ obtained the radiation modes using Maxwell's equation and expanding in powers of the small quantity $\omega R/c$.

The possibility of SPO in spheres was realized a long time ago.⁷⁸ Surface plasma oscillations in spheres were studied theoretically by Fujimoto et al.⁷⁹ and Kreibig and Zacharias⁸¹ and experimentally in absorption or electron loss measurements in Refs. 79 and 81 as well as by Doremus,⁸² Doyle,⁸³ and Greuzburg.⁸⁴ Koumelis et al.⁸⁵ observed spherical SPO in inelastic scattering of X-rays. Finally Kokkinakis and Alexopoulos⁸⁶ observed directly the radiation associated with SPO.

Qualitative results⁸⁷ on inelastic loss in electron microscopy tend to confirm the predictions for SPO in spherical bubbles.

3. Circular Cylinder

We consider here briefly the case of a circular cylindrical plasma of diameter d and dielectric function $\epsilon_p(\omega)$ under vacuum ($\epsilon_0 = 1$). This case has been considered recently by Ngai and Economou,⁸⁸ Miziumski,⁸⁹ and Economou et al.⁹⁰

To study SPO in cylindrical geometries we have to find solutions of Maxwell's equations in cylindrical coordinates with the z -axis along the axis of the cylinder. The present geometry *does not* allow³² the existence of purely electrical waves. Thus the solutions we consider have both E_r and H_r different from zero. For bound solutions with $\nabla \cdot \mathbf{E} = 0$, as the SPO are, the eigensolutions have the following form³²:

$$E_r = \begin{cases} \left[\frac{k_z}{K_p} J'_n(iK_p r) a_n^i + \frac{\omega n}{K_p^2 r} J_n(iK_p r) b_n^i \right] F_n & \text{for } r < \frac{d}{2} \\ \left[\frac{k_z}{K_0} H_n^{(1)'}(iK_0 r) a_n^e + \frac{\omega n}{K_0^2 r} H_n^{(1)}(iK_0 r) b_n^e \right] F_n & \text{for } r > \frac{d}{2} \end{cases} \quad (3.48)$$

with similar³² expressions for the other components E_z , E_θ , H_r , H_z , H_θ , where

$$K_j^2 = k_z^2 - \frac{\omega^2 \epsilon_j(\omega)}{c^2}, \quad j = p, 0$$

$$F_n = \exp(i n \theta + i k_z z - i \omega t)$$

$J_n(x)$, $H_n^{(1)}(x)$ are Bessel and Hankel functions, the prime denotes

differentiation with respect to the corresponding argument x , and $a_n^{i,e}$, $b_n^{i,e}$ are constants to be determined from the boundary conditions. In order to have nonzero solutions the following equation should be satisfied:

$$\left[\frac{2}{iK_p d} \frac{J'_n(iK_p d/2)}{J_n(iK_p d/2)} - \frac{2}{iK_0 d} \frac{H_n^{(1)'}(iK_0 d/2)}{H_n^{(1)}(iK_0 d/2)} \right] \cdot \left[\frac{\omega^2 \epsilon_p(\omega)}{iK_p c^2} \frac{J'_n(iK_p d/2)}{J_n(iK_p d/2)} - \frac{\omega^2}{c^2 iK_0} \frac{H_n^{(1)'}(iK_0 d/2)}{H_n^{(1)}(iK_0 d/2)} \right] = n^2 k_z^2 \left[\frac{4}{K_p^2 d^2} - \frac{4}{K_0^2 d^2} \right]^2 \quad (3.49)$$

In the electrostatic limit ($c \rightarrow \infty$) (3.49) reduces to

$$\epsilon_p(\omega) = \frac{H_n^{(1)'}(x) J_n(x)}{H_n^{(1)}(x) J'_n(x)} \quad (3.50)$$

where

$$x = \frac{ik_z d}{2}$$

The right-hand side of (3.50) is real. From (3.50) we obtain [using $\epsilon_p(\omega) = 1 - \omega_p^2/\omega^2$]

$$\omega_n \xrightarrow{k_z \rightarrow 0} \frac{\omega_p}{\sqrt{2}} \quad (3.51)$$

$$\omega_n \xrightarrow{k_z \rightarrow \infty} \frac{\omega_p}{\sqrt{2}} \quad (3.52)$$

In Fig. 7 we plot the dispersion relation for $n=1$ based on (3.50). We consider next the correct equation (3.49). As can be seen from (3.48), the SPO are radiative if K_0 is imaginary, that is, if

$$\omega > ck_z \quad (3.53)$$

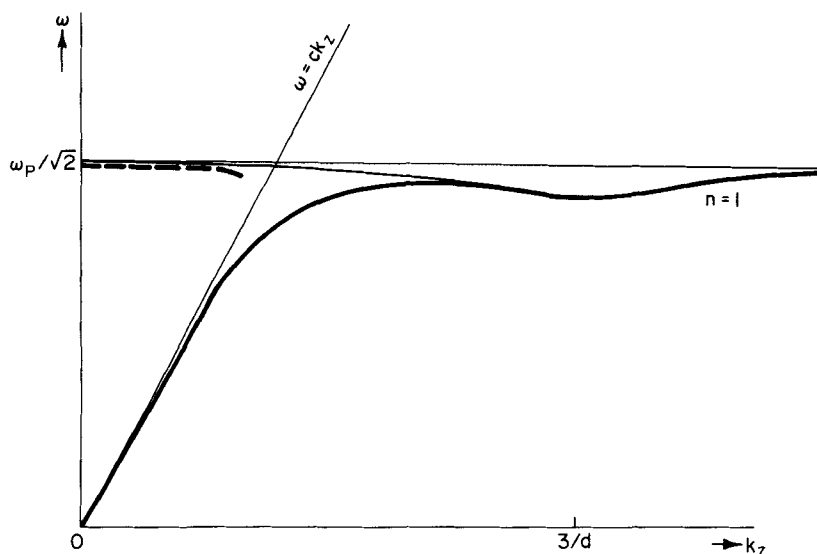


Fig. 7. Dispersion relation for the $n=1$ SP at a circular cylinder of diameter d (schematically). The light solid line is the electrostatic result. The heavy lines are the correct results including RE. There is a nonradiative mode (solid heavy line) and a radiative virtual mode (dashed heavy line); $\omega_p d/c$ is less than unity.

According to the general discussion about the role of RE, we expect that for $k_z c \gg \omega$ the electrostatic results are correct. Also for $d\omega/c \lesssim 1$ and $k_z \rightarrow 0$ the RE should be small. The most dramatic results are for $\omega \approx ck_z$. These expectations are verified by numerical study⁹⁰ of (3.49). The dispersion relation including RE for $n=1$ is plotted schematically in Fig. 7 for the case where $\omega_p d/c < 1$. As d increases, the minimum for $\omega < ck_z$ moves to lower values of k_z and tends to disappear, while the virtual mode for $\omega > ck_z$ moves to lower frequencies and becomes less and less well defined.

The most interesting aspect of the cylindrical geometry is the existence of a well-defined ($\text{Im} \omega_n \lesssim 0.01 \text{Re} \omega_n$ for $\omega_p d/c \lesssim 1$) virtual mode at a frequency just below $\omega_p/\sqrt{2}$. This is a genuine radiative SPO all the way to $k_z = 0$. This mode should be easily observable for thin cylinders in their optical properties which should exhibit a sharp peak at $\omega \approx \omega_p/\sqrt{2}$. As a matter of fact, Miziumski⁸⁹ has already observed the modes in the unfavorable case of a thick cylinder ($\omega_p d/c \sim 10^3$) where they are not so well defined. This mode should also appear as a very sharp peak in the emitted transition radiation as electrons pass by the cylindrical plasma.

Another interesting aspect of the present geometry is the minimum in

the dispersion relation for $k_z > \omega/c$. This minimum creates a peak in the density of states for SPO at a value lower than $\omega_p/\sqrt{2}$ by about 7%. In a carefully designed experiment with high energy resolution, the line shape may exhibit this peak as a satellite peak below the $\omega_p/\sqrt{2}$. Such a peak may also promote a resonant interaction with other modes such as optical phonons in semiconductors.

IV. INTERACTIONS OF PLASMA OSCILLATIONS WITH CHARGED PARTICLES

A. General Remarks

The general method of examining the interaction of an external charged particle (usually an electron) with a material system described by an inhomogeneous dielectric function should start with the interaction Hamiltonian, H_{int} . H_{int} is given by

$$H_{\text{int}} = \int d^3r \rho_e(\mathbf{r}) \phi_s(\mathbf{r}) - \frac{1}{c} \int d^3r \mathbf{j}_e(\mathbf{r}) \cdot \mathbf{A}_s(\mathbf{r}) \quad (4.1)$$

$$= \int d^3r \rho_s(\mathbf{r}) \phi_e(\mathbf{r}) - \frac{1}{c} \int d^3r \mathbf{j}_s(\mathbf{r}) \cdot \mathbf{A}_e(\mathbf{r}) \quad (4.2)$$

where $\rho_{e,s}(\mathbf{r})$, $\mathbf{j}_{e,s}(\mathbf{r})$, $\phi_{e,s}(\mathbf{r})$, $\mathbf{A}_{e,s}(\mathbf{r})$ are the charge density, the current density, scalar potential, vector potential referring to the electron or the system, respectively. Either one of (4.1) or (4.2) can be used, depending on convenience.

There are cases in which first-order effects in H_{int} interest us. In such cases one can easily show that the total fields $\phi(\mathbf{r}) = \phi_e(\mathbf{r}) + \phi_s(\mathbf{r})$ and $\mathbf{A}(\mathbf{r}) = \mathbf{A}_e(\mathbf{r}) + \mathbf{A}_s(\mathbf{r})$ satisfy the general equations (2.5) and (2.6) with

$$\mathbf{j}(\mathbf{r}) = \mathbf{j}_e(\mathbf{r}) + \mathbf{j}_s(\mathbf{r}) \quad (4.3)$$

$$\rho(\mathbf{r}) = \rho_e(\mathbf{r}) + \rho_s(\mathbf{r}) \quad (4.4)$$

where

$$\mathbf{j}_s(\mathbf{r}, \omega) = \int \boldsymbol{\sigma}(\mathbf{r}, \mathbf{r}'; \omega) \cdot \mathbf{E}(\mathbf{r}', \omega) \quad (4.5)$$

with the same $\boldsymbol{\sigma}(\mathbf{r}, \mathbf{r}'; \omega)$ as in the absence of the external electron.

Thus one way to calculate the fields and currents of our total system to first order in H_{int} is to solve the inhomogeneous set of Maxwell's equations for our material system described by $\epsilon_i(\omega)$ with the currents and charges associated with the external charged particle as sources. The general solution of such a system of inhomogeneous equations is the sum of a

particular solution plus the general solution of the corresponding homogeneous set. The latter was systematically studied in Section III. This method of solving the problem, to be referred hereafter as the classical method, is practical only as long as the charges and currents associated with the external particle are known and relatively simple.

There are situations, however, where the external electron must be described quantum mechanically; in this case ρ_e and \mathbf{j}_e are neither known nor simple and the classical method fails. The classical method fails also if higher order terms in H_{int} are important. One is forced then to consider H_{int} in a perturbative quantum mechanical way, in which one calculates transitions due to H_{int} from an initial to a final state. Thus the quantum method requires knowledge of the initial and final states involved in each particular physical problem. To obtain the quantum operator corresponding to H_{int} it is easier to work with (4.1). The operators corresponding to the quantities $\rho_e(\mathbf{r}, t)$ and $\mathbf{j}_e(\mathbf{r}, t)$ are e and $e(\mathbf{p}/m) - (e^2/mc)\mathbf{A}_s$, respectively. We must quantize next the fields $\phi_s(\mathbf{r}, t)$ and $\mathbf{A}_s(\mathbf{r}, t)$. To achieve this the fields ϕ_s , \mathbf{A}_s are written as a linear combination of the modes of the system involved in the particular transition we consider:

$$\phi_s(\mathbf{r}, t) = \sum_i \phi_{is}(\mathbf{r}, t) \quad (4.6a)$$

$$\mathbf{A}_s(\mathbf{r}, t) = \sum_i \mathbf{A}_{is}(\mathbf{r}, t) \quad (4.6b)$$

The fields associated with each mode are quantized following the general technique of field quantization. An example is given in the following subsection. As a result of the quantization, we have that

$$\phi_{is}(\mathbf{r}, t) = f_i^{(+)}(\mathbf{r}, t)c_i^{+} + f_i^{(-)}(\mathbf{r}, t)c_i \quad (4.7a)$$

$$\mathbf{A}_{is}(\mathbf{r}, t) = \mathbf{F}_i^{(+)}(\mathbf{r}, t)c_i^{+} + \mathbf{F}_i^{(-)}(\mathbf{r}, t)c_i \quad (4.7b)$$

where $f_i^{(+)}$, $f_i^{(-)}$, $\mathbf{F}_i^{(+)}$, $\mathbf{F}_i^{(-)}$ are known functions and c_i^{+} , c_i are creation and annihilation operators for the quanta of the eigenmode i . Substituting (4.7) into (4.6) and then into (4.1), we obtain finally the interaction Hamiltonian contributing to the particular transition that we wish to consider:

$$H_{\text{int}} = \sum_{ijj'} (\Lambda_{ijj'} c_i a_j^{+} a_{j'} + \Lambda_{ijj'}^{*} c_i^{+} a_{j'}^{+} a_j) \quad (4.8)$$

where a_j^{+} , a_j are operators which create or annihilate the external electron in the state j or from the state j' , respectively. The first term on the right-hand side of (4.8) describes the physical process where the external

electron changes from state j' to state j , absorbing at the same time a quantum of the i mode of the system; $\Lambda_{ij'}$ gives the amplitude for such a process. The second term on the right-hand side of (4.8) describes the inverse process. Note that our aim is to obtain the amplitude $\Lambda_{ij'}$; the quantization scheme outlined above was used in order to achieve this purpose. Once H_{int} has been brought to the form (4.8), the solution of our problem of transition between the initial and final state requires nothing more than an application of standard techniques of quantum mechanics.

Before we proceed with the cases of interest here, we introduce a simple example to illustrate the application of both the classical and the quantum case.

Consider an electron of high energy (such that its velocity can be considered constant in spite of losses) moving in an infinite plasma described by a dielectric function $\epsilon(\omega)$. The eigenmodes of the medium are the bulk plasmons, $\omega = \omega_p$, and the plane electromagnetic (em) waves with a dispersion $\omega = c|\mathbf{k}|/\sqrt{\epsilon_p}$; both are characterized by a wave number \mathbf{k}_i . The indices j, j' in (4.8) are in the present case the momentum \mathbf{p}, \mathbf{p}' of the electron. If we are interested in calculating the probability of certain transitions, the quantum method is very appropriate. As an example, consider the process where the moving electron excites one of the eigenmodes of the system. The selection rules for this process, that is, conditions specifying whether or not the process will take place, stem from the conservation of energy and momentum, namely

$$\Delta\mathbf{p} \equiv \mathbf{p}' - \mathbf{p} = \hbar\mathbf{k}_i \quad (4.9)$$

$$\Delta E_e = E_e(\mathbf{p}') - E_e(\mathbf{p}) = \hbar\omega_i \quad (4.10)$$

Now because of the assumption of a constant electron velocity, $\Delta E_e \approx \partial E_e / \partial \mathbf{p} \cdot \Delta\mathbf{p} = \mathbf{v} \cdot \Delta\mathbf{p}$, and (4.10) becomes

$$\mathbf{v} \cdot \Delta\mathbf{p} = \hbar\omega_i \quad (4.11)$$

In order to satisfy both (4.9) and (4.11) we should have

$$\omega_i = \mathbf{v} \cdot \mathbf{k}_i \quad (4.12)$$

But, for each mode i , ω_i and \mathbf{k}_i are related through the dispersion relation. For bulk plasmons the dispersion relation is

$$\omega_i \approx \omega_p \quad (4.13)$$

There are always ω_i, \mathbf{k}_i to satisfy both (4.12) and (4.13), which means

that the electron can excite bulk plasmons. The transverse modes, for which $\omega = c|\mathbf{k}|/\sqrt{\epsilon_p}$, can be excited only when

$$|\mathbf{v}| \geq \frac{c}{\sqrt{\epsilon_p}} \quad (4.14)$$

this is the condition for the existence of Cerenkov radiation which is nothing else than the excitation of the transverse em eigenmodes of the system by the moving electron.

In the classical description one can find the complete time-dependent solution of the problem. For this purpose the known charge and current density associated with the moving electron are considered as source terms in Maxwell's equations. The \mathbf{k} -Fourier component of these source terms has a frequency $\omega_{\mathbf{k}} = \mathbf{v} \cdot \mathbf{k}$ where \mathbf{v} is the electron velocity. In the present example one can easily find the Fourier components of the total field⁹ as

$$\mathbf{E}_{\mathbf{k}} = e^{-i\omega_{\mathbf{k}}t} \left[\frac{-ie\mathbf{k}}{2\pi^2\epsilon(\omega_{\mathbf{k}})} - \frac{ie}{2\pi c^2} \frac{\omega_{\mathbf{k}}(\mathbf{v} - \omega_{\mathbf{k}}\mathbf{k}/k^2)}{k^2 - \omega_{\mathbf{k}}^2\epsilon(\omega_{\mathbf{k}})/c^2} \right] \quad (4.15)$$

with a similar expression for the magnetic field $\mathbf{H}_{\mathbf{k}}$.

The first term on the right-hand side of (4.15) is the longitudinal field and the second term is the transverse part.

Whenever the frequency and the wave number of the source terms coincide with the frequency and wave number of an eigenmode of the system, then a resonance occurs and the field should blow up. From (4.15) one sees that the longitudinal field blows up when $\epsilon(\omega_{\mathbf{k}}) = 0$ and the transverse when $k^2 - \omega_{\mathbf{k}}^2\epsilon(\omega_{\mathbf{k}})/c^2 = 0$. These are the equations which give the dispersion relations for bulk plasma oscillations and for plane electromagnetic waves, respectively. The remark above shows that yet another way to obtain the eigenmodes of the system is to find the total field in the presence of an external charge and then determine the frequencies at which this total field blows up. An elementary example of this is the image problem in electrostatics; the total field is $q/r + q[\epsilon(\omega) - 1]/r'[1 + \epsilon(\omega)]$ for a plane surface; this field blows up when $\epsilon(\omega) = -1$ which is the electrostatic condition for a surface plasma oscillation at a single interface. Similarly, one can obtain the condition $\epsilon(\omega) = -1$ for a cylinder and for $k_z = 0$.

In later subsections we discuss the applicability and compare the merits of the quantum and the classical approach for each particular physical situation. Before that, however, we present in the next section a rather

detailed derivation of the quantization procedure to illustrate the methods by which one can obtain the amplitude Λ_{ij} in (4.8).

B. Quantization of Surface Plasma Fields: Electron-Surface Plasmon Interaction Hamiltonian

In Section III we introduced surface plasma oscillations as particular solutions of Maxwell's equations in inhomogeneous media. The nature of the electric and magnetic fields associated with an SPO mode is completely specified. Further the spatial and temporal dependences of these fields are expressible in terms of well-known functions for geometries with high symmetry such as single or multiple parallel films, spheres, and cylinders, all with mathematically sharp boundaries. In some considerations of effects due to electron-SPO interactions, low-energy electrons are involved. Such electrons can no longer be treated as classical particles with well-defined trajectories. The wave character of the low-energy electrons is important and only the quantum method is appropriate to describe the transitions of an electron as it traverses across surfaces. For this reason, a quantized form of the SPO fields is necessary. As a result of field quantization, SPO become field quanta called surface plasmons (SP's). Their associated electromagnetic fields are then expressed in terms of SP creation and annihilation operators which satisfy the basic commutation relations.

Quantization of the complete electromagnetic fields of SPO follows from well-established procedures of field quantization.¹² The sum of the SPO electromagnetic field energy and the kinetic energy of electrons in all conducting regions can be written in terms of selected field variables such as the vector potential. The vector potential is further expressed linearly in terms of mutually conjugate generalized coordinates and momenta. The classical SPO field is then quantized by imposing the appropriate commutation relations to be satisfied by the coordinates and momenta. A simple example follows to demonstrate the procedure.

In contrast to the photon case, quantum transitions of electrons can involve large momentum transfers parallel to the surfaces. Since the phase space of the SPO increases quadratically with k_{\parallel} , for practically all purposes we can ignore the effect of those SPO in the retardation region $k_{\parallel} < \omega_p/c$. The SPO field can then be described by its electric field alone, $[E_z(z)\mathbf{z}_0 + \mathbf{E}_{\parallel}(z)\mathbf{k}_{\parallel}/k_{\parallel}]e^{i(\omega t - \mathbf{k}_{\parallel}\mathbf{R})}$.

We consider a continuum model of an electron gas, with a rigid fixed jellium background of positive charge for any region where the conduction electron density is nonzero in our inhomogeneous medium. The energy of the SPO partly resides in the electric fields and partly in the kinetic energy of the electron motion. It is the charge density fluctuation due to the electron motion that gives rise to the electric fields. The various metallic

regions will be indexed by i . We let n_i be the number density and m_i the effective mass of an electron in the i th region, $\delta\rho_i(\mathbf{r}_i)$ the charge-density fluctuation from the equilibrium value of $\rho_i = n_i e$ of the electron gas at position \mathbf{r}_i , $\phi_i(\mathbf{r}_i)$ the scalar potential of the SPO fields, $\mathbf{u}_i(\mathbf{r}_i)$ the vector displacement of the electron gas, and $\boldsymbol{\pi}_i(\mathbf{r}_i)$ defined as $\partial\mathbf{u}_i(\mathbf{r}_i)/\partial t$. The electric field energy density can be considered as a potential energy density $\frac{1}{2}\delta\rho_i(\mathbf{r}_i)\phi_i(\mathbf{r}_i)$ of the oscillating electron gas. This leads us to consider the Lagrangian density in the i th region,

$$\mathcal{L}(\mathbf{r}_i) = \frac{1}{2}n_i m_i \boldsymbol{\pi}_i(\mathbf{r}_i) \cdot \boldsymbol{\pi}_i(\mathbf{r}_i) - \frac{1}{2}\delta\rho_i\phi(\mathbf{r}_i) \quad (4.16)$$

and the total Lagrangian L for the system

$$L = \sum_i \int \mathcal{L}(\mathbf{r}_i) d\mathbf{r}_i \quad (4.17)$$

By definition, we have the relation

$$\frac{\delta\rho_i(\mathbf{r}_i)}{\rho_i} = -\nabla \cdot \mathbf{u}_i(\mathbf{r}_i) \quad (4.18)$$

The SPO scalar potential $\phi_i(\mathbf{r}_i)$ is then related to the displacement fields $\mathbf{u}_i(\mathbf{r}_i)$ through (4.18) and Poisson's equation,

$$\nabla^2\phi_i(\mathbf{r}_i) = -4\pi\delta\rho_i(\mathbf{r}_i) = 4\pi\rho_i\nabla \cdot \mathbf{u}_i(\mathbf{r}_i) \quad (4.19)$$

We shall illustrate the method of SPO field quantization for the simplest case of a vacuum-metal interface (see Section III.B.1.a). The SPO field can be expressed as a superposition of

$$\mathbf{E} = \sum_{\mathbf{k}_{\parallel}} \left[\frac{E_z(z)\mathbf{z}_0 + E_{\parallel}(z)\mathbf{k}_{\parallel}}{k_{\parallel}} \right] e^{i(\omega t - \mathbf{k}_{\parallel} \cdot \mathbf{R})} \quad (4.20)$$

or, equivalently, in terms of the scalar potentials $\phi_i(\mathbf{r}_i)$

$$\phi = \begin{cases} \sum_{\mathbf{k}_{\parallel}} \phi_{1\mathbf{k}_{\parallel}} e^{-k_{\parallel}z} e^{i(\omega_{\mathbf{k}_{\parallel}}t - \mathbf{k}_{\parallel} \cdot \mathbf{R})}, & z > 0, \text{ vacuum} \\ \sum_{\mathbf{k}_{\parallel}} \phi_{2\mathbf{k}_{\parallel}} e^{+k_{\parallel}z} e^{i(\omega_{\mathbf{k}_{\parallel}}t - \mathbf{k}_{\parallel} \cdot \mathbf{R})}, & z < 0, \text{ metal} \end{cases} \quad (4.21)$$

The displacement field $\mathbf{u}_i(\mathbf{r}_i)$ is decomposed in the same manner,

$$\mathbf{u} = \begin{cases} 0, & z > 0, \text{ vacuum} \\ \sum_{\mathbf{k}_{\parallel}} u_{\mathbf{k}_{\parallel}} e^{k_{\parallel}z} e^{i(\omega_{\mathbf{k}_{\parallel}}t - \mathbf{k} \cdot \mathbf{R})}, & z < 0, \text{ metal} \end{cases} \quad (4.22)$$

and $\mathbf{u}_{k_{\parallel}} = u_{k_{\parallel}z} \mathbf{z}_0 + u_{\mathbf{k}_{\parallel}} \mathbf{k}_{\parallel} / k_{\parallel}$. Charge fluctuations can only reside on the surface, hence from (4.19) we have

$$\operatorname{div} \mathbf{u}(\mathbf{r}) = 0 \quad \text{for } z < 0 \quad (4.23)$$

and from this it follows that $u_{\mathbf{k}_{\parallel}} = -iu_{\mathbf{k}_{\parallel}z}$. The kinetic energy portion of L , $\int \frac{1}{2} nm \boldsymbol{\pi} \cdot \boldsymbol{\pi} d\mathbf{r}$, can be calculated by integration over the half-space $z < 0$, and we find

$$\int \frac{1}{2} nm \boldsymbol{\pi} \cdot \boldsymbol{\pi} d^3r = \sum_{\mathbf{k}_{\parallel}} \left(\frac{Anm}{2k_{\parallel}} \right) \dot{u}_{\mathbf{k}_{\parallel}z} \dot{u}_{-\mathbf{k}_{\parallel}z} \quad (4.24)$$

Here A is the area of the interface.

The charge fluctuation $\delta\rho$ can be obtained from (4.19) and (4.23)

$$\delta\rho = \sum_{\mathbf{k}_{\parallel}} ne u_{\mathbf{k}_{\parallel}z} e^{i(\omega_{\mathbf{k}_{\parallel}}t - \mathbf{k}_{\parallel} \cdot \mathbf{R})} \delta(z) \quad (4.25)$$

and appears as a surface charge. This surface charge density can alternatively be given by $(1/4\pi)(E_{1z} - E_{2z})$, the discontinuity of the normal components of the electric fields. Expressed in terms of ϕ_1 or ϕ_2 , we find

$$\delta\rho = \sum_{\mathbf{k}_{\parallel}} \left(\frac{k_{\parallel}}{2\pi} \right) \phi_{2\mathbf{k}_{\parallel}} e^{i(\omega_{\mathbf{k}_{\parallel}}t - \mathbf{k}_{\parallel} \cdot \mathbf{R})} \quad (4.26)$$

Comparing (4.25) and (4.26), we derive the relationship

$$\phi_{2\mathbf{k}_{\parallel}} = \phi_{1\mathbf{k}_{\parallel}} = \left(\frac{2\pi ne}{k_{\parallel}} \right) u_{\mathbf{k}_{\parallel}z} \quad (4.27)$$

The potential energy portion of L , $\frac{1}{2} \int \delta\rho \phi d\mathbf{r}$, can be expressed via (4.21) and (4.23) in terms of $u_{\mathbf{k}_{\parallel}z}$ as

$$\sum_{\mathbf{k}_{\parallel}} \left(\frac{A\pi e^2 n^2}{k_{\parallel}} \right) u_{\mathbf{k}_{\parallel}z} u_{-\mathbf{k}_{\parallel}z} \quad (4.28)$$

and

$$L = \sum_{\mathbf{k}_{\parallel}} \left\{ \left(\frac{Anm}{2k_{\parallel}} \right) \dot{u}_{\mathbf{k}_{\parallel}z} \dot{u}_{-\mathbf{k}_{\parallel}z} - \left(\frac{A\pi n^2 e^2}{k_{\parallel}} \right) u_{\mathbf{k}_{\parallel}z} u_{-\mathbf{k}_{\parallel}z} \right\} \quad (4.29)$$

The momentum conjugate to the field coordinate, $u_{\mathbf{k}_\parallel z}$, is given by

$$p_{\mathbf{k}_\parallel} = \frac{\partial L}{\partial \dot{u}_{\mathbf{k}_\parallel z}} = \left(\frac{Anm}{k_\parallel} \right) \dot{u}_{\mathbf{k}_\parallel z} \quad (4.30)$$

The Hamiltonian for the SPO is

$$\begin{aligned} H &= \sum_{\mathbf{k}_\parallel} p_{\mathbf{k}_\parallel} \dot{u}_{\mathbf{k}_\parallel z} - L \\ &= \frac{1}{2} \sum_{\mathbf{k}_\parallel} \left(\frac{k_\parallel}{Amn} \right) p_{\mathbf{k}_\parallel} p_{-\mathbf{k}_\parallel} + \sum_{\mathbf{k}_\parallel} \left(\frac{A\pi n^2 e^2}{k_\parallel} \right) u_{\mathbf{k}_\parallel z} u_{-\mathbf{k}_\parallel z} \end{aligned} \quad (4.31)$$

The classical SPO field is now quantized by the Bose-Einstein commutation relations

$$[u_{\mathbf{k}_\parallel z}, p_{\mathbf{k}'_\parallel}] = i\hbar \delta_{\mathbf{k}_\parallel \mathbf{k}'_\parallel} \quad (4.32)$$

SP creation and annihilation operators are introduced as

$$c_{\mathbf{k}_\parallel}^+ = -i \left(\frac{2Anm\hbar\omega_{\mathbf{k}_\parallel}}{k_\parallel} \right)^{-1/2} p_{\mathbf{k}_\parallel} + \left(\frac{A\pi n^2 e^2}{k_\parallel \hbar\omega_{\mathbf{k}_\parallel}} \right)^{1/2} u_{-\mathbf{k}_\parallel z} \quad (4.33)$$

We can easily verify that H in (4.31) is reduced to the harmonic oscillation form

$$H = \sum_{\mathbf{k}_\parallel} \hbar\omega_{\mathbf{k}_\parallel} \left(c_{\mathbf{k}_\parallel}^+ c_{\mathbf{k}_\parallel} + \frac{1}{2} \right) \quad (4.34)$$

with $\omega_{\mathbf{k}_\parallel} = \omega_p / \sqrt{2}$, the dispersionless surface plasmon energy. From (4.27) and (4.33) we can express the potential field in terms of $c_{\mathbf{k}_\parallel}$ and $c_{\mathbf{k}_\parallel}^+$ as follows:

$$\phi(\mathbf{r}, t) = \begin{cases} \sum_{\mathbf{k}_\parallel} \left(\frac{\pi \hbar \omega_{\mathbf{k}_\parallel}}{A k_\parallel} \right)^{1/2} e^{-k_\parallel z} e^{i(\omega_{\mathbf{k}_\parallel} t - \mathbf{k}_\parallel \cdot \mathbf{R})} (c_{\mathbf{k}_\parallel}^+ + c_{-\mathbf{k}_\parallel}), & z > 0 \\ \sum_{\mathbf{k}_\parallel} \left(\frac{\pi \hbar \omega_{\mathbf{k}_\parallel}}{A k_\parallel} \right)^{1/2} e^{k_\parallel z} e^{i(\omega_{\mathbf{k}_\parallel} t - \mathbf{k}_\parallel \cdot \mathbf{R})} (c_{\mathbf{k}_\parallel}^+ + c_{-\mathbf{k}_\parallel}), & z < 0 \end{cases} \quad (4.35)$$

The electron-SP interaction is $e\phi(\mathbf{r})$ where e is the electronic charge.

If $\psi_{\mathbf{q}}(\mathbf{r})$ are the electron wave functions with associated creation and annihilation operators $a_{\mathbf{q}}^+$ and $a_{\mathbf{q}}$, respectively, where \mathbf{q} is the parallel electron momentum, the electron-SP interaction Hamiltonian has the form

$$H_{\text{el-SP}} = \sum_{\mathbf{k}_{\parallel}} \sum_{\mathbf{q}\mathbf{q}'} \Lambda_{\mathbf{q}\mathbf{q}'}(\mathbf{k}_{\parallel}) [c_{-\mathbf{k}_{\parallel}} + c_{\mathbf{k}_{\parallel}}^+] [a_{\mathbf{q}}^+ a_{\mathbf{q}'} + \text{h.c.}] \quad (4.36)$$

The electron-SP interaction vertex function $\Lambda_{\mathbf{q}\mathbf{q}'}(\mathbf{k}_{\parallel})$ is defined by the matrix element of the SP field $\phi(\mathbf{r}, t)$ given in (4.35) as follows:

$$\sum_{\mathbf{k}_{\parallel}} \Lambda_{\mathbf{q}\mathbf{q}'}(\mathbf{k}_{\parallel}) [c_{-\mathbf{k}_{\parallel}} + c_{\mathbf{k}_{\parallel}}^+] = \int d^3r e\phi(\mathbf{r}, t) \psi_{\mathbf{q}}^*(\mathbf{r}) \psi_{\mathbf{q}'}(\mathbf{r}) \quad (4.37)$$

In the model considered here, the electron motion parallel to the surface is free. Hence the wave functions

$$\psi_{\mathbf{q}}(\mathbf{r}) = \frac{\chi_{\mathbf{q}}(z) e^{i\mathbf{q}\mathbf{R}}}{A^{1/2}} \quad (4.38)$$

are the one-electron basis states, and $\Lambda_{\mathbf{q}\mathbf{q}'}(\mathbf{k})$ reduces to

$$\Lambda_{\mathbf{q}\mathbf{q}'}(\mathbf{k}_{\parallel}) = e \left(\frac{\pi \hbar \omega_{k_{\parallel}}}{A k_{\parallel}} \right)^{1/2} \int_{-\infty}^{\infty} dz e^{-k|z|} \chi_{\mathbf{q}}^*(z) \chi_{\mathbf{q}'}(z) \cdot \delta(\mathbf{q} - \mathbf{q}' + \mathbf{k}_{\parallel}) \quad (4.39)$$

The details produced here should serve to demonstrate the method of SPO quantization. The method, in fact, was first applied⁶⁴ to a more complicated geometry of electron tunneling (see Section III.B1.c), and later^{70,64} to the Cs on W geometry⁹¹ (Section III.B.1d). The ease of applying this procedure to any multiple-film geometry should be emphasized. When more than one interface is present, it is still possible to use Maxwell's equations and relations (4.18) and (4.19) to write the Lagrangian L of the entire system in terms of one field variable and its time derivative only. For the vacuum-metal interface, we have seen that this field variable can be chosen to be $u_{\mathbf{k}_{\parallel}z}$, the normal component of the displacement field of the electron gas. We remark also that a similar procedure can be used for the quantization of surface phonon fields.

Another interesting procedure of SPO quantization for the vacuum-metal interface was later given by Wang and Mahan.⁹² They introduced an external charge e at \mathbf{r}_e outside the metal and calculated the interaction energy ΔE with the image charge. The presence of the image charge is identified with states $|1\mathbf{k}_{\parallel}\rangle$ where one quantum of SPO with wave vector \mathbf{k}_{\parallel} is excited from the ground state $|0\rangle$. The SP potential field $\phi(\mathbf{r}, t)$ is

written as

$$\begin{aligned}\phi(\mathbf{r}, t) &= \sum_{\mathbf{k}_{\parallel}} \phi_{\mathbf{k}_{\parallel}}(\mathbf{r}, t) (c_{\mathbf{k}_{\parallel}}^{+} + c_{\mathbf{k}_{\parallel}}) \\ &= \sum_{\mathbf{k}_{\parallel}} U k_{\parallel}^{-1/2} e^{-k_{\parallel} z} e^{i(\omega_{\mathbf{k}_{\parallel}} t - \mathbf{k}_{\parallel} \cdot \mathbf{R})} (c_{\mathbf{k}_{\parallel}}^{+} + c_{\mathbf{k}_{\parallel}})\end{aligned}\quad (4.40)$$

in our present notation. U is an unknown yet to be determined. The interaction of the SPO field with the external charge at \mathbf{r}_e is simply $e\phi(\mathbf{r}_e, t)$. This perturbation on the ground state of the solid plus an external charge gives rise to the extra interaction energy ΔE . Via standard perturbation theory and (4.23)

$$\Delta E = \sum_k \frac{\langle 0 | e\phi_{\mathbf{k}_{\parallel}}(\mathbf{r}_e) c_{\mathbf{k}_{\parallel}} | 1\mathbf{k}_{\parallel} \rangle \langle 1\mathbf{k}_{\parallel} | e\phi_{\mathbf{k}_{\parallel}}^{*}(\mathbf{r}_e) c_{\mathbf{k}_{\parallel}}^{+} | 0 \rangle}{-\hbar\omega_{\mathbf{k}_{\parallel}}} \quad (4.41)$$

The last expression when evaluated and compared with the alternative result for ΔE ,

$$\Delta E = \frac{-e^2}{4\chi_e} \quad (4.42)$$

obtained through image charge interaction considerations, determines U . Their final expression for $\phi(\mathbf{r}, t)$ is identical to (4.35). This is no surprise of course. The relation between surface plasmon and the image charge potential is clearly brought out by these calculations.

Gersten,⁹³ following some earlier considerations of Stern and Ferrell,³⁰ also obtained the same electron-SP vertex function for a vacuum-metal interface as given by (4.39). His method and also that of Wang and Mahan,⁹² though equivalent in physical content to the procedure described in detail earlier in this section, are difficult to generalize for the consideration of more complicated multiple-film geometry as is often encountered in experiments. Lucas, Kartheuser, and Badro⁹⁴ have developed a quantization scheme for surface optical phonon fields of an ionic crystal film. The electron-surface optical phonon interaction Hamiltonian and the corresponding vertex function were first given by them. Sunjic and Lucas⁹⁵ gave the electron-SP interaction Hamiltonian for a thin metallic film. This result can be obtained from the method described in this section. The result for surface phonons requires a simple extension. Instead of electron oscillations, we need to consider motion of ions having an effective charge.

C. Transition Radiation

When a charged particle moves with constant velocity in systems where surfaces are present, radiation is emitted. To illustrate this point we consider here the artificial case of a circular cylinder of radius R and of dielectric function $\epsilon_p(\omega)$ in the vacuum and in the presence of a straight line of uniform charge density q parallel to the axis of the cylinder. The line charge moves with a constant velocity v perpendicular to the axis and passes by a distance $a < R$ from the axis of the cylinder. To simplify the presentation assume further that the parameters are such that the image charges method of electrostatics is a good approximation. Then, as long as the wire is outside the cylinder, the fields for $r > R$ consist of three contributions⁹: one is due to the moving wire, the other to a fictitious wire of charge density $q' = q[\epsilon_p(\omega) - 1]/[\epsilon_p(\omega) + 1]$ moving in a trajectory $\mathbf{r}_{q'}(t)$ where $\mathbf{r}_{q'}(t) = \mathbf{r}_q(t)R^2/r_q^2(t)$, and the third to a wire at the center with charge density equal to $-q'$. During the time the wire is inside the cylinder the field is due to two wires of charge density $q'' = 2q/[\epsilon_p(\omega) + 1]$ and $q - q''$, respectively. The first is moving along the trajectory $\mathbf{r}_{q''}(t) = \mathbf{r}_q(t)$ for $|\mathbf{r}_q(t)| < R$ and the second is at the center of the cylinder.

The picture just given implies immediately that radiation will be emitted because (a) the image charge q' is accelerated during the time the wire is outside the cylinder, and (b) the effective sources of the field change discontinuously at the time the electron crosses the surface. In the case of plane surfaces, only the second cause of radiation is present; this radiation has been termed transition radiation in the literature.^{42, 43, 45, 96-103}

It should be pointed out that the transition radiation is basically different from the Cerenkov radiation. The former, in contrast to the latter, does not require for its existence a resonance condition or the excitation of some eigenmode of the system. However, if a resonance condition is satisfied, that is, if the external source resonates with some bound radiative eigenmode of the system, the transition radiation should exhibit a peak. This is clearly illustrated in the previous description of the cylinder case. If $\epsilon_p(\omega) + 1 = 0$, the image charge and the discontinuity of the source terms blow up and so does the transition radiation. The condition $\epsilon_p(\omega) + 1 = 0$ determines the eigenfrequency of the $k_z = 0$ SPO in a cylinder (without RE). Thus one can interpret the infinity in transition radiation, when $\epsilon_p(\omega) + 1 = 0$, as a resonance effect where the SPO are excited by the incoming electron and greatly enhance the radiation, since the $k_z = 0$ SPO in a cylinder are radiative. Nonradiative bound eigenmodes, although excited by electrons, obviously do not create peaks in the transition radiation; they correspond to infinities in the transition radiation which

occur at nonphysical (complex) values of the parameters. The conclusion is that transition radiation blows up whenever the condition which determines the SPO dispersion relation is satisfied. For radiative SPO this condition is satisfied for almost real (physical) values of the parameters and a peak in the transition radiation appears; for nonradiative solutions this condition is not satisfied for real (physical) values of the parameters and consequently the existence of nonradiative SPO does not influence the strength of transition radiation.

Let us consider briefly the theoretical methods available for studying the problem of transition radiation (TR). The first remark is that the quantum method is not appropriate for the general case of TR. The reason is that the TR is a forced oscillation problem in which the quantum perturbative techniques are not applicable. If, however, a particular radiative bound eigenmode of the system is involved, its contribution can be easily handled by the quantum method. The procedure is to study the excitation of the particular mode by the incoming electron using the Hamiltonian (4.8) and then employing the results of Section III to find the radiation emitted by the already excited mode. This technique has been used by Ferrell⁴² to study the contribution to TR due to the radiative virtual mode of the thin plasma film case.

The classical approach is very well suited for the study of the problem of TR. The procedure is the following: One finds first the fields associated with the incoming electron which are of the type (4.15) with $\epsilon(\omega_k)$ replaced by the corresponding $\epsilon_i(\omega_k)$ in each medium. Such a function is not yet a solution because the boundary conditions are not satisfied. To satisfy them (in analogy with the case of reflection and transmission of em waves) one has to add reflected and transmitted waves. Those waves give rise to transition radiation. Thus the classical approach is conceptually straightforward although mathematically rather complicated. Peaks in the total fields will appear whenever a resonance condition is satisfied. It should be emphasized once more that the classical method calculates the full spectrum of the TR, that is, both the continuous background as well as the peaks which may result when some resonance condition is satisfied. On the other hand, the quantum approach is suited for the calculation of the peaks only and requires a prior realization of the existence of the eigenmodes that resonate.

The details of the classical method are well presented in the original articles.^{96,98} The case of a thin metal film has been studied intensively^{42,43,46,101} because of the strong peak at $\omega \approx \omega_p$ associated with the virtual mode. Most of the extensive experimental work¹⁰⁴⁻¹²² on TR is

reviewed and compared in detail with the theoretical results in the paper by Steinmann.⁵

Recently the phenomenon of transition radiation has found wide application in detecting charged particles in high-energy physics experiments.

D. High-Energy Electron Losses

The problem here is that of a fast electron (usually of kiloelectron-volt energy) passing through matter and losing energy by exciting different eigenmodes of the system. In the present formulation, where the system is described by a complex dielectric function $\epsilon_p(\omega)$, the losses can be of three types:

1. Losses due to $\text{Im}\epsilon_p \neq 0$. This is an approximate way to describe the losses due to eigenmodes of the system which cannot be presented within a dielectric formulation.
2. Losses due to excitations of collective eigenmodes of our system (see Table II) like bulk plasmons, surface plasmons, Cerenkov radiation, and so on.
3. Losses due to radiation while no eigenmode of the system is excited, as for example, the case of transition radiation in a single interface.

Measuring the electron energy loss provides a direct experimental verification of the existence of plasmons.

The classical approach provides a general theoretical method for treating all of the losses mentioned above, as long as the electron trajectory is known. The procedure is as follows⁹: The inhomogeneous set of Maxwell's equations in the presence of the current and charge associated with the external electron is solved for the considered geometry in a way similar to that outlined in Section IV.C. From the calculated total field one subtracts the field produced by the same particle in the vacuum. The resulting field, \mathbf{E}_{eff} , is used to calculate the force \mathbf{F} acting on the particle, that is,

$$\mathbf{F} = e\mathbf{E}_{\text{eff}} \quad (4.43)$$

The energy loss per unit time is then

$$\frac{dW}{dt} = \mathbf{F} \cdot \mathbf{v} = e\mathbf{E}_{\text{eff}} \cdot \mathbf{v} \quad (4.44)$$

This method is explained for the infinite case in the book by Landau and Lifshitz.⁹ In the presence of surfaces the classical method was used first by Ritchie³³ (without RE). The details of the calculations and the final results for different geometries can be found in the original articles.^{20,30,99,79} We do not discuss this subject further since there exist

several excellent review articles^{2,6,36} where the experimental^{35,81,126-130} and theoretical results are presented, discussed, and compared.

We discuss here in some detail the quantum method which has recently found increasing application to the problem of SP-fast electron interaction. As has been explained already, this method is appropriate if one already knows which eigenmodes of the system are involved in the particular physical processes under consideration. In the present case where we are interested in electron losses due to SP excitations, the quantum method starts with the electron-SP interaction Hamiltonian, $H_{\text{el-SP}}$, which is of the form shown in (4.8); the calculation of the quantity Λ_{ij} was considered in detail in Section IV.B. Once the Hamiltonian $H_{\text{el-SP}}$ is known, one applies standard quantum mechanical techniques to calculate electron losses. In this way we can reproduce the classical result for the electron losses due to SPO. The quantum method is really indispensable when either the external electron should be considered as a quantum particle or when processes of higher order in $H_{\text{el-SP}}$ are important. In the present case of high-energy electrons the incoming particle is well described by classical mechanics and consequently quantum methods are needed only when higher order processes are to be considered.

Sunjic and Lucas⁹⁵ have studied the interaction Hamiltonian formulation of the problem of energy-loss spectra of electrons in thin films. They consider the case of high-energy electrons and hence the interaction Hamiltonian formulation is not indispensable. Nevertheless this formulation enables them to reduce the problem to an exactly soluble quantum mechanical model. Their results go beyond the classical theory and predict that, in the energy-loss spectrum, effects of higher order in $H_{\text{el-SP}}$ such as multiple surface plasmon emission can be important. The classical theory can only predict one SP loss. Lucas and Sunjic¹³¹ further applied their theory and calculated loss spectra of fast electrons exciting surface plasmons or surface optical phonons. Their calculations are in agreement with recent experiments of inelastic scattering of low-energy electrons (25 eV) by surface optical phonons in ZnO by Ibach¹³² and inelastic scattering of high-energy (8 keV) electrons by surface plasmons in metallic surfaces by Powell.¹³³ Boersh, Geiger, and Stickel¹³⁴ have measured also the electron energy-loss spectra in thin ionic crystal films such as LiF. Calculations performed by Lucas, Kartheuser, and Badro⁹⁴ agree with the experimental data on LiF. In Ibach's measurements¹³² on ZnO surfaces, low-energy electrons are used. The theory of Lucas and Sunjic¹³¹ treats the electron, however, as classical particles. It is not clear how this will affect the calculation. In the Sunjic and Lucas⁹⁵ treatment of multiple plasmon effects in the energy-loss spectra, they have used the electrostatic

approximation of the SPO dispersion relation for a metallic slab in a vacuum. The true dispersion relation including retardation, given earlier in Section III.B.1.b, is quite different in the retarded region. Hence it is not clear how the broad structures in the loss spectra that Sunjic and Lucas found and attributed to multiple emissions of strongly dispersed surface plasmons will change under the true dispersion relation. Further, in the retarded region, both the electric and the magnetic fields of the SPO are important. There the scalar potential electron-SP interaction Hamiltonian as used by Sunjic and Lucas is inappropriate. In spite of these problems, the works of Lucas and co-workers have certainly demonstrated the usefulness of the interaction Hamiltonian approach.

E. Surface Plasmon Interaction with Low-Energy Electrons

1. Low-Energy Electron Diffraction (LEED)

For electrons of energy less than 100 eV, the atomic scattering cross-sections are typically of the same magnitude as the area occupied by an atom in a single atomic layer. A single atomic layer is, therefore, a very efficient scatterer for low-energy electrons. Since the incoming electron is spending most of its time very close to the surface, one expects relatively large cross-sections for SP excitations. Early experiments on LEED have measured the energy spectrum of backscattered electrons from metal surfaces and found significant inelastic loss due to SP emission. We will quote only one such measurement by A. U. MacRae et al.⁶⁹ Their data on inelastic scattering of a 10-eV primary beam of electrons by multilayers of Cs deposited on a clean tungsten surface have shown that the inelastic components due to one and two SP losses are of the same size as the elastic component of the backscattered electrons. Such a large inelastic SP scattering cross-section of low-energy electrons was first demonstrated theoretically by Ngai, Economou, and Cohen.^{70,64} They employed the electron-SP interaction Hamiltonian formulation. This is absolutely essential for any quantitative theory because the wave character of the low-energy electrons is a necessary feature that gives rise to diffraction of the incident beam. The inelastic electron-SP scattering was considered as the scattering of electrons under the combined influence of two potentials, U and V . U represents all the elastic diffraction and inelastic processes other than SP scattering. V is the electron-SP interaction $H_{\text{el-SP}}$. This problem was reduced to the well-known two-potential scattering for which Gell-Mann and Goldberger's¹³⁵ two-potential formula can be employed. Without giving the analytical details, this two-potential formula essentially tells us how to calculate the transition matrix element T_{fi} between the initial state of an incident electron plus SP ground state, to a final state of a diffracted

electron plus an SP excited state. The prescription is as follows: First solve the electron scattering problem due to U , the semiinfinite crystal potential, only. Call the solutions of the U -potential problem $|\chi\rangle$; that is, these are the LEED wave functions. With $|\chi\rangle$ as the basis set, the transition matrix T_{fi} is then obtained as a Born series of the V potential,

$$T_{fi} = \underbrace{\langle \chi_f^{(-)} | V | \chi_i^{(+)} \rangle}_{1-SP} + \underbrace{\langle \chi_f^{(-)} | V \frac{1}{E_i - H_0 - U + i\epsilon} V | \chi_i^{(+)} \rangle}_{2-SP} + \cdots \quad (4.45)$$

The superscripts (+) and (−) indicate that a scattering wave function has to satisfy outgoing and incoming wave boundary conditions, respectively. The first two terms on the right of (4.45) contribute to the one and two SP emission processes, respectively. The intensities of electrons scattered via one or multiple SP emission were calculated by an approximation to the actual LEED wave functions χ . The result showed that, even for a metal film a few monolayers thick, a large fraction of the backscattered electrons have suffered energy loss due to SP emissions. This means that whenever we consider low-energy electrons traversing across or reflecting from a metal-dielectric interface, excitations of SP are nonnegligible.

In the last few years LEED theory has been improved greatly. Advances in the field are partly due to the recognition that the interaction of the incident electron with the valence electrons in the solid is strong and the elastic electron wave field is damped within 5 to 10 Å of the surface.¹³⁶ Consequently, in any satisfactory LEED theory the effects of both electron multiple scattering from the ion-cores and inelastic scattering including SP excitation must be incorporated on the same footing. Current status of LEED theories is reviewed by Duke in the first chapter of the present volume. The quantum inelastic LEED theory developed by Duke and co-workers¹³⁶ was applied by Bagchi, Duke, Feibelman, and Porteus¹³⁷ to analyze the LEED data taken by Porteus and Faith¹³⁸ on epitaxial Al films. From their analysis, the dispersion relation of the SP excitations for Al(111) is found to be

$$\hbar\omega_s(k_{\parallel}) = (10.1 - 0.7k_{\parallel} + 10k_{\parallel}^2) + i(0.9 + 0.7k_{\parallel}) \quad (4.46)$$

Here energies are measured in electron volts and momenta k_{\parallel} in reciprocal angstroms. This experimentally deduced SP dispersion relation and another deduced earlier from GaAs by electron tunneling measurements⁶⁴ are the only information available in the literature about which we know. The k_{\parallel} dependence of both the real and imaginary parts of the SP frequency is due to quantum effects explained in some detail in a later

section. Its physical origin is due to the failure of any classical theory of SP when the SP has a wavelength ($2\pi/k_{\parallel}$) comparable to or smaller than interelectron distances, and also to deviations from an abrupt boundary surface.

2. Electron Tunneling in Solids

a. Superconductive Tunneling. SPO modes in prototypes of tunnel junctions have been described in Section III.B.1.c. Notably there exists a low-lying mode with dispersion relation

$$\omega = ck_{\parallel} \left[\frac{d_i}{d_i + \lambda_p (\coth k_p d_1 + \coth k_p d_2)} \right]^{1/2} \quad (4.47)$$

for $k_{\parallel} < k_p$. This is an electromagnetic wave with a phase velocity slower than light propagation in the dielectric barrier region. In normal metal junctions, this low-lying mode is no longer present because of very large damping due to collisions both in the bulk and on the surface. However, for superconductors and for frequencies such that $\hbar\omega < 2\Delta$ (2Δ is the superconducting energy gap of the metal), real electromagnetic modes can propagate in the junction. The existence of a similar mode in superconducting tunnel junctions was first pointed out by Swihart.⁶⁵ He called it the junction rf mode. Since then it has been recognized²⁶ to be just a particular case of SPO.

When a dc voltage V_0 is maintained across a superconducting junction, then, according to Josephson,¹³⁹ alternating currents can exist in the barrier along the y -axis, the alternating currents are given by

$$j = \text{Re} j_i e^{i(\omega t - kx)} \quad (4.48)$$

where $\omega = 2eV_0/\hbar$ and $k = 2_e(2\lambda_p + d_i)H_0/\hbar c$ provided ⁶⁷ $d_m \gg \lambda_p$. In the thin film limit,⁶⁷ such that $d_m \ll \lambda_p$, $k = (2e/\hbar c)H_0(2d_m + d_i)$. This is the ac Josephson effect. It predicts that a current density wave as described by (4.48) exists and propagates along the junction in the x direction. Due to large impedance mismatch it is extremely difficult to detect this Josephson radiation directly.

The presence of the low-frequency SP modes in the junction structure suggests that they can be excited by the Josephson radiation as described by the current density wave (4.48). An interesting situation arises when the phase velocity of this current density wave is equal to the SP mode phase velocity. We then expect resonance coupling to occur and manifest itself in

the tunneling characteristics of the superposed films. This is a most unique case of electron-SP interaction where electrons appear in the form of a macroscopic ac current in the dielectric barrier between two metal films. Excitation of the SPO modes is described⁶⁷ simply by Maxwell's equation including the presence of the tunneling currents in the dielectric barrier. Resonance excitation of SP manifests itself as dc current resonant steps or resonant peaks⁶⁶ in the IV characteristic of the Josephson junction. We do not go into the technical details here but the interested reader is referred to a review by Langenberg, Scalapino, and Taylor¹⁴⁰ and also to the paper by Ngai.⁶⁷

b. Metal-Semiconductor Tunnel Junctions. Studies of n -type GaAs-Pb surface-barrier tunnel junctions by Tsui¹⁴¹ have shown evidence for the observation of SP excitation in a degenerate semiconductor-depletion layer interface. Structure is observed in d^2I/dV^2 , the second-order derivative of tunneling current I with respect to bias voltage, which corresponds to an increase in conductance at bias voltages near the conduction electron-surface plasmon energy in doped GaAs. The bias position of the peak structure is strongly dependent on the electron concentration of the GaAs electrode. These measurements led Tsui to interpret his observations as due to the inelastic excitation of SP in GaAs surface by tunneling electrons.

A theoretical model based on SP excitation and amenable to quantitative calculation was given by Ngai, Economou, and Cohen.⁶⁴ Their ideas are essentially summarized as follows. The dynamics of the electron-SP interaction is taken into account by including the SP wave fields in the potential which the electron sees in the insulating region of the junction. Roughly speaking, when an electron is inside the electrodes, its dynamical effects are well screened. This is no longer so when it tunnels into the dielectric region, and its long-range Coulomb field can excite SP. Thereby new tunneling channels are opened by inelastic excitation of SP, and accounts for the conductance increase at bias voltages near the SP energy. For an accurate calculation of the excess tunneling current due to electron-SP interaction, the electron-SP interaction Hamiltonian formalism of Section IV.B must be used. This is not only due to the low-energy nature of the tunneling electrons but also due to the fact that, at the barrier region where the electron cannot classically exist at all, the phenomena are completely quantum mechanical. The calculation of the inelastic current $J_i(V)$ was given within the scheme of the transfer Hamiltonian formalism. Details of the calculation of $J_i(V)$ and its derivatives are quite involved and are not reproduced here. Only the results are quoted. It was found from the expression for d^2J_i/dV^2 that this has a broad peak structure near

the SP energy. The magnitude of d^2J_{\parallel}/dV^2 as calculated agrees¹⁴² with experiment.¹⁴¹ The line shape of d^2J_{\parallel}/dV^2 is a rather sensitive function of the damping of the SP. By fitting the line shape, the k_{\parallel} dependence of the SP damping was for the first time determined from experiment. This k_{\parallel} dependence of both the real and imaginary part of the SP frequency (referred to as quantum effects) is the subject of further discussion in Section X. The magnitude of the k_{\parallel} dependence of the imaginary part of the SP frequency deduced from tunneling measurements agrees with fundamental calculations of quantum effects by Beck and Celli.¹⁴³

3. Photoemission

Photoemission processes (or the photoelectric effect) are viewed as a three-step process.¹⁴⁴ First, the electrons are optically excited within the material to a depth of α^{-1} , where α is the optical absorption coefficient. Second, some of these excited electrons reach the surface, and third, some of these escape across the surface into the vacuum. These photoemitted electrons are collected and their energy distribution determined. For photons of low energy (e.g., 10 eV), it is expected that the excited electrons are of the same energy. Before reaching the surface, however, the electrons may scatter inelastically with other electrons. But all photoemitted electrons must have crossed the surface. From our remark given earlier in the discussion of LEED, such low-energy electrons have very large SP scattering cross-sections. Thus a significant fraction of the photoemitted electrons should suffer a surface plasmon loss. In many ways photoemission resembles LEED as far as electron-SP interaction is concerned.

SP excitation in photoemission was first observed by Callcott and MacRae in Ni.¹⁴⁵ Later Smith and Spicer¹⁴⁶ observed the same effect in a series of alkali metals. The alkali metals have small work functions, small Fermi energies, and small plasma frequencies; hence photons of the order of 10 eV can be used. Smith and Spicer measured the energy distributions of photoelectrons from K, Rb, and Cs. Their energy distribution curves show a peak identified as unscattered or primary electrons, and an intermediate peak at lower energies which is identified to be due to SP loss. The SP loss peak is a significant fraction of the primary photoelectrons, as we would expect for these low-energy electrons. Quantitative calculation was performed by Ngai, Economou, and Cohen^{70,64} with the method discussed in Section IV.E.1. The calculations support the experimental observations of large SP inelastic scattering of low-energy photoelectrons.

4. Field Ion Emission

Ions absorbed on metal can be emitted in the presence of a large electric field. At the locality of a metal tip, the outgoing ion can acquire kinetic

energy of 50 eV when accelerated by an applied field of $5 \text{ V}/\text{\AA}$ to less than 10 Å from the tip surface.¹⁴⁷ These low-energy charged particles, or desorbed ions, can excite SP after they have traveled a few angstroms from the metal tip surface. Lucas¹⁴⁷ has shown that multiple excitations of SP in the metal tip can account for the prominent oscillatory structures in the energy distribution of field-emitted ions observed by Jason¹⁴⁸ from W, Pt, and Mo tips. Lucas's calculations are also based on the electron-SP interaction Hamiltonian method. The ion replaces the role of an electron in this situation.

V. INTERACTION OF SURFACE PLASMONS WITH PHOTONS AND ELECTRONS ON ROUGH SURFACES

A. Theory

Our discussions of SPO up to here have assumed all surfaces to be like mathematical surfaces with well-defined boundaries and perfectly smooth. For real solid surfaces, neither of these assumptions is true. In this section we discuss the effect of roughness on SP modes and their interactions with electrons and photons. It will be seen that surface roughness changes the observable properties of SP which we might expect for a smooth surface. Roughness is shown to have a profound influence on the optical interactions of both radiative and nonradiative SP, thereby introducing interesting new physical effects.

The idea behind these is extremely simple. Presence of random roughness of the surface breaks translational invariance on a smooth plane surface. Momentum parallel to the surface is no longer required to be conserved in any physical interaction process. In a way, random roughness is equivalent to the presence on the surface of a statistical distribution of gratings of different spacings and orientations. These gratings can (1) diffract any incident or emitted radiation, (2) scatter or impart momenta to both the radiative plasmon and the nonradiative SP. Process (1) causes a reduction in reflectivity of the surface. Process (2), when the radiative plasmon is involved, causes a change in the properties of the plasma radiation in thin films, and, when the nonradiative SP are involved, induces a coupling to the radiation.

An excellent review of the experimental works prior to 1968 was given by Steinmann.⁵ We intend to take a different approach. We introduce the concepts and theoretical framework first, then discuss the various types of experiments. The advantage of this approach is that we can discuss the effects of roughness from a unified point of view. The disadvantage is that we have to ignore some of the historical development of the subject.

The physical importance of surface roughness on the optical properties of SP was first suggested by Stern.¹⁴⁹ Quantitative theoretical considerations have been carried out by Stern,¹⁵⁰ Wilems and Ritchie,¹⁵¹ Fedders,¹⁵² Ritchie and Wilems,³⁹ Crowell and Ritchie,¹⁵³ Kretschmann,¹⁵⁴ and Elson and Ritchie.¹⁵⁵ These considerations or calculations have touched upon one aspect of the roughness-induced effects or the other. They all contribute to the development of the field. However, we only review in some detail the most recent work by Elson and Ritchie. This work covers both the photon scattering by roughness and the coupling of nonradiative SP to light mediated by roughness. In many ways this work has absorbed the experiences and merits of previous works and its relation to them is clear. We also apply Elson and Ritchie's theory extensively to roughness effects which have not been described by them.

Elson and Ritchie started out with a perfectly smooth surface bounding a semiinfinite plasma ($z > 0$) from vacuum ($z < 0$). Starting from Maxwell's equations of this inhomogeneous medium, they solve the eigenfunction of the em fields which corresponds to (1) *s*-polarized and *p*-polarized photons that are incident to and reflected from the surface, and (2) nonradiative SP modes whose fields are bound to the surface. They also wrote down the classical Hamiltonian of the system by calculating the sum of the em field energy and the kinetic energy of electrons in the plasma. If \mathbf{A} is the vector potential, the Hamiltonian has the form

$$\mathcal{H} = (8\pi c^2)^{-1} \int d^3r \left[\dot{\mathbf{A}}^2 + \theta(z) \omega_p^2 \mathbf{A}^2 + c^2 (\nabla \times \mathbf{A})^2 \right] \quad (5.1)$$

For any particular em field eigenfunction of type (1) or (2), the boundary continuity requirements on the fields enable one to express H in terms of only one scalar component of \mathbf{A} . In this form, the classical Hamiltonian can be quantized by introducing creation and annihilation operators for the mode under consideration. The vector potential of the mode can then be expressed in terms of these operators. The readers can easily recognize that this quantization scheme is a simple extension of the method explained in Section IV.B. The only difference is that the fields here are electromagnetic since we are interested in photon-photon or photon-SP interactions, while there the fields are electrostatic since we were concerned with electron-SP interactions.

Elson and Ritchie described the rough surface by a function $z = \zeta(x, y)$. The Hamiltonian \mathcal{H} now takes the form

$$\mathcal{H} = (8\pi c^2)^{-1} \int d^3r \left\{ \dot{\mathbf{A}}^2 + \theta[z - \zeta(x, y)] \omega_p^2 \mathbf{A}^2 + c^2 (\nabla \times \mathbf{A})^2 \right\} \quad (5.2)$$

Following Fedders, they transform coordinates to the nonorthogonal system $u_1 = x$, $u_2 = y$, $u_3 = z - \zeta(x, y)$. The vector potentials are expressed in terms of the unit vectors $(\hat{l}_1, \hat{l}_2, \hat{l}_3)$ tangential to the coordinate curves (u_1, u_2, u_3) as $\mathbf{A} = \hat{l}_1 A_1 + \hat{l}_2 A_2 + \hat{l}_3 A_3$. \mathcal{H} can then be expanded in powers of ζ

$$\mathcal{H} = \mathcal{H}_0 + \mathcal{H}_1 + \mathcal{H}_2 + \cdots \quad (5.3)$$

Only the terms \mathcal{H}_0 and \mathcal{H}_1 , which contain terms up to the first power in ζ , were kept.

$$\mathcal{H}_0 = (8\pi c^2)^{-1} \int d^3u \sum_{i=1}^3 \left[\dot{A}_i^2 + \theta(u_3) \omega_p^2 A_i^2 + c^2 H_i^2 \right] \quad (5.4)$$

$$\begin{aligned} \mathcal{H}_1 = \frac{1}{4\pi c^2} \int d^3u \left\{ \dot{D} \dot{A}_3 + \theta(u_3) \omega_p^2 D A_3 \right. \\ \left. - c^2 \left[D \left(\frac{\partial H_1}{\partial u_2} - \frac{\partial H_2}{\partial u_1} \right) + \left(\frac{\partial}{\partial u_3} F \right) H_3 - G \frac{\partial A_3}{\partial u_3} \right] \right\} \end{aligned} \quad (5.5)$$

where

$$D = \frac{\partial \zeta}{\partial u_1} A_1 + \frac{\partial \zeta}{\partial u_2} A_2 \quad (5.6)$$

$$F = \frac{\partial \zeta}{\partial u_1} A_2 - \frac{\partial \zeta}{\partial u_2} A_1 \quad (5.7)$$

$$G = \frac{\partial \zeta}{\partial u_1} H_2 - \frac{\partial \zeta}{\partial u_2} H_1 \quad (5.8)$$

and

$$H_i = \frac{\partial A_k}{\partial u_j} - \frac{\partial A_j}{\partial u_k} \quad (5.9)$$

with cyclic permutations of the coordinate indices. \mathcal{H}_1 is treated as a perturbation on \mathcal{H}_0 . \mathcal{H}_0 describes mutually orthogonal em modes that propagate along the actual rough surface. These zero-order fields are still orthogonal to each other and no physical effects emerge. \mathcal{H}_1 is nondiagonal in these zero-order modes, hence it causes coupling of modes to

occur and induces new effects. Since Elson and Ritchie started doing perturbation theory with zero-order fields that are solutions of the actual surface, their method should be more accurate than earlier theories¹⁵⁶ that proceed from zero-order fields of a smooth surface. Elson and Ritchie applied their theory to calculate the decrease in reflectance of the rough surface for incident photons. In the following sections we discuss various physical phenomena possible on a rough surface and apply Elson and Ritchie's theory whenever possible.

One general comment about Elson-Ritchie's theory is appropriate here. Sometimes it occurs in experiments that a thin film of dielectric is deposited on a rough surface of a thick metal film. An example of this can be found in Jasperson and Schnatterly's¹⁵⁷ experiment where a thin dielectric film of MgF_2 was purposely deposited on Ag foils. This is a special case of more general multifilm rough surfaces that one can envisage. For this general case, the Elson-Ritchie theory can be easily extended. The quantization scheme can be generalized just as simply as was the case with the electrostatic field (Section IV.B). The interaction Hamiltonian can be generated as easily even with the presence of more than one rough surface.

B. Optical Reflectance (Thick Film)

If one carefully examines the interaction Hamiltonian \mathcal{H}_1 of (5.5), and the nature of the vector potential \mathbf{A}_p for an incident photon and \mathbf{A}_s for an SP (nonradiative, of course), it can easily be seen that \mathcal{H}_1 has nonvanishing matrix elements between them. Hence a photon with energy $\hbar\omega$ incident, say, normally on a rough surface can be converted into a surface plasma oscillation. This reduces the reflectance of the solid surface and a dip in the optical reflectance curve (reflectivity versus photon energy) occurs at the surface plasmon energy, $\hbar\omega_p/\sqrt{2}$. The transition rate for photon-SP conversion and the reflectance drop $\Delta R_s(\omega)$ can be easily calculated by the "golden rule." The surface roughness function $\zeta(u_1, u_2)$ can be Fourier analyzed into

$$\zeta(u_1, u_2) = \sum_{\mathbf{\kappa}} \zeta_{\mathbf{\kappa}} e^{-i\mathbf{\kappa} \cdot \boldsymbol{\rho}} \quad (5.10)$$

with $\boldsymbol{\rho} = u_1 \hat{i}_1 + u_2 \hat{i}_2$. Since the roughness is a random process, the variables $\zeta_{\mathbf{\kappa}}$ are stochastic. To obtain meaningful results from theory, a statistical average must be performed for the observables. Elson and Ritchie wrote the average $\langle |\zeta_{\mathbf{\kappa}}|^2 \rangle$ essentially as $\delta^2 g(\kappa)$: δ is the rms variation in the height of the surface around its mean position; and $g(\kappa)$ is the surface structure factor, which is also the two-dimensional Fourier transform of the auto-correlation function for surface roughness. The reflectance drop was given

to be

$$\Delta R_S(\omega) = \frac{\delta^2}{\lambda^4} F(\omega) g[k_{\parallel}(\omega)] \quad (5.11)$$

where $\lambda = 2\pi c/\omega$ is the photon wavelength; $F(\omega)$ is a rather complicated function of $\alpha = \omega/\omega_p$ and blows up at $\omega = \omega_p/\sqrt{2}$, the SP frequency; and $g[k_{\parallel}(\omega)]$ is the surface structure factor evaluated at a wave vector k_{\parallel} equal to that of a surface plasmon having energy $\hbar\omega$. $\Delta R_S(\omega)$ blowing up at $\omega = \omega_p/\sqrt{2}$ is a consequence of the singular density of SP states at energy equal to $\hbar\omega_p/\sqrt{2}$. When damping of the SP, which becomes increasingly important for large k_{\parallel} , is included, $F(\omega)$ or $\Delta R_S(\omega)$ exhibits a peak near $\omega = \omega_p/\sqrt{2}$. Elson and Ritchie had written the quantity $(\alpha\omega_p/c)[(1-\alpha^2)/(1-2\alpha^2)]^{1/2}$ as the argument for the function g . We can easily verify that this quantity is identically $k_{\parallel}(\omega)$.

The decrease in reflectance from rough surfaces has another origin which has nothing to do with SP. This is just the diffuse scattering from the rough surface that removes photons from the specularly reflected beam. The Elson-Ritchie perturbation theory was again used to calculate the decrease in reflectivity. This contribution ΔR_d to the reflectance drop from diffuse scattering is generally comparable with that due to SP coupling.¹⁵⁸ Further, it has no resonance behavior at the SP energy in the reflectance versus photon energy curves.

Experimentally, Jasperson and Schnatterly¹⁵⁷ were the first to observe this photon-SP interaction in optical reflectance of thick Ag foils and established that only surface roughness is responsible for it. On vacuum-depositing thin layers of solid dielectric MgF_2 with dielectric constant $\epsilon_d = 1.93$, they observed a shift to longer wavelengths of the reflectivity resonance structure due to photon-SP conversion. By measuring the shift of the resonance as a function of MgF_2 film thickness, and comparing this result with the SP dispersion relation for such a vacuum-dielectric-metal structure, they determined the dominant wave vector of the surface plasmon, that coupled with the 3450-Å photon, to be $1 \times 10^6 \text{ cm}^{-1}$. The magnitude of the projection of the wave vector of the 3450-Å photon in the plane of the surface is only $1.3 \times 10^5 \text{ cm}^{-1}$, a factor of 8 smaller. Jasperson and Schnatterly were thus able to compare directly the momentum of the incident photon with that of the excited SP and demonstrate the momentum nonconservation. Stanford¹⁵⁹ had also used this method of observing the shift of the resonance at the SP frequency of the reflectance drop, to determine the thickness of a thin dielectric film of silver sulfide on Ag. He obtained good agreement with ellipsometric measurements. Jasperson and

Schnatterly demonstrated also that the reflectivity drop is different for *s*- and *p*-polarized light. Both polarizations couple strongly to SP. Their difference in the coupling strength can be easily understood from the interaction Hamiltonian \mathcal{H}_1 and the difference between the vector potentials for these two polarizations. By increasing the roughness of the surface, they observed a large variation in the size of the reflectance resonance drop. They studied also the temperature dependence of the strength of the resonance and found no change at 290 and 110° K. This rules out the possibility of phonon-assisted photon-SP coupling.

The importance of rough surface absorption effects on reflectance measurements and the complex dielectric constant deduced from them has been repeatedly verified by the recent experimental work of Stanford, Bennett, Bennett, Ashley, and Arakawa,¹⁶⁰ Dobberstein, Hampe, and Sauerbrey,¹⁶¹ Feuerbacher and Steinmann,¹⁶² Beaglehole and Hunderi,¹⁶³ and more recently Endriz and Spicer.¹⁵⁸ In the work by Endriz and Spicer ultraviolet reflectance measurements of Al films of known rms surface roughness δ have good agreement with many aspects of the Elson-Ritchie calculations. The strong dependence of ΔR predicted by the Elson-Ritchie theory on the shape of the surface roughness spectrum $\delta^2 g(\kappa)$ is well observed in their experiment. We can easily see how the shape of $g(\kappa)$ as a function of κ will determine the contributions of ΔR_S and ΔR_d to the total reflectance drop ΔR . For diffuse scattering, the wave vector arguments of $g(\kappa)$ that appear in the expression for ΔR_d are smaller or equal to $\kappa = \omega/c$. On the other hand, for photon-SP conversion, large κ values of the size of the wave vector $k_{||}$ of a surface plasma oscillation with energy $\hbar\omega$ appear as the argument in $g(\kappa)$ in the expression for ΔR_S . In Fig. 8 we try to illustrate for hypothetical shapes of $g(\kappa)$, how the contribution of ΔR_S and ΔR_d changes. We assume $g(\kappa)$ to have a single peak at $\kappa_{\max} = 1/\bar{a}$; \bar{a} , so defined, has the dimension of length and represents a most probable correlation distance of fluctuations on the surface. The two curves in Fig. 8 are intended to correspond to two different correlation lengths. Several facts suggest themselves by inspection of Fig. 8 and the Elson-Ritchie formula for ΔR_d and ΔR_S . First, as the photon energy is increased, the $\kappa < \omega/c$ portion (shaded in Fig. 8) expands to the right, and hence ΔR_d increases. Second, as the correlation length is increased, the peak position κ_{\max} of $g(\kappa)$ shifts to a lower value. The proportionality of ΔR_S to $g[k_{||}(\omega)]$ implies that the most probable SP energy to be excited by a photon has $k_{||} = \kappa_{\max}$. We recall that the SP energy is a monotonic increasing function of $k_{||}$ for a single surface. Hence as the correlation length is increased, the position of the maximum reflectance drop in a plot of reflectivity versus photon energy will shift to lower energy. These expectations have been confirmed by detailed experimental observations by Endriz and Spicer.¹⁵⁸

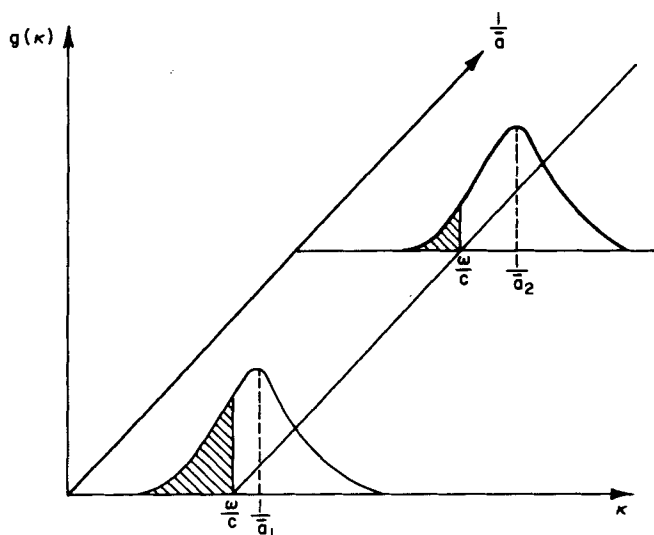


Fig. 8. Surface structure factor $c(\kappa)$ for two different correlation lengths \bar{a}_1 and \bar{a}_2 ($\bar{a}_2 < \bar{a}_1$) (schematically). The point $\kappa = \omega/c$ is indicated for each curve.

Encouraged by the good agreement, they have fitted the Elson-Ritchie theory to the reflectance measurements. Assuming a Gaussian model for $\delta^2 g(\kappa)$, they were able to determine the parameters δ and \bar{a} for Al surfaces.

C. Plasma Radiation Excited by Light (Thin Films) (PREL)

For sufficiently thin films, we have seen in Section III.B1.b that a radiative plasmon mode exists which can radiate energy in the form of photons when excited by fast electrons. A phenomenon suggested by Ferrell and Stern⁴⁷ is the possibility of a resonance in the reflection coefficient of a thin metal film at the bulk plasma frequency. When a p -polarized light is incident on a thin film, it can be understood from classical optics that the effect of the radiative plasma mode is to produce a dip in the transmission and a peak in the reflection. Moreover, the emitted radiation is only in the transmitted and the reflected directions. Brambring and Raether¹⁶⁴ found, however, that the plasma radiation from Ag films occurs at *arbitrary* direction relative to the incident light. The same effect was observed with thin K films by Bösenberg and Raether.¹⁶⁵ These experimental measurements have been adequately reviewed by Steinmann.⁵ Stern¹⁵⁰ gave an explanation of this effect as due to modification of classical electromagnetic theory caused by surface roughness. Kretschmann and Raether¹⁶⁶ obtained essentially the same result and evaluated

numerically the plasma radiation intensity and obtained good agreement with the spectrum and its angular distribution. Wilems and Ritchie¹⁵¹ developed a microscopic theory in which surface roughness and imperfections were assumed to be approximated by random static electron charge density fluctuations. Since the surface irregularities may be considered as a random distribution of periodic irregularities or gratings, the plasma radiation can be elastically scattered by the distribution of gratings and accounts for the PREL effect. In a sense, the PREL effect is the analogue of diffuse scattering on a rough surface discussed in Section V.B.

D. Surface Plasma Radiation Excited by Electrons (SPREE)

Boersch and co-workers^{105-107, 123-125} have measured the radiation emitted from thick silver foils irradiated by electrons at grazing incidence. They found an intense peak at 3500 Å which corresponds to the nonradiative SP energy for semiinfinite Ag bounded by vacuum. The position of the peak was shifted as expected for the SP energy when the surface was covered by a thin dielectric layer. Jones, Cram, and Arakawa¹²³ observed the same effect. The experiment was subsequently repeated with unoxidized Al by Bürker and Steinmann¹¹³ and Braundmeier and Arakawa.^{121, 122} They found a pronounced peak of radiation at 10 eV, the Al SP energy. More recent works on Ag are by Dobberstein and Sauerbrey¹⁶⁷ and Dobberstein.¹⁶⁸ These are rather surprising observations that the supposedly nonradiative SPO can indeed couple with the radiation field. Surface roughness can explain these observations. The relevance of surface roughness was proved by an experiment of Teng and Stern¹²⁵ by using an Al-coated optical reflection grating. Thereby the surface roughness is known and its effects verified.

Quantitative theoretical considerations of SPREE are virtually nonexistent. The calculation of the intensity, angular dependence, and polarization properties of SPREE can be broken into two parts. The first part involves the inelastic excitation of SP by fast electrons. Methods for the treatment have been discussed in Section IV.D. The second part concerns the SP-photon conversion process made possible by surface roughness. This is the inverse of the photon-SP conversion that causes the reflectance drop as discussed in Section V.A. Elson and Ritchie's theory can be employed in this part of the problem. We do not attempt to do the entire problem here. However, we demonstrate that some formal solution of the second part can explain several features of SPREE as were observed experimentally.

One aspect of SPREE that we analyze was reported in a paper by Dobberstein.¹⁶⁸ Dobberstein recognized that for any calculation of the properties of the radiation field of SPREE, the surface structural factor

$g(\kappa)$ [Dobberstein called it $S(g)$] must be known. He devised an interesting method of measuring $g(\kappa)$ of an evaporated 1- μ -thick Ag film on a 0.2- μ rough CaF_2 layer on a glass substrate. He found that $g(\kappa)$ has a prominent peak at $\kappa_0 \approx 7 \times 10^{-3} \text{\AA}^{-1}$. The Ag film was bombarded with a beam of 40-keV electrons at an angle of 5° from the surface. Angular dependence of the intensity of SPREE, observed in the plane defined by the incident electron direction and the surface normal, shows that the main intensity is emitted in the backward direction against the obliquely incident electron beam. This occurs for radiation polarized parallel to the plane of observation, whereas for the perpendicular polarization the angular dependence of the intensity is quite symmetric about the surface normal. The $\lambda = 3850 \text{\AA}$ radiation observed corresponds to those SP with wave vector $k_{\parallel} \approx 5 \times 10^{-3} \text{\AA}^{-1}$. Dobberstein noticed that the equation

$$k_{\parallel} - \kappa_0 = \frac{\omega}{c} \sin \theta$$

for the conservation of overall momentum along the surface, implies $\sin \theta \approx -1$. This means that the main intensity of SPREE should be emitted in the backward direction. However, the difference in behavior of both polarizations has remained unexplained.

The surface lies on the xy or $u_1 u_2$ plane in Fig. 9 and the Ag plasma is

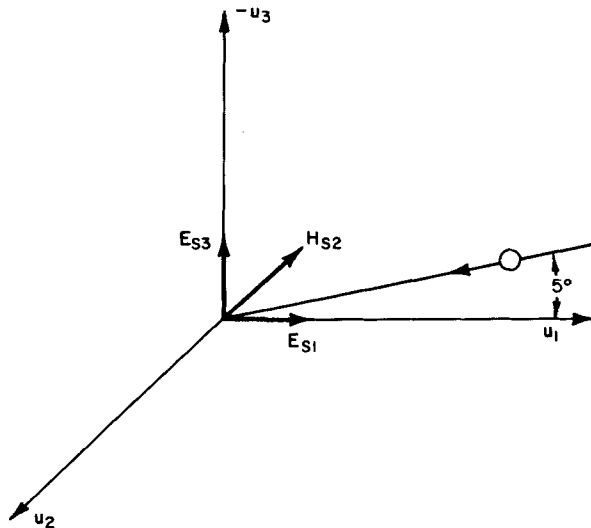


Fig. 9. Coordinate system, SP fields, and incident electron beam for Dobberstein SPREE (see text).

confined to the region $u_3 = [z - \zeta(xy)] > 0$. The surface normal pointing out to vacuum is $-\hat{u}_3$. The plane of incidence of the electrons and the plane of observation of the radiation in Dobberstein's experiment is the u_1u_3 plane. The surface roughness function $\zeta(u_1u_2)$ has Fourier transform ζ_{κ} defined by (5.10) peaked at $\kappa = \kappa_0$. For a surface plasma oscillation with wave vector $k_{\parallel}\hat{l}_1$ along the u_1 -axis, the conservation of momentum in the SP-photon conversion process implies $k_{\parallel} \pm \kappa_0 = (\omega/c)\sin\theta$. Real solutions for θ only exist for the minus sign case, and as Dobberstein pointed out, $\theta = -\pi/2$. The electromagnetic fields of these $k_{\parallel}\hat{l}_1$ SP are shown in Fig. 9. Let \mathbf{A}_S be the vector potential for the SP fields and \mathbf{A}_p the vector potential for the SP-radiation photon. The Elson-Ritchie SP-photon interaction Hamiltonian given by (5.5 to 5.8) will lead us to the nature of the SP radiation photon observed in the u_1u_3 plane. \mathbf{A}_S has only the components A_{S1} and A_{S3} in the \hat{l}_1 and \hat{l}_3 directions, respectively. We found

$$\begin{aligned} \mathcal{H}_{S-p} = & \frac{1}{4\pi c^2} \int d^3u \left\{ \frac{\partial \zeta}{\partial u_1} \dot{A}_{S1} \dot{A}_{p3} + \frac{\partial \zeta}{\partial u_1} \dot{A}_{p1} \dot{A}_{S3} \right. \\ & \left. + \theta(u_3) \omega_p^2 \left[\frac{\partial \zeta}{\partial u_1} (A_{S1} A_{p3} + A_{p1} A_{S3}) \right] \right. \\ & \left. + c^2 \frac{\partial \zeta}{\partial u_1} \left[A_{p1} \frac{\partial H_{S2}}{\partial u_1} - A_{S1} \frac{\partial H_{p2}}{\partial u_1} - \frac{\partial A_{S3}}{\partial u_3} H_{p2} - \frac{\partial A_{p3}}{\partial u_3} H_{S2} \right] \right\} \end{aligned} \quad (5.12)$$

Terms like $-c^2(\partial\zeta/\partial u_1)A_{S1}(\partial H_{p1}/\partial u_2)$ vanish because for photons in the u_1u_3 plane, $\partial H_{p1}/\partial u_2$ is zero. Also terms that contain $\delta\zeta/\partial u_2$ can be ignored since momentum conservation requires that for initial-state SP with $\mathbf{k}_{\parallel} = k_{\parallel}\hat{l}_1$ and final-state photon in the u_1u_3 plane, the κ that appears in ζ_{κ} must also be in the \hat{l}_1 direction. On examining the expression for H_{S-p} in (5.5) to (5.8), we observe that a surface plasma oscillation with $\mathbf{k}_{\parallel} = k_{\parallel}\hat{l}_1$ can be converted into a photon polarized parallel to the u_1u_3 plane only. This accounts for the asymmetry in the intensity of a parallel polarized photon in Dobberstein's data.

SPREE at optical frequencies of 5400 Å from Al grating surfaces has been measured by Teng and Stern.¹²⁵ This radiation comes from SP near the $\omega = ck_{\parallel}$ line, with $k_{\parallel} \approx 10^5 \text{ cm}^{-1}$. In the plane of emission of light, the

intensities of the \perp polarization have two peaks, but no appreciable peaks are discernible in the \parallel polarization. The positions of these peaks, their dependences on the wavelength of the emitted radiation, and the angle of the emission plane relative to the grating rulings have been accounted for by Teng and Stern as SP-photon conversion assisted by the grating which supplies a momentum $\pm \mathbf{g}$, the reciprocal grating vector. They were able to construct, for the first time, the low-energy portion of the dispersion curve for the SP in Al. This is complementary to the LEED determination of the high-energy portion of the dispersion curve discussed in Section IV.E.1.

Teng and Stern noted that the SPREE emitted indicates that the electric field of the 5400-Å radiation is in the plane determined by the normal to the grating surface and \mathbf{g} . On the other hand, for a flat surface, the electric field for the SP is in the plane determined by the surface normal and \mathbf{k}_{\parallel} . This difference in behavior was left unexplained. We apply the Elson-Ritchie formulation to resolve this.

Referring to the same coordinate system as in Fig. 9, we assume that the grating ruling is along the u_1 -axis. The roughness function ζ is then a function of u_2 only;

$$\zeta(u_2) = \sum_n \zeta_{\mathbf{g}_n} e^{i\mathbf{g}_n u_2}$$

where $\mathbf{g}_n = (2\pi n/d)\hat{l}_2$ and d is the ruling spacing. The SP-photon coupling is again describable by the Hamiltonian of (5.5) to (5.9). We first notice that for SP radiation with wave vector k and frequency ω that corresponds to near 5400 Å as observed by Teng and Stern, $\omega = ck$ can be considered to be small compared with ω_p . The group of terms inside the last square brackets in (5.12) is of the order of $(\omega/\omega_p)^2$ compared with the first two terms. Hence they can be neglected and

$$\mathcal{H}_{S-p} = \frac{1}{4\pi c^2} \int d^3u \theta(u_3) \omega_p^2 (A_{S2}A_{p3} + A_{p2}A_{S3}) \frac{\partial \zeta}{\partial u_2} \quad (5.13)$$

This expression implies for an arbitrary emission plane, that the low-frequency SP couples to a photon that has nonzero components of the vector potential in either the \hat{l}_2 or \hat{l}_3 direction. Hence the low-frequency SPREE is polarized in the u_2u_3 plane or, equivalently, the plane defined by the surface normal and the reciprocal grating vector. This is in accord with Teng and Stern's observation.

E. Optical Diffraction Grating and Wood's Anomalies

A diffraction grating is a special form of surface roughness. From the discussions given earlier in this section, it is clear that a p -polarized photon

incident on a grating can be absorbed in creating SP. Teng and Stern¹²⁵ observed sharp dips in the reflectance spectra from Al-coated gratings. These dips correspond to the photon-SP conversion process. That the response of a diffraction grating to *p*-polarized light exhibits Wood's anomalies is well known. Recently Ritchie et al.¹⁶⁹ have explained the occurrence of Wood's anomaly through resonant SP intermediate-state interaction with the photons. The Wood's anomalies result from second- and higher order photon-SP interaction assisted by the grating. Low-frequency portions of the dispersion curves of the SP in Al and Au were constructed from an analysis¹⁶⁹ of the variation in the wave length, at which the Wood's anomalies were observed, as a function of the angle of incidence. Evidence for the existence of zone structures in the SP dispersion curve was observed.¹⁶⁹ These zone structures, which are discontinuities in the SP dispersion curve at multiples of π/d , reflect the Brillouin phenomena of the SP wave because of the periodic structure of the diffraction grating. Similar experiments have been performed recently by Marshall, Fischer and Queisser¹⁷⁰ and Anderson, Alexander, and Bell¹⁷¹ on doped semiconductors.

F. Photoemission; Enhancement of Photoelectron Yield

Endriz and Spicer¹⁷² have performed photoemission measurements on Al films of varied surface roughness. The photoelectron yield has a strong peak when the photon energy approaches the Al SP energy. The size of those peaks correlates strongly with the degree of surface roughness. This led them to interpret this enhancement of photoyield as conversion of photon to SP assisted by roughness and subsequent decay of the excited SP into outgoing electrons. The last step was envisaged as the excitation of electrons by the penetration of the SP fields inside the metal, analogous to the "volume" theory¹⁴⁴ of photoemission. The peak structure of the photoyield near the SP energy arises from the same reason as the reflectance drop due to photon-SP conversion loss discussed in Section V.B. Endriz and Spicer used Elson-Ritchie's formula and computed the photoyield enhancement from the physical processes that they called the volume-photoemission effect, as has just been described. The calculated value of the enhancement was compared with experiments and found to be too small. This discrepancy led them to believe that a photon-excited SP, which has strong field components normal to the surface, can, in addition, give rise to a surface photoelectric effect.¹⁷² Good agreement was obtained only when this surface effect photoemission process by SP was included. These interesting manifestations of SP on rough surfaces, as observed by Endriz and Spicer, bear witness once again to the physical importance of SP.

G. Rough Cylindrical Surfaces

Rough cylindrical surfaces, or the presence of a grating with rulings perpendicular to the direction of the cylinder axis, can bring about photon interaction with the nonradiative SP in a cylinder. These will cause reflectance drops, SPREE, and grating anomalies as for the case of a rough but otherwise flat surface. Perhaps through one of these methods, the interesting dip of the SP dispersion relation for a cylinder can be observed.

VI. PHOTON-SURFACE PLASMON COUPLING; ATTENUATED TOTAL REFLECTION (ATR)

We have seen that the SP of a plane-bounded, semiinfinite electron gas has a phase velocity v_{SP} for propagation along the surface always less than c , the velocity of light. Ordinary photons will not couple with the SP excitations on a smooth flat surface. However, a photon can be totally reflected at the boundary of a vacuum-dielectric medium with refraction index $n_p > 1$. After being totally reflected, the photon state near the boundary has no transmitted wave but an evanescent wave propagating along the surface and decaying exponentially into the vacuum. Let α denote the incident angle of the photon (measured from the surface normal) before being totally reflected back into the dielectric medium. The wave vector k_{ATR} of this evanescent surface wave part of the original photon is given by

$$k_{ATR} = (\omega/c)n_p \sin \alpha \quad (6.1)$$

The condition of total internal reflection requires that α satisfy

$$1 < n_p \sin \alpha < n_p \quad (6.2)$$

From (6.1) and (6.2), we readily observe that $k_{ATR} > \omega/c$, or equivalently, the phase velocity v_{ATR} of the evanescent surface wave is less than c , but no smaller than c/n_p . If the incident photon is p -polarized, then the evanescent wave has a component of the electric field perpendicular to the surface. Hence by the introduction of a dielectric medium, usually in the form of a prism, an external p -polarized photon can be prepared into such a state that, in the vicinity of the total reflection boundary, its fields are of the same type as those of a surface plasma oscillation. This immediately suggests that on bringing the plane-bounded electron gas close to the prism surface within a distance of the order of the decay length of the evanescent wave, SP with $k = k_{ATR}$ can be excited by the photon. By changing the internal angle α of incidence, SP with k_{\parallel} up to but less than $k_{\max} = (\omega/c)n_p$ can be excited. This is a photon-SP conversion process and is observed

experimentally as a dip in the spectrum of the internally reflected photon intensity at the SP frequency. By changing α , the dispersion of SP can be obtained, for $k_{\parallel} < k_{\max}$, from the ATR spectra. This ATR method of exciting SP of metals was proposed by Otto,¹⁷³ and experimentally confirmed.^{173,174} It should also be mentioned that Turbador¹⁷⁵ earlier had used ATR to measure optical constants. Also Harrick¹⁷⁶ studied the optical spectrum of semiconductor surface states from ATR.

It is useful to compare the ATR method of coupling between photons and SP with the excitation of SP in a superconduction junction by Josephson photons. A *p*-polarized photon in ATR can be "slowed down" by total reflection, while the Josephson photon has to be "speeded up" by the application of a static external magnetic field along the junction. In both cases, when the phase velocity of either the slowed-down ATR photon or the speeded-up Josephson photon matches with a surface plasma oscillation, resonant coupling with, or conversion to, the SP occurs.

Recently, the ATR method has been applied extensively to the study of SP and surface optical phonons in semiconductors by Barker,¹⁷⁷ Marschall and Fischer,¹⁷⁸ Bryskin, Gerbshtein, and Mirlin,¹⁷⁹ and Palik et al.¹⁸⁰ Ruppin¹⁸¹ suggested the study of surface optical phonons by the ATR method in ionic crystals. Since the ATR method can only study surface excitations with $k_{\parallel} < k_{\max}$, that is, the vicinity of the retardation region, the interaction between the surface excitation and the photon is significant. In a solid, photons coupled to the elementary excitations such as phonons, plasmons, and magnons are called polaritons. Hence for a surface, the surface excitations such as SP, surface optical phonons, or magnons that interact with a photon in the long-wavelength region, are called collectively surface polaritons. Experimental study of surface polaritons and their dispersion relations have been performed by Marschall and Fischer¹⁷⁸ for GaP, by Bryskin, Gerbshtein, and Mirlin¹⁷⁹ for several alkali halides and CaF₂, by Barker¹⁷² for CaMoO₄, and by Fischer and Tyler¹⁸² for LiF. Observation of the propagation of surface polaritons over macroscopic distances (~ 1.6 cm) along copper-air interfaces at $10.6\text{-}\mu$ wavelength was reported by Schoenwald, Burstein, and Elson.¹⁸³ They have used ATR-prism coupling techniques to generate and detect the surface modes.

Several informative theoretical considerations of surface polaritons and their interactions have been discussed by Kheifets,¹⁸⁴ Chiu and Quinn,¹⁸⁵ and Wallis and Brion.¹⁸⁶ The influence of a magnetic field on SP has been discussed in the nonretarded limit by Pakhomov and Stepanov¹⁸⁷ and Abdel-Shahid and Pakhomov.¹⁸⁸ Chiu and Quinn¹⁸⁹ and also Brion, Wallis, Hartstein, and Burstein¹⁹⁰ have recently studied this problem with retardation effects included.

The problem of surface polaritons associated with surface phonons in

noncubic or anisotropic materials has been treated by Hartstein, Burstein, Brion, and Wallis.¹⁹¹ The problems of surface magnetoplasmons and surface magnons also involve an anisotropic dielectric¹⁹² or permeability tensor with antisymmetric off-diagonal parts. For certain configurations of the magnetic field, the surface, and the wave vector \mathbf{k} , an interesting result¹⁹³ of the nonreciprocity between $-\mathbf{k}$ and $+\mathbf{k}$ was found. Further, this surface excitation does not exist in the absence of the photon field, and the surface polariton is appropriately called a photon-induced surface polariton. Theoretical discussions of the photon-induced surface polaritons have been given by Bryskin, Mirlin, and Reshina.¹⁹⁴ They reported studies of these surface polaritons on uniaxial crystals MgF_2 and TiO_2 . Hartstein, Burstein, Brion, and Wallis¹⁹⁵ have given similar considerations. Experimental observations of photoinduced surface polaritons in α -quartz have been reported by Falge and Otto.¹⁹⁶

VII. SURFACE EXCITATIONS IN SMALL CRYSTALS

It is rather obvious that as the size of a crystal is decreased, the surface modes will become increasingly important relative to the bulk modes. The surface modes will dominate the absorption spectra provided the particle size is small enough. The importance of surface phonons in studies of the infrared properties of small particles has been stressed by Ruppin and Englman.¹⁹⁷ Infrared absorption by SP and surface phonons has been observed by Genzel and Martin¹⁹⁸ in microcrystals of CdO , NaCl , ZnSe , and MgO , by Bryskin, Mirlin, and Reshina¹⁹⁹ in 2 to 40 μ alkali halide crystal, and by Hunt, Steyer, and Huffman²⁰⁰ in small NiO particles. Infrared absorption by coupled SP-surface phonon modes in small crystals of CdO was observed by Rieder, Ishigame, and Genzel.²⁰¹ Raman scattering from surface phonon modes of small crystals has been discussed by Ruppin and Englman¹⁹⁷ and recently observed by Scott and Damen²⁰² in CdS .

The cause of infrared absorption by the surface excitations is due to both absorption and scattering. The theoretical calculations of these cross-sections, usually called the extinction cross-section, have been carried out for small spherical^{81,203} and randomly oriented infinite cylinders.²⁰⁴ We do not describe these calculations but instead offer a physical description of the phenomena in terms of concepts developed earlier in this review. Consider particles so small that their dimensions are small compared with the wavelength of a photon having the same energy as the surface excitation. Interaction of the surface excitations with photons of nearly the same energy no longer has to obey translational invariance in any direction of the surface. Hence all surface excitations are radiative in character. Pho-

tons incident on the particle will have a probability of being elastically scattered and inelastically absorbed by dissipative losses due to incoherent electron excitation, for example. The elastic scattering contributes to diffuse scattering loss in the transmission. The inelastic loss is proportional to the field strengths of the photon field inside the particle. When the photon energy matches that of any surface mode, both the probability for elastic scattering and the inelastic loss become resonantly large. This is due to the fact that direct photon-surface mode conversion becomes possible, and the field energy residing inside the particle, and hence the dissipative losses, is greatly enhanced.

The inverse process of photon emission by surface modes of small particles excited thermally or by incident electron is obviously possible in view of their radiative character. Kálin, Baltes, and Kneubühl²⁰⁵ have reported observation of far infrared (40 to 100 μ) spectral thermal emission at 600°K from 1 to 3 μ small alkahalide crystals.

VIII. INELASTIC X-RAY SCATTERING BY SURFACE PLASMONS

In the phenomena of the em field interacting with matter examined so far the frequency of the outgoing wave was always equal to that of the incoming wave. There are, however, phenomena of the Compton or Raman type where the outgoing photon exhibits a frequency shift relative to the incoming photon. This frequency shift is the energy loss the incoming photon suffers because of inelastic scattering in which an eigenmode of the system is excited. Clearly these phenomena involve two photons and are second order in the field. It follows that a linear response theory is not sufficient to describe such phenomena. We must return to the general Hamiltonian (2.4) of the interacting matter-field system. The inelastic scattering is due to first-order contributions in $\sum_i e^2 \mathbf{A}_i^2 / 2mc^2$ and second-order contributions in $\sum_i e \mathbf{A}_i \cdot \mathbf{p}_i / mc$. These contributions being second order in \mathbf{A} were omitted in deriving the linear current-field relation. From the two contributions the first one turns out to be much larger than the second.²⁰⁶ Thus the term responsible for the X-ray scattering is

$$H_S = \sum_i \frac{e^2 \mathbf{A}_i^2}{2mc^2} \quad (8.1)$$

One then may use standard quantum mechanical methods to obtain the scattering cross-section for the process under consideration.^{18,206-208} The so obtained scattering cross-section depends, for the case of a uniform system,^{18,208} linearly on $\text{Im}[1/\epsilon(\mathbf{k}, \omega)]$. This last factor clearly indicates that

when $\epsilon(\mathbf{k}, \omega) \approx 0$ the scattering cross-section exhibits a peak. This is not a surprise, of course. As in the case of electron loss, the X-ray may be scattered inelastically by bulk plasmons and consequently a peak should appear for energy losses equal to the plasmon energy. For large momentum transfers \mathbf{k} , the plasma loss peak is reduced and the Compton part (i.e., the part where electron-hole pairs are created) is more important.^{207, 209} A physically transparent way of examining the X-ray plasmon scattering is to use a continuous model for the electron gas (a reasonable approximation for low \mathbf{k}); then (8.1) can be written as

$$H_S \approx \int d^3r \frac{e^2 \rho(\mathbf{r}) \mathbf{A}^2(\mathbf{r})}{2mc^2} \quad (8.2)$$

For plasma oscillation the operator $\rho(\mathbf{r})$ can be expressed in terms of plasmon creation and annihilation operators; expressing \mathbf{A}^2 in terms of photon creation and annihilation operators we have that the photon-plasmon part of H_S can be written as

$$H_{S; \text{ph-BP}} = \sum V_{\mathbf{k}, \mathbf{q}} a_{\mathbf{q}}^+ a_{\mathbf{q}+\mathbf{k}} [c_{-\mathbf{k}} + c_{\mathbf{k}}^+] \quad (8.3)$$

where the amplitude $V_{\mathbf{k}, \mathbf{q}}$ is obtained from the method just outlined. The scattering cross-section for plasmon excitation can be trivially obtained from (8.3). This method can be easily generalized to the case where X-rays excite surface plasmons; one has simply to express $\rho(\mathbf{r})$ in (8.2) in terms of SP creation and annihilation operators by following the techniques discussed in Section IV.B.

Bulk plasmon excitation by X-rays was first observed by Priftis et al.²¹⁰ Subsequent work verified^{211, 212} and refined²¹³ the original experiment. Surface plasmons in small spherical particles were recently observed^{85, 214} through inelastic X-ray scattering.

A different plasmon effect during X-ray photoemission is the following: The deep hole created by the X-ray interacts with the plasmons, both surface and bulk, and thereby satellite lines should appear in the photoemission spectrum. The theory of this effect has been worked out by Chang and Langreth.²¹⁵

IX. VAN DER WAALS FORCES BETWEEN SURFACES: SURFACE ENERGY

The close connection between SP excitation and the response of a metal surface to an external charge has been recognized repeatedly in the past.²¹⁶ In actual fact, from linear response theories SP dispersion relation and damping rates can be determined. The SP concept has also found use in

calculating the van der Waals forces between neutral macroscopic bodies whose surfaces are separated by distances d which are typically of the order of 1000 Å. The interaction between the bodies can be easily calculated from consideration of the SP contribution to the ground-state energy of the system. For two bodies whose surfaces are separated by d much larger than interatomic distances, any interaction between them can only occur through electromagnetic fields in the two media and in the space between, namely, the SP and the magnetic bound solutions. In the ground state of the system, those SP and magnetic solution fields execute zero-point motion, and contribute to the total ground-state energy, their sum of zero-point energies. The force between the two bodies can immediately be obtained as the derivative of the total SP plus the magnetic solution's zero-point energy with respect to d . This procedure of calculating the interaction, due originally to Casimir,²¹⁷ was recently applied to the van der Waals force problem by Van Kampen, Nijboer, and Schram²¹⁸ to calculate the attraction between two semiinfinite media. These workers have limited themselves to considering the electrostatic limit and, as a result, only SP excitations are present in the system. Hence their results of the interaction energy and the attraction force are valid in the nonretarded limit. The electrostatic description of those SP with phase velocity not negligible compared with c is inaccurate, as has been pointed out previously in this review. If these SP contribute significantly to the total zero-point energy, the nonretarded formula for the attraction should not be trusted. This situation is expected to occur at large d , such that $d \gg c/\omega_p = 1/k_p$, when all the SP with $k_{\parallel} > k_p$ have fields that have already decayed, and contribute negligible to the attraction. On the other hand, for small d , such that $k_p d \ll 1$, the SP with $k_{\parallel} > k_p$ dominate the contribution to the total zero-point energy and the nonretarded formula is a good approximation. From the classical electrodynamics point of view, when the two surfaces are separated at large distance, the delay in the electromagnetic interaction becomes important, and the instantaneous electrostatic approximation breaks down. For typical metals, $k_p \approx 10^5 \text{ cm}^{-1}$, and, for $d > 1000 \text{ Å}$, $k_p d > 1$ and hence retardation effects are not a priori negligible. Gerlach²¹⁹ has obtained a more general expression for the van der Waals forces by considering the contributions to the zero-point energy of both the SP (with RE included) and the bound magnetic solutions. The SP dispersion relation he used was the same as that derived by Economou²⁶ and discussed in Section III.B.1.c.

Both the nonretarded and the retarded van der Waals attraction force formulas obtained by SP considerations are identical to that derived by Lifshitz.^{9,220} Lifshitz developed a macroscopic theory by attributing the interaction between bodies to fluctuations of the electromagnetic field in

the two bodies and in the space between them. Lifshitz obtained the attraction force using explicit expressions for the fluctuating em fields in the space between the media, satisfying boundary conditions. Inherent in this approach is the assumption that d is much larger than interatomic distances. This Lifshitz formula and its generalizations have been obtained via quantum field theory of electromagnetic radiation in an absorbing medium by Dzyaloshinskii, Lifshitz, and Pitaevskii.²²¹ We have seen that SP and bound magnetic solutions in the system of the two media separated by a distance d constitute all the electromagnetic eigenmodes that are bound to the surfaces. It is therefore not surprising to see that both the eigenmode approach and the Lifshitz and co-workers methods predict the same results. The concepts of fluctuating electromagnetic fields involved in the Lifshitz and quantum field treatments are more difficult to comprehend than those of the eigenmode consideration.

Another interesting and important application of the SP zero-point energy concepts was obtained by Schmit and Lucas²²² in the calculation of surface energy of metals. The surface energy is related to the energy per unit area required to split a solid into two half-solids a large distance apart along a plane. The surface energy σ consists of two parts: (1) the creation energy σ_c which is required to separate the two half-spaces to some distance d , and (2) the van der Waals adhesion energy σ_d at a distance d as discussed earlier. Of course, d is a small distance, but large compared with all interatomic or interelectronic distances l_a and l_e , respectively; σ_d is expected to be small compared with σ_c . Recalling our discussion of retardation effects in σ_d , we recognize that surface plasma oscillation with wave vector $k_{\parallel} \gg 1/d$ never enters into the consideration of σ_d due to the decay of their associated fields. Since d is large compared with l_e , the SP contributing to σ_d have negligible quantum effects, and the calculation of σ_d is exact. This is not the case with σ_c which involves distances of the order of l_e , and SP with large $k_{\parallel} \leq 1/l_e$ contributing to the creation energy. Quantum effects such as SP damping enter into the consideration. Schmit and Lucas handled this by a cutoff SP wave vector k_c arbitrarily chosen to be $\omega_p/\sqrt{2} v_F$, where v_F is the Fermi velocity. When this is applied to alkali and transition metals, Schmit and Lucas²²² obtained good agreement of their calculated σ , its dependences on r_s and temperature, with experiment. Jonson and Srinivasan²²³ have some doubts about these favorable comparisons with experiments and suggest that the agreement may result from the arbitrary cutoff procedure that Schmit and Lucas adopted. Nevertheless, we think that Schmit and Lucas's ideas are quite interesting. Its usefulness depends on the future efforts in handling large k_{\parallel} SP in a more rigorous manner and suitably account for the exchange and correlation energies.

X. QUANTUM EFFECTS

We have already discussed that a quantum treatment of the electrons of the system becomes necessary when

$$\omega \leq v_F k \quad (10.1)$$

From the physical problems we examined one can conclude that there is no need for such quantum treatment in optical properties except perhaps for very rough surfaces. For inelastic scattering of high-energy electrons or X-rays the situation depends on the angle of scattering. Large scattering angles correspond to large k_{\parallel} and one may very well enter into the quantum regime this way. For low-energy electrons as in the case of tunneling, LEED, and photoemission, the quantum regime plays an important role because large k_{\parallel} makes a significant contribution to the observed quantities. The situation is probably even more extreme in the case of surface energy where the large- k_{\parallel} regime makes a dominant contribution for extremely small surface separations. This is evident from the sensitivity of the results to the cutoff, k_c .

As a matter of fact, the quantum treatment of the electrons of the system becomes necessary or desirable even before we approach the regime defined by (10.1). The reason is the following: For $k_{\parallel} \neq 0$, the properties of SP depend on the properties of the surfaces rather strongly. Thus one should incorporate a detailed description of the surface as an input in the theory of SP. However, the classical approaches such as the Boltzmann-Vlasov equation or the hydrodynamic approximation are either limited in the ways they can describe the surface or become extremely complicated so that one is almost forced to the more reliable quantum treatment. The information about the surface can be summarized in the form of the one-particle potential each electron is experiencing, $V(z, \mathbf{R})$. In all the treatments up to date the dependence on the parallel vector \mathbf{R} has been omitted.²²⁴ Bennett,²²⁵ using a classical hydrodynamic approximation, was the first to show the strong dependence of the SP dispersion relation on the form of the surface profile. Feibelman²²⁶ has shown that for any \mathbf{R} -independent $V(z)$ describing the surface, the result for the SP frequency at $k_{\parallel} = 0$ is $\omega_p / \sqrt{2}$ at least as long as the RPA is valid.

In the early treatments²²⁷⁻²³³ the potential $V(z)$ was assumed to be infinite outside the material; this assumption is equivalent to assuming a step function electron density, that is, $n(z) = 0$ for $z > 0$ (outside the material) and $n(z) \neq 0$ for $z < 0$ (inside the material). It is only recently that a more realistic treatment of the surface potential was used. Thus Beck and Celli²³⁴ used a step function for $V(z)$ and Feibelman²²⁴ examined several

forms of $V(z)$ including the self-consistent Lang-Kohn potential.²³⁵ These calculations have shown that the surface potential $V(z)$ is very important in determining the dispersion relation of SP for $k_{\parallel} > 0$.

The theoretical approach is the following: The current field linear relation has the general form

$$j(k_{\parallel}, z, \omega) = \int dz' \sigma(k_{\parallel}, z, z', \omega) E(k_{\parallel}, z', \omega) \quad (10.2)$$

Usually instead of (10.2) an equivalent equation is used relating the charge fluctuation with the electric potential.²³⁴ The response function $\sigma(k_{\parallel}, z, z', \omega)$ (or any corresponding response function) is evaluated within the RPA, which is discussed briefly below. Once σ is known, we substitute (10.2) in Poisson's equation (ρ can be expressed in terms of \mathbf{j} : $\nabla \cdot \mathbf{j} + i\omega\rho = 0$) and an integral equation for the electrostatic potential results.²²⁴ Certain mathematical manipulations combined with numerical evaluation give the dispersion relation. In almost all the treatments the dispersion relation was obtained for low k_{\parallel} (still, however, much larger than k_p so that no RE are present), where a linear expansion is valid^{224, 234}

$$\omega_s(k_{\parallel}) = \frac{\omega_p}{\sqrt{2}} \left[1 + (\alpha_1 + i\alpha_2)k_{\parallel} + O(k_{\parallel}^2) \right] \quad (10.3)$$

The quantities α_1, α_2 are the terms of interest. A discussion of the influence that the form of $V(z)$ has on α_1, α_2 is given in Refs. 224 and 235. Note also that the numbers α_1, α_2 can now be compared with rather accurate experimental results obtained from LEED.¹³⁷ As Feibelman pointed out,²²⁴ small discrepancies between theory and experiment may be due to the omission of the \mathbf{R} dependence in the one-electron potential $V(\mathbf{R}, z)$.

From the integral equation for the electric potential one can derive certain general relations²³² which are independent of the form of $V(z)$. One expects that those relations should be derivable from general consideration. Flores and Garcia-Moliner²³⁹ have shown that this is indeed the case by deriving from simple electrostatic considerations certain relations obtained previously by Harris and Griffin.²³² This alternative derivation is not only simpler but throws some light on the nature of certain approximations.

It should be pointed out that certain physical problems require the knowledge of the dispersion relation for all k_{\parallel} . These are the cases where the results depend rather sensitively on the cutoff k_c , as in the case of tunneling and surface energy discussed above. For those cases one needs to go beyond (10.3). The behavior of the surface plasmon near the cutoff is

a very difficult problem involving rather strong interactions with other elementary excitations such as electrons, holes, other plasmons, and so on. In this extreme regime the form of $V(\mathbf{R}, z)$ should be very important. It seems, however, that such a study is necessary if one wishes to use with confidence the concept of a plasmon all the way to microscopically local effects. The case of surface energy provides evidence that the concept of a plasmon, especially the SP, may be extremely useful in handling questions of a local microscopic nature.

Before we conclude, we present a brief guide to the different ways the RPA is introduced. The subject of the RPA is treated in the standard books on many-body theory^{221, 236-238} and in more specialized books.^{1, 18} Possibly the best way to introduce the RPA is as a self-consistent field approximation¹⁷ to the linearized equation for the density matrix of the many-body system. Several workers have followed this method for the calculation of the response function.^{224, 229-231} The RPA can be used also in the usual²²¹ perturbative approach for the Green's function of the system. Fedders used this formalism.²³³ Finally one can introduce the RPA within the Kadanoff-Baym's Green's function²³⁶ formalism. Harris and Griffin followed this approach. The original way¹⁵ for introducing RPA is not convenient, especially in inhomogeneous systems. It is, of course, obvious that all different formalisms provide identical results; their difference is only in convenience and personal taste. The validity of the RPA is rather difficult to check since the post-RPA approximations are very complicated.¹ There are no calculations using post-RPA approximations for surface problems. These more sophisticated approximations may be important in handling the problem of the dispersion relation near the cutoff.

Acknowledgments

The authors had helpful discussions on the subjects covered in this article with V. Celli, R. Kaplan, D. Licciardello, E. D. Palik, J. J. Quinn, C. Pfeiffer, and R. F. Wallis. The assistance of D. Licciardello and C. Pfeiffer is gratefully acknowledged.

References

1. P. M. Platzman and P. A. Wolff, *Waves and Interactions in Solid State Plasmas* (Solid State Physics, Suppl. No. 13), Academic Press, New York and London, 1973.
2. H. Raether, in *Springer Tracts in Modern Physics*, Vol. 38, G. Höhler, Ed., Springer, New York, 1965, p. 84.
3. C. J. Powell, *Health Phys.*, **13**, 1265 (1967).
4. H. Boersch, *J. Electron Microsc.*, **16**, 39 (1967).
5. W. Steinmann, *Phys. Status Solidi*, **28**, 437 (1968).
6. H. Raether, in *The Structure and Chemistry of Solid Surfaces*, G. A. Somorjai, Ed., Wiley, New York, 1969, p. 10-1.
7. C. J. Powell, *J. Opt. Soc. Am.*, **60**, 78 (1970).
8. R. H. Ritchie, *Surf. Sci.*, **34**, 1 (1973).

9. L. D. Landau and E. M. Lifshitz, *Electrodynamics of Continuous Media*, Pergamon Press, Oxford, 1960, and Addison-Wesley, Reading, Mass., pp. 213–238, 331–337.
10. L. I. Schiff, *Quantum Mechanics*, 2nd ed., McGraw-Hill, New York, 1955, p. 388.
11. The vector potential \mathbf{A} is practically zero whenever the light velocity c is much larger than any other characteristic velocity v_c of the system. If the characteristic lengths are of the order of particle separation, then $c \gg v_c$ since the characteristic times for a condensed system are of the order of 10^{16} sec or less.
12. See, for example, C. Kittel, *Quantum Theory of Solids*, Wiley, New York, 1963, pp. 34–48.
13. If the current $\mathbf{j}(\mathbf{r}, t)$ is known, the charge $\rho(\mathbf{r}, t)$ can be found easily from the equation of continuity $\nabla \cdot \mathbf{j}(\mathbf{r}, t) + \partial \rho(\mathbf{r}, t) / \partial t = 0$. Note also that one can try equivalently to express the polarization $\mathbf{P}(\mathbf{r}, t)$ or the dielectric displacement $\mathbf{D}(\mathbf{r}, t)$ in terms of the field since all these quantities are simply related.
14. D. Pines, *The Many-Body Problem*, Benjamin, New York, 1962.
15. D. Bohm and D. Pines, *Phys. Rev.*, **92**, 609 (1953).
16. U. Fano, *Phys. Rev.*, **103**, 1202 (1956).
17. H. Ehrenreich and M. H. Cohen, *Phys. Rev.*, **115**, 786 (1959).
18. D. Pines, *Elementary Excitations in Solids*, Benjamin, New York, 1964.
19. F. Bloch, *Z. Phys.*, **81**, 363 (1933).
20. R. H. Ritchie, *Phys. Rev.*, **106**, 874 (1957).
21. H. Ehrenreich and H. R. Phillip, *Phys. Rev.*, **128**, 1622 (1962).
22. This damping is basically different from the Landau damping. Landau damping occurs because the plasmons are only approximate eigenstates of the electronic system and consequently they consist of a linear combination of exact eigenstates. The collision damping is a true dissipative mechanism as a result of which all the electronic eigenstates acquire a finite lifetime.¹
23. K. L. Kliewer and R. Fuchs, *Phys. Rev.*, **172**, 607 (1968).
24. G. E. Reuter and E. H. Sondheimer, *Proc. Roy. Soc.*, **A195**, 336 (1948).
25. The quantity c/ω_p , the London penetration depth, is also denoted by λ_p in the literature.
26. E. N. Economou, *Phys. Rev.*, **182**, 539 (1969).
27. R. Englman and E. H. Sondheimer, *Proc. Phys. Soc.*, **B69**, 449 (1956).
28. A. R. Melnyk and M. J. Harrison, *Phys. Rev.*, **B2**, 835 (1970).
29. D. C. Mattis and J. Bardeen, *Phys. Rev.*, **111**, 412 (1958).
30. E. A. Stern and R. A. Ferrel, *Phys. Rev.*, **120**, 130 (1960).
31. The outgoing part of the incident wave solutions is always (except for the case of complete absorption) radiative since the incoming energy is at least partly reemitted.
32. J. A. Stratton, *Electromagnetic Theory*, McGraw-Hill, New York, 1941.
33. R. H. Ritchie, *Phys. Rev.*, **106**, 874 (1957).
34. E. A. Stern and R. A. Ferrell, *Phys. Rev.*, **120**, 130 (1960).
35. C. J. Powell and J. B. Swan, *Phys. Rev.*, **115**, 869 (1959); **116**, 81 (1959); **118**, 640 (1960).
36. H. Raether, *Surf. Sci.*, **8**, 233 (1967).
37. C. Kunz, *Z. Phys.*, **196**, 311 (1966).
38. A. R. Melnyk and M. J. Harrison, *Phys. Rev. Lett.*, **21**, 85 (1968).
39. R. H. Ritchie and R. E. Wilems, *Phys. Rev.*, **178**, 372 (1969).
40. R. L. Guernsey, *The Physics of Fluids*, **12**, 1852 (1969).
41. K. L. Kliewer and R. Fuchs, *Phys. Rev.*, **153**, 498 (1967).
42. R. A. Ferrell, *Phys. Rev.*, **111**, 1214 (1958).
43. R. H. Ritchie and H. B. Elridge, *Phys. Rev.*, **126**, 1935 (1962).
44. A. Otto, *Z. Phys.*, **185**, 232 (1965).

45. I. M. Frank and V. I. Ginsburg, *J. Phys. USSR*, **9**, 353 (1945).
46. E. A. Stern, *Phys. Rev. Lett.*, **8**, 7 (1962).
47. R. A. Ferrel and E. A. Stern, *Am. J. Phys.*, **30**, 810 (1962).
48. A. J. McAlister and E. A. Stern, *Phys. Rev.*, **132**, 1599 (1963).
49. R. H. Huebner, E. T. Arakawa, R. A. Macrae, and R. N. Hamm, *J. Opt. Soc. Am.*, **54**, 1434 (1964).
50. H. Boersch, P. Dobberstein, D. Fritsche, and D. Sauerbrey, *Z. Phys.*, **187**, 97 (1965).
51. A. J. Braundmeier, M. W. Williams, E. T. Arakawa, and R. H. Ritchie, *Phys. Rev.*, **B5**, 2754 (1972).
52. W. E. Jones, K. L. Kliewer, and R. Fuchs, *Phys. Rev.*, **178**, 1201 (1969).
53. S. Y. Shieh, *Phys. Lett.*, **29A**, 46 (1969).
54. T. Kloos, *Z. Phys.*, **208**, 77 (1968).
55. M. Hattari, K. Yamada, and H. Suzuki, *J. Phys. Soc. Japan*, **18**, 203 (1963).
56. M. Skibowski, B. Feuerbach, and W. Steinmann, *Z. Phys.*, **211**, 329 (1968).
57. S. Yamaguchi, *J. Phys. Soc. Japan*, **17**, 1172 (1962).
58. N. Matsudaira, *J. Phys. Soc. Japan*, **18**, 380 (1963).
59. N. Matsudaira, *J. Phys. Soc. Japan*, **17**, 1563 (1962).
60. I. Lindau and P. O. Nilsson, *Phys. Lett.*, **31A**, 352 (1970); *Phys. Scr.*, **3**, 87 (1971).
61. F. Sauter, *Z. Phys.*, **203**, 488 (1967).
62. F. Forstmann, *Z. Phys.*, **203**, 495 (1967).
63. R. P. Godwin, *Phys. Rev. Lett.*, **28**, 85 (1972).
64. (a) K. L. Ngai and E. N. Economou, *Phys. Rev.*, **B4**, 2132 (1971); (b) K. L. Ngai, E. N. Economou, and M. H. Cohen, *Phys. Rev. Lett.*, **22**, 1375 (1969).
65. J. C. Swihart, *J. Appl. Phys.*, **32**, 461 (1961).
66. M. D. Fiske, *Rev. Mod. Phys.*, **36**, 221 (1964).
67. K. L. Ngai, *Phys. Rev.*, **182**, 555 (1969).
68. J. J. Lander and J. Morrison, *Surf. Sci.*, **14**, 465 (1967).
69. A. U. MacRae, K. Muller, J. J. Lander, J. Morrison, and J. C. Phillips, *Phys. Rev. Lett.*, **22**, 1048 (1969).
70. K. L. Ngai, E. N. Economou, and M. H. Cohen, *Phys. Rev. Lett.*, **24**, 61 (1970); E. N. Economou, M. H. Cohen, and K. L. Ngai, Proceedings of the Fourth LEED Theory Seminar, 1970.
71. D. M. Newns, *Phys. Lett.*, **38A**, 341 (1972).
72. J. W. Gadzuk, *Phys. Rev.*, **B1**, 1267 (1970); see also C. J. Powell, *ibid*, **B1**, 4191 (1970).
73. D. C. Licciardello, unpublished.
74. E. N. Economou, unpublished.
75. J. Crowell and R. H. Ritchie, *Phys. Rev.*, **172**, 436 (1968).
76. C. Mie, *Ann. Phys.*, **25**, (4) 377 (1908); see also M. Born and E. Wolf, *Principles of Optics*, Pergamon Press, New York, 1959, p. 630.
77. M. Natta, *Solid-State Commun.*, **7**, 823 (1969).
78. H. Jensen, *Z. Phys.*, **106**, 620 (1937).
79. F. Fujimoto, K. Komaki, and K. Ishida, *J. Phys. Soc. Japan*, **23**, 1186 (1967); F. Fujimoto and K. Komaki, *ibid.*, **25**, 1679 (1968).
80. A. Kawabata and R. Kubo, *J. Phys. Soc. Japan*, **21**, 1765 (1966).
81. U. Kreibig and P. Zacharias, *Z. Phys.*, **231**, 128 (1970); U. Kreibig, *Z. Phys.*, **234**, 307 (1970).
82. R. H. Doremus, *J. Chem. Phys.*, **40**, 2839 (1964); *J. Appl. Phys.*, **35**, 3456 (1964); *J. Chem. Phys.*, **42**, 414 (1965).
83. W. T. Doyle, *Proc. Phys. Soc. (London)*, **75**, 649 (1960).
84. M. Creuzburg and H. Raether, *Z. Phys.*, **171**, 436 (1963).

85. C. Koumelis, D. Leventouri, and K. Alexopoulos, *Phys. Status Solidi (b)*, **46**, K-81 (1971).
86. Th. Kokkinakis and K. Alexopoulos, *Phys. Rev. Lett.*, **28**, 1632 (1972).
87. P. Henoc and L. Henry, *J. Phys. (Paris), Coll. GI, CI*, 55 (1970).
88. K. L. Ngai and E. N. Economou, presented at the Conference on Surface Properties and Surface States of Electronic Materials, Rolla, Mo., June 1972.
89. C. Miziumski, *Phys. Lett.*, **40A**, 187 (1972).
90. E. N. Economou, C. Pfeiffer, and K. L. Ngai, to be published.
91. There is a printing error in Eq. (3.17) of Ref. 64a. The prefactor $(2/|Q|\mathcal{F}_Q)^{1/2}$ should read $(\pi\omega_Q/|Q|\mathcal{S}_Q)^{1/2}$.
92. S. Q. Wang and G. D. Mahan, *Phys. Rev.*, **B6**, 4517 (1972).
93. J. I. Gersten, *Phys. Rev.*, **188**, 774 (1969).
94. A. A. Lucas, E. Kartheuser, and R. G. Badro, *Solid-State Commun.*, **8**, 1075 (1970).
95. M. Sunjic and A. A. Lucas, *Phys. Rev.*, **B3**, 719 (1971).
96. I. M. Frank, *Usp. Fiz. Nauk.*, **87**, 189 (1965) [*Sov. Phys. Usp.*, **8**, 729 (1966)].
97. V. E. Pafomov, *JETP (USSR)*, **33**, 1074 (1957) [*JETP*, **6**, 829 (1958)].
98. G. M. Garibyan, *JETP (USSR)*, **33**, 1403 (1957) [*JETP*, **6**, 1079 (1958)].
99. G. M. Garibyan, *JETP (USSR)*, **37**, 527 (1959) [*JETP*, **10**, 372 (1960)].
100. K. A. Barsukov, *JETP (USSR)*, **37**, 1106 (1959) [*JETP*, **10**, 787 (1960)].
101. V. P. Silin and E. P. Fetisov, *Phys. Rev. Lett.*, **7**, 374 (1961).
102. V. E. Pafomov and E. P. Fetisov, *JETP (USSR)*, **53**, 965 (1967) [*JETP*, **26**, 581 (1968)].
103. R. M. Lewis and J. K. Cohen, *J. Math. Phys.*, **11**, 296 (1970).
104. H. Boersch, C. Radcliff, and G. Sauerbrey, *Z. Phys.*, **165**, 464 (1961).
105. G. Sauerbrey, *Proceedings of the 5th International Congress on Electron Microscopy*, Vol. 1, Academic Press, New York, 1961, p. AA-13.
106. P. V. Blanckenhagen, H. Boersch, D. Fritzsche, G. Sauerbrey, and H. G. Seifert, *Phys. Lett.*, **11**, 298 (1964).
107. H. Boersch, P. Dobberstein, D. Fritzsche, and G. Sauerbrey, *Z. Phys.*, **187**, 97 (1965). See also H. Boersch and G. Sauerbrey, *Optical Properties and Electronic Structure of Metals and Alloys*, F. Abèles, Ed., North Holland, Amsterdam, 1966 p. 386.
108. W. Steinmann, *Phys. Rev. Lett.*, **5**, 470 (1960); *Z. Phys.*, **163**, 92 (1961).
109. W. R. Brown, P. Wessel, and E. P. Trownson, *Phys. Rev. Lett.*, **5**, 472 (1960).
110. A. L. Frank, E. T. Arakawa, and R. D. Birkhoff, *Phys. Rev.*, **126**, 1947 (1962).
111. E. T. Arakawa, N. O. Davis, L. C. Emerson, and R. D. Birkhoff, *J. Phys. Radium*, **25**, 129 (1964).
112. E. T. Arakawa, N. O. Davis, and R. D. Birkhoff, *Phys. Rev.*, **135**, A224 (1964).
113. U. Bürker and W. Steinmann, *Phys. Status Solidi*, **12**, 853 (1965).
114. R. J. Herickhoff, E. T. Arakawa, and R. D. Birkhoff, *Phys. Rev.*, **137**, A1433 (1965).
115. E. T. Arakawa, R. J. Herickhoff, and R. D. Birkhoff, *Phys. Rev. Lett.*, **12**, 319 (1964).
116. R. J. Herickhoff, W. F. Hanson, E. T. Arakawa, and R. D. Birkhoff, *Phys. Rev.*, **139**, A1455 (1965).
117. E. T. Arakawa, R. N. Hamm, W. F. Hanson, and T. M. Jelinek, *Optical Properties and Electronic Structure of Metals and Alloys*, F. Abèles, Ed., North Holland, Amsterdam, 1966, p. 374.
118. W. Steinmann and H. Wille, *Phys. Status Solidi*, **15**, 507 (1966).
119. U. Bürker, to be published.
120. A. J. Braundmeier, Jr., E. T. Arakawa, and M. W. Williams, *Phys. Lett.*, **32A**, 241 (1970).
121. A. J. Braundmeier, Jr., and E. T. Arakawa, *Opt. Commun.*, **2**, 257 (1970).
122. A. J. Braundmeier and E. T. Arakawa, *Z. Phys.*, **239**, 337 (1970).

123. G. E. Jones, L. S. Cram, and E. T. Arakawa, *Phys. Rev.*, **147**, 515 (1966).
124. L. S. Cram and E. T. Arakawa, *Phys. Rev.*, **153**, 455 (1967).
125. Y. Y. Teng and E. A. Stern, *Phys. Rev. Lett.*, **19**, 511 (1967).
126. T. Kloos, *Z. Phys.*, **208**, 77 (1968).
127. J. Daniels, *Z. Phys.*, **203**, 235 (1967).
128. P. Wienhold, *Z. Phys.*, **208**, 313 (1968).
129. C. Kunz and H. Raether, *Naturwissenschaften*, **48**, 711 (1961).
130. P. Schmüser, *Z. Phys.*, **180**, 105 (1964).
131. A. A. Lucas and M. Sunjic, *Phys. Rev. Lett.*, **26**, 229 (1971).
132. H. Ibach, *Phys. Rev. Lett.*, **24**, 1416 (1970); H. Ibach, *Festkörper Probleme*, Vol. XI, O. Madelung, Ed., Pergamon Press, New York, 1971, p. 135; H. Ibach, *Phys. Rev. Lett.*, **27**, 253 (1971).
133. C. J. Powell, *Phys. Rev.*, **175**, 972 (1968).
134. H. Boersh, J. Geiger, and W. Stickel, *Z. Phys.*, **212**, 130 (1968).
135. M. Gell-Mann and M. L. Goldberger, *Phys. Rev.*, **91**, 398 (1953); N. Cabrera, V. Celli, and R. Manson, *Phys. Rev. Lett.*, **22**, 346 (1969).
136. See C. B. Duke in this volume.
137. A. Bagchi, C. B. Duke, P. J. Feibelman, and J. O. Porteus, *Phys. Rev. Lett.*, **27**, 998 (1971).
138. J. O. Porteus and W. N. Faith, in Proceedings of the 5th LEED Seminar, Washington, D. C., 1971, pp. 81-85.
139. B. D. Josephson, *Adv. Phys.*, **14**, 419 (1965).
140. D. N. Langenberg, D. J. Scalapino, and B. N. Taylor, *Proc. IEEE*, **54**, 560 (1966).
141. D. C. Tsui, *Phys. Rev. Lett.*, **22**, 293 (1969).
142. E. N. Economou and K. L. Ngai, *Phys. Rev. Comments and Addenda*, **B4**, 4105 (1971).
143. D. E. Beck and V. Celli, *Phys. Rev. Lett.*, **28**, 1124 (1972).
144. C. N. Berglund and W. E. Spicer, *Phys. Rev.*, **136**, A1030 (1964).
145. T. A. Callcott and A. U. MacRae, *Phys. Rev.*, **178**, 966 (1969).
146. N. V. Smith and W. E. Spicer, *Phys. Rev. Lett.*, **22**, 769 (1969).
147. A. A. Lucas, *Phys. Rev. Lett.*, **26**, 813 (1971); *Phys. Rev.*, **B4**, 2939 (1971).
148. A. J. Jason, *Phys. Rev.*, **156**, 266 (1967).
149. E. A. Stern, as quoted by R. A. Ferrell, Ref. 42.
150. E. A. Stern, *Phys. Rev. Lett.*, **19**, 1321 (1967).
151. R. E. Wilems and R. H. Ritchie, *Phys. Rev. Lett.*, **19**, 1325 (1967).
152. P. A. Fedders, *Phys. Rev.*, **165**, 580 (1968).
153. J. Crowell and R. H. Ritchie, *J. Opt. Soc. Am.*, **60**, 794 (1970).
154. E. Kretschmann and H. Raether, *Z. Naturforsch.*, **23a**, 2135 (1968); **22a**, 1623 (1967); E. Kretschmann, *Z. Phys.*, **241**, 313 (1971).
155. J. M. Elson and R. H. Ritchie, *Phys. Rev.*, **B4**, 4129 (1971).
156. U. Fano, *Ann. Phys. (N.Y.)*, **32**, 393 (1938); *J. Opt. Soc. Am.*, **31**, 213 (1941).
157. S. N. Jaspersion and S. E. Schnatterly, *Phys. Rev.*, **188**, 759 (1969).
158. J. E. Endriz and W. E. Spicer, *Phys. Rev. Lett.*, **24**, 64 (1970); J. E. Endriz and W. E. Spicer, *Phys. Rev.*, **B4**, 4144 (1971).
159. J. L. Stanford, *J. Opt. Soc. Am.*, **60**, 49 (1970).
160. J. L. Stanford, H. E. Bennett, J. M. Bennett, E. J. Ashley, and E. T. Arakawa, *Bull. Am. Phys. Soc.*, **13**, 989 (1968).
161. P. Dobberstein, A. Hampe, and G. Sauerbrey, *Bull. Am. Phys. Soc.*, **13**, 988 (1968); *Phys. Lett.*, **31A**, 328 (1970); **31A**, 307 (1970).
162. B. P. Feuerbacher and W. Steinmann, *Opt. Commun.*, **1**, 81 (1969).
163. D. Beaglehole and O. Hunderi, *Phys. Rev.*, **B2**, 309 (1970); **B2**, 321 (1970).

164. J. Brambring and H. Raether, *Phys. Rev. Lett.*, **15**, 882 (1965).
165. J. Bösenberg and H. Raether, *Phys. Rev. Lett.*, **18**, 397 (1967); J. Bösenberg, *Phys. Lett.*, **26A**, 74 (1967).
166. E. Kretschmann and H. Raether, *Z. Naturforsch.*, **22a**, 1623 (1967).
167. P. Dobberstein and G. Sauerbrey, *Phys. Lett.*, **31A**, 328 (1970).
168. P. Dobberstein, *Phys. Lett.*, **31A**, 307 (1970).
169. R. H. Ritchie, E. T. Arakawa, J. J. Cowan, and R. N. Hamm, *Phys. Rev. Lett.*, **21**, 1530 (1968).
170. N. Marshall, B. Fischer, and H. J. Queisser, *Phys. Rev. Lett.*, **27**, 95 (1971).
171. W. E. Anderson, R. W. Alexander, and R. J. Bell, *Phys. Rev. Lett.*, **27**, 1057 (1971).
172. J. G. Endriz and W. E. Spicer, *Phys. Rev.*, **B4**, 4159 (1971).
173. A. Otto, *Z. Phys.*, **216**, 398 (1968).
174. E. Kretschmann, *Z. Phys.*, **241**, 313 (1971); J. Schoenwald, E. Burnstein, and J. M. Elson, to be published; F. Abelès and T. Lopez-Rios, to be published.
175. T. Turbador, *Proc. Phys. Soc. (London)*, **73**, 40 (1959); *Opt. Acta*, **11**, 207 (1964).
176. N. J. Harrick, *Phys. Rev.*, **125**, 1165 (1962).
177. A. S. Barker, Jr., *Phys. Rev. Lett.*, **28**, 892 (1972).
178. N. Marschall and B. Fischer, *Phys. Rev. Lett.*, **28**, 811 (1972).
179. V. V. Bryskin, Yu. M. Gerbshtein, and D. N. Mirlin, *Sov. Phys. Solid State*, **13**, 1779 (1972); **14**, 453 (1972); *Phys. Status Solidi (b)*, **51**, 901 (1972).
180. E. D. Palik, R. Kaplan, R. Gammon, H. Kaplan, J. J. Quinn, and R. F. Wallis, *Phys. Lett.*, to be published.
181. R. Rupp, *Solid-State Commun.*, **8**, 1129 (1970); see also A. Otto, *Z. Angew. Phys.*, **22A**, 65 (1969).
182. B. Fischer and I. L. Tyler, "Studies of Surface Polaritons," Taormina Research Conference on the Structure of Matter, "Polaritons," October 2-6, 1972, Taormina, Italy.
183. J. Schoenwald, E. Burstein, and J. M. Elson, *Solid-State Commun.*, **12**, 185 (1973).
184. M. I. Kheifets, *Fiz. Tverd. Tela*, **7**, 3485 (1965) [*Sov. Phys. Solid State*, **7**, 2816 (1966)].
185. K. W. Chiu and J. J. Quinn, *Phys. Lett.*, **35A**, 469 (1971).
186. R. F. Wallis and J. J. Brion, *Solid-State Commun.*, **9**, 2099 (1971).
187. V. I. Pakhomov and K. N. Stepanov, *Zh. Tekh. Fiz.*, **37**, 1393 (1967) [*Sov. Phys. Tech. Phys.*, **12**, 1011 (1968)].
188. N. Z. Abdel-Shahid and V. I. Pakhomov, *Plasma Phys.*, **12**, 55 (1970).
189. K. W. Chiu and J. J. Quinn, *Nuovo Cimento*, **10B**, 1 (1972).
190. J. J. Brion, R. F. Wallis, A. Hartstein, and E. Burstein, *Phys. Rev. Lett.*, **28**, 1455 (1972).
191. A. Hartstein, E. Burstein, J. J. Brion, and R. F. Wallis, Taormina Research Conference on the Structure of Matter, Taormina, Italy, 1972; *Solid-State Commun.*, to be published.
192. K. W. Chiu and J. J. Quinn, Taormina Research Conference on the Structure of Matter, Taormina, Italy, 1972, p. 1456; R. F. Wallis, J. J. Brion, E. Burstein, and A. Hartstein, *Proceedings of the 11th International Conference on the Physics of Semiconductors*, PWN—Polish Scientific Publishers, Warsaw, 1972, p. 1448.
193. A. Hartstein, E. Burstein, A. A. Maradudin, R. Brewer, and R. F. Wallis, to be published.
194. V. V. Bryksin, D. N. Mirlin, and I. I. Reshina, *Zh. Eksp. Teor. Fiz. Pis. Red.*, **16**, 445 (1972) [*Sov. Phys. JETP Lett.*, **16**, 315 (1973)].
195. A. Harstein, E. Burstein, J. J. Brion, and R. F. Wallis, *Surf. Sci.*, **34**, 81 (1973) R. F. Wallis, J. J. Brion, E. Burstein, and A. Hartstein, to be published.
196. H. Falge and A. Otto, *Phys. Status Solidi*, **56**, 523 (1973).

197. R. Ruppin and R. Englman, *Rep. Prog. Phys.*, **33**, 149 (1970).
198. L. Genzel and T. P. Martin, *Surf. Sci.*, **34**, 33 (1973).
199. V. V. Bryskin, D. N. Mirlin, and I. I. Reshina, *Solid-State Commun.*, **9**, 669 (1971).
200. A. J. Hunt, T. R. Steyer, and D. R. Huffman, to be published.
201. K. H. Rieder, M. Ishigame, and L. Genzel, *Phys. Rev.*, **B6**, 3804 (1972).
202. J. F. Scott and T. C. Damen, *Opt. Commun.*, **5**, 410 (1972).
203. R. Ruppin, *Surf. Sci.*, **34**, 20 (1973).
204. A. C. Lind and J. M. Greenberg, *J. Appl. Phys.*, **37**, 3195 (1966).
205. R. Kälin, H. P. Baltes, and F. K. Kneubühl, *Solid-State Commun.*, **8**, 1495 (1970).
206. Y. Mizuno and Y. Ohmura, *J. Phys. Soc. Japan*, **22**, 445 (1967).
207. P. M. Platzman, *Comment on Solid-State Physics*, **6**, 8 (1973).
208. K. L. Kliewer and H. Raether, *Phys. Rev. Lett.*, **30**, 971 (1973).
209. Y. Ohmura and N. Matsudaira, *J. Phys. Soc. Japan*, **19**, 1355 (1964); **30**, 1300 (1971).
210. G. Piftis, A. Theodossiou, and K. Alexopoulos, *Phys. Lett.*, **27A**, 577 (1968); G. Piftis, *Phys. Rev.*, **B2**, 54 (1970).
211. T. Suzuki and A. Tanokuba, *J. Phys. Soc. Japan*, **29**, 972 (1970).
212. N. G. Alexandropoulos, *J. Phys. Soc. Japan*, **31**, 1790 (1971).
213. D. M. Miliotis, *Phys. Rev.*, **B3**, 701 (1971).
214. C. Koumelis and D. Leventouri, *Phys. Rev.*, **B7**, 181 (1973).
215. J. J. Chang and D. C. Langreth, to be published.
216. D. M. Newns, *Phys. Rev.*, **B1**, 3304 (1970).
217. H. B. G. Casimir, *Proc. Kon. Ned. Ak. Wet.*, **51**, 793 (1948).
218. N. G. Van Kampen, B. R. A. Nijboer, and K. Schram, *Phys. Lett.*, **26A**, 307 (1968).
219. E. Gerlach, *Phys. Rev.*, **B4**, 393 (1971).
220. E. M. Lifshitz, *Sov. Phys. JETP*, **2**, 73 (1956).
221. J. E. Dzyaloshinskii, E. M. Lifshitz, and L. P. Pitaevskii, *Sov. Phys. JETP*, **10**, 161 (1960).
222. J. Schmit and A. A. Lucas, *Solid-State Commun.*, **11**, 415 (1972); **11**, 419 (1972).
223. M. Jonson and G. Srinivasan, to appear in *Phys. Lett. A*.
224. P. J. Feibelman, *Phys. Rev. Lett.*, **30**, 975 (1973).
225. A. J. Bennett, *Phys. Rev.*, **B1**, 203 (1970).
226. P. J. Feibelman, *Phys. Rev.*, **38**, 220 (1971).
227. D. M. Newns, *J. Chem. Phys.*, **50**, 4572 (1969).
228. D. M. Newns, *Phys. Rev.*, **B1**, 3304 (1970).
229. P. J. Feibelman, *Phys. Rev.*, **176**, 551 (1968).
230. D. E. Beck, *Phys. Rev.*, **B4**, 1555 (1971).
231. D. E. Beck and V. Celli, *Phys. Rev.*, **B2**, 2955 (1970).
232. J. Harris and A. Griffin, *Can. J. Phys.*, **48**, 2592 (1970); *Phys. Lett.*, **34A**, 51 (1971).
233. P. A. Fedders, *Phys. Rev.*, **153**, 438 (1967).
234. D. E. Beck and V. Celli, *Phys. Rev. Lett.*, **28**, 1124 (1972).
235. N. D. Lang and W. Kohn, *Phys. Rev.*, **B1**, 4555 (1970); **B3**, 1215 (1971).
236. L. P. Kadanoff and G. Baym, *Quantum Statistical Mechanics*, Benjamin, New York, 1962.
237. A. L. Fetter and J. D. Walecka, *Quantum Theory of Many-Particle Systems*, McGraw-Hill, New York, 1971.
238. D. Pines, *The Many-Body Problem*, Benjamin, New York, 1962.
239. F. Flores and F. Garcia-Moliner, *Surf. Sci. (Netherlands)*, **24**, 61 (1971).

THEORY OF DYNAMICAL PROPERTIES OF DIELECTRIC SURFACES

K. L. KLIEWER AND R. FUCHS

*Ames Laboratory-USAEC and Department of Physics
 Iowa State University,
 Ames, Iowa*

CONTENTS

I.	Introduction	356
II.	Local Dielectric Continuum Theory for Cubic Crystals	362
	A. Planar Geometry	362
	1. Half-space	362
	2. Slab	371
	3. Radiative Surface Mode	380
	B. Sphere	387
	C. General Geometric Considerations	395
	D. Effects of Damping	404
	1. Half-space	406
	2. Slab	413
	3. Sphere	413
	E. Polar Semiconductors and Magnetic Field Effects	414
	F. Complex Crystals	428
III.	Local Dielectric Continuum Theory for Noncubic Crystals	430
IV.	Long-Wavelength Microscopic Theory	435
V.	Experimental Techniques and Results	435
	A. Optical Investigations	436
	1. Planar Geometry	436
	2. Small Particles	441
	3. Attenuated Total Reflection (ATR)	445
	B. Electron Scattering Investigations	447
VI.	Nonlocal Dielectric Theory	449
	A. Dielectric Function Theory	452
	B. Multiple-Wave Theories	460
	1. Metals and Ionic Crystals	460
	2. Insulators with Exciton States	463
VII.	Microscopic Lattice Dynamics: Introduction	465
VIII.	Microscopic Lattice Dynamics: Monatomic Crystals	467
	A. Slab	467
	1. Procedure and Vibrational Properties	469
	2. Thermal Effects	475

B. Small Particles	483
IX. Microscopic Lattice Dynamics: Ionic Crystals	487
A. Slab	488
1. Procedure and Vibrational Properties	488
2. Optical Properties	500
3. Effects of Retardation	503
4. Thermal Effects	504
B. Small Particles	505
X. Surface Reconstruction	509
A. Monatomic Crystals	509
B. Ionic Crystals	515
XI. Very Recent Developments	517
Acknowledgments	529
References and Notes	530

I. INTRODUCTION

The words "dynamical theory of dielectrics" immediately suggest a theory for the lattice vibrational (or phonon) properties of nonconducting crystals. These words, in connection with "surface," then imply a study of those lattice vibrations that arise from the presence of surfaces, and are, in some sense, concentrated about these surfaces. This is, indeed, the emphasis in the present article.

The expectation of most readers as regards a theory of lattice vibrations for nonconductors would be a microscopic description in which the dynamical properties of the atoms or ions are obtained by explicitly incorporating the interatomic interactions into either classical or quantum mechanical equations of motion which are then solved.¹ This technique is now used extensively in investigations of surface dynamical properties even though the calculations are formidable due to the fact that the translational invariance, which so significantly simplifies the calculations of bulk dynamical properties, is destroyed, totally or in part, by the presence of a surface. We shall discuss such calculations in detail below. However, much of our present understanding of the dynamical character of surfaces is based on quite another point of view. Suppose we consider a medium in which there occurs a surface vibrational excitation with which we can associate an effective dimension λ and an angular frequency² ω . This λ may be a wavelength or some other length which appropriately characterizes the scale of spatial variation. For

$$\lambda \gg d \quad (I.1)$$

where d is a mean interatomic spacing, the response of the medium to the excitation is essentially that of a continuum since, within the length λ , there exists a large number of atoms. At this point, several possible

continuum characterizations are possible; which is selected depends on the type of surface excitation of interest. If one considers the medium to be an elastic continuum describable in terms of an appropriate set of elastic constants, there occur excitations which are the surface analogue of acoustic phonons, the Rayleigh waves.³ Since the properties of these surface acoustic waves have been reviewed recently,⁴⁻⁶ we do not discuss them further here. We turn our attention rather to those lattice vibrations with which are associated significant long-range electromagnetic fields to which the system responds, in the long-wavelength or continuum limit, (1.1), in a fashion describable in terms of the macroscopic dielectric function $\epsilon(\omega)$.^{7,8} The classic examples of such lattice vibrations are the optical vibrational modes in a crystal with ionic character.⁹

The point of view which we are here proposing then is that of a long-wavelength theory of surface lattice dynamics based on $\epsilon(\omega)$, a theory that can be called a dielectric continuum theory. A major fraction of the experimental investigations of surface dynamical properties of dielectrics has dealt with the long-wavelength surface optical (SO) excitations in ionic crystals; this theory has proved very successful in describing the observations made to this time. Thus our detailed treatment of surface dynamical properties below begins with a discussion of this "local" theory. The significance of the appellation "local" and the limitations inherent within such a theory can be understood as follows. Suppose we consider, for simplicity, a bulk, homogeneous, isotropic system. We can then write the relation between the suitably averaged electric field $\mathbf{E}(\mathbf{r}, t)$ and displacement $\mathbf{D}(\mathbf{r}, t)$ as

$$\mathbf{D}(\mathbf{r}, t) = \int_{-\infty}^t dt' \int d^3r' \epsilon_{RA}(\mathbf{r} - \mathbf{r}', t - t') \mathbf{E}(\mathbf{r}', t') \quad (\text{I.2})$$

where $\epsilon_{RA}(\mathbf{r} - \mathbf{r}', t - t')$ is the real-space, real-time response function.¹⁰ Defining the response function $\epsilon_R(\mathbf{r} - \mathbf{r}', t - t')$,

$$\epsilon_R(\mathbf{r} - \mathbf{r}', t - t') = \begin{cases} \epsilon_{RA}(\mathbf{r} - \mathbf{r}', t - t'), & t' < t \\ 0, & t' > t \end{cases} \quad (\text{I.3})$$

and the Fourier transforms

$$\mathfrak{D}(\mathbf{k}, \omega) = \int d^3r \int dt \mathbf{D}(\mathbf{r}, t) e^{i\omega t} e^{-i\mathbf{k} \cdot \mathbf{r}} \quad (\text{I.4a})$$

$$\mathfrak{E}(\mathbf{k}, \omega) = \int d^3r \int dt \mathbf{E}(\mathbf{r}, t) e^{i\omega t} e^{-i\mathbf{k} \cdot \mathbf{r}} \quad (\text{I.4b})$$

$$\epsilon(\mathbf{k}, \omega) = \int d^3r \int dt \epsilon_R(\mathbf{r}, t) e^{i\omega t} e^{-i\mathbf{k} \cdot \mathbf{r}} \quad (\text{I.4c})$$

we find from (I.2)

$$\mathcal{D}(\mathbf{k}, \omega) = \epsilon(\mathbf{k}, \omega) \mathcal{E}(\mathbf{k}, \omega) \quad (\text{I.5})$$

The presence of \mathbf{k} in the dielectric function indicates that the displacement at point \mathbf{r} depends on the electric field over a region of space about \mathbf{r} , that is, the response of the medium is nonlocal or, as it is often stated, spatial dispersion has been included. We can, however, impose a local response requirement on the system by writing

$$\epsilon_R(\mathbf{r} - \mathbf{r}', t - t') = \delta(\mathbf{r} - \mathbf{r}') \epsilon'_R(t - t') \quad (\text{I.6})$$

where δ is the Dirac delta function, which leads to

$$\mathcal{D}(\mathbf{k}, \omega) = \epsilon(\omega) \mathcal{E}(\mathbf{k}, \omega) \quad (\text{I.7})$$

instead of (I.5). Since

$$\epsilon(\omega) = \lim_{\mathbf{k} \rightarrow 0} \epsilon(\mathbf{k}, \omega) \quad (\text{I.8})$$

with $|\mathbf{k}| = 2\pi/\lambda$, where λ is the wavelength, it is apparent that the local theory can only be valid in the long-wavelength regime. A comparison of (I.5) and (I.7) is somewhat disquieting, however, in that the long-wavelength limit leading to the local theory is taken in only part of (I.5). Thus the local theory is in fact rather peculiar and its range of validity can only be ascertained by a study of a nonlocal theory. These few remarks concerning the nonlocal concept have been included here to draw attention to the local-nonlocal relationship. We have only touched a corner of the vast and complex subject of nonlocal response, but we shall return to this subject later.

The formal local theory for surface excitations has been a subject of investigation since the first decade of this century.¹¹⁻¹³ The first developments of this theory in which the emphasis was essentially equivalent to the present attitudes concerning surface excitations, in particular as regards the role of a negative dielectric function, were made by Fano.^{14,15} He was concerned particularly with the surface excitations of the electron gas, excitations which at first glance seem to have little in common with the SO excitations of an ionic crystal. If one, however, recognizes that the oscillations of the negatively charged electrons against the uniform background positive charge of the electron gas model give rise to the same type of electromagnetic fields as those which result from the oscillations of the positive ions against the negative ions in the longitudinal optical mode of an ionic crystal, the possibility that equivalent theories would describe the two phenomena in the long-wavelength limit becomes reasonable. Indeed, the formal theory for the surface excitations of the electron gas, the surface plasmons, is identical, for long wavelengths, to that for the SO surface

excitations we are concerned with here. The work of Refs. 11 to 15 as well as subsequent studies by Ritchie¹⁶ and Stern and Ferrell,¹⁷ the latter two also of the electron gas, dealt with planar surfaces. The initial investigations of the SO modes for planar geometry were made by the authors.^{18,19}

Of interest also are the SO excitations which occur in small particles. Due to mathematical complications associated with the analysis of arbitrary shapes, these investigations have, for the most part, dealt with spheres.²⁰ The earliest work on the sphere problem was that of Mie²⁴ and Debye,²⁵ again in the first decade of this century, and their method has subsequently appeared in a number of textbooks.^{26,27} This technique, which includes the retardation of the Coulomb interaction, was used to calculate the SO excitation modes by the authors²⁸ following an investigation of this problem, in which retardation was neglected, by Englman and Ruppin.²⁹ It is interesting to note that the long-range nature of the fields associated with these SO modes leads to significant geometrical dependence, both in the character of the modes and the theoretical structure needed to describe them. This is particularly true when retardation is included.

Our procedure here is to discuss the local dielectric continuum theory for the SO modes of an ionic crystal in considerable detail, particularly for the important case of planar geometry, as these excitations are, in a real sense, the prototype surface excitations for a dielectric. This discussion is based on the real dielectric function

$$\epsilon(\omega) = \epsilon_{\infty} + \frac{\epsilon_0 - \epsilon_{\infty}}{\omega_{\text{TO}}^2 - \omega^2} \omega_{\text{TO}}^2 \quad (\text{I.9})$$

the single oscillator expression appropriate for diatomic crystals such as the alkali halides in the range of phonon frequencies.³⁰ Here ω_{TO} is the long-wavelength transverse optical phonon frequency and ϵ_{∞} and ϵ_0 are the values of $\epsilon(\omega)$ for $\omega \gg \omega_{\text{TO}}$ and $\omega \ll \omega_{\text{TO}}$, respectively. A sketch of this dielectric function is given in Fig. 1. The longitudinal optical frequency ω_{LO} is that frequency for which $\epsilon(\omega) = 0$ and is given in terms of the transverse optical frequency by the Lyddane-Sachs-Teller relation³¹

$$\omega_{\text{LO}}^2 = \frac{\epsilon_0}{\epsilon_{\infty}} \omega_{\text{TO}}^2 \quad (\text{I.10})$$

Utilizing this expression for ω_{LO}^2 , (I.9) can be written as

$$\epsilon(\omega) = \epsilon_{\infty} \frac{\omega_{\text{LO}}^2 - \omega^2}{\omega_{\text{TO}}^2 - \omega^2} \quad (\text{I.11})$$

Although the emphasis in our presentation of the local theory is on the

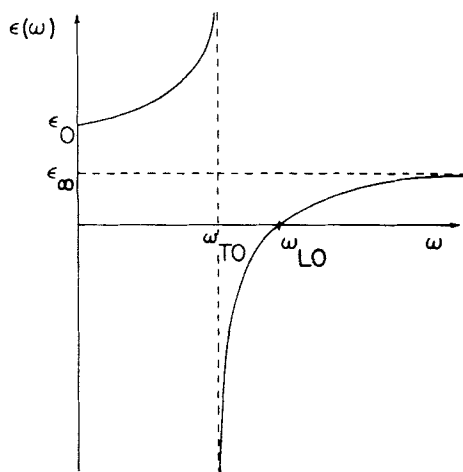


Fig. 1. The frequency-dependent dielectric function for a diatomic ionic crystal. This single-oscillator form is valid for cubic crystals that have a single "reststrahl" or long-wavelength, infrared-active, transverse optical phonon frequency ω_{TO} . The longitudinal optical frequency is denoted ω_{LO} . ϵ_0 , the value of $\epsilon(\omega)$ for $\omega \ll \omega_{TO}$, includes polarization contributions from both nuclear and electronic motion. ϵ_∞ , the value of $\epsilon(\omega)$ for $\omega \gg \omega_{TO}$, includes polarization contributions only from electronic motion. Hence, $\epsilon_0 > \epsilon_\infty$.

properties of ionic crystals, we are also interested in polar semiconductors describable by the dielectric function (I.9) and (I.11) or its generalized form valid if free carriers are present.

A discussion of the SO excitations for a sphere, also based on the dielectric function (I.9), is presented. In this case, there are in fact no genuine normal modes as there are for systems with planar surfaces. The reason for this is discussed as are those excitations which play essentially a normal mode role.

Throughout the presentation we use Gaussian units and refer to the dielectric medium whose surface excitations are of interest as the boundary-active medium. As will become clear below, the active medium will usually be one for which the dielectric function is, over some range of frequencies, negative. Other dielectrics in the problem are referred to as boundary-inactive media. It must here be emphasized that the properties of the boundary-inactive media usually have a pronounced effect on the surface excitations of the active medium. Indeed, the surface excitations of the active medium should really be thought of as boundary excitations which reflect the characteristics of all media that form the boundaries.

Generalizations of the theory to other geometries, to the case where $\epsilon(\omega)$ is complex portending losses in the active medium, to polar semiconductors including magnetic field effects, and to the case of noncubic crystals for which $\epsilon(\omega)$ is a tensor are then discussed. To this point the theory will be local and, as such, restricted to long wavelengths as discussed above. This means, of course, that the actual dynamics of the surface-region atoms must be inferred from the behavior of the electromagnetic fields as the atoms are only implicitly in the theory.

After presenting a collection of experimental results that point up the basic validity of the local description, we return to the theoretical development and eliminate the long-wavelength restriction. This can be accomplished through either a nonlocal dielectric theory or a fully microscopic atomic theory. Although the nonlocal theory is already well developed for the surface plasmons,³²⁻³⁷ such is not the case for the SO modes. To facilitate comparison of the surface plasmon theory with the SO excitation theory, we note that the real local dielectric function for the electron gas is

$$\epsilon(\omega) = 1 - \frac{\omega_p^2}{\omega^2} = \frac{\omega_p^2 - \omega^2}{-\omega^2} \quad (\text{I.12})$$

where ω_p is the plasma frequency. From (I.11) and (I.12) we can make the following formal correspondences: ω_{LO} for the ionic crystal corresponds to ω_p for the electron gas; ω_{TO} for the ionic crystal corresponds to $\omega = 0$ for the electron gas. Since the nonlocal theory for the SO mode problem is only in an early stage of development, our discussion of this theory is rather brief and directed as much toward the problems as the present conclusions.

In turning to the atomic dynamical theory, there exists a level of capability in describing surface phenomena not readily available in a nonlocal dielectric theory. For example, relaxation of surface atoms, actual surface reconstruction, and thermal effects can be readily incorporated. The price paid for this flexibility includes computational complexity and, frequently, results that are not easy to interpret. In addition, the results are often strongly model dependent with the essential parameters not readily identifiable. Our discussion of microscopic lattice dynamics is previewed in Section VII. It is worth noting here, however, that our preoccupation with polar crystals in the presentation of the local theory does not carry over into the sections dealing with the microscopic theory. Surface modes in monatomic crystals and nonpolar semiconductors as well as ionic crystals are discussed for both slabs and small particles.

II. LOCAL DIELECTRIC CONTINUUM THEORY FOR CUBIC CRYSTALS

Within this section we present the local theory of SO excitations for homogeneous isotropic systems or cubic crystals in contact, through sharp boundaries, with other dielectrics of these same types. Thus the dielectric function as well as the magnetic susceptibility for a given dielectric can be written as a single scalar function of the frequency. The generalization of the local theory to crystals of lower symmetry is given in Section III.

A. Planar Geometry^{1, 16, 18, 19, 38, 39}

The developments of Section II.A concern the surface properties of systems consisting of two or more dielectrics in contact through planar boundaries.

1. Half-space

We consider a half-space ($z > 0$) of a boundary-active medium in contact with a half-space ($z < 0$) of a boundary-inactive medium. The dielectric function and magnetic susceptibility of the former we write as $\epsilon(\omega)$ and $\mu(\omega)$; for the inactive medium we write the dielectric function as $\epsilon_I(\omega)$ and take $\mu = 1$. The geometry and notation are given in Fig. 2.

The question we then ask is, what type of electromagnetic field arrangement can such a system support? In particular, for the present

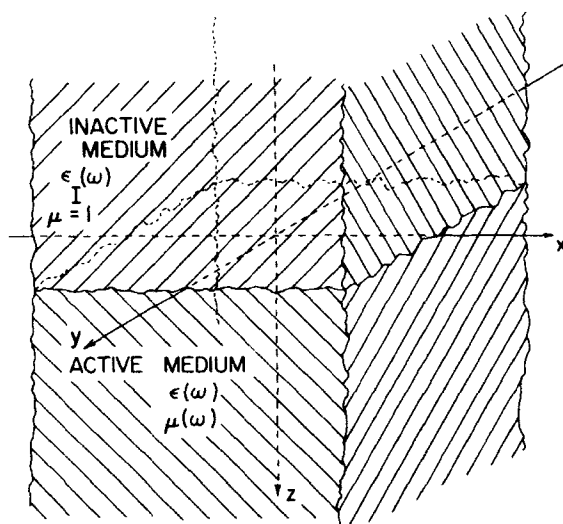


Fig. 2. Geometry and electromagnetic response functions for the analysis of the half-space problem.

purpose, we are interested in that field arrangement which is dependent on the fact that there is a surface present.

Suppose we have an electric field with components both perpendicular and parallel to the $z=0$ boundary of Fig. 2. We take these components as $E_z(x, z, t)$ and $E_x(x, z, t)$. Then, from Maxwell's equations with no external sources,

$$\nabla \cdot \mathbf{D} = 0 \quad (\text{II.1a})$$

$$\nabla \cdot \mathbf{B} = 0 \quad (\text{II.1b})$$

$$\nabla \times \mathbf{E} = -\frac{1}{c} \frac{\partial \mathbf{B}}{\partial t} \quad (\text{II.1c})$$

and

$$\nabla \times \mathbf{H} = \frac{1}{c} \frac{\partial \mathbf{D}}{\partial t} \quad (\text{II.1d})$$

where c is the speed of light in vacuum, there must be a magnetic induction component $B_y(x, z, t)$.⁴⁰ This general field arrangement will be referred to as p -polarized as it is analogous to the p -polarized field orientation of ordinary optical investigations. It should be noted that, in contrast to, say, a calculation of the reflectance for the system of Fig. 2, we are here not dealing explicitly with a source for these fields. Rather, our procedure is to assume that such a p -polarized field arrangement can exist and assess the consequences.

Since we have translational invariance in the x direction, we can make a Fourier transform in this direction (with Fourier transform variable k) as well as in time (with Fourier transform variable ω) and so write all field components in the form

$$E_x(x, z, t) = \mathcal{E}_x(z) e^{ikx} e^{-i\omega t} \quad (\text{II.2})$$

where script letters are used to denote the z -dependent factors in the Fourier transformed field components. From (II.1c) and (II.1d) we then have

$$\frac{d\mathcal{B}_y}{dz} = \frac{i\omega\epsilon\mu}{c} \mathcal{E}_x \quad (\text{II.3a})$$

$$k\mathcal{B}_y = -\frac{\omega\mu\epsilon}{c} \mathcal{E}_z \quad (\text{II.3b})$$

and

$$\frac{d\mathcal{E}_x}{dz} - ik\mathcal{E}_z = i\frac{\omega}{c} \mathcal{B}_y \quad (\text{II.3c})$$

where we have used

$$\mathfrak{D} = \epsilon \mathfrak{E} \quad (\text{II.4a})$$

and

$$\mathfrak{B} = \mu \mathfrak{H} \quad (\text{II.4b})$$

Differentiating (II.3c) with respect to z and using (II.3a) and (II.3b), we find

$$\frac{d^2 \mathfrak{E}_x}{dz^2} - \alpha^2 \mathfrak{E}_x = 0 \quad (\text{II.5})$$

where

$$\alpha^2 \equiv k^2 - \epsilon \mu \left(\frac{\omega}{c} \right)^2 \quad (\text{II.6})$$

Equations (II.5) and (II.6), with ϵ and μ chosen appropriately, are valid for both half-spaces of Fig. 2. In general, for a lossy dielectric, both ϵ and μ will be complex. However, to avoid unnecessary complications at this early stage in our development, let us consider here that these quantities are real.

Consider first the boundary-active medium ($z > 0$). Clearly the solution of (II.5) depends crucially on the sign of α^2 . We assume now that $\alpha^2 > 0$ and $\alpha > 0$.⁴¹ Then, from (II.5) and (II.3), the physically valid solution for the field components is

$$\mathfrak{E}_x(z) = K e^{-\alpha z} \quad (\text{II.7a})$$

$$\mathfrak{E}_z(z) = \frac{ik}{\alpha} K e^{-\alpha z} \quad (\text{II.7b})$$

and

$$\mathfrak{B}_y(z) = -i \frac{\omega}{c} \frac{\mu \epsilon}{\alpha} K e^{-\alpha z} \quad (\text{II.7c})$$

with K an integration constant. Thus we see that the fields decay exponentially from the surface into the medium, indicating that this solution arises as a consequence of the presence of the boundary.

For the inactive medium ($z < 0$), (II.6) is valid if we replace ϵ by ϵ_I and μ by 1. Defining α_I^2 by

$$\alpha_I^2 = k^2 - \epsilon_I \left(\frac{\omega}{c} \right)^2 \quad (\text{II.8})$$

and assuming $\alpha_1^2 > 0$ and $\alpha_1 > 0$, the field components in the boundary-inactive medium are given by

$$\mathcal{E}_x(z) = K' e^{\alpha_1 z} \quad (\text{II.9a})$$

$$\mathcal{E}_z(z) = -\frac{ik}{\alpha_1} K' e^{\alpha_1 z} \quad (\text{II.9b})$$

and

$$\mathcal{B}_y(z) = i \frac{\omega}{c} \frac{\epsilon_I}{\alpha_1} K' e^{\alpha_1 z} \quad (\text{II.9c})$$

with K' the integration constant. Thus the fields in the boundary-inactive medium also decay exponentially from the surface.

From the boundary conditions at the plane $z=0$, \mathcal{E}_x , \mathcal{D}_z , and \mathcal{H}_y continuous, or, equivalently, the continuity of the surface impedance Z which we define here by

$$Z = E_x / H_y \quad (\text{II.10})$$

we find that $K = K'$ and

$$\epsilon = -\frac{\alpha}{\alpha_I} \epsilon_I \quad (\text{II.11})$$

Note that the negative sign in (II.11) appears as a consequence of the exponential decay of the fields in both directions from the surface. After squaring, (II.11) can be rewritten as

$$\frac{\epsilon \epsilon_I (\epsilon - \mu \epsilon_I)}{(\epsilon - \epsilon_I)(\epsilon + \epsilon_I)} = \frac{k^2}{(\omega/c)^2} \quad (\text{II.12})$$

In order that the field arrangement specified by (II.7) and (II.9) can exist, (II.11) and (II.12) must be satisfied. Thus these latter equations specify the eigenvalues with which the eigenfunctions (II.7) and (II.9) are associated. In alternative language, (II.11) and (II.12) specify the dispersion relation $\omega(k)$ of a normal mode of the system. Note that the wave vector involved in this dispersion relation is restricted to a plane parallel to the surface and does not have three-dimensional character.

Although potentially interesting effects could arise from the presence of μ in (II.12), let us specialize now to the usual situation where $\mu = 1$, so (II.12) becomes

$$\frac{\epsilon \epsilon_I}{\epsilon + \epsilon_I} = \frac{k^2}{(\omega/c)^2} \quad (\text{II.13a})$$

or

$$\frac{1}{\epsilon} + \frac{1}{\epsilon_I} = \frac{\omega^2}{c^2 k^2} \quad (\text{II.13b})$$

It is then possible to say a number of things about the character of this normal mode without specifying the functional form of the dielectric functions.

In most cases of interest, the boundary-inactive medium will be chosen so $\epsilon_I > 0$. Then, from (II.11) and our assumptions concerning α and α_I , the normal mode occurs for frequencies such that $\epsilon(\omega) < 0$. It then follows directly that $\epsilon(\omega) < -\epsilon_I$. From (II.13b), we can also see that for $k^2 \gg \omega^2/c^2$, that is, k much larger than the wave vector of a photon of frequency ω , the normal mode frequency is that for which $\epsilon \rightarrow -\epsilon_I$. As is clear physically, this limit is the equivalent of the no-retardation limit, $c \rightarrow \infty$.⁴² If the inactive medium is a vacuum, the normal mode occurs for frequencies such that $\epsilon < -1$ and, for large k , the normal mode frequency is that for which $\epsilon(\omega) = -1$.

We can also at this point discuss the electric field associated with this normal mode. Although the development above was written in a complex notation, we now take the real parts of the complex fields as the physical fields. Keeping the phase factor of (II.2) in mind, we find for the boundary-active medium

$$E_x = e^{-\alpha z} \cos(kx - \omega t) \quad (\text{II.14a})$$

and

$$E_z = -\frac{k}{\alpha} e^{-\alpha z} \sin(kx - \omega t) \quad (\text{II.14b})$$

while in the boundary-inactive medium

$$E_x = e^{\alpha_I z} \cos(kx - \omega t) \quad (\text{II.15a})$$

and

$$E_z = \frac{k}{\alpha_I} e^{\alpha_I z} \sin(kx - \omega t) \quad (\text{II.15b})$$

where we have put the scale factor $K = K' = 1$.⁴³ The electric field within either medium is, of course, transverse and thus satisfies $\nabla \cdot \mathbf{E} = 0$. It should also be noted, however, that for $k \gg \omega/c$, these fields also satisfy the condition $\nabla \times \mathbf{E} \approx 0$. In the no-retardation limit the curl is exactly zero, as it must be from (II.1c), and the fields are electrostatic in character ($\mathbf{B} \equiv 0$). This is approximately true with retardation for $k \gg \omega/c$.

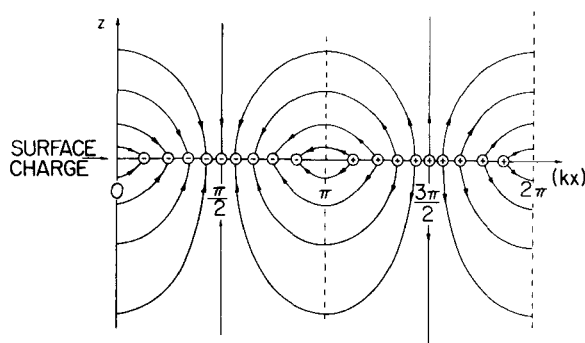


Fig. 3. A sketch of the normal mode electric field for times such that $\omega t = 2\pi n$, where n is an integer. Also shown is the sign of the surface charge with the density of + or - signs indicating roughly the magnitude of the corresponding surface charge density. Note that the product (kx) is plotted along the abscissa.

A sketch of the fields of (II.14) and (II.15) is given in Fig. 3. This electric field arrangement is associated with an induced surface charge density σ proportional to the difference of (II.14b) and (II.15b). Thus,

$$\sigma \propto - \left(\frac{k}{\alpha} + \frac{k}{\alpha_I} \right) \sin(kx - \omega t) \quad (\text{II.16})$$

The normal mode which has emerged from this analysis possesses the following three important characteristics: (1) it is a wave which travels parallel to the surface; (2) it is associated with a surface charge; and (3) the electromagnetic fields of this mode decay exponentially from the surface. Thus this normal mode is appropriately identified as a surface mode and is subsequently so called.

In order to calculate the actual dispersion relation from (II.13), it is necessary to specify the dielectric functions of both the active and the inactive medium. As we are interested here in SO modes, we choose for $\epsilon(\omega)$ of the active medium the single oscillator expression (I.9) appropriate for a diatomic ionic crystal. From Fig. 1, it is apparent that this dielectric function can satisfy the requirements enumerated above for the appearance of the surface mode. In particular, for the usual case of $\epsilon_I > 0$, the requirement that $\epsilon(\omega) < 0$ is satisfied for $\omega_{\text{TO}} < \omega < \omega_{\text{LO}}$.

Expression (I.9) for the dielectric function can be combined with (II.13b) to obtain an analytical expression for the dispersion curve.⁴⁴ Defining

$$\omega_k^2 = c^2 k^2 \left(\frac{1}{\epsilon_\infty} + \frac{1}{\epsilon_I} \right) \quad (\text{II.17})$$

and

$$\omega_{s\infty}^2 = \frac{\epsilon_\infty \omega_{LO}^2 + \epsilon_I \omega_{TO}^2}{\epsilon_\infty + \epsilon_I} = \omega_{TO}^2 \frac{\epsilon_0 + \epsilon_I}{\epsilon_\infty + \epsilon_I} \quad (\text{II.18})$$

where $\omega_{s\infty}$ is the frequency for which $\epsilon(\omega) + \epsilon_I = 0$ or the frequency of the surface mode in the limit of large k , the result is

$$\omega^2 = \frac{(\omega_k^2 + \omega_{LO}^2)}{2} - \frac{1}{2} \left[(\omega_k^2 + \omega_{LO}^2)^2 - 4\omega_k^2 \omega_{s\infty}^2 \right]^{1/2} \quad (\text{II.19})$$

This dispersion curve starts at $\omega = 0$ for $k = 0$ and increases monotonically to the asymptotic limit $\omega_{s\infty}$ as $k \rightarrow \infty$. However, we saw above that the surface mode occurs only when $\alpha_I > 0$ and $\epsilon < -\epsilon_I$. For positive ϵ_I , this means that (II.19) is a legitimate solution only for $k^2 \geq \epsilon_I (\omega_{TO}/c)^2$. When $k^2 = \epsilon_I (\omega_{TO}/c)^2$, $\omega = \omega_{TO}$.

In Fig. 4 the dispersion relation is shown for $\epsilon_I = 1$ corresponding to vacuum and $\epsilon_0 = 9.27$, $\epsilon_\infty = 1.92$, and $\omega_{TO} = 5.78 \times 10^{13} \text{ sec}^{-1}$, values appropriate for LiF.⁴⁵ For large k , the asymptotic frequency is ω/ω_{TO}

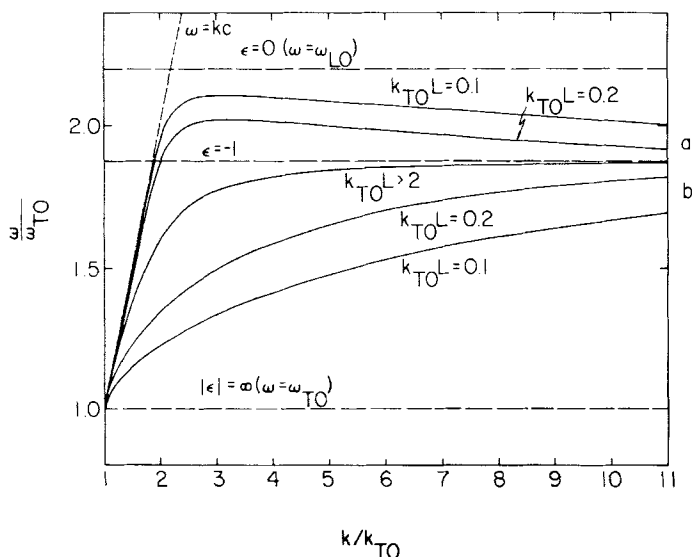


Fig. 4. The frequencies of the surface polariton modes for a LiF slab in vacuum as a function of k/k_{TO} , with $k_{TO} = \omega_{TO}/c$. Slab thickness is expressed by the dimensionless quantity $k_{TO}L$, with L the film thickness. The single curve marked $k_{TO}L > 2$ is that for the half-space discussed above. The other curves, which apply to a slab of finite thickness, occur in pairs: curves (a) are the ω_+ modes, and curves (b) are the ω_- modes, where ω_+ and ω_- are defined in Sec. II.A.2.

$= 1.88$, for which $\epsilon(\omega) = -1$. At small k , as follows from the comments just given, the dispersion curve terminates on the light line ($\omega = ck$) at the frequency $\omega = \omega_{\text{TO}}$.

For large k , $k \gg \omega_{\text{TO}}/c$, we see from (II.6) and (II.8) that $\alpha \cong \alpha_l \cong k$. Thus the electromagnetic fields and the ionic motion associated with the surface polariton⁴² penetrate the crystal only to a depth of order $\alpha^{-1} \cong k^{-1}$. Here it must be kept in mind that the present theory is valid only if $d \ll \alpha^{-1}$ where d is the interionic spacing. The surface polariton frequency has essentially reached its asymptotic value for $k \sim 5k_{\text{TO}}$ where k_{TO} is defined by

$$k_{\text{TO}} = \frac{\omega_{\text{TO}}}{c} \quad (\text{II.20})$$

The value of $5k_{\text{TO}}$ for LiF is about 10^{-4} \AA^{-1} so the conditions for the validity of the local theory are here well satisfied. As k decreases from the asymptotic region, the depth of penetration of the fields, and hence of the ionic motion, increases roughly until the dispersion curve turns rather sharply downward where $k \sim 2k_{\text{TO}}$. The maximum penetration depth $(\alpha^{-1})_{\text{max}}$ thus satisfies

$$(\alpha^{-1})_{\text{max}} \sim (2k_{\text{TO}})^{-1} \quad (\text{II.21})$$

As k decreases from $k \sim 2k_{\text{TO}}$ the penetration decreases rapidly and, as the termination point is approached, $\alpha^{-1} \rightarrow 0$. Thus the polariton is strongly localized at the surface for large k and near the low- k termination point but less so for intermediate values of k . This fact is illustrated in Fig. 5 which shows α^{-1} as a function of k for LiF. Note, however, that α_l^{-1} increases monotonically with decreasing k and becomes infinite at the low- k termination point.

The fashion in which the surface polariton transports energy^{46,47} is rather interesting. The time-averaged Poynting vector

$$\mathbf{S} = \frac{c}{8\pi} \text{Re}(\mathbf{E} \times \mathbf{H}^*) \quad (\text{II.22})$$

has only a component $-(c/8\pi)\mathcal{E}_z \mathcal{H}_y^*$ in the x direction when ϵ and μ are real. Evaluating this and then integrating over z to obtain the time-averaged energy transported in the x direction per unit length in the y direction (see Fig. 2), we find for the active medium

$$\int_0^\infty (S_x)_{\text{act}} dz = \frac{k\omega\epsilon}{16\pi\alpha^3} \quad (\text{II.23a})$$

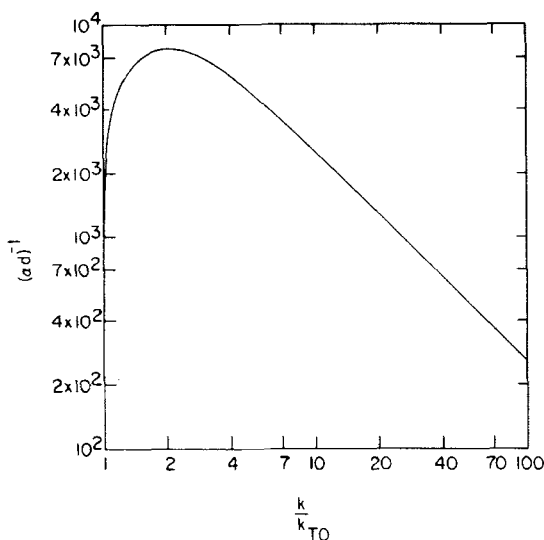


Fig. 5. The penetration depth α^{-1} of the electromagnetic fields associated with the surface polariton for a LiF half-space in vacuum as a function of k/k_{TO} . The penetration depth is defined by the $1/e$ values and is given divided by the anion-cation separation $d=2.01$ Å. For the theory to be valid, $(\alpha d)^{-1} \gg 1$.

and for the inactive medium

$$\int_{-\infty}^0 (S_x)_{\text{inact}} dz = \frac{k\omega\epsilon_I}{16\pi\alpha_I^3} \quad (\text{II.23b})$$

For $\epsilon_I > 0$, we see that the energy transport in the inactive medium is in the $+x$ direction (the direction of propagation) while in the active medium the energy transport is in the $-x$ direction since $\epsilon < 0$. The sum of (II.23a) and (II.23b)

$$\frac{k\omega}{16\pi} \frac{\epsilon_I}{\alpha_I^3} \left\{ 1 - \frac{\alpha_I^2}{\alpha^2} \right\} \quad (\text{II.23c})$$

where we have used (II.11), is, however, positive, indicating net energy transfer in the direction of propagation.

We have then seen that for the usual type of boundary-inactive medium and a boundary-active medium with $\mu=1$, there occurs an SO polariton with p -polarized or transverse magnetic (TM) character. The question then naturally arises as to whether there could occur a surface polariton

associated with the field components B_x , B_z , and E_y , that is, an s -polarized or transverse electric (TE) surface mode. As is clear from the above, the existence of the p -polarized SO mode depends in a vital way on the fact that most ions move with a velocity component normal to the surface so that a spatially oscillatory surface charge results giving rise to the electric field of Fig. 3. Ion motion strictly parallel to the surface will not result in a surface charge and thus cannot produce a long-range dipolar electric field on both sides of the surface. Within the continuum theory, then, there can be no s -polarized SO excitations for systems in which the microscopic character of the optical excitations is electric dipole.

Systems for which the magnetic permeability is of the oscillator form in a range of frequencies over which the dielectric function is more or less constant will behave in the opposite way. The analysis given above can be immediately transcribed to this situation by the interchange⁴⁸ $\epsilon \leftrightarrow \mu$, $\mathbf{D} \leftrightarrow \mathbf{B}$, and $\mathbf{E} \leftrightarrow \mathbf{H}$. Thus, when the microscopic optical excitations have magnetic dipole character the SO excitations will be magnons and the associated electromagnetic field structure will be s -polarized or TE.⁴⁹

2. Slab

A physical picture of the effect of a finite active medium thickness on the surface polariton discussed above can easily be obtained. From (II.21), it is clear that if the film thickness L satisfies

$$L \gtrsim 2(\alpha^{-1})_{\max} \sim \frac{1}{k_{\text{TO}}} \quad (\text{II.24})$$

both surfaces can support such a polariton, and the presence of the second surface has no effect on a polariton propagating along the original surface. Thus a film of thickness $k_{\text{TO}}L \gtrsim 1$ is effectively of infinite thickness insofar as the surface polariton is concerned.

Suppose we have a film such that $k_{\text{TO}}L < 1$. In Fig. 6a we show part of the electric field sketch (Fig. 3) for a semiinfinite medium. The direction of the arrows indicates a particular choice for the sign of the amplitude factor K in (II.7). A corresponding sketch for a second half-space appears in Fig. 6b with the sign of the associated amplitude factor unspecified. Note that the location of the field pattern along x for the two half-spaces is determined by the phase factor $\exp\{i(kx - \omega t)\}$ and, for the same choice of the origins of x and t , the sketches are valid as shown. A rough representation of the field corresponding to a film of thickness L can then be obtained by superposing Figs. 6a and 6b. The superposed fields are given in Fig. 6c and the resultant field in Fig. 6e for the case where the amplitude factors for the two surfaces are of the same sign, that is, the

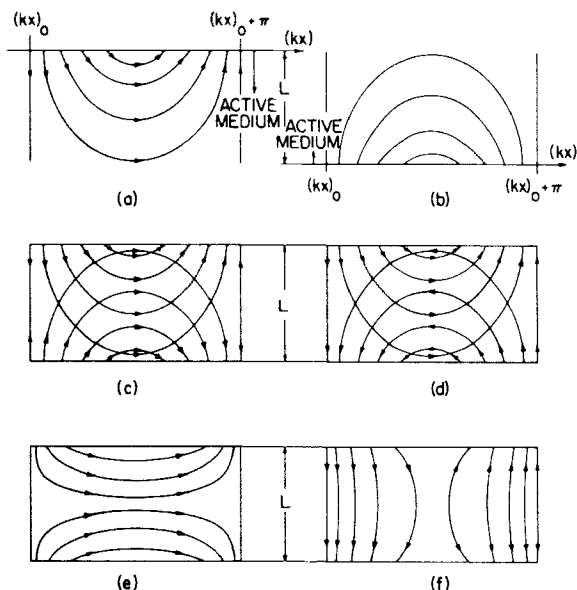


Fig. 6. A physical representation of the surface polariton electric fields within a thin slab (thickness L such that $k_{T0}L \lesssim 1$) as obtained from the fields for the surface polariton in a half-space. (a) Electric field of the half-space from Fig. 3 with the sign of the amplitude factor specified by the arrows. (b) Half-space electric field with the sign of the amplitude factor unspecified. (c) Superposition of the fields of (a) and (b) with the amplitude factors of the same sign. (d) Superposition of the fields of (a) and (b) with amplitude factors of the opposite sign. (e) Resultant field from (c). (f) Resultant field from (d).

electric field components parallel to the surfaces are in the same direction. When the amplitude factors have the opposite sign the corresponding figures are 6d and 6f.⁵⁰ Thus, for a given k , there will in general be two surface polaritons as a result of the interaction of the fields from the two surfaces.

On the basis of Fig. 6 and the considerations of the preceding section, we can draw several conclusions concerning the surface polaritons for a thin film. The polariton of Fig. 6e, for which the electric field and, thus, the polarization is predominantly parallel to the surface, will have a frequency lower than that of the half-space polariton for the same k . (We will call the frequency of this mode ω_- .) This follows from the fact that the fields in the film superpose in such a way that the surface charge, which provides the driving force for the oscillation, is reduced from the corresponding half-space case. In contrast, the polariton of Fig. 6f, with polarization essentially perpendicular to the surface, has a surface charge larger in

magnitude than the corresponding half-space case and thus a higher frequency. (We will call the frequency of this mode ω_+ .) As k increases to values such that $kL \gg 1$, the surface polaritons become highly localized at the surfaces, the fields from the two surfaces no longer overlap, and the polariton frequencies will become those of the associated half-space problems. There will now be, however, two distinct surface mode frequencies in the large- k limit if the inactive media on the two sides of the active film have different dielectric functions. Since the low- k termination point of the polariton corresponds to strong localization at the surface, the polariton frequencies for these values of k must approach the corresponding half-space frequencies. For different inactive media on the two sides of the film, there will, of course, be two distinct termination points, both with $\omega = \omega_{TO}$.

Consider the geometry and notation indicated in Fig. 7 where the possibility of different inactive media on the two sides of the film has been included. The conclusions of the previous paragraph are then sketched in Fig. 8.

We now develop the analytical counterpart of the representations of Fig. 8. To do so, we refer to Fig. 7. Within the active medium $|z| < a$, we have, from (II.3) and (II.5),

$$\mathcal{E}_x(z) = e^{-\alpha z} + Ke^{\alpha z} \quad (\text{II.25a})$$

and

$$\mathcal{E}_z(z) = -i \frac{k}{\alpha} \{ -e^{-\alpha z} + Ke^{\alpha z} \} \quad (\text{II.25b})$$

with α given by (II.6). For $z < -a$, the field components are

$$\mathcal{E}_x(z) = K' e^{\alpha_{Id} z} \quad (\text{II.26a})$$

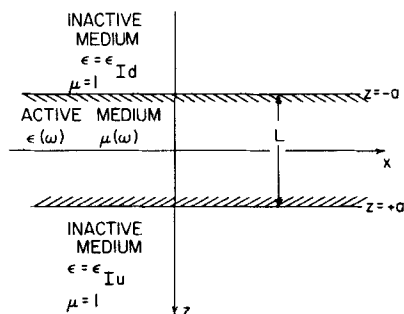


Fig. 7. The geometry and notation for the analysis of the slab problem.

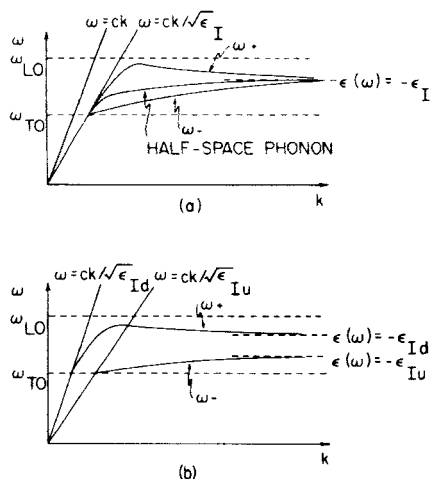


Fig. 8. A sketch of the surface polariton frequencies ω_{\pm} for a slab of thickness such that $k_{TO}L \lesssim 1$. (a) $\epsilon_{Iu} = \epsilon_{Id} = \epsilon_I > 1$. (b) $\epsilon_{Iu} > \epsilon_{Id} > 1$.

and

$$\mathfrak{E}_z(z) = -i \frac{k}{\alpha_{Id}} K' e^{\alpha_{Id} z} \quad (\text{II.26b})$$

with

$$\alpha_{Id}^2 = k^2 - \frac{\epsilon_{Id} \omega^2}{c^2} \quad (\text{II.27})$$

while for $z > a$ we have

$$\mathfrak{E}_x(z) = K'' e^{-\alpha_{Iu} z} \quad (\text{II.28a})$$

and

$$\mathfrak{E}_z(z) = \frac{ik}{\alpha_{Iu}} K'' e^{-\alpha_{Iu} z} \quad (\text{II.28b})$$

with

$$\alpha_{Iu}^2 = k^2 - \frac{\epsilon_{Iu} \omega^2}{c^2} \quad (\text{II.29})$$

K , K' , and K'' are integration constants and α , α_{Iu} , and α_{Id} are all assumed to be positive quantities.⁴¹ Defining

$$S = \frac{\epsilon}{\alpha}, \quad S_u = \frac{\epsilon_{Iu}}{\alpha_{Iu}}, \quad \text{and} \quad S_d = \frac{\epsilon_{Id}}{\alpha_{Id}} \quad (\text{II.30})$$

the equations resulting from the continuity of \mathcal{E}_x and \mathcal{D}_z at $z = \pm a$ are

$$e^{\alpha a} + Ke^{-\alpha a} = K'e^{-\alpha_{Id}a} \quad (\text{II.31})$$

$$S \{ -e^{\alpha a} + Ke^{-\alpha a} \} = S_d K' e^{-\alpha_{Id}a} \quad (\text{II.32})$$

$$e^{-\alpha a} + Ke^{\alpha a} = K''e^{-\alpha_{Iu}a} \quad (\text{II.33})$$

and

$$-S \{ -e^{-\alpha a} + Ke^{\alpha a} \} = S_u K'' e^{-\alpha_{Iu}a} \quad (\text{II.34})$$

Eliminating K' from (II.31) and (II.32), we find for K

$$K = e^{-2\alpha a} \left\{ \frac{S - S_u}{S + S_u} \right\} \quad (\text{II.35a})$$

while the elimination of K'' from (II.33) and (II.34) leads to

$$K = e^{2\alpha a} \left\{ \frac{S + S_d}{S - S_d} \right\} \quad (\text{II.35b})$$

Equating the right-hand sides of (II.35) gives the equation for the dispersion curves of the surface modes. This equation can be solved for S with the result that

$$S_{\pm} = \frac{(S_u + S_d)(e^{-2\alpha a} + e^{2\alpha a}) \mp [(S_u - S_d)^2(e^{-2\alpha a} + e^{2\alpha a})^2 + 16S_u S_d]^{1/2}}{2(e^{-2\alpha a} - e^{2\alpha a})} \quad (\text{II.36})$$

Although (II.36) is complicated, we can nonetheless demonstrate the validity of the principal features of Fig. 8b. Consider $\alpha a \rightarrow \infty$ and $\epsilon_{Iu} > \epsilon_{Id} \geq 1$. Then

$$S_- = -S_u \quad (\text{II.37a})$$

or

$$\left(\frac{\epsilon}{\alpha} \right)_- = -\frac{\epsilon_{Iu}}{\alpha_{Iu}} \quad (\text{II.37b})$$

while

$$S_+ = -S_d \quad (\text{II.38a})$$

or

$$\left(\frac{\epsilon}{\alpha} \right)_+ = -\frac{\epsilon_{Id}}{\alpha_{Id}} \quad (\text{II.38b})$$

For large k , where $\alpha \cong \alpha_{Iu} \cong k$, (II.37b) is just $\epsilon = -\epsilon_{Iu}$ and we obtain the asymptotic frequency for ω_- of Fig. 8b. Thus the dispersion curve associated with S_- is ω_- . Similarly, for large k , the equation resulting from the solution S_+ is $\epsilon \cong -\epsilon_{Id}$ and we obtain the asymptotic frequency of the ω_+ mode.

This limit $\alpha a \rightarrow \infty$, with a fixed, occurs not only for large k , but also near the low- k termination points where $\omega \rightarrow \omega_{TO}$ and $\epsilon \rightarrow -\infty$. From (II.37b) we see that the termination point for the ω_- mode is

$$\alpha_{Iu}|_{\omega=\omega_{TO}}=0 \quad \text{or} \quad k = \frac{\omega_{TO}\sqrt{\epsilon_{Iu}}}{c}$$

while from (II.38b) the termination point for the ω_+ mode is

$$\alpha_{Id}|_{\omega=\omega_{TO}}=0 \quad \text{or} \quad k = \frac{\omega_{TO}\sqrt{\epsilon_{Id}}}{c}$$

These are the limits shown in Fig. 8b.

Finally, we must demonstrate that the frequency ω_+ rises above that of the asymptotic limit while that of ω_- stays below. This is most easily accomplished by considering a very thin film and intermediate values of k so that α is well behaved and we can examine the $\alpha a \rightarrow 0$ limit of (II.36). We find

$$\lim_{\alpha a \rightarrow 0} S_- = -\frac{S_u + S_d}{2\alpha a} + O(\alpha a) \quad (\text{II.39a})$$

and

$$\lim_{\alpha a \rightarrow 0} S_+ = -\frac{\alpha a}{4} \left[\frac{2(S_u + S_d)^2 - (S_u - S_d)^2}{(S_u + S_d)} \right] \quad (\text{II.39b})$$

Since S_u and S_d are here positive, we see from (II.39a) that S_- is a large negative number which means that

$$\omega_- \gtrsim \omega_{TO} \quad (\text{II.40a})$$

a frequency below the asymptotic frequency for the ω_- mode. From (II.39b) we see that S_+ is a small negative number so

$$\omega_+ \lesssim \omega_{LO} \quad (\text{II.40b})$$

a frequency above the asymptotic limit for the ω_+ mode. Thus the validity of the general features shown in Fig. 8b is established.

It is interesting to note that for a thin film and k values such that $aa \ll 1$, the ω_+ mode occurs essentially at the longitudinal optical frequency while the ω_- mode occurs essentially at the transverse optical frequency. These conclusions could have been obtained, more or less directly, from Figs. 6e and 6f.

To simplify the subsequent analysis, we now consider the symmetric case $\epsilon_{lu} = \epsilon_{ld} = \epsilon_l$. Equation (II.36) then simplifies to

$$\left(\frac{\epsilon}{\alpha}\right)_{\pm} = \frac{\epsilon_l}{\alpha_l} \left(\frac{e^{-aa} \mp e^{aa}}{e^{-aa} \pm e^{aa}} \right) \quad (\text{II.41})$$

where we have used the S definitions of (II.30). The corresponding values of K are⁵⁰

$$K_{\pm} = \mp 1 \quad (\text{II.42})$$

and so, from (II.25), the electric field components in the active medium are

$$(\mathcal{E}_x)_{\pm} = e^{-az} \mp e^{az} = 2 \begin{cases} -\sinh az \\ +\cosh az \end{cases} \quad (\text{II.43a})$$

and

$$(\mathcal{E}_z)_{\pm} = + \frac{ik}{\alpha} \{ e^{-az} \pm e^{az} \} = \frac{2ik}{\alpha} \begin{cases} +\cosh az \\ -\sinh az \end{cases} \quad (\text{II.43b})$$

In (II.41) to (II.43), the upper sign or expression is associated with the ω_+ mode and the lower sign with the ω_- mode.

The dispersion curves resulting from (II.41) for LiF and $\epsilon_f = 1$ are shown in Fig. 4 for various film thicknesses. These SO modes are frequently referred to as the Fuchs-Kliwer (FK) modes.

As we noted above, a film of thickness L such that $k_{TO}L \gg 1$ is effectively an infinite crystal, and the properties of the FK modes follow from the results of Section II.A.1. Let us now consider the case of $k_{TO}L \ll 1$. Then, in the large- k limit, $kL \gg 1$, where both polaritons occur at the frequency for which $\epsilon(\omega) = -\epsilon_f$, the electric field is strongly localized at the surfaces, and the magnitudes of the electric field components parallel and perpendicular to the surface are equal [see (II.43)]. For smaller values of k where $\alpha L \ll 1$, the ω_+ mode is associated with $\mathcal{E}_x(z) \sim 0$ and $\mathcal{E}_z(z) \sim \text{Const.}$ while the field components associated with the ω_- mode satisfy $\mathcal{E}_x(z) \sim \text{Const.}$ and $\mathcal{E}_z(z) \sim 0$. In this range of wave vectors, then, ω_- is associated with polarization parallel to the surface and ω_+ with polariza-

tion perpendicular to the surface. However, near the small- k termination point (now common to both modes) the electric field is again highly concentrated near the surface and, in addition, $|\mathcal{E}_z| \ll |\mathcal{E}_x|$ for both surface polaritons.

This last result is a consequence of retardation, as is clear from an examination of the no-retardation limit, $c \rightarrow \infty$, where (II.41) becomes

$$\epsilon_{\pm} = -\epsilon_f \begin{cases} \tanh ka \\ \coth ka \end{cases} \quad (\text{II.44})$$

Equations (II.44) can be solved for ω with the result that

$$(\omega_-)_{\text{NR}}^2 = \frac{\omega_{\text{LO}}^2 + \omega_{\text{TO}}^2 (\epsilon_f / \epsilon_{\infty}) \coth ka}{1 + (\epsilon_f / \epsilon_{\infty}) \coth ka} \quad (\text{II.45a})$$

and

$$(\omega_+)_{\text{NR}}^2 = \frac{\omega_{\text{LO}}^2 + \omega_{\text{TO}}^2 (\epsilon_f / \epsilon_{\infty}) \tanh ka}{1 + (\epsilon_f / \epsilon_{\infty}) \tanh ka} \quad (\text{II.45b})$$

where the subscript NR denotes nonretarded. In the limit $ka \ll 1$, $(\omega_-)_{\text{NR}} \rightarrow \omega_{\text{TO}}$ and the associated fields satisfy $\mathcal{E}_x(z) \sim \text{Const.}$, $\mathcal{E}_z(z) \sim 0$. In this limit $(\omega_+)_{\text{NR}} \rightarrow \omega_{\text{LO}}$, with $\mathcal{E}_z(z) \sim \text{Const.}$, $\mathcal{E}_x(z) \sim 0$. Thus, without retardation, uniform polarization occurs within the slab, parallel to the surfaces for $(\omega_-)_{\text{NR}}$ and perpendicular to the surfaces for $(\omega_+)_{\text{NR}}$, whenever $ka \ll 1$. Physically, it is of course clear that retardation effects should occur only for $k \lesssim \omega_{\text{TO}}/c$.

Generally, in the discussion above, we have been considering inactive media for which $\epsilon_f > 1$. One particularly important exception to this restriction occurs if the active slab is placed on a good conductor, the dielectric function of which we write now in the form

$$\epsilon_c(\omega) = 1 - \frac{\omega_p^2}{\omega(\omega + i/\tau)} \quad (\text{II.46})$$

appropriate to an electron gas in the local limit. Here τ is the mean electron lifetime which, when finite, leads to a complex dielectric function characteristic of a lossy medium. Although a discussion of the effects of losses or damping in the active medium is deferred to Section II.D, it is convenient to introduce these effects here for a conducting backplate. The frequency ω_p in (II.46), the plasma frequency, is for most metals very high, $5 \times 10^{15} \text{sec}^{-1} \lesssim \omega_p \lesssim 30 \times 10^{15} \text{sec}^{-1}$. Since the optical polaritons we are considering here have frequencies in the range of 10^{13}sec^{-1} , the dielectric

function of the conductor in this frequency range will be a very large negative number, $\epsilon_c \sim -10^6$, if we for the moment take $\tau \rightarrow \infty$. This suggests immediately that we can consider a good conductor in the present context as a perfect conductor, $\epsilon \rightarrow \infty$, and thus incapable of supporting an electric field parallel to its surface. For the geometry we have used here, this means that an active medium of thickness ξ placed on a metallic backplate must have $E_x = 0$ at the active medium-metal boundary. From (II.43a), we see that this condition is automatically fulfilled at the center of a slab of thickness L for the FK mode ω_+ but nowhere for ω_- . Hence, an active slab of thickness ξ with a medium of dielectric function ϵ_f on one side and a good conductor on the other can support the ω_+ mode of a slab of thickness 2ξ with media of dielectric function ϵ_f on both sides, but no ω_- mode.

Calculations, utilizing (II.36), of the surface polariton dispersion curves for a dielectric slab on a metallic backing for which the dielectric function is that of (II.46) yield results in essential agreement with the perfect-conductor conclusions if the conductivity σ , defined by

$$\epsilon_c = 1 + \frac{4\pi i \sigma}{\omega} \quad (\text{II.47})$$

is such that $\sigma \gg \omega_{\text{TO}}$ for $\omega \sim \omega_{\text{TO}}$.⁵¹ However, if $\sigma \lesssim \omega_{\text{TO}}$ for $\omega \sim \omega_{\text{TO}}$, the perfect-conductor representation for the metal, not unexpectedly, fails. For these conditions the surface phonon frequencies depend on the values of ω_p and τ as well as on the thickness of the metal.⁵¹

These comments regarding the behavior of the surface polaritons when the dielectric slab is placed on a conductor were based on the local representation (II.46) for the metal dielectric function, that is, the form that results from both the transverse and longitudinal nonlocal dielectric functions of the electron gas in the limit $\omega \gg |\mathbf{q}|v_F$, where \mathbf{q} is the three-dimensional wave vector and v_F is the Fermi velocity. It has been suggested by Heinrichs^{52,53} that for the present problem this local form should be replaced by the nonlocal expression for the longitudinal dielectric function in the limit $\omega \ll |\mathbf{q}|v_F$. Such a procedure is, however, invalid. When nonlocality is included, the boundary conditions are most conveniently satisfied through the continuity of the surface impedance,⁵⁴⁻⁵⁸ given for p -polarized fields by (II.10). For a half-space dielectric, represented by a local dielectric function $\epsilon(\omega)$, placed on a half-space nonlocal electron gas, the equation determining the surface modes is then³⁶

$$\frac{-i\alpha}{\epsilon(\omega)(\omega/c)} = Z_{\text{eg}} \quad (\text{II.48})$$

where α is given by (II.6) and Z_{eg} is the surface impedance for the electron gas. If the electrons of the electron gas reflect specularly upon striking the surface, perhaps the simplest case, this equation becomes^{36,59}

$$-\frac{i(k^2 - \epsilon\omega^2/c^2)^{1/2}}{\epsilon(\omega/c)} = \frac{2\omega ci}{\pi} \int_0^\infty \frac{dq_z}{(k^2 + q_z^2)} \left[\frac{k^2}{\omega^2\epsilon_l(k, q_z, \omega)} + \frac{q_z^2}{\omega^2\epsilon_t(k, q_z, \omega) - c^2(k^2 + q_z^2)} \right] \quad (\text{II.49})$$

where k is still the planar wave vector of the surface excitation, the wave vector within the electron gas has components k and q_z parallel and perpendicular to the surface, and ϵ_l and ϵ_t are the longitudinal and transverse dielectric functions of the electron gas. Thus we see that, even for this simple case, the surface impedance for the electron gas involves not a simple function of the transverse or longitudinal dielectric function with the wave vector components specified, but a wave vector integral (which becomes a sum for a slab) over a function which contains both dielectric functions.

Although (II.49), or its generalization for the case of slabs, has not been solved for ϵ of the form (I.9), it is clear that the solutions ω , for k fixed and real, will, in general, be complex as the modes will be intrinsically damped even for ϵ real. In addition, the solutions of (II.49) will be surface polaritons, surface plasmons, or mixtures thereof.

So the problem of the surface modes for a dielectric in contact with a metal remains unsolved. Since, however, wave vectors $\sim k_{TO}$ are so small on the scale of electronic phenomena, the local representation for the metallic dielectric function is probably valid for k values such that the dielectric can be adequately treated as local.

3. Radiative Surface Mode⁶⁰

We return now to the case where the active medium is surrounded by "normal" kinds of inactive media. In Fig. 9 is shown the $\omega-k$ plane subdivided by lines of importance associated with the parameters which have appeared in the theory above. This figure has been drawn with the geometry of Fig. 7 in mind and $\epsilon_{lu} = \epsilon_{ld} = 1$. The FK modes occur in the region L_2 . A reasonable question is then, are there additional surface excitations associated with any of the other regions? With the exception of modes which can legitimately be characterized as surface modes only when damping is present (see Section II.D), we feel that the answer is a qualified

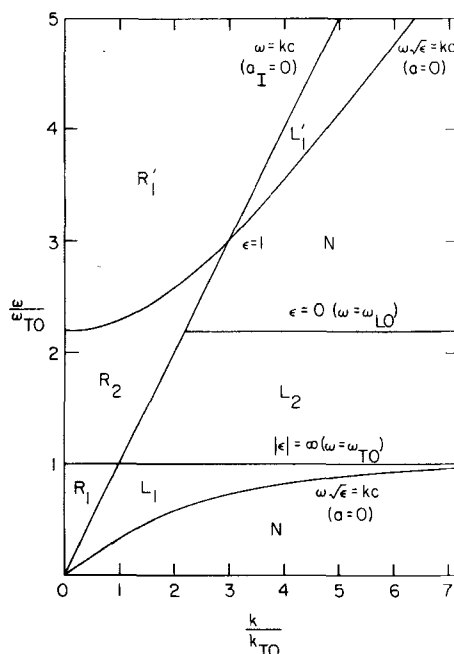


Fig. 9. Regions in the ω - k plane for which different classes of transverse optical modes exist. The curves have been drawn for LiF in vacuum. α is given by (II.6) with $\mu = 1$. α_{\perp} is given by (II.8) with $\epsilon_f = 1$. Radiative solutions exist in the regions R , and nonradiative (localized) solutions in the regions L . The subscripts 1 and 2 denote, respectively, sinusoidal and real exponential solutions inside the slab. There are no solutions in the regions N . The FK modes occur in the region L_2 .

no. In the regions L_1 and L'_1 , both p - and s -polarized polariton modes occur which have fields which decay exponentially outside the slab but vary sinusoidally within.¹⁹ The detailed behavior of these modes depends strongly on the active medium thickness, but they do not have surface character. By this we mean specifically the following: These modes are spread over the active medium, more or less uniformly, independent of its thickness. Under no conditions do they become localized at the surfaces as would a true surface mode such as the FK modes. Thus they can be called "thickness-dependent-bulk" modes.

In the regions R_1 and R'_1 , radiative virtual mode solutions occur, both p - and s -polarized, whose behavior also depends strongly on the slab thickness. But again, these modes have "thickness-dependent-bulk" character rather than the surface character of the FK modes. However, one of the solutions in the region R'_1 has been called a "radiative surface mode"

sufficiently often that we feel a discussion of this mode should be presented here.

We consider the geometry and notation of Fig. 7 with $\epsilon_{Iu} = \epsilon_{Id} = \epsilon_I \geq 1$ and the p -polarized or TM field structure discussed above. Since we are in the region R'_1 , α_I^2 of (II.8) will be negative and we define β_I by

$$\alpha_I = i\beta_I = i \left[\epsilon_I \left(\frac{\omega}{c} \right)^2 - k^2 \right]^{1/2} \quad (\text{II.50})$$

Now, from (II.26) and (II.28), it is clear that for any field arrangement within the slab, the field components outside of the slab will be oscillatory. Requiring the fields to vanish at $z \rightarrow \pm \infty$, as we did above for the fields associated with the FK modes, gives rise to the trivial solution that all fields are zero. Thus, in the regions R , we cannot talk of true normal modes of the system since any excitation of the active medium will radiate its energy and eventually vanish.

The physical effect involved here can be readily identified. Suppose we consider an electromagnetic plane wave of frequency ω propagating in the inactive medium at an angle θ with respect to the normal to the surface (see Fig. 10). The x component k of the wave vector associated with this plane wave then satisfies

$$k = \frac{\omega \sqrt{\epsilon_I}}{c} \sin \theta \quad (\text{II.51})$$

so $k^2 < \epsilon_I (\omega/c)^2$ and thus β_I of (II.50) is positive. Hence, in the regions R , fields within the active medium couple to true radiative solutions without and thereby decay in time through radiative losses. In contrast, the fields of the FK modes are evanescent in the inactive media and couple only very weakly to radiative fields.⁶¹

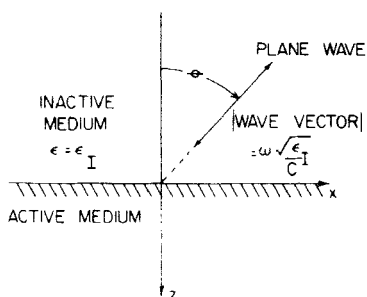


Fig. 10. A sketch illustrating the propagation of a plane wave in the x - z plane of the inactive medium in a direction specified by the angle θ .

Although it is impossible now to characterize the solutions to the electromagnetic field equations as true normal modes, we can nonetheless find "pseudonormal mode" solutions, the virtual modes. These modes are basically the channels by which energy is radiated from the system, that is, if the active medium is excited at time t , then for times $t_1 > t$ the fields associated with the virtual modes correspond to energy flow out of the system and decrease exponentially with increasing time. In the present context we are interested in the modes resulting from the coupling between the photon fields and the polarization fields resulting from optical phonon modes, or the virtual polariton modes.

From the discussion above it is clear that the virtual mode solutions involve a complex frequency

$$\omega = \omega' + i\omega'' \quad (\text{II.52})$$

with $\omega'' < 0$ in order to describe temporal decay properly [see (II.2)]. But this does not fix the nature of the solutions. In most virtual mode applications, the wave vector k is chosen to be real, yielding the real- k virtual modes.⁶⁰ Another possibility is to require that the virtual modes be associated with a given angle θ in the inactive medium as in Fig. 10. Since we can identify the effective wave vector components outside the slab, from (II.2), (II.26), (II.28), and (II.50), as

$$\begin{array}{ll} x \text{ direction} & k \\ z \text{ direction} & \beta_I \end{array}$$

these solutions require both k and β_I to be complex but in such a way that

$$\tan \theta = \frac{k}{\beta_I} \quad (\text{II.53})$$

is real. We will consider here only these real-angle virtual modes since they are the modes which relate directly to the standard optical experiment in which light is directed at the active medium at a fixed angle.

The equations determining the p -polarized virtual modes follow directly from our earlier analysis. Defining β by

$$\alpha = i\beta = i \left[\epsilon \frac{\omega^2}{c^2} - k^2 \right]^{1/2} \quad (\text{II.54})$$

the electric field components within the active medium are, from (II.25) and (II.42),

$$\mathcal{E}_x = K(e^{i\beta z} \mp e^{i\beta z}) \quad (\text{II.55a})$$

and

$$\mathcal{E}_z = \left(\frac{-kK}{\beta} \right) (e^{i\beta z} \pm e^{-i\beta z}) \quad (\text{II.55b})$$

if the arrangement of Fig. 7 is symmetrized so that $\epsilon_{lu} = \epsilon_{ld} = \epsilon_l$. Here K is a constant. For $z > a$, the electric field solution is

$$\mathcal{E}_x = K' e^{i\beta_l z} \quad (\text{II.56a})$$

and

$$\mathcal{E}_z = \left(\frac{-k}{\beta_l} \right) K' e^{i\beta_l z} \quad (\text{II.56b})$$

with K' an integration constant.

Equations (II.56) require some comment. The requirement of temporal decay for the virtual modes means that we can write (II.52) in polar form as

$$\omega = \omega_A e^{-i\varphi} \quad (\text{II.57a})$$

with $0 < \varphi < \pi/2$. The condition (II.53) for the real-angle modes then means

$$k = k_A e^{-i\varphi} \quad (\text{II.57b})$$

and

$$\beta_l = \beta_{lA} e^{-i\varphi} \quad (\text{II.57c})$$

for ϵ_l real. Thus the phase factor e^{ikx} common to all fields *increases* exponentially for increasing x , a necessary consequence of temporal decay as is clear from the following. Consider the energy radiated from the active medium in a time span Δt . This energy will propagate through the inactive medium undiminished in magnitude if ϵ_l is real. However, the fields describing this propagation are decaying exponentially in time. In order that such a temporally decaying field can describe the propagation of a fixed quantity of energy, it is necessary the the field grow exponentially with distance in the direction of propagation. Thus the phase factor e^{ikx} must grow exponentially and so must the phase factor associated with propagation away from the active medium in the z direction. This is the reason that the solution in (II.56) contains the factor $\exp(i\beta_l z)$ rather than $\exp(-i\beta_l z)$.

Applying the usual boundary conditions at $z = a$, we find from (II.55)

and (II.56) the virtual mode condition

$$\frac{\epsilon\beta_I}{\epsilon_I\beta} = \frac{e^{i\beta a} \mp e^{-i\beta a}}{e^{i\beta a} \pm e^{-i\beta a}} \quad (\text{II.58})$$

Using the upper sign in (II.58), we obtain the tangent equation or

$$-i \frac{\epsilon}{\epsilon_I} \frac{\beta_I}{\beta} = \tan \beta a \quad (\text{II.59})$$

with the associated electric field components within the slab being

$$\mathcal{E}_x \propto i \sin \beta z \quad (\text{II.60a})$$

and

$$\mathcal{E}_z \propto -\frac{k}{\beta} \cos \beta z \quad (\text{II.60b})$$

The lower sign in (II.58) yields the cotangent virtual mode equation

$$\frac{i\epsilon\beta_I}{\epsilon_I\beta} = \cot \beta a \quad (\text{II.61})$$

for which the electric field components within the slab are

$$\mathcal{E}_x \propto \cos \beta z \quad (\text{II.62a})$$

and

$$\mathcal{E}_z \propto \frac{-ik}{\beta} \sin \beta z \quad (\text{II.62b})$$

Each of (II.59) and (II.61) has an infinite number of solutions in both regions R_1 and R'_1 . These solutions correspond roughly to spatially oscillatory solutions with n half-wavelengths of oscillation across the slab, that is,

$$2\beta a \sim n\pi \quad (\text{II.63})$$

where n is an integer. The fact that these solutions are oscillatory indicates clearly that we are not dealing with surface waves. However, one of the solutions of the tangent equation involves n of (II.63) equal to zero⁶² and this mode, labeled 0TH in Ref. 60, is the one called the "radiative surface mode." From (II.60) we see that the 0TH mode with βa small has $\mathcal{E}_x \sim 0$ and $\mathcal{E}_z \sim \text{Const}$. These fields within the slab are essentially those of the

FK mode ω_+ for a thin film and k values such that $\alpha L \ll 1$, with L the film thickness.

Let us then examine the properties of this 0TH mode. For $\beta a \ll 1$ we can write (II.59) as

$$-i\epsilon \frac{\beta_I}{\epsilon_I} = a \left\{ \epsilon \left(\frac{\omega}{c} \right)^2 - k^2 \right\} \quad (\text{II.64})$$

Using (II.50), (II.53), and (II.57), this can be written as

$$-i \frac{\epsilon}{\sqrt{\epsilon_I}} \cos \theta = \frac{L}{2} \frac{\omega}{c} (\epsilon - \epsilon_I \sin^2 \theta) \quad (\text{II.65})$$

since $a = L/2$. For $\theta = 0$, the solution of this equation is $\epsilon = 0$ or $\omega = \omega_{LO}$. For $\theta = 90^\circ$ and $\epsilon_\infty > \epsilon_I$, the solution is $\epsilon = \epsilon_I$ or $\omega^2 = (\epsilon_\infty \omega_{LO}^2 - \epsilon_I \omega_{TO}^2) / (\epsilon_\infty - \epsilon_I)$ using (I.11).⁶³ In these limits the solution, for real ϵ , is then a real frequency which is independent of the thickness. Note also that, for $\theta = 0$, the electric field in the inactive medium is identically zero and in the active medium has only a component normal to the surface.

We can further analyze this mode by writing ϵ as

$$\epsilon = \epsilon' + i\epsilon'' = \epsilon_A e^{-i\eta} \quad (\text{II.66})$$

and considering ϵ_I to be real and frequency independent. Then, splitting (II.65) into its real and imaginary parts, we find

$$\frac{\cos(\varphi - \eta)}{\sqrt{\epsilon_I}} \cos \theta = \frac{L}{2} \frac{\omega_A}{c} \sin \eta \quad (\text{II.67a})$$

and

$$\epsilon_A \frac{\sin(\varphi - \eta) \cos \theta}{\sqrt{\epsilon_I}} = \frac{L}{2} \frac{\omega_A}{c} \{ \epsilon_A \cos \eta - \epsilon_I \sin^2 \theta \} \quad (\text{II.67b})$$

Since the 0TH mode is of particular significance for a thin film, the condition from which the appellation "radiative surface mode" arose, let us restrict our analysis to active slabs for which $k_{TO}L = (\omega_{TO}/c)L \ll 1$. Since ω for this mode is of the order ω_{LO} , we then have from (II.67), for θ not too near $\pi/2$, $\eta \cong \pi/2$, $\epsilon'' \cong -\epsilon_A$, $\varphi \cong 0$, and $\epsilon_A \cong [(L/2)(\omega_A/c)]\epsilon_I^{3/2} \times \sin^2 \theta / \cos \theta$. Thus,

$$\omega'' \cong - \left(\frac{L}{4c} \right) \omega_{TO}^2 \epsilon_I^{3/2} \frac{\epsilon_0 - \epsilon_\infty}{\epsilon_\infty^2} \frac{\sin^2 \theta}{\cos \theta} \quad (\text{II.68a})$$

and

$$(\omega')^2 \cong \frac{\omega_{LO}^2 - \omega_{TO}^2 \left\{ \frac{L}{2} \frac{\omega_{LO}\epsilon_I}{c\sqrt{\epsilon_\infty}} \tan\theta \right\}^2}{1 - \left\{ \frac{L}{2} \frac{\omega_{LO}\epsilon_I}{c\sqrt{\epsilon_\infty}} \tan\theta \right\}^2} \quad (\text{II.68b})$$

For small thickness, then, this mode has a frequency near ω_{LO} for $0 \leq \theta \lesssim \theta$, $\sim \cos^{-1}[(L/2)(\omega_{LO}/c)\sqrt{\epsilon_I}]$. In this angular range $|\omega''| \ll \omega_{TO} \sin\theta \tan\theta$ so $|\omega''|/\omega' \ll 1$. Thus the radiative damping of this mode is not very strong. For angles near $\theta = \pi/2$, (II.68) are not valid.⁶⁴ A plot of ω' and ω'' for this mode appears in Fig. 11.

We emphasize that βa for this mode is always small so it is associated with an electric field which is roughly normal to the surface and independent of z for all thicknesses [see (II.55)]. Thus the label surface mode seems inappropriate, even in view of the interesting similarities between this mode and the surface polariton, ω_+ . We return to the effect of this mode in optical studies in Section V.A.

B. Sphere²⁶⁻²⁸

For planar geometry, the surface modes are genuine normal modes of the system when the dielectric function is real; in addition, there occur "pseudonormal" modes, the virtual modes, of which the radiative surface mode is an example. These excitations of the system decay in time through radiative losses. That is, the electromagnetic fields of the active medium couple to electromagnetic fields in the inactive medium which have outgoing radiative wave character at infinity rather than being evanescent as they are for the surface modes. In addition, these virtual modes couple strongly to optical radiation incident upon the system, whereas the nonradiative modes do not. We turn now to the case where the active medium is a sphere, a situation for which the surface modes, and all other transverse excitations, are virtual. This means that a proper description of the surface excitations of a sphere requires a theory in which retardation is included, and it is such a theory which is presented in this section.

We take the active medium to be a sphere of radius a characterized by the local electromagnetic response functions $\epsilon(\omega)$ and $\mu(\omega)$; the inactive medium outside the sphere is represented by the dielectric function $\epsilon_I(\omega)$ and $\mu = 1$. The spherical coordinate system to be used in the analysis is shown in Fig. 12. Many of the relevant mathematical details appear in textbooks^{26,27,65} and are not repeated here.

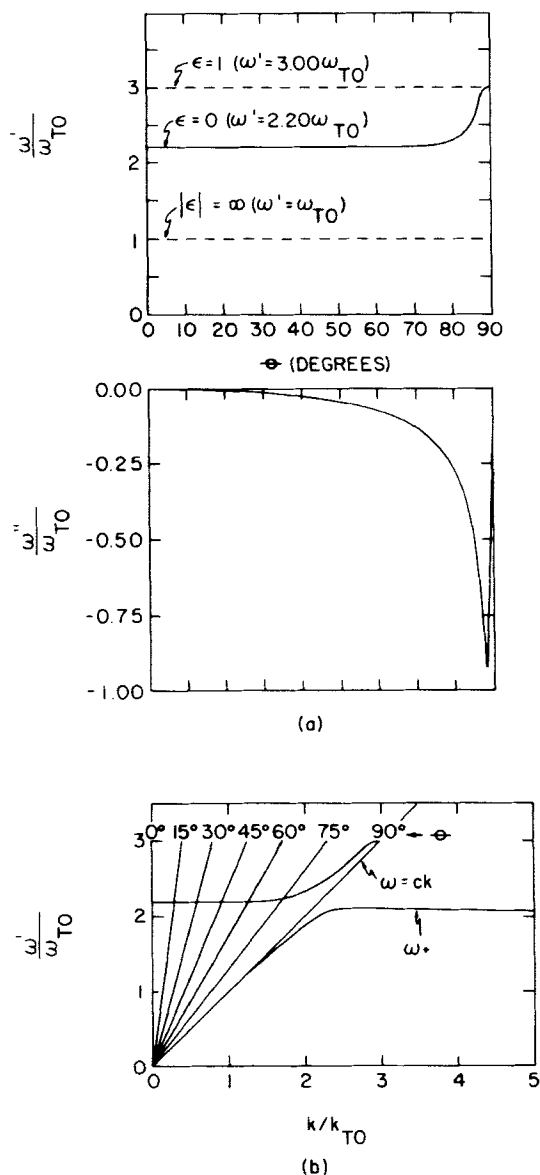


Fig. 11. The complex frequency of the 0TH mode, the "radiative surface mode," for a vacuum-surrounded LiF film of thickness such that $k_{TO}L = 0.1$. (a) The complex frequency as a function of θ . (b) the real part of the complex frequency and the frequency of the surface polariton mode ω_+ as a function of k/k_{TO} . These two modes for thin films have very similar electric fields within the slab if α for the ω_+ mode is such that $\alpha L \ll 1$. However, the electric fields outside the slab for these two modes are very different.

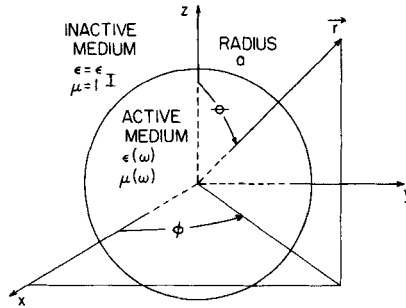


Fig. 12. The spherical coordinate system and the electromagnetic response functions used in the analysis of the sphere problem.

With $\exp(-i\omega t)$ dependence, (II.1c) and (II.1d) lead to the vector wave equation

$$\nabla \times \{ \nabla \times \mathbf{F}(\mathbf{r}, \omega) \} - \xi^2 \mathbf{F}(\mathbf{r}, \omega) = 0 \quad (\text{II.69})$$

where \mathbf{F} can be any of the fields $\mathbf{E}(\mathbf{r}, \omega)$, $\mathbf{D}(\mathbf{r}, \omega)$, $\mathbf{B}(\mathbf{r}, \omega)$, and $\mathbf{H}(\mathbf{r}, \omega)$, and

$$\xi^2 = \frac{\omega^2 \epsilon \mu}{c^2} \quad (\text{II.70})$$

In spherical coordinates, the functions $\mathbf{F}(\mathbf{r}, \omega)$ can be generated from the scalar functions

$$\Psi_{lm}(\mathbf{r}, \omega) = A_{lm} z_l(\xi r) Y_{lm}(\theta, \phi) \quad (\text{II.71})$$

which are solutions of the scalar wave equation

$$\nabla^2 \Psi_{lm}(\mathbf{r}, \omega) + \xi^2 \Psi_{lm}(\mathbf{r}, \omega) = 0 \quad (\text{II.72})$$

In (II.71), A_{lm} is an undetermined coefficient, $Y_{lm}(\theta, \phi)$ is a spherical harmonic, and z_l represents one of that general class of functions usually called the spherical Bessel functions. Three independent solutions of (II.69) are $\mathbf{F} = \mathbf{L}$, \mathbf{M} , and \mathbf{N} , defined by

$$\mathbf{L} = \nabla \Psi \quad (\text{II.73})$$

$$\mathbf{M} = \mathbf{L} \times \mathbf{r} = \xi^{-1} \nabla \times \mathbf{N} \quad (\text{II.74})$$

and

$$\mathbf{N} = \xi^{-1} \nabla \times \mathbf{M} \quad (\text{II.75})$$

\mathbf{L} is longitudinal ($\nabla \times \mathbf{L} = 0$) while \mathbf{M} and \mathbf{N} are transverse ($\nabla \cdot \mathbf{M} = \nabla \cdot \mathbf{N} = 0$).

The characteristic modes are transverse if $\nabla \cdot \mathbf{E} = 0$ and longitudinal if $\nabla \times \mathbf{E} = 0$. Transverse modes can then be obtained from the solutions (II.73) to (II.75) by taking $\mathbf{E} = \mathbf{M}$ or $\mathbf{E} = \mathbf{N}$. If

$$\mathbf{E} = \mathbf{M} \quad (\text{II.76a})$$

then

$$\mathbf{H} = \frac{c}{i\omega} \nabla \times \mathbf{E} = \frac{\xi c}{i\omega} \mathbf{N} \quad (\text{II.76b})$$

and the magnetic field has a nonzero radial component while the radial component of the electric field is zero. Such modes are called transverse electric (TE) or "magnetic." If

$$\mathbf{E} = \mathbf{N} \quad (\text{II.77a})$$

\mathbf{H} is given by

$$\mathbf{H} = \frac{\xi c}{i\omega} \mathbf{M} \quad (\text{II.77b})$$

and \mathbf{E} has a radial component while \mathbf{H} does not. These modes are called transverse magnetic (TM) or "electric." The third choice, $\mathbf{E} = \mathbf{L}$, gives longitudinal modes which have no surface character and are not considered further here.^{66, 66a}

The transverse solutions, (II.76) and (II.77), arise as consequences of our assumption of spherical symmetry. We now make specific application to the present problem. Within the active sphere, $r < a$, where

$$\xi = \frac{\omega}{c} \{ \epsilon(\omega) \mu(\omega) \}^{1/2} \quad (\text{II.78a})$$

the appropriate function z_l in (II.71) is that spherical Bessel function which is finite at $r = 0$ or $j_l(\xi r)$. In the inactive medium, $r > a$,

$$\xi = \xi_l = \frac{\omega}{c} \sqrt{\epsilon_l} \quad (\text{II.78b})$$

and, as required by the nature of the virtual modes, z_l is that function which corresponds to an outgoing wave or the Hankel function $h_l^{(1)}(\xi_l r)$, defined in terms of the spherical Bessel function j_l and the spherical Neumann function n_l by $h_l^{(1)} = j_l + in_l$. The equations determining the frequencies, and thus the radial dependence of the fields, of the transverse virtual modes are obtained by matching the tangential components of \mathbf{E} and \mathbf{H} on the sphere $r = a$. Defining

$$\rho = \xi a \quad (\text{II.79a})$$

and

$$\rho_I = \xi_I a \quad (\text{II.79b})$$

we find for the magnetic modes

$$\frac{(d/d\rho)[\rho j_l(\rho)]}{\mu j_l(\rho)} = \frac{(d/d\rho_I)[\rho_I h_l^{(1)}(\rho_I)]}{h_l^{(1)}(\rho_I)} \quad (\text{II.80})$$

and for the electric modes

$$\frac{(d/d\rho)[\rho j_l(\rho)]}{\epsilon j_l(\rho)} = \frac{(d/d\rho_I)[\rho_I h_l^{(1)}(\rho_I)]}{\epsilon_I h_l^{(1)}(\rho_I)} \quad (\text{II.81})$$

with the requirement that $l \geq 1$. From (II.80) and (II.81) it is apparent that, for given electromagnetic response functions, the characteristic frequencies depend only on the radius of the active medium and the polar angle index l . Since the characteristic frequencies are independent of the azimuthal index m , each solution is $(2l+1)$ -fold degenerate.

We consider now an ionic crystal with $\epsilon(\omega)$ given by (I.9) or (I.11) and $\mu(\omega)=1$, and also assume that $\epsilon_I > 0$. It is convenient to introduce the dimensionless frequency

$$\Omega = \frac{\omega}{\omega_{\text{TO}}} = \Omega' + i\Omega'' \quad (\text{II.82a})$$

where we have written the complex frequency ω as in (II.52), and the dimensionless sphere radius

$$W = k_{\text{TO}} a \sqrt{\epsilon_I} \quad (\text{II.82b})$$

where k_{TO} is given by (II.20). The bulk modes occur in two frequency regions, the "low-frequency" region, $\Omega' < 1$, and the "high-frequency" region, $\Omega' > \omega_{\text{LO}}/\omega_{\text{TO}}$. Infinitely many modes, alternately of the electric and magnetic types as Ω' increases, are associated with *each* value of l in both the low- and high-frequency regions. As $W \rightarrow 0$, all the low-frequency modes have $\Omega' \rightarrow 1$ and the high-frequency modes have $\Omega' \rightarrow \infty$. For $W \rightarrow \infty$, the low-frequency modes have $\Omega' \rightarrow 0$ and the high frequency modes have $\Omega' \rightarrow \omega_{\text{LO}}/\omega_{\text{TO}}$. Additional details concerning these modes appear in Ref. 28.

From our discussion of the half-space in Section II.A.1, it is clear that the surface modes will be of the electric type. In addition, there is but one surface mode for each value of l .⁶⁷ The complex frequencies of several of

these modes are shown in Fig. 13 for a LiF sphere in vacuum.⁶⁸

Let us examine the properties of the surface modes in the limit $W \rightarrow 0$ where both ρ and ρ_I in (II.81) approach zero.^{68a} We have then $j_l(\rho) \cong \rho^l$ and $h_l^{(1)}(\rho_I) \cong \rho_I^{-(l+1)}$, and (II.81) becomes

$$\frac{\epsilon(\omega)}{\epsilon_I} = -\frac{(l+1)}{l} \quad (\text{II.83})$$

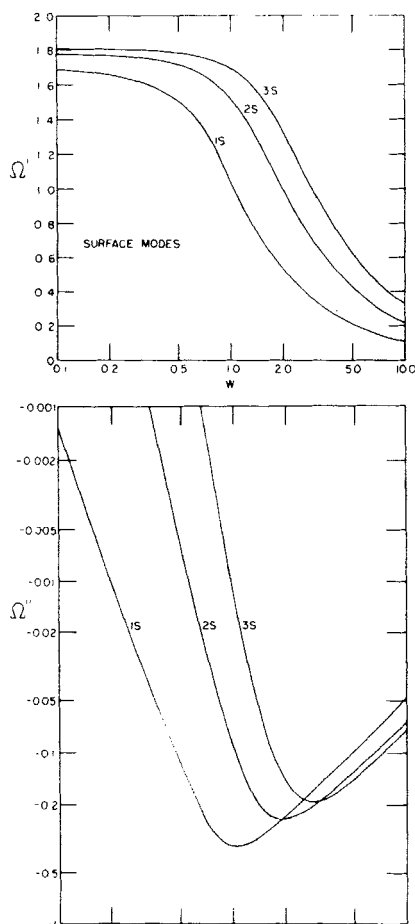


Fig. 13. Complex frequencies of the surface modes as a function of the sphere radius for LiF ($\epsilon_0 = 9.27, \epsilon_\infty = 1.92, \omega_{TO} = 5.78 \times 10^{13} \text{ sec}^{-1}$) in vacuum ($\epsilon_I = 1$). The number in the mode label denotes the value of l . The dimensionless complex frequency Ω is defined in (11.82a) and the dimensionless sphere radius W in (11.82b).

Using (I.10) and (I.11), the frequencies, now real, resulting from (II.83) are

$$\Omega_l^2 = \frac{\omega_l^2}{\omega_{TO}^2} = \frac{\epsilon_0 l + \epsilon_f(l+1)}{\epsilon_\infty l + \epsilon_f(l+1)} \quad (\text{II.84})$$

The expressions (II.83) and (II.84) that determine the surface mode frequencies in the limit $W \rightarrow 0$ in the theory including retardation are identical to the *radius-independent* expressions that result when retardation is neglected.⁶⁹ Thus the nonretarded theory for the surface modes of a sphere is valid only for $W \ll 1$. This conclusion is readily understandable physically. Consistent with their name, most surface modes for $W \ll 1$ are rather well localized at the surface of the active sphere (as is shown immediately below). The associated fields thus extend over a region of length of order a . If the time t_1 necessary for an electromagnetic wave to traverse this distance, $t_1 \sim a\sqrt{\epsilon_f}/c$, is small compared with the period of oscillation of the surface excitation $t_2 \sim 1/\omega_{TO}$, the effects of retardation will vanish. The condition $t_1 \ll t_2$ is just $\omega_{TO} a\sqrt{\epsilon_f}/c \ll 1$ or $W \ll 1$. To give some idea as to the sphere radii involved here, we note that $W=1$ for a LiF sphere in vacuum corresponds to a radius of 5.19×10^{-4} cm.

As W increases, the real parts of the surface mode frequencies decrease. To order W^2 , the still real frequencies of the surface modes are

$$\Omega^2 \cong \frac{\epsilon_0 l + \epsilon_f(1+l)(1+\Delta)}{\epsilon_\infty l + \epsilon_f(1+l)(1+\Delta)} \quad (\text{II.85a})$$

with

$$\Delta = \frac{W^2(l + \frac{1}{2})}{l(l - \frac{1}{2})(l + \frac{3}{2})} \left\{ \frac{\epsilon_0 l + \epsilon_f(l+1)}{\epsilon_\infty l + \epsilon_f(l+1)} \right\} \quad (\text{II.85b})$$

when $\mu = 1$.

As noted above, the surface modes are transverse, $\nabla \cdot \mathbf{E} = 0$ but $\nabla \times \mathbf{E} \neq 0$. In the limit $W \rightarrow 0$, the electric field also satisfies $\nabla \times \mathbf{E} \rightarrow 0$. This is a necessary consequence of the correspondence between the theory with retardation in the limit $W \rightarrow 0$ and the nonretarded theory.

The radial component of the electric field of the surface modes is given by

$$(E_r)_l \propto \begin{cases} (\rho R)^{-1} j_l(\rho R) Y_{lm}(\theta, \phi), & r < a \\ (\rho_l R)^{-1} h_l^{(1)}(\rho_l R) Y_{lm}(\theta, \phi), & r > a \end{cases} \quad (\text{II.86})$$

where $R = r/a$. Since $\rho \rightarrow 0$ as $W \rightarrow 0$ for these modes, $(E_r)_l$ has no radial

nodes. When $W \ll 1$,⁷⁰ the radial dependence of $(E_r)_l$ is $(E_r)_l \propto R^{l-1}$ inside the active sphere and $(E_r)_l \propto R^{-(l+2)}$ outside. As l increases, these modes become increasingly localized at the surface of the sphere and thus are legitimately called surface modes. When $l \rightarrow \infty$, the surface mode frequency is real and satisfies $\omega \rightarrow \omega_{s\infty}$, independent of W . $\omega_{s\infty}$, given by (II.18) and the solution of $\epsilon(\omega) = -\epsilon_f$, is the large- k limit of the surface mode frequency for a planar active medium surface in contact with an inactive medium with dielectric function ϵ_f . In this limit of extreme localization at the surface, the frequency of the surface mode does not depend on whether the boundary is planar or spherical or, for that matter, of any other shape. On physical grounds, it is impermissible to take the $l \rightarrow \infty$ limit here since the strong localization is not compatible with the requirements of the continuum theory. However, for crystals which can legitimately be characterized as macroscopic, this limitation is without physical consequence.

It might be tempting, from the argument just given, to conclude that the surface modes of arbitrary l for a sphere with $W \gg 1$ should be simply related to the surface modes in a half-space. This is, however, not the case and the reason is the long-range nature of the fields associated with these excitations. That is, the fields within the sphere for surface modes with moderate values of l extend throughout the sphere, thereby retaining their "spherical" identity for all W . The mode frequencies then reflect this spherical character as is clear from comparing Figs. 13 and 4.

In the limit $W \rightarrow 0$, the triply degenerate $l=1$ surface modes (denoted 1S in Fig. 13) have uniform electric fields within the active sphere⁷¹ and dipole electric fields without. The threefold degeneracy arises from the fact that the choice of any of the three Cartesian directions for the electric field within the sphere gives rise to an independent mode. The frequency of the 1S modes in this limit is given by the condition $\epsilon(\omega) = -2\epsilon_f$ [see (II.83)] and, interestingly, this is the frequency which results from the wholly invalid assumption that the fields in this problem can in general be written as plane waves characterized by an ordinary three-dimensional wave vector \mathbf{q} together with the long-wavelength limit $|\mathbf{q}|a \ll 1$.⁷²⁻⁷⁶ The fact that this incorrect procedure leads to such a solution is easy to understand. If $|\mathbf{q}|a \ll 1$, the electric field within the sphere for both transverse and longitudinal plane waves is essentially uniform so that three degenerate solutions result, two transverse and one longitudinal, all characterized by the condition $\epsilon(\omega) = -2\epsilon_f$.⁷⁷ In the correct solution, these three solutions also occur but they are all transverse. Thus, the plane-wave solution leads to incorrect implications for the character of the 1S modes, even if it yields the proper frequency for small radius. This can be most readily

appreciated by recognizing that, from the plane-wave point of view, when the sphere radius increases with the wave vector held constant, the fields associated with the transverse and longitudinal plane waves can be distinguished by different depolarization effects and thus the degeneracy, both in field form and frequency, of the "longitudinal" and "transverse" solutions is removed. This is incorrect, as we have seen above that the 1S modes are degenerate under all conditions. Thus, the plane-wave "solution" does not describe properly even the 1S modes. In addition, this plane-wave solution does not yield any of the volume modes or the $l \geq 2$ surface modes, all of which exist as shown above, since these modes involve a more complicated radial and/or angular variation of the fields. So, the plane-wave approach yields totally incorrect results, a conclusion which is in no sense surprising considering that the conditions of translational invariance appropriate for the introduction of an ordinary wave vector do not exist in this problem.

In the discussion just given, we have demonstrated that an "ordinary" approach to a problem sometimes fails completely. We would now like to point out that an unusual approach to this problem, which may be useful in related problems, gives the correct result. Consider the system of Fig. 12 and assume that the active sphere is placed in a uniform, external, *static* electric field \mathbf{E}_0 . Then it follows directly⁷⁸ that the electric field within the sphere is

$$\mathbf{E}_{\text{in}} = \frac{3\epsilon_l}{\epsilon + 2\epsilon_l} \mathbf{E}_0 \quad (\text{II.87})$$

a uniform electric field. Now let us look at this as a normal mode problem and ask, what must be true for a field of the form (II.87) to exist if $\mathbf{E}_0 = 0$? Clearly, $\epsilon + 2\epsilon_l = 0$ must be satisfied so that $\mathbf{E}_0/(\epsilon + 2\epsilon_l)$ remains finite. This is just the condition determining the frequency for the 1S modes as $W \rightarrow 0$ and, in addition, the fields are correctly given, both inside and outside the sphere, by this approach. Why does this electrostatic approach work? The answer lies in the fact that, for the surface modes and $W \rightarrow 0$, the effects of retardation disappear and thus these modes can be described in electrostatic terms. Thus the solution here is rigorously correct when retardation is neglected and also for $W \rightarrow 0$ when retardation is included. A similar procedure can be used to find the other surface modes under these conditions.

C. General Geometric Considerations^{21-23,39}

We have seen that the surface modes for planar surfaces are nonradiative normal modes while the surface modes for the sphere are virtual.

These two types of surface excitations are very different in physical character and the mathematical procedures used above to describe them appear also, at first glance, strongly dissimilar. We will now demonstrate the basic unity in these mathematical procedures, apply the general procedure to an additional example, that of a cylindrical active medium, and then develop a procedure, applicable to a number of geometries, for determining the surface modes without retardation.

Our analysis for the sphere began with (II.69) which, in view of (II.1a) and (II.1b), can also be written

$$(\nabla^2 + \xi^2)\mathbf{F} = 0 \quad (\text{II.88})$$

This vector wave equation, with the coordinate system now unspecified, can be solved in a form in which boundary conditions can be satisfied for six coordinate systems: rectangular, spherical, circular-cylindrical, elliptic-cylindrical, parabolic-cylindrical, and conical. We investigate only the first three. The transverse solutions of (II.88) have the general form⁷⁹

$$\mathbf{M} = \nabla \times \{ \hat{\mu} w \Psi \} \quad (\text{II.89a})$$

or

$$\mathbf{N} = \frac{1}{\xi} \nabla \times (\nabla \times \{ \hat{\mu} w \Psi \}) \quad (\text{II.89b})$$

where $\hat{\mu}$ is an appropriate unit vector, w is a function of the coordinate system variables, and Ψ is a solution of the scalar wave equation (II.72). Both \mathbf{E} and \mathbf{H} satisfy (II.88) so the two independent types of transverse solutions result from selecting \mathbf{E} to be of the form (II.89a) with \mathbf{H} then given by (II.89b), or vice versa. Our solution (Section II.A.1) for the TM surface modes for the active half-space $z > 0$ is obtained by taking \mathbf{E} of the form (II.89a), $\hat{\mu}$ to be a unit vector \hat{y} in the y direction, $w = 1$, and $\Psi \propto \exp(ikx)$ because of the translational invariance parallel to the surface. The sphere surface modes (of the electric type) arise from the choice $w = r$, $\hat{\mu}$ a unit vector \hat{r} in the radial direction, and \mathbf{E} of the form (II.89b). Let us then extend our previous analysis and investigate the characteristic modes of a cylindrical active medium of radius a , described by the functions $\epsilon(\omega)$ and $\mu(\omega)$, encircled by an inactive medium with dielectric function ϵ_f and $\mu = 1$. The coordinate system is sketched in Fig. 14.

We now take $\hat{\mu}$ to be a unit vector in the z direction, $w = 1$, and

$$\Psi(\mathbf{r}, \omega) = \psi(r, \phi, \omega) e^{ihz} \quad (\text{II.90})$$

since we have translational invariance in the direction of the cylinder axis. Then $\psi(r, \phi, \omega)$ of (II.90) is given by

$$\psi(r, \phi, \omega) = e^{in\phi} \begin{cases} J_n(\beta r), & r < a \\ H_n^{(1)}(\beta_f r), & r > a \end{cases} \quad (\text{II.91})$$

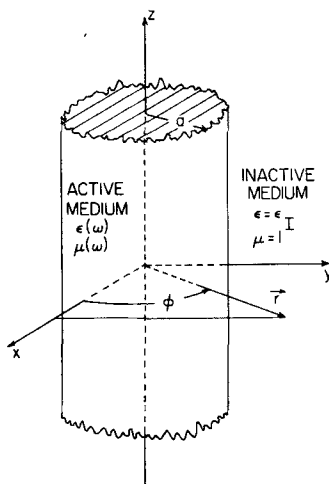


Fig. 14. The cylindrical coordinate system and the electromagnetic response functions used in the analysis of the cylinder problem.

where n is a nonnegative integer, J_n and $H_n^{(1)}$ are cylindrical Bessel and Hankel functions,

$$\beta = \{\xi^2 - h^2\}^{1/2} \quad (\text{II.92a})$$

$$\beta_I = \{\xi_I^2 - h^2\}^{1/2} \quad (\text{II.92b})$$

and ξ and ξ_I are given by (II.78). When $\mathbf{E} \propto \mathbf{M}$ and $\mathbf{H} \propto \mathbf{N}$, the field arrangement is called “magnetic” as the electric field has no z component. With $\mathbf{E} \propto \mathbf{N}$ and $\mathbf{H} \propto \mathbf{M}$, so that \mathbf{H} has no z component, the arrangement is called “electric.” In general, independent electric and magnetic modes do not exist; the satisfaction of the boundary conditions requires fields which have both electric and magnetic character. The equation, resulting from the boundary conditions, which these mixed modes must satisfy is³⁹

$$\left\{ \frac{1}{\beta a} \frac{J'_n(\beta a)}{J_n(\beta a)} - \frac{1}{\beta_I a} \frac{H_n^{(1)'}(\beta_I a)}{H_n^{(1)}(\beta_I a)} \right\} \left\{ \frac{\xi^2}{\beta a} \frac{J'_n(\beta a)}{J_n(\beta a)} - \frac{\xi_I^2}{\beta_I a} \frac{H_n^{(1)'}(\beta_I a)}{H_n^{(1)}(\beta_I a)} \right\} \\ \text{(electric factor)} \qquad \qquad \qquad \text{(magnetic factor)} \\ = \left\{ \frac{nh}{a^2} \left(\frac{1}{\beta^2} - \frac{1}{\beta_I^2} \right) \right\}^2 \quad (\text{II.93})$$

where the primes denote differentiation with respect to the argument. In

the special case where the product (nh) is zero, there are independent magnetic modes [given by setting the magnetic factor in (II.93) equal to zero] and electric modes [obtained from the zeros of the electric factor in (II.93)].

The reason that the two field arrangements, electric and magnetic, do not in general lead to independent excitations in this case is clear. For the slab or the sphere, the field arrangement called electric (or TM) had only an electric field component perpendicular to the surfaces, and that called magnetic (or TE) had only a magnetic field component perpendicular to the surfaces. Thus the two types of field orientation correspond to independent physical situations. For the cylinder, the descriptions electric and magnetic relate to the field components in the z direction and not to the important direction physically, that of the normal to the cylindrical surface. Both electric and magnetic field arrangements in general have both electric and magnetic field components perpendicular to the cylindrical surface and thus the fact that the excitations are of mixed character is merely a labeling problem and does not indicate new features in the behavior of the cylinder modes. When $(nh)=0$, the picture changes. The "magnetic" field arrangement now has an electric field component perpendicular to the surface, while the "electric" field arrangement does not. Thus the excitations of the two types are independent and the electric dipole type of SO excitations, which we have examined in detail above for other geometries, will here be "magnetic" modes. In addition, these surface modes, and the bulk excitations as well, are both radiative and nonradiative in character. Specifically, the surface modes now occur in both regions L_2 and R_2 of Fig. 9 if the abscissa of this figure is considered to be h/k_{TO} rather than k/k_{TO} .

A complete investigation of the surface modes for the cylindrical case has not been made. However, several features are clear. For large h or, more precisely, β_I^2 [(II.92b)], negative and $|\beta_I|a \gg 1$, the surface mode frequencies $\omega_{nh} \rightarrow \omega_{s\infty}$ given by (II.18). This is the now familiar situation of strong localization at the surface. The mode with $n=0$ decreases in frequency from the large h value $\omega_{s\infty}$ to ω_{TO} when h is on the effective light line $\omega = ch/\sqrt{\epsilon_I}$. The modes are real normal modes for $\beta_I^2 < 0$ but most (all?) cross the effective light line and become virtual in the radiative region. Thus the cylindrical geometry provides the interesting situation that the surface modes can be both real and virtual.

In the small-radius limit, $\omega_{TO}a\sqrt{\epsilon_I}/c \ll 1$, (II.93), which determines the mode frequencies, reduces to the corresponding expression as obtained from the nonretarded theory. This is the same physical situation encountered in the case of the sphere.

Our formal development of the continuum theory to this point has been based on the complete set of Maxwell equations, (II.1), and, as such, has included retardation effects. As noted above, the resultant polariton excitations are photon-phonon mixtures. If we neglect retardation, that is, take $c \rightarrow \infty$, and thereby work in an approximation which is formally electrostatic, we eliminate the photon component of these excitations, leaving just phonons. Since we have found occasion above to use the nonretarded results, and since the associated theory is in itself of interest, we develop it here.

The nonretarded long-wavelength dynamics of a finite, cubic, diatomic, ionic crystal can be described by the equations^{1,75,80}

$$\ddot{\mathbf{w}} = b_{11}\mathbf{w} + b_{12}\mathbf{E} \quad (\text{II.94a})$$

$$\mathbf{P} = b_{21}\mathbf{w} + b_{22}\mathbf{E} \quad (\text{II.94b})$$

together with the standard electrostatic boundary conditions. Here \mathbf{w} is the relative anion-cation displacement multiplied by the square root of the reduced mass per unit volume, \mathbf{E} is the macroscopic electric field, and \mathbf{P} the macroscopic polarization. The parameters b_{ij} reflect the properties of the dielectric function (I.9) and are given by

$$b_{11} = -\omega_{\text{TO}} \quad (\text{II.95a})$$

$$b_{12} = b_{21} = \omega_{\text{TO}} \left(\frac{\epsilon_0 - \epsilon_\infty}{4\pi} \right)^{1/2} \quad (\text{II.95b})$$

and

$$b_{22} = \frac{\epsilon_\infty - 1}{4\pi} \quad (\text{II.95c})$$

Equations (II.94) must now be solved along with the electrostatic equations

$$\nabla \cdot \mathbf{D} = \nabla \cdot (\mathbf{E} + 4\pi\mathbf{P}) = 0 \quad (\text{II.96a})$$

and

$$\nabla \times \mathbf{E} = 0 \quad (\text{II.96b})$$

Assuming $\exp(-i\omega t)$ time dependence, the curl of (II.94a) yields

$$(\omega^2 - \omega_{\text{TO}}^2)(\nabla \times \mathbf{w}) = 0 \quad (\text{II.97})$$

indicating that if $\nabla \times \mathbf{w} \neq 0$, $\omega^2 = \omega_{\text{TO}}^2$. From the divergence of (II.94) we

find

$$\left(\omega^2 + b_{11} - 4\pi \frac{b_{12}b_{21}}{1 + 4\pi b_{22}} \right) \nabla \cdot \mathbf{w} = 0 \quad (\text{II.98})$$

But

$$b_{11} - \frac{4\pi b_{12}b_{21}}{1 + 4\pi b_{22}} = -\omega_{\text{LO}}^2 \quad (\text{II.99})$$

so (II.98) can be written as

$$(\omega^2 - \omega_{\text{LO}}^2) \nabla \cdot \mathbf{w} = 0 \quad (\text{II.100})$$

If $\nabla \cdot \mathbf{w} \neq 0$, $\omega^2 = \omega_{\text{LO}}^2$. So, from (II.97) and (II.100), there are three types of solutions:

$$\text{transverse:} \quad \nabla \cdot \mathbf{w} = 0, \quad \omega^2 = \omega_{\text{TO}}^2 \quad (\text{II.101a})$$

$$\text{longitudinal:} \quad \nabla \times \mathbf{w} = 0, \quad \omega^2 = \omega_{\text{LO}}^2 \quad (\text{II.101b})$$

$$\text{surface}^{81}: \quad \nabla \cdot \mathbf{w} = \nabla \times \mathbf{w} = 0 \quad (\text{II.101c})$$

the surface solution appearing since $\omega_{\text{TO}}^2 \neq \omega_{\text{LO}}^2$. The long-wavelength transverse and longitudinal solutions thus occur for the finite crystal at the same frequencies as they do in an infinite crystal.⁸² But there is also a third type of solution.

Equations (II.101) represent well-defined physical situations. However, in dealing with the surface modes it is preferable to be able to work with the electric field rather than with the less familiar function \mathbf{w} . In view of the electrostatic condition (II.96b), it is clear that (II.101) cannot be simply rewritten with \mathbf{w} replaced by \mathbf{E} . However, we can make this replacement in the surface mode conditions since, from (II.94a),

$$\mathbf{w} = - \frac{b_{12}\mathbf{E}}{\omega^2 + b_{11}} \quad (\text{II.102})$$

and this expression indicates a simple proportionality between \mathbf{w} and \mathbf{E} as long as $\omega^2 \neq -b_{11} = \omega_{\text{TO}}^2$. Since this inequality is valid for the surface modes we can characterize them by

$$\nabla \cdot \mathbf{E} = \nabla \times \mathbf{E} = 0 \quad (\text{II.103})$$

The standard procedures of electrostatics then can be used in finding the surface modes. We introduce a potential Φ which satisfies the Laplace

equation,

$$\nabla^2 \Phi = 0 \quad (\text{II.104a})$$

and which is related to \mathbf{E} by

$$\mathbf{E} = -\nabla \Phi \quad (\text{II.104b})$$

Thus the calculation of Φ together with the imposition of the proper boundary conditions yields the nonretarded surface modes. A general procedure for finding the determining equations for the nonretarded surface modes has been presented by Ruppin and Englman.²¹ Consider a system (ξ_1, ξ_2, ξ_3) of curvilinear coordinates with a boundary specified by $\xi_1 = \xi_1^0$. The active medium lies within or without this boundary. If the solution to the Laplace equation (II.104a) can be written in the separated form $y_j(\xi_1)F(\xi_2, \xi_3)$, where $y_j(\xi_1)$ is finite at the origin and at infinity, we write for Φ

$$\Phi_\alpha = A_\alpha y_\alpha(\xi_1) F(\xi_2, \xi_3) \quad (\text{II.105a})$$

$$\Phi_\beta = A_\beta y_\beta(\xi_1) F(\xi_2, \xi_3) \quad (\text{II.105b})$$

where α represents the region $\xi_1 < \xi_1^0$ and β the region $\xi_1 > \xi_1^0$; A_α and A_β are constants. The continuity of the tangential component of \mathbf{E} and the normal component of \mathbf{D} at $\xi_1 = \xi_1^0$ leads to

$$A_\alpha y_\alpha(\xi_1^0) = A_\beta y_\beta(\xi_1^0) \quad (\text{II.106a})$$

and

$$\epsilon_\alpha A_\alpha y'_\alpha(\xi_1^0) = \epsilon_\beta A_\beta y'_\beta(\xi_1^0) \quad (\text{II.106b})$$

where ϵ_α is the dielectric function for $\xi_1 < \xi_1^0$ and ϵ_β that for $\xi_1 > \xi_1^0$. From (II.106) we then have immediately

$$\epsilon_\alpha = \epsilon_\beta \frac{y_\alpha(\xi_1^0) y'_\beta(\xi_1^0)}{y_\beta(\xi_1^0) y'_\alpha(\xi_1^0)} \quad (\text{II.107})$$

the condition determining the frequencies of the surface modes. A corresponding expression for systems with two surfaces has also been obtained by Ruppin and Englman.²¹ We illustrate the use of (II.107) with several examples.

Half-space. Consider the system of Fig. 2. The surface is now $z=0$ and we denote the inactive medium $z < 0$ by α and the active medium $z > 0$ by

β . Then

$$y_\alpha = e^{kz} \quad (\text{II.108a})$$

and

$$y_\beta = e^{-kz} \quad (\text{II.108b})$$

where k is a positive constant which we recognize as the wave vector parallel to the surface. From (II.107) we then have $\epsilon = -\epsilon_f$, a by now well-understood result, from which $\omega = \omega_{s\infty}$, with $\omega_{s\infty}$ given by (II.18). So, for the half-space, the nonretarded theory leads to $\omega = \omega_{s\infty}$ independent of k .

Sphere.²¹ We analyze the system shown in Fig. 12 so that $r = a$ is the boundary. With α corresponding to the region $r < a$ and β the region $r > a$, we have, from the Laplace equation,

$$y_\alpha = r^l \quad (\text{II.109a})$$

and

$$y_\beta = r^{-(l+1)} \quad (\text{II.109b})$$

with l a positive integer. Equation (II.107) then becomes $\epsilon = -\epsilon_f(l+1)/l$, previously found as the $W \rightarrow 0$ limit in the retarded theory [see (II.83)]. The associated frequencies, which approach $\omega_{s\infty}$ for large l , are given in (II.84).

Cylinder.²¹ We now consider the system of Fig. 14, with the surface of interest that for which $r = a$. If we take for α the region $r < a$ and for β the region $r > a$,

$$y_\alpha = I_n(hr) \quad (\text{II.110a})$$

and

$$y_\beta = K_n(hr) \quad (\text{II.110b})$$

where I_n and K_n are the modified Bessel functions, n is a nonnegative integer, and h is the wave vector in the direction of the cylinder axis. The resulting equation for the surface phonon frequencies is

$$\frac{\omega_{nh}^2}{\omega_{\text{TO}}^2} = \frac{\epsilon_0 - \epsilon_f \Delta_{nh}}{\epsilon_\infty - \epsilon_f \Delta_{nh}} \quad (\text{II.111a})$$

where

$$\Delta_{nh} = \frac{K'_n(ha) I_n(ha)}{K_n(ha) I'_n(ha)} \quad (\text{II.111b})$$

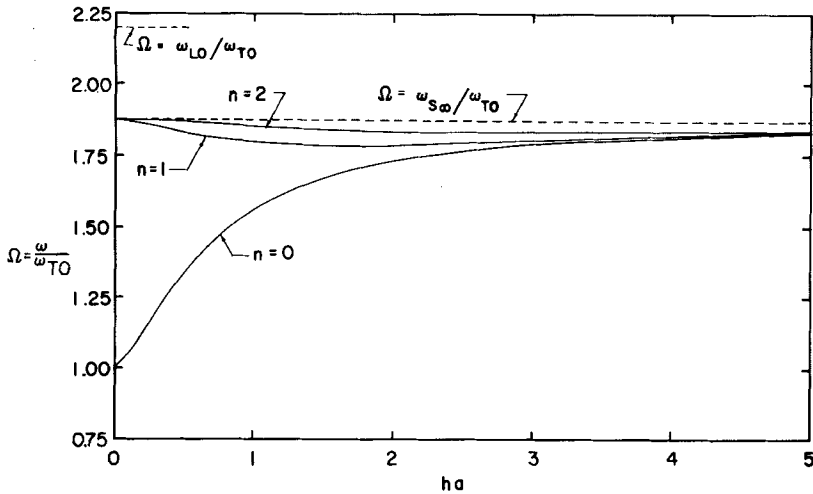


Fig. 15. Some surface mode frequencies (retardation neglected) for an infinite LiF cylinder in vacuum as a function of (ha) , where h is the wave vector parallel to the cylinder axis and a is the cylinder radius. The dielectric function parameters are given in the caption of Fig. 13. All mode frequencies are asymptotic to $\Omega = \omega_{s\infty}/\omega_{TO}$. All modes for which $n \neq 0$ have $\Omega = \omega_{s\infty}/\omega_{TO}$ for $(ha) = 0$.

The prime denotes differentiation with respect to the argument. For $(ha) \gg 1$, $\Delta \cong -1$ and $\omega_{nh}^2 \cong \omega_{s\infty}^2$. Several of these modes are shown in Fig. 15.

Slab.³⁹ This geometry cannot be treated using the single-surface result (II.107). However, the solution can be found in a straightforward fashion from (II.104). We consider the system of Fig. 7 so the potential Φ is of the form

$$\Phi = \begin{cases} K_0 e^{-kz} e^{ikx} & z > a \\ (K'_0 e^{-kz} + K'_1 e^{kz}) e^{ikx}, & |z| < a \\ K_1 e^{kz} e^{ikx}, & z < -a \end{cases} \quad (\text{II.112})$$

where K_j and K'_j are constants, and k is the wave vector parallel to the surfaces. Satisfying the boundary conditions leads to

$$\coth(2ka) = - \frac{\epsilon^2 + \epsilon_{lu} \epsilon_{ld}}{\epsilon(\epsilon_{lu} + \epsilon_{ld})} \quad (\text{II.113})$$

For an ionic crystal and $(ka) \rightarrow 0$, we see that there are two solutions, $\epsilon = 0$ or $\omega = \omega_{LO}$, and $\epsilon \rightarrow -\infty$ or $\omega = \omega_{TO}$. Without retardation, then, the surface

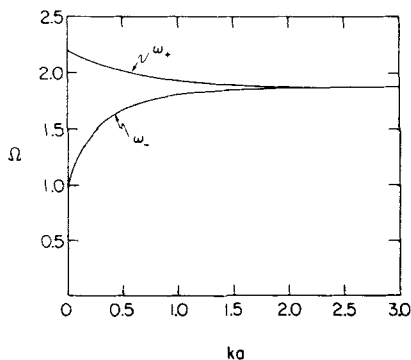


Fig. 16. The frequencies of the surface phonons (retardation neglected) for a LiF slab in vacuum. The length $a=L/2$, with L the slab thickness, and the parameters used in the dielectric function are given in the caption of Fig. 13. The frequencies ω_+ and ω_- , the solutions of (11.114), are given in (11.45).

phonon ω_+ (see Section II.A.2) approaches the longitudinal optical frequency ω_{LO} as $k \rightarrow 0$ while phonon ω_- approaches ω_{TO} . For large (ka) , $\epsilon \rightarrow -\epsilon_{Iu}$ or $-\epsilon_{Id}$, as was discussed in Section II.A.2 in connection with Fig. 8b. In the symmetric case, $\epsilon_{Iu} = \epsilon_{Id} = \epsilon_I$, (II.113) factors into the equation for the ω_+ branch

$$\epsilon = -\epsilon_I \tanh ka \quad (\text{II.114a})$$

and the equation for the ω_- branch

$$\epsilon = -\epsilon_I \coth ka \quad (\text{II.114b})$$

The frequencies resulting from (II.114) are shown in Fig. 16.

We have distinguished carefully between surface polaritons (retardation included) and surface phonons (no retardation). In the literature, both terms are often used to describe what we have called surface polaritons and we also do this below.

D. Effects of Damping

The local lattice dynamics theory developed to this point has been harmonic insofar as the atomic motion is concerned. Our problem here is to include the dissipative effects associated with the anharmonic phonon interactions. Within the local theory this process must begin with a suitable modification of the harmonic response functions $\epsilon(\omega)$ and $\mu(\omega)$. A careful treatment of these modifications leads to expressions of considerable complexity⁸³ in which effects such as temperature dependence are in-

cluded. We shall content ourselves here with a simple phenomenological modification of $\epsilon(\omega)$ which incorporates the features of the "exact" result in a qualitatively correct fashion. In this way, it is straightforward to obtain equations describing the damped surface phonons. However, the same cannot be said concerning the proper interpretation of these equations. This subject has not been thoroughly investigated and a number of unanswered questions remain.

For a divalent cubic ionic crystal, the harmonic dielectric function (I.9) can be obtained classically from an equation of motion for the relative displacement of an anion-cation pair. If we add to this equation of motion a phenomenological damping term proportional to the relative velocity, the anharmonic generalization of (I.9) becomes⁸⁴

$$\epsilon'_A(\omega) = \epsilon_\infty + \frac{(\epsilon_0 - \epsilon_\infty)\omega_{\text{TO}}^2}{\omega_{\text{TO}}^2 - \omega^2 - i\omega\gamma_1} \quad (\text{II.115})$$

where γ_1 represents essentially the proportionality constant in the damping term. This is the complex dielectric function usually used to describe the ionic crystal.

In the limit of zero temperature, the form (II.115), with $\gamma_1 = \gamma_1(\omega)$, is approximately that which emerges from a quantum mechanical treatment.⁸³ Such a treatment also yields an expression for the damping constant $\gamma_1(\omega)$. This expression provides a proper interpretation of $\gamma_1(\omega)$ in that it involves a sum over an appropriate set of matrix elements in which phonon states are anharmonically coupled.

An expression for the dielectric function which describes somewhat better than (II.115) the behavior of the "exact" expression for $\omega \sim \omega_{\text{TO}}$ is

$$\epsilon_A(\omega) = \epsilon_\infty + \frac{(\epsilon_0 - \epsilon_\infty)\omega_{\text{TO}}^2}{\omega_{\text{TO}}^2 - \{\omega + i\gamma_1(\omega)/2\}^2} \quad (\text{II.116})$$

where $\gamma_1(\omega)$ is in general a complicated function of a number of fundamental damping constants. We view $\gamma_1(\omega)$ here as a phenomenological parameter.⁸⁵ For modest damping $\gamma_1 \ll \omega_{\text{TO}}$, expressions (II.115) and (II.116) differ but little. Indeed, it is probably fair to say that if the damping is sufficiently strong that the results using (II.115) or (II.116) differ appreciably, then neither expression is correct. We shall here use (II.116).⁸⁵ For convenience we define the dimensionless variables

$$\Omega = \frac{\omega}{\omega_{\text{TO}}} \quad (\text{II.117a})$$

$$\gamma(\omega) = \frac{\gamma_1(\omega)}{\omega_{\text{TO}}} \quad (\text{II.117b})$$

and, for use below,

$$K = \frac{kc}{\omega_{\text{TO}} \sqrt{\epsilon_I}} \quad (\text{II.117c})$$

Then ϵ_A can be written

$$\epsilon_A(\Omega) = \epsilon_\infty + \frac{\epsilon_0 - \epsilon_\infty}{1 - (\Omega + i\gamma/2)^2} \quad (\text{II.118})$$

This dielectric function is shown in Fig. 17 for LiF and $\gamma = 0.20$.

In principle, $\mu(\omega)$ must be treated in a similar fashion. However, we restrict our analysis to systems for which $\mu(\omega) = 1$. We also consider ϵ_I to be real for simplicity.

1. Half-space

Suppose we simply replace $\epsilon(\omega)$ in the SO phonon dispersion relation

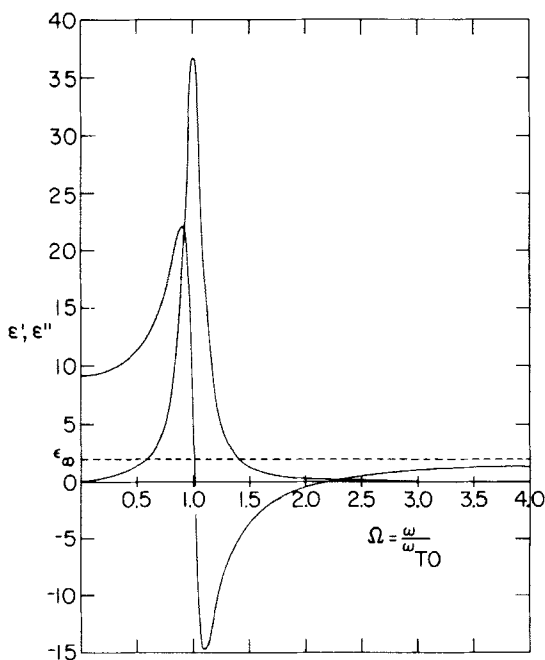


Fig. 17. The complex dielectric function, $\epsilon = \epsilon' + i\epsilon''$, of (11.118) for LiF as a function of frequency Ω . The dielectric function parameters are those given in the caption of Fig. 13 together with $\gamma = 0.20$, a rather large damping constant. Note that $|\epsilon'|$ has maxima for $\Omega \approx 1 \pm \gamma/2$.

(II.13) by $\epsilon_A(\omega)$. Using (II.117) we have then

$$\frac{K^2}{\Omega^2} = \frac{\epsilon_A}{\epsilon_A + \epsilon_I} \quad (\text{II.119})$$

Since ϵ_A is complex, (II.119) will have a solution only if Ω is complex and K is real, K is complex and Ω is real, or both Ω and K are complex. What does this mean? The answer lies in the recognition that anharmonic interactions serve to couple excitations of different frequencies so the excitations at frequency ω_0 contributing to $\epsilon(\omega_0)$ are no longer independent of those contributing to ϵ for frequencies different from ω_0 . Since the dispersion relation relates frequency and wave vector, the possibility of nonindependent wave vectors also arises. So, a complex $\epsilon_A(\omega)$ indicates that the response of the system to an excitation of frequency ω (wave vector k) is spread over a range of frequencies about ω (wave vectors about k) or the excitations have "wave packet" rather than "plane wave" character. This spread in ω and k values can be represented by assigning complex values to these variables. When ω or k is complex, the Fourier-transformed fields \mathfrak{E} and \mathfrak{B} in Section II.A.1 must be thought of as representing superpositions of a group of no longer independent plane waves. In addition, it should be emphasized that the resultant complex nature of ω and k is *not* a consequence of using complex values of ω and k in taking Fourier transforms. These complex quantities are effective values, resulting from the superposition of a spread of real Fourier transform variables ω and k .

The particular wave-packet description selected in solving (II.119) depends on the physical conditions attending the excitation. From (II.2), (II.7), and (II.9) it is apparent from physical considerations that we must have

$$\text{Re } \alpha > 0 \quad (\text{II.120a})$$

$$\text{Re } \alpha_I > 0 \quad (\text{II.120b})$$

and, writing Ω and K as $\Omega = \Omega' + i\Omega''$, $K = K' + iK''$,

$$\Omega'' \leq 0 \quad (\text{II.120c})$$

In addition, for a propagating surface phonon

$$K'' \geq 0 \quad (\text{II.120d})$$

Suppose we consider K real (and thus precisely defined) and Ω complex so that the surface phonon would have the character of a temporal wave

packet. If we then solve (II.119), we find that Ω' is given essentially by (II.19); that is, Ω' starts from 0 for $K=0$ and increases monotonically to $\omega_{s\infty}/\omega_{TO}$ for $K\rightarrow\infty$. Ω'' is also zero for $K=0$ and decreases monotonically to $-\gamma/2$ as $K\rightarrow\infty$. For large K , these frequencies satisfy the familiar equation from the theory without damping, $\epsilon_A + \epsilon_I = 0$.

This is a very interesting result in that there is no low- K cutoff as there was without damping. The solution of (II.119) extends from $K=0$ to $K\rightarrow\infty$ and there is no physical reason for excluding any part of it. For all K , conditions (II.120) are satisfied. When $K \gtrsim 1$ ($k \gtrsim \omega_{TO} \sqrt{\epsilon_I}/c$), this solution looks just as we would expect the damped surface phonon to look. The real part of Ω is very much like the frequency without damping and there is now a finite line width represented by Ω'' . However, without damping the SO phonon did not extend into the radiative region and now it does. To provide a physical picture of what is happening, we consider the equation for the Brewster angle,⁸⁶

$$\tan \theta = \left(\frac{\epsilon_A}{\epsilon_I} \right)^{1/2} \quad (\text{II.121})$$

where θ is the angle measured from the surface normal, and think of ϵ_A as real for the moment.⁸⁷ In the radiative region we can write (see Fig. 10).

$$\sin \theta = \frac{kc}{\omega \sqrt{\epsilon_I}} = \frac{K}{\Omega} \quad (\text{II.122a})$$

so

$$\tan \theta = \frac{K}{(\Omega^2 - K^2)^{1/2}} \quad (\text{II.122b})$$

and (II.121) becomes

$$K^2 = \frac{\epsilon_A \Omega^2}{\epsilon_A + \epsilon_I} \quad (\text{II.123})$$

If we now permit the variables K , Ω , and ϵ_A to assume complex values, this is just (II.119), the surface phonon dispersion relation. Since the generalization of the Brewster angle condition necessary when damping is present leads to the surface phonon dispersion relation and the associated solution satisfies the conditions for the surface phonon, we must conclude that the surface phonon does indeed exist in the radiative region (see Fig. 9) where it and the "Brewster condition" are one and the same. This interpretation suggests an additional possibility. There is another "branch" of the

Brewster angle condition in the radiative region R'_1 of Fig. 9, also described by (II.123).⁸⁷ Does this mean that there is an additional surface phonon branch here? From (II.119), with Ω complex, we find that at $K=0$ there is an additional solution with $\epsilon_A=0$ so $\Omega'=\omega_{LO}/\omega_{TO}$ ($\omega'=\omega_{LO}$) and $\Omega''=-\gamma/2$. With increasing K , Ω' increases monotonically and, as $K\rightarrow\infty$, satisfies

$$\Omega' \rightarrow \left(\frac{\epsilon_\infty + \epsilon_I}{\epsilon_\infty} \right)^{1/2} K \quad (\text{II.124})$$

which is just the very high frequency Brewster condition $\tan\theta=(\epsilon_\infty/\epsilon_I)^{1/2}$. For moderate damping, the frequency Ω' is given essentially by (II.19) with the sign of the second term changed from negative to positive. Ω'' decreases monotonically as K increases, and goes to zero as $K\rightarrow\infty$. Thus this high-frequency Brewster condition must also be thought of as characterizing a surface phonon. So, when the description in terms of temporal wave packets is appropriate, there are two surface mode branches for the half-space, one restricted to the radiative region.

The Brewster angle for ordinary dielectrics is associated with a reflectance minimum for p -polarized light; there is nothing analogous to this condition if the light is s -polarized. Since the SO phonons are associated with p -polarized but not s -polarized fields, the identification of the Brewster condition with a surface phonon is reasonable physically. That the SO phonon should couple strongly to optical radiation in the radiative region can be understood physically from the fact that the fields of the excitation are no longer localized near the surface, neither in the active nor the inactive medium. In contrast to the situation in the nonradiative region, we now have in general $\text{Re}\alpha \ll |k|$ and $|\text{Im}\alpha| \sim |k|$; these relations are valid for α_I as well. Thus the fields associated with these excitations extend well away from the surface and have oscillatory character so the overlap with the fields of incident p -polarized light is large. In this connection it should be noted that the strong surface localization of the active-medium fields for the undamped SO phonons near the low- k termination point ($\omega=\omega_{TO}$, $k=\omega_{TO}c/\sqrt{\epsilon_I}$) does not occur when damping is present. For $\omega/\omega_{TO} \cong 1+\gamma$, α with damping is much like the undamped result. However, as ω decreases below this frequency, $\text{Re}\alpha$ decreases rapidly; $c(\text{Re}\alpha)/\omega_{TO}$ is already small when $\omega/\omega_{TO}=1-\gamma$ (see Fig. 17) and remains small through the radiative region.

It must be emphasized that these radiative region surface phonons are excitations distinct from the virtual modes. In particular, the virtual modes are associated with fields which grow exponentially with increasing distance from the surface while these radiative region surface phonons are associated with fields that decay.

Let us now consider the situation with spatial wave packets, that is, K is complex but Ω is real.⁸⁸ Again the identification of the "Brewster condition" with a surface phonon will occur but in a different way than for the temporal wave-packet description. If we write (II.119) as

$$K = \Omega \left(\frac{\epsilon_A}{\epsilon_A + \epsilon_I} \right)^{1/2} \quad (\text{II.125})$$

then

$$\eta \equiv \frac{K''}{K'} = \frac{\text{Im}(|\epsilon_A|^2 + \epsilon_A \epsilon_I)^{1/2}}{\text{Re}(|\epsilon_A|^2 + \epsilon_A \epsilon_I)^{1/2}} \quad (\text{II.126})$$

where Im denotes the imaginary part and Re the real part. Writing $\epsilon_A = \epsilon' + i\epsilon''$ and taking ϵ_I as real, we find

$$\left(\epsilon' + \frac{\epsilon_I}{2} \right)^2 + \left(\epsilon'' - \frac{1 - \eta^2}{4\eta} \epsilon_I \right)^2 = \left[\frac{\epsilon_I}{4\eta} (\eta^2 + 1) \right]^2 \quad (\text{II.127})$$

In the complex ϵ plane, the lines of fixed η are circles of radius $\epsilon_I(\eta^2 + 1)/4\eta$ centered at $\epsilon' = -\epsilon_I/2$ and $\epsilon'' = (1 - \eta^2)\epsilon_I/4\eta$. We show in Fig. 18 such a complex ϵ plane and the circles of fixed η together with a curve of the dielectric function (II.118) for LiF with $\gamma = 0.20$. This figure, together with the $|K| - \Omega$ relation

$$|K| = \Omega \left(\frac{|\epsilon_A|}{|\epsilon_A + \epsilon_I|} \right)^{1/2} \quad (\text{II.128})$$

provides a clear picture of what happens in this case of spatial wave packets.

For $\Omega \rightarrow 0$, we see from Fig. 18 that $\eta \rightarrow 0$ and from (II.128) that $|K| \rightarrow 0$. As Ω increases from zero, η and $|K|$ both increase but η remains very small (≤ 0.01). As we move through the region of the TO frequency ($\Omega \approx 1$, $\epsilon' \approx 0$, $\epsilon'' \gg 1$, $|K| \approx 1$) nothing dramatic occurs. So, for $\Omega \lesssim 1$,⁸⁹ we see again that the surface phonon and the Brewster condition coincide. The value of Ω in this radiative realm can be obtained to reasonable accuracy from (II.19) by taking $K \approx K'$.

As Ω increases to values somewhat larger than 1, we enter the region in which the SO phonons occur when there is no damping. The dependence of Ω on K' is now much like that for the undamped phonon and, from Fig. 18, the effects of damping continue small ($\eta \ll 1$) until the frequency

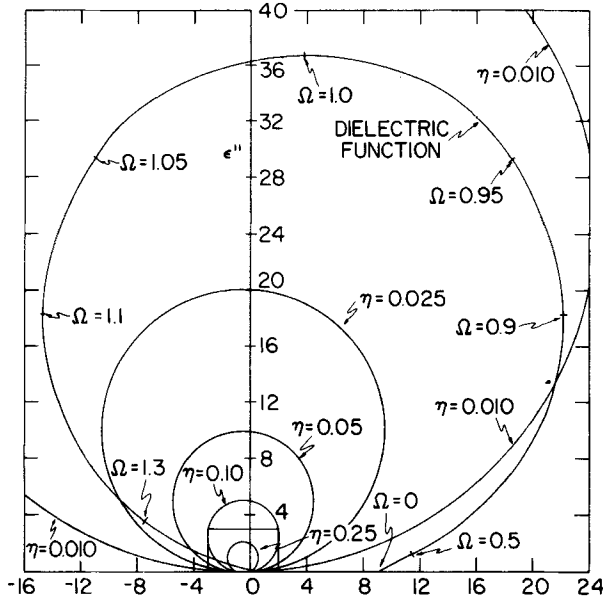


Fig. 18. The complex ϵ plane showing the circles of constant η for $\epsilon_f = 1$ [see (II.126)] and the dielectric function of Fig. 17. Various frequencies are marked on the dielectric function curve.

approaches that corresponding to the condition $|\epsilon_A| \cong -\epsilon_f$. What then occurs is striking and better appreciated from Fig. 19 which is an expanded version of that section of Fig. 18 shown in the box. The damping becomes very strong ($\eta \sim 1$) and $|K|$ reaches a maximum. This maximum value of $|K|$ is, for $\gamma \ll 1$,

$$|K|_{\max} \cong \frac{1}{\epsilon_\infty + \epsilon_f} \left(\frac{\epsilon_0 - \epsilon_\infty}{\gamma} \right)^{1/2} \quad (\text{II.129})$$

at which point $\eta \cong 1$ and $\Omega \cong \omega_{s\infty}/\omega_{\text{TO}}$, with $\omega_{s\infty}$ given by (II.18). The appearance of this maximum in $|K|$ indicates that as Ω increases to a value above $\omega_{s\infty}/\omega_{\text{TO}}$, the dispersion curve bends back to that $d\Omega/dK' < 0$. The frequency region where this derivative is negative extends roughly from $\Omega = \omega_{s\infty}/\omega_{\text{TO}}$, the asymptotic frequency for the undamped phonon, to $\omega_{\text{LO}}/\omega_{\text{TO}}$.

As the frequency increases beyond that for which $|K|$ is a maximum, η continues to increase so $\eta > 1$. However, η itself reaches a maximum, as is clear from Fig. 19, for a frequency Ω between $\omega_{s\infty}/\omega_{\text{TO}}$ and $\omega_{\text{LO}}/\omega_{\text{TO}}$. For

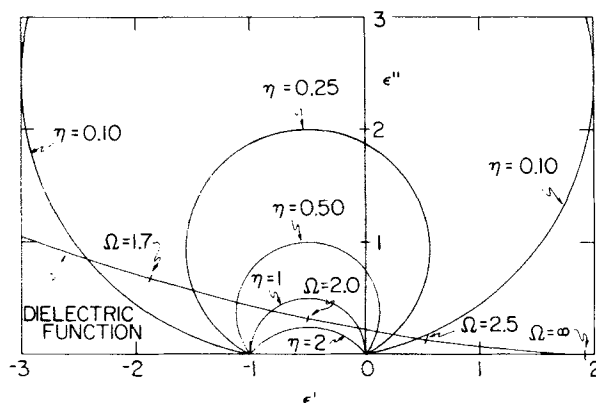


Fig. 19. An expanded version of the part of Fig. 18 within the box. The condition $\epsilon(\omega) = -1$ occurs for $\Omega = 1.88$ if there is no damping.

$\Omega \cong \omega_{LO}/\omega_{TO}$, $\eta \cong 1$ again and $|K|$ is at a minimum of value

$$|K|_{\min} \cong \left(\frac{\epsilon_0}{\epsilon_\infty} \right)^{1/2} \left\{ \frac{\gamma \epsilon_\infty (\epsilon_0 \epsilon_\infty)^{1/2}}{\epsilon_I (\epsilon_0 - \epsilon_\infty)} \right\}^{1/2} \quad (\text{II.130})$$

if $\gamma \ll 1$. Since $\Omega \cong (\epsilon_0/\epsilon_\infty)^{1/2}$ when $|K| = |K|_{\min}$, this point of minimum $|K|$ will usually be in the radiative region. A further increase of Ω is associated with $|K|$ increasing and η decreasing so the dispersion curve approaches the Brewster condition as $\Omega \rightarrow \infty$. A sketch of Ω as a function of K' is shown in Fig. 20.

To our knowledge, a dispersion curve of the form shown in Fig. 20 has not been seen experimentally.^{89a} Indeed, a complete picture of which experimental conditions are associated with the various descriptions of damping does not yet exist. This lengthy discussion of the spatial wave-packet situation has been included to emphasize the interesting and peculiar relation between the surface phonons and the Brewster condition and to point up the complexities which can result in attempting to incorporate losses into even a relatively simple theory.

The final possibility discussed above, that of both Ω and K complex together with a physical requirement linking the two,⁹⁰ has not as yet been investigated.

We saw above that undamped SO phonons are associated with energy transport in the direction of k . When damping is present, there is an additional flow of energy into the active medium.⁴⁶

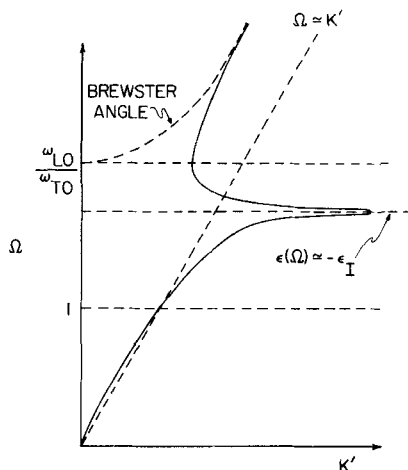


Fig. 20. A sketch of the real frequency $\Omega = \omega/\omega_{TO}$ as a function of the real part (K') of the complex dimensionless wave vector. This curve was constructed using Figs. 18 and 19 and (11.128). The high-frequency branch of the Brewster condition is marked. The low-frequency branch of the Brewster condition coincides with the dispersion curve for $\Omega < 1$. The light line is marked $\Omega \approx K'$ since the light line is no longer sharply defined when damping is included.

2. Slab

No calculations of the surface phonon properties when damping is present have been made. For the temporal wave-packet description, it seems clear that the FK phonon modes will be broadened but not changed significantly. In the radiative region, the surface phonons associated with the Brewster condition should be just as they were for the half-space, if the inactive media on the two sides of the active slab have the same dielectric functions, since the Brewster angle condition is then independent of thickness.⁹¹ The fact that *both* undamped polaritons for this symmetric case approach ω_{TO} along the effective light line $\omega = ck/\sqrt{\epsilon_I}$ is consistent with this suggestion.

The effect of a complex dielectric function on the radiative surface mode is discussed in Ref. 60.

3. Sphere

In this case the inclusion of anharmonic effects is not difficult. There being no wave vector in the problem, the change to a complex dielectric function means only that the already complex frequencies of the virtual surface modes will be modified somewhat. In particular, the imaginary part of the frequency, which is negative, will become larger in magnitude.

This is clear physically. The magnitude of the imaginary part of the frequency is related to the line width of the excitation. When the dielectric function is real, this line width is all due to radiative damping. When anharmonic effects are present there is an additional damping mechanism so the line will be further broadened, or the magnitude of the imaginary part of the frequency will increase. For moderate damping, the real part of the frequency will not change much from that of the harmonic case.

For a very small sphere, the equation describing the surface modes including anharmonicity is

$$\epsilon_A(\omega) = -\frac{l+1}{l}\epsilon_l \quad (\text{II.131})$$

a simple generalization of (II.83). Using (II.118) for ϵ_A , we have immediately that the now complex frequencies of these modes are

$$\frac{\omega}{\omega_{\text{TO}}} = \frac{\omega_l}{\omega_{\text{TO}}} - i\frac{\gamma}{2} \quad (\text{II.132})$$

where ω_l is given by (II.84).

E. Polar Semiconductors and Magnetic Field Effects

The theory described above is applicable to all polar crystals having two ions per unit cell and cubic symmetry. Since this includes polar semiconductors such as InSb and CdO, a special treatment of the surface phonons for these materials is unnecessary. However, these semiconductors can be rendered *n*-type by appropriate doping and the character of the surface excitations can then change significantly. These changes are a consequence of the electron-phonon interaction which can here be thought of as an interaction between the optical phonons and the plasma associated with the added electrons which can be considered free within the effective mass approximation. On physical grounds, it is clear that this interaction will be strongest when the doping is such that the effective plasma frequency ω_p is in the frequency range of the optical phonons. As a result of the interaction, the surface excitations have both SO phonon and surface plasmon character.

These mixed excitations can be modified significantly by placing the system in a magnetic field. If the strength of this field is adjusted so that the cyclotron frequency ω_c of the essentially free carriers satisfies $\omega_c \sim \omega_p \sim \omega_{\text{LO}}$, the behavior of the resulting excitations is particularly interesting. We examine these problems now, first without and then with a magnetic field present.

Suppose we take a polar semiconductor described by the dielectric function (I.9) and dope it such that the conduction electron density is n . Assuming that these conduction electrons populate a simple parabolic

energy band which can be characterized by an effective mass m^* , the undamped local dielectric function for the system can be written as^{38,92-94}

$$\epsilon(\omega) = \epsilon_{\infty} \left\{ 1 + \frac{(\epsilon_0 - \epsilon_{\infty})\omega_{TO}^2/\epsilon_{\infty}}{\omega_{TO}^2 - \omega^2} - \frac{\omega_p^2}{\omega^2} \right\} \quad (II.133)$$

where

$$\omega_p^2 = \frac{4\pi ne^2}{m^* \epsilon_{\infty}} \quad (II.134)$$

is the plasma frequency of the free carriers of charge $-e$.⁹⁵ The dielectric function (II.133) can then be used in (II.11) to find the undamped surface modes for a half-space in contact with an inactive medium of dielectric function ϵ_f . In the large- k limit, or if retardation is neglected, the surface modes satisfy the condition $\epsilon(\omega) = -\epsilon_f$ which now yields the frequencies⁹⁶

$$\omega_{B,A}^2 = \frac{1}{2}(\omega_{s\infty}^2 + \omega_{p\infty}^2) \pm \left[\frac{1}{4}(\omega_{s\infty}^2 + \omega_{p\infty}^2)^2 - \omega_{TO}^2 \omega_{p\infty}^2 \right]^{1/2} \quad (II.135)$$

where ω_B is the larger frequency, $\omega_{s\infty}$ is given by (II.18), and

$$\omega_{p\infty} = \frac{\omega_p}{(1 + \epsilon_f/\epsilon_{\infty})^{1/2}} \quad (II.136)$$

A sketch of the dielectric function (II.133), qualitatively correct for both $\omega_{p\infty} > \omega_{s\infty}$ and $\omega_{s\infty} > \omega_{p\infty}$, is shown in Fig. 21. The frequencies $\omega_{A,B}$ are indicated in this sketch.

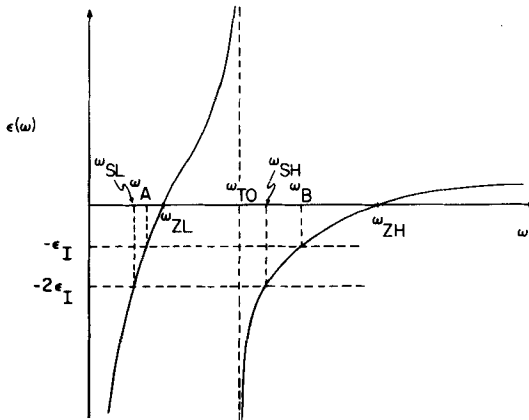


Fig. 21. A sketch of the dielectric function (11.133) for an n -type polar semiconductor as a function of frequency. The frequencies $\omega_{B,A}$ [(11.135)], solutions of $\epsilon(\omega) = -\epsilon_f$, are marked as are the frequencies $\omega_{SH,SL}$ solutions of $\epsilon(\omega) = -2\epsilon_f$, and the frequencies $\omega_{ZH,ZL}$ for which $\epsilon(\omega) = 0$.

This system has two surface excitation branches, a consequence of the fact that two "intrinsic" surface excitations now occur. One "intrinsic" excitation is the SO phonon occurring at the frequency which is the solution of (II.11) with the free carrier term [the last term in braces in (II.133)] neglected; the other is the surface plasmon, also described by (II.11) but now with the phonons, represented by the middle term in (II.133), neglected.^{14-17,33,97} In the limit of large k , the frequency of the former is $\omega_{s\infty}$ and that of the latter is $\omega_{p\infty}$. Although these two excitations arise from distinctly different physical origins, the SO phonon from the oscillating ionic dipole moment and the surface plasmon from the motion of the free electrons with respect to the net positive background ionic charge, they have, for the range of k values permitted in this local theory, essentially identical mathematical descriptions and give rise to macroscopic electromagnetic fields of the same form. In particular, the electric field for both is that of Fig. 3. In a system which can support the two "intrinsic" excitations, they will then interact strongly and the frequencies $\omega_{B,A}$ are those of the resultant mixed-character excitations.

The well-known mode repulsion effect occurs in this problem since ω_B [the higher frequency solution of (II.135)] is greater than the larger of $\omega_{p\infty}$ and $\omega_{s\infty}$, the "intrinsic" mode frequencies, while ω_A is less than the smaller. We note that for $\omega_{p\infty}/\omega_{s\infty} \rightarrow 0$,

$$\begin{aligned} \omega_B &\rightarrow \omega_{s\infty} \\ \omega_A &\rightarrow \frac{\omega_p}{\{(\epsilon_0 + \epsilon_I)/\epsilon_\infty\}^{1/2}} < \omega_{p\infty} \end{aligned} \quad (\text{II.137})$$

while for $\omega_{s\infty}/\omega_{p\infty} \rightarrow 0$,

$$\begin{aligned} \omega_B &\rightarrow \omega_{p\infty} \\ \omega_A &\rightarrow \omega_{\text{TO}} < \omega_{s\infty} \end{aligned} \quad (\text{II.138})$$

so $(\omega_B - \omega_A) > |\omega_{p\infty} - \omega_{s\infty}|$. The frequencies $\omega_{B,A}$ are shown for InSb as a function of the free carrier concentration in Fig. 22.

From Fig. 21, we see that the dielectric function $\epsilon(\omega)$ satisfies $\epsilon(\omega) < -\epsilon_I$ for $\omega < \omega_A$ and $\omega_{\text{TO}} < \omega < \omega_B$. Thus, as k decreases from the asymptotic range, the excitation frequencies will decrease from the asymptotic frequencies $\omega_{B,A}$. The higher frequency mode will terminate at $\omega = \omega_{\text{TO}}$ where $k = \omega_{\text{TO}} \sqrt{\epsilon_I} / c$. Near the termination point, this mode has much the same character as the SO phonon with no free carriers present, a con-

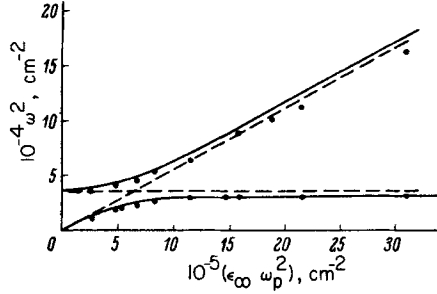


Fig. 22. The asymptotic frequencies $\omega_{B,A}^2$ (solid lines) for a half-space of *n*-type InSb ($\epsilon_0 = 17.7$, $\epsilon_\infty = 15.7$, $\omega_{TO} = 179 \text{ cm}^{-1} = 3.37 \times 10^{13} \text{ sec}^{-1}$) adjacent to a medium for which $\epsilon_f = 2.2$ as a function of $(\epsilon_\infty \omega_p^2)$. The dashed lines are the mode frequencies which would result if there were no surface plasmon-surface polariton interaction, $\omega = \omega_{p\infty}$ and $\omega = \omega_{s\infty}$. The points are experimental results. These experiments were actually performed with the InSb in vacuum, but were done using the ATR technique (see Section V.A.3) under conditions such that the results can be interpreted as the asymptotic frequencies for the InSb adjacent to a medium with $\epsilon_f = 2.2$. (Reprinted from Reshina et al.¹⁴⁵)

sequence of the phonon-related singularity in $\epsilon(\omega)$ at $\omega = \omega_{TO}$. The lower frequency mode will decrease from ω_A and approach zero as $k \rightarrow 0$ on the low-frequency side of the line $\omega = ck/\sqrt{\epsilon_f}$, thus reflecting surface plasmon character for low k as a result of the low-frequency singularity in $\epsilon(\omega)$ due to the free carriers. These features are illustrated in Fig. 23 for InSb doped so that $\omega_{p\infty}/\omega_{s\infty} = 1.42$ and $\epsilon_f = 1$.

If the active medium is a slab, the surface excitations are described by the theory of Section II.A.2. There now occur in general four excitation branches resulting from mixtures of the two "intrinsic" phonons whose electric fields are roughly sketched in Figs. 6e and 6f and the two "intrinsic" plasmons with fields of the same form. If the inactive media on the two sides of the active slab both have the dielectric function ϵ_f , two excitations will occur for large k at each of ω_A and ω_B . As k decreases the two excitations with asymptotic frequency ω_B will remain in the region of Fig. 21 above ω_{TO} where $\epsilon < 0$ and both will terminate at $\omega = \omega_{TO}$ with $k = \omega_{TO}c/\sqrt{\epsilon_f}$. The two excitations whose asymptotic frequency is ω_A will remain in the frequency range of Fig. 21 below ω_{TO} where ϵ is negative and both will approach zero as $k \rightarrow 0$. If the inactive media on the two sides of the slab have different dielectric functions as in Fig. 7, there will still be four surface excitation branches, two in each of the regions of Fig. 21 where $\epsilon < 0$. However, there will now be four asymptotic frequencies, two from each of the equations $\epsilon(\omega) = -\epsilon_{lu}$ and $\epsilon(\omega) = -\epsilon_{ld}$ (see Fig. 8b). The two excitations in the upper frequency region where $\epsilon < 0$ will terminate at

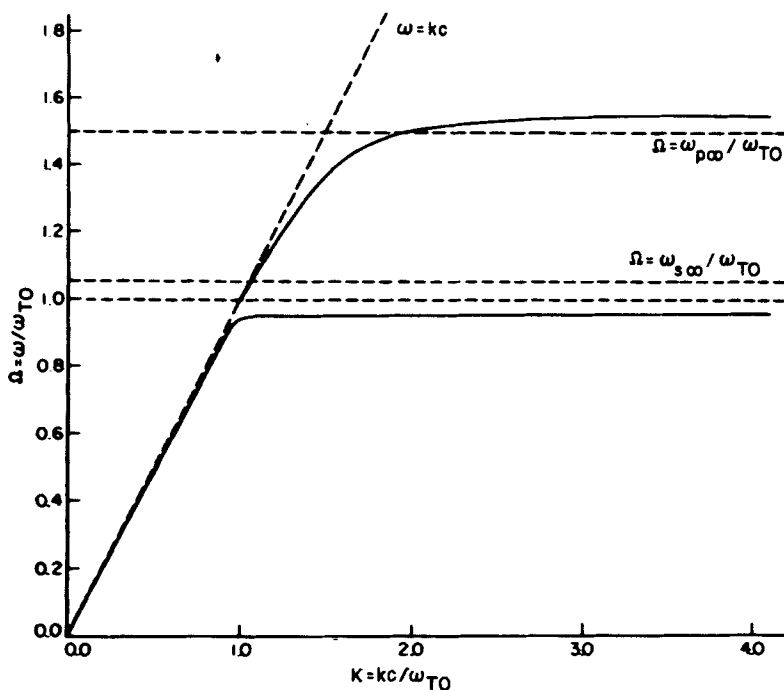


Fig. 23. Dispersion curves for coupled surface modes including retardation for semiinfinite *n*-type InSb ($\epsilon_0 = 17.9$, $\epsilon_\infty = 15.7$) in vacuum. The InSb is doped so that $\omega_{p\infty}/\omega_{s\infty} = 1.42$ ($\omega_{p\infty}/\omega_{TO} = 1.50$). (Reprinted from Wallis and Brion.⁹⁴)

$\omega = \omega_{TO}$, one at $k = \omega_{TO}\sqrt{\epsilon_{lu}}/c$ and the other at $k = \omega_{TO}\sqrt{\epsilon_{ld}}/c$. The two excitations in the lower frequency region for which $\epsilon < 0$ will approach zero as $k \rightarrow 0$, one near the line $\omega = ck/\sqrt{\epsilon_{lu}}$ and the other near the line $\omega = ck/\sqrt{\epsilon_{ld}}$.

Wallis and Brion⁹⁴ examined these modes for InSb with $\epsilon_{lu} = \epsilon_{ld} = 1$ and neglecting retardation. Their results are shown in Fig. 24. The upper (lower) mode in each asymptotically degenerate pair results from (II.114a) [(II.114b)] and the active-medium electric field is that of Fig. 6f (Fig. 6e). Since the two types of modes whose fields are represented by Figs. 6e and 6f are orthogonal, modes of a given type cannot cross, whereas modes of different types can. The consequences of this requirement are clearly evident in Fig. 24.

A study of the surface excitations of a sphere of material described by the dielectric function (II.133) has not been made. However, for small spheres or when retardation is ignored, the discussion of Section II.B can easily be generalized to this case. If the active sphere is embedded in an

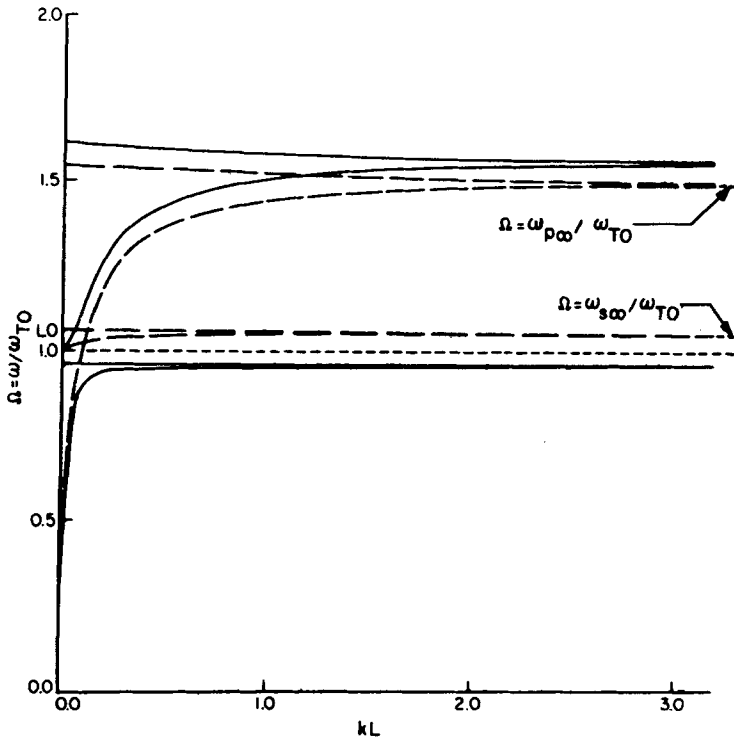


Fig. 24. Frequencies $\Omega = \omega/\omega_{TO}$ of the surface modes (retardation neglected) for slabs of *n*-type InSb in vacuum as a function of (kL) , where L is the slab thickness. The dielectric function parameters and the doping level are given in the caption of Fig. 23. The full lines are the coupled modes and the lines of long dashes the "intrinsic" uncoupled modes resulting if surface plasmon-surface polariton interaction is ignored. Note that the uncoupled surface polaritons are asymptotic to $\omega_{s\infty}$ and the uncoupled surface plasmons to $\omega_{p\infty}$. The position of $\Omega = \omega_{LO}/\omega_{TO}$ is denoted by LO along the ordinate. (Reprinted from Wallis and Brion.⁹⁴)

inactive medium of dielectric function ϵ_f , there will now occur two bands of surface modes with frequencies given by (II.83). These modes will occur in the frequency ranges $\omega_{SL} \leq \omega < \omega_A$ and $\omega_{SH} \leq \omega < \omega_B$, where ω_{SL} and ω_{SH} , solutions of $\epsilon(\omega) = -2\epsilon_f$, are indicated in Fig. 21.

The effects of damping on these mixed excitations have not been investigated. From the discussion of Section II.D, some comments can be made concerning the half-space. In the temporal wave-packet description, the frequency of both modes in the nonradiative region will have a negative imaginary part corresponding to a broadened line. For moderate damping the real parts of the frequencies will not differ much from the undamped values. The undamped mode which terminates at $\omega = \omega_{TO}$

should now continue into the radiative region and again be identified with the Brewster condition. Note that this mode will here occur for $\theta=0$ near the lower frequency for which $\epsilon=0$ in Fig. 21, markedly different behavior than occurs in the pure phonon case. Another radiative region surface excitation will have much the same character as it did without free carriers present. That is, it will occur for $\theta=0$ at the upper frequency zero of $\epsilon(\omega)$ in Fig. 21 and increase with increasing angle (or k) to occur for large frequency, $\omega \gg \omega_{s\infty}$ and $\omega_{p\infty}$, at $\theta = \tan^{-1}(\epsilon_{\infty}/\epsilon_f)^{1/2}$. Again we recognize here the Brewster condition.⁹⁸

It is interesting to note that Wallis and Brion⁹⁴ pointed out the existence of a radiative region solution to their surface mode equations, but they did not discuss its character. Presumably this is the upper frequency excitation associated with the Brewster condition.

The case of the spatial wave-packet description can be discussed as it was in Section II.D. In view of the uncertainty regarding the applicability of this description, we will not do so here.

Let us now add a static magnetic field to the half-space problem. We continue to use the geometry used above; the active medium is taken to fill the region $z > 0$ and the inactive medium of dielectric function ϵ_f to fill the region $z < 0$. The static magnetic field \mathbf{B}_0 lies in the z - y plane and is directed at an angle θ from the z -axis. Since the character of the surface waves depends on the orientation of the wave vector with respect to the magnetic field, we take the surface wave vector \mathbf{k} to lie in the x - y plane at an angle ξ from the x -axis. These geometrical arrangements are shown in Fig. 25.

The dielectric tensor $\epsilon(\omega)$ for the active medium then is⁹⁹

$$\epsilon(\omega) = \begin{bmatrix} \epsilon_1 & -i\epsilon_2 \cos \theta & +i\epsilon_2 \sin \theta \\ +i\epsilon_2 \cos \theta & \epsilon_1 \cos^2 \theta + \epsilon_3 \sin^2 \theta & (\epsilon_3 - \epsilon_1) \sin \theta \cos \theta \\ -i\epsilon_2 \sin \theta & (\epsilon_3 - \epsilon_1) \sin \theta \cos \theta & \epsilon_1 \sin^2 \theta + \epsilon_3 \cos^2 \theta \end{bmatrix} \quad (\text{II.139})$$

where

$$\epsilon_1 = \epsilon_{\infty} \left[1 + \frac{\omega_p^2}{\omega_c^2 - \omega^2} + \frac{(\epsilon_0 - \epsilon_{\infty})\omega_{\text{TO}}^2/\epsilon_{\infty}}{\omega_{\text{TO}}^2 - \omega^2} \right] \quad (\text{II.140})$$

$$\epsilon_2 = \frac{\epsilon_{\infty}(\omega_c/\omega)\omega_p^2}{\omega_c^2 - \omega^2} \quad (\text{II.141})$$

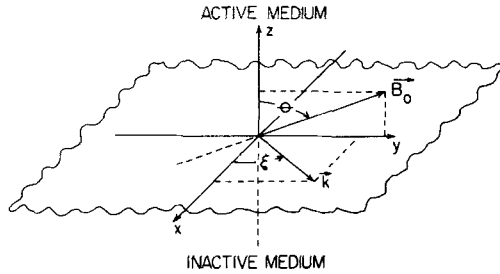


Fig. 25. A sketch showing the boundary separating the active medium ($z > 0$) from the inactive medium ($z < 0$) together with the orientations of the static magnetic field \mathbf{B}_0 and the wave vector \mathbf{k} .

ϵ_3 is given by (II.133), ω_p by (II.134), and the cyclotron frequency ω_c by

$$\omega_c = \frac{eB_0}{m^*c} \quad (\text{II.142})$$

If we neglect retardation, and thereby look only for the nonradiative asymptotic solutions, the equations we must satisfy are $\nabla \times \mathbf{E} = 0$ and (II.1a) with

$$\mathbf{D}(\mathbf{r}, \omega) = \epsilon(\omega) \cdot \mathbf{E}(\mathbf{r}, \omega) \quad (\text{II.143})$$

As discussed in Section II.C, we can in this nonretarded case introduce the potential Φ which then yields \mathbf{E} via $\mathbf{E} = -\nabla\Phi$. So, requirement (II.1a) becomes

$$\nabla \cdot \{ \epsilon(\omega) \cdot \nabla \Phi \} = 0 \quad (\text{II.144})$$

Writing Φ for the surface excitations as

$$\Phi = \begin{cases} \Phi_0 \exp[-\alpha z + i(k_x x + k_y y - \omega t)], & z > 0 \\ \Phi_0 \exp[\alpha_I z + i(k_x x + k_y y - \omega t)], & z < 0 \end{cases} \quad (\text{II.145})$$

and using (II.144) we find

$$\alpha_I^2 = k_x^2 + k_y^2 = k^2 \quad (\text{II.146a})$$

and¹⁰⁰

$$\alpha^2 = \frac{\epsilon_{11}k_x^2 + \epsilon_{22}k_y^2 + 2i\epsilon_{23}\alpha k_y}{\epsilon_{33}} \quad (\text{II.146b})$$

With no damping, ϵ_1 , ϵ_2 , k_x , k_y , and ω are all real and so α is, in general, complex. In addition, the value of α depends on the sign of k_y , a condition sometimes described as nonreciprocal. To find the dispersion relation for the surface excitations we must impose the boundary condition D_z continuous at $z=0$. This leads to

$$-i\epsilon_{31}k_x - i\epsilon_{32}k_y - \alpha\epsilon_{33} = \alpha_I\epsilon_I \quad (\text{II.147})$$

Equation (II.147) with α given by (II.146b) has been solved only for special cases.⁹⁹

1. $\mathbf{B}_0 \perp$ surface so $\theta=0$. In this case we have

$$\alpha^2 = k^2 \left(\frac{\epsilon_1}{\epsilon_3} \right) \quad (\text{II.148a})$$

and the boundary condition equation is

$$\alpha = - \frac{\alpha_I \epsilon_I}{\epsilon_3} \quad (\text{II.148b})$$

Equations (II.148) together then yield

$$(\epsilon_1 \epsilon_3)^{1/2} = -\epsilon_I \quad (\text{II.149})$$

so ϵ_1 and ϵ_3 must be of the same sign. Together with (II.148b), this means that ϵ_1 and ϵ_3 must both be negative.

Comparing ϵ_1 and ϵ_3 , we see that there will be:

two solutions for $\omega_c < \omega_{ZL}$: $\omega_A < \omega < \omega_{ZL}$ and $\omega_B < \omega < \omega_{ZH}$

one solution for $\omega_{ZL} < \omega_c < \omega_{TO}$: $\omega_B < \omega < \omega_{ZH}$

two solutions for $\omega_{TO} < \omega_c < \omega_{ZH}$: $\omega_{TO} < \omega < \omega_{s\infty}$ and $\omega_B < \omega < \omega_{ZH}$

one solution for $\omega_{ZH} < \omega_c$: $\omega_{TO} < \omega < \omega_{s\infty}$.

The frequencies $\omega_{B,A}$ are given by (II.135) and the frequency $\omega_{ZL}(\omega_{ZH})$ is the lower (upper) frequency at which the dielectric function (II.133) is zero. These frequencies are marked in Fig. 21.

Curves of the actual solutions to (II.149) as a function of ω_c are shown for InSb in Fig. 26. Since these are the asymptotic solutions, their number is the minimum number of surface excitation branches. Of course, the unretarded theory cannot yield the radiative region excitations, but there may also be additional nonradiative excitations which do not extend to asymptotic k values.

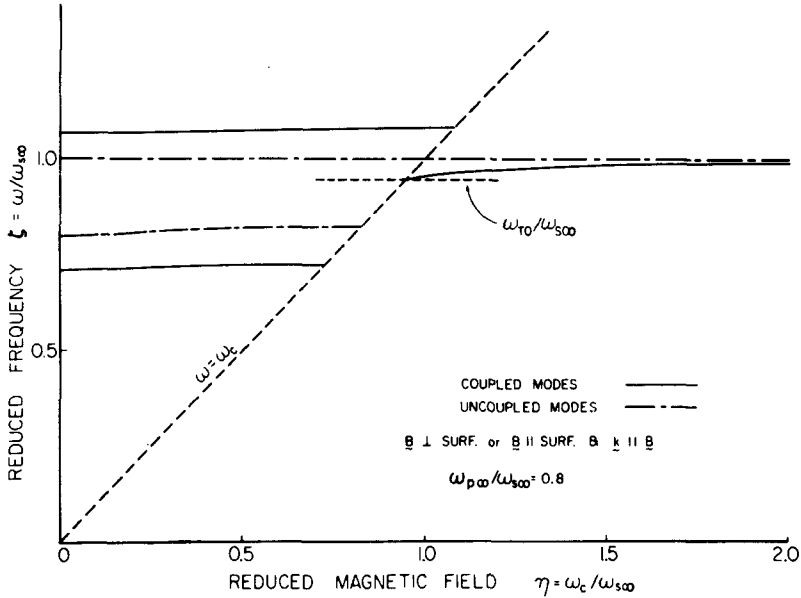


Fig. 26. Coupled mode frequencies $\zeta = \omega/\omega_{s\infty}$ (retardation neglected) as a function of the reduced magnetic field $\eta = \omega_c/\omega_{s\infty}$ for semiinfinite *n*-type InSb ($\epsilon_0 = 17.9, \epsilon_\infty = 15.7, \omega_{TO} = 3.37 \times 10^{13} \text{ sec}^{-1}$) in vacuum. The InSb has been doped so that $\omega_{p\infty}/\omega_{s\infty} = 0.8$. (Reprinted from Brion et al.⁹⁹)

2. $\mathbf{B}_0 \parallel$ surface so $\theta = \pi/2$ and $\mathbf{k} \parallel \mathbf{B}_0$ so $k_x = 0$ and $k = k_y$. Equation (II.146b) now becomes

$$\alpha^2 = \frac{k^2 \epsilon_3}{\epsilon_1} \quad (\text{II.150a})$$

and (II.147) is

$$\alpha = \frac{-\epsilon_I \alpha_I}{\epsilon_1} \quad (\text{II.150b})$$

These equations together yield again (II.149) so the solutions are just as they were for case 1 even though α in the two cases is different.

3. $\mathbf{B}_0 \parallel$ surface so $\theta = \pi/2$ and $\mathbf{k} \perp \mathbf{B}_0$. Equations (II.146b) and (II.147) now are

$$\alpha^2 = k_x^2 = k^2 \quad (\text{II.151a})$$

and

$$\epsilon_2 k_x - \alpha \epsilon_1 = \alpha_I \epsilon_I \quad (\text{II.151b})$$

The dispersion relation then becomes

$$\epsilon_1 - \epsilon_2(\operatorname{sgn} k_x) = -\epsilon_I \quad (\text{II.152})$$

where

$$\operatorname{sgn} a = \begin{cases} +1, & a > 0 \\ -1, & a < 0 \end{cases} \quad (\text{II.153})$$

The nonreciprocal character of the dispersion curve (II.152) is apparent; that is, the dispersion curve depends on the sign of k_x . We note also that α is independent of the dielectric functions and the sign of k_x . In Fig. 27 are shown the solutions of (II.152) for InSb doped so that $\omega_{p\infty}/\omega_{s\infty} = 2.0$ and

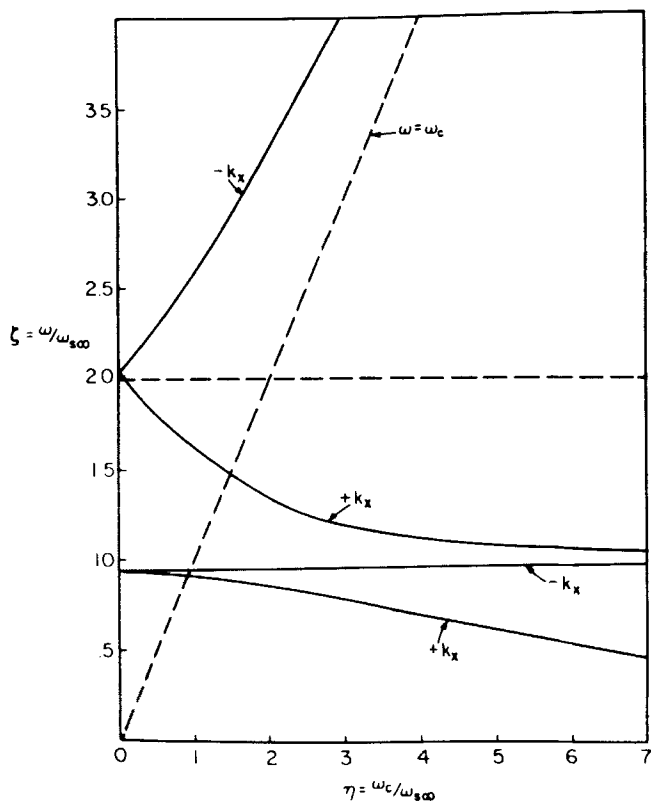


Fig. 27. Coupled mode frequencies $\zeta = \omega/\omega_{s\infty}$ (retardation neglected) as a function of the reduced magnetic field $\eta = \omega_c/\omega_{s\infty}$ for semiinfinite n -type InSb in vacuum. The InSb has been doped so that $\omega_{p\infty}/\omega_{s\infty} = 2.0$. The magnetic field \mathbf{B}_0 is parallel to the surface ($+y$ direction) and \mathbf{k} is perpendicular to \mathbf{B}_0 . (Reprinted from Brion et al.⁹⁹)

$\epsilon_I = 1$. For $k_x > 0$, the upper frequency plasmon-like mode interacts strongly with the lower frequency phonon-like mode. This interaction is weak if $k_x < 0$.

Including retardation in this problem involves, in general, considerable complexity.^{99,101} It turns out to be somewhat simpler mathematically to consider the surface wave as propagating along a Cartesian axis and retain the generality by modifying the dielectric tensor as the physical conditions vary. In anticipation of Section III we now consider the general dielectric tensor

$$\epsilon(\omega) = \begin{bmatrix} \epsilon_{xx} & \epsilon_{xy} & \epsilon_{xz} \\ \epsilon_{yx} & \epsilon_{yy} & \epsilon_{yz} \\ \epsilon_{zx} & \epsilon_{zy} & \epsilon_{zz} \end{bmatrix} \quad (\text{II.154})$$

with no symmetry requirements, and write the electric fields in the two media as

$$\mathbf{E}(x, z, t) = \begin{cases} \mathbf{E}^0 \exp[-\alpha z + i(kx - \omega t)], & z > 0 \\ \mathbf{E}_I^0 \exp[\alpha_I z + i(kx - \omega t)], & z < 0 \end{cases} \quad (\text{II.155a})$$

$$(\text{II.155b})$$

thereby choosing the x -axis as the propagation direction. From (II.1) we can then write the wave equation as

$$\nabla \times (\nabla \times \mathbf{E}) = \frac{\omega^2}{c^2} \mathbf{D} \quad (\text{II.156})$$

Using (II.156), (II.155), (II.154), and (II.143), the equations which determine α and α_I are

$$\alpha_I^2 - k^2 + \epsilon_I \frac{\omega^2}{c^2} = 0 \quad (\text{II.157a})$$

and

$$\begin{aligned} & \alpha^2 \frac{\omega^2}{c^2} F_1(\epsilon) - k^2 \frac{\omega^2}{c^2} F_2(\epsilon) + \left(\frac{\omega^2}{c^2} \right)^2 F_3(\epsilon) + ik\alpha \frac{\omega^2}{c^2} F_4(\epsilon) + (\alpha^2 - k^2) \\ & \times \left[\alpha^2 \epsilon_{zz} - k^2 \epsilon_{xx} + \frac{\omega^2}{c^2} F_5(\epsilon) - ik\alpha (\epsilon_{zx} + \epsilon_{xz}) \right] = 0 \end{aligned} \quad (\text{II.157b})$$

where

$$F_1(\epsilon) = \epsilon_{zz}\epsilon_{yy} - \epsilon_{zy}\epsilon_{yz} \quad (\text{II.158a})$$

$$F_2(\epsilon) = \epsilon_{xx}\epsilon_{yy} - \epsilon_{xy}\epsilon_{yx} \quad (\text{II.158b})$$

$$F_3(\epsilon) = \epsilon_{xx}\epsilon_{yy}\epsilon_{zz} + \epsilon_{xy}\epsilon_{yz}\epsilon_{zx} + \epsilon_{yx}\epsilon_{xz}\epsilon_{zy} \\ - \epsilon_{yy}\epsilon_{xz}\epsilon_{zx} - \epsilon_{xx}\epsilon_{zy}\epsilon_{yz} - \epsilon_{zz}\epsilon_{xy}\epsilon_{yx} \quad (\text{II.158c})$$

$$F_4(\epsilon) = \epsilon_{xy}\epsilon_{yz} + \epsilon_{zy}\epsilon_{yx} - \epsilon_{yy}\epsilon_{zx} - \epsilon_{xz}\epsilon_{zy} \quad (\text{II.158d})$$

and

$$F_5(\epsilon) = \epsilon_{xx}\epsilon_{zz} - \epsilon_{xz}\epsilon_{zx} \quad (\text{II.158e})$$

The next step would be to use the usual boundary conditions on \mathbf{B} , \mathbf{E} and \mathbf{D} at $z=0$ and the requirements $\nabla \cdot \mathbf{D} = \nabla \cdot \mathbf{B} = 0$ to find the equation which, together with (II.157), determines the dispersion relation. This is essentially impossible for so general a case and without a specific system in mind since the electric and magnetic fields in the active medium will involve a sum of terms of the form (II.155a), one for each of the allowed values of α in (II.157b). This problem is discussed further in Section III.

We return now to the semiconductor in a magnetic field. If the magnetic field is either parallel or perpendicular to the surface there will be only one allowed solution of (II.157b). Suppose $\mathbf{B}_0 \parallel$ surface and $\mathbf{k} \perp \mathbf{B}_0$.¹⁰² We can then use for $\epsilon(\omega)$ (II.139) with $\theta = \pi/2$ so \mathbf{B}_0 is in the y direction and \mathbf{k} is in the x direction. From (II.157b) we find

$$\alpha^2 = k_x^2 - \frac{\omega^2}{c^2} \left(\epsilon_1 - \frac{\epsilon_2^2}{\epsilon_1} \right) \quad (\text{II.159})$$

The y components of the fields in (II.155) are now zero so $\nabla \cdot \mathbf{D} = 0$ yields

$$\frac{E_z^0}{E_x^0} = \frac{i(k_x\epsilon_1 + \alpha\epsilon_2)}{k_x\epsilon_2 + \alpha\epsilon_1} \quad (\text{II.160a})$$

and

$$\frac{E_{Iz}^0}{E_{Ix}^0} = -\frac{ik_x}{\alpha_I} \quad (\text{II.160b})$$

while the continuity of D_z and E_x give

$$-i\epsilon_2 E_x^0 + \epsilon_1 E_z^0 = \epsilon_I E_{Iz}^0 \quad (\text{II.161a})$$

and

$$E_x^0 = E_{Ix}^0 \quad (\text{II.161b})$$

so

$$-i\epsilon_2 + \epsilon_1 \frac{E_z^0}{E_x^0} = \epsilon_I \frac{E_{Iz}^0}{E_{Ix}^0} \quad (\text{II.162})$$

Now using (II.160) in (II.162) gives the dispersion relation

$$\alpha_I(\epsilon_1^2 - \epsilon_2^2) = -\epsilon_I(k_x\epsilon_2 + \alpha\epsilon_1) \quad (\text{II.163})$$

We note again the appearance of nonreciprocal effects.

The resulting dispersion curves for $k_x < 0$ are shown in Fig. 28. The lowest excitation branch is plasmon-like and with no magnetic field present it would join the lower phonon-like branch. Since the magnetic field is sufficiently large that the lower surface mode frequency without retardation lies above the lower frequency for which ϵ_1 is zero, the gap results.¹⁰² A similar gap develops when the phonon-like mode which begins on the light line at $\omega = \omega_{TO}$ attempts to join the uppermost plasmon-like branch.

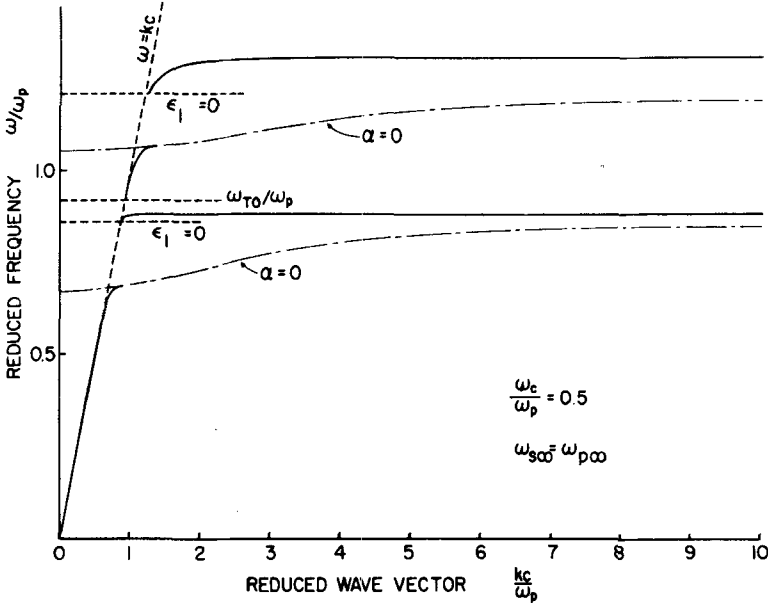


Fig. 28. Dispersion curves for semiinfinite n -type InSb under vacuum. The magnetic field \mathbf{B}_0 is parallel to the surface ($+y$ direction), \mathbf{k} is perpendicular to \mathbf{B}_0 , and $k_x < 0$. The doping and the value of $|\mathbf{B}_0|$ are such that $\omega_c/\omega_p = 0.5$ and $\omega_{3\infty} = \omega_{p\infty}$. (Reprinted from Brion et al.⁹⁹)

We see here occurring a situation alluded to earlier, the number of nonradiative surface excitation branches is larger than the number of branches which extend to asymptotic k values. Some branches extend only a finite distance in k from the light line, the mathematical description of which requires the inclusion of retardation. Although this phenomenon appears here only if the magnetic field is sufficiently large, we will see in Section III that it is not unusual for noncubic crystals without a magnetic field present.

F. Complex Crystals

For a cubic ionic crystal with more than two ions per unit cell, we can, in general, write the dielectric function approximately as

$$\epsilon(\omega) = \epsilon_{\infty} + \sum_{i=1}^n \frac{4\pi\beta_i}{1 - (\omega/\omega_{TOi})^2} \quad (\text{II.164})$$

that is, there will be n infrared-active, long-wavelength, transverse optical frequencies ω_{TOi} . The generalization of the theory to include such crystals is straightforward. In fact, we have already analyzed a formally equivalent situation, the doped polar semiconductor with no magnetic field present, where one of the ω_{TOi} is equal to zero.

Consider first that there is no damping. For a half-space active medium juxtaposed with an inactive medium of dielectric function ϵ_f , there will be n nonradiative surface phonons whose frequencies ω_i will lie in the frequency bands $\omega_{TOi} < \omega_i < \omega_{s\infty i}$, where $\omega_{s\infty i}$ is the first frequency above ω_{TOi} satisfying $\epsilon(\omega_{s\infty i}) = -\epsilon_f$. A slab will have two surface phonons in each of these bands. A sphere whose radius a is such that $W \ll 1$, where W now is

$$W = \frac{\omega_{TOn} \sqrt{\epsilon_f} a}{c}$$

and ω_{TOn} is the largest of the ω_{TOi} , will have bands of surface modes in the frequency regions $\omega_{1Si} < \omega < \omega_{s\infty i}$, with ω_{1Si} the first frequency below $\omega_{s\infty i}$ for which $\epsilon(\omega_{1Si}) = -2\epsilon_f$. The results for a sphere will be complicated and will include considerable overlap between bulk and surface modes if $W \ll 1$ is satisfied for only some or none of the ω_{TOi} . Ruppini and Engelman have discussed several relations involving the dielectric function parameters³⁹ and have studied the long-wavelength optical phonon frequencies for SrTiO_3 .²¹

When damping is included by replacing ω/ω_{TOi} in (II.164) by $(\omega/\omega_{TOi}) + i\gamma_i(\omega)/2$, where $\gamma_i(\omega)$ is the damping parameter associated with the i th TO resonance, there are many possibilities. First consider nonradiative

half-space surface modes with pure spatial decay, that is, ω real and k complex with imaginary part $k'' > 0$. The number of surface mode branches n_{HS} will satisfy $n_{HS} \leq n$; n_{HS} will be less than n if the strength β_i of (II.164) for one or more of the TO optical modes is sufficiently low that the associated minimum in the dielectric function is above $-\epsilon_j$. A slab for which the corresponding half-space has n_{HS} phonon branches will have n_{SL} branches with $2n_{HS} \leq n_{SL} \leq 2n$; n_{SL} can be greater than $2n_{HS}$ if the strengths and damping parameters are such that one or more minima in the dielectric function is above $-\epsilon_j$ but less than zero so that the associated phonon branch ω_+ (see Fig. 8) can exist over a finite range of k values.

Next consider nonradiative "constant-angle" surface modes^{102a} (ω and k complex with ω/k real). Without damping, the dielectric function $\epsilon(\omega)$ of (II.164) has poles at the frequencies ω_{TOj} on the positive real axis of the complex frequency plane. (The poles at the frequencies $-\omega_{TOj}$ do not concern us here.) When damping is included, these poles move to the points $\tilde{\omega}_{TOj}$ lying in the fourth quadrant. For a half-space there will be one surface mode associated with each pole, even if some poles have arbitrarily small, but positive, strengths β_j . The low- k transition points, where the border between radiative and nonradiative modes occurs, coincide with the poles $\omega = \tilde{\omega}_{TOj}$ where ϵ and hence α are infinite, and $\alpha_l = 0$ so $k = \tilde{\omega}_{TOj} \sqrt{\epsilon_l} / c$. For a slab there are two surface modes associated with each pole. The low- k transition points again occur at the poles $\omega = \tilde{\omega}_{TOj}$, one mode in each pair making the transition where $\alpha_{lu} = 0$ or $k = \tilde{\omega}_{TOj} \sqrt{\epsilon_{lu}} / c$, and the other mode, where $\alpha_{ld} = 0$ or $k = \tilde{\omega}_{TOj} \sqrt{\epsilon_{ld}} / c$. The mode or modes associated with a pole having a small strength β_j may exist only over a limited range of k and ω .

If the nonradiative surface modes are chosen to have pure temporal decay (ω complex, k real), the conclusions of the preceding paragraph are essentially unchanged. The most important difference is that the transition points separating radiative from nonradiative modes are now not so sharply delimited.

With damping, each TO resonance frequency ω_{TOj} in the infinite medium, no matter how weak the associated strength β_j , will give rise to a full set of sphere modes, each of which is characterized by a complex frequency ω_{jl} , with l the angular index (see Section II.B). This occurs because $\epsilon(\omega)$ can take on any value in the neighborhood of a complex pole $\tilde{\omega}_{TOj}$, independent of β_j . To demonstrate the validity of these contentions, we separate the effect of the pole at $\tilde{\omega}_{TOj}$ by writing

$$\epsilon(\omega) = \epsilon_{op}(\omega) + \frac{A(\omega)\beta_j}{\tilde{\omega}_{TOj} - \omega} \quad (\text{II.165})$$

where $\epsilon_{op}(\omega)$ is ϵ_∞ plus the contribution to $\epsilon(\omega)$ from poles other than that at $\tilde{\omega}_{TOj}$, $\tilde{\omega}_{TOj} \cong \omega_{TOj}(1 - i\gamma_j/2)$, and $A(\omega) = 4\pi\omega_{TOj}^2/(\tilde{\omega}_{TOj}^* + \omega)$. Then, from (II.165),

$$\omega = \tilde{\omega}_{TOj} + \frac{A(\omega)\beta_j}{\epsilon_{op}(\omega) - \epsilon(\omega)} \quad (\text{II.166})$$

In the small-sphere limit, for example, the l th surface mode occurs where $\epsilon(\omega) = -(l+1)\epsilon_l/l$ [see (II.83)] and there will in general be a solution to (II.166) for these values of $\epsilon(\omega)$. This is especially clear for very small β_j , for then we have $\omega_{jl} \cong \tilde{\omega}_{TOj}$ or, more precisely,

$$\omega_{jl} \cong \tilde{\omega}_{TOj} + \frac{A(\tilde{\omega}_{TOj})\beta_j}{\epsilon_{op}(\tilde{\omega}_{TOj}) + (l+1)\epsilon_l/l} \quad (\text{II.167})$$

These comments concerning the possibilities with damping should be viewed with some caution. Since the dielectric function in these cases will usually be complicated, questions as to specific mode location, resolution, and strength cannot be answered in general. In particular, the frequency dependence of the damping functions $\gamma_j(\omega)$ can have significant effects. If this dependence is sufficiently pronounced, it could give rise to structure in experimental results which might be misinterpreted as being due to additional modes. Each material must be examined individually and meaningful results can be obtained only by detailed calculations in which actual values of the complex dielectric function are used.

III. LOCAL DIELECTRIC CONTINUUM THEORY FOR NONCUBIC CRYSTALS

We consider now the half-space problem with the geometry of Fig. 2 and the active medium to be a biaxial crystal described by the dielectric tensor (II.154) and $\mu=1$. We take $\epsilon(\omega)$ to be real (no damping) so the tensor elements satisfy $\epsilon_{ij} = \epsilon_{ji}$. In this case there do exist principal axes whose orientation is in general frequency dependent.¹⁰³ If the coordinate axes coincide with these principal axes, the dielectric tensor becomes

$$\epsilon_{PA}(\omega) = \begin{pmatrix} \epsilon_x & 0 & 0 \\ 0 & \epsilon_y & 0 \\ 0 & 0 & \epsilon_z \end{pmatrix} \quad (\text{III.1})$$

with $\epsilon_x \neq \epsilon_y \neq \epsilon_z$. The general tensor elements in (II.154) will then involve the quantities ϵ_x , ϵ_y , ϵ_z , and the direction cosines which relate the

coordinate system orientation to the principal axes. We further take the electric field to be of the form (II.155) so that the surface polaritons propagate in the x direction. The equations which α and α_j , the decay parameters for the direction normal to the surface, must satisfy are then given by (II.157).

With no damping, ϵ is real as are k and ω , so α of (II.157b) will in general be complex,

$$\alpha = \alpha' + i\alpha'' \quad (\text{III.2})$$

If, however, α' satisfies⁹⁹

$$\frac{\omega^2}{c^2}(\epsilon_{xy}\epsilon_{yz} - \epsilon_{yy}\epsilon_{xz})(\alpha'^2 - k^2)\epsilon_{xz} = 0 \quad (\text{III.3})$$

the surface polaritons will be "regular"; that is, α will be real. This condition is satisfied if ϵ_{xz} and either of ϵ_{xy} or ϵ_{yz} is zero. So, if any principal axis is parallel to either the surface normal or the surface wave vector \mathbf{k} , the surface polaritons will be regular. For the geometry of Fig. 2 and propagation in the x direction, this means that one principal axis must lie parallel to either the x - or z -axis.

The character of the coupling which distinguishes regular polaritons from "generalized" polaritons (α complex) can be understood with reference to Fig. 29. If the principal axes are oriented along the coordinate directions, electric fields in the three directions are independent and there is no coupling. By this we mean specifically that a polarization, or a component of \mathbf{D} , can appear in a given direction only if there is an electric field component in this direction. The possibility that the field components in the various directions can be coupled through Maxwell's equations must obviously not be excluded. Now consider rotating the crystal axes [and therefore $\epsilon(\omega)$] about the z -axis. An electric field in either the x or y direction will now give rise to both D_x and D_y components, the coupling occurring physically because the field must now be partly longitudinal ($\nabla \cdot \mathbf{E} \neq 0$). However, ϵ_{xz} and ϵ_{yz} are still zero since the z direction, the only "decay" direction, remains independent and the polaritons will be regular although no longer TM as they are for isotropic media. The same is true if we start with the principal axes oriented along the Cartesian axes of Fig. 29 and rotate the crystal axes about the x direction. That is, the displacements D_x and D_z are now coupled but the x direction, the only "propagation" direction, remains independent so we will have regular, non-TM polaritons. If, however, we start with the principal axes aligned with the coordinate axes and then make a simultaneous rotation of the crystal axes about z and x or a single rotation about y , the polaritons will be non-TM and generalized. What happens is that the longitudinal electric field now

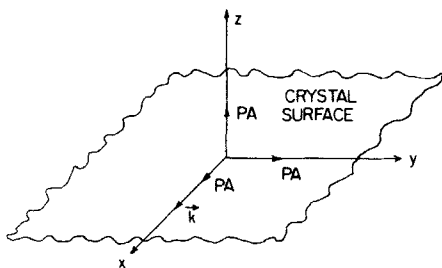


Fig. 29. A sketch of the surface of the noncubic crystal showing the coordinate system aligned with the principal axes (PA) and the wave vector \mathbf{k} . The crystal rotations discussed in the present context should be thought of more properly as cuts of the crystal such that the crystal surface always coincides with the fixed x - y plane.

couples D_x and D_z . The result is that the “decay” associated with the z direction is mixed with the “propagation” associated with the x direction so that both directions end up with both “decay” and “propagation”; that is, α is complex. Note that the active-medium electric field will be partly longitudinal here even if the principal axes and the coordinate axes coincide.

As long as $\epsilon(\omega)$ is real, the Poynting vector \mathbf{S} associated with the surface polaritons will be parallel to the surface but not necessarily parallel to \mathbf{k} .⁹⁹ Modes with $\mathbf{S} \parallel \mathbf{k}$ are referred to as “ordinary” while those with $\mathbf{S} \not\parallel \mathbf{k}$ are called “extraordinary.” Regular surface polaritons are extraordinary if the normal to the surface is along a principal axis while \mathbf{k} is not. If a principal axis is parallel to \mathbf{k} , the now regular surface polaritons are also ordinary.

Let us consider the special case where the principal axes coincide with the Cartesian axes as in Fig. 29.^{99, 101, 104} The dielectric tensor is then given by (III.1) and from (II.157b) we get

$$\alpha^2 = \frac{\epsilon_x}{\epsilon_z} \left(k^2 - \frac{\omega^2}{c^2} \epsilon_z \right) \quad (\text{III.4})$$

Using (II.155) for the electric fields and $\nabla \cdot \mathbf{D} = 0$ leads to

$$\frac{E_z^0}{E_x^0} = \frac{ik\epsilon_x}{\alpha\epsilon_z} \quad (\text{III.5})$$

and E_{Iz}^0/E_{Ix}^0 as given by (II.160b). The boundary equations at $z=0$ require

$$\frac{\epsilon_z E_z^0}{E_x^0} = \frac{\epsilon_I E_{Iz}^0}{E_{Ix}^0} \quad (\text{III.6})$$

which, together with (III.5) and (II.160b), gives the dispersion relation

$$\frac{\epsilon_x}{\alpha} = -\frac{\epsilon_I}{\alpha_I} \quad (\text{III.7})$$

In the nonradiative region and for $\epsilon_I > 0$, α and α_I must be positive so the fields will decay. We see from (III.7) that ϵ_x , the dielectric constant associated with the direction of the surface wave vector, must satisfy

$$\epsilon_x < 0 \quad (\text{III.8})$$

This condition, together with (III.4), suggests interesting possibilities. A mode can reach asymptotic k values only if $\epsilon_x/\epsilon_z > 0$, so for such excitations

$$\epsilon_z < 0 \quad (\text{III.9})$$

However, we can also satisfy $\alpha > 0$ and (III.8) with

$$\epsilon_z > 0 \quad (\text{III.10a})$$

and

$$\epsilon_I \frac{\omega^2}{c^2} < k^2 < \epsilon_z \frac{\omega^2}{c^2} \quad (\text{III.10b})$$

where we have used explicitly the condition $\alpha_I > 0$ or $k > \omega\sqrt{\epsilon_I}/c$ which must always be satisfied in the nonradiative region. Thus there can exist modes which extend in k only a finite distance beyond the effective light line ($\omega = ck/\sqrt{\epsilon_I}$) if $\epsilon_I < \epsilon_z$. We have already seen an example of this kind of behavior in Fig. 28.

These surface polaritons which extend only over a finite range of k values have sometimes been called virtual surface polaritons. We feel that this is most unfortunate since these modes are not virtual in the usual sense of this word. Their fields are of the same form as those for the modes which extend to large k ; their lifetimes are not strongly limited¹⁰⁵ as is generally the case when the term virtual is applied. We would prefer names such as limited- k surface polaritons for those modes which span only a finite range of k , and unlimited- k surface polaritons for modes which can occur to large values of k .

An alternative expression for the dispersion curve can be obtained by squaring (III.7) and then using (II.157a) and (III.4). The result is

$$k^2 = \frac{\omega^2}{c^2} \epsilon_I \epsilon_z \frac{\epsilon_x - \epsilon_I}{\epsilon_x \epsilon_z - \epsilon_I^2} \quad (\text{III.11})$$

From (III.11) it is apparent that the unlimited- k modes must satisfy the asymptotic condition

$$\epsilon_x \epsilon_z = \epsilon_I^2 \quad (\text{III.12})$$

No dispersion curve calculations for biaxial crystals have yet been made. However, there have been several studies of uniaxial crystals, those for which two of ϵ_x , ϵ_y , and ϵ_z are equal. Let us call the dielectric function for the optic axis ϵ_{\parallel} and that for both axes perpendicular to the optic axis ϵ_{\perp} . We can then specialize (III.11) for several cases:

1. Optic axis \perp surface so $\epsilon_z = \epsilon_{\parallel}$ and $\epsilon_x = \epsilon_{\perp}$. Note that all directions of propagation in the x - y plane are now equivalent. From (III.11) we find

$$k^2 = \frac{\omega^2}{c^2} \epsilon_I \epsilon_{\parallel} \frac{\epsilon_{\perp} - \epsilon_I}{\epsilon_{\perp} \epsilon_{\parallel} - \epsilon_I^2} \quad (\text{III.13})$$

Unlimited- k polaritons can occur if

$$\epsilon_{\perp} < 0 \quad \text{and} \quad \epsilon_{\parallel} < 0 \quad (\text{III.14})$$

and limited- k polaritons if

$$\epsilon_{\perp} < 0, \quad \epsilon_{\parallel} > 0 \quad (\text{III.15a})$$

and

$$\epsilon_I \frac{\omega^2}{c^2} < k^2 < \epsilon_{\parallel} \frac{\omega^2}{c^2} \quad (\text{III.15b})$$

2. Optic axis \parallel surface and $\mathbf{k} \perp$ optic axis so $\epsilon_x = \epsilon_z = \epsilon_{\perp}$. Equation (III.11) now becomes

$$k^2 = \frac{\omega^2}{c^2} \frac{\epsilon_{\perp} \epsilon_I}{\epsilon_{\perp} + \epsilon_I} \quad (\text{III.16})$$

Only unlimited- k surface polaritons can occur and they must satisfy

$$\epsilon_{\perp} + \epsilon_I < 0 \quad (\text{III.17})$$

The active-medium electric field is in this case transverse.

3. Optic axis \parallel surface and $\mathbf{k} \parallel$ optic axis so $\epsilon_x = \epsilon_{\parallel}$ and $\epsilon_z = \epsilon_{\perp}$. The dispersion relation (III.11) is

$$k^2 = \frac{\omega^2}{c^2} \epsilon_I \epsilon_{\perp} \frac{\epsilon_{\parallel} - \epsilon_I}{\epsilon_{\parallel} \epsilon_{\perp} - \epsilon_I^2} \quad (\text{III.18})$$

Unlimited- k surface polaritons will now occur when conditions (III.14) are satisfied while the conditions for limited- k polaritons are

$$\epsilon_{\parallel} < 0, \quad \epsilon_{\perp} > 0 \quad (\text{III.19a})$$

and

$$\epsilon_{\parallel} \frac{\omega^2}{c^2} < k^2 < \epsilon_{\perp} \frac{\omega^2}{c^2} \quad (\text{III.19b})$$

Bryskin, Mirlin, and Reshina¹⁰⁶ have investigated some of these modes for MgF_2 and TiO_2 and Falge and Otto^{104,107} have done an exhaustive study of α -quartz. We refer the reader to these papers for dispersion curve calculations.

An investigation of the surface polaritons in noncubic crystals with damping included has not been carried out. This problem will be rather involved for a biaxial crystal since the dielectric tensor cannot, in general, be diagonalized. That is, there does exist a set of axes for which the real part of $\epsilon(\omega)$ is diagonal and the same is true for the imaginary part. However, these two sets of axes do not in general coincide. The complex dielectric tensor for a uniaxial crystal can be diagonalized.

Noncubic magnetic media can be investigated using the formalism given above by making the replacements $\epsilon \leftrightarrow \mu$, $\mathbf{D} \leftrightarrow \mathbf{B}$, $\mathbf{E} \leftrightarrow \mathbf{H}$.

IV. LONG-WAVELENGTH MICROSCOPIC THEORY

We have now completed our presentation of the long-wavelength theory of surface dynamics; the customary formalism of lattice dynamics has not appeared. We would like to point out here that this need not have been the case; that is, our procedure of introducing the electromagnetic response functions at the beginning and then solving Maxwell's equations has a lattice dynamics alternative. One can begin with the equations of motion for the ions vibrating under the influence of both the short-range repulsive and Coulomb interactions. In the long-wavelength limit, the resulting equations can be manipulated into a form in which the dielectric function $\epsilon(\omega)$ appears and the solutions to these equations are just those which are obtained from solving Maxwell's equations with $\epsilon(\omega)$ included. This has been shown for a slab of dielectric (ignoring the change in short-range force constants near the surface) both without¹⁸ and with¹⁹ retardation. Thus when we incorporate $\epsilon(\omega)$ into Maxwell's equations for the problems of interest here, we are implicitly incorporating the results of the usual lattice dynamics procedure.

V. EXPERIMENTAL TECHNIQUES AND RESULTS

We have included this section dealing with the experimental situation before the presentation of the theory valid for large wavevectors since the

experimental results available to this time reflect largely local conditions.

Our discussion begins with results obtained from optical studies other than those involving the use of the attenuated total reflection (ATR) technique. Such investigations can provide a considerable amount of information about the surface excitations if the active sample being investigated is in the form of a slab, and a great deal of information, in principle, if the sample is a small particle. This is followed by a brief description of the ATR technique and a survey of the results obtained using same. We conclude this section with a discussion of the results obtained if the system is excited by electrons.

Ibach¹⁰⁸ has reviewed some of this material previously.

A. Optical Investigations

1. Planar Geometry

Suppose we consider an active slab of homogeneous isotropic material, as in Fig. 7, with smooth surfaces (the implicit assumption in all of the theory above) and surrounded by inactive media with $\epsilon_{lu} = \epsilon_{ld} = \epsilon_f$. Light incident on the active slab will then have $|k| < \omega\sqrt{\epsilon_f}/c$, with k the wave vector component parallel to the slab surface, and interaction with the FK modes of Section II.A.2 is effectively precluded.³³ The virtual modes, in particular the radiative surface mode (see Section II.A.3), and the Brewster angle condition occur within the wave vector region accessible with light. To understand their optical role, we write the reflectance R , transmittance T , and absorptance A for p -polarized incident light as¹⁰⁹

$$T = \frac{1}{4}|P_1 - P_2|^2 \quad (\text{V.1a})$$

$$R = \frac{1}{4}|P_1 + P_2|^2 \quad (\text{V.1b})$$

and

$$A = 1 - T - R = \frac{1}{2}(1 - |P_1|^2) + \frac{1}{2}(1 - |P_2|^2) \quad (\text{V.1c})$$

where

$$P_1 = \frac{2 - L_1}{L_1} \quad (\text{V.2a})$$

and

$$P_2 = \frac{2 - L_2}{L_2} \quad (\text{V.2b})$$

with

$$L_1 = 1 - \frac{i\beta\epsilon_f}{\beta_f\epsilon} \tan\beta a \quad (\text{V.3a})$$

and

$$L_2 = 1 + \frac{i\beta\epsilon_I}{\beta_I\epsilon} \cot \beta a \quad (\text{V.3b})$$

For the constant-angle virtual modes or if ω and k are real, the quantities β and β_I , given by (II.50) and (II.54), can now be written as

$$\beta_I = \frac{\omega}{c} \sqrt{\epsilon_I} \cos \theta \quad (\text{V.4a})$$

and

$$\beta = \frac{\omega}{c} (\epsilon - \epsilon_I \sin^2 \theta) \quad (\text{V.4b})$$

with the angle θ measured from the surface normal as in Fig. 10. The specialization of (V.1) for a half-space yields

$$R = \left| \frac{1 - \epsilon_I \beta / (\epsilon \beta_I)}{1 + \epsilon_I \beta / (\epsilon \beta_I)} \right|^2 \quad (\text{V.5a})$$

and

$$A = 1 - R \quad (\text{V.5b})$$

Let us now take the active slab to be an ionic crystal with $\epsilon(\omega)$ given by (I.9). Equations (V.I) describe the optical properties when ω and k are real. If, however, we allow complex ω and k , the equations $L_1 = 0$ and $L_2 = 0$ are the virtual mode equations (II.59) and (II.61). The cotangent virtual modes [(II.59)] and the tangent virtual modes [(II.61)] have opposite parities.¹⁰⁹ We see from (V.1) that modes of different parity interfere in R and T but not in A . So, the individual modes will in general manifest themselves as individual excitations, particularly in the absorptance.¹¹⁰ This is consistent with our description of these modes as the excitations in which the energy of the system is stored.

The detailed connection between the virtual modes and the optical properties is given in Ref. 109. Since this is of secondary interest in the present context we do not reproduce it here. However, we do note that the radiative surface mode (denoted 0TH in Ref. 109) essentially determines the p -polarized optical properties for $\omega \sim \omega_{LO}$ and $\theta \neq 0$ if $W \lesssim 1$, where

$$W = \frac{\omega_{TO}}{c} \sqrt{\epsilon_I} L \quad (\text{V.6})$$

and L is the slab thickness.¹¹¹ Due to this mode there occur reflectance and absorptance peaks and a transmittance minimum as shown in Fig. 30.

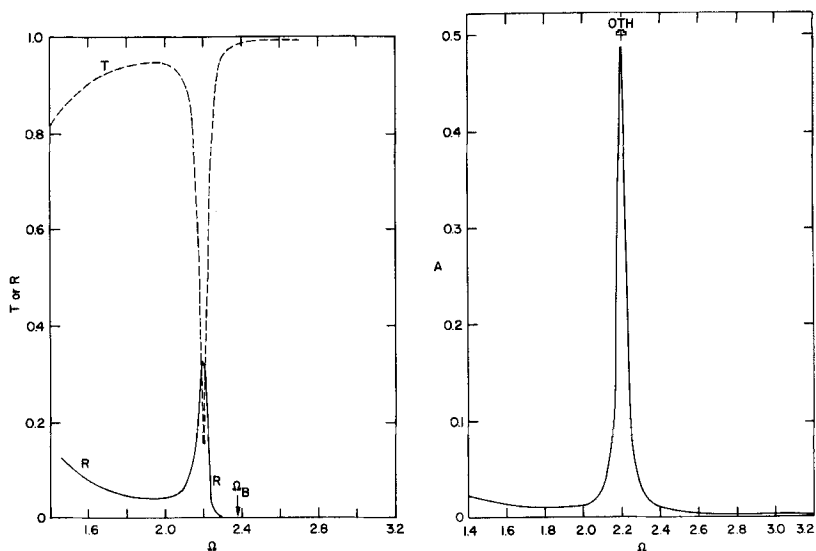


Fig. 30. Transmittance (T), reflectance (R), and absorptance (A) as a function of frequency $\Omega = \omega/\omega_{TO}$ for p -polarized light incident from vacuum at an angle of 30° from the normal on a LiF slab of thickness W [(V.6)]=0.1 (film thickness $= 5.19 \times 10^{-5}$ cm). The dielectric function parameters are $\epsilon_0 = 9.27$, $\epsilon_\infty = 1.92$, $\omega_{TO} = 5.78 \times 10^{13}$ sec $^{-1}$, and $\gamma = 0.02$. The small figure under the mode label indicates the contribution to the line width from both radiative and anharmonic damping and is described in detail by Fuchs, Kliewer, and Pardee.¹⁰⁹ The Brewster angle frequency Ω_B is noted but the Brewster condition is unimportant here.

For s -polarized light there is no analogous structure in the optical properties.

This transmittance dip for p -polarized light was observed by Berreman¹¹² for LiF, thereby confirming the basic properties of the radiative surface mode. However, the line shape was somewhat different from that predicted by the local theory. This point is discussed further in connection with the microscopic theory below.

Since the virtual modes for an ionic crystal are in the phonon frequency range, they correspond to effective temperatures of the order of 100 K. This means that these modes can be studied by observing the far-infrared spectral emissivity. The radiative surface mode has been studied this way for KBr,¹¹³ RbCl,¹¹³ RbBr,¹¹³ NaCl,¹¹³ LiF,^{114–116} MgO,¹¹⁷ and NiF.¹¹⁸ The work on LiF by Hisano and co-workers^{114–116} indicates excellent agreement between the experimental results and the virtual mode theory, both as to line position and width, for $T \lesssim 600$ K. At higher temperatures the damping becomes large and the theoretical line widths are somewhat lower than the measured values. In their analysis, Hisano et al. used dielectric function parameters previously obtained from bulk measurements. These in-

cluded a temperature- but not frequency-dependent γ [see (II.118)]. Since the damping in LiF is strongly frequency dependent⁴⁵ and the inclusion of such effects becomes more important for broad lines, it is likely that better agreement between theory and experiment at high temperatures would result if $\gamma(\omega, T)$ were included.

We note that the virtual modes of an ionic slab of thickness $a/2$ placed on a perfectly conducting backplate will be just the tangent virtual modes for a slab of thickness a . This follows from our comments relating to a metallic backplate in Section II.A.3. In this case (V.1) become¹⁰⁹ $T=0$, $R=|P_1|^2$, and $A=1-|P_1|^2$. The role of an imperfectly conducting backplate is not yet understood (see Section II.A.3).

The Brewster angle condition for the half-space is readily apparent in (V.5a). $R=0$ for¹¹⁹

$$1 = \frac{\epsilon_t \beta}{\epsilon \beta_0} \quad (\text{V.7})$$

This is just the equation which results from the surface phonon equation (II.11) if we move into the radiative region. This transition of (II.11) into the radiative region must be made with some care mathematically. When damping is included, the surface phonon requirements, (II.120), lead to $\text{Im} \alpha_t > 0$ and $\text{Im} \alpha < 0$.¹²⁰ In order that $\text{Re} \beta > 0$ and $\text{Re} \beta_t > 0$, we must take $\alpha_t = i\beta_t$ and $\alpha = -i\beta$ and (II.11) is then (V.7). For a slab we obtain $R=0$ from (V.1b) if $P_1 + P_2 = 0$, which leads again to (V.7). Thus, the Brewster angle condition is independent of thickness. This is clear physically if one thinks of $R=0$ as corresponding to pure refraction.

Reflection minima associated with the Brewster angle are well known and have been observed for years. We do not discuss this point further here except to reiterate our earlier contention that the generalized Brewster condition (V.7) can legitimately be associated with radiative region surface polaritons.

Suppose now that the surface separating the inactive and active media is not smooth but oscillates sinusoidally with periodicity length d in the direction of the surface wave vector \mathbf{k} as sketched in Fig. 31a. If the amplitude A of these oscillations is small compared with the wavelength of the incident light, the effect of this periodicity is to convert $|\mathbf{k}|$ from the single value $k_0 = \omega \sqrt{\epsilon_t} \sin \theta / c$, appropriate to light of frequency ω incident at angle θ from the mean surface normal, into the set of wave vectors

$$k_n = k_0 + \frac{2\pi n}{d} \quad (\text{V.8})$$

with $n=0, \pm 1, \pm 2, \dots$. For sufficiently large $|n|$, the surface wave vector k_n will be in the nonradiative region and, if the frequency of the incident

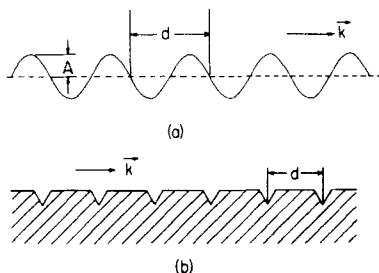


Fig. 31. (a) A cut through a crystal whose surface varies in the direction of the wave vector \mathbf{k} as a sinusoid of amplitude A and period d . (b) A cut through a crystal into whose surface a grating of period d has been inscribed. The grooves are shown running perpendicular to the wave vector \mathbf{k} .

light is properly chosen, direct coupling of the nonradiative surface excitations to the incident light can occur.

A surface with a periodic disturbance can be produced by ruling a grating as indicated in Fig. 31b. This technique was used by Marschall et al.^{121,122} to examine the surface excitation of a thick sample of InSb doped so heavily that the excitation is essentially a surface plasmon. The procedure is to measure the reflectance as a function of frequency and angle and look for dips associated with the various values of n in (V.8). The relation between the dips and the surface excitation dispersion curve can then be obtained from grating theory in which the grating profile is explicitly incorporated.¹²³ The results of Marschall et al. did not agree particularly well with the calculated values. This is not surprising as the process of inscribing grooves probably results not only in grooves but also in extensive surface damage. Such grooves are also most probably of variable shape, making quantitative comparison of the results with grating theory difficult.

A variation of this technique involving the deposition of a thin insulating film upon a metallic grating was used some time ago by Hass.¹²⁴

Surfaces will almost invariably be rough to some extent. A rough surface can be Fourier analyzed and described by a set of surface wave vectors k_α and associated amplitudes A_α . Each k_α will in turn give rise to a set of wave vectors of the form (V.8); that is, $k_{n\alpha} = k_0 + nk_\alpha$. Since these wave vectors extend into the nonradiative region, we expect in general some coupling of light to the nonradiative surface excitations. That this coupling can be significant has been demonstrated clearly for surface plasmons in Ag by Jaspersion and Schnatterly¹²⁵ and shown to be a possibility for surface polaritons in LiF by Berreman.¹²⁶ A discussion of this subject, oriented toward metals, is given in Ref. 33.

A way of obtaining direct coupling of light to the nonradiative surface modes is suggested by Fig. 8b. If we assemble a sample of the type shown in Fig. 7, with $\epsilon_{lu} > \epsilon_{ld}$, and bring the light in from the side where the dielectric function is ϵ_{lu} , that part of the surface excitation associated primarily with the opposite surface and occurring for $\omega\sqrt{\epsilon_{ld}}/c < k < \omega\sqrt{\epsilon_{lu}}/c$ will fall into the radiative region and can thus couple strongly to the incident light. This technique, first used in a quantitative way to investigate surface excitations by Raether and Kretschmann,^{127,128} has not been used for investigations of surface polaritons. It is, however, essentially equivalent to the ATR technique.

2. Small Particles*

For a sphere, all the transverse excitations are virtual modes and thus couple directly with light (see Section II.B). So, in principle, the surface mode properties can be obtained from direct optical experiments, the interpretation of which requires expressions for the cross-sections. For a system as sketched in Fig. 12 with $\mu=1$, the absorption cross-section Q_A for plane-polarized light, in units of the projected area πa^2 , is²⁸

$$Q_A = \frac{1}{(W\Omega)^2} \sum_{l=1}^{\infty} (2l+1) \left(\frac{A_l + A_l^* - 2}{A_l A_l^*} + \frac{B_l + B_l^* - 2}{B_l B_l^*} \right) \quad (\text{V.9})$$

where

$$A_l = \frac{h_l^{(1)}(\rho_l)(d/d\rho)[\rho j_l(\rho)] - j_l(\rho)(d/d\rho_l)[\rho_l h_l^{(1)}(\rho_l)]}{j_l(\rho_l)(d/d\rho)[\rho j_l(\rho)] - j_l(\rho)(d/d\rho_l)[\rho_l j_l(\rho_l)]} \quad (\text{V.10a})$$

and

$$B_l = \frac{\epsilon_l h_l^{(1)}(\rho_l)(d/d\rho)[\rho j_l(\rho)] - \epsilon_l j_l(\rho)(d/d\rho_l)[\rho_l h_l^{(1)}(\rho_l)]}{\epsilon_l j_l(\rho_l)(d/d\rho)[\rho j_l(\rho)] - \epsilon_l j_l(\rho)(d/d\rho_l)[\rho_l j_l(\rho_l)]} \quad (\text{V.10b})$$

with the notation that of Section II.B. The scattering cross-section Q_S is

$$Q_S = \frac{2}{(W\Omega)^2} \sum_{l=1}^{\infty} (2l+1) \left[(A_l A_l^*)^{-1} + (B_l B_l^*)^{-1} \right] \quad (\text{V.11})$$

and the extinction cross-section Q_T , which determines the total power removed from the incident beam, is

$$Q_T = Q_A + Q_S = \frac{2}{(W\Omega)^2} \sum_{l=1}^{\infty} (2l+1) \left(\frac{A_l + A_l^*}{A_l A_l^*} + \frac{B_l + B_l^*}{B_l B_l^*} \right) \quad (\text{V.12})$$

*See also Section IX.B.

The equations $A_l = 0$ and $B_l = 0$ are just the virtual mode equations (II.80) and (II.81) if $\mu = 1$. These equations are satisfied only for complex frequencies, whereas the frequency in an optical scattering experiment is real. Thus A_l or B_l becomes small but not zero when the real frequency in a scattering experiment passes near a complex virtual mode frequency. Because of the denominators $A_l A_l^*$ and $B_l B_l^*$ the cross-sections become large when A_l or B_l becomes small. Each virtual mode is therefore associated with a peak in the cross-sections.

The detailed connection between the virtual modes and the cross-sections is given in Ref. 28. We illustrate the role of the virtual modes by showing cross-sections for a LiF sphere in vacuum in Figs. 32 and 33,

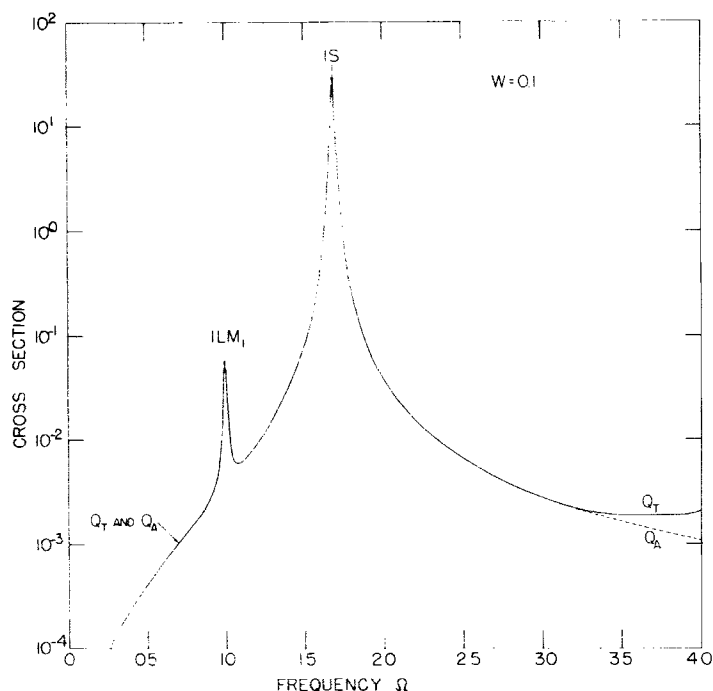


Fig. 32. Absorption cross-section (Q_A) and extinction cross-section (Q_T) as functions of frequency $\Omega = \omega/\omega_{TO}$ for a LiF sphere of radius $W = 0.1$ in vacuum. The dimensionless radius W is defined in (11.82b) and the dielectric function parameters are $\epsilon_0 = 9.27$, $\epsilon_\infty = 1.92$, $\omega_{TO} = 5.78 \times 10^{13} \text{ sec}^{-1}$, and $\gamma = 0.02$, a rather small value. The sphere radius a corresponding to $W = 0.1$ is $5.19 \times 10^{-5} \text{ cm}$. Note that the condition $W = 0.1$ means that the ratio of the wavelength of the light in vacuum, λ , to a is $2\pi/10$ for $\omega = \omega_{TO}$. Although the small radius approximation is valid here, this ratio is not small, indicating that "small radii" are more accurately characterized by $W \ll 1$ than by $a \ll \lambda$, the latter being too restrictive. Mode labels for the bulk modes are described in Ref. 28.

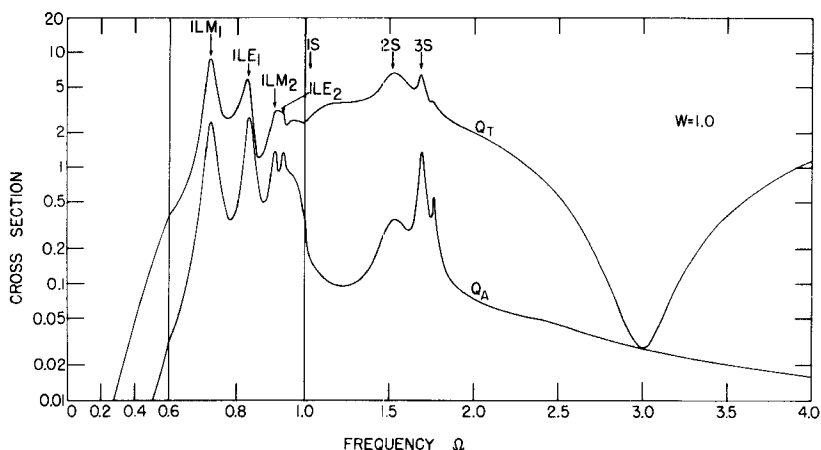


Fig. 33. Absorption cross-section (Q_A) and extinction cross-section (Q_T) as functions of frequency $\Omega = \omega/\omega_{TO}$ for a LiF sphere of radius $W=1.0$ in vacuum. Relevant parameters are given in the caption of Fig. 32. Labels for the bulk modes are described in Ref. 28.

Fig. 32 for $W=0.1$ [see (II.82b)] and Fig. 33 for $W=1.0$. Figure 32 shows the strongly dominant role played by the $1S$ mode if $W \ll 1$. This mode then occurs at the frequency [see (II.89)]

$$\omega_{1S}^2 = \omega_{TO}^2 \frac{\epsilon_0 + 2\epsilon_f}{\epsilon_\infty + 2\epsilon_f} \quad (\text{V.13})$$

For all W , the only identifiable surface mode structure will lie in the frequency range $1 \lesssim \Omega \lesssim \omega_{s\infty}/\omega_{TO}$, with $\omega_{s\infty}$ given by (II.18). Additional calculations of this sort have been made by Ruppin¹²⁹ for ZnS.

On the basis of Figs. 32 and 33, the ready availability of surface information from experiments on small spheres seems apparent. So what is the experimental situation? There occur two serious problems: (1) the production of small genuinely spherical samples, and (2) studying them as independent entities. The cross-sections above are valid for a single sphere; a collection of spheres will give rise to interference effects if their separation is less than or of the order of the wavelength of the incident light so the cross-sections will not merely scale with the number of spheres contributing to the cross-sections. As a result of these problems, most experiments on small particles have been of a qualitative nature. A review of a considerable number of such experiments has been given by Ruppin and Englman.³⁹

The 1S mode for a small sphere involves a uniform electric field within and is three-fold degenerate (see Section II.B). For a small ellipsoid (the most general geometry which can be treated analytically) this degeneracy is split and (II.83) for this mode now becomes¹²⁹

$$\epsilon(\omega_{1Si}) = \epsilon_i \left(1 - \frac{4\pi}{N_i} \right), \quad i = 1, 2, 3 \quad (\text{V.14})$$

where the N_i are the depolarization factors. This illustrates the complications which can result from nonspherical particles and indicates, in particular, that nonsphericity will broaden the 1S peak in Fig. 32. Indeed, the 1S peak for a sphere may give three separate peaks for a properly shaped ellipsoid.¹²⁹

Observations of transmission minima near the frequency ω_{1S} have been made for NaCl,¹³⁰ SnO₂,¹³¹ and BaTiO₃,¹³² among others. These results suggest that roughly spherical particles can be made and that the continuum theory is not seriously inadequate. However, the experimental line widths are much greater than those calculated assuming spherical samples and using damping values characteristic of the bulk. The reason for this is not clear. There is, of course, the possibility that the damping in a small particle is inherently larger than for large samples. However, the effect of nonsphericity of the particles and a distribution of particle sizes and spacings in the samples would also be to increase line widths. Bryskin et al.¹³⁰ and Genzel and Martin¹³³ demonstrated that striking changes occur in the spectra if well-separated particles are moved close together. Genzel and Martin¹³⁴ showed that the transmission structure of small MgO cubes had a small minimum near ω_{1S} but this dip was so broad that a damping factor about eight times that of bulk MgO was needed in the *sphere* calculation to reproduce the experimental width.

The problem of properly characterizing samples of the type needed for these experiments has been treated in an interesting way by Genzel and Martin.¹³⁴ For a sample consisting of small spheres ($W \ll 1$ so the electric field can be considered uniform within) of dielectric function $\epsilon(\omega)$ embedded in a medium of dielectric function ϵ_f , they find that the system can be considered as a medium of dielectric function $\epsilon_{av}(\omega)$,

$$\epsilon_{av}(\omega) = \epsilon_f \frac{\epsilon(\omega)(1+2f) + 2\epsilon_f(1-f)}{\epsilon(\omega)(1-f) + \epsilon_f(2+f)} \quad (\text{V.15})$$

with f the fraction of the sample occupied by the spheres. This expression is valid if f is sufficiently small that the dipole fields outside of the spheres do not overlap appreciably.¹³⁵ Standard optical techniques can then be used to examine films of this material.

Rieder et al.¹³⁶ studied doped CdO and found that the principal features of the experimental results could be understood on the basis of (V.15). These features included absorption peaks associated with the two regions when $\epsilon(\omega)$ is negative (see Fig. 21), a sharp antiresonance near ω_{TO} , a direct consequence of phonon-plasmon coupling, and structure near ω_{LO} quite possibly due to the details of the free carrier-optical phonon interaction. They concluded that the continuum theory for the microcrystals based on bulk dielectric properties was basically correct.

The spectral emission of small, round-edged, closely spaced alkali halide cubes has been studied by Kälín et al.¹³⁷ They also found peaks between ω_{LO} and ω_{TO} as well as a significant temperature dependence of the width of the peaks.

From this discussion it is clear that a solution to the theoretical problem of the optical character of a dielectric cube is needed to aid in the interpretation of these results. It is also clear that a multitude of unanswered questions remain in connection with line widths and their relation to damping.

3. Attenuated Total Reflection (ATR)

The ATR technique,^{138,139} first used by Otto, has become the principal technique for the measurement of surface polariton dispersion curves. We have sketched a possible experimental arrangement in Fig. 34. Ignore the sample for the moment. The light wave incident from vacuum on the prism with index of refraction n_p will be totally reflected at the bottom surface if $n_p \sin \alpha > 1$. Thus, total internal reflection will occur if $n_p^{-1} < \sin \alpha < 1$. The wave vector k_p of the incident light within the prism is $k_p = \omega n_p / c$ and its component k_{pp} parallel to the lower surface of the prism is $k_{pp} = \omega n_p \sin \alpha / c > \omega / c$. In the vacuum below the lower prism surface the electric field will decay as $\exp(-\xi s)$, with s measured perpendicular to the surface and $\xi = \omega(n_p^2 \sin^2 \alpha - 1)^{1/2} / c$. Thus we have an evanescent wave in the vacuum propagating parallel to the surface with $k_{pp} > \omega / c$. If we then bring in the sample as shown in Fig. 34, this evanescent wave can couple to the nonradiative surface excitations, also occurring with surface wave vector greater than ω / c , if a is sufficiently small and ω is that of the surface excitation. This coupling will manifest itself as a reduction in intensity of the wave leaving the prism.

This technique was first used to investigate surface polaritons by Bryskin et al.^{140,141} who studied KBr, NaCl, NaF, LiF, CdF₂, and CaF₂. Other studies on cubic systems include those of Marschall and Fischer¹⁴² on GaP and Fischer et al.¹⁴³ on NaF. The agreement of the experimental dispersion curves with those calculated using (II.13) with $\epsilon(\omega)$ now the real part of (II.115) is excellent for GaP, CaF₂, and CdF₂. The GaP results are shown

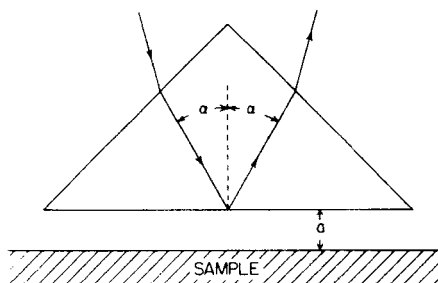


Fig. 34. A sketch of the experimental arrangement used for investigations of surface modes using the ATR technique.

in Fig. 35. For the alkali halides, however, the measured asymptotic frequency is well below the theoretical value obtained using a constant damping parameter γ . The approximation of a constant γ is not good for the alkali halides and Fischer et al.¹⁴³ have shown that the theoretical curve for NaF depends strongly on the behavior of $\gamma(\omega)$. One problem here is that the type of damping description appropriate for surface polaritons *as observed in ATR* has not yet been clarified. In other words, it is not clear

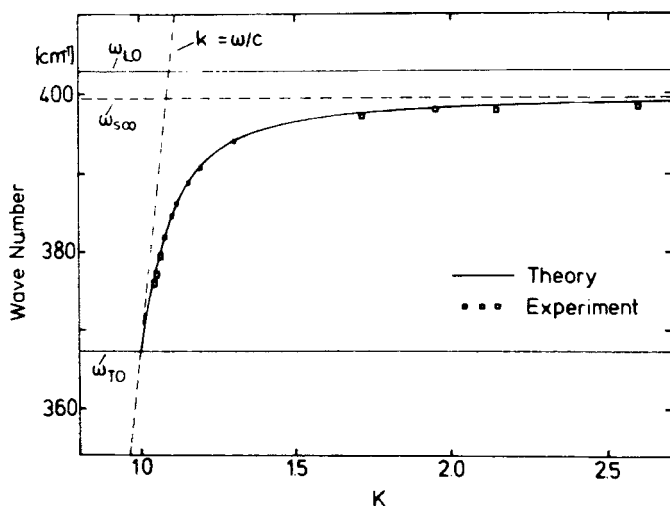


Fig. 35. The surface polariton dispersion curve for semiinfinite GaP ($\epsilon_0 = 10.94$, $\epsilon_\infty = 9.09$, $\omega_{TO} = 367.3 \text{ cm}^{-1} = 6.923 \times 10^{13} \text{ sec}^{-1}$) in vacuum. The frequency is given in reciprocal centimeters and the dimensionless wave vector $K = kc/\omega_{TO}$. The theoretical curve is calculated using (11.13) with $\epsilon(\omega)$ the real part of (11.115) and $\gamma_1 = 0.0035\omega_{TO}$. (Reprinted from Marschall and Fischer.¹⁴²)

just what kind of theoretical curve should be compared with the experimental results. We saw in Section II.D that the theoretical results are strongly dependent on the damping description. Another problem is the proper interpretation of the ATR analysis when the damping is frequency dependent.

Fischer et al.¹⁴³ also imply that nonlocal effects are important by using boundary conditions which include nonlocality.¹⁴⁴ Such effects are discussed in Section VI.

The surface excitations for doped InSb^{143,145,146} have also been measured. Reshina et al.¹⁴⁵ used a number of doping levels with ω_p , the free carrier plasma frequency, ranging from well below to well above ω_{TO} . Their experimental results for the asymptotic frequencies are shown in Fig. 22. The agreement of the lower branch with the theory is excellent. The upper branch will be sensitive to the effective mass of the free carriers and the increasing disparity between the theoretical and experimental results as the carrier concentration increases may well indicate that the effective mass is concentration dependent. The measurements of Fischer et al.¹⁴³ on heavily doped InSb show much better agreement with the theory than did their results using the inscribed grating.

Noncubic crystals can also be examined using the ATR scheme. Experiments on α -quartz have been reported by Falge and Otto¹⁰⁴, on MgF_2 and TiO_2 by Bryskin et al.¹⁰⁶, and on $CaMoO_4$ by Barker.¹⁴⁷ The experiments of Falge and Otto are noteworthy in that 22 surface polariton branches were observed including several limited- k branches. Most were in excellent agreement with the calculated values.

Schoenwald et al.⁴⁷ have demonstrated that surface polaritons can travel distances of the order of centimeters. Their procedure was to use two separated prism couplers, one for excitation and the second for detection. Barker³⁸ has discussed the effects of surface roughness on the ATR signal.

B. Electron Scattering Investigations

The first measurements demonstrating the existence of surface polaritons were performed on LiF films by Boersch, Geiger, and Stickel¹⁴⁸ using the technique of high-energy electron energy loss.¹⁴⁹ The procedure is to shoot high-energy electrons (25 keV in Ref. 148) through the film and then measure the energy change, which gives the energy deposited in the film, and the scattering angle, which gives the momentum imparted to the film. These energy and momentum changes must then be related to the elementary excitations of the system. For a sufficiently thin film, the incident electrons interact principally with the surface modes.

Detailed analyses of the experiment of Boersch et al.¹⁴⁸ have been given by these same authors^{149a} and by Chase and Kliever.⁵¹ Because of the

symmetry of the fields associated with the FK modes ω_+ and ω_- (see Fig. 8a), the electron interaction with mode ω_+ is very small compared with that of mode ω_- for the thicknesses used in the experiments of Ref. 148.⁵¹ Apparatus resolution functions, both in energy and wave vector, have to be included in the analysis as they figure prominently in the experimental results. The range of wave vectors represented by the wave vector resolution is so large that a dispersion curve cannot be determined. The theory then involves essentially the interaction of the electrons with mode ω_- and the inclusion of the apparatus characteristics. Agreement with the experimental results is good. It should be noted that the possibility of energy gain exists here if the temperature is sufficiently high that surface phonons can be thermally excited. This phonon absorption process was also observed by Boersch et al.¹⁴⁸

An alternative electron scattering technique was used by Ibach^{108, 150, 151} to observe surface polaritons in ZnO. He used low-energy electrons ($\lesssim 50$ eV) and observed the energy change resulting when the electrons were reflected from the surface.

Suppose we have a surface wave of frequency ω_s and wave vector k moving along a surface. This wave will interact strongly with an electron outside the surface if the velocity v_p of the electron parallel to the propagation direction of the wave is equal to the phase velocity of the wave, $v_p = \omega_s/k$, the usual "surf-riding" condition. For a 10-eV electron, $v_p \sim 2 \times 10^8$ cm/sec. Surface phonons in ZnO have $\omega_s \sim 70$ meV $\sim 10^{14}$ sec⁻¹ so $k \sim 5 \times 10^5$ cm⁻¹, which is small compared with a reciprocal lattice vector but large compared with the wave vector of a photon of frequency ω_s . Thus we expect the continuum theory to be valid and we can neglect retardation.

ZnO crystallizes in the wurtzite lattice and is uniaxial so the theory of Section III is applicable. Neglecting retardation then means that the surface phonon conditions for the crystal in vacuum are as follows:

1. Optic axis \parallel surface and propagation direction \perp optic axis,

$$\epsilon_{\perp}(\omega) = -1 \quad (\text{V.16})$$

2. Optic axis \parallel surface and propagation direction \parallel optic axis, or optic axis \perp surface,

$$\epsilon_{\parallel}(\omega)\epsilon_{\perp}(\omega) = 1 \quad (\text{V.17})$$

where $\epsilon_{\parallel}(\epsilon_{\perp})$ is the dielectric function parallel (perpendicular) to the optic axis.

Ibach states incorrectly that the surface phonon condition is always of the form $\epsilon = -1$. However, this error causes no real difficulty in his work since the frequencies resulting from $\epsilon_{\perp} = -1$ and $\epsilon_{\parallel} = -1$ differ only by about 2%. Thus, as far as nonretarded surface phonons are concerned, ZnO is essentially isotropic.

The results from Ibach's experiments are very interesting. The surface phonons occur at the frequencies expected from the continuum theory. He finds peaks resulting from multiple surface phonon excitation and their intensities satisfy the Poisson distribution expected theoretically. In the local classical theory, the amplitudes of the electromagnetic fields were essentially irrelevant. However, the interaction of these "slow" electrons with the surface excitations must be treated quantum mechanically and the surface excitations themselves must then be quantized, that is, treated as genuine phonons with energies $\hbar\omega$ and momenta $\hbar k$, where ω and k are the frequency and surface wave vector of the surface excitation. That multiple excitations can then occur follows directly.^{152, 153, 153a}

Ibach also finds that the electrons can gain energy when the temperature is sufficiently high and the ratio of the intensity of the one-phonon gain peak to the intensity of the one-phonon loss peak is the expected Boltzmann factor.

This low-energy electron scattering technique appears to be an excellent scheme for investigating surface phonons. It would be very helpful to have results from such experiments to aid in understanding the problems associated with damping which have appeared in studies of the alkali halides using ATR.

VI. NONLOCAL DIELECTRIC THEORY

In the theory of surface optical phonons discussed in Section II we described the surface active medium with a local dielectric function $\epsilon(\omega)$ which relates the displacement and the electric field: $\mathcal{D}(\mathbf{q}, \omega) = \epsilon(\omega) \mathcal{E}(\mathbf{q}, \omega)$. This description is consistent with the condition (I.1) that a characteristic wavelength or size of the phonon be much larger than the interatomic spacing.

In order to include short-wavelength phonons, one can try to develop a theory in which the medium is described by a nonlocal dielectric function $\epsilon_{\alpha\beta}(\mathbf{q}, \omega)$ ¹⁵⁴ relating the \mathbf{q} th Fourier component of the electric displacement and field by¹⁵⁵

$$\mathcal{D}_{\alpha}(\mathbf{q}, \omega) = \sum_{\beta=1}^3 \epsilon_{\alpha\beta}(\mathbf{q}, \omega) \mathcal{E}_{\beta}(\mathbf{q}, \omega) \quad (\text{VI.1})$$

where α and β denote Cartesian directions. This nonlocal dielectric func-

tion can be written as the Fourier transform of a dielectric function $\epsilon(\mathbf{r}-\mathbf{r}', \omega)$ which gives the response of the infinite medium at \mathbf{r} to the field acting at \mathbf{r}' :

$$D_{\alpha}(\mathbf{r}, \omega) = \int d^3r' \sum_{\beta} \epsilon_{\alpha\beta}(\mathbf{r}-\mathbf{r}', \omega) E_{\beta}(\mathbf{r}', \omega) \quad (\text{VI.2})$$

where

$$\epsilon_{\alpha\beta}(\mathbf{r}-\mathbf{r}', \omega) = \frac{1}{(2\pi)^3} \int d^3q \epsilon_{\alpha\beta}(\mathbf{q}, \omega) e^{i\mathbf{q} \cdot (\mathbf{r}-\mathbf{r}')} \quad (\text{VI.3})$$

Using (VI.1) in Maxwell's equations (II.1),¹⁵⁶ it can be shown that the dispersion relation for plane waves propagating in an infinite medium is given by

$$\det \left[\mathbf{q} \cdot \mathbf{q} \delta_{\alpha\beta} - q_{\alpha} q_{\beta} - \frac{\omega^2}{c^2} \epsilon_{\alpha\beta}(\mathbf{q}, \omega) \right] = 0 \quad (\text{VI.4})$$

The solutions of (VI.4) can be obtained most easily by taking \mathbf{q} in the z direction, assumed to be a crystal symmetry axis for which the off-diagonal components of $\epsilon_{\alpha\beta}$ vanish. Then $\epsilon_{xx}(q_z, \omega)$ and $\epsilon_{yy}(q_z, \omega)$ are transverse dielectric functions, and $\epsilon_{zz}(q_z, \omega)$ is a longitudinal dielectric function. From (VI.4) we find that the dispersion relation for transverse waves ($\mathbf{q} \cdot \mathbf{E} = 0$) is

$$q_z^2 - \frac{\omega^2}{c^2} \epsilon_{xx}(q_z, \omega) = 0 \quad (\text{VI.5})$$

with a similar equation involving ϵ_{yy} , and for longitudinal waves ($\mathbf{q} \times \mathbf{E} = 0$),

$$\epsilon_{zz}(q_z, \omega) = 0 \quad (\text{VI.6})$$

The existence of solutions of (VI.5) and (VI.6) depends on the form of the dielectric functions. For the simple ionic crystal, with the dielectric function in the local limit ($\mathbf{q} \rightarrow 0$) given by (I.9), the doubly degenerate transverse optical (TO) phonon branch and the longitudinal optical (LO) branch are obtained from (VI.5) and (VI.6), respectively, as shown in Fig. 36. The TO branch is split by the effects of retardation into a low-frequency branch (1) and a high-frequency branch (2). If the q dependence of the dielectric functions is neglected, the LO mode has the frequency ω_{LO} independent of \mathbf{q} , and the TO mode approaches the frequency ω_{TO} asymptotically as \mathbf{q} increases.

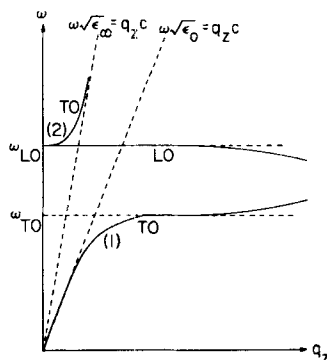


Fig. 36. Dispersion relations for transverse optical (TO) and longitudinal optical (LO) phonons in a bulk ionic crystal.

The foregoing discussion applies only to an infinite medium. In order to calculate the properties of surface optical waves, the manner in which this infinite-medium theory is modified by the presence of the surface must be examined. In particular, (VI.1) and the equivalent equation (VI.2) are no longer applicable.

Two theoretical approaches have been used to discuss surface waves and optical properties in the presence of spatial dispersion. One approach was first employed in the theory of the anomalous skin effect in metals with a specularly scattering surface,¹⁵⁷ and in later work it has been applied to the calculation of the surface plasmon dispersion relation in a metal.^{36, 158} Although the Boltzmann transport equation was used in the first work, this approach can be described more generally with nonlocal dielectric functions, and for this reason we shall refer to it as a dielectric function theory.

The second approach will be denoted the multiple-wave theory, for it depends crucially on the fact that, for a given frequency, it may occur that more waves can propagate in an infinite medium described by a nonlocal dielectric function than can propagate in a local description. Suppose now that the system is a half-space, the dispersion relations of the several propagating waves are known, and fields of the form (II.9) occur outside the medium. If more waves can occur in a nonlocal than a local description, it is possible that the determination of the amplitudes of the waves in the medium requires boundary conditions in addition to those which suffice in a local description. The proper choice of the additional boundary conditions (ABCs) is a controversial matter; different workers have used different ABCs, often with little physical justification.

A. Dielectric Function Theory

Our goal is to find the dispersion relation for the surface optical phonon in a semiinfinite medium with the surface lying in the $z=0$ plane, as shown in Fig. 2. The fields satisfy Maxwell's equations (II.1) with $\mu=1$ and a nonlocal relationship between \mathbf{D} and \mathbf{E} . It is convenient to take advantage of the translational symmetry in the x and y directions by using a dielectric function $\epsilon_{\alpha\beta}(k_x, k_y, z-z', \omega)$ which depends on the x and y components of the wave vector but on the spatial coordinates z and z' (a procedure valid only for k_x and k_y small; see Note 154):

$$\epsilon_{\alpha\beta}(k_x, k_y, z-z', \omega) = \frac{1}{2\pi} \int dq_z \epsilon_{\alpha\beta}(\mathbf{q}, \omega) e^{iq_z(z-z')} \quad (\text{VI.7})$$

where we are again using the symbol \mathbf{k} for a two-dimensional wave vector parallel to the surface, so that the components of the vector \mathbf{q} are (k_x, k_y, q_z) . We take the crystal to be cubic with the cubic axes lying perpendicular and parallel to the surface and also aligned with our coordinate axes. Thus, $\epsilon_{\alpha\beta} = \epsilon_{\beta\alpha}$. We can then consider a p -polarized field arrangement with $k_y=0$, $|k_x|=k$, and $E_y=0$. The equation analogous to (VI.1) and (VI.2) involving the dielectric function (VI.7) is, for an infinite medium,

$$D_\alpha(k_x, z, \omega) = \sum_\beta \int dz' \epsilon_{\alpha\beta}(k_x, z-z', \omega) E_\beta(k_x, z', \omega) \quad (\text{VI.8})$$

We now go to the semiinfinite medium and assume the surface to "scatter" specularly, that is, to affect the fields as would a specularly-scattering metallic surface. Equation (VI.8) must then be replaced and we do so by introducing a polarization vector $P_\alpha(k_x, z, \omega)$ and a susceptibility tensor $\chi_{\alpha\beta}(k_x, z-z', \omega)$ satisfying

$$D_\alpha = E_\alpha + 4\pi P_\alpha \quad (\text{VI.9a})$$

and

$$\epsilon_{\alpha\beta} = \delta_{\alpha\beta} + 4\pi\chi_{\alpha\beta} \quad (\text{VI.9b})$$

The polarization components then are

$$P_x(z) = \int_0^\infty dz' \{ [\chi_{xx}(z-z') + \chi_{xx}(z+z')] E_x(z') + [\chi_{xz}(z-z') - \chi_{xz}(z+z')] E_z(z') \} \quad (\text{VI.10a})$$

and

$$P_z(z) = \int_0^\infty dz' \{ [\chi_{zz}(z-z') - \chi_{zz}(z+z')] E_z(z') + [\chi_{zx}(z-z') + \chi_{zx}(z+z')] E_x(z') \} \quad (\text{VI.10b})$$

for $z > 0$. The k_x and ω indices have been suppressed in (VI.10). These equations, which apply specifically to a metal filling the half-space $z > 0$, have been constructed so that the normal component of the polarization, or equivalently the normal component of the current density, vanishes at the surface.¹⁵⁹ The terms in the susceptibility in which the argument $(z-z')$ occurs represent the response produced at z by electrons which have interacted with the electric field at z' and traveled directly to z , whereas the terms containing $(z+z')$ represent the response produced at z by the electrons which have been reflected off the surface after interacting with the electric field at z' .

Equations (VI.10) can be rewritten in the form of (VI.8), which applies to an infinite medium, by defining fictitious fields for $z < 0$ in an infinite medium such that $E_x(z) = E_x(-z)$ and $E_z(z) = -E_z(-z)$. Replacing the integration variable z' by $-z'$ in the terms containing $(z+z')$, it is easily verified that (VI.9) reduce to (VI.8). A specularly scattering semi-infinite medium $z > 0$ is therefore equivalent to an infinite medium with appropriately chosen fields in the half-space $z < 0$. Maxwell's equations (II.1) can then be solved for the field ratio $E_x(0+)/H_y(0+)$ just inside the surface, that is, the surface impedance, by Fourier transforming the equations with respect to z .^{54, 160} Since E_x and H_y are continuous across the surface $z=0$, the value of $E_x(0+)/H_y(0+)$ must be equal to the corresponding field ratio just outside the surface in the boundary-inactive medium. It is assumed that the boundary-inactive medium can be treated in the local approximation and, therefore, is described by a frequency-dependent dielectric function $\epsilon_l(\omega)$. Under the condition that the fields in the boundary-inactive medium decay exponentially away from the surface, this field ratio is $E_x(0-)/H_y(0-) = -i\alpha_l/\omega\epsilon_l$, according to (II.9a) and (II.9c). The equation $E_x(0-)/H_y(0-) = E_x(0+)/H_y(0+)$ can then be written

$$-\frac{i\alpha_l}{\omega\epsilon_l} = \frac{i\omega}{\pi c} \int_{-\infty}^{\infty} \frac{1}{q^2} \left[\frac{k^2}{(\omega^2/c^2)\epsilon_l(\mathbf{q}, \omega)} + \frac{q_z^2}{(\omega^2/c^2)\epsilon_l(\mathbf{q}, \omega) - q^2} \right] dq_z \quad (\text{VI.11})$$

where $q^2 = k^2 + q_z^2$, $k = |k_x|$, $\alpha_l = [k^2 - \epsilon_l(\omega^2/c^2)]^{\frac{1}{2}}$, $\epsilon_l(\mathbf{q}, \omega)$ is the longitudinal dielectric function, and $\epsilon_t(\mathbf{q}, \omega)$ is the transverse dielectric function. If $\epsilon_l(\mathbf{q}, \omega)$ and $\epsilon_t(\mathbf{q}, \omega)$ are known, (VI.11) yields the surface mode dispersion relation, ω as a function of k_x . As pointed out in Section II.D.1, one can consider surface waves with k_x real and ω complex, k_x complex and ω real, or both k_x and ω complex. In the following discussion we consider k_x ($k = |k_x|$) real and ω complex.

Equation (VI.11) is the nonlocal version of (II.11), and it can be shown that upon replacing $\epsilon_l(\mathbf{q}, \omega)$ and $\epsilon_t(\mathbf{q}, \omega)$ by the local dielectric function $\epsilon(\omega) = \lim_{q \rightarrow 0} \epsilon_l(\mathbf{q}, \omega) = \lim_{q \rightarrow 0} \epsilon_t(\mathbf{q}, \omega)$, a result valid for cubic crystals, (VI.11) reduces to (II.11). In addition, (VI.11) is essentially equivalent to (II.49). The right-hand side of both equations is the nonlocal surface impedance of the medium in the half-space $z > 0$. The left-hand sides differ only trivially because they have been used to describe situations in which the associated media are surface-inactive, with a local dielectric function $\epsilon_l(\omega)$, or surface-active, with a local dielectric function $\epsilon(\omega)$.

If the medium in the half-space $z < 0$ is to be described nonlocally, the left-hand side of (VI.11) must be replaced by the negative of an expression having the same form as the right-hand side, but containing the nonlocal dielectric functions $\epsilon_l(\mathbf{q}, \omega)$ and $\epsilon_t(\mathbf{q}, \omega)$ appropriate for the medium $z < 0$.

It should be noted that whatever surface or bulk phenomena are contained in the original half-space description persist in the "effectively infinite medium" description. That is, the fields in the originally present half-space $z > 0$ contain all the information concerning the excitations of the system. It is these fields that are reflected *mathematically* into the half-space $z < 0$. This reflection is then merely a device to expedite the solution of the equations. However, this device contains the important physical implication that the surface scatters specularly, and this must be kept in mind. The motivation for this procedure is, of course, to satisfy the boundary condition that the normal component of the polarization be zero at the surface. This specular scattering scheme is certainly the simplest, but by no means the only nor, perhaps, even the most appropriate physical way to accomplish this.

Equation (VI.11) has been used to calculate the surface plasmon dispersion relation for a semiinfinite free electron metal, employing RPA expressions for the dielectric functions.³⁶ ω' , the real part of the frequency, does not approach a constant asymptotic value with increasing k_x as it does in a local theory, but continues to rise as k_x increases. Equation (VI.11) has not yet been applied to ionic crystals. One must first ask whether the specular scattering boundary condition (VI.9) is appropriate for an ionic crystal. Second, the integration over q_z must be terminated at finite values so that \mathbf{q}

remains inside the Brillouin zone. Finally, the nonlocal dielectric functions $\epsilon_l(\mathbf{q}, \omega)$ and $\epsilon_t(\mathbf{q}, \omega)$ must be determined. If the [001] crystal axis lies in the z direction, normal to the surface of the crystal, and if k_x is small, \mathbf{q} will remain near the (001) axis in reciprocal space as one integrates over q_z . Then the longitudinal dielectric function $\epsilon_l(\mathbf{q}, \omega)$ is approximately equal to $\epsilon_{zz}(q_z, \omega)$, which must be consistent with the bulk LO phonon dispersion relation according to (VI.6). The transverse dielectric function $\epsilon_t(\mathbf{q}, \omega)$ is approximately equal to $\epsilon_{xx}(q_z, \omega)$, which must be consistent with the bulk TO phonon dispersion relation according to the equation $|\epsilon_{xx}(q_z, \omega)| = \infty$, if we neglect retardation in (VI.5). If k_x becomes so large that it is of the same order of magnitude as a reciprocal lattice vector, \mathbf{q} will move away from symmetry directions into outer parts of the Brillouin zone, where the dielectric tensor cannot be separated into longitudinal and transverse parts, so (VI.11) must become invalid.

Despite these fundamental difficulties, the use of (VI.11) to determine the surface optical mode dispersion relation in an ionic crystal may not be entirely unreasonable. If k_x becomes large enough that retardation effects are unimportant ($k \gg \omega_{TO}/c$), one can alternatively consider (VI.11) in the unretarded limit $c \rightarrow \infty$ where we find

$$-\frac{1}{\epsilon_l} = \frac{k}{\pi} \int_{-\infty}^{\infty} \frac{dq_z}{q^2 \epsilon_t(\mathbf{q}, \omega)} \quad (\text{VI.12})$$

When retardation is neglected, the properties of the surface phonon are therefore governed by the longitudinal dielectric function, which in turn must have a \mathbf{q} dependence consistent with the dispersion relation of the bulk LO mode. In a metal, the increase of the surface plasmon frequency with increasing k is directly related to the fact that the bulk plasmon frequency increases with increasing $|\mathbf{q}|$. In an ionic crystal, however, the frequency of the bulk LO mode decreases with increasing $|\mathbf{q}|$; the frequency of the surface phonon will therefore decrease with increasing k . As k increases from the light line, the frequency of the surface phonon will, in the small k region where retardation is important, increase toward the limit $\omega_{s\infty}$ as given by (II.18). As k continues to increase, the frequency will then decrease as a consequence of the nonlocal effect discussed above. This phenomenon, which has been seen in microscopic lattice-dynamical calculations of the normal modes of an ionic crystal slab using a point-ion model, is discussed further in Section IX.

The same theory can be applied to a slab by replacing the right-hand side of (VI.11), which is the surface impedance for a semi-infinite medium,

by the surface impedance for the slab. We shall assume that the inactive medium on each side of the slab has the same local dielectric function ϵ_I , so the system has reflection symmetry, and the normal modes have definite parities about the center of the slab. It follows that there are two values of the surface impedance, which will be denoted by $Z^{(1)}$ and $Z^{(2)}$, depending on whether the electric field in the z direction has even or odd parity. The expressions for $Z^{(1)}$ and $Z^{(2)}$ are^{55,160}

$$Z^{(1,2)} = \frac{2i\omega}{Lc} \sum_{n=-\infty}^{\infty} \frac{1}{q^2} \left[\frac{k^2}{(\omega^2/c^2)\epsilon_I(\mathbf{q}, \omega)} + \frac{q_z^2}{(\omega^2/c^2)\epsilon_I(\mathbf{q}, \omega) - q^2} \right] \quad (\text{VI.13})$$

where L is the film thickness, $q^2 = k^2 + q_z^2$, and $q_z = n\pi/L$, with n being summed over odd and even integers in the expressions for $Z^{(1)}$ and $Z^{(2)}$, respectively. Because of the finite thickness of the slab, the continuous wave vector q_z in (VI.11) has been replaced by a wave vector assuming discrete values in (VI.13).

The determining equations for the normal modes of the slab are, for odd-parity modes,

$$-\frac{ic\alpha_I}{\omega\epsilon_I} = Z^{(1)} \quad (\text{VI.14a})$$

and for even-parity modes,

$$-\frac{ic\alpha_I}{\omega\epsilon_I} = Z^{(2)} \quad (\text{VI.14b})$$

Equations (VI.14) are the nonlocal versions of the two local equations

$$\frac{S - S_I}{S + S_I} \pm \epsilon^{aL} = 0 \quad (\text{VI.15})$$

where $S = \epsilon/\alpha$ and $S_I = \epsilon_I/\alpha_I$. Equations (VI.15) originate from equating the right-hand sides of (II.35) for this symmetric system in which the inactive medium on each side of the slab is the same.

The solutions of (VI.14) have not been investigated. It is expected that they will yield normal mode dispersion relations which exhibit many of the features of the exact normal modes to be discussed in Section IX. One should find that (a) the two FK surface modes will decrease in frequency for large k instead of approaching a constant asymptotic frequency; and (b) the LO and TO bulk modes, which occur at the frequencies ω_{LO} and ω_{TO} in the local approximation for values of k sufficiently large that

retardation can be neglected, now appear over bands of frequencies. (These features do appear in Figs. 51 and 52, which are discussed in Section IX.) In addition, the modes will exhibit effects of retardation for very small values of k .

Essentially the same nonlocal theory can be used to calculate the nonlocal optical properties of a semiinfinite medium or a slab. Consider, for example, the slab of Fig. 7 with $\epsilon_{lu} = \epsilon_{ld} = 1$ and with p -polarized light incident at an angle θ from the normal in the x - z plane on the upper surface. The fields within the slab can be written as the sum of two parts, one with even parity and the other with odd parity, with the surface impedance (E_x/H_y ratio) for each part given by (VI.13). The wave vector k in the surface impedance expressions is determined by the x component of the wave vector of the incident light: $k = (\omega/c)\sin\theta$, for light incident from vacuum. At the upper surface one then equates the E_x/H_y ratio inside the slab to the E_x/H_y ratio associated with the incident and reflected waves, and at the lower surface, to the E_x/H_y ratio associated with the transmitted wave, the amplitudes of the reflected and transmitted waves being unknown. The resulting equations can be solved for the reflected and transmitted wave amplitudes, and one finally obtains expressions for the reflectance, transmittance, and absorptance of the slab as functions of $Z^{(1)}$ and $Z^{(2)}$.¹⁶¹

This theory yields a series of absorptance peaks associated with bulk plasmon resonances in a very thin metal film, which have been observed experimentally.^{162, 163} In an attempt to determine the applicability of the theory to ionic crystals, one of the authors has used this method to calculate the optical absorptance of a 15-layer NaCl slab with (100) surfaces whose normals are in the z direction,¹⁶⁴ and has compared the result with that of a microscopic lattice-dynamical calculation.¹⁶⁵ The longitudinal dielectric function in (VI.13) was assumed to be of the form

$$\epsilon_l(\mathbf{q}, \omega) \approx \epsilon_l(q_z, \omega) = 1 + \frac{a_1 - 1}{1 - \Omega(\Omega + i\gamma) + a_2(\cos(\pi q_z/q_0) - 1)} \quad (\text{VI.16})$$

where $\Omega = \omega/\omega_{TO}$, γ is a phenomenological damping constant, a_1 and a_2 are adjustable constants, and q_0 is the value of q_z at the edge of the Brillouin zone. The condition $\epsilon_l(q_z, \omega) = 0$, with the damping constant $\gamma = 0$, yields the LO phonon dispersion relation

$$\omega = \omega_{TO} \left[a_1 + a_2 \left(\cos \frac{\pi q_z}{q_0} - 1 \right) \right]^{1/2} \quad (\text{VI.17})$$

which is a good representation of the dispersion relation calculated by Kellermann⁸² if the constants a_1 and a_2 are chosen properly. The local approximation

$$\epsilon_i(\mathbf{q}, \omega) \approx \epsilon(\omega) = 1 + \frac{a_1 - 1}{1 - \Omega(\Omega + i\gamma)} \quad (\text{VI.18})$$

was used for $\epsilon_i(\mathbf{q}, \omega)$. The sum over n in (VI.14) was truncated so that the wave vector remained within the Brillouin zone, that is, $|q_z| \leq q_0$ or $n \leq n_L$, where $n_L = 15$ is the number of atomic layers.

The result of this calculation is shown by the solid line in Fig. 37 which gives the absorbance A as a function of the dimensionless frequency variable $\Omega = \omega/\omega_{\text{TO}}$ for p -polarized light incident at an angle of 75° . The points are obtained from the lattice dynamical theory of Ref. 165. It should be emphasized that a local theory of optical absorption, which is

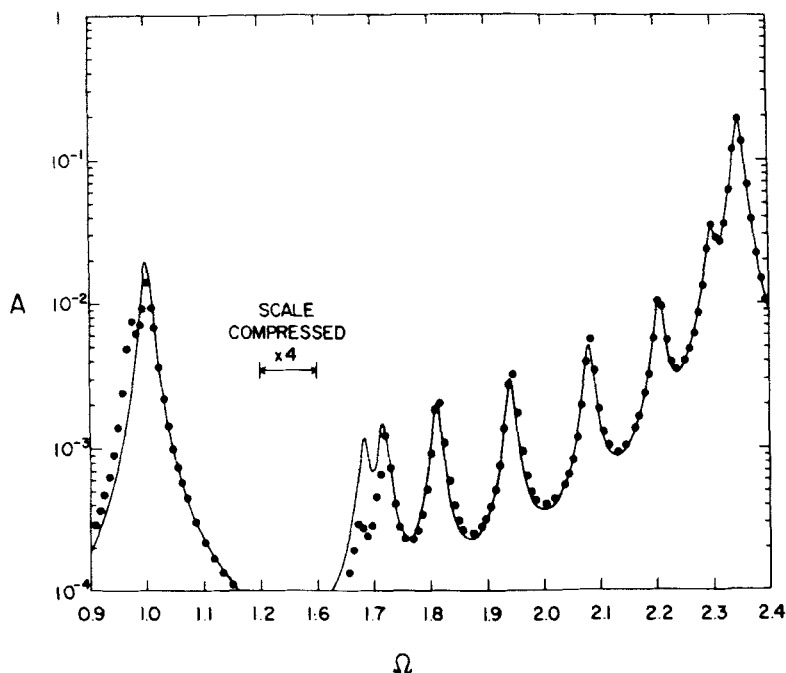


Fig. 37. Absorbance A as a function of frequency $\Omega = \omega/\omega_{\text{TO}}$ for a NaCl film. The points result from a microscopic lattice-dynamics calculation for a 15-layer slab (see Section IX.A) and the line from the nonlocal theory for a film of the same thickness.

based entirely on the local dielectric function (VI.18), would yield only two peaks, one at $\omega = \omega_{\text{TO}}$ or $\Omega = 1$, and the other at $\omega = \omega_{\text{LO}}$ or $\Omega = 2.34$.¹⁶⁶ However, the nonlocal theory yields a series of peaks in the frequency range below ω_{LO} . These peaks are associated with standing-wave or bulk LO modes which fit the slab in such a way that there are $n = 1, 3, 5, \dots, 15$ half-waves of the z component of the polarization across the slab, with nodes at the surfaces.¹⁶⁷ The peak at $\Omega = 2.34$ corresponds to $n = 1$ half-wave; the lowest frequency peak at $\Omega = 1.68$ corresponds to $n = 15$ half-waves.

This nonlocal theory is not entirely correct because it does not produce an absorptance peak at $\Omega = 0.97$ associated with a TO mode strongly localized at the surface (this mode is known as the "Lucas surface mode" in lattice dynamics¹⁶⁸). The discrepancy exists because this surface mode arises as a consequence of the modification of interatomic forces for atoms near the surface; in particular, the restoring force acting on a displaced atom is different for surface and interior atoms. The nonlocal theory, which contains the dielectric function for an infinite medium, therefore does not properly take account of the intrinsically different characteristics of the surface and the bulk. Just as the theory fails to reproduce the optical absorption associated with the Lucas surface mode, the solutions of the normal mode equations (VI.14) will also not include this mode.

A "specular scattering" boundary condition, equivalent to the statement that the normal component of the polarization must be zero at the surface, appears to be reasonable, at least for the LO modes associated with the prominent absorptance peaks appearing in the frequency range $1.6 < \Omega < 2.4$.¹⁶⁹ If this boundary condition were grossly incorrect, one would not expect such good agreement between the nonlocal and the lattice dynamical calculations. The discrepancy in intensity of the peak at $\Omega = 1.68$ may arise as follows: In the lattice dynamical theory there is significant interaction between the LO mode responsible for this peak and lower frequency longitudinal acoustical modes. The absorptance would therefore be smaller in the lattice dynamical theory because some of the optical absorption would be removed from this LO mode and distributed among the acoustical modes which are completely disregarded in the above version of the nonlocal theory.

The fact that the absorptance as calculated using the nonlocal theory agrees as well as it does with that from lattice dynamics suggests that this theory might also give reasonable results for the surface mode frequencies to rather large values of k . Such a calculation would be worthwhile since the corresponding experimental results could possibly be obtained using the experimental technique of Ibach.^{150, 151}

B. Multiple-Wave Theories

1. Metals and Ionic Crystals

Sauter¹⁷⁰ and Forstmann¹⁷¹ have used multiple-wave theories to calculate the optical properties of a semiinfinite metal, Melnyk and Harrison^{172,173} to calculate the optical properties of a metallic slab, and Sturm¹⁷⁴ to determine the surface plasmon dispersion relation. The waves that can propagate in a bulk metal have dispersion relations given by the solutions of (VI.5) and (VI.6). The plasma frequency ω_p in a metal plays the same role as the frequency ω_{LO} in an ionic crystal, for this is the frequency at which the local dielectric function vanishes. As shown in Fig. 38, two waves can propagate in a free electron metal; one is longitudinal (the bulk plasmon), the other is transverse (with two possible directions of polarization), and they both begin at the frequency ω_p when $\mathbf{q}=0$. The rise in frequency of the longitudinal wave with increasing \mathbf{q} is a consequence of nonlocality, the \mathbf{q} dependence of $\epsilon_l(\mathbf{q}, \omega)$.

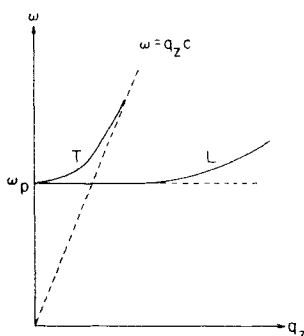


Fig. 38. Dispersion relations for transverse (*T*) and longitudinal (*L*) waves in a bulk free-electron metal.

Consider now a metal filling the semiinfinite region $z > 0$ with light incident from vacuum in the x - z plane at an angle θ from the normal. We investigate the conditions under which these waves can propagate. We again take $k_y = 0$ and, if considering a crystal, orient it such that $E_y = 0$. If one neglects the nonlocality of the transverse dielectric function, then (VI.5), which defines the transverse wave dispersion relation, can be rewritten

$$q_z^2 = \frac{\omega^2}{c^2} \epsilon(\omega) - k^2 = \frac{\omega^2}{c^2} [\epsilon(\omega) - \sin^2 \theta] \quad (\text{VI.19})$$

We assume the free electron form for $\epsilon(\omega)$:

$$\epsilon(\omega) = 1 - \frac{\omega_p^2}{\omega^2} \quad (\text{VI.20})$$

If $\epsilon(\omega) > \sin^2 \theta$ or $\omega/\omega_p > (\cos \theta)^{-1}$, then $q_z^2 > 0$; that is, the transverse wave can propagate into the metal. If $\omega/\omega_p < (\cos \theta)^{-1}$, $q_z^2 < 0$, and the wave is exponentially damped in the z direction. It follows that the absorptance of the metal is small if $\omega/\omega_p < (\cos \theta)^{-1}$, but large for $\omega/\omega_p > (\cos \theta)^{-1}$.^{174a} The longitudinal wave, with the \mathbf{q} dependence of the frequency included, can propagate into the metal for frequencies $\omega \geq \omega_p$.¹⁷⁵ Since this wave has a vanishing y component of the electric field, it cannot be excited with s -polarized light, which has an electric field in the y direction, but only by p -polarized light. If one compares this nonlocal theory with the local theory, in which the \mathbf{q} dependence of the longitudinal wave frequency is neglected, the nonlocal theory gives additional absorptance when $\omega > \omega_p$ for p -polarized light because the longitudinal wave is excited in this frequency range.

We now demonstrate explicitly the emergence of the additional boundary condition requirement by making a calculation of the absorptance for p -polarized light. Taking fields of the form $\mathbf{F}(\mathbf{r}, t) = \mathcal{F}(z)e^{i(kx - \omega t)}$, one writes the fields in the medium ($z > 0$) as the sum of a transverse wave with amplitude a and a longitudinal wave with amplitude b . We begin with

$$\mathcal{E}_z(z) = ae^{iq_z' z} + be^{iq_z'' z} \quad (\text{VI.21a})$$

where q_z' and q_z'' are the z components of the wave vectors for the transverse and longitudinal waves, respectively, at the frequency ω . Using the fact that $\nabla \times \mathbf{E} = 0$ for the longitudinal wave, one finds

$$\mathcal{E}_x(z) = -\frac{q_z'}{k} ae^{iq_z' z} + \frac{k}{q_z''} be^{iq_z'' z} \quad (\text{VI.21b})$$

The magnetic field is then found from Maxwell's equation

$$\mathcal{B}_y(z) = \frac{c}{i\omega} \left[\frac{d\mathcal{E}_x(z)}{dz} - ik\mathcal{E}_z(z) \right] = -\frac{\omega}{kc} ae^{iq_z' z} \quad (\text{VI.21c})$$

Outside the medium ($z < 0$) the fields are expressed as the sum of an incident wave with unit amplitude and a reflected wave with amplitude r :

$$\mathcal{E}_z(z) = e^{iq_z^0 z} + re^{-iq_z^0 z} \quad (\text{VI.22a})$$

$$\mathcal{E}_x(z) = -\frac{q_z^0}{k} [e^{iq_z^0 z} - re^{-iq_z^0 z}] \quad (\text{VI.22b})$$

and

$$\mathfrak{B}_y(z) = -\frac{\omega}{kc} [e^{iq_z^0 z} - r e^{-iq_z^0 z}] \quad (\text{VI.22c})$$

where $q_z^0 = (\omega/c)\cos\theta$ while $k = (\omega/c)\sin\theta$ in both (VI.21) and (VI.22). The usual boundary conditions on the continuity of \mathfrak{E}_x and \mathfrak{B}_y at $z=0$ would be sufficient to solve for the amplitudes r and a if the longitudinal wave amplitude b were zero. However, now an additional boundary condition is needed: It is assumed that the normal component j_z of the conduction current must vanish at the surface, or one can equivalently require that the polarization $P_z(0)=0$. Thus there is no polarization charge on the surface, and E_z must be continuous. This additional boundary condition allows (VI.21) and (VI.22) to be solved for the reflected wave amplitude r and the reflectance $R=|r|^2$.

An equation from which the surface plasmon dispersion relation can be derived is obtained by substituting exponentially decaying fields of the form (II.9) for the incident and reflected wave fields of (VI.22). By using the three boundary conditions on \mathfrak{E}_x , \mathfrak{B}_y , and \mathfrak{E}_z , one gets a homogeneous system of three equations in the three unknowns a , b , and K' , so the determinant of the coefficients of these unknowns must be zero. This is the desired equation. The surface plasmon has a frequency $\omega < \omega_p$, a region where neither a transverse nor a longitudinal wave can propagate. However, the fields within the metal can still be written in the form of (VI.21) with q_z' and q_z'' imaginary, so that both the transverse and longitudinal fields decay exponentially.

The calculations by the previously cited workers differ in detail because of differences in the bulk plasmon dispersion relation, but otherwise the theories are essentially equivalent. It is also of interest that the dielectric function theory discussed in Section VI.B can be made equivalent to the multiple-wave theory by suitably approximating the nonlocal dielectric functions. This is not surprising, since the same boundary condition $j_z(0)=0$ is used in both types of theory. The RPA dielectric functions for an electron gas have a complicated structure which not only describes the transverse and longitudinal wave dispersion relation but also contains the anomalous skin effect in the low-frequency optical properties and the electron-hole pair excitations, which damp the longitudinal wave at large values of the wave vector. By using the local dielectric function $\epsilon(\omega)$ in place of the transverse dielectric function $\epsilon_t(\mathbf{q}, \omega)$ and a longitudinal dielectric function of the form $\epsilon_l(\mathbf{q}, \omega) = 1 - \omega_p^2 / [\omega(\omega + i\gamma) - Aq^2]$, where A is constant, one in effect simplifies the metal so that the only excitations are the transverse and longitudinal waves of the form assumed in the multiple-wave theory. The dielectric function theory for the optical properties of a

slab then becomes equivalent to the multiple-wave theory of Melnyk and Harrison,^{172,173} and (VI.11), which gives the surface plasmon dispersion relation, reduces to an equation derived by Sturm.¹⁷⁴

Since the dielectric function theory, with the $j_z(0)=0$ boundary condition, has been shown to have some validity for ionic crystals, it follows that the multiple-wave theory can also be applied to ionic crystals. Ruppin¹⁷⁶ has used the multiple-wave theory of Melnyk and Harrison to calculate the optical properties of an ionic crystal slab, and has obtained results which are essentially equivalent to those found by one of the authors.¹⁶⁴

2. Insulators with Exciton States

There is a long history of work on the effects of spatial dispersion on the optical properties of insulators with excitonic transitions,¹⁷⁷⁻¹⁸³ and, recently, surface waves¹⁸⁴ and Brillouin scattering¹⁸⁵ have also been studied. The dispersion relations for exciton waves in a bulk crystal are similar to those shown in Fig. 36 for an ionic crystal, except that (1) ω_{LO} and ω_{TO} are very close to each other, and (2) the frequencies of both the lower transverse branch and the longitudinal branch rise rapidly with increasing q_z , so that two transverse branches exist at frequencies $\omega > \omega_{LO}$.

The theories, which are similar in principle to those discussed in Section VI.B.1, are distinguished by the use of various additional boundary conditions. Some authors have also shown how the additional boundary conditions are related to the behavior of the exciton wave function at the surface.^{178,183}

If one first considers light incident normally on a semiinfinite medium, the electric field and polarization can be taken to lie in the x direction. Pekar¹⁷⁷ has used the ABC

$$P_x \Big|_{z=0} = 0 \quad (\text{VI.23})$$

where P_x is the exciton polarization, and Hopfield and Thomas¹⁷⁸ have proposed a more general ABC of the form

$$\left(AP_x + B \frac{dP_x}{dz} \right) \Big|_{z=0} = 0 \quad (\text{VI.24})$$

Zeyher et al.¹⁸³ have shown how the ABC is related to the behavior of the exciton wave function at the surface. They assume that the total polarization can be written as the sum of the exciton polarization P_x and a background polarization $\chi_0 E_x$, where χ_0 is a local dielectric susceptibility. If the exciton is totally reflected by the surface with a phase such that the

exciton wave function vanishes at the surface, they find the ABC

$$(P_x - \chi_0 E_x)|_{z=0} = 0 \quad (\text{VI.25})$$

which reduces to the Pekar condition (VI.23) if $\chi_0 = 0$. If the exciton wave function is simply "chopped off" at the surface, exciton reflection totally disregarded, one obtains an ABC of the Hopfield-Thomas form:

$$\left(\frac{dP_x}{dz} + i\Gamma P_x \right) \Big|_{z=0} = 0 \quad (\text{VI.26})$$

where Γ can be related to parameters appearing in the model dielectric function

$$\epsilon_l(\mathbf{q}, \omega) = \epsilon_0 + \frac{\omega_p^2}{\omega_T^2 - \omega(\omega + i\gamma) + Dq^2} \quad (\text{VI.27})$$

by the equation

$$\Gamma = \frac{\omega(\omega + i\gamma) - \omega_T^2 - Dk^2}{D} \quad (\text{VI.28})$$

Here $k = 0$ since the light is normally incident and D is a constant.

The treatment of obliquely incident p -polarized light, and the closely related problem of surface optical waves, is much less satisfactory. Following the procedure of Sein¹⁸⁰ and Agarwal et al.,¹⁸¹ Maradudin and Mills¹⁸⁴ have assumed that the nonlocal relation between the polarization and the field is given by

$$\mathbf{P}(z) = \int_0^\infty dz' \chi(z - z') \mathbf{E}(z') \quad (\text{VI.29})$$

where the notation is the same as in (VI.9). By using a scalar susceptibility function in (VI.29), any possible difference between transverse and longitudinal susceptibilities is disregarded. Furthermore, (VI.29) does not contain the $\chi(z + z')$ terms of (VI.9), and thus completely neglects the possibility that excitons can be reflected from the surface.¹⁸⁶ Since three waves—two transverse and one longitudinal—can propagate at a given frequency, two ABCs are needed for p -polarized fields. Equation (VI.29), together with the model dielectric function (VI.27), does, in fact, lead to two ABCs: (VI.26) for P_x and a similar equation for P_z .

Maradudin and Mills have found a number of interesting results for both the optical properties and dispersion relations for surface optical

waves. However, the accuracy of these results is questionable because (VI.29) is almost certainly incorrect.

In conclusion, it is not clear how these exciton theories can be applied to ionic crystals because of the uncertainty about the correct ABC. In addition, all multiple-wave theories have the same deficiency as the dielectric function theories in that they disregard the fact that the surface differs dynamically from the bulk,¹⁸⁷ and they would therefore also not be able to treat the properties of the strongly localized Lucas surface mode and analogous features. Further work on the nonlocal approach would be desirable in order to resolve the boundary condition problem and to describe the dynamical properties of the surface correctly. Only for metals has there been progress in these directions.^{32, 34, 35, 37, 188, 189}

VII. MICROSCOPIC LATTICE DYNAMICS: INTRODUCTION

Microscopic lattice-dynamical theories for crystals with planar surfaces have been in existence for over 10 years. Just as in the macroscopic continuum theory, the vibrational modes of such a crystal are characterized by a two-dimensional wave vector \mathbf{k} lying in the plane of the surface. A macroscopic theory can be valid only in the long-wave region $|\mathbf{k}|d \ll 1$, with d a mean atomic spacing, whereas a microscopic theory allows \mathbf{k} to be extended throughout a two-dimensional Brillouin zone compatible with the translational symmetry of the crystal in the plane of the surface.¹⁹⁰

The Green's function method, commonly used for determining the vibrational properties of isolated defects in an otherwise perfect infinite lattice, can also be applied to a crystal with a surface. The formal theory is presented by Ludwig.¹⁹¹ If one begins with an infinite crystal, a semiinfinite crystal can be created mathematically by adding a perturbation to the equations of motion for atoms near the surface in such a way that the forces on these atoms due to atoms outside the surface vanish. The surface (taken to be an x - y plane) is therefore equivalent to an infinite plane of perturbed force constants in the equations of motion. The perturbation can be written in the form of a matrix $J_{\alpha\alpha'}(l_z l'_z; \mathbf{k}, \omega)$ dependent on Cartesian indices α, α' , layer indices l_z, l'_z , wave vector \mathbf{k} , and frequency ω . The Green's function G for the infinite unperturbed crystal also depends on these quantities. The matrix equation $|1 - GJ| = 0$ then yields the surface mode frequencies ω as a function of \mathbf{k} . The order of the determinant is limited by the finite range of the interatomic forces, which makes $J = 0$ if the layers l_z and l'_z are farther from the surface than the range of the forces. However, the difficulty of finding the Green's function

has restricted the use of this method to simple force models and to the simple cubic lattice.^{191,192}

Another method which has been used extensively begins with the equations of motion for the perfect infinite lattice. Instead of determining ω as a function of the three-dimensional wave vector \mathbf{q} as in conventional lattice dynamics, one fixes ω and the wave vector \mathbf{k} parallel to the surface, and solves for q_z , the component of the wave vector normal to the surface. The variation of amplitude with the distance z' of the l th atom from the surface is governed by q_z through the factor $\exp(iq_z z')$. For given values \mathbf{k} and ω , one finds several solutions q_z^s , $s = 1, 2, \dots, 2r$, where the number of solutions, denoted by $2r$, is determined by the range of the interatomic forces.

For a fixed value of \mathbf{k} , one may have a situation such that all of the q_z^s are complex for certain ranges of ω ; if so, exactly half of the q_z^s , that is, r of them, have positive imaginary parts, and the corresponding amplitudes fall off exponentially with distance from the surface. One can then have surface modes for which the amplitudes are expressed as linear combinations of these r basic solutions. Although each of these basic solutions satisfies the equations of motion for an infinite crystal, a solution for a crystal with a surface is found by choosing the coefficients of the linear combination in such a way that the boundary conditions at the surface are satisfied; namely, the forces on atoms below the surface arising from atoms outside the surface must vanish. It is found that these boundary conditions are expressible as a set of r linear homogeneous equations in the atomic displacements. Since there are also r unknown coefficients, this leads to a secular determinant from which the surface mode frequencies can be found as functions of \mathbf{k} .

Again taking \mathbf{k} to be fixed, there occur other frequency regions, known as the bulk mode regions, where several of the q_z^s are real with both positive and negative values; these q_z^s correspond to waves leaving or coming toward the surface. There are more solutions than the r boundary condition equations, so the frequency is not determined as in the case of surface modes, but can take on a continuous range of values within the bulk mode frequency regions.¹⁹³

The formal theory using this method has been discussed by Feuchtwang¹⁹⁴ and by Maradudin et al.,¹ and it has been applied to the calculation of surface mode dispersion relations for simple crystal models.^{6,191,195-200} These investigations have been concerned primarily with the dispersion relations for surface acoustic waves, and have shown that different types of waves can propagate, depending on the direction and magnitude of the two-dimensional wave vector, and on the ratios between elastic constants.

Neither of the foregoing methods has been applied to a realistic model of ionic crystals which includes the Coulomb forces. Also, the possible

appearance of pseudosurface modes, modes with complex frequencies existing within the bulk mode continuum, has not been investigated. These deficiencies have been overcome by a method stimulated by the development of large high-speed computers, which involves the exact determination of the normal modes and eigenfrequencies for a slab of finite thickness. It has been found that for most surface modes, a slab of only 10 to 15 atomic layers approximates closely a half-space; the exceptions are the deeply penetrating surface modes such as the FK modes discussed above. The recent work using this method is discussed, including applications such as calculations of thermal expansion, mean-square vibrational amplitudes, and optical properties. Similar calculations on the normal modes of small rectangular or approximately spherical particles are also discussed.

Another method used in surface studies of late is that of molecular dynamics, the calculation of the positions of the atoms as functions of time using the classical equations of motion with suitable initial conditions. This technique does not yield the individual normal modes, nor does it describe thermal properties correctly at very low temperatures, where zero-point motion is important; however, it has the advantage that it takes account of anharmonicity in the forces exactly, and it can be used to calculate the frequency distribution of normal modes, thermal expansion at the surface, and mean-square vibrational amplitudes.

Finally, we discuss work on the theory of surface reconstruction and the nature of surface modes on a reconstructed surface.

The results of theoretical calculations are presented rather than the formal theory. Those interested in a detailed description of the theoretical background should consult the review by Maradudin et al.¹ Another topic we do not discuss is that of the vibrational properties of impurities on surfaces. This potentially vast subject has not yet reached a state of maturity. With low-energy electron diffraction (LEED) experiments the symmetry of adsorbed monolayers can be determined, but only recently has it been possible to extract information about surface structure and vibrational properties.²⁰¹⁻²⁰⁴ Ibach^{108, 151} has discussed the use of inelastic LEED experiments to determine the vibrational frequencies of adsorbed atoms. Several theoretical treatments of the vibrational properties of adsorbed layers have been given, but only in the most recent work has a realistic model for the adsorbed layer been used.^{191, 199, 203, 205-208}

VIII. MICROSCOPIC LATTICE DYNAMICS: MONATOMIC CRYSTALS

A. Slab

In a series of papers, deWette and his co-workers²⁰⁸⁻²¹² have calculated a number of vibrational properties of slab-shaped monatomic fcc crystals in

which the atoms interact through a Lennard-Jones potential of the form

$$\varphi(r) = 4\epsilon \left[\left(\frac{\sigma}{r} \right)^{12} - \left(\frac{\sigma}{r} \right)^6 \right] \quad (\text{VIII.1})$$

This potential is a good description of the pairwise interaction in noble gas solids. By working with dimensionless frequencies

$$\omega^* = \omega \left(\frac{M\sigma^2}{\epsilon} \right)^{1/2} \quad (\text{VIII.2a})$$

and dimensionless mean-square displacements

$$\langle u^2 \rangle^* = \frac{\langle u^2 \rangle (M\epsilon)^{1/2}}{\hbar\sigma} \quad (\text{VIII.2b})$$

where M is the atomic mass, a single calculation suffices for the analysis of crystals having different values of M , ϵ , and σ . Slabs with (100), (110), or (111) surfaces and containing 11 to 51 atomic planes are considered.

The static equilibrium positions of the atoms in the slab are first determined by minimizing the total potential energy with respect to the displacement of each atomic layer in a direction normal to the surfaces. This procedure does not include the possibility of surface reconstruction. It is found that the layers near the surface are displaced outward from their ideal positions for an infinite medium. The displacements are specified by the fractional changes in interlayer spacing

$$\delta_m = \left\{ \frac{z_m - z_{m+1}}{\text{interlayer spacing in bulk}} \right\} - 1 \quad (\text{VIII.3})$$

where z_m is the coordinate of the m th plane in the direction perpendicular to the surfaces, the planes being numbered in order of increasing distance from a surface. Figure 39 shows the dependence of δ_m on m . For large m , δ_m falls off with distance into the slab as $1/m^{p-3}$, where p is the exponent characterizing the atomic interaction potential for large r , that is,

$$\varphi(r) \xrightarrow{r \rightarrow \infty} r^{-p}$$

For the Lennard-Jones potential, (VIII.1), $p=6$ so $\delta_m \propto 1/m^3$ for large m . There is some deviation from this $1/m^3$ dependence for the outermost layers of all three surface types, and for the (110) surface there is in addition an alternating deviation superimposed on the $1/m^3$ behavior, the

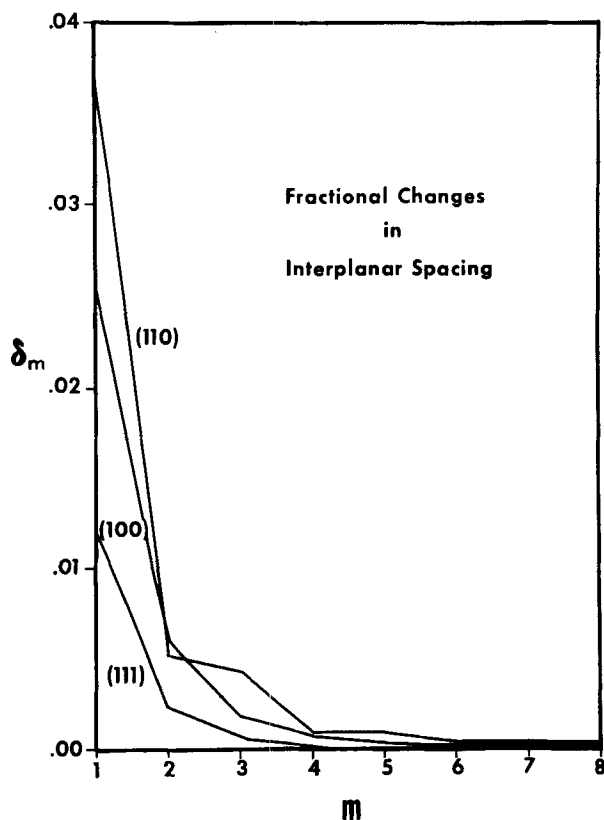


Fig. 39. Static displacements δ_m for (100), (111), and (110) surfaces expressed as fractional changes in the interplanar spacings. (Reprinted from Allen and deWette.²⁰⁹)

δ_m being larger than average for $m = 1, 3, \dots$, and smaller than average for $m = 2, 4, \dots$. The surface displacements are essentially independent of thickness for slabs with more than 30 layers, so such crystals are effectively semiinfinite insofar as static equilibrium properties are concerned.

1. Procedure and Vibrational Properties

After determining the equilibrium positions of the atoms, the dynamical properties of the lattice are calculated. The z direction is taken normal to the slab, so the periodicity of the crystal is defined by a two-dimensional unit cell in the x - y plane. The normal mode solutions are of the form

$$u_\alpha(\mathbf{I}) = M^{-1/2} \xi_\alpha(l_z; \mathbf{k}) e^{i\mathbf{k} \cdot \mathbf{r}_{0l}} e^{-i\omega t} \quad (\text{VIII.4})$$

where $u_\alpha(\mathbf{l})$ is the α th component of the dynamic displacement of the l th atom from its mean position $\mathbf{R}_0' = (x_0', y_0', z_0')$, M is the atomic mass, $\xi_\alpha(l_z; \mathbf{k})$ is the α th component of the eigenvector which depends on an index l_z denoting different atomic layers parallel to the surface, ω is the frequency, \mathbf{k} is a two-dimensional wave vector (k_x, k_y) , and $\mathbf{r}_0' = (x_0', y_0')$. If (VIII.4) is substituted into the equations of motion written in the harmonic approximation, one obtains the eigenvalue equation

$$\sum_{l'_z, \beta} D_{\alpha\beta}(l_z l'_z; \mathbf{k}) \xi_\beta(l'_z; \mathbf{k}, p) = \omega_p^2 \xi_\alpha(l_z; \mathbf{k}, p) \quad (\text{VIII.5})$$

where $p = 1, 2, \dots, 3N_3$ labels the frequency eigenvalues ω_p and the eigenvectors, N_3 being the number of atomic layers in the slab. $D_{\alpha\beta}(l_z l'_z; \mathbf{k})$ is the dynamical matrix, defined by

$$D_{\alpha\beta}(l_z l'_z; \mathbf{k}) = \frac{1}{M} \sum_{l'_x, l'_y} \Phi_{\alpha\beta}(\mathbf{l}, \mathbf{l}') e^{i\mathbf{k} \cdot (\mathbf{r}'_0 - \mathbf{r}_0)} \quad (\text{VIII.6})$$

where the $\sum_{l'_x, l'_y}$ denotes a sum over that plane of atoms for which the z component of the "vector" \mathbf{l}' specifying a specific atom is l'_z . Here

$$\Phi_{\alpha\beta}(\mathbf{l}, \mathbf{l}') = \left(\frac{\partial^2 \Phi}{\partial u_\alpha(\mathbf{l}) \partial u_\beta(\mathbf{l}')} \right)_0 \quad (\text{VIII.7})$$

are the force constants evaluated at the mean positions \mathbf{R}_0' with Φ the total potential energy of the crystal. The allowed values of \mathbf{k} are determined by periodic boundary conditions in the x and y directions, and \mathbf{k} may be taken to lie in the first two-dimensional Brillouin zone, examples of which are shown in Fig. 40.

Several general statements, applicable to an arbitrary crystal, can be made about the effect of crystalline symmetry on the properties of the normal modes.²¹¹ If each atom lies on a 180° rotation axis normal to the surface, the motion of each atom is elliptical, and the normal modes are of two types: The axes of the displacement ellipses are either perpendicular or parallel to the surface. If each atom lies on one of a set of parallel planes perpendicular to the surface and if the perfect infinite crystal has reflection symmetry about each of these planes, then for any two-dimensional wave vector \mathbf{k} parallel to these planes the modes fall into two classes. Two-thirds of the modes have displacements in the sagittal plane, that is, the plane of \mathbf{k} and \hat{z} , where \hat{z} is a unit vector normal to the surface. One-third of the modes are pure shear-horizontal (SH) modes, with displacements perpendicular to the sagittal plane. The foregoing statements apply to either a semiinfinite crystal or a slab. For a slab there may be additional symmetry

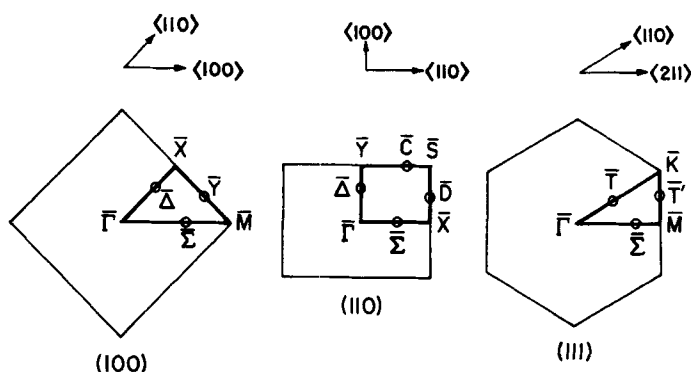


Fig. 40. Brillouin zones for the (100), (110), and (111) surfaces of an fcc crystal. A complete set of $\omega(\mathbf{k})$ values is obtained if \mathbf{k} lies within an irreducible element of the Brillouin zone, the region bounded by the heavy lines. When an x direction is specified below, it is toward the right, that is, along a $\langle 100 \rangle$ crystal axis for the (100) surface, along a $\langle 110 \rangle$ crystal axis for the (110) surface, and along a $\langle 211 \rangle$ crystal axis for the (111) surface. (Reprinted from Allen et al.²¹²)

operations. If the slab has a three-dimensional center of inversion, the normal mode eigenvectors obey the relation $\xi_{\alpha}(-l_z; \mathbf{k}, p) = \xi_{\alpha}^*(l_z; \mathbf{k}, p)$, where l_z and $-l_z$ denote atomic planes equi-distant from the center of inversion and the asterisk denotes the complex conjugate. If the slab has a reflection symmetry plane normal to the z -axis, the eigenvectors have either even or odd parity about this plane. Applications and examples of these symmetry properties are considered in the calculations for a monatomic fcc crystal slab.

In Fig. 41 the ω versus \mathbf{k} dispersion relations are shown for a 21-layer slab with (111) surfaces. Here \mathbf{k} moves along the boundary of the triangular irreducible element of the Brillouin zone in Fig. 40. The modes denoted by S_i are surface modes; they have eigenvectors which fall off with increasing distance from the surface. The other modes are bulk modes, having eigenvectors which depend sinusoidally on distance across the slab. Each curve marked S_i is actually a pair of nearly degenerate modes of even and odd parity. For a semiinfinite crystal each surface mode pair becomes a single surface mode, whereas the bulk modes become infinitely dense.

The surface mode pair S_1 is a generalized Rayleigh wave also found in an elastic continuum model.^{5,213} It lies beneath the bulk bands and persists into the long-wavelength region, where \mathbf{k} is near the point $\bar{\Gamma}$. Near $\bar{\Gamma}$ there is a removal of the degeneracy of this mode pair, which indicates that the penetration depth becomes comparable to the thickness of the slab. At shorter wavelengths the penetration depth of S_1 is much smaller than the thickness, and this is also true of the other S_i , so the mode pairs are

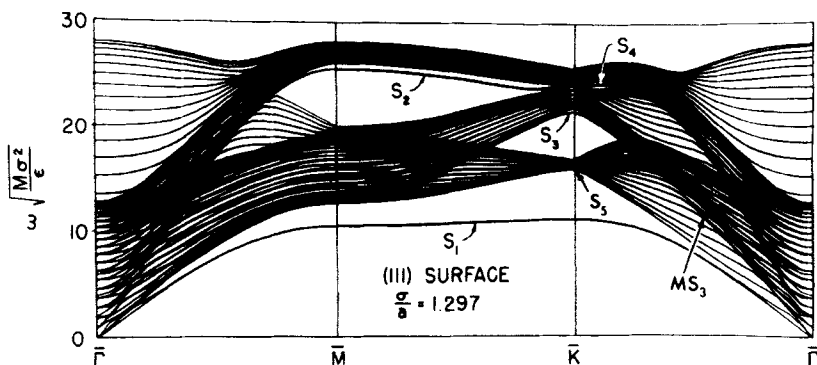


Fig. 41. ω versus k for a 21-layer slab with (111) surfaces. Here a is one-half the lattice spacing, so that $\sqrt{2} a$ is the nearest-neighbor distance; $\sigma/a = 1.297$ corresponds to the density of a static crystal. The lines marked S_i ($i = 1, 2, 3, 4, 5$) correspond to surface mode branches in a semiinfinite crystal. In a slab with two surfaces, there are actually two nearly degenerate modes corresponding to each surface mode in a semiinfinite crystal, so the lines in this figure are actually double lines. Ordinarily the two lines nearly coincide, but for S_1 near the origin ($\bar{\Gamma}$), the penetration depth becomes large, the degeneracy is broken, and the lines separate. In addition to the five distinct surface mode branches, there is a series of mixed modes MS_3 which can be seen as a disturbance in the lowest bulk band along $\bar{K}\bar{\Gamma}$. (Reprinted from Allen et al.²¹²)

essentially degenerate. The modes S_2 , S_4 , and S_5 appear in gaps between the bulk bands and cease to exist as surface modes when they enter the bulk band regions. S_3 still has some surface character within the bulk band, where it is labeled MS_3 and is a mixed mode or a pseudosurface mode. Both S_5 and S_1 are essentially shear-vertical (SV) modes; that is, the displacements are in the plane of \mathbf{k} and \hat{z} and are very nearly in the \hat{z} direction. Near the point \bar{K} the displacements for S_3 are largest in the second layer beneath the surfaces, whereas S_1 has the maximum displacements in the surface layers.

The surface modes S_1 and S_5 can be used to illustrate some general principles relating to the formation of surface modes and their relationship to bulk modes. One can begin with an infinite crystal, for which the modes are characterized by a three-dimensional wave vector \mathbf{q} . The bulk modes in a slab can then be obtained approximately from the modes in the infinite crystal by the following procedure. Defining the z direction to be normal to the surfaces of the slab, only those frequencies in the infinite crystal are allowed for which q_z is compatible with periodic boundary conditions on opposite sides of the slab. For fixed values of q_x and q_y , there are $3N_3$ frequencies corresponding to the allowed values of q_z . As q_x and q_y vary, these $3N_3$ frequencies trace out the bulk mode dispersion relations for the slab. In an actual slab, periodic boundary conditions on the opposite

surfaces are not appropriate; instead, one has missing atoms on either side. The process of removing these atoms perturbs the bulk mode spectrum found previously in such a way that surface modes are pulled out of the bulk mode spectrum. The removal of the atoms outside the slab causes a softening of the forces on the surface atoms, so the surface modes will appear on the low-frequency side of the bulk modes. In fact, one can consider the surface modes as being peeled off one by one as the surface perturbation increases from zero to its final value. In the example being considered, first S_1 is peeled off as the perturbation is turned on, and when the perturbation reaches its final value, S_5 has just begun to be peeled off near the point \bar{K} .

The ω versus \mathbf{k} relations for a (100) surface of a 21-layer fcc slab are shown in Fig. 42. Again there are several series of modes which can be regarded as being peeled off successively from a bulk band as the strength of the perturbation increases. S_6 , S_8 , and S_{10} are an example of such a series; the vibrational amplitudes of these three surface modes are localized primarily in the first, second, and third layers, respectively. Above S_{10} there is an unmarked surface mode which lies slightly within the bulk band region, and is localized primarily in the fourth layer.

Figure 42 also illustrates some consequences of crystal symmetry. When \mathbf{k} is on the line between $\bar{\Gamma}$ and \bar{X} or between $\bar{\Gamma}$ and \bar{M} , it is parallel to a set of reflection symmetry planes. Under these conditions the modes fall into two noninteracting classes, with displacements either in the sagittal plane or normal to the sagittal plane. The surface modes S_4 between $\bar{\Gamma}$ and \bar{X} and S_3 between $\bar{\Gamma}$ and \bar{M} are polarized in the sagittal plane, with displacements predominantly normal to the surface (type SV), whereas the

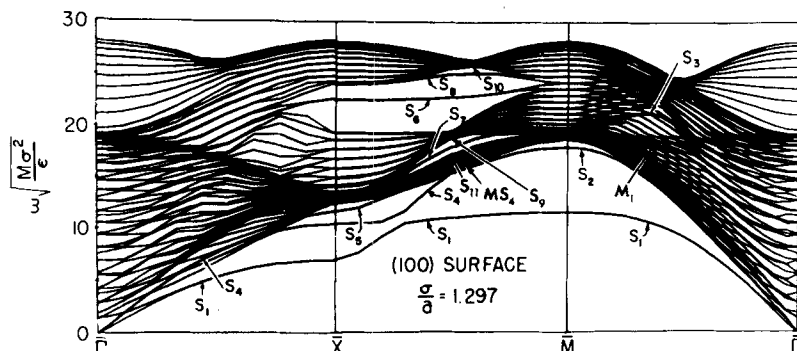


Fig. 42. ω versus \mathbf{k} for a 21-layer slab with (100) surfaces. Besides the indicated surface modes S_1, S_2, \dots, S_{11} , there appear to be two other surface modes at \bar{M} (above S_2), at least five others at \bar{X} (above S_5), one more above S_{10} , and possibly several more above S_9 . There thus appear to be at least 19 distinct surface mode branches for the (100) surface, plus several associated series of mixed modes. (Reprinted from Allen et al.²¹²)

bulk modes among which they lie are polarized normal to the sagittal plane (type SH). Generally surface modes exist only outside bulk bands. In this case, however, there is no mixing between the modes of different types, so the surface modes exist within a bulk band. For \mathbf{k} on the line between \bar{X} and \bar{M} the modes do not fall into noninteracting classes, so when S_4 enters the bulk band it interacts with the bulk modes and becomes a mixed mode or pseudosurface mode MS_4 , with some characteristics of both a surface mode and a bulk mode. Along $\bar{\Gamma}\bar{X}$ the Rayleigh mode S_1 is polarized normal to the sagittal plane (SH), but along $\bar{\Gamma}\bar{M}$ it is polarized in the sagittal plane and predominantly normal to the surface (SV). As one moves from \bar{X} to \bar{M} along $\bar{X}\bar{M}$, where the modes have no definite symmetry, S_1 changes its character from predominantly SH to predominantly SV in the region where it hybridizes or mixes with S_4 , while S_4 changes from SV to SH.

Calculations of ω versus \mathbf{k} have also been carried out for a slab with (110) surfaces, but the results are not discussed here because they are qualitatively similar to those obtained for (111) and (100) surfaces.

The effect on the normal modes of the outward relaxation of the surface layers has also been considered by comparing the foregoing ω versus \mathbf{k} relations, calculated with surface relaxation, with similar calculations in which the force constants were evaluated with the atoms in their unrelaxed ideal positions appropriate for an infinitely extended crystal. It has already been pointed out that the process of removing atoms from an infinite crystal in order to form a slab is equivalent to a softening perturbation on the surface atoms, which leads to the appearance of surface modes at frequencies lower than the bulk modes. Allowing the atoms to relax outward to their static equilibrium positions leads to a further softening, as the force constants for the surface atoms decrease if the atoms are allowed to relax outward. From the previous discussion of the manner in which surface modes are peeled off from the bottom of the bulk bands as the strength of the surface perturbation increases, it follows that fewer surface modes are peeled off when the atoms are held in their unrelaxed positions. For example, of the three surface modes S_6 , S_8 , and S_{10} , shown in Fig. 42, only S_6 appears in the gap between bulk bands if there is no relaxation. S_8 moves up to the bottom of the bulk band region, and S_{10} is missing entirely.

A study by Allen and deWette²¹⁴ on fcc films containing 3 to 21 atomic layers, with (100), (111), and (110) surfaces, should be mentioned. The Lennard-Jones potential was used, the atoms were allowed to relax in a direction normal to the surface, plane by plane, and the frequency spectra were calculated using lattice dynamics. The moments $\langle\omega\rangle$, $\langle\omega^{-1}\rangle$, and $\langle\omega\rangle/\langle\omega^{-1}\rangle$ were calculated in order to study the dependence of the superconducting transition temperature of a metal on film thickness and

orientation. For the three-layer films, the values of $\langle\omega\rangle/\langle\omega^{-1}\rangle$ are reduced from the bulk values by 46, 35, and 63% for the (100), (111), and (110) surfaces, respectively. The relative decrease for the three surfaces can be explained qualitatively by the different numbers of missing bonds for the surface atoms. For the (100), (111), and (110) surfaces, each surface atom has four, three, and five missing nearest neighbors, respectively, and moreover for the (110) surface each atom in the plane beneath the surface has one missing nearest neighbor. When the number of layers reaches 21, the moments of the frequency spectrum are within 5% of their bulk values.

2. Thermal Effects

Calculations of thermal expansion and the mean-square amplitudes of vibration of the atoms at a surface are of interest because these quantities can, in principle, be measured directly by low-energy electron diffraction (LEED). However, only qualitative agreement between theory and experiment has been achieved because of the difficulty of relating the LEED intensities to the surface thermal expansion and vibrational amplitudes.

The calculation of thermal effects in the quasiharmonic approximation begins with a solution of the eigenvalue equation (VIII.5) for the normal mode frequencies $\omega_p(\mathbf{k})$ and eigenvectors $\xi_\alpha(l_z; \mathbf{k}, p)$. The α th component of the mean-square vibrational amplitude of an atom in the layer designated by l_z is given by^{1,209}

$$\langle u_\alpha^2(l_z) \rangle = \frac{\hbar}{2NM} \sum'_{\mathbf{k}, p} |\xi_\alpha(l_z; \mathbf{k}, p)|^2 \frac{\coth[\hbar\omega_p(\mathbf{k})/2k_B T]}{\omega_p(\mathbf{k})} \quad (\text{VIII.8})$$

Here N is the number of atoms in a plane (a monatomic crystal is assumed), k_B is Boltzmann's constant, T is the absolute temperature, and the prime on the summation denotes the omission of the $\omega_p=0$ terms. This expression must be used with care for a thin slab at an elevated temperature because it diverges logarithmically with N . The error should be less than 1% if the periodicity lengths in the x - y plane are taken approximately equal to the thickness, or $\sqrt{N} = N_3$.²⁰⁹

The static equilibrium positions of the atoms are determined by minimizing the potential energy Φ as a function of the atomic positions. Similarly, the "dynamic equilibrium positions," the mean positions when atomic motion is included, are determined by minimizing the total free energy $\Phi + F$. Here F is the vibrational Helmholtz free energy, and is given by^{1,209}

$$F = k_B T \sum'_{\mathbf{k}, p} \ln \left[2 \sinh \left(\frac{\hbar\omega_p(\mathbf{k})}{k_B T} \right) \right] \quad (\text{VIII.9})$$

an expression valid for a finite or an infinite crystal. This quasi-harmonic theory of thermal expansion, equivalent to the Grüneisen theory for an infinite crystal, takes account of the anharmonicity of the forces through the dependence of the force constants (VIII.7) and, hence, the eigenfrequencies $\omega_p(\mathbf{k})$, on the equilibrium atomic positions at which the force constants are calculated. Since the vibrational free energy at $T=0$ has a zero-point contribution that depends on the eigenfrequencies, the dynamic equilibrium positions at $T=0$ are different from the static equilibrium. However, this difference is expected to be small if the mean-square amplitudes are small compared to the square of the interatomic distance.

Using the procedure described above, Allen and deWette²⁰⁹ have calculated the dynamic displacements for an fcc crystal slab with (100) surfaces and a Lennard-Jones interatomic potential, (VIII.1). Just as in their calculation of the static displacements, only the interplanar spacings were allowed to vary when the total free energy was minimized. Since the deBoer parameter Λ ,

$$\Lambda = \hbar(M\epsilon)^{-1/2}\sigma^{-1} \quad (\text{VIII.10})$$

a measure of the ratio of the mean-square vibrational amplitudes at $T=0$ to the square of the interatomic distance, is small for Ar, Kr, and Xe, the dynamic displacements for these substances at $T=0$ are very nearly equal to the static displacements. Figure 43 shows the fractional change in interlayer spacing δ_m , defined in (VIII.3), as a function of the layer index m for Ar at $T=0$ K and Xe at $T=70$ K. The dynamic displacements are essentially the same for Ar, Kr, and Xe. The calculation for Xe shows that the thermal expansion for the outermost layers is greater than that of the interior of the slab by a factor of about 5.

Allen and deWette have also calculated the mean-square vibrational amplitudes for the same model of an fcc crystal slab.²⁰⁹ At $T=0$ the amplitudes are larger at the surface than in the bulk, as shown in Fig. 44 for the (111) and (100) surfaces, and are greater in the z direction, normal to the surface, than in the plane of the surface. For a (110) surface there is additional anisotropy for the x and y directions in the plane of the surface. The mean-square amplitudes increase as the temperature is raised, and at a sufficiently high temperature one has $\langle u_a^2 \rangle \propto T$ (Fig. 45). These calculations underestimate the mean-square amplitudes of the surface atoms because the force constants used to determine the eigenfrequencies and eigenvectors are evaluated with the atoms at their positions of static equilibrium. A more accurate procedure would be to evaluate the force constants for the atoms in their dynamically displaced equilibrium posi-

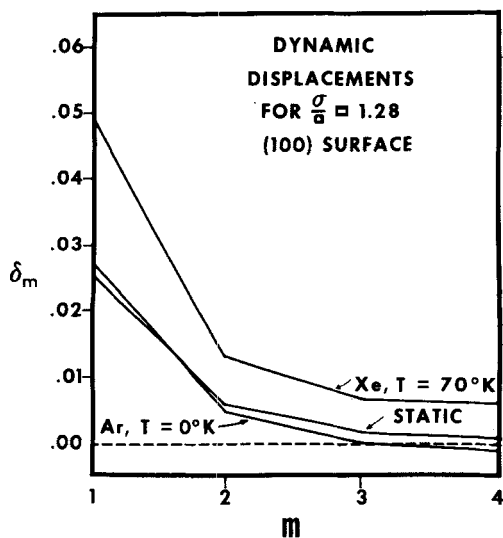


Fig. 43. Static displacements δ_m for a (100) surface compared with dynamic displacements for Ar at $T=0K$ and for Xe at 70K. (Reprinted from Allen and deWette.²⁰⁹)

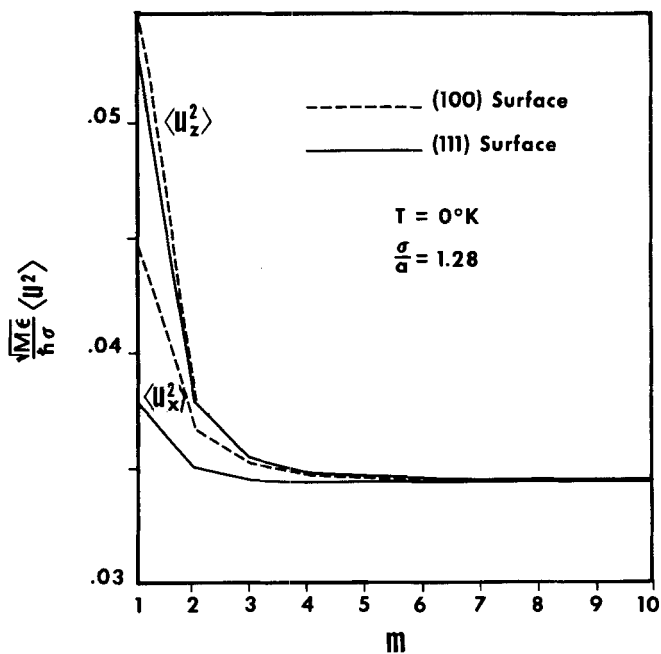


Fig. 44. Mean-square amplitudes $\langle u_x^2 \rangle$ and $\langle u_z^2 \rangle$ for (100) and (111) surfaces at $T=0K$ and $\sigma/a=1.28$. (Reprinted from Allen and deWette.²⁰⁹)

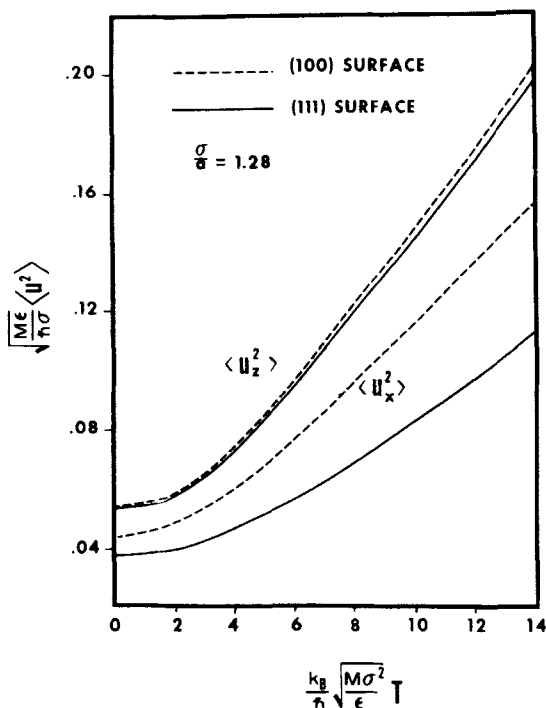


Fig. 45. Temperature dependence of mean-square amplitudes $\langle u_x^2 \rangle$ and $\langle u_z^2 \rangle$ for (100) and (111) surfaces at $\sigma/a = 1.28$. (Reprinted from Allen and deWette.²⁰⁹)

tions for which the interplanar spacing at the surface is greater than for static equilibrium. This procedure would lead to additional softening of the forces on the surface atoms, together with an increase of the mean-square amplitude. A feature not shown in Figs. 44 and 45 is a pronounced increase of the ratio $\langle u^2 \rangle_{\text{surface}} / \langle u^2 \rangle_{\text{bulk}}$ in going from $T=0$ to the high-temperature regime.

To calculate the thermal properties of a crystal one can use a method entirely different from lattice dynamics, that of molecular dynamics. This technique was applied by Allen, deWette, and Rahman²¹⁰ to an fcc crystal slab with a Lennard-Jones interatomic potential. The atoms are given initial random displacements from assumed equilibrium positions, and the motion of each atom is followed as a function of time by computer calculation, using Newton's equations of motion, until thermal equilibrium is attained. The temperature T is found by equating $\frac{3}{2} k_B T$ to the calculated mean kinetic energy per atom. This method takes complete account of anharmonic effects in the determination of the dynamic displacements and

mean-square amplitudes. Being a classical theory, it does not take account of zero-point vibrations, and therefore yields the incorrect result that the mean-square amplitudes go to zero at $T=0$. This deficiency restricts the region of validity of a mean-square amplitude calculation to temperatures higher than the Debye temperature.

Figures 46 and 47 show the mean-square amplitude of the atoms near a (100) surface of an 11-layer fcc slab as a function of the layer index m . A dimensionless temperature

$$T^{**} = \frac{k_B T}{\epsilon} \quad (\text{VIII.11})$$

with ϵ the energy parameter in the Lennard-Jones potential, (VIII.1), is introduced; for Ar, Kr, and Xe the melting temperature corresponds to $T^{**} \approx 0.71$. The dimensionless quantity $(\langle u_\alpha^2 \rangle / \sigma^2) / T^{**}$ is plotted for $\alpha = z$

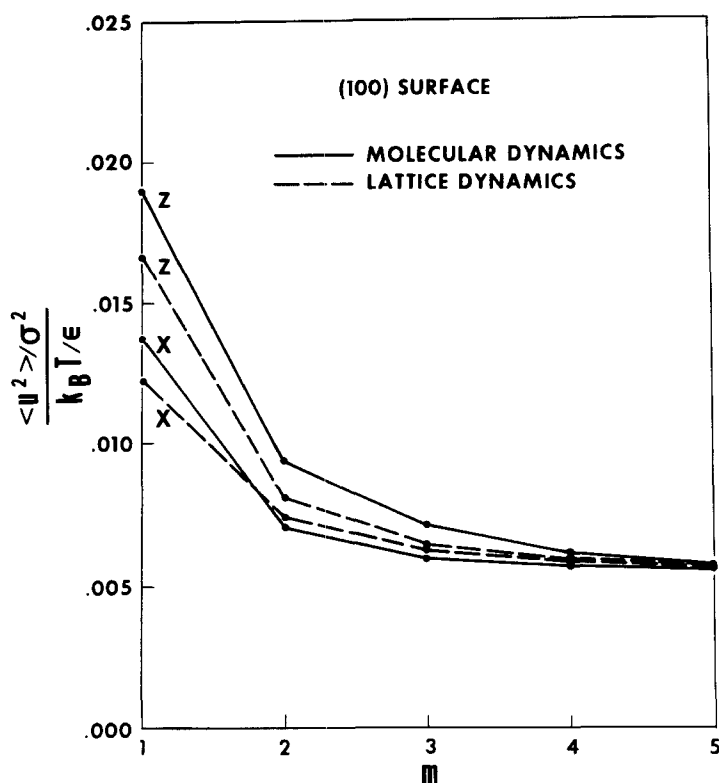


Fig. 46. Mean-square amplitudes $\langle u_x^2 \rangle$ and $\langle u_z^2 \rangle$ for (100) surface at about half the melting temperature ($T^{**} = 0.356$ and $\sigma/a = 1.28$). (Reprinted from Allen et al.²¹⁰)

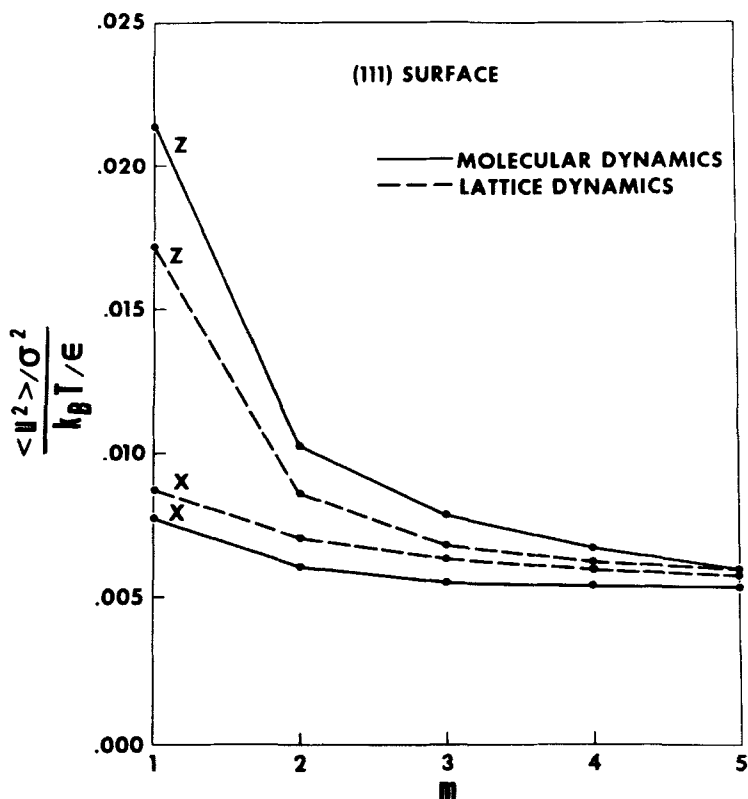


Fig. 47. Mean-square amplitudes $\langle u_x^2 \rangle$ and $\langle u_z^2 \rangle$ for (111) surface at about half the melting temperature ($T^{**} = 0.369$ and $\sigma/a = 1.28$). (Reprinted from Allen et al.²¹⁰)

(normal to the surface) and $\alpha = x$ (parallel to the surface), and for T^{**} corresponding to about one-half the melting temperature. The mean-square vibrational amplitude as calculated by molecular dynamics is larger than that calculated by lattice dynamics, the difference being due to the approximate treatment of anharmonic effects when the lattice dynamics method is used. This difference exists even in an improved lattice dynamical calculation, in which the force constants were calculated with the atoms in their dynamically displaced equilibrium positions, rather than in their static equilibrium positions, as in previous work.²⁰⁹ Calculations of the dynamic equilibrium positions, as expressed by fractional changes in interlayer spacing, are in good agreement for the two methods.

It is of interest that the surface atoms showed no tendency to form a reconstructed structure when the crystal was "cooled" by adding a damp-

ing force to the equations of motion, so that the atoms eventually became motionless. This fact supports the assumption that for atoms interacting with a Lennard-Jones potential, surface relaxation takes place by a uniform motion of each plane of atoms in the direction perpendicular to the surface.

A method for calculating the mean-square vibrational amplitudes of surface atoms, which avoids the use of (VIII.8) and the need to find the normal mode frequencies and eigenvectors, has been applied by Dobrzynski and Masri²¹⁵ to a large number of cubic metals and by Theeten and Dobrzynski²¹⁶ to Si, Ge, and diamond. The method requires the calculation of the diagonal elements of a formal matrix expression^{1,217}

$$\langle u_{\alpha}^2(\mathbf{l}) \rangle = \frac{\hbar}{2M_{\mathbf{l}}} \left[\mathbf{D}^{-1/2} \coth \left(\frac{\hbar \mathbf{D}^{1/2}}{2k_{\mathbf{B}}T} \right) \right]_{\mathbf{l}\alpha, \mathbf{l}\alpha} \quad (\text{VIII.12})$$

where \mathbf{D} is the dynamical matrix, \mathbf{l} labels the position of an atom whose mass is $M_{\mathbf{l}}$, and $\alpha = x, y, \text{ or } z$.²¹⁸ Equation (VIII.12) had been employed by Wallis et al.²¹⁷ in a calculation for a Ni surface. They used a power series expansion in the dynamical matrix at high temperature, while for $T \rightarrow 0$, $\coth(\hbar \mathbf{D}^{1/2}/2k_{\mathbf{B}}T) \rightarrow 1$. The evaluation of diagonal elements of various powers of \mathbf{D} and $\mathbf{D}^{1/2}$ involved much computation which is avoided by using a scheme presented by Theeten and Dobrzynski. The dynamical matrix is written as $\mathbf{D} = \mathbf{d} + \mathbf{R}$, where \mathbf{d} is diagonal, \mathbf{R} is off-diagonal, and it is assumed that, in some sense, $\mathbf{R} \ll \mathbf{d}$. The Taylor's expansion of (VIII.12) near \mathbf{d} then gives

$$\langle u_{\alpha}^2(\mathbf{l}) \rangle = \frac{\hbar}{2M_{\mathbf{l}}} \left\{ [f_0(\mathbf{d})]_{\mathbf{l}\alpha, \mathbf{l}\alpha} + \frac{1}{2} [\mathbf{R}^2]_{\mathbf{l}\alpha, \mathbf{l}\alpha} [f_2(\mathbf{d})]_{\mathbf{l}\alpha, \mathbf{l}\alpha} + \cdots \right\} \quad (\text{VIII.13})$$

where

$$f_0(\mathbf{d}) = \mathbf{d}^{-1/2} \coth \mathbf{a} \quad (\text{VIII.14a})$$

$$f_2(\mathbf{d}) = \frac{1}{4} \mathbf{d}^{-5/2} (3 \coth \mathbf{a} + 3 \mathbf{a} \sinh^{-2} \mathbf{a} + 2 \mathbf{a}^2 \cosh \mathbf{a} \sinh \mathbf{a}) \quad (\text{VIII.14b})$$

and

$$\mathbf{a} = \frac{\hbar \mathbf{d}^{1/2}}{2k_{\mathbf{B}}T} \quad (\text{VIII.14c})$$

For the cubic metals, the dynamical matrix elements in (VIII.13) are calculated using a model due to Clark et al.²¹⁹ in which one has central

nearest- and next-nearest-neighbor forces described by the constants α and β , respectively, and noncentral forces described by a constant γ . These force constants can be calculated from the elastic constants. For selected crystal surfaces, simple expressions can be obtained for $[d]_{l\alpha, l\alpha}$ and $[R^2]_{l\alpha, l\alpha}$, where l denotes either a surface or interior atom.

A similar procedure is used for the diamond structure crystals, except that there are now only two force constants which describe central and noncentral nearest-neighbor forces. Again these two constants can be evaluated from the elastic constants.

Figure 48 gives the result of the calculation for (100) and (111) surfaces of silicon. The mean-square vibrational amplitude $\langle u^2 \rangle$ for surface atoms, in directions parallel and perpendicular to the surface, as well as $\langle u^2 \rangle$ for the bulk atoms, is shown as a function of temperature. At high temperature $\langle u^2 \rangle \propto T$, and the results can be expressed by introducing effective Debye temperatures θ_D related to the slope of $\langle u^2 \rangle$ versus T :

$$\langle u^2 \rangle = \left(\frac{3h^2}{Mk_B} \right) \left(\frac{T}{\theta_D^2} \right) \quad (\text{VIII.15})$$

Table I gives the values of θ_D for both bulk and surface atoms. (In the case

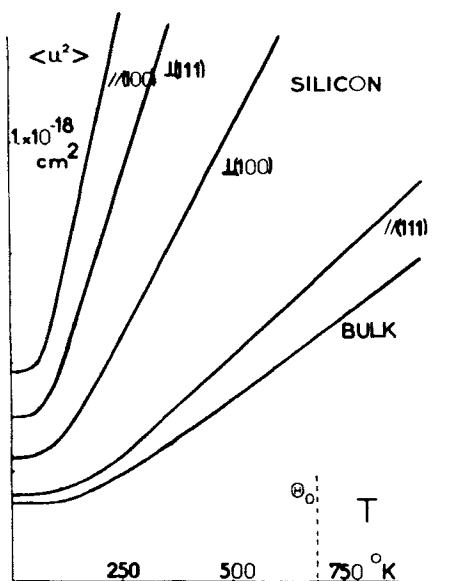


Fig. 48. Thermal dependence of $\langle u^2 \rangle$ for silicon. θ_0 is the experimental bulk Debye temperature. (Reprinted from Theeten and Dobrzynski.²¹⁶)

TABLE I
Debye Temperatures Deduced from High-Temperature Behavior of $\langle u^2 \rangle^a$

	Bulk experimental value	Bulk	$\perp(111)$	$\parallel(111)$	$\perp(100)$	$\parallel(100)$
Silicon	690	750	390	730	510	320
Germanium	350	430	220	410	280	180
Diamond	2230	2300	1350	1940	1510	810

^aAll temperatures in degrees Kelvin.

of surface atoms there is a different value of θ_D associated with motion parallel and perpendicular to the surface.)

The error introduced by terminating the expansion in (VIII.13) at the R^2 term is estimated to be 10 to 20% for high temperatures ($T \gtrsim \theta_D$), but lower for low temperature. For a Si(111) surface, the curves in Fig. 48 are in good agreement with results from LEED experiments of Theeten et al.²²⁰ The agreement for a (100) surface is not as good because each surface atom for a (100) surface is bound to only two bulk Si atoms, while for a (111) surface it is bound to three bulk atoms. The relatively weaker binding for the (100) surface atoms should increase the importance of relaxation and anharmonic effects, which are neglected in the calculation.

B. Small Particles

The vibrational properties of small particles in the shape of spheres and rectangular parallelepipeds are of interest because a large fraction of the atoms may reside on the surface if the particle is sufficiently small. There have been calculations of properties such as the vibrational frequency distribution, the entropy and specific heat, and optical properties and scattering cross sections.

Dickey and Paskin^{221,222} have calculated the frequency spectrum $F(\omega)$ and the moments of this spectrum for small, roughly spherical particles and extremely thin films. A motivation for their thin film calculations is the observation that the superconducting transition temperature of a metal, which can be expressed as a function of various moments of the frequency spectrum, is observed to be higher in the thin film than in a bulk sample.²²³ They consider a monatomic fcc crystal with a Lennard-Jones interatomic potential, a model actually more appropriate for a rare gas solid than for a metal. A molecular dynamics calculation is performed by giving the atoms small initial random displacements and following their subsequent motion using Newton's equations. After the system has come to thermal equi-

librium, the velocity autocorrelation function $\langle \mathbf{v}_i(t) \cdot \mathbf{v}_i(0) \rangle$ is calculated for each atom i , and the frequency spectrum is then given by

$$F(\omega) = \int_0^\infty dt \gamma(t) \cos \omega t \quad (\text{VIII.16})$$

where

$$\gamma(t) = \frac{\sum_i \langle \mathbf{v}_i(t) \cdot \mathbf{v}_i(0) \rangle}{\sum_i \langle \mathbf{v}_i(0) \cdot \mathbf{v}_i(0) \rangle} \quad (\text{VIII.17})$$

The calculations were done with the parameters ϵ and σ in the Lennard-Jones potential, as well as the mass M , set equal to 1. The frequency spectra for a bulk solid, an approximately spherical particle containing 429 atoms, and a five-layer slab with 275 atoms are shown in Fig. 49. The frequency spectra for the slab and the sphere can be understood qualitatively by classifying the atoms as "edge" atoms, with four to six neighbors, "surface" atoms, with seven to nine neighbors, and "bulk" atoms, with 10 to 12 neighbors. By letting the atom index i in the numerator of (VIII.17) run over only a selected class of atoms, one can associate various features of $F(\omega)$ with each class. The frequency spectrum for "bulk" atoms has a double maximum characteristic of the bulk solid, and closely resembles the upper curve in Fig. 49. The "surface" atoms give a frequency spectrum with three peaks: two at $\omega \cong 15$ and $\omega \cong 21$, as for "bulk" atoms, and the largest peak at $\omega \cong 10$. Therefore the peak in $F(\omega)$ at $\omega \cong 10$ for the sphere and the slab can be associated with "surface" atoms. The frequency spectrum for the "edge" atoms has a peak at $\omega \cong 4$ with no prominent structure at higher frequencies.

Dickey and Paskin propose a very simple method for calculating the moments $\langle \omega^j \rangle$ of the frequency spectrum. One considers the crystal in the Einstein approximation, such that each atom vibrates independently in an average potential arising from the nearest neighbors. Then if ω_0 is the vibrational frequency of an atom with $n_0 = 12$ nearest neighbors, $\omega_i = (n_i/n_0)^{1/2} \omega_0$ is taken to be the frequency of an atom with $n_i < 12$ neighbors. ω_0 is selected so as to give the correct moment $\langle \omega^j \rangle$ in the bulk, the value of ω_0 depending on j . The j th moment of the frequency spectrum in a finite crystal is then

$$\langle \omega^j \rangle = \sum_i \alpha_i \omega_i^j \quad (\text{VIII.18})$$

where α_i is the fraction of atoms with n_i nearest neighbors. Calculations of

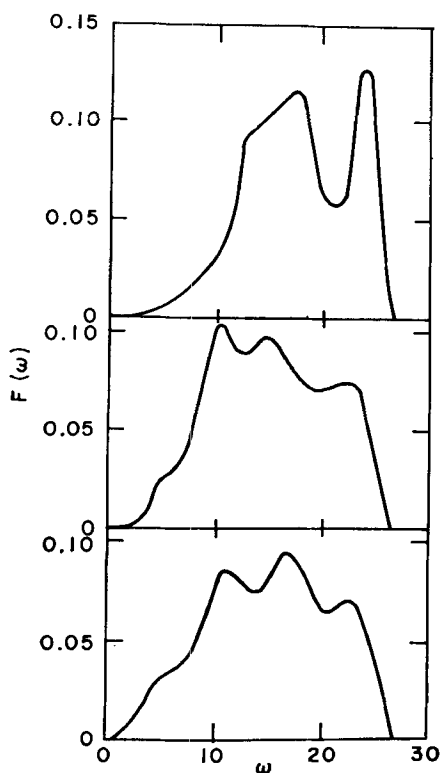


Fig. 49. Frequency spectrum of the bulk solid, the blob, and the five-layer particle, from top to bottom. The relative importance of the bulk modes decreases in this sequence as the surface-to-volume ratio increases. The dimensionless frequency ω here is ω^* of (VIII.2a). (Reprinted from Dickey and Paskin.²²²)

$\langle \omega \rangle$ and $\langle \omega^2 \rangle$ for a spherical particle and a thin slab using (VIII.18) are in good agreement with the results of a molecular dynamics calculation, but the value of $\langle \omega^{-1} \rangle$ from (VIII.18) is as much as 30% below the correct value. This discrepancy occurs for $\langle \omega^{-1} \rangle$ because this moment weights heavily the low-frequency part of the spectrum, which is associated with atoms having a small number of neighbors. Relaxation and anharmonic effects are presumably most important for atoms with few neighbors; such effects are included in the molecular dynamics calculation but not with any care in the approximate calculation.

The vibrational frequency spectrum and entropy for small, approximately spherical fcc and hcp crystals containing 13 to 87 atoms were calculated by Burton²²⁴ who used the Lennard-Jones potential with

parameters representing argon. He first allowed the atoms to relax to the minimum potential energy configuration, and then calculated the vibrational frequencies by diagonalization of the dynamical matrix. The following general statements can be made about the vibrational frequency spectra:

1. There is no high-frequency maximum associated with bulk longitudinal modes, a peak very prominent for bulk crystals, as shown in the upper curve in Fig. 49. The absence of this peak is attributed to the scarcity of atoms with a full set of 12 nearest neighbors; even in an 87-atom cluster, there are only 19 such atoms.
2. For very small clusters, there is a frequency shift of the spectrum toward lower frequencies, reflecting the increasing contribution of edge and surface modes, which lie at low frequencies.
3. The frequency spectra are qualitatively independent of whether the interatomic forces are assumed to act between only nearest neighbors or between all atom pairs, and also are independent of crystal structure; they depend primarily on the cluster size.

Figure 50 shows the calculated entropy per atom, S , as a function of the

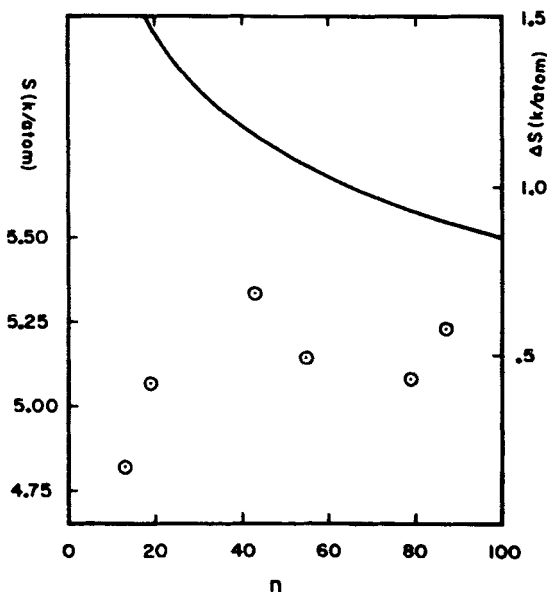


Fig. 50. The entropy per atom of fcc clusters of argon considering all neighbor interactions. Circles show exact results. The solid curve shows the predictions of the classical drop model. The left vertical axis gives the entropy S , and the right axis gives ΔS , the difference between the cluster entropy per atom and that computed for bulk argon. (Reprinted from Burton.²²⁴)

number of atoms in the crystal, at a fixed temperature, $T=93$ K. The solid curve is the entropy per atom as calculated from a classical model, in which one adds to the entropy per atom for a bulk crystal an excess entropy per atom ΔS , proportional to (surface area)/(number of atoms in volume) or to $n^{-1/3}$. In the calculation of ΔS , the excess entropy per unit surface area is taken from work by Allen and deWette²²⁵ on the excess surface entropy of a semiinfinite crystal. The exact results, shown by the circles, are considerably smaller than those of the classical model.

Since low-frequency modes make a larger contribution to the entropy than high-frequency modes, the large value of the entropy for $n > 90$ is attributed to low-frequency surface modes, and the large value at $n \approx 40$, to low-frequency edge modes. The minimum between $n=60$ and $n=80$ is caused by a low-frequency cutoff in the density of states, and the decrease for very small n is a consequence of the fact that a cluster of n atoms has only $3n-3$ vibrational degrees of freedom.

IX. MICROSCOPIC LATTICE DYNAMICS: IONIC CRYSTALS

The long-range Coulomb forces in an ionic crystal produce a diversity of modes not present in crystals with only short-range forces. For this reason, a satisfactory understanding of the vibrational properties of ionic crystals with surfaces has been achieved only recently. The normal modes of both ionic and nonpolar crystals can be considered in two regimes, one in which the vibrational displacements vary slowly from one unit cell to the next, and the other in which the variation is rapid. This distinction is well known for acoustical modes. If the wavelength is much larger than an interatomic distance, one has a macroscopic elastic continuum theory. When the wavelength becomes comparable to the interatomic distance, a microscopic lattice-dynamical theory is required. Since acoustical modes show no unique behavior in ionic crystals, no special emphasis is placed on them.

The optical modes are of particular interest in ionic crystals. For long-wavelength modes, with a slow variation of the displacements from one unit cell to the next, the electric dipole moment in each unit cell can be described by a macroscopic polarization field, and the important properties of the polarization are contained in a frequency-dependent dielectric function $\epsilon(\omega)$. The long-wave optical modes of a finite ionic crystal can then be determined by incorporating $\epsilon(\omega)$ into Maxwell's equations and using suitable boundary conditions at the surfaces, as discussed in Section II. For short-wavelength modes, with a rapid variation of the displacements from one unit cell to the next, a continuous polarization field cannot be used, and a microscopic lattice-dynamical theory is required. The relationship between the optical modes as determined by the macroscopic

theory and by the microscopic theory is not straightforward as will become clear below.

Another unique feature of ionic crystals is the effect of retardation of the Coulomb forces on the optical modes. In the macroscopic continuum theory using Maxwell's equations, retardation can be included by making the velocity of light c finite. There are both magnetic and electric fields for all modes except longitudinal optical modes. Retardation can be neglected by letting $c \rightarrow \infty$; the magnetic fields then disappear and Maxwell's equations reduce to those of electrostatics. The consequences of including or neglecting retardation in the continuum theory have been discussed in Section II. In the microscopic theory, however, the normal modes have been determined *only* in the absence of retardation.

A. Slab

We consider a slab with the NaCl structure, bounded by (001) faces. The z -axis is perpendicular to the surfaces, and the normal modes are characterized by a two-dimensional wave vector \mathbf{k} lying in the x - y plane. We choose the x and y directions to be (100) directions and thus equivalent. The appropriate two-dimensional Brillouin zone is shown in Fig. 40. In the early work on this system, the rigid-ion model of Kellermann was used, in which there are Coulomb forces between all pairs of ions and short-range central forces between nearest neighbors only. In some studies the ions were allowed to relax from their ideal positions to their new static equilibrium positions by letting each ionic layer move in the z direction. This assumption that all ions in the same layer move the same distance may be incorrect; there is recent evidence, discussed later, to the contrary.

1. Procedure and Vibrational Properties

The procedure for finding the normal mode eigenfrequencies and eigenvectors requires diagonalizing the dynamical matrix. The normal mode solutions are of the form

$$u_{\alpha}^{\kappa}(\mathbf{l}) = M_{\kappa}^{-1/2} \xi_{\alpha}^{\kappa}(l_z; \mathbf{k}) e^{i\mathbf{k} \cdot \mathbf{r}_{\mathbf{l}} - i\omega t} \quad (\text{IX.1})$$

and the eigenfrequencies and eigenvectors are solutions of the eigenvalue equation

$$\sum_{l'_z, \kappa', \beta} D_{\alpha\beta}^{\kappa\kappa'}(l_z l'_z; \mathbf{k}) \xi_{\beta}^{\kappa'}(l'_z; \mathbf{k}, p) = \omega_p^2 \xi_{\alpha}^{\kappa}(l_z; \mathbf{k}, p) \quad (\text{IX.2})$$

Equations (IX.1) and (IX.2) are like (VIII.4) and (VIII.5), except that one now has the index $\kappa = 1, 2$ (and $\kappa' = 1, 2$) labeling the two ion types in each unit cell. The dynamical matrix $D_{\alpha\beta}^{\kappa\kappa'}(l_z l'_z; \mathbf{k})$ in (IX.2) is defined as in

(VIII.6), except for the presence of the indices κ and κ' denoting the two ion types, and the replacement of M^{-1} by $(M_\kappa M_{\kappa'})^{-1/2}$.

The dynamical matrix can be written as the sum of two parts, one associated with the short-range forces, and the other with the Coulomb forces. The evaluation of the short-range part using (VIII.6) is straightforward, but the Coulomb part involves a summation over infinitely many ions lying in the plane determined by the fixed value of l'_z . The summation in (VIII.6) is very slowly convergent as it stands, and, for actual calculations, it must be converted into a more rapidly convergent form. The methods used for doing this are not discussed here; the readers interested in this technical detail should consult the original references^{165, 168, 226} or the book by Maradudin et al.¹ It should be noted that the dynamical matrix can be determined either neglecting or including retardation.

Expressions for the dynamical matrix neglecting retardation were determined by Lucas,¹⁶⁸ and the normal modes were examined in detail at $\mathbf{k}=0$, the center of the Brillouin zone. The general case $\mathbf{k}\neq 0$ would require diagonalization of a $6N_3 \times 6N_3$ matrix, where N_3 is the number of atomic layers in the slab. At $\mathbf{k}=0$ the matrix factors into three $2N_3 \times 2N_3$ matrices associated with ionic displacements in the x , y , and z directions, and furthermore the x - and y -polarized modes are degenerate. Thus there are three independent sets of $2N_3$ modes, and each set has N_3 acoustical and N_3 optical modes.

Each set of N_3 acoustical modes with a given polarization has one zero-frequency mode corresponding to uniform translation of the slab; the remaining $N_3 - 1$ modes are bulk modes with a sinusoidal variation of displacements across the slab. There are N_3 z -polarized optical bulk modes which are derived from the longitudinal optical (LO) band in an infinite crystal, and span the frequency range of this band. For the infinite crystal, the LO band extends from the frequency ω_{LO} for which the three-dimensional wave vector $\mathbf{q}=0$, downward to the minimum frequency occurring as \mathbf{q} moves from 0 to the Brillouin zone edge along a (100) direction.

Of the N_3 optical modes with x -polarization, $N_3 - 2$ are bulk modes derived from the transverse optical (TO) band in an infinite crystal and spanning the frequency range of this band. For the infinite crystal, the TO band extends from the frequency ω_{TO} , for which $\mathbf{q}=0$, upward to the maximum frequency occurring as \mathbf{q} moves from 0 to the Brillouin zone edge along a (100) direction. The remaining two x -polarized optical modes are surface modes localized within a few layers of the surfaces. These modes, which have been designated "Lucas modes," lie just below the TO bulk modes: for a seven-layer NaCl slab their frequencies are $\omega = 0.99286\omega_{TO}$ and $\omega = 0.99345\omega_{TO}$, corresponding to even-parity and odd-

parity displacements with respect to the slab center, respectively. The near degeneracy of these modes is a consequence of their weak penetration into the interior of the slab. As the slab becomes thicker their frequencies rapidly approach each other: For an 11-layer slab they differ by only $10^{-5}\omega_{\text{TO}}$. Each of x -polarized modes discussed above is degenerate with a corresponding y -polarized mode.

How do Lucas's results compare with those of the continuum theory in the $\mathbf{k} \rightarrow 0$ limit? To be specific, we take the wave vector \mathbf{k} in the x direction, so that the x - z plane is the sagittal plane, and then summarize, first, the results obtained from the nonretarded continuum theory for the optical modes of a slab¹⁸. For $\mathbf{k} \neq 0$ the modes are polarized either in the sagittal plane or perpendicular to the sagittal plane (y direction). There are bulk modes, with a sinusoidal variation of displacements across the slab, for both directions of polarization. The xz -polarized (or p -polarized) bulk modes occur at both ω_{LO} and ω_{TO} , but the y -polarized (or s -polarized) bulk modes occur only at ω_{TO} . One of the s -polarized bulk modes has uniform polarization (displacements of each ion type independent of z). At $\mathbf{k} = 0$ the p -polarized bulk modes become polarized either in the x or the z direction, with frequencies at ω_{TO} and ω_{LO} , respectively. There occur two deeply penetrating p -polarized surface modes (the FK modes) whose frequencies for $\mathbf{k} \rightarrow 0$ approach ω_{LO} and ω_{TO} while the displacements become uniformly polarized in the z and x directions, respectively (see Fig. 6).

The bulk modes in the microscopic and continuum theories have some differences, as expected. There is a finite number of modes, related to the number of atomic layers in the slab, in the microscopic theory, but an infinite number in the continuum theory. Since the LO and TO phonon branches in an infinite medium occur at ω_{LO} and ω_{TO} without dispersion, according to the continuum theory, the corresponding bulk modes in a film also occur at these two frequencies for any value of \mathbf{k} . The occurrence of the bulk modes over ranges of frequency in the microscopic theory is a consequence of the dispersion of the corresponding LO and TO phonon branches in an infinite crystal.

There is complete disagreement between the continuum and microscopic theories about the nature of the surface modes at $\mathbf{k} = 0$. The nonretarded continuum theory yields strongly localized surface modes only for large values of \mathbf{k} , and, at $\mathbf{k} = 0$ in particular, there are no Lucas modes. The microscopic theory of Lucas for $\mathbf{k} = 0$ indicates that the uniformly polarized optical modes at ω_{TO} and ω_{LO} , which are a prominent part of the continuum theory, do not exist. The continuum theory is therefore invalid at $\mathbf{k} = 0$, but the work of Lucas does not show to what extent or over what range of \mathbf{k} , if any, it is valid.

In an attempt to answer the foregoing questions, Tong and Maradudin²²⁷ determined the normal modes of a 15-layer NaCl slab using the same rigid-ion model as that of Lucas. The surfaces of the film are (001) planes, and the normal modes are found for \mathbf{k} in the x direction, chosen to be a (100) direction. Thus the modes were examined on the line from $\bar{\Gamma}$ to \bar{M} in Fig. 40. At $\mathbf{k}=0$ their results agree with those of Lucas. They determined the region in which bulk modes exist as \mathbf{k} goes from $\bar{\Gamma}$ to \bar{M} , and found that the degeneracy of the Lucas surface modes polarized in the sagittal plane and normal to the sagittal plane is removed as \mathbf{k} moves away from $\bar{\Gamma}$. They also found a pair of surface modes at a frequency between ω_{TO} and ω_{LO} . Although their calculations for the surface modes may be correct for $\mathbf{k} \neq 0$, the results were misinterpreted because the behavior of the surface modes apparently was not examined in sufficient detail near $\mathbf{k}=0$. Tong and Maradudin determined the normal modes both with and without relaxation of the ions to new static equilibrium positions, and found that relaxation resulted in frequency increases up to about 5% but no qualitative changes in the character and general behavior of the modes.^{227a}

In an effort to understand the relationship between the microscopic and continuum theories, Jones and Fuchs¹⁶⁵ also calculated the normal modes of a NaCl slab using a rigid-ion model, taking care to examine the behavior of the modes near $\mathbf{k}=0$. The calculations were carried out for a seven-layer slab neglecting static relaxation of the ions. The modes were determined for \mathbf{k} on the line between $\bar{\Gamma}$ and \bar{X} (see Fig. 40). If \mathbf{k} is on $\bar{\Gamma}\bar{X}$ (or $\bar{\Gamma}\bar{M}$), the 42×42 secular determinant factors into 28×28 and 14×14 determinants associated with displacements polarized in the sagittal plane and normal to the sagittal plane, respectively. For convenience a new coordinate system is introduced, obtained by a 45° rotation about the z -axis, such that the new x -axis is in the direction of \mathbf{k} . The modes polarized in the sagittal plane and normal to the sagittal plane can then be denoted xz -polarized (p -polarized) and y -polarized (s -polarized) modes, respectively. Because the slab has reflection symmetry, the normal modes have definite parity with respect to the center of the slab. If l_z and \tilde{l}_z denote atomic planes equidistant from the central plane, an even-parity mode is one whose eigenvectors satisfy

$$\begin{aligned}\xi_x^*(\tilde{l}_z) &= \xi_x^*(l_z) \\ \xi_y^*(\tilde{l}_z) &= \xi_y^*(l_z) \\ \xi_z^*(\tilde{l}_z) &= -\xi_z^*(l_z)\end{aligned}\tag{IX.3}$$

and an odd-parity mode is one whose eigenvectors satisfy

$$\begin{aligned}\xi_x^*(\tilde{l}_z) &= -\xi_x^*(l_z) \\ \xi_y^*(\tilde{l}_z) &= -\xi_y^*(l_z) \\ \xi_z^*(\tilde{l}_z) &= \xi_z^*(l_z)\end{aligned}\tag{IX.4}$$

where the indices \mathbf{k} and p labeling different normal modes have been suppressed. Modes may cross each other if they are of opposite parity or if they belong to different classes (xz -polarized and y -polarized).

The dispersion relations for the 28 xz -polarized modes are shown in Fig. 51 with the wave vector \mathbf{k} going from $\bar{\Gamma}$ to \bar{X} . The dimensionless wave vector $Q = kr_0\sqrt{2}/2\pi$ is defined in such a way that $Q=0.5$ at the edge of the Brillouin zone (point \bar{X}). The characteristic frequencies for the $\mathbf{k}=0$ TO and LO modes in an infinite crystal were chosen to be $\omega_{\text{TO}} = 2.488 \times 10^{13} \text{ sec}^{-1}$ and $\omega_{\text{LO}} = 5.856 \times 10^{13} \text{ sec}^{-1}$. The frequencies and other properties of the modes at $Q=0$ are shown in Table II. At $Q=0$ the xz -polarized modes have displacements either in the x or z direction, and are so marked. One can consider the displacements of a given ion type as a function of a continuous position variable z which replaces the discrete layer index l_z ; this procedure allows the number of nodes in the z direction to be specified. This number is, of course, the number of sign changes that occur in the eigenvector associated with a given ion type, as one moves across the slab. All modes at $Q=0$ are bulk modes with the exception of the Lucas surface modes at $\omega = 2.4184 \times 10^{13} \text{ sec}^{-1} = 0.9720 \omega_{\text{TO}}$ and $\omega = 2.4191 \times 10^{13} \text{ sec}^{-1} = 0.9723 \omega_{\text{TO}}$.

As one moves away from $Q=0$, the feature of most interest is the pair of modes with frequencies of about $3.9 \times 10^{13} \text{ sec}^{-1}$ at $Q=0.1$ (see Fig. 51). These two modes are the relatively deeply penetrating surface modes also obtained in the continuum theory, the FK modes. At $Q \neq 0$ the displacements are not polarized in either the x or z directions, as they are at $Q=0$. As Q decreases from 0.1, the two FK surface modes move apart, as expected from the continuum theory; the low-frequency mode becomes polarized more nearly in the x direction, and the high-frequency mode polarized more nearly in the z direction.

The ionic displacements of a given ion type for the low-frequency FK mode tend to become constant across the slab as Q decreases, just as in the continuum theory, until $Q \lesssim 0.004$, where this mode enters the TO bulk band region. The fate of the FK mode as it moves through the bulk band region is shown in Fig. 52 by an expanded view of the relevant portion of the dispersion curves. The FK surface mode does not simply cross the bulk

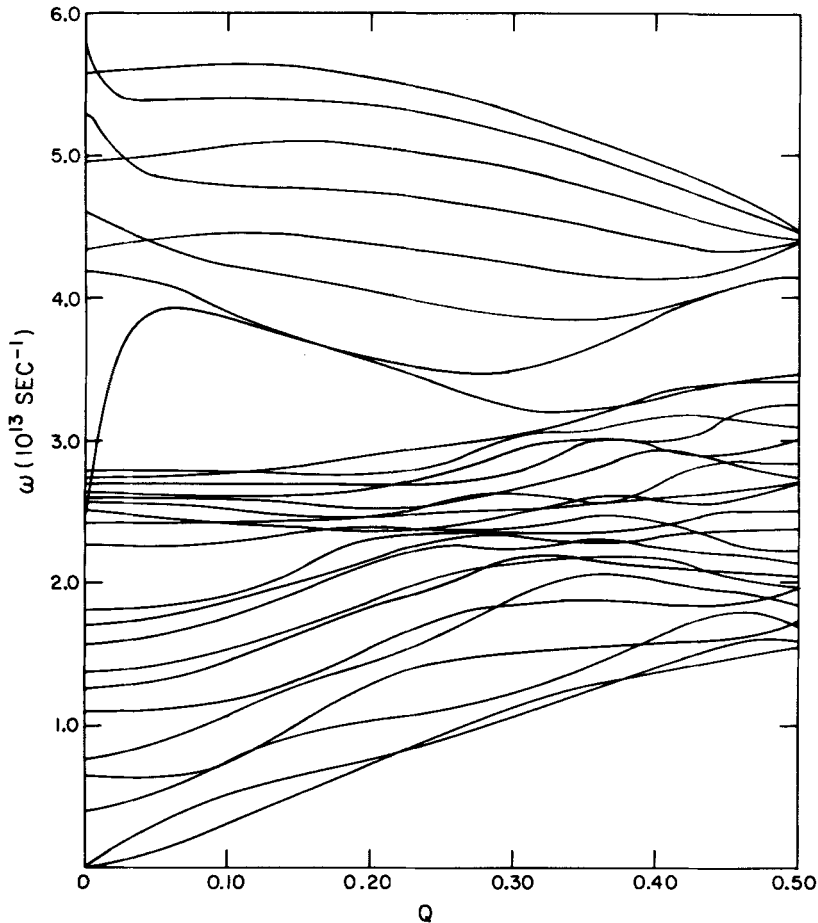


Fig. 51. Dispersion relations in the $\bar{\Gamma}$ to \bar{X} direction (see Fig. 40) for xz -polarized modes of a seven-layer NaCl slab. The dimensionless wave vector Q is defined by $Q = kr_0\sqrt{2}/2\pi$, with r_0 , the nearest-neighbor separation, equal to 2.814 Å. Note that $Q=0.5$ corresponds to the zone edge.

modes, as implied by Fig. 51. Being an even-parity mode, it cannot cross the even-parity bulk modes. Instead, it hybridizes with these modes, passing its nodeless character from one even-parity mode to the other, until at $Q=0$ the low-frequency Lucas mode finally is nodeless. The horizontal lines in Fig. 52 are three odd-parity TO bulk modes which completely ignore the FK mode.²²⁸

The upper FK surface mode is not prominent in Fig. 51, since almost immediately upon leaving the low-frequency FK mode as Q decreases, it

TABLE II
Properties of the xz -Polarized Modes at $\mathbf{k}=0$ for a Seven-Layer NaCl Slab

ω (10^{13} sec^{-1})	Acoustical or optical	Polarization		Odd or even parity	Number of nodes
0	A	x	(TA)	e	0
0	A	z	(LA)	o	0
0.3953	A	x	(TA)	o	1
0.6963	A	z	(LA)	e	1
0.7694	A	x	(TA)	e	2
1.1023	A	x	(TA)	o	3
1.2652	A	z	(LA)	o	2
1.3770	A	x	(TA)	e	4
1.5807	A	x	(TA)	o	5
1.7054	A	x	(TA)	e	6
1.8141	A	z	(LA)	e	3
2.2662	A	z	(LA)	o	4
2.4184	O	x	(surf.)	e	0
2.4191	O	x	(surf.)	o	1
2.5117	O	x	(TO)	e	2
2.5684	O	x	(TO)	o	3
2.5960	A	z	(LA)	e	5
2.6353	O	x	(TO)	e	4
2.6971	O	x	(TO)	o	5
2.7406	O	x	(TO)	e	6
2.7897	A	z	(LA)	o	6
4.1927	O	z	(LO)	o	6
4.3392	O	z	(LO)	e	5
4.6056	O	z	(LO)	o	4
4.9480	O	z	(LO)	e	3
5.2980	O	z	(LO)	o	2
5.5937	O	z	(LO)	e	1
5.7892	O	z	(LO)	o	0

enters the broad LO bulk band region at about $Q=0.07$ and is visible only as a locus of hybridization with the bulk modes. The upper FK surface mode is a nodeless odd-parity mode, polarized predominantly in the z direction. In the hybridization region the nodeless character is passed from one odd-parity mode to the next, until finally near $Q=0$ the highest bulk mode is nodeless.

The FK surface modes begin to split appreciably when $|\mathbf{k}|L < \pi$ or $|\mathbf{k}| < \pi/(N_3 r_0)$, where L is the thickness of the slab, N_3 is the number of atomic layers, and r_0 is the nearest-neighbor distance. The lower FK mode

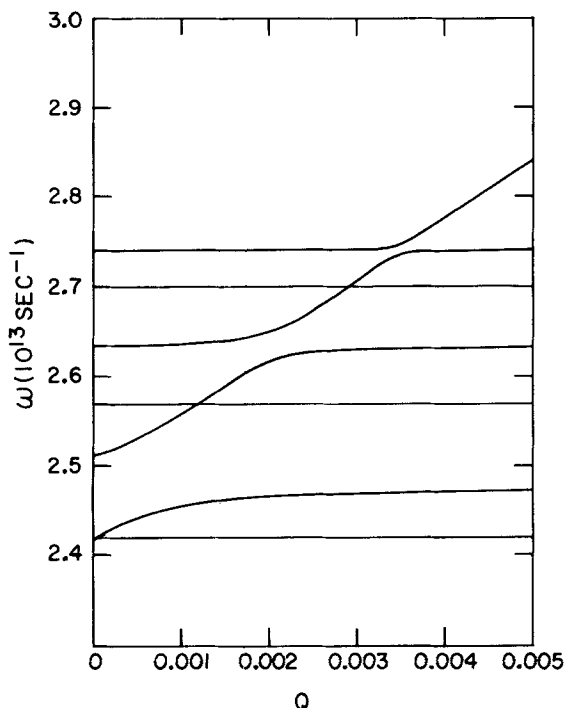


Fig. 52. Dispersion relations for xz -polarized TO modes in the small-wave-vector region where the FK mode lies within the frequency of the TO bulk modes. Note that the FK mode hybridizes with the even-parity bulk mode but passes, without effect, through the odd-parity bulk modes.

moves into the TO bulk mode region for $|\mathbf{k}| < 0.04\pi/(N_3 r_0)$. These results show that for a large number of layers, the splitting of the FK modes and the hybridization of the lower FK mode with the TO bulk modes occur very close to $\mathbf{k}=0$. For the $N_3=7$ -layer slab considered by Jones and Fuchs, the significant behavior of the surface modes can be examined without having to use \mathbf{k} values extremely near $\mathbf{k}=0$.

In order to increase the visibility of the upper FK surface mode, the normal mode calculation of Jones and Fuchs was repeated with the electronic charge multiplied by a factor of 1.26. This procedure increases the frequency gap between the TO and LO bulk bands and allows the high-frequency FK mode to retain its identity over a wide range of Q since it enters the LO bulk band region only for $|Q| < 0.02$. The two FK modes can then be observed to follow closely the behavior predicted by the continuum theory as long as they are in the gap between the bulk bands, with the exception that as $|Q|$ becomes larger than about 0.1, the two

modes do not approach a constant-frequency asymptote, but tend to move to a lower frequency as Q increases.²²⁹

Some additional comments can be made about the Lucas surface modes which are the two lowest modes shown in Fig. 52. The odd-parity mode has the lower frequency except very near $Q=0$, where the two modes cross. This crossing does not show in the figure, but it explains why the even-parity Lucas mode lies lower at $Q=0$. The odd-parity Lucas mode is a surface mode for the entire range of Q , but the even-parity Lucas mode, which begins as a nodeless surface mode at $Q=0$, changes to a bulk mode with two nodes when $|Q| > 0.002$. This behavior of the even-parity Lucas mode is characteristic of this very thin seven-layer slab. In a thicker slab ($N_3 > 13$) the even-parity Lucas mode retains its well-localized surface character for large Q , even though it develops two nodes, and it remains more nearly degenerate with the odd-parity mode.

The force constants for the surface atoms are different from those of the interior atoms because, when a surface atom is displaced, it does not experience a force from the missing ions outside the crystal. If the short-range part of the dynamical matrix is modified in such a way that the forces on the surface atoms are the same as those on the interior atoms, the Lucas surface modes disappear by changing to bulk modes. This shows that the Lucas modes originate from the surface modification of the force constants. The FK surface modes are, however, not affected by this change, showing that these modes arise from the long-range part of the force constants or the Coulomb interaction.

We now turn to the modes polarized normal to the sagittal plane; these can also be denoted as y -polarized, s -polarized, or SH modes. In the seven-layer slab there are seven acoustical modes and seven optical modes. The upper dashed line in Fig. 53 indicates two nearly degenerate Lucas surface modes; the lower pair of dashed lines are acoustical surface modes of opposite parity, and they correspond to the Rayleigh modes obtained by elasticity theory. At $Q=0$ neither of these acoustical modes is localized at the surfaces; the lower one, with even parity, corresponds to uniform translation of the slab. They become surface-like in character with increasing Q , but not remarkably so.

The normal modes of a 15-layer NaCl slab with (001) surfaces have been investigated by Chen et al. using both the Kellermann rigid-ion model²³⁰⁻²³² and an 11-parameter shell model.²³⁰ These authors calculated the ω versus k dispersion curves for values of k around the entire boundary of the triangular irreducible element of the two-dimensional Brillouin zone (Fig. 40) as well as for some values of k within this triangle.

The deeply penetrating FK surface modes and the strongly localized Lucas surface modes are found near the $\bar{\Gamma}$ point and behave in the same

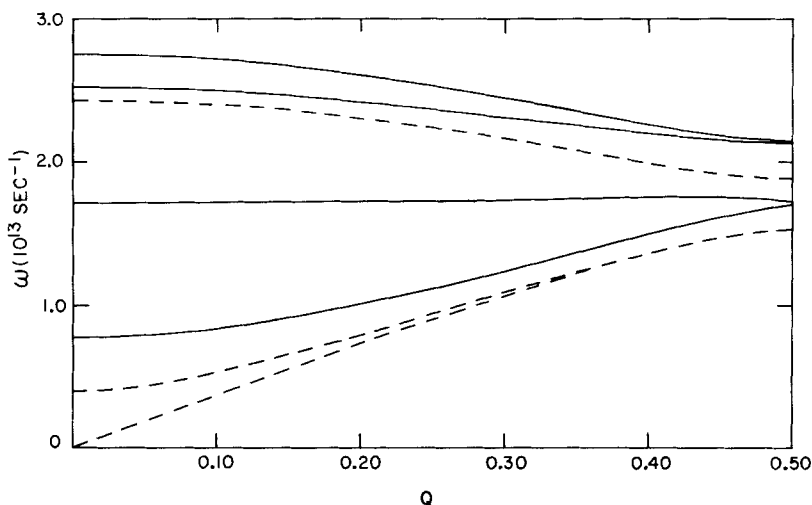


Fig. 53. Dispersion relations for y -polarized modes of a seven-layer NaCl slab. The dimensionless wave vector Q is defined in the caption of Fig. 51.

way, irrespective of the direction of \mathbf{k} . There are, in addition, many surface modes in the outer portions of the Brillouin zone lying in gaps between the bulk band regions, as well as pseudosurface or mixed modes lying within the bulk bands; these modes are shown in Fig. 54*b*. The 15-layer slab is thick enough that all surface modes, with the exception of the deeply penetrating FK modes and the Rayleigh modes near $\mathbf{k}=0$, occur in nearly degenerate pairs of opposite parity. If one goes to thicker slabs, no significant changes in the localized surface modes are expected, and the bulk modes occupy the same regions but fill in these regions more densely.

Results from a shell model calculation for a 15-layer NaCl slab,²³⁰ shown in Fig. 54*a*, differ markedly from those of the rigid-ion model. The most striking difference is that the large gap between the TO and LO bulk bands near the point $\bar{\Gamma}$ for the rigid-ion model is entirely missing for the shell model. Therefore the FK surface modes, which were able to exist as pure surface modes in the rigid-ion model, are now completely buried within the bulk bands as pseudosurface modes. The Rayleigh modes S_1 also show different behavior in the shell model. In the rigid-ion model, S_1 has primarily SV to SH polarization between \bar{M} and \bar{X} , and has SH polarization between \bar{X} and $\bar{\Gamma}$; in the shell model, on the other hand, S_1 has primarily SV polarization throughout the Brillouin zone. The Lucas surface modes are not changed significantly upon going from the rigid-ion model to the shell model.

Chen, Alldredge, and deWette²³³ have also reported calculations on RbF and RbCl, using a shell model for a 15-layer slab with (001) surfaces. Because of the extreme anion-to-cation mass ratio in these ionic crystals, there is a large gap between the optical and acoustical bulk bands, in contrast with NaCl and many other alkali halides, for which the TO bulk bands overlap the acoustical bulk bands. An interesting feature in RbF is a nearly degenerate pair of strongly localized surface modes which exist in a gap between the LO and TO bulk bands near $\mathbf{k}=0$. These modes persist to the $\mathbf{k}=0$ limit, where their frequency of $3.5 \times 10^{13} \text{ sec}^{-1}$ lies between the frequencies $\omega_{\text{TO}} = 3.1 \times 10^{13} \text{ sec}^{-1}$ and $\omega_{\text{LO}} = 5.3 \times 10^{13} \text{ sec}^{-1}$, and they may be detectable optically or with inelastic electron scattering. Apparently these modes are peeled off the LO bulk band by the modification of the surface force constants, just as the Lucas modes are peeled off the TO bulk band. The FK surface modes begin at ω_{TO} and ω_{LO} when $\mathbf{k}=0$, approach each other as \mathbf{k} increases, and finally come together at a frequency of about $4.7 \times 10^{13} \text{ sec}^{-1}$. Since the LO bulk band region extends from 3.6×10^{13} to $5.2 \times 10^{13} \text{ sec}^{-1}$, the FK modes lie almost entirely within this region. They exist as pseudosurface modes, and are visible only as a locus of hybridization within the bulk modes.

The calculations for RbCl do not show the new surface modes at $\mathbf{k}=0$ associated with the LO band, but they have been found in NaI and NaBr. It is not clear why these surface modes are not obtained in the rigid-ion calculation for NaCl, in which a large gap exists at $\mathbf{k}=0$ between the TO and LO bulk bands. A possible explanation is that these modes are suppressed by the presence of the nearby FK surface mode at a frequency near the bottom of the LO bulk band, where one would otherwise expect the new surface modes.

The theories discussed above for the normal modes of an ionic crystal slab require the diagonalization by computer of a $6N_3 \times 6N_3$ dynamical matrix. Bryskin and Firsov^{130,234} have presented a considerably different theory. They rewrite the equations of motion of the slab using normal coordinates for an infinitely extended crystal. The presence of the surfaces produces a coupling between these normal coordinates. By making a further transformation to a new set of coordinates, two of which represent the displacements for the FK modes as given by the continuum theory, they are able to show that the FK modes are approximate normal modes of the slab. Starting with a microscopic theory, this work therefore provides justification for the continuum theory. A more exact study of the equations for the FK modes in a thick slab shows that the FK modes are pseudosurface modes with complex frequencies $\omega = \omega' + i\omega''$ whenever they pass through bulk band regions. The imaginary part of the frequency is the decay rate of the mode which results from its interaction with the bulk

modes. In a thick slab the bulk modes become dense, and it is more convenient to regard the FK modes as taking on a finite lifetime rather than hybridizing with individual bulk modes.

2. Optical Properties

According to the continuum theory, an ionic crystal film much thinner than a wavelength of light may have absorption peaks at ω_{TO} and ω_{LO} . If the light is polarized in the plane of the film, as in the case of normal incidence or oblique incidence with *s*-polarization, there is absorption only at ω_{TO} ; if the light has an electric field component normal to the surface, as in the case of oblique incidence with *p*-polarization, there is absorption at both ω_{TO} and ω_{LO} . It is of interest to see how the results of a microscopic calculation differ from the above-mentioned results.

Tong and Maradudin²²⁷ have used the eigenvectors $\xi_{\alpha}^{\kappa}(l_z; \mathbf{k}, p)$ and eigenfrequencies ω_p obtained from their rigid-ion model of a 15-layer NaCl slab to calculate the susceptibility tensor

$$\chi_{\alpha\beta}(\omega) = \frac{1}{2N_3 r_0^3} \sum_{\substack{\kappa\kappa' \\ l_z, l_z' \\ p}} \frac{e_{\kappa} e_{\kappa'}}{(M_{\kappa} M_{\kappa'})^{1/2}} \frac{\xi_{\alpha}^{\kappa}(l_z; 0, p) \xi_{\beta}^{\kappa'}(l_z'; 0, p)}{\omega_p^2 - \omega^2 - i\gamma\omega} \quad (\text{IX.5})$$

where γ is a phenomenological damping coefficient. This susceptibility relates the induced dipole moment per unit volume to a spatially uniform externally applied electric field of frequency ω through the relationship

$$P_{\alpha} = \sum_{\beta} \chi_{\alpha\beta} E_{\beta} \quad (\text{IX.6})$$

and it therefore involves only the infinite-wavelength ($\mathbf{k}=0$) eigenvectors and frequencies. It is found that $\chi_{\alpha\beta}$ is a diagonal tensor; primarily the TO modes, with *x* and *y* polarizations [(100) directions] at $\mathbf{k}=0$, contribute to χ_{xx} and χ_{yy} , while the LO modes, with *z* polarization at $\mathbf{k}=0$, contribute to χ_{zz} . Absorption peaks occur at the $\mathbf{k}=0$ normal mode frequencies $\omega=\omega_p$, where $\text{Im}\chi_{\alpha\alpha}(\omega)$ has maxima, and the peak heights depend on the properties of the eigenvectors.

The optical properties of the slab can be calculated from the dielectric tensor

$$\epsilon_{\alpha\alpha}(\omega) = 1 + \frac{4\pi P_{\alpha}}{E_{\alpha}^M} \quad (\text{IX.7})$$

where E_{α}^M is the macroscopic field inside the slab. For the *x* and *y* components the macroscopic internal field is equal to the externally

applied field, but the z components of the internal and external fields differ by a depolarization factor:

$$E_z^M = E_z - 4\pi P_z \quad (\text{IX.8})$$

It follows that the dielectric tensor is

$$\epsilon_{xx}(\omega) = 1 + 4\pi\chi_{xx}(\omega) \quad (\text{IX.9a})$$

$$\epsilon_{yy}(\omega) = 1 + 4\pi\chi_{yy}(\omega) \quad (\text{IX.9b})$$

and

$$\epsilon_{zz}(\omega) = [1 - 4\pi\chi_{zz}(\omega)]^{-1} \quad (\text{IX.9c})$$

In the foregoing theory it is assumed that the macroscopic electric field changes negligibly over distances of the order of the interatomic spacing. Because the wavelength of infrared light is much greater than the interatomic spacing and the fields have the same $\exp(i\mathbf{k} \cdot \mathbf{r}_0)$ dependence on the position variable \mathbf{r}_0 in the plane of the surface, both inside and outside the slab, the variation of the electric field in the directions of the surface can indeed be neglected. However, it is not clear how rapidly the field varies in the z direction normal to the slab. Jones and Fuchs¹⁶⁵ developed a theory of the optical properties in which no assumptions are made about the variation of the field from one atomic layer to the next. In this theory, one applies to the slab an electric field \mathbf{E}^a representing the incident plane wave. Within the slab, the total electric field \mathbf{E}' consists of this applied field \mathbf{E}^a plus an induced field \mathbf{E}^i arising from the motion of the ions. From the equations of motion one can determine the motion of the ions as a function of the total field \mathbf{E}' . By appropriate manipulations \mathbf{E}^i can be eliminated, leaving the induced field \mathbf{E}^i as a function of the applied field \mathbf{E}^a . At an infinite distance from the slab, on the side from which the applied wave is incident, it is found that \mathbf{E}^i is a reflected plane wave leaving the slab. The reflectance R is then given by the ratio of Poynting vectors for the reflected and incident waves. Similarly, at an infinite distance from the slab on the side opposite the incident wave, $\mathbf{E}^a + \mathbf{E}^i$ is found to represent the transmitted wave; the transmittance T is the ratio of Poynting vectors for the transmitted and incident waves. The absorptance is finally given by $A = 1 - R - T$. If the treatment is modified by assuming that the fields and ionic displacements are uniform across the slab, the expressions for R , T , and A become equivalent to those of Tong and Maradudin.²²⁷

The calculated absorptance for a 15-layer NaCl slab with the $\langle 001 \rangle$ axis normal to the surfaces is shown in Fig. 55. The light is p -polarized and the

angle of incidence is 75° . A damping factor $\gamma = 5.0 \times 10^{11} \text{ sec}^{-1}$ is included to represent anharmonic effects. In this slab, all absorptance peaks can be associated with unretarded modes at $\mathbf{k}=0$, polarized in the plane of incidence in directions either perpendicular or parallel to the surface. At $\mathbf{k}=0$ the modes polarized parallel to the surface occur in degenerate pairs with mutually perpendicular directions of polarization. Therefore, one can represent each normal mode polarized parallel to the surface in the plane of incidence as an appropriate linear combination of a degenerate pair, for an arbitrary orientation of the plane of incidence. It follows that the absorptance is independent of the orientation of the plane of incidence. The absorptance peak at $\omega = 2.49 \times 10^{13} \text{ sec}^{-1} = \omega_{\text{TO}}$ arises from the lowest even-parity TO bulk mode, and the smaller peak at $\omega = 2.42 \times 10^{13} \text{ sec}^{-1}$ is due to the even-parity Lucas surface mode. Other TO bulk modes lying at frequencies higher than ω_{TO} have absorptance peaks so small that they are not visible when $\gamma > 10^{11} \text{ sec}^{-1}$. The highest frequency peak occurs at $\omega = 5.84 \times 10^{13} \text{ sec}^{-1} = \omega_{\text{LO}}$, which is the frequency of the nodeless odd-parity LO bulk mode, whereas the seven smaller peaks between about 4.1×10^{13} and $5.8 \times 10^{13} \text{ sec}^{-1}$ arise from the other odd-parity LO bulk modes. As one goes to a thicker slab, the peak at ω_{TO} becomes higher, while the Lucas mode peak remains unchanged; also the peaks on the

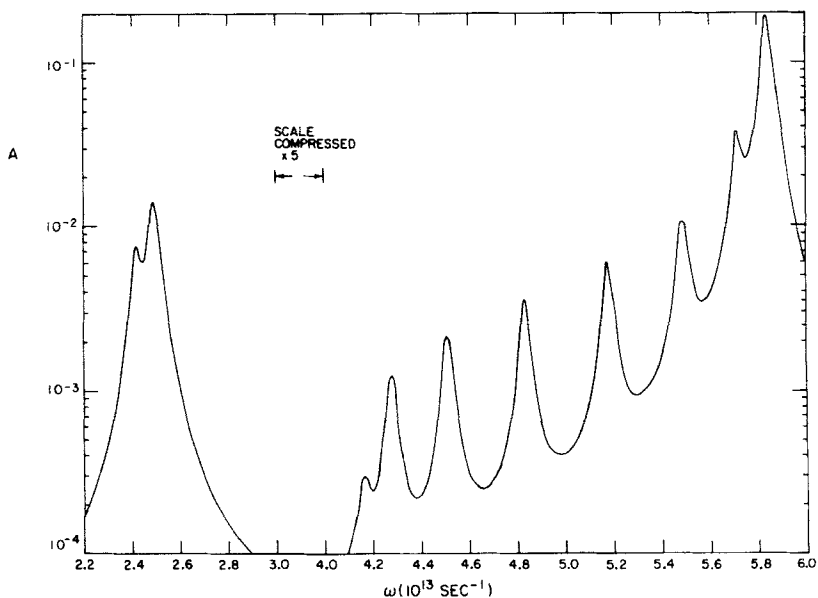


Fig. 55. Absorptance as a function of frequency for *p*-polarized light incident on a 15-layer NaCl slab at an angle of 75° from the normal.

low-frequency side of ω_{LO} become more numerous and diminish in intensity. For a slab thicker than a few hundred layers, there are absorption peaks visible only at ω_{TO} and ω_{LO} , in agreement with the continuum theory.

The absorptance for several slabs was calculated using both the theory of Jones and Fuchs¹⁶⁵ and the approximate theory of Tong and Maradudin,²²⁷ in which it is assumed that the electric field does not vary across the slab. Except for minor differences in the heights of the stronger absorptance peaks, the results are the same for the two theories.

Light that is *s*-polarized has an electric field normal to the plane of incidence, and hence does not interact with the LO bulk modes, which are all polarized in the *z* direction. Only the two lowest frequency peaks in Fig. 55 appear for *s*-polarization, and they are associated with the even-parity Lucas mode and the lowest *y*-polarized TO bulk mode. Berreman¹¹² has made transmittance measurements for a 0.2- μ -thick LiF film which shows a small transmittance minimum on the low-frequency side of a strong minimum at ω_{TO} , for both *s*- and *p*-polarizations. The small minimum might be caused by the Lucas mode. For *p*-polarization Berreman also observed the expected transmittance dip at ω_{LO} , but the dip was asymmetrically broadened on the low-frequency side. It has been suggested¹⁶⁵ that the decreased transmittance below ω_{LO} is caused by unresolved LO bulk modes; however, this effect should not be observable in a film as thick as 0.2 μ . The asymmetry of the peak at ω_{LO} might also be due to a frequency-dependent damping factor $\gamma(\omega)$.

Before going to the next section, it should be noted that the optical properties are completely determined by the normal modes found neglecting retardation.

3. Effects of Retardation

Retardation can be included in the theory of the lattice dynamics of an ionic crystal slab by taking the electric field at the point *r* and a time *t* due to an ion of charge e_j moving with an oscillatory displacement $\mathbf{u}_j(t) = \mathbf{u}_j e^{-i\omega t}$ about the equilibrium position \mathbf{R}_0 to be⁶⁵

$$\mathbf{E}(\mathbf{r}, t) = e_j \left[\frac{\omega^2}{c^2} \mathbf{u}_j + (\mathbf{u}_j \cdot \nabla) \nabla \right] \frac{\exp[i(\omega/c)|\mathbf{r} - \mathbf{R}_0|]}{|\mathbf{r} - \mathbf{R}_0|} e^{-i\omega t} \quad (\text{IX.10})$$

where *c* is the speed of light and ∇ is the gradient operator. The force of ion *j* on a reference ion e_i located at *r* is $\mathbf{f}_i = e_i \mathbf{E}(\mathbf{r}, t)$. The force on the reference ion *i* due to its own displacement is composed of two parts: first, the sum of the unretarded Coulomb forces and short-range forces from all the other ions in their equilibrium positions, just as in the nonretarded

theory; second, a radiation damping force

$$\mathbf{f}_i = \frac{2}{3} \frac{e_i^2}{c^3} \frac{d^2}{dt^2} \mathbf{u}_i(t) \quad (\text{IX.11})$$

Beginning with the foregoing basic expressions, Jones and Fuchs¹⁶⁵ have determined the dynamical matrix including retardation. Letting $c \rightarrow \infty$ yields the dynamical matrix neglecting retardation.

No complete solution for the eigenvectors and eigenfrequencies has been given when retardation is included. Since the dynamical matrix depends on the unknown frequency ω , the frequency cannot be obtained by matrix diagonalization. From the continuum theory it is known that the nature of the modes is determined by the magnitude $|\mathbf{k}|$ of the wave vector parallel to the slab. If $|\mathbf{k}| > \omega/c$, the nonradiative region, the normal mode frequencies are real in the absence of internal damping due to anharmonic forces. Otherwise, one is in the radiative region, where the modes decay radiatively and have complex frequencies. In the microscopic theory the result is similar: It can be shown¹⁶⁵ that the dynamical matrix is Hermitian if $|\mathbf{k}| > \omega/c$ and anharmonicity is ignored, so that the normal mode frequencies are necessarily real in the nonradiative region.

4. Thermal Effects

The mean-square vibrational amplitudes of the atoms near the surface of a NaCl film have been calculated by Chen et al.²³⁵ The calculations were done for a 15-layer NaCl slab with (001) surfaces using the Kellermann rigid-ion model. The results for a slab of this thickness closely approximate those for a semiinfinite crystal, since the bulk bands are densely populated and the surface modes are affected by the finite thickness only for very small values of \mathbf{k} . The expression used to calculate the mean-square amplitudes is basically (VIII.8) with the following minor modifications for a diatomic crystal: In order to calculate the mean-square amplitude $\langle u_{\alpha}^2(l_z, \kappa) \rangle$ of an atom of type κ in the plane l_z , one uses the eigenvector $\xi_{\alpha}^{\kappa}(l_z, \mathbf{k}, p)$ and the mass M_{κ} on the right-hand side of the equation. N is then the number of \mathbf{k} values in the sum over \mathbf{k} .

Results are presented for the mean-square vibrational amplitude as a function of layer index at room temperature, and for the surface mean-square vibrational amplitude $\langle u^2 \rangle_{\text{surface}}$ and the ratio $\langle u^2 \rangle_{\text{surface}} / \langle u^2 \rangle_{\text{bulk}}$ as functions of the temperature. At $T=0$ it is found that $\langle u_z^2 \rangle_{\text{surface}} / \langle u_z^2 \rangle_{\text{bulk}} = 1.24$, whereas $\langle u_x^2 \rangle_{\text{surface}} / \langle u_x^2 \rangle_{\text{bulk}} = 1.08$, where the z direction is normal to the surface. At $T=298$ K these ratios are, respectively, 1.58 and 1.23. For the two ion types, the surface to bulk ratios differ by less than 1% at all temperatures. The mean-square amplitudes of the Na and Cl ions in the

same plane are equal at high temperatures because the force constants for such ions are equal to the Kellermann model, where only nearest-neighbor short range forces are assumed. Preliminary calculations using the shell model show that the mean-square amplitude ratios normal to the surface are higher by about 10% than the values given above for the rigid-ion model. However, the amplitude ratios parallel to the surface are unchanged upon going to the shell model.

B. Small Particles

There has been recent work, both experimental and theoretical, on the dynamical properties of ionic crystal particles. The infrared optical properties of powdered samples of various materials have been measured: for example, the alkali halides,^{130,236-240} barium and strontium titanate,¹³² and magnesium oxide.^{133,241} In addition, the density of phonon states of a magnesium oxide powder has been determined by elastic neutron scattering.²⁴² The usual theoretical approach for the calculation of the optical properties of small particles is to use the continuum theory of Section V.A.2.

For spheres much smaller than a wavelength of light, the dominant feature of the absorptance is a single peak at the Fröhlich frequency ω_{1S} [(V.13)] given by the condition $\epsilon(\omega_{1S}) = -2\epsilon_f$, where ϵ_f is the dielectric function of the surrounding medium (see Fig. 32). The Fröhlich vibrational mode at ω_{1S} is a triply degenerate optical mode with uniform polarization within the sphere, and the associated absorptance peak has been observed by Abaev et al.²³⁸ for tiny NaCl spheres about 50 Å in diameter embedded in a porous glass matrix. This result indicates that the continuum theory continues basically valid even if the smallest dimension of the sample is only of the order of 10 atomic diameters.

The dielectric continuum theory does not yield an exact solution if the particles have shapes other than spheres or ellipsoids. In most experiments, the particles are in the form of cubes or rectangular plates. This discrepancy in shape is probably the most important source of disagreement between the theory, based on a sphere, and experiment. The dielectric continuum theory also cannot describe effects associated with modes having a wavelength comparable to the lattice parameter, such as short-wavelength bulk modes and surface modes localized within a few atoms of the surface. The phonon frequency distribution or density of states, a property that depends on the frequencies of all modes, also cannot be discussed with the dielectric continuum theory.

In an attempt to overcome the limitations of the dielectric continuum theory, there has been work on a microscopic lattice-dynamical theory of small particles, considering a particle to be a large molecule with known

interatomic forces.^{243,244} Using the Kellermann rigid-ion model, Genzel and Martin²⁴³ have studied the lattice dynamics of rectangular MgO crystals containing 48 ($3 \times 4 \times 4$), 64 ($4 \times 4 \times 4$), and 180 ($5 \times 6 \times 6$) atoms, and Martin²⁴⁴ has performed similar calculations for RbF crystals containing 64 and 144 ($4 \times 6 \times 6$) atoms. If the eigenfrequencies are denoted by ω_p and the eigenvectors by $\xi_\alpha^\kappa(l, p)$, where α is a Cartesian index, l is a unit-cell index, $\kappa = (1, 2)$ denotes the atom type, and p labels the normal modes, the optical absorption coefficient of a medium containing N randomly oriented, non-interacting particles per unit volume is given by

$$\alpha(\omega) = \frac{2\pi^2 N}{3c} \sum_{\substack{l, \kappa, \alpha \\ l', \kappa', \alpha'}} \frac{e_\kappa e_{\kappa'}}{(M_\kappa M_{\kappa'})^{1/2}} \xi_\alpha^\kappa(l, p) \xi_{\alpha'}^{\kappa'}(l', p) \delta(\omega_p, \omega) \quad (\text{IX.12})$$

where e_κ and M_κ are the charge and mass, respectively, of the ion κ , and δ is the Kronecker delta function. The total phonon density of states $F(\omega)$ can be calculated, as well as the density of states projected on any desired set of atoms, such as the surface atoms for which the phonon density of states is

$$F_s(\omega) = \sum_{\substack{l, \kappa, p \\ \text{surface}}} |\xi_\alpha^\kappa(l, p)|^2 \delta(\omega_p, \omega) \quad (\text{IX.13})$$

For $F_s(\omega)$, the summation over l, κ is to be carried out only over surface atoms. $F_s(\omega)$ shows, at each frequency, the relative number of modes for which the surface atoms have large amplitudes.

In the normal mode calculations, the atoms were assumed to be in equilibrium at their ideal lattice positions. The density of states $F(\omega)$ of a 64-atom cube of RbF is shown in Fig. 56 (solid line) and is compared with the density of states of a bulk crystal (dashed line). RbF is an especially interesting alkali halide because the density of states of the bulk crystal has a gap, centered at $\omega = 2.5 \times 10^{13} \text{ sec}^{-1}$, between acoustical modes at lower frequencies and optical modes at higher frequencies. Any modes lying in this gap must then be associated with the presence of the surface in a finite crystal. Of the 56 atoms lying on the surface of the $4 \times 4 \times 4$ cube, 8 are corner atoms, 24 are edge atoms, and the remaining 24 can be regarded as the surface atoms in the following discussion. The various features in the density of states in Fig. 56 can then be understood by comparison with the projected densities of states for the edge, corner, and surface atoms. For example, the peak at $\omega = 2.3 \times 10^{13} \text{ sec}^{-1}$ and the low-frequency edge at $\omega = 1.6 \times 10^{13} \text{ sec}^{-1}$ arise primarily from the corner atoms, and the peak at $\omega = 2.9 \times 10^{13} \text{ sec}^{-1}$ is due to edge atoms. The projected density of states for the remaining surface atoms has no distinct peaks, but the general

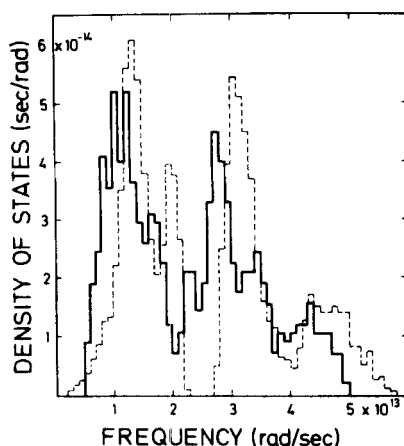


Fig. 56. Calculated rigid-ion density of states of a RbF cube containing 64 atoms (solid line) and RbF using cyclic boundary conditions (dashed line). (Reprinted from Martin.²⁴⁴)

shape resembles that of the total density of states. The density of states for a $4 \times 6 \times 6$ crystal is similar, except that the distinct peaks associated with the corner and edge atoms are absent. The dominant characteristic of the density of states for the $4 \times 6 \times 6$ crystal is that it closely resembles the density of states for a bulk crystal shifted to a lower frequency. There are, in other words, no features in the density of states that can be attributed specifically to surface modes. Chen et al.²⁴⁵ have noted similarly that the density of states of a 15-layer RbF slab corresponds to the density of states of the bulk crystal shifted to a lower frequency. In fact, the calculated difference spectrum (density of states of the finite crystal minus the density of states for the bulk crystal, normalized to the same number of atoms) is essentially the same for the slab and the $4 \times 6 \times 6$ crystal. For a crystal of this size, there are only 8 corner atoms and 40 edge atoms, so the difference spectrum can be attributed primarily to the remaining 64 surface atoms. The surface atoms therefore make the same contribution to the difference spectrum, whether they are located on the very small faces of a rectangular microcrystal or on the infinite surfaces of a film.

The calculated infrared absorption coefficient for a $4 \times 6 \times 6$ RbF crystal is shown in Fig. 57. According to the dielectric continuum theory for a very small ellipsoid with principal axes in the ratio 4:6:6, there should be two absorption peaks associated with uniform polarization modes, the lower frequency peak at ω_{1S}^\perp being associated with the doubly degenerate mode, [see (V.14)] and the upper frequency peak at ω_{1S}^\parallel with the nondegenerate mode. Although there are no uniform polarization modes in the rectangular crystal, there are, in fact, two peaks analogous to those that

occur in the continuum theory, but shifted to lower frequencies. These peaks can be associated with the vibration of surface atoms. There are smaller absorption peaks in the neighborhood of $\omega = 4.6 \times 10^{13} \text{ sec}^{-1}$ which arise from bulk modes having primarily longitudinal optical character, and a peak at $\omega = 2.9 \times 10^{13} \text{ sec}^{-1}$ arising from edge modes. In the frequency range 0.5×10^{13} to $2 \times 10^{13} \text{ sec}^{-1}$ there is additional weak absorption (absorption coefficient $< 50 \text{ cm}^{-1}$) which is too small to show in Fig. 57. This is surface-induced acoustical mode absorption, and it arises because the acoustical modes acquire a dipole moment when a surface is present. Martin^{240,246} has presented a theory of this surface-induced absorption for a semiinfinite NaCl crystal. Experimental results from NaCl powders²⁴⁰ do not exhibit such absorption: the observed absorption is much greater than predicted, and it does not have a peak where the density of states for the acoustical modes has a maximum.

A calculation of the difference spectrum for a $5 \times 6 \times 6$ MgO crystal by Genzel and Martin²⁴³ agrees qualitatively with the difference spectrum for MgO powder as measured by Rieder and Hörl²⁴² (Fig. 58). The discrepancy between theory and experiment can probably be explained by the large size of the powder particles used in the experiment (about 10^4 atoms

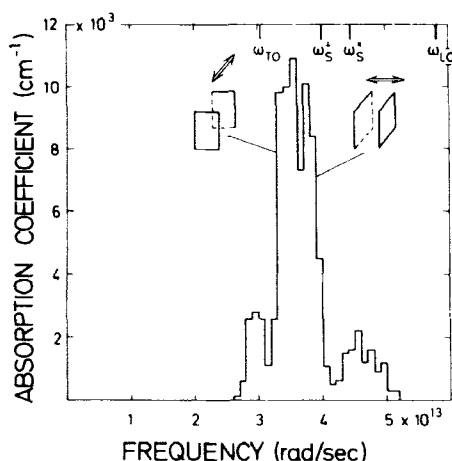


Fig. 57. Calculated infrared absorption coefficient of a powder sample composed of RbF microcrystals, each with atomic dimensions $4 \times 6 \times 6$. The frequencies ω_{TO} and ω_{LO} are indicated as are the frequencies of the surface modes associated with uniform polarization for and ellipsoid with principal axes in the ratio 4:6:6. For such an ellipsoid, the frequency ω_S^\perp (with polarization \perp the short axis and denoted ω_{1S}^\perp in the text) would be doubly degenerate and the frequency ω_S^\parallel (with polarization \parallel the short axis and denoted ω_{1S}^\parallel in the text) would be nondegenerate. These three modes together comprise the triply degenerate 1S mode for a sphere. (Reprinted from Martin.²⁴⁴)

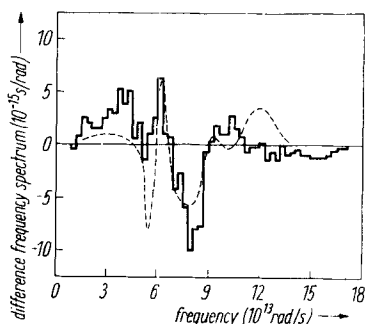


Fig. 58. Calculated difference spectrum (solid line) obtained by subtracting the rigid-ion density of states of MgO with cyclic boundary conditions from the rigid-ion density of states of a microcrystal containing 180 atoms. The experimental difference spectrum was obtained from Rieder and Hörl.²⁴² (Reprinted from Genzel and Martin.²⁴³)

in a crystal). Genzel and Martin²⁴³ also have calculated the infrared absorption coefficient for $3 \times 4 \times 4$ MgO microcrystals; the result is qualitatively similar to that for RbF shown in Fig. 57, except that in MgO, ω_{TO} and ω_{LO} occur, respectively, at frequencies of 7.5×10^{13} and $13.5 \times 10^{13} \text{ sec}^{-1}$. Also, there is no splitting of the central peak in MgO, even though such a splitting might be expected in a rectangular crystal. Measurements of the absorption spectrum of a powder sample consisting of $0.1\text{-}\mu$ MgO cubes show three peaks which agree qualitatively in frequency and relative intensity with the calculated peaks. Genzel and Martin conclude that the vibrational properties of microcrystals containing on the order of 100 atoms already approximate closely those of much larger crystals, containing as many as 10^6 atoms.

X. SURFACE RECONSTRUCTION

A. Monatomic Crystals

It has been observed that the periodic configuration of atoms on certain surfaces of a large variety of crystals is different from a terminated ideal bulk structure.²⁴⁷ For example, a (111) surface of silicon at room temperature has a surface unit cell twice as long in one of the three equivalent directions as it would be for the ideal surface, and it is said to be reconstructed into a (2×1) pattern. Trullinger and Cunningham²⁴⁸ have proposed a soft-surface-mode theory involving dynamic effective charges as a qualitative mechanism for surface reconstruction. They consider a 15-layer slab formed from a simple cubic monatomic crystal by cleavage along two (001) planes. The atoms near the surfaces possess a dynamic effective charge arising from their proximity to the surface. It is assumed

that the dipole moment of the crystal in the z direction (normal to the surface) is of the form

$$M_z = \sum_{lk} e_z(g) u_z(l, g) \quad (\text{X.1})$$

where $u_z(l, g)$ is the displacement from equilibrium of atom l in layer g , and $e_z(g)$ is the effective charge of such an atom. Since the dynamic effective charges decrease rapidly in magnitude with distance into the slab and are of opposite signs for the first two layers,²⁴⁹ it was assumed that $e_z(1) = -e_z(2)$ and $e_z(g) = 0$ for $g > 2$. In addition to long-range Coulomb forces between these effective charges, the atoms interact with short-range central forces between first and second neighbors.

Figure 59 shows the lowest of the 45 branches of the dispersion curves for wave vectors along symmetry lines in the two-dimensional Brillouin zone, with three different choices for the effective charge $e_z(1)$. This mode, which is a surface mode, becomes increasingly soft at the point M as $e_z(1)$ increases; when $e_z(1) > 0.53e$, $\omega^2 < 0$ at the point M , indicating an instability which leads to a $c(2 \times 2)$ reconstructed surface.^{249a} It is found that by including dynamic effective charges for displacements in the x or y directions or by changing the values of the short-range force constants, different surface reconstruction patterns can be obtained.

The existence of dynamic effective surface charges with a magnitude $e_z(1) \sim 0.5e$ is supported by inelastic LEED experiments. Ibach^{151, 250} measured the energy loss of 5-eV electrons scattered inelastically from a cleaved (111) surface of Si at room temperature, and found a 56-meV loss peak. The inelastic intensity is strongly peaked in the direction of the elastically scattered electrons, indicating that the electrons interact with an excitation having a wave vector \mathbf{k} parallel to the surface such that $|\mathbf{k}| \lesssim 10^{-2} k_{BZ}$, where k_{BZ} is the magnitude of a representative Brillouin zone boundary wave vector. This suggests that the excitation is a surface phonon, associated with dynamic charges, having wave vector \mathbf{k} and an energy of 56 meV. If there were no dynamic surface charges, the electrons would not interact preferentially with the surface mode, but rather with the bulk LO phonon branch having $|\mathbf{k}| \ll k_{BZ}$ and q_z , the wave vector normal to the (111) surface arbitrary as momentum normal to the surface need not be conserved. The interaction with this essentially one-dimensional phonon branch, extending from about 52 to 65 meV, might then be expected to yield a loss structure characteristic of the one-dimensional density of states, that is, strongly peaked near the two ends, but with the higher frequency peak reduced by the decrease in electron-phonon coupling at small q_z . If this reduction is sufficiently strong, the LO phonons could indeed yield a loss peak much like that observed by Ibach.

Evans and Mills²⁵¹ developed the theory of inelastic scattering of slow

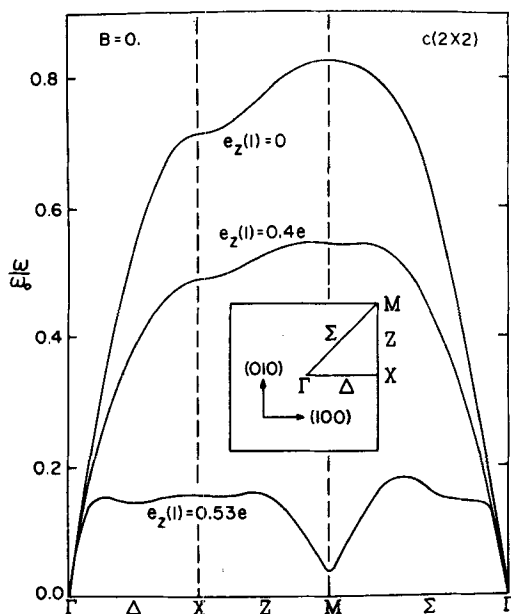


Fig. 59. Dispersion relation for the surface phonon of a 15-layer slab as a function of the surface-induced dynamic effective charge on the first layer. For this case, the short-range force constant parameter $b=0$ and the mode becomes soft at the M point, indicating a $c(2 \times 2)$ reconstructed pattern. The inset shows the irreducible segment of the first Brillouin zone. The normalization frequency ω_0 is defined by $\omega_0 = (a_0 c_{11}/M)^{1/2}$, where a_0 is the lattice parameter for this simple cubic lattice of ions of mass M and the elastic constant c_{11} is taken to be 2.0×10^{12} dynes/cm². (Reprinted from Trullinger and Cunningham.²⁴⁸)

electrons by both ionic crystals such as ZnO and nonionic crystals with surface charges, such as Si. Their analysis of Ibach's results for the intensity of the inelastically scattered electrons yields surface charges with a magnitude of about $0.5e$ if the observed surface mode has an atomic motion normal to the surface. If the motion were parallel to the surface, an unreasonably large effective charge of $4e$ would be required to explain the observed intensity. Evans and Mills also make conjectures about the nature of the surface mode responsible for the scattering. This mode is probably localized within a few atomic layers of the surface, a characteristic typical for surface modes of nonionic crystals.^{200,201,210-212} Since the atoms in the surface layer are bonded to fewer neighbors than an atom in the bulk, a surface mode should be split from the bottom of the optical bulk band and pushed into the gap between the optical and acoustical bands. This picture of the surface mode cannot be strictly correct, since the 56-meV surface mode lies within the 52 to 65 meV LO bulk band, rather than below it. This discrepancy from the behavior

expected for a monatomic lattice may be caused by the presence of the dynamical surface charges.

Ibach has also converted the room-temperature (2×1) reconstructed structure to a (7×7) structure by annealing the Si crystal at 400°C . The 56-meV loss was not found on the annealed surface. This does not mean that the surface phonon is not present on the (7×7) structure; it may indicate that the dynamic charges are reduced.

The fact that the (2×1) surface showed the 56-meV loss while the (7×7) surface did not, provides additional evidence that this loss does not result from excitation of bulk LO modes propagating perpendicular to the surface.

An indication of the manner in which a surface mode can be modified by reconstruction is given by Dobrzynski and Maradudin.²⁵² They consider a semi-infinite simple cubic crystal with an (001) surface and with interatomic forces described by the Montroll-Potts model. On the surface of the crystal there is a layer of light atoms. The surface layer is assumed to reconstruct into a (2×1) structure. In the absence of reconstruction there is a triply degenerate²⁵³ optical surface mode, with a minimum frequency at $\mathbf{k}=0$, lying above a bulk mode continuum throughout the square Brillouin zone with boundaries at $k_x = \pm \pi/a_0$ and $k_y = \pm \pi/a_0$, where a_0 is the bulk nearest-neighbor distance. When reconstruction takes place the new repeat distance in the y direction is $2a_0$ instead of a_0 . New Brillouin zone boundaries appear at $k_y = \pm \pi/2a_0$, where a gap opens up in the surface optical mode dispersion relation. If this dispersion relation is plotted in the reduced zone of the reconstructed crystal, the portion of the mode which was in the regions $-\pi/a_0 < k_y < -\pi/2a_0$ and $\pi/2a_0 < k_y < \pi/a_0$ is moved into the region $-\pi/2a_0 < k_y < \pi/2a_0$, so there are now two surface mode branches in the reduced zone. The low-frequency surface mode at $k_y=0$ corresponds to the same mode in the unreconstructed crystal, whereas the upper mode at $k_y=0$ corresponds to the mode at $k_y = \pm \pi/a$ in the unreconstructed crystal.

Another interesting effect arises from the fact that, in the absence of reconstruction, a portion of the bulk mode continuum near $k_y = \pm \pi/a$ lies at a higher frequency than the surface mode near $k_y=0$. When the bulk modes are moved into the reduced zone of the reconstructed crystal, they will overlap a portion of the lower surface mode branch. The surface mode then becomes a mixed mode and the frequency has a nonzero imaginary part in the region of overlap with the bulk modes.

Although this model is not an accurate representation of Si(111) surface, one can deduce by analogy that a single surface mode branch in the unreconstructed Si crystal will become two branches in the reduced zone of the (2×1) reconstructed crystal, and in particular there should be two

surface modes at $\mathbf{k} \approx 0$, with \mathbf{k} the wave vector parallel to the surface. Since only one mode was observed by Ibach, either the splitting between the two $\mathbf{k} \approx 0$ modes is small or the effective dipole moment associated with one of the modes is small. The latter possibility is likely because the motion of adjacent surface atoms is 180° out of phase for one of the two $\mathbf{k} \approx 0$ surface modes in the reconstructed crystal, giving zero dipole moment for this mode. When the Si surface reconstructs into a (7×7) structure at elevated temperatures, the loss of the signal may occur because of the formation of a large number of $\mathbf{k} \approx 0$ modes in the reduced zone. If many of these modes have dipole moments, and if these modes span a wide frequency range, one may have a large number of small energy-loss peaks that are difficult to detect.

Although there is experimental evidence that the atoms near the surface of a monatomic insulator such as Si have dynamic effective charges, there is at present no theory for the signs and magnitudes of such charges. However, Cunningham and Maradudin²⁴⁹ have examined a simple model consisting of a one-dimensional monatomic chain, which gives considerable insight into the physical origin of dynamic effective charges. They calculate the electronic eigenfunctions and eigenvalues for a finite chain, using a tight-binding theory with s and p orbitals on each atom, and two electrons per atom. This model leads to an insulating state with a lower filled s -like band and an upper empty p -like conduction band. The total dipole moment M of the atomic chain is calculated when a given atom l is displaced in a direction parallel to the chain by a distance $u(l)$ from its ideal lattice position. The dynamic effective charge $e(l)$ of the l th atom is then given by

$$e(l) = \frac{\partial M}{\partial u(l)} \quad (\text{X.2})$$

It is found that the dipole moment of the system can be written in the form

$$M = \sum_l [q_l R(l) + \mu_l] \quad (\text{X.3})$$

Here $R(l)$ is the position of atom l with respect to the center of the atomic chain; q_l , the charge on the l th atom, which arises because the charge of the electron cloud does not exactly neutralize the ion core charge, and μ_l , an electronic dipole moment, which arises from the mixing of s and p states on individual atoms, are appreciably different from zero only for atoms near the surface. The dynamic effective charge of atom l is then

$$e(l) = q_l + R(l) \frac{\partial q_l}{\partial u(l)} + \frac{\partial \mu_l}{\partial u(l)} \quad (\text{X.4})$$

The third term in (X.4) makes a negligible contribution to the dynamic effective charge, since the dipole moment μ_i has little dependence on $u(l)$.

The parameter that determines q_i is the overlap integral between s and p functions on adjacent atoms. The derivative of q_i with respect to displacement, $\partial q_i / \partial u(l)$, is determined by the derivative of the overlap integral with respect to interatomic distance. The first two terms in (X.4) turn out to be of opposite sign, the second term being somewhat larger than the first. Calculations using helium one-electron wave functions and an equilibrium interatomic distance of four times the Bohr radius give the effective charges $e(1) = -0.15e$ ($e > 0$) for surface atoms and $e(2) = +0.1e$ for atoms in the second layer: atoms still farther from the surface have $|e(l)| < 0.03e$. It is also concluded that allowing surface relaxation to take place does not change the dynamic effective charges by more than 5 or 10%. A similar tight-binding approach should also be applicable to a more realistic three-dimensional crystal.

Reconstruction can occur in very thin films without any need for dynamic surface charges. In a calculation of the vibrational frequencies of monatomic fcc films with atoms interacting through a Lennard-Jones potential, deWette and Allen²⁵⁴ concluded that a three-layer film with (110) surfaces is unstable at a sufficiently high density because some of the calculated frequencies are imaginary. The type of distortion can be ascertained by examining the eigenvectors of the normal modes with imaginary frequencies. A molecular dynamics calculation for zero temperature confirmed that the equilibrium structure for such a film is the (1×2) configuration illustrated in Fig. 60. No distortion was found for low-density, thicker films, or in films of any thickness with (100) or (111) surfaces.

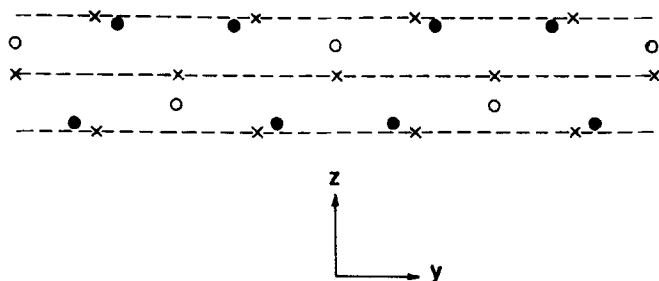


Fig. 60. Schematic side view of film after structural transformation. The positions of the particles before the transformation are indicated by crosses; the positions after the transformation are indicated by solid circles for particles in the outer layers and open circles for particles originally in the center layer. (Reprinted from deWette and Allen.²⁵⁴)

B. Ionic Crystals

Benson and Claxton²⁵⁵ have shown theoretically that the surface layers of an (001) face of alkali halides do not undergo uniform relaxation in a direction normal to the surface, but that the positive and negative ions in a given layer tend to be displaced in opposite directions. It should be noted that a distortion of this type does not increase the size of the two-dimensional unit cell. They base their conclusion on a calculation of the surface energy, allowing the ions in the first five layers to relax. The shell model of Dick and Overhauser^{256,257} is used, with Born-Mayer interactions acting between shells, spring forces acting between the shell and core of a given ion, and Coulomb forces between all shells and cores. Calculations are carried out for 17 alkali halides; some of the results for NaCl and LiF are shown in Table III. Benson and Claxton also computed the shell displacements and the dipole moment of each ion.

The theory of elastic low-energy electron diffraction from a LiF surface has been examined in detail by Laramore and Switendick.²⁵⁸ They show that a distorted surface similar to that proposed by Benson and Claxton is

TABLE III
Displacements of the Ion-Cores near the Surface
for a Semiinfinite Ionic Crystal^a

	λ	z_{λ}^{+}	z_{λ}^{-}
LiF	1	-0.0551	-0.0067
	2	0.0340	0.0117
	3	-0.0090	-0.0008
	4	0.0054	0.0022
	5	-0.0010	0.0001
NaCl	1	-0.0475	0.0194
	2	0.0297	-0.0052
	3	-0.0101	0.0045
	4	0.0053	-0.0011
	5	-0.0016	0.0008

^a λ is the layer index, starting with $\lambda=1$ for the outermost layer. z_{λ}^{+} and z_{λ}^{-} are displacements for the + and - ion-cores in a direction normal to the surface, measured in units of the nearest-neighbor distance in the bulk, a positive value of z denoting an outward displacement.

best able to explain the LEED experiments of McRae and Caldwell,²⁵⁹ who measured the intensity versus electron energy for elastic specular scattering at a fixed angle of incidence. Laramore and Switendick first calculate electron-ion core model potentials from which phase shifts for electron scattering can be determined. It is assumed that each atom vibrates in a spherically symmetric manner that can be characterized by an effective Debye temperature, and that the surface atoms have the same amplitude of vibration as atoms in the bulk. Although the surface atoms actually have larger vibrational amplitudes, at a given temperature the main effect of the larger amplitude would be to reduce the intensities of the peaks in the energy profile and not to change their position.

In the calculation of the intensity profile it is assumed that only the atoms in the first layer relax, as shown in Fig. 61. The bulk layer spacing is taken to be $d=2.03$ Å, and the values of d' and η which give the best agreement with experiment are $d'=1.93$ Å and $\eta=0.25$ Å. The open circles in Fig. 61 denote the fluorine ions; thus the outer fluorine sublayer has an inward displacement of 0.10 Å, whereas the outer lithium sublayer has a much greater inward displacement of 0.35 Å. Measured in units of the nearest-neighbor distance, the displacements are $z_{\lambda}^+ = -0.17$ and $z_{\lambda}^- = -0.05$ for the $\lambda=1$ layer. These values are much larger than the displacements calculated by Benson and Claxton (Table III). Although there is some qualitative similarity, quantitative agreement cannot be expected, since the displacements in Table III are calculated for $T=0$ K, but the LEED experiments were done at $T=573$ K; furthermore the analysis of Laramore and Switendick assumed no displacements for the second ($\lambda=2$)

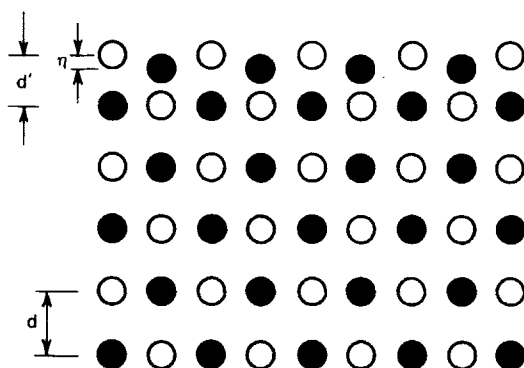


Fig. 61. Schematic illustration of parameters specifying the surface reconstruction for the (100) face of lithium fluoride. d' is the spacing between the second layer and "least-contracted" sublayer in the top layer. η is the separation between the sublayers in the top layer. d is the bulk layer spacing. (Reprinted from Laramore and Switendick.²⁵⁸)

layer. The disagreement is reduced if the difference in displacements for the first two layers, as calculated by Benson and Claxton, is identified as the displacement of the first layer in the analysis of Laramore and Switendick.

XI. VERY RECENT DEVELOPMENTS

Green's Function Treatment of the Lattice Dynamics of a Half-space Ionic Crystal

The lattice dynamics of a semi-infinite NaCl crystal have been studied by Benedik²⁶⁰ using the Green's function method. Starting with an infinite crystal, he chooses a plane denoted by Σ between two adjacent (001) atomic layers and sets equal to zero all interatomic force constants acting between atoms on opposite sides of the plane Σ . By this procedure, the crystal is "cut" along the plane Σ , creating two free (001) surfaces. The vanishing of these force constants is described by a perturbation matrix J in a $3s \times 2N_p$ -dimensional space, where $s=2$ is the number of atoms per unit cell and $2N_p$ is the number of atomic layers involved in the perturbation, N_p , on each side of the plane Σ . The matrix J can be block-diagonalized into two $3s \times N_p$ -dimensional matrices denoted $J_{(+)}$ and $J_{(-)}$, which are associated with coordinates having even and odd symmetry with respect to the plane Σ , and the corresponding unperturbed Green's function matrices $G_{(+)}$ and $G_{(-)}$ for the infinite lattice can also be calculated. Benedik then shows that the perturbed Green's function describing a semi-infinite crystal with a single free (001) surface is

$$\tilde{G} = [I + \bar{G}J]^{-1} \bar{G} \quad (\text{XI.1})$$

where I is the identity matrix,

$$\bar{J} = \frac{J_{(+)} + J_{(-)}}{2} \quad (\text{XI.2})$$

and

$$G^{-1} = \frac{G_{(+)}^{-1} + G_{(-)}^{-1}}{2} \quad (\text{XI.3})$$

A $3s \times N_p$ -dimensional square matrix, \tilde{G} is a function of the frequency ω and the two-dimensional surface wave vector \mathbf{k} . The phonon density of states projected onto the surface can be written

$$\rho(\mathbf{k}, \omega) = \left(\frac{2\omega}{\pi} \right) \text{Tr Im } \tilde{G}(\mathbf{k}, \omega) \quad (\text{XI.4})$$

and the surface-phonon dispersion relations $\omega(\mathbf{k})$ are solutions of the determinantal equation

$$\text{Re} D(\mathbf{k}, \omega) = 0 \quad (\text{XI.5})$$

where

$$D(\mathbf{k}, \omega) = \det \left[I + \bar{G}(\mathbf{k}, \omega) \bar{J}(\mathbf{k}) \right]. \quad (\text{XI.6})$$

By examining the dependence of $D(\mathbf{k}, \omega)$, $\tilde{G}(\mathbf{k}, \omega)$, and $\rho(\mathbf{k}, \omega)$ on ω , it is possible to distinguish among three types of surface phonons: localized, resonant, and pseudo-resonant. A localized surface phonon at a frequency $\omega_i(\mathbf{k})$, characterized by an infinitely sharp peak in the density of states, $\rho(\mathbf{k}, \omega) \propto \delta(\omega - \omega_i(\mathbf{k}))$, occurs where $\text{Re} D(\mathbf{k}, \omega)$, considered as a function of ω , changes sign in a region where $\text{Im} \tilde{G}(\mathbf{k}, \omega) = 0$. A resonant surface phonon and a pseudo-resonant surface phonon are both characterized by a peak in $\rho(\mathbf{k}, \omega)$ of finite width occurring within a broader range of frequencies, a bulk band, in which $\rho(\mathbf{k}, \omega) \neq 0$.²⁶¹ A resonant surface phonon occurs if $\text{Re} D(\mathbf{k}, \omega)$ changes sign at a frequency such that $\text{Im} \tilde{G}(\mathbf{k}, \omega) \neq 0$. If $\text{Re} D(\mathbf{k}, \omega)$ becomes small, without passing through zero, at a frequency where $\text{Im} \tilde{G}(\mathbf{k}, \omega) \neq 0$, one has a pseudo-resonant surface phonon.

The Green's function method appears to be convenient only for short-range interatomic forces, such that the number of layers N_p on either side of the plane Σ involved in the perturbation is small. Benedik points out, however, that even for the long-range Coulomb forces existing in an ionic crystal, the forces acting between layers, at a fixed value of \mathbf{k} , fall off rapidly with increasing distance. He therefore neglects the perturbing forces acting upon all atomic layers more distant than one layer on either side of Σ , so (XI.1) to (XI.6) involve 6×6 matrices.

Calculations of the phonon density of states $\rho(\mathbf{k}, \omega)$ were carried out using a breathing shell model for the interatomic forces, with \mathbf{k} values on the boundary of the irreducible element of the two-dimensional Brillouin zone, and neglecting retardation. In the outer parts of the Brillouin zone, the frequencies of the surface modes and the frequency ranges of the bulk modes are in quite good overall agreement with the shell-model calculations by Chen et al.,²³⁰ for a 15-layer NaCl slab shown in Fig. 54a.

Near $\mathbf{k} = 0$ there are some discrepancies. As $\mathbf{k} \rightarrow 0$, every mode polarized normal to the sagittal plane should become degenerate with a mode polarized in the sagittal plane. However, Benedik finds only one Lucas surface mode lying just below the TO bulk mode region, and it is polarized in the sagittal plane; the corresponding Lucas surface mode polarized normal to the sagittal plane is missing. There is a resonant surface mode at $\mathbf{k} \rightarrow 0$ polarized normal to the sagittal plane, but it lies at a lower frequency than the Lucas mode, and it has no degenerate partner.

Another deficiency of this work near $\mathbf{k}=0$ is the absence of the surface mode between ω_{TO} and ω_{LO} which appears in a dielectric continuum theory and should appear here at the frequency $\omega_{s\infty}$ given by (II.18) with $\epsilon_f = 1$. (When retardation is neglected, the surface mode derived from the dielectric theory lies at the frequency $\omega_{s\infty}$ for all \mathbf{k} , and this mode should therefore appear in the $\mathbf{k} \rightarrow 0$ limit of this microscopic theory.) The origin of these discrepancies is not clear.

Analysis of Attenuated Total Reflection Experiments

The theoretical relationship between the reflectance measured in an attenuated total reflection (ATR) experiment and the surface optical wave on an unperturbed semi-infinite medium (i.e., with the coupling prism absent) has been examined by Otto.²⁶² An ATR experiment may be performed either by holding the frequency ω constant and varying the angle of incidence α (see Fig. 34) or by holding α constant and varying the frequency. In both cases there is a dip in the reflectance at a certain value of the parameter which is varied; if the distance a between the prism and the sample is sufficiently large, the position and width of the dip are related to the properties of the unperturbed surface optical wave. Otto also shows how the position and width of the reflectance dip change as the surface optical wave is perturbed by bringing the prism closer to the sample.

Otto first writes the general expression for the reflectance R of p -polarized light incident within the prism. The dielectric function for the prism is taken to be the real quantity $\epsilon_p = n_p^2$, for the gap of width a $\epsilon = 1$, and for the sample, the complex quantity $\epsilon(\omega) = \epsilon'(\omega) + i\epsilon''(\omega)$. The component of the wave vector parallel to the sample surface is (see p. 445)

$$k = n_p \left(\frac{\omega}{c} \right) \sin \alpha \quad (\text{XI.7})$$

and the reflectance is

$$R = \left| \frac{N r_{pv}}{D} \right|^2 \quad (\text{XI.8})$$

where

$$N = (\epsilon \alpha_v + \alpha) + r_{pv}^{-1} (\epsilon \alpha_v - \alpha) \exp(-2\alpha_v a) \quad (\text{XI.9})$$

and

$$D = (\epsilon \alpha_v + \alpha) - r_{pv} (\epsilon \alpha_v - \alpha) \exp(-2\alpha_v a) \quad (\text{XI.10})$$

r_{pv} is the reflection coefficient at the prism-vacuum interface,

$$r_{pv}(\omega, k) = \frac{\beta_p - i\epsilon_p \alpha_v}{\beta_p + i\epsilon_p \alpha_v} \quad (\text{XI.11})$$

while

$$\alpha_v = \left(k^2 - \frac{\omega^2}{c^2} \right)^{1/2} \quad (\text{XI.12a})$$

$$\alpha = \left(k^2 - \frac{\epsilon \omega^2}{c^2} \right)^{1/2} \quad (\text{XI.12b})$$

and

$$\beta_p = \left(\frac{\epsilon_p \omega^2}{c^2} - k^2 \right)^{1/2} \quad (\text{XI.12c})$$

This expression for R is valid if $n_p \sin \alpha > 1$, that is, the prism-vacuum interface is totally reflecting ($R = 1$) if the sample is absent.

The ratio of the electric field amplitude at the sample-vacuum interface to the electric field amplitude of the incident wave is found to contain the quantity D , given by (XI.10), in the denominator. Setting $D = 0$ specifies the normal-mode condition which in this case is the dispersion relation of the surface optical wave including the perturbing effects of the prism. If the prism is removed by letting $a \rightarrow \infty$, one gets the expression

$$\epsilon \alpha_v + \alpha = 0 \quad (\text{XI.13})$$

which yields the unperturbed surface optical wave dispersion relation. Equation (XI.13) can also be written

$$k = \left(\frac{\omega}{c} \right) \left(\frac{\epsilon}{\epsilon + 1} \right)^{1/2} \quad (\text{XI.14})$$

which is again (II.13a) for the case where the inactive medium has $\epsilon_r = 1$.

To treat the experimental situation in which ω is held constant and α (or k) is varied, Otto expands the expression for R in terms of the quantity $\delta k = k - k_0$, where k_0 is the real wave vector of the surface optical wave in the absence of the prism, neglecting intrinsic damping arising from the presence of $\epsilon''(\omega)$. Thus,

$$k_0 = \left(\frac{\omega}{c} \right) \left(\frac{\epsilon'(\omega)}{\epsilon'(\omega) + 1} \right)^{1/2} \quad (\text{XI.15})$$

Assuming that $\epsilon''(\omega)$ and the second terms in N and D , representing the coupling through the vacuum gap, are small, one finds

$$R = 1 - \frac{4\alpha_{ii}\alpha_{ir}e^{-2\alpha_{vo}a}}{(k - k_0 - \alpha_{rr}e^{-2\alpha_{vo}a})^2 + (\alpha_{ii} + \alpha_{ir}e^{-2\alpha_{vo}a})^2} \quad (\text{XI.16})$$

where

$$\alpha_{rr} = -\frac{2\omega}{c} \frac{g}{|\epsilon'| + 1} \text{Re}\{r_{pv}(\omega, k_0)\} \quad (\text{XI.17a})$$

$$\alpha_{ir} = \frac{2\omega}{c} \frac{g}{|\epsilon'| + 1} \text{Im}\{r_{pv}(\omega, k_0)\} \quad (\text{XI.17b})$$

$$\alpha_{ii} = \frac{\omega}{4c} \frac{g}{(\epsilon')^2} \quad (\text{XI.17c})$$

$$g = \left\{ \frac{|\epsilon'|}{|\epsilon'| - 1} \right\}^{3/2} \quad (\text{XI.18})$$

and

$$\alpha_{vo} = \left(k_0^2 - \frac{\omega^2}{c^2} \right)^{1/2} \quad (\text{XI.19})$$

Equation (XI.16) shows that if the spacing is large so that $\exp(-2\alpha_{vo}a) \ll 1$, the reflectance dip is centered at $k = k_0$ and has the halfwidth α_{ii} characteristic of the unperturbed surface optical wave (intrinsic width). From (XI.16) it is also evident that for an arbitrary spacing a the reflectance dip is centered at the shifted position $k = k_0 + \alpha_{rr} \exp(-2\alpha_{vo}a)$ and the halfwidth is $\alpha_{ii} + \alpha_{ir} \exp(-2\alpha_{vo}a)$ (the sum of intrinsic and radiative widths). The position and width of the reflectance dip can also be found from the dispersion relation of the perturbed surface optical wave, obtained from the condition $D=0$ with ω real and k complex:

$$k = k_0 + \alpha_{rr}e^{-2\alpha_{vo}a} + i(\alpha_{ii} + \alpha_{ir}e^{-2\alpha_{vo}a}) \quad (\text{XI.20})$$

from which it is evident that the real part of k gives the position and the imaginary part of k gives the halfwidth. For the unperturbed surface optical wave, obtained by letting $a \rightarrow \infty$, we have

$$k = k_0 + i\alpha_{ii}, \quad (\text{XI.21})$$

which is the solution of (XI.13) or (XI.14) with ω real. The wave is

attenuated in the direction of propagation, since the imaginary part of k is positive.

It should be emphasized that fixing ω and allowing α to vary lead to results which correspond to a damping description wherein ω is real and k complex. Such a description was discussed at length in Section II.D.1 where it was shown that it leads to the peculiar dispersion curve of Fig. 20.

In the second experimental procedure α is fixed and ω (and k) is varied. The expression for R is now expanded in terms of the quantity $\delta\omega = \omega - \omega_0$, noting that when ω is varied, the variation in k is given by $k = k_0 + (k_0/\omega_0)\delta\omega$. Here k_0 and ω_0 are real quantities determined by the fixed angle α :

$$k_0 = \left(\frac{\omega_0}{c} \right) n_p \sin \alpha \quad (\text{XI.22})$$

and by (XI.14), which gives the surface optical wave dispersion relation under the conditions that intrinsic damping and radiation damping are neglected,

$$k_0 = \left(\frac{\omega_0}{c} \right) \left\{ \frac{\epsilon'(\omega_0)}{\epsilon'(\omega_0) + 1} \right\}^{1/2} \quad (\text{XI.23})$$

The result is

$$R = 1 - \frac{4\omega_{ii}\omega_{ir}e^{-2\alpha_{\omega}a}}{(\omega - \omega_{10} - \omega_{rr}e^{-2\alpha_{\omega}a})^2 + (\omega_{ii} + \omega_{ir}e^{-2\alpha_{\omega}a})^2} \quad (\text{XI.24})$$

where

$$\omega_{rr} = h \operatorname{Re} \{ r_{pv}(\omega_0, k_0) \} \quad (\text{XI.25a})$$

$$\omega_{ir} = h \operatorname{Im} \{ r_{pv}(\omega_0, k_0) \} \quad (\text{XI.25b})$$

$$\omega_{ii} = - \frac{\epsilon_{20}}{\epsilon'_{10}} \quad (\text{XI.25c})$$

$$h = 4\epsilon_{10}/(|\epsilon_{10}| + 1) \quad (\text{XI.26})$$

$$\epsilon_{10} = \epsilon'(\omega_0) \quad (\text{XI.27a})$$

$$\epsilon'_{10} = \left. \frac{d\epsilon'}{d\omega} \right|_{\omega=\omega_0} \quad (\text{XI.27b})$$

and

$$\epsilon_{20} = \epsilon''(\omega_0). \quad (\text{XI.27c})$$

The reflectance dip is centered at the shifted frequency $\omega = \omega_0 + \omega_{rr} \exp[-2\alpha_{vo}a]$ and has the halfwidth $\omega_{ii} + \omega_{ir} \exp(-2\alpha_{vo}a)$, again the sum of intrinsic and radiative damping terms. These properties of the reflectance can also be found from the dispersion relation of the perturbed surface optical wave, obtained from the condition $D=0$ with ω complex, k complex, and $k/\omega = n_p \sin \alpha / c$, a real quantity,

$$\omega = \omega_0 + \omega_{rr} \exp[-2\alpha_{vo}a] + i(\omega_{ii} + \omega_{ir} \exp[-2\alpha_{vo}a]) \quad (\text{XI.28})$$

For the unperturbed surface wave ($a \rightarrow \infty$) we have

$$\omega = \omega_0 + i\omega_{ii} \quad (\text{XI.29})$$

which is the solution of (XI.13) or (XI.14) with ω and k both complex and ω/k real.

The surface wave is now attenuated in time, since the imaginary part of ω is negative. The imaginary part of k also is negative, which means that the amplitude of the surface wave grows in the direction of propagation. This behavior may appear paradoxical, but it is a consequence of the fact that the surface wave, which is nonradiative when the prism is absent, becomes a virtual mode when the prism is brought up because the energy can radiate away through the prism. The requirement that the wave moving in the prism away from the gap have a well-defined direction specified by α is the origin of the condition that ω/k be real. This virtual mode is analogous to the "constant-angle" virtual modes occurring in a slab, for which the amplitude also increases in the direction of propagation.

By making exact calculations, using (XI.8), of the reflectance as a function of k holding ω constant, and as a function of ω holding α constant, with a model dielectric function representing GaP, Otto shows that the approximate equations (XI.16) and (XI.24) give results which agree well with the exact reflectance if the coupling to the prism is not too strong. Equations (XI.16) and (XI.24) also become inaccurate if the intrinsic damping is large, but Otto does not examine such a situation in detail.

Surface Thermal Expansion

A detailed theoretical investigation of surface thermal expansion has been made by Allen²⁶³ and Kenner and Allen.^{264,265} They consider an 11-layer monatomic fcc crystal slab with either (100) or (111) surfaces and

a Lennard-Jones interatomic potential. One can define thermal expansion coefficients $\alpha_i = A_i^{-1}(\partial A_i / \partial T)$, where A_i is the distance between atomic layers i and $i+1$ lying parallel to the surface. The quantity α_1 is the "surface thermal expansion coefficient," whereas α_b , found for i near the center of the slab, is the "bulk thermal expansion coefficient." It is shown that the temperature dependence of α_1 at low temperatures indicates the existence of surface modes. If a surface mode with a nonlinear dispersion relation is present (i.e., as k increases, ω drops below the frequency predicted by the linear relation $\omega \propto k$), the quantity α_1/T^3 has a sharp peak at a temperature below $\frac{1}{4}\hbar\omega_{\max}^S/k_B$, where ω_{\max}^S is the maximum frequency of the surface mode. The α_b/T^3 also has a peak, but it is much broader and occurs at a higher temperature, so the ratio α_1/α_b has approximately the same sharp peak as α_1/T^3 itself. For example, in the case of xenon, α_1/α_b has a maximum value of 6.5 at $T \cong 3$ K for a (100) surface, and a maximum value of 4 at $T \cong 4$ K for a (111) surface. α_1/α_b has a larger peak, occurring at a lower temperature, for a (100) surface because the surface mode denoted S_1 in Figs. 41 and 42 has a greater curvature and a smaller maximum frequency. At higher temperatures α_1/α_b is smaller and is a slowly increasing function of temperature. For example, a (100) surface of xenon has $\alpha_1/\alpha_b \cong 2$ and 3 at the temperatures 23 K and 160 K, respectively, while this ratio is about 20% larger for a (111) surface in this temperature range.

Ignatiev and Rhodin²⁶⁶ have determined the ratio α_1/α_b for a (111) surface of Xe from the temperature shift of the Bragg scattering peaks in a LEED experiment. They find $\alpha_1/\alpha_b \approx 4$ or 5 at temperatures between 55 K and 75 K, a value about twice as large as the theoretical prediction. Kenner and Allen²⁶⁵ suggest that the discrepancy is most probably caused by multiple scattering processes in the LEED experiment which invalidate an analysis based solely on the shift of the Bragg scattering peaks.

Soft Surface Phonons and Surface Reconstruction

A theory of soft surface phonons and surface reconstruction, first proposed by Trullinger and Cunningham,²⁴⁸ has been discussed subsequently in more detail by the same authors.²⁶⁷ It is assumed that dynamic effective charges exist on the two atomic layers next to the surface of a simple cubic lattice. As the magnitude of the charges increase, the frequency of the lowest-lying surface phonon drops and, for an effective charge magnitude of $0.5e$ to $0.6e$, goes to zero at some point in the two-dimensional Brillouin zone. Depending on the ratio between nearest- and next-nearest-neighbor force constants, the resulting surface instability may lead to (2×1) , (4×1) , or $c(2 \times 2)$ ^{249a} reconstruction patterns.

Entropy of Small Particles

Burton²⁶⁸ has made additional calculations of the entropy of small clusters of atoms, with results appreciably different from those reported previously.²²⁴ In the earlier work, the clusters were formed by adding successive near-neighbor shells to the central atom, but in the new work, they were constructed so that their free energy is a minimum. The calculated entropy is now a monotonically increasing function of cluster size, and there is none of the structure shown in Fig. 50. The nature of the changes in the normal mode spectra which lead to these new results are not reported.

Surface Modes which "Bend Back:" Experiments and Interpretation

Arakawa et al.,²⁶⁹ have obtained a surface plasmon dispersion curve for silver which bears a striking resemblance to that of Fig. 20. They employed the technique of Raether and Kretschmann,^{127,128} described at the end of Section V.A.1, wherein a thick silver film is deposited upon a dielectric and light is brought in through the dielectric enabling an examination of the surface plasmon at the vacuum-silver interface. In the experiments of Arakawa, et al., the frequency of the light was held fixed and reflectance dips found by varying the angle of incidence.

These results have been discussed by Alexander et al.,²⁷⁰ who point out that a proper representation of the reflectance for such an experiment requires a three-dimensional plot of the reflectance versus both incident angle and frequency. They go on to show that the usual surface plasmon dispersion curve, extending to large wave vectors with the frequency asymptotic to the frequency given by $\epsilon(\omega) = -\epsilon_f$, is obtained if the experiment is performed at fixed incident angle with variable frequency, while the apparent surface plasmon dispersion curve (i.e., as it manifests itself in reflectance dips) bends back if the experiment is performed at fixed frequency with variable incident angle. The detailed connection between these different experimental procedures and the various descriptions of damping discussed in Section II.D.1 is evident in the analysis given in pp. 519–523. For fixed frequency and variable incident angle, we see from (XI.20) that the "effective" surface excitation is characterized by real frequency and complex wave vector. This situation leads to the bending back of the surface mode, as discussed in Section II.D.1, and is also the appropriate description of the surface mode in the experiments of Arakawa et al.,²⁶⁹ in which bending back was observed. If, on the other hand, the experiment is performed at fixed incident angle with variable frequency, the surface excitation is characterized by the frequency

ω and the wave vector k being complex with the ratio k/ω real [see the discussion below (XI.27c)]. These conditions lead to a surface excitation of the usual sort, no back bending, just as does the real k , complex ω description.

There is an apparent contradiction between Fig. 20, where the "bent-back" portion of the surface mode remains in the radiative region, and the experimental results of Arakawa et al., in which the "bent-back" part of the curve appears in the nonradiative region. The conflict can be resolved by recognizing that the dielectric function of silver cannot be approximated by the simple oscillator expression (modified by letting $\omega_{TO} \rightarrow 0$) which led to Fig. 20. Experiments on materials such as beryllium, aluminum, or the alkali metals should not give rise to "bent-back" parts of the curves lying within the nonradiative region.

Nonlocality and Surface Modes for a Sphere

Using a multiple-wave procedure as described in Section VI.B.1, Ruppin²⁷³ has incorporated longitudinal effects into a theory for the optical properties of a sphere. Since transverse effects in the frequency range of interest for this theory can be accurately represented by $\epsilon(\omega)$, the only effect of the longitudinal fields is to change the quantity B_l of (V.10b) to $B_{l, \text{mod}}$:

$$B_{l, \text{mod}} = \frac{c_l h_l^{(1)}(\rho) + [(d/d\rho_L)j_l(\rho_L)] \times (\text{numerator of } B_l)}{c_l j_l(\rho) + [(d/d\rho_L)j_l(\rho_L)] \times (\text{denominator of } B_l)} \quad (\text{XI.30})$$

Here

$$\rho_L = k_L a \quad (\text{XI.31})$$

with k_L the solution of $\epsilon_l(k_L, \omega) = 0$, where $\epsilon_l(k, \omega)$ is the longitudinal dielectric function of the homogeneous isotropic sphere material, and

$$C_l = l(l+1) \left[\frac{j_l(\rho_L)}{\rho_L} \right] j_l(\rho) (\epsilon - \epsilon_l). \quad (\text{XI.32})$$

The remaining notation is that of Sections II.B and V.A.2.

Calculations²⁷³ of the extinction cross section, (V.12), for a small electron gas sphere show that the frequency of the 1S mode is raised somewhat by the longitudinal fields and a set of plasma resonances appears above the plasma frequency. These resonances are the spherical analogue of the resonances that appear in a thin metallic film,^{55,58} which, in turn, have counterparts in the resonances that appear for an ionic crystal slab below the longitudinal optical frequency as shown in Figs. 37

and 55. Thus, there should also occur longitudinal effects for ionic crystal spheres like those found by Ruppin for metallic spheres. However, in the ionic crystal they should lower the frequency of the 1S mode slightly and give rise to a set of LO phonon resonances for frequencies just below ω_{LO} .

Radiative Surface Modes

Vincent and Silcox²⁷⁴ have studied the radiative surface mode in oxidized aluminum films by means of high-energy electron-energy-loss measurements. The experimental results agree well with the theory.²⁷⁵

Surface Potential, Charge Density, and Dynamic Surface Charge for a Silicon (111) Surface

Appelbaum and Hamann²⁷⁶ have made self-consistent calculations of the ionization potential, charge density, and surface potential for the unreconstructed Si(111) surface. Within the present context, these results will play an important role as starting points for determinations of the dynamic effective charge.^{153a, 248, 249, 267} Indeed, Appelbaum and Hamann²⁷⁶ point out that the dynamic effective charge will be negligible for long-wavelength phonon modes propagating parallel to the Si(111) surface.

This conclusion suggests that the surface-phonon interpretation of the experiments of Ibach (see Section X.A) may be incorrect. However, the experiments of Ibach were performed on reconstructed surfaces and such surfaces may have significant dynamical charges, even if the perfect "terminated-bulk" surface does not.

The conclusion of Appelbaum and Hamann concerning dynamic charges also raises a question as to the validity of theories of surface reconstruction based upon surface phonons which involve dynamic effective charges.

Surface Polaritons for Biaxial and Uniaxial Crystals

We presented in Section III the theory of nonradiative surface polaritons for a half-space active medium, whose surface is an arbitrary face of a biaxial crystal, in contact with a homogeneous isotropic inactive medium. Borstel²⁷⁷ has now enlarged upon this theory. The dielectric properties of the active medium are described by the tensor $\tilde{\epsilon}(\omega)$ and those of the inactive medium by $\epsilon_i(\omega)$. Both $\tilde{\epsilon}$ and ϵ_i are taken to be real so damping effects are not included. Borstel points out that the two components (k_x, k_y) of the surface wave vector \mathbf{k} are not, in general, independent and thus nonradiative modes occur only over specific paths in the \mathbf{k} plane.

Borstel goes on to specialize his results to the case of a uniaxial crystal. If the optic axis is not perpendicular to the surface, he finds a pure transverse regular mode, which he calls a type-A surface polariton, de-

scribed by (III.16), where now $k^2 = k_x^2 + k_y^2$. This is a rather exotic mode in that it loses its surface character if the optic axis is perpendicular to the surface and becomes a bulk mode propagating parallel to the surface. Surface polaritons of type *A* are in general extraordinary but will be ordinary if the real part of the vector $\mathbf{b} = k_x \hat{i} + k_y \hat{j} + i\alpha \hat{k}$ [see (II.155)] is parallel to a principal axis of $\vec{\epsilon}$. Here \hat{i} , \hat{j} , and \hat{k} are unit vectors in the x , y , and z directions. These modes will be ordinary and TM if the optic axis is parallel to the surface and the surface propagation vector \mathbf{k} is perpendicular to the optic axis. The number of type-*A* surface polaritons will equal the number of transverse optical resonance frequencies associated with ϵ_{\perp} .

A second class of polaritons, type *B*, will in general be extraordinary. These modes will be regular if the optic axis is normal to the surface or if the optic axis is parallel to the surface and \mathbf{k} is perpendicular to the optic axis. Dispersion equations (III.16) and (III.18) are again obtained together with an additional special case. If the optic axis is inclined at an angle θ from the surface normal, and the y direction, in the surface, is perpendicular to the optic axis, the dispersion equation for polaritons propagating parallel to y is

$$k_y^2 = \frac{\omega^2}{c^2} \frac{(\epsilon_s \epsilon_{\perp} - \epsilon_{\parallel} \epsilon_I)}{(\epsilon_s \epsilon_{\perp} - \epsilon_I^2)} \quad (\text{XI.33})$$

where

$$\epsilon_s = \epsilon_{\perp} \sin^2 \theta + \epsilon_{\parallel} \cos^2 \theta \quad (\text{XI.34})$$

As for biaxial crystals, k_x and k_y are not independent for an arbitrary active medium surface so nonradiative modes can occur only along certain paths in the $k_x - k_y$ plane.

The maximum number of *B*-type nonradiative surface polaritons is equal to the total number of transverse optical resonance frequencies appearing in ϵ_{\perp} and ϵ_{\parallel} . The actual number for a given active medium surface depends on the crystal cut and the dielectric function of the inactive medium, as does the fraction of the total mode number which will be limited- k modes. All limited- k modes can be eliminated by choosing an inactive medium with a sufficiently high dielectric function.

Microscopic Lattice Dynamics of a CsCl Slab

A calculation of the normal modes of a 14-layer CsCl slab with (001) surfaces has been reported by Srinivasan and Lakshmi.²⁷⁸ A rigid-ion model with a Born-Mayer interaction between nearest neighbors was used. Although the normal mode dispersion relations are similar to those of crystals with the NaCl structure, CsCl has a few unique features. A

strongly localized nearly degenerate pair of surface modes is found in the gap between the TO and LO bulk bands. These modes lie between the two FK modes, they should be observable optically, and at $k=0$ the ionic displacements are perpendicular to the slab. They are similar to the modes found in RbF by Chen et al.²²³ as discussed in Section IX.A.2. Lucas surface modes are also found, but they are much farther from the TO bulk band from which they originate than in the case of the NaCl lattice. Some of the acoustic surface modes have imaginary frequencies, indicating an instability of the CsCl slab or an inappropriate mathematical model.

Local Dielectric Continuum Theory for Small Particles.

One of the authors²⁷⁹ has developed a theory for the optical properties of cubes much smaller than the wavelength of light. As contrasted with a sphere described by the dielectric function (I.9), for which a single absorption peak occurs at a frequency such that $\epsilon(\omega)/\epsilon_I = -2$, a cube has six major absorption peaks occurring where $\epsilon(\omega)/\epsilon_I = -3.68, -2.37, -1.90, -1.27, -0.78$, and -0.42 , with relative strengths 0.44, 0.24, 0.04, 0.05, 0.10, and 0.09, respectively. These values are only approximate, and will change as the accuracy of the calculation is increased. The theory is in fair agreement with transmission measurements of powdered samples of cubes.^{130,134} It should be noted that van Gelder et al.²⁸⁰ have calculated the normal mode frequencies of a cube using a dielectric continuum theory, but they did not estimate the strengths of the associated absorption peaks, and their normal mode frequencies differ considerably from those found in the newer work.

Acknowledgments

Much of the work on this article was done while the authors were visiting professors in Germany, KLK at the Institut für Angewandte Physik, Universität Hamburg, and RF at the Max Planck Institut für Festkörperforschung, Stuttgart. For their hospitality, enthusiasm for physics, and assistance, we would like to thank Prof. Dr. Heinz Raether and his associates at the Institut für Angewandte Physik, Prof. Dr. Ruprecht Haensel and the members of the DESY Synchrotron Radiation Group, and Prof. Dr. L. Genzel and Prof. Dr. H. Bilz and their associates at the MPI Stuttgart. We have benefited from discussions with the aforementioned as well as Drs. E.-E. Koch, E. Kretschmann, E. Kröger, C. Kunz, A. Otto, and M. Skibowski.

For permission to reprint figures we thank the following authors: G. P. Alldredge, R. E. Allen, J. J. Brion, E. Burstein, J. J. Burton, T. S. Chen, S. L. Cunningham, F. W. deWette, J. M. Dickey, L. Dobrzynski, B. Fisher, L. Genzel, Yu. M. Gerbshtein, A. Hartstein, G. E. Laramore, N. Marschall,

T. P. Martin, D. N. Mirlin, A. Paskin, A. Rahman, I. I. Reshina, A. C. Switendick, J. B. Theeten, S. E. Trullinger, and R. F. Wallis. Special thanks are due to Prof. deWette for providing us with originals of a number of published figures.

We wish also to thank Mrs. Mary Thompson of Ames for her yeoman service on the manuscript, Frau R. Höhne of Hamburg for the invaluable assistance she provided KLK, and W. H. Smith and D. Salisbury of the Ames Laboratory staff for their help with the figures.

References and Notes

1. A recent book in which these procedures are discussed at length is that of A. A. Maradudin, E. W. Montroll, G. H. Weiss, and I. P. Ipatova, *Theory of Lattice Dynamics in the Harmonic Approximation*, Academic Press, New York, 1971.
2. We use only the angular frequency ω throughout, but refer to it simply as the frequency.
3. Lord Rayleigh, *Proc. London Math. Soc.* **17**, 4 (1887).
4. T. Wolfram, R. E. DeWames, and E. A. Kraut, *J. Vac. Sci. Technol.*, **9**, 685 (1972).
- 4a. K. Dransfeld and E. Salzmänn, in *Physical Acoustics*, Vol. VII, W. P. Mason, Ed., Academic Press, New York, 1970, p. 219.
5. G. W. Farnell, in *Physical Acoustics*, Vol. VII, W. P. Mason and R. N. Thurston, Eds., Academic Press, New York, 1970, p. 109.
6. D. C. Gazis, R. Herman, and R. F. Wallis, *Phys. Rev.*, **119**, 533 (1960).
7. In general, $\epsilon(\omega)$ is a tensor; for homogeneous isotropic systems or cubic crystals it is a scalar.
8. The term macroscopic here is intended as a reminder that Maxwell's equations, when used for describing long-wavelength phenomena in material media, generally (and often implicitly) relate fields which are appropriate averages of their rapidly varying microscopic counterparts. These averaged fields are referred to as macroscopic fields. Since $\epsilon(\omega)$ relates two of these macroscopic fields, it also has macroscopic character. An excellent discussion of this point appears in L. Rosenfeld, *Theory of Electrons*, Dover, New York, 1965. In general, the macroscopic magnetic permeability $\mu(\omega)$ will also be involved in the response of the medium to an electromagnetic disturbance. We discuss the effect of $\mu(\omega) \neq 1$ below.
9. The standard reference for the bulk properties of these modes is M. Born and K. Huang, *Dynamical Theory of Crystal Lattices*, Oxford University Press, London, 1954.
10. In general ϵ_{RA} will depend on the spatial coordinates independently, that is, $\epsilon_{RA}(\mathbf{r}, \mathbf{r}', t - t')$. It is the assumptions of homogeneity and isotropy which permit us to write the spatial argument as $\mathbf{r} - \mathbf{r}'$.
11. E. Cohn, *Das elektromagnetische Feld*, Leipzig, 1900.
12. J. Zenneck, *Ann. Phys.*, **23**, 846 (1907).
13. A. Sommerfeld, *Ann. Phys.*, IV Folge, **28**, 665 (1909).
14. U. Fano, *Ann. Phys.*, **32**, 393 (1938).
15. U. Fano, *J. Opt. Soc. Am.*, **31**, 213 (1941).
16. R. H. Ritchie, *Phys. Rev.*, **106**, 874 (1957).

17. E. A. Stern and R. A. Ferrell, *Phys. Rev.*, **120**, 130 (1960).
18. R. Fuchs and K. L. Kliewer, *Phys. Rev.*, **140**, A2076 (1965).
19. K. L. Kliewer and R. Fuchs, *Phys. Rev.*, **144**, 495 (1966).
20. The exceptions are the series of papers by Englman and Ruppin.²¹⁻²³
21. R. Englman and R. Ruppin, *J. Phys. C*, **1**, 614 (1968).
22. R. Englman and R. Ruppin, *J. Phys. C*, **1**, 630 (1968).
23. R. Englman and R. Ruppin, *J. Phys. C*, **1**, 1515 (1968).
24. G. Mie, *Ann. Phys.*, **25**, 377 (1908).
25. P. Debye, *Ann. Phys.*, **30**, 57 (1909).
26. J. A. Stratton, *Electromagnetic Theory*, McGraw-Hill, New York, 1947.
27. M. Born and E. Wolf, *Principles of Optics*, Pergamon Press, New York, 1959.
28. R. Fuchs and K. L. Kliewer, *J. Opt. Soc. Am.*, **58**, 319 (1968).
29. R. Englman and R. Ruppin, *Phys. Rev. Lett.*, **16**, 898 (1966).
30. Ref. 9, p. 83 and Chapter VII. This dielectric constant applies to crystals that have a single "reststrahl" or long-wavelength, infrared-active, transverse optical phonon frequency, crystals of the NaCl, CsCl, ZnS, and fluorite structures.
31. R. H. Lyddane, R. G. Sachs, and E. Teller, *Phys. Rev.*, **59**, 673 (1941).
32. P. J. Feibelman, *Phys. Rev. Lett.*, **30**, 975 (1973).
33. R. H. Ritchie, *Surf. Sci.*, **34**, 1 (1973).
34. D. E. Beck and V. Celli, *Phys. Rev. Lett.*, **28**, 1124 (1972).
35. D. E. Beck, *Phys. Rev.*, **B**, **4**, 1555 (1971).
36. R. Fuchs and K. L. Kliewer, *Phys. Rev.*, **B**, **3**, 2270 (1971).
37. A. J. Bennett, *Phys. Rev.*, **B**, **1**, 203 (1970).
38. A. S. Barker, Jr., *Surf. Sci.*, **34**, 62 (1973).
39. R. Ruppin and R. Englman, *Rep. Prog. Phys.*, **33**, 149 (1970).
40. Maxwell's equations separate into two groups in the present case, one of which relates E_x , E_z , and B_y , and the other E_y , B_x , and B_z . The two groups can be analyzed independently and we begin with the former, frequently called transverse magnetic (TM) to emphasize the fact that the magnetic field is parallel to the surface while the electric field is not. Since the x and y directions were equivalent physically, prior to the introduction of the fields, the use of E_x for the electric field component in the surface plane involves no loss of generality. That is, an electric field component with an arbitrary direction in the x - y plane can be made to lie along the x -axis by merely rotating the system, dielectric media plus fields, about the z -axis.
41. The effects of losses or damping are discussed in Section II.D. In anticipation of this discussion we note there that our assumption $\alpha > 0$ must be generalized, if ϵ or μ is complex, to the assumption that $\text{Re}\alpha > 0$, where Re indicates the real part. This is the implication whenever we describe the α parameters as being positive.
42. A dielectric function not equal to 1 indicates the possibility of polarization within the system; the development of the theory from the dynamic Maxwell's equations indicates that photons are also involved. For c finite, we are then dealing with a normal mode which is a mixture of polarization and photons. Such excitations are frequently called polaritons, and so our concern here is with surface polaritons.
43. In this classical, linear analysis, the amplitude associated with the normal mode plays an unimportant role. Such would not be the case in the corresponding quantum mechanical treatment.

44. S. Q. Wang and G. D. Mahan, *Phys. Rev., B*, **6**, 4517 (1972).
45. H. Bilz, L. Genzel, and H. Happ, *Z. Phys.*, **160**, 535 (1960).
46. A. Otto, *Optik* (in press).
47. J. Schoenwald, E. Burstein, and J. M. Elson, *Solid-State Commun.*, **12**, 185 (1973).
48. A. Harstein, E. Burstein, J. J. Brion, and R. F. Wallis, *Surf. Sci.*, **34**, 81 (1973).
49. D. L. Mills, *J. Phys. (Paris)* **31** C1-33 (1970); T. Wolfram and R. E. DeWames, *Phys. Rev. Lett.* **24**, 1489 (1970); S. Stojanovic and B. S. Tosic, *Phys. Status Solidi* **32**, 229 (1969). See also R. Alexander, R. Graham, and R. Bell (to be published) who discuss the case where both inactive and active media are characterized by complex dielectric functions and complex magnetic permeabilities.
50. The procedure of setting the amplitude factors of the fields for the two surfaces equal or opposite in sign can also be thought of as the fields from the two surface being in phase or out of phase. Only if the media on the two sides of the active slab are the same will this procedure be rigorously valid.
51. J. B. Chase and K. L. Kliewer, *Phys. Rev., B*, **2**, 4389 (1970).
52. J. Heinrichs, *Phys. Rev., B*, **5**, 4792 (1972).
53. J. Heinrichs, *Phys. Rev., B*, **8**, 1708 (1973).
54. K. L. Kliewer and R. Fuchs, *Phys. Rev.*, **172**, 607 (1968).
55. W. E. Jones, K. L. Kliewer, and R. Fuchs, *Phys. Rev.*, **178**, 1201 (1969).
56. A. Otto, *Phys. Status Solidi*, **42**, K31 (1970).
57. R. Fuchs, unpublished.
58. R. Fuchs and K. L. Kliewer, *Phys. Rev.*, **185**, 905 (1969).
59. It should be noted that the electron gas surface impedance used here was derived assuming a step-function electron charge density at the surface. For the surface plasmon, and presumably in the present problem as well, the large wave vector results depend significantly on the detailed position dependence of the charge density near the surface.^{32,34,35,37} For such wave vectors, however, the local representation for the ionic crystal dielectric function will also be invalid.
60. K. L. Kliewer and R. Fuchs, *Phys. Rev.*, **150**, 573 (1966).
61. R. H. Ritchie, *Surf. Sci.*, **4**, 497 (1965).
62. More properly, $|\beta a| \ll 1$.
63. For $\epsilon_l > \epsilon_\infty$, the region L'_1 disappears, the region R'_1 is compressed, and the region R_2 extends to ∞ between R'_1 and N . The OTH mode then has $\omega \rightarrow \infty$ at an angle θ such that $\sin \theta = (\epsilon_\infty / \epsilon_l)^{1/2}$.
64. Expressions valid for this case appear in Ref. 60 for $\epsilon_l = 1$.
65. J. D. Jackson, *Classical Electrodynamics*, Wiley, New York, 1962.
66. For an ionic crystal sphere for which $\epsilon(\omega)$ is given by (I.9), these longitudinal modes all occur at the frequency $\omega = \omega_{LO}$, have $\mathbf{H} = 0$ everywhere, and have $\mathbf{E} = 0$ outside the sphere. The longitudinal modes are independent of whether or not retardation is included.²⁸
- 66a. Longitudinal effects in this problem are discussed in Section XI.
67. It should be kept in mind that here, as well as for the bulk modes, there occurs the $(2l+1)$ -fold degeneracy associated with the azimuthal index m .
68. For W sufficiently large, many of the surface modes have Ω' in the frequency region of the low-frequency bulk modes. These two types of modes remain distinct, however, in

- that $|\Omega''|$ for the surface modes is considerably larger than $|\Omega''|$ for the bulk modes when Ω' for the two types of modes is comparable.
- 68a. It is in the $W \rightarrow 0$ limit that the distinction between transverse bulk modes and surface modes can be stated. Denoting the macroscopic polarization by \mathbf{P} , transverse bulk modes have $\nabla \cdot \mathbf{P} = 0$ everywhere, and $\nabla \times \mathbf{P} \neq 0$ within the particle. Surface modes have $\nabla \cdot \mathbf{P} = \nabla \times \mathbf{P} = 0$ within the particle, but $\nabla \cdot \mathbf{P} \neq 0$ on the surface of the particle. See also equations (II.101).
 69. This is shown in Section II.C.
 70. More generally, when $|\rho| \ll l$ and $|\rho_l| \ll l$.
 71. The fact that the "surface" mode here extends uniformly throughout the active sphere points up the impossibility of distinguishing definitively surface modes from bulk modes by a casual examination of the penetration depth of the fields. See also footnotes 68a and 81.
 72. H. Fröhlich, *Theory of Dielectrics*, Oxford University Press, New York, 1949, pp. 149–155.
 73. H. B. Rosenstock, *Phys. Rev.*, **121**, 416 (1961).
 74. A. A. Maradudin and G. H. Weiss, *Phys. Rev.*, **123**, 1968 (1961).
 75. T. H. K. Barron, *Phys. Rev.*, **123**, 1995 (1961).
 76. J. Grindlay, *Can. J. Phys.*, **43**, 1605 (1965).
 77. It was this result that led to the incorrect conclusion that, for $q \rightarrow 0$, the TO and LO phonons in an ionic crystal were degenerate in frequency.
 78. See, for example, Ref. 26, p. 206.
 79. P. M. Morse and H. Feshbach, *Methods of Theoretical Physics*, McGraw-Hill, New York, 1953, Chapter 5.
 80. Ref. 9, p. 82.
 81. We can immediately call such a solution a surface solution since, in an infinite medium, a vector field is uniquely specified by giving its divergence and curl. Solutions for which both the divergence and curl are zero then must be associated with "noninfinite medium" features, that is, surfaces.
 82. E. W. Kellermann, *Phil. Trans. Roy. Soc.*, **238**, 513 (1940).
 83. Ref. 9, Chapter VII.
 84. Ref. 9, p. 120.
 85. Our definition of the damping constant γ_1 corresponds to 2γ in the notation of Born and Huang.⁹ Consistent with the phenomenological character of our γ_1 , we can write those terms of Born and Huang's Eq. (47.11) which specifically involve the frequency as $1/(4\omega_{\text{TO}}^2) + i/(\omega_{\text{TO}}\gamma_{\text{eff}})$, with $2/\gamma_{\text{eff}}$ equal to the expression in the square brackets of (47.11). Putting $\omega = \omega_{\text{TO}}$ in (II.116) and expanding to lowest order in $(\gamma_1/\omega_{\text{TO}})$, we obtain $1/(4\omega_{\text{TO}}^2) + i/(\omega_{\text{TO}}\gamma_1)$, which is just the Born and Huang result if we identify γ_1 with γ_{eff} . If we put $\omega = \omega_{\text{TO}}$ in (II.115), the real part of the frequency-dependent factor vanishes. Thus, we prefer (II.116).
 86. Ref. 27, p. 43.
 87. The frequencies $\omega(\theta)$ which satisfy this equation for LiF are shown in Figs. 3 and 4 of Ref. 60.
 88. See also Ref. 46. One of the authors (KLK) would like to acknowledge a stimulating discussion with Dr. Otto concerning the appearance of the Brewster angle condition in the surface excitation theory.

89. When damping is present, the various regions of Fig. 9 are no longer well defined.
- 89a. However, see p. 525.
90. An example of the type of physical requirement that might serve to link the two is that there be a real angle associated with the excitation process. This requirement appears in the discussion of the real-angle virtual modes in Section II.A.3. See also pp. 519–523.
91. This is shown in Section V.A.1.
92. I. Yokota, *J. Phys. Soc. Japan*, **16**, 2075 (1961).
93. B. B. Varga, *Phys. Rev.*, **137**, A1896 (1965).
94. R. F. Wallis and J. J. Brion, *Solid-State Commun.*, **9**, 2099 (1971).
95. In practice m^* is usually dependent on n since the conduction band is not rigorously parabolic. See, for example, E. J. Johnson and D. H. Dickey, *Phys. Rev.*, **B**, **1**, 2676 (1970).
96. K. W. Chiu and J. J. Quinn, *Phys. Lett.*, **35A**, 469 (1971).
97. K. L. Kliewer and R. Fuchs, *Phys. Rev.*, **153**, 498 (1967).
98. Keep in mind here that the “pure” Brewster angle condition is associated with a real dielectric function. With damping, and in the temporal wave-packet description, the effective Brewster angle condition involves in general a complex frequency. The remarks above relate to the real part of the frequency.
99. J. J. Brion, R. F. Wallis, A. Hartstein, and E. Burstein, *Surf. Sci.*, **34**, 73 (1973).
100. This equation is given incorrectly in Ref. 99.
101. V. N. Lyubimov and D. G. Sannikov, *Sov. Phys. Solid State*, **14**, 574 (1972).
102. J. J. Brion, R. F. Wallis, A. Hartstein, and E. Burstein, *Phys. Rev. Lett.*, **28**, 1455 (1972).
- 102a. Such modes are called “constant-angle” because of their correspondence with the so-labeled virtual modes.⁶⁰ See also Section XI, pp. 519–523.
103. See, for example, L. D. Landau and E. M. Lifshitz, *Electrodynamics of Continuous Media*, Pergamon Press, New York, 1960, Chapter 11.
104. H. J. Falge and A. Otto, *Phys. Status Solidi (b)*, **56**, 523 (1973).
105. With damping these modes do have a finite lifetime, but then so do the modes which extend to large k .
106. V. V. Bryskin, D. N. Mirlin, and I. I. Reshina, *Sov. Phys. JETP Lett.*, **16**, 315 (1972).
107. Note that these authors have used the terms ordinary and extraordinary differently than we did in our discussion above.
108. H. Ibach, in *Festkörper Probleme*, Vol. XI, O. Madelung, Ed., Pergamon Press, Vieweg, 1971.
109. R. Fuchs, K. L. Kliewer, and W. J. Pardee, *Phys. Rev.*, **150**, 589 (1966).
110. Modes of given parity can of course interact in A .
111. The condition $W=1$ means the wavelength of the incident light $\lambda=2\pi L$ if $\omega=\omega_{TO}$.
112. D. W. Berreman, *Phys. Rev.*, **130**, 2193 (1963).
113. J. E. Mooij, W. B. van de Bunt, and J. E. Schrijvers, *Phys. Lett.*, **28A**, 573 (1969).
114. K. Hisano, Y. Okamoto, and O. Matamura, *J. Phys. Soc. Japan*, **28**, 425 (1970).
115. K. Hisano, *J. Phys. Soc. Japan*, **25**, 1091 (1968).
116. K. Hisano, Y. Okamoto, T. Kubota, and O. Matamura, *J. Phys. Soc. Japan*, **23**, 1422 (1967).
117. Y. Okamoto, N. Ohama, and O. Matamura, *J. Phys. Soc. Japan*, **30**, 1208 (1971).

118. R. Källin, R. Brusa, H. P. Baltes, and F. K. Kneubühl, *Soc. Suisse Phys.*, **45**, 3 (1972).
119. In a calculation of the optical properties for a real system with ϵ complex, ω is real and (V.7) cannot be satisfied exactly. The Brewster angle will then correspond to a reflectance minimum rather than $R=0$. We can solve (V.7) exactly if we permit ω and/or k to be complex.
120. These conditions are related to the fact that the nonradiative surface polaritons have the electric field component normal to the surface directed oppositely in the active and inactive media while the radiative region surface excitations have these components in the same direction.
121. N. Marschall, B. Fischer, and H. J. Queisser, *Phys. Rev. Lett.*, **27**, 95 (1971).
122. B. Fischer, N. Marschall, and H. J. Queisser, *Surf. Sci.*, **34**, 50 (1973).
123. See, for example, J. Hägglund and F. Sellberg, *J. Opt. Soc. Am.*, **56**, 1031 (1966).
124. M. Hass, *Phys. Rev. Lett.*, **13**, 429 (1964).
125. S. N. Jaspersion and S. E. Schnatterly, *Phys. Rev.*, **188**, 759 (1969).
126. D. W. Berreman, *Phys. Rev.*, **B**, **1**, 381 (1970).
127. E. Kretschmann, and H. Raether, *Z. Naturforsch.*, **23a**, 2135 (1968).
128. E. Kretschmann, *Z. Phys.*, **241**, 313 (1971).
129. R. Ruppin, *Surf. Sci.*, **34**, 20 (1973).
130. V. V. Bryskin, Yu. M. Gerbshtein, and D. N. Mirlin, *Solid-State Commun.*, **9**, 669 (1971).
131. J. R. Luxon and R. Summitt, *J. Chem Phys.*, **50**, 1366 (1969).
132. J. T. Luxon, D. J. Montgomery, and R. Summitt, *J. Appl. Phys.*, **41**, 2303 (1970).
133. L. Genzel and T. P. Martin, *Phys. Status Solidi (b)*, **51**, 91 (1972).
134. L. Genzel and T. P. Martin, *Surf. Sci.*, **34**, 33 (1973).
135. Another approach to the "mixed-medium" dielectric function has been presented by O. Hunderi, *Phys. Rev.*, **B**, **7**, 3419 (1973).
136. K. H. Rieder, M. Ishigawa, and L. Genzel, *Phys. Rev.*, **B**, **6**, 3804 (1972).
137. R. Källin, H. P. Baltes, and F. K. Kneubühl, *Helv. Phys. Acta*, **43**, 488 (1970).
138. A. Otto, *Z. Phys.*, **216**, 398 (1968).
139. An analysis of ATR experiments due to Otto is discussed in Section XI. For comparison the modified ATR technique of Raether and Kretschmann is discussed in Ref. 128.
140. V. V. Bryskin, Yu. M. Gerbshtein, and D. N. Mirlin, *Sov. Phys. Solid State*, **13**, 1779 (1972).
141. V. V. Bryskin, Yu. M. Gerbshtein, and D. N. Mirlin, *Fiz. Tverd. Tela*, **14**, 543 (1972).
142. N. Marschall and B. Fischer, *Phys. Rev. Lett.*, **28**, 811 (1972).
143. B. Fischer, N. Marschall, and H. J. Queisser, *Surf. Sci.*, **34**, 50 (1973).
144. See footnote 2 of Ref. 143.
145. I. I. Reshina, Yu. M. Gerbshtein, and D. N. Mirlin, *Fiz. Tverd. Tela*, **14**, 1280 (1972). [*Sov. Phys. Solid State*, **14**, 1104 (1972)].
146. W. E. Anderson, R. W. Alexander, Jr., and R. J. Bell, *Phys. Rev. Lett.*, **27**, 1057 (1972).
147. A. S. Barker, Jr., *Phys. Rev. Lett.*, **28**, 892 (1972).
148. H. Boersch, J. Geiger, and W. Stickel, *Phys. Rev. Lett.*, **17**, 379 (1966).
149. H. Raether, *Springer Tracts in Modern Physics*, **38**, 84 (1965).
- 149a. H. Boersch, J. Geiger, and W. Stickel, *Z. Phys.*, **212**, 130 (1968).

150. H. Ibach, *Phys. Rev. Lett.*, **24**, 1416 (1970).
151. H. Ibach, *J. Vac. Sci. Technol.*, **9**, 713 (1972).
152. A. A. Lucas and M. Šunjić, *Phys. Rev. Lett.*, **26**, 229 (1971).
153. M. Šunjić and A. A. Lucas, *Phys. Rev.*, **B**, **3**, 719 (1971).
- 153a. See also Ref. 251.
154. This dielectric function is not valid, in general, for a crystal, as the local field corrections, which result in the appearance of reciprocal lattice vectors in the argument of $\epsilon_{\alpha\beta}$, have been ignored. This means that we should, in principle, restrict our considerations to \mathbf{q} values that satisfy $|\mathbf{q}| \ll |\mathbf{G}|$, where \mathbf{G} is any reciprocal lattice vector. Since the nonlocal theory for the problems of interest here is in such an early stage of development and our intent is to emphasize the physical distinctions between local and nonlocal descriptions, we will be cavalier about this restriction. Several related mathematical deficiencies in our discussion should be noted. We will write the spatial argument of the real-space dielectric function as $(\mathbf{r}-\mathbf{r}')$ which is consistent with the Fourier-transformed dielectric function having argument \mathbf{q} and subject to the same limitations. The wave vector \mathbf{q} is restricted to the first Brillouin zone and the process of taking Fourier transforms, when done properly, involves an integral over this zone and a sum over reciprocal lattice vectors. Consistent with the procedure above, we will merely integrate over the first zone. Comprehensive discussions of the general dielectric function theory appear in S. L. Adler, *Phys. Rev.*, **126**, 413 (1962); N. Wiser, *ibid.*, **129**, 62 (1963); and H. Ehrenreich, in *The Optical Properties of Solids*, J. Tauc, Ed., Academic Press, New York, 1966, p. 106.
155. Equation (VI.1) is more general than (I.5) because the dielectric function is a tensor, allowing for the possibility that \mathfrak{D} and \mathfrak{E} may not be parallel. Even in an isotropic system such as a free electron gas, the \mathbf{q} vector establishes a preferred direction, and it turns out that \mathfrak{D} and \mathfrak{E} are, in fact, not parallel. An equivalent statement is that the transverse and longitudinal dielectric functions are not equal for $\mathbf{q} \neq 0$.
156. We use the convention that $\mathbf{B} = \mathbf{H}$, so that all physical currents, including the magnetization current, $c\nabla \times \mathbf{M}$ are included in the displacement current. Therefore (II.1d) is replaced by

$$\nabla \times \mathbf{B} = \frac{1}{c} \frac{\partial \mathbf{D}}{\partial t} = \frac{1}{c} \left[\frac{\partial \mathbf{E}}{\partial t} + 4\pi \left(\mathbf{j} + \frac{\partial \mathbf{P}}{\partial t} + (c\nabla \times \mathbf{M}) \right) \right]$$

with \mathbf{P} the polarization, \mathbf{M} the magnetization, and \mathbf{j} the conduction current. After taking Fourier transforms the system is fully characterized by the dielectric tensor defined by $\mathfrak{D}(\mathbf{q}, \omega) = \epsilon(\mathbf{q}, \omega) \cdot \mathfrak{E}(\mathbf{q}, \omega)$. One obtains a magnetic permeability different from 1 by moving the magnetization current to the left-hand side of the equation and changing the dielectric function from ϵ to ϵ' . We have

$$\nabla \times (\mathbf{B} - 4\pi \mathbf{M}) = \frac{1}{c} \left[\frac{\partial \mathbf{E}}{\partial t} + 4\pi \left(\mathbf{j} + \frac{\partial \mathbf{P}}{\partial t} \right) \right]$$

or

$$\nabla \times \mathbf{H} = \frac{1}{c} \frac{\partial \mathbf{D}'}{\partial t}$$

Following Fourier transformation we can write $\mathfrak{B} = \mu \mathfrak{H}$ and $\mathfrak{D}' = \epsilon' \cdot \mathfrak{E}$, where we

- have assumed magnetic isotropy. The dielectric functions $\epsilon_{\alpha\beta}(\mathbf{q}, \omega)$ and $\epsilon'_{\alpha\beta}(\mathbf{q}, \omega)$ are related by $\epsilon_{\alpha\beta} = \mu\epsilon'_{\alpha\beta}$. In the following discussion, we shall not distinguish between different physical origins of the current, and all three terms $\mathbf{j} + \partial\mathbf{P}/\partial t + c\nabla \times \mathbf{M}$ will be lumped together into a total polarization current $\partial\mathbf{P}/\partial t$, or alternatively, into a total conduction current \mathbf{j} .
157. G. E. H. Reuter and E. H. Sondheimer, *Proc. Roy. Soc. (London)*, **A195**, 336 (1948).
 158. R. H. Ritchie and A. L. Marusak, *Surf. Sci.*, **4**, 234 (1966).
 159. This can be shown by setting $z=0$ and noting that the diagonal elements of the susceptibility tensor for a free electron gas are even functions of the spatial variable, whereas the off-diagonal elements are odd functions.
 160. R. Fuchs and K. L. Kliewer, *Phys. Rev.*, **185**, 905 (1969).
 161. The expressions for R , T , and A for a slab are $R = \frac{1}{4}|P^{(1)} + P^{(2)}|^2$, $T = \frac{1}{4}|P^{(1)} - P^{(2)}|^2$, and $A = 1 - T - R$, where $P^{(1,2)} = (\cos\theta - Z^{(1,2)})/(\cos\theta + Z^{(1,2)})$.
 162. I. Lindau and P.-O. Nilsson, *Phys. Scr.*, **3**, 87 (1971).
 163. M. Anderegg, B. Feuerbacher, and B. Fitton, *Phys. Rev. Lett.*, **27**, 1565 (1971).
 164. R. Fuchs, *Phys. Lett.*, **43A**, 42 (1973).
 165. W. E. Jones and R. Fuchs, *Phys. Rev.*, **B**, **4**, 3581 (1971).
 166. Additional structure arising from anharmonic processes, expressible approximately by a frequency-dependent damping parameter $\gamma(\omega)$, is neglected in this discussion.
 167. In this nonlocal theory, the dielectric is still being considered as a continuum, and the question of the exact position of the surfaces in relation to the atoms does not arise. If one wishes to make a connection with the lattice dynamics of the slab, which is discussed later, these surfaces should be taken to lie one-half the interlayer spacing outside the surface atomic layers. For a standing-wave LO mode in which n half-waves fit between the surfaces, there are $n-1$ nodes within the slab, as well as the two nodes at the surfaces outside the slab. The $n=15$ mode, for example, has nodal surfaces which lie between the atomic layers, and the atoms themselves are at antinodes, with like atoms in adjacent layers moving in opposite directions. The eight LO modes in this 15-layer slab which produce optical absorption peaks correspond to the four LO modes in a seven-layer slab with zero, two, four, and six nodes. (This is discussed in Section IX.)
 168. A. A. Lucas, *J. Chem. Phys.*, **48**, 3156 (1968).
 169. Lattice dynamical calculations show that these LO modes do, in fact, have nodes in the z displacement at the surfaces, provided that one chooses the position of the surfaces properly as discussed in footnote 167.
 170. F. Sauter, *Z. Phys.*, **203**, 488 (1967).
 171. F. Forstmann, *Z. Phys.*, **203**, 495 (1967).
 172. A. R. Melnyk and M. J. Harrison, *Phys. Rev. Lett.*, **21**, 85 (1968).
 173. A. R. Melnyk and M. J. Harrison, *Phys. Rev.*, **B**, **2**, 835; 851 (1970).
 174. K. Sturm, *Z. Phys.*, **209**, 329 (1968).
 - 174a. The assertion that the absorptance is large for $(\omega/\omega_p) > (\cos\theta)^{-1}$ is a consequence of our assumption of a semi-infinite medium. We are really saying that the reflectance here is small. For a finite thickness, this could mean small absorptance and large transmittance.
 175. If the bulk plasmon dispersion relation is given by $q^2 = f(\omega)$, the wave will propagate in the z direction if $q_z^2 > 0$ or $k^2 = f(\omega) - q_z^2 < f(\omega)$. Since k^2 is very small on the scale of the bulk plasmon dispersion relation, we have $f(\omega) \gtrsim 0$ or $\omega \gtrsim \omega_p$.

176. R. Ruppin, private communication.
177. S. I. Pekar, *Sov. Phys. JETP*, **6**, 785 (1958).
178. J. J. Hopfield and D. G. Thomas, *Phys. Rev.*, **132**, 563 (1963).
179. V. M. Agranovich and V. L. Ginzburg, *Spatial Dispersion in Crystal Optics and the Theory of Excitons*, Wiley-Interscience, New York, 1966.
180. J. J. Sein, *Phys. Lett.*, **32A**, 141 (1970).
181. G. S. Agarwal, D. N. Pattanayak, and E. Wolf, *Phys. Rev. Lett.*, **27**, 1022 (1971).
182. J. L. Birman and J. J. Sein, *Phys. Rev.*, **B**, **6**, 2482 (1972).
183. R. Zeyher, J. L. Birman, and W. Brenig, *Phys. Rev.*, **B**, **6**, 4613 (1972).
184. A. A. Maradudin and D. L. Mills, *Phys. Rev.*, **B**, **7**, 2787 (1973).
185. W. Brenig, R. Zeyher, and J. L. Birman, *Phys. Rev.*, **B**, **6**, 4617 (1972).
186. Equation (VI.24) has been used in theories of optical properties of a metal with a diffusely scattering surface, for which the reflection of electrons from the surface can indeed be disregarded. However, it is correct only for normally incident or *s*-polarized light. It leads to incorrect results for *p*-polarized light because it violates the condition that the normal component of the current must be zero at the surface. See J. M. Keller, R. Fuchs, and K. L. Kliewer, to be published.
187. This statement is perhaps not entirely correct, because Hopfield and Thomas¹⁷⁸ have assumed that an inactive layer exists on the surface of the insulator, which takes into account the fact that excitons may be reflected not at the surface, but at some distance below the surface.
188. P. A. Fedders, *Phys. Rev.*, **153**, 438 (1967).
189. P. J. Feibelman, *Phys. Rev.*, **B**, **3**, 2974 (1971).
190. This statement does not imply that the macroscopic theory is necessarily valid near $q=0$; one cannot use it to find any modes, such as strongly localized surface modes, in which the atomic displacements vary rapidly on the scale of the interatomic distance.
191. W. Ludwig, *Springer Tracts in Modern Physics*, **43**, 206 (1967).
192. P. Masri and L. Dobrzynski, *Surf. Sci.*, **34**, 119 (1973).
193. Surface modes may exist in the bulk mode regions, however, if they are decoupled from the bulk modes by symmetry.
194. T. E. Feuchtwang, *Phys. Rev.*, **155**, 731 (1967).
195. R. Stonely, *Proc. Roy. Soc. (London)*, **A232**, 447 (1955).
196. D. C. Gazis and R. F. Wallis, *J. Math. Phys.*, **3**, 190 (1962).
197. D. C. Gazis and R. F. Wallis, *Surf. Sci.*, **3**, 19 (1964).
198. D. C. Gazis and R. F. Wallis, *Surf. Sci.*, **5**, 482 (1966).
199. B. Lengler and W. Ludwig, *Phys. Status Solidi*, **7**, 463 (1964).
200. R. F. Wallis, D. L. Mills, and A. A. Maradudin, in *Localized Excitations in Solids*, R. F. Wallis, Ed., Plenum Press, New York, 1968, p. 403.
201. S. Andersson and J. B. Pendry, *J. Phys. C*, **5**, L41 (1972).
202. C. W. Tucker, Jr., and C. B. Duke, *Surf. Sci.*, **29**, 237 (1972).
203. J. B. Theeten, L. Dobrzynski, and J. L. Domange, *Surf. Sci.*, **34**, 145 (1973).
204. G. A. Somorjai, *Surf. Sci.*, **34**, 156 (1973).
205. H. Kaplan, *Phys. Rev.*, **125**, 1271 (1962).
206. B. Lengler and W. Ludwig, in *Lattice Dynamics*, R. F. Wallis, Ed., *J. Phys. Chem. Solids*, Suppl. 1, 1965. (Pergamon Press).

207. L. Dobrzynski, *Surf. Sci.*, **20**, 99 (1970).
208. G. P. Alldredge, R. E. Allen, and F. W. deWette, *Phys. Rev.*, **B**, **4**, 1682 (1971).
209. R. E. Allen and F. W. deWette, *Phys. Rev.*, **179**, 873 (1969).
210. R. E. Allen, F. W. deWette, and A. Rahman, *Phys. Rev.*, **179**, 887 (1969).
211. R. E. Allen, G. P. Alldredge, and F. W. deWette, *Phys. Rev.*, **B**, **4**, 1648 (1971).
212. R. E. Allen, G. P. Alldredge, and F. W. deWette, *Phys. Rev.*, **B**, **4**, 1661 (1971).
213. G. P. Alldredge, R. E. Allen, and F. W. deWette, *J. Acoust. Soc. Am.*, **49**, 1453 (1971).
214. R. E. Allen and F. W. deWette, *Phys. Rev.*, **187**, 883 (1969).
215. L. Dobrzynski and P. Masri, *J. Phys. Chem. Solids*, **33**, 1603 (1972).
216. J. B. Theeten and L. Dobrzynski, *Phys. Rev.*, **B**, **5**, 1529 (1972).
217. See R. F. Wallis, B. C. Clark, and R. Herman, in *The Structure and Chemistry of Solid Surfaces*, G. A. Somorjai, Ed., Wiley, New York, 1968, p. 17-1.
218. The matrix on the right of (VIII.12) has rows and columns labeled by the pair of numbers (α), the atom position and component of interest.
219. B. C. Clark, D. C. Gazis, and R. F. Wallis, *Phys. Rev.*, **134**, A1486 (1964).
220. J. B. Theeten, J. L. Domange, J. Bonnerot, and J. P. Hurault, *Solid-State Commun.*, to be published.
221. J. M. Dickey and A. Paskin, *Phys. Rev. Lett.*, **21**, 1441 (1968).
222. J. M. Dickey and A. Paskin, *Phys. Rev.*, **B**, **1**, 851 (1970).
223. M. Strongin, O. F. Kammerer, J. E. Crow, R. D. Parks, D. H. Douglass, Jr., and M. A. Jensen, *Phys. Rev. Lett.*, **21**, 1320 (1968).
224. J. J. Burton, *J. Chem. Phys.*, **56**, 3133 (1972).
225. R. E. Allen and F. W. deWette, *J. Chem. Phys.*, **51**, 4820 (1969).
226. F. W. deWette and G. E. Schacher, *Phys. Rev.*, **137**, 78 (1965).
227. S. Y. Tong and A. A. Maradudin, *Phys. Rev.*, **181**, 1318 (1969).
- 227a. Surface relaxation for an ionic crystal involves inward motion of the surface ions; the opposite occurs for monatomic crystals and a Lennard-Jones potential. This is not surprising if one recognizes that the equilibrium separation between the ions in a diatomic ionic molecule is smaller than the nearest-neighbor distance in an infinite crystal of such molecules, while an isolated pair of identical atoms interacting via a Lennard-Jones potential has a larger separation than occurs in a crystal of such atoms. Thus, a relaxed ionic crystal surface is less soft than its unrelaxed counterpart and it follows that the highly-localized surface modes, e.g., the Lucas modes, move closer to the bulk bands from which they originate when relaxation is included.
228. It should be noted that in several places in the literature, figures analogous to Fig. 52 have appeared which imply incorrectly that the surface mode hybridizes with all of the bulk modes as it passes through the bulk band region. As pointed out in the text and shown in Fig. 52, the surface mode hybridizes with only the even-parity bulk modes, and crosses the odd-parity modes without interaction.
229. This effect, caused by the dispersion introduced by the discrete lattice, is also evident in Fig. 51. In the range $Q \gtrsim 0.1$, the two FK modes move appreciably below the asymptotic frequency $\omega = [\frac{1}{2}(\omega_{LO}^2 + \omega_{TO}^2)]^{1/2} = 4.499 \times 10^{13} \text{ sec}^{-1}$ predicted by the continuum theory when $\epsilon_{\infty} = 1$.
230. T. S. Chen, G. P. Alldredge, F. W. deWette, and R. E. Allen, *Phys. Rev. Lett.*, **26**, 1543 (1971).

231. T. S. Chen, R. E. Allen, G. P. Alldredge, and F. W. deWette, *Solid-State Commun.*, **8**, 1205 (1970).
232. T. S. Chen, R. E. Allen, G. P. Alldredge, and F. W. deWette, *Phys. Rev., B*, **6**, 627 (1972).
233. T. S. Chen, G. P. Alldredge, and F. W. deWette, *Solid-State Commun.*, **10**, 941 (1972).
234. V. V. Bryskin and Y. A. Firsov, *Sov. Phys. Solid State*, **14**, 981 (1972).
235. T. S. Chen, G. P. Alldredge, F. W. deWette, and R. E. Allen, *Phys. Rev., B*, **6**, 623 (1972).
236. V. V. Bryskin, Yu. M. Gerbshtein, and D. N. Mirlin, *Sov. Phys. Solid State*, **13**, 1342 (1971).
237. T. P. Martin, *Phys. Rev.*, **177**, 1349 (1969).
238. M. I. Abaev, V. N. Bogomolov, V. V. Bryskin, and N. A. Klushin, *Sov. Phys. Solid State*, **13**, 1323 (1971).
239. T. P. Martin, *Solid-State Commun.*, **9**, 623 (1971).
240. T. P. Martin, *Phys. Rev., B*, **1**, 3480 (1970).
241. J. T. Luxon, D. J. Montgomery, and R. Summitt, *Phys. Rev.*, **188**, 1345 (1969).
242. K. H. Rieder and E. M. Hörl, *Phys. Rev. Lett.*, **20**, 209 (1968).
243. L. Genzel and T. P. Martin, *Phys. Status Solidi (b)*, **51**, 101 (1972).
244. T. P. Martin, *Phys. Rev., B*, **7**, 3906 (1973).
245. T. S. Chen, G. P. Alldredge, and F. W. deWette, *Solid-State Commun.*, **10**, 941 (1972).
246. T. P. Martin, *Phys. Rev.*, **170**, 779 (1968).
247. G. A. Somorjai and H. H. Farrell, *Adv. Chem Phys.*, **20**, 215 (1971).
248. S. E. Trullinger and S. L. Cunningham, *Phys. Rev. Lett.*, **30**, 913 (1973).
249. S. L. Cunningham and A. A. Maradudin, *Phys. Rev., B*, **7**, 3870 (1973).
- 249a. This is a face-centered square lattice with nonprimitive basis vectors $2a_0\hat{i}$ and $2a_0\hat{j}$, where a_0 is the bulk nearest-neighbor separation and \hat{i} and \hat{j} are Cartesian unit vectors.
250. H. Ibach, *Phys. Rev. Lett.*, **27**, 253 (1971).
251. E. Evans and D. L. Mills, *Phys. Rev., B*, **5**, 4126 (1972).
252. L. Dobrzynski and A. A. Maradudin, *Phys. Rev., B*, **7**, 1203 (1973).
253. The degeneracy is a consequence of the Montroll-Potts model.
254. F. W. deWette and R. E. Allen, *Phys. Rev.*, **187**, 878 (1969).
255. G. C. Benson and T. A. Claxton, *J. Chem. Phys.*, **48**, 1356 (1968).
256. B. G. Dick and A. W. Overhauser, *Phys. Rev.*, **112**, 90 (1958).
257. B. G. Dick, *Phys. Rev.*, **145**, 609 (1966).
258. G. E. Laramore and A. C. Switendick, *Phys. Rev., B*, **7**, 3615 (1973).
259. E. G. McRae and C. W. Caldwell, Jr., *Surf. Sci.*, **2**, 509 (1964).
260. G. Benedik, *Phys. stat. sol. (b)*, **58**, 661 (1973).
261. A localized surface mode may lie within a region of bulk modes if the two types of modes belong to non-interacting classes. This can occur only if \mathbf{k} lies in a symmetry direction (see Sec. VIII. A.1).
262. A. Otto, Taormina Conference on Polaritons, (to be published).
263. R. E. Allen, *J. Vac. Sci. Technol.*, **9**, 934 (1972).
264. V. E. Kenner and R. E. Allen, *Phys. Letters*, **39A**, 245 (1972).

- 265. V. E. Kenner and R. E. Allen, *Phys. Rev. B*, **8**, 2916 (1973).
- 266. I. Ignatiev and T. N. Rhodin, *Phys. Rev. B*, **8**, 893 (1973).
- 267. S. E. Trullinger and S. L. Cunningham, *Phys. Rev. B*, **8**, 2622 (1973).
- 268. J. J. Burton, Faraday Trans., *J. Chem Soc.*, **69**, 540 (1973).
- 269. E. T. Arakawa, M. W. Williams, R. N. Hamm, and R. H. Ritchie, *Phys. Rev. Letters* **31**, 1127 (1973).
- 270. R. W. Alexander, G. S. Kovener, and R. J. Bell, *Phys. Rev. Letters* **32**, 154 (1974).
- 271. When ω and k are both complex and k/ω is real, the exciting surface wave vector in an ATR experiment, or the modified ATR arrangement used by Arakawa, et al., is $k = \omega n_p \sin \alpha$ or $(k/\omega) = n_p \sin \alpha = \text{real}$. This provides additional justification for calling such modes "constant-angle" modes. See also footnote 102a.
- 272. See, for example, H. Ehrenreich and H. R. Phillip, *Phys. Rev.* **128**, 1622 (1962), or P. B. Johnson and R. W. Christy, *Phys. Rev. B*, **6**, 4370 (1972).
- 273. R. Rupp, *Phys. Rev. Letters* **31**, 1434 (1973).
- 274. R. Vincent and J. Silcox, *Phys. Rev. Letters* **31**, 1487 (1973).
- 275. The mode of interest is the OTH mode of reference 97.
- 276. J. A. Appelbaum and D. R. Hamann, *Phys. Rev. Letters* **32**, 225 (1974).
- 277. G. Borstel, *Phys. stat. sol. (b)* **60**, 427 (1973).
- 278. R. Srinivasan and G. Lakshmi, *J. Phys. Chem. Solids*, **34**, 2149 (1973).
- 279. R. Fuchs, *Phys. Lett.*, to be published.
- 280. A. P. van Gelder, J. Holvast, J. H. M. Stoelinga, and P. Wyder, *J. Phys. C*, **5**, 2757 (1972).

SOME COMMENTS ON THE ELECTRONIC PROPERTIES OF LIQUID METAL SURFACES

**STUART A. RICE, DANIEL GUIDOTTI, AND
HOWARD L. LEMBERG**

*The Departments of Chemistry and Physics and The James
Franck Institute The University of Chicago, Chicago, Illinois*

and

WILLIAM C. MURPHY AND AARON N. BLOCH

*The Department of Chemistry Johns Hopkins University
Baltimore, Maryland*

CONTENTS

I.	Introduction	544
II.	Inferences Concerning Some Structural Properties of Liquid Metal Surfaces	545
	A. General Remarks	545
	B. Why Liquid Metals?	546
	C. The Transition Zone in Liquid Insulators	547
	D. The Transition Zone in Liquid Metals	549
III.	Simple Reflection Spectroscopy as a Tool for the Study of Liquid Metal Surfaces	554
	A. General Remarks	554
	B. Formal Development	556
	C. A Model of the Surface and Its Properties	562
	D. Application of the Surface Zone Model	570
	E. Inferences Concerning the Structure of the Liquid Metal Surface	576
IV.	Surface Plasmon Dispersion: A Probe of the Structure of a Liquid Metal Surface	577
	A. General Considerations	577
	B. Surface Plasmons—An Overview	578
	C. The Nonradiative Surface Plasmon Basic Theory	580
	D. Coupling to NRSP	586
	1. Excitation via Surface Roughness	586
	2. Evanescent Waves and the Method of Frustrated Total Reflection (FTR)	590
	E. Some Simple Models	594
	1. Intrinsic Damping of the Electron Gas—The Sharp-Surface Case	594

2. Resonance Effects on the NRSP Dispersion596
3. Effects of an Inhomogeneous Surface597
F. The NRSP at an Epstein-Stratified Mercury Surface610
V. Conclusions and Speculative Remarks618
Appendix624
References630

I. INTRODUCTION

Within the last few years there has been a dramatic increase in the study of the electronic properties of metallic surfaces. Although available theoretical models and methods, as well as experimental techniques, are primitive relative to those used to study the bulk electronic structure, enough has been learned to outline the problems that must be solved before a satisfactory description of surfaces can be achieved. Typical of these problems are the following:

1. What is the nature and extent of surface reconstruction?
2. What is the nature of the electronic structure at and near the surface, for example, does the metal undergo an extended state-localized state transition?
3. What is the nature of collective electron excitations at and near the surface, and how do they depend on the surface reconstruction?
4. Do solutes which introduce scattering resonances, or deep-lying narrow bands, have any special influence on the electronic properties of a surface?
5. What is the nature of the interaction of adsorbates with a metallic surface? How is the density of states influenced by adsorption?

It is the purpose of this review to examine several of these problems for the particular case of liquid metals. It must be acknowledged at the outset that almost nothing definitive is known about the electronic structure of liquid metal surfaces. Despite this, we shall argue that a variety of arguments, augmented by common sense, suggest these materials to be ripe for further study at this time.

The following text is organized around attempts to discuss, for liquid metals, items 1 and 3 above, although considerations related to 2 and 4, and to a lesser extent 5, also creep into the discussion. Thus we rephrase 1, 2, and 3 for the case of liquid metals to read:

- 1'. How does the ion-core distribution near a (liquid metal) surface differ from that in the bulk?
- 2'. How is the distribution of electron density near the surface related to the ion-core distribution?
- 3'. Is the dispersion relation for surface plasmons measurably influenced by the forms of the ion-core and electron density distributions?

It will be seen that the interpretation we offer is often speculative. Hopefully, our work will stimulate others to improve the theory and the experimental information available, so as to more firmly ground our understanding of liquid metal surfaces.

This review is organized as follows. In Section II we examine arguments which suggest that the ion-core density near a liquid metal surface differs considerably from that in the bulk over a range of a few interionic separations. It is suggested that the electron density is also inhomogeneous on a similar length scale near the surface. We then examine, in Section III, the interaction of electromagnetic radiation with an inhomogeneous conductor and discuss how reflectivity measurements can be used to probe the gross properties of the surface zone. It is shown that reflectivity measurements have some, but only limited, sensitivity to the form of the surface conductivity profile, so better probes must be sought. Section IV is, then, devoted to an examination of the possibility that the surface plasmon dispersion relation can be used to probe the electronic structure of the surface. It is shown that the surface plasmon dispersion relation is modestly sensitive to the nature of the surface, and that the difference between dispersion relations corresponding to different surface structures is measurably large. It is also shown that the information obtainable from the study of surface plasmons only probes gross features of the electronic structure of the surface, so better methods must still be sought. Finally, in Section V we summarize our analysis and point to obvious extensions and connections with other approaches.

It should be obvious that this review is not intended to be comprehensive. We are confident that other authors will, by focusing attention on topics of interest to them, cover the gaps in the treatment of this paper.

II. INFERENCES CONCERNING SOME STRUCTURAL PROPERTIES OF LIQUID METAL SURFACES

A. General Remarks

In a simple metal most of the bulk cohesive energy is, essentially, the density-dependent, but structure-independent, delocalization energy of the electron gas. Relative to this the contributions determining the crystal structure of the metal are small, and with adequate pseudopotentials can usually be treated by perturbation theory.¹ Hence, although the atomic volumes of the allotropes of a given metal are nearly independent of structure,² metallic structures themselves are sensitive to small variations in screening and to chemical trends in the weak pseudopotential.¹ They are likewise susceptible to distortions and phase transitions with alloying or with temperature and pressure.

We have stressed these familiar observations as a basis for inquiring whether analogous statements can be made about a metal surface. In part, such an analogy has already been implicitly drawn. Schmit and Lucas³ have proposed recently that most of the excess energy of a metal surface is in effect the density-dependent, but structure independent, surface energy of a semiinfinite electron gas. Similar suggestions had been made before,⁴⁻⁶ but Schmit and Lucas appear to be the first to have elucidated the central importance of the collective modes. Specifically, they found that about 90% of the surface energy of the most simple metals can be assigned to the shift in zero-point energy of the plasma oscillations which accompanies the cleavage of an infinite crystal and separation of the surfaces formed to infinity. The decrease in the frequency ω_p of a longitudinal plasma mode to the surface plasmon frequency $\omega_s = \omega_p / \sqrt{2}$ is more than offset by the increase in the frequency of a *p*-polarized transverse mode* from zero to ω_s , leading to a positive net surface energy.

It follows from the results of Schmit and Lucas that the stability of a metal surface depends but weakly on structure. In light of these observations we are encouraged to draw a further inference from the energetics of bulk metals: If the structure of a metal is sensitive to comparatively mild perturbations in the ionic pseudopotential in the bulk should it not also be affected by the severe alteration of local electronic properties which must occur in the vicinity of a surface? It was such reasoning which led two of us to suggest that it is appropriate to regard the surfaces of certain metals not as geometrically sharp boundaries between bulk and vapor, but as finite, inhomogeneous transition zones whose ionic and electronic structures may be quite distinct from those of the bulk. We found, for example, that the anomalous optical properties of liquid mercury could be understood in terms of a structured interface whose conductivity parallel to the nominal surface plane substantially exceeds that of the bulk. In later sections of this article we review these optical results and explore the prospects for more definitive experimental testing of the hypothesized surface structure. The present section is intended to place that discussion in the context of a small but growing body of independent evidence for an anomalous surface zone in certain liquid metals.

B. Why Liquid Metals?

Qualitatively, the considerations outlined above should, in principle, be general for the surfaces of all simple metals. In practice, however, the

*The contribution of the transverse collective modes appears to have been overlooked in the work of Lang and Kohn,⁷ who therefore find a negative surface energy for a high-density electron gas with a "jellium" positive background, and must invoke a large lattice contribution to account for the surface energy of polyvalent metals.

optimum conditions for their study are met when the metal is a liquid. Experimentally, it is relatively easy to generate fresh surfaces which are automatically flat and defect-free, and the surface tension and its thermodynamic derivatives are readily measured. From a theoretical point of view, the nearly spherical Fermi surfaces and the absence of Umklapp processes provide important simplifications relative to the electronic structures of most crystalline metals. Most important, we expect intuitively that in a liquid, the relative freedom of motion of the ions will facilitate the formation of the sort of inhomogeneous transition zone we seek.

Certainly this is true in the vicinity of the critical point, where the width of the transition zone becomes macroscopically large. For simple dielectric fluids, this region has been studied optically by Huang and Webb⁹; they find a continuous, monotonic decrease in density from bulk liquid to vapor, in agreement with theoretical predictions.^{10,11} For conducting fluids, the corresponding electronic properties of the critical interfacial zone are of considerable intrinsic interest. In our view, however, such a topic belongs more properly to a discussion of the metal-to-insulator transition in dense metal vapors^{12,13} than to a study of liquid metal surfaces, and we consider it beyond the scope of this article.

Rather, we are concerned here with the character of the liquid surface far from the critical region, where the singlet density profile varies rapidly over a mean interatomic distance. Under these conditions, the assumptions underlying the continuum theory^{10,11} appropriate to the critical region no longer obtain, and two questions immediately arise. First, is it physically meaningful to speak of a transition zone at all, or is the zone so narrow that it can be described adequately by the traditional expedient¹⁴⁻¹⁶ of shrinking its width to zero? Second, if an inhomogeneous surface zone of nonzero width does exist, is its density necessarily a monotonic function of the depth, as in the critical regime,⁹⁻¹¹ or can there exist a distinct interfacial structure, as suggested by Bloch and Rice?⁸

C. The Transition Zone in Liquid Insulators

Experimental studies of dielectric fluids are again an instructive starting point from which to approach the first question. In a long series of ellipsometric investigations dating back to Lord Rayleigh,¹⁷ the thickness of the optical surface profile for a number of transparent liquids has been measured directly.¹⁸⁻²⁰ Although the ellipsometric method is notoriously sensitive to surface contamination, it has become clear with the gradual improvement of experimental technique that, for the liquids studied, the width of the surface zone is not negligible. In water at room temperature, for example, a minimum thickness of one molecular layer seems well established.²⁰

Despite these findings, it has remained common for theoretical investigations of liquid surfaces to treat the density profile as a step function.¹⁴⁻¹⁶ Much of the impetus for such work was generated by the early success of Fowler,¹⁴ who calculated the surface tension with reasonable accuracy under the assumptions that the singlet density profile $\rho(z)$ remains constant, and the radial distribution function $g(r)$ homogeneous and spherically symmetric, up to a sharp discontinuity at the Gibbs dividing surface. Exploiting the mechanical approach due to Lord Rayleigh,²¹ Fowler obtained for the surface tension γ , the famous formula,

$$\gamma = \frac{\pi}{8} \rho^2 \int_0^\infty u_2'(r) g(r) r^4 dr \quad (\text{II.1})$$

where $u_2(r)$ is the intermolecular pair potential. If the dividing surface is so chosen that the excess superficial density of matter Γ_S is zero, the corresponding expression for the excess surface energy U_S is

$$U_S = -\frac{\pi}{2} \rho^2 \int_0^\infty u_2(r) g(r) r^3 dr \quad (\text{II.2})$$

Equations (II.1) and (II.2) also represent the limit, as the width of the transition zone is decreased to zero, of the results of the more general statistical mechanical theory of Kirkwood and Buff.²² The expressions have been evaluated for a variety of simple liquids, with $u_2(r)$ and $g(r)$ deduced from experimental properties of the bulk.^{15,16,22} Considering the experimental and theoretical uncertainties inherent in this procedure, and the difficulty²³ in obtaining reliable measurements of γ and U_S , the agreement between observed and calculated values is generally deemed fairly good.

Closer inspection, however, reveals that the discrepancies between theory and experiment are not random: for simple dielectric liquids the Fowler expressions systematically underestimate U_S and overestimate γ .¹⁵ If we take the existence of a transition zone seriously, such results are not difficult to understand. Relative to the dividing surface defined by (II.2), the surface tension is just the excess Helmholtz free energy per unit area,

$$\gamma = U_S - TS_S \quad (\text{II.3})$$

where S_S is the excess entropy per unit area. Intuitively, one expects that if the real surface density profile is monotonic and of nonzero width, it will represent a state of higher internal energy, but also of higher entropy, than the corresponding step-function interface. In (II.3), the two effects will tend to cancel, so that the agreement between (II.1) and experiment may

be deceptively good, but in the end the free energy of the real system must be lower than that of the step-function model. All this is precisely what is observed.¹⁵ Further, the agreement between theory and experiment deteriorates as the temperature is raised,¹⁵ as expected for a transition zone whose width increases with temperature.

This interpretation is reinforced by the work of Buff, Lovett, and Stillinger,²⁴ who have made the distinction between sharp and extended surfaces explicit and quantitative in the neighborhood of the critical point. Here the diffuseness of the surface is due almost entirely to thermal agitation, so that departures from a step-function ground state can be decomposed into a sum of capillary wave excitations. From the known dependence of the ripplon frequencies on surface tension, the drop in γ below the Fowler value can be calculated, and the width of the corresponding surface zone determined. The final results agree closely with experiment.⁹ Although the model cannot be transposed to the region far from the critical point, where thermal effects need not dominate the surface profile, it does serve as a direct demonstration of the trends one expects when a diffuse surface is represented by a step-function model.

These trends are absent in the results of calculations which explicitly include the transition zone,²⁵⁻²⁸ whether by varying its width so as to minimize the free energy,²⁵⁻²⁷ or by determining its width a priori using the Yvon-Born-Green equation.²⁸ With a careful choice of $g(r)$, theory and experiment agree for liquid argon to better than 1%,^{27,28c} with a transition zone width of a few atomic layers.^{27,28c}

It is worth remarking that the thermodynamic reasoning outlined above does not depend on the physical model chosen for the bulk liquid or the physical origin of the density transition. Hence, sharp-surface calculations based on the so-called cellular methods^{29,30}—in which the liquid is treated essentially as a quasicrystalline solid and its configurational energy and entropy evaluated at the surface—exhibit the same trends, and about the same accuracy, as do the results of the Fowler formula. They are improved³¹ if γ is minimized by varying the occupation of the “cells” in the first surface layer, a crude but mathematically convenient representation of the transition zone. Likewise, in certain cases the predictions of the significant structure model theory of Eyring and co-workers³² become more accurate when the surface depth is increased to several molecular layers.^{32b}

D. The Transition Zone in Liquid Metals

The weight of experimental and theoretical evidence, then, teams with common sense to support the view that the surface of a simple dielectric liquid is characterized by a transition zone a few molecular diameters thick. We see no reason for these considerations to be obviated when the

liquid is a conductor. Indeed, there is good cause to suspect that in some liquid metals the effect may be greatly pronounced, to the point where the density profile exhibits an oscillatory structure having anomalous thermodynamic and electronic properties. We offer two arguments, closely interrelated.

First, whatever the behavior of its ionic density profile, the surface zone in a metal represents the termination of a semiinfinite electron gas. It is well known^{7,33-36} that reflection of conduction electrons from such a region gives rise to quantum interference effects. For example, if the electrons are otherwise free and the potential barrier at the surface is sharp and infinite, the Friedel oscillations of the electron density $n(z)$ take the form

$$n(z) = n_0 \left\{ 1 + \frac{3 \cos(2k_f z)}{4k_f^2 z^2} - \frac{3 \sin(2k_f z)}{8k_f^3 z^3} \right\} \quad (\text{II.4})$$

where z is the coordinate perpendicular to the surface, k_f is the Fermi wave number, and n_0 is the average electron density in the bulk. This behavior is by no means peculiar to the infinite-barrier model. Equation (II.4) closely resembles³⁷ the results of a self-consistent calculation⁷ for an electron gas with a positive "jellium" background terminating in a step function at the surface; and the oscillations are known to persist even when the ions are included explicitly.^{7,38} In any event, the precise form of the equation is not at issue here: The point is that surface-induced oscillations in the charge density exist, that the first and largest maximum occurs at approximately one-half a Fermi wavelength from the nominal surface plane, and that it is not unreasonable to suppose that these charge oscillations can play a role in a self-consistent readjustment of the positions of the ions in the vicinity of the surface.

Our second argument is based on the fact that the effective pair potential $u_2(r)$ is fundamentally different for a liquid metal than for a liquid dielectric.^{1,16,39} In contrast with the weak Lennard-Jones potential which adequately represents the pair interaction in liquid argon,^{27,28} $u_2(r)$ for a liquid metal derives from the screening of the strong interionic Coulomb repulsion by the conduction electrons. To second order in the screened ionic pseudopotential, the self-consistent result is*¹

*The potential (II.5) bears only a qualitative resemblance to the pair potentials deduced by March and co-workers¹⁶ from experimental radial distribution functions, using Born-Green theory. Their results were used to calculate surface tensions from the Fowler formula, with only modest success. It is not clear to what extent this work has suffered from the inadequacies of the Fowler formula itself, of the Kirkwood superposition approximation introduced for the triplet correlation function, or of the experimental values for $g(r)$ and $u_2(r)$. In any case Harrison³⁹ has observed that the March potentials do not exhibit the Friedel oscillations of a true interaction potential in a metal; rather, the wavelength of the oscillations is independent of valence, as expected for the simple stacking of noninteracting hard spheres.

$$u_2(r) = \frac{Z^2 e^2}{r} + \frac{\Omega^2}{8\pi^3 e^2} \frac{1}{r} \int_0^\infty [v(q)]^2 \epsilon(q) [\epsilon(q) - 1] \sin(qr) q^3 dq \quad (\text{II.5})$$

where Z is the ionic charge, Ω is the atomic volume, $v(q)$ is the screened pseudopotential form factor,¹ and $\epsilon(q)$ is the wave-number-dependent static dielectric constant of the electron gas. Strictly, (II.5) should be modified to account for exchange, correlation, and nonlocality in the screening.^{40,41} For our purposes, however, (II.5) is sufficient⁴¹ to illustrate the salient behavior of $u_2(r)$. At large r , its asymptotic form is oscillatory¹:

$$u_2(r) \xrightarrow{r \rightarrow \infty} \frac{18\pi Z^2 e^2}{k_f^2} [v(2k_f)]^2 \frac{\cos 2k_f r}{8k_f^3 r^3} \quad (\text{II.6})$$

where the Friedel oscillations enter (II.5) through the well-known singularity in $\epsilon(q)$ due to the Fermi cutoff at $q=2k_f$. At smaller r , this effect, together with the form¹ of $v(q)$ leads to enhanced oscillations and a deep minimum in the vicinity of the nearest-neighbor distance.^{1,41}

The unique form of $u_2(r)$ in a liquid metal assumes particular significance in light of the recent work of Croxton and Ferrier,²⁸ who have carried out the first detailed theoretical study of the structure of a liquid vapor interface near the triple point. Their analysis is grounded in a modified form of the Yvon-Born-Green equation for the singlet particle density:

$$\nabla_1 \rho(r_1) = - \frac{\rho_0^2}{k_B T} \int_2 \nabla_1 \{ u_2(\mathbf{r}_{12}) u_2^{0*}(z_2) \} g(\mathbf{r}_{12}) d^3 r_2 \quad (\text{II.7})$$

Here $u_2^{0*}(z)$ is a phenomenologically chosen operator which, as the surface zone is traversed, gradually changes $u_2(r_{12})$ from its functional form in the bulk liquid to that in the vapor. Solving the equation numerically, Croxton and Ferrier^{28a} find that for a simple liquid sufficiently close to its triple point, the density profile is not monotonic but exhibits stable oscillations suggestive of atomic layering at the interface. These can be traced^{28a} largely to the effect on (II.7) of the oscillations in the product $g(r_{12})u_2(r_{12})$. In a Lennard-Jones fluid with parameters appropriate to liquid argon, these oscillations are relatively weak: The effect persists only over about two atomic diameters in the immediate vicinity of the triple point. Nevertheless the structure is confirmed by molecular-dynamics calcula-

tions,^{28d} and brings the calculated surface tension into excellent agreement with experiment.*

For a fluid in which the first minimum in $u_2(r)$ is deep and narrow, the tendency toward a layered interface becomes much stronger, and Croxton and Ferrier surmise that this is the case for liquid metals.^{28a,c} Their arguments take no account of the long-range oscillatory nature of $u_2(r)$, but we nevertheless believe them to be qualitatively correct. Indeed, insofar as the oscillations in $u_2(r)$ and $g(r)$ tend to coincide,^{1,41} they will reinforce each other in (II.7) to enhance the tendency toward a structured interface. We speculate, then, that in certain cases the effect may persist to greater depths, and to higher temperature, than Croxton and Ferrier suggest. Further, in polyvalent liquid metals such as Sn and Hg, whose liquid structure factors are notoriously sensitive¹ to the details of the screening and hence the electron density distribution, there is reason to suspect that such effects can initiate a major structural rearrangement in the vicinity of the surface—a liquid-state analogue of surface reconstruction.⁸

Given such possibilities, it is tempting to undertake a full calculation of the interfacial structure of a liquid metal. The surface Friedel oscillations and the Croxton-Ferrier effect are not, of course, independent of one another. We have separated them here for pedagogical convenience, but a good calculation should include both together in a self-consistent way. Unfortunately, the method of Croxton and Ferrier itself seems poorly suited to such a task, largely because of the inordinate complexity of $u_2^{0*}(r_{12})$ and $u_2(r_{12})$ when they are modified to take into account the complicated dielectric screening in the vicinity of the surface.³⁷ It seems preferable to attempt an approach which includes both electrons and ions

*It is true that no such structure is found in the calculations of Hill,²⁵ Plesner and Platz,²⁶ or Toxvaerd²⁷ on the surface profile of liquid argon. The first two papers have been criticized by Croxton and Ferrier²⁸ on double grounds. First, any density oscillations are explicitly suppressed at the beginning by arbitrarily setting $g(r)$ equal to a constant for distances greater than an atomic diameter. Second, both calculations adopt the mathematical artifact of subdividing the surface zone into homogeneous films of infinitesimal width. This device is justified for computation of, say, the optical response,⁸ but its use in a thermodynamic calculation requires the further assumption that the films are in equilibrium with one another.²⁵⁻²⁷ For films whose thickness is a tiny fraction of an interatomic distance, such an assumption must be applied with care.²⁸ The work of Toxvaerd²⁷ is also subject to this second criticism, although not to the first. Toxvaerd's method involves assuming a form for the density profile, and then parametrizing it so as to minimize the surface energy. Arbitrarily, Toxvaerd chose a monatomic form; whether he would have been equally successful with the form obtained by Croxton and Ferrier²⁸ is not clear. Note added in proof: Dr. J. Barker, IBM Laboratories, San Jose, has carried out Monte Carlo simulations of a three dimensional liquid Ar surface in equilibrium between liquid and vapor. He finds surface structure consisting of 8-9 density oscillations, so the structure extends into the liquid phase $\sim 25-30$ Å. [Private communication and *J. Chem. Phys.* **60**, 1976 (1974).]

from the beginning, with the electronic wave functions attenuated above the surface and matched to the bulk wave functions in the interior, and which self-consistently computes the surface potential and electron density profile. Such a calculation was recently accomplished by Appelbaum and Hamann³⁸ for the (100) face of crystalline sodium. They find that the first Friedel maximum in the electron density and the first maximum due to the electron-ion interaction linearly reinforce one another, producing a substantial electron density oscillation in the neighborhood of the surface. Since the ions are taken as fixed at their bulk positions, the Croxton-Ferrier effect is precluded. As Appelbaum and Hamann³⁸ point out, however, there is in principle no reason why the calculation cannot be extended to allow the ion positions and charge density oscillations to adjust self-consistently to one another. For liquid metals this seems a promising, if laborious, avenue.

The accumulation of experimental information has been as slow as the development of the theory. Nevertheless, there have emerged some isolated but striking thermodynamic results which, if correct, strongly corroborate the point of view outlined here.

We have remarked that we do not expect the surface energy of a liquid metal³ to be strongly structure-dependent. The same is not true, however, of the surface entropy. In fact, since the layered interface proposed by Croxton and Ferrier represents in effect a structure more ordered than the bulk, the excess surface entropy for such a system would be negative.²⁸ According to (II.3), this would be manifested as a positive temperature coefficient of the surface tension.

Croxton and Ferrier²⁸ have observed that such an effect cannot persist over an indefinite temperature range. As the critical point is approached and the surface zone becomes extended, the structure is necessarily "washed out" and the familiar monotonic profile⁹⁻¹¹ is recovered. The surface tension must therefore pass through a maximum and, of course, approach zero at the critical point.

The large body of experimental data on the surface tensions of liquid metals has been thoroughly reviewed^{42,43} and is not recapitulated here. Instead, we concentrate on the few cases in which the "inversion"²⁸ of the temperature dependence of γ discussed above has been observed. It should be recalled however, that the effects expected for a structured interface—a somewhat reduced surface tension, together with an "inversion"—are also the effects expected for a liquid contaminated with a surface-active impurity.⁴³ Such data must therefore be interpreted with caution.

Even with this in mind, there remain one and possibly two sets of data which remain difficult to gainsay. The first is the careful work of White⁴⁴ on on 99.9999% pure zinc. What distinguishes this study is White's recognition of the necessity of performing the measurement of an equilibrium

property under equilibrium conditions. When he took care to ensure that the liquid and its saturated vapor had reached equilibrium—that is, that there was no net flux of vapor across the interface—White measured a comparatively low surface tension with a large positive temperature coefficient. When he deliberately allowed progressive degrees of continuous vaporization, the surface tension at the melting point rose toward its conventional value⁴³ and the temperature range over which the coefficient remained positive decreased, until the usual negative value⁴³ was regained. These results have a double significance. First, they corroborate the predictions of Croxton and Ferrier^{28c} in complete detail. Second, they cast serious doubt on surface tension measurements in which the need for equilibrium conditions is ignored—in other words, on the great majority of the measurements which have been reported.

The second set of data is the early work of Sauerwald and co-workers^{45,46} on molten copper. The low surface tension and positive temperature coefficient they report have been reproduced by some workers^{42,43} and contradicted by others⁴³; in no case is it clear how closely equilibrium conditions were approached. The Sauerwald experiments, however, also included molten silver and gold, for which “normal” negative coefficients were found. When copper was alloyed with increasing concentrations of either silver or gold, the temperature range of the positive coefficient gradually decreased in a manner quite analogous with the results of White’s experiments on zinc.

Positive temperature coefficients have from time to time also been reported, though less convincingly, for cadmium and mercury.⁴² Clearly, further work is in order, and confirmation in other types of experiments must be sought as well. Such experiments are the subject of the succeeding sections of this paper.

III. SIMPLE REFLECTION SPECTROSCOPY AS A TOOL FOR THE STUDY OF LIQUID METAL SURFACES

A. General Remarks

By simple reflection spectroscopy we mean both the study of the intensity of reflection of unpolarized radiation as a function of wavelength (and possibly angle of incidence) and ellipsometry. Other methods, such as surface plasmon excitation via optical coupling, are discussed in Section IV. As is well known, the application of ellipsometry and amplitude reflection spectroscopy to the study of metals has a long history, and the results thus obtained have played a useful role in the evolution of our understanding of the properties of bulk metals. However, the purpose of this article is to examine our knowledge of the properties of liquid metal

surfaces. For this reason we do not remark on the special features of the optics of bulk metals, nor on the circumstances which led to the suggestion that reflection spectroscopy could be used to learn something of the gross features of the surface of a liquid metal. Rather, we focus attention exclusively on the following questions:

1. Under what conditions is it possible to obtain information about surface properties from reflection spectroscopy?
2. What is the nature of the information about surfaces that can be so obtained?

Is there any reason to expect the optical properties of a liquid metal to be sensitive to the structure of its surface? After all, under almost all experimental conditions the penetration depth for electromagnetic radiation is much larger than both the atomic spacing and the coherence length characteristic of any reasonable surface structure. In the limit that the ratio of the surface structure coherence length to the penetration depth is small should not the classical Fresnel relations completely describe the reflection spectrum? We argue below that the existence of an inhomogeneous region at the surface of a liquid metal *does* influence the reflection spectrum of the metal in a subtle fashion, and that the Fresnel relations cannot be used under all circumstances.

The following observations provide sufficient justification for suspecting that the nature of the surface of a liquid metal will have a measurable influence on its reflection spectrum.

1. It is well known, both from theory and experiment, that dielectric films on metal surfaces can grossly alter the reflectivity. To be effective such films must be of the order of magnitude of a wavelength in thickness.

2. Ellipsometric studies of many kinds are consistent in showing that even a monolayer of dielectric on a metal surface measurably influences the polarization relationship between incident and reflected light.

3. In the case of dielectrics, for which the penetration depth is sensibly infinitely large, it can be shown that the field of the reflected wave is equivalent to the field arising from an infinitesimally thin layer placed on the surface and having a dipole moment per unit area which is dependent on the properties of the bulk dielectric medium. Furthermore, should an inhomogeneous surface layer exist, the measured reflectivity will depend in a complicated way on the properties of both the equivalent surface dipole layer (representing the net field arising from the bulk dielectric) and the real surface dipole layer.

4. Experimental studies of reflection from dielectric materials show that there are small deviations from the Fresnel formulas.^{46a} For example, the component of the electric field of the reflected radiation that is parallel to the plane of incidence should vanish at the Brewster angle, and the

phase difference between it and the component of the electric field of the reflected radiation that is perpendicular to the plane of incidence should change discontinuously from π to zero. Experiment shows that the parallel component does not vanish (although it becomes very small) and that the phase change varies smoothly over an angular range $\pm 5'$ about the Brewster angle. Similarly, the Fresnel formulas predict that when the refractive indices of two dielectrics in contact are the same the interface reflectivity should vanish, but it does not. In both instances cited it has been argued that the only possible cause of the breakdown of the Fresnel relations is the existence of a surface layer with structure different from that of the bulk.^{46a}

Aside from item 1, each of the above suggests that a very thin inhomogeneous layer at the surface of a liquid, one very much less than a wavelength in thickness, can lead to measurable deviations from the optical properties predicted under the assumption that the liquid is homogeneous up to a mathematical plane at which its properties change discontinuously to those of the contiguous phase. Conversely, the measured optical properties of a liquid metal must contain some information, albeit deeply buried, about the properties of the liquid metal surface. It is this aspect of the subject which we now examine.

B. Formal Development

As is well known, an electromagnetic field only partially penetrates a conducting medium. In the special case of a homogeneous metal filling the half-space $z > 0$, that is one for which the structure and properties of the metal adjacent to the surface are identical with those deep in the bulk, the penetration depth is related to the frequency and optical constants by a formula of the form

$$\delta \propto \frac{c}{\omega [|\epsilon(\omega)|]^{1/2}} \quad (\text{III.1})$$

where $\epsilon(\omega)$ is the dielectric function of the metal. In the optical region it is ordinarily the case that $\delta \ll c/\omega$. But this implies that the derivatives of the field components inside the metal along the normal to the surface are large relative to the tangential derivatives. It is then further implied that the field inside the metal near the surface can be regarded as the field of a plane wave, whereupon the tangential components of \mathbf{E} and \mathbf{H} are related by ($\mu = 1$ for a nonmagnetic metal)

$$\mathbf{E}_t = \frac{1}{[\epsilon_b]^{1/2}} \mathbf{H}_t \times \mathbf{n} \quad (\text{III.2})$$

where \mathbf{n} is a unit vector along the inward normal to the surface and ϵ_b is the bulk dielectric function. Since \mathbf{E}_t and \mathbf{H}_t are continuous across the

surface, their values just outside the metal surface must be related in the same way. For the case of a metal that is isotropic, as is always true of a liquid of monatomic species, Ginzburg^{46b} has shown that the propagation of transverse waves is generally consistent with the linear relation

$$\mathbf{D}(\omega) = \epsilon(\omega)\mathbf{E}(\omega) \quad (\text{III.3})$$

That is, there is a local relationship between the electric field and the current density and the polarization inside the metal. Equation (III.3) is not necessarily valid, even in an isotropic medium, for the description of the propagation of longitudinal waves, but for the present we focus attention on transverse waves, for which (III.3) can be used.

Adopting (III.3) the surface impedance

$$Z = \frac{4\pi}{c[\epsilon_b]^{1/2}} \quad (\text{III.4})$$

where Z is complex

$$Z = Z_1 + iZ_2 \quad (\text{III.5})$$

completely characterizes the reflection of electromagnetic waves from the metallic surface. Indeed, the rate of absorption of energy by the metal is, from the Poynting vector averaged over one period,

$$\begin{aligned} \dot{Q} &= \frac{c}{4\pi} \int d\Sigma \operatorname{Re}(\mathbf{E}_t \times \mathbf{H}_t^*) = \frac{c[\epsilon_b]^{1/2} |E_t|^2 |\mathbf{n}|}{8\pi} \\ &= \frac{|E_t|^2}{2Z_1} \end{aligned} \quad (\text{III.6})$$

We thus find that when $\delta \ll c/\omega$ and $\mathbf{D} = \epsilon\mathbf{E}$, the reflectivity is expressible in terms involving only the values of the electric field and its space derivative on the surface.

The preceding refers to the case where the metal is homogeneous for all $z > 0$. Suppose the structure of the metal is different near the surface from what it is in the bulk and, correspondingly, that the surface impedance is different from (III.4). This situation arises, even in a homogeneous metal, under conditions such that the anomalous skin effect is important. In that case the diffuse reflection of electrons from the surface introduces an extra resistive component, so the surface behaves as if its conductivity is different from that of the bulk. When the metal is inhomogeneous near the surface we likewise expect the surface conductivity to differ from that of the bulk. Despite the existence of the inhomogeneity, if the distance an electron moves in one period of the field is small relative to δ , we can use (III.3) to connect \mathbf{D} and \mathbf{E} ; this condition is satisfied throughout the region of interest to us.

Following the analogy outlined,^{46a,c} we assume that the net effect of differences in structure between the surface and the bulk leads, in the presence of an incident electromagnetic field, to an excess surface current density \mathbf{j}_s which is related to an excess surface conductivity $\Delta\sigma_s$ and the tangential components of the electric field by

$$\mathbf{j}_s = \Delta\sigma_s(\omega)\mathbf{E}_t = \Delta\sigma_s(\omega)[\mathbf{E} - (\mathbf{n} \cdot \mathbf{E})\mathbf{n}] \quad (\text{III.7})$$

The presence of an excess surface current places restrictions on the tangential component of the magnetic field, since the difference $\mathbf{H}_t^{\text{metal}} - \mathbf{H}_t^{\text{vac}}$ is proportional to the total surface density, $\mathbf{J}_{S,\text{total}}$ of which \mathbf{j}_s is merely the part defined by $\Delta\sigma_s$. The condition referred to is

$$\mathbf{H}_t^{\text{metal}} - \mathbf{H}_t^{\text{vac}} = \frac{4\pi}{c} \mathbf{J}_{S,\text{total}} \quad (\text{III.8})$$

Further, the components of the magnetic field normal to the surface, and the components of the electric field tangent to the surface, are continuous

$$\mathbf{H}_n^{\text{metal}} = \mathbf{H}_n^{\text{vac}} \quad (\text{III.9a})$$

$$\mathbf{E}_t^{\text{metal}} = \mathbf{E}_t^{\text{vac}} \quad (\text{III.9b})$$

In contrast, the normal component of the displacement field changes discontinuously on passing the surface because the excess surface current \mathbf{J}_s leads, via the equation of continuity, to an excess surface charge density $\Delta\rho_s$ given by

$$\Delta\rho_s = \frac{i}{\omega} \nabla \cdot \mathbf{j}_s \quad (\text{III.10})$$

where we have taken the field time dependence to be $\exp(i\omega t)$. The change in \mathbf{D}_n is related to the total surface current density by

$$\mathbf{D}_n^{\text{vac}} - \mathbf{D}_n^{\text{metal}} = \frac{4\pi i}{\omega} \nabla \cdot \mathbf{J}_{S,\text{total}} \quad (\text{III.11})$$

Although \mathbf{j}_s alone does not determine the boundary conditions, we shall find that its introduction is conceptually useful. Equations (III.8), (III.9), and (III.11) are taken as the boundary conditions which define the interaction between the liquid metal and the incident radiation field.

The flux of energy through the surface of the metal is again obtained

from the Poynting vector which now leads to

$$\begin{aligned} \frac{c}{4\pi} \int d\Sigma [\mathbf{n} \cdot \mathbf{E}^{\text{vac}} \times \mathbf{H}^{\text{vac}}] &= \frac{1}{4\pi} \int dV \left[\mathbf{E}^{\text{vac}} \cdot \frac{\partial \mathbf{D}^{\text{vac}}}{\partial t} + \mathbf{H}^{\text{vac}} \cdot \frac{\partial \mathbf{B}^{\text{vac}}}{\partial t} \right] \\ &+ \int d\Sigma [\mathbf{j}_s \cdot \mathbf{E}^{\text{vac}}] \end{aligned} \quad (\text{III.12})$$

in terms of the excess surface current and the properties of the bulk metal. To obtain the right-hand side of (III.12) we have used Gauss's theorem. Following the introduction of (III.7) into (III.12), and averaging over one period of the field, the heat released per unit time as a result of dissipation in the metal is found to be

$$\dot{Q} = -\frac{\omega\epsilon_2}{8\pi} \int dV E^2 + \frac{1}{2} \text{Re} \Delta\sigma_s \int d\Sigma [E^2 - (\mathbf{n} \cdot \mathbf{E})^2] \quad (\text{III.13})$$

The first term on the right-hand side of (III.13) can be transformed into the form displayed in (III.6), but we do not wish to do so in the present case.

We can, without specifying $\Delta\sigma_s$, also determine the complex reflection coefficients. For radiation falling on the surface of a semiinfinite liquid metal with the features already described, the ratio of the amplitudes of the reflected to incident radiation are

1. when the electric vector is perpendicular to the plane of incidence,

$$r_s = \frac{\cos\varphi - [\epsilon_b(\omega) - \sin^2\varphi]^{1/2} - (4\pi/c)\Delta\sigma_s}{\cos\varphi + [\epsilon_b(\omega) - \sin^2\varphi]^{1/2} + (4\pi/c)\Delta\sigma_s} \quad (\text{III.14})$$

where φ is the angle of incidence (the angle between the direction of the incident radiation and the normal to the surface); and

2. when the electric vector lies in the plane of incidence the ratio of the projections of the incident and reflected radiation along the normal to the surface,

$$r_p = \frac{\cos\varphi \left[(\epsilon_b(\omega) - \sin^2\varphi)^{1/2} + (4\pi\Delta\sigma_s/c) + \sin^2\varphi / (\epsilon_b(\omega) - \sin^2\varphi)^{1/2} \right] - 1}{\cos\varphi \left[(\epsilon_b(\omega) - \sin^2\varphi)^{1/2} + (4\pi\Delta\sigma_s/c) + \sin^2\varphi / (\epsilon_b(\omega) - \sin^2\varphi)^{1/2} \right] + 1} \quad (\text{III.15})$$

Thus we see that the rate of energy absorption by the nonmagnetic metal is determined by excess surface losses ($\text{Re}\Delta\sigma_s$) and volume losses ($\text{Im}\epsilon = \epsilon_2$). We conclude from this, as well as from (III.14) and (III.15), that the optical properties of the inhomogeneous metal require the specification of the real and imaginary parts of the bulk dielectric function, $\epsilon_b \equiv \epsilon_1 + i\epsilon_2$, and of the excess surface conductivity. Only when $\Delta\sigma_s \equiv 0$, so that there is neither increment nor decrement in the conductivity of the surface relative to the bulk, are the optical properties determined fully by $\epsilon_b(\omega)$.

One further comment is in order: If it is assumed that $\Delta\sigma_s(\omega)$ does not become singular as $\omega \rightarrow 0$, and that $\Delta\sigma_s(\omega) \rightarrow 0$ as $\omega \rightarrow \infty$, then the Kramers-Kronig relations between $\text{Re}\Delta\sigma_s$ and $\text{Im}\Delta\sigma_s$ assume the form

$$\text{Re}\Delta\sigma_s(\omega) = \frac{2}{\pi} \mathcal{P} \int_0^\infty \frac{x \text{Im}\Delta\sigma_s(x)}{x^2 - \omega^2} dx \quad (\text{III.16a})$$

$$\text{Im}\Delta\sigma_s(\omega) = \frac{2\omega}{\pi} \mathcal{P} \int_0^\infty \frac{\text{Re}\Delta\sigma_s(x)}{x^2 - \omega^2} dx \quad (\text{III.16b})$$

Although the preceding arguments reveal the potential importance to the interpretation of optical studies of an inhomogeneous layer at the surface of the liquid metal, they do not yet connect observable phenomena with any measure of the structure of that layer. To do so we must make some assumption about the structure of the inhomogeneous zone. Very few studies of this type have been carried out. Landau and Lifschitz⁴⁷ consider the case of propagation of waves in an inhomogeneous medium in the limit that the dielectric function varies slowly on the scale of length determined by the wavelength of the incident radiation. This case is of no interest to us, since the only likely inhomogeneous surface zones have coherence lengths small relative to the wavelength of incident radiation in the energy range of interest. But when the dielectric function changes markedly on a microscopic scale are Maxwell's equations adequate to describe the interaction of matter and radiation? Although it is true that Maxwell's equations are used to describe this interaction under the most extreme form of variation, namely a step discontinuity in $\epsilon(\omega)$, the solution of the field equations is then replaced with a boundary condition and the solution is usually used only in a macroscopic sense and not to elucidate any features of the region where $\epsilon(\omega)$ changes rapidly. From the pragmatic point of view, it is known that the macroscopic interpretation of the ellipsometry of metals and films is successful even when the films are only one or two molecular layers; that the ellipsometry of pure dielectric liquid surfaces leads to the very sensible and internally consistent result that the

surface zone on a dielectric liquid maintained at a temperature and pressure point distant from the critical point, is of the order of one to three molecular diameters thick; that the optics of films much thinner than a wavelength and with linearly varying refractive index are accurately described by classical electrodynamics; and so forth. These observations embolden us to use macroscopic theory as an analytical tool to examine how the optical properties of a liquid metal depend on the specific (rather than generic) structure of the surface zone.

Let us consider, then, an isotropic, inhomogeneous, nonmagnetic conductor whose properties are constant in planes perpendicular to the z -axis. Let the surface zone be centered about the plane $z=0$. We assume that all macroscopic intensive properties of the system are scalar functions of the coordinate z only and define as positive the z direction in which the conductivity $\sigma(z, \omega)$ tends to its bulk value. Suppose an electromagnetic wave of frequency ω , linearly polarized at an angle θ to the plane $y=0$, propagates in that plane at an angle φ to the z -axis. We now make the key assumption, perhaps dubious, that Maxwell's equations will hold over regions as small as the effective width of our transition zone, or that if they do not, they remain approximations sufficiently good that their breakdown can be corrected for by suitable parametrization of our results. It is not at present possible to offer justification for this assumption other than its apparent success in ellipsometry and for the case of dielectric liquids, as discussed above, and the necessity to have some well-defined starting point for an analysis of the interaction of radiation with the inhomogeneous conductor described.

Under the conditions stated, if $\mathbf{E}(x, z, \omega, t)$ is the electric vector and $\mathbf{H}(x, z, \omega, t)$ is the magnetic vector of the electromagnetic wave, it is necessary that

$$\nabla \times \mathbf{E} = -\frac{1}{c} \frac{\partial \mathbf{H}}{\partial t} \quad (\text{III.17a})$$

$$\nabla \times \mathbf{H} = \frac{1}{c} \left[\frac{\partial \mathbf{E}}{\partial t} + 4\pi \mathbf{J}(x, z, \omega, t) \right] \quad (\text{III.17b})$$

where $\mathbf{J}(x, z, \omega, t)$ is the current density. Except under conditions when the anomalous skin effect is important it is also true that

$$\mathbf{J}(x, z, \omega, t) = \sigma(z, \omega) \mathbf{E}(x, z, \omega, t) \quad (\text{III.18})$$

We assume that the time dependences of \mathbf{E} and \mathbf{H} are given by

$$\mathbf{E}(x, z, \omega, t) = \mathbf{E}(x, z, \omega) \exp(i\omega t)$$

and

$$\mathbf{H}(x, z, \omega, t) = \mathbf{H}(x, z, \omega) \exp(i\omega t)$$

so that (III.17a) and (III.17b) become

$$\nabla \times \mathbf{E} = -\frac{i\omega}{c} \mathbf{H} \quad (\text{III.19a})$$

$$\nabla \times \mathbf{H} = \frac{i\omega}{c} \epsilon(z, \omega) \mathbf{E} \quad (\text{III.19b})$$

where the complex dielectric constant is given by

$$\epsilon(z, \omega) \equiv 1 - i \frac{4\pi\sigma(z, \omega)}{\omega} \quad (\text{III.20})$$

Following standard procedure, by taking the curl of (III.19a) and the divergence of (III.19b) we can eliminate \mathbf{H} and obtain

$$\nabla^2 \mathbf{E} + \nabla \left(\mathbf{E} \cdot \frac{\nabla \epsilon(z, \omega)}{\epsilon(z, \omega)} \right) = -\frac{\omega^2}{c^2} \epsilon(z, \omega) \mathbf{E} \quad (\text{III.21a})$$

Similarly, eliminating \mathbf{E} ,

$$\nabla^2 \mathbf{H} + \left(\frac{\nabla \epsilon(z, \omega)}{\epsilon(z, \omega)} \right) \times \nabla \times \mathbf{H} = -\frac{\omega^2}{c^2} \epsilon(z, \omega) \mathbf{H} \quad (\text{III.21b})$$

Equations (III.21) have plane-wave solutions only if the second term on the left-hand side of each is zero, that is only if $\epsilon(z, \omega) \rightarrow \epsilon(\omega)$, a constant in space. Where this is not so, the problem is complicated immeasurably—in fact, there are very few such cases for which the equations can be solved analytically at all.

C. A Model of the Surface and Its Properties

We can gain some idea of the consequences of retaining the z dependence of ϵ by considering a specific example. A wide variety of possible variations of $\epsilon(z)$ can be approximated by assigning to the conductivity the so-called Epstein profile, introduced by Epstein⁴⁸ in a study of the reflection of radio waves from the ionosphere, and by Eckart⁴⁹ in a treatment of

reflection of electrons from a potential barrier:

$$\sigma(w) = -\frac{w}{1-w} \left(\sigma_b + \frac{\sigma_s}{1-w} \right) \quad (\text{III.22})$$

$$w \equiv -\exp\left(\frac{2\pi z}{\Delta}\right)$$

As $z \rightarrow \infty$, we have $\sigma(w) \rightarrow \sigma_b$, the bulk value of the conductivity, while the "surface term" in σ_s vanishes. As we pass through $z=0$, the bulk term drops monotonically with z , while the surface term passes through an extremum. The profile is sketched in Fig. 1, which is due to Eckart.⁴⁹

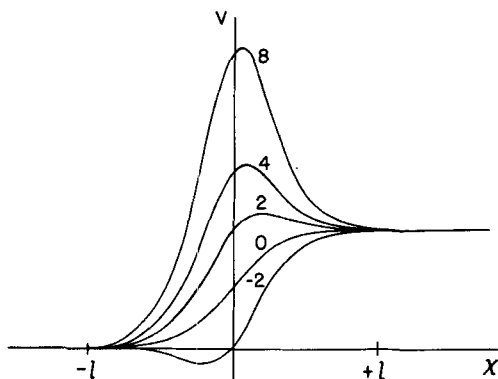


Fig. 1. The Epstein profile, after Eckart. In Eckart's paper the coordinate χ corresponds mathematically to our z , the parameter l to our Δ , and the quantity V to our $\sigma(\omega)$. The numbers labeling the curve are values of the ratio σ_s/σ_b .

A simple separation of variables suffices to show that (III.21) have the usual x dependence $\exp[-(i\omega x/c)\sin\varphi]$, so that (III.19) assumes the form

$$\frac{\partial E_y}{\partial z} = \frac{i\omega}{c} H_x$$

$$\frac{\partial H_x}{\partial z} = \frac{i\omega}{c} [\epsilon(z) - \sin^2\varphi] E_y \quad (\text{III.23a})$$

$$H_z = E_y \sin\varphi$$

$$\begin{aligned}\frac{\partial E_x}{\partial z} &= -\frac{i\omega}{c} \left(\frac{\epsilon(z) - \sin^2 \varphi}{\epsilon(z)} \right) H_y \\ \frac{\partial H_y}{\partial z} &= -\frac{i\omega}{c} \epsilon(z) E_x \\ E_z &= -\frac{\sin \varphi}{\epsilon(z)} H_y\end{aligned}\tag{III.23b}$$

As in the case of a homogeneous conductor, these two sets of equations are independent, and can be treated mathematically as characterizing separate waves. Equation (III.23a), of course, represents the transverse electric (TE) component, and (III.23b) the transverse magnetic (TM) component, in the terminology of Born and Wolf.⁵⁰ For the tangential components of the TE wave, (III.21) are

$$\begin{aligned}\frac{\partial^2 E_y}{\partial z^2} &= -\frac{\omega^2}{c^2} [\epsilon(z) - \sin^2 \varphi] E_y \\ \frac{\partial^2 H_x}{\partial z^2} - \frac{\partial \ln[\epsilon(z) - \sin^2 \varphi]}{\partial z} \frac{\partial H_x}{\partial z} &= -\frac{\omega^2}{c^2} [\epsilon(z) - \sin^2 \varphi] H_x\end{aligned}\tag{III.24a}$$

and for those of the TM wave

$$\begin{aligned}\frac{\partial}{\partial z} \left(\frac{\epsilon(z)}{\epsilon(z) - \sin^2 \varphi} \frac{\partial E_x}{\partial z} \right) &= -\frac{\omega^2}{c^2} \epsilon(z) E_x \\ \frac{\partial}{\partial z} \left(\frac{1}{\epsilon(z)} \frac{\partial H_y}{\partial z} \right) &= -\frac{\omega^2}{c^2} (\epsilon(z) - \sin^2 \varphi) H_y\end{aligned}\tag{III.24b}$$

At normal incidence ($\varphi=0$), the two sets of equations become identical, and can be solved in the case of the Epstein profile. The equation for E is then an example of Riemann's P equation, and will in general have 24 hypergeometric solutions, of which we can choose the appropriate ones by

demanding, as boundary conditions, convergence to plane-wave forms at infinity. The solution for H is then obtained directly from (III.23).

For oblique incidence, the TE system can, obviously, also be solved in this way. Instead of plane waves, we obtain for the electric vector in the inhomogeneous medium

$$E_y(x, z, \omega) = E_0 \exp\left[-\frac{i\omega x}{c} \sin \varphi\right] (1-w)^\beta \left(\frac{w}{w-1}\right)^\alpha F\left(U, V, W; \frac{1}{1-w}\right) \quad (\text{III.25a})$$

and for the magnetic vector:

$$\begin{aligned} H_x(x, z, \omega) = & [\epsilon_b - \sin^2 \varphi]^{1/2} E_0 \exp\left[-\frac{i\omega x}{c} \sin \varphi\right] (1-w)^\beta \left(\frac{w}{w-1}\right)^\alpha \\ & \times \left[\left(\frac{\alpha + \gamma}{w-1} - \frac{\alpha}{w(w-1)} \right) F\left(U, V, W; \frac{1}{1-w}\right) \right. \\ & \left. + \frac{U}{1-w} F\left(U+1, V, W; \frac{1}{1-w}\right) \right] \quad (\text{III.25b}) \end{aligned}$$

Here w is defined as in (III.22), ϵ_b is the bulk dielectric constant, $\epsilon_b = 1 - i(4\pi\sigma_b/\omega)$, F is the hypergeometric function, $U \equiv \alpha - \beta + \gamma$, $V \equiv \alpha - \beta + 1 - \gamma$, and $W \equiv 1 - 2\beta$ where

$$\begin{aligned} \alpha &\equiv -\frac{i\omega\Delta}{c} \sin \varphi \\ \beta &\equiv -\frac{i\omega\Delta}{c} [\epsilon_b - \sin^2 \varphi]^{1/2} \\ \gamma &\equiv \frac{1}{2} + \frac{[c^2 - i(16\pi\omega\sigma_s\Delta^2)]^{1/2}}{2c} \end{aligned} \quad (\text{III.26})$$

Our notation and choice of parameters differ slightly from those of Eckart.

After some labor along the lines he sketches, we obtain for the amplitude reflection coefficient r_s for light polarized perpendicular to the plane of incidence, the relation

$$r_s = \frac{\Gamma(1-\beta-\alpha-\gamma)\Gamma(-\beta-\alpha-\gamma)\Gamma(2\alpha)}{\Gamma(-\beta+\alpha+\gamma)\Gamma(1-\beta+\alpha+\gamma)\Gamma(-2\alpha)} \quad (\text{III.27})$$

As $\Delta \rightarrow 0$, this reduces to the usual expression

$$r_s \rightarrow \frac{-\beta+\alpha}{-\beta-\alpha} = \frac{\cos\varphi - [\epsilon_b - \sin^2\varphi]^{1/2}}{\cos\varphi + [\epsilon_b - \sin^2\varphi]^{1/2}} \quad (\text{III.28})$$

To obtain the amplitude reflection coefficient r_p for light polarized parallel to the plane of incidence, and hence the full set of optical properties, it is necessary to solve the set of equations for the TM component. However, examination of (III.23b) after change in variable from z to w reveals that both contain irregular singular points, and we are not able to solve them directly. Moreover, the analytic solutions for a TE wave lead to reflection coefficients which, as we have seen, are a product of gamma functions of complex arguments, not amenable to numerical evaluation. We can approximate the true solutions for both cases as closely as we like, however, by considering the inhomogeneous layer as a pile of homogeneous films of differential thickness, lying perpendicular to the z -axis. The conductivity in the j th thin film is given by the value of the Epstein profile (III.22) at $z = z_j$, the plane of the film's low- z surface. The solutions of Maxwell's equations within each film are plane waves, and are subject to the usual boundary conditions at the (ideal film surfaces. The advantage of such a stratified model over the continuous one is that not only can the results for both types of wave be easily calculated, but the model is more versatile: the dispersion law for the conductivity can be varied almost arbitrarily with z_j without raising any serious mathematical complications.

In standard treatments of stratified media it has become customary to introduce at this point the characteristic matrices of Abeles,⁵¹ and to use them to calculate the optical properties. We find it conceptually somewhat more direct to turn instead to a simple extension of the equivalent matrices of Herpin,⁵² from which those of Abeles may be derived.

We summarize this extension as follows. Let us consider a stack of L homogeneous thin films separating two semiinfinite, continuous, homogeneous media. Let one of these media be the vacuum, and the other our bulk liquid metal. We characterize the j th film, of thickness δ_j , by the

complex dielectric constant $\epsilon_j(\omega) = 1 - i(4\pi\sigma_j(\omega)/\omega) = n_j^2(\omega)$ where $n_j(\omega)$ is the complex index of refraction. From Snell's law, the complex angle of refraction φ_j is related to the angle of incidence φ on the first film by

$$\begin{aligned}\cos\varphi_j &\equiv (1 - \sin^2\varphi_j)^{1/2} \\ &= \left(1 - \frac{\epsilon_{j-1}}{\epsilon_j} \sin^2\varphi_{j-1}\right)^{1/2} \\ &= \left(1 - \frac{\epsilon_{j-2}}{\epsilon_{j-1}} \sin^2\varphi_{j-2}\right)^{1/2} = \dots = \left(1 - \frac{\sin^2\varphi}{\epsilon_j}\right)^{1/2}\end{aligned}\quad (\text{III.29})$$

Then the plane-wave solutions in the j th film can be written for the tangential components of the TE wave in the form

$$\begin{aligned}E_y &= a \exp(-ip_j z) + b \exp(ip_j z) \\ H_x &= -g_j a \exp(-ip_j z) + g_j b \exp(ip_j z)\end{aligned}\quad (\text{III.30a})$$

and of the TM wave in the form

$$\begin{aligned}E_x &= c \exp(-ip_j z) + d \exp(ip_j z) \\ H_y &= h_j c \exp(-ip_j z) - h_j d \exp(ip_j z)\end{aligned}\quad (\text{III.30b})$$

where $p_j = (\omega/c)[\epsilon_j - \sin^2\varphi]^{1/2}$, $g_j = [\epsilon_j - \sin^2\varphi]^{1/2}$ and $h_j = \epsilon_j[\epsilon_j - \sin^2\varphi]^{-1/2}$; the functions a , b , c , and d are all of the form

$$a(x, \omega, t) = a_0 \exp[i\omega(t - x \sin\varphi)] \quad (\text{III.30c})$$

Since the development from this point is of the same form for both cases, we treat only the TE wave in detail, and present the results for the TM wave at the end.

We consider first the sum and difference of the two equations (III.30a) and define

$$\begin{aligned}X &\equiv -g_j E_y + H_x = -zg_j a \exp(-ip_j z) \\ Y &\equiv -g_j E_y - H_x = -zg_j b \exp(ip_j z)\end{aligned}\quad (\text{III.31})$$

representing waves traveling in the positive and negative z directions,

respectively. Then the column matrix

$$(A) \equiv \begin{pmatrix} E_y \\ H_x \end{pmatrix} \quad (\text{III.32})$$

is related to the column matrix

$$(\mathcal{Z}) \equiv \begin{pmatrix} X \\ Y \end{pmatrix} \quad (\text{III.33})$$

by

$$\begin{aligned} (\mathcal{Z}) &= (T_j)(A) \\ (A) &= (T_j)^{-1}(\mathcal{Z}) \end{aligned} \quad (\text{III.34})$$

where

$$(T_j) = \begin{pmatrix} -g_j & 1 \\ -g_j & -1 \end{pmatrix} \quad (\text{III.35})$$

If we write (\mathcal{Z}'_j) for the value of (\mathcal{Z}) at one film surface $z = z_j$, and (\mathcal{Z}_j) for the value at $z = z_j + \delta_j$, we have the relation

$$(\mathcal{Z}'_j) = (P_j)(\mathcal{Z}_j) \quad (\text{III.36})$$

where

$$(P_j) = \begin{pmatrix} \exp(i\psi_j) & 0 \\ 0 & \exp(-i\psi_j) \end{pmatrix}; \quad \psi_j \equiv p_j \delta_j \quad (\text{III.37})$$

Moreover, the boundary condition requiring continuity of the tangential field components at the interface of, say, the j th and $(j-1)$ th films leads immediately to the continuity of (A) , so that

$$(A_{j-1}) = (A'_j) \quad (\text{III.38})$$

where the notation is analogous to that just described in (\mathcal{Z}) .

Combining (III.34), (III.36), and (III.38), we obtain the following recurrence relations for (\mathcal{Z}_j) :

$$\begin{aligned} (\mathcal{Z}_{j-1}) &= (T_{j-1})(A_{j-1}) = (T_{j-1})(A'_j) \\ &= (T_{j-1})(T_j)^{-1}(\mathcal{Z}'_j) \\ &= (T_{j-1})(T_j)^{-1}(P_j)(\mathcal{Z}_j) \end{aligned} \quad (\text{III.39})$$

and hence for (A_j) ,

$$(A_{j-1}) = (T_{j-1}) = (T_j^{-1})(P_j)(T_j)(A_j) = S_j(A_j) \quad (\text{III.40})$$

where

$$S_j \equiv (T_j)^{-1}(P_j)(T_j) \quad (\text{III.41})$$

This last expression is readily evaluated as

$$(S_j)_{TE} = \begin{pmatrix} \cos \psi_j & -\frac{i}{g_j} \sin \psi_j \\ -ig_j \sin \psi_j & \cos \psi_j \end{pmatrix} \quad (\text{III.42})$$

which is identical with the corresponding Abeles matrix (M_j) .

If we now apply the recurrence relation (III.40) repeatedly over the entire set of L films, we relate the vacuum (A_0) to the bulk value (A_{L+1}) by

$$(A_0) = (Q)(A_{L+1}) \quad (\text{III.43})$$

where

$$(Q) \equiv \prod_{j=1}^L (S_j) \quad (\text{III.44})$$

Then if q_{mn} are the matrix elements of (Q) , we have the following relationships between the incident, reflected, and transmitted electric vectors E_{yi} , E_{yr} , and E_{yt} :

$$\begin{aligned} E_{yi} + E_{yr} &= (q_{11} - g_b q_{12}) E_{yt} \\ -\cos \varphi (E_{yi} - E_{yr}) &= (q_{21} - g_b q_{22}) E_{yt} \end{aligned} \quad (\text{III.45})$$

In (III.45), g_b is simply the bulk (here Drude) value of g . We immediately obtain the complex amplitude reflection coefficients in the form

$$r_s \equiv \frac{E_{yr}}{E_{yi}} = \frac{\cos \varphi (q_{11} - g_b q_{12}) - (g_b q_{22} - q_{21})}{\cos \varphi (q_{11} - g_b q_{12}) + (g_b q_{22} - q_{21})} \quad (\text{III.46})$$

In the limit of a sharp surface the ψ_j vanish and r_s becomes the familiar expression

$$\begin{aligned} r_s(\text{sharp surface}) &= \frac{\cos \varphi - g_b}{\cos \varphi + g_b} \\ &= \frac{\cos \varphi - [\epsilon_b - \sin^2 \varphi]^{1/2}}{\cos \varphi + [\epsilon_b - \sin^2 \varphi]^{1/2}} \end{aligned} \quad (\text{III.47})$$

In the case of the TM wave the (S_j) are found to be

$$(S_j)_{\text{TM}} = \begin{pmatrix} \cos \psi_j & \frac{i}{h_j} \sin \psi_j \\ ih_j \sin \psi_j & \cos \psi_j \end{pmatrix} \quad (\text{III.48})$$

If the elements of (Q) are Q_{mn} , use of (III.48) leads to an amplitude reflection coefficient given by

$$r_p = \frac{(Q_{11} + h_b Q_{12}) - \cos \varphi (Q_{21} + h_b Q_{22})}{(Q_{11} + h_b Q_{12}) + \cos \varphi (Q_{21} + h_b Q_{22})} \quad (\text{III.49})$$

Again, as the ψ_j approach zero (III.49) reduces to the usual form

$$r_p(\text{sharp surface}) = \frac{[\epsilon_b - \sin^2 \varphi]^{1/2} - \epsilon_b \cos \varphi}{[\epsilon_b - \sin^2 \varphi]^{1/2} + \epsilon_b \cos \varphi} \quad (\text{III.50})$$

The energy reflection coefficients ($R_s = r_s r_s^*$, $R_p = r_p r_p^*$) and the ellipsometric properties are obtained from (III.46) and (III.49) in the conventional manner. The important feature of this treatment, however, is that a given set of these properties is not unique to a single set of films. Herpin⁵² demonstrates that any product of two or more (S_j) can be expressed as a sum of Pauli matrices, and hence that the optical properties of an arbitrary stratified medium are equivalent to those of a system of two appropriately chosen homogeneous films. The proof of this theorem leads directly to the conclusion that there are possible an infinite number of such media which are optically equivalent to any given double layer.

The consequences for the calculation given above are far reaching. They assert that in choosing and parametrizing a particular conductivity profile for the surface zone, we are in effect choosing an equivalent double layer. Since there are an infinite number of possible profiles equivalent to the same double layer, it follows that the conclusions we shall reach from the calculation are independent of the particular form we have chosen. Admittedly, this implies that we have no direct way of confirming the physical speculations that led to the choice of profile; on the other hand, it encourages us not to be unduly upset if parameters that are physically unlikely are required to fit the choice of profile to the observed data.

D. Application of the Surface Zone Model

We have described, in Section III.C, a model of the electrical properties of the surface of a liquid metal, and how those properties influence the

optical properties of the metal. Although we have shown that the presence of a surface transition layer of nonzero width can change markedly the solutions of Maxwell's equations as compared to the solutions for a conductor with a "classical" discontinuous planar surface we have not shown how the excess conductivity is related to the structure. The magnitude of the deviations from the Fresnel solutions depends directly on the effective width of the transition zone and the magnitude of the surface conductivity relative to the bulk conductivity. When these are large enough for the complex quantity γ [see (III.27)] to differ appreciably from unity, the relation between the real and imaginary parts of r_s and r_p will be affected more than their absolute values. Even without detailed calculations we may then confidently expect some difference between the optical constants deduced from ellipsometric data via the Fresnel equations and those deduced from reflectance data via the Fresnel equations. This effect, that is the difference in deduced optical constants, is the direct analogue of the phase change across the transition zone which is responsible for the ellipsometric properties of dielectric liquids. Note, however, that in the case of a conducting liquid there is no way of distinguishing this phase change from that due to bulk absorption. The effect of a surface zone on the reflectance of the metal is much less pronounced, but not completely negligible.

The only systems to which the analysis of Section III.C has been applied are liquid Hg and liquid Hg-In alloys. It would take us too far afield to indicate why these systems were chosen. For the present it suffices to say that if the surface transition layer has a coherence length of the order of 10 Å these materials are likely candidates for investigation because in them the penetration depth in the energy region of interest is of the order of magnitude of 100 Å, and the electron mean free path and Fermi energy wavelengths are about 10 Å and 5 Å, respectively. Although the surface zone coherence length is only of the order of one-tenth of the penetration depth, all other natural lengths are about equal, and the several kinds of optical measurements have become modified electron diffraction experiments, and should be somewhat sensitive to the properties of the surface zone.

Direct evidence that the surface zone influences the optical properties of liquid Hg was first presented by Bloch and Rice.⁸ They showed that, using the optical constants deduced from the ellipsometric data of Faber and Smith⁵³ via the Fresnel relations, the calculated metallic reflectivity did not agree with their measured reflectivity (see Fig. 2). The ellipsometric and reflectance measurements were repeated by Choyke, Vosko, and O'Keefe,⁵⁴ and by Crozier and Murphy.⁵⁵ The latter investigators, so as to eliminate all possibility of error arising from the use of different samples in

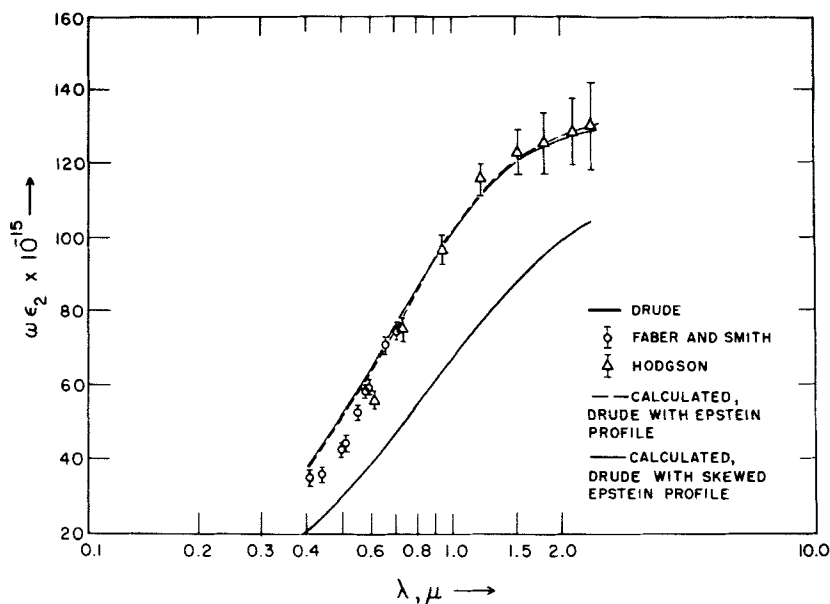


Fig. 2. Effect of a surface transition zone on the ellipsometrically determined $\omega\epsilon_2$ for mercury, $\phi=78.05^\circ$. The theoretical curves for this and the next figure were calculated using parameters chosen to give the best simultaneous fit to the data of Hodgson and Faber and Smith.⁵³ The sharp-surface Drude curve is given in each figure for comparison.

different experiments, made ellipsometric and reflectance measurements on the same sample. The work of Bloch and Rice was completely confirmed by all these investigators. The experimental data permit the following strong conclusion: The optical properties of liquid Hg are different for *p*- and *s*-polarization of the incident radiation; the liquid cannot be described with only a single dielectric function such as is the case for a homogeneous isotropic medium.

It now remains to be established that the discrepancy revealed above can be removed by including in the analysis of the data the influence of an inhomogeneous surface layer in the liquid metal. That this is the case was shown by Bloch and Rice,⁸ and verified by Crozier and Murphy.⁵⁵ The resolution of all the differences is not perfect, as will be seen below, but it is on the whole very good.

Following Bloch and Rice, and as detailed in Section III.C, we adopt the conductivity profile (III.22). Bloch and Rice proposed that σ_b be taken to have the Drude quasi-free-electron form $\sigma_{0b}[1 + i\omega\tau_b]^{-1}$, where σ_{0b} is the dc conductivity and τ_b the corresponding relaxation time, and that σ_s have a

frequency dependence that depends on position in the transition region. Drawing on arguments concerning the metal \rightarrow nonmetal transition, it was suggested that in the low-density tail of the surface zone the electrons were localized; these contribute to the ac (but not the dc) conductivity via the Lorentzian form $\sigma_{0S}[1 + i\omega\tau_S(1 - \omega_0^2/\omega^2)]^{-1}$, where the localized states are centered around ω_0 . In the rest of the transition zone, as z increases and the density increases toward the bulk value, the surface zone becomes more like the bulk. In this region Bloch and Rice took σ_S to have the form $\sigma_{0S}[1 + i\omega\tau_S]^{-1}$, quasi-free-electron behavior but with different dc conductivity and relaxation time. Thus the conductivity profile is completely specified by σ_{0S} , τ_S , Δ [see (III.22)], ω_0 , and the position z_0 at which the transition from quasi-free-electron to Lorentzian frequency dependence occurs.

We show in Figs. 2 and 3 Bloch and Rice's calculations of the real and imaginary parts of the dielectric function, as compared to the values calculated under the assumption that liquid Hg is homogeneous and isotropic up to a discontinuous density change (the surface), and has a Drude-like conductivity. The parameter values used were $\Delta = 6.28 \text{ \AA}$, $\sigma_{0S} = 48\sigma_{0b}$ and $\tau_S = 0.9\tau_b$. Calculations are also shown for a skewed profile, defined by taking Δ_1 and Δ_2 , the values of Δ on the bulk and vapor sides of

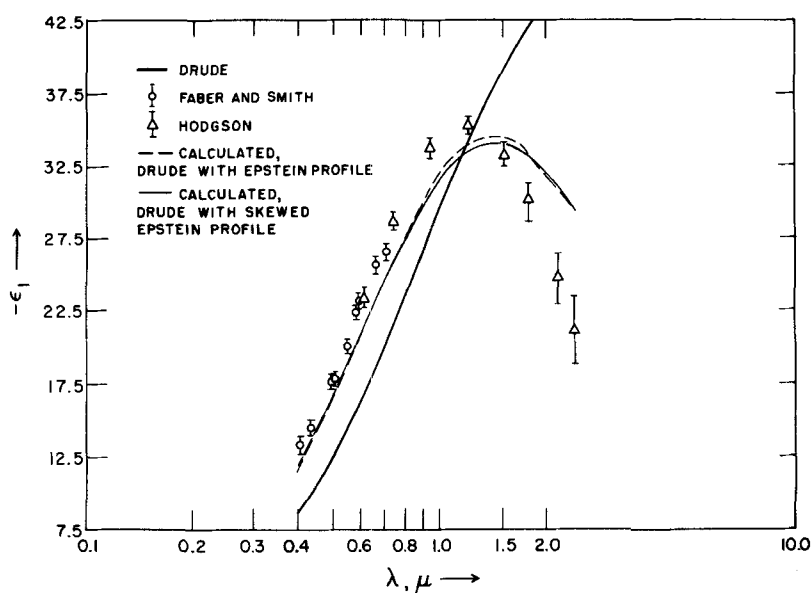


Fig. 3. Effect of a surface transition zone on ellipsometrically determined ϵ_1 for mercury, $\phi = 78.05^\circ$. Calculations as in Fig. 2.

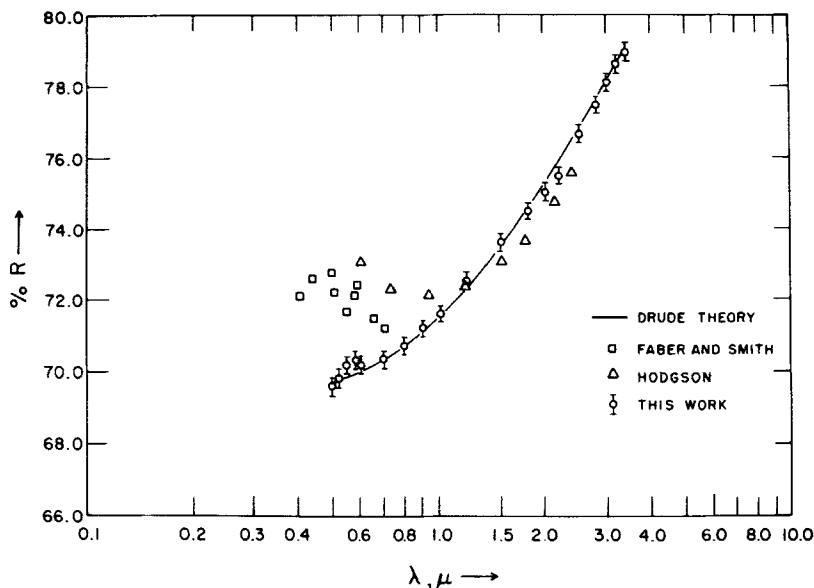


Fig. 4. Reflectivity of Hg-LiF interface, 0.495 to 3.40 μ . The results of Faber and Smith, and of Hodgson, recalculated to normal incidence, are displayed for comparison. We do not show the experimental uncertainty in their data, which amounts to as much as $\pm 1.8\%$ in the reflectivity. As usual, the Drude theory is represented by the solid curve.

the maximum in the profile, to be different. The effective width of the profile is, in this case, proportional to $\Delta_1 + \Delta_2$. The curves shown in Figs. 2 and 3 correspond to $\Delta_1 = 6.28\text{\AA}$, $\Delta_2 = 31.40\text{\AA}$, $\sigma_{0S} = 17\sigma_{0b}$ and $\tau_S = 0.9\tau_b$.

Crozier and Murphy applied the Bloch-Rice theory to the interpretation of their data, with the results shown in Fig. 5. They used the same parameters as did Bloch and Rice (simple profile) but assumed that the presence of a dielectric window in contact with the liquid metal removes the low-density tail. They therefore truncated the low-density tail at $z = -3.6\text{\AA}$. Crozier and Murphy note that at this point in the surface zone its refractive index at 5000 \AA is 1.43, very close to that of the silica with which the Hg was in contact. They also carried out calculations for the skewed profile with $\sigma_{0S} = 36\sigma_{0b}$, $\tau_S = 1.4\tau_b$, $\Delta_1 = 6.28\text{\AA}$ for $z > 0$ and $\Delta_2 = 12.56\text{\AA}$ for $z < 0$, and $\omega_0 = 18.84 \times 10^{14} \text{sec}^{-1}$.

The agreement between calculation and experiment speaks for itself—it is possible to account reasonably well (though not completely) for the optical properties of liquid Hg by including the effects on the radiation-matter coupling of an inhomogeneous surface zone.

As mentioned before, the only other liquid metal systems to which this

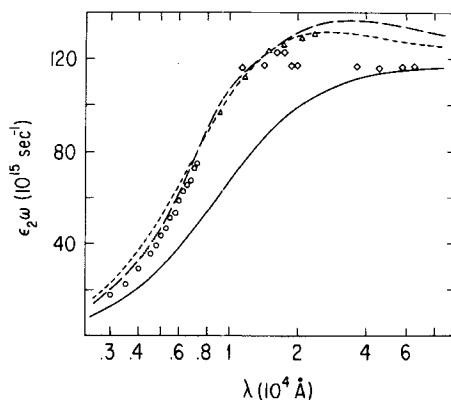


Fig. 5. Comparison between experimental results and calculations of $\omega\epsilon_2$ versus wavelength for mercury (after Crozier and Murphy). The solid curve represents the Drude behavior. The long-dashed curve is given by a skewed Epstein profile. The short-dashed curve by a modified Bloch-Rice profile. The ellipsometry results of the C. M. work for the silica-mercury interface are given by O, the results of Comins by \diamond , and the results of Hodgson by \triangle .

type of analysis has been applied are liquid Hg—In alloys. Siskind, Boiani, and Rice⁵⁶ note that elementary thermodynamic analysis shows that a solute which raises the surface tension of a mixture will have a smaller concentration in the surface region than in the bulk. Of course, the necessary change in concentration cannot occur discontinuously, so there will be a concentration gradient between the surface and the bulk, and the condition of local electroneutrality requires that there be a corresponding electron concentration (hence conductivity) gradient. This surface effect, which can also influence ellipsometric and reflectance measurements, is different from the one postulated for single-component liquids by Bloch and Rice and must be considered in addition to possible physical surface structure effects.

The Hg—In alloy systems are obviously more complicated than pure Hg. It suffices for our present purposes to note that Siskind, Boiani, and Rice present a qualitatively and semiquantitatively consistent interpretation of all the available data by incorporating the necessary concentration gradient into the Epstein-Eckart profile framework by assuming that $\sigma_b(\omega)$ is a function of z as well as of ω . More specifically, they assume that

$$\sigma_b(\omega, z) = \sigma_b(\omega, 0); \quad z < 0$$

$$\sigma_b(\omega, z) = \sigma_b^*(\omega) + [\sigma_b(\omega, 0) - \sigma_b^*(\omega)] \exp\left(-\frac{z}{\Lambda}\right); \quad z \geq 0$$

where $\sigma_b^*(\omega)$ is the conductivity of the bulk alloy and Λ a characteristic length which is a measure of the size of the region over which $\sigma_b(\omega, z)$ changes from its surface value, $\sigma_b(\omega, 0)$, to its bulk value, $\sigma_b^*(\omega)$. The fitting of the data show that $\Lambda = 30\text{\AA}$, sensibly the same for all alloy concentrations. We refer the reader to the original paper for more details.⁵⁶

E. Inferences Concerning the Structure of the Liquid Metal Surface

The results described in the preceding section, although gratifying, also illustrate the weakness of this particular approach to the study of the structure of surfaces. Simply put, although the optical constants are sensitive to the nature of the surface zone on the liquid, the significance to be attached to any particular set of profile parameter is uncertain, since any stratified layer can be replaced by two equivalent layers. Thus, ellipsometric and reflectance measurements permit the sorting of surface zone models into gross categories, but cannot provide answers to questions concerning subtle details. On the other hand, since the method permits a gross sorting out of models, it is to be expected that at least the gross (common) features of models that work will be characteristic of the real surface. In support of this we note that in both the Bloch-Rice and Crozier-Murphy calculations the part of the profile adjacent to the dielectric (or vacuum) had a mixture of localized and delocalized states, while the part adjacent to the bulk metal had a conductivity larger than the bulk. All model surface zones that fit the experimental data have these features. It is quite reasonable that the surface zone of liquid Hg really does have these properties. Thus, measurements of the thermoelectric power and Hall coefficient of Hg as a function of density support the existence of a pronounced dip in the electronic density of states at the Fermi energy when the atomic density is of the order of two-thirds the liquid density. Of course, the opening up of such a gap in low-density fluid Hg is consistent with the assumed existence of localized states in the tail of the model surface zone. Similarly, a variety of calculations of the electronic and nuclear density profiles near the surface indicate that a peak in the electron concentration just inside the metal is likely to occur (see Section II.B), just as is assumed to be the case in the part of the model surface zone close to the bulk.

We conclude that ellipsometric and reflectance studies of a liquid metal can provide useful information about the gross properties of its surface, but that we must seek more powerful tools if we wish to know much about its detailed electronic structure. In the next section we propose that the surface plasmon dispersion relation, while still not overly sensitive to details of the electronic structure of the surface, is more so than the optical

constants. We also show how the surface plasmon dispersion relation may be studied.

IV. SURFACE PLASMON DISPERSION: A PROBE OF THE STRUCTURE OF A LIQUID METAL SURFACE

A. General Considerations

Given the formal development of Section III.B, and the analysis of data discussed in Section III.D, we are lead to ask the following question: What experimental probe will be most sensitive to the existence and structure of the transition zone that is proposed to characterize the surface of a liquid metal? Although we do not have a definitive answer to this question we attempt to convince the reader that the study of the dispersion relation for nonradiative surface plasmons can provide useful information about the surface of a liquid metal (or any other surface).

For the present we restrict attention to those experimental methods which utilize electromagnetic radiation, since these are relatively simple to use over a wide range of energy. More sophisticated, and at least seemingly direct methods exist, for example, low-energy electron diffraction (LEED). However, at present the energy and angular resolution in LEED experiments is far inferior to that achievable with electromagnetic radiation and, more serious, there are uncertainties in the fundamental interpretation of the data collected. Taken together, these difficulties considerably reduce the attractiveness of LEED experiments vis-à-vis experiments based on some variant of ellipsometry or reflection spectroscopy. We expect that in the future, when the experimental technology is improved and the theory of LEED fully established, LEED experiments will be a very powerful tool for the investigation of liquid metal surfaces.

Since we are interested in probing the properties of the surface, an important qualitative characteristic of any given kind of spectroscopy is the existence of a penetration depth of the sort described by (III.1). Physical intuition tells us, of course, that the spectroscopic method of choice for our purpose is that which has the smallest penetration depth. For metallic conductors, the penetration depth is essentially independent of the angle of incidence of the radiation, for the derivation of (III.1) is based on the assumption that $\text{Re}(4\pi\sigma/\omega) \gg 1$. In ellipsometric and normal-incidence studies of liquid mercury, therefore, attenuation of the incident beam in the direction normal to the metal surface is described by a common decay length.

This observation prompts us to inquire why ellipsometric investigations of mercury seem more sensitive to the existence of a surface transition

zone than do reflectance studies. We argue now that this enhanced sensitivity arises because ellipsometric experiments sample the response of the metal to incident electric fields that are both normal and parallel to the interface, while in near-normal incidence (typical of reflectance experiments) most of the incident field strength is in the parallel direction. Consideration of the boundary conditions across a metallic interface provides supports for this viewpoint, for the requirement of continuity on the tangential electric field implies that the normal field must vary much more rapidly in the surface region—even near a sharp, zero-thickness interface. Hence any deviation from zero thickness, such as the existence of a transition zone, should exert a more pronounced influence on the reflection of p -polarized radiation than it does for s -polarization.

From the preceding discussion one is led to conclude that the class of experiments which should permit one to study the transition zone of a liquid metal with reasonable sensitivity is comprised of those which allow for a small penetration depth, and which also employ an incident field that induces a large electronic response in the normal direction. One means of accomplishing this is selection of a probe that obeys a dispersion relation different from those associated with the standard optical methods, and which makes maximum use of p -polarized radiation. The nonradiative surface plasmon (NRSP)⁵⁷ is just such a probe. The NRSP couples exclusively to p -polarized light and has a dispersion curve which lies primarily to the right (higher momentum) of the light line of the adjacent contact (dielectric) medium, in contrast to the radiative dispersion relations which define other optical properties. Moreover, as an electronic excitation which is intrinsically localized to the surface region of a conductor, we suspect that the NRSP should manifest some degree of sensitivity to the gross electronic structure of a surface zone such as that described by (III.22). Before showing that this is true on a quantitative level, we review the basic electromagnetic theory which leads to the existence of surface plasmons, and point out those features which should distinguish NRSP spectroscopy from ellipsometry and reflectance spectroscopy.

B. Surface Plasmons—An Overview

The properties of surface plasmons in a metal that is homogeneous up to a planar interface are discussed elsewhere in this volume. Nevertheless, since the point of view taken in our analysis requires an understanding of features of the surface plasmon dispersion relation only briefly touched upon we shall, for convenience, sketch the background required for the application to liquid metals.

Surface plasmons, like bulk plasmons, are collective excitations of the electrons wherein the density fluctuations are connected through a phase

relation. Bulk plasmons were first observed by Ferrell⁵⁸ via the energy losses experienced by fast electrons transmitted through thin metal foils. These energy losses are integral multiples of $\hbar\omega_p$ with ω_p the classical plasma frequency of the metal. Surface plasmons, which are localized to the region immediately adjacent to the metal surface,⁵⁹ have at short wavelengths a wavelength-independent characteristic frequency $\omega_s < \omega_p$; their existence can also be inferred from electron energy-loss experiments.⁶⁰ Ritchie⁶¹ showed that in the short-wavelength limit

$$\omega_s = \frac{\omega_p}{(1 + \epsilon_0)^{1/2}} \quad (\text{IV.1})$$

where ϵ_0 is the (frequency-independent) dielectric constant of the medium in contact with the metal surface. Equation (IV.1) leads to the expectation that ω_s depends on the character of the metal surface, and this is found to be the case.⁶⁰ For example, for an unoxidized Al surface (contact medium is the vacuum) $\hbar\omega_s = 10.3$ eV, whereas for an oxidized Al surface (contact medium is Al_2O_3) $\hbar\omega_s = 7.0$ eV.⁶²

As the plasmon wavelength increases the fact that field fluctuations propagate with finite speed becomes important.^{59,63} The consequences of retardation were first considered by Ferrell⁶³ who predicted the decay of bulk plasmons by emission of photons in thin metal foils. This was subsequently verified by Steinmann⁶⁵ and Brown et al.⁶⁶ by observing the fluorescence radiation emitted by thin metal foils which were subjected to bombardment by energetic electrons. In later experiments,⁶⁷ X-ray bombardment of thin metal foils again produced fluorescent radiation whose angular distribution was in agreement with the predictions of Ferrell.

Retardation can have important consequences for surface plasmons as well. Taking this into account one finds that the energy of a surface plasmon is now wavelength dependent, and that the dispersion relation now contains two modes distinguishable by their ability to couple directly to the electromagnetic field. Those surface modes which at long wavelengths are characterized by the plasma frequency ω_p independent of wavelength, and which radiate at increasing frequencies as their wavelength decreases in such a way that their phase velocity is always greater⁶⁴ than that of light in the bounding dielectric medium, are referred to as radiative surface plasmons (RSP). These are not "true" normal modes of the system and are sometimes referred to as "virtual modes." They are discussed at length by Kliever and Fuchs.^{57,59} We do not discuss these "modes" further as they are not of primary importance in our study of liquid metal surfaces. There are, however, collective oscillations at a metal

surface which do not couple directly to the electromagnetic field, and which are localized in a region about the metal surface⁵⁹ that varies from a few angstroms for short-wavelength surface plasmons to a few hundred angstroms in the long-wavelength limit. These modes are the already referred to nonradiative surface plasmons. At the short wavelengths which are typical of electron scattering experiments, the frequency of the nonradiative modes is independent of wavelength and is given by (IV.1). At longer wavelengths, however, the frequency decreases in such a way that the phase velocity is always less⁶⁴ than that of light. Consequently, NRSP can neither emit nor absorb light directly. Besides their appearance in electron energy-loss experiments described above, NRSP have also been detected in ellipsometric studies of solid metal surfaces.⁶⁸ Recently, there has been evidence from photoemission experiments which links the observed increase in the photoyield at discrete frequencies, depending on the angle of incidence of the ionizing radiation, with the onset of nonradiative surface plasma oscillations.^{69,86} In both the ellipsometric and the photoemission studies the nonradiating plasma modes at the metal surface are stimulated by the incident plane electromagnetic waves via intervention of the surface roughness which inevitably exists on all solid metal samples. The role of surface roughness in coupling the plane electromagnetic field with the field of nonradiating surface plasma modes is discussed later, as is a different coupling mechanism which makes possible the stimulation of NRSP by plane electromagnetic waves at surfaces which are smooth. This technique is particularly useful for studying surface plasma oscillations at a liquid metal surface in contact with an optically polished dielectric.

C. The Nonradiative Surface Plasmon Basic Theory

The microscopic basis of surface plasma waves has been a subject of sophisticated theoretical development⁷⁰ and elaborate model-based calculations^{71,72} in recent years. In the optical regime which interests us, however, it is sufficient to consider the NRSP within a macroscopically oriented, local dielectric framework of the type employed by Bloch and Rice^{8,55,56} for the analysis of classical reflectivity and ellipsometry experiments on liquid metals. Including retardation via Maxwell's equations, we outline first, in the present section, the macroscopic treatment of surface plasma waves, specializing to the "idealized" surface mode which occurs at a geometric boundary of zero thickness in order to elucidate the basic features of the resonance.

The simplest approach to the theory of surface plasmons is based on the form that Maxwell's equations assume in a conducting medium. The two curl equations are given by (III.19a) and III.19b), with position-

independent dielectric functions; the appropriate divergence equations are

$$\nabla \cdot \mathbf{D} = 0 \quad (\text{IV.2a})$$

$$\nabla \cdot \mathbf{H} = 0 \quad (\text{IV.2b})$$

Equations (III.19a), (III.19b), (IV.2a), and (IV.2b) express Maxwell's equations in the form most convenient for the present analysis, as they may be applied to either dielectric or metallic media simply by substituting the appropriate dielectric constant ϵ_i of medium i . These dielectric constants may, in general, depend on the frequency ω , and in the liquid metals which are discussed here, we allow for possible coordinate dependence of ϵ_i because of the existence of a surface transition zone. In the long-wavelength limit which the present section treats, nonlocal effects are completely neglected, it being assumed that all of the ϵ_i are independent of wave vector \mathbf{k} in spite of spatially dependent dielectric screening in the nonuniform region of the liquid metal surface. This assumption is consistent with the local relation (III.18) between the current density and the electric field. Surface plasmons interact only with p -polarized radiation, since for s -polarization $\nabla \cdot \mathbf{E} = \nabla \cdot \mathbf{E}_t \equiv 0$ and there are no charge fluctuations. Therefore, taking the plane of incidence to be the xz plane, we set $E_y = 0$ and assume that all fields are independent of the coordinate y . The identities $H_x \equiv 0$ and $H_z \equiv 0$ follow directly from Maxwell's equations. Our geometry is specified, in addition, by supposing the half-space $z \geq 0$ to be occupied by liquid metal, and the region $z < 0$ by a semiinfinite dielectric. Given this arrangement we may further assume, without loss of generality, that all fields are of the form $\mathbf{F}(\mathbf{x}, t) = \mathbf{F}(z)e^{ik_x x - i\omega t}$. With these assumptions the field equations for transverse magnetic (TM) waves become

$$\frac{\partial E_x}{\partial z} = ik_x E_z + \frac{i\omega}{c} H_y \quad (\text{IV.3a})$$

$$\frac{\partial H_y}{\partial z} = \frac{i\omega\epsilon}{c} E_x \quad (\text{IV.3b})$$

$$E_z = -\frac{ck_x}{\omega\epsilon} H_y \quad (\text{IV.3c})$$

After some straightforward algebra, (IV.3) yield a second-order differential equation for the tangential magnetic field,

$$\frac{\partial}{\partial z} \left[\frac{1}{\epsilon} \frac{\partial H_y}{\partial z} \right] = \frac{K^2}{\epsilon} H_y \quad (\text{IV.4})$$

with $K^2 = k_x^2 - (\omega/c)^2 \epsilon$. We remark that (IV.4) is still quite general, allowing for a possible coordinate dependence $\epsilon_m = \epsilon_m(z)$ in the dielectric function of the liquid metal.

In order to gain some understanding of the fundamental nature of surface plasma waves, we now consider one of the simplest geometries for which they are known to occur: a semiinfinite, homogeneous metal bounded by a semiinfinite, homogeneous dielectric. In this configuration (IV.4) simplifies to

$$\frac{d^2}{dz^2} H_y^i = K_i^2 H_y^i \quad (\text{IV.5})$$

the indices i referring to properties and fields in medium i . Employing the relations (IV.3b) and (IV.3c) between the electric and magnetic field components, we can readily determine the most general solutions for the fields within the two media (neglecting the common x and t dependence):

$$\begin{aligned} H_y^i &= A_i e^{K_i z} + B_i e^{-K_i z} \\ E_x^i &= \frac{cK_i}{i\omega\epsilon_i} (A_i e^{K_i z} - B_i e^{-K_i z}) \\ E_z^i &= -\frac{ck_x}{\omega\epsilon_i} (A_i e^{K_i z} + B_i e^{-K_i z}) \end{aligned} \quad (\text{IV.6})$$

The dispersion of the surface plasma waves may be found from (IV.6) by applying appropriate boundary conditions to the field amplitudes. Making the usual loop and pillbox arguments at the zero-thickness metal-dielectric boundary, one finds that E_x and H_y , the tangential fields, as well as D_z , the normal displacement, must be continuous across the interface. Boundary conditions as $z \rightarrow \pm \infty$ require, moreover, that all fields remain finite; for $\text{Re}(K_i) > 0$, this implies that B_d and A_m vanish identically. Applying the continuity conditions at $z=0$, we find that the dispersion relation at a simple metal-dielectric interface is given implicitly by

$$\frac{K_m}{\epsilon_m} + \frac{K_d}{\epsilon_d} = 0 \quad (\text{IV.7})$$

or

$$k_x = \pm \frac{\omega}{c} \left(\frac{\epsilon_m \epsilon_d}{\epsilon_m + \epsilon_d} \right)^{1/2} \quad (\text{IV.8})$$

in more transparent form. The degeneracy in the sign of k_x arises from the degeneracy in the direction of H_y .

We may deduce, from (IV.8) alone, some of the general properties of surface plasmons. First, for real ω , because $\epsilon_m(\omega)$ is in general complex so also must be k_x . Second, for the case that $\epsilon_{2m} \ll \epsilon_{1m}$ ($\epsilon_m = \epsilon_{1m} + i\epsilon_{2m}$), which is valid in the absence of interband transitions and/or strong scattering, (IV.8) has propagating solutions only for those values of ω for which $\epsilon_{1m}(\omega) < -\epsilon_d$ or $\epsilon_{1m}(\omega) > 0$. The first domain contains all the nonradiative modes, and the second all the modes that can radiate. That this is so follows from the observation that ω/k_x is the phase velocity of the plasmon. Hence, from (IV.8),

$$V_{\text{phase}} = \frac{c}{n_d} \left(\frac{\epsilon_{1m}(\omega) + \epsilon_d}{\epsilon_{1m}(\omega)} \right)^{1/2}$$

$$n_d = \epsilon_d^{1/2} \quad (\text{IV.9})$$

When $\epsilon_{1m}(\omega) < -\epsilon_d$ we find that $V_{\text{phase}} < c/n_d$, hence decay into electromagnetic radiation is forbidden. When $\epsilon_{1m}(\omega) > 0$ we find $V_{\text{phase}} > c/n_d$, and the prohibition on decay into radiation is removed. The range of frequencies for which $0 > \epsilon_{1m}(\omega) > -\epsilon_d$ constitutes a forbidden band in which no plasmon modes exist. In this region the corresponding charge fluctuations decay exponentially in both space and time. The reader should note the similarities between the general properties of surface plasmons just mentioned and the general properties of the mixed photon-matter mode in ionic crystals and the photon-magnon mode in magnetic crystals. In all these cases there are radiative and nonradiative modes separated by a gap in which no modes exist.

A simple and very useful model for which the surface plasmon dispersion relation can be obtained explicitly is defined by taking for ϵ_m the free electron form

$$\epsilon_m(\omega) = 1 - \frac{\omega_p^2}{\omega^2} \quad (\text{IV.10a})$$

and for $\epsilon_d(\omega)$ the dispersionless form

$$\epsilon_d(\omega) = \epsilon_d = \text{Const.} \quad (\text{IV.10b})$$

Then (IV.8) can be solved explicitly to yield ω as a function of k_x . It is

found that

$$\omega^2 = \frac{\omega_p^2 \epsilon_d + c^2 k_x^2 (1 + \epsilon_d) - \left[(\omega_p^2 \epsilon_d + c^2 k_x^2 (1 + \epsilon_d))^2 - 4 \omega_p^2 c^2 k_x^2 \epsilon_d \right]^{1/2}}{2 \epsilon_d} \quad (\text{IV.11})$$

The functional form ω versus k_x is displayed in Fig. 6. As shown, the upper branch corresponds to the RSP and the lower branch to the NRSP. The NRSP branch represents the energy-momentum relation for the normal modes of charge oscillation at the metal-dielectric interface. Note that as $k_x \rightarrow \infty$, $\omega_{\text{NRSP}} \rightarrow \omega_s$, whereas as $k_x \rightarrow 0$, $\omega_{\text{RSP}} \rightarrow \omega_p$, while both branches approach the dispersion curve of light in the bounding (passive) dielectric at the other ends of the ranges of k_x mentioned. Thus ω_{RSP} becomes photon-like as $k_x \rightarrow \infty$, but ω_{NRSP} becomes photon-like as $k_x \rightarrow 0$.

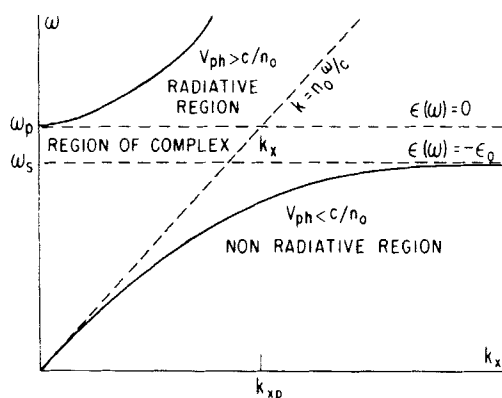


Fig. 6. The surface plasmon dispersion relation of an undamped free electron gas at a homogeneous metal-dielectric interface.

Since we shall later be concerned with optical excitation of the NRSP it is worthwhile restating, in slightly different language, why it is not possible to excite the NRSP simply by shining light on the dielectric metal interface. The condition on the phase velocity shown in Fig. 6 is equivalent to noting that light of given energy $\hbar\omega = \hbar\omega_{\text{NRSP}}$ does not possess enough momentum parallel to the interface to couple directly to the surface plasmon (see Fig. 7). This is a translation of the observation that everywhere in the nonradiative region $\omega < ck_x/n_d$ (see Fig. 6), hence

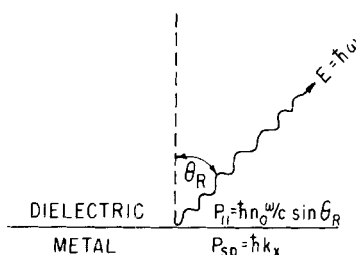


Fig. 7. At the boundary between a semiinfinite metal and semiinfinite dielectric, the NRSP momentum P_{sp} is always greater than the surface component P_{\parallel} of the momentum of a photon (with corresponding energy) for all real angles at which the photon can be emitted. At such a boundary, momentum conservation prevents the decay of a NRSP into a photon.

$\text{Re}(K_{d,m}) > 0$ (recall that $K_{d,m}^2 = k_x^2 - \omega^2 \epsilon_{d,m}/c^2$) and electromagnetic waves propagate in neither the dielectric nor the metal, but are exponentially attenuated as $\exp(K_d z)$ and $\exp(-K_m z)$.

We recall, at this point, some of the general remarks made in Section IV.A. The NRSP dispersion, it is to be noted, differs quite noticeably from the radiative dispersion relations which characterize the standard method of optical experimentation. All of these standard methods are associated with skin depths of the form (III.1) describing the attenuation of electromagnetic waves in the metal, and in a rough sense, at least, these decay lengths are similar to the evanescent nature of the NRSP waves.

It may be seen from the arguments above that $\text{Re}(K_m)$ is proportional to the absorption coefficient for surface plasmons which propagate at the dielectric-metal boundary. Actually, $[\text{Re}(K_m)]^{-1}$ is the skin depth characteristic of all optical probes. [Note, however, that this differs somewhat from the more customary form given in (III.1).] Now, ellipsometric and reflectance experiments are confined to measurements along the k_x - ω line defined by

$$k_x = \frac{n_d \omega}{c} \sin \theta \quad (\text{IV.12})$$

where θ is the angle of incidence. Normally, in these experiments, θ is a fixed parameter, so the k_x - ω relation is linear. Furthermore, since $\sin \theta \leq 1$, ellipsometry and reflectance studies are obviously confined to the radiative region $k_x \leq n_d \omega/c$. Consequently, a lower limit to the normal penetration depth is given by

$$\frac{c}{\omega} \cdot \frac{1}{\text{Re}[(\epsilon_d - \epsilon_m)^{1/2}]} \quad (\text{IV.13})$$

corresponding to (near) normal incidence reflectivity.

In contrast with the behavior described by (IV.11), the dispersion curve for the NRSP, although linear for small k_x , is markedly nonlinear for large k_x ; this nonlinearity plays an important role in determining their properties. In the frequency range between $\omega \ll \omega_s$ and $\omega \approx \omega_s$, k_x varies from $k_x \approx n_d \omega / c$ to $k_x \gg n_d \omega / c$. It is readily seen, then, that the skin depth for NRSP absorption, if such can be made to occur, will generally be smaller than the skin depths at the same frequency for reflectivity and ellipsometry. Of course, the NRSP dispersion relation must depend, to some extent, on the details of the structure of the surface, especially in the intermediate- and high-energy regions where deviation from the light line is large. Thus, if some method of exciting the NRSP can be found, the measured dispersion relation ought to contain information, albeit in concealed form, about the structure of the metal surface.

D. Coupling to NRSP

Having set forth the general properties of the NRSP we now turn to the analysis of how they may be excited in laboratory experiments. We consider two methods, one exploiting the difference between rough and smooth surfaces and the other, the properties of evanescent waves.

1. Excitation via Surface Roughness

It was suggested by Stein⁷³ that whereas at a smooth surface the direct optical excitation of NRSP is not possible, surface roughness can provide a coupling through which optical excitation can occur. Indeed, Beaglehole⁷⁴ has shown that when light is incident perpendicular to the grooves of a vacuum-metal grating interface the momentum component along the surface and perpendicular to the grooves is given by

$$k_x = \frac{\omega}{c} \sin \theta + \frac{2\pi m}{d} \quad (\text{IV.14})$$

where θ is the angle of incidence relative to the normal, d is the grating spacing, and m is an integer corresponding to the order of the diffraction. For a given $m \neq 0$ it is possible, at some angle θ_R , for momentum to be conserved across the metal-vacuum interface, and for the NRSPs to couple to the plane electromagnetic field and absorb or emit light (see Fig. 8). In a particular order m , the NRSPs absorb or limit light at some angle θ_R such that

$$k_{\text{NRSP}} = \frac{\omega}{c} \sin \theta_R + \frac{2\pi m}{d} > \frac{\omega}{c} \quad (\text{IV.15})$$

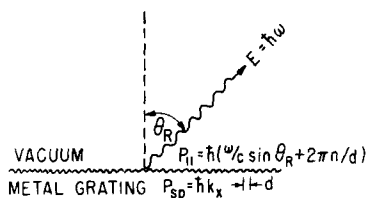


Fig. 8. At a metal grating-vacuum (or dielectric) interface, the NRSP momentum P_{sp} can be conserved across the boundary in a particular grating order m , and a NRSP can decay into a photon.

Direct experimental evidence of NRSP fluorescence was first obtained by Teng and Stern⁷⁵ in experiments with a metal surface on which an optical grating had been ruled. Upon bombardment of the grating surface with energetic electrons, they found that electromagnetic radiation with frequencies much less than the metal's plasma frequency was emitted. The angular dependence of the intensity of fluorescence agreed with (IV.14). Furthermore, when light of the same frequency as the fluorescence radiation was specularly reflected from the same grating, minima were observed in the reflected beam intensity at angles which corresponded to the maxima in the fluorescence spectrum excited by electron bombardment.

The diffraction grating technique has since been used to study NRSP dispersion on a variety of metal⁷⁶ and semiconducting⁷⁷ surfaces. To our knowledge the converse, namely the use of NRSP dispersion as a tool for scanning a conducting surface and retrieving information about its electronic properties, has never been suggested. For the case of interest to us, a liquid metal, a grating could be "ruled" with an ultrasonic transducer. Just as for the solid metals, such grating grooves would have macroscopic depth. Viewed in the reduced zone scheme, which is inherent in (IV.15), there is no reason to expect that the NRSP dispersion at the surface of the grating differs in any but the trivial way (addition of arbitrary multiples of the grating reciprocal lattice vector) from that observed at a smooth surface. Some slight additional structure has been observed, though, at the zone boundaries of the grating, resulting from plasmon-photon interactions in second and higher orders^{77,78} [(IV.15) is a first-order description]. Thus, if there is inherent structure at the surface, and the coherence length of that structure is short relative to the grating groove depth and spacing, the NRSP dispersion should contain some information about the inherent properties of the surface charge distribution.

Just as we may regard thermal waves in a liquid as providing effective gratings for the scattering of light (Brillouin spectrum), so also may we

regard random roughness on a surface as the random superposition of a large number of diffraction gratings. An experiment, then, merely picks out of all possible Fourier components the one to which a coupling, defined by conservation of energy and momentum, is possible. Using this idea, the second class of studies that have been performed on rough surfaces are those done on metals with random roughness, which is nevertheless controlled in magnitude. Stanford, Bennett, and co-workers⁷⁹ have investigated the reflection of light from carefully prepared silver films, while Endriz and Spicer^{80,81} have reported ultraviolet reflectance measurements from aluminum films. In both cases, the dependence of the surface plasmon on surface structure is much more pronounced than for metalized gratings. Figures 9 and 10, which are based on these results, illustrate observable wavelength shifts in the peak reflectance drops due to surface plasmon absorption. In the context of the present review, the scale of the inhomogeneities of Figs. 9 and 10 should be emphasized: the reflectance peaks display significant roughness dependence for rms peak height variations as small as 10 to 30 Å.

It would be misleading to the reader to leave the subject matter of this section without mentioning some of the interesting historical antecedents to the studies we have mentioned. A type of surface wave that does not

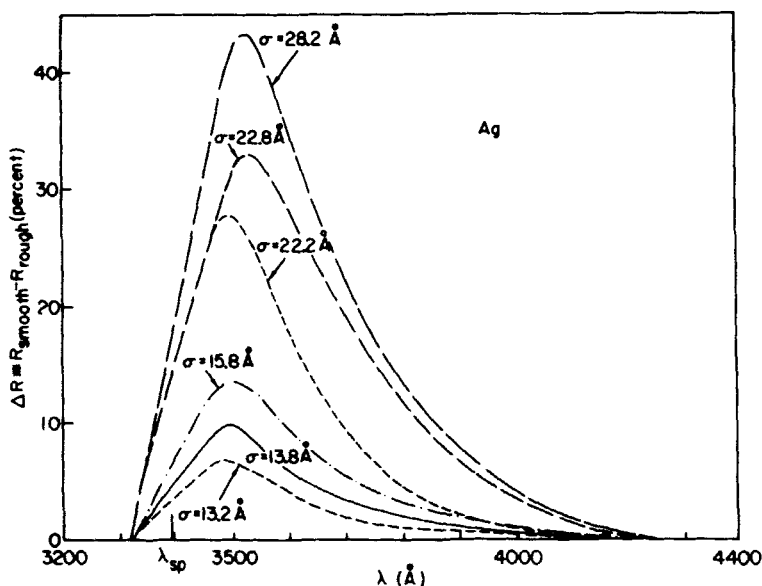


Fig. 9. (After Endriz and Spicer. Experimentally observed reflectance drops in Ag as a function of surface roughness σ (Stanford et al. as quoted in Endriz and Spicer).

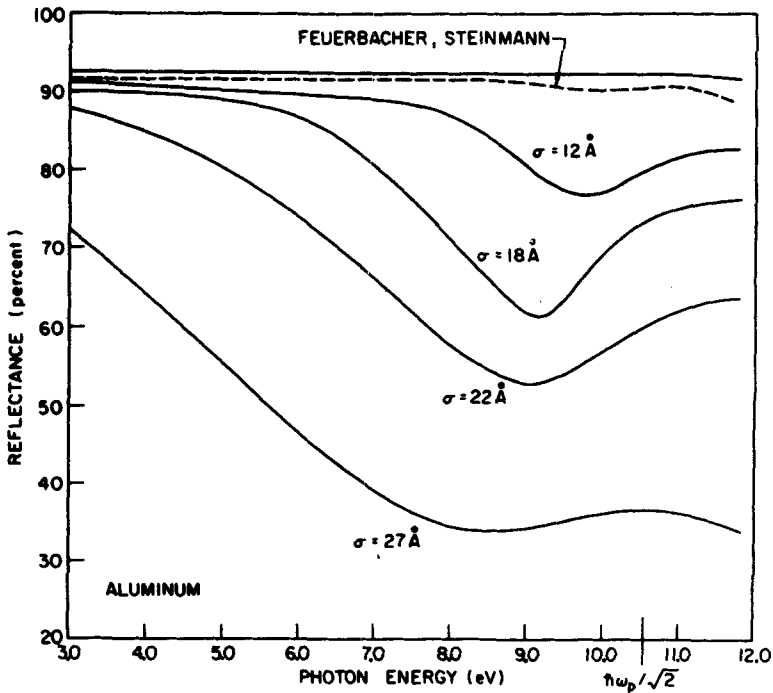


Fig. 10. (After Endriz and Spicer.) Al reflectance for films of varying roughness. The rougher films are characterized by their measured rms roughness σ . Also shown is the smooth surface Al reflectance obtained by Feuerboeher and Steinman (see Endriz and Spicer for reference).

radiate was first described in 1909 by Sommerfeld⁸² in connection with the propagation of radio waves along the ocean's surface. Nonradiating surface waves have also been used to account for the Wood⁸³ anomalies in the response of a metallicly overcoated diffraction grating to p -polarized light. The Wood anomalies are essentially of two types. One has to do with the emergence of a new spectral order at grazing incidence angles. This is observed with s -polarized light and is explained by Lord Rayleigh.⁸⁴ The other has to do with a resonance effect in the intensity of the diffracted light at certain discrete frequencies depending on the angle of incidence. This is observed only with p -polarized light. Fano⁸⁵ was apparently the first to give an account of the resonance anomaly in terms of surface waves. More recently, a detailed treatment and historical review of both anomalies was given by Hessel and Oliner⁸⁶ but the first explanation in terms of nonradiative surface plasma resonances was put forth by Ritchie

et al.^{76,78} who understand the resonance anomaly in terms of surface photon-surface plasmon interaction in second and higher orders. In fact these authors obtain a detailed construction of the NRSP curve by plotting the wavelengths at which the resonance anomaly occurred as a function of the angle at which the p -polarized light was incident on a metallic grating. They find good agreement with the dispersion curve predicted by (IV.8).

2. *Evanescent Waves and the Method of Frustrated Total Reflection (FTR)*

A different technique for coupling the electromagnetic and NRSP fields was devised by Otto.⁸⁷ This method takes advantage of the fact that when light is totally reflected from the boundary between two media with dissimilar indices of refraction, there exists an evanescent electromagnetic field in the medium with smaller index of refraction. This inhomogeneous field has a longitudinal component and decays exponentially away from the surface⁸⁸ and is, therefore, of the same form as that arising from the NRSP calculated in the local approximation [e.g., see (IV.6)].

A plane electromagnetic wave incident on the boundary at $z=0$ can be represented by fields of the form

$$\begin{aligned} \mathbf{F}_2 &= \mathbf{F}_{02} \exp [i(\mathbf{k} \cdot n_2 \mathbf{x} - \omega t)] \\ &= \mathbf{F}_{02} \exp \left[in_2 \frac{\omega}{c} (x \sin \theta_i - z \cos \theta_i) \right] \exp(-i\omega t) \end{aligned} \quad (\text{IV.16})$$

If both media are semiinfinite and if $\theta_i > \theta_c$ (θ_c is the critical angle), all the incident light is reflected back into medium 2, giving rise to the familiar phenomenon of total reflection. When this happens, the average energy flow across the medium 1-medium 2 boundary is zero. Nevertheless, there is still a nonvanishing, electromagnetic field in medium 1 of the form

$$\mathbf{F}_1 = \mathbf{F}_{01} \exp \left(ixn_2 \frac{\omega}{c} \sin \theta_i \right) \exp(K'z) \exp(-i\omega t) \quad (\text{IV.17})$$

where $K' = (\omega/c)(n_2^2 \sin^2 \theta_i - n_1^2)^{1/2}$. This, of course, represents an inhomogeneous wave which propagates parallel to the interface and is in the plane of incidence, but which is attenuated exponentially as the distance from the interface at $z=0$ grows.

If, on the other hand, the optically less dense medium (medium 1) is of some finite thickness d , (see Fig. 11), then taking into account the wave reflected from the medium 1-metal boundary, one finds that the average energy flow across the spacer is no longer identically zero. In fact, the

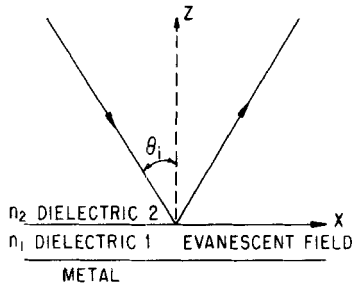


Fig. 11. The principle of frustrated total reflection. An evanescent field exists in medium 1 when $\theta_i > \theta_c$. This field makes it possible to conserve momentum across the metal-dielectric 1 interface, and thus for the photon decay of NRSP. The emitted photons are seen to emerge from the dielectric 1-dielectric 2 boundary at some angle θ_R in accordance with (IV.20).

average z component of the Poynting vector in the spacer is now of the form

$$\langle S_z \rangle = -Qe^{2K'z} \quad (\text{IV.18})$$

where Q is a factor which depends on the spacer thickness, the angle of incidence θ_i , and the optical constants of all three media involved. The evanescent field in the finite spacer is of the form

$$\mathbf{F}_1 = \exp\left(ixn_2 \frac{\omega}{c} \sin \theta_i\right) [\mathbf{F}_{01} e^{K'z} + \mathbf{F}_{01'} e^{-K'z}] e^{-i\omega t} \quad (\text{IV.19})$$

By varying the angle θ_i , it is possible to match the x component of the momentum carried by the evanescent field with the momentum of the NRSP which is always greater than $n_1\omega/c$. Thus, at some angle $\theta_R > \theta_c$

$$k_{\text{NRSP}} = n_2 \frac{\omega}{c} \sin \theta_R \quad (\text{IV.20})$$

Coupling now occurs between the plane electromagnetic field in medium 1 and the NRSP field on the metal surface, and, as shown by Otto,⁸⁷ an alteration in the intensity of the reflected light is observed. Over the last two years, the frustrated total reflection (FTR) technique has been widely used as a tool for studying surface plasma waves in metals^{87,89} and semiconductors^{77,89,90} and surface polarization waves in ionic^{59,91} and molecular crystals.⁸⁹ As pointed out by Fischer et al.,⁹⁰ the FTR technique has several advantages over the grating technique. First, the second-order interactions⁷⁸ of the NRSP with the periodic structure, which give rise to

zone gaps and increased damping, are eliminated. Second, the FTR response can be calculated exactly (in the local approximation and assuming wave fronts of infinite extent) with the well-known formulas for reflection from a stratified medium. The evaluation of the grating response, on the other hand, is much more complicated and only approximate because the grating profile is usually unknown. The reflectivity minima in FTR yield the dispersion curve directly and the widths of the dips are related to the NRSP damping.⁸⁷

There are two drawbacks to this technique, however. The first is the obvious limitation imposed by the lack of optical materials that will transmit beyond the near ultraviolet. The second is a limit on the highest wave vector obtainable. The range of available k values is limited by the difference of the indices of refraction of the two dielectric media, as shown in Fig. 12. One finds⁸⁷

$$n_2 \frac{\omega}{c} < k_x < n_1 \frac{\omega}{c}$$

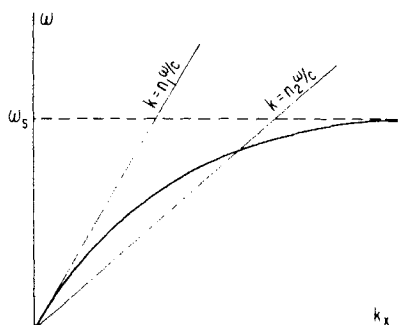


Fig. 12. The range of the dispersion curve observable by the FTR method corresponds to the range $\theta_c < \theta < 90^\circ$ in the angle of incidence. The highest wave vector, $n_2\omega/c$, is obtained at the upper limit, while the smallest, $n_1\omega/c$, is obtained at the critical angle.

for the range of attainable wave vectors by FTR. Thus, only a small portion of the dispersion curve is determinable by the FTR method, even with the highest index of refraction materials now available. Nevertheless, the FTR method is particularly useful in the study of surface plasma oscillations in liquid metals, which as far as we are able to ascertain has not yet been done.

An FTR experiment is usually carried out with a prism-film coupler (see Fig. 13). It is very important to note that the dispersion relation for surface

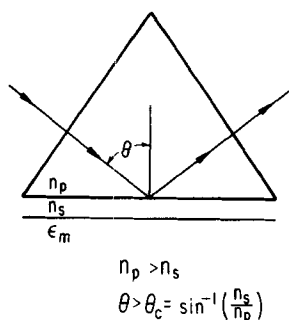


Fig. 13. Experimental configuration for the method of frustrated total reflection. A prism of high refractive index (n_p), undercoated with a low-index (n_s) dielectric spacing film, is bounded by a semiinfinite metal with dielectric function ϵ_m . For angles of incidence greater than the critical angle for total reflection, θ_c , light may be absorbed by the NRSP which propagates along the s - m interface.

plasmons excited through the FTR prism-film coupler is actually more complicated than that predicted by (IV.8), for introducing the thin dielectric layer s changes the character of the boundary value problem that must be solved. Within the film s there are evanescent waves decaying in the $+z$ and $-z$ directions [see (IV.19)], one resulting from the response of the polarization to surface plasma waves at the s - m interface; the other associated with total reflection at the p - s interface. In a simple picture, the two decaying waves undergo multiple reflection at the two interfaces, and a self-consistent field is established in the dielectric s which differs from the field that would exist in a semiinfinite dielectric. The self-consistency requirement, contained implicitly in the boundary conditions, introduces a small quantitative change into the character of the dispersion relation in addition to allowing optical coupling to occur.

Employing the usual continuity conditions at both s - m and p - s interfaces, we can easily find the dispersion of surface plasmons excited by frustrated total reflection⁸⁷:

$$(\epsilon_m K_s + \epsilon_s K_m) + \frac{(\epsilon_m K_s - \epsilon_s K_m)(\epsilon_s K_p + i\epsilon_p K_s)}{(\epsilon_s K_p - i\epsilon_p K_s)} e^{-2K_s d} = 0 \quad (\text{IV.21})$$

where d is the thickness of the spacing layer, and

$$K_p = \left[\epsilon_p \left(\frac{\omega}{c} \right)^2 - k_x^2 \right]^{1/2} \quad (\text{IV.22})$$

E. Some Simple Models

In what follows, we propose that an accurate determination of the surface plasmon dispersion relation can provide considerable information on the structure of liquid metal surfaces. This information may include existence or nonexistence of bound electron states, the surface free electron density, and the nature of scattering by impurities near the surface. The succeeding paragraphs are devoted to examination of the influence on the NRSP dispersion relation of a bound resonance state, and a spatially inhomogeneous free electron density near the surface. We find that a resonance state will manifest itself as a sharp spike on the dispersion curve, and that an inhomogeneous free electron density near the surface has the effect of displacing the dispersion curve relative to that corresponding to a homogeneous surface. Furthermore, we find a second dispersion branch appearing as a direct consequence of the surface inhomogeneity in the density of conduction electrons. The slope of this branch depends on whether the free electron density near the surface is greater or less than the free electron density in the bulk. We suggest that experimental observation of this second branch could provide direct confirmation that the surface region of metals is characterized by an inhomogeneous density of conduction electrons.

1. *Intrinsic Damping of the Electron Gas—The Sharp-Surface Case*

We return to the model of Section IV.C and write for the dielectric function of the metal

$$\begin{aligned}\epsilon_{1m} &= 1 - \frac{4\pi e^2 \tau^2}{m(1 + \omega^2 \tau^2)} N_b \\ \epsilon_{2m} &= \frac{4\pi e^2 \tau}{m\omega(1 + \omega^2 \tau^2)} N_b\end{aligned}\quad (\text{IV.23})$$

where τ is the characteristic lifetime of a charge fluctuation in the free electron gas and N_b is the density of free electrons that have a mass m and charge e . Substituting this into the dispersion relation (IV.7) and writing $k = k_1 + ik_2$ for the complex wave vector, we obtain

$$\begin{aligned}k_1^2 &= \frac{\frac{1}{2}(\omega/c)^2 \epsilon_d}{(\epsilon_{1m} + \epsilon_d)^2 + \epsilon_{2m}^2} \left[\epsilon_{1m}(\epsilon_{1m} + \epsilon_d) \right. \\ &\quad \left. + \epsilon_{2m}^2 + \left([\epsilon_{1m}(\epsilon_{1m} + \epsilon_d) + \epsilon_{2m}^2]^2 + (\epsilon_{2m}\epsilon_d)^2 \right)^{1/2} \right]\end{aligned}\quad (\text{IV.24a})$$

$$k_2 = \frac{1}{2} \left(\frac{\omega}{c} \right)^2 \frac{\epsilon_d}{k_1} \frac{\epsilon_{2m} \epsilon_d}{(\epsilon_{1m} + \epsilon_d)^2 + \epsilon_{2m}^2} \quad (\text{IV.24b})$$

Of course, $\text{Re}(k) \equiv k_1$ defines the momentum of the plasmon. Its mean propagation length is $\Lambda = 2\pi/\text{Im}(k)$ or $2\pi/k_2$.

For most metals, $|\epsilon_{2m}/\epsilon_{1m}|$ is very small over a large range of frequency so that the effects of damping may be ignored to a good approximation. Therefore, on setting $\epsilon_{2m} = 0$ in (IV.24a) we retrieve the usual undamped dispersion relation and the mean propagation length is now infinite. For a few metals, for example Hg, $|\epsilon_{2m}/\epsilon_{1m}|$ is rather large over much of the frequency range of interest and ϵ_{2m} cannot be ignored. Figure 14 shows the effects of various damping strengths on the dispersion relation. The undamped limit is shown by the solid curve. The damping is seen to mix the surface plasmon modes, characterized by the lower branch, with the propagative electromagnetic field associated with the upper branch. The gap between the upper and lower branches is seen to become a region of anomalous dispersion in the presence of damping. Here ϵ_{2m} plays a major role. Outside this region, the two branches retain their undamped characteristics.

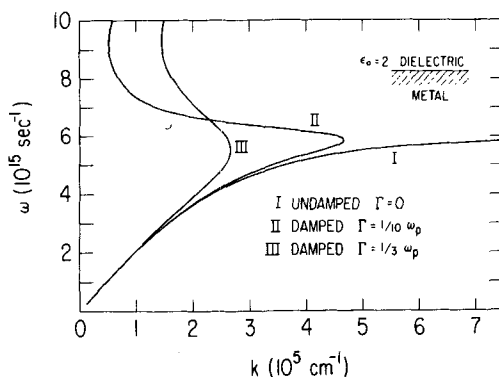


Fig. 14. The effects of damping on the surface plasmon dispersion curve of a free electron gas with a homogeneous surface. We have used (IV. 24a) with the parameters as shown in the figure.

From (IV.24b) we deduce that, for some metals, the long-wavelength surface plasmons can propagate over macroscopic distances. We take $\epsilon_{2m} = 0.3$ and $\epsilon_{1m} = -20$ as typical values. The surface plasmon frequency and wave vector are generally of the order of $k_1 \sim 10^5 \text{ cm}^{-1}$ and $\omega \sim 10^{15}$

sec^{-1} . $\epsilon_d \sim 2$ is common for many optical materials. We then find

$$\Lambda \sim 1 \text{ cm}$$

Thus, long-wavelength surface plasmons in metals with large $|\epsilon_{1m}|$ can propagate along the surface over distances which are several orders of magnitude greater than their wavelength.

A rather convincing experiment exhibiting this effect was reported by Schoenwald et al.⁹¹ who find propagation of surface plasmons on copper over distances of several centimeters.

2. Resonance Effects on the NRSP Dispersion

In this section we consider the effects of a possible interaction between the surface plasmon and other collective or single-particle excitations which may exist in the liquid metal. Single-particle modes can arise from the excitation of inner-core electrons or interband excitations and may interact with the plasmon. Furthermore, it has been shown that if a charged impurity is introduced into a metal, the aggregation of screening charge which accumulates around the impurity⁹² can support collective oscillations in its immediate neighborhood.^{93,94} These localized plasma oscillations (LPO) may also interact with surface plasmon modes. Both the single-particle excitations and LPO give rise to terms, in the wave-vector-independent dielectric function, which display the Lorentzian form $(\omega_i^2 - \omega^2 - i\omega\Gamma)^{-1}$. Therefore, to examine the gross effects of such an interaction

on the surface plasmon dispersion it is sufficient to include in $\epsilon_m(\omega)$ a characteristic Lorentzian resonance in addition to the free electron term.

To obtain an approximation to the dielectric function of a liquid metal we consider a system of N atoms each having Z electrons. f_0 of these electrons are bound with the natural frequency ω_0 while f are free. The dielectric function for such a system is

$$\epsilon(\omega) = 1 - \frac{4\pi N f e^2}{m\omega(\omega + i\Gamma)} + \frac{4\pi N e^2}{m} \frac{f_0}{\omega_0^2 - \omega^2 - i\omega\Gamma_0} \quad (\text{IV.25})$$

and $Z = f_0 + f$. f_0 may be looked upon as a resonance strength while $\tau \equiv 1/\Gamma$ and $\tau_0 \equiv 1/\Gamma_0$ are the characteristic relaxation times of the free electron gas and the bound electron resonance, respectively. Nf and Nf_0 are, of course, just the density of free electrons and the density of bound electrons.

The real and imaginary parts of the dielectric function defined in (IV.25)

are

$$\epsilon_1(\omega) = 1 - \frac{\omega_p^2}{\omega^2 + \Gamma^2} + \xi^2 \frac{(\omega_0^2 - \omega^2)}{(\omega_0^2 - \omega^2) + \omega^2 \Gamma_0^2} \quad (\text{IV.26a})$$

$$\epsilon_2(\omega) = \frac{\omega_p^2 \Gamma}{\omega(\omega^2 + \Gamma^2)} + \xi^2 \frac{\omega \Gamma_0}{(\omega_0^2 - \omega^2)^2 + \omega^2 \Gamma_0^2} \quad (\text{IV.26b})$$

where

$$\omega_p^2 = \frac{4\pi(Nf)e^2}{m}, \quad \xi^2 = \frac{4\pi(Nf_0)e^2}{m} \quad (\text{IV.27})$$

The essential feature of this dielectric function is that it contains a free electron term and a resonance term. Its influence on the NRSP dispersion curve is displayed in Figs. 15a to 15c for different values of ω_0 . Figure 15c also shows the effects of changing the relaxation time τ_0 and the resonance strength f_0 of the bound electron. From Figs. 15 we infer that if surface plasmons interact with other excitations in a liquid metal, the effects of this interaction can appear as an anomaly in the dispersion curve. The anomaly is in the form of a spike which extends into the radiative region and which peaks near the natural frequency of the interacting mode. The half-width of the resonance is primarily dependent on the density of bound states, and increases as Nf_0 increases. This should be expected because increasing the density of states interacting with the surface plasmons also increases the interaction probability and decreases the lifetime of the plasmon excitation.

3. Effects of an Inhomogeneous Surface

Only over the past few years has interest been renewed concerning the possibility that a metal-vacuum transition may not be, after all, abrupt.⁹⁵ The abrupt (zero width) transition is an idealized concept which, taken together with the continuity conditions across the discontinuous boundary, makes the mathematical solution of various problems more tractable. This problem-solving technique is by no means restricted to electrodynamics. We know, for example, that in quantum mechanical problems one often uses square-well potentials and continuity conditions on the wave function and its derivative as a first approximation to more complicated situations. However, just as more realistic potentials in quantum mechanical problems can lead to more realistic and indeed physically different results, so too might a more realistic model of the metal-vacuum transition be expected to

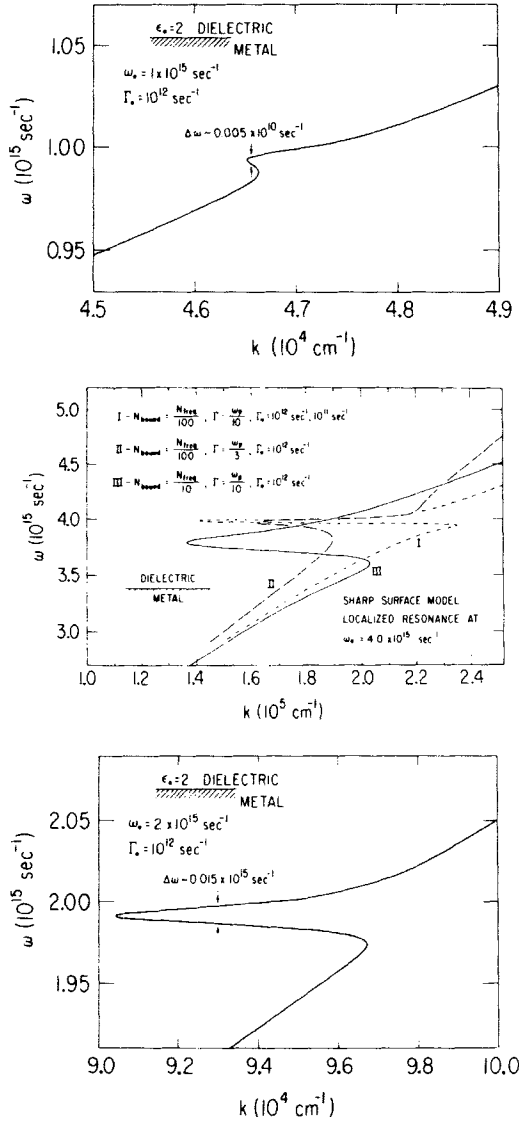


Fig. 15. The homogeneous surface dispersion relation for a semi-free-electron gas characterized by the dielectric function (IV.25). The parameters used are shown in each figure. In both (a) and (b) $Nf_0/Nf = 10^{-2}$. In (c), this ratio is varied as shown. Comparison of the three figures shows a substantial increase in both the depth and half-width of the resonance spike as $\omega_0 \rightarrow \omega_e$. This indicates a trend toward increasing coupling between surface plasmons and the electromagnetic field. In (c), curve I shows the insensitivity of the resonance spike to the bound-state damping, Γ_0 . Both $\Gamma_0 = 10^{12} \text{ sec}^{-1}$ and $\Gamma_0 = 10^{11} \text{ sec}^{-1}$ coincide with curve I. The resonance spike is highly sensitive to the damping Γ of the free electron gas as seen on comparing curves I and II. Finally, comparison between curves I and II displays the effect of varying the density of localized resonances.

lead to physically significant results, at least as far as the surface plasmon dispersion is concerned.

The development of theories of liquid metal surfaces has lagged far behind theories of the bulk properties. The extra difficulty arises of course from the loss of translational symmetry near the surface, where the electron density falls off very rapidly. Early work on metal surfaces was carried out by Frenkel⁹⁶ and Bardeen,³³ but in the quarter century or so that followed, metal surfaces were practically forgotten. In the last few years, however, the theory of metals has been generalized⁹⁷ to treat the case of inhomogeneous Fermi systems. This formulation is particularly suitable to investigations of the electronic structure of metal surfaces and has been used by several authors^{7,37,98} to calculate the free electron density profile near a metal surface, the work function, and the surface energy. But while work functions and surface energies have been measured and agreement with the generalized electron theory is reasonably good, we know of no experiment which has been successful in obtaining definitive information on the distribution of free electrons near a metal surface.

Seeking a possible tool which could be used to study the electronic structure of metal surfaces, Bennett⁷¹ has considered the influence of a nonabrupt metal-vacuum transition on the short-wavelength surface plasmon dispersion. Using a hydrodynamic model he finds that the surface plasmon dispersion, in this limit, is sensitive to the spatial variation of the electron density in the transition region, and suggests that surface plasmon spectroscopy can be a useful tool for investigating the electronic densities at metal surfaces.

Recently, Feibelman^{72,99} has investigated in more detail the influence of an inhomogeneous density of electrons on the short-wavelength surface plasmon dispersion relation. He calculated the linear dispersion coefficient and found it to be very sensitive to the spatial extent of the transition region. As yet, however, we know of no direct experimental evidence which unambiguously establishes the existence of a diffuse metal-vacuum transition. There is, of course, indirect evidence from the reflectivity-ellipsometry measurements discussed in Section III.

We consider now the effects which a spatially dependent density of electrons near a metal-dielectric interface may have on the long-wavelength surface plasmons. We take the metal to extend from $z=0$ to $z=\infty$. A dielectric medium is assumed to occupy the remaining half-space. The free carrier density in the metal is given the form

$$N(z) = \begin{cases} N_b \pm (N_s - N_b)e^{-z/a}, & z \geq 0 \\ 0, & z < 0 \end{cases} \quad (\text{IV.28})$$

N_b is the free carrier density in the bulk, while N_s may be considered as a maximum surface free electron density. We do not pretend that (IV.28) actually represents a realistic free electron density near a metal surface. Rather, our model electron density profile was chosen primarily to facilitate analytic representation of the surface plasmon dispersion. However, we believe that this model profile incorporates the most important features of the inhomogeneous electron density in a real metal, that is, a continuous variation from the bulk to the surface value. We therefore expect the qualitative results of our analysis to be indicative of the characteristic features of the surface plasmon dispersion at a real metal surface. As a consequence of (IV.28) the free electron dielectric function also becomes spatially dependent and takes the form

$$\epsilon(\omega, z) = \epsilon_1(\omega, z) + i\epsilon_2(\omega, z) \quad (\text{IV.29})$$

where both ϵ_1 and ϵ_2 are real and can be separated into bulk and surface contributions denoted by b and s :

$$\epsilon_1(\omega, z) = b_1(\omega) - s_1(\omega)e^{-z/a} \quad (\text{IV.30a})$$

$$\epsilon_2(\omega, z) = b_2(\omega) - s_2(\omega)e^{-z/a} \quad (\text{IV.30b})$$

For a free electron metal, and in the long-wavelength limit, the bulk and surface terms are

$$b_1(\omega) = 1 - \frac{4\pi e^2 \tau^2}{m(1 + \omega^2 \tau^2)} N_b \quad (\text{IV.31a})$$

$$b_2(\omega) = \frac{4\pi e^2 \tau}{m\omega(1 + \omega^2 \tau^2)} N_b \quad (\text{IV.31b})$$

$$s_1(\omega) = \frac{4\pi e^2 \tau^2}{m(1 + \omega^2 \tau^2)} (N_s - N_b) \quad (\text{IV.31c})$$

$$s_2(\omega) = \frac{4\pi e^2 \tau}{m\omega(1 + \omega^2 \tau^2)} (N_s - N_b) \quad (\text{IV.31d})$$

From (IV.29) and (IV.30) we may write the dielectric function in the more compact form

$$\epsilon(\omega, z) = b(\omega) - s(\omega)e^{-z/a} \quad (\text{IV.32})$$

where

$$b(\omega) = b_1(\omega) + ib_2(\omega), \quad s(\omega) = s_1(\omega) + is_2(\omega) \quad (\text{IV.33})$$

In the long-wavelength limit, where retardation effects play a leading role, the complete set of Maxwell's equations must be used in conjunction with a suitable transport equation. The dispersion relation is obtained by evaluating the electromagnetic fields which arise from the surface charge oscillations. These fields are present in both the metal and the dielectric. The appropriate continuity conditions are then used at the boundary ($z=0$) as a self-consistency condition which gives the surface plasmon dispersion.

In the metal, where the dielectric function is spatially dependent, the electric and magnetic fields are determined by (IV.3) and (IV.4) which we rewrite here explicitly showing the z dependence of the dielectric function

$$H_y''(z) - \frac{\epsilon'(\omega, z)}{\epsilon(\omega, z)} H_y'(z) - K^2(z) H_y(z) = 0 \quad (\text{IV.34a})$$

$$E_x(z) = - \frac{i}{\epsilon(\omega, z)(\omega/c)} H_y'(z) \quad (\text{IV.34b})$$

$$E_z(z) = - \frac{k_x}{\epsilon(\omega, z)(\omega/c)} H_y(z) \quad (\text{IV.34c})$$

where

$$K^2(z) = k_x^2 - \epsilon(\omega, z) \frac{\omega^2}{c^2} \quad (\text{IV.35})$$

In the dielectric, where the dielectric function is assumed to be spatially independent, the fields are determined by

$$H_y''(z) - K_0^2 H_y(z) = 0 \quad (\text{IV.36a})$$

$$E_x(z) = - \frac{i}{\epsilon_0(\omega/c)} H_y'(z) \quad (\text{IV.36b})$$

$$E_z(z) = - \frac{k_x}{\epsilon_0(\omega/c)} H_y(z) \quad (\text{IV.36c})$$

where

$$K_0^2 = k_x^2 - \epsilon_0 \frac{\omega^2}{c^2} \quad (\text{IV.37})$$

We have assumed throughout fields of the form

$$\mathbf{F}(\mathbf{x}, t) = \mathbf{F}(z) e^{i(k_x x - \omega t)} \quad (\text{IV.38})$$

which represents an inhomogeneous plane wave propagating along the surface in the x direction. The primes, of course, denote differentiation with respect to z .

The solution of (IV.36a), which converges for $z < 0$ (in the dielectric), is

$$H_y(z) = A e^{K_0 z} \quad (\text{IV.39a})$$

where A is an arbitrary constant. From this and (IV.36b) we obtain the electric field component parallel to the surface:

$$E_x(z) = -A \frac{i}{\epsilon_0(\omega/c)} K_0 e^{K_0 z} \quad (\text{IV.39b})$$

Now, the solution of (IV.34a) is more complicated. An approximate solution is derived in the Appendix. This solution is valid when the relative excess electron density in the surface region is small ($|g| \equiv |(N_s - N_b)/N_b| \lesssim 0.1$) and when the characteristic extent a of this region satisfies the relation $ak_x \lesssim 0.1$. The first condition limits us to excess electron densities of the order of 10% or less, while the second restricts a to a few hundred angstroms or less. Both of these requirements are easily met by what we believe to be the surface structures of most metals.^{85,95,97} Here we quote the results obtained in the Appendix:

$$H_y(z) = B e^{-K_b z} \left[1 + \frac{s}{b} \frac{bq - aK_b}{1 + 2aK_b} e^{-z/a} \right] \quad (\text{IV.40a})$$

Then, using (IV.34b), we obtain the surface component of the electric field inside the metal:

$$\begin{aligned} E_x(z) = & B \frac{i}{\epsilon(\omega, z)(\omega/c)} K_b e^{-K_b z} \left[1 + \frac{s}{b} \frac{bq - aK_b}{1 + 2aK_b} e^{-z/a} \right] \\ & - B \frac{s}{b} \frac{1}{a} e^{-K_b z} \frac{bq - aK_b}{1 + 2aK_b} e^{-z/a} \end{aligned} \quad (\text{IV.40b})$$

where $K_b = [k_x^2 - b(\omega^2/c^2)]^{1/2}$, B is an arbitrary constant, and $q = a^2(\omega/c)^2$. The dispersion relation is now obtained by matching the magnetic fields (IV.39a) and the electric field components parallel to the surface, (IV.39b) and (IV.40b), at $z=0$. The result is, after rearranging

terms,

$$\left[\frac{K_0}{\epsilon_0} + \frac{K_b}{\epsilon(0)} \right] = \frac{s}{b} \frac{aK_b - qb}{1 + 2aK_b} \left[\frac{K_b + 1/a}{\epsilon(0)} + \frac{K_0}{\epsilon_0} \right] \quad (\text{IV.41})$$

where $\epsilon(0)$ is just $b - s$.

Equation (IV.41) represents the surface plasmon dispersion at the semi-diffuse metal surface defined by the density profile (IV.28). In the limit that $|N_s - N_b| \rightarrow 0$, the metal surface becomes homogeneous, $s \rightarrow 0$, and (IV.41) reduces to the sharp-surface dispersion relation. The solution of (IV.41) for the undamped electron gas is shown in Figs. 16*a* and 16*b* for $N_s > N_b$ and $N_s < N_b$, respectively. Here as in all subsequent figures relating to (IV.41) we take the bulk plasma frequency, ω_p , to be 7.0 eV. The dielectric constant of the contact medium is assumed to be 2.0, which is a common value. The surface plasmon branch (I) and the photon branch (III) are in one-to-one correspondence with the branches of the homogeneous surface dispersion relation shown in Fig. 6, which is the limiting case of our model. In contrast, the existence of branch II in place of the usual gap between branches I and III is directly attributable to the assumed inhomogeneous electron density profile near the surface. Indeed, we note that

1. branch II vanishes in the limit $|N_s - N_b| \rightarrow 0$;
2. as shown in Figs. 16*a* and 16*b* the slope of branch II depends on the sign of $(N_s - N_b)$. It is negative when $N_s > N_b$, but becomes positive when $N_s < N_b$.

To bring out more clearly the dependence of the surface plasmon dispersion relation on the parameters which define the electron density profile, namely g and a , Fig. 17 shows branch I for various values of these parameters. It is evident that increasing g while keeping a constant shifts the dispersion curve away from the "homogeneous surface" (i.e., $g = 0$) dispersion curve, and vice versa. Keeping g constant and varying a leads to similar results. The "surface plasmon frequency" ω_s (i.e., the limit of branch I as $k_x \rightarrow \infty$) depends on a and g as is intuitively expected.

Figures 18*a* and 18*b* show how branch II is affected by the profile parameters. The slope of branch II seems to be predominantly dependent on a , while the region where branch II enters the light line (asymptotically) shows a very sensitive dependence on g and little dependence on a .

It should be noted that the energy band in which branch II exists is very narrow. It is typically of the order of a few tenths of an electron volt for the parameters which we have used.

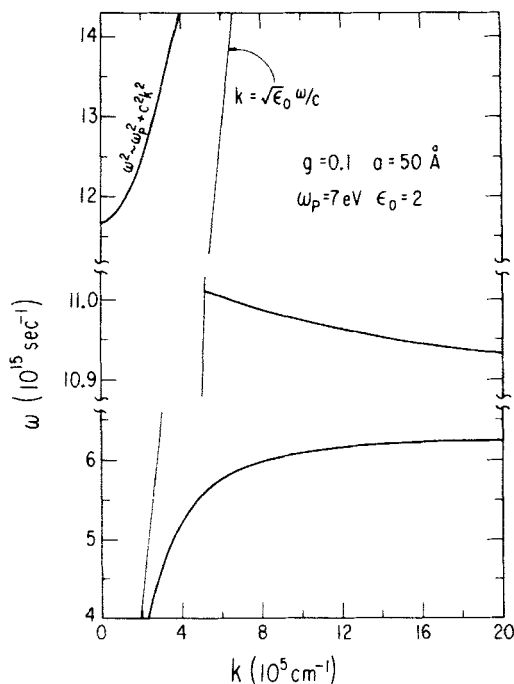


Fig. 16. The three branches of the dispersion curve as predicted by (IV.41) for (a) $g > 0$ and (b) $g < 0$. Throughout the text, branch I refers to the lower curve, branch II to the middle curve, and branch III to the upper curve. Note the scale breaks and the $10\times$ scale magnification for branch II. Branch III is almost coincident with the trivial solution $\omega^2 = \omega_p^2 + c^2 k_x^2$, but does not seem to be a trivial solution.

Figure 19 shows the detail of branch II near the light line. It is important to note that the slope of branch II is not discontinuous at the light line as might be suggested by the scale of the figures just discussed. In fact, branch II approaches the light line asymptotically just as branch I does, only much more rapidly.

To understand the origin of branch II we consider the following even simpler model, and obtain its surface plasmon dispersion relation. A homogeneous metal substrate of plasma frequency ω_{p1} is overlaid with a homogeneous thin film of thickness d and plasma frequency ω_{p2} . The film is, in turn, in contact with a semiinfinite dielectric with index of refraction $n_0 = \sqrt{\epsilon_0}$. Therefore, the free electron density is of the form (assuming $N_2 > N_1$)

$$N(z) = \begin{cases} N_1, & z > d \\ N_2, & 0 < z < d \\ 0, & z < 0 \end{cases} \quad (\text{IV.42})$$

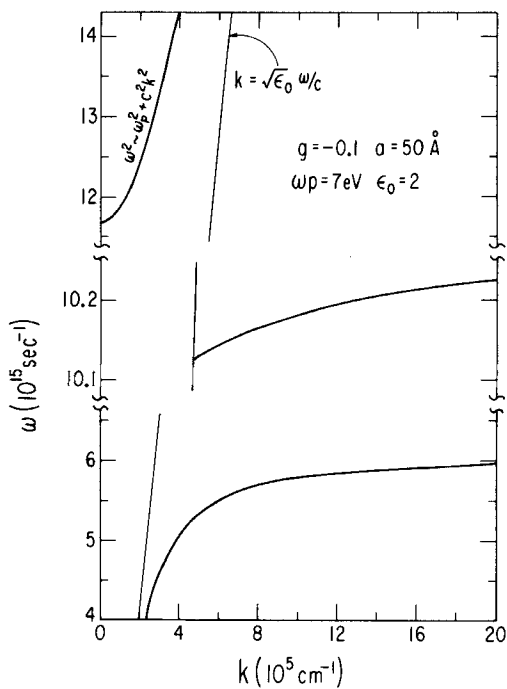


Fig. 16 (continued).

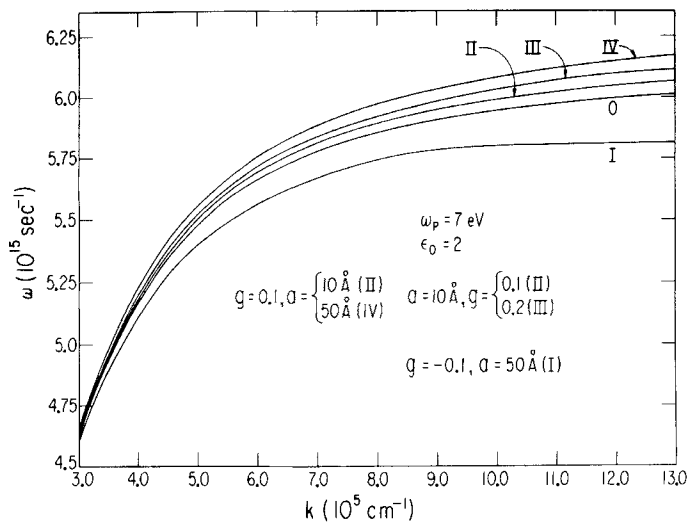


Fig. 17. Branch I for various values of the parameters a and g . Curve 0 corresponds to ; (homogeneous surface). Curves II, III, and IV correspond to $g > 0$, curve I to $g < 0$.

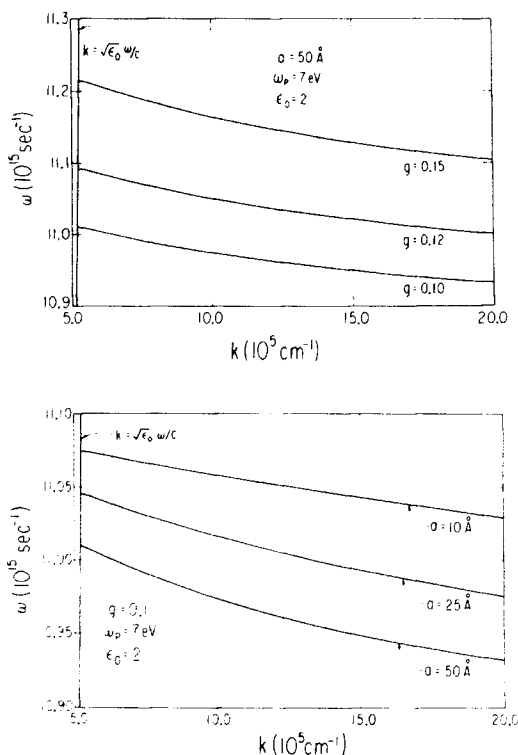


Fig. 18. The dependence of branch II on (a) g and (b) a . The slope of this branch is seen to depend primarily on a , while the region where branch II approaches the light line ($k_x = n_0 \omega / c$) depends little on a , but varies considerably with g .

In this case there are, of course, two boundaries, one at $z = d$ and one at $z = 0$; hence, two surface plasmon branches and one photon branch must appear in the dispersion relation. Indeed, the surface plasmon dispersion relation for such a system^{57,87} is

$$(\epsilon_2 K_1 + K_2 \epsilon_1)(K_0 \epsilon_2 + K_2 \epsilon_0) + (\epsilon_1 K_2 - K_1 \epsilon_2)(K_0 \epsilon_2 - \epsilon_0 K_2) e^{-2K_2 d} = 0 \quad (\text{IV.43})$$

where 1, 2, 0 refer to the substrate, film, and dielectric, respectively, and $K_j = [k_x^2 - \epsilon_j(\omega^2/c^2)]^{1/2}$ ($j = 0, 1, 2$).

The solution of (IV.43) is qualitatively similar to that of (IV.41) displayed in Figs. 16a and 16b. A second branch again appears in the gap between the lower and the upper branch and behaves just as branch II does. Figure 20 shows the behavior of this intermediate branch near the light line. Its behavior is remarkably similar to that of branch II shown in Fig. 19.

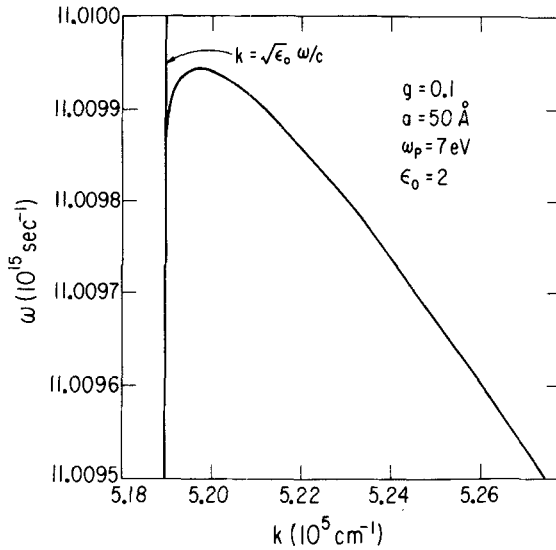


Fig. 19. Details of the asymptotic behavior of branch II near the light line for the parameters listed in the figure. Note the branch II approaches the light line some three orders of magnitude faster than does branch I.

For further comparison we display, in Fig. 21a, the dependence of branch II on a as predicted by (IV.41). In Fig. 21b we display the dependence on d of the corresponding branch as predicted by (IV.43). Note the two are remarkably similar. From Fig. 21b we see that at large wave vectors, the intermediate branch is asymptotic to $\omega_{\text{rms}} \equiv [(\omega_{p1}^2 + \omega_{p2}^2)/2]^{1/2}$. This is actually the case for all values of d . We see a similar

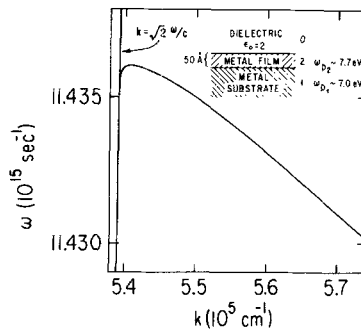


Fig. 20. Details near the light line of the second dispersion branch which appears as a solution of (IV.43) for the undamped free electron gas. Note the striking similarity with Fig. 19. There we have used $d = 50 \text{ \AA}$ and $(N_2 - N_1)/N_1 = 0.1$ as parameters comparable to the a and g of Fig. 19.

behavior in Fig. 21a although an analytical expression for this limit is not easily obtained from (IV.41).

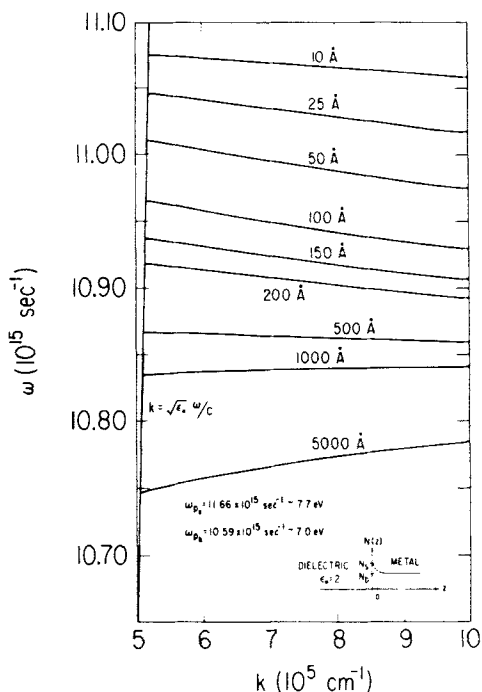


Fig. 21. Comparison between (a) the dependence of branch II on a for the exponential surface profile, and (b) the dependence of the corresponding branch on d for the homogeneous thin film model. In (a), the curves are labeled by the surface diffusiveness parameter a . In (b), the labels denote the thickness d of the homogenous surface film.

Figure 21b further shows clearly the origin of the intermediate branch, at least as far as this simple model is concerned. We can imagine what happens as d starts out very small and gradually increases and becomes very large. For small d we expect the charge fluctuations at the two boundaries to interfere through their overlapping fields. As d increases, however, because of the exponential attenuation of the surface plasmon fields, the overlap and therefore the interaction also decreases. When d has become sufficiently large (two or three decay lengths, or roughly 1000 Å for the parameters used here) interaction should not occur and the intermediate branch should coincide with the dispersion curve corresponding to two semiinfinite metals. This is indeed what Fig. 21b shows. The inter-

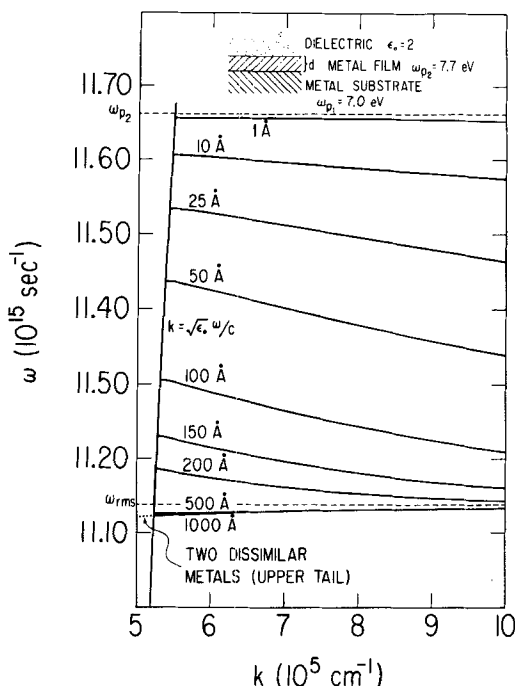


Fig. 21 (continued).

mediate branch, as predicted by (IV.43) for $d = 1000 \text{ \AA}$, coincides with the upper tail (that part which would be accessible in an FTR measurement) of the dispersion curve corresponding to surface plasmons at the interface between two semiinfinite metals with corresponding parameters (dashed curve). This behavior is indeed inherent in (IV.43). Taking the limit $d \rightarrow \infty$, two noninteracting modes are clearly seen to arise:

$$\epsilon_2 K_1 + \epsilon_1 K_2 = 0 \quad (\text{IV.44a})$$

$$\epsilon_2 K_0 + \epsilon_0 K_2 = 0 \quad (\text{IV.44b})$$

Equation (IV.44a) is just the dispersion relation for a metal-metal interface, while (IV.44b) is the dispersion relation at a metal-dielectric interface. The full dispersion curve predicted by (IV.44a) is shown in Fig. 22. Of course, such a simple analysis is not possible for Fig. 21a because there we have only one actual boundary. This observation itself is very important, for we may infer from it that localized plasma oscillations do not arise as a

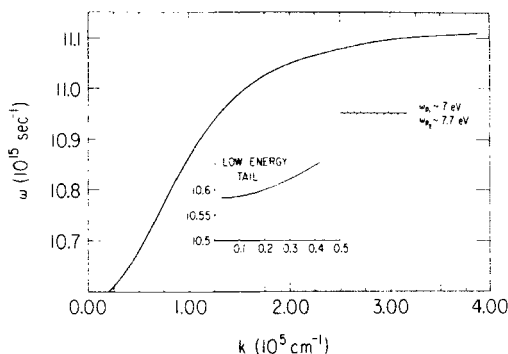


Fig. 22. The dispersion curve of surface plasmons at a bimetallic interface. Damping is neglected and the free electron densities of the two metals are taken to differ by 10%.

consequence of consistency conditions at boundaries as such, but that they can exist as local excitations in the vicinity of any charge inhomogeneity.^{93,94,100} Another way of putting the same thing is to note that when the density inhomogeneity occurs on a scale small compared with a plasmon wavelength it mimics a discontinuous boundary, and when that inhomogeneity occurs on a scale commensurate with the plasmon wavelength, it cannot be seen at all.

F. The NRSP at an Epstein-Stratified Mercury Surface

In this section we describe the results of calculations that evaluate the sensitivity of the surface plasmon dispersion relation in the optical regime to the presence of the inhomogeneous surface zone which Bloch and Rice⁸ have proposed for liquid mercury. Retardation of the electromagnetic fields has been included in these computations, in contrast to the approximation $c^{-1} \rightarrow 0$ which is frequently made in hydrodynamic and RPA treatments that attempt to include electronic relaxation near the surface. The latter treatments are consequently valid only in the high-energy ($E \approx \hbar\omega_{sp}$), high-momentum ($k \gtrsim \omega_p/c$) region and are more useful for the description of plasmon excitation by electron energy-loss techniques than for optical studies. As emphasized earlier, we expect the surface profile to have greatest impact where the dispersion of the plasma waves departs most from linearity. It should be noted, therefore, that the inclusion of retardation in the electrodynamic treatment of surface plasmons is responsible for the curvature characteristic of the dispersion relation (see Fig. 6).

Whatever else its shortcomings, the adoption of the Bloch-Rice profile in these calculations is an attempt to test the hypothesis that NRSP disper-

sion can be used to probe the structure of a liquid metal surface while simultaneously requiring consistency with other data for the same system. Thus, the calculations represent a realistic first test of whether or not NRSP dispersion can be useful in the context envisioned.

In these calculations the means of coupling light waves to the surface excitation of the liquid metal was taken to be the frustrated total reflection method, for the prism-film coupling system should disturb the fundamental nature of the surface zone least among the possible coupling techniques and is mathematically simplest.

The surface plasmon dispersion has been determined by applying Maxwell's equations (III.23b) for incident p -polarized radiation to the skewed Epstein-stratified transition layer. As pointed out by Bloch and Rice, the analytic structure of the Epstein profile (III.22) does not permit direct analytical solution of the TM components of Maxwell's equations, precisely those components which give rise to surface plasma waves. It is therefore impossible to obtain a dispersion relation of the type (IV.41) in closed form for the mode which is strictly bound to the Epstein-stratified mercury surface. Numerical evaluation of such a dispersion relation is possible, but as these bound surface plasmons are not directly observed optically, it is preferable to solve for the modes of a prism-spacer-mercury system. In doing so, one must take proper account of the radiative damping of the NRSP as described by Otto.⁸⁷

The Herpin matrices of Section III.C have been used to calculate the optical response of mercury to NRSP excitation, with an additional layer s , corresponding to the spacing film of the coupler, and with appropriate additional boundary conditions at the prism-film and metal-film interfaces. The refractive index of the prism was taken as $n_p = 2.53$, that of the spacer as $n_s = 1.39$, and the film thickness d , a critical parameter in determining the degrees of photon-surface plasmon coupling and radiative damping, depended on the frequency in a manner which is described in detail below.

Results which are typical of the optical response calculations are illustrated in Figs. 23 to 25, which show that the surface plasmon at a diffuse interface should behave quite differently from the NRSP at a perfectly sharp boundary with effective optical constants as measured by ellipsometry or reflectivity. The ellipsometric curves shown are based on the measurements of Faber and Smith,⁵³ which extended to a maximum energy of about 3 eV. The plasmon is photon-like at lower energies, its dispersion approaching the light line $\omega = ck_x/n_s$ as $\omega \rightarrow 0$. Even at these low energies (≈ 1 to 2 eV) there is a noticeable difference between the Drude free electron and transition zone reflectivity minima. The ellipsometric sharp surface, although displaying behavior that is much closer to calculations for the diffuse surface model, should still be distinguishable from the

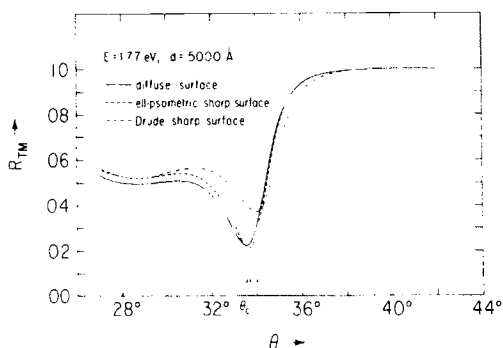


Fig. 23. Transverse magnetic reflectivity R_{TM} for $E = 1.77$ eV and three models of the liquid mercury surface: diffuse, with skewed Epstein profile; sharp surface, with ellipsometric optical constants; sharp surface, with Drude optical constants. All computations performed for FTR geometry with spacer thickness d and parameter values described in the text. Arrows locate the abscissas of minimum reflectivity, or maximum coupling to the NRSP.

latter by careful experimentation. This closer agreement is of course to be expected, since the ellipsometric optical constants reflect a nonzero contribution from p -polarized light.

It is apparent from the figures that as the energy increases, the three possible surface models give rise to NRSP absorption which becomes increasingly different. Thus, at 1.77 eV, the angular separation of the reflectivity drops for diffuse and ellipsometric surfaces is only about 0.1° ; by 3.06 eV, it has increased to approximately 0.2° . The diffuse and free electron minima, by way of comparison, are separated by 0.5° at 1.77 eV and 1.1° at 3.06 eV.

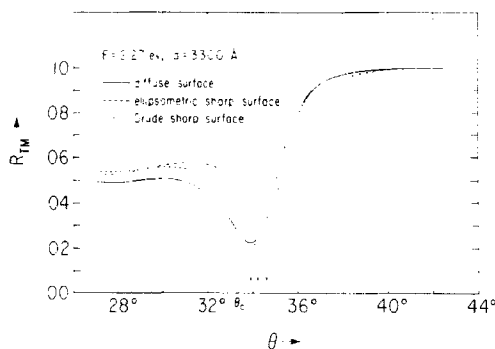


Fig. 24. Transverse magnetic reflectivity R_{TM} for $E = 2.27$ eV and three models of the liquid mercury surface. Computations as in Fig. 5.

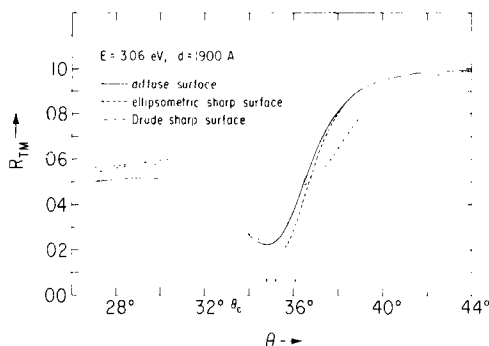


Fig. 25. Transverse magnetic reflectivity R_{TM} for $E = 3.06$ eV and three models of the liquid mercury surface. Computations as in Fig. 5.

In order to evaluate “ellipsometric” sharp-surface reflectivities at still higher energies (> 3.06 eV), where the differences between models are expected to be even more pronounced, it was first necessary to compute a set of apparent optical constants characterizing the Hg surfaces. These calculations were performed in the same manner that Bloch and Rice originally found effective optical constants in good agreement with existing ellipsometric data: by calculating r_p and r_s , the amplitude reflection coefficients of a vacuum-Hg nonuniform interface, at 78° incidence, and then inverting the sharp-surface Fresnel relations to give apparent values for the real and imaginary parts of the dielectric constant ϵ_m .

By employing this expedient, the apparent optical constants were evaluated for energies between 3 and 5 eV. It is worth reemphasizing the significance of these constants for the subsequent analysis: They are the values of $\text{Re}(\epsilon_m)$ and $\text{Im}(\epsilon_m)$ that would be measured in an ellipsometric experiment at 78° incidence *if the skewed profile were completely accurate*. The optical response of Hg to NRSP excitation is illustrated in Figs. 26 to 28 at these higher energies for the full profile, a free electron sharp surface, and an equivalent “ellipsometric” sharp surface. Once again, the absorption should be measurably different for the three cases. The differences between the lower two curves in these figures illustrate quite convincingly that the shifts observed in Figs. 23 to 25 are due to the structure of the transition region, and are not simply an artifact of the slight deviation in the Bloch-Rice fit to ellipsometric measurements.

The NRSP dispersion relation may be determined over a range of energies by measuring the angle of minimum reflectivity, corresponding to maximum coupling to the excitation, from several sets of calculations. The effect of the surface zone, most noticeable at high energies, has been

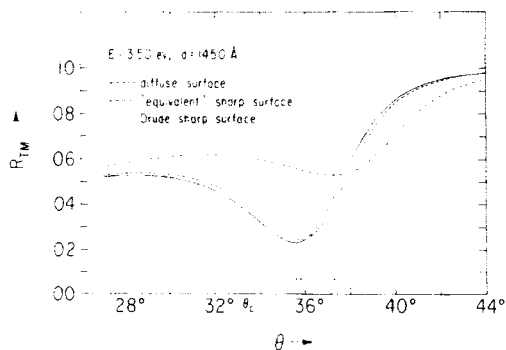


Fig. 26. High-energy reflectivity calculations, for $E = 3.50$ eV and three models of the liquid mercury surface: diffuse, with skewed Epstein profile; sharp surface, with “equivalent” optical constants; sharp surface, with Drude optical constants. FTR parameters as in Fig. 5.

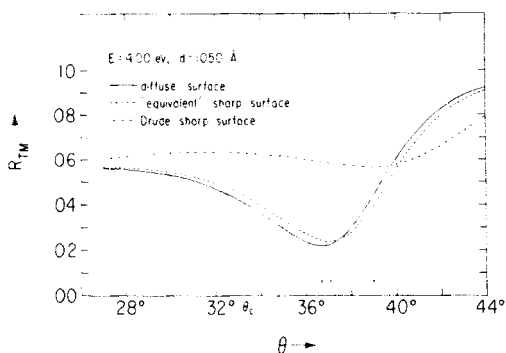


Fig. 27. High-energy reflectivity calculations, for $E = 7.00$ eV and three models of the liquid mercury surface. Computations as in Fig. 9.

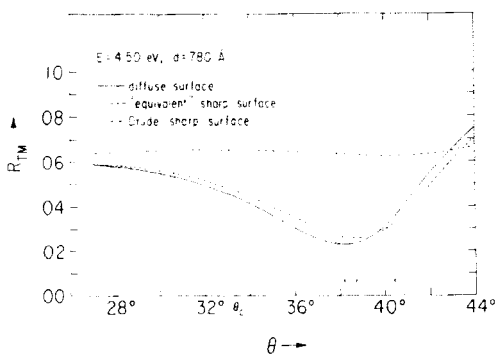


Fig. 28. High-energy reflectivity calculations, for $E = 4.50$ eV and three models of the liquid mercury surface. Computations as in Fig. 9.

evaluated from 3.5 to 5.5 eV, where interband effects start to become important, and is shown in Fig. 29. We note, in particular, the shift of the dispersion relation toward the radiative regime. This finding is consistent with the higher effective electron density in the transition region, and with the semidiffuse surface profile discussed in Section IV.E.3.

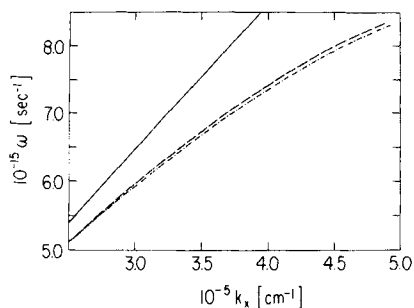


Fig. 29. Dispersion relation for surface plasmons at a liquid mercury-dielectric interface, for FTR geometry. Dashed curve is dispersion relation for full inhomogeneous profile; dot-dashed line, for an ellipsometrically equivalent sharp surface. Absorption at a Drude sharp surface is heavily damped at these energies, so the resulting dispersion is not shown. Solid curve represents the light line $\omega = ck_x/\hbar$, in the dielectric spacer layer.

In the determination of the NRSP dispersion which has been presented above and summarized in Fig. 29 for a mercury surface possessing a nonuniform conductivity profile, there are a number of fine points which deserve further elaboration. For the sake of simplicity, though, we first bring out these subtleties for the surface plasmons which have been studied in Section IV.B at a sharp boundary of zero thickness. At a homogeneous metal surface, the NRSP was identified as that mode of electronic excitation which was completely bound to the metal-dielectric boundary. In the FTR geometry of Fig. 13 this defining condition had to be generalized somewhat; because of the existence of two boundaries in close proximity, there was no mode which was strictly bound to the metal-thin film interface. The surface plasmon was in that case specified by assuming only incoming light waves in the prism. Application of this condition results in a normal mode for which energy can be transported in one direction only if one takes k_x real: from the incoming waves in the prism to the NRSP at the metal-spacer interface. In effect, the normal modes of (IV.21) correspond to complete frustration of the total reflection that is ordinarily anticipated for $\theta > \theta_c$.

In actual practice the surface plasmon is rarely observed with complete absorption of the incident radiation. It is customary, rather, to observe a

distinct reflectance drop as a function of angle of incidence (for p -polarization), with the minimum of R_{TM} located in the neighborhood of the resonance angle defined by (IV.20). The magnitude of these dips may range from as little as 10% to more than 90% with half-widths from fractions of a degree to several degrees. The exact nature of a particular drop depends, of course, on the parameters of the coupler, the metal, and the frequency employed.

The distinction between a surface plasmon defined by total absorption and the experimentally observed structure which displays a small but nonzero reflectivity may not be merely academic in the context of small but observable surface effects which we expect liquid mercury to manifest. The residual reflectivity is associated with radiative damping of the surface plasma excitation, a phenomenon which arises because light can couple out a prism-thin film system as well as coupling to the nonradiative mode in the first place. But the existence of such a damping mechanism should cause a shift in the location of the surface resonance, this shift being engendered by the reactive effects of the outgoing radiation. The general principles governing such a shift apply to all radiatively damped resonances. We wish now to consider the importance of this effect, a task most readily accomplished by evaluating the displacement of the angle of minimum reflectivity as the spacer thickness d is varied. From the work of Otto⁸⁷ on the NRSP in silver it may be seen that, at a constant frequency $\omega = 3.45 \times 10^{15} \text{ sec}^{-1}$, when the spacer thickness decreases from 3000 to 1000 Å, the reflectivity (in this case, actually the reflectivity ratio $R_{\text{TM}}/R_{\text{TE}}$) increases from approximately 0 to roughly 80%. The change in position of the resonance as a result of this drastic shift in radiative damping is from approximately 54° incidence on the prism base to approximately 58° incidence—certainly a significant change when compared with the peak separations which have been noted for the three “plausible” surface models of mercury.

The calculations presented in Fig. 29 represent the dispersion relation over several electron volts, a relatively large energy range. Because of this fact, it proved impossible to achieve coupling to the NRSP over the entire energy range with a single spacer thickness, so d was allowed to vary with frequency in such a way that observable surface plasmon absorption occurred. Furthermore, d was varied so as to maintain constant radiative damping at each frequency for which the reflectivity was calculated. The condition was imposed largely in an ad hoc way: Appropriate values of d were determined by requiring the residual reflectivity R_{TM} to remain roughly constant, $R_{\text{TM}} \approx 0.2$, as the frequency was varied. In doing this we took advantage of the fact that the calculations described here were not limited in the same way as most experiments by the availability of prisms with only a few coating (spacer) thicknesses.

Having described the methods of computation and the numerical results of our study of NRSP excitation in liquid mercury, it is instructive to backtrack for a moment and analyze the surface plasmon calculations in the light of Herpin's theorem⁵² in order to gain a better understanding of why the type of surface plasmon experiment proposed here is capable of yielding information which is basically distinct from that generated by the classical optical methods. A well-known principle in optics, Herpin's theorem states that any stratified medium—and therefore, any continuous, nonuniform medium approximated by a large number of thin homogeneous films—can be reduced to an equivalent system composed of only two layers. The proof of this assertion rests on the fact that each of the Herpin matrices \mathbf{S}_j may be expressed as a linear combination of Pauli spin matrices, and therefore any continued matrix product of the \mathbf{S}_j can also be so expressed. By appropriate choice of optical constants and thicknesses of the equivalent double layer, the continued product may thus be represented as

$$\mathbf{Q} = \prod_{j=1}^N \mathbf{S}_j = \mathbf{S}_A \cdot \mathbf{S}_B \quad (\text{IV.45})$$

In considering the implications of Herpin's theorem for a stratified diffuse transition layer at a liquid metal surface, one is struck immediately by the fact that a particular double layer may be associated with several very different transition zones. Indeed the investigations of Bloch and Rice⁸ revealed a number of models for the diffuse mercury surface, all based on the Epstein profile (III.22), but with different values for the parameters of the quasi-free-electron and localized-state surface regions. From a naive point of view, the equivalence of several profiles to a single double-layer system might be taken as evidence that optical methods, surface plasmon absorption included, are fundamentally limited in the scope of information they can reveal about an inhomogeneous surface layer. It might be further supposed, according to this line of reasoning, that all optical experiments will exhibit the same sensitivity to the structure of an inhomogeneous region, since they all appear to sample the same equivalent double layer, and should therefore produce results which are basically equivalent rather than complementary. While we accept the former argument that the relation between transition zones and a set of optical results is homeomorphic rather than isomorphic, we reject the latter assertions. To support this conclusion, and to show why optical excitation of plasma waves at a liquid metal surface should provide a new and reasonably sensitive probe of surface structure, it is useful to reexamine Herpin's theorem somewhat more carefully.

It is to be noted, first of all, that each of the elements of the Herpin matrix \mathbf{S}_j is a function of several variables: the parameters characterizing

the j th layer, ϵ_j and δ_j , and, in addition, the frequency ω , angle of incidence θ in the homogeneous contact medium, and the dielectric constant of that medium, ϵ_c . As a result, each element of the product matrix \mathbf{Q} incorporates a rather complicated dependence on these parameters, which in turn is exhibited in the discrepancies that occur among apparent optical constants calculated from normal incidence and ellipsometric measurements.

Let us now assume the existence of several diffuse profiles, each fitting the apparent optical constants at a metal-dielectric interface over a wide range of angles and frequencies. We are interested in the behavior of the Herpin matrices and the equivalent double layer for a surface plasmon experiment under conditions of frustrated total reflection. Light that is incident on the prism-film surface in such an experiment gives rise to a characteristic exponential decay of the field amplitudes in the coupling film. As is well known, this sort of field modulation corresponds to a complex angle of transmission within the spacer layer, so that the radiation is incident on the thin film-mercury interface at a complex angle, too. It is this complex angle of incidence which distinguishes surface plasma excitation by frustrated total reflection from other optical techniques, and which leads to its greater sensitivity to surface structure. In physical terms, the complex angle of incidence at the mercury surface results in a larger parallel momentum transfer than is possible by classical optical methods, as stressed in Section III. Consequently, the decay length for the fields, given by $(\text{Re}(K_m))^{-1}$ in a homogeneous metal, is smaller, and the surface plasmon excitation should reflect surface anomalies more strongly.

V. CONCLUSIONS AND SPECULATIVE REMARKS

The primary objective of this section is to evaluate the results which have been obtained in Section IV regarding the use of NRSP spectroscopy in the study of liquid metal surfaces, and, more generally, in the investigation of any conducting surface with nonuniform electronic structure. In performing this evaluation we analyze both the strengths and the limitations which the analysis has revealed, and we suggest ways in which the sensitivity of NRSP absorption might be increased beyond that of the FTR technique. From the comparison of the NRSP dispersion predicted for simple models and the "realistic" Bloch-Rice model, a number of important conclusions emerge which clarify our interpretation of surface plasmon absorption at the liquid metal surface. In particular, we establish several criteria concerning the appearance of distinctive structure in the NRSP dispersion relation—structure which is associated with "anomalous" electronic properties at the surface.

One of the limitations on NRSP spectroscopy in liquid mercury is the fact that the differences which have been calculated in optical response

between an Epstein-stratified mercury surface and a zero-thickness Drude or ellipsometric surface are not as large as might have been expected, in view of the 10% discrepancy between the apparent optical constants measured by ellipsometry and reflectivity. Nonetheless, one should be able to detect these differences experimentally, particularly at higher energies where the reflectance drops are separated by several tenths of a degree or more. We note with special interest the fact that reflectivity calculations for the two Bloch-Rice profiles mentioned in Section III, one symmetric and the other skewed, indicate that the two profiles should be distinguishable in a surface plasmon experiment at high energies, although they correspond very nearly to the same equivalent double-layer system at lower energies and for the conventional optical techniques.

A second limitation is posed by the high degree of internal damping that exists in mercury, a phenomenon which is mathematically represented by the large imaginary part of the dielectric constant. With increasing energy this internal damping results in broadening of the resonance to a point where definition of the mode becomes problematical. As a result, it would appear difficult to observe surface plasmons in mercury by the FTR technique above 5 or 6 eV.

By imposing an external electric field at the mercury surface one might be able to overcome the limitations mentioned above and distinguish more readily the surface plasmon absorption due to different surface models. One would expect the surface dipole layer in mercury to be enhanced by such a technique; indeed, a recent microscopic treatment of metal surfaces by Lang and Kohn^{7,95} shows that a static external field should have precisely this effect of drawing the centers of positive and negative charge apart. An additional means of increasing the sensitivity of a surface plasmon experiment might be to impose a modulating electric field which is slowly varying in time in conjunction with a static external field. The resulting experimental configuration would be much like the electoreflectance technique which has been widely applied to semiconductors in recent years.¹⁰¹

In addition to the measurably large shift of the NRSP dispersion in mercury toward the radiative regime, caused by the fact that the effective electron density at the surface is greater than that in the bulk metal, there are a number of additional features which, on theoretical grounds, might be expected to play a role in the spectrum of surface plasma oscillations at a diffuse mercury surface. Among these features we note the possibility of interaction between the localized electronic states assumed in the Bloch-Rice model and the collective surface plasma mode. Just as the NRSP is known to interact with phonon modes which are localized at a surface, one might anticipate a mixing of plasmon and localized electronic states. Such

an interaction, if not occurring naturally between the NRSP and the localized states arising from the metal-to-nonmetal transition in the low-density region of the surface zone, might always be introduced by alloying or by adsorption of suitable species at the mercury surface.

In Section IV.E we described a simple model of the NRSP-localized state interaction. The model is based on the premise that the nonuniform structure of a metal surface can be neglected, in a first approximation, when one considers interactions between the two types of electronic states. Thus, throughout the metal the dielectric function is assumed to contain a Lorentzian contribution arising from a small fraction of localized resonances in addition to the predominant contribution due to nearly free electrons. The dispersion relation which results from this localized-state model departs significantly from the free electron case.

In order to evaluate the effect that localized states might have on the NRSP in mercury, we have also carried out several FTR calculations of the sort described in Section IV.F at low energies, close to the localized-state resonance of the Epstein profile. The NRSP at these energies was found to be shifted entirely to the radiative regime, continuing the general trend for decreasing energy which is depicted in Fig. 29. While this appears to be the first time that such a drastic change has been noted for the surface plasma excitation—from nonradiative to radiative character—there is no noticeable structure which can be ascribed to the localized states. In fact, the optical response undergoes little change even when the region of localized states is partially or completely removed from the surface transition zone, in accord with the suggested cutoff of Crozier and Murphy.⁵⁵

Faced with an apparent discrepancy between surface plasmon calculations in mercury and the normal mode model described in Section IV.E, we now take note of some important differences between the two treatments. First of all, we point out that localized states in the Bloch-Rice transition zone occur over a region of only a few Ångströms, a distance which is quite small when compared with the decay length for surface plasmons in mercury at optical frequencies (≈ 200 Å). By contrast, the localized resonances in Section IV.E are assumed to occur throughout the entire metal sample. Second, in the Bloch-Rice surface layer, there is a sharp cutoff between the region of localized-state conduction and nearly free electron conduction. Since surface plasma waves originate basically in oscillations of the nearly free electrons, spatial separation of the two types of electronic states undoubtedly decreases the tendency for localized and plasmon states to interact.

In spite of the negative findings of the just-mentioned Epstein profile calculational search for surface plasma-localized resonance interactions, the normal mode model should be of significant value in interpreting

surface diagnostic studies of liquid metals. As mentioned above, localized states may be introduced by alloying. In this connection we note that the alloy transition zones which have been fitted to experiment by Siskind, Boiani, and Rice⁵⁶ give reason to suspect that the interaction of the collective surface mode and individual electronic states may be stronger in the alloy than in a pure liquid metal. The decay length Λ associated with the differential concentration gradient in an amalgam of mercury and indium is found to be about 30 Å, a distance much larger than the region suggested to be occupied by localized states in pure mercury.

There is another way in which the normal mode calculation may aid in understanding surface plasmon absorption in mercury. We recognize that the Epstein profile advanced by Bloch and Rice is based on a fit to experimental results, and as such lacks a fundamental theoretical justification. It is reasonable to suppose, therefore, that the corresponding modeled nonuniform conductivity does not fully incorporate all features which a realistic transition zone might possess. If the Mott transition is broadened at the liquid metal surface so that the zones of free and localized conduction processes overlap, for instance—an effect which might be brought about by the mobility of the liquid metal ions—the NRSP-localized state mixing may well be manifested more prominently in the surface plasmon dispersion relation.

The semidiffuse surface model described in Section IV.E takes account of inhomogeneity in the charge distribution but not of localized resonances. The nonuniformity is expressed in terms of an exponential profile for the electronic density, and the assumption is made that all electrons can be treated as quasifree particles. In calculations with this exponential model, an additional nonradiative branch has been found in the surface plasmon dispersion relation which is located in a narrow frequency band between the surface plasma frequency and the plasma frequency. The new branch appears to result from the fact that an inhomogeneous structure with a large gradient in its electronic properties mimics, to a certain extent, a system composed of a homogeneous metal substrate overlaid by a thin metal film, which is in turn bounded by a semiinfinite dielectric. In an idealized system such as this, with two metal boundaries, two surface plasmon branches should occur, corresponding to charge oscillations which are localized at either the substrate-film or film-dielectric interfaces.

If the monotonic approximation (IV.28) for the electron density at a metal surface contains an additional branch in the spectrum of surface plasma oscillations, it may be expected, a fortiori, that the Epstein profile postulated by Bloch and Rice should give rise to a second branch also. We anticipate this because the sharply peaked Epstein profile resembles a

discrete film-substrate system much more closely than the exponential form (IV.28). In the exponential calculations a second branch is predicted for relative surface excesses $|N_s - N_b|/N_b$ as low as 10%; by comparison, the symmetric Epstein profile with $\sigma_{0s} = 48\sigma_{0b}$ corresponds to an excess surface concentration many times larger. Moreover, the gradient of the electronic properties (e.g., conductivity) is much greater for the Epstein profile than it is for the exponential model.

Despite these favorable signs for the appearance of a second surface plasmon branch in mercury, a number of additional factors must be considered when we attempt to predict the behavior of a real physical system such as mercury from a simple model like the one defined by (IV.28). Since the work of Ehrenreich and Phillips on the optical properties of silver,¹⁰² it has been known that the effect of interband transitions on the plasma oscillations of a conducting medium is to renormalize the plasma frequency from a quasi-free-electron value given by

$$\omega_p = \left(\frac{4\pi N e^2}{m} \right)^{1/2} \quad (\text{V.1})$$

to a value defined by the condition that the real part of the dielectric constant vanish:

$$\text{Re}[\epsilon_m(\omega_p)] = 0 \quad (\text{V.2})$$

In a similar way, it should be apparent that the change in dielectric screening resulting from interband absorption renormalizes the surface plasmon frequency so that it satisfies

$$\text{Re}[\epsilon_m(\omega_{sp})] + \epsilon_d = 0 \quad (\text{V.3})$$

when the conductor is bounded by a medium of dielectric constant ϵ_d .

If we apply conditions (V.2) and (V.3) to liquid mercury bounded by vacuum, we find from the near-normal reflection measurements of Wilson and Rice¹⁰³ that the plasma energy $E_p = \hbar\omega_p$ is renormalized from a quasi-free value of 15 eV to about 7 eV for the electron gas with interactions screened by interband effects. Analogously, the surface plasma energy $E_{sp} = \hbar\omega_{sp}$ is shifted from 10.5 eV to a screened value of 6 eV. The two energies are shifted to within about 1 eV of one another, similar to the change that is observed in silver.¹⁰²

The importance of taking interband transitions into account becomes apparent when we consider the second NRSP branch in the light of Feibelman's microscopic analysis of interfacial plasmons at bimetallic junctions.⁹⁰ The surface plasma frequency characterizing the bimetallic

interface is given by

$$\omega_{sp}^2 = \frac{1}{2}(\omega_{p_1}^2 + \omega_{p_2}^2) \quad (\text{V.4})$$

where ω_{p_1} and ω_{p_2} are plasma frequencies of the two semiinfinite metals. In the short-wavelength limit. Feibelman points out that if $\omega_{p_1} > \omega_{p_2}$, then surface plasma oscillations localized at the boundary in metal 1 will be degenerate in energy with bulk plasmons in metal 2. Therefore, surface plasmons occurring in the frequency range between ω_{p_1} and ω_{p_2} should be able to decay by continuous transfer of energy to the bulk modes which propagate on the low-electron-density side of the junction. Furthermore, Feibelman demonstrates that when the electron densities are in the relation $n_1 \gtrsim 3n_2$, Landau damping of the bulk mode in metal 2 becomes very important, the bulk plasma oscillations then decaying into single-particle excitations of the low-density electron gas. This additional damping mechanism should be reflected in the "real" dispersion and the width of surface plasmon absorption at the bimetallic interface.

Turning once again to the propagation of surface plasmons in mercury in the presence of a surface transition layer, it is of particular interest to apply Feibelman's analysis of the surface mode at a diffuse bimetallic junction to the second branch which has been found at an inhomogeneous conducting surface that is bounded by a dielectric. As was pointed out earlier in Section IV, such a surface mimics the behavior of a metal film-metal substrate system. For the particular case of mercury, a film-substrate combination may be numerically determined¹⁰⁴ (by a fitting procedure similar to the one employed by Bloch and Rice) which possesses apparent optical constants in good agreement with ellipsometric and reflectometric measurements. The effective dc conductivity σ_{0f} of the film in this equivalent system is many times larger than the dc conductivity of bulk mercury, σ_{0b} . We observe, therefore, that the effective density of free electrons in the film is much larger than that in the bulk. Because of the latter relation, Feibelman's treatment suggests that the upper surface plasmon branch in mercury, which corresponds to charge oscillations at the bimetallic film-substrate boundary, should be strongly damped by decay into bulk plasmons in the substrate which may be subsequently subjected to strong Landau damping themselves.

The renormalization of plasma energies which occurs because of interband transitions may alter this conclusion significantly. If interband effects in the surface layer—which are probably different from those in the bulk—lower the film plasma frequency sufficiently, the degree of Landau damping will be altered and its influence perhaps largely eliminated. The appearance of a distinct second branch in the surface plasmon spectrum of

mercury can thus serve as a measure of the electronic interactions occurring in the surface transition zone.

The analyses presented above are, of course, highly speculative. They have not been aimed at achieving a conclusive and rigorous theory of surface plasma waves in liquid mercury, as the exact nature of the surface transition zone is still largely unknown. Rather, it has been our purpose in this section to suggest several lines of profitable inquiry and to develop a conceptual structure within which a rigorous theory may eventually be defined. We believe that the present investigation marks surface plasmon absorption by frustrated total reflection as a useful technique for the study of conducting surfaces. In conjunction with appropriate modulation, alloying, or adsorption techniques to emphasize various features of the surface, the study of surface plasma waves should provide much information in the future on the microscopic structure of liquid metal surfaces.

Acknowledgments

SAR, DG and HL thank the National Science Foundation for support of their research. WCM and ANB thank the donors of the Petroleum Research Fund, sponsored by the American Chemical Society, for partial support of their research.

APPENDIX

Here we show how we may obtain a first-order solution of (IV.34a). Making use of the transformation

$$\begin{aligned} H_y(z) &= x^\alpha U(x) \\ x &\equiv e^{-z/a} \end{aligned} \quad (\text{A.1})$$

where α is a constant yet to be determined, (IV.34a) becomes

$$\begin{aligned} \frac{x^2}{a^2} U''(x) + \frac{x}{a} \left[\frac{2\alpha}{a} + \left(\frac{1}{a} + \frac{\epsilon'(x)}{\epsilon(x)} \right) \right] U'(x) \\ + \left[\frac{\alpha(\alpha-1)}{a^2} + \frac{\alpha}{a} \left(\frac{1}{a} + \frac{\epsilon'(x)}{\epsilon(x)} \right) - K^2(x) \right] U(x) = 0 \end{aligned} \quad (\text{A.2})$$

The primes, of course, indicate differentiation with respect to x . Equations (IV.32) and (IV.35) may be rewritten in terms of x :

$$\epsilon(x) \equiv \epsilon(\omega, x) = b(\omega) - s(\omega)x \quad (\text{A.3})$$

$$K^2(x) = K_b^2 + s \frac{\omega^2}{c^2} x \quad (\text{A.4})$$

where $K_b^2 = (K_x^2 - b\omega^2/c^2)$. Substituting (A.3) and (A.4) into (A.2) we obtain

$$\frac{x^2}{a^2} U'' + \frac{x}{a} \left[\frac{2\alpha}{a} + \left(\frac{1}{a} + \frac{(s/a)x}{b-sx} \right) \right] U' + \left[\frac{\alpha^2}{a^2} + \frac{\alpha}{a} \frac{(s/a)x}{b-sx} - K_b^2 - s \frac{\omega^2}{c^2} x \right] U = 0 \quad (\text{A.5})$$

We see that choosing $\alpha = \pm aK_b$ removes the constant term from the last coefficient. Then (A.5) becomes

$$x(b-sx)U'' + [b(2\alpha+1) - 2\alpha sx]U' + \left[s \left(\alpha - ba^2 \frac{\omega^2}{c^2} \right) + s^2 a^2 \frac{\omega^2}{c^2} x \right] U = 0 \quad (\text{A.6})$$

Upon making the further substitution

$$x = \frac{b}{s} y \quad (\text{A.7})$$

we obtain, as a final form,

$$y(y-1) \frac{d^2 U}{dy^2} + [2\alpha y - (2\alpha+1)] \frac{dU}{dy} - \left[\alpha + ba^2 \frac{\omega^2}{c^2} (y-1) \right] U = 0 \quad (\text{A.8})$$

This is a linear equation with two regular singular points. Therefore we try to find solutions of the form

$$U \equiv U(y) = y^p \sum_{n=0}^{\infty} a_n y^n \quad (\text{A.9})$$

where p is a constant to be determined from the indicial equation. Substituting (A.9) into (A.8) we obtain the recursion relation for the coefficients a_n

$$[(p-1) + (2\alpha+1)] p a_0 = 0 \quad (\text{A.10a})$$

$$-[p + (2\alpha+1)](p+1)a_1 + \left\{ p[(p-1) + 2\alpha] - \left(\alpha + ba^2 \frac{\omega^2}{c^2} \right) \right\} a_0 = 0 \quad (\text{A.10b})$$

and for $n \geq 2$

$$\begin{aligned}
 & -[(n+p-1)+(2\alpha+1)](n+p)a_n \\
 & + \left\{ (n+p-1)[(n+p-2)+2\alpha] - \left(\alpha - ba^2 \frac{\omega^2}{c^2} \right) \right\} a_{n-1} - ba^2 \frac{\omega^2}{c^2} a_{n-2} = 0
 \end{aligned} \tag{A.10c}$$

Equation (A.10a) is satisfied nontrivially when

$$[(p-1)+(2\alpha+1)]p = 0 \tag{A.11}$$

whose solutions are

$$p = 0, \quad p = -2\alpha \tag{A.12}$$

The recursion relation for $p = 0$ then becomes

$$a_1 = - \frac{\alpha - ba^2(\omega^2/c^2)}{2\alpha+1} a_0 \tag{A.13a}$$

$$\begin{aligned}
 & -n(n+2\alpha)a_n + \left\{ (n-1)[(n-2)+2\alpha] \right. \\
 & \quad \left. - \left(\alpha - ba^2 \frac{\omega^2}{c^2} \right) \right\} a_{n-1} - ba^2 \frac{\omega^2}{c^2} a_{n-2} = 0
 \end{aligned} \tag{A.13b}$$

(for $n \geq 2$) while for $p = -2\alpha$ we have

$$a_1 = - \frac{\alpha + ba^2(\omega^2/c^2)}{2\alpha-1} a_0 \tag{A.14a}$$

$$\begin{aligned}
 & -n(n-2\alpha)a_n + \left\{ (n-2)[(n-1)-2\alpha] \right. \\
 & \quad \left. - \left(\alpha - ba^2 \frac{\omega^2}{c^2} \right) \right\} a_{n-1} - ba^2 \frac{\omega^2}{c^2} a_{n-2} = 0
 \end{aligned} \tag{A.14b}$$

(for $n \geq 2$).

The first four coefficients are written below explicitly for the two cases. Letting $q \equiv a^2(\omega^2/c^2)$ we find for $p = 0$

$$a_1 = - \frac{\alpha - bq}{1+2\alpha} a_0$$

$$a_2 = - \frac{(\alpha^2 - b^2 q^2)}{2(2\alpha+1)(2\alpha+2)} a_0 - \frac{bq}{2(2\alpha+2)} a_0$$

$$a_3 = - \frac{(2+3\alpha+bq)}{2 \cdot 3(2\alpha+2)(2\alpha+3)} \left[\frac{\alpha^2 - b^2 q^2}{2\alpha+1} + bq \right] a_0 + \frac{bq(\alpha - bq)}{3(2\alpha+1)(2\alpha+3)} a_0$$

$$\begin{aligned}
 a_4 = & -\frac{(6+5\alpha+bq)(2+3\alpha+bq)}{2 \cdot 3 \cdot 4(2\alpha+2)(2\alpha+3)(2\alpha+4)} \left[\frac{\alpha^2 - b^2 q^2}{2\alpha+1} + bq \right] a_0 \\
 & + \frac{(6+5\alpha+bq)(\alpha-bq)bq}{3 \cdot 4(2\alpha+1)(2\alpha+3)(2\alpha+4)} a_0 \\
 & + \frac{bq}{2 \cdot 4(2\alpha+2)(2\alpha+4)} \left[\frac{\alpha^2 - b^2 q^2}{2\alpha+1} + bq \right] a_0
 \end{aligned} \tag{A.15}$$

and for $p = -2\alpha$

$$\begin{aligned}
 a_1 = & -\frac{\alpha + bq}{1-2\alpha} a_0 \\
 a_2 = & -\frac{(\alpha^2 - b^2 q^2)}{2(1-2\alpha)(2-2\alpha)} a_0 - \frac{bq}{2(2-2\alpha)} a_0 \\
 a_3 = & -\frac{(2-3\alpha+bq)}{2 \cdot 3(2-2\alpha)(3-2\alpha)} \left[\frac{\alpha^2 - b^2 q^2}{1-2\alpha} + bq \right] a_0 - \frac{bq(\alpha+bq)}{3(1-2\alpha)(3-2\alpha)} a_0 \\
 a_4 = & -\frac{(6-5\alpha+bq)(2-3\alpha+bq)}{2 \cdot 3 \cdot 4(2-2\alpha)(3-2\alpha)(4-2\alpha)} \left[\frac{\alpha^2 - b^2 q^2}{1-2\alpha} + bq \right] a_0 \\
 & - \frac{(6-5\alpha+bq)(\alpha+bq)bq}{3 \cdot 4(1-2\alpha)(3-2\alpha)(4-2\alpha)} a_0 \\
 & + \frac{bq}{2 \cdot 4(2-2\alpha)(4-2\alpha)} \left[\frac{\alpha^2 - b^2 q^2}{1-2\alpha} + bq \right] a_0
 \end{aligned} \tag{A.16}$$

These coefficients depend only on the constants α and bq whose magnitude is much less than 1 in the optical region:

$$|\alpha| = |aK_b| = \left| a \left(k_x^2 - b^2 \frac{\omega^2}{c^2} \right)^{1/2} \right| \sim 10^{-2} \text{ to } 10^{-3}$$

$$bq = b \frac{\omega^2}{c^2} a^2 \sim 10^{-4} \text{ to } 10^{-5}$$

In the optical region K_b and ω/c both range from 10^4 to 10^5 cm^{-1} . For the surface diffusiveness parameter a , we have taken an upper value of 10 \AA .

This is a reasonable upper limit in view of the calculations of Bloch and Rice⁸ and Lang and Kohn.⁹⁵

From the recursion relation (A.13b) and (A.14b) we see that all of the coefficients will be small, with the largest being $a_1 \sim 10^{-2}a_0$. In fact, keeping only linear terms in α and bq we find

$$\begin{array}{ccc}
 p=0 & & p=-2\alpha \\
 \hline
 a_1 \sim -(\alpha - bq)a_0 & & a_1 \sim (\alpha + bq)a_0 \\
 \hline
 & p=0 \text{ and } p=-2\alpha & \\
 \hline
 a_2 \sim -\frac{bq}{(2!)^2}a_0 & & a_4 \sim -\frac{3!2!}{(4!)^2}bqa_0 \\
 a_3 \sim -\frac{2!1!}{(3!)^2}bqa_0 & & a_5 \sim -\frac{4!5!}{(5!)^2}bqa_0 \\
 \\
 a_k \sim -\frac{(k-1)!(k-2)!}{(k!)^2}bqa_0 = -\frac{bq}{k^2(k-1)}a_0 & & \quad (A.17)
 \end{array}$$

The solutions of (A.8) are then given approximately by

$$U(y) \sim a_0 \left[1 + \frac{bq - \alpha}{1 + 2\alpha} y \right] - bqa_0 \sum_{n=2}^{\infty} \frac{y^n}{n^2(n-1)} \quad (A.18a)$$

for $p=0$, and

$$U(y) \sim a_0 \left[1 + y \frac{bq + \alpha}{1 - 2\alpha} \right] y^{-2\alpha} - bqa_0 y^{-2\alpha} \sum_{n=2}^{\infty} \frac{y^n}{n^2(n-1)} \quad (A.18b)$$

for $p = -2\alpha$.

The sums in (A.18) are absolutely convergent for $|y| < 1$. We can further simplify the two equations above by noting that y itself is small. This we now proceed to show. Since we have assumed that the metal occupies the half-space of positive values of the coordinate z , $x (= e^{-z/a})$ is always less than 1 except at the boundary ($z=0$). Furthermore, the fractional difference between the bulk and surface values of the free electron density which we denote by $g [(N_s - N_b)/N_b]$ is typically of the order of 0.1.⁹⁵

For a free electron metal, $\text{Im}(\epsilon(\omega))$ is typically much smaller than $\text{Re}(\epsilon(\omega))$ and in this calculation we ignore it altogether. Therefore, for an undamped free electron gas, (IV.31) give

$$\frac{s}{b} = \frac{s_1}{b_1} = \frac{R(\omega)(N_s - N_b)}{1 - R(\omega)N_b} = \frac{\omega_p^2}{\omega^2} \frac{g}{1 - \omega_p^2/\omega^2}$$

where $R(\omega) = 4\pi e^2 / m\omega^2$. Thus $s/b \sim g$ when $\omega \lesssim \omega_s$ (the surface plasma frequency). These considerations in turn imply that $|y| = |s/b|x \lesssim 0.1$ for all $z > 0$ and $\omega \lesssim \omega_s (\sim \omega_p / \sqrt{2})$. To first order, then, we keep only the linear terms in y in (A.18):

$$U(y) \underset{p=0}{\sim} a_0 \left(1 + \frac{bq - \alpha}{1 + 2\alpha} y \right) \quad (\text{A.19a})$$

$$U(y) \underset{p=-2\alpha}{\sim} a_0 \left(1 + \frac{\alpha + bq}{1 - 2\alpha} y \right) y^{-2\alpha} \quad (\text{A.19b})$$

In terms of z

$$U(z) \underset{p=0}{\sim} a_0 \left(1 + \frac{s}{b} \frac{bq - \alpha}{1 + 2\alpha} e^{-z/a} \right) \quad (\text{A.20a})$$

$$U(z) \underset{p=-2\alpha}{\sim} a_0 \left(\frac{s}{b} \right)^{-2\alpha} e^{2\alpha z/a} \left(1 + \frac{s}{b} \frac{\alpha + bq}{1 - 2\alpha} e^{-z/a} \right) \quad (\text{A.20b})$$

Finally

$$H_y(z) \underset{p=0}{=} e^{-(\alpha/a)z} U(z) \underset{p=0}{=} a_0 e^{-(\alpha/a)z} \left(1 + \frac{s}{b} \frac{bq - \alpha}{1 + 2\alpha} e^{-z/a} \right) \quad (\text{A.21a})$$

$$H_y(z) \underset{p=-2\alpha}{=} e^{-(\alpha/a)z} U(z) \underset{p=-2\alpha}{=} a_0 e^{(\alpha/a)z} \left(1 + \frac{s}{b} \frac{bq + \alpha}{1 - 2\alpha} e^{-z/a} \right) \quad (\text{A.21b})$$

where $\alpha = \pm aK_b$, and we have set $(s/b)^{-2\alpha} = 1$ because $\alpha \sim 10^{-2}$ to 10^{-3} . Equations (A.21a) and (A.21b) give identical results for either choice of the sign of α . If $\alpha > 0$, we reject (A.21b) as it diverges for $z \rightarrow \infty$, and (A.21a) is the solution of (IV.34a). If $\alpha < 0$, we reject (A.21a) for the same reasons, and (A.21b) is the solution in this case [identical to (A.21a) when $\alpha > 0$]. The y component of the magnetic field described by (IV.34a) is therefore given, to good approximation, by

$$H_y(z) = a_0 e^{-K_b z} \left(1 + \frac{s}{b} \frac{bq - aK_b}{1 + 2aK_b} e^{-a/a} \right) \quad (\text{A.22})$$

This is just (IV.40a). Note, incidentally, that the first term in (A.22) is just the y component of the magnetic field in the case of a homogeneous surface.

References

1. For example, V. Heine and D. Weaire, in *Solid State Physics*, Vol. 24, H. Ehrenreich, F. Seitz, and D. Turnbull, Eds., Academic Press, New York, 1970.
2. B. J. Austin and V. Heine, *J. Chem. Phys.*, **45**, 928 (1966).
3. J. Schmit and A. A. Lucas, *Solid-State Commun.*, **11**, 415, 419 (1972).
4. J. Frenkel, *Phil. Mag.*, **33**, 297 (1917).
5. H. Samoilovich, *Acta Physicochim. (USSR)*, **20**, 97 (1945).
6. K. Huang and G. Wyllie, *Proc. Phys. Soc.*, **A62**, 180 (1949).
7. N. D. Lang and W. Kohn, *Phys. Rev.*, **B1**, 4555 (1970).
8. A. N. Bloch and S. A. Rice, *Phys. Rev.*, **185**, 933 (1969).
9. J. S. Huang and W. W. Webb, *J. Chem. Phys.*, **50**, 3677 (1969).
10. J. van der Waals, *Z. Phys. Chem. (Leipzig)*, **13**, 657 (1894).
11. J. W. Cahn and J. E. Hilliard, *J. Chem. Phys.*, **28**, 258 (1958).
12. F. Hensel and E. U. Franch, *Rev. Mod. Phys.*, **40**, 697 (1968), and references therein; F. Hensel, *Phys. Lett.*, **31A**, 88 (1970).
13. U. Even and J. Jortner, *Phys. Rev. Lett.*, **28**, 31 (1972); U. Even and J. Jortner, *Phil. Mag.*, **25**, 715 (1972).
14. R. H. Fowler, *Proc. Roy. Soc.*, **A159**, 229 (1937).
15. P. D. Shoemaker, G. W. Paul, and L. E. Marc de Chazal, *J. Chem. Phys.*, **52**, 491 (1970).
16. M. D. Johnson, P. Hutchinson, and N. H. March, *Proc. Roy. Soc.*, **A282**, 283 (1964); N. H. March, *Liquid Metals*, Pergamon Press, Oxford, 1968.
17. Lord Rayleigh, *Phil. Mag.*, **33**, 1 (1892).
18. C. V. Raman and L. A. Ramdas, *Phil. Mag.*, **3**, 220 (1927).
19. J. W. McBain, R. C. Bacon, and H. D. Bruce, *J. Chem. Phys.*, **7**, 818 (1939).
20. K. Kinoshita and H. Yokota, *J. Phys. Soc. Japan*, **20**, 1086 (1965).
21. Lord Rayleigh, *Scientific Papers*, **3**, Articles 176, 186, 193 (1890, 1892).
22. J. G. Kirkwood and F. P. Buff, *J. Chem. Phys.*, **17**, 338 (1949).
23. M. C. Wilkinson, *J. Colloid Interfac. Sci.*, **40**, 14 (1972).
24. F. P. Buff, R. A. Lovett, and F. H. Stillinger, Jr., *Phys. Rev. Lett.*, **15**, 621 (1965); F. P. Buff and R. A. Lovett, in *Simple Dense Fluids*, H. L. Frisch and F. W. Salsburg, Eds., Academic Press, New York, 1968, pp. 17 ff.
25. T. L. Hill, *J. Chem. Phys.*, **20**, 141 (1952).
26. C. W. Plesner and O. Platz, *J. Chem. Phys.*, **48**, 5361 (1968).
27. S. Toxvaerd, *J. Chem. Phys.*, **55**, 3116 (1971).
28. (a) C. A. Croxton and R. P. Ferrier, *J. Phys C*, **4**, 1909 (1971); (b) **4**, 1921 (1971); (c) **4**, 2433 (1971); (d) **4**, 2447 (1971).
29. J. W. Belton and M. G. Evans, *Trans. Faraday Soc.*, **37**, 1 (1941).
30. J. E. Lennard-Jones and J. Corner, *Trans. Faraday Soc.*, **36**, 1156 (1940); J. Corner, *ibid.*, **44**, 1036 (1948).
31. I. Prigogine and L. Saraga, *J. Chim. Phys.*, **49**, 399 (1952).
32. (a) T. S. Ree, T. Ree, and H. Eyring, *J. Chem. Phys.*, **41**, 524 (1964); (b) W. C. Lu, M. S. Jhon, T. Ree, and H. Eyring, *ibid.*, **46**, 1073 (1967).

33. J. Bardeen, *Phys. Rev.*, **49**, 653 (1936).
34. W. J. Swiatecki, *Proc. Phys. Soc.*, **A64**, 226 (1961).
35. P. P. Ewald and H. Juretschke, in *Structure and Properties of Solid Surfaces*, R. Gomer and C. S. Smith, Eds., University of Chicago Press, Chicago, 1953, p. 82.
36. R. D. Berg and L. Wilets, *Proc. Phys. Soc.*, **A68**, 229 (1955).
37. D. M. Newns, *Phys. Rev.*, **B1**, 3304 (1970).
38. J. A. Appelbaum and D. R. Hamann, *Phys. Rev.*, **B6**, 2166 (1972).
39. W. Harrison, *Pseudopotentials in the Theory of Metals*, Benjamin, New York, 1966.
40. R. W. Shaw, Jr., *J. Phys. C*, **2**, 2335 (1969).
41. R. W. Shaw, Jr., and V. Heine, *Phys. Rev.*, **B5**, 1646 (1972).
42. V. K. Semenchenko, *Surface Phenomena in Metals and Alloys*, Pergamon Press, Oxford, 1961.
43. B. C. Allen, in *Liquid Metals: Chemistry and Physics*, S. Z. Beer, Ed., Marcel Dekker, New York, 1972, pp. 161 ff.
44. D. W. G. White, *Trans. ACME*, **236**, 796 (1966).
45. G. Drath and F. Sauerwald, *Z. Allg. Chem.*, **162**, 301 (1927); W. Karause, F. Sauerwald, and M. Michalke, *ibid.*, **181**, 353 (1929).
46. (a) V. A. Kizel, *Sov. Phys. U.P.*, **10**, 485 (1968); (b) V. L. Ginzburg, *Sov. Phys. JETP*, **34** (7), 1096 (1958); (c) V. P. Silin, *ibid.*, **35**, 700 (1959); **36**, 1025 (1959).
47. T. D. Landau and E. M. Lifschita, *Electrodynamics of Continuous Media*, Addison-Wesley, Reading, Mass., 1960, pp. 256 ff.
48. P. S. Epstein, *Proc. Natl. Acad. Sci. U.S.*, **16**, 627 (1930).
49. C. Eckart, *Phys. Rev.*, **35**, 1303 (1930).
50. M. Born and E. Wolf, *Principles of Optics*, 3rd ed., Pergamon Press, New York, 1965, pp. 52 ff.
51. F. Abeles, *Ann. Phys. (Paris)*, **3**, 504 (1948); **5**, 596 (1950).
52. A. Herpin, *Compt. Rend.*, **225**, 182 (1947).
53. T. E. Faber and N. V. Smith, *J. Opt. Soc. Am.*, **58**, 102 (1968); J. N. Hodgson, *Phil. Mag.*, **4**, 189 (1959); N. R. Comins, *ibid.*, **25**, 817 (1972).
54. W. J. Choyke, S. M. Vosko, and T. W. O'Keefe, *Solid-State Commun.*, **9**, 361 (1971).
55. E. D. Crozier and E. Murphy, *Can. J. Phys.*, **50**, 1914 (1972).
56. B. Siskind, J. Boiani, and S. A. Rice, *Can. J. Phys.*, **51**, 894 (1973).
57. K. L. Kliewer and R. Fuchs, *Phys. Rev.*, **153**, 498 (1967); E. N. Economou, *ibid.*, **182**, 539 (1969).
58. R. A. Ferrell, *Phys. Rev.*, **101**, 554 (1956); R. A. Ferrell and J. J. Quinn, *ibid.*, **108**, 570 (1957).
59. R. M. Ritchie and M. B. Eldridge, *Phys. Rev.*, **126**, 1935 (1962); K. L. Kliewer and R. Fuchs, *ibid.*, **144**, 495 (1966).
60. See, for example, H. Raether, *Surf. Sci.*, **8**, 233 (1967); A. Bagchi and C. B. Duke, *Phys. Rev.*, **B5**, 2784 (1971); V. E. Heenrich, *ibid.*, **B7**, 3512 (1972); E. A. Stein and R. A. Ferrell, *ibid.* **120**, 130 (1960).
61. R. H. Ritchie, *Phys. Rev.*, **106**, 874 (1957). See also Ref. 63.
62. C. J. Powell and J. B. Swan, *Phys. Rev.*, **118**, 640 (1960); C. Kunz, *Z. Phys.*, **196**, 311 (1966); **176**, 53 (1962).

63. R. A. Ferrell, *Phys. Rev.*, **111**, 1214 (1958). See also Economou. Ref. 57.
64. E. A. Stein as quoted by R. A. Ferrell in Ref. 63.
65. W. Steinmann, *Phys. Rev. Lett.*, **5**, 470 (1960).
66. R. W. Brown, P. Wessel, and E. P. Trounson, *Phys. Rev. Lett.*, **5**, 472 (1960).
67. D. M. Miliotis, *Phys. Rev.*, **B3**, 701 (1971); N. G. Alexandropoulos, *J. Phys. Soc. Japan*, **31**, 1790 (1971); K. L. Kliewer and M. Roether, *Phys. Rev. Lett.*, **30**, 971 (1973).
68. R. E. Palmer and S. E. Schnatterly, *Phys. Rev.*, **B4**, 2329 (1971); T. F. Gesell et al., *ibid.*, **B7**, 5141 (1973).
69. J. C. Phillips, *Phys. Rev.*, **137** A1835 (1965); W. Steinmann, *Phys. Status Solidi*, **28**, 437 (1968).
70. R. Fuchs and K. L. Kliewer, *Phys. Rev.*, **B3**, 2270 (1971); J. Harris and A. Griffin, *Can. J. Phys.*, **48**, 2592 (1970); J. Harris and A. Griffin, *Phys. Rev.*, **B3**, 749 (1971); J. Harris, *ibid.*, **B4**, 1022 (1971).
71. A. J. Bennett, *Phys. Rev.*, **B1**, 203 (1971).
72. P. J. Feibelman, *Phys. Rev. Lett.*, **30**, 975 (1973).
73. See Stein as quoted in Ref. 71.
74. D. Beaglehole, *Phys. Rev. Lett.*, **22**, 708 (1968).
75. Y. Y. Teng and E. A. Stern, *Phys. Rev. Lett.*, **19**, 511 (1967).
76. R. H. Ritchie, E. T. Arakawa, J. J. Cowan, and R. N. Mamm, *Phys. Rev. Lett.*, **21**, 1530 (1968).
77. N. Marschall, B. Fischer, and H. J. Queisser, *Phys. Rev. Lett.*, **27**, 95 (1971); W. F. Anderson, R. W. Alexander, and R. J. Bell, *ibid.*, **27**, 1057 (1971); a general treatment of surface roughness is given by J. M. Elson and R. H. Ritchie, *Phys. Rev.*, **B4**, 4129 (1971); A. S. Barker, Jr., *Surf. Sci.*, **34**, 62 (1973).
78. R. H. Ritchie, *Surf. Sci.*, **34**, 1 (1973).
79. J. L. Stanford, *J. Opt. Soc. Am.*, **60**, 49 (1970); J. L. Stanford, H. E. Bennett, J. M. Bennett, E. J. Ashley, and E. T. Arakawa, *Bull. Am. Phys. Soc.*, **13**, 989 (1968).
80. J. G. Endriz and W. E. Spicer, *Phys. Rev.*, **B4**, 4144 (1971).
81. J. G. Endriz and W. E. Spicer, *Phys. Rev.*, **B4**, 4159 (1971).
82. A. Sommerfeld, *Ann. Phys.*, **28**, 665 (1909).
83. R. W. Wood, *Phil. Mag.*, **4**, 396 (1902).
84. Lord Rayleigh, *Proc. Roy. Soc. (London)*, **A79**, 309 (1907).
85. U. Fano, *J. Opt. Soc. Am.*, **31**, 213 (1941).
86. A. Hessell and A. A. Oliner, *Appl. Opt.*, **4**, 1275 (1965).
87. A. Otto, *Z. Phys.*, **216** 398 (1968).
88. M. Born and E. Wolf, *Principles of Optics*, Pergamon Press, New York, 1959, Section 1.5.4.
89. A. S. Barker, Jr., *Phys. Rev. Lett.*, **28**, 892 (1972); R. Bruns and H. Roether, *Z. Phys.*, **237**, 98 (1970); A. Otto, *ibid.*, **219**, 227 (1969); **224**, 65 (1969); H. J. Falge and A. Otto, *Phys. Status Solidi. (b)*, **56**, 523 (1973); G. C. Morris and M. G. Sceats, *Molecular Crystallography and Liquid Crystallography*, 1973 (in press).
90. V. V. Bryxin, D. M. Mirlin, and I. I. Reshina, *Solid-State Commun.*, **11**, 695 (1972); I. I. Reshina, Yu. M. Gerbshtein, and D. M. Mirlin, *Sov. Phys. Solid State*, **14**, 1104 (1972); B. Fischer, N. M. Marschall, and H. J. Queisser, *Surf. Sci.*, **34**, 50 (1973).

91. W. E. Jones and R. E. Fuchs, *Phys. Rev.*, **B4**, 3581 (1971); A. Otto and W. Sohler, *Opt. Commun.*, **3**, 254 (1971); J. Schoenwold, E. Bernstein, and J. M. Elson, *Solid-State Commun.*, **12**, 185 (1973); R. J. Bell, R. W. Alexander, Jr., W. F. Parks, and G. Kovener, *Opt. Commun.*, **8**, 147 (1973).
92. J. Fridel, *Phil. Mag.*, **43**, 153 (1953).
93. E. A. Sziklas, *Phys. Rev.*, **138**, A1070 (1965); B. V. Paranjape and W. J. Heaney, *ibid.*, **B6**, 1743 (1972).
94. D. E. Beck, V. Celli, G. LoVecchio, and A. Magnaterra, II, *Nuovo Cimento*, **68B**, 230 (1970).
95. N. D. Lang and W. Kohn, *Phys. Rev.*, **B7**, 3541 (1973); **B3**, 1215 (1971).
96. J. Frenkel, *Z. Phys.*, **51**, 232 (1928).
97. P. Hohenberg and W. Kohn, *Phys. Rev.*, **136**, B864 (1964); W. Kohn and L. J. Sham, *ibid.*, **140**, A1133 (1965).
98. R. J. Smith, *Phys. Rev.*, **181**, 522 (1969); N. D. Lang, *Solid-State Commun.*, **7**, 1047 (1969); A. J. Bennett and C. B. Duke, in *Structure and Chemistry of Solid Surfaces*, G. A. Somorjai, Ed., New York, 1969.
99. P. J. Feibelman, *Phys. Rev.*, **B3**, 2974 (1971); P. J. Feibelman, C. B. Duke, and A. Bagchi, *ibid.*, **B5**, 2436 (1972).
100. J. V. Parker, J. C. Nickel, and R. W. Gould, *The Physics of Fluids*, **7**, 1489 (1964); F. C. Hoh, *Phys. Rev.*, **133**, A1016 (1964).
101. See, for example, M. Cordona, *Modulation Spectroscopy, Solid State Physics*, Supple. II, Academic Press, New York and London, 1969.
102. H. Ehrenreich and H. R. Phillips, *Phys. Rev.*, **121**, 1622 (1962).
103. E. G. Wilson and S. A. Rice, *Phys. Rev.*, **145**, 55 (1966).
104. H. L. Lemberg, unpublished results.

AUTHOR INDEX

- Abaev, M. I., 505, 540
 Abdel-Shahid, N. Z., 340, 353
 Abelès, F., 340(174), 353, 566, 569, 631
 Aberdam, D., 156(376), 173(376), 209
 Adawi, I., 245(45), 263
 Albridge, R. G., 27(135), 32(206), 203, 205
 Adler, S. L., 449(154), 536
 Agarwal, G. S., 463(181), 464, 538
 Agranovich, V. M., 463(179), 538
 Alexander, R., 371(49), 532
 Alexander, R. W., 338, 353, 447(146), 525, 535, 540, 587(77), 591(77,91), 632, 633
 Alexandropoulos, N. G., 343(212), 354, 579(67), 632
 Alexopoulos, K., 305(85), 343(85,210), 351, 354
 Alferieff, M. E., 225, 235, 263
 Alldredge, G. P., 467(208,211,212), 470(211), 471-473(212,213), 496(230-232), 497(297), 498(230), 499, 504(235), 507, (245), 511(211,212), 518(230), 529(233), 539, 540
 Allen, B. C., 553-554(43), 631
 Allen, R. E., 467(208-212), 469(209), 470(211), 471(212-213), 472-473(212), 474(214), 475(209), 476-480, 487, 496(230-232), 497-498(230), 504(235), 511(210-212), 514, 518(230), 523, 524, 529, 539, 540
 Amelio, G. F., 32(207,209), 205
 Amus'ya, M. Ya., 22(80), 202
 Anderegg, M., 457(163), 537
 Anderson, J., 250(50), 263
 Anderson, J. R., 45(248), 77(248), 80(248), 85(248), 89-90(248), 106(248), 116, 147(351-353), 156(248), 174(248), 182(351-353), 206, 208
 Anderson, P. W., 214, 221(9), 262
 Anderson, W. E., 338, 353, 447(146), 535
 Anderson, W. F., 587(77), 591(77), 632
 Andersson, D. E., 182(394), 209
 Andersson, S., 31(182), 85(310), 90-91(310), 107(310), 108, 114(310), 124(310), 159(382), 160(310,382), 164, 165, 169(386), 174(390), 182(394), 204, 207, 209, 467(201), 511(201), 538
 Appelbaum, J. A., 527(276), 541, 550(38), 553, 631
 Arakawa, E. T., 294(49,51), 319(110-112, 114-117, 120-122), 332, 334, 338(169), 350-353, 525, 526, 540, 587-588(76), 590(76), 632
 Ashcroft, N. W., 244(43), 263
 Ashley, E. J., 332, 352, 588(79), 632
 Augustus, P. D., 32(210), 205
 Austin, B. J., 545(2), 630
 Axelsson, G., 19-20(68), 25(68), 27(68), 202
 Bacon, R. C., 547(19), 630
 Badro, R. G., 321, 317
 Baer, Y., 28(150), 203
 Bagchi, A., 9(30), 14(46), 42(30), 44-46(30), 47(212), 62(212), 77-78(30), 79(30,46), 81(30), 87(46), 89(30), 90(30,46), 106(46), 122(30), 126, 127(212,335), 131(212,335), 132, 133, 186, 189(212,335), 190(212), 197(30), 201, 205, 208, 221(8), 234(30), 262, 323, 347(137), 352, 579(60), 599(99), 631, 633
 Baker, A. D., 251(53), 263
 Baker, C., 251(53), 263
 Baker, J. M., 27(147), 33(147,220), 203, 205, 244(39), 246(39), 250, 251, 261, 263
 Ball, D. J., 28(154), 204
 Baltes, H. P., 342, 354, 438(118), 445(137), 535
 Bambynek, W., 18-19(63), 27(63), 201
 Bardeen, J., 279(29), 280, 349, 550(33), 599, 631
 Barker, Jr., A. S., 340, 353, 362(38), 415(38), 447, 531, 535, 587(77), 591(77,89), 632
 Barnes, R. F., 58(258), 64(258), 140(258), 206
 Barnett, E. F., 28(152), 32(152), 204
 Barron, T. H. K., 394(75), 399(75), 532
 Barsukov, K. A., 318(100), 351
 Bartel, M., 28(153), 204
 Bastow, T. J., 31(187), 204
 Baudoin, R., 31(190), 98(321), 100(321), 122(321), 156(376), 173(376), 204, 207, 209
 Bauer, E., 13(41), 42(244), 141(342), 146(350), 154(342), 173(342), 184(342), 201, 206, 208
 Bauer, W., 24(100), 26(100), 202
 Baym, G., 348(236), 354

- Beach, N. A., 258(64), 264
 Beaglehole, D., 332, 352, 586, 632
 Beck, D. E., 326, 346(230,231), 347(234), 348(230,231), 352, 354, 361(34,35), 465(34,35), 531, 596(94), 610(94), 633
 Becker, G. E., 167, 209
 Beeby, J. L., 79(267), 90(267), 155(267), 206
 Bell, A. E., 240(32), 242(32), 246, 248, 249(32), 250, 255(56), 263, 264
 Bell, R. J., 338, 353, 371(49), 447(146), 540(270), 532, 535, 540, 587(77), 591(77,91), 632, 633
 Belton, J. W., 549(29), 630
 Benedik, G., 517, 518, 540
 Bennett, A. J., 346, 354, 361(37), 465(37), 531, 580(71), 599(98), 632, 633
 Bennett, H. E., 332, 352, 588, 632
 Bennett, J. M., 332, 352, 588(79), 632
 Benson, G. C., 515-517, 540
 Berg, R. D., 550(36), 631
 Berglund, C. N., 326(144), 338(144), 352
 Bergmark, T., 20(76), 22(76), 25(76), 28(76), 32(76), 202
 Berndt, W., 41(240), 85(240), 87(240), 90(240), 124(240), 160(240), 165-167(240), 205
 Bernstein, E., 591(91), 596(91), 633
 Berreman, D. W., 438, 440, 534, 535
 de Bersuder, L., 98(321), 100(321), 122(321,327), 207
 Bethe, H., 14(50), 81, 82(50), 201
 Bilz, H., 368(45), 439(45), 529, 352
 Birkhoff, R. D., 319(110-112,114-116), 351
 Birman, J. L., 463(182,183), 538
 Bishop, H. E., 25(106), 27(129,142), 33(142), 202, 203
 Blakely, J. M., 182(393), 209
 Blanckenhagen, P. V., 319(106), 334(106, 107), 351
 Blandin, A., 262
 Bledsoe, J. R., 31(163), 204
 Bloch, A. N., 547, 552(8), 571-576, 580, 610, 611, 613, 617-621, 623, 628, 630
 Bloch, F., 274, 349
 Boersch, H., 268-269(4), 294(50), 319(104, 106,107), 321, 334, 348, 350-352, 447, 448, 535
 Bogomolov, V. N., 505(238), 540
 Bohm, D., 273, 348(15), 349
 Boiani, J., 575, 576(56), 580(56), 621, 631
 Bond, G. C., 10(34), 201
 Bonnerot, J., 31(189,191), 204, 483(220), 539
 Bonzel, H. P., 4(5), 6(5), 7, 8(5), 19(5), 26(5), 28(5), 36(5), 40(5), 141-142(5), 154(5), 173(5), 184(5), 200
 Born, M., 350, 357(9), 359(27), 387(27), 405(85), 515, 530, 531, 564, 590(88), 631, 632
 Borstel, G., 527, 541
 Bosenberg, J., 333, 353
 Boudreaux, D. S., 14, 43(245), 82(53,270, 274), 83(245), 87, 106(53,274), 201, 206
 Brambring, J., 333, 353
 Braundmeier, A. J., 294(51), 319(120-122), 334, 350, 351
 Brenig, W., 463(183), 538
 Brewer, R., 341(193), 353
 Brion, J. J., 340, 341(192), 353, 371(48), 415(94), 418, 419, 420(99), 244-245(99), 426(102), 427(99,102), 431-432(99), 529, 532, 534
 Brown, R. W., 319(109), 351, 579, 632
 Bruce, H. D., 547(19), 630
 Brundle, C. P., 26(120), 203, 251(53), 263
 Bruns, R., 591(89), 633
 Brusa, R., 438(118), 535
 Bryskin, V. V., 340, 341, 353, 364, 435, 444(130), 445, 447, 499, 505(130,236, 238), 529(130), 534, 535, 539, 540
 Bryxin, V. V., 591(90), 622(90), 632
 Buck, T. M., 28(154), 204
 Buerger, M. J., 154(364,365), 208
 Buff, F. P., 548, 549, 630
 van de Bunt, W. B., 438(113), 534
 Burhop, E. H. S., 18(61), 201
 Bürker, U., 319(113,119), 334, 351
 Burkstrand, J. M., 38(236), 122(330), 123, 129-130(236), 132(236), 205, 207
 Burnstein, E., 340(174), 341(192,193), 353, 369(47), 371(48), 420(99), 422-425(99), 426(102), 427(99,102), 431-432(99), 447(47), 529, 532, 534
 Burton, J. J., 485, 486, 525, 529, 539, 540
 Buttner, P., 41(240), 85(240), 87(240), 90(240), 124(240), 160(240), 165-167(240), 205
 Cabrera, N., 23(96), 31(162), 202, 204
 Cahn, J. W., 547(11), 553(11), 630
 Caldwell, C. W., 74(263), 108, 206, 207, 516, 540
 Callcott, T. A., 33(215), 205, 326, 352
 Campbell, B. D., 25(108), 202
 Capart, G., 14(43), 82(271), 83(43), 87(43), 90(43), 106(43), 201, 206
 Carlson, T. A., 28(151), 32(151), 203
 Caroli, C., 226, 263
 Carotte, C., 204
 Carroll, C. E., 147(355), 182(355), 208
 Carter, G., 9(27), 28(27), 201

- Cashion, J. K., 33(216,217), 205
 Casimir, H. B. G., 344, 354
 Castaing, R., 10(33), 23(33), 25(33), 28(33), 201
 Celli, V., 31(162), 204, 326, 346(231), 347 (234), 248(231), 352, 354, 361(34), 465 (34), 531, 596(94), 610(94), 633
 Chang, C. C., 19(72), 25-27(72), 202
 Chang, J. J., 343, 354
 Chase, J. B., 379(51), 447-448(51), 532
 Chen, T. S., 496, 497-498(230), 499, 504, 507, 518, 529, 539, 540
 Cherepkov, N. A., 22(80), 202
 Chernysheva, L. V., 22(80), 202
 Chiu, K. W., 340, 341(192), 353, 415(96), 534
 Choyke, W. J., 571, 631
 Christy, R. W., 541
 Chung, M. F., 27(127), 203
 Clark, B. C., 481(217), 539
 Clark, H. E., 263
 Clarke, T. A., 157(378,379), 158, 174(378, 379), 180(378), 209
 Claxton, T. A., 515-517, 540
 Coad, J. P., 25(110), 27(138,142), 33(138, 142), 203
 Cochran, W., 157-158(380), 209
 Cohen, J. K., 318(103), 351
 Cohen, M., 29(155,158), 32(231), 204, 205
 Cohen, M. H., 221(8), 225, 235, 262, 263, 273, 296(64), 297, 298(64,70), 299, 316 (64,70), 322, 323(64), 325, 326, 348(17), 349, 350
 Cohn, E., 358-359(11), 530
 Comins, N. R., 575, 631
 Cooper, J. W., 20(75), 202
 Cordona, M., 619, 633
 Corner, J., 549(30), 630
 Corotte, C., 31(190), 204
 Cowan, J. J., 338(169), 353, 587(76), 590 (76), 632
 Craesmann, B., 18-19(63), 27(63), 201
 Cram, L. S., 334(123,124), 352
 Crow, J. E., 483(223), 539
 Crowell, J., 304, 328, 350, 352
 Croxton, C. A., 549-551(28), 552-554, 630
 Crozier, E. D., 571, 572, 574-576, 580(55), 620, 631
 Cunningham, S. L., 509, 510(249), 511, 513, 524, 527(248,249,267), 529, 540
 Curien, H., 21-22(77), 202
 Damen, T. C., 341, 354
 Danforth, W. E., 147(353), 182(353), 208
 Daniels, J., 321(127), 352
 David, G., 156(370), 173-174(370), 208
 Davies, J. A., 9(28), 23(28), 25(28), 28(28), 201
 Davies, N. O., 319(111,112), 351
 Davison, C. J., 4(16), 6, 14, 38(16), 49, 77, 82, 83, 125(16), 184, 200
 Debye, P., 359, 531
 Dederichs, P. H., 83(289), 207
 Delong, A., 52(257), 206
 Demuth, J. E., 107, 108, 171, 207
 Dennis, R. L., 140(338), 208
 DeVille, J. P., 156(370), 173-174(370), 208
 DeWames, R. E., 357(4), 371(49), 530, 532
 Dick, B. G., 515, 540
 Dickey, D. H., 415(95), 534
 Dickey, J. M., 483-485, 529, 539
 Dixon, R. D., 32(211), 205
 Dobberstein, P., 294(50), 319(107), 332, 334-336, 350-353
 Dobrzynski, L., 466(192), 467(203,207), 481, 482, 512, 529, 538-540
 Domange, J. L., 31(189,191), 204, 467(203), 483(220), 538, 539
 Dooley, G. J., 27(140,141), 33(140,141), 203
 Doremus, R. H., 305, 350
 Doyle, W. T., 305, 350
 Douglass, Jr., D. H., 483(223), 539
 Dransfeld, K., 357(4a), 530
 Drath, G., 554(45), 631
 Ducharme, A. R., 19(65), 25(65), 201
 Duke, C. B., 4(1,6,8-13), 6(19), 7(1,6,8,11), 9(19,21,24,29,30), 12(1), 14(46,47), 18, 23(21), 28(1,6), 29(19), 30(8), 31(8,9,21), 32(8-10,47,197), 33(12,13,47), 34(6,8-13, 47), 40(6,8,21,29), 41(47, 241,242), 42 (30), 44(6,30), 45(6,11,19,24,30,47,247, 248,250,252), 46(30,47,242,250), 47(11- 13,212), 51(6,255), 54(21), 59(259), 62 (212), 64, 72(6,8), 73(8,10), 74(19), 76 (6,255), 77, 78(30), 79, 80(6,9,248,266), 81, 82(19), 85(19,29,54,197,248,255), 86(47,242), 87(6,46,47,241), 88, 89, 90 (6,10,30,46,197,241,242,248,251,266), 91(29), 94, 95(250), 96(6,250), 97, 98 (250), 99, 100(47,241,242,250), 101(9), 102(8,10,47), 103(10,11,47,197,242), 104(10), 105, 106(46,47,197,242,248, 250,255), 107, 109(326), 110, 111, 112 (242), 114(241,242), 115(242, 326), 116, 118(241,242), 119(6,250), 120, 122(30, 197,250), 123, 124(241,242), 125(247, 252,332), 126, 127(12,212,252,332-337), 129(252,333,334,336,337), 130(333,334), 131(212,332-337), 132(212), 133-138, 139(12,336), 140, 141(1,6), 142-143(1), 144, 148-150, 151(357), 154, 156(6,29,

- 54,197,248,250,255,326,366-369), 157
(368), 158(19,255,368,326), 159(21,29,
197,250,326,366-369), 160(241,242,326,
366-368), 161-163, 167, 168, 169(387),
170-172, 173(366-369), 174, 175(255,
366-369), 178-181, 182(397), 183(197,
397), 186, 188, 189(12,13,212,252,332-
337), 190-197, 198(404), 200, 201, 205-
209, 225, 235, 263, 323, 347(137), 352,
467(202), 538, 579(60), 599(98,99), 631,
633
Dunning, W. J., 143(345), 151(345), 208
Dvoryankin, V. F., 82(272), 141-142(341),
154(341), 173(341), 184(341), 206, 208
Dzyaloshinskii, J. E., 345, 348(221), 354
Eastman, D. E., 32(201), 33(216-218,220,
221), 205, 244, 246, 248, 250, 251, 261,
263
Eckart, C., 562, 563, 565, 575, 631
Economou, E. N., 33(231), 205, 280, 282,
286, 293(26), 296(64), 297(26), 298(64,
70), 299, 301(26), 304(74), 305, 307(90),
316(64,70), 322, 323(64), 324(26), 325,
326(142), 344, 349-352, 578-579(57),
606(57), 631
Ehrenreich, H., 145(347), 208, 273, 275
(21), 348(17), 349, 449(154), 536, 541,
622, 633
Eldridge, M. B., 579-580(59), 591(59), 631
Ellis, W. P., 25(108), 150-151(358), 202,
208
Elridge, H. B., 294(43), 318-319(43), 349
Elson, J. M., 197(402), 209, 328, 330-333,
336-338, 340(174), 352, 353, 369(47),
447(47), 532, 587(77), 591(77,91), 596
(91), 632, 633
Emerson, L. C., 319(111), 351
Endriz, J. E., 332, 338, 352, 353, 588, 589,
632
Engel, T., 256(63), 264
Englman, R., 278(27), 341, 349, 354, 358
(20), 359, 362(39), 395(21-23,39), 397
(39), 401, 402(21), 428, 442(29), 443,
531
Epstein, P. S., 562-564, 566, 575, 611, 612,
614, 617, 620-622, 631
Ert, G., 147(354), 182(354), 183, 208
Escard, J., 156(370), 173-174(370), 208
Estermann, I., 23(89), 202
Estrup, P. J., 4(3), 8(3), 14, 28(3), 31(179),
40(3), 91, 141(3), 147(351-353), 151(3),
154(3), 173(3), 182(179,351-353), 184
(3), 200, 204, 208, 250(50), 263
Evans, E., 510, 511, 540
Evans, M. G., 549(29), 630
Even, U., 547(13), 630
Ewald, P. P., 550(35), 631
Eyring, H., 549, 630
Faber, T. E., 571-574, 611, 631
Fahlman, A., 19(66-68), 20(66-68,76), 22
(76), 25(66-68,76), 27(66-68,134,135),
28(76), 32(76,206), 201-203, 205
Faith, W. N., 38(238), 129-130(239), 141
(339), 189(238,401), 194, 205, 208, 209,
323, 352
Falge, H., 341, 353, 591(89), 632
Falge, H. J., 432(104), 435, 447, 534
Fano, U., 20(75), 202, 273, 330, 349, 352,
358, 359(14,15), 416(14,15), 530, 589,
620(85), 632
Farnell, G. W., 357(5), 471(5), 530
Farnsworth, H. E., 38(232), 125(232), 175,
205, 209
Farrell, H. H., 4(4), 6(4), 7, 8(4), 28(4), 31
(170), 36(4), 40(4), 72(170), 141-142(4),
154(4), 156(371), 173(4,371), 174(371,
388), 184(4), 200, 204, 208, 209, 509
(247), 540
Fauchier, J., 225, 263
Fedders, P. A., 328, 329, 346(233), 348,
352, 354, 465(188), 538
Feibelman, P. J., 9(30), 42(30), 44-46(30),
77(30), 78, 79, 80(30), 89-90(30), 122
(30), 190(30), 197(30), 201, 323, 346
(229), 347(137), 248(244,229), 352, 354,
361(32), 465(32,189), 531, 538, 580(72),
599, 622, 623, 632, 633
Fellner-Feldegge, H., 28(152), 32(152), 204
Ferrell, R. A., 201, 280(30), 289, 294(47),
317, 318(42), 319, 320(30), 333, 349,
350, 359, 416(17), 531, 579, 631, 632
Ferrier, R. P., 549-551(28), 552-554, 630
Feshbach, H., 396(79), 532
Fetisov, E. P., 318(101,102), 319(101), 351
Fetter, A. L., 348(237), 354
Feuchtwang, T. E., 466(194), 538
Feuerbach, B., 294(56), 350
Feuerbacher, B., 33(223), 205, 332, 352,
457(163), 537
Fink, M., 14(49), 201
Fink, R. W., 18-19(62,63), 27(62,63), 201
Firsov, Y. A., 499, 539
Fischer, B., 338, 340, 353, 440(121,122),
445-447, 529, 535, 587(77), 591, 622(90),
632
Fischer, S. S., 31(163), 204
Fiske, M. D., 298(66), 325(66), 350
Fitton, B., 33(223), 205, 457(163), 537
Flores, F., 347, 354
Florio, J. V., 182(396), 209

- Forstman, F., 41(240), 85(240), 87(240), 90(240), 124(240), 160(240), 165-167, 205, 294(62), 350, 460, 537
- Fortner, R. J., 27(139), 32(208), 33(139), 203, 205
- Fowler, R. H., 547(14), 548, 630
- Franch, E. U., 547(12), 630
- Frank, A. L., 319(110), 351
- Frank, I. M., 294(45), 318(45,96), 319(96), 350, 351
- Frenkel, J., 546(4), 599, 630, 633
- Freund, H. U., 18-19(63), 27(63), 201
- Fridel, J., 596(92), 633
- Friedel, J., 214, 262
- Fritzsch, D., 294(50), 319(106,107), 334(106,107), 350, 351
- Fröhlich, H., 394(72), 532
- Fuchs, R., 276(23), 278-279(23), 290, 293(41,52), 349, 350, 359(18,19,28), 361(36), 362(18,19), 379(36,54,55,57,58), 380(36,60), 381(19), 383(60), 387(28), 391(28), 413(60), 416(97), 435(18,19), 436-437(109), 438, 439(109), 441-443(28), 451(36), 453(54,160), 454(36), 456(55,160), 457(164,165), 458(165), 463(164), 489(165), 490(18), 491, 501, 504, 526(55,58), 529, 531, 532, 534, 537, 541, 578(57), 579, 580(59,70), 591(59,91), 606(57), 631-633
- Fujimoto, F., 305, 320(79), 350
- Gadzik, J. W., 225, 232, 242(33), 246-248, 249(33), 263, 299, 350
- Gallon, T. E., 19(73), 25(73), 26(73,121), 27(73,123), 202, 203
- Gammon, R., 353
- Garcia-Moliner, F., 347, 354
- Garibyan, G. M., 318(98,99), 319(98), 351
- Gazis, D. C., 357(6), 466(196-198), 481(219), 530, 538, 539
- Gaubert, G., 98(321), 100(321), 122(321), 207
- Geiger, J., 321, 352, 447(148,149a), 448(148), 535
- von Gelder, A. P., 529, 541
- Gell-Man, M., 322, 352
- Genzel, L., 341, 354, 368(45), 439(45), 444, 445(136), 505(133), 506, 508, 509, 529(134), 532, 535, 540
- Gerbstein, Yu. M., 340, 353, 417(145), 444(130), 445(140,141,145), 447(145), 449(130), 505(130,236), 529(130), 535, 540, 591(90), 622(90), 632
- Gerlach, E., 18, 19(65), 25(103,107,109,65), 201-203, 344, 354
- Germer, L. H., 4(16), 6, 14, 31(175), 36(16), 49, 77, 82, 83, 125(16), 156(370), 173-174(370), 182(392), 184, 200, 204, 208, 209
- Gersten, J. I., 317, 351
- Gesell, T. F., 580(68), 632
- Gibbons, A. M., 32(197), 74(264), 85(197, 264,303), 90(197,264,303), 103(197), 106(197), 122(197), 156(197), 159(197), 174(197), 183(197), 205, 206, 207
- Ginsburg, V. I., 294(45), 318(45), 350, 463(179), 538, 554(46), 557(46a), 631
- Godwin, R. P., 294(63), 350
- Goldberger, M. L., 322, 352
- Goldstaub, S., 156(370), 173-174(370), 208
- Goldstein, Y., 9(25), 10(37), 201
- Gomer, R., 11(38), 201, 224, 225, 226(23), 234(30), 235, 237(23), 239(23), 242(35), 243(23,37), 244(23), 248-249(35), 252-254, 255(56,57,59,61), 256(57,59,61-63), 257(61), 258, 263, 264
- Good, R. H., 226-227(22), 229, 237(22), 263
- Goodman, F. O., 23(95,96), 31(167,168), 72(170), 202, 204
- Goodman, R. M., 31(170), 156(371), 173-174(371), 204, 208
- Gould, R. W., 610(100), 633
- Graham, R., 371(49), 532
- Grant, J. T., 27(136,137,140,141,143), 33(136,137,140,141,143), 203
- Gray, H. B., 258(64), 264
- Greenberg, J. M., 341(204), 354
- Greuzburg, M., 305, 350
- Griffin, A., 346(232), 347, 348, 354, 580(70), 632
- Grimley, T. B., 214, 262
- Grindlay, J., 394(76), 532
- Grobman, W. D., 33(221), 205
- Group d'Etude des Surfaces, 98(322), 100(322), 122(322), 207
- Grover, N. B., 9(25), 10(37), 201
- Guernsey, R. L., 291, 249
- Guinier, A., 182(399), 183
- Hass, T. W., 27(136,137,140,141,143), 33(136,137,140,141,143), 203
- Hägglund, J., 440(123), 534
- Hagström, S. B. M., 32(202), 205
- Hagstrum, H. D., 23-24(97,98), 25(101,102), 32-33(101,102), 167, 202, 209, 212, 262
- Hamann, D. R., 527, 541, 550(38), 553, 631
- Hamm, R. N., 294(49), 319(117), 338(169), 350, 351, 353, 525(269), 540
- Hammon, D., 28(152), 32(152), 204
- Hampe, A., 332, 352

- Hamrin, K., 19(68), 20(68,76), 22(76), 25(68,76), 27(68,134,135), 28(76), 32(76, 206), 202, 203, 205
- Hannum, R. W., 74(264), 85(264,303), 90(264,303), 206, 207
- Hanson, W. F., 319(116,117), 351
- Happ, H., 368(45), 439(45), 532
- Harrick, N. J., 340, 353
- Harris, J., 346(232), 347, 348, 354, 580(70), 632
- Harris, L. A., 19(71), 25(71), 26(71), 27(128,130), 202, 203
- Harrison, M. J., 278(28), 291, 294(28,38), 349, 460, 463, 537
- Harrison, W. A., 48(254), 206, 550(39), 631
- Hartstein, A., 340, 341(192,193), 353, 371(48), 420(99), 422-425(99), 426(102), 427(99, 102), 431-432(99), 529, 532, 534
- Hass, M., 440, 535
- Hattari, M., 294(55), 350
- Hays, W. L., 23(87), 202
- Heaney, W. J., 596(93), 610(93), 633
- Heckingbottom, R., 182-183(398), 209
- Heden, P. F., 28(150), 203
- Hedin, L., 90(318), 207
- Hedman, J., 20(76), 22(76), 25(76), 28(76, 150), 32(76,203), 202, 203, 205
- Heenrich, V. E., 579(60), 631
- Heine, V., 82(270), 206, 545(1,2), 550(1), 551-552(1,41), 630, 631
- Heinrichs, J., 197(403), 209, 379, 532
- Helms, C. R., 33(219), 205, 244(41), 246(41), 263
- Hennequin, J. H., 10(33), 23(33), 25(33), 28(33), 201
- Henoc, P., 305(87), 351
- Henrion, J., 31(195), 182(195), 204
- Henry, L., 305(87), 351
- Hensel, F., 547(12), 630
- Henzler, M., 150-151(359,361), 208
- Herickhoff, R. J., 319(114-116), 351
- Herman, F., 41, 88(243), 206
- Herman, R., 357(6), 481(217), 530, 539
- Herpin, A., 566, 570, 611, 617, 618, 631
- Hessell, A., 580(86), 589, 632
- Hill, G. E., 29(159), 204
- Hill, T. L., 549(25), 552, 630
- Hilliard, J. E., 547(11), 553(11), 630
- Hirabayashi, K., 83, 85, 90(281,299,301, 302), 206, 207
- Hisano, K., 438(114-116), 534
- Hodgson, J. N., 572, 574, 575, 631
- Hoffman, F., 83(283), 90(283), 206
- Hoffstein, V., 14, 82(53,274), 87, 98(321), 100(321), 106(53,274), 122(321,327), 201, 206, 207
- Hoh, F. C., 610(100), 633
- Holenberg, P., 599(97), 602(97), 633
- Holland, B. W., 31(194), 32(197,198), 74(264), 75, 76, 77-81(266), 85(197,264, 303), 90(197,264,266,303), 103(197,198), 105(194), 106(197), 111(194), 122(197), 123(194), 156(197), 159(197), 174(197), 183(197), 204-207
- Holvast, J., 529, 541
- Honig, J. M., 145(346), 147(346), 208
- Hopfield, J. J., 463(178), 464, 538
- Hopkins, B. J., 29(159), 204
- Hörl, E. M., 505(242), 508, 509, 540
- Hörnfeldt, O., 19-20(66), 25(66), 27(66), 201
- Houston, J. E., 25(104,107), 26(111-116), 27(113-116), 33(113,114,116), 52(256), 122(329), 144(329), 147(256,356), 148, 151(329,356,362,363), 159(363), 182, 183, 202, 203, 206-208
- Howmsom, A. J., 127(334), 129-131(334), 189(334), 208
- Huang, K., 357(9), 405(85), 530, 546(6), 547, 549(9), 553(9), 630
- Huber, D. L., 62(260), 64(260), 69(260), 206
- Hudis, J., 28(149), 203
- Huebner, R. H., 294(49), 350
- Huffman, D. R., 341, 354
- Hüfner, S., 32(204), 205
- Hunderi, O., 332, 352, 444(135), 535
- Hunt, A. J., 341
- Hurault, J. B., 31(191), 204
- Hurault, J. P., 225(16), 263, 483(220), 539
- Hutchinson, P., 547-548(16), 550(16), 630
- Ibach, H., 31(172-174), 204, 321, 352, 436, 448, 459, 467, 510, 511, 527, 534, 536, 540
- Ignatiev, I., 524, 540
- Ignatjevs, A., 31(193), 204
- Ipatova, I. P., 356(1), 362(1), 399(1), 466-467(1), 475(1), 481(1), 489(1), 530
- Ishida, K., 305(79), 320(79), 350
- Ishigame, M., 341, 354
- Ishigawe, M., 445(136), 535
- Jackson, J. D., 387(65), 503(65), 532
- Janak, J. F., 33(214), 205
- Jason, A. J., 327, 352
- Jasperson, S. N., 330, 331, 352, 440, 535
- Jelinek, T. M., 319(117), 351
- Jenkins, L. H., 27(127), 203
- Jennings, P. J., 82(279), 84(279), 206
- Jensen, H., 305(78), 350
- Jensen, M. A., 483(223), 539

- Jepsen, D. W., 13(42), 41(239), 45-46(42, 251), 82(278), 85, 86, 87(239), 90-91 (42,251), 92, 93, 94, 96-99, 101, 106 (42,251), 122(251), 159(251,381), 201, 205-207, 209
- Jhon, M. S., 549(32), 630
- Johansson, G., 20(76), 22(76), 25(76), 27(135), 28(76), 32(76,206), 202, 203, 205
- Johnson, A. L., 27(132), 203
- Johnson, E. J., 415(95), 534
- Johnson, M. D., 547-548(16), 550(16), 630
- Johnson, P. B., 541
- Jona, F., 13(42), 41(239), 45-46(42,251), 82(278), 83(286), 85(42,306), 86, 87 (239), 90-91(42,251,286), 92(42,286), 93-94(42), 96(251), 97(42), 98-99(251), 101, 106(42,251,286), 120, 122(251,320), 159(251,381,383), 201, 205-207, 209
- Jones, E. R., 31(169), 69(169,262), 70, 71, 204, 206
- Jones, G. E., 334(123), 352
- Jones, R. O., 83(284-286), 86(284,285), 87, 90-92(284-286), 106(284-286), 206, 207
- Jones, W. E., 294(52), 350, 379(55), 456 (55), 457-458(165), 489(165), 491, 501, 504, 526(55), 532, 537, 591(91), 633
- Jonson, M., 345, 354
- Jopson, R. C., 18-19(62), 27(62), 201
- Jortner, J., 547(13), 630
- Josephson, B. D., 324, 340, 352
- Joyce, B. A., 27(144), 33(144), 203
- Joyner, B. W., 10(36), 150-151(36), 201
- Juretschke, H., 550(35), 631
- Kadanoff, L. P., 348(236), 354
- Kälin, R., 342, 354
- Källin, R., 438(118), 445(137), 535
- Kambe, K., 14(48), 84, 85, 201, 207
- Kammerer, O. F., 483(223), 539
- Kane, P. F., 26(117), 28(117), 203
- Kaplan, H., 340(180), 353, 467(205), 538
- Kaplan, R., 31(192), 204, 340(180), 348, 353
- Karause, W., 554(46), 631
- Karlson, S. E., 20(76), 22(76), 25(76), 28 (76), 32(76), 202
- Kartheuser, E., 317, 321, 351
- Kasemo, B., 31(182), 107, 108, 169(386), 174(390), 204, 207, 209
- Kawabata, A., 350
- Kellerman, E. W., 400(82), 458(82), 488, 496, 504, 506, 532
- Kennedy, D. J., 22(81), 26(81), 202
- Kenner, V. E., 523, 524, 540
- Kheifets, M. I., 340, 353
- King, D. A., 255(58), 256, 258, 264
- Kinosita, K., 547(20), 630
- Kirkwood, J. G., 548, 630
- Kittel, C., 22(83), 43(246), 48(83), 59(83), 62(83), 82(275), 202, 206, 272(12), 274, 279(12), 312(12), 349
- Kinzel, V. A., 554-556(46a), 558(46a), 631
- Klasson, M., 28(150), 32(203), 203, 205
- Kliwer, K. L., 276(23), 278-279(23), 290, 293(41,52), 342(208), 349, 350, 354, 359(18,19,28), 361(36), 362(18,19), 379(36,51,54,55,58), 380(36,60), 381 (19), 383(60), 387(28), 391(28), 413(60), 416(97), 435(18,19), 436-437(109), 438, 439(109), 441-443(28), 447-448(51), 451 (36), 453(54,160), 454(36), 456(55,160), 490(18), 528(55,58), 531, 532, 534, 547, 578(57), 579(67), 580(59,70), 591(59), 606(57), 631, 632
- Kljushnikov, O. I., 32(203), 205
- Kloos, T., 294(54), 321(126), 350, 352
- Klushin, N. A., 505(238), 540
- Kneubühl, F. K., 342, 354, 438(118), 445 (137), 535
- Knuth, E. L., 23(87), 202
- Kohn, W., 84, 207, 225, 263, 347, 354, 546, 550(7), 597(95), 599(7,97), 602 (95,97), 619, 628, 630, 633
- Kohrt, C., 255-256(57), 258, 264
- Kokkinakis, Th., 305, 351
- Komaki, K., 305(79), 320(79), 350
- Korringa, J., 84, 207
- Kouener, G. S., 525(270), 540
- Koumelis, C., 305(85), 343(85,214), 351, 354
- Kovener, G., 591(91), 633
- Kraut, E. A., 357(4), 530
- Kreibig, U., 305, 321(81), 341(81), 350
- Kretschmann, E., 328, 333, 340(174), 352, 353, 441(127,128), 525, 529, 535
- Kronig, R. de L., 81, 82(269), 206
- Kubo, R., 350
- Kubota, T., 438(116), 534
- Kumar, J., 83(286), 90-92(286), 106(286), 207
- Kunz, A. B., 14(46), 79(46), 87(46), 90(46), 106(46), 201
- Kunz, C., 290, 321(129), 349, 352, 631
- Küppers, J., 147(354), 182(354), 183, 208
- Kusch, P., 23(94), 202
- Kuyatt, C. E., 242(36), 243, 263
- Lakshmi, G., 528, 541
- Landau, L. D., 270, 290, 294(9), 311(9), 318(9), 320, 344(9), 349, 430(103), 534

- Landau, T. D., 560, 623, 631
 Lander, J. J., 14(57), 32(205), 33(226,227), 83, 85, 141-142(340), 154(340), 173(340), 182(340), 184(340), 201, 205, 206, 208, 298(68,69), 332(69), 350
 Landman, U., 4(12,13), 14(47), 32(47), 33-34(12,13,47), 41(47), 45(47,252), 46(47), 47(12,13), 77(12,252), 79(47), 86(47, 242), 87(47), 88(47,242), 89(47,242), 94(47), 96-106(47), 110-111(47), 112(242), 122-123(47), 125(252), 126, 127(12,252, 336,337), 129(252,336,337), 131(336, 337), 134(13,337), 135-138, 139(12,336), 140, 141, 144, 148-150, 151(357), 154, 186(12,13,337), 189(12,13,252,336,337), 190(12,13,337), 191, 192(13), 193-197, 200, 201, 206-208
 Lang, B., 10(36), 150, 151(36), 201
 Lang, N. C., 347, 354, 546, 550(7), 597(95), 599(7,98), 602(95), 619, 628, 630, 633
 Langenberg, D. N., 325, 352
 Langreth, D. C., 343, 354
 Laramore, G. E., 4(4,7,10), 14(46), 31(9), 32(9,10,197,199), 34(7,9,10,199), 40(7), 41(241,242), 45-46(247,250), 73(10, 199), 75(265), 77(9,10,247), 79(9,10,46, 250), 80(9), 81, 85(197), 87(46,241,312), 90(10,46,197,241,242,250,265), 94, 95-96(250), 97, 98(250), 100(241,242,250, 312), 101(9), 102(10), 103(10,197,199, 242), 104(10,199), 105(199), 106(46,197, 242,265,312), 107(312), 108, 109(326), 111(199), 114(241,242), 115(242, 326), 118(241,242), 119(250), 120, 122(197, 250,328,329), 123, 124(241,242), 125(247,332), 126, 127(332-334), 128, 129(333,334), 130(333,334), 131(332-334), 144(329), 151(329,363), 156(197,250, 265,326,363), 160(240,241,326), 161-162(241), 163(241,242), 167(241,242), 168-172(242), 174(197,250,326), 180, 183(197), 189(332-334), 200, 201, 205-208, 515-517, 529, 540
 Larrabee, G. B., 26(117), 28(117), 203
 von Laue, M., 83-85, 207
 Lauzier, J., 98(321), 100(321), 122(321, 327), 207
 Lawless, K. R., 29(156,157), 204
 Lea, C., 242(35), 248-249(35), 263
 Lederer, D., 226(21), 263
 Lee, A. E., 29(161), 204
 Legally, M. G., 58(258), 64(258), 140(258), 156(372-374), 173-175(372-374), 176, 178(372-374), 206, 208
 LeJeune, E. J., 32(211), 205
 Lemberg, H. L., 623(104), 633
 Lengler, B., 466(199), 467(199,206), 538
 Lennard-Jones, J. E., 549(30), 551, 630
 Leung, C., 255-257(61), 264
 Leventouri, D., 305(85), 343(85,214), 351, 354
 Lewis, R. M., 318(103), 351
 Licciardello, D. C., 301(73), 348, 350
 Liebsch, A., 182-183(397), 209
 Lifshitz, E. M., 270, 290, 294(9), 311(9), 318(9), 320, 344, 345, 348(221), 349, 354, 430(103), 534, 560, 631
 Lind, A. C., 341(204), 354
 Lindau, I., 294(60), 350, 457(162), 537
 Lindberg, B., 20(76), 22(76), 25(76), 28(76), 32(75), 202
 Lindgren, I., 20(76), 22(76), 25(75), 28(75), 32(76), 202
 Lipari, N. O., 14(47), 32-34(47), 41(47, 241,242), 45(47), 46(47,242), 77(47), 86(47,242), 87(47,241), 88-89(47,242), 90(241,242), 94(47), 96-99(47), 100(47,241,242), 102(47), 103(47,242), 105(47), 106(47,242), 107(242), 110-111(47), 112(242), 114(241,242), 115(242), 118(241,242), 122-123(47), 124(241,242), 160(241,242), 161-163(241,242), 167(241,242), 168-172(242), 200, 201, 206
 Lipson, H., 157-158(380), 209
 Liu, W. S., 23(96), 202
 Lopez-Rios, T., 340(174), 353
 Löt, W., 15, 19(64), 201
 LoVecchio, G., 596(94), 610(94), 633
 Lovett, R. A., 549, 630
 Löwdin, P. O., 88, 207
 Lu, W. C., 549(32), 630
 Lucas, A. A., 317, 321, 322, 327, 345, 351, 352, 354, 449(152,153), 459(168), 489-491, 497, 499, 536,537, 546, 553(3), 630
 Ludwig, W., 465, 466(191,199), 467(191, 199,206), 538
 Lundquist, B. I., 31(193), 204
 Lundquist, S., 90(318), 207
 Luxon, J. R., 444(131,132), 505(132,241), 535, 540
 Lyddane, R. H., 359, 531
 Lyon, H. B., 31(177), 204
 Lyubimov, V. N., 425(101), 432(101), 534
 McAlister, A. J., 294(48), 350
 McBain, J. W., 547(19), 630
 MacDonald, N. C., 19(74), 25(74), 202
 McKinney, J. T., 31(169), 69(169,262), 70(169), 71(169), 204, 206
 McLane, S. B., 25(105), 202

- McMillan, W. L., 221(9), 262
 MacNair, D., 28(154), 204
 McNatt, J. L., 27(147), 33(147), 203
 MacRae, A. U., 31(175,176), 33(215,227), 204, 205, 298(69), 332, 326, 350, 352
 McRae, E. G., 4(3), 8(3), 14, 28(3), 40(3), 74(263), 82(276,277,279), 84, 85, 91, 108, 141(3), 147, 151(3), 154(3), 173(3), 184(3), 200, 206, 207, 516, 540
 Macrae, R. A., 294(49), 350
 Madden, Jr., A. H., 146-147(348), 152(348), 208
 Madey, D. W., 250(52), 263
 Madey, T. E., 10(32), 201
 Magnaterra, II, A., 596(94), 610(94), 633
 Maguire, H. G., 32(210), 205
 Mahan, G. D., 316, 317, 351, 367(44), 532
 Mamm, R. N., 587(76), 590(76), 632
 Mandl, A., 19(69), 25(69), 27(69), 202
 Manson, R., 31(162), 204
 Manson, S. T., 22(81), 26(81), 202
 Many, A., 9(25), 10(37), 201
 Maradudin, A. A., 341(193), 353, 356(1), 362(1), 394(74), 399(1), 464, 466(200), 467, 475(1), 481(1), 489, 491, 498, 500, 501, 510(249), 511(200), 512, 513, 527(249), 530, 532, 538-540
 Marc de Chazal, L. E., 547-549(15), 630
 March, N. H., 547-548(16), 550(16), 630
 Marcus, P. M., 13(42), 41(239), 45-46(42, 251), 82(278), 85, 86, 87(239), 90-91(42,251), 92-95(42), 96(251), 97(42), 98-99(251), 101, 106(42,251), 122(251), 159(251,381), 201, 205-207, 209
 Mark, H., 18-19(62,63), 27(62,63), 201
 Marklund, I., 29(159), 204
 Marschall, N., 338, 340, 353, 440, 445, 446-447(143), 529, 535, 587(77), 591(77, 90), 622(90), 632
 Martin, M. R., 14(49), 201
 Martin, T. P., 341, 354, 444, 505(133,237, 239,240), 506-509, 529(134), 530, 535, 540
 Martinson, J., 29(159), 204
 Marusak, A. L., 451(158), 537
 Mascall, A., 31(190), 204
 Mason, R., 157-158(378,379), 174(378, 379), 180(378), 209
 Masri, P., 466(192), 481, 538, 539
 Massey, H. S. W., 6(17), 14(17), 23(93), 100(17), 200, 202
 Matamura, O., 438(114,116,117), 534
 Matsudaira, N., 294(58,59), 343(209), 350, 354
 Mattheiss, L. F., 88, 207
 Matthew, J. A. D., 19(73), 25(73), 26(73, 121), 27(73), 202, 203
 Mattis, D. C., 219(6), 279(29), 280, 349
 May, J. W., 4(2), 8(2), 28(2), 40(2), 141(2), 151(2), 154(2), 173(2), 182(392), 184(2), 200, 209
 Mayer, J. W., 23(86), 25(86), 28(86), 202
 Mel'nik, P. V., 26(118,119), 203
 Melnyk, A. R., 278(28), 291, 294(28,38), 349, 460, 463, 537
 Menadue, J. F., 29(160), 204
 Menzel, D., 250(51), 255(59,60), 256(59), 263, 264
 Merrill, R. P., 23(91), 29(91), 202
 Merzbacher, E., 21(78), 202
 Metze, V., 125(332), 127(332), 131(332), 189(332), 208
 Meyer, F., 27(124), 203
 Michalke, M., 554(46), 631
 Mie, G., 350, 359, 531
 Miliotis, D. M., 343(213), 354, 579(67), 632
 Miller, D. R., 31(164,165), 204
 Mills, D. L., 62(261), 206, 371(49), 464, 466(200), 510, 511(200), 532, 538, 540
 Mirlin, D. N., 340, 341, 353, 354, 417(145), 435, 444(130), 445(140,141,145), 447(106,145), 499(130), 505(130,236), 529(130), 530, 534, 535, 540, 591(90), 622(90), 632
 Mitchell, D. F., 29(156,157), 204
 Mitchell, I. V., 23(86), 25(86), 28(86), 202
 Mityagin, A. Yu., 82(272,273), 141-142(341), 154(341), 173(341), 184(341), 206, 208
 Mizuno, Y., 342(106), 354
 Miziumski, C., 305, 307, 351
 Modinos, A., 225, 263
 Moliere, K., 83, 206
 Montgomery, D. J., 444(132), 505(132), 535
 Montroll, E. W., 356(1), 362(1), 399(1), 466-467(1), 475(1), 481(1), 489(1), 512, 530
 Mooiju, J. E., 438(113), 534
 Morabito, Jr., J. M., 31(178), 204
 Morris, G. C., 591(89), 632
 Morrison, J., 14(57), 33(226,227), 83, 85, 201, 205, 206, 298(68,69), 322(69), 350
 Morse, P. M., 14(51), 81-83, 201, 396(79), 532
 Moruzzi, V. L., 33(214), 205
 Mott, N. F., 6(17), 14(17), 23(93), 100(17), 200, 202
 Mularie, W. M., 27(125), 203
 Müller, E. W., 11(39), 25(39,105), 28(39), 29, 30(39), 201, 202, 226-227(22),

- 229, 237, 239, 263
 Müller, K., 33(227), 205, 298(69), 322
 (69), 350
 Murphy, E., 571, 572, 574-576, 580(55),
 620, 631
 Musket, R. G., 24(100), 26(100), 27(139),
 28(148), 32(208), 33(139), 202, 203, 205
- Nakhodkin, N. G., 26(118,119), 203
 Natta, M., 304, 305, 350
 Neave, J. A., 27(144), 33(144), 203
 Nemnov, A., 32(203), 205
 News, D., 214, 219-220(4), 249(4), 262
 News, D. M., 299, 343, 346(227,228), 350,
 354, 550(37), 552(37), 599(37), 631
 Ngai, K. L., 33(231), 205, 296(64), 297,
 298(64,67,70), 299, 301(67), 305, 307
 (90), 316(64,70), 322, 323-324(67), 325,
 326(142), 350-352
 Ngoc, T. C., 156(372-374), 173-176(372-
 374), 178(372-374), 208
 Nicholas, J. F., 8(20), 142, 150, 200
 Nickel, J. C., 610(100), 633
 Nicolet, M. A., 23(86), 25(86), 28(86), 202
 Nijboer, B. R. A., 344, 354
 Nilsson, P. O., 294(60), 350, 457(162), 537
 Nilsson, R., 32(203), 205
 Nordberg, R., 19(67), 20(67,76), 22(76),
 25(67,76), 27(67,134), 28(76), 32(76),
 202, 203
 Nordling, C., 19(66-68), 20(66-68,76), 22
 (76), 25(66-68,76), 27(66-68,134), 28
 (76,150), 32(76,203), 201-203, 205
- Offergeld, G., 28(153), 204
 Ohama, N., 438(117), 534
 Ohmura, Y., 342(206), 343(209), 354
 Ohtsuki, Y. H., 85, 207
 Okamoto, Y., 438(114,116,117), 534
 O'Keefe, D. R., 23(90), 29(90), 202
 O'Keefe, T. W., 571, 631
 Oliner, A. A., 580(86), 589, 632
 van Oostrom, A., 242(34), 263
 Otto, A., 294(44), 340, 341, 349, 353,
 369(46), 379(56), 412(46), 432(104),
 435, 445(138), 447, 519, 520, 529, 532,
 534, 535, 540, 590, 591(89,91), 592-593
 (87), 606(87), 611, 616, 632, 633
 Ouder, J., 167, 209
 Overhauser, A. W., 515, 540
- Pafomov, V. E., 318(97,102), 351
 Pakhomov, V. I., 340, 353
 Palik, E. D., 340, 348, 353
 Palmberg, P. W., 4(15), 7(15), 19(15,74),
 25(15,74), 26-27(15), 200, 202, 244(42), 263
- Palmer, R. E., 580(68), 632
 Palmer, R. L., 23(90), 29(90), 202
 Panitz, J. A., 25(105), 202
 Pankove, J. I., 9(22), 20(22), 200
 Paranjape, B. V., 596(93), 610(93), 633
 Pardee, W. J., 436-437(109), 438, 439
 (109), 534
 Park, R. L., 4(1), 7(1), 12(1), 18, 25(104,
 107), 26(111-116), 27(113-116), 28(1),
 33(113,114,116), 52(256), 122(329),
 141-142(1), 144(329), 146(348), 147
 (256,348,356), 148, 151(329,356,362,
 363), 152(348), 159(363), 182, 183
 (400), 200, 202, 203, 206-209
 Parker, J. V., 610(100), 633
 Parks, R. D., 483(223), 539
 Parks, W. F., 591(91), 633
 Parratt, L. G., 26(122), 203
 Paskin, A., 483-485, 530, 539
 Pattanayak, D. N., 463(181), 464, 538
 Pattinson, E. B., 27(126), 33(126), 203
 Paul, G. W., 547-549(15), 630
 Paulson, R. H., 224, 263
 Pekar, S. I., 463(177), 538
 Pendry, J. B., 14(45), 31(193), 45(249),
 79, 82(52), 83(45,249,287), 85-87, 90
 (249,287,310), 91(249,310), 92(249),
 100(307,308), 106(45,52,287), 107,
 114, 115(45,307,308), 124(310), 159
 (382), 160(310,382), 164, 165, 169(386),
 201, 204, 206, 207, 209, 467(201), 511
 (201), 538
 Penn, D., 220, 222(7), 225, 226, 230, 232
 (26), 233, 234(30), 235, 244(44), 262,
 263
 Penny, W. G., 81, 82(269), 206
 Perdereau, M., 27(133), 150-151(360),
 167, 203, 208, 209
 Peria, W. T., 27(125,131), 203
 Perlman, M. L., 28(149), 203
 Perry, J. J., 43(245), 83(245), 206
 Pessa, M., 4(14), 7(14), 20(14), 25-26(14),
 200
 Pfeiffer, C., 305(90), 307(90), 348, 351
 Phillip, H. R., 275(21), 349, 541
 Phillips, H. R., 622, 633
 Phillips, J. C., 33(227), 205, 298(69), 322
 (69), 350, 580(69), 632
 Pines, D., 273(14,18), 342(18), 348(15,18,
 238), 349, 354
 Pinsker, Z. G., 83(288), 207
 Piper, T. C., 31(171), 204
 Pitaevskii, L. P., 345, 348(221), 354
 Platz, O., 549(26), 552, 630
 Platzman, P. M., 266, 270(1), 272-275(1),

- 342-343(207), 348(1), 348, 354
Plesner, C. W., 549(26), 552, 630
Plummer, E. W., 33(222), 205, 230(26),
231, 232(26), 233, 242(33), 243, 244,
246-248, 249(33), 250-252, 261, 262,
263
Pogorel'skii, K. S., 82(272,273), 206
Porteus, J. O., 4(13), 33-34(13), 38(235,
238), 47(13), 122(331), 129-130(238),
134(13), 141, 186(13), 189(13,40,235,
238), 190(13), 192(13), 193, 194, 200,
205, 208, 209, 323, 347(137), 352
Powell, C. J., 19(69,70), 25(69,70), 27(69),
202, 268-269(3,7), 289, 321(35), 348,
352, 631
Pratt, R. H., 22(79), 202
Price, R. E., 18-19(63), 27(63), 201
Priftis, G., 343, 354
Prigogine, I., 549(31), 630
Pritchard, J., 10(35), 201
Propst, F. M., 31(171), 38(236), 129-130
(236), 132(236), 204, 205
Prutton, M., 141-142(344), 184(344), 208

Queisser, H. J., 338, 353, 440(121,122),
445-447(143), 535, 587(77), 591(77,90),
622(90), 632
Quinn, J. J., 340(180), 341(192), 348, 353,
415(96), 534, 631
Quinto, D. T., 27(145), 31(194), 33(145),
105, 111, 123, 156(375), 159(145), 173
(375), 203, 204, 209

Radcliff, C., 319(104), 351
Raether, H., 15(59), 201, 268-269(2,6),
275(2), 290, 305(84), 321(2,6,36,129),
328(154), 333, 342(208), 348-350, 352-
354, 441(127), 525, 529, 535, 579(60),
631
Rahman, A., 467(210), 478, 479-480(210),
511(210), 530, 539
Raman, C. V., 547(18), 630
Ramdas, L. A., 547(18), 630
Rao, P. V., 18-19(63), 27(63), 201
Raskin, D., 23(94), 202
Lord Rayleigh, 357, 471, 497, 530, 547,
548, 589, 630, 632
Ree, T., 549(32), 630
Ree, T. S., 549(32), 630
Reid, R. J., 31(183,184,196), 76(196), 204
Reshina, I. I., 341, 353, 354, 417, 435, 447
(106), 530, 534, 535, 591(90), 622(90),
632
Reuter, G. E., 278(24), 349
Reuter, G. E. H., 451(157), 537
Rhead, G. A., 31(195), 150-152(360),
182(195), 204, 208
Rhodin, T. N., 14(44), 31(193), 79(44),
81(44), 86(311), 89-91(44), 96(319),
106(44), 107-108(323), 201, 204, 207,
524, 540
Riach, G. E., 19(74), 25(74), 202
Rice, S. A., 547, 552(8), 571, 572-576, 580,
610, 611, 617-623, 628, 630, 631, 633
Rieder, K. H., 341, 354, 445, 505(242),
508, 509, 535, 540
Ritchie, R. H., 197(402), 209, 268-269(8),
274(20), 289, 291(8,39), 294(8,43,51),
304, 318-319(43), 320(20), 328, 330-
334, 336-338, 349, 350, 352, 353, 358,
361(16), 382(61), 416(16,33), 436(33),
440, 451(158), 525(269), 530-532, 537,
540, 579-580(59), 587(76-78), 589, 590
(76,78), 591(59,77,78), 631, 632
Riviere, J. C., 25(106,110), 27(129,138,
142), 33(138,142), 202, 203
Robert, T., 28(153), 204
Robertson, W. C., 27(145), 31(194), 33
(145), 105(194), 111(194), 123(194),
141(343), 156(375), 159(145), 173(343,
375), 182(396), 184(396), 203, 204, 208,
209
Rodgers, W. E., 23(87), 202
Roether, M., 579(67), 591(89), 632
Rosenfeld, L., 357(8), 530
Rosenstock, H. B., 394(73), 532
Rostoker, N., 84, 207
Roundy, V., 62(261), 206
Rudge, M. R. H., 6(18), 14, 15, 24(18),
200
Ruppin, R., 340, 341(203), 353, 354,
358(20), 359, 362(39), 395(21-23,39),
397(39), 401, 402(21), 428, 442(29),
443, 444(129), 463, 526, 527, 531, 535,
538, 541

Sachs, R. G., 359, 531
St. James, D., 226(21), 263
Saltsburg, H., 9(26), 23(26,90), 29(26,90),
31(26), 201, 202
Salzmann, E., 357(4a), 530
Samoilovich, H., 546(5), 630
Samson, J. A. R., 245(46), 263
Sannikov, D. G., 425(101), 432(101), 534
Saraga, L., 549(31), 630
Sauerbrey, G., 294(50), 319(104-107), 332,
334(105-107), 350-353
Sauerwald, F., 554, 631
Sauter, F., 294(61), 350, 460, 537
Scalapino, D. J., 325, 352
Sceats, M. G., 591(89), 632
Schacher, G. E., 539

- Schaich, W. L., 244(43)
 Scheibner, E. J., 32(207), 33(224,225), 205
 Schiff, L. L., 47(253), 87(253), 206, 270(10), 349
 Schmickley, R. D., 22(79), 202
 Schmidt, L. D., 250(49), 263
 Schmit, J., 345, 354, 546, 553(3), 630
 Schmöser, P., 321(130), 352
 Schnatterly, S. E., 330-332, 352, 440, 535, 580(68), 632
 Schoenwald, J., 340(174), 353, 369(47), 447(47), 532, 591(91), 596, 633
 Schram, K., 344, 354
 Schreiner, D. G., 26(111), 203
 Schrieffer, J. R., 219(6), 224, 250, 262, 263
 Schrijvers, J. E., 438(113), 534
 Schull, C. G., 22(82), 202
 Schwartz, L., 145(347), 208
 Schwoebel, R. L., 150(358), 151(358), 208
 Scott, J. F., 341, 354
 Scrivisan, R., 541
 Seah, M. P., 31(180,181), 38(234), 129 (234), 204, 205
 Seifert, H. G., 319(106), 334(106), 351
 Sein, J. J., 463(180,182), 464, 538
 Sellberg, F., 440(123), 535
 Semenchenko, V. K., 553-554(42), 631
 Sewell, T. B., 29(155,158), 204
 Sham, L. J., 599(97), 602(97), 633
 Shaw, R. W., 551(40,41), 551(41), 631
 Shieh, S. Y., 294(53), 350
 Shoemaker, P. D., 547-549(15), 630
 Sickafus, E. N., 4(5), 6(5), 7, 8(5), 19(5), 26-27(5), 33(229,230), 36(5), 40(5), 141-142(5), 154(5), 173(5), 184(5), 200, 205
 Siegbahn, K., 19(67,68), 20(67,68,76), 22(76), 25(67,68,76), 27(67,68,134), 28(76,152), 32(76,152), 202-204
 Silcox, J., 527, 541
 Silin, V. P., 318(101), 319(101), 351, 554 (46), 558(46c), 631
 Simmons, G. W., 29(156,157), 204
 Simms, D. L., 23-24(88), 202
 Sinharoy, S., 174(389), 209
 Siskind, B., 575, 576(56), 580(56), 621, 631
 Skibowski, M., 294(56), 350
 Skillman, S., 41, 88(243), 206
 Slater, J. C., 14, 45(55), 83, 201, 207
 Smith, D. L., 77(266), 79-81(266), 90(266), 156(369), 159(369), 173-175(369), 178, 179, 206, 208
 Smith, D. P., 23(85), 25(85), 28(85), 202
 Smith, Jr., H. P., 83(283), 90(283), 206
 Smith, J. N., 9(26), 23(26,90), 29(26,90), 31(26), 201, 202
 Smith, J. R., 225(13), 263
 Smith, N. V., 33(213), 205, 244(38), 263, 326, 352, 571, 572, 574, 611, 631
 Smith, R. J., 599(98), 632
 Snow, E. C., 94, 97, 101, 120, 134, 191, 207
 Sohler, W., 591(91), 633
 Sommerfeld, A., 358(13), 359, 530, 589, 632
 Somorjai, G. A., 4(4), 6(4), 7, 8(4), 10(36), 14(49), 28(4), 31(170,177,178,192), 36 (4), 40(4), 72(170), 141-142(4), 150-151 (36), 154(4), 156(371), 173(371), 174 (371,388), 184(4), 200, 201, 204, 208, 209, 467(204), 509(247), 538, 540
 Sondheimer, E. H., 278(24,27), 349, 451 (157), 537
 Sorokina, M. F., 32(203), 205
 Spicer, W. E., 32(200), 33(200,213,219), 205, 244, 246(41), 263, 326, 332, 338, 352, 253, 588, 589, 632
 Srinivasan, G., 345, 354
 Srinivasan, R., 528, 541
 Stanford, J. L., 331, 332, 352, 588, 632
 Steiger, R. F., 31(178), 204
 Stein, E. A., 579(60,64), 580(64), 586, 631, 632
 Stein, R. J., 38(237), 129-130(237), 205
 Steinhardt, R. G., 28(149), 203
 Steinmann, W., 268-269(5), 275(5), 294 (5,56), 319(108,113,118), 320, 327, 332-334, 348, 350-352, 579, 580(69), 632
 Steinrisser, F., 33(229,230), 205
 Stepanov, K. N., 340, 353
 Stern, E. A., 280(30), 289, 317, 319(46), 320(30), 328, 333, 334(125), 336-338, 349, 350, 352, 358, 416(17), 531, 587, 632
 Stern, O., 23(89), 202
 Stern, R. M., 38(237), 43(245), 83, 129-130(237), 174(389), 205, 206, 209
 Steyer, T. R., 341, 354
 Stickel, W., 321, 352, 447(148,149a), 448 (148), 535
 Stickney, R. E., 23(92), 29(92), 202
 Stillinger, Jr., F. H., 549(24), 630
 Stoelinger, J. H. M., 529(280), 541
 Stojanovic, S., 371(49), 532
 Stone, F. S., 10(31), 201
 Stonely, R., 466(195), 538
 Stratton, J. A., 286(32), 301(32), 305(32), 349, 359(26), 387(26), 531
 Stratton, R., 227(24), 263
 Strongin, M., 483(223), 539

- Strozier, Jr., J. A., 83(284-286), 86(284, 285), 87, 90-92(284-286), 106(284-286), 159(383), 206, 207, 209
- Sturm, K., 460, 463, 537
- Subbarao, R. B., 31(164,165), 204
- Suleman, M., 27(126), 33(126), 203
- Summitt, R., 444(131,132), 505(132,241), 535, 540
- Sunjie, M., 317, 321, 322, 352, 449(152, 153), 536
- Suzuki, H., 294(55), 343(211), 350, 354
- Swan, J. B., 289, 321(35), 349, 631
- Swanson, L. W., 240(32), 242(32), 246, 249, 253, 256(62), 263, 264
- Swiatecki, W. J., 550(34), 631
- Swift, C. D., 18-19(62,63), 27(62,63), 201
- Swihart, J. C., 298(65), 324, 350
- Switendick, A. C., 33(217), 75(265), 90 (265), 106(265), 108, 109, 159(265), 205, 206, 515-517, 530, 540
- Sziklas, E. A., 596(93), 610(93), 633
- Szostak, R. J., 182(392), 209
- Tabor, D., 31(185-188), 204
- Tait, R. H., 86(311), 207
- Takeishi, Y., 85, 90(299), 207
- Tamm, P. W., 250(49), 263
- Tanokuba, A., 343(211), 354
- Taub, H., 98(321), 100(321), 122(321), 207
- Taylor, B. N., 325, 352
- Teller, E., 359, 531
- Tendulkar, D. V., 23(92), 29(92), 202
- Teng, Y. Y., 334(125), 336-338, 352, 587, 632
- Terakura, K., 263
- Tescari, M., 157-158(378,379), 174(378, 379), 180(378), 209
- Tharp, L. N., 33(224,225), 205
- Theeten, J. B., 31(189,191), 41(242), 46 (242), 86(242), 88-90(242), 100(242), 103(242), 106-107(242), 112(242), 114-115(242), 118(242), 124(242), 160(242), 163(242), 167-172(242), 200, 204, 206, 467(203), 481-483, 530, 538, 539
- Theodosiou, A., 343(210), 354
- Thomas, D. G., 463(178), 464, 538
- Tolk, N. H., 23(88), 24(88,99), 202
- Tong, S. Y., 14(44), 31(193), 79(44), 81 (44), 86(311), 89-91(44), 96(319), 106 (44), 107-108(323), 204, 207, 491, 498, 500, 501, 539
- Tosic, B. S., 371(49), 532
- Toxvaerd, S., 549-550(27), 552, 630
- Tracy, J. C., 182(393), 209
- Trapezikov, V. A., 32(203), 205
- Trounson, E. P., 319(109), 351, 579(66), 632
- Trullinger, S. E., 509, 511, 524, 527(248, 267), 530, 540
- Tsong, T. T., 11(39), 25(39), 28(39), 29, 30(39), 201
- Tsui, D. C., 325, 326(141), 352
- Tucker, Jr., C. W., 6(19), 9(19,29), 14, 29(19), 40(29), 45(19,248), 51(255), 76(255), 77(19,248,255), 79(29), 80 (248), 81, 82(19), 85(19,29,54,248,255), 116, 146(349), 156(29,54,248,255,366-368), 157(368,377), 158(19,255,368), 159(29,366-368), 160(366-368), 173 (366-368), 174, 175(255,366-368), 178-181, 200, 201, 206, 208, 209, 467(202), 538
- Turbador, T., 340, 353
- Turnbull, J. C., 38(232), 125(232), 205
- Turner, D. W., 251(53), 263
- Tyler, I. L., 340, 353
- Van Hove, M. W., 169(386), 209
- Van Kampen, N. G., 344, 354
- Varga, B. B., 415(93), 534
- Vass, M., 255-257(61), 264
- Vincent, R., 527, 541
- Vosko, S. M., 571, 631
- Vrakking, J. J., 27(124), 203
- van der Waals, J., 547(10), 553, 630
- Waclawski, B. J., 22(222), 205
- Walecka, J. D., 348(237), 354
- Wallis, R. F., 340(180), 341(192,193), 348, 353, 357(6), 371(48), 415(94), 418, 419, 420(99), 422-425(99), 426 (102), 427(99,102), 431-432(99), 466 (196,198,200), 481(219), 511(200), 530, 532, 534, 538, 539
- Wang, S. Q., 316, 317, 351, 367(44), 532
- Weaire, D., 545(1), 550-552(1), 630
- Webb, M. B., 31(169), 38(233), 58(258), 64(258), 69(169,262), 70-71(169), 140(258,338), 156(372-374), 173-176 (372-374), 178(372-374), 189(233), 204, 206, 208
- Webb, W. W., 547, 549(9), 553(9), 630
- Weber, R. E., 19(74), 25(74), 27(131,132), 202, 203
- Weber, W. H., 38(233), 189(233), 205
- Wei, P. S. P., 33(228), 205
- Weinberg, W. H., 23(91), 29(91), 202
- Weiss, G. H., 356(1), 362(1), 394(74), 399(1), 466-467(1), 475(1), 481(1), 489(1), 530, 532
- Wertheim, G. K., 32(204), 205

- Wessel, P., 319(109), 351, 579(66), 632
 de Wette, F. W., 467(208-212), 469(209),
 470(211), 471(212,213), 472-473(212),
 474(214), 475(209), 476-478, 479(210),
 480(209,210), 487, 496(230-232), 497-
 498(230), 499, 504(235), 507(245), 511
 (210-212), 514, 518(230), 529(233), 539,
 540
 Wheatly, G. H., 28(154)
 Whitaker, M. A. B., 27(146), 33(146), 203
 White, C. W., 23(88), 24(88,99), 202
 White, D. W. G., 553, 631
 Wienhold, P., 321(128), 352
 Wilems, R. E., 291(39), 334, 328, 334,
 349, 352
 Wilets, L., 550(36), 631
 Wilkinson, M. C., 548(23), 630
 Wille, H., 319(118), 351
 Williams, A. R., 33(214), 205
 Williams, B. R., 31(166), 204
 Williams, M. W., 294(51), 319(120), 350,
 351, 525(269), 540
 Wilson, E. G., 622, 633
 Wilson, J. M., 31(185-188), 204
 Winkel, D. E., 82(277), 84(277), 206
 Wise, H., 23(84), 202
 Wiser, N., 449(154), 536
 Wolf, E., 350, 359(27), 387(27), 463(181),
 464, 531, 538, 564, 590(88), 631, 632
 Wolff, P. A., 266, 270(1), 272-275(1),
 348(1), 348
 Wolfram, T., 357(4), 371(49), 530, 532
 Wollan, E. O., 22(82), 202
 Wong, C., 159(383), 209
 Wood, B. J., 23(84), 202
 Wood, E. A., 84, 142, 145(291), 146,
 155(291), 207
 Wood, R. W., 589, 632
 Woodruff, D. P., 31(180,181), 85(303),
 90(303), 204, 207
 Wooten, F., 9(23), 20(23), 200
 Wyder, P., 529(280), 541
 Wyllie, G., 546(6), 630
 Yamada, K., 294(55), 350
 Yamaguchi, S., 294(57), 350
 Yates, Jr., J. T., 10(32), 201, 255-256(58),
 258, 264
 Ying, S. C., 225(13), 263
 Yokota, H., 547(20), 630
 Yokota, I., 415(92), 534
 Yoshioka, H., 14(56), 201
 Young, P. L., 252-256, 263
 Young, R. D., 12(40), 29(40), 142-144(40),
 201, 229-230, 240, 246-248, 263
 Zacharias, P., 305, 321(81), 341(81), 350
 Zenneck, J., 358-359(12), 530
 Zeyher, R., 463(183), 538
 Zyryanov, V. G., 32(203), 205

SUBJECT INDEX

- Absorptance, 436, 437, 457, 461, 501-502
Absorption, 332
Absorption coefficient, 507
 surface-induced, 508
Absorption cross section, 441
Active medium, definition, 360
Adsorption, 218
 electronegative, 218
 electropositive, 218
Ag, 440, 525-526
Al, 526
Ar, 476, 479, 486
Alkali metals, 526
Angular profiles, 128-131, 133, 135, 188
Anharmonic effects, 404-414, 476, 480, 483
Anomalous skin effect, 278, 281, 282, 290, 291
Appearance potential spectroscopy, 26, 27
Attenuated total reflection, (ATR) 339, 445-449, 519-523, 525-526
Atomic basis, 142
Atomically flat surface, 8, 142
Auger processes, 18
Auger spectroscopy, 26

Backplate, metallic, 378
Bank structure effects, 275
Barium titanate, 44, 505
Be, 526
Biaxial crystals, 430-433, 435, 527
Binding energy, 218
Bloch Rice model for liquid mercury, 572
Boltzmann-Vlasov equation, 269, 274, 276
Boundary-active medium, definition, 360
Boundary conditions, 365, 375, 379, 390, 399, 422, 426, 432, 453
 additional, 451, 461-465
 microscopic theory, 466
Boundary-inactive medium definition, 360
Bound modes, 283, 284, 293, 294, 302, 319
 virtual, 285, 293, 294, 319
Bragg envelope concepts, 174
Bravais net, 50, 142, 152
Brewster angle, 408-410, 412, 420, 436, 439
Brillouin scattering, 463
Brillouin zone, 455, 458, 470-471, 510, 524

NaCl structure, 488, 510
 reconstructed surface, 512
Bulk modes, 381, 391, 456, 471-474, 490-491, 510
Bulk plasmons, 457

CaF₂, 445
CaMoO₄, 447
CdO, 414, 445
CdR₂, 445
Cerenkov radiation, 311, 318, 320
Characteristic loss spectroscopy, 25
Chemisorption, theory of, 212
 linear response (Kohn-Smith-Ying method), 225
 Newns-Anderson model, 214
 resonance, 213
 Surface molecule, 217
 Bonding and antibonding levels
 valence bond (Schrieffer-Paulson, Gomer) approach, 224
CO adsorption, 255
 beta or beta precursor, 256
 electron impact desorption, 256
 electron structure of virgin CO, 258
 virgin, 255
Coherence zone, 52, 53
Coincidence site structures, 146
Collision, 267
 damping, 275
 time, 267, 275, 276, 281
Conductivity, 272
 longitudinal, 272
 transverse, 272
Conductor, 278; *see also* Metal
Constant-angle modes, 429, 523
Continuum theory, 357, 490, 505, 529
Coordinate system, 396
 cylindrical, 396-397, 402
 general, 395-401
 rectangular, 401, 403
 spherical, 387-389, 402
Coster-Kronig transitions, 27
Coulomb forces, 359, 435, 489, 503-504, 510, 518
CsCl, 528-529
Cube modes, 444, 529
Cutoff wavevector, 345, 347
Cyclotron frequency, 267, 270

- Cylinder modes, 396, 402
- Damping, 380, 404-414, 419, 429-430, 438
 ATR measurement of, 446-447
 frequency-dependent, 439, 447, 503
 intrinsic, 522
 radiative, 382, 387, 438, 522
 small particles, 444
- DeBoer parameter, 476
- Debye temperature, 479, 482, 516
- Debye Waller factor, 63, 69
- Degeneracy, 471, 472
 slab modes, 471
 sphere modes, 391, 394, 444
- Density of states, phonons, *see* Frequency spectrum, 417, 484
- Density profile, 550
 in liquid metals, 550
- Diamond, 481
- Diatomic crystals, 359, 367
- Dielectric function, 272, 273, 279, 357, 358
 alkali halides, 359, 407
 complex, 371, 405
 complex crystals, 428, 430
 damping in, 361, 378, 380, 404-405, 429
 diatomic crystals, 359, 367
 electron gas, 361, 378
 insulators, 280
 local, 357, 362, 364, 379, 415
 longitudinal, 272, 379-380, 450, 455, 457
 metal, 361, 378
 mixture, 444
 nonlocal, 357-362, 379, 415, 449-459
 polar semiconductor, 415, 420
 poles in, 429
 RPA, 459, 462
 semiconductors, 279, 280
 transverse, 272, 379-380, 450
- Dielectric susceptibility, 452, 500
- Dielectric tensor, 420, 425, 430, 450
 complex, 435
- Differential inelastic scattering cross-section, 59, 60
- Diffuse surface, 603
 second dispersion branch, 603
 in step inhomogeneity, 604
 in truncated exponential profile, 603
- Dipole moment, 444
- Dispersion relation, 289, 292, 323
- Dispersion relations of electronic excitations, 2
 Al (111), 194-196
 bulk excitations, 56
 bulk plasmons, 131
 determination of surface excitation dispersion, 185
 surface excitations, 57
 surface plasmons, 131, 191
- Dispersion relation of surface modes,
 asymptotic behavior, 368-369, 376-377, 393, 404, 408-409, 411, 416-417, 419, 422, 433, 456
 half-space, 365-369
 nonreciprocal, 422, 424, 427
 slab, 368, 374-375, 377
 metallic backing, 379
 microscopic theory, 492-493
 termination point, 369, 373, 376-378, 416, 419, 429, 453, 518-519
- Drude sharp surface, 611
- Dynamic effective charges, 509-511, 513-514, 524, 527
- Dynamic equilibrium 475-576, 480
- Dynamical matrix, 470, 481, 488-489
- Effective Debye temperature, 70, 102
- Electric field, 367
 half-space, 367
 slab, 372, 383-385
 sphere, 393
- Electric modes, 391-397
- Electric Solutions, 283, 286, 294
 P-waves, 283, 286, 294
- Electromagnetic fields, 393
 localization at surface, 393-394, 409
 penetration of, 364, 367, 373, 377-378, 381
 p-polarized, 363, 379, 382, 409, 436, 452, 461
 s-polarized, 371
- Electron gas, 358, 361, 550, 594
 damping effects, 594
- Electron loss, 305, 310, 320
- Electron scattering, 447-449, 510-511
- Electron tunneling, 323-325
 semiconductor, 323-325
- Electrostatic approximation, 285, 289, 295, 303
- Electrostatic theory, 399; *see also* Non-retarded theory
- Ellipsoid modes, 444, 507
- Ellipsometric method, 547
- Ellipsometric surface, 612
- Emissivity, 438
- Energy analyzers, 239
 differential types, 242
 retarding type, 240
- Energy profiles, 128
- Energy transport, 369, 412, 432
- Entropy, 485-487, 525

- Epstein profile, 562
 P-polarized reflectivity, 570
 S-polarized reflectivity, 566, 569
ESCA, 28; *see also* X-ray photodissociation spectroscopy
Evanescent wave, 382, 445
Excitons, 463-465
 optical properties, 463
Extinction cross section, 441, 526

Fermi velocity, 379
Field, 271, 282
 longitudinal, 271, 282
 transverse, 271, 282
Field emission, 225, 226
 energy distribution in the presence of adsorbates, 233
 experimental aspects of, 237
 microscope, 237
 resolution, 238
 theory of energy distribution, 225
 total energy distribution, 227
 transfer Hamiltonian, 231
Field and photoemission distributors, 246
 Ba on W, 246
 carbon monoxide on tungsten, 250
 H₂ on W, 248
 Mo (110), 247
Field ion emission, 326
Field ion microscopy, 28
Fiske steps, 298
Fowler-Norheim equation, 227
Frequency, 380
 complex, 380, 391, 407, 414
 longitudinal optical (LO), 359, 376, 390, 404, 450, 460
 plasma, 361, 378, 415, 460
 reststrahl, 360
 transverse optical (TO), 359, 376, 404, 410, 429, 450
Frequency difference spectrum, 507, 509
Frequency spectrum, 417, 484
 moments of, 474-475, 483-485
 projected, 506
Friedel oscillations, 550, 551
Frohlich mode, 505
FTR method, 590, 592
 limitations, 592
Fuchs-Kliwer (FK) mode, definition, 377
 hybridization with bulk modes, 492-495

GaP, 445
Ge, 481
Geometry, 286
 cylindrical, 286
 planar, 286
 spherical, 286, 301
 tunneling, 296
Grating, 336, 337, 440
Green's Function, 213, 465, 517-519
 Green's operator, 213
Gruneisen theory, 476

Half space modes, 527-528
 biaxial and uniaxial crystals, 527-528
 complex crystals, 428-429
 cubic crystals, 362-371
 damping included, 406-412
 excitons, 463-465
 lattice-dynamics theory, 517-518
 noncubic crystals, 430-435
 nonlocal theory, 452-457
 nonretarded theory, 401
 polar semiconductors, 414-417
 with magnetic field, 420-427
 reconstruction effects, 512-514
Hartree Fock Approximation, 213, 214
 theory, 223
Heisenberg representation, 61
Helmholtz free energy, 475
Homogeneous surface, 557
 Poynting vector, 557
Hydrodynamic approximation, 269, 274, 346

Ideal surface, 142
Image charge, 317, 318
Image interaction, 213
Impurities, 467
Inactive medium, definition, 360
Incoherent overlayer structure, 146
Inelastic electron solid collisions, 14, 54, 127, 188
 electron diffraction calculations, 136
 dynamical inelastic diffraction, 2, 136
 line broadening mechanisms, 2
 electron impact ionization, 14
 energy tuned resonances, 127
 inelastic diffraction, 133
 Al (100), 133
 Al (111), 135, 138, 188
 model inelastic low-energy electron diffraction calculations, 2, 124
 dynamical inelastic diffraction, 136
 two step inelastic diffraction, 124
 momentum-tuned resonances, 127
 plasmon emission cross sections, 15
 side band diffraction, 127, 129, 133
Inelastic low energy electron diffraction, 55; *see also* LEED
Inhomogeneous surface, 557
 energy flux through, 558

- InSb, 414, 416-427
 Intensity patterns, 36
 Intensity profiles, 36
 Interaction, 312, 321, 325
 electron-surface plasmon, 312, 315, 316, 321, 325
 Interference function, 48
 definition, 48
 multilayer diffraction, 50
 single layer diffraction, 49
 Intra-atomic Coulomb repulsion, 213
 effective U, 218
 Ion-induced excitations, 24
 Ionization spectroscopy, 25
 Ion neutralization, 23

 Josephson effect, 298, 301, 324, 340

 KBr, 438, 445
 Kr, 476, 479
 Kramers-Kronig relations, 560
 for surface conductivity, 560

 Landau damping, 274, 326
 Lattice dynamics, 361, 435, 465-509
 ionic crystals, 489-500, 528-529
 monatomic crystals, 467-475
 small particles, 483-487, 505-509
 LEED, 298, 322
 Lennard-Jones potential, 468, 479
 LiF, 368-370, 377, 392, 406, 438, 440, 442, 445, 447, 415-416
 Light line, 369, 413, 417, 428, 433
 Linear approximation, 272, 273
 Line width, 438
 Liquid Hb, 574
 inhomogeneous properties of, 574
 Liquid structure factor, 552
 Local approximation, 276, 278, 281
 Local density of states, 213
 Ga, 214
 Local theory, 357-359, 362, 435, 438
 condition for validity, 369
 Longitudinal modes, 390, 450
 Longitudinal optical (LO) frequency, 359, 377
 Loss profiles, 132, 134, 138, 188
 Loss spectra, 17, 38; *see also* Secondary electron
 Low energy electron diffraction (LEED), 1, 2, 5, 29, 37, 66, 83, 70, 118, 467, 475, 483, 510, 515-516, 524
 acoustical phonon assisted diffraction, 67
 Al (100), 93, 94, 97, 101, 105, 111, 120, 123
 Al (111), 99, 105, 111, 192
 beam parameters, 40
 conservation laws, 5
 elastic diffraction, 5, 6
 inelastic diffraction, 56
 Cu(100), 75, 76
 diffracted intensities, 70
 dynamical theory, 73, 77, 83
 distorted wave multiple scattering analysis, 1, 77
 laminar multiple scattering analysis, 1, 83
 wave-function matching analysis, 1, 81
 elastic diffraction from a rigid lattice, Born approximation, 1
 electron diffraction from a rigid lattice, Born approximation, 47
 four step approach to intensity analysis, 41
 inelastic low energy electron diffraction, 37, 55
 instrumental effects, 52
 instrumental parameters, 40
 insulator analyses, 107
 intensity analysis, 35
 layer KKR method, 85, 92
 LiF(100), 74, 109
 model elastic low energy electron diffraction calculations, 1, 86, 118, 121, 160
 standards for assessment, 118
 tabulation, adsorbed overlayers, 160
 tabulation, clean methods, 121
 Ni (100), 107, 108
 Ni (100)-C(2x2)-S, 161, 162, 164, 170, 171, 172
 Ni (100)-C(2x2)-Na, 164
 optical phonon assisted diffraction, 66
 qualitative features, 4
 quasi elastic diffraction from a vibrating lattice, Born approximation, 58
 Rh (100)-C(2x8)-O, 181
 Lucas modes, 459, 489-491, 496, 518, 529
 Lyddane-Sachs-Teller relation, 359

 Macroscopic theory, 357; *see also* Continuum theory
 Magnetic field, 420
 Magnetic modes, 390-391
 Magnetic solutions, 283, 286
 S-waves, 283, 286
 Magnetic susceptibility, 362, 364-365
 frequency-dependent, 371
 Maxwell's equations, 269, 271, 280, 363, 389, 399, 435, 450, 461
 Melting temperature, 479
 Metallic backplate, 378-380
 Metals, 378-379, 460

- MgF₂, 435, 447
 MgO, 438, 444, 505-506, 508-509
 Microscopic theory, 435, 465-519, 523-525, 528
 Miller indices, 142
 Models of electron solid interaction, 77, 81, 88, 89, 90
 adsorbed overlayer potentials, 112
 boundary conditions, 91
 bulk electron ion core potential, 106
 elastic collision model, 95
 electron-electron interaction, 44, 77
 electron-ion core phase shifts, 87
 electron-ion core potential, 86
 electron phonon interaction, 44
 electron plasmon coupling, 45
 Hartree-Fock approximation, 106
 inelastic collision damping, laminar models, 84
 multiple scattering models, 77
 inelastic collision damping length, 45
 inelastic collision model, 90, 92
 ion core potentials, 78
 lattice vibrations, 43, 101
 local complex potential model, 90
 number of phase shifts, 98, 103
 rigid lattice, 98
 vibrating lattice, 103
 optical potential, 45, 46, 89
 overlapping atomic charge density model, 88, 106
 qualitative features, 13
 specifically surface phenomena; clean surfaces, 110
 static potential model, 42, 81, 83
 Molecular dynamics, 467, 478-481, 483
 Monatomic crystals, 467-487, 509-514
 Monolayer, 298
 Multiphonon scattering, 64
 Multiple technique strategy, 33
 Multiple-wave theory, 451, 460-465

 NaCl, 438, 444-445, 505, 515, 517-519
 NaF, 445-446
 Neutron scattering, 505
 NiF, 438
 Noncubic crystals, 430-435, 527-528
 Nonlocal theory, 358, 447, 449-465, 526
 Nonorthogonality, 220
 Nonpolar semiconductors, 361, 481-483, 510-514
 Nonradiative modes, 381, 429, 440-441
 Nonradiative region, 381, 440
 Nonradiative surface plasmons, 580
 review of basic theory, 580
 Nonretarded theory, 366, 393, 399, 415, 418, 421, 518
 No-retardation limit, 366, 378
 NRSP, 585, 586
 coupling to the electromagnetic field, 585, 586
 diffraction grating, 587
 FTR method, 590
 grating method, 586, 587
 random roughness, 588
 surface roughness, 586
 dispersion, 596
 diffuse surface, 611
 Epstein profile, 611
 Lorentzian resonance, 596
 Second dispersion branch in truncated exponential profile, 603

 Optic axis, 434, 448, 527
 Optical modes, 487
 Optical properties, 436-447, 500-503, 529
 Oscillations, 550
 surface induced, 550
 Overcompleteness, 220
 nonorthogonality, 220
 Overlayer structures, labeling procedures, 146
 coincidence site, 146
 incoherent, 146
 matrix method, 146
 net quotient method, 146
 simple, 146
 notation, 112
 diffusion of impurities, 145
 inequivalent domains, 148
 nonuniform, 145
 out of phase domains, 148
 reflection registry degeneracy, 149
 registry degeneracy, 148
 rotational registry degeneracy, 149
 translational registry degeneracy, 148
 uniform, 145

 Pair correlation function, 62
 Particles, 359, 441-445, 483-487, 505-509, 525, 529
 Particle solid interactions, 1, 12
 atoms, molecules, ions, 13, 22
 electrons, 13
 photons, 13, 20
 qualitative survey, 12
 Penetration depth, 556
 Periodic boundary conditions, 472
 Phase velocity, 583
 of surface plasmons, 583
 Phonons, 490
 bulk, 381, 391; *see also* Bulk modes

- surface, 473; *see also* Surface modes
- Photoemission, 244, 326, 338, 343
 - ESCA, 245
 - experimental aspects, 245
 - surface, 245
 - x-ray, 343
- Photon, 294, 328
 - coupling with surface plasmons, 294, 304, 328, 331, 339
 - coupling with surface polaritons, 340
 - s-and p-polarized, 332
- Plane waves, nonlocal, 450
- Plasma, 266
 - bulk oscillations, 238
 - degenerate, 267, 274, 281
 - frequency, 266, 274, 361, 378, 414, 415
 - gaseous, 266
 - nondegenerate, 267, 274
 - radiation excited by light, 33
 - solid-state, 266
 - surface oscillations, 286
 - wavelength, 278
- Polaritons, 369, 404
- Polarization, 360, 487
- Polar semiconductors, 360, 414-428
 - in magnetic field, 420-428
- Poynting vector, 432
 - energy transport, 369, 412, 432
- Principal axes, 430
- P-polarization, 363, 370, 381-383, 409, 452, 491, 502
- Pseudo-rocking curve, 36, 38
- Pseudosurface modes, 467, 472, 497, 518; *see also* Surface modes
- Quantum regime, 276, 278, 282, 323, 326, 346
- Quartz, 435
- Quasi-elastic scattering cross sections, 56, 64, 65
- Quasi-harmonic approximation, 475-476
- Radiative modes, 283, 285, 292, 303, 306, 307, 319, 341, 381-387, 390, 395, 414, 436, 527
- Radiative region, 381, 408, 420, 439, 441
- Random phase approximations, 273, 275, 346
- Rayleigh waves, 357, 471, 496-497
- RbBr, 438
- RbCl, 438
- Real-angle modes, 383
- Reciprocal lattice, 5, 152, 154
- Reciprocal lattice vector, 448
- Reconstruction, 468, 480, 509-517, 524
 - in thin films, 514
- Reflectance, 290, 293, 330, 332, 436-440, 462, 501
 - minimum, 409, 439, 519, 521-523, 525
- Reflection high-energy electron diffraction, 29
- Reflectivity, 559
 - P-polarization, 559
 - semi-infinite, 559
 - S-polarization, 559
- Relaxation, 474, 483
- Repulsion of modes, 416
- Resonance, 311
- Retardation, 366, 425, 435, 488, 503
- Retardation effects, 282, 292, 295, 303, 381
- RHEED (reflection high energy electron diffraction), 29
- Rigid-ion model, 488, 491, 496, 528
- Rough surface, 439-441
- Rotation diagrams, 38
- Sagittal plane, 470, 491
- Scattering, 277
 - diffuse, 277
 - specular, 277
- Scattering cross section, 441
- Screened pseudopotential, 550, 551
- Screening, 266
 - length, 267, 274
- Secondary electrons, 17
- Secondary emission spectra, 16
- Selvedge, 145
- Semi-infinite medium, *see* half-space, 512-514
- Shear-horizontal (SH) modes, 470, 474
- Shear-vertical (SV) modes, 472-473
- Shell model, 496, 499, 515, 518
- Short-range forces, 435, 489, 510
- Si, 481-483, 509-510, 527
- Simple overlayer structure, 146
- Simple reflection spectroscopy, 554
- Single site t matrix, 79
- Slab, dielectric, 378-380
 - on grating, 440
 - on metal, 378-380, 439
- Slab modes, 428
 - complex crystals, 428
 - cubic crystals, 371-387
 - damping included, 413
 - experimental studies, 436-441
 - lattice-dynamics theory, 467-483, 488-505, 528
 - nonlocal theory, 455-459
 - polar semiconductors, 417
 - reconstruction effects, 509
 - unretarded, 403-404

- Slab, reconstruction in, 514
Small crystals, 341
Snell's law, 290
 SnO_2 , 444
Spatial dispersion, see nonlocal theory, 449-465
Spectral emission, 445
Specular scattering, 380, 452, 459
Sphere modes, 359-360
 complex crystals, 428
 cubic crystals, 387-396, 505
 damping included, 413
 nonlocal theory, 526
 optical studies, 441-445
 polar semiconductors, 418
 unretarded, 402
Spherical cavity, 304
S-polarization, 371, 381, 409, 491, 502
Spot pattern, 36
Static equilibrium, 468-469, 474-475
Strontium titanate, 428, 505
Substrate, 145
Surface, 268, 269
 charge, 283, 284, 286, 367, 372
 density, 558
 excess, 558
 energy, 343
 experiments, 268
 modes, 268, 269
 profile, 346
 roughness, 327
 semiconductors, 340, 345
Surface atomic composition, 1, 25
Surface atomic motion, 1, 30
Surface characterization, 4
Surface crystallography, 176
 analytical approaches, 1, 2, 154
 atomic geometry and symmetry, 2, 142, 143, 150
 of ideal surfaces, 142, 143
 terrace ledge Kirk model, 143
 of nonideal surfaces, 2, 150
 classification of imperfections, 2, 142
 disorder of the first kind, 183
 disorder of the second kind, 183
 disorder of the third kind, 183
 multi-step topographies, 2
 single step imperfections, 2, 143
 statistical mechanical model, 182
constant-momentum transfer averaging method, 176
data reduction methods, 155, 156, 173
energy averaging methods, 180
Fourier transform methods, 157
kinematic methods, see data reduction methods, 173
microscopic model methods, 155
multistep topography, 143
Patterson function methods, 157
relation between intensity pattern symmetry and atomic geometry, 2, 7, 151
structural analysis for disordered surfaces, 181
structure determinations for disordered surfaces, 181
 via dynamical models, 159
structure of adsorbed overlayers, 159
structure of clean surfaces, 159
uniform overlayer model, 155
Surface current density, 558
 excess, 558
Surface electronic structure, 1, 32
Surface energy, 546, 553
 of a liquid metal, 553
Surface geometry, 1, 28
Surface impedance, 365, 379, 453
Surface modes, 357
 extraordinary, 528
 generalized, 431
 mixed, 467, 472, 497, 518
 nonradiative, 440, 441, 429, 527-528
 nonretarded, 401, 455
 ordinary, 528
 peeling off, 473, 499
 radiative, 380-387, 408, 527
 regular, 431
 resonant, 518
 strongly-localized, 490
 transverse, 450
Surface optical (SO) phonons, see surface modes, 357
Surface plasma radiation excited by electrons, 334
Surface plasmon, 286, 309, 312, 358, 361, 416, 440, 454, 460, 462
Surface plasmons, 578
 an overview, 578
Surface plasmon dispersion relation, 582
 homogeneous metal dielectric boundary, 582
 simple metal-dielectric interface, 582
Surface polaritons, 369; *see also* Surface modes
Surface reactions, 3
Surface sensitivity of electron spectroscopies, 9
Surface tension, 552
 of liquid copper, 554
 of liquid metals, 553
 under equilibrium conditions, 554
Surface zone, 550

- Surf-riding condition, 448
Swihart's mode, 324
Symmetry, crystalline, 470-471
- Thermal diffuse scattering, 64, 69
Thermal effects, 438, 448
 ionic crystals, 504-505
 monatomic crystals, 475-483, 523-524
TiO₂, 435, 447
Total internal reflection, 445
Transfer Hamiltonian, 231
Transition radiation, 318, 320
Transition zone, 546
 inhomogeneous, 546
 in liquid insulators, 547
 in liquid metals, 549
Translational invariance, 356, 363, 396, 452
Transmittance, 436, 501
Transverse electric (TE) modes, 371, 390
Transverse magnetic (TM) modes, 370, 382, 383, 390, 528
Transverse optical (TO) frequency, 359, 377
- Ultra high vacuum, 3, 11
Uniaxial crystals, 434, 448, 527
Unit meshes, 142, 152
- Van der Waals forces, 343
Velocity autocorrelation function, 484
Vertex renormalization subplane multiple scattering, 80
 lattice vibration, 101
- Vibrational amplitude, mean-square, 475-482, 504-505
 anisotropy of, 476
Virtual modes, 383, 436-439, 442
- Wave equation, 389, 396, 425
 scalar, 389
 vector, 389, 396, 425
Wave, evanescent, 445
Wave packet, 407, 410
Waves, 450
 longitudinal, 450, 460
 transverse, 450
Wave vector, 407
 complex, 407, 410, 429, 525-526
 three-dimensional, 365, 394, 489
 two-dimensional, 365, 436, 445, 452, 465, 527
Wood's anomalies, 337
Work functions, determination of, 230
Wurtzite lattice, 448
- Xe, 476, 479, 524
X-ray fluorescence, 18
X-ray photoelectron spectroscopy, 28
X-ray scattering, 342
xz-polarized modes, 491-497
- y-polarized modes, 491-497
- Zero point energy, 344
Zero-point vibration, 479
ZnO, 448-449, 510
ZnS, 443